Edited by
Michael J. Zehetbauer, Yuntian T. Zhu

WILEY-VCH

Bulk Nanostructured Materials

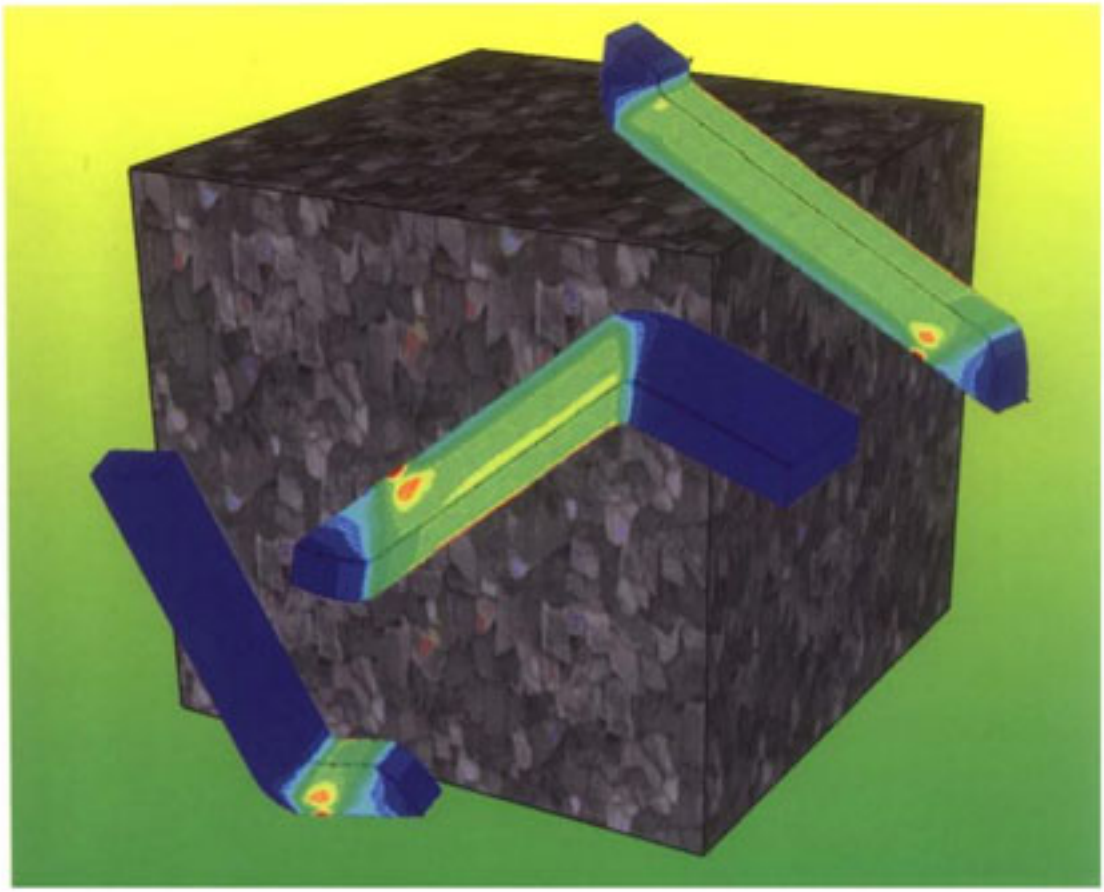

Bulk Nanostructured Materials

Edited by
Michael J. Zehetbauer
and Yuntian Theodore Zhu

Bulk Nanostructured Materials. Edited by M. J. Zehetbauer and Y. T. Zhu

ISBN: 978-3-527-31524-6

Related Titles

Champion, Y., Fecht, H.-J. (eds.)

Nano-Architectured and Nanostructured Materials

2004. Hardcover
ISBN: 978-3-527-31008-1

Zehetbauer, M. J., Valiev, R. Z. (eds.)

Nanomaterials by Severe Plastic Deformation

2004. Hardcover
ISBN: 978-3-527-30659-6

Köhler, M., Fritzsche, W.

Nanotechnology
An Introduction to Nanostructuring Techniques

2004. Hardcover
ISBN: 978-3-527-30750-0

Schmid, G. (ed.)

Nanoparticles
From Theory to Application

2004. Hardcover
ISBN: 978-3-527-30507-0

Trebin, H.-R. (ed.)

Quasicrystals
Structure and Physical Properties

2003. Hardcover
ISBN: 978-3-527-40399-8

Bulk Nanostructured Materials

Edited by
Michael J. Zehetbauer
and Yuntian Theodore Zhu

WILEY-VCH Verlag GmbH & Co. KGaA

The Editors

ao. Univ. Prof. Dr. Michael J. Zehetbauer
University of Vienna
Chair of Group 'Physics of Nanostructured Materials'
Faculty of Physics
Boltzmanngasse 5
1090 Wien
Austria

Yuntian T. Zhu, Ph. D.
Associate Professor
Department of Materials Science & Engineering
North Carolina State
University Rm 308, Research Building II
1009 Capability Dr.
Raleigh, NC 27695-7919
USA

Library of Congress Card No.: applied for

British Library Cataloguing-in-Publication Data
A catalogue record for this book is available from the British Library.

Bibliographic information published by the Deutsche Nationalbibliothek
Die Deutsche Nationalbibliothek lists this publication in the Deutsche Nationalbibliografie; detailed bibliographic data are available in the Internet at http://dnb.d-nb.de.

Composition K+V Fotosatz GmbH, Beerfelden

Printing betz-druck GmbH, Darmstadt

Bookbinding Litges & Dopf GmbH, Heppenheim

Printed in the Federal Republic of Germany

Printed on acid-free paper

ISBN 978-3-527-31524-6

Contents

Bulk Nanostructured Materials. Edited by M. J. Zehetbauer and Y. T. Zhu

ISBN: 978-3-527-31524-6

Preface

Nanostructured materials have been at the cutting edge of modern materials science. This exciting field started in 1981 when Herbert Gleiter published his first papers on the unique and outstanding properties of nanostructured materials. The second surge in the field occurred in 1993 when Ruslan Valiev attempted to process nanostructured materials by the top-down approach of severe plastic deformation (SPD). The advantage of SPD is that it can process nanomaterials with large dimensions and no porosity, which paves the way to nanomaterials in bulk shape or, as we call them here, 'bulk nanostructured materials – BNMs'. Since 1993, SPD techniques have experienced exponential development, which is why the majority of the chapters in this book are concerned with them. At the same time, bottom-up techniques such as ball milling and consolidation, and crystallization from the amorphous state are also significantly represented in this book as these methods are promising techniques and have their own advantages. Moreover, the processing techniques largely determine the properties and dimensional limits of BNMs. For this reason we have devoted several chapters of the book to various processing methods for producing BNMs.

This book aims to collect the whole spectrum of current knowledge on BNMs. In addition to metals and alloys, it also includes nonmetallic nanomaterials such as semiconductors and ceramics. Several large chapters are devoted to the mechanical properties because they have been well investigated and understood, probably due to their close relevance to commercial applications. Certainly, another reason for their thorough understanding is due to the progress made by molecular dynamics (MD) simulations, which have become increasingly important to the field of nanomaterials. Therefore, one chapter of this book has been devoted to MD simulations.

BNMs also exhibit unique and interesting magnetic properties. Two chapters of this book present the magnetic properties of BNMs, which focus on hard and soft magnetism, magnetostriction and magnetoelectric properties.

A good understanding of properties demands reliable acquisition of microstructural data. This book comprises several chapters that describe characterization methods being used to study nanostructural features of BNMs. Naturally,

Bulk Nanostructured Materials. Edited by M. J. Zehetbauer and Y. T. Zhu

ISBN: 978-3-527-31524-6

HRTEM is the first choice for characterizing the nanostructures down to atomic resolution. Recently, advanced diffraction techniques, especially in combination with high-intensity synchrotron and neutron diffraction for *in-situ* investigations, have also proven to be very powerful in global structural information such as texture, internal strains, dislocation density and type, twin density, etc., which means that HRTEM and diffraction techniques yield complementary information on the nanostructures of BNMs.

The two final sections of the book discuss unique applications of BNMs, which not only benefit from the refined grain structure but also – as in case of SPD-processed BNM – from the high densities of SPD-induced lattice defects. On the one hand, these nanostructures allow for significant enhancement of diffusion processes, e.g., in applications like hydrogen storage and nitriding of steels. On the other hand, high defect densities promote the occurrence of phases that usually do not form under normal temperature, pressure and alloy content. Nanostructurization also promises attractive potentials in improving the mechanical properties of micro-electronic-mechanical systems (MEMS) and of material surfaces, as well as in increasing the properties of materials for medical applications, including biocorrosion resistance. The last chapter of the book discusses the advantages and viability of BNMs in commercial applications, in terms of technological innovation, industrial areas and possible turnovers.

In our opinion, the research and development of BNMs will make significant progress in the next few years to make them ready for several commercial applications. This will be achieved by further improving several material properties including ductility and fatigue strength. Different processing methods that are described in this book might be combined to produce BNMs with the desired material properties.

Our thanks go to the colleagues who contributed to this book, and to the Wiley-VCH publishing team, who kindly advised and helped us in editing this book. We are also grateful to our families, who showed much understanding and patience during the work. We hope that the readers of this book will find it informative and useful in their research and development of BNMs.

October 2008

Michael J. Zehetbauer & Yuntian T. Zhu
Editors

List of Contributors

Igor V. Alexandrov
Ufa State Aviation Technical University
12 K. Marx Str.
450000 Ufa
Russia

Irene J. Beyerlein
Theoretical Division
Los Alamos National Laboratory
Los Alamos, NM 87545
USA

Wolfgang Blum
University of Erlangen-Nürnberg
Institut für Werkstoffwissenschaften
LS 1
Martensstr. 5
91058 Erlangen
Germany

Sergey Dobatkin
Russian Academy of Sciences
A. A. Baikov Institute of Metallurgy and Materials Science
Laboratory of Bulk Nanomaterials
Leninsky prospekt 49
119991 Moscow
Russia

Philip Eisenlohr
Institut für Werkstoffwissenschaften
LS 1
University of Erlangen-Nürnberg
Martensstr. 5
91058 Erlangen
Germany

Yuri Estrin
Monash University
ARC Centre of Excellence for Design in Light Metals
Department of Materials Engineering
Clayton, Vic. 3800
Australia
and
CSIRO Division of Manufacturing and Materials Technology
Clayton, Vic. 3168
Australia

Roland Grössinger
Vienna University of Technology
Institute of Solid State Physics
1040 Vienna
Austria

Jenö Gubicza
Eötvös University
Department of Materials Physics
Budapest
Hungary

Bulk Nanostructured Materials. Edited by M. J. Zehetbauer and Y. T. Zhu

ISBN: 978-3-527-31524-6

Bing Q. Han
University of California
Department of Chemical Engineering
and Materials Science
One Shields Avenue
Davis, CA 95616
USA

Timothy Hanlon
GE Global Research
1 Research Circle
Niskayuna, NY 12309
USA

Zenji Horita
Kyushu University
Department of Materials Science
and Engineering,
Faculty of Engineering
Fukuoka 819-0395
Japan

Heinz-Werner Höppel
University of Erlangen-Nürnberg
Institute I: Allgemeine
Werkstoffeigenschaften
Department of Materials Science
and Engineering
Martensstr. 5
91058 Erlangen
Germany

Xiaoxu Huang
Risø National Laboratory
Center for Fundamental Research:
Metal Structures in Four Dimensions
Materials Research Department
4000 Roskilde
Denmark

Dustin M. Hulbert
University of California
Chemical Engineering &
Materials Science Department
One Shields Avenue
Davis, CA 95616
USA

Dongtao T. Jiang
University of California
Chemical Engineering &
Materials Science Department
One Shields Avenue
Davis, CA 95616
USA

H. Peter Karnthaler
University of Vienna
Faculty of Physics
Physics of Nanostructured Materials
Boltzmanngasse 5
1090 Vienna
Austria

Carl C. Koch
Department of Materials Science
and Engineering
North Carolina State University
Campus Box 7907
Raleigh, NC 27695
USA

Hyoung Seop Kim
Chungnam National University
Department of Metallurgical
Engineering
305-764 Daejeon
Korea

Terence G. Langdon
University of Southampton
Materials Research Group
School of Engineering Sciences
Southampton SO17 1BJ
UK
and
University of Southern California
Departments of Aerospace &
Mechanical Engineering
and Materials Science
Los Angeles, CA 90089-1453
USA

Enrique J. Lavernia
University of California
Department of Chemical Engineering and Materials Science
One Shields Avenue
Davis, CA 95616
USA

Xiaozhou Liao
The University of Sydney
School of Aerospace, Mechanical & Mechatronic Engineering
NSW 2006
Australia

Terry C. Lowe
Los Alamos National Laboratory
Los Alamos, NM 87545
USA

Ke Lu
Chinese Academy of Sciences
Shenyang National Laboratory for Materials Science
Institute of Metal Research
Shenyang 110016
P.R. China

Evan Ma
Johns Hopkins University
Department of Materials Science and Engineering
Baltimore, MD 21218
USA

Rajiv S. Mishra
University of Missouri
Center for Friction Stir Processing and
Department of Materials Science and Engineering
Rolla, MO 65409
USA

Hael Mughrabi
University of Erlangen-Nürnberg
Institute I: Allgemeine Werkstoffeigenschaften
Department of Materials Science and Engineering
Martensstr. 5
91058 Erlangen
Germany

Amiya K. Mukherjee
University of California
Chemical Engineering & Materials Science Department
One Shields Avenue
Davis, CA 95616
USA

Benedikt Moser
EMPA
Feuerwerker Str.36
3602 Thun
Switzerland

Airat A. Nazarov
Ufa State Aviation Technical University
Institute of Physics of Advanced Materials
12 K. Marx Str.
450000 Ufa
Russia

A. Piers Newbery
University of California
Department of Chemical Engineering and Materials Science
Davis, CA 95616
USA

Reinhard Pippan
Erich Schmid Institute of Materials Science
Austrian Academy of Sciences
Jahnstr. 12
8700 Leoben
Austria

and
Christian Doppler Laboratory
for Local Analysis
of Deformation and Fracture
Jahnstr. 12
8700 Leoben
Austria

Christian Rentenberger
University of Vienna
Physics of Nanostructured Materials
Faculty of Physics
Boltzmanngasse 5
1090 Vienna
Austria

Xavier Sauvage
Université de Rouen
Groupe de Physique des Matériaux –
UMR CNRS 6634
Institut of Material Research
76801 Saint-Etienne-du-Rouvray
France

Julie M. Schoenung
Department of Chemical Engineering
and Materials Science
University of California
Davis, CA 95616
USA

Erhard Schafler
Institute of Materials Physics
University Vienna
Austria

Ruth Schwaiger
Forschungszentrum Karlsruhe
Eggenstein-Leopoldshafen
Germany

Alla V. Sergueeva
University of California
Chemical Engineering &
Materials Science Department
One Shields Avenue
Davis, CA 95616
USA

Leon Shaw
University of Connecticut
Department of Materials Science &
Engineering
Institute of Materials Science
3136 Storrs, CT 06269
USA

Vaclav Sklenička
Institute of Physics of Materials
Academy of Sciences
Žižkova 22
616 62 Brno
Czech Republic

Wolfgang Sprengel
Technische Universität Graz
Institute of Materials Physics
Petersgasse 16
8010 Graz
Austria

Dorotheé Vinga Szabó
Forschungszentrum Karlsruhe
P. O. Box 3640
76021 Karlsruhe
Germany

Katherine E. Thomson
University of California
Chemical Engineering &
Materials Science Department
One Shields Avenue
Davis, CA 95616
USA

László S. Tóth
Université de Metz
Laboratoire de Physique et Mécanique des Matériaux
Ile du Saulcy
57045 Metz
France

Nobuhiro Tsuji
Osaka University
Department of Adaptive Machine Systems
Graduate School of Engineering
2-1 Yamadaoka
Suita, Osaka 565-0871
Japan

Reiko Sato Turtelli
Vienna University of Technology
Institute of Solid State Physics
1040 Vienna
Austria

Tamás Ungár
Eötvös University
Department of Materials Physics
Budapest
Hungary

Ruslan Z. Valiev
Ufa State Aviation Technical University
Institute of Physics of Advanced Materials
12 K. Marx Str.
450000 Ufa
Russia

Alexej Vinogradov
Osaka City University
Department of Intelligent Materials Engineering
Faculty of Engineering
Osaka 558-8585
Japan

Dieter Vollath
NanoConsulting
Primelweg 3
76297 Stutensee
Germany

Thomas Waitz
University of Vienna
Physics of Nanostructured Materials
Faculty of Physics
Boltzmanngasse 5
1090 Vienna
Austria

Yinmin M. Wang
Chemistry and Materials Science Directorate
Lawrence Livermore National Laboratory
Livermore, CA 94550
USA

Gerhard Wilde
Westfälische Wilhelms-Universität Münster
Institute of Materials Physics
Wilhelm-Klemm-Str. 10
48149 Münster
Germany

Roland Würschum
Graz University of Technology
Institute of Materials Physics
Petersgasse 16
8010 Graz
Austria

Dieter Wolf
Center for Advanced Modeling and Simulation
Idaho National Laboratory
Idaho Falls, ID 83415
USA

Vesselin Yamakov
National Institute of Aerospace
100 Exploration Way
Hampton, VA 23666
USA

Jichun Ye
University of California
Department of Chemical Engineering
and Materials Science
Davis, CA 95616
USA

Michael J. Zehetbauer
University of Vienna
Research Group Physics
of Nanostructured Materials
Faculty of Physics
Boltzmanngasse 5
1090 Wien
Austria

Yuntian T. Zhu
Department of Materials Science
and Engineering
North Carolina State Unversity
Raleigh
USA

Part One
Introduction and Overview

Bulk Nanostructured Materials. Edited by M. J. Zehetbauer and Y. T. Zhu

ISBN: 978-3-527-31524-6

1
Nanostructured Materials: An Overview

Carl C. Koch

1.1
Introduction

Since the title of this book is "Bulk Nanostructured Materials" it seems appropriate to first discuss what we mean by "bulk" and "nanostructured" and to consider where the topics covered in this book fit into the general large and diverse field of nanoscience and nanotechnology. Nanostructured materials have been defined as materials that have at least one dimension in the "nanoscale" (typically 1 to 100 nm). Thus, depending on the dimensions in which the length scale is nanoscale, they can be classified into a) nanoparticles, b) layered or lamellar structures, c) filamentary structures, and d) bulk nanostructured materials [1]. The nanoparticles can be considered to be of "zero" dimensionality and examples include a large range of nanoscale powders of interest for diverse applications such as dispersions in cosmetics and pharmaceuticals. Quantum dots for optoelectronic applications may also fall into this category. A layered or lamellar structure is a one-dimensional nanostructure in which the magnitudes of length and width are much greater than the thickness that is nanoscale. Thin films for electronic device applications are examples of this category. Two-dimensional nanostructures have the length much larger than the width or diameter and nanowires or nanotubes may fit this division. The nanostructures that contain the "bulk" definition relevant to this book are three-dimensional and consist of crystallites, or in certain cases quasicrystals and/or amorphous material that are nanoscale in dimension. While it has been the convention to classify "nanocrystalline" bulk crystalline materials as those with a grain size <100 nm, this arbitrary classification may not always be the most appropriate. Perhaps a definition based on the specific size-dependent property that exhibits a critical dimension in the nanoscale regime would be more fitting. An example of this dimensionality of certain properties is the ferromagnetic coercive force, H_c. It has been found that the dependence of H_c on grain size (D) changes dramatically from a $1/D$ dependence for larger grains to a D^6 for grain sizes less than about 100 nm as shown in Fig. 1.1 [2]. This occurs when the grain size becomes smaller than the ferromagnetic domain (Bloch) wall thickness such that

Bulk Nanostructured Materials. Edited by M. J. Zehetbauer and Y. T. Zhu

ISBN: 978-3-527-31524-6

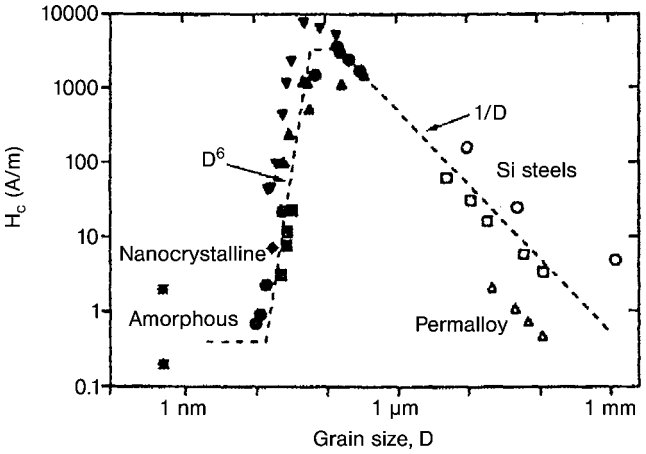

Fig. 1.1 Coercive force, H_c, as a function of grain size. (reproduced with permission from Ref. [2], page 415).

the domain wall now samples several, or many, grains and fluctuations in magnetic anisotropy on the grain size length scale that are then irrelevant to domain-wall pinning and therefore to H_c. Another example of size dependent properties is the critical current density in type-II superconductors. The size scale property of interest in this case is the superconducting coherence length that is approximately the distance over which there are strong correlations between superconducting electrons [3]. For high-field type-II superconductors this distance is of the order of 5–10 nm. This, in turn, determines the geometry of the fluxoid lattice that occurs in an applied magnetic field and must be pinned to obtain high values of critical current density (J_c). In fact, it is found that grain boundaries are very effective pinning sites that result in high values of J_c. The J_c of the commercial superconducting Nb_3Sn is controlled by grain size and is inversely proportional to grain size, with grain sizes of 50–80 nm providing high values [4]. The situation for mechanical strength is less clear since there is an essentially continuous increase in strength or hardness as the grain size is reduced to the nanoscale. This is reflected in the empirical Hall–Petch behavior that has been modeled by the interaction of dislocations with grain boundaries [5]. Pile-up of dislocations at grain boundaries is considered to be the mechanistic process responsible for the resistance to plastic flow from grain refinement. Several authors [6–8] have suggested divisions of the grain size scale into regions wherein dislocation-based plasticity is dominant (typically from about 10 nm grain sizes and larger) versus the regime below about 10 nm ("nano-1" [6]), where grain-boundary deformation processes are likely. The scheme according to Cheng et al. [6] is shown in Fig. 1.2. The dislocation regime is further divided [6] into the "traditional" regime (typically greater than 1 μm grain size) where both grain boundary and intragranular dislocation sources are operative, from the regime (from about 10 nm up to nearly 1 μm)

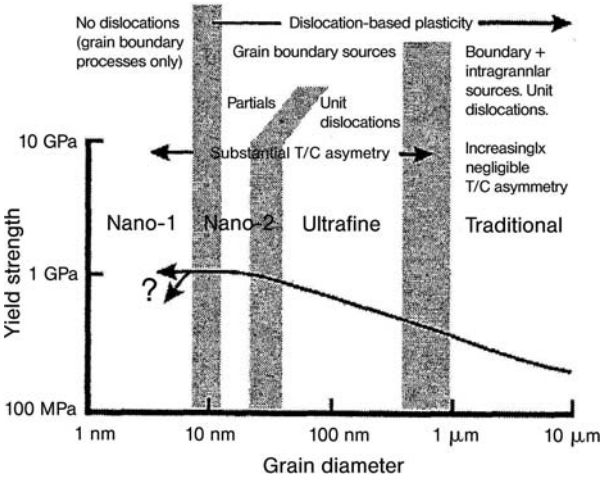

Fig. 1.2 Deformation mechanism map for fcc metals. Strength curve is based upon copper. (reproduced with permission from Ref. [6], Fig. 1).

where only grain-boundary dislocation sources exist, and even further subdivision into an "ultrafine" regime (from about 30 nm to 1 μm) where unit dislocations are dominant and a "nano-2" regime where partial dislocations are responsible for the deformation. These divisions were based upon both experimental results and computer simulations. However, recent *in-situ* straining experiments in the electron microscope [9–11] suggest dislocation activity, including pile-ups, may occur at grain sizes down to at least about 20 nm. While more experimental studies, along with modeling and simulations, are needed to better clarify this topic, it seems clear that an arbitrary cutoff of 100 nm below which we define "nanocrystalline" may not be realistic and indeed many interesting mechanical properties are found at grain sizes from 100 nm to 500 nm ("ultrafine grains"), a regime more accessible for many of the processing methods. However, hardness and strength typically reach maximum values at grain sizes below about 50 nm so this regime would appear to be of most interest from a scientific point of view. So we can leave the "nanostructured materials" definition somewhat cloudy, and move to the definition of "bulk". This presumably refers to samples that are not particulates, thin films, or nanoscale wires, but to materials containing many nanoscale grains being of potential usefulness for applications requiring their geometry. If thick enough, perhaps coatings should fall into this category.

In 1997 the author was part of a panel sponsored by the US National Science Foundation and other agencies through the World Technology (WTEC) Division of the International Technology Research Institute that assessed the R & D status and trends in nanoparticles, nanostructured materials, and nanodevices. The present author was responsible for the area of "consolidated materials", that

is, bulk nanostructured materials and wrote the chapter in the book that summarized the panel's findings [12]. This chapter, like the present book, emphasized mechanical behavior, with some discussion of ferromagnetic materials as well as hydrogen storage and corrosion behavior. Thus, the topics of this book are part of the large field of nanoscience and nanotechnology. However, bulk nanostructured materials are often "left out" of topical conferences and journals specific to nanoscience and technology. In many cases, "nano" refers to the size of a component – particle, thin film, or wire – and not to the microstructure of a bulk sample. It is the author's perception that most of the papers published in the topics of this book are found in the conventional materials science and engineering and physics journals rather than in specialized "nano" journals. For example, looking at a recent issue of the Virtual Journal of Nanoscale Science & Technology (a weekly multijournal compilation of the latest research on nanoscale systems) not a single paper of the 110 papers in the issue were in the area covered by this book. This is typical of many other new journals devoted to nanoscience and technology, and to many topical conferences in the field. Of course, the topics of this book are well covered in numerous symposia that are parts of materials science meetings such as TMS or MRS, or in topical meetings devoted to the subject. It is well known that the impetus for the interest in this now large subfield of materials science came from the research of H. Gleiter and coworkers in the early 1980s when materials with nanoscale grain sizes were prepared by the inert gas condensation method and their properties were found in many cases to be dramatically different from those of conventional grain-size materials [13]. The explosion of research in this field that has occurred since these initial discoveries has been influenced by the advances in three important technological areas [14]:

1. new and improved processing methods to provide nanocrystalline materials
2. new and improved characterization of materials at the nanoscale in terms of spatial resolution and chemical sensitivity
3. new and improved understanding of the relationships between nanostructure and properties.

The remainder of this overview chapter will be devoted to a description of the state-of-the-art of these three technological streams and their influence on bulk nanostructured materials.

1.2 Processing

Processing of bulk nanostructured materials can in principle be accomplished by either the "bottom-up" assembly of atoms or molecules into nanoscale clusters that require subsequent consolidation into bulk material, or the "top-down" methods that start with a bulk solid and obtain a nanostructure by structural decomposition. The bottom-up methods include the inert gas condensation and

compaction technique that stimulated the field. This technique consists of evaporating a metal inside a chamber containing a partial pressure (typically a few hundred Pascals) of an inert gas, e.g. He, such that the evaporated atoms collide with the gas atoms inside the chamber, lose their energy, and condense in the form of small discrete crystals of loose powder. The condensed fine powders collect on a liquid-nitrogen-cooled cold finger and are stripped off by an annular Teflon ring into a compaction device. The details of this process and improvements to the original design have been published [15]. While this method has provided the materials for the seminal early studies of the properties of nanocrystalline materials, it suffers from both the limited size of samples that can be prepared and from the common problem of two-step methods in that the compaction step may not provide completely dense or bonded material in spite of improvements to the process.

Chemistry is based upon the reactions and manipulations of atoms and molecules and the synthesis of nanocrystalline materials by chemical reactions predates the recent development of this field. Chemical synthesis of nanoscale materials has been reviewed by Chow and Kurihara [16]. In terms of bulk nanostructured materials these methods are two-step in that the particulates formed by the chemical reactions require consolidation. Of course, historically and in the present, the resultant nanoscale particulates can be used as such in applications ranging from catalysts to cosmetic powders. An example of a structural bulk material prepared by chemical reactions is WC-Co. Kear and coworkers [17] have developed a process in which fine and uniform precursor powders are obtained by spray-drying (solvent removal) of homogeneous aqueous solutions of soluble salts of W and Co. This precursor powder is reduced with hydrogen and reacted with CO in a fluidized-bed reactor to yield nanophase WC/Co powder. After consolidation by sintering, the grain size was on the order of 200 nm. These materials provided superior mechanical properties in terms of hardness and toughness compared to larger grain size conventional WC-Co.

Electrodeposition can be classified as a "bottom-up" method of preparation of nanocrystalline materials and also as "one-step" since no consolidation step is needed. Thick electrodeposits may be considered to be bulk materials. Since the late 1980s electrodeposition has been studied as a method to produce nanocrystalline materials and it has moved into the commercial production of such materials. Much of the work was pioneered by Erb and coworkers and this subject has been reviewed by Erb et al. [18]. Using special processing methods, a large number of metals, alloys, composites, and ceramics have been electrodeposited with nanocrystalline microstructures. Electrodeposition occurs by the nucleation of crystallites on the substrate surface and their subsequent growth along with nucleation of new crystallites. In order to obtain a nanocrystalline grain size, nucleation events should be favored over growth. The variables in electrodeposition include bath composition, bath pH, temperature, overpotential, bath additives, and direct current vs. pulse electrodeposition. It has been stated [18] that the two most important mechanisms that are rate-determining steps for formation of nanoscale grains in electrodeposition are charge transfer at the electrode

surface and surface diffusion of adions on the crystal surface. One method to inhibit growth of nucleated crystallites is by reducing the surface diffusion of adions by adsorption of foreign species (which may be referred to as "grain refiners" or "additives") on the growing surface. Most such additives are organic materials and may become trapped at the grain boundaries and are presumably responsible for the brittle mechanical behavior observed in nanocrystalline materials processed by electrodeposition with additives. Since high overpotential favors extensive nucleation, pulse plating, as a powerful method to achieve high overpotentials is a technique to synthesize a nanocrystalline structure without the use of additives. In the codeposition of alloys, the solute ion can act like an organic additive but without the deleterious embrittlement effects. Therefore, there are several processing strategies that can be used to provide artifact-free bulk nanocrystalline materials by electrodeposition. Some of the examples of bulk nanocrystalline materials that exhibit optimized combinations of strength and ductility, to be discussed in the section on properties, were made by electrodepostion.

The ball milling of powders – mechanical attrition – has been a popular method to produce materials with a nanocrystalline grain size [19]. The ball milling of powders can be divided into two categories: 1. the milling of elemental or compound powders – "mechanical milling", and 2. the milling of dissimilar powders – "mechanical alloying", in which material transfer occurs. This subject has been reviewed by a number of authors [20, 21]. Besides being discussed in the examples of general reviews of ball milling, this specific topic has also been reviewed [19]. Mechanical attrition has been found to refine the grain size to the nanoscale of all solid elements studied. The minimum grain size achieved is dependent upon a number of process and material variables [19]. The minimum grain size obtainable by milling has been attributed to a balance between the defect/dislocation structure introduced by the plastic deformation of milling and its recovery by thermal processes [22]. The minimum grain size is plotted against the melting temperature of the element in Fig. 1.3. At least for the lower melting metals, there appears to be an inverse dependence of minimum grain size on melting temperature that is consistent with the competition between defect creation and removal. It is clear that mechanical attrition can produce nanocrystalline materials with fine grain sizes such that for higher melting point metals, grain sizes below 10 nm can be achieved. However, in order to attain bulk material, the powders need to be consolidated. The ability to maintain the very small grain sizes in as-milled material and obtain artifact-free bulk samples with minimal grain growth remains a challenge.

For all the "two-step" processes for formation of nanostructured materials the first step provides a nanoscale particulate, or as in mechanical attrition, a powder particle with a nanoscale microstructure. These particulates must then be consolidated into bulk form. The consolidation problem remains an active area for more research and development and has not been adequately resolved to date. The problem is to form good atomic bonding between the particulates by a combination of pressure and temperature such that theoretical densities are

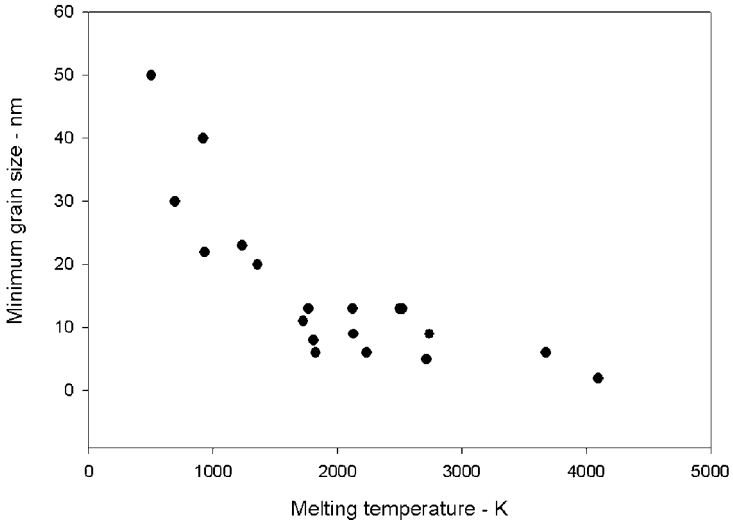

Fig. 1.3 Minimum nanocrystalline grain size for ball-milled elements versus their melting temperature (data given in Ref. [19]).

reached along with the complete interparticle bonding. This should be done without significant coarsening of the nanoscale microstructure or by introduction of any structural defects or unwanted phases. This topic has been reviewed, for example, by Groza [23] and Mayo [24]. Most consolidation methods have used pressure-assisted sintering approaches. Shear stresses are most effective in collapsing pores and also disrupt surface oxide layers. Since deformation processes that have significant shear stress components are desired we can list the processes in order of decreasing effectiveness as follows: extrusion – sinterforging – uniaxial hot pressing – hot isostatic pressing (HIP). Nonconventional consolidation methods for densification of nanocrystalline particulates include microwave sintering, field-assisted sintering methods, and shockwave consolidation.

The possibility of producing very fine grain structures by severe plastic deformation was suggested by research using conventional deformation methods taken to very high degrees of strain. It has been known for many decades, going back to the 1950s, that the structure of deformed metals can change with increasing plastic deformation such that random dislocation arrays can lower the energy of the system by "self-assembly" into "cells" or "subgrains" such that there is a high dislocation density in the cell walls and a lower dislocation density within the cells. The cells are typically the result of plastic deformation, the cell boundaries are somewhat diffuse. Subgrains, like cells, show small misorientations with their neighbors, but have sharper boundaries, and are formed by plastic deformation and thermal recovery processes. In most cases, the early studies of microstructures produced by severe plastic deformation gave cell or

subgrain sizes in the micrometer down to submicrometer size scale, but not into the nanoscale. One exception to these results is from the work of Rack and Cohen [25], who reported the cell structure developed in a series of Fe-Ti alloys deformed by wire drawing to large values of true strain up to about 7. The size of the cells decreased with increasing deformation, and reached values of about 50 nm at the highest strains. However, these were all cells with very low angle misorientations. In recent years special methods of mechanical deformation have been developed for producing submicrometer and even nanoscale grains with high-angle grain boundaries. These methods, the microstructure developed, and the properties of the materials with the refined grains so produced have been reviewed by Valiev et al. [26] and form much of the content of this book. The major methods of severe plastic deformation, in addition to mechanical attrition, are severe plastic torsion straining under high pressure (HPT) and equal-channel angular pressing (ECAP). In the case of HPT a disk-shaped sample is compressed to pressures of about 2 to 6 GPa and then one of the dies is moved with respect to the other. With enough rotation very large values of strain can be achieved, well into the 100s. This method has been used to achieve submicrometer grain sizes and in some cases even nanocrystalline grain sizes. The ECAP method that allows for the deformation of bulk samples by pure shear was first developed by Segal et al. [27]. In this method a billet is pressed through a die with two channels at angles of intersection typically 90 to 120°. The billet is subjected to severe deformations without changing its dimensions. Multiple passes through the die provide accumulative strain. The grain sizes developed by this method are typically in the submicrometer, 200 to 300 nm, range. A large body of experimental research and modeling studies has been reported for this technique. There are examples of submicrometer-size grain structures induced by the severe strain of ECAP in several metals that provide an excellent combination of both increased strength along with good ductility [28]. Other severe plastic deformation methods that will be described in more detail in the book include accumulative roll bonding [29] and friction stir welding [30]. It appears that the total strain provided by a given deformation process is in large part responsible for the final grain size that can be obtained. This must be a function of the dislocation density that can be obtained and its subsequent rearrangement by thermal processes. The processes that can provide the highest practical strain levels would be HPT and mechanical attrition of powders. The former has typically been limited to rather small disk samples although recent work is directed to scaling this to larger cylinders [31]. Mechanical attrition typically results in a powder product that then requires consolidation. Recent results on *in-situ* consolidation during ball milling of several ductile metals and alloys have been reported. The processing challenge is to produce nanocrystalline materials with the finest grain sizes to maximize strength, but without artifacts that might compromise ductility, and in sufficient size for mechanical testing and applications.

1.3 Characterization

An important aspect of the ability to study and develop nanocrystalline materials is the improvement of techniques to probe the spatial and chemical nature of nanoscale regions such as grains, precipitates, and grain-boundary chemistry. X-ray diffraction line-broadening analysis has been used to estimate the grain size and lattice strain of nanocrystalline materials. These techniques for the most part are not new and have been reviewed and discussed in a number of papers. There are several factors that can cause broadening of X-ray diffraction peaks and care must be taken in the separation of these effects. Instrumental broadening (quality of the alignment, receiving slit, *etc.*) must be corrected for. The problems with such corrections and the use of reference standards have been discussed [32]. A number of different analyses can be performed to deduce the crystalline size and the internal strain present in the sample. The most used of these methods are the Scherrer [33], the Williamson–Hall [34], and the Warren–Averbach [35] methods. While the simple Scherrer method only provides an average unit cell column length, the Williamson–Hall and Warren–Averbach techniques also give estimates of the lattice strain. If the grain-size distributions are narrow, then the X-ray technique can give good values for the average grain sizes [36]. Ungar and coworkers [37, 38] further modified the peak profile analysis methods of Williamson–Hall and Warren–Averbach to estimate grain-size distributions as well as dislocation density and dislocation arrangements. Generally, grain-size determination by the use of X-ray diffraction line-broadening analysis is only advised if the average grain size does not exceed 100 nm and the grain-size distribution is narrow. Correction for instrumental broadening becomes critical for grain sizes greater than about 30 nm. In cases where an inhomogeneous grain-size distribution exists, with some grains >100 nm, other methods, in particular, transmission electron microscopy, must be used.

Transmission electron microscopy, TEM, is one of the most direct methods for the determination of the grain size. High-resolution TEM can reveal grains at the smallest sizes as well as information on the nature of the grain boundaries. More sophisticated Z-contrast imaging can provide chemical information regarding grain-boundary segregation [39]. The advantages of TEM are obvious in terms of providing direct images of the grain size, shape, and size distribution. The analysis of the micrographs involves the application of straightforward stereological relationships, which provide various possibilities to characterize the grains. In order to get accurate statistical information on nanocrystalline grain size by TEM, dark-field TEM must be carried out on many fields of view in many samples.

Other methods that can be used in certain cases to measure nanocrystalline grain size are high-resolution scanning electron microscopy [40], atomic force and scanning tunneling microscopy [41] and Raman spectroscopy [42].

1.4 Properties

1.4.1 Mechanical Properties

One of the areas of research on nanocrystalline materials that has received extensive study is their mechanical behavior. The great interest in the mechanical behavior of nanocrystalline materials originates from the unique mechanical properties first observed and/or predicted by the pioneers of this field, Gleiter and coworkers [13]. Among these early observations or predictions were:

- Lower elastic moduli than for conventional grain size materials – by as much as 30–50%,
- Very high hardness and strength – hardness values for nanocrystalline pure metals (~10 nm grain size) that are 2 to 10 or more times higher than those of larger grained (>1 μm) metals,
- Increased ductility – perhaps even superplastic behavior – at low homologous temperatures in even normally brittle ceramics or intermetallics with nanoscale grain sizes, believed to be due to grain boundary, diffusional deformation mechanisms.

While some of these early observations and predictions have been verified by subsequent studies, in particular the high hardness and strength values, some have been found to be due to high porosity in the early bulk samples (for example the low elastic moduli observed) or to other processing artifacts, and not inherent properties of the nanocrystalline materials. The ductility issue remains a subject of present research, and while most nanocrystalline materials do not exhibit the high predicted ductilities, and in fact show little ductility in tension [43], there are recent examples of good ductility along with high strength in a limited number of cases [44–46].

Three major limitations to ductility for nanocrystalline materials can be identified. These are: 1. artifacts from processing; 2. force instability in tension; 3. crack nucleation or propagation instability. Porosity was a major artifact, especially for earlier studies of metals made by the inert gas condensation method. Even when theoretical density is attained, complete particle bonding may be lacking. Nanocrystalline materials made by ball milling of powders also can suffer from lack of complete bonding after power consolidation. The surfactant that is sometimes used to prevent excessive cold welding during milling can prevent complete bonding during consolidation and therefore limit ductility. Another popular method for producing nanocrystalline materials is electrodeposition. While this method is "one-step" in that it does not require consolidation of particulates and the problems associated with this, most of the nanocrystalline materials made by electrodeposition have also exhibited very poor ductility, presumably due to the additives often used to attain a nanocrystalline microstructure, as discussed in Section 1.2. However, as will be described below, several

examples of high strength and good ductility are observed with electrodeposited nanocrystalline materials produced without the use of organic additives.

Necking generally begins at maximum load during tensile testing. The amount of uniform elongation depends upon the strain hardening such that true uniform strain $\varepsilon_u = n$ in a cylindrical specimen (or $\varepsilon_u = 2n$ for a sheet) where n is the strain hardening coefficient. For an ideally plastic material (such as amorphous alloys) where $n = 0$, the necking instability would begin just as soon as yielding occurred. This criterion implies that the sample is mechanically stable until the rate of strain hardening falls to a level determined by the flow stress (and prior strain) at that time. Materials with a high capacity for strain hardening are therefore stable, while those with little capacity for strain hardening are potentially unstable.

Elongation to failure in tension is plotted vs. grain size in Fig. 1.4 for a variety of metals and alloys. It is clear that for most metals with grain sizes below about 30 nm the elongation to failure values are very low, typically less than 2–3%. Since this graph was originally published [43] several new datum points have been added that show significant ductility for grain sizes of ≤30 nm. These more recent breakthroughs in ductility will be described below.

As described above, strain hardening is needed in order to minimize mechanical instabilities that lead to local deformation (necking) and failure. The ability to strain harden therefore becomes an important criterion for ductility in nanostructured materials. An approach that has been used to provide strain hardening in nanostructured materials is to introduce a bimodal grain-size distribution by appropriate processing methods. The supposition was that the larger grains should deform by the usual dislocation mechanisms and provide strain harden-

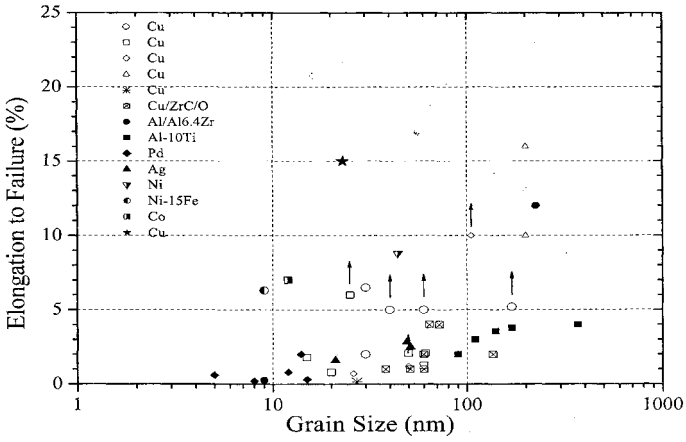

Fig. 1.4 Elongation to failure in tension versus grain size for a variety of metals and alloys. (reproduced with permission from Ref. [43], Fig. 1).

ing, while the smaller nanoscale grains would provide the strength and hardness.

Results of Ma and coworkers [46] have provided a dramatic example of combinations of high strength and high tensile ductility. Copper was rolled at liquid-nitrogen temperature to high strains of 93% to create a high dislocation density that does not dynamically recover. The as-rolled microstructure showed the high dislocation density along with some resolvable nanoscale grains with dimensions less than 200 nm. Annealing for short times at temperatures up to 200 °C provided for the development of grains with high-angle boundaries that were in the nanoscale or submicrometer size range. Some abnormal recrystallization was observed such that for annealing at 200 °C for 3 min, about 25% volume fraction of the samples consisted of grains 1–3 μm in diameter. Rolling the Cu at room temperature did not provide sufficient dislocation density to accomplish the subsequent nanoscale/submicrometer grain sizes on annealing. This work on Cu gave stress–strain curves for annealed coarse-grained Cu, Cu rolled to 95% at room temperature, Cu rolled to 93% at liquid-nitrogen temperature, and these samples annealed for 3 minutes at either 180 or 200 °C. The optimum properties were obtained for the mixed grain size material with the 1–3 μm grains embedded in the matrix of nanoscale and submicrometer-size grains. This material had a high yield stress of about 340 MPa, a total elongation to failure of 65% and uniform elongation of about 30%. The ductility was thus comparable to that of annealed conventional grain size Cu, but the yield strength was almost 7 times higher.

Lavernia and coworkers have prepared a commercial Al alloy, 5083 [47] and an Al-7.5% Mg alloy [48] by cryomilling followed by powder compaction by hot isostatic pressing and extrusion. The cryomilling of Al alloy 5083 [48] resulted in a nanoscale microstructure with average grain size about 30 nm. After hipping and extrusion the grain size remained mostly nanoscale at an average value of about 35 nm. However, some larger grains were also observed in the TEM analysis. The stability of the nanoscale grain size during the elevated temperature compaction steps was attributed to the large number of various precipitates including several intermetallic compounds such as Mg_2Si and Al_3Mg_2 as well as compounds formed from interstitial impurity atoms, namely AlN and Al_2O_3, which presumably retard grain growth by Zener pinning of the grain boundaries. A few larger micrometer-size grains were formed by secondary recrystallization. These large grains were believed to be responsible for the good ductility observed in these materials along with large increases in strength. Guided by these results, an Al-7.5% Mg alloy was cryomilled to nanostructured grain sizes [49]. The cryomilled powder was then combined with either 15 or 30% by volume of unmilled alloy powder, which was made by powder atomization and had micrometer-scale grain sizes. The powders were then consolidated by hipping and extrusion to bulk samples for tensile testing. The additions of larger grains to the nanocrystalline matrix increased the tensile ductility from about 1.4% to 5.4% elongation, with some decrease in strength values but still about four times the yield strength of conventional Al 5083.

While nanoscale grain boundaries have been the focus for increasing strength in studies of nanocrystalline materials, twin boundaries can also be an effective obstacle to dislocation motion and a potent strengthener. Lu and coworkers [49] have reported the synthesis of nanoscale growth twins in electrodeposited Cu. The Cu grain sizes were of the order of 400–500 nm and the twin lamellae thicknesses ranged from averages of about 100 nm down to < 20 nm. The yield strength of the Cu followed Hall–Petch behavior with increased strength as twin lamellae spacing decreased. Increased ductility also was observed with decreasing twin lamellae spacing. The Cu with the finest twin lamellae spacing shows both high strength and ductility. Higher strain hardening than conventional grain size Cu is also noted.

While some strategies for optimization of strength and ductility, such as bimodal grain-size distributions, compromise some strength for ductility, there are several recent results on nanostructured materials where strength levels are high and good ductility can still be achieved. These results are for nanocrystalline materials with small grain sizes (< 30 nm) and with relatively narrow grain-size distributions such that no grains > 50 nm are present.

Electrodeposited Co metal has been prepared with a small average grain size of about 12 nm and with a fairly narrow grain-size distribution of ±7 nm [44]. This material had the hcp structure with no trace of the fcc phase, that is, it had the equilibrium structure for room temperature. The hardness, yield strength, and ultimate tensile strength for this nanostructured Co were 2–3 times higher than for conventional grain size Co. The nanocrystalline Co exhibited elongation to fracture values of 6 to 9%, which are comparable to those for the conventional grain size Co. Of great interest is the dependence of the mechanical behavior of the nanostructured Co on the strain rate of the tensile tests. Applying lower strain rates resulted in higher flow stress and tensile strength at relatively constant yield strength. This behavior is in contrast to the usual response of a material in which dislocation slip is the dominant mechanism. In such materials higher strain rates result in higher tensile strength. The authors suggest this response of nanocrystalline Co to changes in strain rate are typical of materials that deform predominantly by deformation twinning. That is, higher strain rates result in lower flow stress and tensile strength. They therefore suggest that the dominant deformation mechanism in their nanocrystalline Co is twinning. More studies, in particular high-resolution TEM or *in-situ* TEM under stress, are needed to confirm these ideas about twinning deformation.

Li and Ebrahimi [45] have prepared nanocrystalline Ni and Ni-Fe alloys by electrodeposition without the use of any additives that might induce embrittlement. Their samples exhibited excellent strength values along with good ductility. The Ni sample had a grain size of 44 nm and the Ni–15% Fe sample had a 9 nm grain size. The fracture behavior of the alloys was very different even though both exhibited good values of elongation. The Ni sample had an elongation of about 9% and also showed significant reduction of area and ductile fracture behavior consistent with that for other ductile fcc metals and deformation

by dislocation motion. While the Ni–15% Fe sample also showed reasonable 6% elongation, the reduction in area was negligible and fracture appeared to be brittle. TEM revealed grain-boundary cracking. The authors suggest that the Ni–15% Fe alloy with the average grain size of 9 nm was below the "crossover" grain size from dislocation dominated deformation processes to grain-boundary deformation processes such as grain boundary sliding. In spite of this apparent brittle fracture behavior good ductility along with high strength were observed, suggesting processing artifacts did not affect the mechanical properties.

The *in-situ* consolidation of ball milled powders in several metals has allowed for the production of artifact-free samples for tensile testing. Bulk nanocrystalline Cu spheres were synthesized using a combination of liquid-nitrogen temperature and room-temperature milling [9]. Spheres with diameters up to about 8 mm were obtained that could be pressed into disks from which samples for mechanical testing could be machined. TEM results shown in Fig. 1.5 A indicate

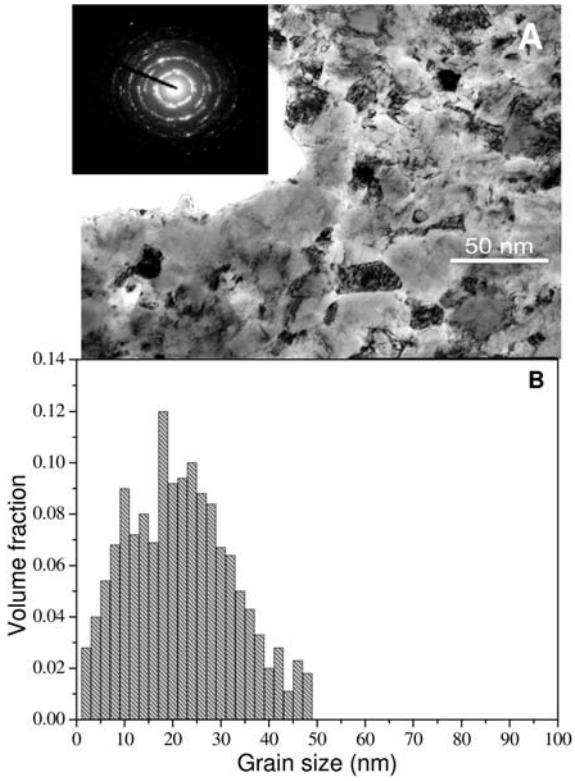

Fig. 1.5 TEM observations of the typical microstructure in the *in-situ* consolidated nanocrystalline Cu. The bright-field TEM micrograph (A) and the SADP [the upper left inset in A] show roughly equiaxed grains with random orientations. The statistical distribution of grain size (B) was obtained from multiple dark-field TEM images of the same sample (reproduced with permission from Ref. [9], Fig. 1).

that the consolidated Cu consists of equiaxed nanograins oriented randomly, as can be seen from the corresponding selected area diffraction pattern, the upper left inset in Fig. 1.5 A. Statistical analysis of multiple dark-field images reveals a monotonic lognormal grain-size distribution with an average grain size of 23 nm (Fig. 1.5 B). Density measurements, scanning electron microscopy of the sample surfaces, and TEM analysis show that no porosity is introduced during the *in-situ* consolidation of nanocrystalline Cu. The chemical analysis of the consolidated nanocrystalline Cu indicated that the oxygen content increased from 0.10 at.% in the starting powder to 0.29 at.% in the final product. The measured Fe contamination was less than 0.1 at.%. Therefore, it may be concluded that the nanocrystalline Cu made by the above procedure is free of artifacts in that there is no porosity, no debonding, and minimal impurity contamination.

Tensile test data for the *in-situ* consolidated nanocrystalline Cu is compared with the stress–strain curve for conventional grain size Cu in Fig. 1.6 [9]. In the case of the nanocrystalline Cu, the 0.2% offset yield strength (σ_y) and the ultimate tensile strength (σ_u) reach values of 971±12 MPa and 1120±29 MPa, respectively. This σ_y value is at least one order of magnitude higher than that of coarse-grained pure Cu samples, and σ_u of the nanocrystalline Cu is about five times higher than that of the coarse-grained Cu sample. The hardness value of this nanocrystalline Cu is 2.3 GPa, which is consistent with the Hall–Petch behavior of Cu. Therefore, it is concluded that the high values of hardness and yield strength are due to the small grain size (23 nm). These strength values are

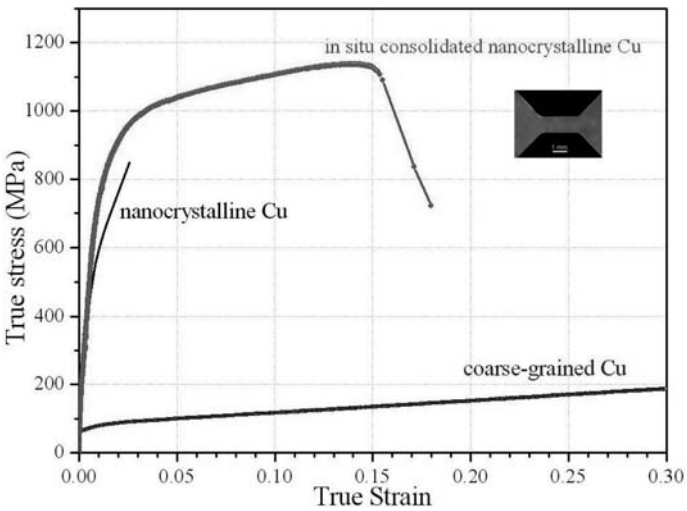

Fig. 1.6 True stress versus true strain for bulk *in-situ* consolidated Cu in comparison with that for coarse-grained Cu and nanocrystalline Cu made by the inert gas condensation and compaction technique. (reproduced with permission from Ref. [9], Fig. 2).

comparable to the highest values observed for nanocrystalline Cu but more significant is the good tensile ductility observed with 14% uniform elongation and 15% elongation to failure. This ductility is much greater than previously reported for nanocrystalline materials of this grain size and even somewhat greater than the ductility of the nanotwinned Cu [49]. Another important feature of the stress–strain curve (Fig. 1.6) is the large strain hardening observed in the plastic region that suggests a high lattice dislocation accumulation during the plastic deformation up to failure. Strain hardening is often limited in nanocrystalline materials at grain sizes where dislocation activity is believed to be difficult. *In-situ* dynamic straining transmission electron microscope observations of the nanocrystalline Cu were also carried out, which showed individual dislocation motion and dislocation pile-ups. This suggests a dislocation-controlled deformation mechanism that allows for the high strain hardening observed. Trapped dislocations were also seen in individual nanograins.

An artifact-free bulk nanocrystalline Al-5% Mg alloy was also prepared using *in-situ* consolidation during ball milling at liquid nitrogen and room temperatures [50]. The average grain size, determined by TEM, was 26 nm with a relatively narrow grain-size distribution. The nanocrystalline structure produced was a supersaturated solid solution of Mg in Al. The tensile behavior of the nanocrystalline alloy showed an extremely high strength. The tensile yield strength reached 620 MPa (four times that of the coarse-grained Al-5083 alloy), and the ultimate tensile strength was 740 MPa. A significant tensile ductility was obtained with an elongation to failure value of 8.5%. Strain hardening was also observed, which is suggested to originate from dislocation accumulation during plastic deformation.

1.4.2
Magnetic and Other Properties

Nanocrystalline materials have been studied for possible use in applications of soft magnetic materials, hard magnetic materials, and magnetic storage media [51]. The first two topics may be classed with bulk nanostructured materials. Soft ferromagnetic materials for potential use in transformer cores, inductive devices, *etc*. have been mainly developed by the partial crystallization of amorphous precursors to precipitate the nanocrystalline phase which may be α FeSi (FINEMET), α Fe (NANOPERM), α FeCo, (bcc), α' FeCo (B2) (HITPERM) [52]. The small single-domain nanocrystalline ferromagnetic precipitates in the amorphous matrix give these alloys their unique magnetic behavior. The averaging of the magnetocrystalline anisotropy over many grains coupled within an exchange length gives the very low coercive force and low energy losses (narrow B/H hysteresis loop).

Hard ferromagnetic nanocomposites have been found to exhibit a variety of interesting properties [53]. For example, exchange coupling in magnetically hard and soft phases can increase magnetic induction by the phenomenon of "remanence enhancement". In the $Fe_{90}Nd_7B_3$ composition, a nanoscale mixture of the

hard $Fe_{14}Nd_2B$ phase and the soft α Fe phase exhibit high coercivity along with high values of remanent magnetization. This is associated with exchange coupling between the hard and soft phases which forces the magnetization vector of the soft phase to be rotated to that of the hard phase. The requirements for this behavior are a nanocrystalline grain size and a degree of coherence across the interphase boundaries sufficient to enable adjacent phases to be exchange coupled.

Other properties of bulk nanocrystalline materials that are important and will be addressed in the book are hydrogen-storage materials and surface properties such as corrosion resistance.

The following chapters written by authors with expertise in their fields will expand on the brief overview given here as well as related areas not covered in this short introduction. The result should definitely show that bulk nanostructured materials are an important part of the "nanocrystalline revolution".

References

1 R. W. Siegel **1994**, *Nanostruc. Mater.* 4, 121.
2 G. Herzer **1997**, in *Handbook of Magnetic Materials,* (ed.) K. H. J. Buschow, Elsevier Science, Amsterdam, Vol. 10, Chap. 3, p. 415.
3 D. Saint-James, G. Sarma, E. J. Thomas **1969,** *Type II Superconductivity,* Pergamon Press, Oxford, p. 10.
4 R. M. Scanlan, W. A. Fietz, E. F. Koch **1975**, *J. Appl. Phys.* 46, 2244.
5 A. H. Cottrell **1958**, *Trans. TMS-AIME,* 212, 192.
6 S. Cheng, J. A. Spencer, W. W. Milligan **2003**, *Acta Mater.* 51, 4505.
7 K. S. Kumar, H. Van Swygenhoven, S. Suresh **2003**, *Acta Mater.* 51, 5743.
8 H. Conrad **2003**, *Mater. Sci. Eng. A,* 341, 216.
9 K. M. Youssef, R. O. Scattergood, K. L. Murty, J. A. Horton, C. C. Koch **2005**, *Appl. Phys. Lett.* 87, 091904-1.
10 K. S. Kumar, S. Suresh, M. F. Chisholm, J. A. Horton, P. Wang **2003**, *Acta Mater.* 51, 387.
11 R. Mitra, W-A. Chiou, J. R Weertman **2004**, *J. Mater. Res.* 19, 1029.
12 C. C. Koch **1999**, in *Nanostructure Science Technology,* (eds.) R. W. Siegel, E. Hu, M. C. Roco, Kluwer Academic Publishers, Dordrecht, The Netherlands, Chap. 6, p. 93.
13 H. Gleiter **1989**, *Prog. Mater. Sci.* 33, 223.
14 R. W. Siegel **1999**, in *Nanostructure Science Technology,* (eds.) R. W. Siegel, E. Hu, M. C. Roco, Kluwer Academic Publishers, Dordrecht, The Netherlands, Chap. 1, p. 10.
15 R. W. Siegel **1991**, in *Processing of Metals Alloys,* (eds.) R. W. Cahn, P. Haasen, E. J. Kramer, Vol 15 of Materials Science Technology-A Comprehensive Treatment, VCH, Weinheim, Germany, p. 583.
16 G-M. Chow, L. K. Kurihara **2002**, in *Nanostructured Materials: Processing, Properties and Applications,* (ed.) C. C. Koch, William Andrew Publishers, Norwich, NY, p. 3.
17 L. E. McCandlish, B. H. Kear, B. K. Kim **1992**, *Nanostruct. Mater.* 1, 119.
18 U. Erb, K. T. Aust, G. Palumbo **2002**, in *Nanostruct. Mater.: Process., Prop.s, Applic.,* ed. C. C. Koch, William Andrew Publishers, Norwich, NY, p. 179.
19 C. C. Koch **1993**, *Nanostruct. Mater.* 2, 109.
20 C. C. Koch **1991**, in *Processing of Metals Alloys,* (eds.) R. W. Cahn, P. Haasen, E. J. Kramer, Vol. 15 of Materials Science Technology: A Comprehensive Treatment, VCH, Weinheim, Germany, p. 193.

21 C. Suryanarayana **2004**, *Mechanical Alloying Milling*, Marcel Dekker, New York.
22 J. Eckert, J. C. Holzer, C. E. Krill, W. L. Johnson **1992**, *J. Mater. Res.*, 7, 1751.
23 J. R. Groza **2002**, in *Nanostructured Materials: Processing, Properties, Application,*. (ed.) C. C. Koch, William Andrew Publishers, Norwich, NY, p. 115.
24 M. J. Mayo **1996**, *Int. Mater. Rev.* 41, 85.
25 H. J. Rack, M. Cohen **1970**, *Mater. Sci. Eng.* 6, 320.
26 R. Z. Valiev, R. K. Islamgaliev, I. V. Alexandrov **2000**, *Prog. Mater. Sci.* 45, 103.
27 V. M. Segal, V. I. Reznikov, A. E. Drobyshevkij, V. I. Kopylov **1981**, *Metally* 1, 115.
28 R. Z. Valiev, I. V. Alexandov, Y. T. Zhu, T. C. Lowe **2002**, *J. Mater. Res.* 17, 5.
29 Y. Saito, H. Utsunomiya, N. Tsuji, T. Sakai **1999**, *Acta Mater.* 47, 579.
30 S. Benavides, Y. Li, L. E. Murr **2000**, in *Ultrafine Grained Materials,* (eds.) R. S. Mitra, S. L. Semiatin, C. Suryanarayana, N. N. Thadhani, T. C. Lowe, TMS, Warrendale, PA, p. 155.
31 G. Sakai, K. Nakamura, Z. Horita, T. G. Langdon **2005**, *Mater. Sci. Eng. A* 406, 268.
32 C. E. Krill, R. Birringer **1998**, *Philos. Mag. A* 77, 621.
33 A. Guinier **1963**, *X-ray Diffraction*, W. H. Freeman Co., San Francisco, CA, p. 121.
34 G. K. Williamson, W. H. Hall **1953**, *Acta Metall.* 1, 22.
35 B. E. Warren B. L. Averbach **1950**, *J. Appl. Phys.* 21, 595.
36 G. W. Nieman, J. R. Weertman **1991**, in *Morris E. Fine Symposium,* (eds.) P. K. Liaw, J. R. Weertman, H. L. Marcus, J. S. Santer, TMS, Warrendale, PA, p. 243.
37 T. Ungar, A. Borbely **1996**, *Appl. Phys. Lett.* 69, 3173.
38 T. Ungar, S. Ott, P. G. Sanders, A. Borbely, J. R. Weertman **1998**, *Acta Mater.* 46, 3693.
39 G. Duscher, M. F. Chisholm, U. Alber, M. Ruhle **2004**, *Nature Mater.* 3, 621.
40 H. Chang, C. J. Altstetter, R. S. Averback **1992**, *J. Mater.* 7, 2962.
41 K. Sattler, G. Raina, M. Ge, N. Venkatiswaran, J. Xhie, Y. X. Liao, R. W. Siegel **1994**, *J. Appl. Phys.* 76, 546.
42 T. D. Shen, C. C. Koch, T. L. McCormick, R. J. Nemanich, J. Y. Wang, J. G. Huang **1995**, *J. Mater. Res.* 10, 139.
43 C. C. Koch, D. G. Morris, K. Lu, A. Inoue **1999**, *MRS Bull.* 24, 54.
44 A. A. Karimpoor, U. Erb, K. T. Aust, G. Palumbo **2003**, *Scr. Mater.* 49, 651.
45 H. Li, F. Ebrahimi **2004**, *Appl. Phys. Lett.* 84, 4307.
46 Y. Wang, M. Chen, F. Zhou, E. Ma **2002**, *Nature* 419, 912.
47 V. L. Tellkamp, A. Melmed, E. J. Lavernia **2001**, *Metall. Mater. Trans. A* 32, 2335.
48 D. Witkin, Z. Lee, R Rodreguez, S. Nutt, E. J. Lavernia **2003**, *Scr. Mater.* 49, 297.
49 Y. F. Shen, L. Lu, Q. H. Lu, Z. H. Jin, K. Lu **2005**, *Scr. Mater.* 52, 989.
50 K. M. Youssef, R. O. Scattergood, K. L. Murty, C. C. Koch **2005**, *Scr. Mater.* 54, 251.
51 M. E. McHenry, D. E. Laughlin **2000**, *Acta Mater.* 48, 223.
52 M. E. McHenry, M. A. Willard, D. E. Laughlin **1999**, *Prog. Mater. Sci.* 44, 291.
53 D. J. Sellmyer, R. Skomski **2002**, *Scr. Mater.* 47, 531.

2
Bulk Nanostructured Materials by SPD Processing: Techniques, Microstructures and Properties

Ruslan Z. Valiev and Airat A. Nazarov

2.1
Introduction

During the last decade, fabrication of bulk nanostructured metals and alloys using severe plastic deformation (SPD) has been evolving as a rapidly progressing direction of modern materials science that is aimed at developing materials with new mechanical and functional properties for advanced applications [1]. The principle of these developments is based on grain refinement down to the nanoscale level in bulk billets using severe plastic deformation.

SPD processing refers to various experimental procedures of metal forming that may be used to impose very high strains on materials leading to exceptional grain refinement. Recently, the main principles and definitions in SPD processing have been discussed in detail [2, 3]. Following these principles, the unique feature of SPD processing is that high strain is imposed at relatively low temperatures (usually less than 0.4 T_m) without any significant change in the overall dimensions of the workpiece. Another feature is that the shape is retained due to the use of special tool geometries which prevent free flow of material and thereby produce a significant hydrostatic pressure. The presence of this hydrostatic pressure is essential for achieving high strains and introducing high densities of lattice defects that are necessary for exceptional grain refinement.

SPD-produced nanomaterials are fully dense and their large geometric dimensions make them attractive for efficient practical applications.

Fabrication of bulk nanostructured materials using severe plastic deformation is becoming one of the most actively developing areas in the field of nanomaterials [4–6], and SPD materials are viewed as structural and functional materials of the next generation of metals and alloys.

Today, SPD techniques are emerging from the domain of laboratory-scale research into commercial production of various ultrafine-grained (UFG) materials. This change is manifested in several ways. First, it is characterized by the fact that not only pure metals are investigated, but also commercial alloys for special applications; second, by the requirements of economically feasible production of

Bulk Nanostructured Materials. Edited by M. J. Zehetbauer and Y. T. Zhu

ISBN: 978-3-527-31524-6

ultrafine-grained metals and alloys associated with developing SPD techniques. In the following we will consider these new trends in SPD processing and highlight some key results on the developments of the nanoSPD materials science and applications. We also report here new results on finding novel SPD processing routes used to produce bulk ultrafine-grained materials with a small grain size refined down to a typical nanorange of 40–50 nm and less.

2.2 Developing SPD Techniques for Grain Refinement

2.2.1 The Principles of SPD Techniques

High-pressure torsion (HPT) and equal-channel angular pressing (ECAP) are the SPD techniques that were used in the first works to produce nanostructured metals and alloys possessing submicrometer- or even nano-sized grains [7, 8]. Since the time of the earliest experiments, processing regimes and routes have been established for many metallic materials, including some low-ductility and hard-to-deform materials. High-pressure torsion and ECAP die sets have also been essentially modernized [2, 9]. Several other techniques of SPD processing are now available as well. The major methods of the fabrication of UFG materials that are already established alongside with HPT and ECAP include multidirectional forging (MDF), accumulative roll bonding (ARB), cyclic extrusion and compression (CEC), repetitive corrugation and straightening (RCS) and twist extrusion (TE). These various processes have been considered recently [2] and here their principles are outlined for comparison.

High-pressure torsion refers to processing in which the sample, generally in the form of a thin disk, is subjected to torsional straining under a high hydrostatic pressure: the principle of HPT is illustrated schematically in Fig. 2.1 (a) [2, 10, 11]. The disk is located within a cavity, a hydrostatic pressure is applied, and plastic torsional straining is achieved by rotation of one of the anvils. In order to achieve pressures higher than 2 GPa, it is generally preferable to use a modified geometry with the cavities placed in each of the two anvils, as shown in Fig. 2.1 (b) [11]. If there is no outward flow of material, the disk thickness remains constant and the true torsional strain, γ, is given by $\gamma = (r/h)\varphi$, where r is the distance from the center of the disk, φ is the torsional angle in radians, and h is the sample thickness. An alternative relationship is also available if there is some outward flow of material between the two anvils and a corresponding reduction in the value of h [10]. For comparison with other SPD methods, the true equivalent strain, ε, can be calculated using the relation $\varepsilon = (1/a)\gamma$, where the parameter a takes either the values from a plastic flow criterion (where $a = 2$ for Tresca and $a = \sqrt{3}$ for von Mises) or from the Taylor theory for polycrystals (where $a = 1.65$ for texture-free face-centered cubic [fcc] metals and decreases slightly to lower values during continued deformation). The relatively

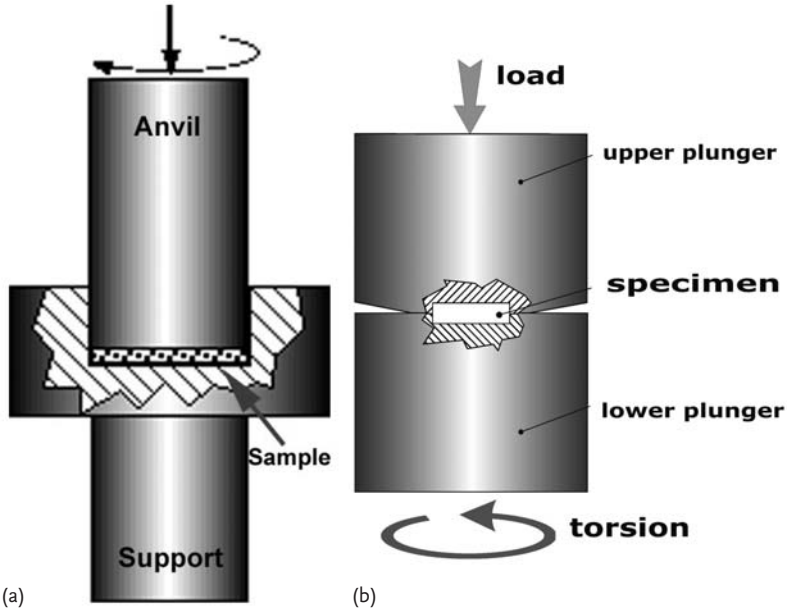

Fig. 2.1 The principle of HPT: (a) tool with a sample located within a cavity in the support anvil and (b) tool with cavities in both anvils.

small disks used in conventional HPT are attractive for products such as small bulk nanomagnets with enhanced soft and hard magnetic properties, arterial stents, and devices for microelectromechanical system applications. There have also been recent attempts to extend HPT to include the processing of larger bulk samples [12].

Equal-channel angular pressing (ECAP) [13] is at present the most developed SPD processing technique. The progress in ECAP processing has been discussed quite recently and has been reported elsewhere [9]. As illustrated in Fig. 2.2, during ECAP a rod-shaped billet is pressed through a die constrained within a channel that is bent at an abrupt angle. A shear strain is introduced when the billet passes through the point of intersection of the two parts of the channel. Since the cross-sectional dimensions of the billet remain unchanged, the pressings may be repeated to attain exceptionally high strains. The equivalent strain, ε introduced in ECAP is determined by a relationship incorporating the angle between the two parts of the channel, Φ, and the angle representing the outer arc of curvature where the two parts of the channel intersect, Ψ. The relationship is given by [14]:

$$\varepsilon = (N/\sqrt{3})[2\cot\{(\Phi/2) + (\Psi/2)\} + \Psi\mathrm{cosec}\{(\Phi/2) + (\Psi/2)\}] \tag{2.1}$$

where N is the number of passes through the die.

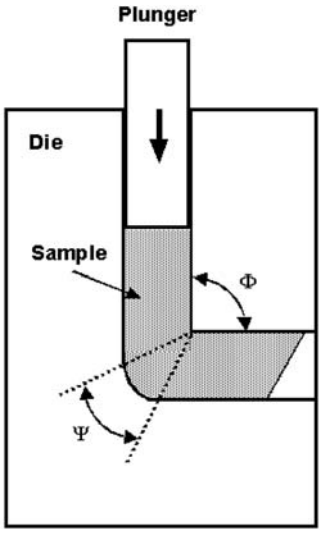

Fig. 2.2 The principle of ECAP.

During repetitive pressings, the shear strain is accumulated in the billet, leading ultimately to a UFG structure. In practice, different slip systems may be introduced by rotating the billet about its longitudinal axis between each pass [15] and this leads to four basic processing routes: there is no rotation of the billet in route A, rotations by 90° in alternate directions or the same direction in routes B_A and B_C, respectively, and rotations by 180° in route C [16]. When using a die with a channel angle of $\Phi = 90°$, route B_C is generally the most expeditious way to develop a UFG structure consisting of homogeneous and equiaxed grains with grain boundaries having high angles of misorientation.

There have also been numerous recent modifications of conventional ECAP that are designed to yield more efficient grain refinement including the incorporation of a backpressure, the development of continuous processing by ECAP, and others [9].

The technique of *accumulative roll bonding* (ARB) makes use of a conventional rolling facility. As illustrated in Fig. 2.3 [17], a sheet is rolled so that the thickness is reduced to one-half of the thickness in a prerolled condition. The rolled sheet is then cut into two halves that are stacked together. To achieve good bonding during the rolling operation, the two contact faces are degreased and wire brushed before placing them in contact and the stacked sheets are then rolled again to one-half thickness. Thus, a series of rolling, cutting, brushing, and stacking operations are repeated so that ultimately a large strain is accumulated in the sheet. It is possible to heat the sheet when rolling but at a temperature where there is no recrystallization. For the ARB process, the equivalent strain after N cycles, ε_N, is given by $\varepsilon_N = 0.80\ N$ [17].

In practice, the UFG structure produced by ARB is not three-dimensionally equiaxed but rather there is a pancake-like structure that is elongated in the lat-

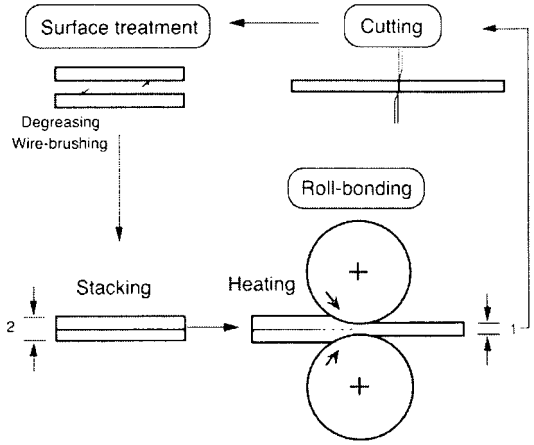

Fig. 2.3 Schematic illustration of ARB [17].

eral direction. This microstructural feature is the same irrespective of the types of metals and alloys. The ARB process has recently been applied successfully for the production of metal-matrix composites as well [18].

Multidirectional forging (MDF) was applied for the first time in the first half of the 1990s for the formation of UFG structures in bulk billets [19, 20]. The process of MDF is usually associated with dynamic recrystallization in single-phase metals/alloys.

The principle of MDF is illustrated in Fig. 2.4 and it assumes multiple repeats of free-forging operations including setting and pulling with changes of the axes of the applied load. The homogeneity of the strain produced by MDF is lower than in ECAP and HPT. However, the method can be used to obtain a nanostructured state in rather brittle materials because processing starts at elevated temperatures and the specific loads on tooling are relatively low. The choice of the appropriate temperature–strain rate regimes of deformation leads to the desired grain refinement. The operation is usually realized over the temperature interval of 0.1–0.5 T_m, where T_m is the absolute melting temperature, and it is useful for producing large-sized billets with UFG structures [21].

Cyclic extrusion and compression (CEC, also sometimes called "hourglass pressing") is performed by pushing a sample from one cylindrical chamber of diameter d_o to another with equal dimensions through a die with diameter d_m that is markedly smaller than d_o [22]; the principle is illustrated in Fig. 2.5. Thus, the processing induces extrusion and the chambers provide compression so that, during one cycle, the material is pushed to first experience compression, then extrusion, and finally compression again. The true strain produced in one cycle is calculated as $\Delta\varepsilon = 4 \ln(d_o/d_m)$. In the second cycle, the extrusion direction is reversed, leading to the same sequence of deformation modes. The process can be repeated N times by pushing the sample back and forth to give an accumu-

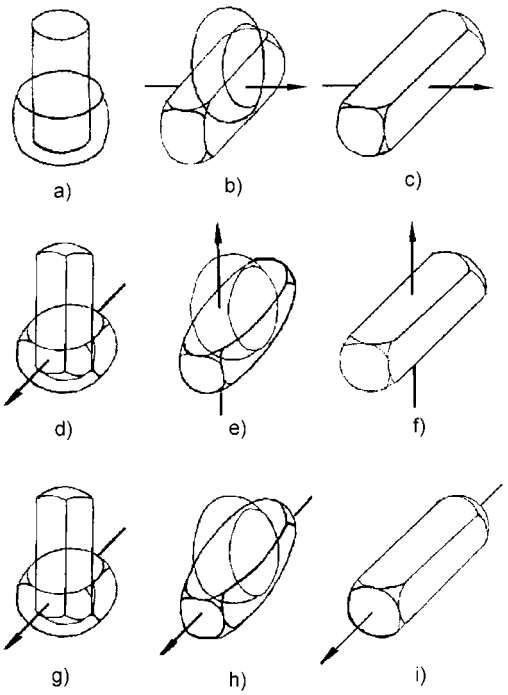

Fig. 2.4 The principle of MDF: (a), (b) and (c) show setting and pulling along the first axis, (d), (e) and (f) show setting and pulling along the second axis, and (g), (h) and (i) show setting and pulling along the third axis [19].

lated true strain of ($N\Delta\varepsilon$). With a diameter ratio of typically $d_m/d_o \approx 0.9$, the strain imposed on the material in one cycle is $\Delta\varepsilon \approx 0.4$. Accumulated true strains of up to 90 have been reported [22] with sample dimensions of about 25 mm in length and 10 mm in diameter. The deformation speed is as low as ~ 0.2 mm/s in order to limit heating of the specimen to < 5 K. Although the strains reached with this method are much higher than those with any unidirectional SPD technique, the microstructure and/or mechanical properties are similar because of the extra annihilation of dislocations due to the cyclic character of the straining [23].

Repetitive corrugation and straightening (RCS) was introduced recently and the principle is illustrated in Fig. 2.6 [24]. In a repetitive two-step process, the workpiece is initially deformed to a corrugated shape and then straightened between two flat platens using a processing cycle that may be repeated many times. The RCS facility illustrated in Fig. 2.6 subjects the workpiece to both bending and shear, which promotes grain refinement. Processing by RCS was used to produce nanostructures in a copper sample with an average initial grain size of 760 μm [24, 25]. A similar procedure was used later for grain refinement of aluminum [26].

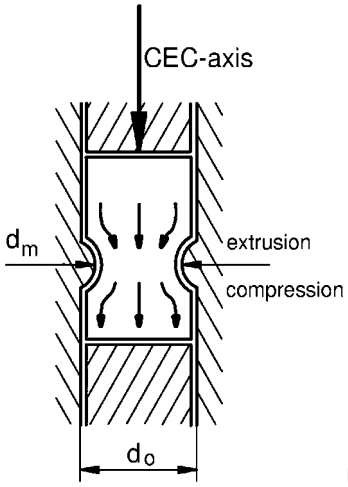

Fig. 2.5 The principle of CEC.

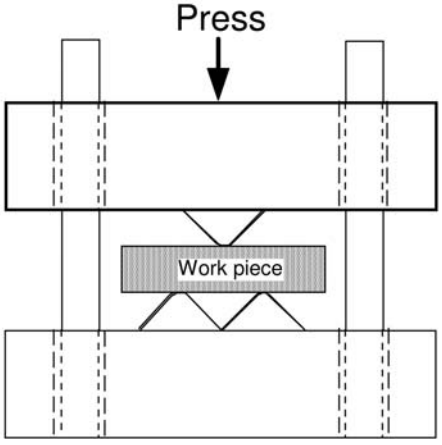

Fig. 2.6 The principle of RCS [24, 25].

An advantage of RCS is that it can be adapted easily to current industrial rolling facilities. It is not difficult to machine a series of corrugating teeth into the rollers of a conventional rolling mill, thus enabling the RCS process, and this has the potential of producing nanostructured materials in a continuous and economical way [27]. The RCS technique is currently in the early stages and further research is needed to develop the process to a mature SPD technique for producing nanostructured materials. One critical issue is the need to design equipment and processing schedules for improving microstructural homogeneity.

The use of *twist extrusion* (TE) for grain refinement was introduced in 2004 [28] and the principles are illustrated in Fig. 2.7. During TE, a workpiece is

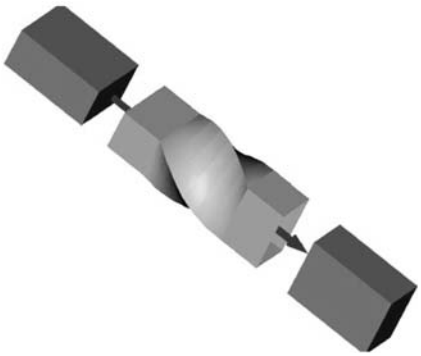

Fig. 2.7 The principle of TE [28].

pushed through an extrusion die whose cross section maintains its shape and size while it is twisted through a designated angle around its longitudinal axis. As a result, the workpiece regains its shape and size after each TE pass and thus it is possible to repetitively process a sample for excellent grain refinement. A variety of cross-sectional shapes, but not circular geometries, are possible with this technique. In practice, and by analogy to HPT, the plastic strain is not uniform across the cross section but the plastic strain increases with the distance from the axis so that the more distant regions have a finer grain size. This microstructural heterogeneity leads to inhomogeneous mechanical properties with the cross-sectional center having the lowest strength. It is anticipated that the microstructural homogeneity may improve with increasing numbers of TE passes.

To date, the developed SPD techniques have been typically used for laboratory-scale research. The requirement of economically feasible production of ultrafine-grained metals and alloys that is necessary for successful commercialization raises several new problems in the SPD techniques development. The most topical tasks are to reduce the material waste, to obtain uniform microstructure and properties in bulk billets and products, and to increase the efficiency of SPD processing.

One example of solving these tasks is by way of developing continuous ECA pressing [29] and multistep combined SPD processing [30] for fabrication of long-sized rods aimed at setting up commercial production of nanostructured Ti materials for medical applications. Some new results of these works are presented below.

2.2.2 Continuous ECA Pressing

It is known that the ECAP technique in its original design has some limitations for practical utilization, in particular, a relatively short length of the workpiece that makes ECAP a discontinuous process with low production efficiency and high cost. In addition, the ends of a workpiece usually contain nonuniform mi-

crostructure or macrocracks and have to be cut off, thus a significant portion of the workpiece is wasted and the cost of the UFG materials produced by ECAP is further increased.

The key to wide commercialization of UFG materials is to lower their processing cost and waste through continuous processing. Several attempts have been made to this end. For example, repetitive corrugation and straightening (RCS) [24, 25] is designed for processing of metal sheets and rods in a continuous manner. The coshearing process [31] and the continuous constrained strip shearing (C2S2) process [32] were recently also reported for continuous processing of thin strips and sheets to produce UFG structures. However, the question of further improvement of microstructure uniformity and properties remains topical in the development of these techniques.

Among recent interesting studies, combining the Conform process with ECAP to continuously process UFG materials for large-scale commercial production has been demonstrated [29]. In this invention, the principle used to generate frictional force to push a workpiece through an ECAP die is similar to the Conform process [33], while a modified ECAP die design is used so that the workpiece can be repetitively processed to produce UFG structures.

The principle of the ECAP-Conform setup is schematically illustrated in Fig. 2.8. As shown in this figure, a rotating shaft in the center contains a groove, into which the workpiece is fed. The workpiece is driven forward by frictional forces on the three contact interfaces with the groove, which makes the workpiece rotate with the shaft. The workpiece is constrained to the groove by a stationary constraint die. The stationary constraint die also stops the workpiece and forces it to turn an angle by shear as in a regular ECAP process. In the current setup, the angle is about 90°, which is the most commonly used channel intersection angle in ECAP. This setup effectively makes ECAP continuous. Other ECAP parameters (die angle, strain rate, etc.) can also be used.

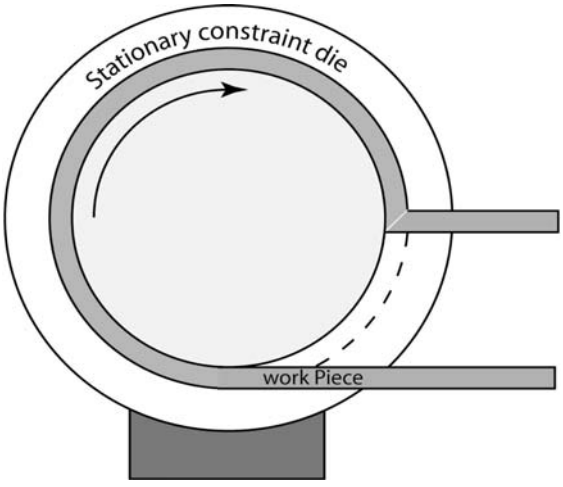

Fig. 2.8 Schematic illustration of an ECAP-Conform setup.

In [29] there has been used commercially pure (99.95%) coarse-grained long Al wire with a diameter of 3.4 mm and over 1 m in length for processing by ECAP at room temperature with 1–4 passes with route C, i.e. the sample was rotated 180° between ECAP passes. The initial Al wire had a grain size of 5–7 μm. Presently, processing of similar rods from CP Ti (Grade 2 and 4) is underway.

Figure 2.9 shows an Al workpiece at each stage of the ECAP-Conform process, from the initial round feeding stock to rectangular Al rod after the first ECAP pass. As shown, the rectangular cross section was formed shortly after the wire entered the groove (see the arrow mark). The change was driven by the frictional force between the groove wall and the Al workpiece. The frictional force pushed the wire forward, deformed the wire to make it conform to the groove shape. After the wire cross-section changed to the square shape, the frictional force per unit of wire length became larger because of larger contact area between the groove and the wire. The total frictional force pushed the wire forward from the groove into the stationary die channel, which intersects the groove at a 90° angle. This part of the straining process is similar to that in the conventional ECAP process.

TEM observations showed that ECAP-Conform led to microstructure evolution typical of the ECAP process [34, 35]. Figure 2.10 clearly indicates that the ECAP-Conform process can effectively refine grains and produce UFG structures in Al and now in CP Ti. The tensile mechanical properties of the as-processed Al samples after 1 to 4 passes are listed in Table 2.1. It is obvious that the ECAP-Conform process has significantly increased the yield strength ($\sigma_{0.2}$) and the ultimate tensile strength (σ_u), while preserving a high elongation to failure (ductility) of 12–14%. These results are consistent with those for Al processed by conventional ECAP [34]. We also found that in the case of CP Ti strength grows by more than 2 times after the processing as compared with the initial material, and this fact is also consistent the results obtained for Ti subjected to conventional ECAP.

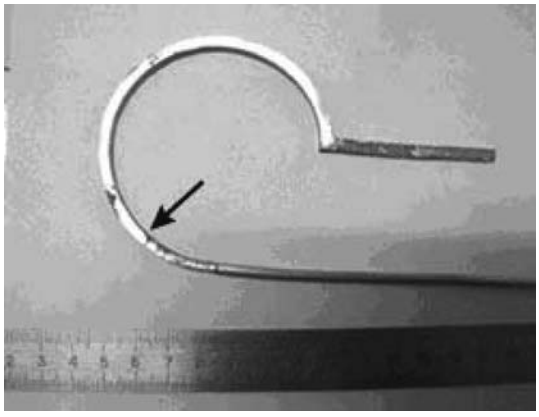

Fig. 2.9 An Al workpiece in the process of ECAP-Conform.

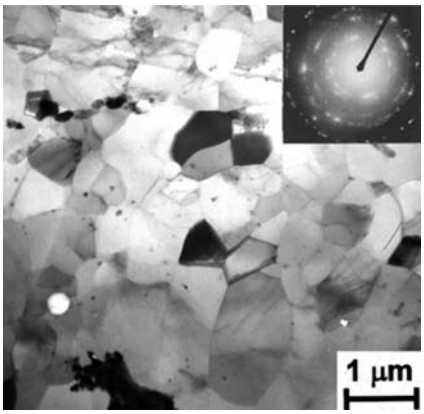

Fig. 2.10 TEM micrograph from the longitudinal section of Al wire processed by ECAP-Conform with four passes.

Table 2.1 Yield strength $\sigma_{0.2}$, ultimate tensile strength σ_u, elongation to failure δ, and cross-sectional reduction (necking) ψ of Al samples processed with 1 to 4 passes.

Processing state	$\sigma_{0.2}$ [MPa]	σ_u [MPa]	δ [%]	ψ [%]
initial Al rod	47	71	28	86
after 1 pass	130	160	13	73
after 2 passes	130	170	12	72
after 3 passes	130	160	14	76
after 4 passes	140	180	14	76

Thus, the newly developed continuous SPD technique, ECAP-Conform can successfully produce UFG materials. The continuous nature of the process makes it promising for production of UFG materials on a large scale, in an efficient and cost-effective manner. However, further study is needed to investigate its ability with respect to grain refinement and properties improvement of various UFG materials.

2.2.3 Combined SPD Processing

While solving the problem of fabrication of nanostructured Ti materials for medical applications, the advantage of combining ECAP with other techniques of metal forming such as rolling, forging or extrusion has been demonstrated [36, 37]. These advantages are connected with effective shaping of long-sized semiproducts (sheets, rods) as well as further enhancement of properties of UFG materials. For example, in Grade 2 CP Ti high strength (YS = 980 MPa, UTS = 1100 MPa) with elongation to failure $\delta = 12\%$ was attained using ECAP

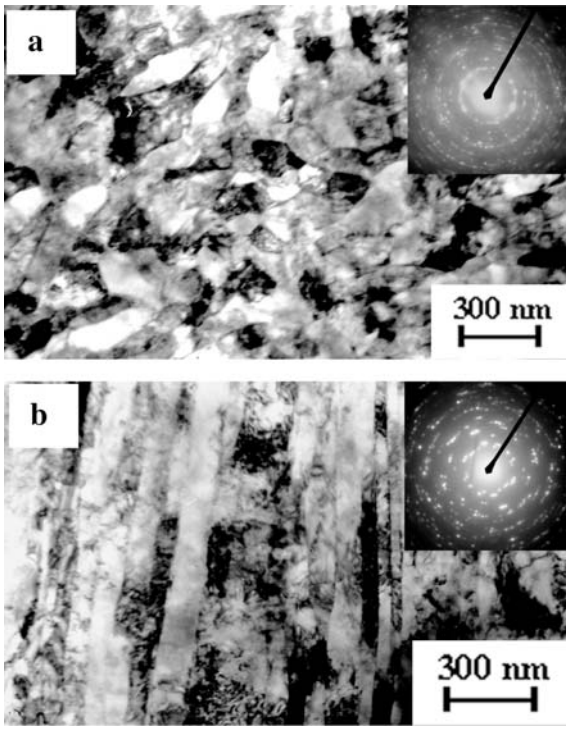

Fig. 2.11 TEM micrographs displaying the microstructure of Grade 2 Ti after ECAP+TMT, $\varepsilon = 80\%$:
(a) cross section;
(b) longitudinal section.

Table 2.2 Mechanical properties of Grade 2 Ti billets at different stages of processing.

State	σ_u [MPA]	$\sigma_{0.2}$ [MPA]	δ [%]	ψ [%]
Initial	440	370	38	60
ECAP 4 passes	630	545	22	51
ECAP 4 passes+TMT $\varepsilon = 80\%$	1150	1100	11	56

and extrusion. Also, the results of studies on processing of Ti rods of over 800 mm in length and 6.5 mm in diameter by a combination of ECAP and thermomechanical treatment (TMT) including forging and rolling are very impressive [30].

Figure 2.11 presents TEM micrographs of CP Ti subjected to ECAP+TMT, $\varepsilon = 80\%$. It can be seen that the combined processing results in significant additional grain refinement down to 100 nm in comparison with 300–400 nm after ECAP; however, a considerable elongation of grains takes place. Mechanical testing has shown (Table 2.2) that TMT after ECAP results in strength growth of CP Ti and the record values of $\sigma_{0.2}$ and σ_u are observed; at the same time, sufficient

ductility is preserved. It is important that these strength values of nanostructured CP Ti are visibly higher than those values of the Ti-6%Al-4%V alloy that is presently widely used in medicine and engineering.

It is also interesting that the microstructure and properties of the obtained rods are rather uniform, the dispersion of mechanical properties along the rod length does not exceed ±5% [38]; at the same time, material utilization rate totals 0.65. This shows great prospects for the use of combined SPD processing for commercial production of semiproducts made of Ti for medical application.

2.3
The New SPD Processing of Bulk Nanocrystalline Materials

Since the first works dating back to the early 1990s [7, 8], SPD techniques have been used mostly because of their ability to produce ultrafine-grained materials through microstructure refinement in initially coarse-grained metals [3]. The final grain size produced depends strongly on both processing regimes and the type of material. For pure metals the mean grain size is typically about 100–200 nm after processing by HPT and about 200–300 nm after processing by ECAP. For alloys and intermetallics the grain size is usually smaller and in some cases it is in the range of 50–100 nm. However, it is very important for fundamental tasks and many advanced applications to have bulk nanocrystalline materials with a mean grain size less than 30–50 nm. Is it possible to produce such materials using SPD techniques? In recent years this problem has become the object of special investigations using two approaches: SPD consolidation and SPD-induced nanocrystallization of amorphous alloys.

2.3.1
SPD Consolidation

Already in the early work on consolidation of powders [39, 40] it was revealed that during HPT high pressures of several GPa can provide a rather high density close to 100% in the processed disc-type nanostructured samples. For fabrication of such samples via severe torsion straining consolidation, not only conventional powders but also powders prepared by ball milling can be used.

HPT consolidation of nanostructured Ni and Fe powders prepared by ball milling [39, 40] can be taken as an example. The conducted investigations showed that the density of the samples processed at room temperature is very high and close to 95% of the theoretical density of bulk coarse-grained metals. After HPT consolidation at 200 or 400 °C the sample density is even higher and reaches 98%. TEM examinations showed the absence of porosity. The mean grain size is very small; it is equal to 17 nm and 20 nm for Ni and Fe, respectively. It is also very interesting that the value of microhardness of the Ni samples produced by HPT consolidation was 8.60 ± 0.17 GPa, the highest value of microhardness mentioned in literature for nanocrystalline Ni. It is worth men-

tioning that SPD consolidation is the most successful in conditions of low-temperature superplasticity.

2.3.2 SPD-induced Nanocrystallization

Recent investigations also show that SPD processing can control crystallization of initially amorphous alloys that may result in the formation of bulk nanocrystalline alloys with a very small grain size and new properties [41–43]. In [43] this approach is used to produce and to investigate Ti-Ni alloys widely known as alloys with shape-memory effects.

As the material for this investigation, two alloys of the Ti-Ni system were used: melt-spun $Ti_{50}Ni_{25}Cu_{25}$ alloy [41, 43] and cast $Ti_{49.4}Ni_{50.6}$ alloy [44, 45].

The amorphous structure of $Ti_{50}Ni_{25}Cu_{25}$ alloy was confirmed by TEM and X-ray investigations (Figs. 2.12 and 2.13) [4, 43]. However, after HPT at room temperature, although the diffraction methods still indicated the amorphous struc-

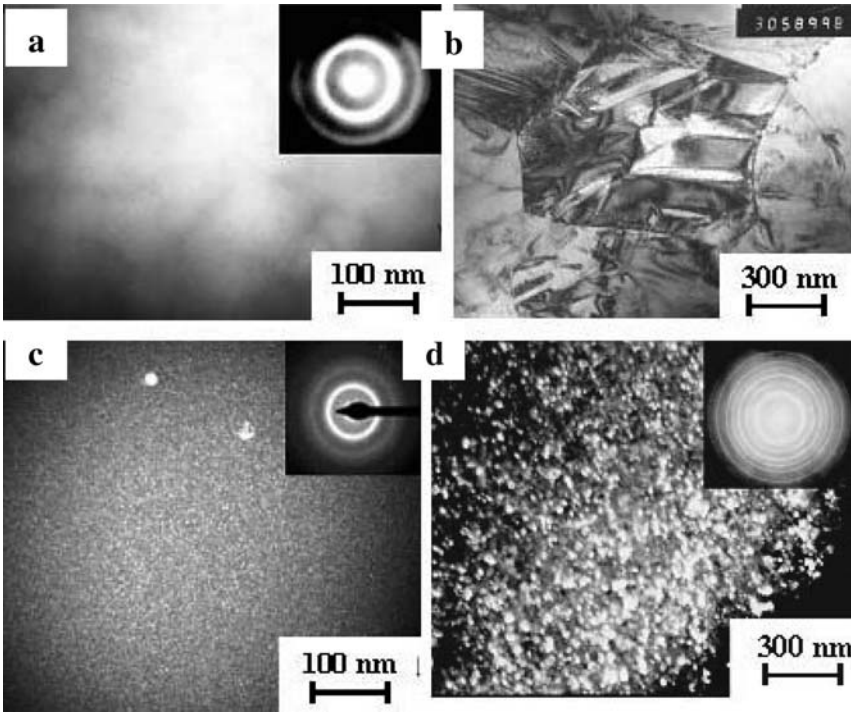

Fig. 2.12 TEM images of rapidly quenched alloy $Ti_{50}Ni_{25}Cu_{25}$: (a) initial state (dark field); (b) after annealing at 450 °C for 10 min; (c) after HPT (dark field); (d) after HPT and annealing at 390 °C for 10 min.

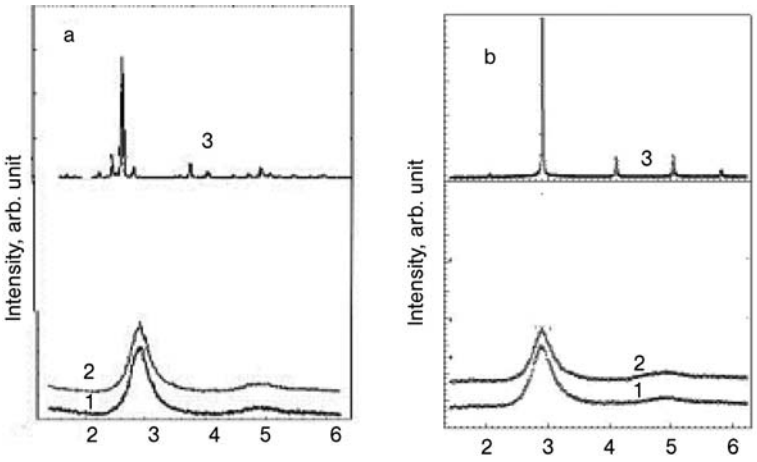

Fig. 2.13 X-ray diffraction patterns of the $Ti_{50}(Ni, Cu)_{50}$ alloy: (a) initial rapidly quenched alloy (1); after annealing at 300 °C 5 min (2); after annealing at 450 °C 5 min (3) with the phase B19; (b) alloy after HPT(1); after HPT and annealing at 300 °C 5 min (2); after HPT and annealing at 400 °C 5 min, with the phase B2 (3).

ture of the alloy, TEM studies showed the appearance of many nanocrystallites with very small sizes of about 2–3 nm (Fig. 2.12(c)).

The essential difference in behavior of this alloy in the amorphous state and after HPT was revealed during subsequent annealing. As can be seen in Fig 2.13, the amorphous alloy was crystallized and changed its phase composition after the annealing and further cooling to room temperature.

In the coarse-grained alloy $Ti_{50}Ni_{25}Cu_{25}$, the temperature of martensite transformation upon cooling is ~ 80 °C, which is why there is a martensite phase in the alloy at room temperature. In this connection, the existence of only the austenitic phase after HPT and nanocrystallization can be related to the martensite transformation retardation in the alloy with a nanocrystalline grain size. This fact was previously reported in literature for ultrafine-grained Ti-Ni alloys [46]. Concerning the alloy $Ti_{50}Ni_{25}Cu_{25}$, the critical point is the grain size of about 100 nm. Martensite transformation does not take place at room temperature below this size.

The amorphous state in the $Ti_{49.4}Ni_{50.6}$ alloy can be obtained directly as a result of HPT processing ($P = 6$ GPa, $n = 5$ revolutions) [44, 45]. Then the homogenous nanocrystalline structure was produced by annealing of the HPT material (Fig. 2.14). For instance, after annealing at 400 °C for 0.5 h the mean grain size is about 20 nm (Figs. 2.14(a) and (b)), and after annealing at 500 °C it is about 40 nm (Figs. 2.14(c) and (d)). It is worth mentioning that according to HRTEM observations after such annealing there are no regions of amorphous phase and grain boundaries are well defined, although there are still small distortions of the crystal lattice near some of the boundaries.

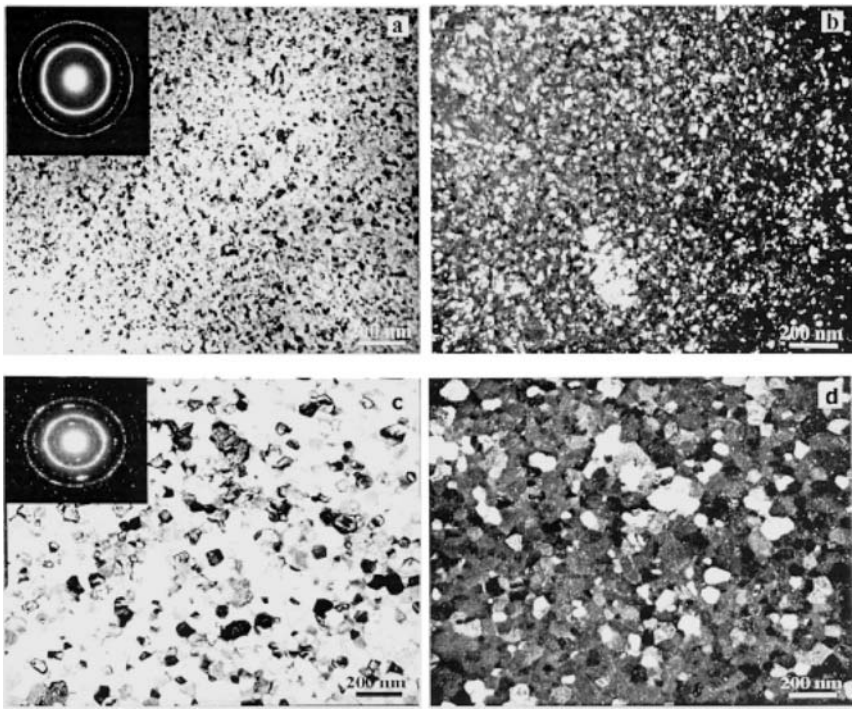

Fig. 2.14 TEM micrographs of the $Ti_{49.4}Ni_{50.6}$ alloy after HPT and annealing at 400 °C (a, b) and at 500 °C (c, d) for 0.5 h: (a, c) bright-field images; (b, d) dark-field images.

Tensile mechanical tests showed that the amorphous nitinol produced by HPT had much higher strength in comparison with the initial microcrystalline state [44], but it was essentially brittle. Nanocrystallization results in the record value of strength for this material equal to 2650 MPa with an elongation to failure of about 5%.

Thus, SPD consolidation of powders and SPD-induced nanocrystallization can be regarded as new SPD processing routes for fabrication of bulk nanocrystalline materials. One of the advantages of this technique is its ability to produce fully dense samples with a uniform ultrafine-grained structure having a grain size under 40–50 nm. Studies of the properties of these materials are of great interest for ongoing research because deformation mechanisms and, as mentioned above, phase transformations can basically change in materials with a small grain size [1, 47].

2.4
Structural Features and Enhanced Properties in SPD-produced Nanomaterials

As was noted above, the average grain size achieved in pure metals using various SPD techniques usually lies in the range of about 150–300 nm, but in alloys it may be significantly smaller [3]. For example, using HPT with the intermetallic Ni_3Al produced a grain size of 60 nm and in TiNi alloys processing by HPT led to a complete amorphization [44, 48]. At the same time, the structural features of SPD-processed metals are quite complex and they are characterized not only by the formation of ultrafine grains but also, as a consequence of this, by high density of interfaces. Numerous structural studies of SPD nanomaterials have led to an important conclusion that the grain boundaries (GBs) in these materials have a specific, nonequilibrium structure [3, 46], which is characterized by the presence of a high density of dislocations.

The concept of nonequilibrium GBs was established due to earlier investigations of the behavior of GBs under external influences [49]. Trapping of dislocations in GBs during plastic deformation results in an accumulation of specific defects in the GBs called extrinsic grain-boundary dislocations (EGBDs). The GBs containing EGBDs induce noncompensated long-range internal strains and have an enhanced energy and are commonly referred to as nonequilibrium GBs. As very large plastic strains are applied for the preparation of nanomaterials and, therefore, the density of EGBDs can be very high, the role of nonequilibrium GBs in the properties of these materials is expected to be particularly important.

The nonequilibrium character of GBs in SPD nanomaterials is proved by a number of experimental data obtained using various complementary methods. First evidences were obtained during TEM studies, which showed that for nanomaterials prepared by SPD a specific strain contrast on GBs and extinction contours near the GBs are typical [3, 46]. Moderate annealing results in a relaxation of the GB structure that does not involve any significant grain growth. The extinction contours in the grains disappear, and the GBs acquire their usual band contrast. Direct HRTEM studies of severely deformed metals and alloys [25, 50, 51], also showed that GBs caused a significant, up to 1 to 3% lattice distortions in a layer of 6 to 10 nm thickness near the GBs, had a curved shape and contained many EGBDs. X-ray diffraction methods provided plenty of data on the specific structural characteristics of SPD nanomaterials that resulted in an increased integral background intensity, a significant decrease of the intensity and broadening of peaks in X-ray spectra [52]. Root mean square (rms) strains calculated from an analysis of these spectra are as high as 0.3% to 1.2%, depending on the material, method of SPD used and deformation and post-deformation storage conditions.

The nonequilibrium GB structure in as-prepared UFG materials is evidenced also by a direct relationship between the structural relaxation and the evolution of different properties of UFG materials during annealing. For example, the coefficient of diffusion along GBs in as-prepared nanostructured materials is

several orders of magnitude higher than that along the GBs of coarse-grained polycrystals; preannealing of UFG samples before diffusion experiments results in a significant recover of the diffusion coefficient [53]. Young and shear moduli of as-prepared UFG Cu are approximately 10% less than those of coarse-grained polycrystals [54]. After 1 h annealing at $T = 400$ K a sharp increase of the moduli to their ordinary values occurs, and this increase is directly associated with an attainment of equilibrium structure by GBs.

The genesis of UFG structures produced by SPD techniques is not yet fully understood. Some authors relate them to *in-situ* recrystallization [55]. Others place the origin in the formation and evolution of a dislocation cell structure whose size scale decreases as the stress rises during SPD processing [56–58]. The accumulation of the misorientation between neighboring dislocation cells occurs in parallel with the decrease of the average cell size and leads to a gradual transformation of the dislocation cell structure. In particular, predominantly polarized dipole walls yield a new refined grain structure in which polarized tilt walls are prevalent, causing high angles of misorientation between the grains [57, 58]. Qualitatively, the formation of UFG structure can be understood also by extrapolating numerous experimental data obtained in the studies of large plastic deformations by conventional methods such as die compression, cold rolling, *etc.* [59–61]. From these studies, it follows that the substructure evolves by the formation of misoriented regions containing blocks of several cells. These regions have a certain alignment with the applied stress and are separated by dense dislocation walls and microband boundaries with misorientation angles larger than those of cell walls, which continuously increase with the strain. For monotonic loading conditions typical of conventional methods, the subgrains delineated by such boundaries called geometrically necessary boundaries (GNBs), are elongated. The formation of GNBs is thought to occur due to an operation of different combinations of slip systems in microbands [59]. A similar elongated substructure is observed also after one pass ECAP and subsequent passes using route A [62]. This suggests that the grain subdivision might occur by the formation of GNBs through a microbanding mechanism. However, with respect to ECAP, it is not clear how this mechanism can result in the formation of equiaxed UFG structure after several passes with the strain-path change.

According to the above-mentioned models, the smallest grain size achievable by SPD cannot be smaller than the length scale of the precursor dislocation-cell structure, which normally is in the range of a few hundred nanometers. Recently, it was found that HPT processing of electrodeposited nickel induced the growth of grains to a final size close to the lower grain-size limit for HPT refinement of coarse-grained nickel, suggesting that there exists a final grain size determined by the processing parameters rather than by the total imposed strain [63].

An alternative concept of structural evolution during large plastic deformation, which assumes a dominating role of the grain interactions, has been developed by Rybin et al. [64, 65]. According to this concept, plastic strain of differ-

ently oriented grains results in an accumulation of incompatibilities of the plastic strain, which can be described in terms of specific mesodefects in GBs consisting of the systems of gliding dislocations having Burgers vectors tangential to the GB plane and systems of sessile dislocation, equivalent to disclinations at triple junctions. Junction disclinations have been shown to act as main carriers of grain subdivision during deformation. When triple junctions accumulate disclinations with the strength Ω sufficient for an activation of additional dislocation activity near the junctions, they initiate the formation of low-angle boundaries crossing the grains. This process of disclination accumulation and relaxation is repeated during deformation resulting in the grain fragmentation and increase of the misorientations of new grains. At very large strains typical for SPD processing, this can result in the formation of an equiaxed ultrafine grained structure. Disclinations at junctions of grains and subgrains in SPD-processed metals have been observed by special methods of electron microscopy [66] that gives support for this fragmentation model of grain subdivision.

Quite recently, a quantitative model of grain subdivision based on this disclination concept has been developed for a study of the grain refinement during simple shear and ECAP straining [67, 68]. In essence, this model combines the viscoplastic self-consistent model of polycrystal deformation [69], which has been recently use to simulate ECAP straining [70], and the disclination model. The former allows one to find the strain incompatibilities on GBs necessary to calculate the accumulation rate for junction disclinations and the latter provides a grain subdivision criteria. It has been shown that this model results in a better description of textures formed during ECAP processing of metals, than the models taking no account for the grain subdivision. Evolution of GB misorientation distribution during SPD has also been described for the first time. It seems that the proposed approach can have a significant potential in understanding the mechanisms of nanostructure formation using SPD methods. However, at present there is no satisfactory model that could predict the ultimate grain size in the disclination approach.

Although the formation mechanisms of the UFG structure are not completely clear, at present the nature of the nonequilibrium structure of GBs in the product nanomaterials is fairly well understood. Defects formed on GBs and their junctions during SPD are inherited by as-prepared nanomaterials. A structural model of nanomaterials based on the concept of nonequilibrium GBs was proposed in [71–74]. In this model, the authors distinguished three basic types of nonequilibrium dislocation arrays formed on GBs and their junctions during plastic deformation: disordered networks of EGBDs, arrays of EGBDs with Burgers vectors normal to the GB plane (sessile EGBDs), which are equivalent to dipoles of junction disclinations, and arrays of EGBDs with Burgers vectors tangential to the GB plane (gliding EGBDs). This model has been used to calculate the characteristics of UFG materials such as rms strain, excess GB energy and volume expansion due to defects. The estimates yield the values consistent with the experimental data. Moreover, studies of the kinetics of GB recovery performed in these models and a comparison with experimental data on the evolu-

tion of GB diffusion coefficient and elastic moduli during annealing of SPD nanometals show a good correlation [75] that gives an additional support on the relation between the nonequilibrium GB structure and properties of nanomaterials.

The nonequilibrium GB structure is considered to have a significant effect on the properties of SPD nanomaterials. In particular, atomic computer simulations of nonequilibrium GBs show several orders of magnitude increase of vacancy concentrations as compared to equilibrium ones [76] that must result in a significant increase of the GB diffusion coefficient. Indeed, experimental studies show very high vacancy concentrations [77] and, as mentioned above, enhanced GB diffusion coefficient [53] in SPD materials.

The nonequilibrium GB structure, in combination with the very small grain size and high GB diffusion coefficient results in an operation of deformation mechanisms different from those in coarse-grained polycrystals. In particular, grain boundary sliding at much lower temperatures than for coarser-grained polycrystals is possible in SPD nanomaterials [78, 79]. As a consequence, unusual mechanical properties of nanomaterials processed by SPD can be expected.

It is well known that any grain refinement promotes mechanical strength, and thus one can expect ultrafine-grained materials to possess very high strength. Moreover, introduction of a high density of dislocations in SPD-processed nanometals may result in even greater hardening. However, both of these factors normally decrease ductility. Strength and ductility are the key mechanical properties of any material, but they typically have opposite trends. Materials may be strong or ductile, but rarely both at once. Recent studies have shown that nanostructuring of materials may lead to a unique combination of exceptionally high strength and ductility (Fig. 2.15), but this task calls for original approaches [8, 38, 80, 81].

One such new approach to the problem was suggested recently by Wang et al. [81]. They created a nanostructured copper by rolling the metal at low temperature – the temperature of liquid nitrogen – and then heating it to around 450 K. The result was a "bimodal" structure of micrometer-sized grains (at a volume fraction of around 25%) embedded in a matrix of nanocrystalline grains. The material showed extraordinarily high ductility, but also retained its high strength. The reason for this behavior is that, while the nanocrystalline grains provide strength, the embedded larger grains stabilize the tensile deformation of the material. Other evidence for the importance of grain-size distribution comes from work on zinc [82], copper [83], and aluminum alloy [84]. What is more, the investigation of copper [83] has shown that bimodal structures can increase ductility not only during tensile tests, but also during cyclic deformation. This observation is important for improving fatigue properties.

Another approach suggested recently [85] is based on formation of second-phase particles in the nanostructured metallic matrix, which modify shear-band propagation during straining, thereby increasing the ductility. A systematic study of both hard and soft second-phase particles with varying sizes and distributions is required here, to allow mechanical properties to be optimized.

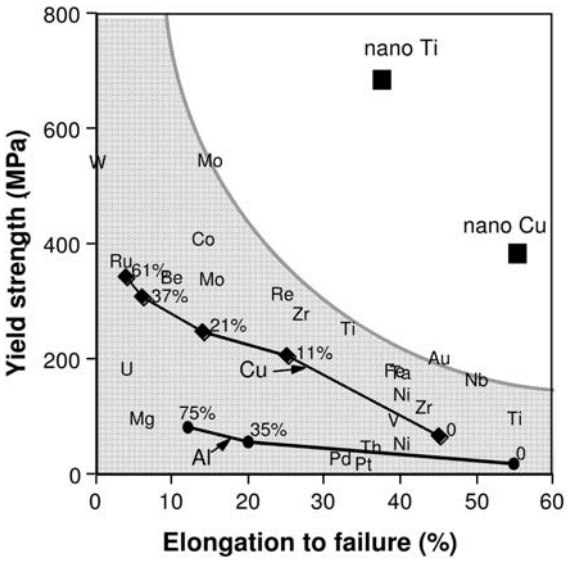

Fig. 2.15 Strength and ductility of nanostructured metals compared with coarse-grained metals. Conventional cold rolling of copper and aluminum increases their yield strength but decreases their ductility. The two lines represent this tendency for Cu and Al and the % markings indicate a percentage on rolling. In contrast, the extraordinarily high strength and ductility of nanostructured Cu and Ti clearly sets them apart from coarse-grained metals [8].

A third approach to the problem of strength and ductility is probably the most universal of the three, because it can be applied both for metals and for alloys. The approach introduced in [1] is based on formation of ultrafine-grained structures with high-angle and nonequilibrium grain boundaries capable of grain-boundary sliding (GBS). It is well known that sliding, which increases ductility, normally cannot develop at low-angle boundaries. The importance of high-angle grain boundaries was verified in work [8] on the mechanical behavior of metals subjected to different degrees of severe plastic deformation resulting in the formation of various types of grain boundaries. As was noted above, sliding can be easier when nonequilibrium boundaries are present. Another example that supports this suggestion is the extraordinary influence of annealing conditions on the mechanical behavior found recently in nanostructured titanium produced by HPT [86]. Here, a short annealing at 300 °C results in a noticeable increase in strength combined with greater ductility than in the HPT-produced state or after annealing at higher temperatures. Structural studies show that after annealing at 300 °C the grains become free of dislocations, but GBs retain their nonequilibrium structure. At higher temperatures, the GBs attain a more equilibrated structure and also grain growth starts. As a result, strength and ductility fell after peak values at 300 °C.

The growth of strength and ductility in the cited work was associated with higher strain-rate sensitivity of flow stress. An increased strain-rate sensitivity has also been reported in other works investigating high strength and ductility in nanometals [3, 8, 78]. High strain-rate sensitivity indicates viscous flow and plays a key role in superplasticity in materials [87], but on the other hand it is associated with the development of grain-boundary sliding, and therefore depends on grain-boundary structure.

The fact that grain-boundary sliding can operate at low temperatures in nanocrystals is in agreement with the recent results of large-scale atomistic computer simulation aimed at a study of deformation mechanisms active in nanostructured metals [88–90]. Such molecular dynamics simulations have provided valuable insight into the deformation behavior of nanometals. For coarse-grained metals, dislocation movement and twinning are well-known primary deformation mechanisms. But the results of simulation show that ultrafine grains may also aid in specific deformation mechanisms such as grain-boundary sliding or nucleation of partial dislocations [89–92]. Moreover, the sliding may have a cooperative (grouped) character similar to that observed in earlier studies on superplastic materials [93, 94]. It should be stressed that recent experiments investigating deformation mechanisms in nanostructured materials have confirmed a number of the results of computer simulation [86, 95, 96].
However, atomic simulations so far have been carried out for nanocrystals with equilibrium GBs containing no extrinsic defects. Further research is needed to obtain an insight into the role of the nonequilibrium GB structure in the deformation mechanisms of nanocrystals.

In practice, processing of nanomaterials to improve both strength and ductility is of primary importance for fatigue strength and fracture toughness [83, 97, 98]. An extraordinary increase in both low-cycle and high-cycle fatigue strength may take place; there exists a theoretical explanation and the first experimental evidence of this interesting phenomenon [97, 98].

2.5
Using SPD-produced Nanostructured Metals

Markets for bulk nanostructured materials exist in virtually every product sector where superior mechanical properties (in particular, strength, strength-to-weight ratio and fatigue life) are critical design parameters. Formal market analyzes have identified a wide range of potential applications for nanometals in aerospace, transportation, medical devices, sports products, food and chemical processing, electronics and conventional defense [99]. Among them we can single out the following directions: (1) development of extra-strong nanostructured light alloys (Al, Ti, Mg), for example Al-based commercial alloys with yield strength over 800–900 MPa, for the motor industry and aviation; (2) development of metals and alloys with ultrafine-grained structure for use at cryogenic temperatures [100]; (3) development of nanostructured ductile refractory metals

and high-strength TiNi alloys with advanced shape-memory effect for space, medical and other applications. The applications of nanostructured materials in engineering new-generation aviation engines [101] are worth a special mention.

Out of the broad range of possible applications of advanced nanostructured metals, we focus here on the one that is representative of the high-tech market: biomedical implants and devices. High mechanical and fatigue properties are the essential requirements for metallic biomedical materials, in particular titanium and its alloys [102], which have excellent biological compatibility and high biomechanical properties. For example, in trauma cases, plates and screws made of new titanium materials are planned to be widely used for fixing bones. These plates need very high compressive and bending strength, and sufficient ductility. Different implant–plate constructions for osteosynthesis have been analyzed, resulting in the design and processing of a series of nanostructured titanium plates (Figs. 2.16 (a) and (b)). Figure 2.16 (c) illustrates another application of nanostructured titanium for a special conic screw, which requires high fatigue strength as well. In this case all the advantages of nanostructured titanium are fully used [37] – high static and fatigue strength (yield tensile strength $\geq$950 MPa at strain rate 10^{-3} s^{-1}, endurance of more than 500 MPa at 2×10^7 cycles) and excellent biological compatibility.

Alongside applications of bulk nanostructured materials driven by their superior properties that were considered above, in recent years applications driven by their superior manufacturability have been attracting ever-growing attention of researchers and engineers [103]. For instance, UFG metals can be readily fabricated into the desired shapes in an efficient and cost-effective manner. Machining, forging and forming may be easier in SPD-processed metals than in their conventional counterparts.

In particular, for products that are directly machined to shape from SPD-processed mill products, the feed rates and cutting depths can be increased because of the manner in which the deformation occurs under the machining conditions [104]. Processing by SPD leads to a smoother surface finish and a reduction in tool wear. For some specialized products, the largest portion of the cost may be associated with the machining. In some cases the superior surface finish from machining of the SPD-processed metals may obviate the need for subsequent surface-finishing steps. This will reduce the manufacturing cost by eliminating or simplifying the processing steps.

The UFG alloys processed by SPD can also be formed superplastically at lower temperatures and faster rates than is possible in conventional superplastic alloys [3, 105]. In the superplastic-forming industry, complex components, often having multiple curved surfaces, are formed from superplastic sheet metals. The essential requirements for achieving a superplastic-forming capability are small grain sizes, typically less than $\sim$10 μm, and high forming temperatures, typically above $\sim$0.5 T_m, where T_m is the absolute melting point of the material. At present, the superplastic-forming industry occupies a small but viable cost-effective niche through the production of high-cost low-volume components associated primarily with the aerospace, architectural and sports industries [106]. Ex-

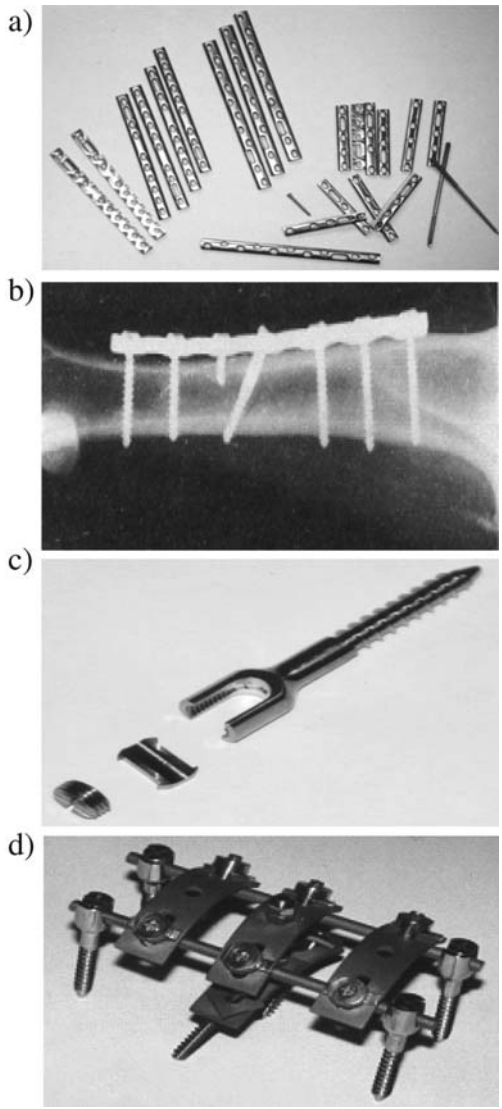

Fig. 2.16 Medical implants made of nanostructured titanium: (a, b) plate implants for osteosynthesis; (c) conic screw for spine fixation; (d) device for correction and fixation of spinal column.

pansion beyond this niche, into automotive and other high-volume applications, is currently restricted by the slow strain rates involved in the forming process (typically $\sim 10^{-3}\ s^{-1}$) and the consequent long forming times ($\sim$20–30 min) associated with the production of each separate component.

The introduction of bulk UFG materials provides a potential for overcoming the inherent limitations associated with conventional coarse-grained superplastic materials. Thus, it is now well established, both theoretically and experimentally [107, 108], that the rate of flow within the superplastic regime varies inversely

with the grain size raised to a power that is close to ~2. It is anticipated, therefore, that a decrease in the grain size by one order of magnitude will lead to an increase in the optimal superplastic forming rate by approximately two orders of magnitude and thus, in effect, the total forming time will be reduced to ~20–30 s. It can be shown also that this reduction in grain size will lead to the advent of a superplastic forming capability that occurs at lower temperatures than those generally associated with conventional superplastic flow. Early experimental results provided very clear demonstrations of the occurrence of both high strain rate superplasticity [109] and low-temperature superplasticity [110] in bulk nanostructured materials, where high strain rates refer to the tensile testing of samples at rates at and above 10^{-2} s^{-1} and low temperatures refer to tensile testing at homologous temperatures below 0.5 T_m.

The production of bulk nanostructured alloys in sheet form, with ultrafine grains that are fairly stable at elevated temperatures, has the potential to expand the superplastic-forming niche into a processing regime that will be effective in producing components for a very wide range of commercial applications.

2.6 Conclusions

Several new trends in SPD processing for fabrication of bulk nanostructured materials have been presented in this chapter, based on recent results in the sphere of the development of SPD techniques for fabrication of nanostructured materials for medical and some other applications. Presently new tasks, connected with economically feasible production of UFG metals and alloys, started to be solved through decreasing the material waste, obtaining homogeneous structure and advanced properties in bulk billets and products.

From the fundamental point of view, studies focused on fabrication of bulk nanocrystalline materials using SPD techniques, as well as their structural features and potential for obtaining extraordinary properties, are of special interest. This chapter also has presented two new approaches – SPD consolidation of powders and SPD-induced crystallization – both enabling fabrication of bulk nanostructured materials with a grain size of 40–50 nm or smaller. Another important fundamental problem are studies of grain boundaries in UFG materials; the possibility to control the structure of grain boundaries in UFG materials paves the way for achievement of unique properties of nanomaterials.

Acknowledgements

The present paper was supported in part by the NIS-IPP Program of DOE (USA), the Russian Foundation for Basic Research and the Russian Federal Science and Technology Program. Cooperation with coauthors mentioned in references is gratefully acknowledged as well.

References

1 R. Z. Valiev **2004**, *Nature Mater.* 3, 511–516.
2 R. Z. Valiev, Y. Estrin, Z. Horita, T. G. Langdon, M. J. Zehetbauer, Y. T. Zhu **2006**, *JOM* 58 (4), 33–39.
3 R. Z. Valiev, R. K. Islamgaliev, I. V. Alexandrov **2000**, *Prog. Mater. Sci.* 45, 103–189.
4 Y. T. Zhu, et al. (eds.) **2006**, *Ultrafine Grained Materials IV*, The Minerals, Metals Materials Society, Warrendale, PA, USA.
5 M. Zehetbauer (ed.) **2003**, *Adv. Eng. Mater.* 5 (Special Issue on Nanomaterials by Severe Plastic Deformation (SPD)).
6 Z. Horita (ed.) **2006**, *Proc. of the 3rd Inter. Conf. on Nanomaterials by Severe Plastic Deformation*, *Mater. Sci. Forum* 503–504.
7 R. Z. Valiev, N. A. Krasilnikov, N. K. Tsenev **1991**, *Mater. Sci. Eng.* A137, 35–40.
8 R. Z. Valiev, I. V. Alexandrov, Y. T. Zhu, T. C. Lowe **2002**, *J. Mater. Res.* 17, 5–8.
9 R. Z. Valiev T. G. Langdon **2006**, *Prog. Mater. Sci.* 51, 881–981.
10 A. P. Zhilyaev, G. V. Nurislamova, B.-K. Kim, M. D. Baró, J. A. Szpunar, T. G. Langdon **2003**, *Acta Mater.* 51, 753–765.
11 T. Hebesberger, H. P. Stüwe, A. Vorhauer, F. Wetscher, R. Pippan **2005**, *Acta Mater.* 53, 393–402.
12 G. Sakai, K. Nakamura, Z. Horita, T.G. Langdon **2005**, *Mater. Sci. Eng. A* 406, 268–273.
13 V. M. Segal, V. I. Reznikov, A. E. Drobyshevskiy, V. I. Kopylov **1981**, *Russ. Metall.* 1, 99–105.
14 Y. Iwahashi, J. Wang, Z. Horita, M. Nemoto, T. G. Langdon **1996**, *Scr. Mater.* 35, 143–146.
15 V. M. Segal **1995**, *Mater. Sci. Eng A* 197, 157–164.
16 M. Furukawa, Y. Iwahashi, Z. Horita, M. Nemoto, T. G. Langdon **1998**, *Mater. Sci. Eng. A* 257, 328–332.
17 Y. Saito, H. Utsunomiya, N. Tsuji, T. Sakai **1999**, *Acta Mater.* 47, 579–583.
18 S.-H. Lee, T. Sakai, Y. Saito, H. Utsunomiya, N. Tsuju **1999**, *Mater. Trans. JIM* 40, 1422–1428.
19 O. R. Valiakhmetov, R. M. Galeyev, G. A. Salishchev **1990**, *Fiz. Met. Metall.* 10, 204.
20 R. M. Galeyev, O. R. Valiakhmetov, G. A. Salishchev **1990**, *Russ. Metall.* 4, 97.
21 S. V. Zherebtsov, G. A. Salishchev, R. M. Galeyev, O. R. Valiakhmetov, S. Yu. Mironov, S. L. Semiatin **2004**, *Scr. Mater.* 51, 1147–1151.
22 J. Richert M. Richert **1986**, *Aluminium*, 61, 604.
23 M. Richert, H. P. Stüwe, M. J. Zehetbauer, J. Richert, R. Pippan, Ch. Motz, E. Schafler **2003**, *Mater. Sci. Eng. A* 355, 180–185.
24 Y. T. Zhu, H. Jiang, J. Huang, T. C. Lowe **2001**, *Metall. Mater. Trans.* 32A, 1559–1562.
25 J. Y. Huang, Y. T. Zhu, H. Jiang, T. C. Lowe **2001**, *Acta Mater.* 49, 1497–1505.
26 D. H. Shin, J. J. Park, Y.-S. Kim, K.-T. Park **2002**, *Mater. Sci. Eng. A* 328, 98–103.
27 J. Huang, Y. T. Zhu, D. J. Alexander, X. Liao, T. C. Lowe, R. J. Asaro **2004**, *Mater. Sci. Eng. A* 371, 35–39.
28 D. V. Orlov, V. V. Stolyarov, H. Sh. Salimgareyev, E. P. Soshnikova, A. V. Reshetov, Ya. Ye. Beygalzimer, S. G. Synkov, V. N. Varyukhin **2004**, *Ultrafine Grained Materials III*, (eds.) Y.T. Zhu, et al. Warrendale, PA: TMS, p. 457.
29 G. J. Raab, R. Z. Valiev, T. C. Lowe, Y. T. Zhu **2004**, *Mater. Sci. Eng. A* 382, 30–34.
30 V. V. Latysh, I. P. Semenova, G. H. Salimgareeva, I. V. Kandarov, Y. T. Zhu, T. C. Lowe, R. Z. Valiev **2006**, *Mater. Sci. Forum* 503–504, 763–768.
31 Y. Saito, H. Utsunomiya, H. Suzuki, T. Sakai **2000**, *Scr. Mater.* 42, 1139–1144.
32 J. C. Lee, H. K. Seok, J. Y. Suh **2002**, *Acta Mater.* 50, 4005–4019.
33 D. Green **1972**, *J. Inst. Met.* 100, 295–300.
34 Y. Iwahashi, Z. Horita, M. Nemoto, T. G. Langdon **1997**, *Acta Mater.* 45, 4733–4741.
35 M. Furukawa, Z. Horita, M. Nemoto, T. G. Langdon **2001**, *J. Mater. Sci.* 36, 2835–2843.
36 V. V. Stolyarov, Y. T. Zhu, T. C. Lowe, R. Z. Valiev **2001**, *Mater. Sci. Eng. A* 303, 82–89.
37 Y. T. Zhu, T. C. Lowe, R. Z. Valiev, V. V. Stolyarov, V. V. Latysh, G. I. Raab **2002**, U.S. Patent 6,399,215.

38 W. M. Wang E. Ma **2004**, *Acta Mater.* 52, 1699–1709.
39 R. Z. Valiev, R. S. Mishra, J. Grosa, A. K. Mukherjee **1996**, *Scr. Mater.* 34, 1443.
40 R. Z. Valiev **2006**, *Mater. Sci. Forum* 503–504, 3–10.
41 R. Z. Valiev **2003**, *Adv. Eng. Mater.* 5, 296–300.
42 G. Wilde, N. Boucharat, G. P. Dinda, H. Rösner, R. Z. Valiev **2006**, *Mater. Sci. Forum* 503–504, 425–432.
43 R. Z. Valiev, V. G. Pushin, D. V. Gunderov, A. G. Popov **2004**, *Doklady RAN* 398, 1–3.
44 A. V. Sergueeva, C. Song, R. Z. Valiev, A. K. Mukherjee **2003**, *Mater. Sci. Eng. A* 339, 159–165.
45 J. Y. Huang, Y. T. Zhu, X. Z. Liao, R. Z. Valiev **2004**, *Philos. Mag. Lett.* 84, 183–190.
46 R. Z. Valiev, A. V. Korznikov, R. R. Mulyukov **1993**, *Mater. Sci. Eng. A* 186, 141–148.
47 Y. T. Zhu T. G. Langdon **2004**, *JOM* 56 (10), 58–63.
48 X. Z. Liao, Y. H. Zhao, S. G. Srinivasan, Y. T. Zhu, R. Z. Valiev, D. V. Gunderov **2004**, *Appl. Phys. Lett.* 84, 592–594.
49 R. Z. Valiev, V. Yu. Gertsman, O. A. Kaibyshev **1986**, *phys. stat. sol. (a)* 97 (1), 11–56.
50 R. Z. Valiev R. Sh. Musalimov **1994**, *Phys. Met. Metallogr.* 78 (6), 666–670.
51 Z. Horita, D. J. Smith, M. Nemoto, R. Z. Valiev, T. G. Langdon **1998**, *J. Mater. Res.* 13 (2), 446–450.
52 I. V. Alexandrov, K. Zhang, K. Lu **1996**, *Ann. Chim.–Sci. Mater.* 21, 407–416.
53 Yu. R. Kolobov, G. P. Grabovetskaya, M. B. Ivanov, A. P. Zhilyaev, R. Z. Valiev **2001**, *Scr. Mater.* 44, 873–878
54 N. A. Akhmadeev, N. P. Kobelev, R. R. Mulyukov, Ya. M. Soifer, R. Z. Valiev **1993**, *Acta Metall. Mater.* 41, 1041–1046.
55 R. Lapovok, P. F. Thomson, R. Cottam, Y. Estrin **2005**, *J. Mater. Sci.* 40, 1699–1708.
56 Y. Estrin, L. S. Tóth, Y. Brechet, H. S. Kim **2006**, *Mater. Sci. Forum* 503–504, 675–680.
57 T. Ungár M. Zehetbauer **1996**, *Scr. Mater.* 35, 1467.
58 M. Zehetbauer, T. Ungár, R. Kral, A. Borbély, E. Schafler, B. Ortner, H. Amenitsch, S. Bernstorff **1999**, *Acta Mater.* 47, 1053.
59 N. Hansen **1990**, *Mater. Sci. Technol.* 6, 1039.
60 D. A. Hughes, Q. Liu, D. C. Chrzan, N. Hansen **1997**, *Acta Mater.* 45, 105–112.
61 D. A. Hughes N. Hansen **2000**, *Acta Mater.* 48, 2985.
62 T. G. Langdon, M. Furukawa, M. Nemoto, Z. Horita **2000**, *JOM* 52(4), 30–33.
63 X. Z. Liao, A. R. Kilmametov, R. Z. Valiev, H. Gao, X. Li, A. K. Mukherjee, J. F. Bingert, Y. T. Zhu **2006**, *Appl. Phys. Lett.*, 88, 021909.
64 V. V. Rybin, A. A. Zisman, N. Yu. Zolotarevskii **1985**, *Phys. Solid State* 27 (1), 181–186.
65 V. V. Rybin, A. A. Zisman, N. Yu. Zolotarevsky **1993**, *Acta Metall. Mater.* 41, 2211–2217.
66 M. Motylenko, V. Klemm, P. Klimanek, T. Pavlovitch, H. Straube **2004**, *J. Alloys Compd.* 378 (1-2), 93-96.
67 A. A. Nazarov, N. A. Enikeev, A. E. Romanov, T. S. Orlova, I. V. Alexandrov, I. J. Beyerlein, R. Z. Valiev **2006**, *Acta Mater.* 54, 985–995.
68 A. A. Nazarov, N. A. Enikeev, T. S. Orlova, A. E. Romanov, I. V. Aleksandrov, R. Z. Valiev **2005**, *Russ. Metall.* 5, 431–437.
69 R. A. Lebensohn C. N. Tome **1993**, *Acta Metall. Mater.* 41, 2611–2624.
70 I. J. Beyerlein, R. A. Lebensohn, C. N. Tomé **2003**, *Mater. Sci. Eng. A* 345, 122.
71 A. A. Nazarov, A. E. Romanov, R. Z. Valiev **1995**, *Nanostr. Mater.* 6, 775.
72 R. Z. Valiev **1995**, *Nanostruct. Mater.* 6 (1), 73–82.
73 A. A. Nazarov, A. E. Romanov, R. Z. Valiev **1996**, *Scr. Mater.* 34, 729-734.
74 A. A. Nazarov **1997**, *Scr. Mater.* 37, 1155.
75 A. A. Nazarov **2000**, *Interface Sci.* 8, 315–322.
76 R. T. Murzaev A. A. Nazarov **2006**, *Phys. Met. Metallogr.* 100, 228.
77 E. Schafler, G. Steiner, E. Korznikova, M. Kerber, M. J. Zehetbauer **2005**, *Mater. Sci. Eng. A* 410–411, 169.
78 R. Z. Valiev, E. V. Kozlov, Yu. F. Ivanov, J. Lian, A. A. Nazarov, B. Baudelet **1994**, *Acta Metall. Mater.* 42, 2467–2475.

79 N. Q. Chinh, P. Szommer, Z. Horita, T. G. Langdon **2006**, *Adv. Mater.* 18, 34–39.

80 R. Valiev, **2002**, *Nature* 419, 887–889.

81 Y. Wang, M. Chen, F. Zhou, E. Ma **2002**, *Nature* 419, 912–915.

82 X. Zhang, H. Wang, R. O. Scattergood, J. Narayan, C. C. Koch, A. V. Sergueeva, A. K. Mukherjee **2002**, *Acta Mater.* 50, 4823–4830.

83 H. Mughrabi, H. W. Höppel, M. Kautz, R. Z. Valiev **2003**, *Z. Metall.* 94, 1079–1083.

84 Y. S. Park, K. H. Chung, N. J. Kim, E. J. Lavernia **2004**, *Mater. Sci. Eng. A* 374, 211–216.

85 C. C. Koch **2003**, *Scr. Mater.* 49, 657.

86 R. Z. Valiev, A. V. Sergueeva, A. K. Mukherjee **2003**, *Scr. Mater.* 49, 669–674.

87 T. G. Nieh, J. Wadsworth, O. D. Sherby **1997**, *Superplasticity in Metals Ceramics*, Cambridge University Press, Cambridge,.

88 H. Van Swygenhoven, **2002** *Science* 296, 66–67.

89 V. Yamakov, D. Wolf, S. R. Phillpot, A. K. Mukherjee, H. Gleiter **2002**, *Nature Mater.* 1, 1–5.

90 J. Schiøtz K. W. Jacobsen **2003**, *Science* 301, 1357–1359.

91 Z. Budrovic, H. Van Swygenhoven, P. M. Derlet, P. Van Petegem, B. Schmitt **2004**, *Science* 304, 273–276.

92 H. Van Swygenhoven, P. M. Derlet, A. G. Frøseth **2004**, *Nature Mater.* 3, 399–403.

93 M.G. Zelin, N. A. Krasilnikov, R. Z. Valiev, M. W. Grabski, H. S. Yang, A. K. Mukherjee **1994**, *Acta Metall. Mater.* 42, 119–126.

94 H. Hahn K.A. Padmanaban **1997**, *Philos. Mag. B* 76, 559.

95 M. Chen, E. Ma, K.J. Hemker, H. Sheng, Y. Wang, X. Cheng **2003**, *Science* 300, 1275–1277.

96 X. Z. Liao, F. Zhou, E. J. Lavernia, D.W. He, Y. T. Zhu **2003**, *Appl. Phys. Lett.* 83, 5062–5064.

97 H. W. Höppel, Z. M. Zhou, H. Mughrabi, R. Z. Valiev **2002**, *Philos. Mag. A* 82, 1781–1794.

98 A. Vinogradov S. Hashimoto **2003**, *Adv. Eng. Mater.* 5, 351–358.

99 T. C. Lowe Y. T. Zhu **2003**, *Adv. Eng. Mater.* 5, 373–378.

100 Y. Wang, E. Ma, R. Z. Valiev, Y. T. Zhu **2004**, *Adv. Mater.* 16, 328–331.

101 M. Gell **1994**, *JOM* 46, 30–34.

102 D. M. Brunette, P. Tengvall, M. Textor, P. Thomen **2001**, *Titanium in Medicine*, Springer, Berlin Heidelberg.

103 Y. T. Zhu, T. C. Lowe, T. G. Langdon **2004**, *Scr. Mater.* 51, 825–830.

104 M. D. Morehead, Y. Huang, Y. T. Zhu, T. C. Lowe, R. Z. Valiev **2006**, *Transactions of the North American Manufacturing Research Institute of SME* 34, 539–546.

105 C. Xu, M. Furukawa, Z. Horita, T. G. Langdon **2003**, *Acta Mater.* 51, 6139–6149.

106 A. J. Barnes **2001**, *Mater. Sci. Forum* 357–359, 3.

107 A. Ball M. M. Hutchison **1969**, *Metal Sci. J.* 3, 1.

108 T.G. Langdon **1994**, *Acta Metall. Mater.* 42, 2437.

109 R. Z. Valiev, D. A. Salimonenko, N. K. Tsenev, P. B. Berbon, T. G. Langdon **1997**, *Scr. Mater.* 37, 1945–1950.

110 S. X. McFadden, R. S. Mishra, R. Z. Valiev, A. P. Zhilyaev, A. K. Mukherjee **1999**, *Nature* 398, 684–686.

3
Nonmetallic Bulk Nanomaterials

Dieter Vollath and Dorothée V. Szabó

3.1
Introduction

Nonmetallic nanomaterials are very interesting as they may be ceramic or semiconducting materials. Of special interest are the mechanical, magnetic, electrical, and optical properties. A whole chapter has been devoted to mechanical properties, hence this contribution is restricted to the other physical properties. In most cases, the interesting physical properties of nanomaterials are those of one isolated particle. Two or more nanoparticles together will interact and modify the properties. This interaction may destroy the properties of the particles and lead to new altered ones. As for technical applications, one particle is not sufficient, it is necessary to bring many particles together to form bulk material. The application of such a bulk material is controlled by the properties of the individual particles and their interaction. This interaction has to be controlled in order to tailor the properties for the envisaged application in an optimum way. Consequently, this leads to nanocomposites. In most cases, such composites consist of an active phase represented by nanoparticles, embedded in a second phase. This second phase may be polycrystalline or glassy, ceramic or polymer. In a simplified way, Fig. 3.1 displays the structure of such a composite.

In some cases, especially in ceramic–ceramic nanocomposites, there is a mutual solubility between the nanoparticles and the host phase. In this case it is necessary to have a diffusion barrier between these two phases. The most famous example of such a highly developed nanocomposite is the well-known gold ruby glass [1]. In this case, the red color is a consequence of gold nanoparticles with sizes in the range between 20 and 50 nm. As the gold is soluble in alkaline containing glasses, a tin oxide layer protects these nanoparticles. This arrangement is displayed schematically in Fig. 3.1 (b). However, this second phase is not necessarily just a distance holder. In many cases, it contributes directly to the properties of the bulk material. Additionally, the nanoparticulate phase may be distributed stochastically or well ordered. Both cases are observed. It is well known that the ordering process contributes significantly to the properties of the material. The structure of an ordered nanocomposite is displayed schematically in Fig. 3.1 (c).

Bulk Nanostructured Materials. Edited by M. J. Zehetbauer and Y. T. Zhu

ISBN: 978-3-527-31524-6

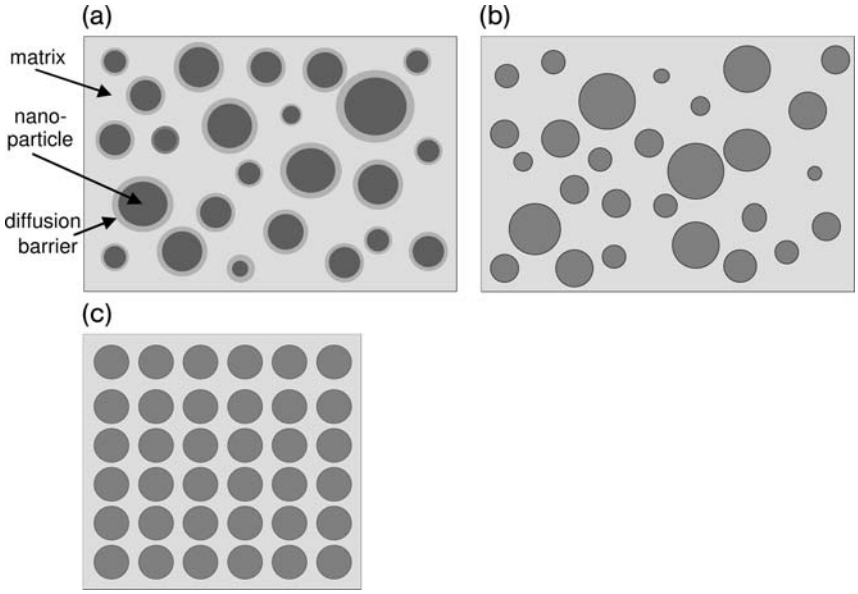

Fig. 3.1 (a) Schematic structure of a nanocomposite, consisting of nanoparticles stochastically distributed in a matrix. (b) Nanocomposite consisting of nanoparticles coated with a diffusion barrier, distributed in a matrix. This corresponds schematically to the structure of gold ruby glass. (c) Structure of an ordered nanocomposite consisting of nanoparticles in a matrix.

It is quite difficult to produce nanocomposites with structures close to the ideal ones. Figure 3.2 shows typical examples for different nanocomposites. The elementary case of a ceramic–ceramic composite is displayed in Fig. 3.2 (a) [2]. In this case, the nanoparticles consisted of zirconia and the matrix of alumina. This combination of materials was selected because of the good contrast in electron microscopy. A little different is the material displayed in Fig. 3.2 (b), a ceramic–polymer composite. In this case, the ceramic phase consisted of maghemite, γ-Fe_2O_3; the polymer was PMA [2]. Absolutely different is the composite displayed in Fig. 3.2 (c), which is close to a perfectly ordered one. This electron micrograph displays a mixture of particulate Fe_3O_4 in a $Fe_{58}Pt_{42}$ matrix. This well-ordered mixture is the starting product to obtain a Fe_3Pt–FePt nanocomposite [3].

Furthermore, one must keep in mind that properties of nanoparticles are grain-size dependent. Therefore, to obtain a product with well-defined properties a narrow particle-size distribution is essential. However, in some cases a broad distribution of properties is requested, as for the emission of white light. In this case, the size distribution of the active nanoparticulate phase must be very broad. The technical realization of these two requirements is equally difficult.

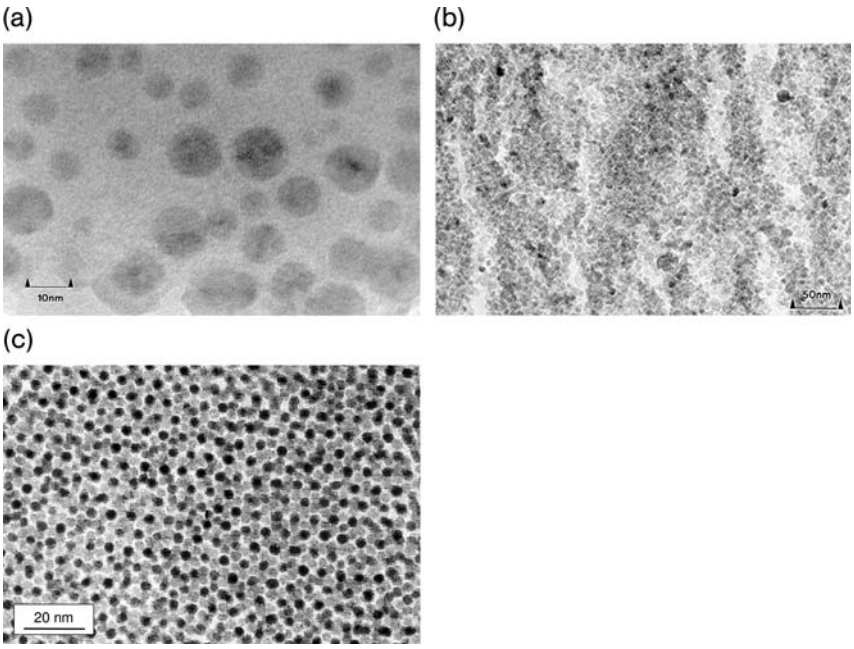

Fig. 3.2 (a) Nanocomposite made of zirconia nanoparticles and an alumina matrix, after (Fig. 5 in [2]). (b) Nanocomposite made of γ-Fe_2O_3 and PMA after (Fig. 6 in [2]). (c) Electron micrograph showing a mixture of particulate Fe_3O_4 in a $Fe_{58}Pt_{42}$ matrix after (Fig. 1a in [3])

3.2 Optical Properties

Looking at optical properties, one has to distinguish four different cases.

- adjustment of the index of refraction by adding nanoparticles to polymers
- nanoparticulate pigments in glasses or polymers
- design of special transparent UV absorbers
- luminescent material.

As each one of these cases may fill a book, only the most important basic facts are explained here.

In many applications, it is necessary to adjust the index of refraction of a polymer precisely to a given value. One of the possibilities to do this is the addition of nanoparticles with different indices of refraction. For small concentrations c of nanoparticles, the index of refraction of such a composite $n_{\text{composite}}$ consisting of a matrix with the indices of refraction n_{matrix} for the matrix and n_{particle} for the nanoparticle may be estimated by

$$n_{\text{composite}} = (1 - c)n_{\text{matrix}} + cn_{\text{particle}} \tag{3.1}$$

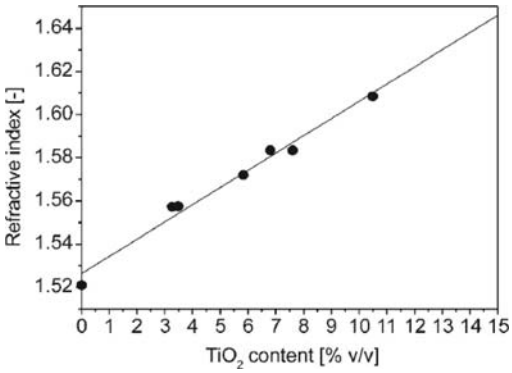

Fig. 3.3 Index of refraction of TiO_2–polyvinyl alcohol (PVA) composite for different TiO_2 particle concentrations after (Fig. 6 in [4]).

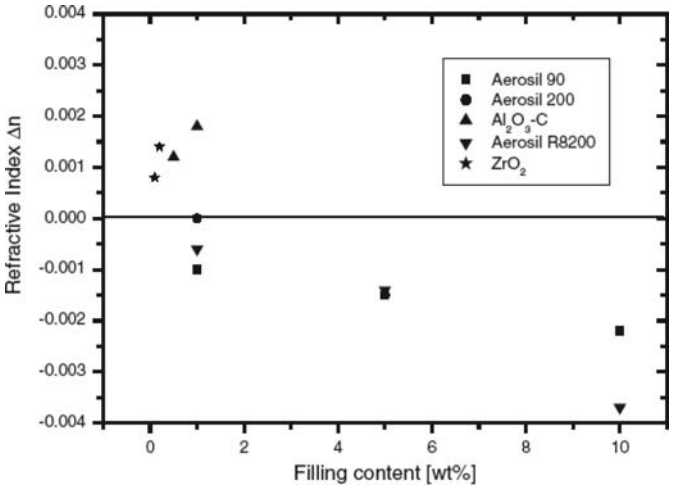

Fig. 3.4 Variation of the index of refraction of PMMA filled with different ceramic nanoparticles according to Boehm et al. (Fig. 10 in [5]).

Equation (3.1) shows that to adjust a certain index of refraction one needs either a smaller concentration c of nanoparticles with high index of refraction or a larger amount of particles with lower index of refraction. This linear relationship of the index of refraction with particle volume concentration is displayed in Fig. 3.3 – which shows the index of refraction of TiO_2–polyvinyl alcohol (PVA) composite for different TiO_2 particle concentrations. Within the accuracy of the experiment, the linear correlation given in Eq. (3.1) is fulfilled exactly, even at concentrations of more than 10 vol% that are not longer "small" concentrations [4].

Figure 3.4 displays the change of the index of refraction of PMMA with different ceramic nanoparticles [5]. Table 3.1 gives the indices of refraction for the different materials used for the graph in Fig. 3.4.

Table 3.1 Indices of refraction for different materials.

Material	Index of refraction
PMMA used as matrix	1.49
ZrO_2	2.20
Aerosil[a)] 90	1.45
Aerosil[a)] 200	1.45
Aerosil[a)] R8200	1.45
Al_2O_3-C	1.76

a) Aerosil are SiO_2 powders produced by DEGUSSA

Figure 3.4 shows clearly that adding particles with refractive index higher than the matrix, such as ZrO_2 and Al_2O_3, leads to an increase of the refractive index and vice versa, as shown with the silica additions. As Fig. 3.4 gives weight and not volume contents, a significant deviation from Eq. (3.1) is observed.

To obtain transparent material it is necessary to reduce light scattering at the nanoparticles in the composite. The total power P_{scatter} of the scattered light in such a composite is given by:

$$P_{\text{scatter}} = KP_0c\frac{n_{\text{particle}} - n_{\text{matrix}}}{n_{\text{matrix}}^2}\frac{D^6}{\lambda^4} \tag{3.2}$$

In Eq. (3.2) the symbols have the following meaning: K is a constant factor, D is the particle size, and λ is the wavelength of the scattered light. From Eq. (3.2) it is obvious that the particle size is very crucial as it enters with the power of six. Therefore, a very narrow particle-size distribution is indispensable as even a few larger particles contribute more than proportional to the scattering power. It is important to note the D is the optically active particle size that means the size of nanoparticle clusters, if some are present. Obviously, Eq. (3.2) does not allow clusters of particles. Generally, as a rule of thumb, one may assume perfect transparent composite, if the largest particles are smaller than a tenth of the wavelength under consideration. As the shortest wavelength visible to the human eye is 400 nm; this rule says that the largest particle must not exceed 40 nm if a material has to be transparent for the whole range of visible light. However, Eq. (3.2) is not proposing a small difference between the indices of refraction between matrix and particles, as a small difference necessarily leads to a higher concentration of particles. An optimization may be obtained looking at the concentration. Assuming perfect blending of the particles in the matrix the concentration c_n for clusters consisting of n particles is, to a first approximation:

$$c_n = c^n \tag{3.3}$$

Therefore, only small concentrations of particles with high refractive index can reduce the number of scattering clusters and thereby the amount of scattered

light. However, the use of coated particles – in this case ceramic particles individually coated with the matrix polymer – alleviates this problem totally. Typical examples are alumina-coated particles, as alumina does not show any catalytic activity. This allows the optimization of the system using particles with small index of refraction.

Essentially the same considerations are necessary in the design of transparent UV absorbing materials, such as paints or lacquers. The only difference is the necessary strong absorption in the UV region. Typical absorbers, colorless to the human eye, are TiO_2, ZnO, ZrO_2, and so forth. However, one has to be very careful in selection of these absorbing materials, as there are two important points to be considered:

- All oxides used as UV absorber are photocatalytically active materials.
- The onset wavelength of the absorption is wavelength dependent.

The photocatalytic activity of the nanoparticles must not lead to a self-destruction of the composite system. This point must be checked carefully before fixing a combination of polymer matrix and nanoparticles. When in doubt, the active UV absorbing nanoparticle must be coated with a second catalytically inactive ceramic material such as alumina.

As an example of the particle-size dependency of the UV absorption, the absorption of light in wavelength range from 200 nm to 600 nm is plotted in Fig. 3.5 [6]. The pigmentary material has a mean value of the particle size of 200 nm, whereas that of the ultrafine material is around 20 nm. In this figure, the blue shift of the absorption maximum is evident. This blue shift with de-

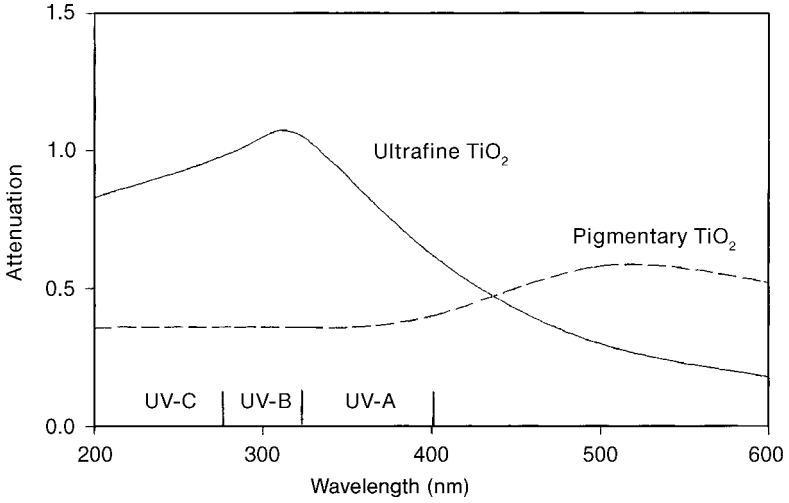

Fig. 3.5 UV absorption of different TiO_2 particles in the wavelength range from 200 nm to 600 nm after (Fig. 1 in [6]).

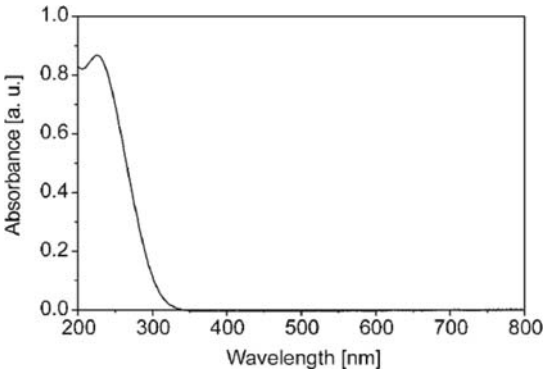

Fig. 3.6 UV/VIS spectrum of a 0.037 wt% TiO_{22} in PVA nanocomposite, showing the absorption maximum of TiO_2 nanoparticles at 225 nm, after (Fig. 4 in [4]).

creasing particle size is typical of the optical properties of nanoparticles. This will be discussed later in this section.

For both types of materials, the onset of absorption is quite flat, indicating a relatively broad particle-size distribution. This is significantly different in the absorption spectrum displayed in Fig. 3.6 [4]. In this figure, the absorption of a 0.037 wt% TiO_2 in PVA nanocomposite is displayed. The nearly negligible background absorption arising from the PVA is subtracted. Additionally, in this case, the particle size was significantly smaller, as one may realize by the remarkable blue shift of the onset of absorption.

Furthermore, as a consequence of the narrow particle-size distribution, the maximum of the absorption is very narrow, in contrast to the products displayed in Fig. 3.5. Provided the particles are isolated, a material as shown in Fig. 3.6 is perfectly transparent in the visible region.

A further interesting optical application of ceramic/polymer nanocomposites is their use as magneto-optical materials. The phenomena in question are in this context the Faraday effect, the rotation of the plane of polarization of light in transmission, and the Kerr effect, the rotation of the polarization plane after reflection at the surface of magnetic materials. Usually, for optomagnetic devices, thin films of ferromagnetic materials are used. The first attempts in this directions use nanoparticulate ferrites in polymer matrix [7]. However, better results are obtained with ferrite–silica nanocomposites. All these materials are hampered by the high absorption of visible light by ferrites. Therefore, useful applications are possible only in the range of red light. Zhou et al. [8] synthesized $ZnFe_2O_4$ nanoparticles in silica. The magnetization curves of this material were, at least down to a temperature of 78 K, free of hysteresis. Figure 3.7 displays the optical absorption coefficient as a function of the wavelength for a particle concentration of 30 (curve a) and 5 wt% (curve b).

As expected, it is obvious that the increase of ferrite concentration increases the optical absorption. Furthermore, the strong increase of absorption for the

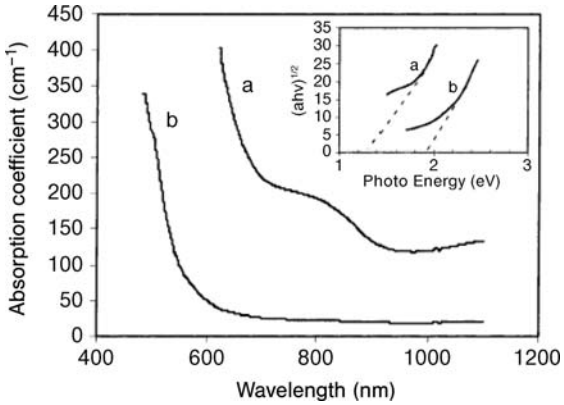

Fig. 3.7 Optical absorption coefficient as a function of the wavelength for $ZnFe_2O_4$ nanoparticles in a silica matrix. Two different particle concentrations are measured, (a) 30%, (b) 5%. Data according to (Fig. 5 in [8]).

shorter wavelengths is shifted significantly to shorter wavelengths. This blue shift may be attributed to a smaller particle size or surface phenomena in the bandgap. The insert in Fig. 3.7 is related to the relationship between optical absorption and bandgap energy E_g [9],

$$(ahv)^{0.5} = const\,(hv - E_g) \tag{3.4}$$

with h = Plank's constant and v = the frequency of the light. Extrapolating the energy-rich, linear part of the graph described by Eq. (3.4), $(ahv)^{0.5} \rightarrow 0$ gives the optical bandgap. In this case, for the specimen with 30 wt% ferrite the value is 1.25 eV and for the 5 wt% one the energy gap is 1.9 eV. Data on the optical reflectance in the UV-VIS range of γ-Fe_2O_3–SiO_2 nanocomposites are given by Moreno et al. [10].

Most important are optical properties connected to light emission. Especially in this field, one observes a series of phenomena characteristic of nanoparticles. One of the most important groups of properties is connected to quantum confinement. Quantum confinement is observed in the case of interaction of very small nanoparticles with light, when free electrons and holes are created. In this case, the hole and the electron form a hydrogen-like complex, an exciton. Depending on the properties of the particle, the exciton radius, called the "exciton Bohr radius" may be in the range between a tenth and a few nanometers. Quantum confinement occurs when one or more of the dimensions of a nanocrystal are smaller than the diameter of the exciton. In this case, absorption and emission of light is particle-size dependent. It is one of the few cases where a quantum phenomenon can be described in good approximation without applying Schrödinger's equation.

In the simplest case, quantum-confinement systems of nanoparticles are described like a particle in a box with infinitely high walls. The assumption of infinite walls is justified in the case of insulating ceramic materials and – in most cases with good approximation – for semiconductors, too. This is an idealized description of a free electron in a nanoparticle with the diameter of L. Generally, this problem of a confined particle is solved using the Schrödinger equation. However, this model can be described with a simplified approach using the basic rules of quantum mechanics. The condition for a standing wave consisting of n half-waves in a box is:

$$\frac{n\lambda}{2} = L \tag{3.5}$$

Substituted into the de-Broglie relationship this leads to:

$$p = mv = \frac{h}{\lambda} = \frac{nh}{2L} \tag{3.6}$$

In Eq. (3.6), p is the momentum, m the mass and v the velocity of the electron; h is Plank's constant. Now, one can calculate the energy E_n and obtains

$$E_n = \frac{mv^2}{2} = \frac{p^2}{2m} = \frac{n^2h^2}{8mL^2} = K\frac{n^2}{L^2} \tag{3.7}$$

Equation (3.7) gives the main characteristic of quantum-confinement systems, as it shows that the energy of the electron is inversely quadratic to the particle size. Lastly, this describes the blue shift of the absorption edges. The energy difference between two energy levels n and n+1 describes the energy of an emitted wave.

$$\Delta E = \frac{(2n+1)h^2}{8mL^2} \quad \text{leading to} \quad \lambda = \frac{8mcL^2}{(2n+1)h} \tag{3.8}$$

This equation clearly shows the blue shift with decreasing particle size L. However, one has to bear in mind that blue shift is not only observed in the quantum-confinement case. Even Pauli's principle enforces a blue shift with decreasing particle size. This is illustrated in Fig. 3.8. This figure elucidates the transition from the energy levels of one atom to the energy bands in a crystal. In an atom, each electron sits on one distinct energy level. Each energy level can be populated by one electron only. (Strictly speaking, taking the two possible spins into account these are two electrons, however, this is not important for these considerations.) Bringing two atoms together that form a molecule leads to a splitting of each energy level. This splitting continues with each atom added. Finally, in a crystal, the energy levels form energy bands. The energy difference E_g between two energy bands decreases with increasing size of the crystal. This is shown in Fig. 3.8.

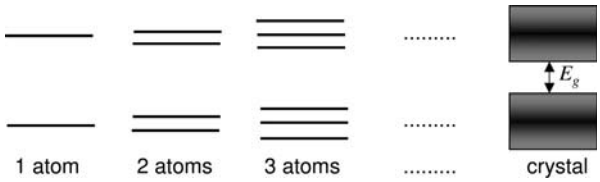

Fig. 3.8 Transition of the energy levels of one atom to the energy bands in a crystal.

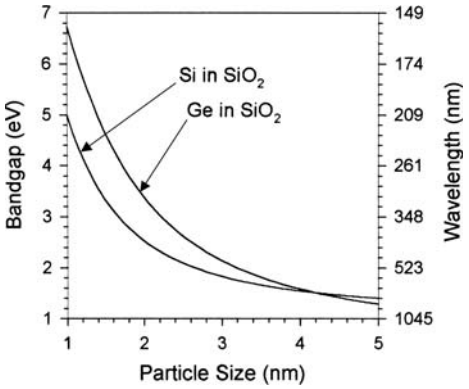

Fig. 3.9 Particle-size-dependent bandgap energy E_g after [11].

An increase of E_g with decreasing particle size leads necessarily to a blue shift of any absorption or emission of photons. A typical example of the particle-size-dependent bandgap energy E_g is given in Fig. 3.9 for silicon and germanium nanoparticles [11]. In this graph the parabolic increase of the bandgap with decreasing particle size is perfectly visible. However, this graph demonstrates in addition that these phenomena are of any importance in the range below approximately 5 nm only.

As mentioned above, the change in the bandgap and quantum-confinement phenomena leads to a blue shift of any interaction with photons. A great example is given by Pratsinis and coworkers [12–14] and is displayed in Fig. 3.10. This figure shows the absorbance due to ZnO as a function of wavelength and particle size. The blue shift with decreasing particle size from 12 nm over 4 nm to 3 nm is clearly visible. This demonstrates the possibility of tailoring optical properties of nanoparticles just by the particle size.

These elementary considerations are valid for isolated particles and composites with low concentrations of particles. In this case, the concentration is rather defined by the distance between the particles and not by the number of particles. Most of the excited nanoparticles form a dipole. As in organic lumophores, these dipoles may interact. The distance of interaction is at a maximum 10 or 15 nm. Interacting dipoles give rise to excimer formation, altering the

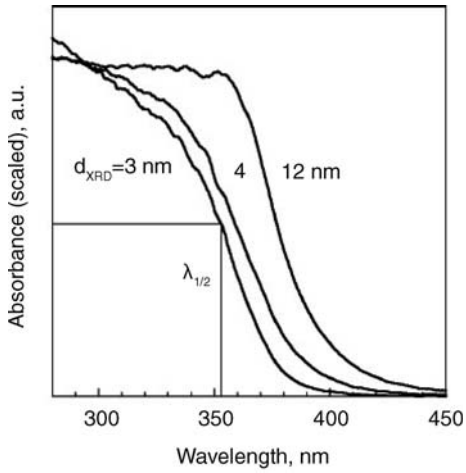

Fig. 3.10 Absorbance of ZnO as a function of wavelength and particle size. Data according to (Fig. 1 in [13]).

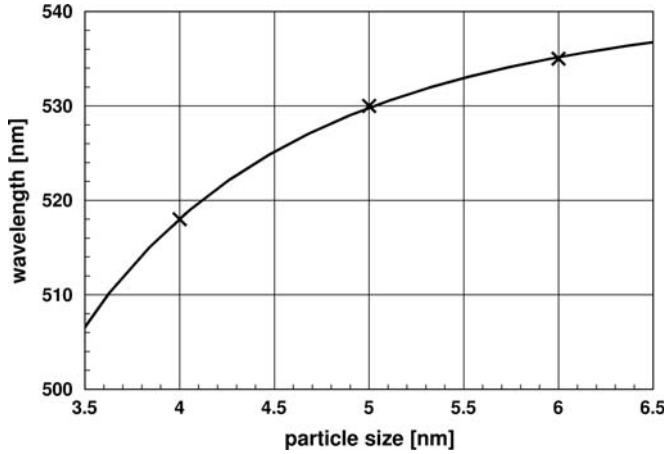

Fig. 3.11 Emission wavelength of ZnO coated with PMMA as a function of the particle size after (Fig. 17 in [2]).

emission spectra significantly. A good example of this is ZnO [15]. In the excited state ZnO exhibits a dipole moment leading to a permanent dipole-induced dipole interaction. This influences the emission wavelength of the composites significantly. In this situation the size dependency of the emitted wavelength is no longer $1/D^2$, rather a dependency with $1/D^3$ is found [2, 15]. As an example, Fig. 3.11 displays the emission wavelength of ZnO coated with PMMA as a function of the particle size [2].

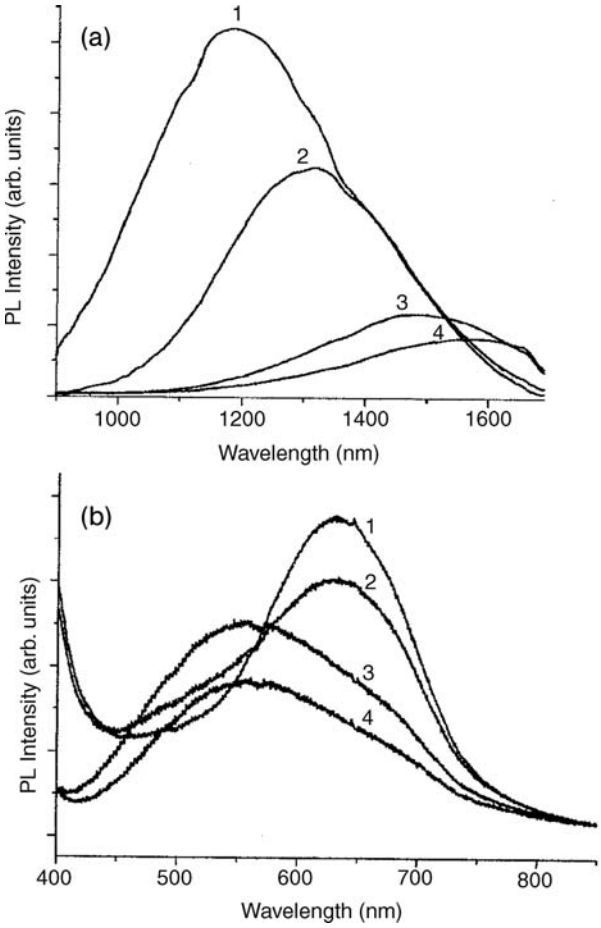

Fig. 3.12 Photoluminescence spectra of PbS in polystyrene in (a) IR and (b) visible light. Data according to (Fig. 10 in [16]).

The materials that are used for quantum-confinement phenomena are ZnO, CdSe, CdS, GaAs, GaN, and so on. In most cases these nanoparticles are applied as particle, especially in biotechnology or as thin films. Applications in bulk materials are relatively rare. In most cases, in bulk materials they are used as pigments or, most interesting, used to enhance electroluminescence. From an economic viewpoint, electroluminescence applications have the highest potential.

Figure 3.12 displays photoluminescence spectra of PbS in polystyrene in the IR (Fig. 3.12 (a)) and in the visible range (Fig. 3.12 (b)) [16].

The emission in the IR was excited by 532-nm photons, whereas the excitation wavelength for the emission in the visible range was 325 nm. Table 3.2 gives the particle size and the maxima of the emission peaks of the samples

Table 3.2 Particle sizes and the maxima of the emission peaks of the samples presented in Fig. 3.12.

Sample number	Particle size (nm)	Emission peak in the IR (nm)
1	6.1	1190
2	6.6	1320
3	7.2	1480
4	7.9	1570

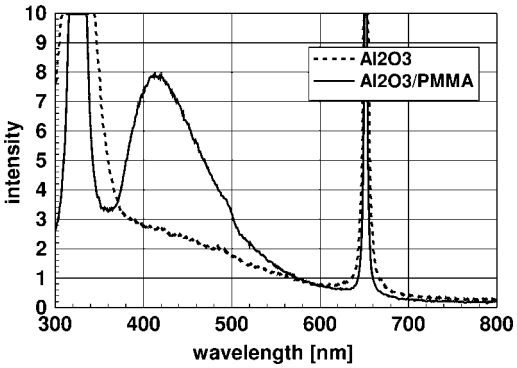

Fig. 3.13 Photoluminescence of bare alumina nanoparticles and alumina core/shell nanoparticles with PMMA coating. Data according to [18].

used for these measurements and indicated by the numbers 1, 2, 3, and 4 in Fig. 3.12.

As expected from the theory of quantum confinement, the wavelength of the emission in the IR decreases with decreasing particle size. This is a further example of the blue shift with decreasing particle size. However, the emission in the visible range does not follow this general rule. The authors do not give any explanation. However, it is well known that the incorporation of nanoparticles in polymers may lead – in case of chemical bonding at the particle surface – to interaction phenomena in bulk polymer parts. Additionally, polymer coating or incorporation in a polymer protects the particles of degrading by interaction with the surrounding atmosphere [17]. A typical example of a luminescence based on the interaction of oxide particles with PMMA is given in Fig. 3.13. In this figure, photoluminescence of alumina without and with PMMA coating is plotted [18]. It is interesting to note that this emission is only dependent on the combination PMMA–oxide and not on the type of the oxide, as long as it is an insulator [19].

Similar phenomena are described for many other combinations of oxides with polymers. Typical examples are the incorporation of oxide nanoparticles in PPV

(poly(p-phenylene vinylene), and CN-PPP (poly[2-(6-cyano-6′methylheptyloxy)1,4-phenylene]) by Musikhin et al. [20].

3.3
Metallic and Semiconducting Nanoparticles in Transparent Matrices

One of the oldest applications of nanoparticles is their use as a pigment in glass. The first known application of these composites goes back to the Assyrians. Approximately 700 BC they documented the composition of a red glass with gold nanoparticles as pigment. Until now the composition of this "gold-ruby-glass" did not change significantly. However, this colored glass is not only used for decoration but also, after grinding, as a pigment. Figure 3.14 displays the absorbance of gold as $HAuCl_4$ in solution (curve a) and as nanoparticles dispersed in polymer (curve b) as demonstrated by Park et al. [21]. In this case the nanoparticles had a size in the range from 5 to 15 nm. Certainly, the position and, therefore, the width of the absorption peak depend strongly on the particle size. This allows adjusting the hue, for example, by temperature treatment of the composite.

In most cases, high-quality products excelling in a clear color are obtained by a narrow particle-size distribution. In a glass, the particle size of the gold is stabilized by adding tin oxide into the glass matrix. Besides gold, nanoparticles of silver, copper, and platinum are often used as colorants for glasses. Additionally, the color can be adjusted by replacing pure metal particles by alloys of gold with other metals. A typical example of a gold–silver alloy with a Au/Ag ratio of 1/2 is displayed in Fig. 3.15 [22].

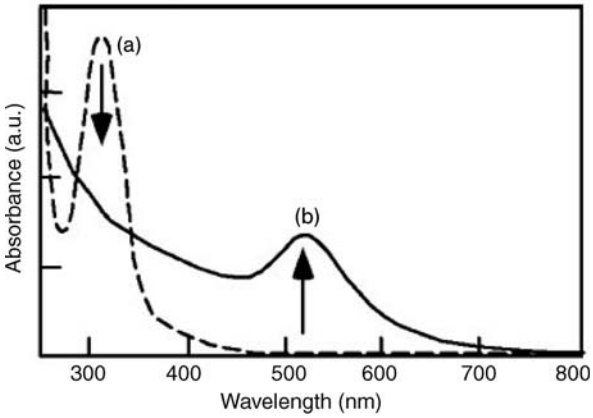

Fig. 3.14 UV/Vis absorbance of gold as $HAuCl_4$ in solution (curve a) and as nanoparticles dispersed in polymer (curve b). Data according to [21].

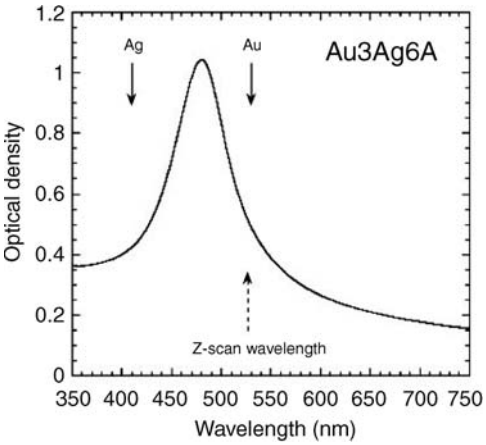

Fig. 3.15 Optical absorption spectrum of a gold–silver alloy. Data according to [22].

In Fig. 3.15, the positions of the absorption maxima of pure silver and gold nanoparticles with equivalent size are indicated. A complete theoretical description of the color of metal nanoparticles in glass is given by Quinten [23].

With regard to the recent technological development, nanoparticles made of semiconducting compounds are getting more and more attention. Originally, nanoparticles made of mixed crystals from the system CdSe–CdS–ZnS–ZnSe dispersed in glass were used as pigments. Nearly all hues from deep red to orange and yellow are obtained in this system. More recently, the luminescence properties of these materials are gaining more and more attention. As an example, Fig. 3.16 (a) displays the absorbance of a series of solid solutions in the system CdSe–CdTe dispersed in silicate glass [24]. The concentration of nanoparticles in the glass was 0.75 wt%. This figure clearly demonstrates the red shift with increasing Te content in the nanoparticles. However, it must be pointed out that this is not a straightforward process. In the phase diagram of the CdSe–CdTe system one observes two phases, on the selenium-rich side the particles crystallize in the wurtzite and on the tellurium side in the sphalerite structure. In the two-phase area, around a ratio Se/Te = 1 a minimum of the absorption is observed. Furthermore, Fig. 3.16 (b) demonstrates that the absorption bands become clearly visible at higher concentrations. The specimen used for this figure consisted of $CdSe_{0.2}Te_{0.8}$. Therefore, they were clearly in the sphalerite one-phase field.

Semiconducting nanoparticles are the original example of quantum-confinement systems. A wonderful series of examples on the behavior of semiconducting nanoparticles was given by Reisfeld [25]. Reisfeld demonstrates the blue shift of nanoparticles with decreasing particle size, using the example of PbS. Figure 3.17 (a) displays the absorbance of PbS nanoparticles as a function of the wavelength for the particle sizes 4.8 nm (curve 1), 5.4 nm (curve 2), and 6.0 nm

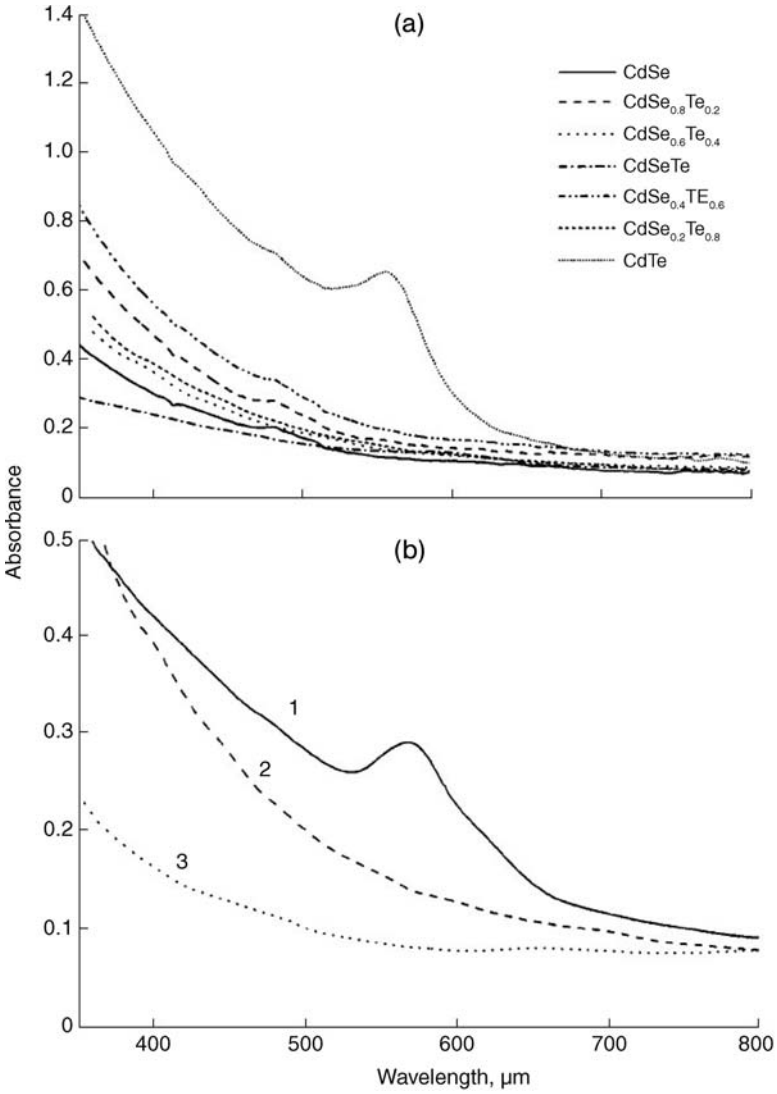

Fig. 3.16 (a) Absorbance of a series of solid solutions in the system CdSe–CdTe dispersed in silicate glass, after [24]. The concentration of nanoparticles in the glass is 0.75 wt%. (b) Absorbance as a function of particle concentration.

(curve 3). Curve 4 gives the absorption of the zirconia substrate. The blue shift of the absorbance is correlated with a widening of the bandgap.

Figure 3.17 (b) displays a plot according to Eq. (3.4). The intersection of the extrapolation of the linear part of the graph gives the bandgap. One clearly sees the widening of the bandgap from 1.42 eV for the 6 nm particles to 1.92 for the

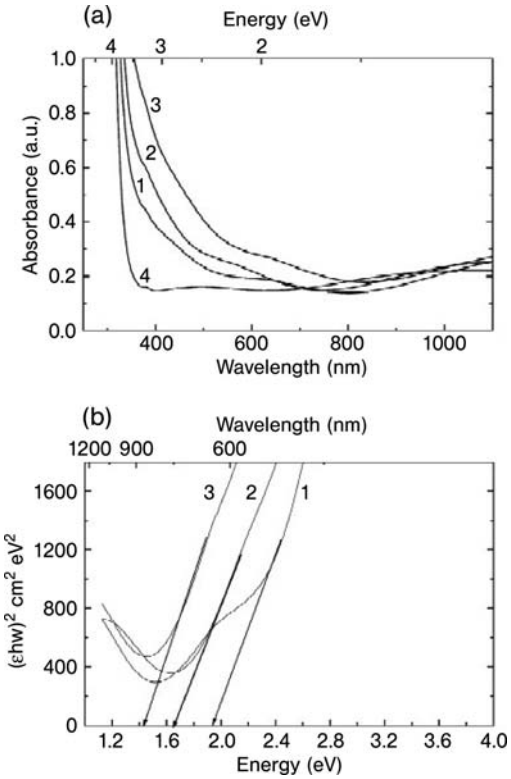

Fig. 3.17 (a) Absorbance of PbS nanoparticles as a function of the wavelength for different particle sizes. (b) Plot according to Eq. (3.4). Data according to [25].

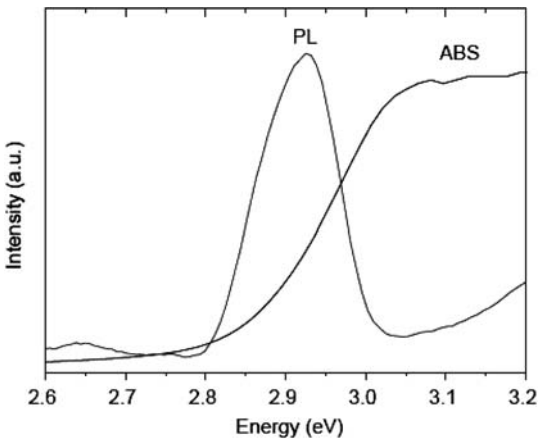

Fig. 3.18 Absorption and photoluminescence spectra of ZnSe in SiO_2. Data taken from [26].

4.8 nm particles. This demonstrates the possibility of adjusting the optical properties, in this case the color, by the particle size, which is, in this example, adjusted by annealing at different temperatures.

As mentioned above, semiconducting particles in a transparent matrix are extremely interesting with respect to their luminescence properties. In this context, Fig. 3.18 displays the absorption and photoluminescence spectra of ZnSe in SiO_2 [26]. The interesting point in Fig. 3.18 is that absorption and luminescence spectra are overlapping. Therefore, the emission of one particle can excite a further particle of the same kind. This allows the transport of information from one to the next particle.

3.4 Magnetic Properties of Bulk Nanomaterials

Magnetic materials based on bulk nanocomposites are of great interest. As in all the other cases, the interaction of the nanoparticles is of crucial importance. In this case, in both directions, in the case of superparamagnetic materials, interaction between the magnetic particles destroys the new properties, in the case of exchange-coupled materials, the properties are the result of particle interaction. Both groups of materials are beginning to show industrial relevance.

3.4.1 Superparamagnetic Nanocomposites

Ferro- or ferrimagnetic materials keep the orientation of their magnetization by their magnetic anisotropy. In the case of nanoparticles consisting of soft magnetic material, the orientation of the magnetization vector is fluctuating. Therefore, in such materials, remanent magnetization is impossible; the coercivity is zero. This most dramatic effect is observed when the thermal energy of the particle is larger than the energy of anisotropy.

For a single isolated magnetic nanoparticle, the condition leading to superparamagnetism is:

$$kT \geq KV \tag{3.9}$$

(K is the constant of magnetic anisotropy, V is the volume of the particle; KV is the energy of magnetic anisotropy, k is Boltzmann's constant, T is the temperature, kT is the thermal energy). From Eq. (3.9) one can derive a temperature T_B

$$T_B = KV/k \tag{3.10}$$

called the blocking temperature. Obviously, the blocking temperature depends on the particle volume, therefore, monosized particles are assumed. In cases where this assumption is not valid, the volume V is replaced by the volume-

weighted mean volume. In superparamagnetic particles, the vector of magnetization is fluctuating thermally between different easy directions of magnetization overcoming the hard directions.

The magnetization M of noninteracting superparamagnetic particles mathematically follows the same law (Langevin's formula) as for paramagnetic materials.

$$M = nm[\coth(mH/kT) - kT/mH] \tag{3.11}$$

m is the magnetic moment of one particle, which is, in a first approximation, proportional to the volume of the particle, n is the number of particles, and H the magnetic field. nm gives the saturation moment of the specimen.

Expanding Eq. (3.11) into a Taylor series for small values of H, one can calculate the susceptibility. For the magnetization M one obtains:

$$M = nm\left[\frac{kT}{mH} + \frac{mH}{3kT} - \frac{\mathrm{kT}}{mH}\right] = \frac{nm^2H}{3kT} \tag{3.12}$$

After differentiating with respect to the susceptibility μ:

$$\mu = \frac{\partial M}{\partial H} = \frac{nm^2}{3kT} \tag{3.13}$$

Equation (3.13) shows that the susceptibility increases quadratically with the magnetic moment of the individual particles. Comparing two specimens with the same saturation moment nm, the one with the larger moment m per particle has the higher susceptibility.

The properties of superparamagnetic materials are often given as temperature independent and as a function of a temperature-independent magnetic quantity $a = mH/kT$, frequently called the "reduced magnetic field". Plotting the magnetization M versus H/T gives a good indication of the validity of Langevin's formula. Figure 3.19 exhibits a typical magnetization curve of a superparamagnetic material, $MnFe_2O_4$ coated with PMMA, for different temperatures [27]. In this graph, it is obvious that at 100, 200, and 300 K the magnetization curves do not show any hysteresis.

However, as an additional consequence of the Langevin function, at low fields there is no linear part existing in the magnetization curve.

As an example of a temperature-reduced magnetization curve Fig. 3.20 displays the graph for a γ-Fe_2O_3 specimen consisting of pressed PMMA-coated particles at 200 and 300 K. The two magnetization curves are nearly identical. The slight difference is caused by a minor interaction of the particles. Obviously, the coating was not thick enough to avoid any interaction between the particles.

This proves that by using coated nanoparticles it is possible to maintain superparamagnetism also in technical parts. The structure of such a pressed body was previously shown in Fig. 3.2 (b). The specimen for electron microscopy

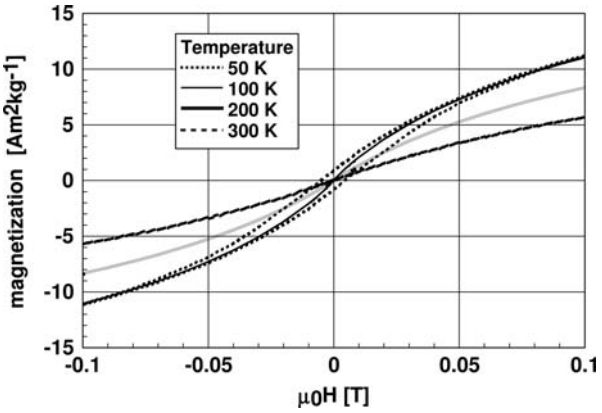

Fig. 3.19 Magnetization curves of a superparamagnetic material, $MnFe_2O_4$ coated with PMMA measured at different temperatures. Data taken from [27].

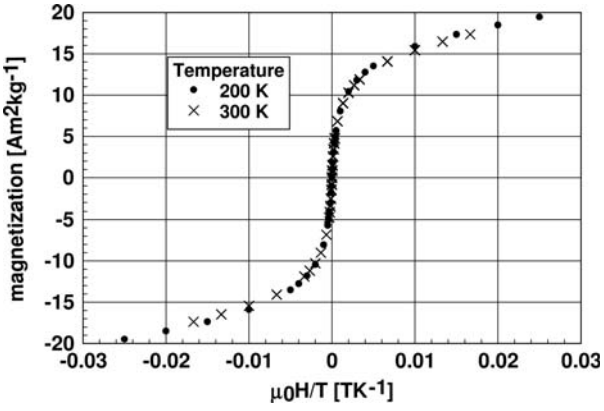

Fig. 3.20 Temperature-reduced magnetization for a γ-Fe_2O_3 specimen consisting of pressed PMMA-coated particles. Data taken from [27].

was prepared by cutting the pressed and sintered body with an ultramicrotome into 20 nm slices. Slip-stick phenomena during this cutting process led to the artefacts visible in this micrograph.

Below the blocking temperature the situation is more complex as hysteresis appears. According to the theory of superparamagnetism [28] the experimentally determined coercitivity H_C at the temperature T is related to H_{C0} the coercivity at 0 K, and T_B the blocking temperature:

$$\frac{H_C}{H_{C0}} = 1 - \left(\frac{T}{T_B}\right)^{0.5} \tag{3.14}$$

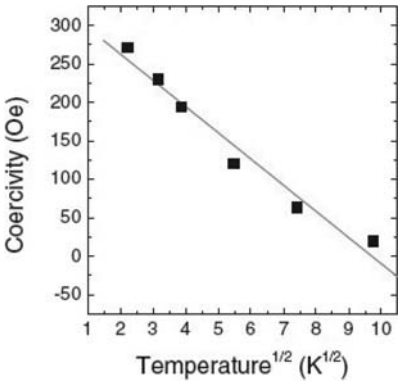

Fig. 3.21 Coercitivity as a function of $T^{0.5}$. Data taken from (Fig. 4a in [29]).

Figure 3.21 displays a graph showing coercitivity as a function of $T^{0.5}$ presented by Jeong et al. [29]

This linearization is well suited to determine the blocking temperature and coercitivity at 0 K. In the example given in Fig. 3.21 one finds $T_B = 119.5$ K and $H_{C0} = 0.0337$ T.

Comparing the saturation magnetization visible in Fig. 3.20 with those of material with grain sizes in the micrometer region, one realizes significantly lower values of the saturation magnetization. The relaxation time governs the ability of the particles to follow a change in external magnetic field with the frequency f. When $\tau < 1/f$ the particle is able to follow the external frequency, therefore, remanence and coercitivity are zero. When $\tau > 1/f$ hysteresis is observed.

Theoretically, the saturation magnetization of γ-Fe_2O_3 is approximately 75 Am^2 kg^{-1}. For nanoparticles this value is not observed, experimentally. This is caused by a surface layer of each particle in the matrix with reduced magnetization. Due to spin-canting phenomena at the surface of magnetic particles, the spins are not as well ordered as is observed in the interior [30]. This phenomenon is only of importance in the case of nanoparticles, since for conventional materials, the surface/volume ratio is a few orders of magnitude smaller than that of nanomaterials. Figure 3.22 displays the dependency of the saturation magnetization of the particle size according to Han et al. [31]. This graph clearly shows the expected decrease of the saturation magnetization.

Further experimental results show a linear decrease of the saturation magnetization with inverse surface area [32]. In a simplified manner, ferrite nanoparticles with a diameter d consist of a magnetic active core and a nonmagnetic surface layer with the thickness δ. This leads to a reduced saturation magnetization of:

$$M_{\text{nanoparticle}} = \frac{(d - 2\delta)^3}{d^3} M_{\text{macroscopic}} \tag{3.15}$$

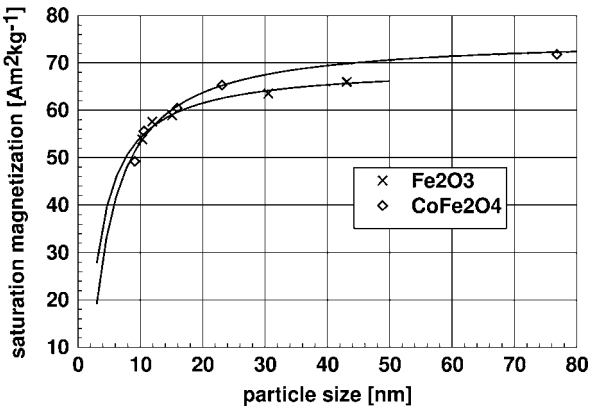

Fig. 3.22 Saturation magnetization as a function of the particle size for two different nanoscaled ferrites. Data taken from [31].

$M_{\text{nanoparticle}}$ is the saturation magnetization of the nanoparticles and $M_{\text{macroscpic}}$ that expected theoretically for macroscopic particles. The fit shown in Fig. 3.22 is based on this formula. In the case of γ-Fe_2O_3 the fits lead to a thickness of the nonmagnetic surface layer of 0.8 nm and 1.0 nm for $CoFe_2O_4$. Considering a particle size of 5 nm and a thickness of the nonmagnetic surface layer of 1.0 nm, one can expect only 20% of the saturation magnetization of bulk materials. This reduces the possibilities of application.

In bulk materials, dipole–dipole interaction of the particles cannot be excluded completely. In this case one has to find an optimum between the superparamagnetic properties and the density of magnetically active particles in the matrix. The interaction of the particles in a matrix leads to magnetically larger particles that may be no longer superparamagnetic. Caizer et al. [33] describe the fictitious increase of the particle size of γ-Fe_2O_3 in an amorphous silica matrix by a reduction of the thickness of the nonmagnetic layer. These authors show that even a concentration as low as 0.68 vol% does not eliminate particle interaction. In the discussed case a virtual decrease of the particle size from 11.7 nm at 70 K to 10.1 nm at room temperature was observed. The detailed results are presented in Fig. 3.23. It is interesting to see that with increasing temperature the thermal energy more and more overcomes the dipole–dipole interaction, apparently resulting in a decreased particle size.

The magnetization curves depicted in Figs. 3.19 and 3.20 are related only to the time constant of the measuring device, in most cases approximately 100 s. However, for the definition of superparamagnetism, time constants are crucial. Looking at superparamagnetism of bulk materials, one has to realize that the magnetic particles are spatially fixed particles. This is Néel or intrinsic superparamagnetism [34]. The time needed by the particles to follow a change in the direction of the magnetic field is called the relaxation time, limiting the maximum frequency of application. However, superparamagnetism is a consequence

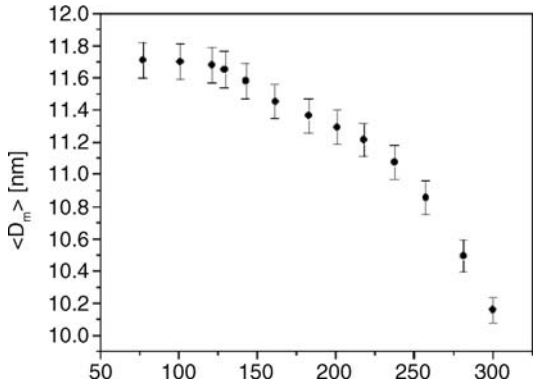

Fig. 3.23 Calculated mean magnetic diameter of nanoparticles as a function of temperature. Data according to (Fig. 10 in [33]).

of thermal fluctuations of the magnetization vector, a random process. Therefore, one cannot give a frequency of fluctuation, rather the mean value of the time between two fluctuations, the relaxation time τ. The relaxation time governs the ability of the particles to follow a change of an external magnetic field with the frequency f. When $\tau < 1/f$ the particle is able to follow the external frequency; therefore, remanence and coercitivity are zero. When $\tau > 1/f$, hysteresis is observed. According to Néel [34] the relaxation time is given by

$$\tau = \tau_0 \exp(KV/kT) \tag{3.16}$$

where τ_0 is a material-dependent constant factor in the range between 10^{-9} and 10^{-13} s. At room temperature, the frequency of thermal relaxation may be well beyond 1 GHz, provided that the composition and particle size of the ferrite are selected properly. The basis for selection is the Aharoni [35] relationship for τ_0:

$$\tau_0 \propto m/K \propto V/K \tag{3.17}$$

Equation (3.17) shows that small values of τ_0 are obtained only with materials showing large values of the magnetic anisotropy K, as τ_0 increases with increasing magnetic moment m of the particles, which is proportional to the particle volume. However, according to Eq. (3.17), a small volume leading to short relaxation times reduces the magnetic moment of the particle too much.

As described by Eq. (3.13), for noninteracting particles, μ increases quadratically with the magnetic moment of the particle. For technical applications, a small value of the relaxation time and a large susceptibility is desired. In this respect, Eqs. (3.13) and (3.17) are contradictory; superparamagnetic materials can be optimized for either high susceptibility or short relaxation time.

Figure 3.24 exhibits the magnetic susceptibility of different ferrite nanoparticles as a function of frequency in comparison to a conventional ferrite [2].

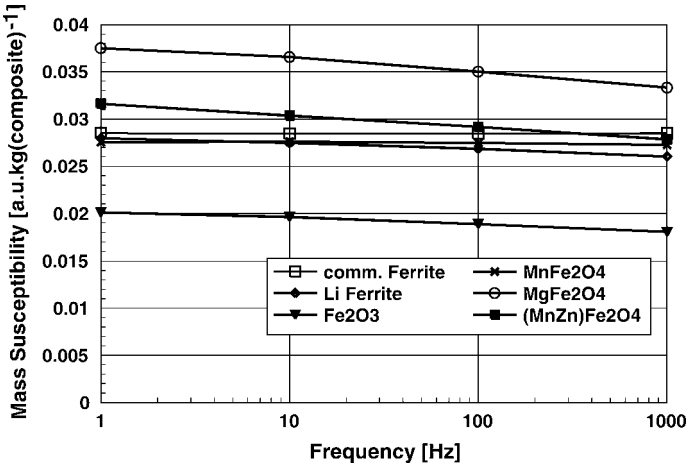

Fig. 3.24 Magnetic susceptibility of different ferrite nanoparticles as a function of frequency in comparison to a conventional ferrite (Fig. 10 in [2]).

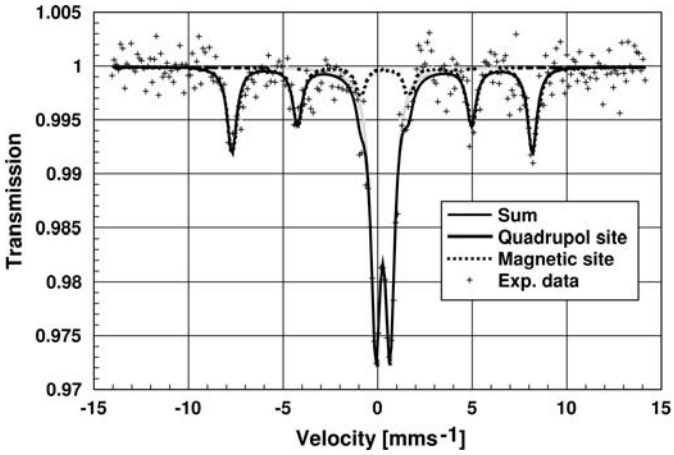

Fig. 3.25 Mößbauer spectrum of a partly superparamagnetic sample. Data according to (Fig. 9 in [36]).

It is remarkable that the magnetic susceptibility of the nanocomposites is in the same range as it is for conventional ferrites. In contrast to conventional ferrites, the susceptibility of nanoparticulate ferrites decreases with increasing frequency. The reason for the decreasing susceptibility is found in the interaction and energy distribution of the different particles. This phenomenon can be reduced with smaller particle size and a larger distance between the magnetic particles. This measure reduces susceptibility.

Lastly, the Mößbauer spectrum is the ultimate proof of Néel superparamagnetism and, the only proof accepted nowadays. Figure 3.25 shows the Mößbauer

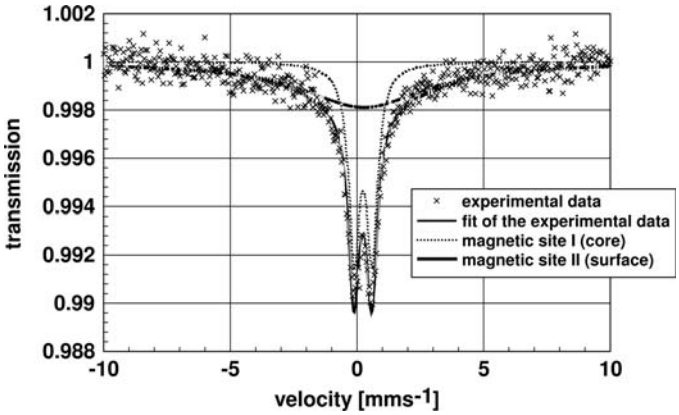

Fig. 3.26 Mößbauer spectrum of a nanoscaled ferrite, consisting of two components. One is the superparamagnetic ferrite core of the particle and the other one represents the surface of the particles. Data according to (Fig. 11 in [2]).

spectrum of a partly superparamagnetic specimen [36]. One realizes a superposition of a doublet with a sextet.

In Fig. 3.25, the sextet represents the conventional ferrite, whereas the doublet is characteristic of superparamagnetic material. The splitting of the sextet is directly proportional to the magnetic crystal field. However, it must be pointed out that this is the mean value of the crystal field that is seen by the nucleus during one revolution. Above the blocking temperature, this mean value is zero because the fluctuation frequency of the magnetic crystal field is larger than the Lamor frequency of the nucleus. Therefore, in superparamagnetic materials the Mößbauer spectrum consists only of the doublet, which is typical of nonmagnetic materials.

Looking in great detail at the Mößbauer data of superparamagnetic materials, often one realizes an imperfect fit at the minima and the maximum of the doublet. This is because Mößbauer spectra of such materials consist of two components. One is the superparamagnetic ferrite core of the particle and the other one represents the surface of the particles. As mentioned above, due to spin-canting phenomena, the surface is magnetically less ordered than the core. Therefore, the core is represented by a doublet, whereas the surface layer is characterized by a broad maximum. An example displaying a complete fit taking into account the surface is depicted in Fig. 3.26 [2].

The analysis of the Mößbauer spectrum in Fig. 3.26 revealed the surface layer to represent 60% of the volume, and a magnetic core to represent 40% of the particle. Therefore, the saturation magnetization is, at maximum, only 40% of the theoretically possible value. Assuming a 0.8-nm nonmagnetic surface layer, leads to a particle size of approximately 6 nm. Both estimations fit perfectly with the experimental results.

A special property of bulk superparamagnetic materials is superferromagnetism. Morup and Christiansen [37] were the first to observe this phenomenon. As in the case of paramagnetic materials, where the interaction of the atomic dipoles leads to ferromagnetism, in superparamagnetic materials, an interaction of the magnetic dipoles, as being represented by the particles, leads to superferromagnetism. It is essential for superferromagnetism that all particles have nearly the same size.

3.4.2 Magnetic Refrigeration

A potentially important application of bulk superparamagnetic materials is magnetic refrigeration. Instead of ozone-depleting refrigerants and energy-consuming compressors, this application uses nanocomposites in a magnetic field. Magnetic cooling has been used for decades in low-temperature physics. Magnetic cooling applies the fact that in a magnetic field magnetic dipoles are oriented in parallel. Therefore, the entropy of paramagnetic particles in a magnetic field is lower than outside of the magnetic field. Additionally, magnetic dipoles arranged in a row attract each other. This reduces the enthalpy of the system. Therefore, removing paramagnetic particles from the magnetic field leads to a reduction of the temperature. For this process, called adiabatic demagnetization, paramagnetic salts of rare-earth elements are applied in low-temperature physics. In the range of higher temperatures, the entropy contribution increases with increasing number of aligned spins in a particle. Therefore, the efficiency of this process increases significantly when using superparamagnetic materials instead of paramagnetic molecules.

Shull and coworkers [38] showed that the temperature difference ΔT caused by a change of the magnetic field ΔH depends on total number of N spins in an assembly, distributed into n noninteracting particles with magnetic moment m,

$$\Delta T \propto n\left(\frac{N}{n}\right)^2 \frac{H}{T}\Delta H = Nm\frac{H}{T}\Delta H \tag{3.18}$$

$\left(\frac{N}{n}\right) = m$ is the number of spins per particle. Assuming a constant number of spins in the system, Eq. (3.18) leads to the conclusion that the temperature difference ΔT is directly proportional to the number of spins per particle and the total number of spins in the system. Therefore, the application of superparamagnetic particles in a nanocomposite instead of other paramagnetic compounds makes magnetic refrigeration more efficient, allowing the use of conventional coils or permanent magnets instead of superconducting ones.

Furthermore, Eq. (3.18) shows that magnetic cooling is most efficient at low temperatures. However, in the case of superparamagnetism the lowest temperature of application is the blocking temperature. By selecting appropriate materials, the application of magnetic refrigeration is now extended from close to absolute zero to room temperature.

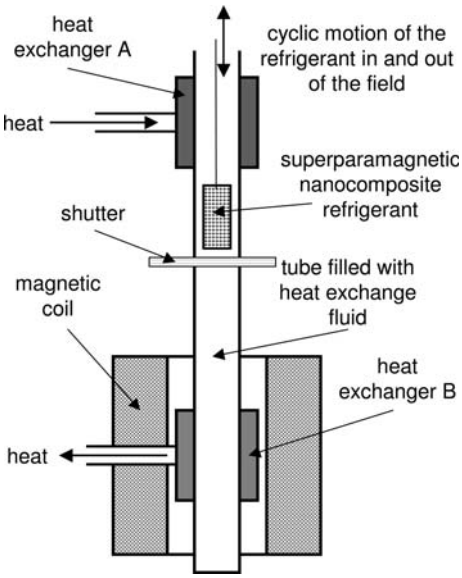

Fig. 3.27 Basic principle of magnetic refrigeration.

Figure 3.27 displays the basic principle of such a system. The superparamagnetic material is moved between two heat exchangers. One of these heat exchangers is placed in a magnetic field represented by a coil. At first, the material is moved into the magnetic field, where it is cooled in the heat exchanger. Afterwards, the material is pulled out of the magnetic field. This leads, according to Eq. (3.18), to a temperature reduction. In the second heat exchanger, the temperature of the cooled material is increased again by cooling the fluid in the heat exchanger. Now the cycle starts by moving the superparamagnetic material into the magnetic field again. In technical realization, a rotational movement replaces this linear cyclic one.

3.4.3
Exchange-coupled Magnetic Nanocomposites

Except for superferromagnetism, the interaction of superparamagnetic nanoparticles in nanocomposites is disadvantageous. However, Kneller and Hawig [39] developed a new composite consisting of hard and soft magnetic nanoparticles with interesting new properties. This development led to new hard and soft magnetic materials with exceptional properties. The new class of hard magnetic materials consists of soft magnetic particles, usually superparamagnetic ones, directly adjacent to a hard magnetic particle. In such an arrangement, the magnetic dipole moments of the magnetically hard particles force the vector of magnetization of the soft magnetic particles into the same direction. As a result, the vectors of magnetization of the soft magnetic particles around the hard mag-

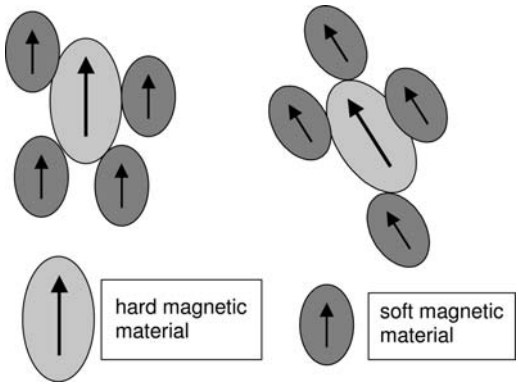

Fig. 3.28 Sketch of an exchange-coupled material.

netic one are magnetically oriented into the same direction. This arrangement is sketched in Fig. 3.28.

The hard and soft magnetic nanoparticles are "exchange coupled". Within the material, they form randomly oriented islands, within these islands, all particles show the same magnetic orientation. It is an assembly of exchange-coupled nanocrystals. Dipolar interactions need not be considered because these particles touch each other. In contrast to dipolar interaction, exchange coupling leads – as far as is possible because magnetic crystal anisotropy prefers the alignment of the magnetic moments in the easy direction of magnetization of each particle – to parallel orientation of the moments over the whole sample.

The exchange energy is proportional to the surface, whereas the energy of anisotropy is proportional to the volume of the particles. This size-dependent interplay of two energetic terms results in a "correlation volume" filled with parallel-aligned magnetic moments. These are the islands mentioned above. According to Herzer [40] the size of the correlation volume is described by

$$V_{\mathrm{corr}} = \left(\frac{A}{K}\right)^6 \frac{1}{V_{\mathrm{partcile}}^3} \quad \text{or} \quad N = \frac{V_{\mathrm{corr}}}{V_{\mathrm{particle}}} = \left(\frac{A}{K}\right)^6 \frac{1}{V_{\mathrm{particle}}^4} \tag{3.19}$$

In Eq. (3.19), V_{corr} is the correlation volume, K the constant of magnetic anisotropy and V_{particle} the volume of each particle, assuming that all particles are equal in size. A is the exchange constant of nanoparticles, usually it is found to be in the range of 10^{-12} J m^{-1}. According to Eq. (3.19), the correlation volume increases with decreasing particle size. As the smallest size of the particles is limited, so is the maximum possible size of the correlation volume or equivalently, the number of exchanging particles N is limited. Assuming magnetic particles with 5 nm diameter, in most cases, the diameter of the correlation volume is in the range of 100 nm.

Until now, the explanations followed the historical path. However, a close look at Eq. (3.19), shows that the correlation volume may be very large for materials

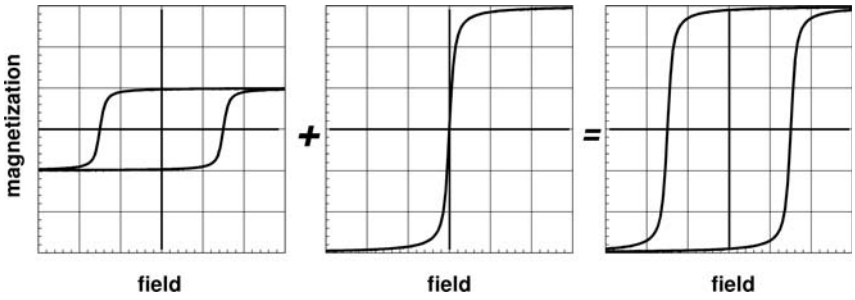

Fig. 3.29 Schematic diagram of exchanged-coupled materials, combining superparamagnetism and hard magnetic properties.

with small constants of anisotropy. As the coercivity increases with the square of the magnetic moment of the particles, in this case of the exchange-coupled islands, soft magnetic materials with extremely high susceptibility can be designed. This leads to "ultrasoft" magnetic material. The constant of anisotropy of these, in most cases metallic materials, is more than an order of magnitude smaller than for soft ferrites, leading to large exchange-coupled islands. Therefore, exchange-coupled soft oxide materials are also described.

The advantage of exchange-coupled magnetic nanoparticles for hard magnetic materials is obvious as these composites combine the advantages of hard and soft magnetic materials. Hard magnetic materials have high coercitivity and low saturation magnetization and remanence, whereas soft magnetic materials are characterized by a very small, or in the case of superparamagnetic particles zero, coercivity and high saturation magnetization. Exchange-coupled composites combine both properties. In a simplified manner, this is demonstrated in Fig. 3.29.

Figure 3.29 shows that the combination of a hard magnetic material with a soft one gives a new hard magnetic material with significantly higher remanence; the coercitivity is more or less unchanged. This combination allows the design of permanent magnets with higher energy products (energy product = coercivity times remanence), as they are possible by using conventional materials. This makes an additional advantage of exchange-coupled permanent magnets obvious. Additionally, there is a large economical advantage. With a reduced amount of the expensive hard magnetic material a superior and cheaper product is obtained.

These nanocomposites may either use hard or soft magnetic materials as the matrix with the appropriate inclusions of the other type of magnetic materials. However, there are experimentally well-supported theoretical reasons that the application of hard magnetic islands in a soft magnetic matrix leads to the best possible results. Figure 3.30 displays such composite magnets.

This figure shows a magnet with random-oriented hard magnetic particles and one with optimized structure. As expected, the latter show the better prop-

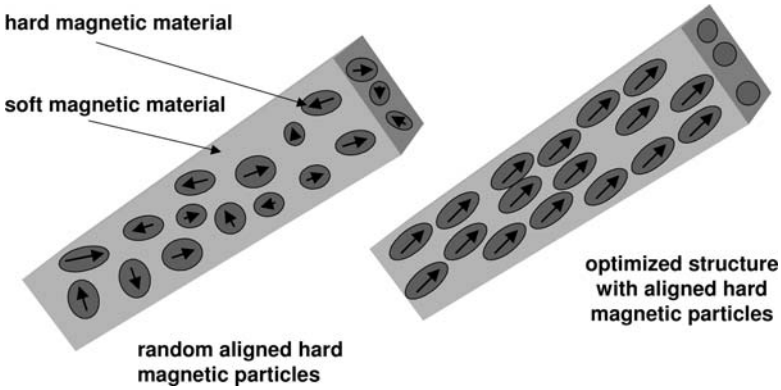

Fig. 3.30 Composite magnet consisting of hard magnetic islands embedded in a soft magnetic material.

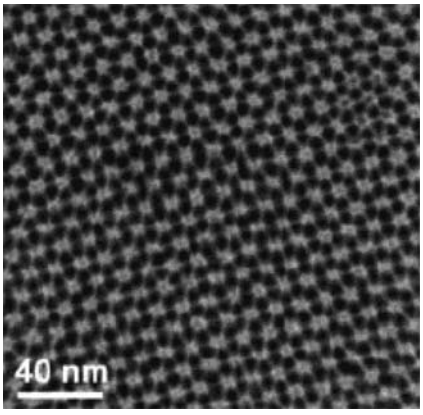

Fig. 3.31 Structure of a ceramic-containing nanocomposite made of $Fe_{58}Pt_{42}/Fe_3O_4$, as shown by Zeng et al. (Fig. 1A in [41]).

erties. In most cases, the optimized structure is obtained by self-organization or precipitation processes.

In most cases, exchange-coupled hard materials are metallic ones. Until now, the best results are obtained with $FePt/Fe_3Pt$ nanocomposites. In this composite, FePt is the magnetically hard phase and Fe_3Pt the soft one [3]. Looking at ceramic composites, in most cases, there is one ceramic and one metallic phase. A typical example of a ceramic containing nanocomposite is $Fe_{58}Pt_{42}/Fe_3O_4$ [41].

Figure 3.31 displays the structure of such a composite. In this figure, the darker regions are $Fe_{58}Pt_{42}$ particles with 4 nm in diameter coated with 0.5 nm Fe_3O_4 being the brighter regions. Sintering of this material was performed at 650 °C for one hour in an argon atmosphere with 5% hydrogen. The magnetiza-

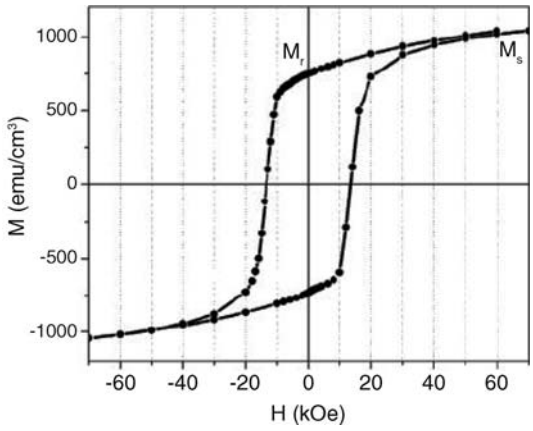

Fig. 3.32 Room-temperature magnetization curve of an exchanged-coupled material, a ceramic-containing nanocomposite made of 4 nm $Fe_{58}Pt_{42}$ coated with 1 nm Fe_3O_4, as shown by Zeng et al. (Fig. 4 in [41]).

tion curve of such a product with different coating thickness of 1 nm is displayed in Fig. 3.32.

This magnetization curve displays a remarkable saturation magnetization and high coercitivity. The energy product of this composite is approximately 38% higher than the highest value theoretically possible for the pure PtFe bulk material. Similar interesting results and high coercitivities are found Ni/NiO composites [42].

As mentioned in the introduction, theoretically, not only hard magnetic materials but also exchange-coupled soft magnetic materials are possible. Due to the small anisotropy constant, the correlation volume for this type of materials may be huge. Like the hard exchange-coupled materials, research is primarily into the direction of metallic systems. There exists a broad range of literature for materials like FeSiBNbCu or FeZrB with a constant of anisotropy well below 10^3 J m^{-3}. In this case, the estimated correlation volume is of macroscopic size leading to extremely high values of the susceptibility.

However, pure metallic particles do not lead to useful materials for high-frequency applications. Also in this case, nanocomposites are essential. It is an important prerequisite for successful high-frequency applications that each one of the particles is coated with an insulating layer. In the case of technical realization, this layer is realized by coating the particles with silica or oxidizing the surface of the particles. This design leads to soft magnetic materials with unmatched high susceptibilities for electronic applications. Composite materials based on this design are already commercialized [43]. Typical examples are (Ni,Fe)/SiO_2 [44], Co/SiO_2, Fe,Co/SiO_2, $NiFe_2O_4$/SiO_2, or (Ni,Zn)Fe_2O_4/SiO_2. Research in this field is now typically related to synthesis processes.

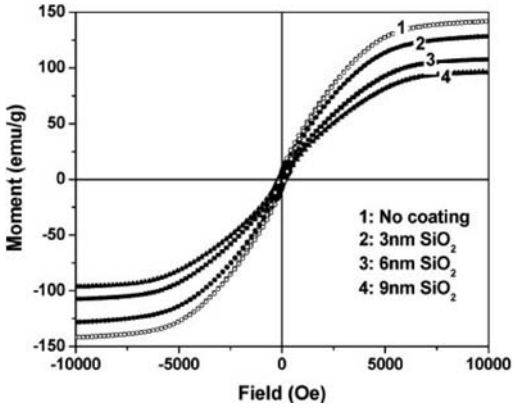

Fig. 3.33 Room-temperature magnetization curve of FeNi coated with silica of different coating thickness after Zhao et al. (Fig. 1 in [44]).

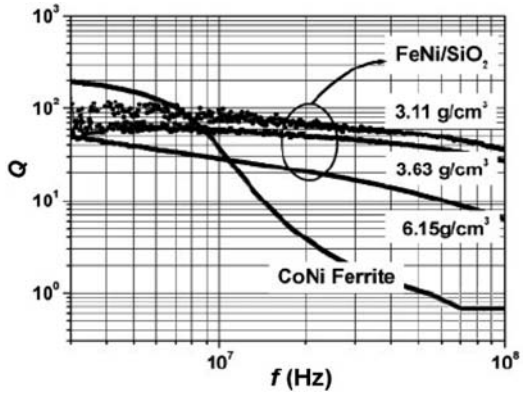

Fig. 3.34 Quality factor of $FeNi/SiO_2$ nanocomposite material as a function of frequency compared to conventional CoNi-ferrites. Data according to Zhao et al. (Fig. 3 b in [44]).

Figure 3.33 displays typical room-temperature magnetization curves of this type of materials. The magnetically active material was FeNi coated with silica. In Fig. 3.33, the thickness of the coating is used as parameter. It is important to realize that in these magnetization curves, hysteresis is not visible. The size distribution of these particles was quite broad; it ranged from 10 to 150 nm. Most important for this type of materials is the high-frequency behavior. Figure 3.34 depicts the quality factor of this type of material in comparison to the competing conventional $(Co,Ni)Fe_2O_4$ ferrites. The quality factor Q is the inverse of the energy loss, an important figure of merit for high-frequency materials. It is obvious that, above 10^7 Hz, the exchange-coupled nanocomposites are better than

the conventional materials. Furthermore, the quality factor increases with increasing coating thickness, visible in the magnetization curves connected to a reduced susceptibility. However, it must be stated that the permeability of the conventional material is better.

3.5 Electrical Conductivity

Electrical conductivity of nanocomposites depends on percolation. The theory of percolation treats the properties of two-phase mixtures. Details of this theory consider shape and concentration of the constituents. In the case of electrical conductivity, the crucial question is the critical concentration p_c, the percolation threshold, where the minority phase of the mixture forms a continuous network. Assuming a two-phase mixture, an insulating and an electric conductive one, the percolation threshold simplyfied represents the concentration of the onset of electrical conductivity. Above the percolation threshold p_c, the electrical conductivity σ is described by:

$$\sigma = \sigma_0 \, (p - p_c)^t \tag{3.20}$$

In Eq. (3.20) σ_0 is the conductivity and p the volume fraction of the conducting phase. In a $\log(\sigma)$ versus $\log(p–p_c)$ plot, Eq. (3.20) is linearized [45]. The exponent t reflects the dimensionality of the network; usually, it is found in the range between 1.3 and 3.

Certainly, it is obvious that percolation is extremely sensitive to the shape and the aspect ratio of the second-phase particles. There are a large number of stochastic theories in the literature; most of them are so complex that technical use is practically excluded. As an example, one of these descriptions of percolation published by Balberg [46] leads for the percolation threshold to the equation:

$$p_c = 0.7 \frac{\langle L \rangle^3}{\langle L^3 \rangle} \frac{D}{\langle L \rangle} \tag{3.21}$$

In Eq. (3.21), L is the length of the particles and D the particle diameter. The brackets $\langle \, \rangle$ denote mean values. It is an important characteristic of percolation that the percolation threshold increases with the mean value of the aspect ratio $a = \frac{\langle L \rangle}{D}$. Therefore, the concentration of particles necessary for percolation of fibers is up to many orders of magnitude larger than for spherical particles. To obtain optically transparent electrically conductive composites one has to apply extremely thin long fibers, usually realized with nanotubes or nanowires. In any real length distribution, $\frac{\langle L \rangle^3}{\langle L^3 \rangle} < 1$ is valid. Furthermore, as the nanomaterial used as electrically conductive filler is significantly more expensive than the polymer matrix, the application of nanotubes or nanowires is an economical necessity, too.

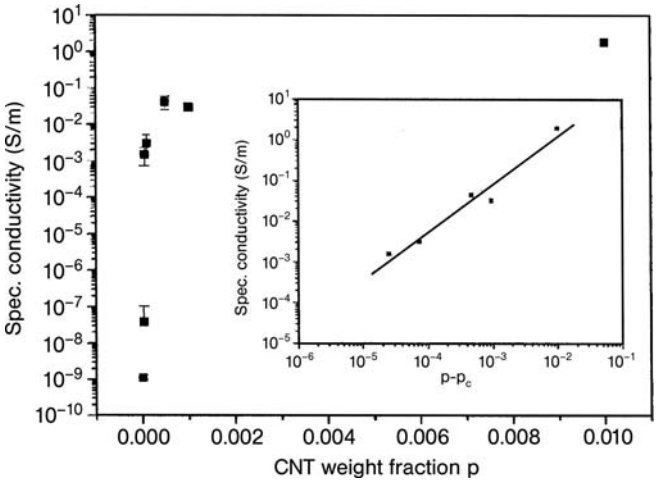

Fig. 3.35 Electrical conductivity of a carbon nanotube–epoxy composite [47]. The insert shows the double-logarithmic plot according to Eq. (3.20).

Figure 3.35 displays the electrical conductivity of a carbon nanotube–epoxy composite [47]. It is remarkable that the percolation threshold is as low as 2.5×10^{-3} wt%, which is equivalent to a volume fraction of 1×10^{-5}. The electrical conductivity of these composite is in the range of 1 Sm^{-1} in the case of 1 wt% nanotubes in the composite. According to Eq. (3.21), the low percolation threshold indicates a large aspect ratio, which is expected for nanotube composites. However, such low percolation thresholds are not always obtained. Coleman et al. [48] report on a nanotube–PMPV (poly(*p*-phenylenevinylene-co-2,5-dioctoxy-m-phenlyenevinylene)) composite. In this composite, the percolation threshold was in the range from 7 to 8 wt% nanotubes. These huge differences may be explained by insufficient singularization of the fibers in the composite. According to Eq. (3.21), in this case the percolation threshold goes to higher concentrations because the diameter of fiber bundles is larger than that of one fiber.

The insert in Fig. 3.35 displays the double-logarithmic plot according to Eq. (3.20). One may realize that the experimental data exactly follow this law up to a volume content of nearly 0.1 above the percolation threshold.

Figure 3.36 shows the electrical conductivity of a carbon-nanotube-filled epoxy [49]. In Fig. 3.36, VGCF stands for vapor-grown carbon fibers. These fibers had a length of 10–20 μm and a diameter of 150 nm. Therefore, the aspect ratio was roughly in the range of 100. Two different methods of epoxy preparation were applied. The first method, denoted as "low viscosity" in Fig. 3.36, used epoxy resin diluted in acetone to reduce viscosity. The second one just used commercial epoxy resin. In both cases, the carbon fibers were dispersed in the liquid by stirring and sonification at room temperature. Looking at Fig. 3.36, one realizes the remarkable fact that the resistivity decreases in the low-viscosity case for more

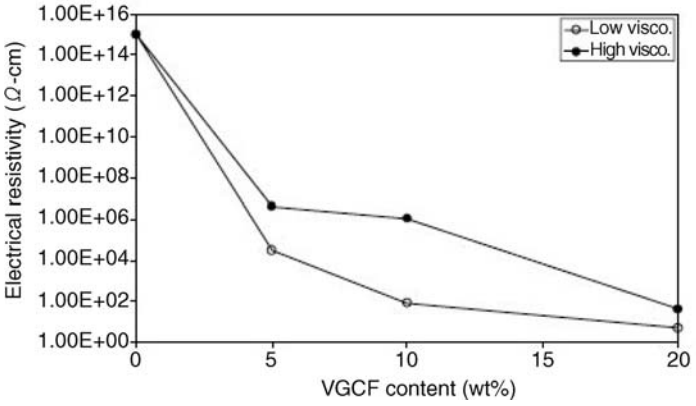

Fig. 3.36 Electrical resistivity of a carbon-nanotube-filled epoxy as a function of fiber loading for low and high-viscosity epoxy nanocomposite sheets. Data according to Choi et al. [49] (Fig. 5).

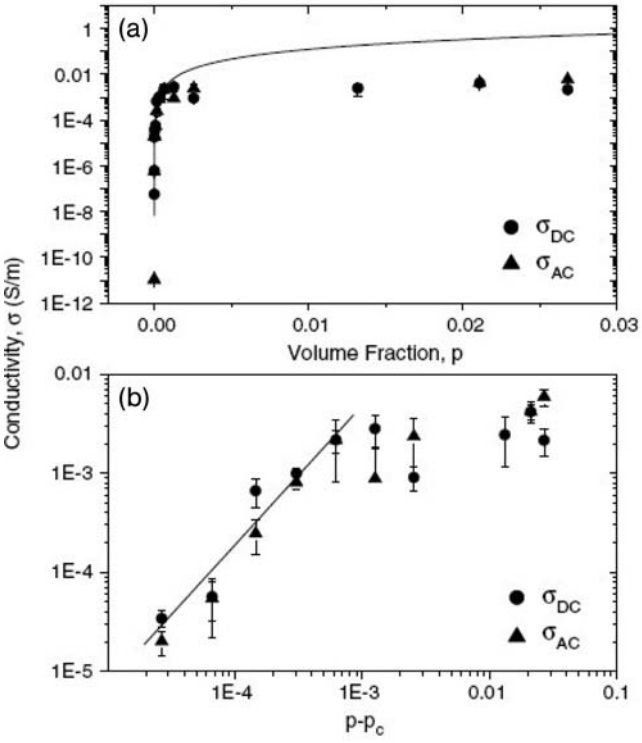

Fig. 3.37 Electrical conductivity of a composite of PMMA and $Mo_6S_{4.5}I_{4.5}$ fibers, after Murphy et al. (Fig. 3 in [50]). The solid line in (a) is a fit of Eq. (3.20). In (b) the data taken from (a) is linearized according to Eq. (3.20).

than ten orders of magnitude in the concentration range from zero to five weight per cent carbon fibers. A significantly more advanced system was introduced by Murphy et al. [50]. Instead of carbon fibers, these authors use $Mo_6S_{4.5}J_{4.5}$ fibers. This material crystallizes linearly in wires with a diameter of approx. 1 nm. However, one must point out that these fibers form bundles that can be reduced in diameter by sonification. Figure 3.37 shows the electrical conductivity of a composite of PMMA and these fibers. In Fig. 3.37 (a), the electrical conductivity is plotted versus the volume fraction of nanowires. The conductivity was measured by DC and AC methods. Interestingly, there was no difference found. The full line in Fig. 3.37 (a) was obtained by fitting the experimental results with the percolation law. This fit is not satisfactorily, it gives just first indications, leading to a percolation threshold of $p_c = 1.3 \times 10^{-5}$. This is an extremely low value; similar ones are found for carbon nanotubes, too. According to Eq. (3.21), this indicated a huge aspect ratio, probably larger than 1000. The conductivity of the nanowires is estimated to be in the range of 80 Sm^{-1}. Figure 3.37 (b) displays the electrical conductivity versus $(p–p_c)$. Both graphs together show that in this case, in the extremely narrow concentration range from 10^{-5} (percolation threshold) to 10^{-3}, the electrical conductivity increases from 10^{-5} to nearly 10^{-2} Sm^{-1}. Additionally, Fig. 3.37 shows that, in this case, Eq. (3.20) is valid only up to a volume fraction of nanowires of approximately 10^{-3}. This is a significantly smaller value that is found for carbon nanotubes. Probably, this effect is correlated to insufficient debundling of the fibers at high concentrations.

References

1 Gmelins Handbuch der anorganischen Chemie: Gold, **1954**, Verlag Chemie, Weinheim, pp. 92 ff, 397 ff.

2 D. Vollath, D. V. Szabó **2004**, *Adv. Eng. Mater.* 6, 117–127.

3 H. Zeng, J. Li, J. P. Liu, Z. L. Wang, S. H. Sun **2002**, *Nature* 420, 395–398.

4 R. J. Nussbaumer, W. R. Caseri, P. Smith, T. Tervoort **2003**, *Macromol. Mater. Eng.* 288, 44–49.

5 J. Böhm, J. Hausselt, P. Henzi, K. Liftin, T. Hanemann **2004**, *Adv. Eng. Mater.* 6, 52–57.

6 M. K. Wu, **1995**, in *Nanostructured Materials and Coatings*, Gorham/Intertech Consulting, Fig. 1 KEMIRA Pigments Inc.

7 R. F. Ziolo, E. P. Giannelis, B. A. Weinstein, M. P. Ohoro, B. N. Ganguly, V. Mehrotra, M. W. Russel, D. R. Huffman **1992**, *Science* 257, 219–223.

8 Z. H. Zhou, J. M. Xue, H. S. O. Chan, J. Wang **2002**, *Mater. Chem. Phys.* 75, 181–185.

9 G. Mills, Z. G. Li, D. Meisel **1988**, *J. Phys. Chem.* 92, 822–828.

10 E. M. Moreno, M. Zayat, M. P. Morales, C. J. Serna, A. Roig, D. Levy **2002**, *Langmuir* 18, 4972–4978.

11 J. B. Khurgin, E. W. Forsythe, S. I. Kim, B. S. Sywe, B. A. Khan, G. S. Tompa **1995**, *Mater. Res. Soc. Symp. Proc.* Vol. 358, 193–198.

12 *www.ptl.ethz.ch/research/res_top_Qdots*

13 L. Mädler, W. J. Stark, S. E. Pratsinis **2002**, *J. Appl. Phys.* 92, 6537–6540.

14 T. Tani, L. Mädler, S. E. Pratsinis **2002**, *J. Mater. Sci.* 37, 4627–4632.

15 S. Monticone, R. Tufeu, A. V. Kanaev **1998**, *J. Phys. Chem. B* 102, 2854–2862.

16 W.P. Lim, H. Y. Low, W. S. Chin **2004**, *J. Phys. Chem. B* 108, 13093–13099.

17 S. Muhamuni, B. S. Bendre, V. J. Leppert C. A. Smith, D. Cooke, S. H. Risbud, H. W. H. Lee **1996**, *Nanostruct. Mater.* 7, 659–666.

18 D. Vollath, I. Lamparth, D. V. Szabó **2002**, *Berg und Hüttenmännische Monatshefte* 147, 350–358.

19 D. Vollath, D. V. Szabó, S. Schlabach **2004**, *J. Nanoparticle Res.* 6, 181–191.

20 S. Musikhin, L. Bakueva, E. H. Sargent, A. Shik **2002**, *J. Appl. Phys.* 91 6679–6683.

21 J.-E. Park, M. Atobe, T. Fuchigami **2005**, *Electrochimica Acta* 51, 849–854.

22 E. Cattaruzzaa, G. Battaglina, P. Calvellia, F. Gonellaa, G. Matteib, C. Mauriziob, P. Mazzoldib, S. Padovanib, R. Pollonia, C. Sadab, B.F. Scremina, F. D'Acapitoc **2003**, *Compos. Sci. Technol.* 63, 1203–1208

23 M. Quinten **2001**, *Appl. Phys. B* 73, 317–326

24 I. V. Bodnar', V. S. Gurin, A. P. Molochko, and N. P. Solovei **2004**, *Inorg. Mater.* 40, 115–121. Translated from *Neorgan. Mater.* **2004**, 40, 158–165.

25 R. Reisfeld **2002**, *J. Alloys Compd.* 341, 56–61.

26 Y. Wang, 3.i Yao, M. Wang, F. Kong, J. He **2004**, *J. Cryst. Growth* 268, 580–584.

27 D. Vollath, D. V. Szabó, **2000**, unpublished data.

28 B. D. Cullity **1972**, *Introduction to Magnetic Materials*, Addison-Wesley, Reading, USA, 410 ff.

29 J.-R. Jeong, S.-L. Lee, S.-C. Shin **2004**, *phys. stat. sol. (b)* 241, 1593–1596.

30 R. H. Kodama, A. E. Berkowitz, E. J. McNiff, S. Foner **1997**, *J. Appl. Phys.* 81, 5552–5557.

31 D. H. Han. J. P. Wang, H. L. Luo **1994**, *J. Magn. Magn. Mater.* 136, 176–182.

32 Z. 3. Tang, C. M. Sorensen, K. J. Klabunde, G. C. Hadjipanayis **1991**, *Phys. Rev. Lett.* 67, 3602–3605.

33 C. Caizer, I. Hrianca **2003**, *Eur. Phys. J. B* 31, 391–400.

34 L. Néel **1949**, *Comt. Rend.* 228, 664–666.

35 A. Aharoni **1964**, *Phys. Rev.* 132, A447–A449.

36 D. V. Szabó, D. Vollath, W. Arnold **2001**, *Ceram. Trans.* 111, 217–224.

37 S. Morup, G. Christiansen **1993**, *J. Appl. Phys.* 73, 6955–6957.

38 R. D. McMichael, R. D. Shull, L. J. Swartzendruber, L. H. Bennet, R. E. Watson **1992**, *J. Magn. Magn. Mater.* 111, 29–33.

39 E. F. Kneller, R. Hawig **1991**, *IEEE Trans. Magn.* 27, 3588–3600.

40 G. Herzer **1997**, *Handbook of Magnetic Materials*, (ed.) K. H. J. Buschow, Vol. 10, Chapter 3, Elsevier Science, Amsterdam, p. 415.

41 H. Zeng, J. Li, J. P. Liu, S. Sun **2004**, *Nano Lett.* 4, 187–190.

42 J. B. Yi, J. Ding, Z. L. Zhao, B. H. Liu **2005**, *J. Appl. Phys.* 97, 10K306.

43 *http://www.inframat.com/magnetic.htm.*

44 Y. Zhao, C. Ni, D. Kruczynski, X. Zhang, J.Q. Xiao **2004**, *J. Phys. Chem. B* 108, 3691–3693.

45 D. Stauffer, A. Aharoni **1994**, *Introduction to Percolation Theory*, 2nd edn. Taylor and Francis, London.

46 I. Balberg **1985**, *Phys. Rev. B* 31, 4053–4055.

47 J. K. W. Sandler, J. E. Kirk, I. A. Kinloch, M. S. P. Shaffer, A. H. Windle **2003**, *Polymer* 44, 5893–5899.

48 J. N. Coleman, S. Curran, A. B. Dalton, A. P. Davey, B. McCarthy, W. Blau, R. C. Barklie **1998**, *Phys. Rev. B* 58, R7492–R7495.

49 Y.-K. Choi, K.-I. Sugimoto, S.-M. Song, Y. Gotoh, Y. Ohkoshi, M. Endo **2005**, *Carbon* 43, 2199–2208.

50 R. Murphy, V. Nicolosi, Y. Hernandez, D. McCarthy, D. Rickard, D. Vrbanic, A. Mrzel, D. Mihailovics, W. J. Blau, J. Coleman **2006**, *Scr. Mater.* 54, 417–420.

Part Two
Fundamentals

Bulk Nanostructured Materials. Edited by M. J. Zehetbauer and Y. T. Zhu

ISBN: 978-3-527-31524-6

4
Deformation Mechanisms of Nanostructured Materials

Yuntian T. Zhu, Bing Q. Han, and Enrique J. Lavernia

4.1
Introduction

Nanostructured materials can be defined as solids with nanoscale (typically 1–100 nm) grain structure or substructures in at least one dimension [1–3]. Siegel [2] has classified nanostructured materials into four categories according to their dimensionality: 0D – nanoclusters (particles); 1D – multilayers; 2D – nanograined layers; and 3D – equiaxed bulk solids. In short, he has described the 3D nanostructured materials as "…three-dimensionally modulated, synthetic materials with average grain, phase, or other structural domain sizes below 100 nm." *Nanostructured* materials cover materials with a broader grain-size range than the term, *nanocrystalline* materials. The latter is defined as materials with grain sizes in the range of 1–100 nm [4].

Two complementary approaches have been developed to synthesize nanostructured materials. The first one is a "bottom-up" approach, in which bulk nanostructured materials are assembled from individual atoms or nanoscale building blocks such as nanoparticles [5]. Gleiter's pioneering work [6] is a typical example of a "bottom-up" approach. Various chemical and physical methods have been developed to synthesize nanopowders for small-scale laboratory investigations as well as for large-scale commercial use. Such methods include inert gas condensation (IGC) [6], high-energy ball milling [7], spray conversion processing [8], sputtering [9], physical vapor deposition [10], chemical vapor deposition [11], sol-gel process [12], sliding wear [13], and spray forming [14]. The bottom-up approach has a number of applications such as films, coatings, electronic devices, drug deliveries, cosmetics, paints, lubricants, rocket fuels, catalysts, and reinforcements for nanocomposites.

Most bottom-up approaches produce nanopowders. For structural applications, the nanopowders need to be consolidated into bulk nanomaterials. However, consolidation of nanopowders has been a challenge. Gleiter [6] and Nieman *et al.* [15] cold-compacted IGC-produced nanopowders *in situ* in ultrahigh vacuum and obtained nanostructured discs that are typically a few hundred micrometers in thickness and less than 10 mm in diameter. Their as-produced samples contained

Bulk Nanostructured Materials. Edited by M. J. Zehetbauer and Y. T. Zhu

ISBN: 978-3-527-31524-6

many flaws that masked the intrinsic mechanical properties [16, 17]. Flaws included gas-filled pores, cracks, poorly bonded grains, *etc*. These flaws render the material brittle, especially under tension. A series of other conventional and new techniques, such as hot pressing, hot isostatic pressing (HIP) [18], rapid hot forging [19, 20] and plasma activated sintering [21], have been used to consolidate nanopowders. Most of these techniques involve the applications of heat and pressure. Grain growth usually occurs during consolidation, although nanopowder oxidation and contaminants may help impede grain growth.

An exception to the above problem is an approach that combines cryomilling followed by hot extrusion which could produce nanostructured materials with 100% density while maintaining their nanostructures [22–24]. In such an approach, nanosized second-phase oxide and nitride particles are produced during the cryomilling, which significantly increases the thermal stability of the materials and consequently allows hot extrusion to obtain full density without significant grain growth. When mixed with large grain sizes to form a bimodal structure, reasonable ductility is obtained while maintaining high strength.

The second approach for producing nanostructured materials is a "top-down" approach, in which existing coarse-grained materials are refined into nanostructured materials. The most successful "top-down" approach has been *via* severe plastic deformation (SPD) techniques, among which the most developed are equal-channel angular pressing (ECAP) and high-pressure torsion (HPT) [25]. The ECAP technique was first invented by Segal in 1972 [26], and was later used to produce nanostructured materials [27]. Recently, new SPD techniques have been developed, such as accumulative roll bonding [28], twist extrusion [29], repetitive corrugation and straightening (RCS) [30], and surface nanostructuring [31, 32]. SPD-produced materials such as Cu, Fe and Ti typically have an average grain size of 60–200 nm [33], somewhat above 100 nm, the upper bound often used to define the *nanocrystalline* materials. However, subgrains with low misorientation angles, dislocation cell structures [30], and the coherent crystallite domains as measured by X-ray analysis are usually smaller than 100 nm. These materials produced by SPD can be classified as *nanostructured* materials [34].

Nanostructured materials produced by SPD techniques are free of porosity and contaminants, and can be used to study their intrinsic deformation mechanisms. These materials have unique micro- and nanostructures such as high dislocation density, nonequilibrium grain (subgrain) boundaries and dislocation cells [30], which give them high strength and also much better ductility than those synthesized by the first approach. However, even these nanostructured materials often exhibit a very low ductility [35, 36], due to low strain-hardening rate [37]. There are two reasons for this. First, nanostructured materials with grain sizes less than 100 nm often deform by dislocation emission from, and annihilation at, grain boundaries without accumulation in the grain interior [38]. Second, nanostructured materials with larger grain sizes often have saturated dislocation densities due to the fact that grain refinement is realized by dislocation activities.

In recent years much attention has been paid to developing strategies for improving the poor ductility of UFG materials [23, 36, 39–48]. Approaches for increasing the ductility include bimodal (or multimodal) grain-size distribution [23, 41], second-phase particle hardening [36, 45, 46], growth twins [43, 44], and adjusting stacking-fault energy for deformation twinning [49]. Each approach has its own limitations and is suitable for only certain material systems. For a single-phase UFG metal or alloy where dislocation slip is the primary deformation mechanism, it has been difficult to find an effective way to improve its ductility without trading-off strength. Recently, some encouraging findings have been reported on the ductility of this type of UFG materials. A UFG Cu produced by equal-channel angular pressing (ECAP) for 16 passes with backpressure showed both very high ductility and strength [50]. A UFG Al processed by accumulative roll bonding (ARB) was found to have both higher ductility and strength with increasing ARB strain [40]. A nanocrystalline Cu produced by a combination of cryomilling and room-temperature milling also exhibited both high ductility and strength [42]. However, these reports are exceptions rather than usual cases. It is not clear what structural feature(s) are responsible for the observed high ductility and high strength or if any processing-introduced artifacts such as impurities and oxides have played a role in the high ductility.

The unique mechanical properties of nanostructured materials are attributed to their unique deformation mechanisms, which, in many cases, are different from those in their coarse-grained counterparts [51–55]. Some deformation mechanisms, e.g., partial dislocation emission from grain boundaries, homogeneous nucleation of twins inside grain interior, heterogeneous twin nucleation on grain boundaries, and twin lamellae formed via the splitting and migration of grain boundaries, have been predicted by molecular-dynamics (MD) simulations [53–58], and experimentally observed [59–63] to operate in nanocrystalline face-centered-cubic (fcc) metals. In this chapter, recent progresses on the deformation mechanisms of nanostructured materials will be systematically described.

4.2
Deformation Mechanisms of Nanostructured Materials

A majority of studies on the deformation mechanisms of nanostructured materials have focused on face-centered-cubic (fcc) metals. As a result, we have more knowledge on deformation mechanisms of fcc metals than hexagonal-close-packed (hcp) and body-centered-cubic (bcc) metals. More specifically, most molecular-dynamics simulation and experimental studies are on three fcc metals: Al, Ni and Cu, because of their medium-to-high stacking-fault energies as well as unique unstable stacking-fault energies and unstable twin-fault energies. As discussed later, these fcc metals display an activation of different deformation mechanisms as their grain sizes are reduced to the nanoscale. Metals with very low stacking-fault energies demonstrate less variation in deformation mecha-

nisms with decreasing grain sizes and therefore have been less studied. In the following sections, nanostructured Al, Ni and Cu are primarily used to demonstrate the unique deformation mechanisms of nanostructured materials.

Deformation mechanisms in nanostructured materials include slip of full dislocations and partial dislocations, deformation twinning, wide stacking faults, grain-boundary sliding, and grain rotations. While these deformation mechanisms also exist in coarse-grained materials, their activations, sources and behaviors are very different in nanostructured materials. These deformation mechanisms are discussed in the following sections.

4.2.1 Slip of Full Dislocations

For coarse-grained materials with medium to high stacking-fault energy (e.g. Cu, Ni and Al), slip of full dislocations is the primary deformation mechanism at room temperature and quasistatic strain rates. The dislocation sources are usually Frank–Read type inside the grain interiors. However, when the grain sizes decreases to a few hundred nanometers and subgrain sizes decreased to below 100 nm, as in the case of most nanostructured materials produced by SPD, the Frank–Read dislocation source may no longer exist, and grain boundaries become the source and sink for slipping dislocations. In other words, dislocations are emitted from a grain-boundary segment and disappear into another grain-boundary segment without accumulation inside grain interior. This is clearly demonstrated in nanostructured hcp Ti processed by severe plastic deformation, in which grains and subgrains smaller than 60 nm contains almost

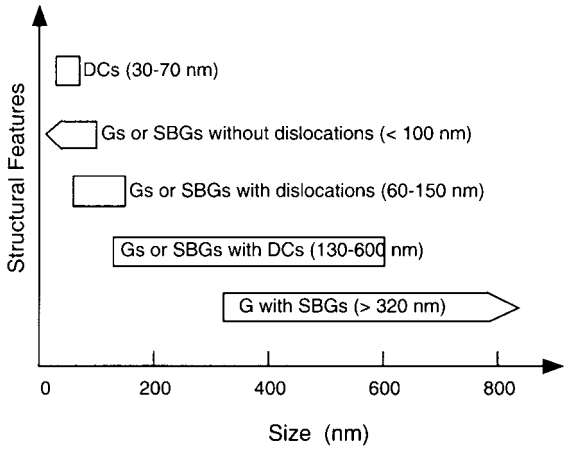

Fig. 4.1 The hierarchy and size ranges of different structural features in nanostructured Ti processed by ECAP plus cold rolling. DC denotes dislocation cells, G denotes grain, SBG denotes subgrain.

no dislocations, while grains larger than 100 nm generally contains a high density of dislocations (see Fig. 4.1) [64].

It should be noted that it is possible for full dislocations to be trapped inside very small grains via dislocation interlocking and other mechanisms. For example, full dislocations were observed in nanostructured Ni grain with sizes as small as 10–20 nm [65, 66]. Dislocations were also observed in 20 nm grains in nanostructured Cu processed by ball milling [42]. As will be discussed later, the activation of full dislocations depends on the applied external stresses. For nanostructured fcc metals and alloys with grain sizes below 100 nm, as the grain sizes decrease, the slip of full dislocations may become less significant with decreasing grain sizes and other deformation mechanisms such as partial dislocation slip and deformation twinning become more significant. However, such a trend may not be true for hcp metals such as Ti, which was found to deform by twinning in its coarse-grained state but not in the nanostructured state [67, 68].

4.2.2 Slip of Partial Dislocations and Deformation Twinning

4.2.2.1 MD Simulations and Experimental Observations

Partial dislocation slip and deformation twinning are two different but related deformation processes. Our early understanding of the partial dislocations and deformation twins in nanocrystalline metals were largely from the results of MD simulations [53–58] because of experimental difficulties.

MD simulations predict that partial dislocation emission from grain boundaries [54, 56] is a dominant deformation mechanism in grains with diameters in the range of several tens of nanometers. The activation of partial dislocations provides a critical precondition for the formation of deformation twins. Figure 4.2 is a high-resolution transmission electron microscopy (HRTEM) image that

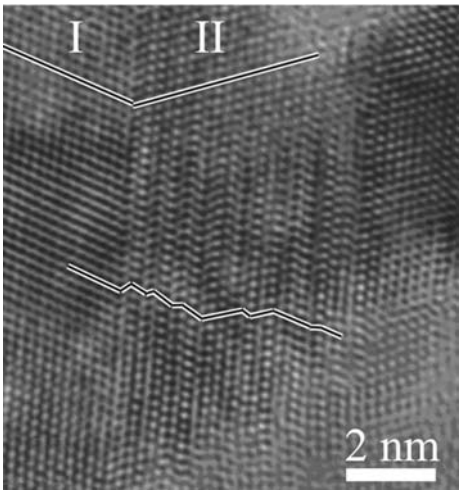

Fig. 4.2 HRTEM micrograph from Cu processed by HPT [11]. Regions I and II form a twinning relationship. Stacking faults shown in region II were generated by partial dislocations emitted from the lower grain boundary, which stopped in the interior of the grain.

shows direct evidence of partial dislocation emission from grain boundaries in nanocrystalline Cu processed by HPT [62]. As shown, there is only one twin boundary at the upper part of Fig. 4.2 that divides twin domains I and II. However, there are high densities of microtwins and stacking faults at the lower part of domain II. These microtwins and stacking faults do not go across the whole grain but stop in the grain interior with Shockley partial dislocations located at the fronts of the microtwins and stacking faults. It is obvious that these twins and stacking faults were formed by partial dislocations emitted from the lower grain-boundary segment. As will be discussed later, the microtwins shown in Fig. 4.2 were formed by heterogeneous twinning.

Deformation twins have been predicted by MD simulations in nanocrystalline Al [54, 57], Ni [53, 56] and Cu [69]. Three twinning mechanisms were predicted [54]: 1) homogeneous twinning inside nanosized grains by coincidental overlapping of wide stacking-fault ribbons. The stacking-fault ribbons were formed by dissociated lattice dislocations, and become very wide due to the effect of small grain size as well as external stress [70]. 2) heterogeneous twinning from the grain boundaries. 3) twinning by grain-boundary splitting and migration. These deformation twinning mechanisms were recently verified in nanocrystalline Al [51, 59, 60, 70], Cu [62], Ni [71] and Pd [63] by HRTEM. Al in its coarse-grained (CG) state has never been observed to deform by twinning, except at crack tips [72], because of Al's very high stacking-fault energy. CG Cu does not deform by twinning [73, 74] except at very high strain rates [75, 76] and/or low temperatures [77]. Moreover, in CG Cu smaller grain sizes were found to impede deformation twinning, which is also true for many other metals [78, 79]. In contrast, twinning becomes a major deformation mechanism in nanocrystalline Cu processed by HPT at room temperature and a low strain rate [62]. In addition, it was also found that under the same HPT condition, twinning only occurred in crystalline domains that are smaller than 50 nm [80]. These results indicate that the nanocrystalline materials indeed deform via mechanisms not accessible to their coarse-grained counterparts, and grain size plays a critical role in the formation of deformation twins.

Figure 4.3 (a) shows a deformation twin formed by homogeneous twinning inside a nanocrystalline Al grain. It has a thickness of two atomic planes and is therefore a twin nucleus. It was clearly formed by dynamic overlapping of two extended partial dislocations with stacking faults on adjacent slip planes [59]. As shown, the two stacking faults are only partially overlapped. This twin may grow by overlapping with more wide stacking faults. Figure 4.3 (b) shows another scenario of twin nucleation in nanostructured Ni [81]. As marked by the black arrow on the left, one dislocation on a grain boundary was dissociated into two Shockley partials with a wide stacking fault, and another dissociated dislocation near the grain boundary overlapped with it to form a twin nucleus. This is a unique mechanism of twin nucleation at grain boundaries.

Figure 4.4 shows twins formed by grain-boundary splitting and migration. As shown, some segments of the boundary are straight, coherent $(1\bar{1}1)$ twin boundaries as indicated by white arrows. These segments, which are connected by

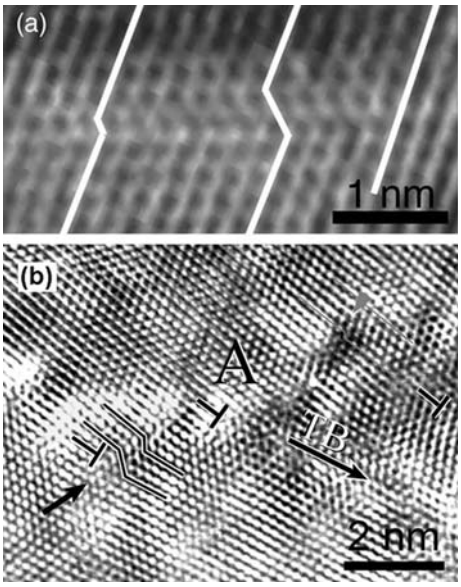

Fig. 4.3 (a) A deformation twin formed by the overlapping of two extended dislocations on adjacent slip planes in nanostructured Al produced by cryogenic ball milling [59]. (b) A twin nucleus formed by the overlapping of an extended dislocation from a grain boundary and a slipping extended dislocation from the grain interior [81].

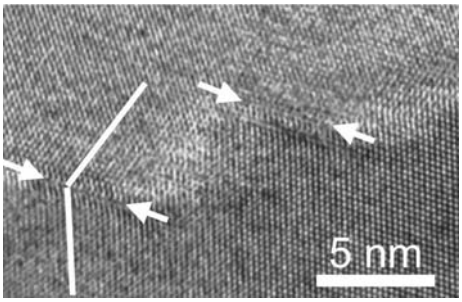

Fig. 4.4 An HRTEM image of a twin formed by grain-boundary splitting and migration. It consists of short, straight, coherent $(1\bar{1}1)$ twinning planes (marked by arrows) connected by incoherent, noncrystallographic segments.

noncrystallographic segments, form a zigzag boundary between the two twinning areas. To form such a twin, a grain-boundary segment was dissociated into a twin boundary and a new grain boundary [16]. A twin lamella was formed via the migration of the new grain boundary. The boundaries of twin lamellae formed at different time frames joined together to form the zigzag boundary. The noncrystallographic segments observed here were actually the new grain boundaries in this mechanism. Readers are referred to the work by Yamakov *et al.* [58] for a more detailed description of this twinning mechanism.

Deformation twins formed by heterogeneous twinning in nanostructured Cu are shown in Fig. 4.2. These twins were nucleated on a grain boundary. Most twins observed in nanocrystalline Al and Cu are this type. Figure 4.5 shows a) a multiple-fold twin and b) a five-fold twin in nanostructured Cu produced by HPT [82]. They were formed by sequential twinning by partial dislocation emis-

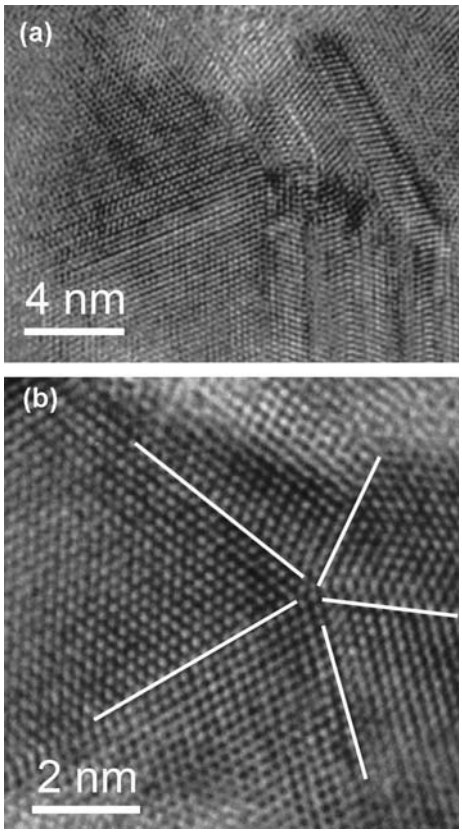

Fig. 4.5 (a) A multiple twin and (b) a five-fold twin formed in nanostructured Cu processed by HPT.

sion from grain boundaries or twin boundaries. Multiorientation applied stresses or stress orientations are needed to form the five-fold twins. This experimental observation and proposed formation mechanism have been recently verified by MD simulations [83]. In addition, the five-fold twins were observed only in grains smaller than 20 nm, indicating a size effect.

Both MD simulations and experimental data indicate that such deformation twins are formed by partial dislocation emissions from grain boundaries [51, 54, 60, 62, 66]. It is of interest to understand under what conditions the deformation twins will nucleate and grow. MD simulations do not tell what critical stress is needed for the deformation twin to nucleate and grow or what grain size is optimum for deformation-twin nucleation. Moreover, MD simulations [54–56] usually use extremely high strain rates in the order of 10^6 to 10^8 s^{-1}, which correspond to explosive deformations in a real experiment. It is well known that the strain rate significantly affects the deformation mechanisms of materials [62, 69]. This adds complexity to the interpretation of the MD simulation results. It is of interest to study the grain-size effect on the deformation twinning without the complication of high strain rates. In the following section,

we shall review and examine analytical dislocation models on the formation of deformation twins.

4.2.2.2 Analytical Dislocation Models

Conventional Dislocation Models Two similar models were proposed to explain the formation of deformation twins in nanocrystalline metals [51, 61]. In the model by Chen *et al.* [51], the stress needed to activate a full dislocation is described as

$$\tau_{\mathrm{L}} = \frac{2\eta G b}{d} \tag{4.1}$$

where η is a parameter that reflects the characteristics of the dislocation ($\eta = 0.5$ for an edge dislocation and $\eta = 1.5$ for a screw dislocation), G is the shear modulus, and b is the magnitude of the Burgers vector of the full dislocation. The stress to activate a partial dislocation is described as

$$\tau_{\mathrm{p}} = \frac{2\eta G b_1}{d} + \frac{\gamma}{b_1} \tag{4.2}$$

where b_1 is the magnitude of the Burgers vector of the partial dislocation, and γ is the stacking-fault energy. When $\eta = 0.5$, these two equations become identical to those in the work by Liao *et al.* [61].

Because $b > b1$, τ_{p} will increase at a slower rate than τ_{L}, which means that it will be easier to activate a partial dislocation than a full dislocation when the grain is below a critical size. These two models seem very straightforward in explaining the activation of partial dislocations, which is a prerequisite of deformation twinning.

Unfortunately, experimental data show that smaller grain size hinders, not promotes, deformation twinning [78, 79], which directly contradicts these two models [51, 61]. It has been found that the critical stress for twinning follows a Hall–Petch relationship

$$\sigma_{\mathrm{T}} = \sigma_{\mathrm{T}_0} + \kappa_{\mathrm{T}} d^{1/2} \tag{4.3}$$

where σ_{T_0} is a constant and κ_T is the Hall–Petch slope for twinning. Equation (4.3) is similar to the well-known Hall–Petch relationship for a lattice dislocation:

$$\sigma_{\mathrm{F}} = \sigma_{\mathrm{F}_0} + \kappa_{\mathrm{F}} d^{1/2} \tag{4.4}$$

where σ_{F_0} is a constant and κ_{F} is the Hall–Petch slope for the slip of a full dislocation.

Table 4.1 lists the Hall–Petch slopes for both twinning and for slip of full dislocations [78]. As shown, the Hall–Petch slope for twinning is higher than that

Table 4.1 The Hall–Petch slopes for bcc, fcc and hcp metals and alloys [78].

Material	H–P slope for slip, κ_F MPa mm$^{1/2}$	H–P slope for twinning, κ_T MPa mm$^{1/2}$
bcc		
Fe-3 wt%Si	12	100
Armco Fe	20	124
Steel: 1010, 1020, 1035	20	124
Fe-25 at%Ni	33	100
Cr	10.08	67.75
Va	3.46 (20 K)	22.37
fcc		
Cu	5.4 (RT)	21.66 (77 K)
Cu-6 wt%Sn	7.1	11.8 (77 K), 7.9 (RT)
Cu-9 wt%Sn	8.2	15.77 (77 K)
Cu-10 wt%Zn	7.1	11.8 (77 K)
Cu-15 wt%Zn	8.4	16.7 (295 K)
hcp		
Zr	8.26	79.2
Ti	6 (78 K)	18 (4 K)

for the slip of full dislocation for body-centered-cubic (bcc), face-centered-cubic (fcc), and hexagonal close-packed (hcp) metals and alloys. Therefore, the models are not supported by experimental data. Moreover, these two models predict an unrealistically high critical stress for twinning [51], which is perhaps part of their inherent limitation. The models also made an implicit assumption that activation of partial dislocation equals formation of twinning, which, as shown later, is not correct.

A Recent Model Based on the Emission of Partial Dislocations from Grain Boundaries A recent analytical dislocation model by Asaro *et al.* [84] utilized the simulation and experimental results that partial dislocations are emitted from boundaries of nanosized grains. The critical stress needed to move a full dislocation is described as

$$\tau_F = \frac{Gb}{d} \tag{4.5}$$

and the critical stress needed to move a partial dislocation is described as

$$\tau_p \approx \frac{Gb}{3d} + (1-\delta)\frac{\gamma}{Gb} \tag{4.6}$$

where δ is the ratio of equilibrium stacking fault width to grain size.

This model predicts that below a certain critical grain size partial dislocations from grain boundaries need a lower stress to move than do full dislocations in nanocrystalline metals. Most importantly, it predicts a realistic, low twinning stress that is obtainable under experimental conditions such as ball milling. However, the model does not address two critical issues. First, the emission of a partial dislocation does not guarantee the nucleation of a deformation twin because a trailing partial could easily follow to erase the stacking fault formed by the first partial. Second, random emissions of partial dislocations from a grain boundary would give a deformation twin equal probability to grow or to shrink, which cannot explain the deformation twin growth and the observed large deformation twins in nanocrystalline Al, Cu and Pd [59–63].

A New Model Addressing the Nucleation and Growth of Deformation Twins To address the above two issues, Zhu *et al.* [85, 86] recently developed an analytical model to describe the nucleation and growth of deformation twins in fcc nanocrystalline metals. To nucleate a twin, a stacking fault needs to be produced first. The stacking fault can be produced by either the emission of a partial dislocation from a grain boundary or dissociation and spread of a full dislocation. Their model reveals that the latter needs a lower stress to activate. In other words, to produce a deformation twin, a full dislocation is first dissociated and spread across/into a nanograin under an external stress, and then a second partial is emitted on an adjacent plane to produce a twin nucleus. The dissociated full dislocation can be either an edge dislocation or a screw dislocation. Both have an optimum grain size at which the critical stress for nucleating a twin is lowest. In practice, a dislocation can be of mixed nature, with the lowest stress lying in the range of [86]

$$\frac{1.715(4-3\nu)}{2.089-\nu}\frac{\gamma}{a} \leq \tau_{\min} \leq \frac{12.211}{3.727+\nu}\frac{\gamma}{a} \tag{4.7}$$

where $\tau_{\min}$ is the critical stress for nucleating a twin. For the same reason, the optimum grain size, $d$op, for deformation twinning can be described as

$$\frac{2.089-\nu}{54.985(1-\nu)}\frac{Ga^2}{\gamma} \leq \frac{d_{\mathrm{op}}}{\ln(\sqrt{2}d_{\mathrm{op}}/a)} \leq \frac{3.727+\nu}{97.053(1-\nu)}\frac{Ga^2}{\gamma} \tag{4.8}$$

The physics behind the optimum grain size and critical twinning stress arises from the fact that when the grain size is relatively large, as the grain size becomes smaller, it is easier for the full dislocation to dissociate into two partials with the help of the grain boundaries [85]. However, when the grain size is too small, it takes a higher applied stress to emit partial and full dislocations.

For fcc metals and alloys, neither the Poisson's ratio ν nor lattice parameter changes dramatically from material to material. However, the SFE γ could vary by more than an order of magnitude. In addition, a slight change in alloy composition could significantly change the SFE [87]. Therefore, it is reasonable to

Table 4.2 Parameters for Cu and Al used in our model.

	G (GPa)	ν	γ (mJ/m^2)	a (Å)	τ_{min} (GPa)	d_{op} (nm)
Al	26.5	0.345	122	4.04	0.88–0.91	5–7
Ni	94.7	0.312	125	3.5232	1.05–1.07	19–27
Cu	54.6	0.343	45	3.6146	0.36–0.37	38–54

say from Eq. (4.7) that the minimum twin nucleation stress is largely determined by the SFE. Lower SFE leads to lower twin nucleation stress. Equation (4.8) indicates that the optimum grain size for twin nucleation is largely determined by the ratio of shear modulus to SFE (G). Higher shear modulus and lower SFE leads to larger optimum grain size for twin nucleation.

Table 4.2 lists the critical stresses and optimum grain-size ranges calculated using Eqs. (4.7) and (4.8), for nanostructured Al, Ni and Cu, along with their material parameters used for the calculation. For nanostructured Al the optimum grain size for twin nucleation is in the range of 4.9 to 7.4 nm. However, MD simulations predicted grain-boundary sliding as the primary deformation mode in nanostructured Ni [88] and nanostructured Cu [69] when their grain sizes are below 10 nm. Such a trend also likely exists in nanostructured Al, but again, this behavior will be affected by processing history. In other words, grain-boundary sliding, instead of deformation twinning, is the likely deformation mode in nanostructured Al with grain sizes smaller than 10 nm. Indeed, deformation twins were not observed in grains smaller than 10 nm in a nanostructured Al produced by cryogenic ball milling [59]. Twins were only observed at small corners of grains of several tens of nanometers (see Fig. 4.6) [60]. Such a grain is too large for grain-boundary sliding, but its small corners can nucleate deformation twins at (111) planes with a size between 4.9 nm and 7.4 nm, and then grow larger near the grain corner. The deformation twins were not observed in large grains because their nucleation requires very high stress.

Table 4.2 shows that the optimum grain-size range for nanostructured Ni to deform by twinning is 19–27 nm. This agrees very well with experimental observations that nanostructured Ni produced by electrodeposition with an average grain size of 25 nm deforms extensively by twinning at liquid-nitrogen temperature [71, 81]. In addition, in nanostructured Ni produced by surface mechanical attrition treatment (SMAT) [31], twins were observed in 50% of small grains (20–50 nm), but only in 10% of large grains (50–100 nm), agreeing well with Eqs. (4.7) and (4.8), and also indicating a grain-size effect.

The model also predicts that the optimum grain size for twin nucleation in Cu is 38.4–54.2 nm. In the HPT-processed nanostructured Cu, deformation twins were only observed in Cu grains smaller than 50 nm [80], which is consistent with our model prediction. In addition, the critical twinning stress for Cu is 0.36–0.37 GPa (Table 4.2), which can be easily reached under the HPT condition. This also explains the high densities of twins in the HPT-processed nano-

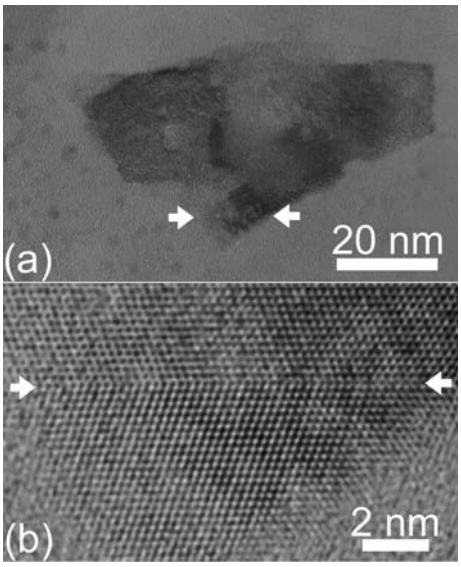

Fig. 4.6 (a) A deformation twin at the lower corner of a large grain with the twin boundaries marked by two white arrows, and (b) HRTEM image of the twin.

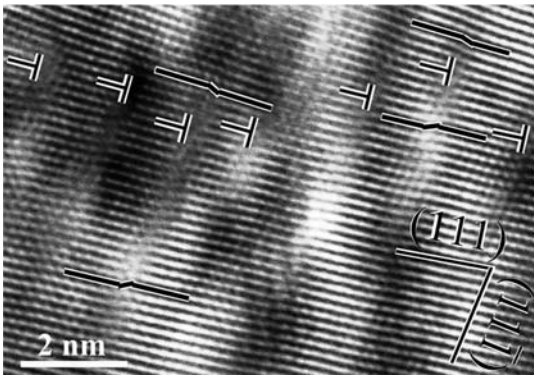

Fig. 4.7 HREM images showing 60° dislocations formed by (111) planes on a nonequilibrium grain boundary are dissociated into Shockley partials bounding stacking faults [81].

structured Cu, which suggests that deformation twinning played a significant role in the deformation of nanostructured Cu.

This model does not consider dislocation nucleation from grain boundaries, and assumes that nongeometrically necessary dislocations already exist at grain boundaries and can readily move under a sufficient external stress. Such dislocations are abundant in SPD-processed nanostructured materials and such grain boundaries have been termed nonequilibrium grain boundaries [61, 81, 89]. Furthermore, as seen in Fig. 4.7, such dislocations could be already dissociated into partials, which are ready to emit into the grain interior under an external stress. Therefore, this model should work very well in nanostructured materials synthesized by SPD techniques, which may be why it can explain well the ex-

perimental observations in cryomilled Al [60, 70], SMAT-processed Ni and HPT-processed Cu [62, 80]. For nanostructured materials without nongeometrically necessary dislocations, e.g. nanostructured materials synthesized by methods such as CVD and electro-deposition, dislocation nucleation is a critical step and deformation twinning would require higher external stresses than predicted by our current model.

4.2.2.3 **Wide Stacking Faults**

As discussed in Sections 4.2.2.1 and 4.2.2.2, the formation of wide stacking faults is a precondition for homogeneous twin nucleation and heterogeneous twin nucleation. Traditional wisdom would tell us that it is not possible to form such a wide stacking fault in high stacking fault metals such as Al and Ni, at least it has not been observed in their coarse-grained state, except at crack tips [90, 91]. However, due to the effect of small grain size, wide stacking faults have been indeed observed in nanostructured Al [70] and Ni [92] (see Figs. 4.8 (a) and (b)). An analytical model, based on assumptions similar to those used to develop Eqs. (4.7) and (4.8), predicted that both grain size and applied shear stress affects the width of the stacking fault in nanostructured Al [70] (see Fig. 4.9).

4.2.2.4 **Effect of Generalized Planar Fault Energy**

Recent MD simulations predicted that generalized planar fault energy (GPFE) curves significantly affect the deformation mechanisms of nanocrystalline materials [93]. Specifically, the GPFE curves were predicted to affect the nucleation of partials and twins from grain boundaries [93]. Similar conclusions were also

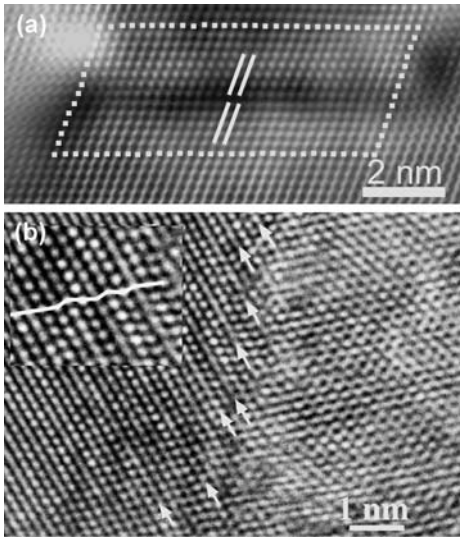

Fig. 4.8 Wide stacking faults in (a) nanostructured Al produced by cryogenic ball milling [70], and (b) nanostructured Ni produced by electrodeposition and tested in tension at liquid-nitrogen temperature [92].

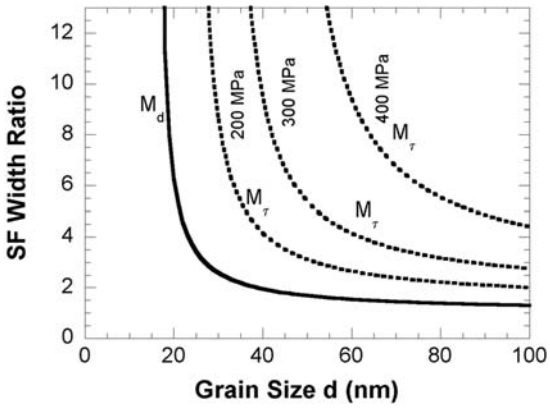

Fig. 4.9 The ratio of the stacking fault width predicted in nanostructured Al to that in coarse-grained Al vs grain size. The solid curve (M_d) considers only the grain-size effect, while the dashed curves (M_τ) consider the effect of both grain size and dynamic stresses. The value of shear stress is indicated near each M_τ curve.

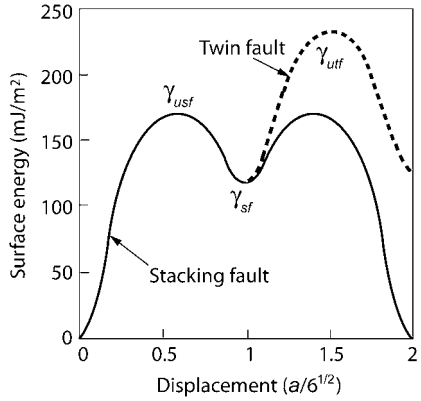

Fig. 4.10 Schematics of the generalized planar fault energy curves for Ni [92, 93]. γ_{sf} is the stable stacking-fault energy; γ_{usf} is the unstable stacking-fault energy; γ_{utf} is the unstable twin-fault energy; a is the lattice constant.

obtained by analytical modeling [94], using an approach similar to dislocation emissions from a crack tip [90, 91]. However, a recent study indicates that the unstable stacking-fault energy γ_{usf} and unstable twin-fault energy γ_{utf} obtained from GPFE curves vary significantly with the models used for their calculation and it is not clear if these values even qualitatively agree with the real values [95], which so far cannot be experimentally measured.

Ni is a perfect candidate for studying the effect of GPFE curves on the deformation mechanisms of nanostructured materials. As shown in Fig. 4.10 [92, 93],

Ni has a very high stable stacking-fault energy (SFE), γ_{sf}, which makes it energetically unfavorable to form a stacking fault by emitting only a leading partial from a grain boundary. However, basing on the GPFE curve features shown in Fig. 4.10, the MD simulation demonstrated that it is the GPFE curves, not the stable SFE, that determines the formation of stacking faults in nanostructured Ni [93]. Specifically, at an applied stress level that can overcome γ_{usf} but not γ_{utf}, only stacking faults will be observed, despite the high γ_{sf}, and no twins will be observed.

To experimentally verify this MD result, Wu *et al.* recently did tensile testing on electrodeposited Ni with an average grain size of 25 nm at liquid-nitrogen temperature, at which the flow stress happens to be able to overcome γ_{usf} but not γ_{utf}, according to Fig. 4.10. However, HREM observations revealed both stacking faults and deformations twins, suggesting that the GPFE curves can reasonably predict stacking faults but not twinning. This discrepancy is attributed to three factors that are beyond the control of GPFE curves: 1) stress concentrations exist at local grain-boundary locations, 2) extremely high stress concentrations near stacking faults [96], and 3) the twinning partial orientation advantage, i.e. it has the same Burgers vector as the leading partial that generated the stacking fault, while the orientation of the trailing partial is very different. Therefore, the applied stress that caused the emission of the leading partial also promotes the emission of the twinning partial instead of the trailing partial. Lastly, the GPFE curves themselves can only be calculated qualitatively [95] and cannot be experimentally verified, which puts any predictions from these curves in doubt.

4.2.3
Grain-boundary Sliding and Grain Rotations

When the grain size is very small, grain-boundary sliding has been predicted to be a deformation mechanism by MD simulations [97–99]. This has also been verified in nanostructured Al and Cu processed by SPD [100, 101]. Note that the grain sizes of the SPD-processed Al and Cu are several hundred nanometers. As the grain sizes become smaller, the grain-boundary sliding becomes more significant. In addition, because of the small grain sizes, it is easier for grains to align to accommodate the grain-boundary sliding. Figure 4.11 [102], an atomic force microscopy (AFM) image of nanostructured Ti deformed in tension at 250 °C, shows that grains, and grain boundaries, appear to align, which indicates that extensive grain-boundary sliding occurred during the deformation.

The grain rotation was first observed through *in-situ* transmission electron microscopy (TEM) by Ke *et al.* [103] in 1995. Recently, Shan *et al.* [66] found under *in-situ* TEM that in nanocrystalline Ni with grain sizes around 10 nm, groups of neighboring grains changed their orientations during straining and formed grain agglomerates. This grain rotation was believed to be accommodated by diffusion. Because of the small grain size, the grain rotations were extremely rapid. Surprisingly, dislocation activity was also observed in a few

Fig. 4.11 An AFM topograph (left) taken from the surface of an HPT-processed Ti sample after being tested in tension at 250 °C for a strain about 30% (see curve 3 in Fig. 4.10). The right micrograph is a derivative of the left one [102].

grains, but dislocation slip was not considered a dominant deformation mechanism. These observations are consistent with molecular-dynamics (MD) simulation, which predicted that nanocrystalline metals deform *via* grain-boundary sliding and rotation at very fine grain sizes (e.g. 3–10 nm) [52, 56]. Note that the grain rotation in nanocrystalline metals and alloys is still controversial. Although TEM has provided direct evidence of grain rotation during deformation, the thin-foil nature of TEM samples casts a doubt as to whether the bulk nanocrystalline materials deform in the same way as thin foils. Recently, it has been found that large plastic deformation by HPT randomized the initial fiber texture of nanocrystalline Ni produced by electrodeposition [104]. This provides indirect evidence that grain rotation indeed happened during the HPT in bulk nanocrystalline Ni. Although all experimental evidence has pointed to the existence of grain rotation, more study is needed to provide clear-cut, undeniable evidence.

4.3 Summary

In summary, nanocrystalline metals and alloys deform via mechanisms different from their coarse-grained counterparts. Deformation mechanisms in nanostructured materials include slip of full dislocations and partial dislocations, deformation twinning, wide stacking faults, grain-boundary sliding, and grain rotations. The activation and significance of each mechanism depend on intrinsic material properties such as stacking-fault energy and shear modulus, structural features such as grain size, and external factors such as applied stress and de-

formation temperature. The following key points can be drawn from available MD simulations and experimental observations:

- Full dislocation slip is found active in grains as small as 10 nm; however, its significance decreases with decreasing grain size.
- Emission of partial dislocations and deformation twinning become significant in nanostructured metals and alloys, even for those with high stacking-fault energy such as Al and Ni.
- There is a clear grain-size effect in the nucleation and growth of deformation twins. For metals and alloys with medium to high stacking-fault energy, deformation twins were observed in grains smaller than a certain value.
- The grain-size effect is explained by an analytical model [85, 86], which, despite its simplicity, shows remarkable agreement with experimental observations for nanostructured Al, Ni and Cu. The model also predicts that deformation twins are difficult to nucleate but easy to grow via a *stress-controlled growth* mechanism.
- Wide stacking faults were observed in nanostructured Al due to a grain-size effect.
- General planar fault-energy curves may be able to explain the stacking faults observed in nanostructured Ni but cannot reasonably predict the nucleation and growth of deformation twinning.
- Grain-boundary sliding and grain rotation may become significant deformation mechanisms with decreasing grain size.

References

1 H. Gleiter **2000**, *Acta Mater.* 48, 1–29.
2 R.W. Siegel **1993**, in *Fundamental Properties of Nanostructured Materials* (eds.) D. Fiorani G. Sberveglieri, World Scientific, Singapore, pp. 3–19.
3 C. Suryanarayana **1995**, *Int. Mater. Rev.* 40, 41–64.
4 C. C. Koch **2003**, *Scr. Mater.* 49, 657–662.
5 E. L. Hu, D. T. Shaw **1999**, in *Nanostructure Science and Technology, A Worldwide Study* (eds.) R.W. Siegel, E. Hu, M.C. Roco, Final Report by WTEC Panel p. 15.
6 H. Gleiter **1981**, in *Deformation of Polycrystals: Mechanisms and Microstructures.* (eds.) Hansen, A. Horsewell, T. Leffers, M. Linolt, Roskilde, Denmark, Risø National Laboratory, p. 15.
7 C. C. Koch **1993**, *Nanostruct. Mater.* 2, 109–129.
8 B. H. Kear, L. E. McCandish **1993**, *Nanostruct. Mater.* **3**, 19–30.
9 H. Chang, C. J. Altstetter, R. S. Averback **1992**, *J. Mater. Res.* 7, 2962–2970.
10 R. Bickerdike, D. Clark, J. N. Easterbrook, G. Hughes, W. N. Mair, P.G. Partridge, H. C. Ranson **1985**, *Int. J. Rapid Solidif.* 1, 305–325.
11 W. Chang, G. Skandan, S. C. Danforth, M. Rose, A. G. Balogh, H. Hahn, B. Kear **1995**, *Nanostruct. Mater.* 6, 321–324.
12 R. A. Roy, R. Roy **1984**, *Mater. Res. Bull.* 119, 69–177.
13 D. A. Rigney **1988**, *Ann. Rev. Mater. Sci.* 18, 141–163.
14 B. Li E. J. Lavernia **1999**, in *Non-Equilibrium Processing of Materials,* (ed.) C. Suryanarayana, Pergamon, New York, p. 153–189.
15 G. W. Nieman, J. R. Weertman, R. W. Siegel **1989**, *Scr. Metall.* 23, 2013–2018.
16 S. R. Agnew, B. R. Elliott, C. J. Yongdahl, K. J. Hemker, J. R. Weertman **2000**, *Mater. Sci. Eng. A* 285, 391–396.
17 P. G. Sanders, G. E. Fougere, L. J. Thompson, J. A. Eastman, J. R. Weertman **1997**, *Nanostr. Mater.* 8, 243–252.

18 J. Rawers, G. Slavens, D. Govier, C. Dogan, R. Doan **1996**, *Metall. Mater. Trans. A* 27, 3126–3134.

19 L. He E. Ma **1996**, *J. Mater. Res.* 11, 72–80.

20 G. R. Shaik W. W. Milligan **1997**, *Metall. Mater. Trans. A* 28, 895–904.

21 R. S. Mishra, J. A. Schneider, J. F. Shackelford, A. K. Mukherjee **1995**, *Nanostruct. Mater.* 5, 525–544.

22 B. Q. Han, J. Y. Huang, Y. T. Zhu, E. J. Lavernia **2006**, *Acta Mater.* 54, 3015–3024.

23 B. Q. Han, Z. Lee, D. Witkin, S. R. Nutt, E. J. Lavernia **2005**, *Metall. Mater. Trans. A* 36, 957–965.

24 B. Q. Han, J. Y. Huang, Y. T. Zhu, E. J. Lavernia **2006**, *Scr. Mater.* 54, 1175–1180.

25 R. Z. Valiev, R. K. Islamgaliev, I. V. Alexandrov **2000**, *Prog. Mater. Sci.* 45, 103–189.

26 V. M. Segal **1999**, *Mater. Sci. Eng. A* 271, 322–333.

27 R. Z. Valiev, O. A. Kaibyshev, R. I. Kuznetsov, R. Sh. Musalimov, N. K. Tsenev **1988**, *Dokl. Akad. Nauk SSSR* 301, 864–866.

28 N. Tsuji, Y. Ito, Y. Koizumi, Y. Minamino, Y. Saito **2002**, in *Ultrafine Grained Materials II* (eds.) Y. T. Zhu, T. G. Langdon, R. S. Mishra, S. L. Semiatin, M. J. Saran, T. C. Lowe. TMS (The Minerals, Metals & Materials Society) p. 389.

29 D. V. Orlov, V. V. Stolyarov, H. Sh. Salimgareyev, E. P. Soshnikova, A. V. Reshetov, Ya. Ye. Beygelzimer, S. G. Synkov, V. N.Varyukhin **2004** in *Ultrafine Grained Materials III* (eds.) Y. T. Zhu, T. G. Langdon, R. Z. Valiev, S. L. Semiatin, D. H. Shin, T. C. Lowe, TMS p. 457.

30 Y. T. Zhu, H. Jiang, J. Huang, T. C. Lowe **2001**, *Metall. and Mater. Trans.* 32A, 1559–1562.

31 K. Lu, J. Lu **1999**, *J. Mater. Sci. Technol.* 15, 193–197.

32 K. Dai, J. Villegas, L. Shaw **2003**, *Acta Mater.* 51, 2647–2663.

33 I. V. Alexandrov, Y. T. Zhu, T. C. Lowe, R. K. Islamgaliev, R.Z. Valiev **1998**, *Metall. Mater. Trans. A* 29, 2253–2260.

34 T. C. Lowe, R. Z. Valiev **2000**, *Investigations and Applications of Severe Plastic Deformation*, (eds.) T. C. Lowe, R. Z. Valiev, Kluwer Academia Publishers, Dordrecht, p. xiii.

35 Y. T. Zhu, X. Z Liao **2004**, *Nature Mater.* 3, 351–352.

36 Y. H. Zhao, X. Z. Liao, S. Cheng, E. Ma, Y.T. Zhu **2006**, *Adv. Mater.* 18, 2280.

37 G. E. Dieter **1986**, *Mechanical Metallurgy*, 3rd edn, McGraw-Hill, Boston, p. 290.

38 Z. Budrovic, H. Van Swygenhoven, P. M. Derlet, S. V. Petegem, B. Schmitt **2004**, *Science* 304, 273–276.

39 E. Ma *JOM* **2006**, 58, 49–53.

40 H. W. Höppel, J. May, M. Göken **2004**, *Adv. Eng. Mater.* 6, 781–784.

41 Y. Wang, M. Chen, F. Zhou, E. Ma **2002**, *Nature* 419, 912–915.

42 K. M. Youssef, R. O. Scattergood, K. L. Murty, J. A. Horton, C. C. Koch **2005**, *Appl. Phys. Lett.* 87, 091904.

43 L. Lu, Y. Shen, X. Chen, L. Qian, K. Lu **2004**, *Science* 304, 422–426.

44 E. Ma, Y. M. Wang, Q. H. Lu, M. L. Sui, L. Lu, K. Lu **2004**, *Appl. Phys. Lett.* 85, 4932–4934.

45 Z. Horita, K. Ohashi, T. Fujita, K. Kaneko, T. G. Langdon **2005**, *Adv. Mater.* 17, 1599–1602.

46 Y. B. Lee, D. H. Shin, K. T. Park, W. J. Nam **2004**, *Scr. Mater.* 51, 355–259.

47 J. K. Kim, H. K. Kim, J. W. Park, W. J. Kim **2005**, *Scr. Mater.* 53, 1207–1211.

48 H. W. Kim, S. B. Kang, N. Tsuji, Y. Minamino **2005**, *Acta Mater.* 53, 1737–1749.

49 Y. H. Zhao, Y. T. Zhu, X. Z. Liao, Z. Horita, T. G. Langdon **2006**, *Appl. Phys. Lett.* 89, 121906.

50 R. Z. Valiev, I. V. Alexandrov, Y. T. Zhu, T. C. Lowe **2002**, *J. Mater. Res.* 17, 5–8.

51 M. W. Chen, E. Ma, K. J. Hemker, H.W. Sheng, Y. M. Wang, X. M. Cheng **2003**, *Science* 300, 1275–1277.

52 K. S. Kumar, S. Suresh, M. F. Chisholm, J. A. Horton, P. Wang **2003**, *Acta Mater.* 51, 387–405.

53 H. Van Swygenhoven **2002**, *Science* 296, 66–67.

54 V. Yamakov, D. Wolf, S. R. Phillpot, A. K. Mukherjee, H. Gleiter **2002**, *Nature Mater.* 1, 45–48.

55 J. Schiøtz, F. D. Ditolla, K. W. Jacobsen **1998**, *Nature* 391, 561–563.

56 H. Van Swygenhoven, P. M. Derlet, A. Hasnaoui **2002**, *Phys. Rev. B* 66, 024101.

57 V. Yamakov, D. Wolf, M. Salazar, S. R. Phillpot, H. Gleiter **2002**, *Acta Mater.* 50, 5005–5020.

58 V. Yamakov, D. Wolf, S. R. Phillpot, A. K. Mukherjee, H. Gleiter **2004**, *Nature Mater.* 3, 43–47.

59 X. Z. Liao, F. Zhou, E. J. Lavernia, S. G. Srinivasan, M. I. Baskes, D. W. He,

Y. T. Zhu **2003**, *Appl. Phys. Lett.* 83, 632–634.
60 X. Z. Liao, F. Zhou, E. J. Lavernia, D. W. He, Y. T. Zhu **2003**, *Appl. Phys. Lett.* 83, 5062–5064.
61 X. Z. Liao, J. Y. Huang, Y. T. Zhu, F. Zhou, E. J. Lavernia **2003**, *Philos. Mag.* 83, 3065–3075.
62 X. Z. Liao, Y. H. Zhao, S. G. Srinivasan, Y. T. Zhu, R. Z. Valiev, D. V. Gunderov **2004**, *Appl. Phys. Lett.* 84, 592–594.
63 H. Rösner, J. Markmann, J. Weissmüller **2004**, *Philos. Mag. Lett.* 84,321–334.
64 Y. T. Zhu, J. Y. Huang, J. Gubicza, T. Ungár, Y. M. Wang, E. Ma, R. Z. Valiev **2003**, *J. Mater. Res.* 18, 1908–1917.
65 X. L. Wu, E. Ma **2006**, *Appl. Phys. Lett.* 88, 231911.
66 Z. W. Shan, E. A. Stach, J. M. K. Wiezorek, J. A. Knapp, D. M. Fallstaedt, S. X. Mao **2004**, *Science* 305, 654–657.
67 I. Kim, J. Kim, D.H. Shin, X.Z. Liao, Y.T. Zhu **2003**, *Scr. Mater.* 48, 813–817.
68 X. Z. Liao, Y. T. Zhu unpublished data.
69 J. Schiøtz, K. W. Jacobsen **2003**, *Science*, 301, 1357–1359.
70 X. Z. Liao, S. G. Srinivasan, Y. H. Zhao, M. I. Baskes, Y. T. Zhu, F. Zhou, E. J. Lavernia, H. F. Xu **2004**, *Appl. Phys. Lett.* 84, 3564–3566.
71 X. Wu, Y. T. Zhu, M. W. Chen, E. Ma **2006**, *Scr. Mater.* 54, 1685–1690.
72 S. Hai, E. B. Tadmor **2003**, *Acta Mater.* 51, 117–131.
73 C. D. Liu, M. N. Bassim, D. X. You **1994**, *Acta Met. Mater.* 42, 3695–3704.
74 N. Hansen, B. Ralph **1982**, *Acta Metall.* 30, 411–417.
75 O. Johari, G. Thomas **1964**, *Acta Metall.* 2, 1153–1159.
76 C. S. Smith **1958**, *Trans. Met. Soc. AIME.* 212, 574–589.
77 T. H. Blewitt, R. Coltman, J. K. Redman **1957**, *J. Appl. Phys.* 28, 651–660.
78 M. A. Meyers, O. Vöhringer, V. A. Lubarda **2001**, *Acta Mater.* 49, 4025–4039.
79 E. El-Danaf, S. R. Kalidindi, R. D. Doherty **1999**, *Metall. Mater. Trans.* 30A, 1223–1233.
80 X. Z. Liao, Y. H. Zhao, Y. T. Zhu, R. Z. Valiev, D. V. Gunderov **2004**, *J. Appl. Phys.* 96, 636–640.
81 X. Wu, Y. T. Zhu **2006**, *Appl. Phys. Lett.* 89, 031922.
82 Y. T. Zhu, X. Z. Liao, R. Z. Valiev **2005**, *Appl. Phys. Lett.* 86, 103112.
83 A. J. Cao, Y. G. Wei **2006**, *Appl. Phys. Lett.* 89, 041919.
84 R. J. Asaro, P. Krysl, B. Kad **2003**, *Philos. Mag. Lett.* 83, 733–743.
85 Y. T. Zhu, X. Z. Liao, Y. H. Zhao, S. G. Srinivasan, F. Zhou, E. J. Lavernia **2004**, *Appl. Phys. Lett.* 85, 5049–5051.
86 Y. T. Zhu, X. Z. Liao, S. G. Srinivasan, E. J. Lavernia **2005**, *J. Appl. Phys.* 98, 034319.
87 L. E. Murr **1975**, *Interfacial Phenomena in Metals and Alloys*, Addison-Wesley, London, p. 145.
88 H. Van Swygenhoven, M. Spaczer, A. Caro, D. Farkas **1999**, *Phys. Rev. B* 60, 22–25.
89 J. Y. Huang, Y. T. Zhu, H. Jiang, T. C. Lowe **2001**, *Acta Mater.* 49, 1497–1505.
90 J. R. Rice **1992**, *J. Mech. Phys. Solids* 40, 239–271.
91 E. B. Tadmore, S. Hai **2003**, *J. Mech. Phys. Solids* 51, 765–793.
92 X. Wu, Y. T. Zhu, E. Ma **2006**, *Appl. Phys. Lett.* 88, 121905.
93 H. Van Swygenhoven, P. M. Derlet, A. G. Frøseth **2004**, *Nature Mater.* 3, 399–403
94 R. J. Asaro, S. Suresh **2005**, *Acta Mater.* 53, 3369–3382.
95 J. A. Zimmerman, H. J. Gao, F. F. Abraham **2000**, *Model. Simul. Mater. Sci. Eng.* 8, 103–115.
96 J. Wang, H. Huang **2004**, *Appl. Phys. Lett.* 85, 5983–5985.
97 H. Van Swegenhoven P. M. Derlet **2001**, *Phys. Rev. B* 63, 134101.
98 M. A. Meyers, A. Mishra, D. J. Benson **2006**, *Prog. Mater. Sci.* 51, 427–556.
99 M. A. Meyers, A. Mishra, D. J. Benson **2006**, *JOM* 58, 41–48
100 N. Q. Chinh, P. Szommer, Z. Horita, T. G. Langdon **2006**, *Adv. Mater.* 18, 34–39.
101 R. Z. Valiev, E. V. Kozlov, Yu. F. Ivanov, J. Lian, A. A. Nazarov, B. Baudelet **1994**, *Acta Mater.* 42, 2467–2475.
102 Y. T. Zhu, M. Hawley, R. Z. Valiev unpublished result.
103 M. Ke, S. A. Hackney, W. W. Milligan, E. C. Aifantis **1995**, *Nanostruct. Mater.* 6, 689–697.
104 X. Z. Liao, R. Z. Valiev, H. S. Gao, X. D. Li, A. K. Mukherjee, J. F. Bingert, Y. T. Zhu **2006**, *Appl. Phys. Lett.* 88, 021909.

5
Modeling of Strength and Strain Hardening of Bulk Nanostructured Materials

Michael J. Zehetbauer and Yuri Estrin

5.1
Introduction

To date, processing of bulk nanostructured materials has been achieved through a limited number of methods that may be classified broadly as "bottom-up" and "top-down" techniques. According to other articles within this book, e.g. Chapter 1 by C.C. Koch, the first group is represented by electrodeposition techniques, or by those utilizing consolidation of nanostructured powders produced by ball milling or inert-gas condensation. Although some growth of the average grain size achieved with ball milling or inert-gas condensation occurs during compaction at elevated temperatures, it can be kept at bay, within the order of a few 100 nm. Currently, bulk nanomaterials several millimeters in thickness can be synthesized by these methods (see Chapter 12 by B. Q. Han et al. and Chapter 1 by C. C. Koch). The second group involves materials that are in bulk shape before the nanocrystalline structure is produced. This has the advantage that contamination with impurities and also health hazards associated with handling of nanopowders are avoided. Since some classes of alloys can be synthesized in both glassy and bulk shape (see Chapter 13 by G. Wilde), bulk nanomaterials can be produced by well-defined thermal treatment of such alloys. Arguably the most successful method has been nanostructuring by severe plastic deformation, or SPD, introduced by R. Z. Valiev (see Chapter 2). SPD techniques achieve nanostructuring of a bulk workpiece by keeping its shape unchanged, yet introducing an extremely high degree of plastic deformation under simultaneous application of high hydrostatic pressure. Most commonly, this occurs in a repetitive process, which is possible due to the shape of the workpiece being preserved.

The aim of this chapter is to review models that have been developed to describe and predict the strength and plasticity of ultrafine or nanocrystalline metallic materials. We also address modeling of the evolution of the microstructure towards nanocrystallinity under severe plastic deformation and the attendant enhancement of strength characteristics. This chapter focuses on the range of grain sizes well above ≈ 20 nm where strength and strain hardening are still

Bulk Nanostructured Materials. Edited by M. J. Zehetbauer and Y. T. Zhu

ISBN: 978-3-527-31524-6

governed by dislocation mechanisms. Models covering the range below this value have been described in detail in the articles of Y. Zhu et al. (Chapter 4, analytical models) and D. Wolf et al. (Chapter 7, molecular dynamics "MD" model simulations) in this book.

5.2
Modeling of Strength and Strain Hardening of Ultrafine-grained and Nanocrystalline Materials

Models addressing the strength and/or the strain hardening of nanomaterials in most cases imply that there is a monomodal grain-size distribution without any crystal lattice defects within the grain interior. Such models will be treated in Section 5.2.1. As concerns SPD processed nanomaterials, these models will apply only if SPD nanomaterials have undergone a particular thermal treatment and attained a well-recovered, equilibrated grain structure. Usually, SPD nanomaterials – at least in their as-processed state – show an ultrafine-grained or nanoscaled structure with highly nonequilibrium grain boundaries as well as considerable densities of lattice defects left in the grain interior by plastic deformation. These process-inherited features have decisive consequences for the macroscopic properties of the resulting nanomaterials. Thus, in order to achieve reliable model predictions of the properties of SPD nanomaterials, it is necessary to simulate the processing procedure and the ensuing nanostructure, rather than referring to a simplified quasiequilibrated nanostructure. Models describing the strength and strain hardening of SPD nanomaterials are to be discussed separately, and this will be done below in Section 5.2.2.

5.2.1
Modeling of Hardening of Equilibrated Nanostructures

One of the most apparent and well-known effects of nanoscaled structure on the macroscopic strength has been the lowering of the Hall–Petch slope with decreasing grain size. In some cases the slope even becomes negative after a strength maximum is passed, which behavior is referred to as the inverse Hall–Petch one. Most of the models available attribute this effect to grain-boundary sliding, or to the formation of shear bands.

Motivated by the fact that neither Coble creep (controlled by grain-boundary diffusion) nor Nabarro–Herring creep can account for the measured exponents of the grain size governing the measured stress data [1–3], Hahn and Padmanabhan [4, 5] tried to model this effect by quantifying the balance between the generation and annihilation of the grain-boundary area. They did that by assuming a special mechanism of grain-boundary sliding (Fig. 5.1), on the basis of minimizing the grain-boundary energy as the driving force, and received Hall–Petch type laws (τ proportional to $1/L^2$, where τ is the shear stress and L is the grain size) both for the part with a positive slope below a critical stress/grain

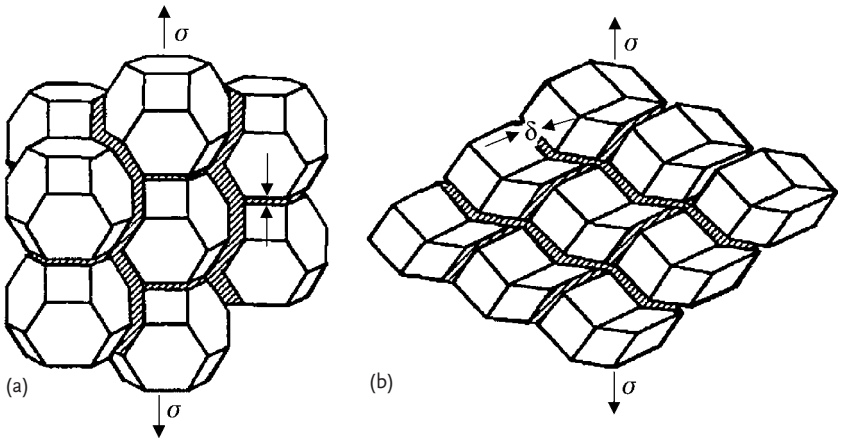

Fig. 5.1 Illustration of the rate-controlling sliding of grain boundaries surrounding arrays of essentially nondeforming (a) tetrakai-decahedral and (b) rhombic dodecahedral grains (after Hahn and Padmanabhan [4, 5]).

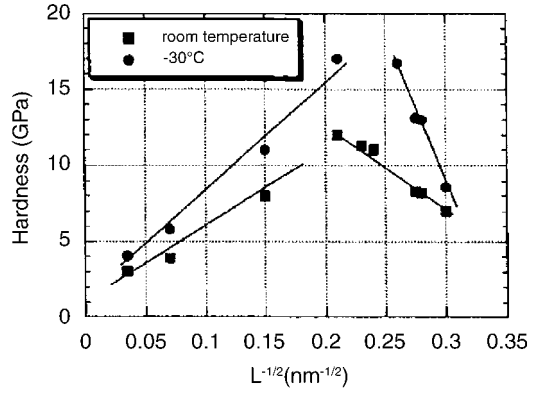

Fig. 5.2 Hardness of nanocrystalline Ti-Al measured at two temperatures. Down at a critical grain size of about $L = 25$ nm, there occurs Hall–Petch "hardening", whereas below that grain size Hall–Petch "softening" is observed. The lines corresponding to model calculations fit the experimental data reasonably well (after Hahn and Padmanabhan, [4]).

size where dislocation mechanisms are predominant, and the part with negative slope owing to grain-boundary sliding (Fig. 5.2).

It should be noted that various molecular-dynamics simulations agree with the Hahn–Padmanabhan model, although the unrealistically high strain rates used in the simulations are still problematic (see also Chapter 7 by D. Wolf in this book). The problem is also a challenge to experimentalists, for example, to

those investigating texture that can decide on the question whether the grain boundary mechanism has a pure shear character or consists in grain rotation as in classical superplasticity.

The fact that Hahn and Padmanabhan assumed a grain-boundary sliding mechanism that differs from both Coble and Nabarro–Herring creep is the reason why they obtained the creep rate $d\varepsilon/dt$ (time derivative of strain ε) to be inversely proportional to the grain size L, i.e. $d\varepsilon/dt \propto 1/L$ [6], which differs from the creep rate laws for superplasticity [7, 8] and from those of many other models, e.g. that of Kim, Estrin and Bush first formulated in 2000 [9] where a $d\varepsilon/dt \propto 1/L^2$ law for the grain-boundary phase follows. Like all models described in this section, the model in ref. [9] simulates the hardening behavior of materials that already possess a nanocrystalline structure. Basically it is a phase-mixture model that builds on early work by Carsley et al. [10] considering the total stress as a weighted sum of the contributions of grain-boundary regions and of grain interiors, similar to the composite ansatz of the models discussed in Section 5.2.2. The specific features of Kim et al.'s model [9] are that the plastic flow of the grain-boundary phase obeys a viscous law characteristic of a pseudoamorphous structure, while the flow in the grain interior is described by a one-internal-variable dislocation model [11], and by diffusion-controlled plastic flow. In 2005, Kim and Estrin [12] published a further version of [9] where the viscous flow of the grain-boundary phase was expressed in terms of a diffusion-controlled process, too. As distinct from the model of Hahn and Padmanabhan, the phase-mixture models [9, 12] describe the strength maximum in the Hall–Petch plot (Fig. 5.3) by the transition from dislocation slip dominated deformation of the grain interiors (positive Hall–Petch slope) to diffusion-controlled deformation of both phases (negative Hall–Petch slope) with decreasing grain size. They

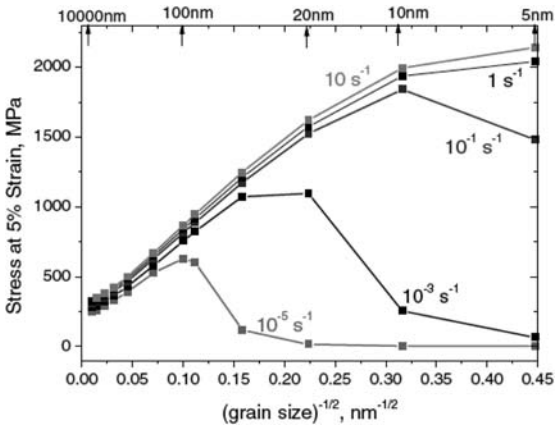

Fig. 5.3 Grain-size dependence of the flow stress of Cu at a proof strain of 5% presented in a Hall–Petch diagram (from [12]).

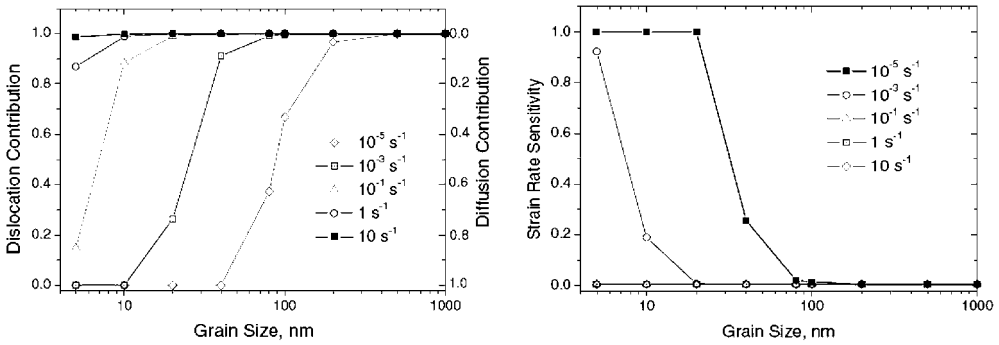

Fig. 5.4 Left-hand side: Relative contributions from dislocation-glide-controlled deformation mechanism (left axis) and the diffusion controlled ones (right axis). Right-hand side: Concomitant variation of strain-rate sensitivity of the flow stress, for different strain rates as indicated (from [12]).

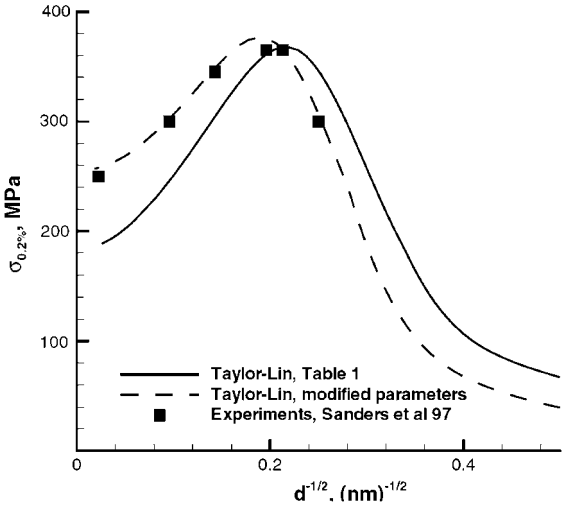

Fig. 5.5 Hall–Petch dependences for copper calculated by two variants of the model by Mercier et al. (lines, [14]) and compared to experimental data by Sanders et al. (symbols, [15]); from [14].

also make quantitative predictions concerning the strain-rate dependence of the critical grain size at which the predominant mechanism changes (Fig. 5.4).

Capolungo et al. [13] modified Kim et al.'s model [9] and implemented it in a self-consistent formulation in which the grain interior is represented as an ellipsoidal Eshelby-type inclusion. However, this modification did not bring about any principal improvement of predictive capability. The latest development of [9] is the work by Mercier et al. [14] who used the Taylor–Lin homogenization

scheme to include elasticity. The quantitative agreement of the predicted grain-size dependence of the yield stress of Cu with experiments by Sanders et al. [15] both in the normal and in the inverse Hall–Petch range is quite remarkable (Fig. 5.5).

Investigations of negative Hall–Petch slope have recently been complemented by the work of Trelewitz and Schuh [16] giving evidence that the shear banding/grain-boundary sliding effects in amorphous metals may have the same basic physical reasons. More work has to be done in the future to further substantiate this idea.

For further approaches and details to modeling the grain-size effects in the range of ultrafine and nanoscale grain sizes, the reader is referred to the detailed review of Meyers et al. [17].

5.2.2 Modeling of Strength and Structure Evolution during Nanostructuring by Severe Plastic Deformation: SPD models

5.2.2.1 Constitutive Models for Strain Hardening at Large Strains

The history of most of these models goes back to the seminal concept of Kocks [18] who derived macroscopic strain hardening from a constitutive description based on statistical generation, interaction and annihilation of dislocations. This type of model employing the total dislocation density as an internal variable provides an adequate description of stages II and III of strain hardening, but fails to cover stages IV and V that are predominant at large strains [19]. Considering a dislocation-cell-forming material and adopting the successful concept of Mughrabi [20] in which the dislocation structure is regarded as a "composite" of dislocation-poor areas ("cell interiors") and dislocation-rich areas ("cell walls"), Prinz and Argon [21], and later Nix et al. [22] were able to account for stage-IV and stage-V hardening by applying the concept of Kocks for both "phases". Zehetbauer [23] formulated this idea in terms of different types of dislocations and succeeded in describing stage-IV and stage-V hardening characteristics for both low [23] and high [24] deformation temperatures, and different strain rates. Moreover, generation and annihilation of vacancies were considered that appear in high concentrations especially under large strain plastic deformation (Fig. 5.6, right-hand side). While promoting dislocation annihilation via climb, the profuse presence of these vacancies accounts for the saturation of strength in stage V even at deformation temperatures as low as $T \cong 0.2\ T_m$, where T_m is the melting temperature in K (Fig. 5.6, left-hand side). Zehetbauer's model also provides a fair description of the cell/grain-size evolution [25].

In 1998, Estrin et al. [26, 27] published a model that also builds on the composite principle. They did not distinguish between different types of dislocations but put more emphasis on the exchange of dislocations between cell interior and cell walls, and included a basic thermally activated contribution to stress. In contrast to the model of Zehetbauer [23], which postulated a constant volume fraction of cell walls, Estrin et al. found that this volume fraction must decrease

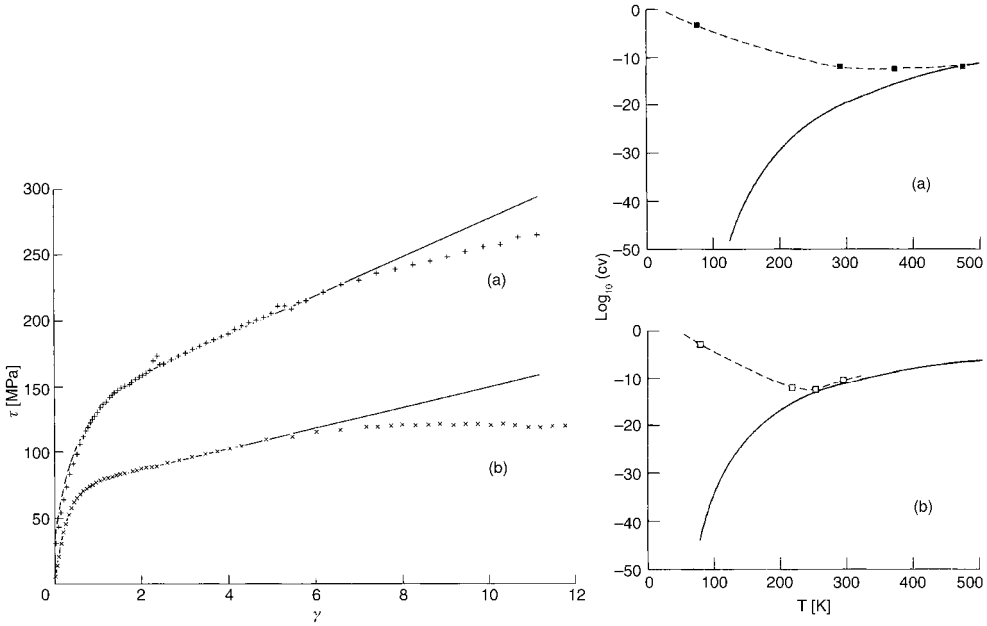

Fig. 5.6 Left-hand side: Fits of Zehetbauer's model to (a) Cu and (b) Al stress–strain characteristics measured by room-temperature torsion. Without the presence of deformation-induced vacancies, the model (full line) fails to represent the experimental data points (symbols). Right-hand side: The concentration of vacancies (cv) as a function of deformation temperature for the case of (a) Cu and (b) Al. Below 0.2 T_m, the real vacancy concentration (cv) (dashed line and experimental data points) vastly exceeds that of thermal vacancies (full line, from [23]).

during stage IV (see Fig. 5.7 right-hand side) in order to account for the nearly constant hardening coefficient characteristic of stage IV.

Starting in 1997, Nes and Marthinsen [29–31] developed a model that combines strain hardening/softening from storage/annihilation of free dislocations with that from the Hall–Petch-type hardening/softening due to formation and dissolution of dislocation cell/subboundaries. It is assumed that the softening mechanisms (i.e. those of dynamic recovery) are governed by the same activation enthalpy, of either cross-slip or climb of dislocations. The model well describes the variation of strain hardening during the deformation stages IV and V as well as its strain-rate dependence (Fig. 5.8).

The composite models of Roters et al. [32] and Gördeler et al. [33, 34] have in common that they consider three types of dislocations: sessile cell wall and cell interior ones, and the mobile dislocations carrying the plastic deformation. The models also account for possible reactions between dislocations of these different types by a set of coupled differential equations describing the evolution of the three dislocation populations. Furthermore, the models distinguish between thermally activated and athermal stress components.

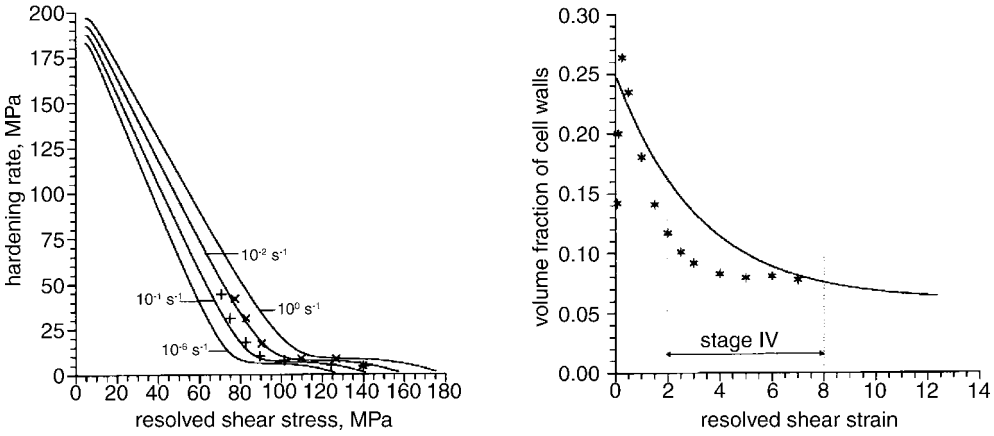

Fig. 5.7 Left-hand side: Calculations of the strain-rate dependence of the strain hardening rate in Cu according to the model by Estrin et al. [26]. The calculated curves are in good accord with the experimental data obtained by Zehetbauer et al. [19]. Right-hand side: The volume fraction of cell walls as a function of resolved shear strain. The solid line corresponds to a fit function used in [26] while the stars represent X-ray profile broadening measurements by Müller et al. [28].

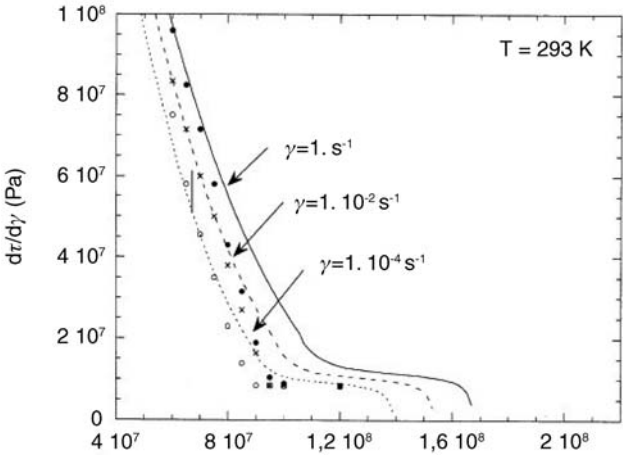

Fig. 5.8 Strain-rate dependence of strain hardening of Cu at large strains for torsional straining (from Nes [31]). The symbols represent the measurements by Zehetbauer and Seumer [19], while the lines represent predictions based on the model by Nes and Marthinsen [31].

Another concept suitable for describing strain-hardening curves at large strains has been suggested by Hughes and Hansen [35]: In their approach, strain hardening is brought into connection with the main elements of microstructure (notably geometrically necessary boundaries (GNBs), and incident dislocation boundaries, IDBs. see Fig. 5.9). By using individual established harden-

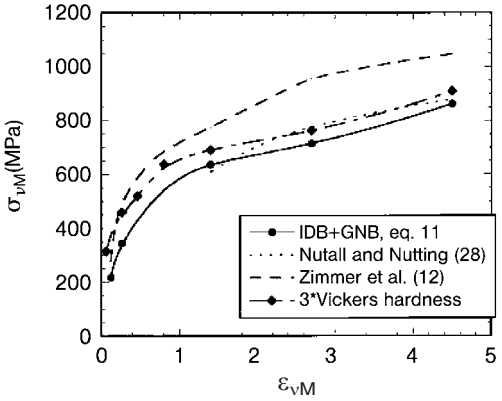

Fig. 5.9 Overall stress as a function of the von Mises strain in severely plastically deformed Ni (from Hughes and Hansen, [35]). Modeling of strength by IDB and GNB hardening matches the experimental data.

ing laws with these elements, and by adding up the individual contributions to strength, this formalism provides a reasonably good description of strength and strain hardening up to large strains. However, this approach does not describe the deformation-induced evolution of the microstructure. Neither does it derive the variation of strength from this evolution; it only shows that the hardening laws for the different structural elements work well and that the stress from these different stress sources can be linearly added to provide a good fit to the macroscopic overall strength.

By contrast, the model by Pantleon and coworkers [36–38] is based on elementary microstructural processes implemented in dislocation flux balances and specific dislocation storage and annihilation in IDBs and GNBs. Although it is of the one-internal-variable type and uses the original concept of Kocks [18] of statistical dislocation kinetics, the model is able to predict the strain-hardening coefficient for the deformation stages II, III and IV. The power of the model lies in the accurate prediction of details of the microstructural evolution, i.e. that of the misorientation angles of both IDBs and GNBs (Fig. 5.10, left-hand side), and the evolution of grain size. The misorientation evolution of both types of boundaries is a consequence of the imbalance of dipole and/or tilt dislocations of different signs as they meet at grain boundaries. It was shown [38] that the strain hardening in stage IV results from the misorientation of GNBs only (Fig. 5.10, right-hand side).

An interesting approach that focuses on the aspect of grain fragmentation, i.e. the evolution of misorientation and grain division during large strain plastic deformation, is to use the concept of disclinations described in detail by Romanov and Vladimirov [39]. Such defects are thought to develop from groups of excess dislocations formed in double cross-slip events. The end lines of these groups correspond to lines of discontinuity of misorientation and are repre-

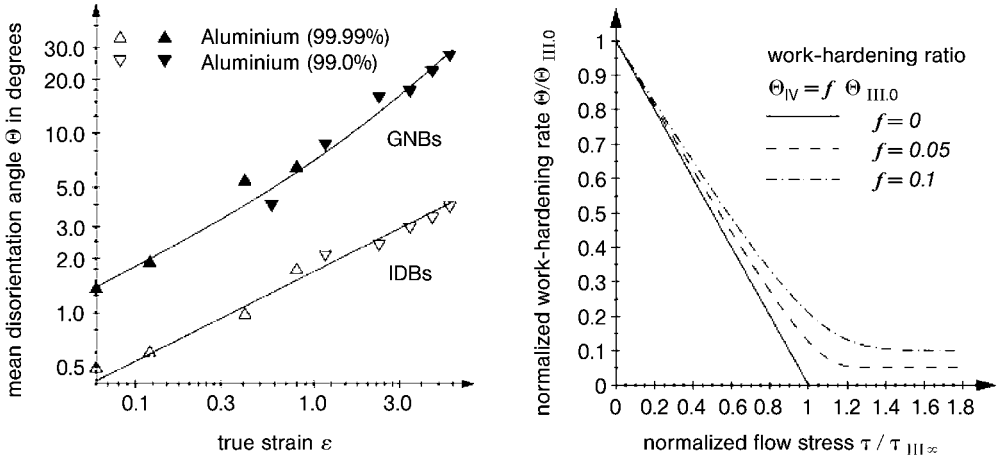

Fig. 5.10 Modeling of misorientation and strain hardening for large-strain cold-worked Al. The growth of misorientation of IDBs and GNBs follows different laws that are confirmed by TEM data (left figure). Stage-IV hardening is intimately connected with the volume fraction f of GNBs (right figure, after Pantleon [38]).

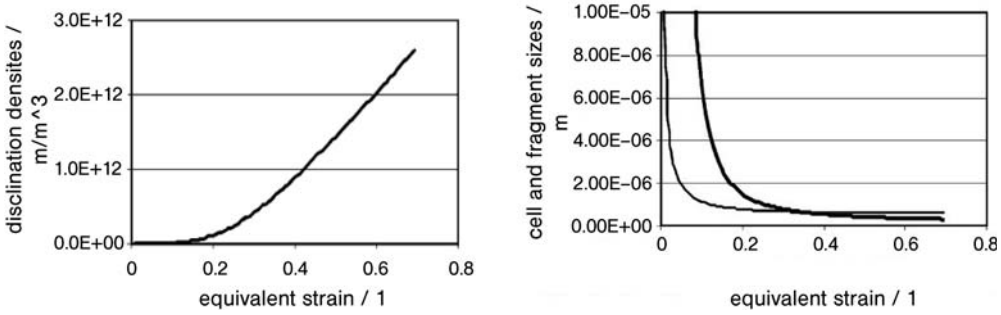

Fig. 5.11 Calculated evolution of disclination density (left-hand side), as well as of cell size (thin line) and fragment size (thick line) in the right figure, as a function of compression strain for a [112] Cu single crystal (from Seefeldt, [40]).

sented by dipoles of partial disclinations with mutually compensating noncrystallographic Frank vectors. These vectors determine the rotation axes and angles by which the crystal lattice around the disclinations has been rotated. Seefeldt [40–42] suggested a model describing the fragmentation in terms of generation, propagation and immobilization of partial disclinations. The model was successfully applied to the compression of [112] Cu single crystals at room temperature. As shown in Fig. 5.11, the size of dislocation cells with equally oriented crystal lattice, d_c, obeying a Holt-type scaling law, $d_c = K(\rho_{tot})^{-1/2}$ [43], and the fragment size d_f of misoriented crystal regions given by $d_f = (2\theta_{tot})^{-1/2}$ were derived. Here, ρ_{tot} and θ_{tot} denote the total dislocation density and the average

misorientation angle, respectively; K is a numerical constant. The results of Seefeldt's model compare favorably with the experimental findings.

It should be noted that already in 1999 Seefeldt et al. formulated a constitutive composite model concerning both disclination and dislocation interactions and proposed to apply it for modeling SPD processes [42]. Meanwhile, a number of other authors also considered their models for SPD applications as is described in detail in the next section.

5.2.2.2 Application of Large-strain Models to SPD Processes

Models for SPD Processes with Low Hydrostatic Pressure Some of the models described above, which have been originally designed for large-strain plastic deformation, have been successfully applied to cases of severe plastic deformation (SPD). Thus, the model of Zehetbauer [23] has been used by Zeipper et al. [44] to describe the deformation behavior on an ECAP-processed commercial purity (CP) Ti alloy.

The model also provides an adequate description of the evolution of dislocation density, the vacancy concentration (Fig. 5.12, left-hand side) and the dislocation cell size (Fig. 5.12, right-hand side) that is equivalent to the crystallite size as determined from X-ray profile broadening measurements [44].

The strain-hardening model of Estrin [26, 27] was applied to describe the microstructure evolution and the strength characteristics associated with it for ECAP processing of Cu and Al [45–47]. Simulations of the stress, strain and dislocation structure were coupled with simulations of the texture evolution. Extensive experimental measurements of strength, microstructure and misorientation

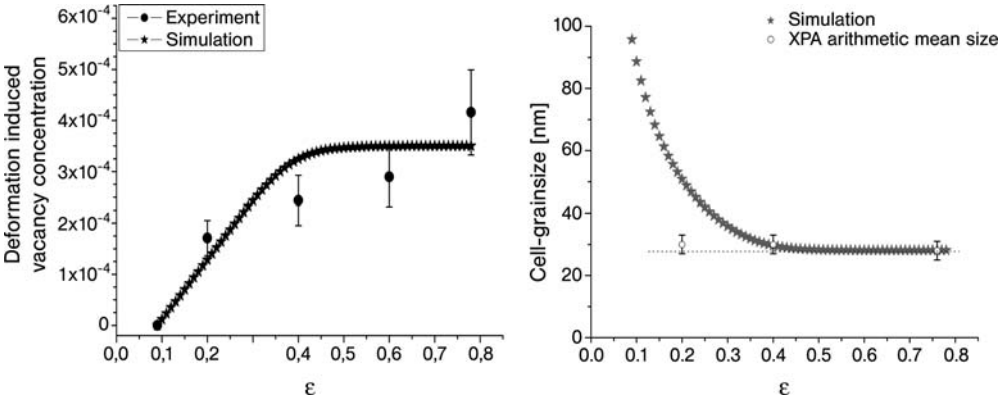

Fig. 5.12 Uniaxial room-temperature tensile deformation of CP-Ti after ECAP processing at 473 K. Left-hand side: Evolution of vacancy concentration, right-hand side: Evolution of cell size. Symbols represent data from residual electrical resistivity measurements and X-ray profile broadening, respectively (after Zeipper et al., [44]).

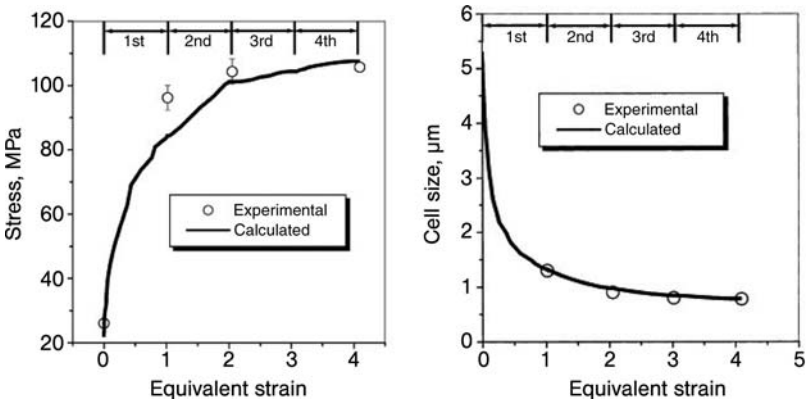

Fig. 5.13 Experimental and calculated values of stress and cell size after different amounts of ECAP deformation in pure Al (Baik et al., [47]).

distribution (see, e.g. Fig. 5.13 [47]) have proven the validity of the model with respect to strength, grain size and texture. Recently, Estrin et al. [48] extended the model to describe the evolution of misorientation-angle distribution, in the way similar to Pantleon's approach [36–38] of specific dislocation storage and annihilation in IDBs and GNBs, and a stochastic description in terms of the Fokker–Planck equation.

It should be mentioned that the role of dislocation storage in the grain-boundary formation and the grain-fragmentation process has also been considered by Mohamed [49] for the case of ball milling. Based on the idea of balance between generation and annihilation of dislocations, the smallest grain size $d_{\min}$ attainable by a material at a given milling strain rate and temperature was calculated. The role of strain imparted to the material is played by the milling time, $d_{\min}$, is calculated as a function of strength σ, the melting temperature T_m, and the stacking-fault energy γ. An interesting parallel to the strain-hardening model of Zehetbauer [23] is the consideration of deformation-induced excess vacancies with concentration $c(\varepsilon)$, with ε denoting the strain. Mohamed performs the same substitution of thermal vacancies c_{th} by deformation induced ones $c(\varepsilon)$, and assumes linearity, i.e. $c(\varepsilon) = k\varepsilon$. The rate of grain-size decrease is proportional to the energy of milling, while the rate of grain-size increase is determined by climb-controlled dislocation annihilation. Thus, as in Zehetbauer's model using a derivation by Argon and Moffat [50], the dislocation annihilation rate is proportional to σ, D (coefficient of self diffusion), γ^2 and indirectly proportional to kT, where k is the Boltzmann constant and T the absolute temperature. From the fact that the minimum grain size requires a balance between decreasing and increasing rates of grain size, Mohamed found $d_{\min}$ to depend on the stress through $d_{\min} \propto \sigma^{-1.25}$, a relation that has been clearly confirmed by ball-milling experiments with a number of metals yielding, within experimental

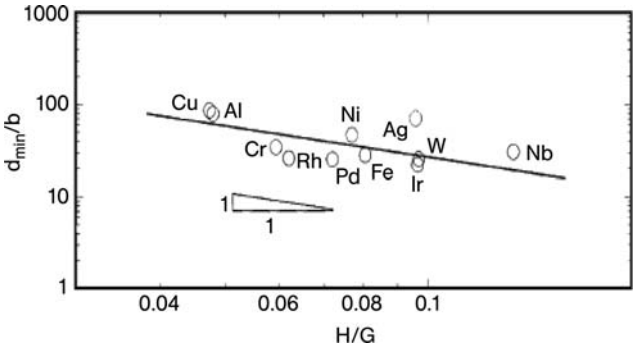

Fig. 5.14 The normalized minimum grain size achievable by ball milling as a function of hardness H normalized with respect to the shear modulus *G*. The model predicts a stress exponent of –1.25 (full line) which is roughly fulfilled by the experimental data (circles, from Mohamed [49]).

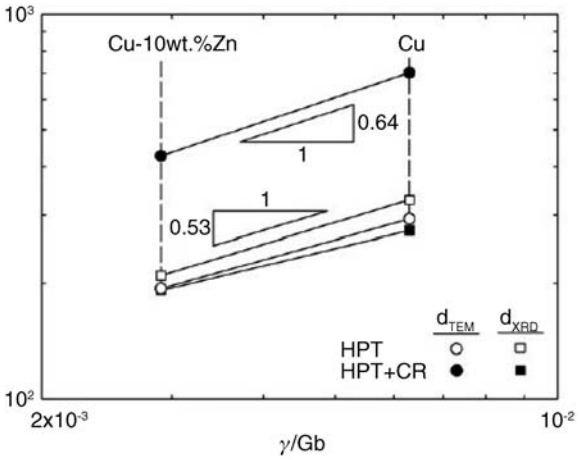

Fig. 5.15 The normalized minimum grain size as a function of the normalized stacking-fault energy. Data are from TEM and XRD measurements for HPT, and HPT followed by rolling (after Zhao et al., [51]).

error, $d_{min} \approx \sigma^{-1.3}$ (see Fig. 5.14). The experimental dependence of d_{min} on γ^n is also in accord with the model predictions, albeit less clearly than the stress dependence. Indeed, the experiment gives an exponent of $n = 0.65$ instead of the predicted one of 0.5. Since this dependence has recently been confirmed for HPT deformed as well as HPT and post-rolled Cu and CuZn specimens [51], it seems to hold also for SPD-processed nanomaterials (Fig. 5.15).

Relatively good agreement of the modeled value of d_{min} with experimental data was also achieved with regard to its dependence on the self diffusion en-

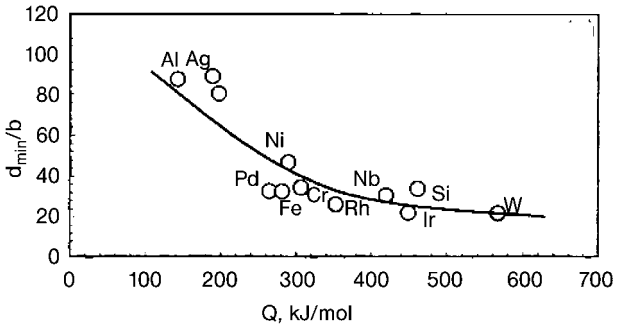

Fig. 5.16 The normalized minimum achievable grain size in ball milling as a function of self-diffusion enthalpy Q. The model fits the experimental data reasonably well (from Mohamed, [49]).

thalpy Q (see Fig. 5.16), bulk modulus, and the equilibrium spacing of two piled-up edge dislocations. There are indications that the dependence of $d_{\min}$ on the milling temperature is well reproduced, too, but more experimental data on cryomilled materials and especially on SPD-processed ones are required to ascertain agreement between modeling and experiment.

The models of Estrin [26, 27, 45–47] and Zehetbauer [23, 44] have been further developed by a number of authors. For example, the former has been used (in a slightly modified form) by Enikeev and coworkers [52] to describe quantitatively the evolution of misorientation with proceeding strain. Following the ideas of Pantleon (see Section 5.2.2.1) they start from the Read–Shockley relation for the misorientation $\Theta = bd\Delta\rho$, where d is the grain size calculated after Estrin et al. [26] and $\Delta\rho$ is the increase of the sessile part of the dislocation density in the grain boundary due to the incorporation of dislocations from the grain interior. $\Delta\rho$ is calculated by solving the evolution equations for two dislocation densities introduced by analogy to those in [26, 27], i.e. for grain-boundary dislocations and grain-interior ones. The calculated misorientation data well match the measuring results of Belyakov et al. [53] on multiforged Cu (Fig 5.17). Enikeev et al. also calculated the evolution of total dislocation density with increasing strain for both ECAP and HPT deformation. They found a reasonable agreement with measurements by X-ray diffraction, which exhibited a steady decrease of the dislocation density as a function of SPD-induced strain (Fig. 5.18).

An example of a further development of Zehetbauer's model [23] is an approach by Alexandrov et al. [54] where deformation by twinning was considered in addition to that by dislocation slip, as twinning appears to play an important role in the deformation of materials with small grain sizes and/or low stacking-fault energies [55, 56]. Alexandrov et al. used the relations of Barnett et al. [57] and Remy [58] for the Hall–Petch type hardening by twinning, and assumed the (edge) dislocations in grain boundaries act as the nuclei of the twins. The total strain was taken as a sum of the strains due to dislocation slip and twinning weighted by the respective volume fractions.

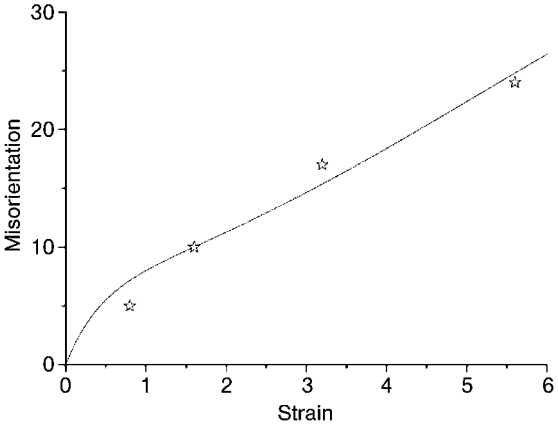

Fig. 5.17 Misorientation as a function of true equivalent strain for Cu subjected to multiple forging. Stars: measured data [53], lines: model fit (after Enikeev et al., [52]).

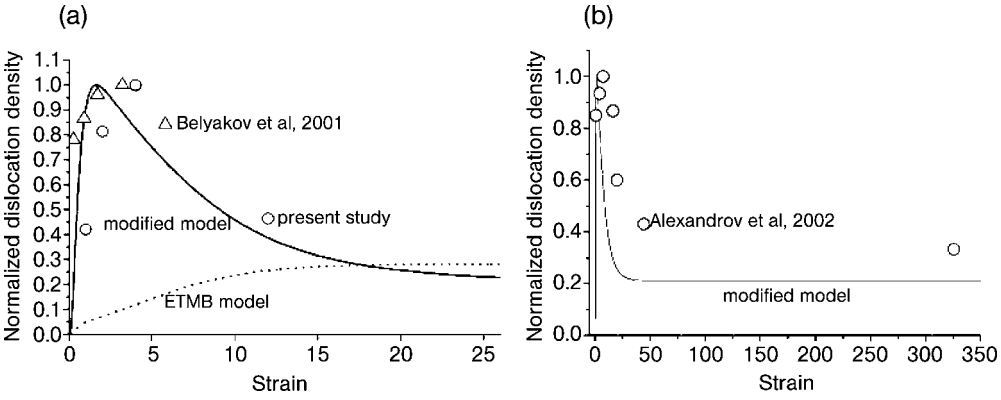

Fig. 5.18 Evolution of dislocation density as a function of strain. While the full lines represent the results from the Enikeev model, the dotted line corresponds to calculations according to the model of Estrin et al. [26, 27]. Experimental data in the left figure are for Cu processed by multiple forging (triangles), and by ECAP (circles), whereas those in the right figure (circles) are from Cu processed by HPT (from [52]).

Nes et al. [59] have also applied their earlier model ([29–31], see above) to materials with grain sizes below 1 μm, and obtained good agreement with the observed stress–strain curves as well as with microstructural evolution. The total stress obeys the classical Hall–Petch relation although the parameters in this relation depend on alloy content and strain. The model can be used either for the description of microstructure or for simulating the stress/strain characteristics of an ultrafine-grained (UFG) material as it evolves during straining. As long as the grain size is larger than about $D = 500$ nm, the pileup stress is sufficient for

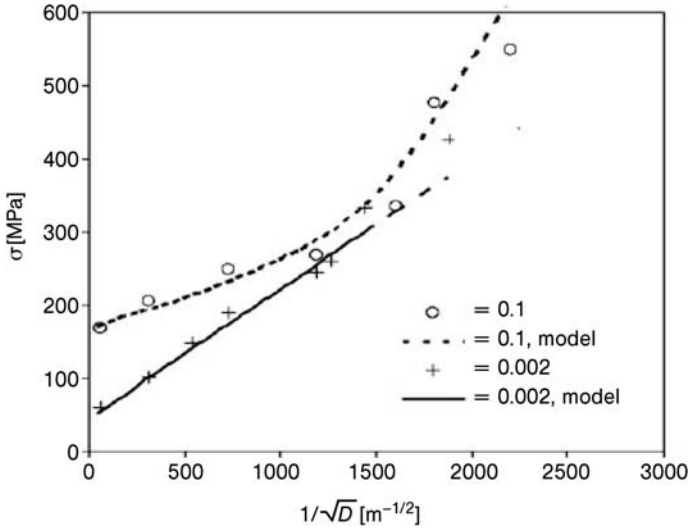

Fig. 5.19 Hall–Petch plot for $AlMg_3$, of measured yield stresses (ε=0.002) and flow stresses (ε=0.1) (symbols), and simulated ones using the extended model of Nes et al. [59] (lines).

propagating deformation across grain boundaries – representing the Hall–Petch regime with the classical exponent of –1/2. For smaller grain sizes, now in the range of 500 nm ("ultrafine grains") and below, the spacing between high-angle boundaries no longer allows for pileups, and the new large-angle grain boundaries become effective for dislocation bowing out, the bowing-out stress amounting to Gb/D. This means that the grain-size exponent now is –1 instead of –1/2 (Fig. 5.19). From these considerations it also follows that the model does not apply for grain sizes in the range where dislocations cannot bow out any longer.

The concept of Hughes and Hansen [35] described above was recently extended to SPD-processed materials, particularly HPT processed Ni [60]. Again from careful evaluation of TEM data, the most important microstructural parameters, such as the spacing between high-angle boundaries, and that between low-angle boundaries, as well as the density of free dislocations between the boundaries were determined. By substitution of these parameters in the Hall–Petch and the Orowan equations for the corresponding strain-hardening contributions, a good agreement with the measured strength data as a function of deformation strain applied was achieved (Fig. 5.20) although, as already mentioned above, no description of the deformation-induced evolution of the microstructure nor of the related strength was given.

Since the main feature of SPD is enhanced fragmentation of grains due to (1) the enhanced hydrostatic pressure and (2) changes of the deformation path, recent modeling efforts have focused on these two peculiarities, and are described in the next two sections.

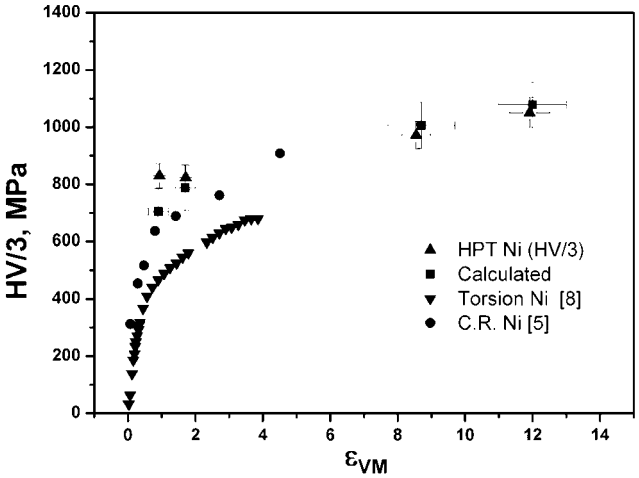

Fig. 5.20 The stress–strain relation for HPT Ni, torsion deformed Ni and cold-rolled Ni (from [60]). The full squares represent the calculated values for HPT Ni.

Models for SPD Cases with Enhanced Hydrostatic Pressure For SPD methods where the hydrostatic pressure is about 1 GPa or larger, it has been shown that the microstructure that emerges is finer than for cases of normal (atmospheric) pressure deformation [61–68]. The smaller grain size thus leads to an enhancement of strength (Fig. 5.21 a).

Therefore, the role of hydrostatic pressure in modeling of the fragmentation process needs to be taken into account. This was first done by Zehetbauer et al. [61, 62] who suggested that the pressure primarily restricts the diffusion that underlies the annihilation of edge dislocation in the composite model [23] described in Section 5.2.2.2. Therefore, the deformation-induced vacancies are hindered in reaching edge dislocations, and hence dislocation climb and annihilation are effectively reduced. The consequence is that the balance between generation and annihilation of dislocations will be shifted to the generation and that an increased density of dislocations will show up in the material if a higher hydrostatic pressure is applied (Fig. 5.21 b). This enhanced density of edge dislocations gives rise to an increase of total grain-boundary area, which is equivalent to a decrease in average grain size (Fig. 5.22, Holzleithner et al. [63]). The restriction of diffusion and edge-dislocation annihilation also leads to an enhanced concentration of deformation-induced vacancies as has been found by experiments [64] as well as by model calculations [65].

Recently, the model of Estrin et al. [26, 27] has also been modified to account for the experimental evidence of back and/or hydrostatic pressure effects in Al-Mg alloys, see Mckenzie et al. [66]. In the spirit of Zehetbauer's model [61, 62], an additional annihilation mechanism specific of cell wall dislocations was introduced that is governed by dislocation climb and thus by pressure-dependent

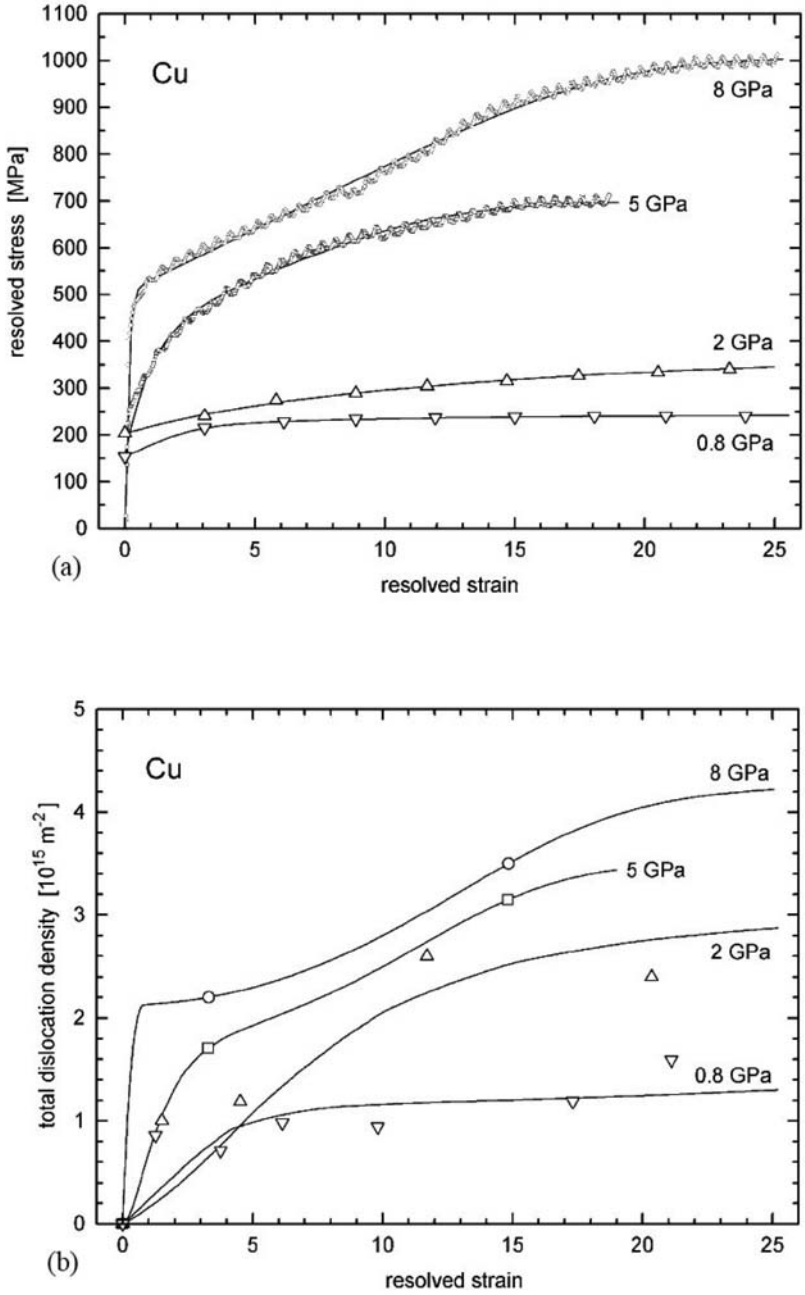

Fig. 5.21 Measured data (symbols), and fits (lines) calculated using the model of Zehetbauer and Kohout [61] for different hydrostatic pressures as indicated, for HPT-deformed Cu: (a) stress–strain relationships; (b) dislocation-density evolution (after Zehetbauer et al. [62]).

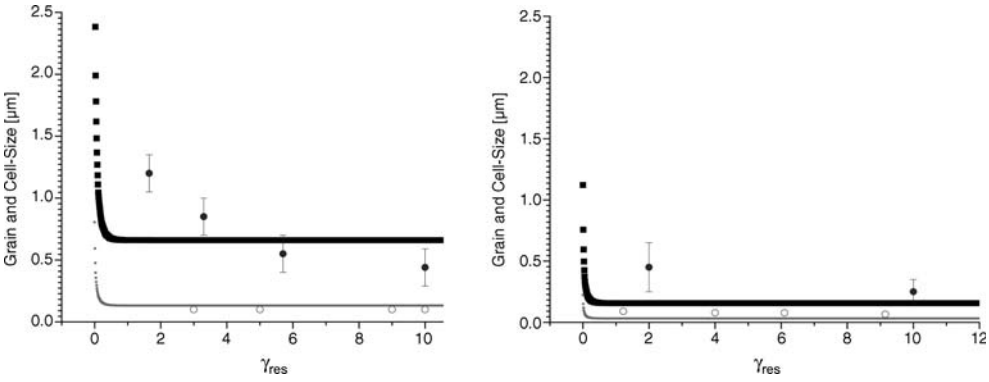

Fig. 5.22 Evolution of grain/cell size (black line) and grain/cell wall size (grey line) vs resolved shear strain, during HPT processing of Cu with hydrostatic pressure $p = 2$ GPa (left figure) and $p = 8$ GPa (right figure) (Holzleithner et al., [63]).

diffusion. The simulations based on this model exhibit an increase of dislocation density with increasing hydrostatic pressure, too. By making use of Holt's relation $d = K/\sqrt{\rho}$ [43], it was possible to simulate the evolution of measured cell size and of cell-wall-thickness evolution as a function of both true strain and hydrostatic pressure applied (Fig. 5.23). The simulations reproduced the experimental trends [67, 68] showing a decrease of cell size decreases with increasing strain and also with increasing hydrostatic pressure.

Models Accounting for Strain-path Changes An important feature of SPD fragmentation is that at least 60% of grain boundaries achieve a misorientation angle between adjacent grains in excess of 10°. This condition can be met either by applying very large strains, as in the case of HPT or accumulative roll bonding (ARB), or by regular changes of the strain path as is true, e.g., for ECAP where different routes of consecutive passes can be applied (see Chapter 8 by Z. Horita). This kind of grain boundaries that are characteristic of a particular mode of SPD process, are often referred to as "geometrically necessary boundaries – GNBs". They consist of arrays of geometrically necessary dislocations, as a consequence of specific strain gradients that build up in the SPD mode considered. Petryk and Stupkiewicz [69] have devised a model for calculating the number and/or density of high-angle grain boundaries not only as a function of strain but also of the strain path, which can be a unidirectional or cyclic one. As in Pantleon's [38] and Nes' [29] concepts described above, the model distinguishes between the GNB-type "cell block" walls, and low-angle "cell" walls. In principle, the model uses a composite ansatz involving a stress component associated with thermally activated deformation processes, and two hardening terms $\sigma \propto 1/d$ and $\sigma \propto 1/d^2$ for grains of size d with low- and high-angle boundaries, respectively. It also utilizes the experimentally well-established finding that both the dislocation cell size and the cell-block size saturate with strain.

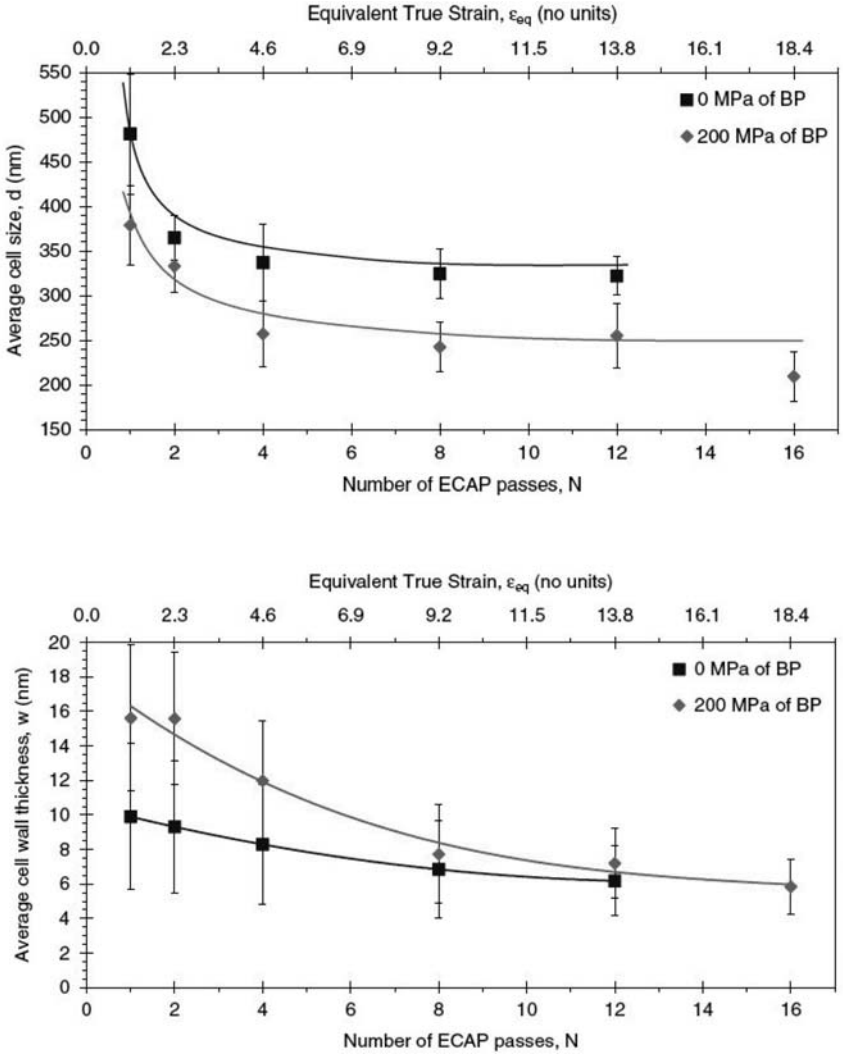

Fig. 5.23 Cell size (top) and cell-wall thickness (bottom) as a function of number of ECAP passes in Al alloy 6016 (from Mckenzie et al., [66]). Symbols: data from TEM measurements, lines: calculations based on the model [26, 27] modified to include a dependence on hydrostatic pressure. BP stands for the back pressure applied during ECAP processing.

Petryk et al. [69] describe the deformation paths in terms of multiplicative split of the deformation gradient, and calculate "effective" strains for different deformation paths ("routes") of ECAP-, CEC- (cyclic extrusion and compression) and HPT deformation. These "effective strains" can strongly differ from the equivalent von Mises strain, as demonstrated clearly in Fig. 5.24: HPT and rolling turn out to have the highest effective strains, followed by the different

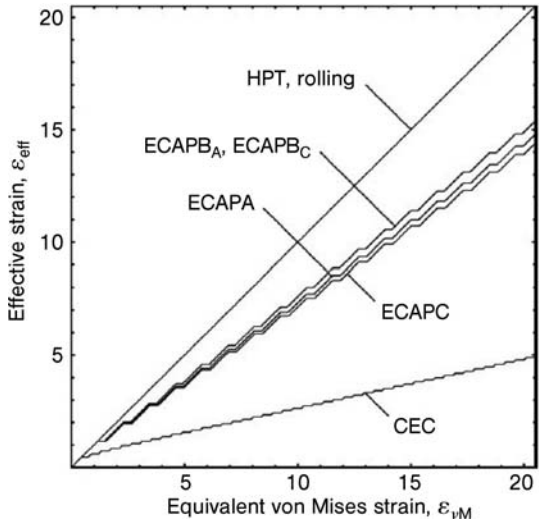

Fig. 5.24 Comparison of the effectiveness of different SPD deformation modes (after Petryk and Stupkiewicz, [59]).

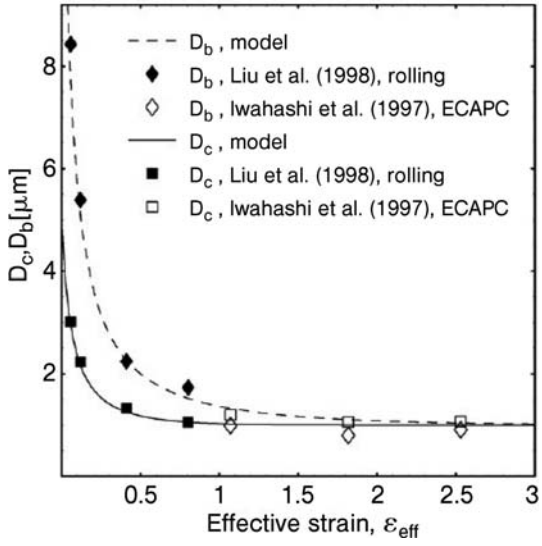

Fig. 5.25 The evolution of the dislocation cell size (D_c) and the cell block size (D_b) with the effective strain. The data were collected from rolling and ECAP processing of Al 99.99% (symbols) and compared with the curves calculated using Petryk's model (after [69]).

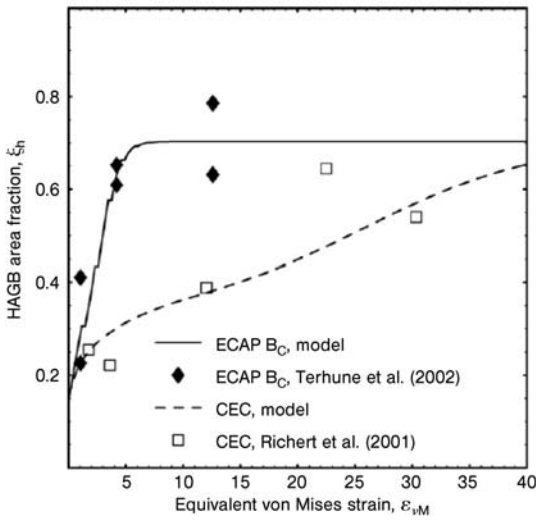

Fig. 5.26 Percentage of high-angle grain boundaries as a function of the von Mises equivalent strain. The data have been collected from different SPD techniques on Al 99.99% (symbols) and compared with the curves calculated using Petryk's model (after [69]).

routes of ECAP (which do not vary in effectiveness very much, Fig. 5.24). Deformation by CEC turns out to be the most ineffective SPD mode. Petryk et al. also calculated the size of cells and cell blocks as a function of effective strain and found that the former saturates more quickly than the latter (Fig. 5.25) which conforms – at least for the case of commercially pure Al – with experimental data from the literature. Although the data correspond to different SPD modes, they line up along monotonic curves, thus supporting the relevance of the model. By taking into account high-angle grain boundaries that are specific to a particular SPD mode and also those developing due to deformation path changes, the model has the ability to calculate the fraction of the high-angle grain boundaries as a function of the von Mises strain (see Fig. 5.26). Also, this plot clearly shows the differences in efficiency of the various SPD methods in achieving high-angle grain boundaries. It should be mentioned, however, that the model is not fully satisfactory in predicting stress–strain behavior: the set of fit parameters chosen for a certain SPD mode does not apply for another SPD mode. The reason may lie in the difference of internal stress levels characteristic of the various SPD modes, although this contradicts the opinion of the authors of the model.

Models Accounting for Strain Gradients The first paper that considered strain gradients in connection with SPD processed materials was published by Lapovok et al. [70], with the purpose of quantitatively describing microhardness in-

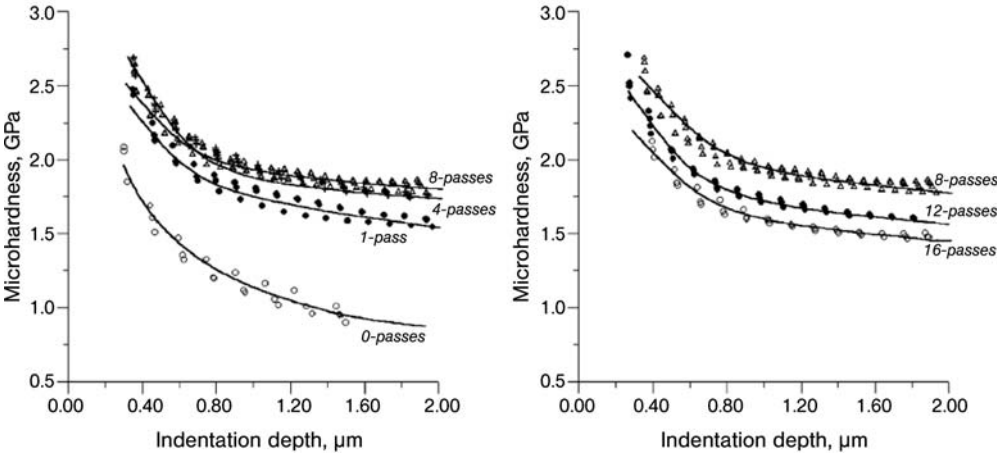

Fig. 5.27 Indentation curves obtained in experiments (symbols) and calculated using a strain gradient model (lines) for annealed and ECAP processed Cu after different numbers of passes (from [70]).

dentation characteristics for ECAP-processed Cu after different numbers of passes. The mechanism-based strain-gradient plasticity model by Nix and Gao (1998, [71]) was for the first time combined with a composite dislocation structure that usually develops at large plastic deformation. For the evolution of this structure, the models by Estrin et al. [26, 27] and Baik et al. [45–47] were linked to the strain-gradient model by defining the cell size as the most important intrinsic length scale parameter. Figure 5.27 demonstrates how well the model reflects the experimentally found dependence of the microhardness $H \propto \sigma$ on the indentation depth h that follows a law $\sigma^2 = C_1 + C_2\ 1/h$, where C_1, C_2 are constants. Using this model it was found that the density of geometrically necessary dislocations starts to dominate that of statistically stored ones for indentation depths smaller than about 1 μm.

The role of strain gradients for the SPD deformation itself has been first discussed by Gil Sevillano [72], being primarily motivated by the fact that HPT deformation achieves markedly smaller grain sizes than other SPD methods. From a quantitative expression for the strain gradient achieved in torsion (Martinez et al. [73]) the density of geometrically necessary dislocations connected with the strain gradient was estimated to be of the order $n \times 10^{14}$ m^{-2} (where n denotes the number of revolutions). This, however, amounts to just about 2% of the measured total dislocation density [62] at least at shear strains of $\gamma \approx 15$.

A recent detailed model developed by Estrin et al. [74] attempts to account for strain gradients and/or geometrically necessary dislocations (GNDs) in SPD processing by HPT. As in the ansatz by Gil Sevillano, GNDs are considered to form *in addition* to the statistically generated dislocations that had been calculated by the model of Mckenzie [66] described in Section 5.2.2.2.2. As in their previous work [70], the authors utilized the mechanism-based strain-gradient plasticity

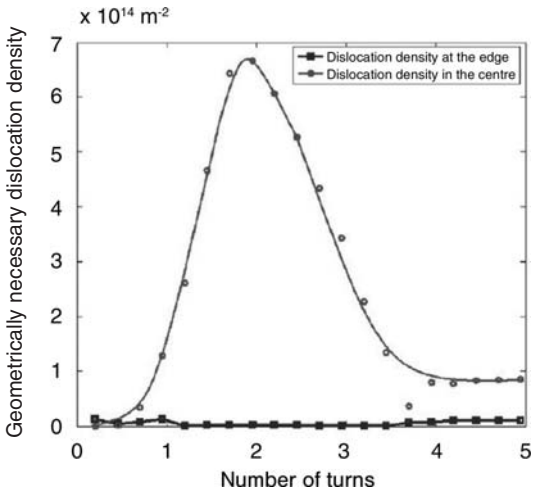

Fig. 5.28 Density of geometrically necessary dislocations near the center of an HPT sample and at its edge (from [74]). Note that the figure in the original paper [74] contains a misprint in the order of magnitude of dislocation density, which has been corrected here.

model of Nix and Gao (1998, [71]). Again, the cell size d serves as the length scale parameter of the model. It enters in combination with the Burgers vector b and a stiffness parameter that scales with the elastic modulus. As expected, most of the GNDs accumulate in the center of the sample where the strain gradient is largest (Fig. 5.28).

As a consequence of the gradient effects, a significant amount of strain is produced also in the center of the sample, as shown in Fig. 5.29 for the numbers of turns above one. The calculations match the experimental results of Zhilyaev et al. [75] reasonably well. In a further variant of their gradient plasticity approach, Estrin et al. [74] introduced a second-order gradient term, as in an earlier paper (Estrin and Mühlhaus [76]. As could be expected, the strain distribution becomes more homogeneous than in the case of the previous gradient model: homogeneity is achieved already for HPT anvil rotations less than one full turn. The calculated values of statistical dislocation densities in cell walls and interiors are closer to the available experimental data [62], and the cell sizes in the center of the specimen and at its edge are in good agreement with recent experimental results by Horita and Langdon [77], see insert in Fig. 5.30. The question whether the first or second strain-gradient model is more adequate is not resolved at this stage for two reasons: (i) the available data on radial stress and strain distribution seem to depend on the HPT equipment they were obtained with [75, 77], and (ii) much more data on local dislocation-density and grain-size measurements need to be collected in order to decide on the relevance of the two models, and on that of the strain-gradient models in general.

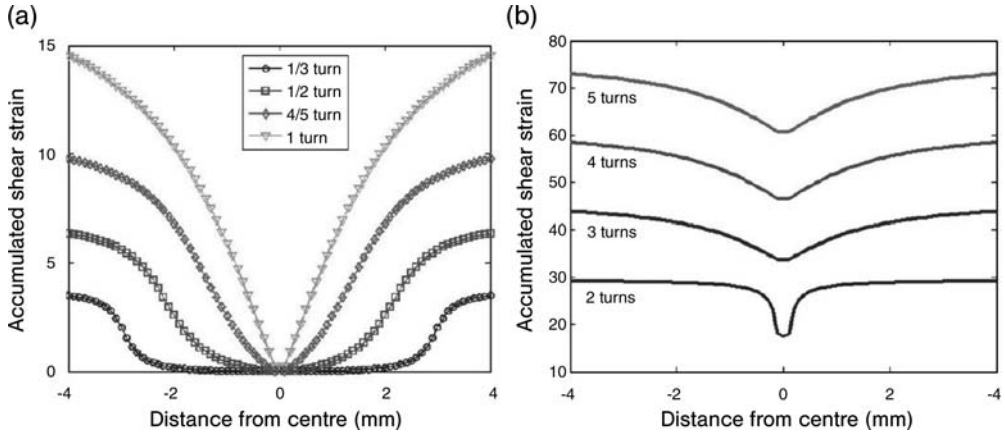

Fig. 5.29 Accumulated shear-strain profiles along the cross section of an HPT sample after different numbers of turns, as calculated by the mechanism-based strain-gradient plasticity model (from Estrin [74]).

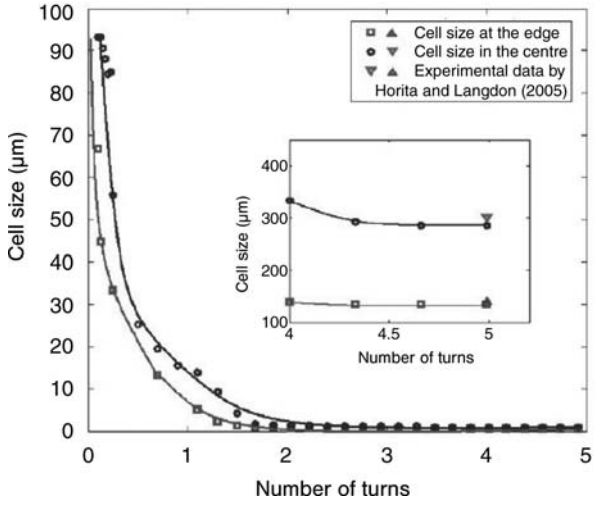

Fig. 5.30 Evolution of the dislocation cell size at the edge and in the center of the HPT sample calculated with the second-order strain-gradient model. The model predictions are in agreement with the measurements of Horita and Langdon on HPT Cu [77] (from Estrin [74]).

5.3 Summary and Outlook

Modeling of strength and strain hardening of bulk nanostructured materials concerns two cases: (i) the simulation of the mechanical response of genuinely nanocrystalline materials, and (ii) the modeling of procedures, namely that of SPD that *leads* to nanocrystallinity. In both cases, composite (also called "phase-mixture") models utilizing a superposition of weighted stresses in the grain or dislocation cell interior and the grain or cell boundary have proven to perform well.

For materials that possess a nanocrystalline structure, the Hall–Petch-type hardening governed by the dislocation slip confined to a grain prevails. An inverse Hall–Petch dependence of the yield strength or flow stress on the grain size is obtained when the grain size is below about 20 nm. It is undisputed that below this critical grain size, the deformation of the grain boundaries governs the strength of the material, but no consensus regarding the exact underlying deformation mechanisms exists so far. The significance of the various mechanisms being currently discussed in the literature, including diffusion-controlled dislocation motion, translational shear, motion of partial partial dislocations, or twinning, needs to be critically proven.

For the other modeling goals aiming at accounting for the evolution of the grain size towards the submicrometer or nanometer scale, composite (phase-mixture) models have been quite successful. With their capability to adequately describe late strain-hardening stages at large strains, they are well suited for modeling the SPD processes. Process parameters, such as the hydrostatic pressure, the deformation path, and the temperature can be used to obtain a most refined microstructure. Modeling appears as a potent tool for optimizing these parameters in such a way that saturation in the dislocation accumulation is postponed. Some more recent models, which consider twinning mechanisms and/or the formation of disclinations, were shown to account for the experimental results quite aptly, and they need to be developed further, along with the earlier, dislocation-density-based models. The same is true for models that involve gradient plasticity in connection with nonuniform SPD modes or with specific strain paths. A particular challenge for modeling is a correct consideration of deformation-induced vacancy-type defects produced by SPD in very high concentration, as these may have an effect on strain-hardening characteristics, diffusion and thermal stability of SPD-processed nanomaterials.

The models discussed in this overview are multiscale in that they link modeling at the level of macroscopic continuum to models of deformation at the scale of nanosized grains or submicrometer-scale dislocation cell. We believe the strength of these models is that they "jump" intermediate length scales and provide a basis for engineering computations, e.g. by finite-element simulations. However, these models use certain assumptions about the dislocation generation, motion and interaction with grain boundaries, which – in want of experimental evidence – need verification by other modeling approaches, particularly

molecular-dynamics simulations. The field is large, and the prospects for viable structural applications of bulk nanomaterials being promising, the need for advanced modeling in this area is significant.

References

1 R.W. Siegel, G.E. Fougere, Nanophase Materials: Synthesis, Properties, Applications (Kluwer, Dordrecht, 1993), p. 233.
2 H. Hahn, R.S. Averback, H.J. Höfler, I. Logas, Proc. MRS Symposium vol. 206 Pittsburgh, Penn., 1991), p. 569.
3 H. Hahn, R.S. Averback, Nanostruct. Mater. 1 (1992) 95.
4 H. Hahn, K.A. Padmanabhan, Philos. Mag. B 76 (1997) 559.
5 H. Hahn, P. Mondial, K.A. Padmanabhan, Nanostruct. Mater. 9 (1997) 603
6 K.A. Padmanabhan, J. Schlipf, J. Mater. Sci. Technol. (1996) 391.
7 A.K. Mukherjee, Mater. Sci. Eng. A 322 (2002) 1.
8 Y.T. Zhu, T.G. Langdon, Mater. Sci. Eng. A 409 (2005) 234.
9 H.S. Kim, Y. Estrin, M.B. Bush, Acta Mater. 48 (2000) 493.
10 J.E. Carsley, J. Ning, W.W. Milligan, S.A. Hackney, E.C. Aifantis, Nanostruct. Mater. 4 (1995) 441.
11 Y. Estrin, in: Unified Constitutive Laws of Plastic Deformation, eds. A.S. Krausz, K. Krausz, (Academic Press, New York, 1996) p. 69.
12 H.S. Kim, Y. Estrin, Acta Mater. 53 (2005) 765.
13 L. Capolungo, M. Cherkaoui, J. Qu, J. Eng. Mater. Technol. 127 (2005) 400.
14 S. Mercier, A. Molinari, Y. Estrin, J. Mater. Sci. 42 (2007) 1455.
15 P.G. Sanders, J.A. Eastman, J.R. Weertman, Acta Mater. 45 (1997) 4019.
16 J.R. Trelewitz, Ch. A. Schuh, Acta Mater. 55 (2007) 5948.
17 M.A. Meyers, A. Mishra, D.J. Benson, Prog. Mater. Sci. 51 (2006) 427.
18 U.F. Kocks, J. Eng. Mater. Technol. 98 (1976) 76.
19 M. Zehetbauer, V. Seumer, Acta Metall. Mater. 41 (1993) 577.
20 H. Mughrabi, Acta Metall. 31 (1983) 1367.
21 F.B. Prinz, A.S. Argon, Acta Metall. 32 (1984) 1021.
22 W.D. Nix, J. Gibeling, D.A. Hughes, Metall. Trans.16A (1985) 2215.
23 M. Zehetbauer, Acta Metall. Mater. 41 (1993) 589.
24 M. Zehetbauer, P. Les, Proc. Int. Symp. Hot Workability of Steels & Light Alloys & Composites, eds. H.J. McQueen et al., 35th Annual Conference of Metallurgists, Met. Soc. Can. Inst. Mining & Metallurgy, Montreal, Quebec (Canada) 1996, p. 205.
25 P. Les, M. Zehetbauer, Key Eng. Mater. 97–98 (1994) 335.
26 Y. Estrin, L.S. Toth, A. Molinari, Y. Brechet, Acta Mater. 46 (1998) 5509.
27 L.S. Toth, A. Molinari, Y.Estrin, J. Eng. Mater. Technol. 124 (2002) 71.
28 M. Müller, M. Zehetbauer, A. Borbely, T. Ungar, Z. Metallk. 86 (1995) 827.
29 K. Marthinsen, E. Nes, Mater. Sci. Eng. A234–236 (1997) 1095.
30 E. Nes, Prog. Mater. Sci. 41 (1998) 129.
31 E. Nes, K. Marthinsen, Mater. Sci. Eng. A 322 (2002) 176.
32 F. Roters, D. Raabe, G. Gottstein, Acta Mater. 48 (2000) 4181.
33 M. Goerdeler, G. Gottstein, Mater. Sci. Eng. A 309–310 (2001) 377.
34 G.V.S.S. Prasad, M. Goerdeler, G. Gottstein, Mater. Sci. Eng. A 400–401 (2005) 231.
35 D.A. Hughes, N. Hansen, Acta Mater. 48 (2000) 2985.
36 W. Pantleon, Acta Mater. 46 (1998) 451.
37 W. Pantleon, J. Mater. Res. 17 (2002) 2433.
38 W. Pantleon, Mater. Sci. Eng. A 387–389 (2004) 257.
39 A.E. Romanov, V.I. Vladimirov, Disclinations in crystalline solids, in: F.R.N. Nabarro (ed.), Dislocations in Solids, vol. 9, North Holland, Amsterdam 1992, p. 191.
40 M. Seefeldt, J. Alloys Compd. 378 (2004) 102.
41 M. Seefeldt, P. Klimanek, P. Van Houtte, The role of disclinations for substructure

evolution, Proc. 25th Riso Int. Symp. Mater. Sci., eds. C. Gundlach et al., Riso Nat.Lab., Roskilde, Denmark (2004) p. 97.
42 M. Seefeldt, V. Klemm, P. Klimanek, Proc. NATO Adv. Res. Workshop Investigations & Applications of Severe Plastic Deformation, August 2–6 (Moscow, Russia 1999), eds. T.C. Lowe and R.Z. Valiev, (Kluwer Academic Publishers, The Netherlands, 2000), p. 197.
43 D.J. Holt, J. Appl. Phys. 41 (1970) 3197.
44 L. Zeipper, M. Zehetbauer, Ch. Holzleithner, Mater. Sci. Eng. A 410–411 (2003) 217
45 S.C. Baik, R.J. Hellmig, Y. Estrin, H.S. Kim, Z. Metallk. 94 (2003) 754.
46 S.C. Baik, Y. Estrin, R.J. Hellmig, H.T. Jeong, H.G. Brokmeier, H.S. Kim, Z. Metallk. 94 (2003) 1189.
47 S.C. Baik Y. Estrin, H.S. Kim, R.J. Hellmig, Mater. Sci. Eng. A 351 (2003) 86.
48 Y. Estrin, L.S. Toth, Y. Brechet, H.S. Kim, Mater. Sci. Forum 503–504 (2006) 675.
49 F.A. Mohamed, Acta Mater. 51 (2003) 4107.
50 A.S. Argon, W.C. Moffat, Acta Metall. 293 (1981) 29.
51 Y.H. Zhao, Y.T. Zhu, X.Z. Liao, Z. Horita, T.G. Langdon, Mater. Sci. Eng. A 463 (2007) 22.
52 N. Enikeev, H.S. Kim, I.V. Alexandrov, Mater. Sci. Eng. A 460–461 (2007) 619.
53 A. Belyakov, T. Sakai, H. Miura, K. Tsuzake, Philos. Mag. 81 (2001) 2629.
54 I. Alexandrov, R. Chembarisova, V. Sitdikov, V. Kahyhanov, Mater. Sci. Eng. A, doi :10.1016/j.msea.2007.11.073.
55 L. Balogh, T. Ungar, Y. Zhao, Y.T. Zhu, Z. Horita, C. Xu, T.G. Langdon, Acta Mater. 56 (2008) 809.
56 X.L. Wu, Y.T. Zhu, Phys. Rev. Lett. 101 (2008) 025503.
57 M.R. Barnett, C.H.J. Davies, X. Ma, Scripta Mater. 52 (2005) 627.
58 L. Remy, Acta Metall. 26 (1978) 443.
59 E. Nes, B. Holmedal, E. Evangelista, K. Marthinsen, Mater. Sci. Eng. A 410–411 (2005) 178.
60 H.W. Zhang, X. Huang, N. Hansen, R. Pippan, M.J. Zehetbauer, Mater. Sci. Forum (2008), in print.
61 M. Zehetbauer, J. Kohout, Proc. 9th Int. Symp. Plasticity & Current Appl. "Plasticity '02", Aruba, Netherlands, 2002, eds. A.S. Khan, O. Lopez-Pamies, NEAT Press, Maryland (USA), p. 543.
62 M.J. Zehetbauer, H.P. Stuewe, A. Vorhauer, E. Schafler, J. Kohout, Adv. Eng. Mater. 5 (2003) 330.
63 Ch. Holzleithner, M. Zehetbauer, Presentation at the Conf. Ultra Fine Grained Materials 2006 (UFG 2006), Irsee (Germany) 2006, to be published.
64 E. Schafler, G. Steiner E. Schafler, G. Steiner, E. Korznikova, M. Kerber, M.J. Zehetbauer, Mater. Sci. Eng. A 410–411 (2005) 169–173.
65 M. Zehetbauer, E. Schafler, G. Steiner, E. Korznikova, A. Korznikov. Mater. Sci. Forum, 503–504 (2006) 57–64.
66 P.W.J. Mckenzie, R. Lapovok, Y. Estrin, Acta Mater. 55 (2007) 2985.
67 E. Schafler, A. Dubravina, B. Mingler, H.P. Karnthaler, M. Zehetbauer Mater. Sci. Forum, 503–504 (2006) 51.
68 R. Lapovok, Mater. Sci. Forum 503–504 (2006) 37.
69 H. Petryk, S. Stupkiewicz, Mater. Sci. Eng. A 444 (2007) 214.
70 R. Lapovok, F.H. Dalla Torre, J. Sandlin, C.H.J. Davies, E.V. Pereloma, P.F. Thomson, Y. Estrin, J. Mech. Phys. Solids 53 (2005) 729.
71 H. Gao, Y. Huang, W.D. Nix, J.W. Hutchinson, J. Mech. Phys. Solids 47 (1999) 1239.
72 J. Gil Sevillano, Strengthening by Plastic Work: From LPS to SPD. A 25 Years Perspective, Proc. 25th Riso Int. Symp. Mater. Sci., eds. C. Gundlach et al., Riso Nat. Lab., Roskilde, Denmark (2004), p. 1.
73 J.M. Martinez-Esnaola, M. Montagnat, P. Duval, J. Gil Sevillano, Scripta Mater. 50 (2004) 273.
74 Y. Estrin, A. Molotnikov, C.H.J. Davies, R. Lapovok, J. Mech. Phys. Solids 56 (2008) 1186.
75 A.P. Zhilyaev, K. Oh-ishi, T.G. Langdon, T.R. McNelley, Mater. Sci. Eng. A 410–411 (2005) 277.
76 Y. Estrin, H.B. Muelhaus, in: Proc. Int. Conf. Eng. Mathem., AEMC Sidney, IEAust (1996) p. 161.
77 Z. Horita, T.G. Langdon, Mater. Sci. Eng. A 410–411 (2005) 422.

6
Finite-element Method Simulation of Severe Plastic-deformation Methods

Hyoung Seop Kim

6.1
Introduction

Plastic-deformation processing is a viable method for grain refinement of metallic materials, since average subgrain/cell size of metals decreases with plastic strain at room temperature. In recent years, severe plastic deformation (SPD) [1–5] was developed as a new method of manufacturing bulk specimens having ultrafine grained (UFG) structure. The SPD process has been the subject of intensive investigations in recent years due to the unique physical and mechanical properties inherent in various UFG materials. Also, SPD-processed materials have a number of advantages over nanostructured materials manufactured by other methods through powder processing. Among various SPD methods, such as multiple forging, high-pressure torsion (HPT), accumulative roll bonding (ARB), equal-channel angular pressing (ECAP) shown in Fig. 6.1, twist extrusion, and various developed and modified processes, the ECAP process is a promising and interesting method. Hence, most of this chapter will be assigned to ECAP.

ECAP involves large shear strains in a workpiece that deforms while moving through a die containing two intersecting channels of identical cross sections, see Fig. 6.1(a). This process has been the subject of intensive study due to its capability of producing large fully dense UFG samples including nanometer scale by repeating the process several times while maintaining the original cross section of the workpiece.

In the HPT process, Fig. 6.1(b), a workpiece is held between anvils (upper ram and lower support) and strained in compression under the applied pressure of several GPa. After pressing and holding the workpiece the holder rotates and surface friction forces between the workpiece and the rotating die deform the workpiece by shear force. By this method nanostructures can be formed both by the consolidation of powders as well as the refinement of the coarse-grained microstructures. The presence of high-angle grain boundaries and high intrinsic stresses are the main features of the nanostructured materials obtained by HPT.

Bulk Nanostructured Materials. Edited by M. J. Zehetbauer and Y. T. Zhu

ISBN: 978-3-527-31524-6

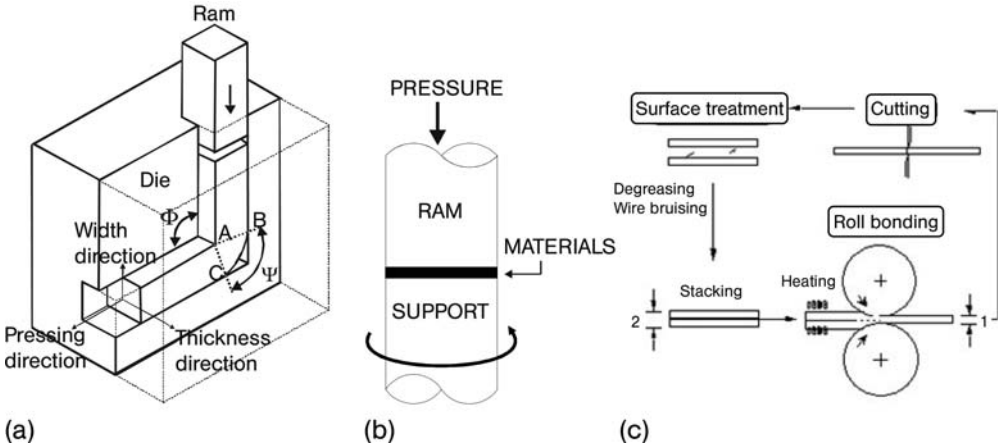

Fig. 6.1 Schematic diagrams of (a) ECAP showing the channel angle Φ and the corner angle Ψ, (b) HPT and (c) ARB [6].

The principle of ARB invented by Tsuji *et al.* [6] is as follows: two sheets of the same thickness are subjected to simultaneous rolling, see Fig. 6.1 (c). In one pass, the thickness of the two sheets is reduced down to the thickness of one initial sheet. This operation is repeated several times. The alignment of sheets relative to each other can be changed between consecutive rolling cycles. As a result of such combined rolling, the sheets are bonded together; this process is accompanied by microstructure refinement.

To obtain the UFG materials with a good quality by exposing coarse-grained materials to SPD, it is essential to combine experimental research with a theoretical analysis of inhomogeneous deformation behavior in the workpiece during the process. Significant progress has been made in the analysis of the process itself as well as in the understanding of fundamental properties of the SPD-processed materials by using theoretical [7] and experimental methods. The microstructures and the concomitant mechanical properties of SPD-processed materials are closely related to the degree of plastic deformation, hence, understanding the phenomena associated with the plastic stress and strain development is very important for an optimum SPD process design. The plastic-deformation behavior of a workpiece during the ECAP process is controlled, in addition to pressing temperature and ram speed, by both the die design parameters, for example, die shape, die length, channel intersection angle, die-corner angle, the friction condition, and so forth, and parameters related to material properties, hardening exponent, strain-rate sensitivity. The finite element method (FEM) has been widely used in the plastic-forming process in order to analyze the global and local deformation response of the workpiece with nonlinear conditions of boundary, loading and material properties, to compare the effects of various parameters, and to search for optimum process conditions for a given material. Since materials and processing parameters that affect the flow behav-

ior during ECAP are interdependent, it is difficult to evaluate the effect of the single parameter on the flow behavior even in well-designed and prepared ECAP experiments. For example, to evaluate the sole effect of pressing speed on deformation behavior during ECAP is difficult since the local temperature rise is significantly influenced by the pressing speed and the mechanical properties change during the process. For better understanding of the independent effect of various materials and processing parameters and better process control, it is more effective to study the effects of various parameters by theoretically simulating the ECAP process.

In the current review, the plastic-deformation behavior of metals during the ECAP process is analyzed using the FEM in order to investigate the effects of external and internal factors on the deformation inhomogeneity during ECAP.

6.2
Characteristics of ECAP and Main Factors Affecting Plastic Deformation

Ideally, ECAP involves *perfectly homogeneous* simple shear plastic deformation within a very thin layer of a workpiece pressed through a die containing two intersecting channels of identical cross sections that meet a predetermined angle. Figure 6.1 (a) shows the principle of ECAP, where two channels of equal cross section intersect at a designed channel angle Φ. The deformation during ECAP occurs within the localized zone in the intersecting region of the two channels. The dashed region (fan-shaped area ABC) in Fig. 6.1 (a) indicates a so-called "main deforming zone" (MDZ). In particular, if the die-corner angle Ψ is 0, that is B = C, deformation occurs in the immediate vicinity of the plane, i.e. the shear plane. In this case, the deformation mode in ECAP under ideal condition is "simple shear" as in the case of torsion. The major difference of ECAP from torsion or other plastic-deformation processes, which is unique in ECAP, is that deformation occurs in the immediate vicinity of the shear plane. Therefore, the deformation in the ECAP sample is very homogeneous. Segal [8] has demonstrated that, providing the workpiece is constrained to fully fill the die channel and the die corner is sharp, on traveling through the die an element will be sheared abruptly on crossing the join line between the two channels by an amount dependent on the die-channel angle. Under these conditions, the magnitude of the shear strain decreases with increasing channel angle.

A generally used equation for the equivalent strain ε generated in the workpiece after one pass of ECAP is given by the following relation [9]:

$$\varepsilon = \frac{1}{\sqrt{3}}\left[2\cot\left(\frac{\Psi}{2}+\frac{\Phi}{2}\right) + \Psi\,\mathrm{cosec}\left(\frac{\Psi}{2}+\frac{\Phi}{2}\right)\right] \tag{6.1}$$

According to Eq. (6.1), the equivalent strain decreases with the die-corner angle Ψ and the channel angle Φ. It can be shown that the effective strain during ECAP decreases from the maximum of 1.15 to the minimum of 0.907 on

changing the corner angle from the minimum value $\Psi = 0^\circ$ to the maximum value $\Psi = 90^\circ$ when the channel angle is fixed as $\Phi = 90^\circ$.

Most of the SPD processes are simpler than any other metal-forming processes in terms of deformation homogeneity, which is understandable from the viewpoint of the purpose of SPD; to modify microstructures of a workpiece not to manufacture the final complex shape parts. Indeed, the shapes of the dies and workpiece in SPD cannot be complex for repeating the processes. In spite of relatively simple processing compared to conventional metal-forming processes such as forging and extrusion, different combinations of many processing variables produce quite unpredictable results associated with deformation degree, deformation homogeneity and processed material properties. It should be stressed that one of the unique characteristics of ECAP is its highly homogeneous deformation of workpiece, which cannot be easily found in any other metal-forming processes. Hence, ECAP has one more viable industrial application in addition to grain refinement; homogenization of microstructures of bulk engineering parts.

However, it has been revealed that unlike the ideal simple shear case, the real ECAP deformation characteristics are not perfectly homogeneous. Consequently, the microstructures of the ECAP-processed materials are inhomogeneous. Because of this nonideal deformation and microstructural inhomogeneity in ECAP, to control die and process design local deformation behavior needs to be considered, otherwise only control of a major variable (i.e. total amount of plastic strain based on the die channel and corner angles) is necessary. In spite of a lot of research results published recently, many factors and mechanisms of the inhomogeneous deformation were not fully understood.

The ECAP process comprises all the input variables applicable to general bulk forming processes, such as workpiece material, dies, the conditions at the die/

Table 6.1 Processing variables of ECAP.

Main variables	Technical area
Workpiece properties	shape (block, cylinder) and size, chemical composition and microstructure, flow properties under processing conditions (flow stress in function of strain, strain rate and temperature), thermal and physical properties
Dies and tools	geometry (shape, channel angle, corner angle, backpressure, number of angles, channel size), surface conditions, material hardness, surface coating, temperature, stiffness and accuracy
Interface conditions	surface finish, lubrication, friction, heat transfer
Deforming zone	mechanics of plastic deformation, material flow, stresses, velocities, temperatures
Equipment	speed, production rate, force and energy capabilities, rigidity and accuracy
Processing route	number of passes, route (A, Ba, Bc, C or modified one), input direction

workpiece interface, the mechanics of shape change in the deforming, and the characteristics of the processing equipment [11]. Thus, in designing, developing and optimizing the ECAP process, key technical problem areas that must be addressed are included in Table 6.1. The understanding of these variables allows the prediction of the characteristics of the ECAP-processed product, namely, geometry and tolerance, surface finish, microstructure and properties. If the processing variables are not well adjusted, it is common to meet incorrect workpiece geometries including fracture, die fracture and wear, jam of workpiece and die as well as inappropriate microstructure and properties.

6.3 Plasticity and Calculation Theories

Computer simulation of metal forming including SPD is a technique that enables the behavior of the workpiece material in a forming operation to be predicted [12]. This primarily concerns the plasticity of the workpiece material and associated tools and can be described in terms of stresses, strains and microstructural changes that are brought about as a result of the process. Accommodated in the technique can also be the effects of thermal flow within the workpiece and between the workpiece and the tools, the frictional heat-transfer conditions on the tool/workpiece interface, the elastic and thermal expansions and contractions of the workpiece and the tools and the coupling of the changing constitutive characteristics of the workpiece. This relates material composition, structure and process parameters to end-product performance and design. In practical terms, simulations can predict the loads and energies required to perform the operation, the filling or lack of the dies, the occurrence of flow defects and the resultant properties of the workpiece. Various different approaches have been taken to simulate the plastic-deformation behavior of the workpiece in ECAP; namely, slip-line-field (SLF) method, upper-bound technique (UBT), FEM and finite-volume method (FVM). A brief of the computer simulations in metal forming, the plasticity theory and the analysis methods related to ECAP will be described below.

Since the development of "plasticity theory" in the mid-19th century with the hypothesis of Tresca relating to the prediction of yielding, mathematicians and engineers developed the slab method, the SLF theory and the UBT in the early and mid-20th century [13, 14]. The SLF method [15–17], which gives exact solutions for plane strain boundary value problems for rigid plastic solids, has been losing its weight with the development of the FEM based on high computing power because it can treat a two-dimensional plane strain geometry and rigid-perfect plastic materials, although it is still found useful in understanding basic metal-forming phenomena. In particular, Segal [15, 16] and Stoica *et al.* [17] analyzed the plasticity of ECAP using the SLF calculations; material flow, stress, strain and the effects of corner angle, friction and multi-passes. The UBT [18, 19], which constructs and solves the kinematic admissible velocity field, pro-

vides a quick way to estimate collapse loads for plastic solids and structures. Lee [18] has analyzed the stresses and strains for channel angular deformation taking friction between dies and material into account using the UBT. Alkorta and Gil Servilano [19] have simulated ECAP using the UBT and compared their results with the FEM, considering the material strain hardening and the back-pressure effect.

The nonlinear FEM based on continuum plasticity theory and formulations became a most popular and reliable computer-aided analysis tool for metal-forming simulations. In the FEM, the workpiece is divided into subregions called elements. The elements are connected at discrete nodal points on the boundaries. Then, at each element, a set of trial functions or admissible velocity fields are usually assigned with constant parameters, which are identified with the nodal point velocities. The trial functions in each region are combined to form an admissible velocity field, which satisfies the necessary requirements, except for that of volume constancy. The volume constancy is applied through the variational principle. The major advantage of the FEM is that it can be applied to a range of problems with little restriction on the workpiece geometry [12]. The FEM is in principle able to solve problems whose complexity is limited only by the power of the computing facilities that are available.

Many SPD research groups analyzed ECAP using the commercial FEM packages. Since geometries of dies and workpieces are not complex in ECAP, compared to the other metal-forming processes, pre/postprocessing time is not long, mesh distortions are regular during the calculations and the FEM simulations are not so difficult. Almost any software having contact-surface-treating functions can reproduce the SPD processing; general purpose FEM packages such as ABAQUS [20], MSC/MARC [21] and LS-DYNA [22], bulk-forming-oriented packages such as DEFORM [23], SUPERFORGE [24] and QFORM [25], and in-house code [26] were used for SPD simulations. It should be noted that among the above packages, SUPERFORM is not the FEM- but the FVM-based package, which calculates the values of conserved variables averaged across the control volume. However, the FVM has not been fully evaluated and the validity of their results was not accessed, yet. For accurate and efficient use of SPD simulations as a process-development tool, it is not only necessary to have a reliable FEM solver and appropriate input data of material and processing conditions but also to have analysis capability based on the knowledge of plasticity theory, solution schemes and characteristics of each package. The first step to simulate is to decide which scheme to use; static/dynamic time integration, two/three-dimensional modeling, stress/coupled stress–temperature analysis, material model, friction model, calculation domain of workpiece/die–workpiece, remeshing and so on, in that a specific software needs to be used.

Over 60 papers on SPD simulations using the FEM including the FVM have been published [19, 27–88] until 2005 since Prangnell *et al.* in 1997 [27]. Most of them applied the continuum model. The models based on dislocation-crystal-plasticity [43, 46–48, 66, 83] and crystal-plasticity [86, 87] analyses are now being introduced to develop quantitative descriptions of microstructure and crystallo-

graphic texture evolution during SPD. There is only one paper on the simulation of HPT [82] and none on ARB. However, in principle, ARB has the same mechanics as clad rolling [88–94], and microstructure-related ARB simulations are expected.

6.4
Simulation Results

6.4.1
Two-dimensional vs Three-dimensional Simulations

In a rectangular workpiece of ECAP, the thickness direction is perpendicular to the width and length directions (see Fig. 6.1(a) for the definition of directions), so that the strain along the thickness direction is zero, i.e. plane strain condition prevails. That is, the deformation during the ECAP process of rectangular specimens becomes 2-dimensional. Therefore, 2-dimensional plane-strain FEM simulations of the ECAP process are valid. However, strictly speaking, cylindrical workpiece cannot be modeled as a 2-dimensional plane strain or axisymmetric condition. If heat transfer or friction is to be quantitatively and correctly considered, 3-dimensional simulation is necessary, because the heat flows in any directions and the friction exists between the contact pairs of the thickness directions as well. However, when the friction is ignored in block-shape workpieces, the problem can be reasonably assumed to be 2-dimensional.

Figure 6.2 shows a mesh system of 3-dimensional simulation; (a) initial mesh and (b) deformed mesh under frictionless condition. The number of elements is 240 000, which is much more than usual number (< 10 000) in 2-dimensional ECAP simulations. The running time of a calculation was less than several minutes on an IBM p690 (666 GFLOPS) supercomputer. The predicted effective

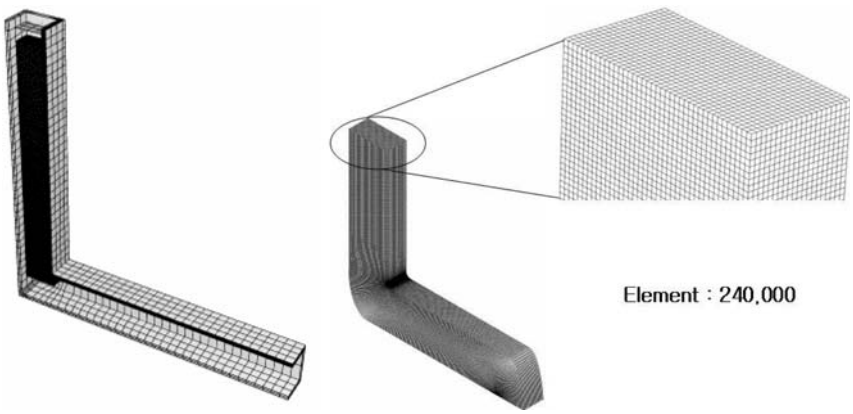

Fig. 6.2 Mesh system of 3-dimensional. (a) initial mesh and (b) deformed mesh.

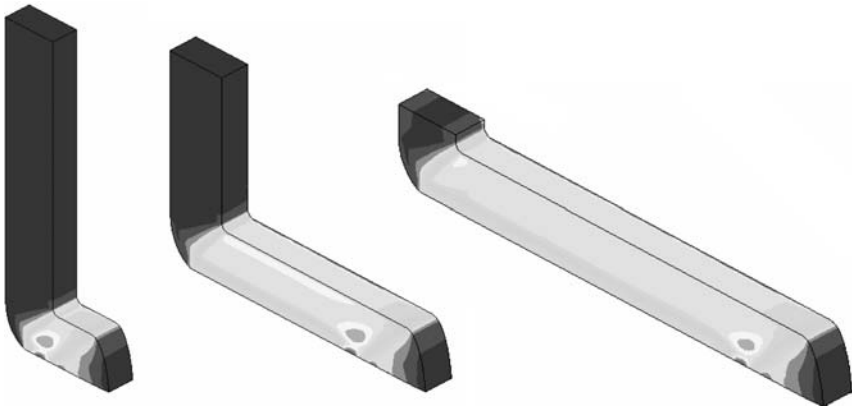

Fig. 6.3 Three-dimensional effective strain distributions of the frictionless ECAP.

strain distributions in Fig. 6.3 illustrate that the plain-strain condition prevails in the frictionless ECAP deformation because the strain contours are perpendicular to the thickness direction.

6.4.2
Benchmark Testing of ECAP Simulations [81] in NANOSPD3

There are many simulation results of the material flow in ECAP at different laboratories, obtained with different software packages, considering different geometries of the die set, models of the ECAP process and the materials. As a result, the correlation between the modeling results obtained at different laboratories as well as their adequacy, hence, possibilities of their application for the analysis of the experimental data become topical issues. At this technical stage, it is meaningful to compare the simulation results for benchmarking. For this purpose, the first benchmark testing was done and presented in NANOSPD3, Fukuoka, 2005; FEM simulations of the material flow at the 1st ECAP pass were conducted in Russia (Ufa and Sarov), Hungary (Budapest) and Korea (Daejeon) for the same processing parameters and the same material, but with the use of different software packages and their own techniques by the authors to solve these tasks. The calculations were made with the use of different computer software packages: Ufa (Deform3D ver. 5.0), Sarov (DRACON code based on the variation-difference method of solving continuum-mechanics equations), Daejeon (ABAQUS ver. 6.4 explicit), Budapest (QFORM3D ver. 4). The numbers of elements were 18240 in Ufa, 20026 in Sarov, 240000 in Daejeon and 24044 in Budapest.

Comparisons of the obtained simulation results were made by means of matching the calculated values of the level of the accumulated strain along the bulk of the billet, pressing loads, and the geometrical form of the billet after ECAP. It is seen from Fig. 6.4 that the zone with the maximal plastic strain

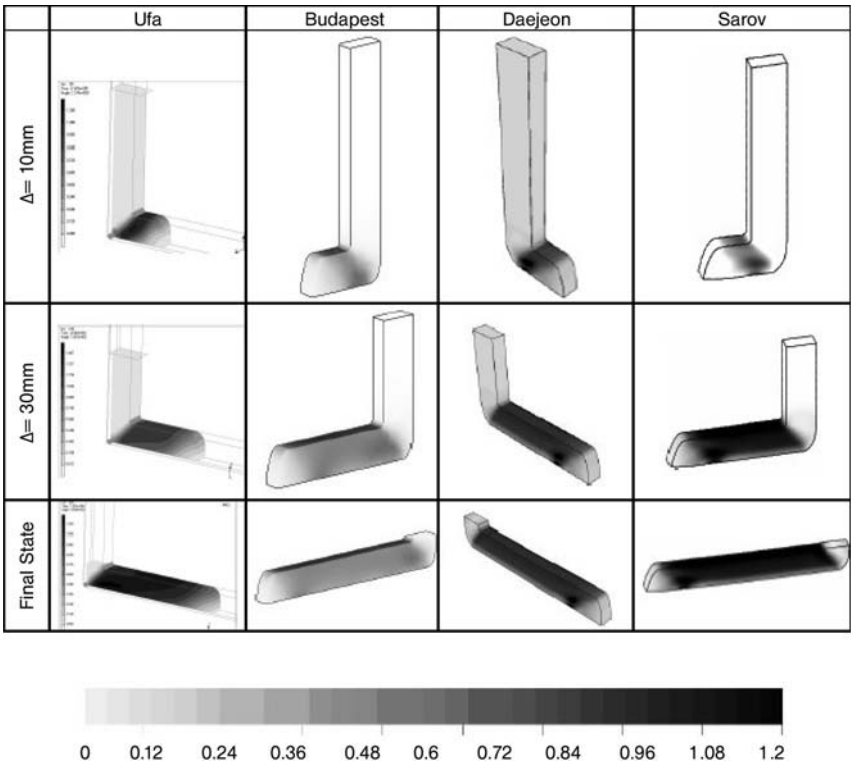

Fig. 6.4 Distribution of the accumulated strain along the section of the sample at different values of the punch travel.

value corresponds to the zone of formation and growth of the plastic deformation zone. It has been established that the zone of the local accumulated strains maximum is formed at a distance of 2–3 mm from the bottom supplying surface in the zone of the outer radius transition. The profile gap zones as well as the character of the billet's nose zones are similar and correspond to the experimental data. One observes the presence of a clearly defined undeformed zone of 1.5–2 mm in width, for the final stage of the workpiece deformation process. The zone of homogeneous strains, defined according to the isoline boundary $\varepsilon = 1.08$ for all cases, is comparable and it consists 75–80% of the initial workpiece volume, which is the peculiarity of the ECAP process. The place of the plastic deformation in the bulk of the bill*et al*so differs to some extent when different codes are applied, however, the differences are not more than 10%.

Figure 6.5 shows the dependence of the press force on the punch travel. It was also revealed that the character of the force variation depending on the punch travel was not practically influenced by the applied code during calculations. Small oscillations of the force, observed in Fig. 6.5 are typical for numerical calculation methods and they depend on the FE value. The obtained punch

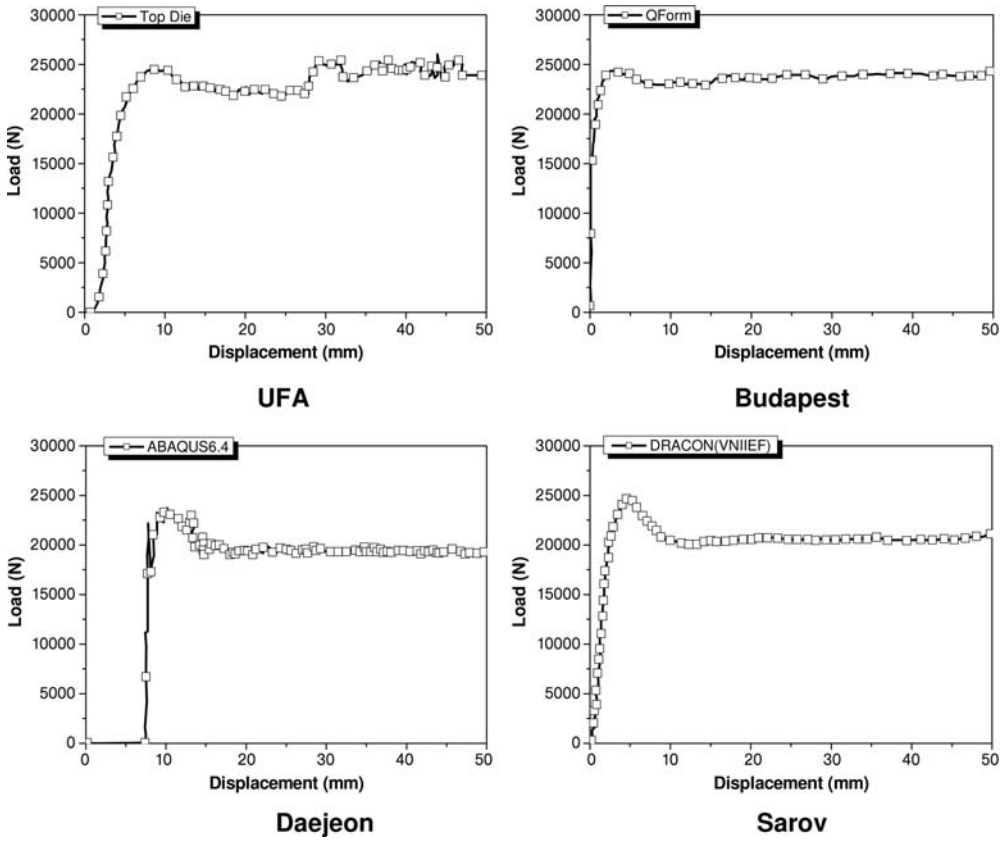

Fig. 6.5 Punch-force dependence on the punch travel.

force values on the smooth section of the curve are as follows: 22 kN (DEFORM); 24 kN (QFORM); 19 kN (ABAQUS) and 21 kN (DRACON). The character of curves for all strain components is similar for all of the tested codes. The benchmark testing of ECAP is scheduled to continue in accordance with the nanoSPD conference held every 3 years.

6.4.3 Mesh-size Sensitivity

The mesh-size sensitivity in ECAP was investigated [42, 61]. Figure 6.6 shows the calculated deformed geometries of a perfect plastic material in the steady state of the frictionless ECAP process for (a) $\Phi = 90^\circ$, $\Psi = 0^\circ$ with coarse meshes (0.6 mm in side length of a mesh) and (b) $\Phi = 90^\circ$, $\Psi = 0^\circ$ with fine meshes (0.2 mm in side length of a mesh). At a glance, the deformed shapes of coarse mesh in Fig. 6.6 (a) and fine mesh in Fig. 6.6 (b) look the same, but it can be obviously

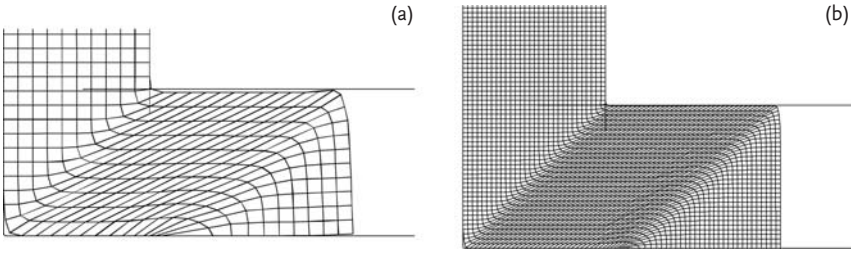

Fig. 6.6 ECAP simulation for the mesh-size sensitivity; ABAQUS standard ver. 6.4, frictionless, $\Phi = 90^\circ$, $\Psi = 0^\circ$ with (a) coarse meshes and (b) fine meshes.

found that there are two gaps between the die and workpiece in the calculated results of the coarse mesh of 0.6 mm; (i) the corner gap in MDZ and (ii) the exit-channel gap between the billet top and die-exit channel. On the other hand, the size of the corner gap in the fine mesh, Fig. 6.6 (b), is smaller than that in the coarse mesh, Fig. 6.6 (a). Moreover, the exit-channel gap does not occur in the fine-mesh calculation, Fig. 6.6 (b). Since the corner gap is formed in strain-hardening materials and the exit-channel gap is formed in rate-sensitive materials during the frictionless ECAP process of $\Phi = 90^\circ$, $\Psi = 0^\circ$, the corner gap and the exit-channel gap found in Fig. 6.6 (b) are attributed to the too coarse mesh size in the analysis, which cannot simulate fully the die-filling situation. Although the corner gap was expected to disappear completely for perfect plastic materials with zero hardening rate, the arc curvatures generated on the surface of the workpieces are 12°, 5° and 19° for the die shapes of $\Phi = 90^\circ$, $\Psi = 0^\circ$ with the coarse meshes, $\Phi = 90^\circ$, $\Psi = 0^\circ$ with the fine meshes and $\Phi = 135^\circ$, $\Psi = 0^\circ$, respectively.

6.4.4
Influence of Die-channel Angle

The influence of die-channel angle on the plastic deformation during ECAP was investigated by some groups [19, 27, 37, 52, 53, 61, 69, 71]. When the channel angle Φ is 135°, a corner gap is generated in EAP of a perfect plastic material, hence, the corner angles of the workpiece are greater than 0°, regardless of the die-corner angles, see Fig. 6.7. It is apparent that the shear strain in ECAP using the high channel angle die is lower than that using the low channel angle.

6.4.5
Influence of Die-corner Angle

The effect of the corner angle on the plastic deformation of the perfect plastic material during ECAP was simulated by [16, 19, 33, 36, 52, 56, 59, 62, 71, 75, 85]. Figure 6.8 shows that as the corner angle Ψ increases to 45° and to the maximum value 90°, under $\Phi = 90^\circ$, the less shear zone (LSZ) in the bottom

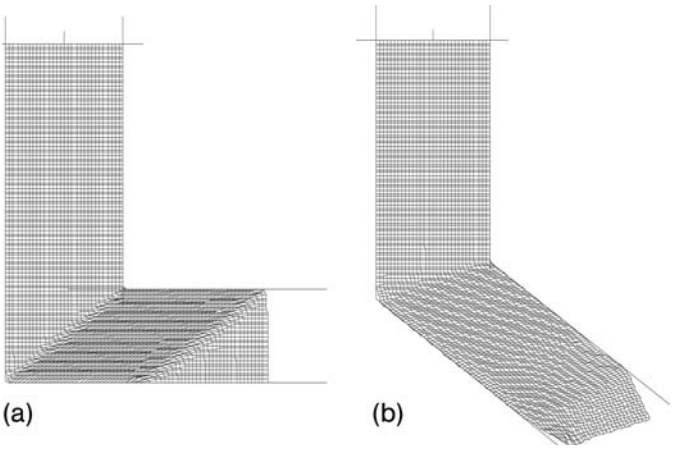

Fig. 6.7 ECAP simulation for the mesh-size sensitivity; ABAQUS standard ver. 6.4, frictionless, (a) $\Phi = 90^\circ$, $\Psi = 0^\circ$ and (b) $\Phi = 135^\circ$, $\Psi = 0^\circ$.

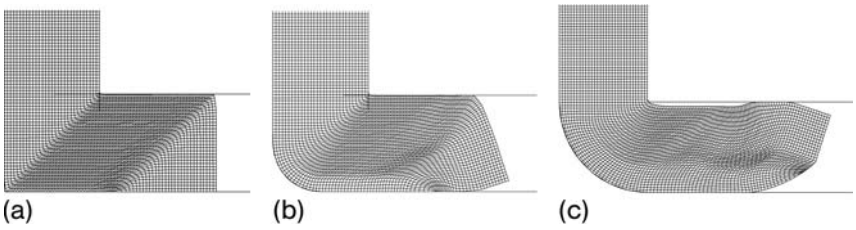

Fig. 6.8 Deformed finite-element mesh of nonhardening material during ECAP, showing corner-angle dependence of deformation homogeneity; corner angles (a) $\Psi = 0^\circ$, (b) $\Psi = 45^\circ$ and (c) $\Psi = 90^\circ$.

region of the workpieces increase. This expanded LSZ is the characteristic of the round-corner die ECAP process, due to the shorter length of the die outer part in $\Psi > 0^\circ$ than in the case of a sharp corner ($\Psi = 0^\circ$). The exit-channel gap in $\Psi = 90^\circ$ is attributed to the large bending effect in the round-corner dies compared to the case of $\Psi = 0^\circ$ or 45°.

A mechanism for the LSZ in the bottom can be understood from the velocity field during ECAP. The velocity distribution at the steady stage is shown in Fig. 6.9 in order to investigate the formation of the LSZ. The outer part of the workpiece within the MDZ (area ABC in Fig. 6.1) moves faster because of the generated tensile stress in that region; it travels longer, and goes further than the inner part. Although the outer part goes further in the MDZ because of the faster velocity than the inner part, the inner part leaves the MDZ earlier than the outer part because the inner region of the MDZ is shorter that the outer re-

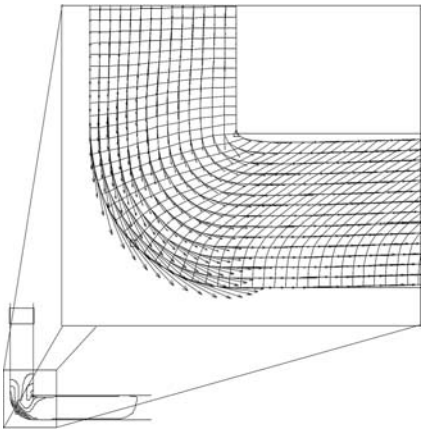

Fig. 6.9 Velocity vector in ECAP using the round-corner die.

gion. The material outside of the MDZ flows with the same horizontal velocity regardless of the position. In other words, the overall shear deformation in the workpiece is generated due to the fact that the inner part leaves the MDZ earlier than the outer part. The LSZ in the outer part is attributed to the faster velocity in the outer part than in the inner part within the MDZ.

6.4.6 Effect of Friction

Friction is an important factor controlling flow behavior of workpiece near die-contacting surface. In general, friction generates deformation differences in a workpiece between surface region and internal region. Hence, it is generally suggested that friction should be reduced using lubricants in metal forming. The effect of friction on the plastic-deformation behavior was simulated by sev-

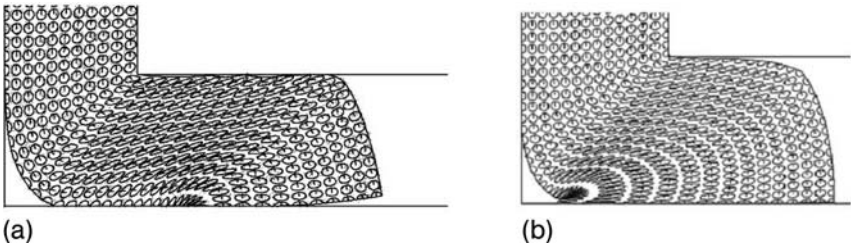

Fig. 6.10 Finite-element analysis (DEFORM) results of pure Al showing the deformation of grids superimposed on the specimen during ECAP with a die angle of 90°. The deformation of the sample is shown for the condition of (a) without and (b) with friction. After Ref. [49].

eral groups [16, 27, 29, 30, 49, 52, 56, 61, 62, 68, 75]. The work of Oh and Kang [49] is introduced below. It should be remembered that their results need to be understood only qualitatively because their approach is 2-dimensional.

Figures 6.10 (a) and (b) show the deformation behavior of the billets that has been partially deformed for the channel angle of 90°, without and with friction. There is a difference in material deformation at the outer corner. The deformation with friction shows the severe distortion at the outer corner, which resulted

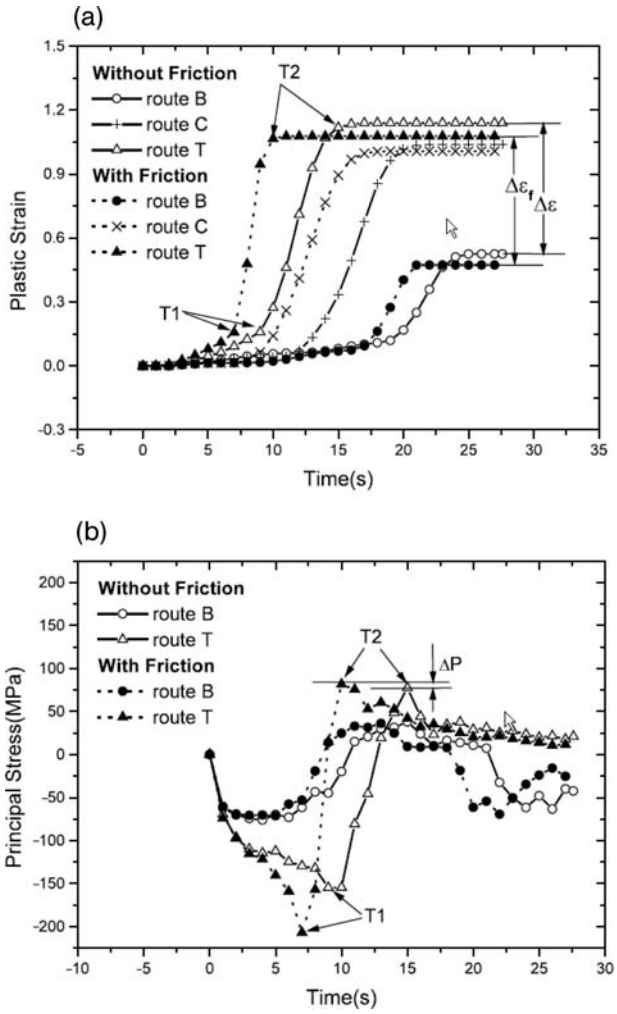

Fig. 6.11 The friction effect of pure Al on plastic strain in various positions plotted against time of passage through the ECAP die for a channel angle of 90° with and without friction. Routes B, C and T represent the positions of bottom, center and top, respectively. After Ref. [49].

in cutting a fragment. The friction induced by the bottom part of the mold limited the material flow at the outer corner. So, the outer-corner distortion became so big that the fragment can not maintain the continuity, is separated from the billet and is left as a dead zone.

Figure 6.11 (a) shows the comparisons of plastic-strain differences between the top and bottom parts. The top part completed deformation in a short time, but that of the bottom part took more time. The friction acts as a backpressure, so the beginning of plastic deformation for the friction case was earlier than that of the no-friction case. The maximum plastic strain at the top part without friction was 1.14 and that of the friction case was 1.08. The friction resisted the flow of material at the surface part, so the material deformation at the inside part of billet decreased. The constraint that was produced by friction decreased the material flow at the bottom part, therefore, the differences in strain values between top and bottom part became reduced from $\Delta\varepsilon = 0.62$ to $\Delta\varepsilon = 0.60$. Figure 6.11 (b) shows the comparison of the histories for principal stress between with and without friction. The top part shows the peak compressive stress before the passage of the corner. The compressive stress became high tensile stress during the passage of the corner. At this stage, there is a high possibility to form cracks at the top part. The stress at the bottom part is much smaller than that at the top part. The difference of peak tensile stress at the top part between with and without friction is 5 MPa. It is so small that the billet surface is not sensitive to cracking due to friction. This means that the friction effect of pure Al is not critical for practical application of the cold working having the friction coefficient of around 0.2. While, in the hot ECAP case, the friction coefficient increases to 0.6–0.8, so the friction provokes additional peak tensile stress. However, the increase of friction does not mean increasing the possibility of cracking. Because the ductility is also increased at the higher temperature, it yields a lower resistance to material flow and results in the easier ECAP process.

6.4.7 Effect of Backpressure

The effect of the backpressure was treated in Refs. [30, 49, 76, 83, 85]. The backpressure has been introduced theoretically in the earlier papers of Segal [15]. However, practically, backpressure has not been widely used or often used in a primitive form of the consequent extruded sample and its role has not been understood. In this section, the work done by Lapovok [76] is introduced.

The stress and strain distribution during ECAP with different levels of backpressure has been simulated by the FEM software "Q-Form" [25] designed specially for simulating forging and extrusion processes. The modeling of ECAP without backpressure confirmed the nonuniformity of strain–stress distribution. The effective strain and mean stress distribution during ECAP of the specimen from Al alloy 2024 are shown in Fig. 6.12. As can be seen, the mean stress at the outer surface and middle flow line is similar and has a negative value dur-

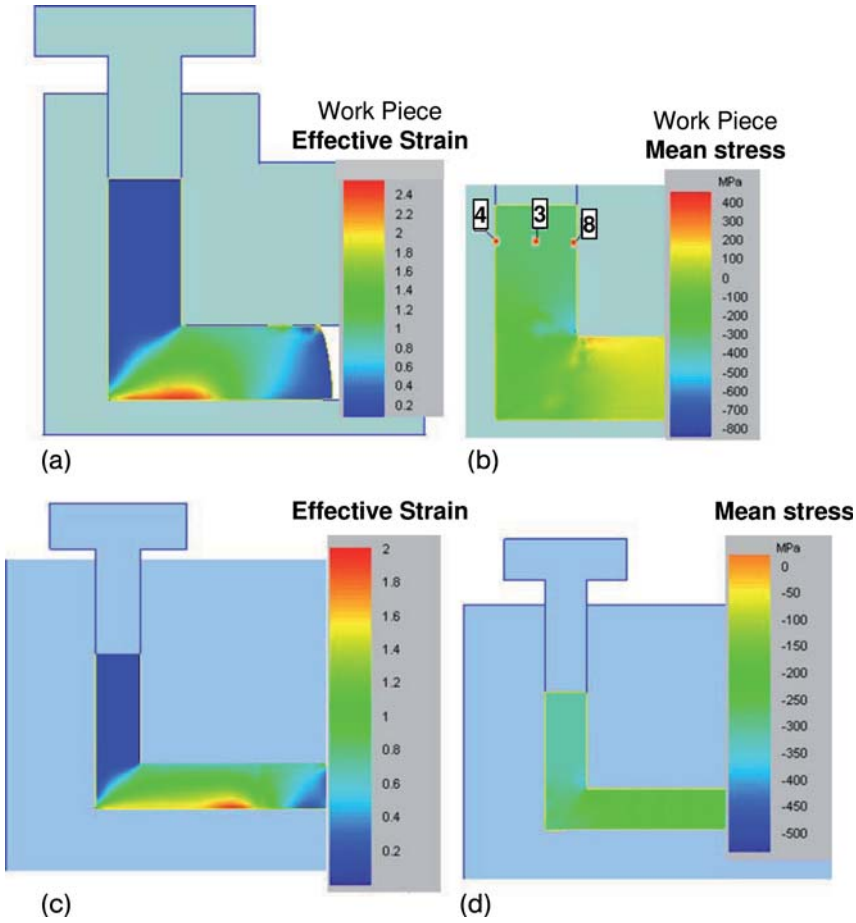

Fig. 6.12 The distribution of stress–strain during ECAE without (a, b) and with backpressure (c, d). (a, c) – effective strain; (b, d) – mean stress.

ing deformation. At the inner surface, the mean stress changes sign from negative to positive as soon as a particle passed the corner of the die, which is the reason for the cracking starting from the inner surface. To create a uniform stress distribution along the cross section of the sample, backpressure can be applied. In the presence of backpressure the mean stress histories for the points at the outer and inner surfaces become the same. The value of a mean stress is negative during deformation what helps to prevent cracking and extrude the low-ductile samples. Hence, the application of backpressure would eliminate a gap between a specimen and the die and change the mode of deformation to a simple shear as described theoretically for an ideal rigid-plastic material. The distribution of strain and stress becomes uniform and the low ductile materials can be extruded without failure. Backpressure is an important factor for industrial applications of ECAP

such as closing of porosity in cast ingots for forging stock and a compacting of light alloys swarf for the following transportation and remelting.

6.4.8
Effects of Material Properties: Strain Hardening and Strain-rate Sensitivity [19, 28, 32]

The external factors described above are controlled usually in the metal-forming processes, aiming at shaping of parts. On the other hand, internal factors (i.e. material properties of the workpiece) need to be considered in SPD processing aiming at microstructural modifications, because the hardening characteristics of materials affect the deformation homogeneity and final microstructural homogeneity of the processed materials.

Two kinds of materials were utilized to investigate the strain-hardening effect on the formation of the die-corner gap using the isothermal two-dimensional plane-strain FEM. Firstly, 6061Al-T6 was used as a (nearly) nonhardening, i.e. quasiperfect plastic, material. Secondly, 1100Al was used as a strain-hardening material. The stress–strain relationship for 1100Al is $\sigma = 119.28\varepsilon^{0.297}$ MPa and for 6061Al is $\sigma = 413.68\varepsilon^{0.05}$ MPa. The stress–strain curves used are plotted in Fig. 6.13 (a). The stress values were normalized by the flow stress at 1% strain

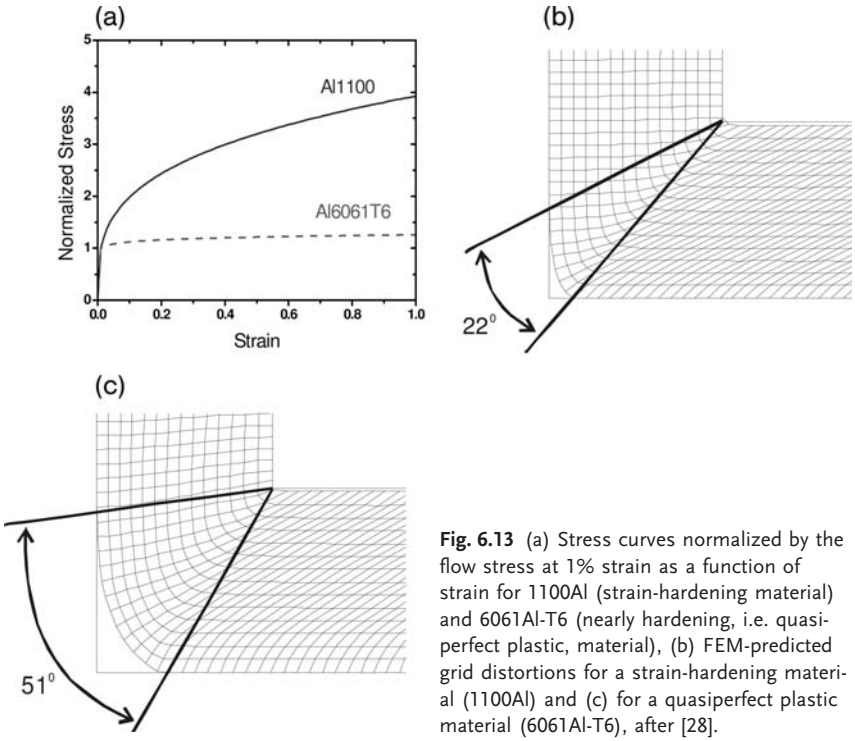

Fig. 6.13 (a) Stress curves normalized by the flow stress at 1% strain as a function of strain for 1100Al (strain-hardening material) and 6061Al-T6 (nearly hardening, i.e. quasi-perfect plastic, material), (b) FEM-predicted grid distortions for a strain-hardening material (1100Al) and (c) for a quasiperfect plastic material (6061Al-T6), after [28].

to compare the strain-hardening behavior explicitly. Figure 6.13 shows the calculated deformed meshes for (b) the strain-hardening material (1100Al) and (c) the quasiperfect plastic material (6061Al-T6). It can be obviously found that the die-corner-filling behavior of the strain-hardening and quasiperfect plastic materials are quite different. The corner gap between the die and the workpiece is large in 1100Al, which has high strain-hardening behavior and relatively small in 6061Al-T6 with low strain-hardening behavior. The corner gap is expected to disappear completely for real perfect plastic materials with zero hardening rate, see Figs. 6.7 and 6.8. Although the die-corner angle Ψ was 0°, the arc curvatures generated on the surface of the workpiece are $\Psi = 51°$ for 1100Al and $\Psi = 22°$ for 6061Al-T6, due to the corner-gap formation between the die and the workpiece. Therefore, it can be concluded that a sharp die-corner angle is not essential for the high strain generation in the workpiece because the workpiece does not exactly follow the corner shape of the die.

The mechanism of the formation of the die-corner gap can be explained using the stress distribution developed in the workpiece. For the nonhardening material, the workpiece deforms as the ram presses and the die corner is filled with the workpiece. On the other hand, for the strain-hardening material, the inside part of the workpiece within the deforming zone, which receives more severe deformation, is harder than the outer part of the deforming zone. The outside part of the workpiece, which receives lower deformation and is therefore softer than the inside part within the deforming zone, can flow faster to the exit channel. The outside surface of the strain-hardening workpiece goes through the shorter distance, and hence, the bottom surface of the final workpiece of the strain-hardening material shows lower shear deformation than the nonhardening workpiece.

Two-dimensional FEM simulations of the ECAP process have been carried out in order to assess the effects of strain hardening and strain-rate sensitivity. In the simulations, the simple model die with the prototype geometry of $15\times15\times120\ \text{mm}^3$, $\Phi = 90°$ and $\Psi = 0°$ was used. In order to investigate the effects of strain hardening and strain-rate sensitivity of materials, nonhardening (perfect plastic) materials of strain hardening exponent $n=0$, strain-hardening materials of $n=0.5$, strain-rate-insensitive materials of srain rate sensitivity $m=0$, and rate-sensitive materials of $m=0.5$ were considered. The example for the strain-rate-sensitive materials may correspond to ECAP processing of materials at high temperatures. The stress σ-strain ε curves for the model materials can be expressed by the following equation;

$$\sigma = \varepsilon^{n}\dot{\varepsilon}^{m} \tag{6.2}$$

Constant ram speeds of 1 and 10 mm/s were employed. Figure 6.14 shows the deformed geometries (flow net) for various materials of different material parameters at two different pressing speeds. In the case of (a) the nonhardening and rate-insensitive materials ($n=0$ and $m=0$), the deformed geometry represents almost ideal and homogeneous behavior within the workpiece. The work-

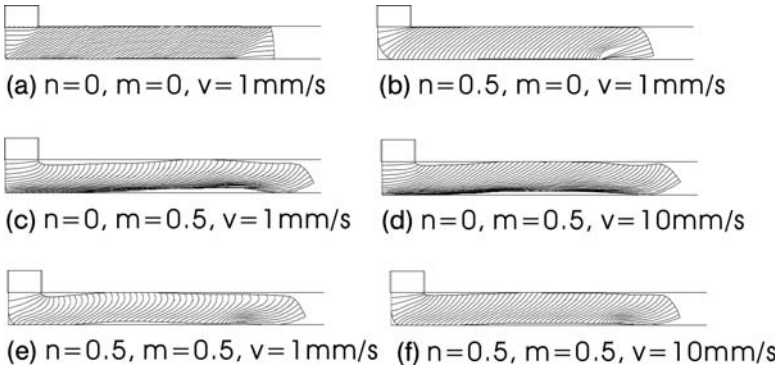

Fig. 6.14 Deformed geometry changes during ECAP. (a) $n=0$, $m=0$; (b) $n=0.5$, $m=0$; (c) $n=0$, $m=0.5$, $v=1$ mm/s; (d) $n=0$, $m=0.5$, $v=10$ mm/s; (e) $n=0.5$, $m=0.5$, $v=1$ mm/s; (f) $n=0.5$, $m=0.5$, $v=10$ mm/s.

piece flows along the die filling all the inside channel. On the other hand, in the case of (b) the strain-hardening and rate-insensitive material ($n=0.5$, $m=0$), two important points should be noted. First, the corner gap between the die and the workpiece develops. The size of the corner gap was found to increase with increase of the hardening exponent n. Secondly, the center part and the inner part of the workpiece are heavily sheared, whereas the outer part appears to be much less sheared. The strain-rate-sensitive ($m=0.5$) material in Fig. 6.14 (c) shows a quite different deformation distribution in ECAP compared to the perfect plastic or strain-hardening materials. The outer (bottom after pressed) part of the workpiece experiences more severe deformation and the inner (top after pressed) part of the workpiece shows less shear deformation. Contrary to the strain-hardening materials, the formation of the corner gap is insignificant. However, the upper-channel gap instantly develops upon shearing of the billet from the vertical entrance channel to the horizontal exit channel. The strength near the inner corner increases rapidly due to the high strain-rate sensitivity, which would tend to decrease the shear strain. This would result in the formation of the upper-channel gap between the billet top and die-exit channel, which has the same effect as increasing the die-channel angle. In the outer-corner region, the strain rate is higher than the center part, but the tendency for increasing the channel angle due to high strain-rate sensitivity is limited by the rigid bottom wall of the channel. The reaction force from the bottom wall would promote the bending of the billet, resulting in the formation of the lower-channel gap between the billet bottom and the die. In Fig. 6.14 (d), the deformation distribution for the strain-rate-sensitive materials with $n=0$ and $m=0.5$ at a higher pressing speed is shown. The strain distribution and the shape are similar to those at a lower pressing speed, Fig. 6.14 (c). However, the rate-dependent deformation characteristics (i.e. local inhomogeneity, less shear zone and exit-channel gaps) are reduced at high deformation speeds. In the case of strain-hardening

and rate-sensitive materials with $n=0.5$ and $m=0.5$ (Figs. 6.14(d) and (f)), the corner gap develops due to the strain-hardening effect and the upper-channel and exit-channel gaps develop due to the strain-rate-sensitivity effect. It should be noted, however, that the strain-rate sensitivity acts to reduce the corner gap promoted by the hardening exponent (compare Figs. 14(b) and (e)) and the hardening exponent tends to reduce the upper-channel and the bottom exit-channel gaps (compare Figs. 14(d) and (f)). It should also be stressed that the inhomogeneity of the shear deformation strongly depends on the relative effects of the strain-hardening exponent and the strain-rate sensitivity.

6.5
Multiscale Modeling: Dislocation-cell Modeling [82]

The deformation behavior and microstructural evolution of metals during ECAP was analyzed using a 3-dimensional version of a dislocation-based strain-hardening model implemented in a finite-element code ABAQUS. A "phase mixture" approach that the material is partitioned in two phases of the dislocation cell walls and the cell interiors with dislocation density which is much lower than cell-wall dislocation density, is used to calculate the local mechanical behavior throughout the workpiece. The model is embedded in a texture analysis code, so that texture evolution can be determined alongside the microstructure variation. In this model, the dislocation population is considered to decompose into two: dislocations with a density ρ_w forming a cell-wall structure and those contained within the cell interiors, with density ρ_c. The evolution of the dislocation densities in the cell interiors and cell walls is described by the following coupled differential equations:

$$\dot{\rho}_c = \alpha^* \frac{1}{\sqrt{3}} \frac{\sqrt{\rho}_w}{b} \dot{\gamma}_w - \beta^* \frac{6\dot{\gamma}_c}{bd(1-f)^{1/3}} - k_0 \left(\frac{\dot{\gamma}_c}{\dot{\gamma}_0}\right)^{-1/n} \dot{\gamma}_c \rho_c \tag{6.3}$$

$$\dot{\rho}_w = \frac{6\beta^* \dot{\gamma}_c (1-f)^{2/3}}{bdf} + \frac{\sqrt{3}\beta^* \dot{\gamma}_c (1-f)\sqrt{\rho}_w}{fb} - k_0 \left(\frac{\dot{\gamma}_w}{\dot{\gamma}_0}\right)^{-1/n} \dot{\gamma}_w \rho_w \tag{6.4}$$

where f, d, G, b and $\dot{\gamma}^r$ denote the volume fraction of the cell walls, the average cell size, the shear modulus, the magnitude of the Burgers vector and the resolved plastic shear rate, respectively. The parameters, α^*, β^* and k_0 are considered to be constant, while the exponent $1/n$ characterizes the strain-rate sensitivity of the dynamic recovery rate represented by the last term in the equations. A scaling relation between the average cell size d and the inverse square root of the total dislocation density, $d = K/\sqrt{\rho}_{total}$ is further assumed. Finally, a decrease of the cell-wall volume fraction with strain from an initial value f_o towards a (lower) saturation value f_∞ is given by $f = f_\infty + (f_o - f_\infty)\exp(-\gamma_r/\tilde{\gamma}_r)$. The latter relation suggests that the rate of "sharpening" of cell walls with strain

Table 6.2 The parameter values used in the simulations.

$\rho_w^{t=0}$	$\rho_c^{t=0}$	f_0	f_∞	$\tilde{\gamma}^r$	$\dot{\gamma}_0^r$	m	n
1.0×10^{13} m^{-2}	1.0×10^{14} m^{-2}	0.29	0.16	2.5	1.0	120	50
a	G	b	K	α^*	β^*	k_0	
0.25	81.7 GPa	2.48×10^{-10} m	30	0.030	1.8×10^{-7}	0.046	

outstrips the concurrent growth of cell-wall area due to cell refinement owing to growth of total dislocation density.

While most of the simulations so far were carried out for fcc materials, here we report some new results relating to ECAP of bcc IF steel. In the simulations presented below, a channel angle of 90° and a zero die-corner angle were taken. Two-dimensional FEM calculations were carried out assuming plane strain conditions. The $\{110\}\langle111\rangle$, $\{112\}\langle111\rangle$ and $\{123\}\langle111\rangle$ slip systems were considered to be active. The contribution of the Peierls stress was neglected in a first approximation. All model parameters used in the dislocation-based hardening model are summarized in Table 6.2. In this calculation, 1 to 8 ECAP pressings were simulated.

Another relatively new result is the prediction of the variation of the average misorientation angle between neighboring cells under ECAP, alongside the prediction of the cell-size evolution. Following Ref. 21, experimental power-law relations between the average misorientation angles in incidental dislocation boundaries (IDBs) and geometrically necessary boundaries (GNBs) and the applied effective strain were adopted:

$$\theta_{\mathrm{IDB}} = k_{\mathrm{IDB}}\varepsilon^{1/2} \tag{6.5}$$

$$\theta_{\mathrm{GNB}} = k_{\mathrm{GNB}}\varepsilon^{2/3} \tag{6.6}$$

The parameters k_{IDB} and k_{GNB} can be determined experimentally in deformed microstructures by TEM or EBSD analysis. Here, we used $k_{\mathrm{IDB}}=1.5$ and $k_{\mathrm{GNB}}=7$. For a reliable analysis and trustworthy predictions, more experimental data from cell/grain-boundary studies are needed, however.

Figure 6.15 shows calculated results on effective stress and misorientation angle distributions in an IF steel sample during the 8th pass of route A ECAP. An initial low strength of less than 100 MPa increases up to an average value of more than 600 MPa. The spatial distribution in Fig. 6.15 (a) shows the lowest strength in the top region and a lower strength magnitude in the bottom region than in the central area of the workpiece. The misorientation angle distribution in Fig. 6.15 (b) increases up to 16° in most of the central area. In this case the cell structure produced can be reinterpreted as a new grain structure. Although not shown here, it was predicted that the dislocation cell size (and hence the new grain size) saturates after a few ECAP passes.

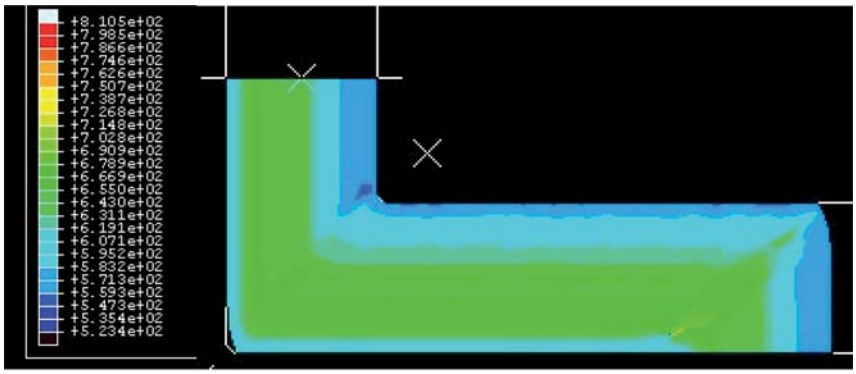

(a) **Effective Stress, MPa**

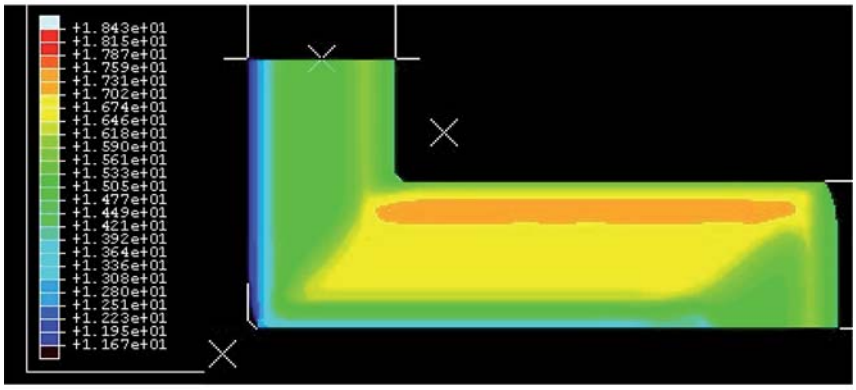

(b) **Misorientation Angle, degree**

Fig. 6.15 Calculated distributions of effective (von Mises equivalent) stress and average misorientation angle in the 8th pass of route A ECAP of steel.

6.6 HPT Simulation [84]

In this process, knowledge of the internal stress and strain distribution is fundamental to the determination of the optimum process conditions for a given material, such as the number of rotations, rotational speed and the temperature. The ABAQUS was applied to obtain a better understanding the plastic-deformation behavior of the workpiece during the torsion straining process. Figure 6.16 shows the deformed geometry of a Cu sample after the HPT processes of (a) compressed and unloaded state with 5 GPa, (b) compression (5 GPa) – die rotation (36°) – unloading and (c) compression (5 GPa) – die rotation (72°) – unloaded state. The outer part of the workpiece out of the die was thickened. Although the geometry of the deformed workpiece is not distinguishable in

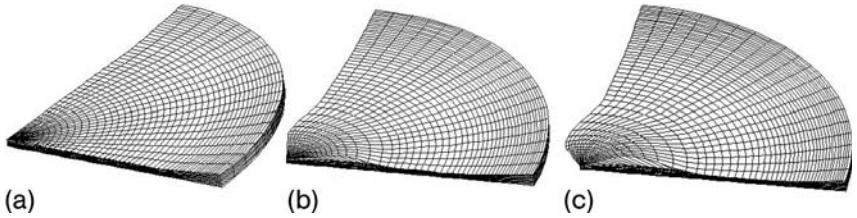

Fig. 6.16 Deformed geometries of Cu sample after the HPT processes of (a) compressed – unloaded state with 5 GPa, (b) compression (5 GPa) – die rotation (36°) – unloading and (c) compression (5 GPa) – die rotation (72°) – unloaded states.

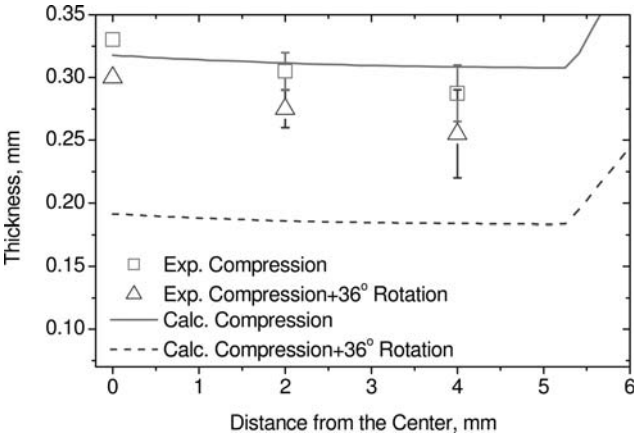

Fig. 6.17 Comparison of the calculated thickness profiles and the experimental ones.

Fig. 6.16, it can be shown that the thickness profile of the unloaded workpiece is not the same as that of the loaded workpiece because of an elastic recovery, see Fig. 6.17. The shear-deformed geometry after compression-rotation represents an unexpected result. The circumferential displacement in the sheared workpiece is apparently inhomogeneous with radius. This nonuniform circumferential displacement profile with radius is related maybe with the stress distribution and a friction hill. The discrepancy of the thickness values between the calculated and the experimental results may be attributed to the uncertainties of: 1) the compressive pressure, which can vary from the initial setting value during the rotation of the die but set to be a constant value of 5 GPa, 2) the coefficient of friction, and 3) gradient effect. Despite the discrepancy, the tendency of the calculated results remains the same as the experimental results and the calculated results provide a lot of important information on the HPT process. The circumferential displacement profile (rotation angle) on the upper surface of the workpiece in Fig. 6.16 (c) shows that it is constant in the center

region and decreases afterwards with the distance from the center. In the central region the friction stress is high enough to achieve a sticking condition between the surfaces of the die and the workpiece. As a result, the angular displacement of the upper surface of the workpiece is the same as that of the workpiece (0.314 rad).

Figure 6.17 shows a comparison of the calculated thickness profiles and the experimental ones of the compressed and the compressed-rotated workpieces. In both the experimental and the calculated results, the thickness of the workpiece decreases with distance from the center. This nonuniform thickness profile is attributed to the stress inhomogeneity. The inner part of the workpiece is under a compressive stress state, the pressure decreases with the radius and the outer part is under a tensile stress state during the compression-rotation loading. The more compressed parts expand more than the less compressed parts, and the outer parts under tensile stress state are compressed after the die is removed. Hence, the final thickness of the inner part is higher than the outer part, as can be seen in Fig. 6.17. The thickness profile of the compression and shear-deformed workpiece can be described as the same situation as the case of the compressed one, but the value of the pressure of the former case is higher than the latter.

6.7 Conclusions

In this chapter, the major developments in finite-element simulation of ECAP are reviewed. The efforts are directed to the understanding differences in software and skills, element sizes, processing parameters and material properties. It was shown that useful insights not only in the average strain and strain rate but also a more detailed analysis of strain nonuniformities and the concomitant microstructure nonhomogeneity in a workpiece undergoing ECAP can be obtained using the FEM. Examples of FEM results obtained by using a dislocation-density-based "phase mixture" model and HPT were given.

Acknowledgements

The author would like to thank his colleagues Y. Estrin, S. B. Kang, I. Alexandrov, R. Lapovok, M. Zehetbauer and Y. Zhu, and his students M. H. Seo, B. S. Moon, W. S. Ryu, Y. S. Jang, S C. Yoon, Y. G. Jeong and P. Quang for their useful work, discussion and help in preparing the manuscript. This work was supported by a Korea Research Foundation Grant (KRF-2005-202-D00205) and the POSTECH New Fellow Grant. The author's finite-element calculations were performed using the supercomputing resources of the Korea Institute of Science and Technology Information (KISTI).

References

1 R. Z. Valiev, R. K. Islamgaliev, I. V. Alexandrov **2000**, *Prog. Mater. Sci.* 45, 103–189.
2 T. C. Lowe, Y. T. Zhu **2003**, *Adv. Eng. Mater.* 5, 373–378.
3 Y. T. Zhu, D.P. Butt **2004**, *Nanomaterials by Severe Plastic Deformation* in *Encyclopedia of Nanotechnology*, American Scientific Publishers, Stevenson Ranch, CA, Vol. 6, 843–856.
4 Y. T. Zhu, T. G. Langdon **2004**, *JOM* 58–63.
5 T. C. Lowe, R. Z. Valiev **2004**, *JOM* 64–68.
6 N. Tsuji, Y. Saito, S–H. Lee, Y. Minamino **2003**, *Adv. Eng. Mater.* 5, 338–344.
7 S. L. Semiatin, A. A. Salem, M. J. Saran **2004**, *JOM* 58–63.
8 V. M. Segal **1995**, *Mater. Sci. Eng. A* 197, 157–164.
9 Y. Iwahashi, J. Wang, Z. Horita, M. Nemoto, T. G. Langdon **1996**, *Scr. Mater.* 35, 143–146.
10 T. Altan, S. I. Oh, H. L. Gegel **1983**, *Metal Forming: Fundamentals and Applications*, American Society of Metals, Metal Park, Ohio.
11 T. Altan, V. Vazquez **1997**, *J. Mater. Proc. Tech.* 71, 49–63.
12 A. N. Bramley, D. J. Mynors **2000**, *Mater. Des.* 21, 279–286.
13 R. Hill **1950**, *The Mathematical Theory of Plasticity*, Oxford University Press, Oxford.
14 J. Chakrabarty **1987**, *Theory of Plasticity*, McGraw-Hill International Editions, Singapore.
15 V. M. Segal **1999**, *Mater. Sci. Eng. A* 271, 322–333.
16 V. M. Segal **2003**, *Mater. Sci. Eng. A* 345, 36–46.
17 G. M. Stoica, D. E. Fielden, R. McDaniels, Y. Liu, B. Huang, P. K. Liaw, C. Xu, T. G. Langdon **2005**, *Mater. Sci. Eng. A* 410–411, 239–242.
18 D. N. Lee **2000**, *Scr. Mater.* 43, 115–118.
19 J. Alkorta, J. Gil Sevillano, *J. Mater. Proc. Tech.* 141, **2003**, 313–318.
20 ABAQUS, http://www.abaqus.com.
21 MSC/MARC, http://www.marc.com.
22 LS–DYNA, http://www.lstc.com.
23 DEFORM, http://www.deform.com.
24 SUPERFORGE, http://www.mscsoftware.com.
25 QFORM, http://www.qform3d.com.
26 CAMPFORM, http://imp.kalst.ac.kr.
27 P. B. Prangnell, C. Harris, S. M. Roberts **1997**, *Scr. Mater.* 37, 983–989.
28 H. S. Kim, M. H. Seo, S. I. Hong **2000**, *Mater. Sci. Eng. A* 291, 86–90.
29 S. L. Semiatin, D. P. DeLo, E. B. Shell **2000**, *Acta Mater.* 48, 1841–1851.
30 J. R. Bowen, A. Gholinia, S. M. Roberts, P. B. Prangnell **2000**, *Mater. Sci. Eng. A* 287, 87–99.
31 S. L. Semiatin, D. P. DeLo **2000**, *Mater. Des.* 21, 311–322.
32 H. S. Kim, S. I. Hong, M. H. Seo **2001**, J. Mater. Res. 16, 856–864.
33 H. S. Kim **2001**, *Mater. Sci. Eng. A* 315, 122–128.
34 H. S. Kim **2001**, *Mater. Trans.* 42, 536–538.
35 H. S. Kim, M. H. Seo, S. I. Hong **2001**, *J. Mater. Proc. Tech.* 113, 622–626.
36 J.-Y. Suh, H.-S. Kim, J.-W. Park, J.-Y. Chang **2001**, *Scr. Mater.* 44, 677–681.
37 J.-W. Park, J.-Y. Suh **2001**, *Metall. Mater. Trans. A* 32, 3007–3014.
38 K. Xia, J. Wang **2001**, *Metall. Mater. Trans. A* 32, 2639–2647.
39 H. S. Kim, Mater **2002**, *Sci. Eng. A* 328, 317–323.
40 H. S. Kim, M. H. Seo, S. I. Hong **2002**, *J. Mater. Proc. Tech.* 130–131, 497–503.
41 B. S. Moon, H. S. Kim, S. I. Hon, **2002**, *Scr. Mater.* 46, 131–136.
42 H. S. Ki, **2002**, *J. Mater. Res.* 17, 172–179.
43 S. C. Baik, Y. Estrin, H. S. Kim, R. Hellmig, H.-T. Jeong **2002**, *Mater. Sci. Forum* 408–412, 697–702.
44 A. Rosochowski, L. Olejnik **2002**, *J. Mater. Proc. Tech.* 125–126, 309–316.
45 J. W. Lee, J. J. Park **2002**, *J. Mater. Proc. Tech.* 130–131, 208–213.
46 S. C. Baik, R. Hellmig, Y. Estrin, H. S. Kim **2003**, *Z. Metallk.* 94, 754–760.
47 S. C. Baik, Y. Estrin, R. J. Hellmig, H. T. Jeong, H.-G. Brokmeier, H. S. Kim **2003**, *Z. Metallk.* 94, 1189–1198.

48 S. C. Baik, Y. Estrin, H. S. Kim, R. J. Hellmig **2003**, *Mater. Sci. Eng. A* 351, 86–97.

49 S. J. Oh, S. B. Kang **2003**, *Mater. Sci. Eng. A* 343, 107–115.

50 J.-Y. Suh, J.-H. Han, K.-H. Oh, J.-C. Lee **2003**, *Scr. Mater.* 49, 185–190.

51 Q. X. Pei, B. H. Hu, C. Lu, Y. Y. Wang **2003**, *Scr. Mater.* 49, 303–308.

52 Y.-L. Yang, S. Lee **2003**, *J. Mater. Proc. Tech.* 140, 583–587.

53 C. J. L. Pérez, P. González, Y. Garcés **2003**, *J. Mater. Proc. Tech.* 143–144, 506–511.

54 C. J. L. Pérez, C. Berlanga, J. Pérez–Ilzarbe **2003**, *J. Mater. Proc. Tech.* 143–144, 105–111.

55 H. S. Kim, P. Quang, M. H. Seo, S. I. Hong, K. H. Baik, H. R. Lee, D. M. Nghiep **2004**, *Mater. Trans.* 45, 2172–2176.

56 V. M. Segal **2004**, *Mater. Sci. Eng. A* 386, 269–276.

57 L. S. Tóth, R. A. Massion, L. Germain, S. C. Baik, S. Suwas **2004**, *Acta Mater.* 52, 1885–1898.

58 S. C. Lee, S. Y. Ha, K. T. Kim, S. M. Hwang, L. M. Huh, H. S. Chung **2004**, *Mater. Sci. Eng. A* 371, 306–312.

59 V. Nagasekhar, Y. Tick-Hon **2004**, *Comput. Mater. Sci.* 30, 489–495.

60 S. Li, I. J. Beyerlein, C. T. Necker, D. J. Alexander, M. Bourke **2004**, *Acta Mater.* 52, 4859–4875.

61 S. Li, M. A. M. Bourke, I. J. Beyerlein, D. J. Alexander, B. Clausen **2004**, *Mater. Sci. Eng. A* 382, 217–236.

62 C. J. Luis-Pérez, R. Luri-Irigoyen, D. Gastón-Ochoa **2004**, *J. Mater. Proc. Tech.* 153–154, 846–852.

63 S. W. Chung, H. Somekawa, T. Kinoshita, W. J. Kim, K. Higashi **2004**, *Scr. Mater.* 50, 1079–1083.

64 S. W. Chung, W. J. Kim, K. Higashi **2004**, *Scr. Mater.* 51, 1117–1122.

65 I. V. Alexandrov **2004**, *Mater. Sci. Eng. A* 387–389, 772–776.

66 H. S. Kim, Y. Estrin **2005**, *Mater. Sci. Eng. A* 410–411, 285–289.

67 S. Li, S. R. Kalidindi, I. J. Beyerlein **2005**, *Mater. Sci. Eng. A* 410–411, 207–212.

68 S. Dumoulin, H. J. Roven, J. C. Werenskiold, H. S. Valberg **2005**, *Mater. Sci. Eng. A* 410–411, 248–251.

69 A. V. Nagasekhar, Y. Tick–Hon, S. Li, H. P. Seow **2005**, *Mater. Sci. Eng. A* 410–411, 269–272.

70 W. J. Zhao, H. Ding, Y. P. Ren, S. M. Hao, J. Wang, J. T. Wang **2005**, *Mater. Sci. Eng. A* 410–411, 348–352.

71 F. Yang, A. Saran, K. Okazaki **2005**, *J. Mater. Proc. Tech.* 166, 71–78.

72 C. J. Luis, R. Luri, J. León **2005**, *J. Mater. Proc. Tech.* 164–165, 1530–1536.

73 S. Li, I. J. Beyerlein, D. J. Alexander, S. C. Vogel **2005**, *Acta Mater.* 53, 2111–2125.

74 S. Li, I. J. Beyerlein, M. A. M. Bourke **2005**, *Mater. Sci. Eng. A* 394, 66–77.

75 B. S. Altan, G. Purcek, I. Miskioglu **2005**, *J. Mater. Proc. Tech.* 168, 137–146.

76 R. Y. Lapovok **2005**, *J. Mater. Sci.* 40, 341–346.

77 P. N. Nizovtsev, A. A. Smolyakov, A. I. Korshunov, V. P. Solovyev **2005**, *Rev. Adv. Mater.* 10, 479–482.

78 P. N. Nizovtsev, A. A. Smolyakov, V. P. Solovyev, A. I. Korshunov **2005**, *TMS Lett.* 2, 121–122.

79 S. C. Yoon, S. I. Hong, H. S. Kim **2006**, *Mater. Sci. Forum* 503–504, 221–226.

80 P. Quang, S. C. Yoon, S. I. Hong, H. S. Kim **2006**, *Mater. Sci. Forum* 503–504, 931–936.

81 I. V. Alexandrov, I. N. Budilov, G. Krallics, H. S. Kim, S. C. Yoon, A. A. Smolyakov, A. I. Korshunov, V. P. Solovyev **2006**, *Mater. Sci. Forum* 503–504, 201–208.

82 Y. Estrin, L. S. Tóth, Y. Bréchet., H. S. Kim **2006**, *Mater. Sci. Forum* 503–504, 675–680.

83 G. I. Raab **2006**, *Mater. Sci. Forum* 503–504, 739–744.

84 H. S. Kim, Y. S. Lee, S. I. Hong, A. A. Tarakanova, I. V. Alexandrov **2003**, *J. Mater. Proc. Tech.* 142, 334–337.

85 I.-H. Son, J.-H. Lee, Y.-T. Im **2006**, *J. Mater. Proc. Tech.* 171, 480–487.

86 S. Li, A.A. Gazder, I. J. Beyerlein, E. V. Pereloma, C. H. J. Davies **2006**, *Acta Mater.* 55, 1087-1100.

87 S. Li, S. R. Kalidindi, I. J. Beyerlein **2005**, *Mater. Sci. Eng. A* 410-411, 201-206.

88 A. Segawa, T. Kawanami **1995**, *J. Mater. Proc. Tech.* 53, 544–551.
89 G.-Y. Tzou, M.-N. Huang **2003**, *J. Mater. Proc. Tech.* 140, 622–627.
90 J. Yong, P. Dashu, L. Dong, L. Luoxing **2000**, *J. Mater. Proc. Tech.* 105, 32–37.
91 Y.-M. Hwang, G.-Y. Tzou **1996**, *J. Mater. Proc. Tech.* 62, 249–259.
92 Y.-M. Hwang, T.-H. Chen, H.-H. Hsu **1996**, *Int. J. Mech. Sci.* 38, 443–460.
93 A. Segawa, T. Kawanami **1995**, *J. Mater. Proc. Tech.* 47, 375–384.
94 A. Afonja, D. H. Sansome **1973**, *Int. J. Mech. Sci.* 15, 1–14.

7
MD Simulation of Deformation Mechanisms in Nanocrystalline Materials

Dieter Wolf and Vesselin Yamakov

7.1
Introduction

The plastic-deformation behavior of nanocrystalline (nc) materials has been the subject of considerable debate ever since polycrystalline metals with a grain size of typically less than 0.1 μm were first synthesized in bulk form approximately 25 years ago (for recent reviews see [1, 2]). As far as the mechanical behavior of these materials is concerned, it is remarkable how little experimental information on the underlying grain-boundary (GB) and dislocation processes that control their deformation and fracture behavior has become widely accepted, the suggestions ranging from greatly enhanced ductility [3–5] to dramatically increased strength and hardness due to the Hall–Petch effect [6, 7]. What seems to be more or less accepted, however, is that (a) for the larger grain sizes (of 50–100 nm) deformation is dominated by dislocation processes and (b) in the lower grain-size range (< 30 nm) a GB-based deformation process takes over, leading to a reduction of the yield and flow stress with decreasing grain size [8–15]; this phenomenon is known as the "inverse Hall–Petch effect". The crossover from "normal" to "inverse" Hall–Petch behavior at a critical grain size, d_c, of typically 20–30 nm, observed in some experiments [13–15], is therefore thought to be due to a change in the dominant deformation mechanism, from one based on dislocations to one mediated by GB processes. The existence of such a crossover implies that a "strongest grain size" [6, 16] exists at which the material is hardest to deform.

Given the extremely rapid increases in recent years in processor speed coupled with the development of ever larger massively parallel computing architectures, atomic-level molecular-dynamics (MD) simulations of nanocrystalline materials have begun to provide novel insights into their structure and thermomechanical behavior. While the first simulations involved relatively modest system sizes [17, 18], simulations have now advanced to a level where they provide a powerful new tool for elucidating – in a degree of detail not possible experimentally – the atomic-level mechanisms controlling the complex dislocation and GB processes in heavily deformed materials with a submicrometer grain

Bulk Nanostructured Materials. Edited by M. J. Zehetbauer and Y. T. Zhu

ISBN: 978-3-527-31524-6

size. In particular, these simulations have now become large enough that they have begun to capture the entire range of grain sizes where the transition from a dislocation to a GB-based deformation mechanism occurs. (For a recent review see [19].)

Apart from their atomic-level spatial and temporal resolution, several unique features of MD simulations are particularly relevant to the deformation studies reviewed here. One is their ability to elucidate the behavior of a fully characterized, albeit usually idealized, nanocrystalline model system in terms of the underlying interfacial structure, driving forces and atomic-level mechanisms. Another arises from the ability to deform to rather large plastic strains, thus enabling the observation of deformation under very high GB *and* dislocation densities. This enables identification of the intra- and intergranular dislocation and GB processes in a deformation regime where they compete on an equal footing, thus providing atomic-level insights into the underlying mechanisms not available from experiments. Recent successes include, for example, identification of the atomic-level mechanisms for dislocation nucleation from, and annihilation at, the GBs [20–22]; the prediction [23] and subsequent experimental verification [24] of mechanical twinning in nc Al [25]; elucidation of the mechanistic causes for the crossover from a dislocation- to a GB-based deformation mechanism with decreasing grain size [26]; the observation of shear bands [27] and their relation to dimpled fracture surfaces [28].

The fundamental limitations inherent to the MD approach are well known. In addition to being limited to relatively small model systems consisting of typically millions of atoms, important issues are the reliability of the interatomic potentials used and the relatively short time period (of typically 10 ns, or about 10^7 MD time steps) over which the dynamics of the system can be probed. The interatomic force descriptions used in most MD simulations are of empirical or semiempirical origin. While these have the advantage of being computationally extremely efficient, they are unable to fully capture the many-body nature of electronic bonding, particularly its complex, self-consistent variation as a function of local structure and chemistry in the vicinity of defects. (For a review of interatomic potentials used in atomistic simulations and a discussion of their limitations, see e.g. [29].)

The short time duration to which MD simulations are inherently limited is particularly relevant to the simulation of plastic deformation. As a consequence, such simulations always involve extremely high strain rates (of typically $>10^7$/s, corresponding to 1% strain in 1 ns), that is, many orders of magnitude higher than in experiments. This issue and the question as to whether MD simulations can actually capture experimentally observed deformation processes were addressed when MD simulations of nc materials first became feasible [30]. As first proposed by Gleiter and coworkers [3, 8, 9], the extrapolation of the Coble-creep formula [31] describing GB diffusion creep in coarse-grained materials to a nm grain size predicts extremely high strain rates, well within the MD range. To test whether MD simulations can, indeed, capture this well-known deformation process, Keblinski et al. [30] simulated GB diffusion creep in nc Si model micro-

structures that were tailored to (i) suppress grain growth (by selecting a uniform grain size and grain shape) and (ii) facilitate GB-diffusion-controlled deformation (by designing mostly high-energy GBs into the microstructure). Indeed, in spite of the extremely high strain rates, these simulations *quantitatively* validated the Coble-creep equation [31, 32].

The chapter is organized as follows. In Section 7.2 we discuss the insights into dislocation plasticity gained from MD simulations of columnar microstructures with the largest grain sizes (up to $d \sim 0.1$ μm). Section 7.3 focuses on the GB-based deformation processes in materials with the smallest grain sizes ($d < d_c$) and the insights gained from these simulations on the "inverse Hall–Petch effect". In Section 7.4 we discuss recent simulations on fully 3d microstructures, which, for the first time, capture the full range of grain sizes where the crossover from a dislocation to a GB-based deformation process takes place with decreasing grain size.

7.2
Dislocation Plasticity for Larger Grain Sizes and the Existence of d_c

The common low-temperature plastic-deformation mechanism in coarse-grained metals and ceramics involves the continuous nucleation of dislocations from Frank–Read sources and their glide through the crystal on well-defined slip systems. In a polycrystalline material the size of these sources cannot exceed the grain size. Since the stress needed for their operation is inversely proportional to the size of the source, this deformation mechanism can operate only down to a grain size of typically about 1 μm. For smaller grain sizes, mobile dislocations must be nucleated from other sources, such as the GBs or grain junctions. In this section we review recent MD simulations of columnar nc Al microstructures [22, 23, 33] that revealed the existence of a length-scale competition between the grain size and the dislocation splitting distance; this competition renders dislocation processes less and less effective until, at a critical grain diameter, d_c, GB-based deformation processes take over. These simulations also revealed a propensity for deformation twinning and subsequent strain hardening. While the high degree of periodicity imposed in the columnar direction restricts the dislocations to being straight lines rather than loops, these simulations have the advantage of enabling rather large grain sizes to be considered and they are easily visualized and quantified. Although the lack of dislocation-line curvature in such columnar-model simulations fails to reproduce the grain-size dependence of the nucleation stress in the bulk material, we demonstrate the experimental support gained for some of the key predictions from these simulations.

7.2.1 Columnar Simulation Model for Al

Yamakov et al. [22] determined the behavior of ⟨110⟩-textured microstructures consisting of four grains of identical size and a regular-hexagonal shape in the simulation cell. These microstructures have the advantage over fully 3d microstructures that a considerably larger grain size can be considered. As illustrated in Fig. 7.1 the four grains in the 3d periodically repeated simulation cell are oriented relative to the tensile (x) axis by rotations about [110] by the angles 0°, 30°, 60° and 90°. The 12 high-angle GBs in the system therefore consist of three groups of identical asymmetric [110] tilt GBs: whereas the 30° and 90° boundaries are high-energy GBs, with a highly disordered atomic structure [34–37], the 60° tilt GBs have a dislocation structure because their misorientation is vicinal to the $\Sigma = 3$, 70.53° tilt misorientation. The ⟨110⟩ column axis (z direction) ensures that, following their nucleation, dislocations can glide on either of two {111} slip planes, activating six slip systems in each grain (out of the 12 that are possible in a fully 3d microstructure), unimpeded by the 3d periodic border conditions imposed on the simulation cell.

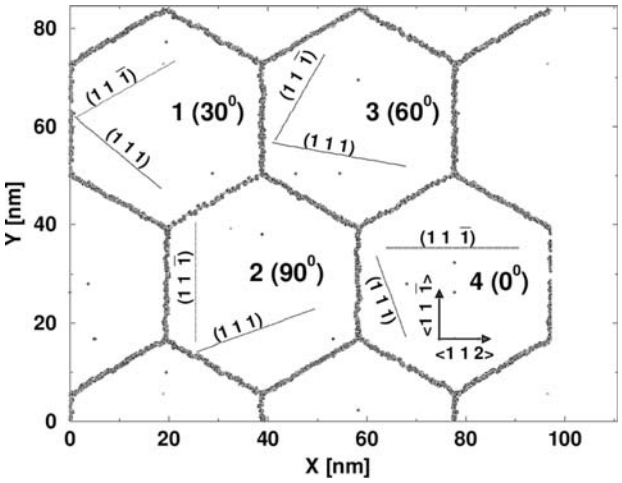

Fig. 7.1 Orientations of the four grains relative to the edge of the simulation cell (x direction, corresponding to the ⟨112⟩ direction in grain 4; i.e. the misorientation angle of each grain is given by the angle between its ⟨112⟩ direction and the (x) axis. The orientations are mapped onto a [110]-projected snapshot of the system with a grain size of $d = 45$ nm after its thermal equilibration at $T = 300$ K but prior to application of external stress. Also indicated are the orientations of the two sets of {111} slip planes in each grain. Only atoms with nearest-neighbor coordination deviating from the fcc perfect-crystal value of 12 are shown. The continuous network of these miscoordinated atoms tracing the GBs indicates that all these [110] tilt GBs are high-angle GBs. The GBs remain perfectly straight until the threshold stress for the nucleation of dislocations is reached [33].

The minimum thickness of the simulation cell in the columnar (z) direction is determined by the cutoff radius, $R_c = 1.37a_0$, of the EAM potential for Al of Ercolessi and Adams [38] used for the simulations. This potential yields a zero-temperature lattice parameter $a_0 = 4.03$ Å. The simulation cell contains only 5 periodically repeated (110) planes (or 10 (220) planes, giving a simulation-cell thickness of $\sim 3.5a_0$ in the (z) direction, the net effect being that any dislocations nucleated from the GBs are constrained to being straight lines. By contrast with the (z) direction, the simulation-cell size in the x–y plane is determined solely by the grain size, d; for values ranging between $d = 20$ and 100 nm, the simulated systems thus contained between 97 000 and 2 425 000 atoms. The potential was slightly modified for a higher degree of smoothness at the cutoff radius; this modification increases the stacking-fault energy from 104 mJ/m^2 to 122 mJ/m^2, that is, closer to the experimental values, ranging between 120 and 142 mJ/m^2 [39].

All simulations were carried out under constant tensile loads of 2.3–2.5 GPa and at a temperature of $T = 300$ K. Ercolessi and Adams [38] estimated the melting point for this potential at 940 K, compared to the experimental value of 933 K. For further details, see Ref. [22].

7.2.2
Length-scale Effects in the Nucleation of Dislocations from the Grain Boundaries and the Existence of d_c

The most common dislocations responsible for the slip deformation of fcc metals are extended dislocations, their cores being split into two Shockley partials connected by a stacking fault. The length of the stacking fault, that is, the dislocation splitting distance, r, depends on the stacking-fault energy, Γ, and the resolved shear stress, σ, on the glide plane as [40]

$$r = K_1 b^2/(\Gamma - K_2\sigma) \tag{7.1}$$

where $b = a_0/\sqrt{6}$ is the length of the Burgers vector of the partials; K_1 and K_2 are numerical factors depending on the elastic constants of the material and the types of partials forming the extended dislocation. Under the high stress required to nucleate dislocations from the GBs, the magnitude of r can be significant and, for a nanocrystalline grain size become comparable to, or even larger than, d. Thus r introduces a new length scale into the problem in addition to d, because a complete extended dislocation cannot be nucleated unless $d > r(\sigma)$ (see Figs. 7.2 (a) and (b)).

The requirement that $d > r(\sigma)$ represents a necessary condition for the dislocation-glide mechanism to be fully operational. When d becomes comparable to r (see Fig. 7.2 (a)), only single partials can be nucleated, producing stacking faults in their glide through the grains. This regime has been considered previously for nc Ni and Cu [20, 41–44], with the same result. The interplay between $r(\sigma)$ and d thus results in a grain size below which the slip process becomes less

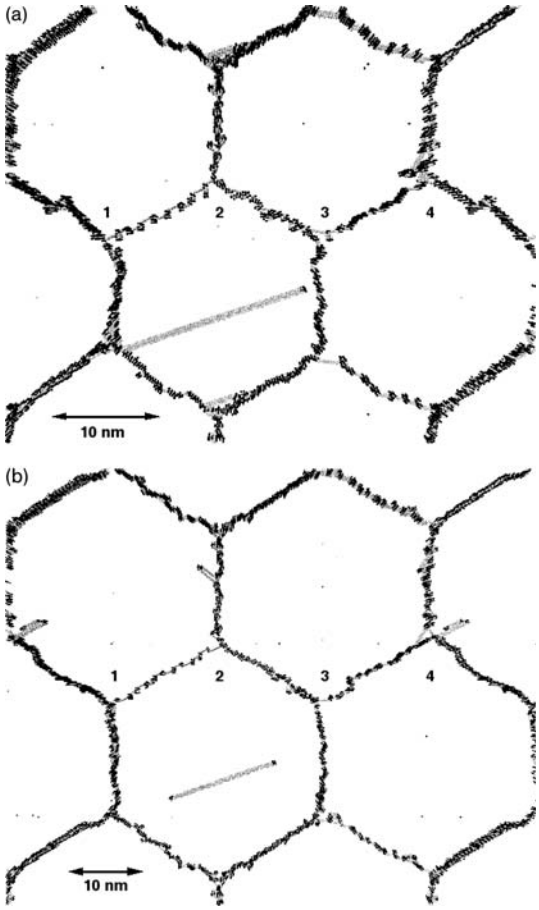

Fig. 7.2 (a) Snapshot of the $d = 20$ nm system at 14.6 ps of deformation time; a nucleated partial 1/6 [112] dislocation is observed, leaving behind an intrinsic stacking fault. (b) Snapshot of a crystallographically identical system, however, with a 30 nm grain size, at 27.6 ps of deformation time. A fully developed extended 1/2 [011] dislocation dissociated into two partials is observed. In both snapshots the applied tensile stress is 2.3 GPa; however, the average internal stress in grains 2 and 4 is 2.77 GPa [33]. Here and throughout, common-neighbor analysis was used to identify perfect-crystal atoms as being either in a local hcp (gray atoms) or fcc environment (atoms not shown). Black atoms are "defected", i.e. neither in an fcc nor hcp environment, including atoms not having 12 nearest neighbors.

and less effective in producing plastic strain and the GB based deformation starts to dominate. This suggests that a critical grain size, $d_c \sim r$, exists below which the material starts to soften due to the domination of a GB-based deformation mechanism. However, as discussed in Section 7.4.2, the grain-size dependence of the dislocation-nucleation stress also enters into d_c.

An interesting observation is that when the applied stress is turned off, any previously nucleated dislocation (see Fig. 7.2 (b)) tends to get reabsorbed *reversibly* by the GB at the same place from which it was nucleated [22]. The initial dislocation-free structure is thus restored, provided the plastic strain was small enough that no dislocation reactions or entanglements had taken place. This plastic reversibility suggests that, in agreement with experimental observations (see Section 7.2.4), at this extremely small grain size the grains cannot sustain single, mobile dislocations without external stress.

7.2.3
Deformation Twinning in Nanocrystalline Al

As the plastic strain increases, the dislocation concentration in the grain interiors continues to increase, giving rise to various types of intragranular dislocation–dislocation interaction processes associated with the glide of extended dislocations on different slip systems. Most of these processes are well known from extensive deformation studies in single crystals and coarse-grained polycrystals [40, 45, 46]. Among the best known is the formation of Lomer–Cottrell locks [46, 47] seen in each of the four grains in Fig. 7.3.

In addition to these *intra*granular processes, these simulations also reveal a variety of unanticipated and intriguing *inter*granular processes, involving the interaction of dislocations with GBs and deformation twins formed during the

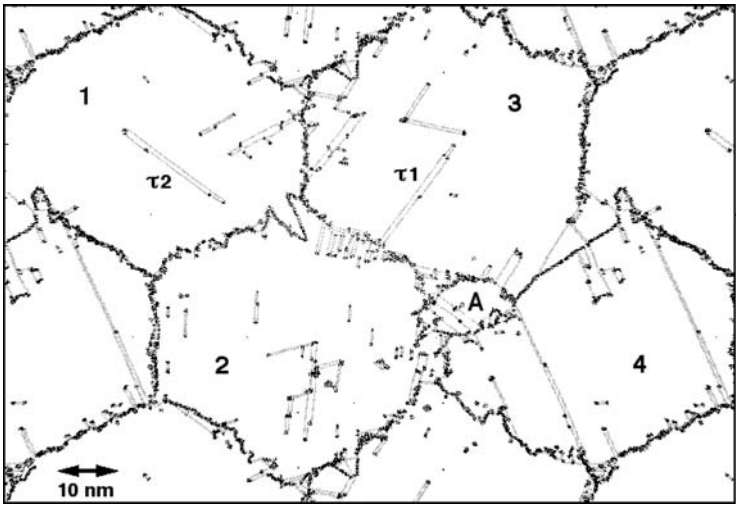

Fig. 7.3 Snapshot at 11.9% plastic strain for the microstructure in Fig. 7.1 ($d = 45$ nm) [23]. A variety of processes involving dislocation–dislocation and dislocation–GB interactions are shown to take place. Formations $\tau 1$ and $\tau 2$ in grains 3 and 1 mark two distinct types of deformation twins. Whereas $\tau 1$ was heterogeneously nucleated from the GB, $\tau 2$ was homogeneously formed inside the grain interior via dislocation–dislocation reactions. Formation of a new grain, labeled A, is also seen.

simulation [33]. Their net combined effect after ~12% plastic strain is shown in the snapshot in Fig. 7.3 for a grain size of 45 nm.

The considerable roughness of the initially flat GBs is particularly noticeable (compare with Fig. 7.1). This roughness arises entirely from dislocation–GB interaction processes, as evidenced by the fact that for a stress slightly below the dislocation-nucleation threshold, the GBs remained perfectly straight during the entire deformation simulation. Moreover, a new grain labeled A has been nucleated at those GBs that were especially active during these emission/absorption/twin-formation events [23]. In addition, Fig. 7.3 reveals a mechanism for what at first sight appears to be GB splitting (see, e.g., the GB between grains 2 and 3). However, detailed analysis reveals that the ordered deformation substructure in grain 2 arises from a massive emission of Shockley partials trailed by *extrinsic* stacking faults. Interestingly, the cores of the partials are aligned, presumably due to elastic interactions among them; this eventually leads to the formation of a new dislocation boundary [23].

A unique aspect of this work, arising from the ability to deform to rather large plastic strains and to consider a relatively large grain size, is the observation of extensive deformation twinning under the very high GB and dislocation densities that can be present in these materials [23, 33, 48]. In fact, three distinct mechanisms for deformation twinning have been observed (see also Fig. 7.3). The simulations revealed a high concentration of stacking-fault planes in the grains produced by single partials or by dissociated perfect dislocations. These stacking faults confined by the dense GB network of the nanocrystal were found to initiate deformation twinning, the underlying twinning mechanisms involving partial dislocations and their interaction with the GBs, including stacking-fault overlapping and the coordinated nucleation of partial dislocations from the GBs [33]. In view of the classic understanding of deformation twinning (see e.g., [49]) as a phenomenon limited to relatively large grain size and materials with relatively low stacking-fault energy, such as Cu [50], these observations for nc Al are very surprising. Interestingly, previous simulations for nc Cu had already revealed the emission of *extrinsic* stacking faults from the GBs early during the deformation [41]; however, their coordinated nucleation and propagation across the grain interiors giving rise to deformation twinning during the later stages of the deformation had eluded detection because of the small grain size to which these simulations were limited. But recent simulations of nc Cu with a grain size of up to 50 nm also revealed the formation of deformation twins [51].

Yamakov et al. [48] suggested that the process of deformation twinning can have a two-fold effect on the mechanical behavior of the material. First, early on during the deformation when the grain interiors are practically free of dislocations, it can facilitate the deformation by adding additional slip systems or by facilitating the transfer between existing slip systems through dislocation–twin reactions. Secondly, once twins have been formed they can repel certain types of gliding dislocations and give rise to pile-ups (see Fig. 7.4), with consequent strain hardening of the material.

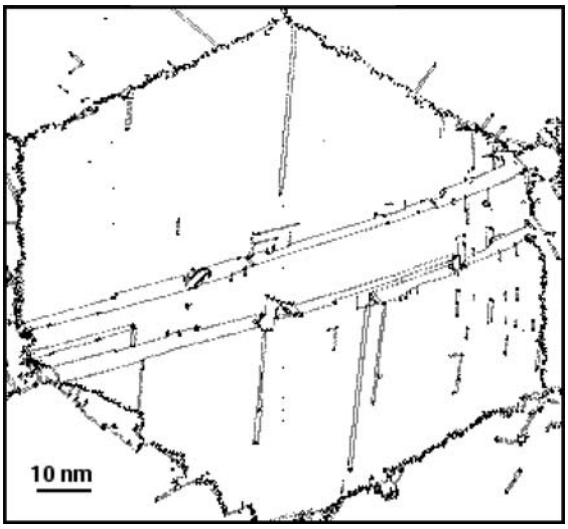

Fig. 7.4 Grain from the microstructure in Fig. 7.1 with a grain size of 100 nm at about 10% plastic strain. Dislocation–twin reactions lead to the formation of complex twin networks consisted of twin boundaries on both (111) and (11$\bar{1}$) planes, connected by stair-rod dislocations at the crossing points. These networks trap the dislocations to form pile-ups, as can be seen in the right part of the grain; these pile-ups probably give rise to work hardening in our model system [48].

The ability of the GBs in nanocrystalline metals to nucleate dislocations and twins continues to be intensively investigated by MD simulation. For example, using a fully 3d microstructure of nc Cu of grains of general shape and varying size, Schiotz and Jacobsen [51] were able to show active dislocation nucleation from the GBs and even the formation of pile-ups. While partial dislocations and stacking faults were dominant in the smaller grains, perfect dislocations and twins were found in 50 nm grains [51]. Bringa et al. [52] studied nc Cu under shock loading. The governing deformation mechanism at ultrahigh stresses (from 5 to 230 GPa) and strain rates (from 10^9 to 10^{11} s^{-1}) was found to be dislocation-based plasticity initiated from the GBs and GB sliding. Considering columnar microstructures similar to those described in Refs. [22, 23], Shimokawa et al. [53] have studied in greater detail the role of the grain size on the detailed GB mechanism of dislocation nucleation in Al. In support of these simulation results, Zhu et al. [54, 55] presented a detailed theoretical analysis on the conditions under which a deformation twin can be nucleated from the GBs and subsequently grow into the grain interior.

All the MD studies reviewed above were focused on fcc metals. The question arises whether the observed dislocation-based deformation mechanisms are specific only to the fcc crystallography or whether they can be generalized to a broader class of nanocrystalline materials. A pioneering MD simulation to answer this question was performed on nc cobalt by Zheng et al. [56]. Surpris-

ingly, this hcp metal showed a different deformation mode. Twinning was not found to occur, and the deformation was governed by partial dislocation slip that lead to a continuous accumulation of stacking faults that gradually produced an allotropic transformation into an fcc phase.

7.2.4 Experimental Validation of Key Predictions

Some of the key predictions from the columnar-model simulations by Yamakov et al. have gained solid experimental support. Among these is the observation in nc Al of the nucleation of perfect dislocations by the successive emission from the GBs of leading and trailing Shockley partial dislocations [5], resulting in a transition with increasing grain size from partial-dislocation slip to the conventional slip mechanism [40]. Several TEM studies on the deformation mode in pure nc Al [24, 57], Al-7.5% wt% Mg [57, 58] and Al-7.6 wt% Mg [59] at different grain sizes revealed that below a critical grain size of the order of 10–20 nm, deformation twinning becomes a dominant deformation mode, even if deformation twinning has never been seen in coarse-grained samples due to the high stacking-fault energy. Similar findings have been reported for other fcc metals, such as Cu [60, 61], Ni [62] and Pd [63]. Moreover, direct TEM observation by Liao et al. [64] in nc Al confirmed the existence of all three twinning mechanisms observed in the simulations [33], namely via stacking-fault overlapping in the grain interiors, coordinated nucleation of partial dislocations from the GBs [59], recently also found in nc Cu [61], and GB splitting [64].

Taking advantage of the inherently highly nonuniform deformation during high-pressure torsion, in a recent study Liao et al. [65] used severe plastic deformation to produce three regions with vastly different grain sizes (ranging from about 200–10 nm) and with varying grain shapes (elongated *vs.* equiaxed) and deformation histories in the same copper sample. This approach thus avoided the problems of comparing the mechanical behavior in samples with different deformation histories, enabling TEM deformation studies for grain sizes ranging from the submicrometer range down to the nm range under identical deformation conditions. A detailed analysis of the TEM images obtained in the three regions demonstrated that different deformation mechanisms dominate in each. Specifically, the regions with the smallest grain sizes contained a considerably higher dislocation density combined with extensive deformation twins; the latter were formed by the mechanism of coordinated partial-dislocation emission from GBs seen in the MD simulations (see, e.g., Figs. 7.3 and 7.4). By contrast, in the submicrometer grain-size region the grain-size effect of twinning could be described by the conventional pole mechanism known from the study of coarse-grained materials.

A more detailed analysis on the role of grain size on deformation twinning in Cu was performed by Huang et al. [66] using equal-channel angular pressing at room temperature and low strain rate (10^{-2} s^{-1}). Samples with grain size ranging from micrometers to nanometers were tested. The transition from the pole

mechanism for deformation twinning in coarse-grained samples to a GB-assisted mechanism in the nanocrystalline samples predicted by MD simulations, was found to occur in the range between 1 μm and 100 nm. These experiments [65, 66] thus confirm the predictions based on the MD simulations of distinct new twinning mechanisms operating in nanocrystalline materials.

Of particular interest is the report by Rösner et al. [63] of similar deformation-twinning processes in another high stacking-fault energy fcc metal, Pd. A comparison between their Al [24] and Pd [63] experiments showed similarities with the MD results in the way the deformation twins were formed. However, in contrast to the MD simulations, in both Pd and Al the twins were found to form on only one slip plane per grain; thus, the twins were always coplanar within each grain. As one slip plane is not enough to accommodate a general deformation, an additional deformation mechanism is required. Rösner et al. suggested that grain rotation will allow the grains to orient their active twin plane along the principal shear direction. By contrast, the MD simulations [48] indicated the appearance of twin networks where two twin planes operate on an equal basis. A possible reason for this might be the much higher strain rates in the MD simulations compared to the experimental studies.

A common criticism of most experimental observations on deformation twinning is that, while the MD simulations were carried out under uniform tensile load, the experimental samples were subject to high nonuniform stresses such as, for example, in ball milling or angular-channel extrusion techniques. A recent study by Wu et al. [67] avoids this problem by deforming nc Ni with a grain size of $\sim$25 nm under uniform tensile load at room temperature (RT) and at liquid nitrogen temperature (LNT). The RT samples did not exhibit deformation twinning apart from the growth of pre-existing twins. In particular, no partial dislocations leaving stacking faults behind have been found, suggesting that the GB-nucleated dislocations were perfect dislocations that quickly traveled across the grains and disappear at the opposite GB. By contrast, the LNT samples conclusively revealed deformation twinning initiated from the GBs through nucleation of series of twinning dislocations, similar to the MD observations of Yamakov et al. [23, 48] for Al at RT. The absence in the RT-deformed samples of a sufficient number of partial dislocations and stacking faults contradicts the MD simulations on Ni reported by Swygenhoven [68] in which partial dislocation slip initiated from the GBs dominated the deformation in this grain-size regime and no perfect dislocations were observed. Noting that theoretical calculations [69] give a lower nucleation stress for perfect dislocations at RT than for twinning dislocations, Wu et al. [67] suggested that the discrepancy with the MD results may come mainly from the very high strain rates in the simulation, leaving not enough time for the trailing partial to be nucleated. Also, the very high local stress concentrations in a Voronoi-type MD microstructure are thought to contribute to the much higher partial dislocation density than seen experimentally [67].

Because deformation twinning is not observed in coarse-grained Al, the formation of deformation twins in nanosized grains seems to be directly related to

the nanocrystalline microstructure [25]. Regarding the mechanical twinning of fcc metals, several models have been proposed [54, 55] in which deformation twins are created by stacking faults led by 1/6 ⟨112⟩ Shockley partials. In terms of these models, the preference for twinning in nanocrystalline materials may be understood by comparing the critical shear stress needed to nucleate a perfect (1/2 ⟨110⟩) dislocation with the stress required to initiate the Shockley-partial twinning dislocation, assuming the size of the dislocation source to be proportional to the grain size. If the GBs are assumed to act as dislocation sources, as suggested by the MD simulations, the stress required to nucleate a Shockley partial is found [24] to be less than that required for a perfect dislocation, when the grain size becomes smaller than a critical value, d_c. For Al, d_c is estimated to be approximately 10 to 15 nm. This model implies that deformation twinning occurs when the GBs start to nucleate more partial dislocations then perfect ones. Rösner et al. [63] argued that this condition alone is not enough as they observed that twin nucleation had started at 3 times higher strain rates then that needed for partial dislocation nucleation. Thus, although it may be energetically favorable to nucleate a partial instead of a perfect dislocation, this does not necessarily imply that twinning occurs; an additional condition, such as high strain rate, seems to be required.

In summary, the MD observations of the preferential generation of partial dislocations, resulting in the formation of stacking faults and deformation twins in nanocrystalline grains [23, 33, 41, 48], are now fully supported by experimental data. Twinning may also offer an alternative interpretation to explain the grain-size strengthening in terms of dislocation pile-ups against the twins.

7.3 Grain-boundary-based Deformation Mechanisms for the Smallest Grain Sizes ($d < d_c$)

The various simulations performed to date on the deformation behavior for the smallest grain sizes ($d < d_c$) agree in that all suggest that (a) the deformation process is governed by GB-mediated processes and (b) the material should soften with decreasing grain size. However, the simulations differ with respect to the specific GB mechanism(s) proposed to be responsible for this behavior.

7.3.1 Simulation of Low-temperature Deformation

About six years ago, inspired by experimental reports of inverse Hall–Petch behavior below some critical grain size, Schiotz et al. [20, 41] and Swygenhoven et al. [21, 70] started to simulate low-temperature plastic deformation of fully 3d microstructures containing typically about 10–50 grains with distributions in their shapes and sizes (of less than $d \sim 20$ nm). To render the deformation observable by MD simulation, very high stresses of $\sim$1–3 GPa had to be applied.

Similar to the experiments, Schiotz et al. determined the yield stress, σ_Y, as a function of the grain size, whereas Swygenhoven's team focused on the strain *versus* time behavior from which the strain rate and its activation energy can be extracted. Consistent with previous suggestions based on experiments [6, 7] both teams identified GB sliding as the dominant deformation mechanism.

The early simulations of Schiotz et al. [20, 41] reported mechanical softening of the low-temperature *yield stress* of nc Cu with decreasing grain size (from 6.6–3.3 nm). By identifying and visualizing the areas with the most inhomogeneously displaced atoms relative to the overall *homogeneous* deformation in the simulated sample, they presented evidence for the existence of GB sliding combined with grain rotation. In some of the larger grains ($d \geq 5.2$ nm), they also observed the nucleation of partial dislocations from the GBs. Following their nucleation, these incomplete extended dislocations traveled across the grains, leaving behind intrinsic stacking faults.

Using a similar approach for simulations of nc Ni with an average grain size of 3.4–5.2 nm at 70 K, Swygenhoven et al. [21, 70] showed that under the low-temperature, high-stress conditions in these simulations, GB sliding and grain rotation were the elementary mechanisms responsible for the observed deformation behavior; moreover, the strain rate was found to increase with decreasing grain size. These observations were confirmed in subsequent simulations in the temperature range of 300–500 K and for grain sizes of up to 12 nm [42, 43] and later 20 nm [71] and it was suggested that GB sliding takes place through atom shuffling and "stress-induced" (i.e. athermal) GB diffusion [43, 71] Similar to the work of Schiotz et al., these simulations also revealed the nucleation of Shockley partials above a certain minimum grain size, d_m, which was shown to depend on the stacking-fault energy ($d_m \sim 8$ nm for Cu and ~ 12 nm for Ni; [43]).

In spite of these rather similar observations, the two groups have offered qualitatively different interpretations. Schiotz et al. plotted their yield and flow stresses against $d^{-1/2}$ (see Fig. 7.5), supposedly confirming the proposed form for the inverse Hall–Petch effect [8], however, without offering a physical explanation of the $\sigma_Y \sim d^{1/2}$ dependence. Also, while observing extensive partial-dislocation nucleation from the GBs, they showed that these dislocations were responsible for only about 1/3 of the total plastic strain, leading them to conclude that GB sliding is the dominant deformation mechanism, rather than dislocation slip. Unfortunately, however, the accommodation process required for GB sliding to proceed was not addressed.

By contrast, Swygenhoven et al. [43, 71] plotted their strain rates against d^{-1} (see Fig. 7.6(a); that is, assuming that $\sigma_Y \sim d$ rather than $\sigma_Y \sim d^{1/2}$). Whereas the strain rates for the three smallest grain sizes were shown to be associated with GB sliding as the sole deformation mechanism, the deformation behavior for the two largest grain sizes involved both GB sliding and dislocation processes. The GB-sliding dominated behavior was rationalized on the basis of a simple model that, like Schiotz et al., assumes that the entire macroscopic deformation arises from GB sliding. Assuming further that deformation occurs by a viscous-type flow of the grains, with a viscosity governed by stress-driven, thermally acti-

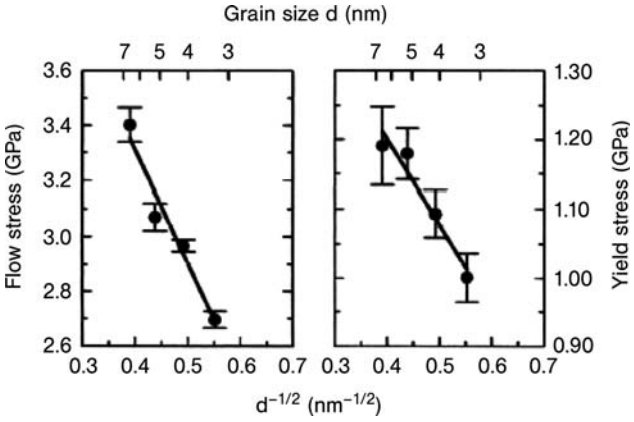

Fig. 7.5 Grain-size dependence of yield stress (left) and flow stress (right) extracted from room-temperature MD simulations of Schiotz et al. [20].

vated GB sliding, a simple GB-area to GB-volume argument was then shown to lead to a d^{-1} dependence of the strain rate, according to [43]

$$\dot{\varepsilon} \sim 1/\sigma_{\mathrm{Y}} = \frac{\dot{d}_0}{d} \mathrm{e}^{-(U/kT)} \sinh\left(\frac{\sigma v}{kT}\right) \tag{7.2}$$

where $\dot{d}_0$ is a characteristic elongation rate of a grain of size d [71], v is the activation volume and U the activation energy for GB sliding. We note that this expression, and the manner in which it was derived, differs fundamentally from (i) the expression for dislocation-induced GB sliding as a mechanism controlling the strain rate in superplastic deformation (yielding the usual $\varepsilon \sim d^{-2}$ dependence; [72]) and (ii) from Coble's expression [31] for GB diffusion accommodated GB sliding (see Eq. (7.3) below).

The key question about these simulations is this: if (i) GB sliding is, indeed, the dominant deformation mechanism and if, indeed, (ii) dislocation processes play no role in the deformation – at least for the smallest grain sizes – and if (iii) microcracking does not occur, then what choices are left for the (rate-limiting) accommodation mechanism? The suggestion that "stress-assisted GB diffusion" may accompany the observed GB sliding [71] might offer a clue. If this were the case, then the accommodation mechanism should be the same as in Coble creep, the only difference being the absence of an activation energy for this athermal process; the Coble-creep formula should then apply. To test this hypothesis, in Fig. 7.6 (b) the data from Fig. 7.6 (a) [43] are replotted, however, as a double-logarithmic plot. Remarkably, the data points for the three smallest grain sizes fall on a straight line with a slope of 2.73. As expected for the Coble-creep mechanism [31], the magnitude of this slope confirms that GB diffusion, albeit likely of athermal origin, accommodated by GB sliding or, conversely, GB sliding accommodated by stress-induced atom reshuffling that resem-

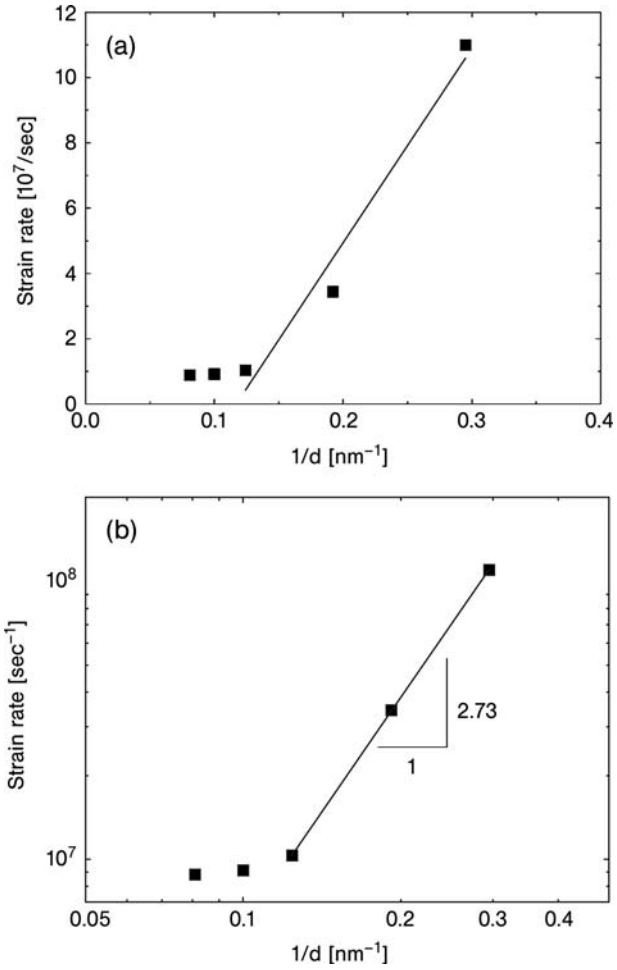

Fig. 7.6 Grain-size dependence of strain rates extracted from room-temperature MD simulations of Swygenhoven et al. [43] of a nc Ni model system containing only high-angle GBs. The grain sizes ranged between 3.4 and 12 nm. Whereas for the two largest grain sizes the deformation is governed by a dislocation process, the deformation behavior for the three smallest grain sizes is due to GB processes [43]. (a) Strain rates plotted against $1/d$, as in the original work [43]; the straight line suggests that Eq. (7.3) is obeyed. (b) Double-logarithmic plot of the same data, revealing a perfect fit of the data points for the three smallest grain sizes to the Coble-creep equation (7.3).

bles GB diffusion, is responsible for the simulated deformation behavior (see also Section 7.3.2).

As discussed in detail in Section 7.3.4, the above analysis illustrates a response of the system in a temperature/strain-rate/stress regime where the underlying thermal-equilibrium, steady-state deformation process cannot be probed due to the far too short MD time window at room temperature. How-

ever, it is interesting to observe that in the absence of any of the usual accommodation processes, the simulated system nevertheless finds a deformation mode that can at least be rationalized.

7.3.2 Simulation of Grain-boundary Diffusion Creep

Apart from GB sliding, it has been proposed that even at relatively modest temperatures, nanocrystalline fcc metals with the smallest grain size may deform by the mechanism of Coble creep and that this might explain the observations of inverse Hall–Petch behavior for $d < d_c$ [8, 9]. To test this suggestion, Yamakov et al. [32] performed MD simulations of fully 3d nc Pd microstructures with a grain size of up to 15.2 nm. To render the process observable on an MD time scale and at relatively low stresses (of 100 to 400 MPa, that is, well below the dislocation-nucleation threshold; see Section 7.2.1), the simulations were performed at elevated temperatures ranging from 900–1300 K, that is, (0.6–0.9) T_m for the Pd (EAM) potential [54, 55]. As in the earlier simulations of GB diffusion creep in nc Si [30], in order to suppress grain growth and thus enable steady-state diffusion creep to take place, model microstructures were tailored to have a uniform grain size and shape. The random grain orientations chosen in this study ensured that all the GBs in the system were high-energy boundaries, whose structure and self-diffusion behavior had been studied previously [30, 73] using the same interatomic potential for Pd.

According to Fig. 7.7, following an elastic regime the simulations reveal the onset of steady-state creep, characterized by constant strain rates. These rates

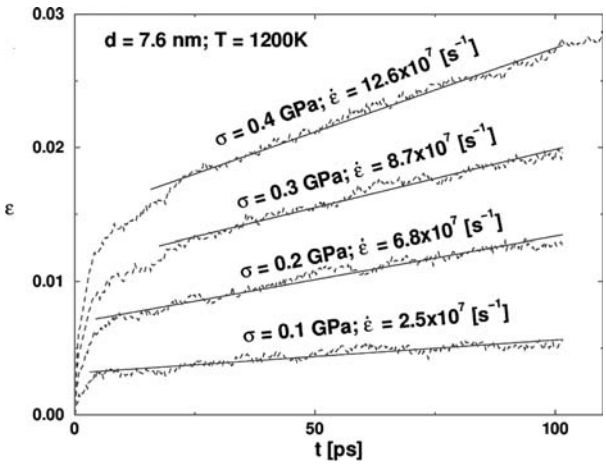

Fig. 7.7 Total (elastic + plastic) strain *vs* simulation time of a tailored, 3d periodic nc Pd microstructure consisting of 16 grains of identical shape and grain size (of 7.6 nm) arranged on a bcc lattice at 1200 K under different tensile stresses [32].

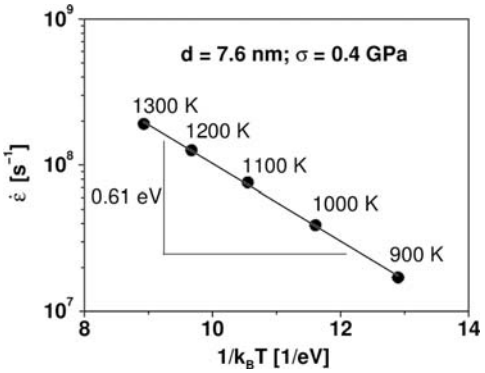

Fig. 7.8 Arrhenius plot for the creep rate in a system containing 16 grains in the simulation cell [32].

were found to increase linearly with the applied stress, σ, for the entire range of grain sizes and temperatures investigated [32]. Moreover, by following the displacements of the centers of mass of individual grains, as in the earlier nc Si deformation simulations [30], the deformation was verified to be homogeneous, that is, the deformation of each grain mirrors the overall deformation.

The activation energy represents an important fingerprint of the underlying deformation mechanism. The Arrhenius plot in Fig. 7.8 for the strain rates extracted from the simulations (Fig. 7.7) yields an activation energy of 0.61 ± 0.1 eV. This value is in remarkable agreement with the universal high-temperature activation energy of 0.60 ± 0.05 eV determined earlier [73] for high-energy *bicrystalline* GBs in Pd in the absence of stress and of any of the microstructural constraints present in the polycrystal. This comparison reveals that, indeed, GB diffusion is the deformation rate-limiting process.

The grain-size dependence of the strain rate represents another important characteristic of the deformation mechanism. The observed linear relation between $\dot{\varepsilon}$ and σ [32] suggests that, for a given grain size and temperature, the strain rates obtained for different stresses (Fig. 7.7) should – within the error bars – collapse into a single point, $\dot{\varepsilon}/\sigma$. The log–log plot of $\dot{\varepsilon}/\sigma$ *versus* the grain size in Fig. 7.9 collects all the data points thus obtained at 1200 K. In this representation the strain rates, indeed, fall on a universal curve, showing a d^{-3} dependence for the larger grain sizes and close to a d^{-2} dependence for the smaller ones.

Taken together, the observations of (i) the linearity between $\dot{\varepsilon}$ and σ, (ii) the homogeneity of the deformation, (iii) the correct activation energy (namely that for GB diffusion), and (iv) the d^{-3} dependence found for the larger grain sizes demonstrate that the simulation results for the larger grain sizes are consistent with the well-known Coble-creep formula [31],

$$\dot{\varepsilon} = A \frac{\sigma \Omega_D}{k_B T} \frac{\delta_D D_{GB}}{d^3} \tag{7.3}$$

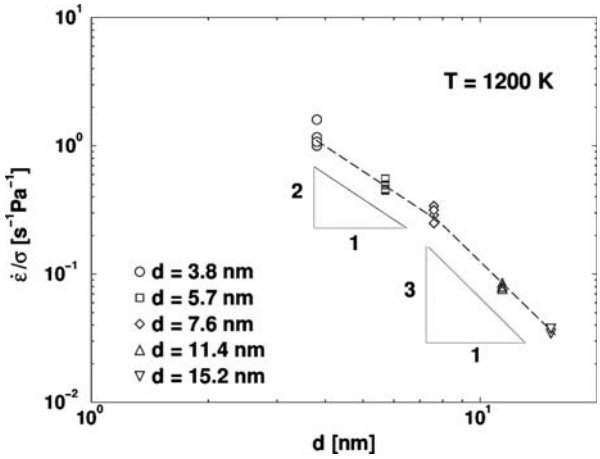

Fig. 7.9 Scaling plot of $\dot{\varepsilon}/\sigma$ *vs.* grain size, d, showing that all the data points obtained for different stresses at 1200 K collapse onto a single curve, and indicating that the strain rate increases linearly with stress (see Eq. (7.1)). The dashed curve is merely a guide to the eye. The increase in error bars with decreasing grain size is due to the greater equilibrium fluctuations in the smaller systems [32].

Here, $\delta_D D_{GB}$ is the diffusion flux in the GBs with diffusion constant D_{GB}, grain-boundary width δ_D and activation volume $\Omega_D \cdot \sigma\Omega_D$ is the work performed by the stress during an elementary diffusion jump in the GB; $k_B T$ is the thermodynamic temperature and A is a geometric constant that depends on the grain shape. To test whether the underlying mechanism is indeed that assumed by Coble, the authors followed the diffusion of individual GB atoms, verifying that, indeed, they diffused from the grain equators to the poles [32].

By contrast with Eq. (7.3), for the two smallest values of d deviations from the d^{-3} dependence are clearly visible in Fig. 7.9. This reduced grain-size dependence for the smallest values of d was shown to follow naturally from Coble's derivation under the assumption that the GB width can no longer be neglected relative to d. In this limit, Coble creep and Nabarro–Herring creep become identical processes, with a grain-size exponent of –2 (see Fig. 7.9) [32].

7.3.3
Geometrically Necessary Coupling between Grain-boundary Diffusion Creep and Grain-boundary Sliding

From the deformation of coarse-grained materials under conditions where dislocation processes are unimportant and microcracking does not occur, it is well known that, just as GB sliding must be accommodated by GB diffusion [74], GB diffusion creep in turn requires GB sliding (known as Lifshitz sliding [75, 76]) as an accommodation mechanism. The interplay between the two mechanisms therefore represents two different aspects of the same deformation process.

Throughout their simulations, Yamakov et al. [32] verified that no dislocations were nucleated from the GBs and that no microcracking occurred. Under these conditions, the GB diffusion creep should be accommodated by Lifshitz sliding [75, 76]. Experimentally, GB sliding can be observed directly by scratching marker lines across the GBs [77]. Since in MD simulations the atoms are already labeled, this idea was implemented [32] by "painting" straight lines of atoms across the surface of the unstrained system. These simulations revealed that after $\sim$4% elongation in the tensile direction, the marker lines had, indeed, undergone shifts across all the GBs. A detailed analysis of the magnitudes of these shifts showed them to be in complete agreement with the geometrically necessary "Lifshitz sliding" required to accommodate the GB diffusion creep [75, 78]. We note that this type of GB sliding is distinct from Rachinger sliding [76, 79] that occurs when, during *large-strain* deformation, entire grains move through the polycrystalline matrix. Rachinger sliding is therefore an *inhomogeneous* deformation process and involves topological discontinuities, such as neighbor switching [80].

7.3.4 Discussion

The results of the significant number of simulations of inverse Hall–Petch behavior reviewed above strongly suggest that in the absence of grain growth, the nanocrystalline microstructures considered in these simulations deform via the well-known Coble-creep mechanism. The inverse Hall–Petch effect therefore appears to be merely a manifestation of GB diffusion creep, with the characteristic d^{-3} decrease of the creep rate with decreasing grain size. The apparently contradictory suggestions that GB sliding, on the one hand, and GB diffusion creep, on the other, are responsible for the inverse Hall–Petch effect can thus be reconciled as originating from one and the same deformation mechanism.

However, given that GB diffusion is a thermally activated process, one cannot hope to prove directly by MD simulation that the observation of thermally equilibrium Coble creep [32] can be extrapolated to room temperature where most deformation experiments are performed. Whereas the observation window accessible to MD simulations is limited to typically less than about 10^{-8} s, the experimental time window is typically ten orders of magnitude longer. In order for MD simulations to nevertheless capture the *equilibrium* steady-state response of the material at lower temperatures *and* under experimental conditions, much longer simulation times than those presently possible would therefore be required. Since this is not an option, the challenge consists in capturing and elucidating the rate-limiting experimental processes, however, within the short MD time window, while avoiding probing some poorly defined, "MD only" deformation-rate-dependent transient response of the material.

To analyze quantitatively whether in Pd, at least experimentally, Coble creep can be expected to facilitate the deformation even at room temperature and at a more typical stress level of $\sigma = 0.1$ GPa, Eq. (7.3) can be extrapolated to deter-

mine the predicted strain rate based on the simulation results described in Sections 7.3.2 and 7.3.3 [32]. Starting from the simulated strain rate of $\dot{\varepsilon}(900\ \mathrm{K},\ 0.4\ \mathrm{GPa}) = 1.7 \times 10^{7}\ \mathrm{s}^{-1}$ obtained for a grain size of 7.6 nm at 900 K for $\sigma = 0.4$ GPa (see Fig. 7.8), with the activation energy of 0.61 eV one finds:

$$\dot{\varepsilon}(300\ \mathrm{K},\ 0.1\ \mathrm{GPa}) = 1.1 \times 10^{-7}\dot{\varepsilon}(900\ \mathrm{K},\ 0.4\ \mathrm{GPa} = 1.87\ \mathrm{s}^{-1} \tag{7.4}$$

that is, a strain rate entirely within the experimental range. Under these conditions, particularly in the absence of dislocations, GB sliding can, indeed, be accommodated by GB diffusion. This is remarkable because for Pd, with a melting point for the potential used here of about 1500 K, room temperature represents a homologous temperature of only ~ 0.15.

Since experimental strain rates are usually even lower than the limit in Eq. (7.4), it seems entirely plausible that, as predicted over a decade ago by Gleiter and his coworkers [3, 8, 9] even at room temperature most nanocrystalline fcc metals can, indeed, deform via the Coble-creep mechanism. Unfortunately, however, this assertion cannot be proven directly by MD simulation since an MD time window of ~ 1 s would be required to observe thermally activated GB diffusion. However, as illustrated in Fig. 7.6(b), even the room-temperature MD simulations are consistent with the Coble-creep mechanism [43, 70], in spite of the fact that the time window in these simulations was far too short to capture the equilibrium GB-diffusion process. It is interesting to observe that in the absence of any of the usual accommodation processes, including *thermally activated* GB diffusion, microcracking and dislocation processes, and under simulation conditions corresponding to no experimentally realizable situation, the simulated system [43, 70] finds a deformation mode that can at least be rationalized. These observations suggest that Coble creep, that is, GB-diffusion accommodated GB sliding, represents a very robust mechanical response of a nanocrystalline material, even at low temperatures. The reasons for this probably lie in the fact that GB diffusion, or even athermal stress-induced shuffling of GB atoms, represents a very powerful stress-relaxation mechanism.

The study of Yamakov et al. [32] demonstrates that under carefully chosen simulation conditions, the well-known time-scale and high-stress limitations inherent to MD simulations can be overcome to enable probing the intrinsic equilibrium steady-state response of a nanocrystalline microstructure to external loading. Although limited to elevated temperatures, under these thermodynamically and kinetically well-defined conditions Yamakov et al. were able to elucidate the role of GB diffusion as an accommodation mechanism for GB sliding, and *vice versa*. However, this study also demonstrates the considerable difficulties of such simulations in capturing the equilibrium steady-state response of the material at lower temperatures, the challenge being to avoid probing some poorly defined, deformation-rate-dependent transient response of the material that cannot easily be related to the deformation conditions present in experiments.

7.4
Crossover from "Normal" to "Inverse" Hall–Petch Behavior

Facilitated by rapid increases in computational power, two recent simulation studies on fully 3d microstructures [26, 51] have been able to capture the full range of grain sizes over which the crossover from a dislocation process (see Section 7.2) to a GB process (see Section 7.3) takes place, and thus to elucidate the nature of the "strongest grain size", d_c, in nanocrystalline fcc metals. In the first of these studies, Yamakov et al. [26] considered nc Al microstructures consisting of four grains in a periodically repeated simulation cell. This simple set-up enabled exploration of a range of grain sizes from 7–32 nm, that is, both above and below d_c for Al, and hence allowed the transition from GB-dominated processes (for $d < d_c$) to dislocation-dominated processes (for $d > d_c$) to be directly probed (see Section 7.4.2). Most importantly, these simulations demonstrated for the first time directly the coupling between the crossover in the deformation mechanism and the mechanical behavior. In addition to yielding a value of $d_c \sim 18$ nm for Al, these simulations demonstrated unambiguously that the crossover in the mechanical behavior is, indeed, due to a transition in the dominant deformation process.

In the second study, Schiotz and Jacobsen [51] determined the flow stress of nc Cu with a grain size ranging between 5 and 50 nm. These simulations also revealed the expected crossover in the flow stress, from Hall–Petch to inverse Hall–Petch behavior, at a value of $d_c \sim 14$ nm for Cu. As in the study of Yamakov et al., this crossover in the mechanical behavior was accompanied by a change in the underlying mechanism, from dislocation-mediated plasticity to GB sliding.

In the following, we summarize some of the key insights gained from these studies.

7.4.1
Grain Boundaries as Dislocation Sources

In the simulations by Yamakov et al. [26] four grains of identical size and a rhombic-dodecahedral shape (the shape of the fcc Wigner–Seitz cell) were arranged on a 3d periodic fcc lattice. The 24 GBs in the simulation cell thus meet at 32 triple lines at 120° angles, that is, close to the equilibrium Herring angles, ensuring a high degree of stability against grain growth. By selecting random grain orientations and applying a Monte-Carlo procedure to avoid low-angle and vicinal (i.e. dislocation) boundaries as well as "special" high-angle misorientations, they ensured that, as in their columnar model all the GBs in the system were general, high-energy GBs with a highly disordered atomic structure. This simulation geometry ensures a rather uniform stress distribution across the microstructure [81]. In spite of the small number of grains, elevated-temperature simulations of GB-diffusion creep in nc Si [30] and Pd model systems with the same geometry quantitatively reproduced the Coble-creep formula for the strain rate (see Eq. (7.3)).

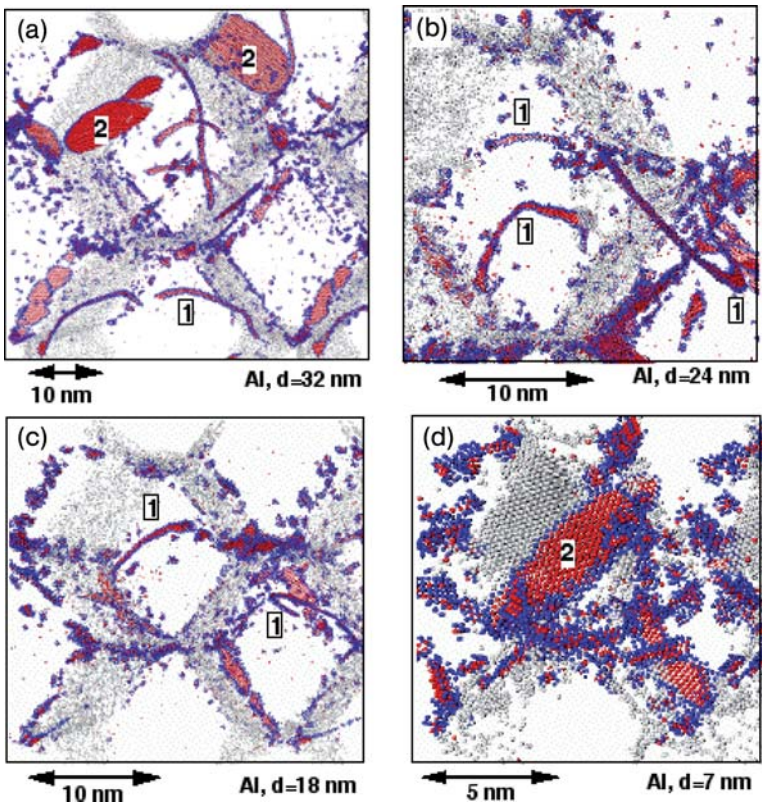

Fig. 7.10 Snapshots of the four-grain, fully 3d Al microstructure at about 1.5% plastic strain for four different grain sizes: (a) $d = 32$ nm; (b) $d = 18$ nm; (c) $d = 10$ nm and (d) $d = 7$ nm. Common-neighbor analysis was used to identify atoms as being either in a local hcp or fcc environment (not shown). The GBs are seen as walls of gray atoms (representing "disordered" atoms, i.e. atoms neither in a local fcc nor hcp environment). To better visualize the grain interiors, only parts of the GBs are shown. "Highly disordered" atoms are defined as (i) atoms with more than half of their neighbors within the cutoff radius of the potential being disordered or (ii) atoms interacting with at least two hcp-coordinated atoms. Three distinct types of dislocation configurations are labeled as (1), indicating a complete, extended 1/2 [110] dislocation; (2), indicating a stacking-fault plane produced by a single Shockley-partial dislocation and (3), split stacking-fault plane [26].

The first important result of Yamakov et al. [26] was the observation (see Fig. 7.10) that the GBs in their fully 3d microstructure, indeed, nucleate perfect dislocations, as suggested by Li [82] over 40 years ago. As in their columnar model geometry [22], these dislocations were found to be 1/2[110] dislocations dissociated into two 1/6[112] Shockley partials connected by a stacking fault, that is, the type of extended dislocations commonly seen in fcc metals [40]. In the formations labeled 1 in Figs. 10 (a) and (b), these dislocations are seen as red loops

representing the stacking-fault atoms in an hcp environment, delineated by two thin lines of atoms representing the dislocation lines of the two partials. The simulations revealed that the mechanism of nucleation of these extended dislocations involves the successive emission of both the leading and trailing Shockley partials from the GB (see also [22]). As in the columnar simulations, the width of the stacking-fault region, that is the splitting distance, r, of the extended dislocation, depends on the resolved shear stress and the stacking-fault energy (SFE) as expressed by Eq. (7.1). Once nucleated, these dislocation grow and extend into the grain interiors.

It is well known that dislocation loops in coarse-grained materials are formed by Frank–Read sources. The difference here is that the range of grain sizes (of 7–32 nm; see Fig. 7.10) is too small for complete loops to develop. As the loop radius is inversely proportional to the resolved shear stress, it cannot be made smaller than the grain size for any reasonable value of the stress; the dislocation is thus forced to terminate at the GBs. Hence, although Figs. 10 (a) and (b) reveal the onset of the dislocation-slip mechanism, the GBs still strongly affect the process by modifying the dislocation mobility. In particular, it seems likely that the dislocation mobility is decreased due to its termination on GBs, suggesting a GB-induced mechanism for hardening with decreasing grain size. This mechanism could supplement the conventional dislocation pile-up mechanism in which the GBs act as barriers impeding the free movements of the dislocations.

A comparison of these observations for a fully 3d microstructure with those obtained for a columnar simulation geometry [22] reveals that, not surprisingly, the main difference lies in the fact that in the 3d microstructure, the dislocation lines are no longer constrained to being straight lines. This allows the development of dislocation loops, the curvature of which introduces a grain-size effect into the nucleation stress. By relating the size of the dislocation loops nucleated from the GBs to the grain size, Cheng et al. [83] recently suggested that the nucleation stress should be inversely proportional to the grain size, $\sigma_n \sim 1/d$. As a consequence, when the grains become larger (say of μm size), the mechanism changes to the one considered by Li [82] involving the nucleation of dislocations from GB ledges and their propagation through the forest dislocations commonly present in coarse-grained materials. This mechanism gives a Hall–Petch type of nucleation stress, $\sigma_n = \sigma_0 + k/\sqrt{d}$, where σ_0 is the single-crystal yield stress and k is a constant that depends on the strength of the GB. Combining the two mechanisms one gets:

$$\sigma_n = \sigma_0 + \kappa/\sqrt{d} \quad \text{for coarse-grained metals [82]} \tag{7.5 a}$$

$$\sigma_n \sim 1/d \quad \text{for nanocrystalline metals [83]} \tag{7.5 b}$$

A similar Hall–Petch form of Eq. 7.5 (a) has recently been discussed also by Bata and Pereloma [84]. The increase of σ_n with decreasing grain size would imply a decrease in the dislocation activity in smaller grains. This decrease is

clearly seen in Figs. 7.10 (a)–(c). The absence of such a decrease in the columnar-model simulations [22] supports the role of the dislocation-line curvature in the nucleation process. Also, for the same grain size and interatomic potential the 3d model microstructures exhibited a slightly lower threshold stress for dislocation nucleation from the GBs (of $\sim$1.9 GPa; [26]) than the columnar systems (of $\sim$2.3 GPa). This difference is probably due to (i) the fact that the dislocations are no longer restricted to being straight lines (see Fig. 7.10) and (ii) the presence of a complete set of 12 slip systems (compared to only six in the columnar microstructures).

We finally mention that, in addition to the nucleation mechanism involving the successive emission of two complementary partial dislocations, Fig. 7.10 (c) reveals a second mechanism for producing a perfect dislocation. This mechanism starts by the nucleation of a single partial from the GB, leaving an intrinsic stacking fault behind (formation 3 in Fig. 7.10 (c)). At some point, instead of nucleating a follow-up second partial, the stacking-fault plane breaks from inside, producing a loop of another partial dislocation which restores the fcc lattice (see formation 3). The result is a perfect dislocation loop in close vicinity to the GB.

Such an event has also been observed in atomistic simulations of a Frank–Read source using the same EAM potential for Al [85]. The authors refer to this effect as "anomalous dislocation multiplication in fcc metals" [85]. A careful estimate of the resolved shear stress required to split the stacking fault gave a value of 0.93 $\pm$0.05 GPa. This value is consistent with a previous estimate of 1 GPa for the resolved shear stress on the (111) planes using the same potential [22]. While the size of the Frank–Read source considered in Ref. [85] is only a few nanometers (rendering it very unlikely to exist and operate inside the grain of a real material), the above simulations suggest that it may be operational at the GBs and in reality may contribute to the dislocation slip in nanocrystalline fcc metals. It is also worth noting that the columnar simulations have shown that this anomalous dislocation multiplication can be assisted by dislocations that happen to pass by [48].

7.4.2 Crossover in the Mechanical Behavior

Both simulation studies of the mechanical behavior in the crossover regime [26, 51] revealed that the transition from a dislocation-based to a GB-mediated deformation mechanism with decreasing grain size leads to a crossover in the mechanical behavior, from Hall–Petch hardening to softening. Here, we analyze this crossover in some detail.

Figures 7.10 (a)–(d) provide clear evidence for a change in the deformation mechanism as the grain size decreases from 32 nm in (a), via 18 nm and 10 nm in (b) and (c), to 7 nm in (d) [26]. As in the columnar model, when the grain size becomes comparable to, or even smaller than, the size of these extended dislocations, nucleation of complete dislocations is no longer possible.

Instead, as seen in Fig. 7.10 (d), only single partials can then be nucleated, leaving behind stacking faults generated by the glide of the partials through the grains (configurations labeled (2) in Fig. 7.10). Having been limited to similarly small grain sizes as that in Fig. 7.10 (d), the earlier simulations of nc Ni and Cu by Schiotz et al. [20, 41] and Swygenhoven et al. [42–44] yielded qualitatively the same behavior as that seen in Fig. 7.10 (d). Interestingly, such incomplete nucleation events can occur even for larger grain sizes, as seen for example in Fig. 7.10 (a). In this particular case the emission of the trailing partial appears to have been prevented by the local GB and triple-junction environments and the associated local stress fields [26]. The key question now is how this change in the deformation mechanism affects the mechanical behavior. Instead of focusing on the yield stress as a function of the grain size, Yamakov et al. [26] probed the mechanical behavior in the flow regime, by determining how the strain rate under the applied tensile stress is affected by this change in mechanism.

The plastic strain *versus* time plots, $\varepsilon(t)$, shown in Fig. 7.11 for three of the five grain sizes studied, reveal a pronounced change in the strain rate, $\dot{\varepsilon}$, as the dislocation-slip process is gradually pre-empted by a GB-mediated deformation mechanism. The lack of smoothness of these curves arises from the discreteness of the deformation process, involving two distinct deformation mechanisms (see below), which is particularly noticeable due to the small number of grains in the simulation cell. It is, nevertheless, clear from Fig. 7.11 that (i) as the grain size decreases from $d = 24$ nm to 18 nm, the average strain rate

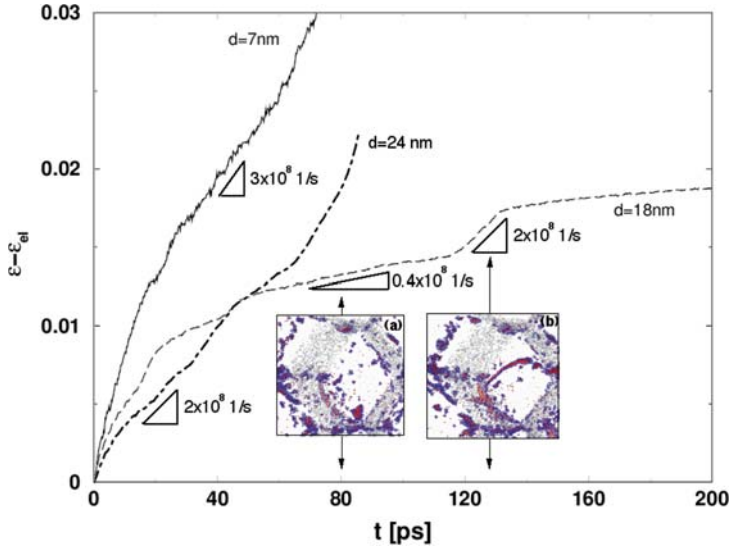

Fig. 7.11 Plastic strain *vs* time for four-grain, fully 3d Al microstructures with grain sizes of $d = 7$, 18 and 24 nm. The strain rates indicated in several regions are given in units of 10^8 s^{-1}. The two insets (a) and (b) represent enlarged snapshots of the grain in the upper left corner in Fig. 7.10 (c) taken at (a) $t = 70$ ps and (b) $t = 110$ ps [26].

decreases, and (ii) $\dot{\varepsilon}$ increases again as the grain size decreases further to $d=7$ nm. Remarkably, although the deformation mechanism for $d=7$ nm involves only GB processes (see Fig. 7.10 (d)), the average strain rate obtained for this system exceeds even that obtained for the $d=24$ nm system (see Fig. 7.11).

The deformation behavior of the system with the intermediate grain size of 18 nm is particularly revealing. The discontinuities in the slope of $\varepsilon(t)$ for this system can be correlated directly with the underlying dislocation activity (illustrated in the two insets (a) and (b) in Fig. 7.11, representing enlarged snapshots of the grain in the upper left corner in Fig. 7.10 (b) taken, respectively, at $t=70$ and 110 ps). Most importantly, the sudden, approximately five-fold increase in the strain rate occurring at about $t=105$ ps (from ~ 0.4 to $\sim 2.0\times10^8$ s^{-1}) is caused by the glide of a dislocation across the grain interior (see also Fig. 7.10 (b), taken at the same instant as inset (b) in Fig. 7.11). As soon as the dislocation has been annihilated in the surrounding GBs (at $t\approx 115$ ps), the strain rate decreases again. The same process is responsible for the "deformation bursts" occurring at the onset of plastic deformation and at $t\approx 25$–30 ps.

In the time intervals between these deformation bursts, no mobile dislocations exist in the structure (see inset (a) in Fig. 7.11). The strain *versus* time behavior, for example, between $t=30$ ps and $t=105$ ps is therefore completely determined by GB processes. This results in a much lower strain rate of $\sim 0.4\times10^8$ s^{-1}, compared to a rate of $\sim 2.0\times10^8$ s^{-1} during the deformation bursts. The much lower deformation rate associated with the GB processes indicates that the grain size of 18 nm is still too large to enable these GB processes to fully overcome the rapidly decreasing dislocation contribution to the strain rate with decreasing grain size. On the other hand, since the dislocation-slip process is no longer fully operational for the much smaller grain size of $d=7$ nm (see Fig. 7.10 (d)), the strain rate obtained for this system must be dominated by these GB processes (see Fig. 7.11).

The crossover in the mechanical behavior with decreasing grain size extracted from these simulations is summarized in Fig. 7.12 [26]. Although for the reasons discussed above, the $\varepsilon(t)$ curves exhibit large variations, Fig. 7.12 shows the *average* strain rates extracted from plots like those in Fig. 7.11 for all five grain sizes. The minimum near $d=18$ nm is clearly seen. This "strongest size" [16] of $d_c\sim 18$ nm for this simple Al model system is reached when the grains have become too small to nucleate complete dislocations, but are still too large for GB processes to dominate the deformation.

In qualitative agreement with all previous simulations, in the inverse Hall–Petch regime (see Section 7.3), the strain rate for $d=7$ nm (ranging between $\sim 3.0\times10^8$ s^{-1} and $\sim 4.4\times10^8$ s^{-1}; see Fig. 7.11) is considerably higher than that associated with the GB processes in the $d=18$ nm system (of $\sim 0.4\times10^8$ s^{-1}). A quantitative analysis of these results yields a ratio of the strain rate for $d=7$ nm to that from 30–105 ps for the $d=18$ nm system of between 2.1 and 2.6. Remarkably, this range of values is consistent with the mechanism of GB diffusion creep, for which Yamakov et al. [32] showed that $\dot{\varepsilon}\sim d^{-n}$, with $2<n\leq 3$ (see Sec-

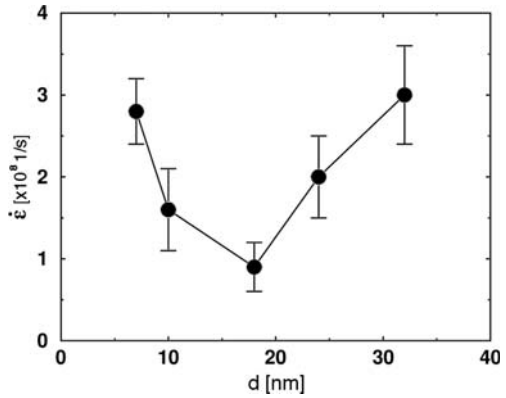

Fig. 7.12 Grain-size dependence of the overall strain rate for all the grain sizes studied. The minimum in the strain rate at $d = 18$ nm suggests the existence of a "strongest size" at which the grains have become too small to sustain the dislocation-slip process, but are still too large for GB processes to dominate the deformation [26].

tion 7.3.2). This analysis suggests that in Al, even at $T/T_m \approx 0.32$, the Coble-creep mechanism is, indeed, responsible for the observed grain-size softening in the inverse Hall–Petch regime.

The recent, very large simulations of Schiotz and Jacobsen [51] for nc Cu avoided some of the geometrical limitations of the simulation model used by Yamakov et al. discussed above. In particular, their model system incorporated a larger number of grains and a distribution in the grain size, the average size ranging between 5 and 50 nm. The crossover in the flow stress of nc Cu thus obtained [51] is in full qualitative agreement with the minimum in the average strain rate discussed above. Interestingly, although the stacking-fault energy of Cu is only about one third of that of Al, a comparison with the Al simulations reveals rather similar grain sizes where the crossover from Hall–Petch to inverse Hall–Petch behavior occurs in the two materials ($d_c \sim 14$ nm for Cu [51] and $d_c \sim 18$ nm for Al [26]). As in the study of Yamakov et al. [26], this crossover in the mechanical behavior was found to be correlated with a transition in the dominating deformation mechanism [51].

While for the smallest grain sizes, Schiotz and Jacobsen [51] identified GB sliding as the dominant deformation mode, they also found that with increasing grain size the dislocation activity increases significantly. Also, as in the study of Yamakov et al., starting at 2.5–3% plastic strain dislocations were seen to nucleate from the GBs; these were mostly partial dislocations, although in some of the larger grains several perfect extended dislocations, split into partials, were also observed. Noting that Cu has a lower SFE than Al (which decreases the energy penalty associated with the formation of a stacking fault and thus favors partial-dislocation slip over perfect-dislocation slip at grain sizes below ~ 50 nm), these observations are consistent with the earlier Al simulations [26]. Remarkably, in one particularly large simulation Schiotz and Jacobsen were able to

reach a 10% plastic strain for a grain size of 50 nm. These simulations revealed deformation twins in a grain-size, plastic-strain and strain-rate regime that is very close to that probed in the columnar Al microstructures [23], in which extensive deformation twinning was also observed (see Section 7.2.3). However, whereas the columnar simulations for a grain size of 100 nm suggested pile-ups against twin networks as the cause for the Hall–Petch hardening effect [48], for their largest grain sizes Schiotz and Jacobsen observed dislocation pile-ups against the GBs, suggesting that even in a nanocrystalline material such pile-ups can be responsible for the observed hardening.

7.4.3 Effect of the Stacking-fault Energy

Although the above comparison between Al and Cu seems to imply that the crossover grain size, d_c, may not depend very strongly on the material, the discussion in Section 7.2.2 has suggested that the value of d_c should be governed by the competition between the two length scales defined by the dislocation splitting distance r (see Eq. (7.1)) and the grain size d. Also, since the splitting distance depends on the level of applied stress, the latter should also affect the value of d_c.

By comparing the deformation behavior of Al with that of a low-SFE material with an identical microstructure and grain size, Yamakov et al. [86] eliminated any of the topological differences between the Al and Cu microstructures considered in [26] and [51], respectively. As representative for a low-SFE metal, they considered a hypothetical material, "low-SFE Pd", described by the EAM potential of Foiles et al. [87] for Pd. This potential, fitted to bulk properties of Pd, yields the very low SFE of only 8 mJ/m^2. Although this value does not compare well at all to the experimental value of $\sim$180 mJ/m^2 [88], the potential can be used to compare the deformation behavior of a hypothetical low-SFE model material with that of Al(high-SFE) described by the Ercolessi and Adams's EAM potential [38]; with a SFE of 122 mJ/m^2, the latter is representative of a high-SFE metal.

These simulations revealed a very strong influence of the SFE on the deformation process. As seen in Figs. 7.13 (a) and (b) obtained for a grain size of 24 nm, already after only 1% plastic strain the difference in the SFE has produced very different dislocation patterns in the two systems. The Al(high-SFE) system shown in (a) exhibits a series of loops of perfect dislocations propagating through the grain interiors. By contrast, in the Pd(low-SFE) system shown in (b), the grain interiors are transected by a number of stacking-fault planes lying on several slip systems.

Figure 7.14 shows the plastic strains *versus* time obtained for the two model materials after subtracting the appropriate elastic strains. Remarkably, although initially (i.e. up to a plastic strain of $\sim$0.4%) the two materials behave quite similarly, for the larger strains the two systems evolve qualitatively rather differently. Following a steady-state deformation regime, after $\sim$1% plastic strain the

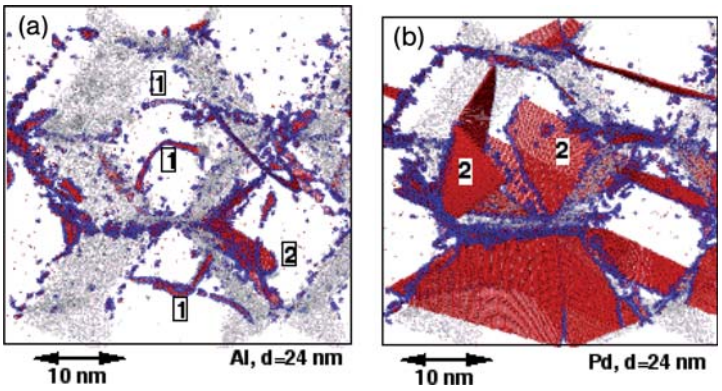

Fig. 7.13 Comparison of the deformation behaviors of (a) Al (with a SFE of 122 mJ/m^2) and (b) a hypothetical low-SFE material, called low-SFE Pd, with a SFE of 8 mJ/m^2. The snapshots were taken after 1.0% plastic straining for a grain size of 24 nm. To ensure similar deformation conditions, each system was loaded under uniform tensile stress approximately 0.1 GPa above its dislocation-nucleation threshold stress for this grain size [86].

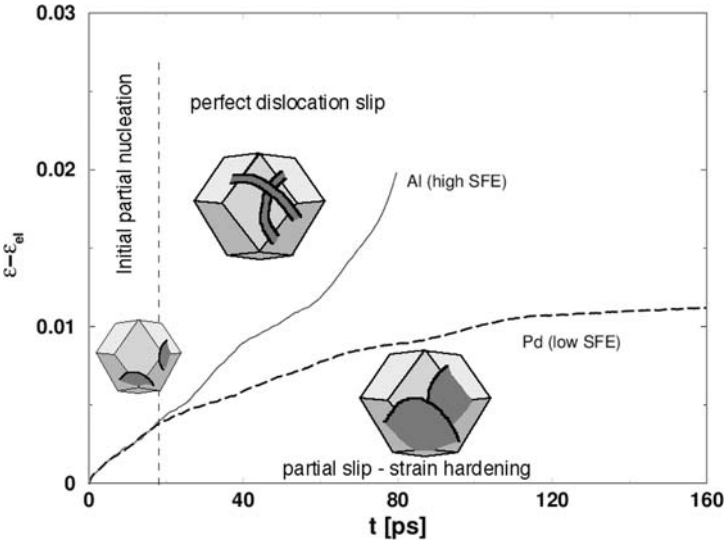

Fig. 7.14 Comparison of the plastic strain *vs* time behavior of Al and low-SFE Pd for a grain size of 24 nm [86].

strain rate in the Al(high-SFE) system is approximately constant; by contrast, after a much smaller steady-state regime, the strain in the Pd(low-SFE) system *decreases* steadily. In each material the plastic deformation starts at the moment when the first partial dislocations are nucleated from the GBs (labeled the "initial partial nucleation" regime in Fig. 7.14). (We note that, so as to create similar

deformation conditions, for each case the stress level was chosen ~ 0.1 GPa above the respective nucleation-threshold stress; [86]; the rather similar initial strain rates in Fig. 7.14 are therefore to be expected.)

The different behaviors of the two materials seen in Fig. 7.14 can be understood in terms of the Orowan equation [89],

$$\dot{\varepsilon} = ab\rho(\sigma)v(\sigma) \tag{7.6}$$

where a is a geometrical factor relating the active slip system to the shear-strain direction. $\rho(\sigma)$ is the concentration of mobile dislocations, which depends on the nucleation rate and, hence, the stress, σ, $v(\sigma)$ is the velocity of the dislocation, which is also a function of σ. According to Eq. (7.6), equal strain rates will be reached at a given stress when the product $\rho(\sigma)v(\sigma)$ is the same in the two systems.

Up to about 0.4% plastic strain, both systems nucleate only partial dislocations propagating with about equal velocity into the grain interiors, giving rise to rather similar strain rates. At this point the two curves in Fig. 7.14 start to diverge. The Al(high-SFE) system is able to emit second partials that terminate these stacking faults to form complete, perfect dislocations (see Fig. 7.13 (a)). As a result of many dislocation nucleation/absorption events, the GBs become more and more rough (see also Ref. [23]); this roughness increases the nucleation rate and leads to a continuously increasing strain rate (see the "perfect dislocation slip" regime in Fig. 7.14). At the same time, in the low-SFE system the second partials do not appear because, for equal stacking-fault lengths, the system energy has increased less than in the high-SFE material. Instead, the stacking faults continue to extend via the glide of the single partial dislocations. Quickly, some of these transect the entire grain interior and, inevitably, block the propagation of any later formed stacking faults (see Fig. 7.13 (b)). The inability of the low-SFE metal to produce perfect dislocations consequently leads to strain hardening, as evidenced by a continuously decreasing strain rate (see the "partial slip" regime in Fig. 7.14).

This situation, in which $d < r$, is similar to that in a high-SFE metal with a very small grain size (compare Fig. 7.13 (b) with Fig. 7.10 (d)). However, an important difference between the two materials arises from the strong d^{-3} grain-size dependence of the competing GB-based deformation process (See Section 7.3.2). Whereas in the high-SFE metal the small grain size enables the GB-mediated deformation process to dominate, the larger grain size in the low-SFE metal favors the partial-dislocation-slip process. Thus in low-SFE metals the transition from dislocation-based to GB-based deformation with decreasing grain size is more complex as these materials first undergo a transition from perfect to partial slip. As was noted by Yip [90], the existence of the partial-slip region would push the normal Hall–Petch hardening further down towards smaller grain sizes, as the partial slip produces strain hardening, as seen in the MD simulations [86]. This reasoning suggests that lowering the SFE would result in a decrease of d_c. Indeed, a comparison of the MD simulations for Al [26]

(yielding a value of $d_c = 18$ nm) with those for Cu [20] (with a SFE that is lower than that for Al, yielding a value of $d_c = 14$ nm) and with bubble-raft experiments (presumably with a very low or zero SFE, yielding a value of $d_c = 7$ nm) [91] seems to support this view [90].

These observations can be captured in a novel deformation-mechanism map based on the knowledge of dislocation nucleation and dislocation structure in nanocrystalline fcc metals [86]. The underlying physics for this map arises from the length-scale competition between the grain size, d, and the splitting distance, r (see Eq. (7.1)), and from the grain-size dependence of the dislocation nucleation stress from a source at the GB proposed by Cheng et al. [83] (see Eq. (7.5)). In this way, the map connects the mechanical properties of nanocrystalline fcc metals with the structure and physics of the dislocations present in the deformation process. Based on Eq. (7.1) the map is expressed in coordinates of reduced stress, σ/σ_∞, and reduced inverse grain size, r_0/d. In contrast to the use of b and G that normalize the variables d and σ in the phenomenological constitutive equations on which the prevalent deformation maps are built [92–95], r_0 (the equilibrium splitting distance at zero stress) and σ_∞ (the stress at which the splitting distance becomes infinite) are material-defining parameters in this novel map. (For more details, see Ref. [86]).

According to this map the "strongest size", d_c, may arise from two different scenarios for high- and low-SFE metals or at low and high stress. For high-SFE metals Region II involves very high stress and the crossover from normal to inverse Hall–Petch behavior should be governed mainly by the transition from perfect slip to GB-mediated deformation, that is, the $1/d$ line between Region I and III. By contrast, for low-SFE metals or under high-stress conditions, the transition involves partial slip in Region II as an intermediate stage; however, the influence of the partial slip on d_c is still not very clear. For example, Yip [90] suggested that the resulting strain hardening during partial slip may push the normal Hall–Petch behavior down to smaller grain sizes. Another consideration may be that because of the intragrain hardening, the GB processes may become dominant at larger grain sizes in the partial-slip than in the perfect-slip regime.

Swygenhoven et al. [96] suggested that both the stable and unstable stacking-fault energies are required for predicting whether the deformation proceeds via partial- or perfect-dislocation slip. While the stable SFE gives the excess energy of the SF once it is formed, the difference between the stable and unstable SFE defines the energy barrier that has to be overcome to generate the trailing partial dislocation to end the SF and to form a perfect dislocation. It was argued that the higher ratio between the unstable and the stable SFE in Ni compared to Al may suppress the nucleation of a trailing partial, thus explaining the failure of the MD simulations to observe perfect dislocations in nc Ni [96]. While valid, this argument serves mostly to explain a simulation result performed under extremely high strain rates under which the kinetics of dislocation nucleation from the GBs may be different from that based on the equilibrium energy balance. By contrast, the deformation mechanism map proposed by Yamakov et al. [86] aims to capture the nucleation process under quasistatic conditions.

7.5 Discussion and Conclusions

Only a decade ago, deformation simulations of the kind reviewed above were virtually unthinkable. These simulations have now advanced far enough where they have begun not only to elucidate the structural differences between nanocrystalline and coarse-grained materials but also to capture the grain-size-dependent mechanical behavior of nanocrystalline fcc metals. These simulations suggest the following four-stage scenario for the room-temperature mechanical behavior.

(a) For the largest (submicrometer) grain sizes, the GBs act as dislocation sources for the nucleation of complete, extended dislocations that subsequently glide across the grains where they become reincorporated into the GB structure. Other than for the inability of Frank–Read sources to operate within such small grains, the material therefore still seems to deform by the conventional dislocation-slip mechanism, including for example dislocation-dislocation reactions (such as Lomer–Cottrell lock formation) and cross-slip, two processes well known from the study of coarse-grained materials and single-crystal plasticity.

(b) As the grain size decreases well below 100 nm, the deformation behavior changes fundamentally, as evidenced by the observation of deformation twinning in a high stacking-fault-energy material like Al. Remarkably, this critical prediction from the MD simulations has recently been validated experimentally, including observation of all three twinning mechanisms identified in the simulations. Whether or not in this regime the yield-stress increase with decreasing grain size, indeed, follows the $\sigma \sim d^{-1/2}$ Hall–Petch relation has not yet been determined by simulation. However, the simulations have begun to capture two possible hardening mechanisms, including dislocation pile-ups against the GBs and pile-ups against complex networks formed by deformation twins, dislocations and extended stacking faults.

(c) As the grain size becomes even smaller and comparable to the size of the extended dislocations (which depends not only on the stacking-fault energy but also the applied stress; see Eq. (7.1)), complete-dislocation slip seems to be gradually replaced by partial-dislocation slip. This important prediction from simulations of nc Al has also been verified by experiment.

(d) The transition from complete- to partial-dislocation slip is accompanied by a rapid increase with decreasing grain size in the stress required to nucleate dislocations from the GBs. The overall dislocation activity and its effectiveness in producing strain decreases rapidly until, eventually, a GB-based deformation process takes over. The simulations reveal that this crossover in the dominating deformation mechanism gives rise to a maximum in the yield stress at the "strongest grain size" d_c. Although the simulations appear to disagree as to the exact nature of the dominating deformation mechanism for $d < d_c$ (i.e. GB sliding *vs* GB diffusion), it seems that the two mechanisms can be reconciled as originating from one and the same deformation process, namely Coble creep (i.e. GB-diffusion-induced grain elongation accommodated by Lifshitz sliding).

In spite of the well-known limitations of the MD approach, such simulations enable the study of well-characterized, albeit still idealized, model systems and can thus provide insights not readily obtainable from experiments. Nevertheless, a number of important differences in the deformation behavior between coarse-grained and nanocrystalline metals predicted by MD simulation seem to be borne out by experimental observations. Furthermore, one of the early findings of the MD simulations, that is, that the atomic structures of the highly constrained GBs in nanocrystalline materials do not really differ fundamentally from those of entirely unconstrained high-energy bicrystalline GBs, is also supported by experimental observations. Also consistent with the MD simulations, a significant number of nanocrystalline materials reveal adequate plasticity in experiments where diffusional processes, including GB sliding, dominate. However, we see the strength of these simulations less in their ability to one day mimic the "real material" but in their ability to probe the behavior of carefully designed, fully characterized and progressively more complex model systems. This, we believe, will enable gradual deconvolution of the complex interplay among various deformation and microstructural processes in well-defined model systems, something that has proven difficult to achieve in experiments.

Acknowledgements

This work is supported by the US Department of Energy, BES-Materials Science under contract W-31-109-Eng-38. V. Yamakov is sponsored through cooperative agreement NCC-1-02043 with the National Institute of Aerospace.

References

1 H. Gleiter **2000**, *Acta Mater.* 48, 1.
2 C. C. Koch, C. Suryanarayana **2000**, in *Microstructure and Properties of Mater.*, J. C. M. Li (ed.) World Scientific Publishing, Singapore, p 380.
3 J. Karch, R. Birringer, R. H. Gleiter **1987**, *Nature* 330, 556.
4 S. X. McFadden, R. S. Mishra, R. Z. Valiev, A. P. Zhilyaev, A. K. Mukherjee **1999**, *Nature* 398, 684.
5 B. N. Kim, K. Hiraga, K. Morita, Y. Sakka **2001**, *Nature* 413, 288.
6 T. G. Nieh, J. Wadsworth **1991**, *Scr. Metall.* 25, 955.
7 R. W. Siegel **1997**, *Mater. Sci. Forum* 235–238, 851.
8 A. H. Chokshi, A. Rosen, J. Karch, H. Gleiter **1989**, *Scr. Metall.* 23, 1679.
9 V. Y. Gertsman, M. Hoffmann, H. Gleiter, R. Birringer **1994**, *Acta Metall. Mater.* 42, 3539.
10 U. Erb, G. Palumbo, R. Zugic, K. T. Aust **1996**, in *Processing and Properties of Nanocrystalline Materials*, C. Suryanarama, et al. (eds.), TMS: Warrendale, PA, p 96.
11 R. A. Masamura, P. M. Hazzledine, C. S. Pande **1998**, *Acta Mater.* 46, 4527.
12 H. Alves, M. Ferreira, U. Koster, B. Muller **1996**, *Mater. Sci. Forum* 225–227, 769.
13 G. E. Fougere, J. R. Weertman, R. W. Siegel, S. Kim **1992**, *Scr. Metall. Mater.* 26, 1879.
14 G. McMahon, U. Erb **1989**, *Microstruct. Sci.* 17, 447.
15 R. O. Scattergood, C. C. Koch **1992**, *Scr. Metall.* 27, 1195.

16 S. Yip **1998**, *Nature* 391, 532.
17 S. R. Phillpot, D. Wolf, H. Gleiter **1995**, *J. Appl. Phys.* 78, 847.
18 S. R. Phillpot, D. Wolf, H. Gleiter **1995**, *Scr. Metall. Mater.* 33, 1245.
19 K. S. Kumar, H. V. Swygenhoven, S. Suresh **2003**, *Acta Mater.* 51, 5743.
20 J. Schiotz, F. D. DiTolla, K. Jacobsen **1998**, *Nature* 391, 561.
21 H. V. Swygenhoven, A. Caro **1997**, *Appl. Phys. Lett.* 71, 1652.
22 V. Yamakov, D. Wolf, M. Salazar, S. R. Phillpot, H. Gleiter **2001**, *Acta Mater.* 49, 2713.
23 V. Yamakov, D. Wolf, S. R. Phillpot, A. K. Mukherjee, H. Gleiter **2002**, *Nature Mater.* 1, 45.
24 M. Chen, E. Ma, K. J. Hemker, H. Sheng, Y. Wang, X. Cheng **2003**, *Science* 300, 1275.
25 J. B. Sorensen, J. Schiotz **2003**, *Science* 300, 1244.
26 V. Yamakov, D. Wolf, S. R. Phillpot, A. K. Mukherjee, H. Gleiter **2003**, *Philos. Mag. Lett.* 83, 385.
27 A. Hasnaoui, H. V. Swygenhoven, P. M. Derlet **2002**, *Phys. Rev. B* 66, 184112.
28 A. Hasnaoui, H. V. Swygenhoven, P. M. Derlet **2003**, *Science* 300, 1550.
29 M. S. Daw, S. M. Foiles, M. I. Baskes **1993**, *Mater. Sci. Rep.* 9, 251.
30 P. Keblinski, D. Wolf, H. Gleiter **1998**, *Interface Sci.* 6, 205.
31 R. L. Coble **1963**, *J. Appl. Phys.* 34, 1679.
32 V. Yamakov, D. Wolf, S. R. Phillpot, H. Gleiter **2002**, *Acta Mater.* 50, 61.
33 V. Yamakov, D. Wolf, S. R. Phillpot, H. Gleiter **2002**, *Acta Mater.* 50, 5005.
34 D. Wolf **2001**, in *The Encyclopedia of Materials Science and Engineering*, R. W. Cahn, (ed.) Pergamon Press, Oxford.
35 P. Keblinski, S. R. Phillpot, D. Wolf, H. Gleiter **1996**, *Phys. Rev. Lett.* 77, 2965.
36 P. Keblinski, S. R. Phillpot, D. Wolf, H. Gleiter **1997**, *J. Am. Ceram. Soc.* 80, 717.
37 P. Keblinski, S. R. Phillpot, D. Wolf, H. Gleiter **1997**, *Acta Mater.* 45, 987.
38 F. Ercolessi, J. B. Adams **1994**, *Europhys. Lett.* 26, 583.
39 J. R. Noonan, H. L. Davis **1984**, *Phys. Rev. B* 29, 4349.
40 J. P. Hirth, J. Lothe **1992**, *Theory of Dislocations*, Krieger Publishing Company, Malabar, FL.
41 J. Schiotz, T. Vegge, F. D. DiTolla, K. W. Jacobsen **1998**, *Phys. Rev. B* 60, 11971.
42 H. V. Swygenhoven, M. Spaczer, A. Caro **1999**, *Acta Mater.* 47, 3117.
43 H. V. Swygenhoven, M. Spaczer, A. Caro, D. Farkas **1999**, *Phys. Rev. B* 60, 22.
44 H. V. Swygenhoven **2002**, *Science* 296, 66.
45 S. J. Zhou, D. L. Preston, P. S. Lomdahl, D. M. Beazley **1998**, *Science* 279, 1525.
46 V. Bulatov, F. F. Abraham, L. Kubin, B. Devincre, S. Yip **1998**, *Nature* 391, 669.
47 J. Weertman, J. R. Weertman **1992**, *Elementary Dislocation Theory*, Oxford University Press, Oxford.
48 V. Yamakov, D. Wolf, S. R. Phillpot, H. Gleiter **2003**, *Acta Mater.* 51, 4135.
49 E. El-Danf, S. R. Kalindi, R. Doherty **1999**, *Met. Mater. Trans.* 30A, 1223.
50 T. Ungar, S. Ott, P. G. Sanders, A. Borbely, J. R. Weertman **1998**, *Acta Mater.* 46, 3693.
51 J. Schiotz, K.W. Jacobsen **2003**, *Science* 301, 1357.
52 E. M. Bringa, A. Caro, Y. Wang, M. Victoria, J. M. McNaney, B. A. Remington, R. F. Smith, B. R. Torralva, H. Van Swygenhoven **2005**, *Science* 309, 1838.
53 T. Shimokawa, A. Nakatani, H. Kitagawa **2005**, *Phys. Rev. B*. 71, 224110-1.
54 Y. T. Zhu, X. Z. Liao, S. G. Srinivasan, Y. H. Zhao, M. I. Baskes **2004**, *Appl. Phys. Lett.* 85, 5049.
55 Y. T. Zhu, T. G. Langdon **2005**, *Mater. Sci. Eng. A* 409, 234.
56 G. P. Zheng, Y. M. Wang, M. Li **2005**, *Acta Mater.* 53, 3893.
57 J. He, E. J. Lavernia **2001**, *J. Mater. Res.* 16, 2724.
58 J. He, K. H. Chung, X. Liao, Y. T. Zhu, E. J. Lavernia **2002**, *Met. Trans.* 33A, 1.
59 X. Z. Liao, J. Y. Huang, Y. T. Zhu, F. ZhouE. J. Lavernia **2003**, *Philos. Mag.* 83, 3065.
60 Y. Wang, M. Chen, F. Zhou, E. Ma **2002**, *Nature* 419, 912.
61 X. Liao, Y. Zhao, S. Srinivasan, Y. Zhu, R. Valiev, D. Gunderov **2004**, *Appl. Phys. Lett.* 84, 592.
62 K. Kumar, S. Suresh, M. Schisolm, J. Horton, P. Wang **2003**, *Acta Mater.* 51, 387.

63 H. Rosner, J. Markmann, J. Weissmuller **2004**, *Philos. Mag. Lett.* 84, 321.

64 X. Z. Liao, F. Zhou, E. J. Lavernia, S. G. Srinivasan, M. I. Baskes, D. W. He, Y. T. Zhu **2003**, *Appl. Phys. Lett.* 83, 632.

65 X. Z. Liao, Y. H. Zhao, Y. T. Zhu, R. Z. Valiev, D. V. Gunderov **2004**, *J. Appl. Phys.* 96, 636.

66 C. X. Huang, K. Wang, S. D. Wu, Z. F. Zhang, G. Y. Li, S. X. Li **2006**, *Acta Mater.* 54, 655.

67 X. Wu, Y. T. Zhu, M. W. Chen, E. Ma **2006**, *Scr. Mater.* 54, 1685.

68 H. V. Swygenhoven **2006**, *Mater. Sci. Forum* 503–504, 193.

69 Y. T. Zhu, X. Z. Liao, S. G. Srinivasan, E. J. Lavernia **2005**, *J. Appl. Phys.* 98, 034319.

70 H. V. Swygenhoven, A. Caro **1998**, *Phys. Rev. B* 58, 11246.

71 H. V. Swygenhoven, P. Derlet **2001**, *Phys. Rev. B* 64, 224105.

72 R. C. Gifkins **1976**, *Metall. Trans.* 7A, 1225.

73 P. Keblinski, D. Wolf, S. R. Phillpot, H. Gleiter **1999**, *Philos. Mag. A* 76, 2735.

74 R. Raj, M. F. Ashby **1971**, *Metall. Trans.* 2, 1113.

75 I. M. Lifshitz **1963**, *Soviet Phys. JETP* 17, 909.

76 T. G. Langdon **2000**, *Mater. Sci. Eng.* 283, 266.

77 D. G. Attwood, P. M. Hazzledine **1976**, *Metallography* 9, 483.

78 W. R. Cannon **1972**, *Philos. Mag.* 25, 1489.

79 W. A. Rachinger **1952**, *J. Inst. Met.* 81, 33.

80 M. F. Ashby, R. A. Verall **1973**, *Acta Metall.* 21, 49.

81 D. Moldovan, D. Wolf, S. R. Phillpot, A. K. Mukherjee, H. Gleiter **2003**, *Philos. Mag. Lett.* 83, 29.

82 J. C. M. Li **1963**, *Trans. Metall. Soc. AIME* 227, 239.

83 S. Cheng, J. A. Spencer, W. W. Milligan **2003**, *Acta Mater.* 51, 4505.

84 V. Bata, E. Pereloma **2004**, *Acta Mater.* 52, 657.

85 M. de Koning, W. Cai, V. Bulatov **2003**, *Phys. Rev. Lett.* 91, 025503.

86 V. Yamakov, D. Wolf, S. R. Phillpot, A. K. Mukherjee, H. Gleiter **2004**, *Nature Mater.* 3, 43.

87 S. M. Foiles, J. B. Adams **1986**, *Phys. Rev. B* 40, 5909.

88 I. L. Dillamore, R. E. Smallman **1965**, *Philos. Mag.* 12, 191.

89 E. Orowan **1940**, *Proc. Roy. Soc. (London)* 52, 8.

90 S. Yip **2004**, *Nature Mater.* 3, 11.

91 K. J. Van Vliet, S. Tsikata, S. Suresh **2003**, *Appl. Phys. Lett.* 83, 1441.

92 J. Weertman, J. R. Weertman **1965**, in *Physical Metallurgy*, J. W. Cahn (ed.), North-Holland, Amsterdam, p. 793.

93 A. K. Mukherjee, J. E. Bird, J. E. Dorn **1969**, *Trans. Am. Soc. Met.* 62, 155.

94 M. F. Ashby **1972**, *Acta Metall.* 80, 887.

95 H. J. Frost, M. F. Ashby **1982**, *Deformation-Mechanism Maps: The Plasticity and Creep of Metals and Ceramics*, Pergamon Press, Oxford.

96 H. Van Swygenhoven, P. M. Derlet, A. G. Froseth **2004**, *Nature Mater.* 3, 399.

Part Three
Processing

Bulk Nanostructured Materials. Edited by M. J. Zehetbauer and Y. T. Zhu

ISBN: 978-3-527-31524-6

8
ECAP: Processing Fundamentals and Recent Progresses

Zenji Horita

8.1
Principle of ECAP

Equal-channel angular pressing (ECAP) is a typical processing technique of severe plastic deformation (SPD), which is capable of imparting large plastic strain to polycrystalline materials. As illustrated in Fig. 8.1, a sample is pressed through a channel having an equal cross section but bending in a solid die [1]. Thus, shear strain is introduced when the sample passes at the bending point. Since the sample cross section remains unchanged at both entrance and exit channels, repetitive pressing is feasible. For the pass number of N, the total equivalent strain ε_N is given by the following equation with the two angles, Φ and Ψ which are the channel bending angle (internal angle) and the angle at the outer arc of curvature (outer angle) at the bending point [2].

$$\varepsilon_N = (N/\sqrt{3})[2\cot\{(\Phi/2) + (\Psi/2)\} + \Psi\mathrm{cosec}\{(\Phi/2) + (\Psi/2)\}] \tag{8.1}$$

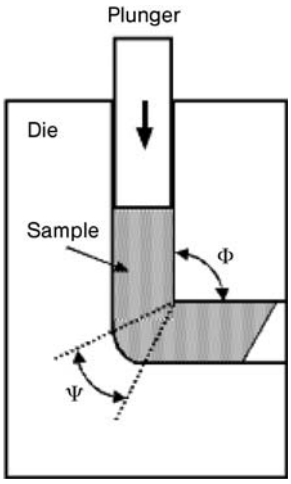

Fig. 8.1 Schematic illustration of ECAP facility showing angles of Φ and Ψ.

Bulk Nanostructured Materials. Edited by M. J. Zehetbauer and Y. T. Zhu

ISBN: 978-3-527-31524-6

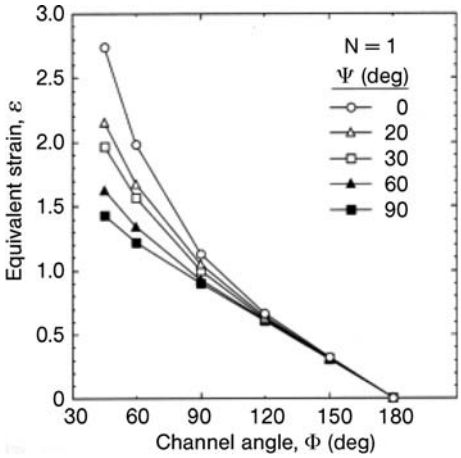

Fig. 8.2 Variation of equivalent strain, ε, with channel internal angle, Φ, for outer angles of Ψ: the strains are shown for a single pass with $N=1$.

Figure 8.2 shows the equivalent strain after a single passage through the die, ε_1 ($N=1$), calculated as a function of Φ for several different angles of Ψ [3]. The strain is determined mainly with Φ for up to $\Phi = 90^\circ$ irrespective of the angles of Ψ and the effect of Ψ becomes significant when Φ is smaller than 90°. The strain given by Eq. (8.1) is theoretical and it may be released if heat generation occurs or it may be increased if the friction between the sample and the channel wall creates additional strain.

8.2 Shearing Characteristic

When repetitive pressing is performed, the sample may be rotated between the two consecutive pressings around the longitudinal axis [4]. This rotation then activates different shearing systems and there may be four distinct processing routes. These routes are designated route A, route B_A, route B_C and route C as illustrated in Fig. 8.3 [5]. In route A, the sample is pressed without rotation, in route B the sample is rotated by 90° between each pressing with the rotation occurring either in alternative directions in route B_A or in the same direction in route B_C, and in route C the sample is rotated by 180° between each pressing. The influence of these pressing routes may be elucidated by considering the change in a cube element through a channel having angles of $\Phi = 90^\circ$ and $\Psi = 0^\circ$. The first pass deforms the cube element into a rhombohedral element as illustrated in Fig. 8.4 [6]. The three inserts in Fig. 8.4 show the elements after deformation and the associated shearing planes on the *X*, *Y*, and *Z* planes. The further changes in the corresponding elements on the *X*, *Y*, and *Z* planes are illustrated in Fig. 8.5 for up to a total of eight pressings in the four processing routes [5]. Thus, route A leads to increasing distortions in the *X* and *Y* planes but no deformation in the *Z* plane, route B_A leads to increasing distortions on

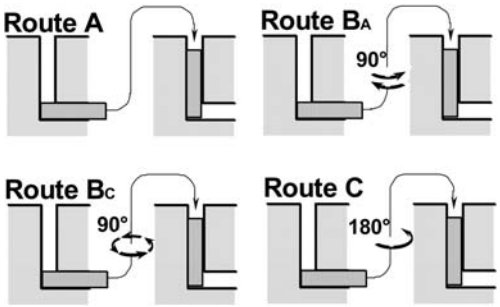

Fig. 8.3 Schematic illustration of four processing routes.

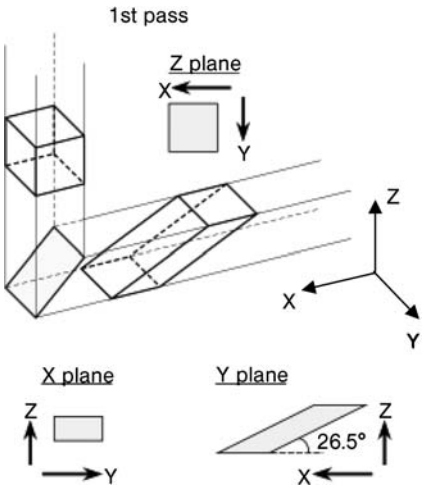

Fig. 8.4 Shearing associated with single passage through die.

all three orthogonal planes, and in route B_C and C the cubic element is restored every four and two pressings, respectively. However, there is a clear difference between routes B_C and C: route B_C includes deformation on all three orthogonal planes, whereas route C has no deformation on the *Z* plane.

8.3 Microstructural Evolution

Transmission electron microscopy (TEM) observations have shown that for small numbers of pressings, microstructures consist of grains with elongated structures having low-angle boundaries for any routes. An equiaxed grain structure with high-angle grain boundaries tends to be developed more expeditiously through route B_C than other routes: for instance, an equiaxed grain size of $\sim$1.3 μm is achieved in pure Al (99.99%) after four pressings through route B_C as shown in Fig. 8.6, but elongated structures with low-angle boundaries are retained for the other routes even after further numbers of pressings [7, 8]. This

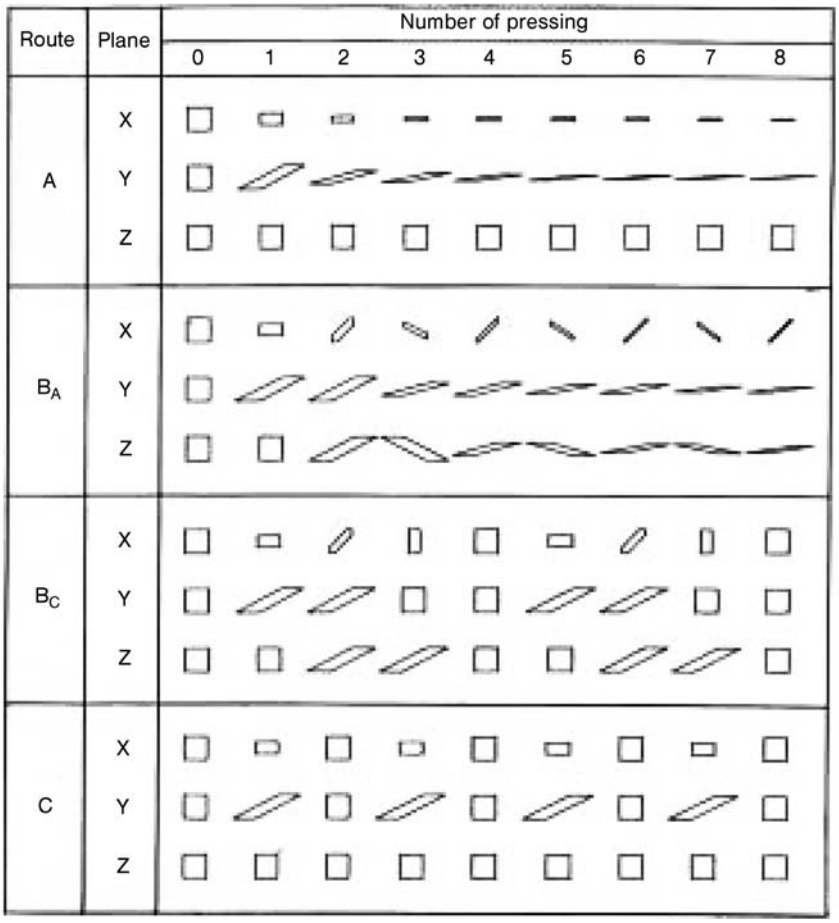

Fig. 8.5 Shearing characteristics for four processing routes.

observation is also confirmed with crystal orientation image analysis using electron backscatter diffraction (EBSD) [9]. An important conclusion deduced from the use of route B_C is that large strain should be introduced from different orientations to obtain a fine-grained structure having high-angle boundaries.

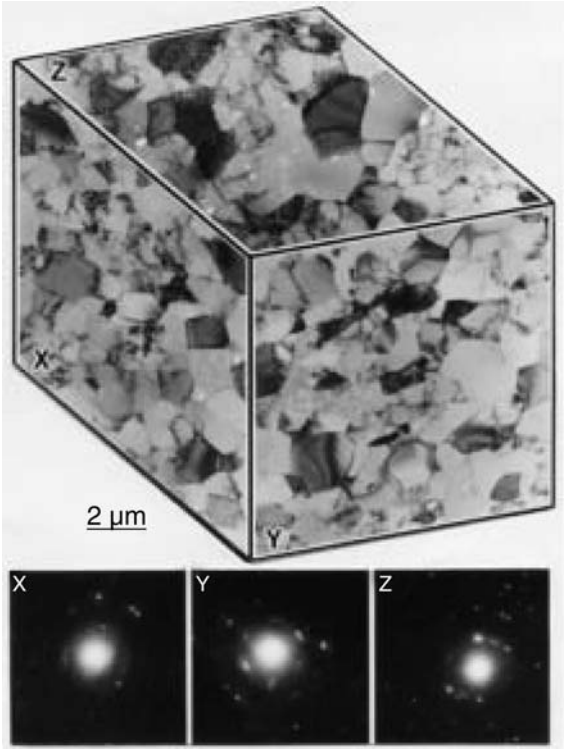

Fig. 8.6 Microstructures and SAED patterns in pure (99.99%) Al after ECAP for 4 passes through route B_C.

8.4 Effect of Channel Angles on Microstructures

8.4.1 The Effect of Φ

Figures 8.7 (a) to (d) show transmission electron micrographs of pure (99.99%) Al together with selected-area electron diffraction (SAED) patterns after processing with ECAP dies having four different internal angles as $\Phi = 90^\circ$, 112.5°, 135°, and 157.5° [10]. Route B_C is used because this route is most expeditious in producing fine-grained structures having high-angle grain boundaries as described in Section 8.3. It is noted that, as Φ is increased, less strain is introduced in the sample. Therefore, a comparison is made in Fig. 8.7 at an equivalent strain of ~ 4 for all dies by selecting the appropriate total numbers of pressings: 6 passes for $\Phi = 112.5^\circ$, 9 passes for $\Phi = 135^\circ$, and 19 passes for $\Phi = 157.5^\circ$. The microstructures are observed on the plane perpendicular to the longitudinal axis. Whereas the diffraction spots in the SAED patterns in Fig. 8.7 tend to form rings for $\Phi = 90^\circ$ and 112.5°, those for $\Phi = 135^\circ$, 157.5° exhibit

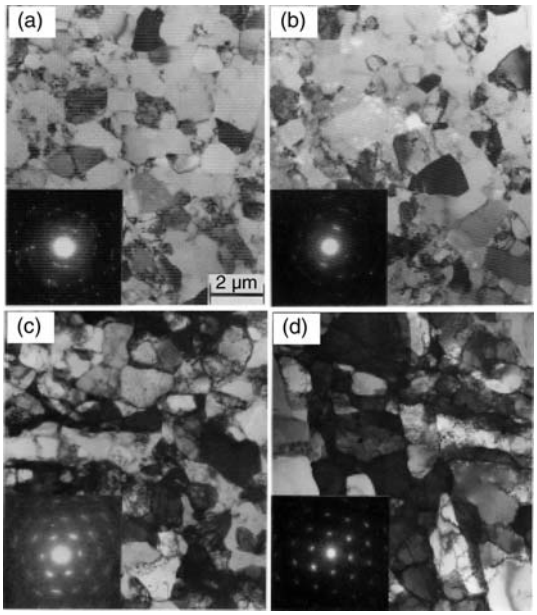

Fig. 8.7 Microstructures and SAED patterns in pure (99.99%) Al after ECAP to strain of ~4 using dies with four different channel angles: (a) $\Phi = 90$, (b) $\Phi = 112.5^\circ$, (c) $\Phi = 135^\circ$ and (d) $\Phi = 157.5^\circ$.

well-defined net patterns. It is noted that the SAED patters were taken from an area of 12.3 μm, which is the same size as in Fig. 8.6. It is concluded from these observations that the microstructure tends to consist of subgrains with low-angle grain boundaries when the channel angle is increased. It is then necessary to use a die having an internal channel angle of $\Phi = 90^\circ$ in order to produce fine-grained structure. The use of a die having $\Phi = 60^\circ$ with $\Psi = 30^\circ$ showed that there is no overall change in microstructure except that the grain size is slightly decreased [3].

8.4.2 The Effect of Ψ

Figure 8.8 shows optical micrographs after 1 pass and 4 passes with angles of $\Psi = 0^\circ$ and $= 90^\circ$ [11]. The micrographs were taken on the Y plane from the top edge to the bottom edge of the pressed sample. For the sample after 1 pass with an angle of $\Psi = 0^\circ$, most of the grains are equally elongated to the direction with an angle of $\sim 30^\circ$ from the longitudinal axis (X axis) except for those grains located at the very top and bottom parts of the section where the grain elongation is more intense and the elongated direction becomes almost parallel to the longitudinal axis. It is considered that the intense elongation of the

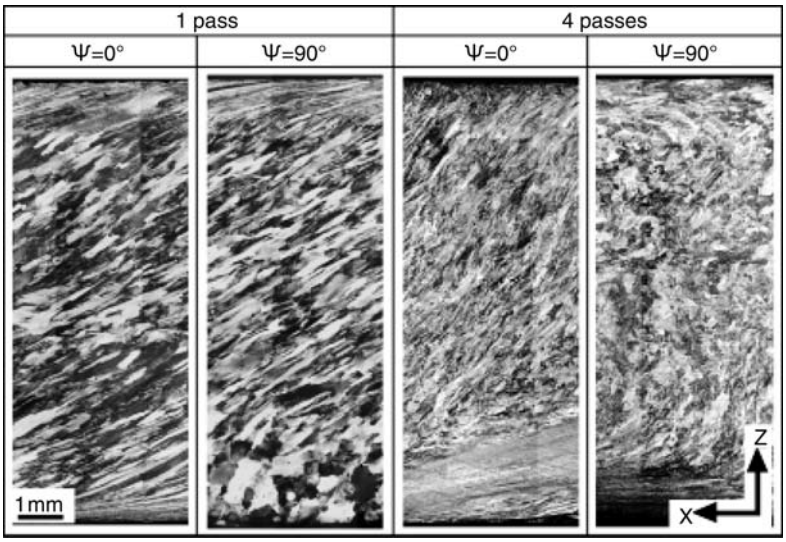

Fig. 8.8 Optical micrographs in pure (99.99%) Al after ECAP for 1 pass and 4 passes with outer angles of $\Psi = 0^\circ$ and $\Psi = 90^\circ$.

grains at the top and bottom parts is due to the friction between the sample and the channel wall. The sample after 1 pass with the angle of $\Psi = 90^\circ$ contains an area consisting of equiaxed grains at the lower part of the section. Although the other features are essentially the same, this is a major difference when compared with the microstructure formed with $\Psi = 0^\circ$. The microstructures after 4 passes with $\Psi = 0^\circ$ and $\Psi = 90^\circ$ look complicated and it is no longer possible to identify individual grains. Except at the lower parts of the sections, there appears to be a unidirectional right-upwards flow of the structure for the sample processed with $\Psi = 0^\circ$ but no such flow exists for the sample processed with $\Psi = 90^\circ$.

8.5 Pressing Speed

Microstructures after pressing with speeds of $\sim 8.5 \times 10^{-3}$ mm/s and ~ 7.6 mm/s are shown in Fig. 8.9 together with SAED patterns taken from an area of 12.3 μm [12]. Here, samples of pure (99.99%) Al were pressed with a die having a channel angle of $\Phi = 90^\circ$ to a total equivalent strain of ~ 4 (4 passes) through route B_C. Comparison shows that there is little difference in both the fine-grained structures and the appearance of the SAED patters. The average grain sizes for both structures were measured to be ~ 1.3 μm. However, close observation of the microstructures reveals that there are more extrinsic dislocations both within the grain interior and in the grain boundaries after pressing at the faster speed. This sug-

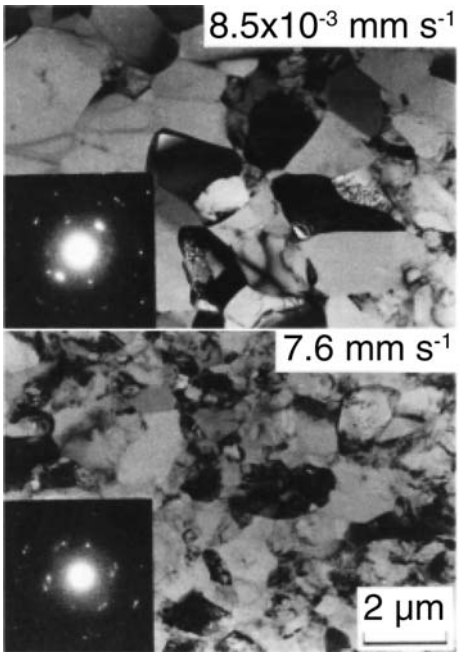

Fig. 8.9 Microstructures and SAED patterns in pure (99.99%) Al after ECAP for 4 passes at two different pressing speeds.

gests that recovery occurs more easily at the slower speed and the corresponding microstructures are in an equilibrated condition.

8.6 ECAP Temperature

ECAP was operated at elevated temperatures to examine the effect of pressing temperature on the microstructural evolution. Samples of pure (99.99%) Al were pressed at temperatures of 373, 473, and 573 K using a die having a channel angle of $\Phi = 90^\circ$. All samples were subjected to 6 pressings through route B_C. Figure 8.10 shows the microstructres and the associated SAED patterns taken from the samples pressed at the corresponding temperatures [13]. The ECAP at 373 K yielded an equiaxed grain structure containing high-angle grain boundaries. This structure is essentially similar to that for room-temperature pressing, although there is a slight increase in the averaging grain size: $\sim$1.5 μm for the 373 K pressing in comparison with $\sim$1.3 μm for the room-temperature pressing. The grain structures produced by ECAP at 473 K and 573 K are also equiaxed but the SAED analysis exhibits net patterns. These microstructural observations reveal that subgrain structures are developed during ECAP of pure (99.99%) Al at temperatures of 473 K or higher. The grain size or the subgrain size is plotted in Fig. 8.11 against the ECAP temperature including for the room-temperature pressing [14]. Figure 8.11 also plots the 0.2% proof

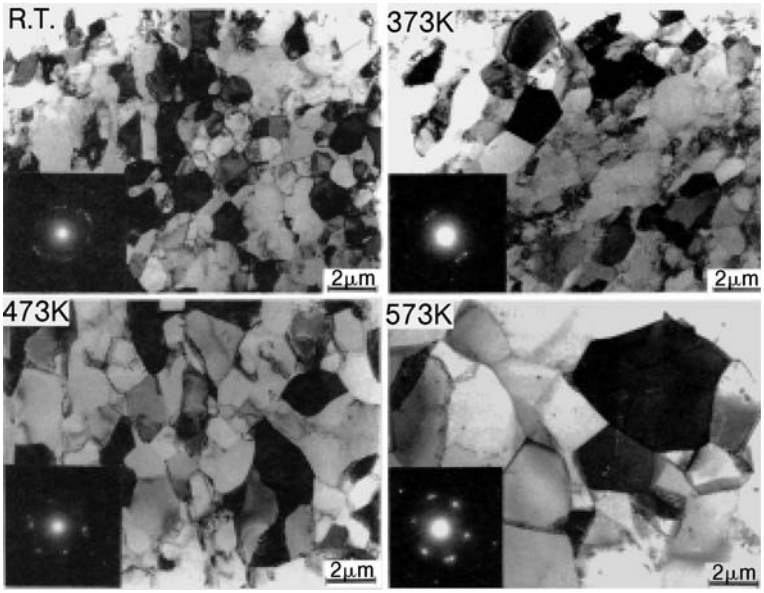

Fig. 8.10 Microstructures and SAED patterns in pure (99.99%) Al after ECAP at four different temperatures.

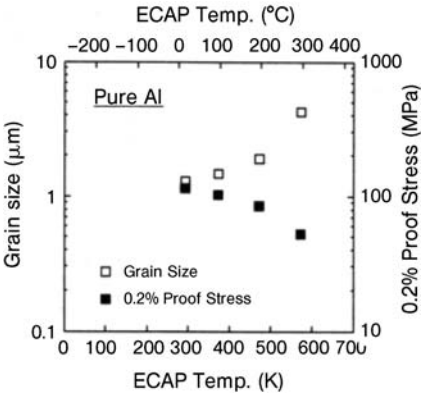

Fig. 8.11 Grain size and 0.2% proof stress with respect to ECAP temperature.

stress that was obtained by compression testing at room temperature with an initial strain rate of $3.3\times10^{-4}\ s^{-1}$. The grain size increases with an increase in ECAP pressing temperature and this trend is opposite to that for the 0.2% proof stress. It is noted that an addition of 3%Mg to pure Al increases the temperature where the subgrain structure develops during ECAP [13]. Further addition of 0.2%Sc to the Al-3%Mg alloy yielded microstructures that consist of fine grains having high-angle grain boundaries [13].

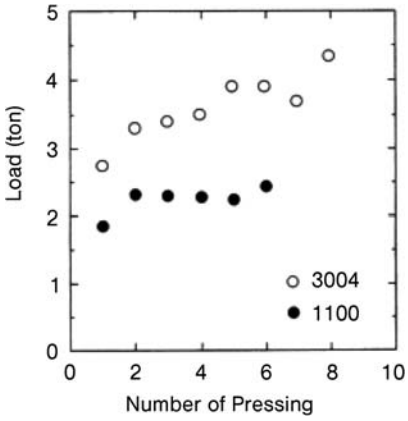

Fig. 8.12 Load variation with respect to number of ECAP pass.

8.7
Applied Load

The applied load required for ECAP pressing was measured for fully annealed Al-1100 and Al-3004 alloys. The maximum applied load is plotted against the number of pressings in Fig. 8.12 [15]. For such load measurements, samples with a diameter of 10 mm were used. The measurements show that maximum loads of 1.9 and 2.8 tons are required for the first pressing of the annealed Al-1100 and Al-3004 alloys, respectively. For the second pressings, slightly larger loads are required for both alloys. The applied load is then almost invariant with further pressings in the Al-1100 alloy but gradually increases up to 4.4 tons in the Al-3004 alloy. These trends are similar to those of the tensile strength examined with respect to the number of pressings [16].

The applied load was also measured for a sample of the Al-1100 alloy having a diameter of 40 mm. It was found that a maximum load of 31.5 tons is required for the first pressing of the fully annealed Al-1100 alloy. When compared with the load of 1.9 tons required for the first pressing of the fully annealed Al-1100 sample having the 10 mm diameter, it follows that the increase in the load is $\sim$16 times. This extent of the load increase is consistent with the increase in the cross section of the sample. It is concluded that, with use of an appropriate lubricant, the maximum load required for ECAP is determined by the sample strength.

8.8
Temperaturere Measurement during ECAP

For a measurement of the sample temperature during ECAP, a hole was drilled parallel to the longitudinal axis of the sample and thermocouple was placed directly at the bottom of the hole. The temperature was continuously monitored during ECAP.

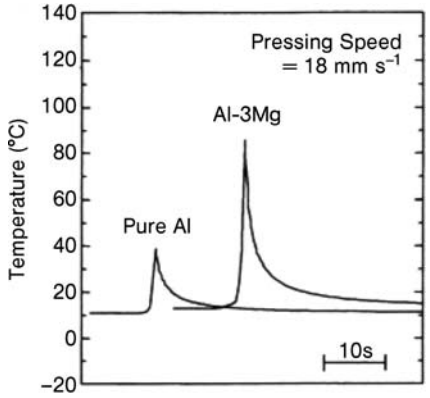

Fig. 8.13 Temperature change during ECAP for pure (99.99%) Al and Al-3%Mg alloy at a pressing speed of 18 mm/s.

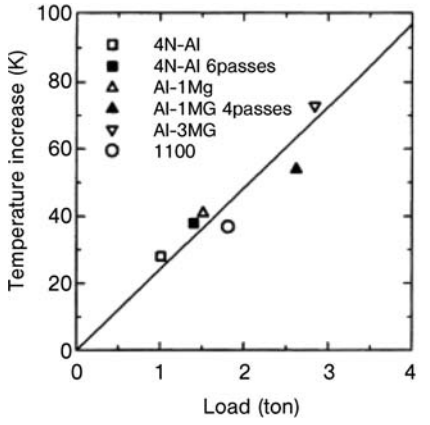

Fig. 8.14 Temperature increase with applied load during ECAP for different materials and conditions.

Figure 8.13 shows representative results obtained in pure (99.99%) Al and an Al-3%Mg alloy that are both in fully annealed conditions [15, 17]. Reproducibility was confirmed by repeating three times with three samples of each material. For pure (99.99%) Al, the temperature increased abruptly to a maximum of $\sim 40\,^{\circ}C$ upon shearing but thereafter the temperature decreased to $< 15\,^{\circ}C$ within ~ 10 s. Identical behavior was recorded for the Al-3%Mg alloy except that the temperature increased to a maximum of $\sim 85\,^{\circ}C$ upon shearing with a subsequent decrease to $< 20\,^{\circ}C$ within ~ 10 s.

Further measurements of the temperature during ECAP were conducted in fully annealed Al-1100 and Al-1%Mg alloys including pure (99.99%) Al subjected to 6 pressings and the Al-1%Mg alloy subjected to 4 pressings. The temperature variations of these materials were essentially similar to those for the fully annealed pure (99.99%) Al and Al-3%Mg alloy shown in Fig. 8.13. Figure 8.14 plots the temperature rise against the maximum applied load for all materials examined. There is a linear correlation between the two quantities, indicating that adiabatic heating is more significant in the ECAP for a pressing speed

of ~18 mm/s. The temperature measurements were also conducted in pure (99.99%) Al at a speed of 0.18 mm/s, which is slower by two orders of magnitude. It was found that the temperature rise was negligible so that adiabatic heating is of no practical significance at this lower pressing speed.

8.9 Sample Size

ECAP was conducted using samples of Al-1100 having diameter of 6, 10 and 40 mm. All samples were subjected to 6 pressings at room temperature. Compression specimens with dimensions of $3\times3\times5$ mm^3 were cut from the center portion of the ECAP samples such that the compression axis was parallel to the longitudinal axis of the ECAP samples. Compression tests were repeated twice for each samples size at an initial strain rate of 3.3×10^{-4} s^{-1}. The 0.2% proof stress is plotted in Fig. 8.15 and it is confirmed that the results are almost identical irrespective of the sample size [18]. Microstructural observations using

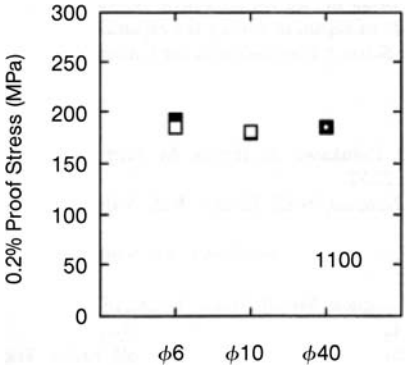

Fig. 8.15 0.2% proof stress for three different sizes of ECAP samples in Al-1100.

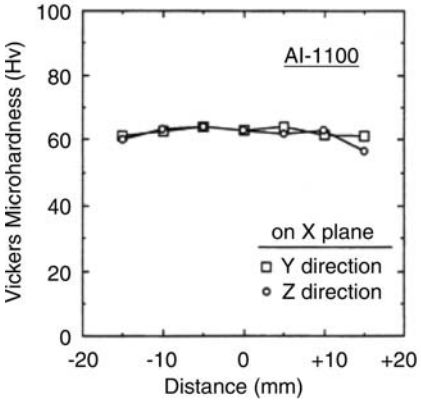

Fig. 8.16 Variation of Vickers microhardness across cross section of ECAP sample in Al-1100.

TEM revealed that there is no significant difference in grain size. The Vickers microhardness was measured on the plane perpendicular to the longitudinal axis of the ECAP samples with a diameter of 40 mm. The measurements were made every 5 mm in the *Y* and *Z* directions which are defined in Fig. 8.4. The results are plotted in Fig. 8.16. It is shown that there is no appreciable difference in hardness across the cross section of the ECAP sample. It is suggested that scaling up the sample size should be feasible without introducing any significant change in grain sizes and mechanical properties.

References

1 V. M. Segal, V. I. Reznikov, A. E. Drobyshevskiy, V. I. Kopylov **1981**, *Russ. Metall.* 1, 99–105.
2 Y. Iwahashi, J. Wang, Z. Horita, M. Nemoto, T. G. Langdon **1996**, *Scr. Mater.* 35, 143–146.
3 K. Furuno, H. Akamastu, K. Ohishi, M. Fukukawa, Z. Horita, T. G. Langdon **2004**, *Acta Mater.* 52, 2497–2507.
4 V. M. Segal **1995**, *Mater. Sci Eng. A* 197, 157–164.
5 M. Furukawa, Y. Iwahashi, Z. Horita, M. Nemoto, T. G. Langdon **1998**, *Mater. Sci Eng. A* 257, 328–332.
6 Y. Iwahashi, M. Furukawa, Z. Horita, M. Nemoto, T. G. Langdon **1998**, *Metall. Mater. Trans. A* 29, 2245–2252.
7 Y. Iwahashi, Z. Horita, M. Nemoto, T. G. Langdon **1996**, *Acta Mater.* 46, 3317–3331.
8 K. Ohishi, Z. Horita, M. Furukawa, M. Nemoto, T. G. Langdon **1998**, *Metall. Mater. Trans. A* 29, 2011–2013.
9 S. D. Terhune, K. Ohishi, Z. Horita, T. G. Langdon, T. R. McNelley **2002**, *Metall. Mater. Trans. A* 33, 2173–2184.
10 K. Nakashima, Z. Horita, M. Nemoto, T. G. Langdon **1998**, *Acta Mater.* 46, 1589–1599.
11 M. Kamachi, T. Fujinami, Z. Horita, T. G. Langdon **2004**, *Mater. Sci. Forum* 447–448, 477–482.
12 P. B. Berbon, M. Furukawa, Z. Horita, M. Nemoto, T. G. Langdon **1999**, *Metall. Mater. Trans. A* 30, 1989–1997.
13 A. Yamashita, D. Yamaduchi, Z. Horita, T. G. Langdon **2000**, *Mater. Sci. Eng. A* 287, 100–106.
14 Z. Horita, M. Furukawa, M. Nemoto, T. G. Langdon **2000**, *Mater. Res. Soc. Symp. Proc.* 601, 311–322
15 D. Yamaguchi, Z. Horita, T. Fujinami, M. Nemoto, T. G. Langdon **2000**, *Mater. Sci. Forum* 331–337, 607–612.
16 Z. Horita, T. Fujinami, M. Nemoto, T. G. Langdon **2000**, *Metall. Mater. Trans.* 31A, 691–701.
17 D. Yamaguchi, Z. Horita, M. Nemoto, T. G. Langdon **1999**, *Scr. Mater.* 41, 791–796.
18 Z. Horita, T. Fujinami, T. G. Langdon **2001**, *Mater. Sci Eng.* A318, 34–41.

9
High-pressure Torsion – Features and Applications

Reinhard Pippan

9.1
Introduction

Torsion has been a frequently used deformation technique for a long time, especially to determine the stress–strain behavior at large strains. In free torsion the geometrical changes of a cylindrical sample usually permit simple determination of the stress–strain behavior. The fracture strain is usually significantly larger than in a tensile experiment, due to the vanishing macroscopic hydrostatic tension component of the stress. By applying an additional hydrostatic compression stress the fracture strain can be further enhanced. At very high hydrostatic compression stresses the strain to fracture can be increased to infinity. High-pressure torsion is a realisation of such a torsion experiment at very high hydrostatic pressure [1–4]. In the following chapters this highly changed due to excessive use of "very" efficient method to study the material behavior under very high strains will be discussed.

The following points will be discussed in detail:

- the determination of an equivalent strain,
- deviation of the real HPT from ideal torsion,
- the strain distribution in a HPT sample,
- advantages and disadvantages of the technique,
- some general remarks on the microstructural evolution during HPT,
- upscaleability and possibility for industrial application.

9.2
The Equivalent Strain in Torsion

In order to compare strains achieved by different deformation methods, it is helpful to define an equivalent strain. There are different ways to define a strain, which can differ significantly at large strains. The most common definition of equivalent strain, ε_v, is based on the proposition that two samples deformed via different strain paths should be comparable, when the same specific

Bulk Nanostructured Materials. Edited by M. J. Zehetbauer and Y. T. Zhu

ISBN: 978-3-527-31524-6

plastic work, W_{pl}, has been done on them. For a tensile test this can be written as:

$$\frac{A}{V} = W_{pl} = \int_0^{\varepsilon} \sigma \, d\varepsilon_v \, , \tag{9.1}$$

where σ is the tensile flow stress, A is the total plastic work and V the active volume of the specimen.

For an ideally plastic material:

$$W_{pl} = \sigma \cdot \varepsilon_v \, . \tag{9.2}$$

For axially symmetric tensile deformation in the x_1 direction, the principle plastic strains are: ε_{pl1}, ε_{pl2} and ε_{pl3}, where $\varepsilon_v = \varepsilon_{pl1}$, and $\varepsilon_{pl2} = \varepsilon_{pl3} = 1/2\,\varepsilon_{pl1}$.

Torsional deformation can be modeled by a simple shear. In analogy to Eq. (9.1):

$$\frac{A}{W} = W_{pl} = \int_0^{\gamma} \tau \, d\gamma \tag{9.3}$$

where τ is the shear flow stress, and γ is the plastic shear strain (equal to: tan (plastic shear angle)).

For ideal plasticity:

$$W_{pl} = \tau\gamma \, . \tag{9.4}$$

Comparing tensile and torsional specimens that have undergone the same plastic work gives:

$$\int_0^{\varepsilon_v} \sigma \, d\varepsilon_v = \int_0^{\gamma} \tau \, d\gamma \, . \tag{9.5}$$

This equation is fulfilled, when:

$$\sigma = a\,\tau \tag{9.6}$$

and:

$$d\varepsilon_v = \frac{1}{a} d\gamma \, . \tag{9.7}$$

Obviously Eqs. (9.6) and (9.7) are fulfilled for any arbitrary value of a, called the Taylor factor, thus an additional assumption is needed. Many have been pro-

posed but only three have been widely accepted; they are $a = 2$, $a = \sqrt{3}$, $a = M$, the Taylor factors corresponding to the Tresca yield locus, the von Mises yield locus and Taylor yield criterion [1)], respectively.

The equivalent strain is not a parameter to characterize the change of shape of a volume element or grain [5, 6]. Consider a cubic volume element of edge length 10 μm. This volume element may be one phase in a dual-phase alloy. After 15 passes of accumulative roll bonding and homogeneous deformation, the thickness of the volume element should be 0.3 nm. The corresponding equivalent strain (true strain) is 10.4. According to Eq. (9.5) and using the Tresca criterion ($a = 2$), the same amount of plastic work is done for $\gamma = 20.8$. Considering a homogenously sheared cubic volume element gives the element thickness to be 480 nm [5]. This indicates that simple shear – which is typical for HPT and ECAP – is not as efficient as rolling or drawing in changing the geometry of the original "grain" structure at very large strains.

9.2.1 Idealized and Real HPT

In Fig. 9.1 (a) a sketch of an idealized HPT process is depicted. A disc-shaped specimen is deformed by simple shear between two anvils, which rotate with respect to one another. In order to avoid sliding between the anvils and the specimen high contact stresses are necessary. To build up a high contact stress, also at the edge of the specimen the deformation is constrained in the radial directions. In the idealized case, the sample is deformed by pure torsion under a hydrostatic pressure, and the dimensions of the sample remain constant during processing. For this case the shear strain γ can be calculated according to Eq. 9.8:

$$\gamma = \frac{2\pi n}{t} r \quad \text{or} \quad \varepsilon_v = \frac{2\pi \cdot n}{a \cdot t} r \tag{9.8}$$

where r, n and t are the distance from the center of the axis of rotation, the number of revolutions and the thickness of the sample, respectively.

In order to realize an idealized torsion, no friction at the outside of the cylindrical sample should occur. Since such frictionless constraint of radial deformation is impossible, the maximum height of the sample is limited in order to ensure a homogeneous deformation in the axial direction (over the height of the sample) [7]. To avoid sliding between the anvil and the top and bottom faces of the sample, the necessary pressure is usually very high. As a rule of thumb the pressure should be larger than the hardness of the material, or about 3 times the yield stress of the as-processed material. Furthermore, a sufficient microroughness of the top and bottom surface of the anvil is required. The strength of SPD materials is very high, therefore the necessary pressure is typically between 1–10 GPa, depending on the material to be processed. 1 GPa is usually

1) The Taylor theory is a kinetic analysis, which takes into account the texture of a material.

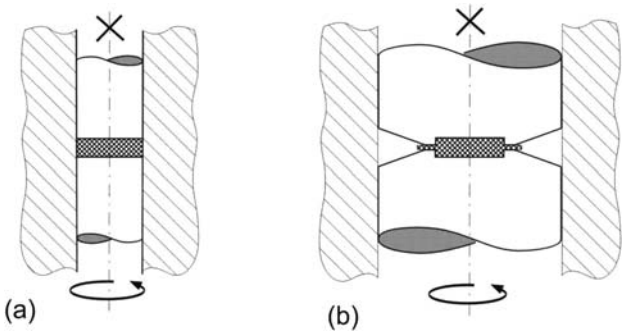

Fig. 9.1 Schematic illustration of high-pressure torsion equipment: (a) idealized and (b) practical setup.

sufficient to deformed pure Al or pure Cu. In many materials 5 GPa is sufficient to avoid sliding between the anvils and the sample. Only with very high strength material are larger pressures necessary. 5 GPa is a very high stress, therefore the idealized version in Fig. 9.1 (a), with a cylindrical stamp of the same diameter as the sample, is not possible to realize. In such an experimental set-up the yield stress of the stamps should be larger than the applied pressure.

A practical set-up, which overcomes this problem and permits a deformation very similar to the idealized HPT, is depicted in Fig. 9.1 (b). The applied pressure in such a set-up can be about 3 times the yield stress of the stamp material (like in an indentation experiment, where the hardness is about 3 times of the flow stress). Both anvils are provided with a cylindrical cavity of the same dimensions. The diameter of the cylindrical cavities and the initial diameter of the HPT sample are identical. The sum of both depths of the cavities should be somewhat smaller than the initial height of the HPT sample. Thus, during loading, a small amount of the material flows between the ring shaped region between the anvils. The friction in this ring region confines the free flow of the material out of the HPT tool, this leads to a back pressure and therefore induces a well-defined hydrostatic pressure within the processing zone of the tool. In addition, the material between the two anvils prevents touching, and therefore failure, of the anvils during the torsional deformation. The bottom and the top face of the cylindrical cavity of the tool are sandblasted in order to clean the surface and to provide the necessary micro roughness, which delivers sufficient friction for a continuous torsional deformation. Furthermore, the surface of the sample should also be cleaned. As mentioned above, during the axial loading of the anvils a certain amount of material flows into the ring shaped region. During subsequent torsional deformation an additional somewhat small amount of material flows out, which again reduces the height of the sample. The amount of material that flows out of the cavity between the anvils is dependent upon the difference in volume between the sample and the anvil cavity as well as upon the strength of the material. Even if the cavity formed by the anvils has a perfectly cylindrical shape, due to the inhomogeneous elastic deformation of the

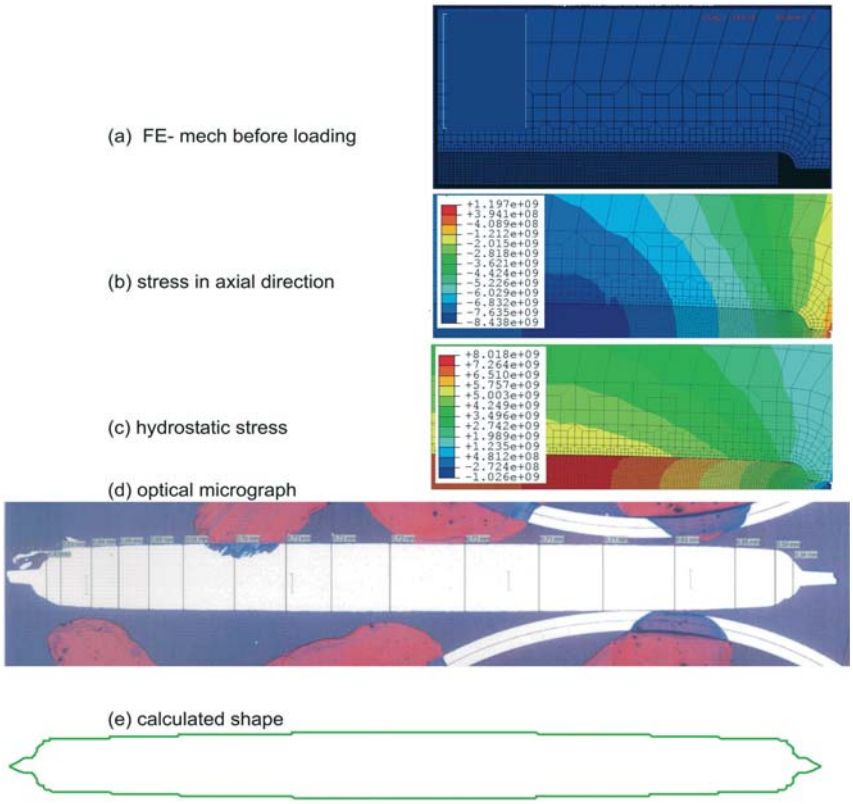

Fig. 9.2 Illustration of the finite-element simulation of the compressive loading of a rail steel in a HPT tool with a nominal pressure of about 7 GPa. (a) shows a detail of the FE mechanism used, due to the symmetry only a quarter of the sample and the anvil has to be considered. (b) and (c) exhibit the axial stress and the hydrostatic component of the stress [N/m^{2}]. In (d) and (e) the calculated shape (only few selected points are presented) and the real shape of the originally cylindrical sample are compared.

tool the height of the sample in the center is somewhat larger than at the edge. This effect increases with increasing pressure and increasing strength of the material. The results of a finite element (FE) simulation of this deformation is depicted in Fig. 9.2. Figures 9.2 (b) and (c) show the stress distribution in an anvil and the sample. The applied "nominal" hydrostatic pressure (load divided by the sample cross section) was in this case 7 GPa; the sample material and the tool material are a rail steel and a high-strength tool steel, respectively [8].

In this figure the different height of the originally cylindrical sample in the centre and at the edge, and the material flow between the two anvils, is visible. Figures 9.2 (d) and (e) compare the resulting shape of the FE simulation and the experimentally determined shape after applying the compression load. The figures show a good agreement between the calculated and measured shapes.

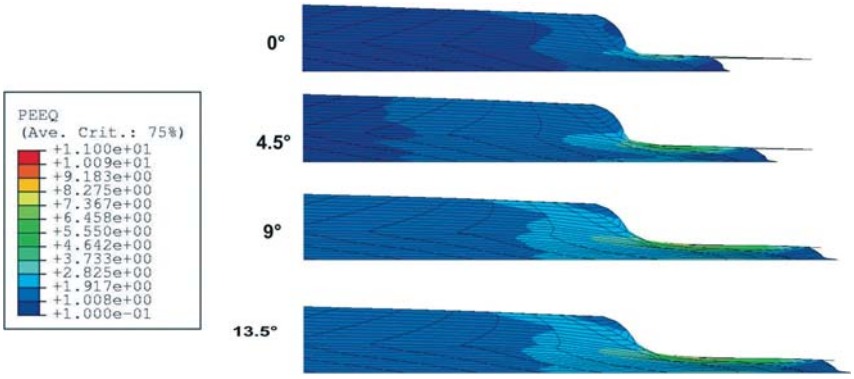

Fig. 9.3 Illustration of the flow of the material between the two anvils for different angle of rotation, only the edge of the sample is depicted. The color code represents the equivalent strain.

The simulation indicates that after the first compressive loading the hydrostatic pressure in the HPT sample is not very homogeneously distributed, especially when a high strength material is deformed. However, after a very "small" rotation of the anvils a relatively homogeneous distribution of the hydrostatic stress in the HPT-sample is observed [8]. Figure 9.3 shows, furthermore, the additional flow of material between the anvils during rotation in the simulation, which is in good agreement with the observed behavior. The very high von Mises stress in the anvil, which is indicated in Fig. 9.2 (b), induces a small amount of plastic deformation of the anvils. Therefore the anvils are usually remachined after the first load if such a very large load is applied.

9.3 The Homogeneity of the Deformation

9.3.1 The Radial Distribution

In an ideal HPT experiment the strain should increase linearly with the distance from the axis of rotation (Eq. (9.8)). It is therefore very surprising that a uniform severely deformed microstructure in HPT samples with no significant radial dependence of the hardness has been reported at a relatively small number of revolutions (see, for example, [9, 10]). However, a very carefully performed HPT experiment showed clearly the opposite [11]. A typical result of this study is shown in Fig. 9.4. HPT samples of an austenitic steel (~15 wt Cr, 25 wt Ni) with a initial thickness of about 0.8 mm had been deformed to $n = 2.27$ and $n = 16$ revolutions. The centre of the samples was polished and a special etching procedure was applied. At shear strains smaller than about 1, the original grain

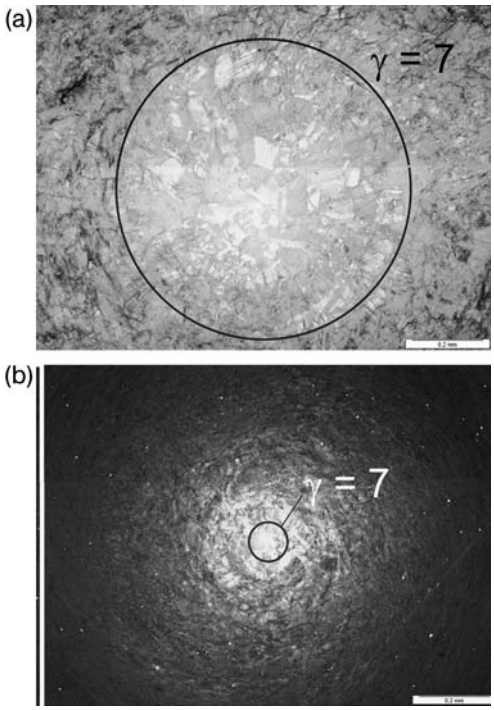

Fig. 9.4 Optical micrographs of the central region of about 0.7 mm thick samples after (a) 2.27 and (b) 16 revolutions. The region with the nominal shear strain at 7 is indicated. Clearly visible is the "low" deformed central region in both samples. The material is an austenitic steel (~15 wt Co, 25 wt Ni).

structure is visible and at a shear strain γ larger than 8, the microstructure appeared unstructured and dark in the optical microscope. The micrographs in Fig. 9.4 indicate clearly that the centre of the HPT sample remains nearly undeformed even at very large numbers of revolutions. Furthermore, the radial dependence of strain and the variation of the microhardness could be clearly demonstrated [11]. What may be the reasons that many authors reported that in HPT deformed samples a uniform microstructure develops after only a few revolutions. In the following, different reasons are listed:

- In addition to the shear deformation of the sample, a compressive deformation during compressive loading and during the initial phase of the following torsional deformation takes place as already mentioned. In our experiments, where we use a tool as depicted in Fig. 9.1 (b), the typical compressive deformations are between 5% and 20%. This deformation is usually very small compared to deformation introduced by torsion. For a HPT sample with a thickness of 0.8 mm deformed by 1 revolution, the equivalent strain at a radius of 4 mm introduced by torsion is about 20. Therefore, the few % com-

pressive deformation is negligible, except in the centre of the sample. However, it is important to note that the change in thickness of the sample should be taken into account for the calculation of the shear strain [6, 11]. We usually use the mean height given from the thickness after simple compression and the final thickness after HPT deformation for calculation of the shear strain by Eq. (9.8). Since the difference is usually small, sometimes we use the final thickness only. Furthermore, it should be noted that some groups use tools and initial sample shape combinations where the compressive deformation can be significantly larger, hence, they may find a more homogeneous microstructure and hardness distribution.

- A parallel shift of the axes of the upper and the lower anvils can introduce an additional shear deformation also in the centre of the sample [11]. Furthermore, a misalignment of the axes of the anvils can make the deformation during compression complex and that during rotation even more so.
- Finally, it should be noted that the weakly deformed region in a HPT-sample can be very small. The sample in Fig. 9.4 (b), which had been HPT deformed to 16 revolutions shows only a cylindrical central region of about 50 μm in diameter, where the equivalent strain is smaller than 4. Such a region is not easy to find on a HPT sample.

9.3.2 The Axial Homogeneity

For the derivation of Eq. (9.8) it is assumed that shear in the axial direction is homogeneously distributed. In order to prove this assumption different experiments have been performed on split HPT samples [12, 13]. Figures 9.5 and 9.6 show two examples. A HPT sample, split in the plane through the axis of rotation, was deformed to 1/4 revolution. A photo of the sample is depicted in Fig. 9.5. The helical shape of the split sample clearly indicates the homogeneous deformation in the axial direction and it also shows that the shear strain is proportional to the radius, only at the edge of the sample is a small deviation from the ideal helical shape observed. This observed deviation is in good agreement with the FE simulations [8]. Similar experiments are also performed at very high strains, where no further hardening of the material takes place. Two HPT samples were deformed to very high strains ($\varepsilon_v \sim 100$) then the samples were

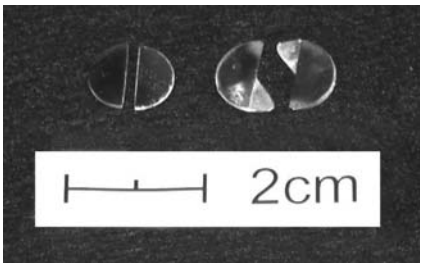

Fig. 9.5 Split HPT sample before and after a deformation to ¼ revolution. The expected fan shape is clearly visible.

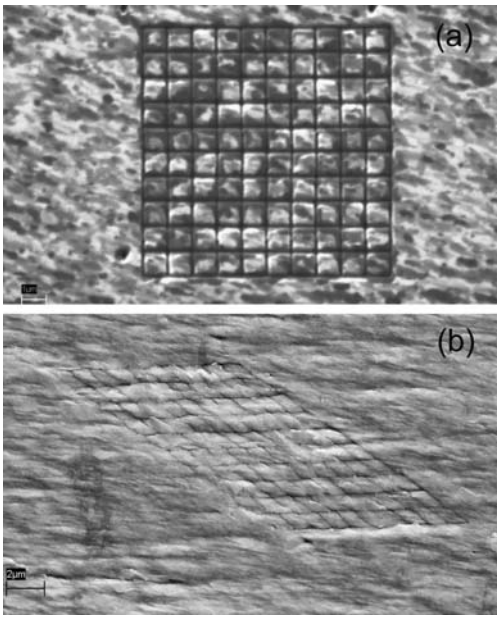

Fig. 9.6 (a) illustrates the microgrid on a polished, split HPT sample at a radius of 2 mm from the axis of rotation. The Ni sample was deformed, $\varepsilon_V \approx 100$. (b) shows the grid after further shear deformation ($\gamma \approx 1.4$), which demonstrates the very homogeneous deformation in axial direction even on the microscale.

split at a radius of 2 mm from the axis of rotation. The splitting surface was polished and marked with a grid by a focused ion beam. The corresponding parts of samples were then put together and a further small amount of HPT deformation was applied. A SEM-image of the deformed grid is depicted in Fig. 9.6, demonstrating the very homogeneous deformation in the axial direction. This is the case even in the micrometer range in a material with no further capacity for hardening. Finally, it should be noted that many different experiments in dual phase materials [14, 15] clearly support these observations of homogeneous shear in the axial direction and the radius dependence of the shear strain. In the author's experience this nearly ideal torsional deformation is fulfilled as long as the diameter of the HPT sample is larger than 8 times the thickness of the sample. A very large deviation from the axial homogeneity is demonstrated in [8], where the thickness to diameter ratio was about 1. For ratios smaller than 1/8 up until now our group has observed only one exception, in some magnesium alloys the formation of a crack in the central plane, at the edge of the sample, can induce a localization of the deformation to a very narrow band, and finally to a partly fractured and re-welded sample. How about the recent work by Zenji Horita and Terry Langdon on very thick samples? They have presented their results in several confs. You may want to include their results.

9.4
Advantages and Disadvantages of the HPT Process

Compared to other severe plastic deformation processes the HPT-technique offers a large number of advantages, listed in the following.

- Most severe plastic deformations offers only a stepwise application of strain. HPT permits a defined continuous variation of the strain.
- The most important advantage of HPT is the very simple way in which extremely high shear strains can be achieved. One revolution of a 0.8 mm thick HPT specimen correspond to a equivalent strain of about 18, at a radius of 4 mm. An application of 100 revolutions simple corresponding then to an equivalent strain of 1800 (or 180 000%). Such large equivalent strains are nearly impossible to obtain by any other technique.
- A further important advantage is that HPT permits the severe plastic deformation of relatively brittle materials, or high strength materials at low temperatures, which are often impossible to deform severely (see, for example, [14–16]).
- The pressure can be varied in a defined way, however, a certain minimum pressure is always necessary.
- The strain rate at a specified radius of the sample can be precisely controlled.
- Heating or cooling of the anvils permits a severe plastic deformation at a well defined temperature.
- The total torque vs the angle of rotation can be comfortably measured, see Fig. 9.7. This permits a control that slip between the anvil and the sample does not occur during the processing and, furthermore, it can be used to esti-

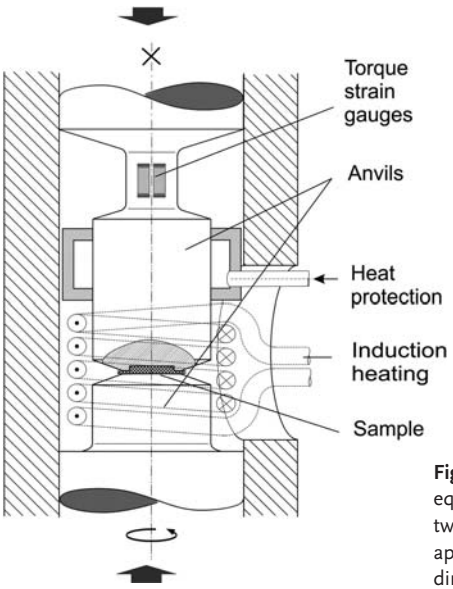

Fig. 9.7 Schematic illustration of the HPT equipment used. It permits deformation between –196 and 500 °C, measurement of the applied torque, and the ability to change the direction of rotation.

mate the evolution of shear flow stress *in situ*, during the severe plastic deformation [17]. The measured total torque contains the torque to deform the sample and the torque due to sliding between the burr (the material pressed between anvils) and the tool, as well as some deformation of the burr. Depending on the geometry of the tool, the formed burr and the pressure, the torque to deform the sample is typically about 70% of the total torque. Despite the uncertainty in the *in-situ* measured shear flow stress, this direct measurement is a very helpful tool to analyze the severe plastic-deformation processes.

- A change of the direction of rotation permits one to apply a severe cyclic plastic deformation, which is typical for many other SPD processes (Equal Channel Angular Pressing route C, Cyclic Extrusion Compression [18, 19] or constrained groove pressing [20], Cyclic Channel Die Compression [21]). Hence, this cyclic version allows one to study the effect of strain path on the evolution of the microstructure up to extremely large accumulative strains [21].

In summary; HPT is a simple and efficient tool enabling study of material behavior under severe plastic deformation. From HPT-samples one can machine (miniaturized) specimens, allowing determination of the mechanical properties of SPD-materials. Typical specimen geometries for tensile or fracture mechanics tests are depicted in Fig. 9.8.

Despite these advantages of HPT – especially for fundamental studies of the potential of SPD – there are some disadvantages, especially for large-scale industrial application. In industrial applications one usually needs homogeneous material properties. Due to the radial dependence of the shear strain, a radial dependence of the properties is expected. In most metals and alloys at strains larger than 10 or 20, a saturation in refinement, local and global texture is observed (see the following chapters). By application of such large strains, even at relatively small radii, a large part of the HPT-sample have a homogenous microstructure and therefore homogeneous properties. Only the very central region of the HPT-sample shows then an inhomogeneous property distribution. A further disadvantage for the industrial application is the magnitude of the equipment necessary to produce HPT-deformed materials with larger dimensions (see upscaling of HPT deformation).

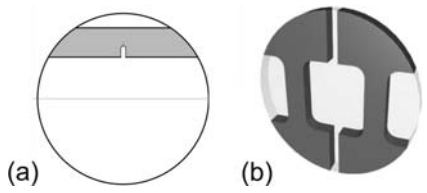

Fig. 9.8 Illustration of (a) small fracture mechanics and (b) tensile samples machined from HPT samples.

9.5 Upscaling of the HPT Deformation and the Possibility of Large Scale Industrial Production

In principle, there exists no limit to an increase in the diameter of the HPT-sample, only the ratio of the diameter of the HPT-sample to the height should not be smaller than a critical value to obtain a homogeneous deformation in the axial direction. The typical pressure to permit HPT deformation of steels at room temperature is about 5 GPa (or 3 times the yield stress of the SPD deformed materials). In order to produce a HPT sample of 100 mm in diameter, this requires a HPT-press with a load capacity of 40 000 kN. Such large presses and especially larger ones, where the stamp can be rotated, are rare. Hence, samples significantly larger than 100 mm can not be produced by a simple HPT arrangement as depicted in Fig. 9.1(b). However, it should be noted that for certain industrial applications this sample size is sufficient.

A severe torsion process that permits mass production has recently been proposed [22]. The principle of this technique is illustrated in Fig. 9.9. One end of the rod is rotated around the longitudinal axis of the rod, while the other one is fixed. Local heating and local cooling provide "free" torsional deformation in a localized region. The movement of the rod along the longitudinal axis permits a continuous production of a severely plastically deformed rod. Due to the necessary heating and the limited amount of torsional straining, because cracking is not suppressed by the pressure, the refinement of microstructure is rather limited. However, the improvement in formability of certain materials offers a large scale application in industry.

A further technique that permits mass production is the torsion extrusion process [23]. This technique is characterized by the rotation of die or container during the extrusion process. Figure 9.10 shows the principle of this process. Due to the rotation of the die and the friction in the container and die channel, a torsion deformation in the transition region between the container and the die takes place. A deviation from the cylindrical shape of the container and die in the vicinity of the transition region should restrict the torsional deformation

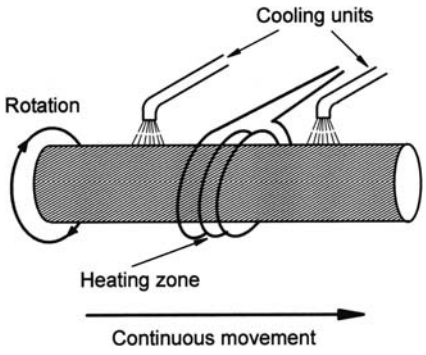

Fig. 9.9 Schematic illustration of a severe torsional straining process.

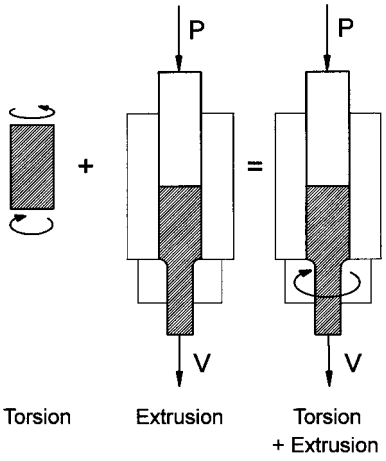

Fig. 9.10 Schematic illustration of the principle of the torsional extrusion process.

to a very defined zone. A clever design of the shape of the die channel shape allows to control of the pressure in the torsion zone. Due to the high pressure the torsional straining is not limited, as in the case of the "standard" HPT. As in the standard HPT, where the torsional deformation can be several orders of magnitudes larger than the compression deformation, in this case torsional deformation can be several orders of magnitude larger than the extrusion strain. Therefore, this technique could really be denoted as a continuous HPT, and would permit simple large scale production of SPD-materials.

Finally, it should be noted that the mechanism, which may be responsible for the "homogeneous" HPT-samples (see discussion above), for example the shift of the rotation axis, may improve the homogeneity of such an SPD-deformed rod.

9.6
Some General Remarks on the Evolution of Microstructure

Figure 9.11 shows a sequence of micrographs taken using back-scattered electrons, with increasing strains in a ferritic steel with 17 Co [24]. The field of vision is a few μm^2 only, each picture presents therefore the microstructure within one original grain or a small region comprising two neighbouring original grains.

At an equivalent strain of 1, one observes rather hazily the beginning of the formation of a substructure on the microscale, which is especially pronounced at the original grain boundary. With increasing strain the contrasts become more obvious and the scale of the substructure decreases. Beyond a certain strain – in the present case at a strain of 16 – there is no clear change in the microstructure. At larger strains and especially in the saturation regime, the microstructure observed in the axial direction shows equiaxed "grains" with a more

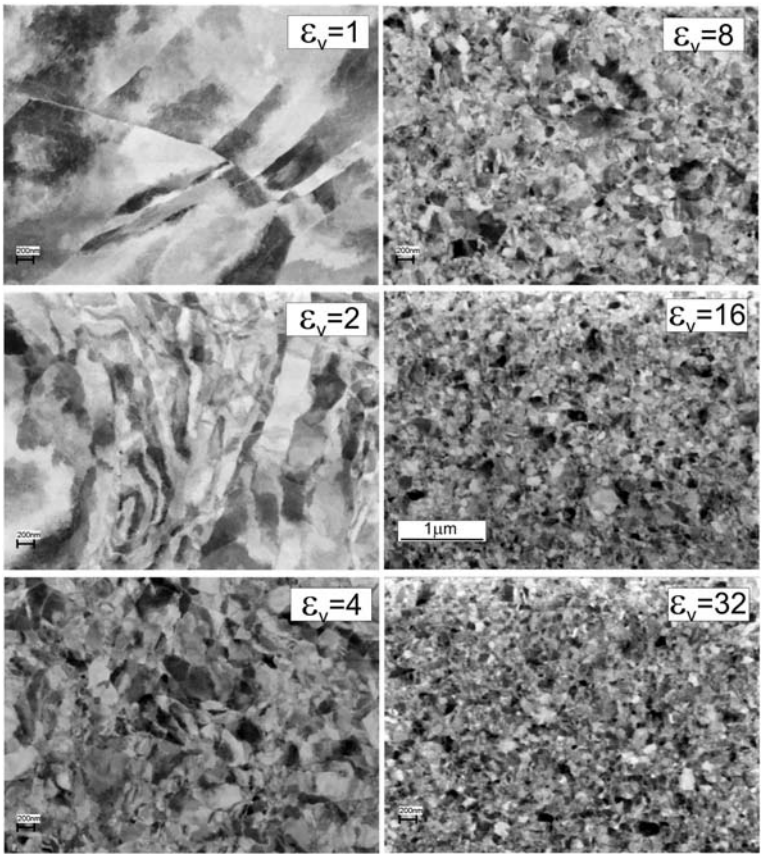

Fig. 9.11 Back Scattered Electron (BSE) micrographs of a ferritic steel (17 weight per cent Co) at different equivalent strains; the micrographs are taken in the axial direction and were performed at the same magnification.

or less pronounced bi-modality, depending on the deformation temperature and the material.

The microstructure in the radial direction exhibits a preferred direction inclined at an angle to the axial direction [6], an example is presented in Fig. 9.12. One might suppose that this preferred direction is a "souvenir" of the original grain structure. This, however, is not so, the angle in the saturation regime does not agree with the shear angle and remains constant in the saturation regime [6]. The described features of the structural refinement are typical of HPT deformation of single phase materials. This general evolution behavior of the microstructure can be observed in all SPD deformation processes.

The speciality of HPT is only that it is very easy to reach these strains, where the saturation in refinement can be observed [13], with the other techniques it is sometimes impossible or it can be very time consuming. The necessary strain

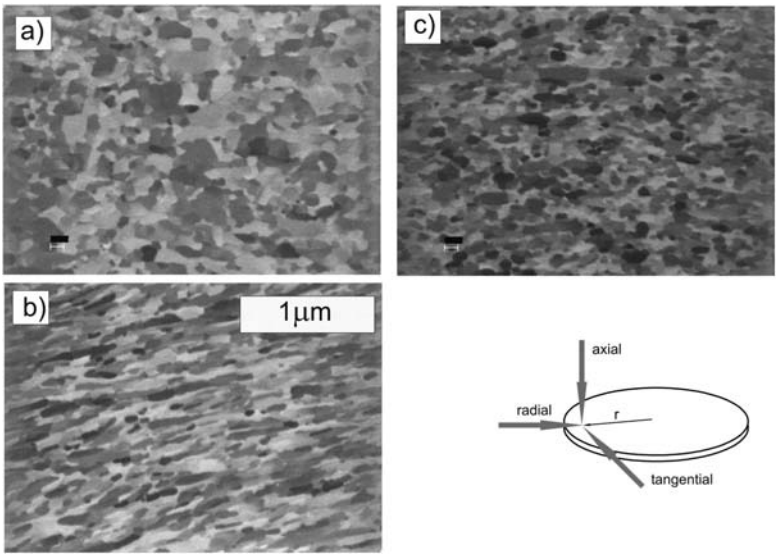

Fig. 9.12 Focused iron beam micrographs of HPT deformed pure Fe, deformed to $\varepsilon_V \approx 100$, obtained in the three principle observation directions ((a) axial, (b) radial and (c) tangential).

to reach the saturation and the minimum size of the "grains" (structural elements, which are separated by high angle boundaries) are affected by the temperature, strain rate, strain path, alloying, crystal structure and pressure. The importance of parameters is qualitatively evaluated in Table 9.1 (for details, see for example [4, 13, 25, 26]).

The structural evolution of dual or multiphase materials is much more complex [15, 27–30]. The minimum sizes of the phases and grains, which can be achieved by HPT, are usually smaller than in single phase material. In the author's opinion one should, in principle, also reach a saturation in the micro-

Table 9.1 Effect of different parameters on the onset strain of saturation and the size of the structural elements in the saturation regime.

	***d* at saturation**	**Onset of saturation**
temperature	very high	very high
strain rate	medium	medium
strain path	high	medium
pressure	low–medium	low
alloying	very high	medium
precipitations	high	?
crystal structure	low	medium
stacking-fault energy	medium	?

structural evolution, which can be a (nano)composite, a solution of the phases or a transformation to an amorphous state. The strain to reach such saturation might be very high, or due to the extreme strength, difficult to obtain. In summary; the structural evolution in a HPT deformation should be similar to all SPD processes at the same processing parameters, where the plastic deformation occurs by simple shear. The advantage of HPT is that it is relatively easy to achieve very large strains at different processing parameters and due to the inherent high pressure, it can be applied to materials that are usually difficult to deform.

Acknowledgements

The work was supported by the Austrian "Fonds zur Förderung der wissenschaftlichen Forschung", Project P17096-NO2.

References

1 J. Bridgmen **1936**, in: *Processing of Metals under High Pressure Conditions*, M. Techizdat (ed.), Moscow, p. 230.
2 V. A. Zhorin, D. P. Shashkin, N. S. Yenikoponyan **1984**, *DAN SSR* 278, 144.
3 R. I. Kuznetsov, V. I. Bykov, V. P. Cheryshov, V. P. Pilyugin, Na. Yefremov, V. V. Posheyev **1985**, *Plastic deformation of solid bodies under pressure*, Sverdlovsk, *IFM NTS RAN*, 4/85.
4 R. Z. Valiev, R. K. Islamgaliev, I. V. Alexandrov **2000**, *Prog. Mater. Sci.* 45, 101.
5 H. P. Stüwe **2003**, *Adv. Eng. Mater.* 5, 291–295.
6 T. Hebesberger, H. P. Stüwe, A. Vorhauer, F. Wetscher, R. Pippan **2005**, *Acta Mater.* 53, 393–402.
7 W. Ecker **2004**, *Diploma Thesis* Montanuniversität Leoben.
8 G. Sakai, K. Nakamura, Z. Horita, T. G. Langdon **2006**, *Mater. Sci. Forum* 503–504, 391–396.
9 A. P. Zhilyaev, G. V. Nurislamova, B.-K. Kim, M. D. Bar, J. A. Szpunar, T. G. Langdon **2003**, *Acta Mater* 51, 753.
10 A. P. Zhilyaev, S. Lee, G. V. Nurislamova, R. Z. Valiev, T. G. Langdon **2001**, *Scr. Mater.* 44, 2753.
11 A. Vorhauer, R. Pippan **2004**, *Scr. Mater.* 51, 921–925.
12 T. Hebesberger **2002**, *PhD Thesis* Montanuniversität Leoben.
13 R. Pippan, F. Wetscher, M. Hafok, A. Vorhauer, I. Sabirov, **2006** *Adv. Eng. Mater.* 8, in press.
14 F. Wetscher, A. Vorhauer, R. Stock, R. Pippan, **2004** *Mater. Sci. Eng. A* 387–389, 809–816.
15 I. Sabirov, R. Pippan, **2005** *Scr. Mater.* 52, 1293–1298.
16 A. Vorhauer, W. Knabl, R. Pippan, **2003** *Mater. Sci. Forum* 426–432, 2747–2752.
17 A. Vorhauer, R. Pippan, On the onset of steady state in bcc iron during severe plastic deformation at low homologous temperatures, submitted to *Metall. Mater. Trans. A*.
18 J. Richert, M. Richert **1986**, *Aluminium* 62, 604.
19 M. Richert, H. P. Stüwe, M. Zehetbauer, J. Richert, R. Pippan, C. Motz, E. Schafler **2003**, *Mater. Sci. Eng. A* 355, 180–185.
20 D. H. Shin, J.-J. Park, Y.-S. Kim, K.-T. Park **2002**, *Mater. Sci. Eng. A* 328, 98.
21 A. Vorhauer, R. Pippan **2004**, in: *Nanomaterials by Severe Plastic Deformation*, M. Zehetbauer, R. Z. Valiev (eds.), Wiley-VCH Verlag GmbH & Co, Weinheim, p. 684.

22 Y. Miyahara, N. Emi, K. Neishi, K. Nakamura, K. Kaneko, M. Nakagaki, Z. Horita **2006**, *Mater. Sci. Forum* 503–504, 949–954.

23 S. Mizunuma **2006**, *Mater. Sci. Forum* 503–504, 185–190.

24 A. Vorhauer, S. Kleber, R. Pippan **2005**, *Mater. Sci. Eng.* 410–411, 281.

25 X. Huang, G. Winther, N. Hansen, T. Hebesberger, A. Vorhauer, M. Zehetbauer **2003**, *Mater. Sci. Forum* 426–432, 2819.

26 M. J. Zehetbauer, H. P. Stüwe, A. Vorhauer, E. Schafler, J. Kohout **2003**, *J. Adv. Eng. Mater.* 5, 330.

27 F. Wetscher **2006**, *PhD Thesis*, University Leoben.

28 I. Sabirov, O. Kolednik, R. Pippan **2005**, *Metall. Mater. Trans.* 36A, 2861.

29 X. Sauvage, F. Wetscher, P. Pareige **2005**, *Acta Mater.* 53, 2127.

30 Yu. V. Ivanisenko, R. Z. Valiev, W. Lojkowski, A. Grob, H.-J. Fecht **2002**, in: *Ultrafine Grained Materials II*, T. C. Lowe (ed.), The Minerals, Metals and Materials Society, Warrendale, USA, p. 47.

10
Fabrication of Bulk Nanostructured Materials by Accumulative Roll Bonding (ARB)

Nobuhiro Tsuji

10.1
Introduction

Ultrafine-grained (UFG) metallic materials whose mean grain size is smaller than 1 μm are a candidate for the advanced structural materials in the future, because they have excellent mechanical properties in simple chemical compositions. One of the promising ways to fabricate the UFG or nanocrystalline materials is the severe plastic-deformation (SPD) process [1]. Various special SPD processes, which make it possible to deform the materials up to very large plastic strain, have been developed [1, 2]. The famous examples of such SPD processes are equal-channel angular extrusion (ECAE) and high-pressure torsion (HPT) [1, 3]. Those SPD processes have succeeded in producing UFG materials, but most of the SPD processes previously developed are batch processes that can only fabricate limited amounts of material. As an alternative, we [2, 4, 5] have invented a novel SPD process using the rolling deformation that is known as the most advantageous metal working process for continuous production of bulk materials, such as plates, sheets and bars. The process, named *accumulative roll bonding (*ARB*),* has succeeded in fabricating bulk sheet materials having the UFG structures and brought many findings into the field of SPD and UFG. The aim of the present chapter is to summarize the features of the ARB processing and to overview the structures and properties of the ARB-processed materials.

10.2
ARB Process

The principle of the ARB process is illustrated in Fig. 10.1. In conventional rolling, it is almost impossible to apply a huge amount of strain to the materials, because of the decrease in thickness of the materials accompanied with increasing total strain. In the ARB process, 50% of rolled material is cut into two pieces, stacked so as to be in the initial dimensions, and rolled again. In order

Bulk Nanostructured Materials. Edited by M. J. Zehetbauer and Y. T. Zhu

ISBN: 978-3-527-31524-6

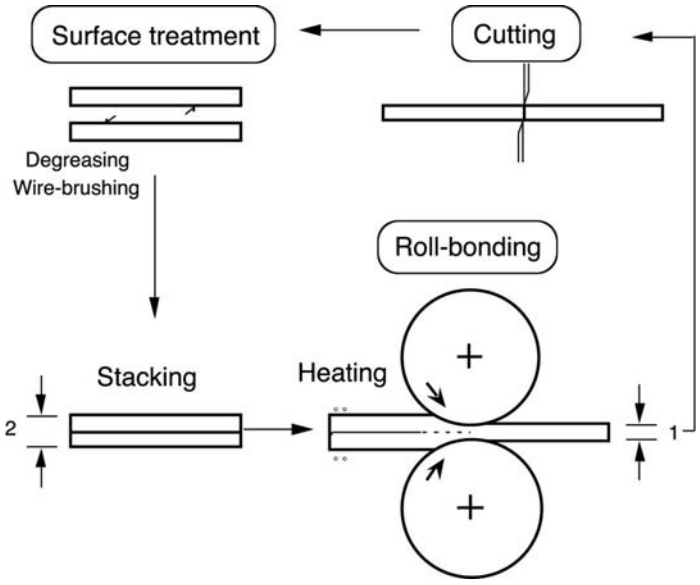

Fig. 10.1 Schematic illustration showing the principle of the accumulative roll-bonding (ARB) process.

to obtain one-body solid materials, the rolling in the ARB process is not only a deformation process but also a bonding process (roll bonding). For good bonding, the contacting surfaces of the sheets are degreased and wire brushed before stacking. Sometimes the stacked sheets are heated at an elevated temperature below the recrystallization temperature to achieve good bonding and to reduce the rolling force. These procedures can be repeated limitlessly in principle, so that the plastic deformation up to very high strain is realized, resulting in UFG structures. Because the (von Mises) equivalent strain (ε) of 50% rolling is 0.8, the total strain accumulated by n cycles of the ARB is $0.8n$. After 10 cycles of the ARB, for example, 8.0 of strain is applied to the material. In contrast, in order to fabricate a 1-mm thick sheet with 8.0 of total strain in conventional rolling, it is necessary to start from a big ingot having a thickness of 1024 mm (over one meter).

The ARB process does not require any special equipment except for a rolling mill with enough capacity, which is another advantage of this method. Figure 10.2 shows (a) a rolling mill, (b) a hand grinder with a stainless wire brush, and (c) a shearing machine used for the ARB process in Osaka University. The rolling machine is a conventional two-high mill with a 310 mm roll diameter. Because large reduction in one pass is necessary to achieve good bonding [6] and the roll bonding is often carried out without lubrication to realize quick UFG formation [7], the rolling force during the ARB becomes very large. For instance, the rolling force for commercial-purity aluminum sheet 40 mm in width reaches to 49 tons in the seventh cycle of the ARB without lubrication at room

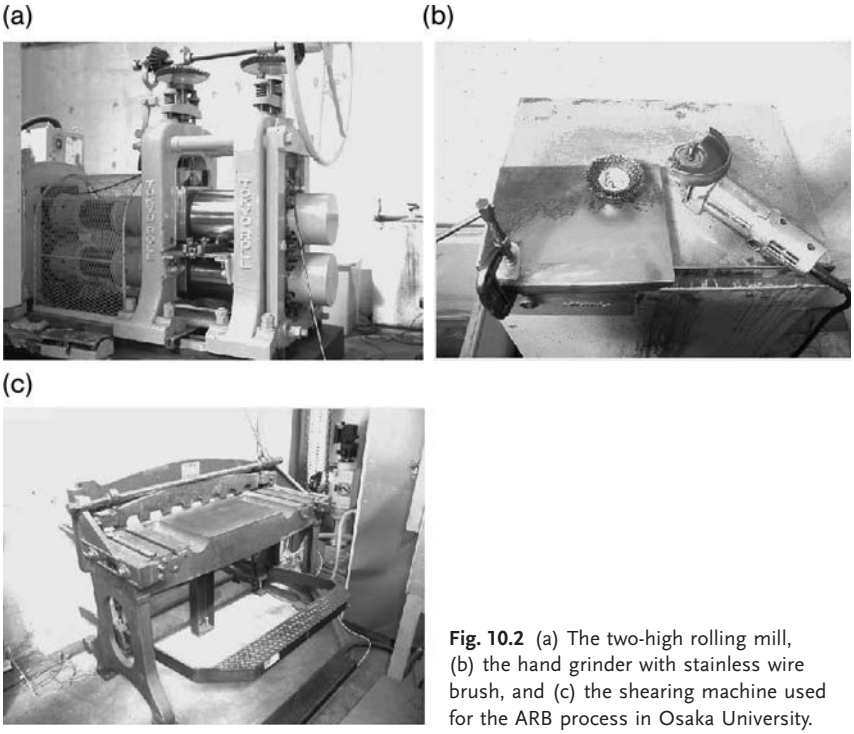

Fig. 10.2 (a) The two-high rolling mill, (b) the hand grinder with stainless wire brush, and (c) the shearing machine used for the ARB process in Osaka University.

temperature (RT). Thus, the only requirement for the rolling mill is high capacity. The rolling mill shown in Fig. 10.2 (a) has a capacity of 150 tons.

The ARB process has been successfully applied to various kinds of metallic materials and has produced bulk sheets having ultrafine structures. All materials processed by the ARB in Osaka University until now are summarized in Table 10.1 [8–29]. In every material, ultrafine lamellar boundary structure or pancake-shaped ultrafine grains whose boundary spacing or grain thickness is much smaller than 1 μm, which will be shown in the following section, formed uniformly in the materials after several cycles of the ARB. The ARB-processed sheets having the ultrafine structures possess very high strength that is two to four times higher than that of the starting coarse-grained materials. Besides Table 10.1, many scientists in various countries have also used the ARB process for SPD research [30–34].

Unexpectedly, the roll bonding in the ARB process was not so difficult for most of the materials, although degreasing by acetone and wire brushing before stacking were indispensable for good bonding. The minimum rolling reduction in one pass to achieve bonding exists, as is well known [6], which depends on the kind of the materials and the rolling conditions. During the course of the ARB cycles, bonding at interfaces becomes more and more perfect. As a result, even after fracture in tensile test, exfoliation of the bonded interfaces could be

Table 10.1 Various kinds of metallic materials ARB-processed in Osaka University.

Material (mass%)	Conditions	Mircostructures	Grain Size	Tesnile Strength	Reference
4N-Al	7 cycles at RT	pancake UFG	670 nm	125 MPa	[8]
1100-Al (99%Al)	8 cycles at RT	pancake UFG	210 nm	310 MPa	[9]
5052-Al (Al-2.4Mg)	4 cycles at RT	ultrafine lamellae	260 nm	388 MPa	[10]
5083-Al (Al-4.5Mg-0.57Mn)	7 cycles at 100 °C	ultrafine lamellae	80 nm	530 MPa	[11]
6061-Al (Al-1.1Mg-0.63Si)	8 cycles at RT	ultrafine lamellae	100 nm	357 MPa	[12]
7075-Al (Al-5.6Zn-2.6Mg-1.7Si)	5 cycles at 250 °C	pancake UFG	300 nm	376 MPa	[13]
8011-Al (Al-0.63Si-0.72Fe)	8 cycles at RT	pancake UFG	320 nm	240 MPa	[14]
Al-2Cu	6 cycles at RT	ultrafine lamellae	67 nm	(HV 115)	[15]
Al-4Cu	6 cycles at RT	ultrafine lamellae			[16]
Al-5vol%SiC	8 cycles at RT	–	–	170 MPa	[17]
OFHC-Cu	6 cycles ar RT	ultrafine lamellae	260 nm	520 MPa	[18]
Cu-0.27Co-0.09P	8 cycles at 200 °C	ultrafine lamellae	150 nm	470 MPa	[19]
Cu-30Zn	5 cycles at RT	ultrafine lamellae	47 nm	801 MPa	[20]
Ni	5 cycles at RT	ultrafine lamellae	140 nm	885 MPa	[10]
IF steel	7 cylces at 500 °C	pancake UFG	210 nm	870 MPa	[9]
IF steel	10 cycles at RT	ultrafine lamellae	88 nm	1020 MPa	[21]
0.041P-added IF steel	5 cycles at 400 °	pancake UFG	180 nm	820 MPa	[22]
SS400 steel (Fe-0.13C-0.37Mn)	5 cycles at RT	ultrafine lamellae	110 nm	1030 MPa	[23]
Fe-26Cr-7Ni (a)	4 cycles at RT	ultrafine lamellae	120 nm	1000 MPa	[24]
Fe-30Ni	7 cycles at 500 °C	ultrafine lamellae	170 nm	750 MPa	[25]
Fe-36Ni	7 cycles at 500 °C	ultrafine lamellae	87 nm	780 MPa	[26]
cp-Ti	6 cycles at RT	ultrafine lamellae + equiaxed ultrafine grains	80–100 nm	892 MPa	[27]
Cu-71.9Ag (eutectic)	5 cycles at RT	ultrafine lamellae + shear bands	Ag: 30 nm Cu: 10 nm	(HV 208)	[28]
Ni+1100-Al multi-layer	7 cycles at RT	–	–	292 MPa	[10]
Zr+Cu	10 cycles at RT	ultrafine lamellae + shear bands, partial amorphization			[29]

seen only at the center of the sheet that corresponds to the bonded interface in the last ARB cycle. Figure 10.3 shows an optical microstructure of a plain low-carbon steel (JIS-SS400) ARB processed up to strain of 4.0 at RT. Sound one-body sheets were obtained even in steels processed at ambient temperature. The bonded interfaces expected to exist at positions indicated by the arrows in Fig. 10.3 are mostly invisible in spite of deep etching before observation, though

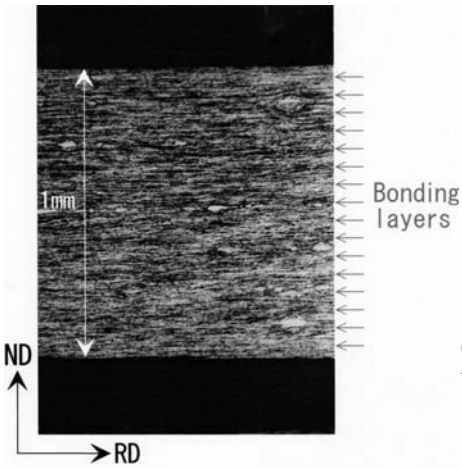

Fig. 10.3 Optical microstructure of the 0.13C steel (JIS-SS400) ARB-processed up to $\varepsilon = 4.0$ at RT. Observed from TD. The arrows indicate the expected positions of the bonded interfaces.

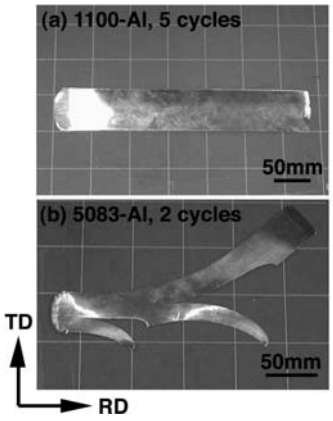

Fig. 10.4 Appearance of ARB-processed aluminum alloys sheets. (a) 1100-Al ARB-processed by 5 cycles ($\varepsilon = 4.0$) at RT. (b) 5083-Al ARB-processed by 2 cycles ($\varepsilon = 1.6$) at RT.

some inclusions that are presumably retained during wire brushing and stacking are observed along some interfaces. Concerning the microstructure, it has been found in aluminum that the thin regions near the bonded interfaces, the thickness of which is below 1 μm, show characteristic microstructures including both nanograins and oxide particles formed during wire brushing [35, 36].

A possible and rather serious problem in the ARB process is cracking during rolling in some hard materials. The typical appearance of the ARB processed aluminum alloys is shown in Fig. 10.4. In very ductile materials, such as pure aluminum, pure Cu and IF steel, almost no cracking occurred even after many cycles of the ARB. As a result, sound and large sheets filled with UFG structures could be obtained even in university laboratories. Figure 10.4 (a) is an example of the 1100-Al (99%Al) sheet ARB processed by 5 cycles ($\varepsilon = 4.0$) at RT, whose size is 1 mm thick, 55 mm wide and 320 mm long. On the other hand,

some kinds of materials considerably lose workability, as the strength increased with increasing number of ARB cycles (strain). An example of a severely cracked sheet of a 5083-Al (Al-4.7%Mg) ARB processed by 2 cycles ($\varepsilon = 1.6$) at RT is shown in Fig. 10.4 (b). The cracks generally start at side edges of the sheet due to tensile stress, and they sometimes propagate into the center of the sheet, as shown in Fig. 10.4 (b). The severe cracking tends to occur especially in high-strength aluminum alloys, such as 5000 and 7000 series. Once such cracking occurs, it is difficult to proceed to the next cycle. However, there are some techniques or know-how to avoid the cracking during roll bonding. As a result, the ARB process has been applicable to most of the metallic materials that can be rolled (Table 10.1).

10.3 Microstructure of ARB-processed Materials

Only one or two cycles of the ARB gives a normal plastic deformation corresponding to 50% or 75% rolling. Therefore, the microstructure after one or two cycles showed typical deformation microstructures composed of dislocation cells and subgrains [37]. Above three cycles, the lamellar boundary structure, which has been typically observed in heavily rolled materials [38], developed, and the materials ARB processed above five cycles were uniformly filled with the ultrafine lamellar boundary structure or the pancake-shaped UFGs. Together with this microstructural evolution, the mean misorientation of the deformation-induced boundaries increased with increasing strain [39]. The evolution of ultrafine microstructure during the ARB can be understood in terms of grain subdivision [37, 39]. It should be noted, however, that the evolution of microstructure and the increase in misorientation of boundaries in the ARB process were much faster than those in conventional rolling [39]. One of the main reasons for this quick grain subdivision in the ARB process is the additional shear strain due to friction between the rolls and the materials under the unlubricated roll-bonding condition [7, 21, 39].

A typical TEM micrograph of the ultrafine structure in the interstitial free (IF) steel ARB processed by 7 cycles ($\varepsilon = 5.6$) at 500 °C is shown in Fig. 10.5 (a). The microstructure is elongated along the rolling direction (RD). Because the ARB process was carried out at a temperature of 500 °C in this case, recovery and short range of grain-boundary migration turned the lamellar structure into a pancake-shaped grain structure [37]. For this microstructure, Kikuchi-line analysis was carried out in TEM. The misorientation map obtained from the accurate crystallographic analysis by the TEM/Kikuchi-line method is shown in Fig. 10.5 (b), where the high-angle grain boundaries with misorietation angles larger than 15° are drawn in bold lines and the misorientations in degrees are superimposed. It is clearly shown that most of the boundaries are high-angle grain boundaries, so that it is possible to consider that this is already a kind of ultrafine "grain" structure having large misorientations to each other. At the

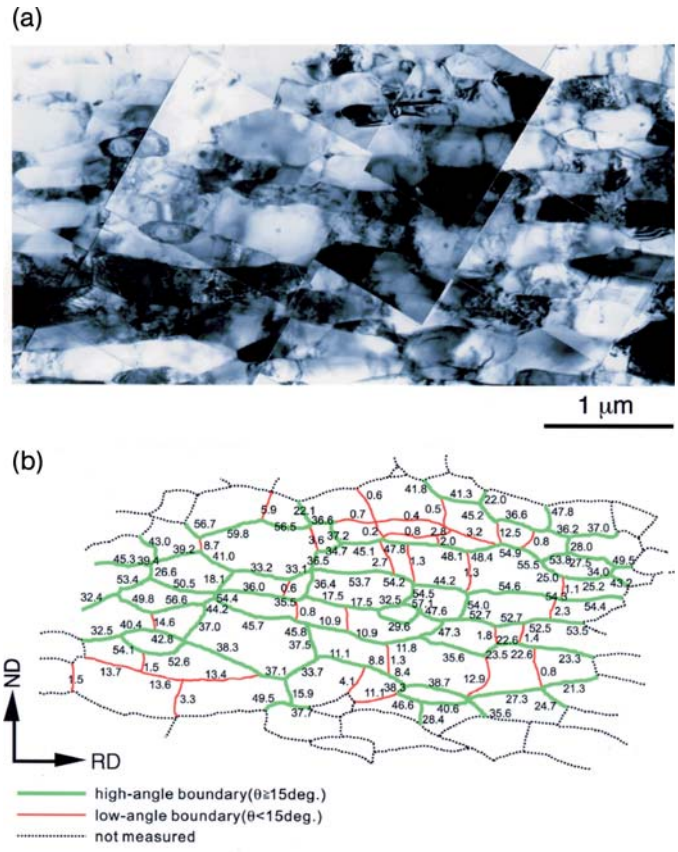

Fig. 10.5 TEM microstructure (a) and corresponding misorientation map (b) of the IF steel ARB-processed by 7 cycles ($\varepsilon = 5.6$) at 500 °C. Observed from TD.

same time, however, the as-ARB-processed materials have the character of deformation microstructures, because the microstructure is elongated along the direction of metal flow (RD) and there are many low-angle boundaries as well as some dislocations within the grains. Quite similar results have been obtained in pure Al as well [39].

It has been recently confirmed by detailed SEM/EBSD analysis that the ultrafine microstructure in the ARB-processed materials is quite uniform throughout the thickness of the sheets [21, 40]. Figure 10.6 shows the mean grain thickness of the pancake-shaped UFGs and the fraction of high-angle grain boundaries as a function of the thickness location in the IF steel ARB processed by 7 cycles ($\varepsilon = 5.6$) at 500 °C. The grain size is homogeneous around 200 nm and the fraction of high-angle boundaries is always above 75% throughout the thickness. Similar homogeneity has been confirmed in the ARB-processed pure Al, pure

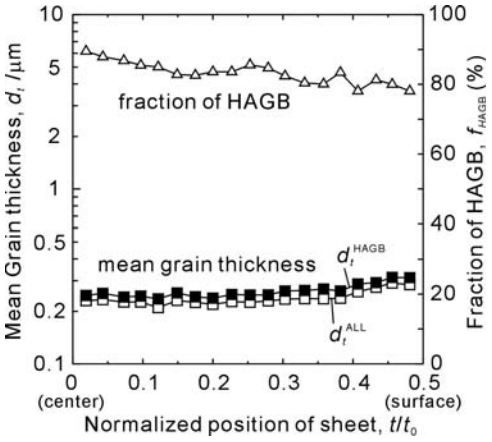

Fig. 10.6 Mean grain thickness and fraction of high-angle boundaries throughout the thickness of the UFG IF steel ARB processed by 7 cycles ($\varepsilon = 5.6$) at 500 °C.

Cu and Fe-36%Ni alloy [40]. It can be concluded, therefore, that the ARB is a promising SPD process to fabricate bulk sheets filled with UFG structure uniformly. On the other hand, the ARB-processed materials, especially those processed without lubrication, had a complicated distribution of texture through the thickness location [4, 7, 21, 40, 41]. This is due to the additional shear deformation caused by large friction between rolls and sheets and the repetition of cutting, stacking and rolling [7]. Roughly speaking, the sheets ARB-processed without lubrication have strong shear texture at subsurface regions, while the texture in the other parts is relatively weak [21].

As was shown in Table 10.1, the ultrafine grain size obtained by the ARB considerably differs depending on the alloy systems. Though the typical grain size obtained by the ARB process was several hundred nm, sometimes quite fine structures down to several tens of nm could be obtained. Basically, coarser microstructure was obtained in purer materials, probably due to the enhanced recovery including the short range of grain-boundary migration. The solute atoms [15] and low stacking-fault energy [20] seemed quite effective to refine the microstructure. The size of the microstructure decreased with increasing strain [39, 42], however, the rate of decrease became smaller and smaller and sometimes the grain size nearly saturated after a certain amount of strain. Since the formation of the ultrafine structure can be understood in terms of grain subdivision, the balance between the accumulation and annihilation of strain (dislocations) should be considered for the nanostructure evolution. The lower processing temperature, of course, resulted in finer structure. The effects of strain rate and strain path on the ultrafine grain subdivision are the remaining issues to be studied. When considering very high strain rates, it should be noted that the amount of heat generation due to plastic working is significant [42]. Especially

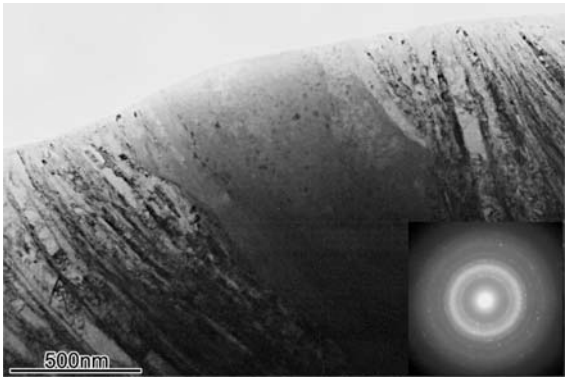

Fig. 10.7 TEM micrograph and a corresponding SAD pattern near a shear band in the specimen ARB-processed up to $\varepsilon = 13.7$. Observed from TD.

in the SPD of bulk materials, the heat generation due to large plastic working plays an important role in the microstructure evolution [42]. On the other hand, nanostructures down to several ten nm of grain sizes have been obtained in limited regions of the materials, such as surface, in various kinds of processing (wire brushing [35, 36], shot-peening [43, 44], sliding wear [45] and hot rolling [46]). In addition to the grain refinement, the ARB process can be also used as a bulk mechanical alloying process to fabricate nonequilibrium materials in bulk shape [28, 29, 47]. Figure 10.7 shows an example of the amorphous phase formed in the Cu/Zr multilayered sheets ARB-processed up to strain of 13.7 [29].

10.4 Mechanical Properties of the ARB-processed Materials

Figure 10.8 shows the engineering stress–strain curves of the materials ARB-processed by various cycles. Many materials show similar tendency of change in mechanical properties, which has been also reported in materials severely deformed by other processes such as ECAE [48]. In the case of the IF steel ARB-processed at 500 °C (Fig. 10.8 (a)), for example, the strength increased somewhat after only one cycle of the ARB, while the elongation greatly decreased. The strength continued to increase with increasing strain, and it reached 900 MPa after 7 cycles, which is 3.2 times higher than that of the starting materials. When the ARB process was conducted at ambient temperature, the strength became above 1 GPa in this material [49]. The elongation remained at nearly the same value or slightly decreased with increasing number of cycles. The commercial-purity aluminum (1100, Fig. 10.8 (c)) showed nearly the same tendency as the IF steel. The characteristic feature of the severely deformed materials is a

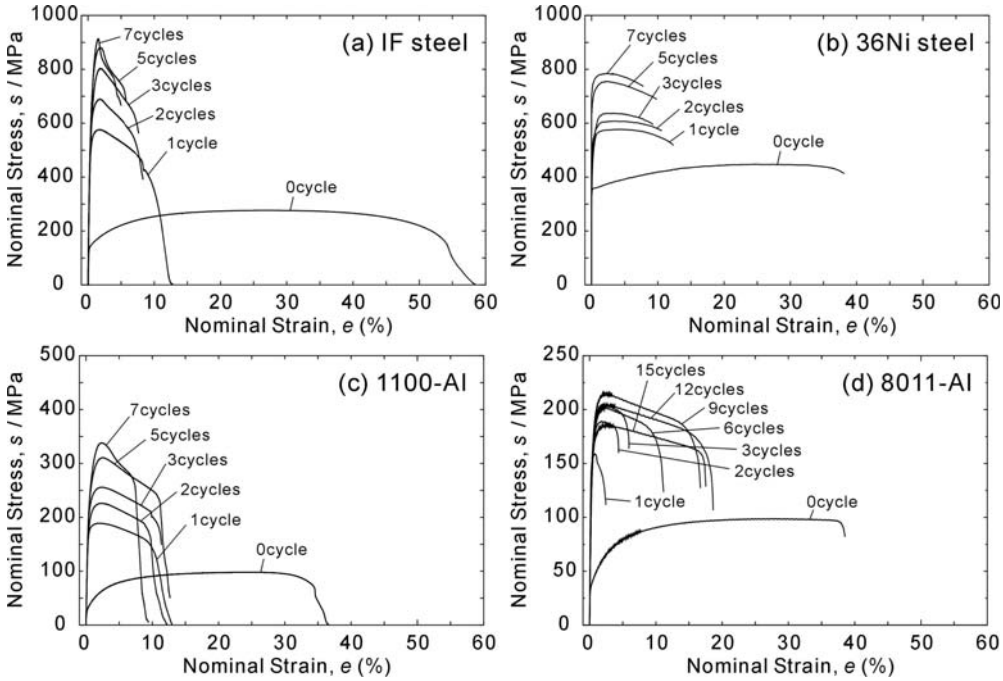

Fig. 10.8 Engineering (nominal) stress–strain curves of the various ARB-processed materials. (a) IF steel processed at 500°C. (b) 36 Ni steel processed at 500°C. (c) 1100-Al processed at RT. (d) 8011-Al processed at RT.

lack of uniform elongation. It is well known that work-hardened materials show limited ductility. Though the ARB-processed materials certainly exhibited UFG structures, they had a character of deformation microstructure, as was described before (Fig. 10.5). Therefore, it is not surprising that the as-ARB-processed materials performed limited ductility. The 36Ni steel, which had austenite (fcc) single phase, showed a similar change in mechanical properties to the ferritic (bcc) steel (IF steel) and pure aluminum. Strength increased with increasing strain and ductility rapidly decreased by 1 cycle of the ARB. However, the shapes of the stress–strain curves in the 36Ni were significantly different from the IF steel and pure aluminum. The 36%Ni exhibited a relatively large amount of uniform deformation, which was also observed in the ARB-processed Cu having similar stacking-fault energy [18]. This is probably because the austenite and Cu originally have large strain-hardening ability compared with ferrite and aluminum having high stacking-fault energies, avoiding the early plastic instability that will be discussed in the following section.

Subsequent annealing could change the microstructures of the ARB-processed materials [9, 22, 50, 51]. Figure 10.9 shows the TEM microstructures of the 1100-Al ARB-processed and then annealed at various temperatures [9]. During

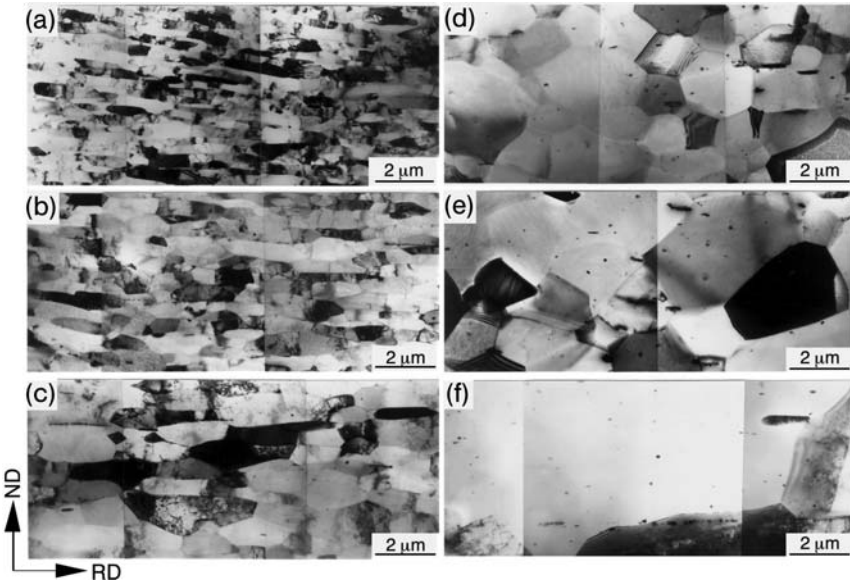

Fig. 10.9 TEM microstructures of the 1100 aluminum annealed for 1.8 ks at (a) 100 °C, (b) 150 °C, (c) 200 °C, (d) 225 °C, (e) 250 °C and (f) 300 °C after 6 cycles of ARB ($\varepsilon = 4.8$) at 200 °C. Observed from TD.

low-temperature annealing, recovery decreases the dislocation density inside the elongated ultrafine grains, and the ultrafine grains slightly grow. In the specimen annealed at 225 °C for 1.8 ks, equiaxed grains free of dislocations are observed. It is quite difficult to distinguish these grains from conventionally recrystallized grains. It should be noted, however, that the mean grain size is still around 1 μm, which cannot be achieved through a conventional deformation and recrystallization process. Further annealing causes normal grain growth, resulting in equiaxed grain structures having various mean grain sizes. A similar microstructural change has been observed in the ARB-processed IF steel [9]. Anyhow, it is possible to fabricate bulk sheets having various mean grain sizes ranging from 100 nm to 100 μm through an ARB and annealing process.

Figure 10.10 shows the stress–strain curves of commercial-purity aluminum (1100-Al) and ultralow carbon interstitial free (IF) steel specimens having various mean grain sizes [9]. Assuming uniform deformation, true stress and true strain are indicated in the figure. The specimens were fabricated by the ARB and subsequent annealing process. The flow stress of both materials increases with decreasing mean grain size. Once the mean grain size becomes smaller than 1 μm, elongation of both Al and Fe suddenly dropped, though the strength still increases with decreasing grain size. The stress–strain curves of the UFG specimens reveal similar shapes. The flow stress rapidly rises at the beginning of tensile tests and reaches the maximum at a plastic strain of a few per cent,

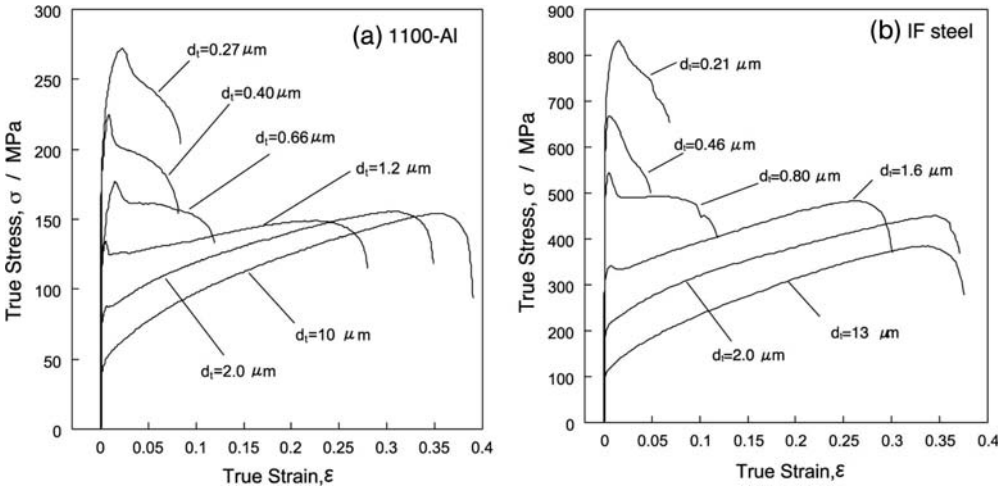

Fig. 10.10 True stress–true plastic strain curves of the 1100-Al (a) and IF steel (b) with various mean grain sizes fabricated by the ARB and subsequent annealing process.

followed by macroscopic necking toward fracture. That is, uniform elongation is especially limited to within a few per cent in the UFG Al and Fe, resulting in small total elongation below 10%. This is the typical tensile behavior of the UFG materials.

The limited uniform elongation of the UFG materials is simply understood in the following way [9, 52]. Equation (10.1) is the Considére criterion for plastic instability of rate-insensitive materials.

$$\sigma \geq \left(\frac{d\sigma}{d\varepsilon}\right) \tag{10.1}$$

Here, σ and ε are true stress and true strain, respectively, so that $(d\sigma/d\varepsilon)$ is the strain-hardening rate. When the strain-hardening rate coincides with the flow stress, plastic instability, in other words necking, starts in the tensile test, which determines the uniform elongation. Figure 10.10 shows that the flow stress, especially yield strength, greatly increases with decreasing mean grain size, as has been observed in typical grain-refinement strengthening. Generally speaking, the strain-hardening rate monotonously decreases as the tensile test proceeds. As a result, flow stress (σ) meets the strain-hardening rate ($d\sigma/d\varepsilon$) at smaller plastic strain when the strength of the material increases, which is schematically shown in Fig. 10.11. This is the basic mechanism for the decrease in the uniform elongation. Moreover, Fig. 10.10 indicates that the strain-hardening rate (slope of the true stress–strain curve) after macroscopic yielding also decreases with decreasing grain size, though the mechanism of this phenomenon is still unclear. Consequently, it is expected that the plastic instability condition

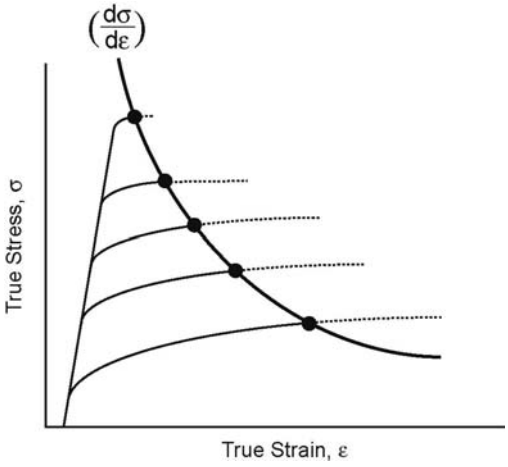

Fig. 10.11 Schematic illustration showing the decrease in the uniform elongation with increasing yield strength based on the plastic instability condition.

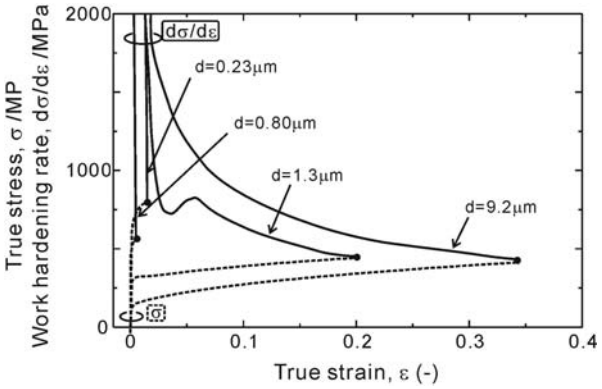

Fig. 10.12 True stress–true strain curves and work-hardening rate–true strain curves of the IF steel with various mean grain sizes fabricated by the ARB and subsequent annealing process.

expressed in Eq. (10.1) is achieved at a very early stage of the tensile test in the UFG Al and Fe, resulting in limited uniform elongation below a few per cent.

The strain-hardening rate of the IF steel specimens with various mean grain sizes was calculated from the actual stress–strain data and is shown together with the stress–strain curves in Fig. 10.12. In Fig. 10.12, the broken lines are the stress–strain curves, while the solid lines indicate the strain-hardening rate ($d\sigma/d\varepsilon$). It is clearly shown that the plastic instability is achieved at smaller strains as the grain size is finer. The point of plastic instability coincides well

with the value of the observed uniform elongation for each specimen. Additionally, the strain-hardening rate seems to become smaller with finer grain size at the same plastic strain. It can be concluded, anyhow, that the limited ductility (limited uniform elongation) of the UFG Al and Fe is explained in terms of early plastic instability.

It is noteworthy, however, that the UFG Al and Fe have fairly large local elongation (Fig. 10.10). It should be remembered that the original UFG specimen was made by rolling (ARB) without fracture. That is, the plasticity itself is not lost even in the UFG materials. They are plastically unstable only for tensile stress conditions. In that sense, it is not so surprising that nanocrystalline Cu was deformable in rolling [53]. Thus, it is expected that the UFG materials are applicable to some kinds of plastic working applications where tensile stress conditions are suppressed.

It was shown in the previous section that the limited uniform elongation in the UFG Al and ferritic steel is attributed to the high yield strength and lack of strain hardening in the UFG microstructures. It should be noted here that the strain-hardening ability in both Al with high stacking-fault energy FCC structure and ferritic Fe with BCC structure is originally low. The understanding based on Eq. (10.1) tells us that it is possible to increase the uniform elongation if the strain hardening rate ($d\sigma/d\varepsilon$) can be increased by any means. One of the possible ways to enhance strain hardening is to disperse fine second-phase particles within the matrix. Ueji et al. [54–56] have found a simple way to obtain a multiphased UFG microstructure in low-carbon steels without SPD. When the starting microstructure is Martensite, ultrafine ferrite grains with mean grain size of about 100 nm can be obtained only after conventional 50% cold rolling and subsequent annealing at around 500 °C [54]. Because Martensite in carbon-steels is a supersaturated solid solution of carbon, a number of fine carbides having nanometer dimensions precipitate homogeneously in the matrix during annealing. Figure 10.13 shows a typical example of the multiphased UFG steel (0.13%C plain low-C steel: JIS-SS400) fabricated by the Martensite method [54]. Nearly equiaxed ultrafine ferrite grains including nanocarbides are observed in most of the area. It has been clarified that most of the UFGs are surrounded by high-angle grain boundaries [55].

Stress–strain curves of the SS400 low-carbon steel (0.13%C) fabricated by the Martensite method are shown in Fig. 10.14. The specimens annealed at 500 °C or 550 °C show both high strength and adequate ductility. It is noteworthy that the 550 °C annealed specimen having the multiphased UFG structure like Fig. 10.13 exhibits tensile strength of 870 MPa, uniform elongation of 8% and total elongation of 20%. As the starting material (SS400) is a 400 MPa class steel, the strength more than doubled. Compared with the ferrite single-phased UFG steel (Fig. 10.10(b)), the stress–strain curve of the multiphased UFG steel clearly indicates strain hardening. The Considére criterion was again examined for the multiphased UFG steel fabricated by the Martensite method, and it was obviously shown that the strain-hardening rate increased by dispersing the nanocarbide within the UFG ferrite matrix. This way seems adaptive to other

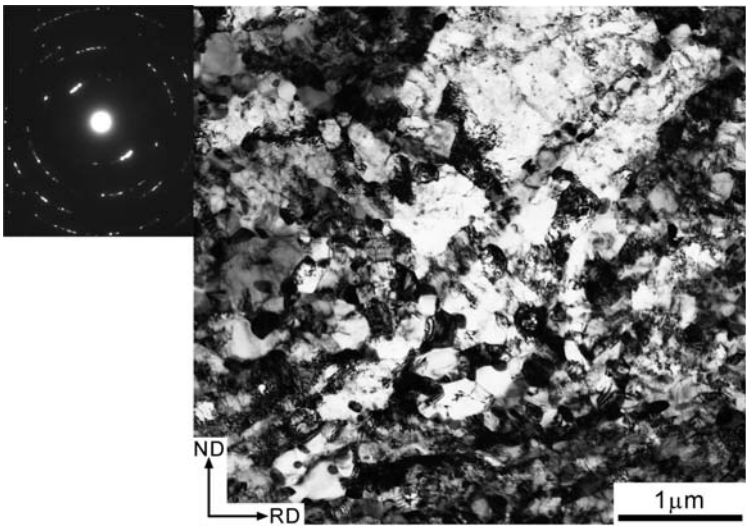

Fig. 10.13 Multiphased UFG structure in the 0.13%C steel (JIS-SS400). The specimen having Martensite starting phase was cold rolled by 50% and then annealed at 500 °C for 1.8 ks. Observed from TD.

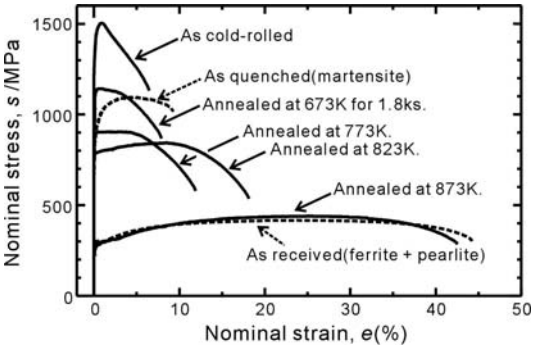

Fig. 10.14 Nominal stress–strain curves of the 0.13%C steel (SS400) 50% cold rolled and annealed at various temperatures for 1.8 ks. The starting microstructure was Martensite.

kinds of metals, such as Al alloys, since Horita et al. [57] recently reported that the Al-Ag alloy having nanoscale γ' particles within the UFG Al matrix shows both high strength and large elongation. It was also found by Zhao et al. [58] recently that the same strategy was effective in 7075 Al alloy including fine GP zones. It can be concluded now that to enhance strain hardening by dispersing fine second-phase particles is a promising way to prevent the occurrence of early plastic instability and to realize adequate ductility in UFG materials.

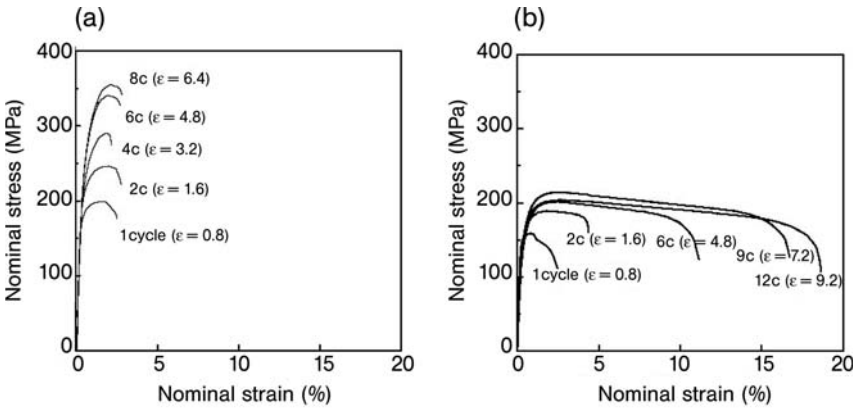

Fig. 10.15 Nominal stress–strain curves of the AA1100 (a) and AA8011 (b) alloys ARB-processed by various cycles at RT.

The way to increase the uniform elongation in the UFG materials was discussed in the former section. Another possibility to increase the substantial elongation in the SPD materials has been shown recently. Figure 10.15 shows the stress–strain curves of two kinds of Al alloys ARB-processed by various cycles at RT [14]. In the commercial-purity aluminum (AA1100), the strength monotonously increases with increasing number of the ARB cycle (strain). On the other hand, elongation greatly dropped only by one cycle, and it maintains nearly the same value. These are the typical changes in the mechanical properties of the SPD-processed materials not only in the case of ARB (Fig. 10.8) but also in case of other SPD processes like ECAP [48]. The AA8011 alloy (Al-0.17wt%Si-0.57wt%Fe-0.11wt%Cu), however, shows a unique behavior. The elongation of the AA8011 significantly decreases by 1 cycle of the ARB, similar to AA1100. However, total elongation of the AA8011 sheet increases with increasing number of the ARB cycles, and it reaches 18% after 12 cycles. This unique increase in ductility was first found by Kim et al. [14] only in the Al-Si-Fe system.

It should be noted that the stress–strain curves of the AA8011 do not show enhanced strain hardening but nearly a constant flow stress or rather negative slope after initial hardening. This suggests that the increase in ductility in this case is different from the case in the previous section that could be understood in terms of plastic instability. The strain-hardening analysis similar to Fig. 10.12 is again carried out for the AA8011 ARB-processed by 9 cycles. Here, the Hart criterion for strain-rate-sensitive materials,

$$\sigma\left(1-\left(\frac{\partial \log \sigma}{\partial \log \bar{\varepsilon}}\right)_{\bar{\varepsilon}}\right) \geq \left(\frac{\partial \sigma}{\partial \bar{\varepsilon}}\right)_{\bar{\varepsilon}} \tag{10.2}$$

is also investigated in addition to the Considére criterion (Fig. 10.16). The results do not show a significant difference between the two criteria and the

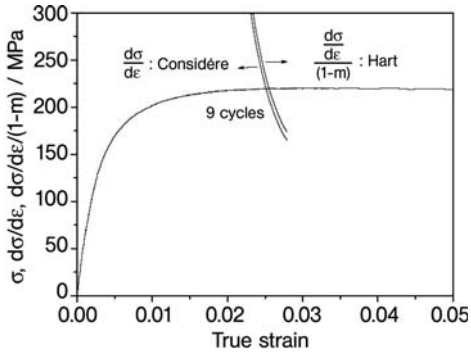

Fig. 10.16 True stress–true strain curves and work-hardening rate–true strain curves of the AA8011 alloy ARB-processed by 9 cycles at RT. Both Considére and Hart criteria are investigated.

strain-hardening rate curves meet the stress–strain curve at very small strain, around three per cent. This indicates that necking initiates at an early stage of tensile test as well as other kinds of ARB-processed materials like AA1100 but it does not develop locally. That is, the post-uniform elongation significantly increases as the SPD proceeds in the AA8011 alloy by any means. It is noteworthy that substantially uniform elongation is realized in the AA8011 alloy (Fig. 10.15 (b)) because the propagation of necking is so diffuse, which is thought to be advantageous for practical applications.

It has been also clarified that the strain-rate sensitivity of the AA8011 alloy increases with increasing number of ARB cycles [14]. The strain-rate sensitivity (so-called *m* value) of the starting sheet with conventional coarse-grained structure was about 0.01 but it reached 0.047 after the 8 ARB cycles [14]. It is phenomenologically known that such an increase in *m* value results in a significant improvement of the post-uniform elongation [59]. The increase in the strain-rate sensitivity is attributed to enhanced dynamic recovery caused by the increase in the density of high-angle grain boundaries with increasing strain [14]. High strength and large elongation in the as-ECAP-processed Cu reported by Valiev et al. [60] might be classified into this category. Another reason for the enhanced dynamic recovery in the Al-Si-Fe system is the relatively high purity of the matrix owing to the scavenging effect by addition of Si+Fe [14].

Besides the previous understanding described above, several unknown properties, such as surprisingly high strength and high ductility both managed in bimodal nanostructured Cu [52], have been found in the nanostructured materials. Recently, other unique phenomena, namely hardening by annealing and softening by deformation, were found in the ARB-processed pure aluminum. The details of these curious properties can be found in the original literature [61].

10.5 Conclusions

The details of the accumulative roll bonding (ARB), which is a severe plastic deformation process using rolling deformation were introduced. The microstructures and the mechanical properties of the ARB-processed materials were shown in detail. The advantages of the ARB process are applicability to bulk sheet materials and ease of installation without special equipments. The ARB can be applied to most of the workable metallic materials, and quite uniform ultrafine microstructures can be obtained after several cycles of the ARB. The ARB-processed materials have very high strength, but the uniform elongation is generally limited. The limited uniform elongation can be explained by lack of strain hardening, which points out directions for new materials design for the ultrafine microstructures with excellent mechanical properties.

Acknowledgement

This work was financially supported by the 21st Century COE Program (the Center of Excellence for Advanced Structural and Functional Materials Design) at Osaka University through MEXT Japan and the Industrial Technology Research Grant Program in 2005 from NEDO of Japan (project ID 05A27502d).

References

1 R. Z. Valiev, Y. Estrin, Z. Horita. T. G. Langdon, M. J. Zehetbauer, Y. Zhu **2006**, *JOM* 33–39.
2 N. Tsuji, Y. Saito, S. H. Lee, Y. Minamino, **2003**, *Adv. Eng. Mater.* 5, 338–344.
3 R. Z. Valiev, R. K. Islamgliev, I. V. Alexrov, **2000**, *Prog Mater. Sci.* 45, 103–189.
4 Y. Saito, N. Tsuji, H. Utsunomiya, T. Sakai and R. G. Hong, **1998**, *Scr. Mater.* 39, 1221–1227.
5 Y. Saito, H. Utsunomiya, N. Tsuji, T. Sakai, **1999**, *Acta Mater.* 47, 579–583.
6 R. F. Tylecote, **1968**, *The Solid Phase Welding of Metals*, Edward Arnold, London.
7 S. H. Lee, Y. Saito, N. Tsuji, H. Utsunomiya, T. Sakai, **2002**, *Scr. Mater.* 46, 281–285.
8 Y. Koizumi, M. Ueyama, N. Tsuji, Y. Minamino, **2003**, *J. Alloys Compd.* 355 47–51.
9 N. Tsuji, Y. Ito, Y. Saito, Y. Minamino, **2002**, *Scr. Mater.* 47, 893–899.
10 M. Ueyama, **2001**, Master Thesis, Osaka University.
11 N. Tsuji, K. Shiotsuki, Y. Saito, **1999**, *Mater. Trans. JIM* 40, 765–771.
12 S. H. Lee, Y. Saito, T. Sakai, H. Utsunomiya, N. Tsuji, **2000**, *Mater. Sci. Forum* 331–333, 1169–1174.
13 A. Tsuji, **2000**, Bachelor Thesis, Osaka University.
14 H. W. Kim, S. B. Kang, N. Tsuji, Y. Minamino, **2005**, *Acta Mater.* 53, 1737–1749.
15 N. Tsuji, T. Iwata, M. Sato, S. Fujimoto, Y. Minamino, **2004**, *Sci. Tech. Adv. Mater.* 5, 173–180.
16 N. Kamikawa, N. Tsuji, T. Sakai, Y. Minamino, **2004**, *Proc. of the 25th Riso Int. Symp. On Mater. Sci.*, Riso National Laboratory, Roskilde, Denmark, pp. 369–376.
17 S. H. Lee, T. Sakai, Y. Saito, H. Utsunomiya, N. Tsuji, **1999**, *Mater. Trans. JIM* 40, 1422–1428.
18 N. Tamaki, **2000**, Bachelor Thesis, Osaka University.

19 T. Sakai, Y. Saito, T. Kanzaki, N. Tamaki, N. Tsuji, **2001**, *J. JCBRA* 40, 213–217.
20 T. Nishiyama, **2002**, Master Thesis, Osaka University.
21 N. Kamikawa, N. Tsuji, Y. Minamino, **2004**, *Sci. Tech. Adv. Mater.* 5, 163–172.
22 N. Tsuji, S. Okuno, Y. Koizumi, Y. Minamino, **2004**, *Mater. Trans.* 45, 2272–2281.
23 N. Tsuji, R. Ueji, Y. Minamino, **2004**, *Trans. Mater. Res. Soc. Jpn.* 29, 3529–3532.
24 H. Koyama, **2003**, Bachelor Thesis, Osaka University.
25 H. Kitahara. T. Kimura, N. Tsuji, Y. Koizumi, Y. Minamino, **2004**, *Ultrafine Grained Materials III*, TMS, Ohio, pp. 369–374.
26 K. Inoue, N. Tsuji, Y. Saito, **2001**, *Proc. of the Int. Symp. On Ultrafine Grained Steels ISUGS–2001*, ISIJ, Tokyo, pp. 126–129.
27 D. Terada, S. Inoue, N. Tsuji, **2007**, *J. Mater. Sci.* 42, 1673–1681.
28 S. Ohsaki, **2006**, PhD Thesis, Tsukuba University
29 N. Tsuji, S. Kato, S. Ohsaki, K. Hono, Y. Minamino, **2005**, *J. Metastable Nanocryst. Mater.* 24–25, 643–646.
30 K. T. Park, H. J. Kwon, W. J. Kim, Y. S. Kim, **2001**, *Mater. Sci. Eng. A* 316, 145–152.
31 Z. P. Xing, S. B. Kang, H. W. Kim, **2001**, *Scr. Mater.* 45, 597–604.
32 C. P. Heason and P. B. Prangnell, **2002**, *Mater. Sci. Forum* 396–402, 429–434.
33 W. Q. Cao, Q. Liu, A. Godfrey, N. Hansen, **2002**, *Mater. Sci. Forum* 408–412, 721–726.
34 P. J. Hsieh, Y. P. Hung, J. C. Huang, **2003**, *Scr. Mater.* 49, 173–178.
35 M. Sato, N. Tsuji, Y. Minamino, Y. Koizumi, **2003**, *Mater. Sci. Forum* 426–432, 2753–2758.
36 M. Sato, N. Tsuji, Y. Minamino, Y. Koizumi, **2004**, *Sci. Tech. Adv. Mater.* 5, 145–152
37 N. Tsuji, R. Ueji, Y. Ito, Y. Saito, **2000**, *Proc. of the 21st Riso Int. Symp. on Mater. Sci.*, Riso National Laboratory, Roskilde, Denmark, pp. 607–616.
38 N. Hansen and D. Juul Jensen, **1999**, *Philos. Trans. R. Soc. Lond., A* 357, 1447–1469.
39 X. Huang, N. Tsuji, N. Hansen, Y. Minamino **2003**, *Mater. Sci. Eng. A* 340, 265–271.
40 B. L. Li, N. Tsuji, N. Kamikawa, **2006**, *Mater. Sci. Eng. A*, 423, No.1–2 331–342.
41 N. Tsuji, R. Ueji, Y. Minamino, **2002**, *Scr. Mater.* 47, 69–76.
42 N. Tsuji, T. Toyoda, Y. Minamino, Y. Koizumi, M. Kiritani, M. Komatsu, T. Yamane, **2003**, *Mater. Sci. Eng. A.* 350/1–2, 108–116.
43 N. R. Tao, Z. B. Wang, W. P. Tong, M. L. Sui, J. Lu, K. Lu, **2002**, *Acta Mater.* 50, 4603–4616.
44 M. Umemoto, Y. Todaka, K. Tsuchiya, **2003**, *Mater. Trans.* 44, 1488–1493.
45 D. A. Hughes and N. Hansen, **2001**, *Phys. Rev. Lett.* 87, 135501/1–135503/4.
46 G. M. Scamans, A. Afseth, G. E. Thompson, X. Zhou, **2002**, *Mater. Sci. Forum* 396–402, 1461–1466.
47 S. Ohsaki, S. Kato, N. Tsuji, T. Ohkubo, K. Hono, **2007**, *Acta Mater.* 55, 2885–2895
48 Z. Horita, M. Furukawa, K. Oh-ishi, M. Nemoto, T. G. Langdon, **1999**, *Proc. of the 4th Int. Conf. on Recrystallization and Related Phenomena, JIM* 301–308.
49 N. Kamikawa, **2006**, PhD Thesis, Osaka University.
50 Y. Ito, N. Tsuji, Y. Saito, H. Utsunomiya, T. Sakai, **2000**, *J. Jpn. Inst. Met.* 64, 429–437.
51 N. Tsuji, Y. Ito, H. Nakashima, F. Yoshida, Y. Minamino, **2002**, *Mater. Sci. Forum* 396–402, 423–428.
52 Y. Wang, M. Chen, F. Zhou, E. Ma, **2002**, *Nature* 419, 912–915.
53 L. Lu, M. L. Sui, K. Lu, **2000**, *Science* 287, 351.
54 N. Tsuji, R. Ueji, Y. Minamino, Y. Saito, **2002**, *Scr. Mater.* 46, 305–310.
55 R. Ueji, N. Tsuji, Y. Minamino, Y. Koizumi, **2002**, *Acta Mater.* 50, 4177–4189.
56 R. Ueji, N. Tsuji, Y. Minamino, Y. Koizumi, **2004**, *Sci. Tech. Adv. Mater.* 5, 153.
57 Z. Horita, K. Ohashi, T. Fujita, K. Kaneko, T. G. Langdon, **2005**, *Adv. Mater.* 17, 1599.
58 Y. H. Zhao, X. Z. Liao, S. Cheng, E. Ma, Y. T. Zhu **2006**, *Adv. Mater.* 18, 2280–2283.
59 R. H. Wagoner and J. L. Chenot, **1997**, *Fundamentals of Metal Forming*, John Wiley & Sons, Inc. 11.
60 R. Valiev, I. V. Alexrov, Y. T. Zhu, T. C. Lowe, **2002**, *J. Mater. Res.* 17, 5.
61 X. Huang, N. Hansen, N. Tsuji, **2006**, *Science* 312, 249–251.

11
Bulk Nanomaterials from Friction Stir Processing: Features and Properties

Rajiv S. Mishra

11.1
Introduction

Friction stir processing (FSP) is a relatively new solid-state microstructural modification technique. This processing technique can be viewed as a severe plastic-deformation technique because of the high processing strain involved. It is also unique from the viewpoint of its applicability to a localized region. In this chapter, the current state of understanding and development of FSP for processing of bulk nanomaterials are addressed. Much of the review is taken from two recent reviews on friction stir processing by the author [1, 2]. Particular emphasis has been placed on: (a) mechanisms responsible for the microstructural refinement, (b) effects of FSP parameters on resultant microstructure and final mechanical properties, and (c) addition of second phase in selective regions. The scope is this chapter is limited to aluminum alloys, although conceptually these results can be obtained for other metals and alloys.

Recently friction stir processing (FSP) was developed by Mishra et al. [3, 4] as a generic tool for microstructural modification based on the basic principles of friction stir welding (FSW), that was invented at The Welding Institute (TWI) of UK in 1991 as a solid-state joining technique, and it was initially applied to aluminum alloys [5, 6]. The details of FSW and the current status of the field has been recently reviewed by Mishra and Ma [1]. The basic concept of FSP is remarkably simple. A nonconsumable rotating tool with a specially designed pin and shoulder is inserted into the monolithic material to be processed and traversed along the line of interest to produce a processed volume (Fig. 11.1). The tool serves two primary functions: (a) heating of the workpiece, and (b) movement of material to produce the microstructural modification. The heating is accomplished by friction between the tool and the workpiece and plastic deformation of the workpiece. The localized heating softens the material around the pin and combination of tool rotation and translation leads to movement of material from the front of the pin to the back of the pin. As a result of this process a joint is produced in "solid state". Because of various geometrical features of the tool, the material movement around the pin can be quite complex [7]. During

Bulk Nanostructured Materials. Edited by M. J. Zehetbauer and Y. T. Zhu

ISBN: 978-3-527-31524-6

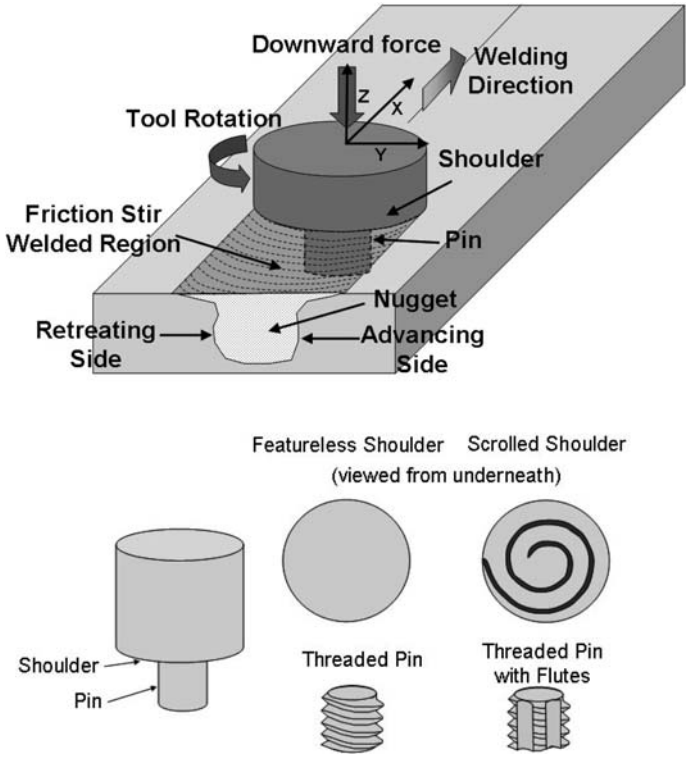

Fig. 11.1 Schematic drawing of friction stir welding process and friction stir welding tools.

the FSP process, the material undergoes intense plastic deformation at elevated temperature, resulting in generation of fine and equiaxed recrystallized grains [8–11]. The fine microstructure in the friction stirred region produces specific property enhancement. For example, high strain rate superplasticity was obtained in commercial 7075Al alloy by FSP [3, 12]. Furthermore, the FSP technique has been used to produce surface composite on aluminum substrate [13], homogenization of powder metallurgy aluminum alloy [14], microstructural modification of metal matrix composites [15] and property enhancement in cast aluminum alloys [16].

In order to perform FSP, the processing tool must be given two basic parameters: tool rotation rate (ω, rpm) in clockwise or counterclockwise direction and tool traverse speed (v, mm/min) along the traverse direction. As mentioned earlier, the rotation of the tool results in stirring and mixing of material around the rotating pin and the translation of tool moves the stirred material from the front to the back of the pin and finishes the microstructural modification process. Higher tool rotation rates generate higher temperatures because of higher friction heating and results in more intense stirring and mixing of material as will be discussed later. However, it should be noted that frictional coupling of

tool surface with the workpiece is going to govern the heating. So, a monotonic increase in heating with increasing tool rotation rate is not expected as the coefficient of friction at the interface will change with increasing tool rotation rate.

In addition to the tool rotation rate and traverse speed, another important process parameter is the angle of spindle or tool tilt with respect to the workpiece surface. A suitable tilt of the spindle towards trailing direction ensures that the shoulder of the tool holds the stirred material by the threaded pin and consolidates material effectively at the trailing side of the shoulder. Further, the insertion depth of pin into the workpiece (also called target depth) is important for producing sound welds or processed zones with smooth tool shoulders. For addition of second-phase particles this can be critical. It should be noted that the recent development of a "scrolled" tool shoulder allows FSP with 0° tool tilt (Fig. 11.1).

11.2 Temperature Distribution

For producing bulk nanomaterials using FSP, the most important factor is to control the temperature. However, temperature must be kept high enough to produce defect-free consolidation of sheared or stirred layers behind the pin. As mentioned earlier, FSP results in intense plastic deformation around the rotating tool and friction between the tool and workpieces. Both these factors contribute to the temperature increase within and around the stirred zone. Since the temperature distribution within and around the stirred zone directly influences the microstructure of the welds, such as grain size, grain-boundary character, coarsening and dissolution of precipitates, and resultant mechanical properties of the welds, it is important to obtain information about temperature distribution during FSP. The control of temperature is critical for maintaining ultrafine-grained microstructure. This can be achieved by (a) controlling the process parameters, and/or (b) tool geometry. The temperature measurements within the stirred zone are very difficult due to the intense plastic deformation produced by the rotation and translation of tool. Therefore, the maximum temperatures within the stirred zone during FSW/P have been either estimated from the microstructure of the weld [8, 9, 17] or recorded by embedding thermocouples in the regions adjacent to the rotating pin [18, 19].

Mahoney et al. [18] conducted friction stir welding of 6.35-mm thick 7075Al-T651 plate and measured the temperature distribution around the stirred zone both as a function of distance from the stirred zone and through the thickness of the sheet. Figure 11.2 shows the peak temperature distribution adjacent to the stirred zone. Maximum temperature was recorded at the locations close to the stirred zone, i.e. the edge of the stirred zone, and the temperature decreased with increasing distance from the stirred zone. A maximum temperature of 475 °C was recorded near the corner between the edge of the stirred zone and the top surface. The temperature at the edge of the stirred zone increased from

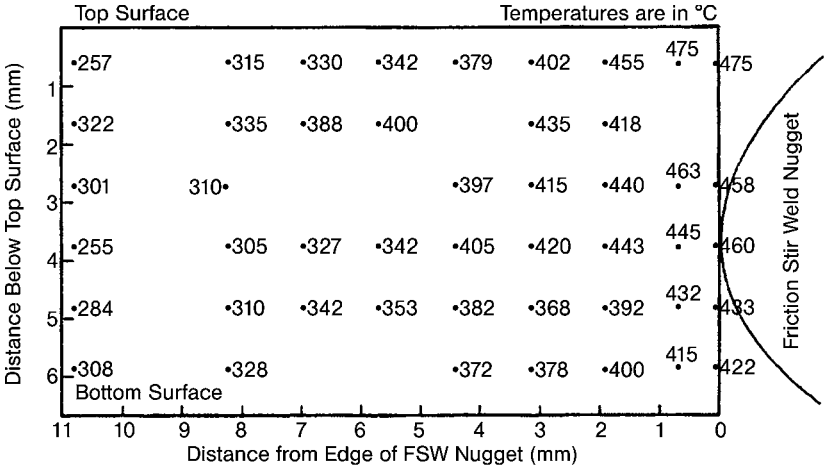

Fig. 11.2 Peak temperature distribution adjacent to a friction stir weld in 7075Al-T651 (after Mahoney et al. [18]).

the bottom surface of the plate to the top surface. Based on these results the temperature within the stirred zone is likely to be above 475 °C. However, the maximum temperature within the stirred zone should be lower than the melting point of 7075Al because no evidence of material melting was observed in the weld [8, 18].

In a recent investigation, a numerical three-dimensional (3D) heat-flow model for friction stir welding of age hardening aluminum alloy has been developed by Frigaard et al. [20], based on the method of finite differences. The average heat input per unit area and time according to their model is [20],

$$q_0 = \frac{4}{3}\pi^2 \mu P N R^3 \tag{11.1}$$

where, q_0 is the net power (W), μ is the friction coefficient, P is the pressure (Pa), N is the tool rotational speed (rot/s) and R is the tool radius (m). Frigaard et al. [20] suggested that the tool rotation rate and shoulder radius are the main process variables in FSW/P, and the pressure P cannot exceed the actual flow stress of the material at the operating temperature if a sound weld without depressions is to be obtained. The process model was compared with *in-situ* thermocouple measurements in and around the FSW zone. FSW of 6082Al-T6 and 7108Al-T79 was performed at constant tool rotation rate of 1500 rpm and a constant welding force of 7000 N, at three welding speeds of 300, 480, and 720 mm/min. They reported a peak temperature of above ~500 °C in the FSW zone. The peak temperature decreased with increasing traverse speeds from 300 to 720 mm/min. The effect of FSW parameters on the temperature of the FSW process was further examined by Arbegast and Hartley [21]. They reported that for a given tool geometry and depth of penetration, the maximum temperature

was observed to be a strong function of the rotation rate (ω, rpm), while the rate of heating was a strong function of the traverse speed (v, ipm). It was also noted that there was a slightly higher temperature on the advancing side of the joint where the tangential velocity vector direction was the same as the forward velocity vector. They measured the average maximum temperature on 6.35 mm aluminum plates as a function of the pseudo-"heat index $w(w = \omega^2/v)$". It was demonstrated that for several aluminum alloys a general relationship between maximum welding temperature (T, °C) and FSW parameters (ω, v) can be explained by

$$\frac{T}{T_m} = K\left(\frac{\omega^2}{v \times 10^4}\right)^a \tag{11.2}$$

where the exponent a was reported to range from 0.04 to 0.06, the constant K is between 0.65 and 0.75, and T_m (°C) is the melting point of the alloy. The maximum temperature observed during FSW of various aluminum alloys is found to be between 0.6 T_m and 0.9 T_m, which is within the hot working temperature range for those aluminum alloys. Furthermore, the temperature range is generally within the solution heat-treatment temperature range of precipitation-strengthened aluminum alloys.

11.3 Microstructural Evolution

The contribution of intense plastic deformation and high-temperature exposure within the stirred zone during FSW/FSP results in the occurrence of recrystallization and development of texture within the stirred zone [11, 12, 17, 18, 22–30]. Based on microstructural characterization of grains and precipitates, three distinct zones, stirred (nugget) zone, thermomechanically affected zone (TMAZ), and heat-affected zone (HAZ), have been identified as shown in Fig. 11.3. The microstructural changes in various zones exert a significant effect on postweld mechanical properties. Therefore, the microstructural evolution during FSW/FSP has been studied by a number of investigators.

Fig. 11.3 A typical macrograph showing various microstructural zones in FSP 7075Al-T651 (standard threaded pin, 400 rpm and 51 mm/min).

11.3.1 Nugget Zone

Intense plastic deformation and frictional heating during FSW/FSP result in generation of a recrystallized fine-grained microstructure within the stirred zone. This region is usually referred to as the nugget zone (or weld nugget) or dynamically recrystallized zone (DXZ). Under some FSW/FSP conditions, an onion-ring structure was observed in the nugget zone. In the interior of the recrystallized grains, usually there is low dislocation density [8, 9]. The interface between the recrystallized nugget zone and the parent metal is relatively diffuse on the retreating side of the tool, but quite sharp on the advancing side of the tool [31].

11.3.2 Shape of Nugget Zone

Depending on processing parameter, tool geometry, temperature of workpiece, and thermal conductivity of the material, various shapes of nugget zone have been observed. Basically, the nugget zone can be classified into two types, a basin-shaped nugget that widens near the upper surface and an elliptical nugget. Sato et al. [19] reported the formation of a basin-shaped nugget on friction stir welding of 6063Al-T5 plate. They suggested that the upper surface experiences extreme deformation and frictional heating by contact with a cylindrical-tool shoulder during FSW, thereby resulting in generation of a basin-shaped nugget zone. On the other hand, Rhodes et al. [8] and Mahoney et al. [18] reported an elliptical nugget zone in the weld of 7075Al-T651.

Recently, an investigation was conducted on the effect of FSP parameter on the microstructure and properties of cast A356 [32]. The results indicated that a lower tool rotation rate of 300–500 rpm resulted in generation of a basin-shaped nugget zone, whereas an elliptical nugget zone was observed by FSP at higher tool rotation of >700 rpm. This indicates that with same tool geometry, different nugget shapes can be produced by changing processing parameters.

11.3.3 Grain Size

It is well accepted that the dynamic recrystallization during FSW/FSP results in generation of fine and equiaxed grains in the nugget zone [11, 12, 17, 18, 22–30]. FSW/FSP parameters, tool geometry, composition of workpiece, temperature of the workpiece, vertical pressure, and active cooling exert significant influence on the size of the recrystallized grains in the FSW/FSP materials. While the typical recrystallized grain size in the FSW/FSP aluminum alloys is in the micrometer range, ultrafine-grained (UFG) microstructures (average grain size $<1\ \mu m$) have been achieved by using external cooling or special tool geometries (Table 11.1).

Table 11.1 A summary of ultrafine-grained microstructures produced via FSW/FSP in aluminum alloys.

Material	Plate thickness, mm	Tool geometry	Special cooling	Rotation rate, rpm	Traverse speed, mm/min	Grain size, μm	Ref.
2024Al-T4	6.5	Threaded cylindrical	Liquid nitrogen	650	60	0.5–0.8	[11]
1050Al	5.0	Conical pin without thread	N/A	560	155	0.5	[33–35]
7050 Al	1	N/R	Dry ice, Isopropyl alcohol	200–500	N/A	0.025–0.1	[36]
7075Al	2	N/R	Water, Methanol, Dry ice	1000	120	0.1	[37]
Cast Al-Zn-Mg-Sc	6.7	Threaded cylindrical	N/A	400	25.4	0.68	[38, 39]
6061 Al	3.2	Cylindrical, 12.7 and 19.1 mm shoulder	Water	1000	76.2	0.2	[40]
Al-4Mg-1 Zr	N/R	Cylindrical threaded	N/A	600	25.4	0.7	[41]
7075 Al	N /R	Cylindrical, 1.9 mm pin	Water, Methanol, Dry ice	1000	120	0.1– 0.5	[42]

Benavides et al. [11] investigated the effect of the workpiece temperature on the grain size of FSW 2024Al. They [11] reported that decreasing the starting temperature of the workpiece from 30 to –30 °C with liquid-nitrogen cooling resulted in a decrease in the peak temperature from 330 to 140 °C at a location 10 mm away from the weld centerline, thereby leading to a reduction in the grain size from 10 to 0.8 μm in FSW 2024Al. Following the same principles, Su et al. [37] prepared bulk nanostructured 7075Al with an average grain size of ~100 nm via FSP, using a mixture of water, methanol and dry ice for cooling the plate rapidly behind the tool. On the other hand, Kwon et al. [33–35] adopted a cone-shaped pin with a sharpened tip to reduce the amount of frictional heat generated during FSP of 1050Al. A peak temperature of only 190 °C was recorded in the FSP zone at a tool rotation rate of 560 rpm and a traverse speed of 155 mm/min, which resulted in a grain size of 0.5 μm. Similarly, Charit and Mishra [38, 39] reported that a grain size of 0.68 μm was produced, by using a small diameter tool with normal threaded pin, in FSP of cast Al-Zn-Mg-Sc at a tool rotation rate of 400 rpm and a traverse speed of 25.4 mm/min. These observations are consistent with the general principles for recrystalliza-

tion [43] where the recrystallized grain size decreases with decreasing annealing temperature.

More recently, Li et al. [23], Ma et al. [12], Sato et al. [44], and Kwon et al. [33–35] studied the influence of processing parameter on the microstructure of FSW/FSP aluminum alloys. It was noted that the recrystallized grain size can be reduced by decreasing the tool rotation rate at a constant tool traverse speed [23, 33–35, 44] or decreasing the ratio of tool rotation-rate/traverse-speed [12]. For example, Kwon et al. [33–35] reported that FSP resulted in generation of the grain size of ~0.5, 1–2, and 3–4 μm in 1050Al at tool rotation rates of 560, 980, 1840 rpm, respectively, at a constant traverse speed of 155 mm/min. Similarly, Sato et al. [44] reported the grain size of 5.9, 9.2, and 17.8 μm in FSW 6063Al at tool rotation rates of 800, 1220, 2450 rpm, respectively, at a constant traverse speed of 360 mm/min. Decreasing the ratio of tool rotation-rate/traverse-speed from 400 rpm/102 mm/min to 350 rpm/152 mm/min resulted in a decrease in the recrystallized grain size from 7.5 to 3.8 μm [12]. FSW/P at higher tool rotation rate or higher ratio of tool rotation-rate/traverse-speed results in an increase in both degree of deformation and peak temperature of thermal cycle. The increase in the degree of deformation during FSW/FSP results in a reduction in the recrystallized grain size according to the general principles of recrystallization [43]. On the other hand, the increase in peak temperature of FSW/FSP thermal cycle leads to generation of coarse recrystallized grains, and also results in remarkable grain growth. A recent investigation on FSP 7050Al has revealed that the initial size of newly recrystallized grains is on the order of 25–100 nm [36]. When heated for 1–4 min at 350–450 °C, these grains grow to 2–5 μm, a size equivalent to that found in FSP aluminum alloys [36]. Therefore, the variation of recrystallized grain size with tool rotation rate or traverse speed in FSW/FSP aluminum alloys depends on which factor is dominant. The investigations on FSP 1050Al and 7075Al-T651 appear to indicate that the peak temperature of the FSW/FSP thermal cycle is the dominant factor in determining the recrystallized grain size. Thus, the recrystallized grain size in the FSW/FSP aluminum alloys generally increases with increasing tool rotation rate or increasing ratio of tool rotation-rate/traverse-speed. Figure 11.4 shows the variation of grain size with the pseudo-heat index in 2024Al and 7075Al [1]. It shows that there is an optimum combination of tool rotation rate and traverse speed for generating

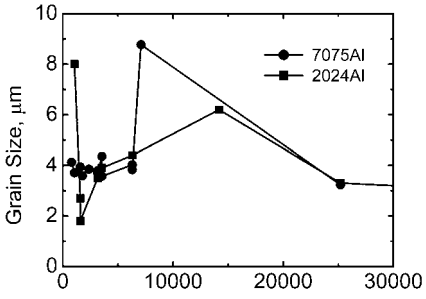

Fig. 11.4 Variation of grain size with pseudo-heat index [1]. Note that the grain size does not monotonically increase with increasing heat index.

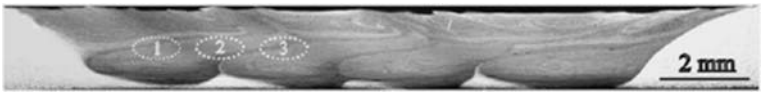

Fig. 11.5 Macroimage of FSP 7075 Al after 4 passes with average grain size of ~250 nm (after Su et al. [48]).

the finest grain size in a specific aluminum alloy with same tool geometry and temperature of the workpiece.

The grain size within the weld zone tends to increase near the top of the weld zone and it decreases with distance on either side of the weld-zone centerline, and this corresponds roughly to the temperature variation within the weld zone [18, 23, 45]. For example, Mahoney et al. [46] reported a variation in grain size from the bottom to the top as well as from the advancing to the retreating side in a 6.35-mm thick FSP 7050Al. The average grain size ranges from 3.2 μm at the bottom to 5.3 μm at the top and 3.5 μm from the retreating side to 5.1 μm on the advancing side. Similarly, in a 25.4-mm thick plate of FSW 2519Al, it was found that the average grain sizes were 12, 8 and 2 μm, respectively, in the top, middle, and bottom region of the weld nugget [47]. Such variation in grain size from bottom to top of the weld nugget is believed to be associated with the difference in temperature profile and heat dissipation in the nugget zone. Because the bottom of workpieces is in contact with the backing plate, the peak temperature is lower and the thermal cycle is shorter compared to the nugget top. The combination of lower temperature and shorter excursion time at the nugget bottom effectively retards the grain growth and results in smaller recrystallized grains. It is evident that with increasing plate thickness, the temperature difference between the bottom and top of the weld nugget increases, resulting in increased difference in grain size. Recently, Su et al. [48] produced large area with ~250 nm grain size (Fig. 11.5). The influence of friction stir zone shape on the bottom region profile can be noted. As mentioned earlier, this shape can be controlled by the process parameter, but some variability should be expected.

11.3.4 Recrystallization Mechanisms

A discussion of recrystallization mechanisms and the applicability to FSP has been reviewed in references [1, 2] and readers are encouraged to read these references. Very briefly, several mechanisms have been proposed for dynamic recrystallization process in aluminum alloys, such as discontinuous dynamic recrystallization (DDRX), continuous dynamic recrystallization (CDRX), and geometric dynamic recrystallization (GDRX) [43]. Aluminum and its alloys normally do not undergo DDRX because of their high rate of recovery due to aluminum's high stacking-fault energy. As for dynamic nucleation process in the nugget zone of FSW aluminum alloys, CDRX [24, 27, 49], DDRX [36, 37, 44],

GDRX [20, 50], and DRX in the adiabatic shear bands [51] have been proposed to be possible mechanisms. Jata and Semiatin [10] were the first to propose CDRX as operative dynamic nucleation mechanism during FSW. They suggested that low-angle boundaries in the parent metal are replaced by high-angle boundaries in the nugget zone by means of a continuous rotation of the original low-angle boundaries during FSW. In their model, dislocation glide gives rise to a gradual relative rotation of adjacent subgrains. Similarly, Heinz and Skrotzki [24] also proposed that CDRX is operative during FSW/FSP. In this case, strain induces progressive rotation of subgrains with little boundary migration. The subgrain rotation process gradually transforms the boundaries to high-angle grain boundaries.

However, it is important to point out that many of the recrystallized grains in the nugget zone are finer than the original subgrain size. Thus, it is unlikely that the recrystallized grains in the nugget zone result from the rotation of original elongated subgrains in the base metal. Rhodes et al. [36] obtained recrystallized grains of 25–100 nm in FSP 7050Al-T76 by using a "plunge and extract" technique and rapid cooling. These recrystallized grains were significantly smaller than the pre-existing subgrains in the parent alloy, and identified as nonequilibrium in nature, predominantly high angled, relatively dislocation free. Su et al. [37] and Rhodes et al. [36] proposed that DDRX mechanism is responsible for the nanostructure evolution. The fact that recrystallized grains in the nugget zone of FSW/P aluminum alloys are significantly smaller than the pre-existing subgrains in the parent alloy strongly suggests that DDRX is the operative mechanism for recrystallization during FSW/P of aluminum alloys.

11.4 Superplasticity in FSP Ultrafine Grained Materials

As presented in Section 11.3.3, FSW/P results in generation of ultrafine-grained microstructure of <1 μm in various aluminum alloys. As emphasized by Mishra et al. [3, 4], this microstructure is ideal for superplasticity. Recently, Charit et al. [39] and Ma et al. [41] examined the effect of FSP on superplastic deformation behavior of ultrafine-grained aluminum alloys. These studies found exceptional high strain rate superplasticity (HSRS) and low-temperature superplasticity. For example, optimum ductility of 1165% at a strain rate of 3×10^{-2} s^{-1} and 310 °C was obtained [39]. This demonstrated the effectiveness of FSP for processing ultrafine-grained materials that are amenable to HSRS. Figure 11.6 (a) shows the stress–strain curves at various temperatures and an initial strain rate of 10^{-2} s^{-1} for the FSP alloy. With increasing temperature the flow stress falls down consistently until 410 °C, when an abrupt increase in the flow stress occurs due to abnormal grain growth (AGG). Also, the effect of increasing strain rate on the flow behavior at 310 °C is shown in Fig. 11.6 (b). The FSP alloys show enhanced superplastic deformation kinetics. For example, the superplastic behavior of FSP 7075Al and Al-4Mg-1Zr can be described by a united equation:

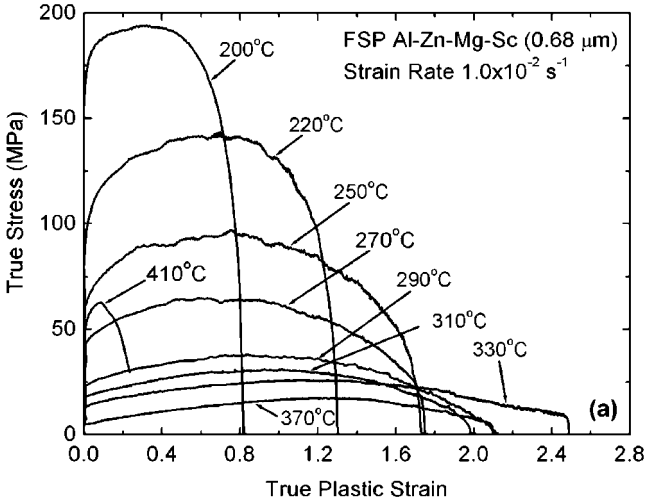

Fig. 11.6 Stress–strain curves of ultrafine grained FSP Al-Zn-Mg-Sc alloy, (a) at an initial strain rate of 10^{-2} s^{-1}, and (b) at a temperature of 310 °C [39].

$$\dot{\varepsilon} = 700\frac{D_0 Eb}{kT}\exp\left(\frac{-84000}{RT}\right)\left(\frac{b}{d}\right)^2\left(\frac{\sigma}{E}\right)^2 \tag{11.3}$$

where $\dot{\varepsilon}$ is the strain rate, D_0 is the pre-exponential constant for diffusivity, E is the Young's modulus, b is the Burger's vector, k is the Boltzmann's constant, T is the absolute temperature, R is the gas constant, d is the grain size, σ is the applied stress, and σ_0 is the threshold stress. The dimensionless constant of 700 in Eq. (11.3) is more than one order of magnitude larger than that the value of 40. As analyzed by Mishra et al. [52], the dimensionless contact of 40 is applicable for conventionally processed aluminum alloys. Ma et al. [12, 28] attributed the enhanced deformation kinetics in the FSP aluminum alloys to the high per cent of high-angle boundaries produced by friction stir processing [3].

It should be pointed out that the basic requirement of fine grain size is a necessary but not always sufficient condition to obtain superplasticity. If the fine grain microstructure is not stable at high temperature, superplastic elongation will be significantly reduced. A recent investigation showed that FSP 7475Al exhibited no superplastic elongation due to abnormal grain growth at high temperatures, though this alloy had a very fine original grain size of 2–3 μm [30]. Similarly, abnormal grain growth was also observed at high temperature in FSP 7050 and 2519 aluminum alloys [53]. The thermal stability in FSP 7075Al alloy and Al-4Mg-1Zr alloy was attributed to the effective pinning of grain growth by fine Cr-bearing dispersoids and $MgZn_2$-type precipitates, and Al_3Zr dispersoids, respectively. Therefore, it is important to understand the effect of alloy chemis-

try, FSP parameters on the thermal stability of fine microstructure of FSP aluminum alloys.

11.5
FSP for Surface Composite Fabrication and Microstructural Homogenization

Compared to unreinforced metals, metal-matrix composites (MMCs) reinforced with ceramic phases exhibit high strength, high elastic modulus, and improved resistance to wear, creep and fatigue. These properties make MMCs promising structural materials for aerospace and automobile industries. However, MMCs also suffer from a great loss in ductility and toughness due to incorporation of nondeformable ceramic reinforcements, and are relatively costly. These restrictions limit their wider application. For many applications, the useful life of components often depends on surface properties such as wear resistance. In these situations, only the surface layer needs to be reinforced by ceramic phases while the bulk of the component should retain the original composition and structure with higher toughness. There is also an emphasis on added functionality. For example, a structural component can be designed to serve additional nonstructural functions. This approach has the possibility of integrating subsystems.

The existing processing techniques for forming surface composites are based on liquid phase processing at high temperatures. In this case, it is hard to avoid an interfacial reaction between the reinforcement and metal matrix and the formation of some detrimental phases. Furthermore, critical control of processing parameters is necessary to obtain the ideal solidified microstructure in the surface layer. Obviously, if processing of a surface composite is carried out at temperatures below the melting point of the substrate, the problems mentioned above can be avoided. In the last five years, attempts have been made to use FSP to incorporate ceramic particles into the surface layer of aluminum alloys to form a surface composite [13, 54, 62], as well as to modify the powder metallurgy processed alloys and composites [14, 63–67].

11.5.1
Localized Surface Modification

Localized surface modifications can be a very powerful tool to achieve the right combination of properties, i.e. a gradient of properties within a monolithic structure. The potential exists to broaden design possibilities using metal matrix composites surfaces. The short thermal cycle and relatively low temperature during FSP can help to avoid or eliminate reaction products. Table 11.2 provides a summary of various efforts to date [13, 54, 62]. The initial results are very encouraging and clearly demonstrate the viability of FSP.

Table 11.2 A summary of surface modification and *in-situ* composite efforts.

Material system	Remarks
5083 Al-SiC (Mishra et al. 2003) [13]	SiC particles were put on the surface and stirred into the matrix.
A356 Al-SiC (Ma and Mishra 2003) [56]	SiC particles were put on surface and stirred into the matrix.
7050 Al-WC (Newkirk et al. 2003) [57]	WC particles were put a machined surface slot and stirred.
1100 Al-SiO_2 and TiO_2 (Howard et al. 2005) [55]	Introduced the concept of reaction processing during FSP. The reaction product was placed subsurface with a three-layer setup and friction stir processed.
7050 Al and 6061 Al-WC, SiC, Al_2O_3, MoS_2, Fe, Zn, Cu (Ramadorai et al. 2005) [58]	Powders were placed in subsurface drilled holes. The hole geometry provided good control of the volume fraction. A number of ceramic and metallic phases were explored, including a combination of SiC and MoS2.
AZ61-SiO2 (Lee et al. 2006) [59, 60]	Distributed nanoparticles by using repeated runs.
Al-SWCNT (Johannes et al. 2006) [61]	Demonstrated the survivability of single-wall carbon nanotubes (SWCNT) during FSP. The nanotubes were placed subsurface by drilling a hole from top and using a plug.
AZ31-MWCNT (Morisada et al. 2006) [54]	Multiwall carbon nanotubes (MWCNT) were distributed in a Mg alloy.
Al-NiTi (Dixit et al. 2006) [62]	Shape-memory alloy (NiTi) was distributed using the hole method without any interfacial reaction with Al.

Figures 11.7 (a) and (b) show examples of SiC distributed using the surface addition method [13, 56]. The uniform SiC distribution is demonstrated and a reaction and defect-free composite/matrix interface illustrated. Figure 11.7 (c) shows the fracture surface of a single wall carbon-nanotube–aluminum-composite tested in tension [61]. The survivability following large processing strains and the thermal cycle is noteworthy. This illustrates the possibility of developing sensors and actuators by locally embedding functional particles. In another attempt to embed functional particles, Dixit et al. [62] have observed clean Al/NiTi interfaces after friction stir processing (Fig. 11.7 (d)).

11.5.2 Processing of Powder Metallurgy Alloys

Powder-metallurgy-processed aluminum alloys suffer from three major microstructural problems that limit their full potential: (a) prior particle boundaries with an aluminum oxide film, (b) microstructural inhomogeneity, and (c) remnant porosity. These microstructural features particularly hamper the ductility in very high strength aluminum alloys. Berbon et al. [14, 63] have shown that

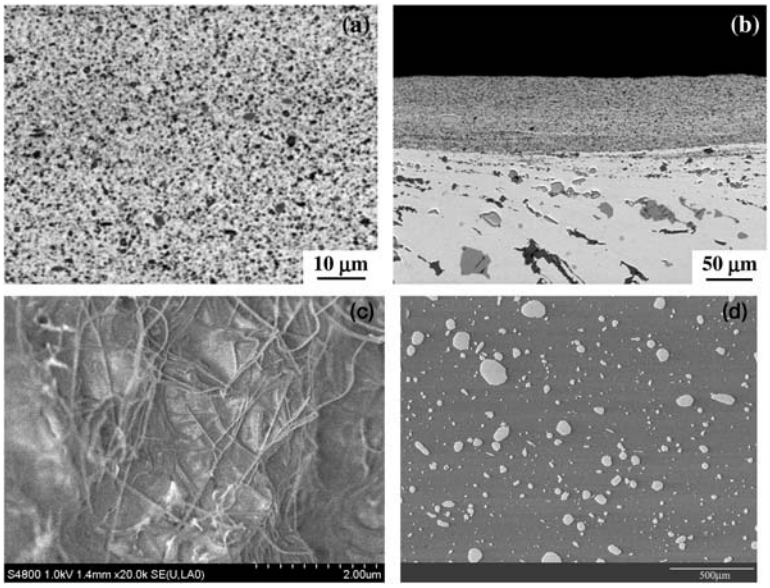

Fig. 11.7 Optical micrograph showing (a) uniform distribution of SiC particles (~15 vol.%) in A356 matrix, and (b) perfect bonding between surface composite and aluminum alloy substrate (600 rpm rotation rate and 6.4 mm/min traverse speed) [13, 56]. (c) SEM image showing SWCNTs bundles on the fracture surface of a friction stir processed aluminum matrix [61]. (d) SEM image showing uniformly distributed NiTi particles in Al matrix [62].

FSP can be used a homogenization tool. Figure 11.8 shows the microstructural difference in an Al-Ti-Cu alloy processed by extrusion and by FSP. The FSP microstructure is remarkably different from the as-extruded microstructure. This leads to an excellent combination of strength and ductility. Combining the trends observed by various studies cited in this section, the potential of FSP as a tool to create homogeneous nanocomposites on a local scale can be visualized. Designers and fabricators can take this approach to design components and subsystems to take advantage of localized property enhancements to augment conceptual design elements.

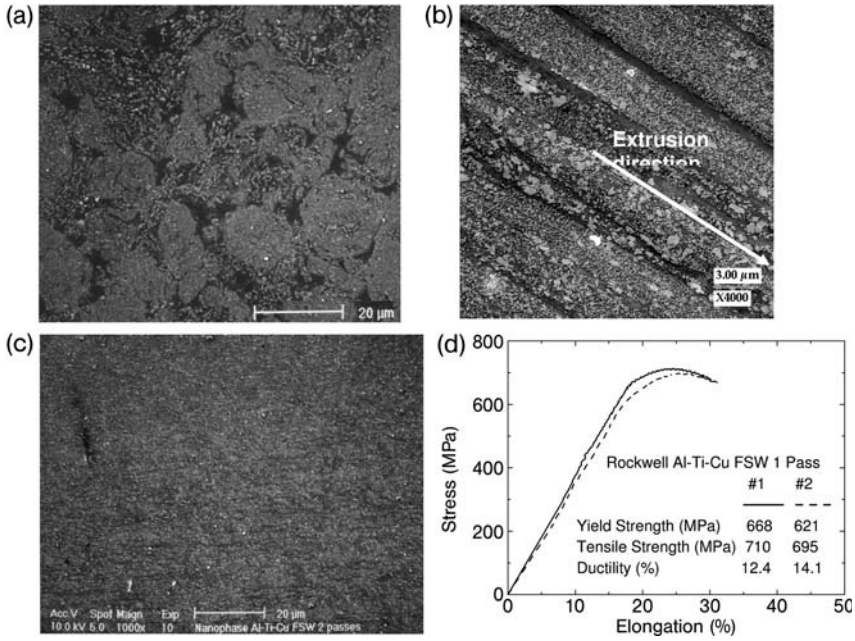

Fig. 11.8 (a) Typical microstructure in the as-HIPed condition. Dark regions consist of pure Al, grey regions consist of fine intermetallics dispersed in an Al matrix, and light regions consist of coarse intermetallics in an Al matrix. (b) Typical as-extruded microstructure shows the same three microstructural features, now elongated in the extrusion direction. (c) Typical microstructure observed in the FSP nugget. The three different microstructural features seen in the starting material have been homogenized. (d) Tensile tests of the friction stir processed material show an excellent strength and more than 10% ductility [14].

Acknowledgement

Much of this review is taken from two previous reviews by the author. The author gratefully acknowledges the support of the US National Science Foundation through various grants over the last six years that has helped in the development of many concepts presented in this chapter.

References

1 R. S. Mishra, Z. Y. Ma **2005**, Friction stir welding and processing, *Mater. Sci. Eng. R-Rep.* 50, 1.

2 R. S. Mishra, M. W. Mahoney **2007**, Friction Stir Processing. In, R. S. Mishra, M. W. Mahoney, (eds.) *Friction Stir Welding and Processing*, ASM International. Materials Park, OH, p. 311.

3 R. S. Mishra, M. W. Mahoney, S. X. McFadden, N. A. Mara, A. K. Mukherjee **1999**, High strain rate superplasticity in a friction stir processed 7075 Al alloy, *Scr. Mater.* 42, 163.

4 R. S. Mishra, M. W. Mahoney **2001**, Friction stir processing, A new grain refinement technique to achieve high strain rate superplasticity in commercial alloys, *Superplasticity in Advanced Materials*, ICSAM-2000, 357–3, 507.

5 C. Dawes, W. Thomas **1995**, *TWI Bull.* 6, 124.

6 W. M. Thomas, J. C. Needham, M. G. Murch, P. Templesmith, C. J. Dawes **1991**, G. B. Patent Application No, 9125978.8 Dec. 1991.

7 B. London, M. Mahoney, B. Bingel, M. Calabrese, D. Waldron **2001**, *Proceedings of the Third Int. Symposium on Friction Stir Welding*. Kobe, Japan, TWI.

8 C. G. Rhodes, M. W. Mahoney, W. H. Bingel, R. A. Spurling, C. C. Bampton **1997**, Effects of friction stir welding on microstructure of 7075 aluminum, *Scr. Mater.* 36, 69.

9 G. Liu, L. E. Murr, C. S. Niou, J. C. McClure, F. R. Vega **1997**, Microstructural aspects of the friction-stir welding of 6061-T6 aluminum, *Scr. Mater.* 37, 355.

10 K. V. Jata, S. L. Semiatin **2000**, Continuous dynamic recrystallization during friction stir welding of high strength aluminum alloys, *Scr. Mater.* 43, 743.

11 S. Benavides, Y. Li, L. E. Murr, D. Brown, J. C. McClure **1999**, Low-temperature friction-stir welding of 2024 aluminum, *Scr. Mater.* 41, 809.

12 Z. Y. Ma, R. S. Mishra, M. W. Mahoney **2002**, Superplastic deformation behaviour of friction stir processed 7075Al alloy, *Acta. Mater.* 50, 4419.

13 R. S. Mishra, Z. Y. Ma, I. Charit **2003**, Friction stir processing, a novel technique for fabrication of surface composite, *Mater. Sci. Eng. A-Struct. Mater. Prop. Microstruct. Process.* 341, 307.

14 P. B. Berbon, W. H. Bingel, R. S. Mishra, C. C. Bampton, M. W. Mahoney **2001**, Friction stir processing, A tool to homogenize nanocomposite aluminum alloys, *Scr. Mater.* 44, 61.

15 J. E. Spowart, R. S. Mishra **2003**, In, K. V. Jata, R. S Mishra, S. L Semiatin, T. Lienert, (eds.) *Friction Stir Welding and Processing II*, TMS, Warrendale, PA, p. 243.

16 Z. Y. Ma, S. R. Sharma, R. S. Mishra, M. W. Mahoney **2003**, Microstructural modification of cast aluminum alloys via friction stir processing, *Thermec '2003*, Pts 1–5, 426–4, 2891.

17 L. E. Murr, G. Liu, J. C. McClure **1997**, Dynamic recrystallization in friction-stir welding of aluminum alloy 1100, *J. Mater. Sci. Lett.* 16, 1801.

18 M. W. Mahoney, C. G. Rhodes, J. G. Flintoff, R. A. Spurling, W. H. Bingel **1998**, Properties of friction-stir-welded 7075 T651 aluminum, *Metall. Mater. Trans. a-Phys. Metall. Mater. Sci.* 29, 1955.

19 Y. S. Sato, H. Kokawa, M. Enomoto, S. Jogan **1999**, Microstructural evolution of 6063 aluminum during friction-stir welding, *Metall. Mater. Trans. a-Phys. Metall. Mater. Sci.* 30, 2429.

20 O. Frigaard, O. Grong, O. T. Midling **2001**, A process model for friction stir welding of age hardening aluminum alloys, *Metall. Mater. Trans. a-Phys. Metall. Mater. Sci.* 32, 1189.

21 W. J. Arbegast, P. J. Hartley **1998**, *Fifth International Conference on Treads in Welding Research. Pine Mountain*, GA, USA, p. 541.

22 L. E. Murr, Y. Li, R. D. Flores, E. A. Trillo, J. C. McClure **1998**, Intercalation vortices and related microstructural features in the friction-stir welding of dissimilar metals, *Mater. Res. Innov.* 2, 150.

23 Y. Li, L. E. Murr, J. C. McClure **1999**, Flow visualization and residual microstructures associated with the friction-

stir welding of 2024 aluminum to 6061 aluminum, *Mater. Sci. Eng. A-Struct. Mater. Prop. Microstruct. Process.* 271, 213.

24 B. Heinz, B. Skrotzki **2002**, Characterization of a friction-stir-welded aluminum alloy 6013, *Metall. Mater. Trans. B-Process Metall. Mater. Process. Sci.* 33, 489.

25 Y. S. Sato, S. H. C. Park, H. Kokawa **2001**, Microstructural factors governing hardness in friction-stir welds of solid-solution-hardened Al alloys, *Metall. Mater. Trans. a-Phys. Metall. Mater. Sci.* 32, 3033.

26 H. G. Salem, A. P. Reynolds, J. S. Lyons **2002**, Microstructure and retention of superplasticity of friction stir welded superplastic 2095 sheet, *Scr. Mater.* 46, 337.

27 J. Q. Su, T. W. Nelson, R. Mishra, M. Mahoney **2003**, Microstructural investigation friction stir welded 7050-T651 aluminum, *Acta. Mater.* 51, 713.

28 Z. Y. Ma, R. S. Mishra, M. W. Mahoney, R. Grimes **2003**, High strain rate superplasticity in friction stir processed Al-Mg-Zr alloy, *Mater. Sci. Eng. A-Struct. Mater. Prop. Microstruct. Process.* 351, 148.

29 I. Charit, R. S. Mishra **2003**, High strain rate superplasticity in a commercial 2024 Al alloy via friction stir processing, *Mater. Sci. Eng. A-Struct. Mater. Prop. Microstruct. Process.* 359, 290.

30 I. Charit, R. S. Mishra, M. W. Mahoney **2002**, Multi-sheet structures in 7475 aluminum by friction stir welding in concert with post-weld superplastic forming, *Scr. Mater.* 47, 631.

31 M. James, M. Mahoney **1999**, Proceedings of the first International Symposium on Friction Stir Welding, *First International Symposium on Friction Stir Welding*, Thousand Oaks, CA, USA.

32 Z. Y. Ma, R. S. Mishra, M. W. Mahoney **2003**, In, K. V. Jata, M. W. Mahoney, R. S. Mishra, S. L. Semiatin, T. J. Lienert, (eds.) *Friction Stir Welding and Processing II*, TMS, Warrendale, PA, p. 221.

33 Y. J. Kwon, N. Saito, I. Shigematsu **2002**, Friction stir process as a new manufacturing technique of ultrafine-grained aluminum alloy, *J. Mater. Sci. Lett.* 21, 1473.

34 Y. J. Kwon, I. Shigematsu, N. Saito **2003**, Production of ultra-fine grained aluminum alloy using friction stir process, *Mater. Trans.* 44, 1343.

35 Y. J. Kwon, I. Shigematsu, N. Saito **2003**, Mechanical properties of fine-grained aluminum alloy produced by friction stir process, *Scr. Mater.* 49, 785.

36 C. G. Rhodes, M. W. Mahoney, W. H. Bingel, M. Calabrese **2003**, Fine-grain evolution in friction-stir processed 7050 aluminum, *Scr. Mater.* 48, 1451.

37 J. Q. Su, T. W. Nelson, C. J. Sterling **2003**, A new route to bulk nanocrystalline materials, *J. Mater. Res.* 18, 1757.

38 I. Charit, R. S. Mishra **2004**, In, Y.T. Zhu, R.Z. Valiev, S.L. Semiatin, D.H. Shin, T.C. Lowe, (eds.) *Ultrafine Grained Materials III*, TMS, Warrendale, PA, p. 95.

39 I. Charit, R. S. Mishra **2005**, Low temperature superplasticity in a friction-stir-processed ultrafine grained Al-Zn-Mg-Sc alloy, *Acta. Mater.* 53, 4211.

40 D. C. Hofmann, K. S. Vecchio **2005**, Submerged friction stir processing (SFSP), An improved method for creating ultra-fine-grained bulk materials, *Mater. Sci. Eng. A-Struct. Mater. Prop. Microstruct. Process.* 402, 234.

41 Z. Y. Ma, R. S. Mishra **2005**, Development of ultrafine-grained microstructure, low temperature (0.48 T-m) superplasticity in friction stir processed Al-Mg-Zr, *Scr. Mater.* 53, 75.

42 J. Q. Su, T. W. Nelson, C. J. Sterling **2006**, Grain refinement of aluminum alloys by friction stir processing, *Philos. Mag.* 86, 1.

43 F. J. Humphreys, M. Hotherly **1995**, *Recrystallization and Related Annealing Phenomena*, Pergamon Press, New York.

44 Y. S. Sato, M. Urata, H. Kokawa **2002**, Parameters controlling microstructure and hardness during friction-stir welding of precipitation-hardenable aluminum alloy 6063, *Metall. Mater. Trans. a-Phys. Metall. Mater. Sci.* 33, 625.

45 Y. Li, E. A. Trillo, L. E. Murr **2000**, Friction-stir welding of aluminum alloy 2024 to silver, *J. Mater. Sci. Lett.* 19, 1047.

46 M. Mahoney, R. S. Mishra, T. Nelson, J. Flintoff, R. Islamgaliev, Y. Hovansky **2001**, In, K. V. Jata, R. S. Mishra, S. L.

Semiatin, D. P. Field, (eds.) *Friction Stir Welding and Processing*, TMS, Warrendale, PA, USA, p. 183.

47 P. S. Pao, E. Lee, C. R. Feng, H. N. Jones, D. W. Moon **2003**, In, K. V. Jata, M. W. Mahoney, R. S. Mishra, S. L. Semiatin, T. Lienert, (eds.) *Friction Stir Welding and Processing II*, TMS, Warrendale, PA, USA, p. 113.

48 J. Q. Su, T. W. Nelson, C. J. Sterling **2005**, Friction stir processing of large-area bulk UFG aluminum alloys, *Scr. Mater.* 52, 135.

49 L. E. Murr, R. D. Flores, O. V. Flores, J. McClure, G. Liu, D. Brown **1998**, Friction-stir welding, Microstructural characterization, *Mater. Res. Innov.* 1, 211.

50 K. A. A. Hassan, A. F. Norman, P. B. Prangell **2001**, *Third International Symposium on Friction Stir Welding*, Kobe, Japan, TWI,.

51 L. E. Murr, E. A. Trillo, S. Pappu, C. Kennedy **2002**, Adiabatic shear bands and examples of their role in severe plastic deformation, *J. Mater. Sci.* 37, 3337.

52 R. S. Mishra, T. R. Bieler, A. K. Mukherjee **1995**, Superplasticity in powder metallurgy aluminum alloys and composites, *Acta Metall. Mater.* 43, 877.

53 R. S. Mishra, R. K. Islamgaliev, T. W. Nelson, Y. Hovansky, M. W. Mahoney **2001**, In, K. V. Jata, M. W. Mahoney, R. S. Mishra, D. P. Field, (eds.) *Friction Stir Welding and Processing*, TMS, Warrendale, PA, p. 205.

54 Y. Morisada, H. Fujii, T. Nagaoka, M., Fukusumi **2006**, MWCNTs/AZ31 surface composites fabricated by friction stir processing, *Mater. Sci. Eng. A-Struct. Mater. Prop. Microstruct. Process.* 419, 344.

55 S. M. Howard, B. K. Jasthi, W. J. Arbegast, G. J. Grant, D. R. Herling **2005**, Friction surface reaction processing in aluminum substrates, *Friction Stir Welding and Processing III*, TMS, Warrendale, PA, p. 139.

56 Z. Y. Ma, R. S. Mishra **2003**, Friction stir surface composite fabrication, *Surface Engineering, in Materials Science II*, TMS, Warrendale, PA, p. 243.

57 J. W. Newkirk, R. S. Mishra, J. Thomas, J. A. Hawk **2003**, Friction Stir Processing to Create Surface Composites, *Advances in Powder Metallurgy & Particulate Materials, MPIF*, Princeton, NJ, p. 6.60.

58 U. Ramadorai, J. W. Newkirk, R. S. Mishra, J. A. Hawk **2005**, Surface Modification of Aluminum Alloys to Create in Situ Surface Composites, *4th ASM International Surface Engineering Congress and 19th International Conference on Surface Modification Technologies*, ASM, Materials Park, OH, p. 22.

59 C. J. Lee, J. C. Huang, P. J. Hsieh **2006**, Mg based nano-composites fabricated by friction stir processing, *Scr. Mater.* 54, 1415.

60 C. J. Lee, J. C. Huang, P. L. Hsieh **2006**, Using friction stir processing to fabricate Mg based composites with nano fillers, *Compos. Mater.* IV, 313, 69.

61 L. B. Johannes, L. L. Yowell, E. Sosa, S. Arepalli, R. S. Mishra **2006**, Survivability of single-walled carbon nanotubes during friction stir processing, *Nanotechnology*, 17, 3081.

62 M. Dixit, J. W. Newkirk, R. S. Mishra **2006**, *Scr. Mater.* 56, 541.

63 J. Zheng, R. S. Mishra, P. B. Berbon, M.W. Mahoney **2001**, Microstructure and mechanical behavior of friction stir processed Al-Ti-Cu alloy, *Friction Stir Welding and Processing*. Indianapolis, IN, USA, TMS, p. 235.

64 J. E. Spowart, Z.-Y. Ma, S. Mishra **2003**, The effect of friction stir processing (FSP) on the spatial heterogeneity of discontinuously-reinforced aluminum (DRA) microstructures, Friction Stir Welding and Processing II, TMS, Warrendale, PA, p. 243.

65 C. J. Hsu, P. W. Kao, N. J. Ho **2005**, Ultrafine-grained Al-Al_2Cu composite produced in situ by friction stir processing, *Scr. Mater.* 53, 341.

66 J. C. H. Chuang, J. C. Huang, P. J. Hsieh **2005**, Using friction stir processing to fabricate MgAlZn intermetallic alloys, *Scr. Mater.* 53, 1455.

67 A. Tewari, J. E. Spowart, A. M. Gokhale, R. S. Mishra, D. B. Miracle **2006**, Characterization of the effects of friction stir processing on microstructural changes in DRA composites, Material Science and Engineering α-Structural Materials Properties Microstucture and Processing, 428, 80.

12
Bulk Nanostructured Metals from Ball Milling and Consolidation

Bing Q. Han, Jichun Ye, A. Piers Newbery, Yuntian T. Zhu, Julie M. Schoenung, and Enrique J. Lavernia

12.1
Introduction

Bulk nanostructured materials (BNMs) are emerging as a new class of materials with unusual structures and, as a result, have attracted considerable attention in recent years [1]. The relatively high strength in BNMs as compared to conventional materials of similar composition offers interesting possibilities related to many structural applications. The successful synthesis of large-scale BNMs with a grain size in the range of 10–200 nm represents a major achievement in the wide field of nanotechnology [2]. BNMs usually have grain sizes of less than 100 nm, resulting from processing nanostructured powders (<50 nm) via such techniques as mechanical milling, a ball-milling technique [3], followed by consolidation into three-dimensional components.

Ball milling is a widely used approach for the preparation of nanostructured metallic powders [4]. The grain-size refinement in the powder occurs by the repeated fracturing and rewelding of powder particles in a highly energetic ball mill. The process usually requires at least one fairly ductile metal to act as a host or binder. Other components can consist of other ductile metals, brittle metals, and intermetallic compounds or nonmetals and refractory compounds. After consolidation into fully dense nanocrystalline compacts, the material has unusual physical and mechanical properties compared to their conventionally processed counterparts. This technology was originally developed by Benjamin for the fabrication of nickel-based oxide dispersion strengthened (ODS) superalloys in the early 1970s [5]. Gilman and Benjamin [6] also applied milling to produce an oxide-reinforced aluminum by fragmenting the naturally formed surface oxide film and dispersing the oxide particles homogeneously in the aluminum. The greatly improved mechanical properties of the milled ODS alloys have been attributed to the limited grain growth by Zener pinning as well as the high level of plastic deformation introduced during the milling. The final grain size of BNMs is largely determined by the inherent thermal stability of the microstructure in combination with the parametric space used during milling [3].

Bulk Nanostructured Materials. Edited by M. J. Zehetbauer and Y. T. Zhu

ISBN: 978-3-527-31524-6

In this chapter, the mechanisms of ball milling of metallic powders for nanostructured grains and subsequent consolidation techniques are delineated. The following topics are emphasized: microstructural evolution of powder particles during ball milling; metal matrix composites processed by milling; grain-size variation following consolidation and processing; and mechanical behavior of consolidated materials. Recent mechanical behavior data for cryomilled Al alloys are emphasized and the associated mechanisms are introduced in an effort to shed light on the fundamental behavior of ultrafine grained and nanostructured materials.

12.2
Mechanisms of Nanostructure Formation

During milling, the material experiences severe plastic deformation, resulting in grain refinement. The process involves five stages of evolution in the powder particle, i.e. particle flattening as a result of plastic deformation, welding-dominance stage, fracturing and equiaxed particle formation, random welding orientation of the powder particles and a steady state, during which microstructural refinement continues, as shown in Fig. 12.1 (a) [7–9]. It is critical to establish a balance between fracturing and cold welding in order to mechanically mill successfully. Two techniques are employed to reduce cold welding and promote fracturing [5]. The most common technique is to modify the surface of powder particles by adding a processing control agent (PCA) that impedes the clean metal-to-metal contact necessary for cold welding. The other is to modify the deformation mode of powder particles so that they fracture before they are able to deform to the large compressive strain necessary for flattening and cold welding. Two events, coalescence and fragmentation of particles occur simultaneously during ball milling, as shown in Fig. 12.1 (b) [4]. In the coalescence event, particles are effectively welded to each other during plastic deformation. In the fragmentation event, particles are broken down by dynamic fracture, forging fracture and shear fracture.

The formation of a nanocrystalline structure by ball milling is considered to take place via three stages, as proposed by Fecht [10]. In the first stage, severe plastic deformation is applied on powder particles during milling. This deformation is localized in shear bands containing a dense network of dislocations. In the second stage, by the arrangement of the dislocations, the grains become divided into subgrains that are separated by low-angle grain boundaries. The formation of these subgrains is attributed to the annihilation and recombination of dislocations, as well as a decrease of the atomic-level strain. In the final stage, further deformation leads to the reduction of subgrain sizes, as well as the reorientation of the subgrains to form grains with high-angle misorientations.

In view of the fact that the severe plastic deformation introduced during milling is a repetitive process, the milling time dominates the overall deformation strain. Basically, all metals and compounds investigated exhibit similar be-

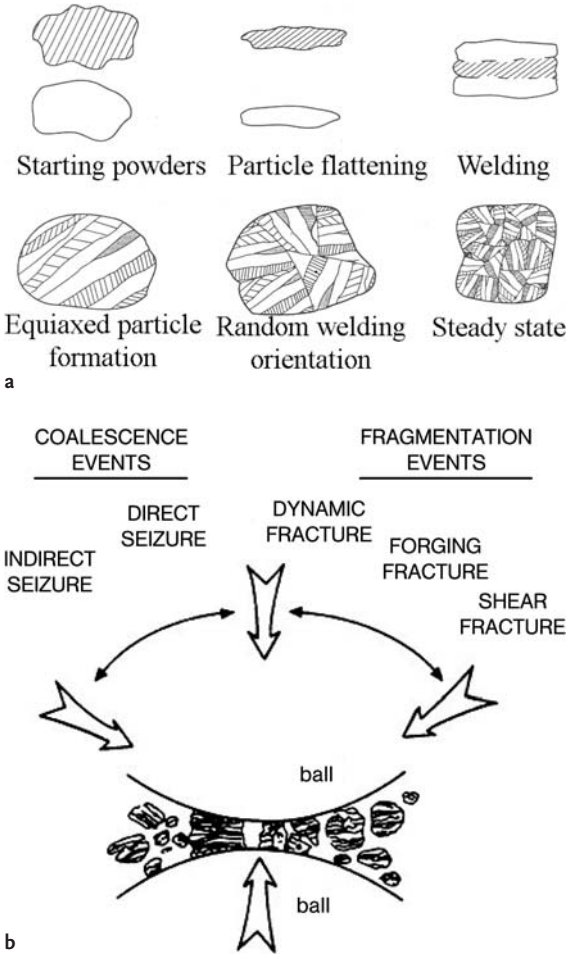

Fig. 12.1 (a) The five stages of powder evolution during mechanical alloying [7–9]; and (b) A schematic sketch of the process of mechanical attrition of metal powders [4, 10].

havior in terms of grain-size reduction and increase in atomic-level strains [11]. A factor to consider in the grain-refinement process is microstructural inhomogeneity. In order to obtain a microstructure with nanoscale grain sizes, adequate milling time is required. The empirical model cited previously [10] describes deformation as localized into shear bands, which ultimately comprise the entire sample. It would not be surprising, therefore, to find microstructural features that manifest different relative degrees of deformation, and not simple lognormal distributions of randomly oriented equiaxed grains.

As revealed by the variations of X-ray diffraction patterns, the grain size in powder particles initially decreases with increasing milling time and ultimately

reaches a minimum grain size [10]. The minimum grain size obtainable by milling of metals has been attributed to a balance between the grain refinement introduced by the severe impact deformation of milling and the thermal recovery by the material itself [3, 10, 12]. These studies have led to the following important observations and findings: (1) the minimum grain-size varies inversely with the melting point or the bulk modulus, (2) there is a linear relationship between the minimum grain size and the critical equilibrium distance between two edge dislocations in FCC metals, and (3) limited experimental evidence suggests that smaller grain sizes are achieved at lower milling temperatures. Most recently, Mohamed [13] developed a dislocation model to quantitatively describe the minimum grain size obtainable by milling. According to this model, the minimum grain size is governed by a balance between the strain-hardening rate introduced by dislocation generation and the recovery rate arising from dislocation annihilation and recombination. By balancing the rate of grain-size decrease and the rate of grain-size increase, the minimum grain size is found to decrease with increasing hardness and self-diffusion activation energy, as well as decreasing stacking-fault energy

Cryomilling is a variation of ball milling, in which metallic powders are milled in a liquid-nitrogen slurry using a modified ball-milling attritor, connected to a liquid-nitrogen source [14–16]. The processing parameters that influence cryomilling are very similar to those relevant to ball milling, e.g., the size of the mill, the milling media (material and ball diameter), the time of milling, and the ball-to-powder mass ratio. The extremely low temperature in cryomilling suppresses recovery and recrystallization, leading to finer grain structures and more rapid grain refinement [4]. The milling time required to attain a nanostructure is significantly reduced, because the low temperature suppresses the annihilation of dislocations and the accumulation of a higher dislocation density is possible. Cooling the mill media and powder is an effective approach to accelerate the fracture and to rapidly establish a steady-state process. Powder agglomeration, and welding to the milling media are suppressed, resulting in more efficient milling results (e.g., improved yield and microstructure refinement). Even so, for cryomilling of aluminum, a process-control agent (PCA), often stearic acid, is required to prevent excessive welding of aluminum to itself, the ball charge, the attritor tank, and the impellers. The variation of microstructure of a cryomilled Al-7.5Mg-0.3Sc alloy powder during cryomilling has been investigated by TEM and inspection of the results revealed that the elongated lamellar structure was formed initially during milling and eventually evolved into equiaxed grains [17]. A random distribution of equiaxed grains between 10 and 30 nm diameter in a cryomilled Al-7.5wt%Mg alloy after cryomilling for eight hours is shown in Fig. 12.2 [16, 18]. Finally, oxidation during milling is significantly reduced. Potential chemical reactions between a reinforcement and the matrix are also suppressed.

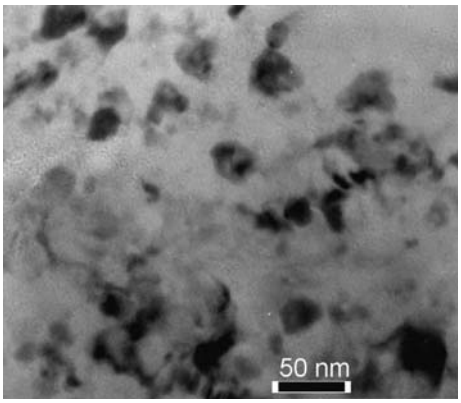

Fig. 12.2 Equiaxed-grained nanostructures of the as-milled Al-7.5%Mg alloy powder [16, 18].

12.3 Ball Milling of Metal Matrix Composites

Ball milling can be used to fabricate Al matrix composites [19, 20]. In these studies, the purpose of the milling was to effectively mix the reinforcements with the matrix and to enfold the matrix material around each reinforcing particle, eliminating voids between the Al alloy matrix and the reinforcement and achieve solid-state bonding between them. However, the microstructure of the Al matrix was not taken into consideration in those early studies. Thus, the milling time used was much shorter than that needed with normal mechanical milling as applied to fabricate nanocrystalline metallic materials. In addition to the capabilities of uniformly distributing the reinforcement and developing good matrix/reinforcement interfaces, mechanical milling, especially the variation called cryomilling, is capable of producing a nanocrystalline grain structure in the metallic matrix [21–23].

During ball milling of a matrix/reinforcement mixture, the ductile matrix, even with the hard reinforcing particles on/in it, can still be deformed, flattened and cold welded in the same manner as monolithic metal. The presence of hard particles facilitates the fracturing process, thus shortening the time to achieve equiaxed powder [24]. The morphology of milled composite particles is important to the ultimate mechanical properties of consolidated materials. For example, Fogagnolo et al. [25] found that bulk material made from the extrusion of Al/Si_3N_4 powder milled for 4.5 h had a minimum tensile elongation, and that it required a 45% higher load than was necessary to extrude powder milled for 10 h [25]. The higher extrusion load, attributed to the flake-like morphology of the powder, created defects such as microcracks or surface irregularities, degrading the material's ductility [25]. Thus, it is preferable that sufficient milling time should be used to achieve a steady state and obtain equiaxed morphology for the milled powder.

The change in the size of the reinforcement depends not only on the milling parameters, but also on the intrinsic properties of the reinforcement and ma-

trix. Because the material used for milling is a ductile-brittle system, the reinforcing particles became trapped and embedded in the ductile metal. It is believed that the metallic phases behave like a cushion, damping the forces acting on the reinforcement, and, thus, reducing the amounts of energy available to fracture the reinforcement. Ye et al. [26] observed only a small change in the B_4C size during cryomilling, decreasing from an average particle size of 2.5 μm down to 1.1 μm after 10 h of cryomilling, which was attributed to the extremely high hardness and impact resistance of B_4C. Similar behavior has been observed for Si_3N_4, where the size of the Si_3N_4 changed from 8.6 μm to 1 μm after the mechanical milling of Al/Si_3N_4 [25]. In contrast, the size of AlN can decrease to 30 nm after cryomilling with Ni or Al [22, 23, 27] and SiC particles can reduce from 100 μm to 1 μm while many nanoscaled SiC particles were also observed [28].

One of the advantages of the mechanical milling technique as a method to synthesize metal matrix composite powders is the uniform distribution of the reinforcement, which normally cannot be obtained via blending. Prasad et al. [29] observed that more homogeneously distributed ceramic particles in composites resulted in higher yield strengths, as well as a higher ductility. The reinforcing particles adhere onto the metal particles when milling starts. The metal surfaces with reinforcement stuck to them are cold welded with other metal surfaces. As a result, the reinforcing particles became entrapped in the Al matrix. It seems reasonable to assume that ceramic particulate clusters within the metal matrix would lead to easier crack initiation. These cracks would propagate through the metal matrix and fracture the metal particles. The freshly fractured surfaces with B_4C particles on them would then weld with other metal surfaces. Upon continued milling, reinforcing particles will become uniformly distributed within the metal matrix. Ye et al. [26] observed that there are numerous B_4C particles on the surface of Al powder cryomilled for 1 h. However, after 6 h of cryomilling, most of the B_4C is dispersed uniformly within the Al matrix. No clusters of B_4C were detected after cryomilling for 6 h. Homogeneity is harder to obtain when the size of the reinforcement becomes smaller. For example, nanosized mullite particles agglomerate in an Al/mullite composite fabricated by blending [30]. However, composites with uniformly distributed nanosize hard particles, which fragmented from larger particles, can be formed via mechanical milling [22, 27]. It is expected that, if a reinforcement with a starting size in the nanometer scale was used, a uniform distribution can also be achieved through the aforementioned repeated cold-welding and fracturing processes that occur during milling. Nanosized diamond particles (4–5 nm) [31] and nanosized SiC particles (25 nm) [32] have been uniformly introduced into an Al-Mg alloy and 5083 Al, respectively, by cryomilling.

The presence of hard reinforcing particles may influence the process of the grain refinement in the metal matrix. Chung et al. [27] found that the introduction of a small amount of AlN particles with an initial size of 2 μm facilitated the grain-refinement process for Ni during cryomilling, and greatly reduced the grain size from 132 nm for pure Ni down to 65 nm and 37 nm for Ni with

0.5 wt.% and 2.0 wt.% AlN, respectively, after milling for 8 h. During cryomilling, the AlN particles broke into nanoscaled particles, from 2 μm down to 20–300 nm in size. This enhancement in the grain-refinement process for the Ni matrix was interpreted by a mechanism involving the interactions of dislocations with small hard particles, and dislocation generation due to the difference in thermal expansion coefficient between matrix and reinforcement [27]. Since cryomilling is conducted in liquid nitrogen, the temperature variation is minimal and the dislocation generation due to the mismatch of the thermal expansion coefficient can be neglected. In another related study, Ye et al. [26] observed that different amounts of B_4C (0–25 wt.%) in the Al matrix had little effect on the final Al grain sizes (25 nm) after 8 h of cryomilling, which indicates that the presence of B4C did not affect the microstructural evolution of the Al matrix. These fractured B4C particles are not small enough to provide sufficient interaction with dislocations, i.e. to act as a source of dislocations, which is why the presence of the B4C particles did not affect the formation of the nanocrystalline structure in the Al matrix. In conclusion, only when the reinforcing particles are very small (less than 100 nm), either by fracturing during mechanical milling or as raw material, can they facilitate the grain-refinement process in the metal matrix.

12.4 Consolidation of Ball-milled Powders

Widespread application of ball-milled powders, in common with nanostructured particles produced by other techniques, requires efficient methods of consolidation to produce useful shapes, of sufficient size, with close to 100% theoretical density [33–35]. The final microstructure of the material in a form suitable for application depends not only on the milling parameters, but also on the method used to consolidate the powder. Since conventional consolidation processes usually require time at elevated temperature, care must be taken to avoid losing the beneficial structure present in the as-milled powders. Thus, consolidation parameters are restricted to prevent coarsening of the structure, precipitation of metastable or stable phases, transformation of metastable crystalline and quasicrystalline phases into equilibrium phases, and/or crystallization of amorphous phases.

Because particle sizes of milled powders are generally in the range of tens of micrometers, the problems associated with densifying nanosize particles, i.e. aggregate formation and high interparticulate frictional forces, are usually not encountered. Also, the extremely strong driving force for sintering of ultrafine particles with a small radius of curvature will not exist. Even so, the small grain size of ball-milled powders may enhance sintering through increased grain-boundary diffusion. Certainly, the large grain-boundary area acts as a strong driver for growth when exposed to elevated temperatures. Although pressure, ranging from a few tens of MPa to a few GPa, can assist densification by stress-

assisted diffusion plus plastic and creep deformation, thus reducing the time spent at temperature, enhanced deformation-induced grain growth can occur.

Like most powder metallurgical processes, before consolidation, the ball-milled powders must be handled with care, since they can be, depending on the material, vulnerable to reaction with atmospheric constituents, such as oxygen and moisture. This type of reaction can lead to the formation of oxides and hydroxides, which would severely embrittle the final material. The powders are usually handled in the clean, dry atmosphere of a glovebox, and sealed in an airtight can before they are transferred to the open air. Prior to primary consolidation, ball-milled powders normally require degassing at an elevated temperature, to remove contaminants, e.g., hydrogen and carbon, caused by the addition of the PCA before milling. The degassing process involves heating under vacuum the powder at a temperature well above the breakdown temperature of the PCA. For large amounts of powder, to enable the contaminant species to move through the powder bed and exit the vessel, the degassing can last for several days. This will generally lead to grain growth in lower-melting materials [36]. Once the degassing cycle is completed, the can is then sealed at the stem to preserve the vacuum. For Al, annealing data suggests that grains grow at the degassing temperature from about 25 to about 65 nm, based on XRD and TEM measurements [37]. The presence of oxide and carbide dispersoids, arising from incorporation of the PCA during milling, can aid retention of a small grain size due to grain-boundary pinning.

Conventional powder metallurgy processes that have been used to densify ball-milled powders include sintering, uniaxial cold pressing, cold isostatic pressing (CIP), vacuum hot pressing, and, most commonly, hot isostatic pressing (HIP). Since sintering usually is operated at very high temperatures, significant grain growth inevitably occurs. Thus, it is rarely used to consolidate nanostructured materials.

A review of the available literature shows that in early studies [14], the most common primary consolidation route was HIP. The densification during the HIP process has been described as a three-step process, beginning with loose packing of powder in the can, elimination of connected porosity due to the growth of necks at contact points between adjacent particles, and reduction of the size of individual pores [38, 39]. The growth of necks and filling in of pores at each stage are accomplished by a combination of plastic deformation of the powder particles, power-law creep, and mass diffusion to the remaining free surfaces. For HIP, the combination of pressure and temperature can be used to achieve almost 100% density at a lower temperature than would be required for sintering alone and at a lower pressure than required for CIP [39]. The driving force to achieve densification is associated with the reduction in surface area and, hence, surface energy of the pores. The pressure and temperature are two critical parameters for consolidation [35].

Since the consolidation of the milled powder usually requires high temperatures for long times, there is a challenge for retaining nanoscale grain size. The diffusion processes can lead to relatively coarse, micrometer-size grains forming

in the interstices between the nanograined prior powder particles [32, 40]. This has been shown to be beneficial in increasing the ductility and fracture toughness of the final material, because the coarser grains act to prevent crack growth [41]. In some cases, to avoid the grain growth during HIP in cryomilled Al alloys [42, 43], CIP was applied to consolidate cryomilled powders [44]. Compared to HIP processing, CIP is operated at room temperature, but with a much higher isostatic pressure. Therefore, the microstructure after CIP and extrusion in cryomilled Al alloys is generally homogeneous.

Despite obtaining nearly full density, the ductility of as-HIPped material is generally low [45]. This is most likely due to the presence of prior particle boundaries, usually decorated with surface oxide, that are not removed by isostatic deformation. To break up the prior particle boundaries, a shear stress needs to be applied to the material, which can also remove small amounts of residual porosity. Therefore, secondary processing such as extrusion or forging is necessarily performed. HIP and extrusion have been performed on cryomilled Al/Al_2O_3 [14] and $NiAl/Y_2O_3$ composites [46, 47]. Nanostructured Fe-10Cu alloys have been prepared by ball milling, followed by HIP and forging at different conditions [48], obtaining grain sizes in the range of 30 nm to 1.7 μm. Cryomilled Al alloys, such as Al 5083, have excellent thermal stability due to the presence of nanoscale nitrogen-containing dispersoids, which means that they can be HIPped and extruded without excessive grain growth [36, 43, 49, 50]. As shown in Fig. 12.3, it has been reported that the average grain size of cryomilled 5083 Al alloy increases from 130 nm in the as-HIPped status to 250 nm after extrusion [36]. At room temperature, the strength of the extrusions are ~20% higher than that of the as-HIPped material, despite the larger grain size, giving a strength that is more than twice that of conventional wrought, strain-hardened Al 5083, with comparable ductility.

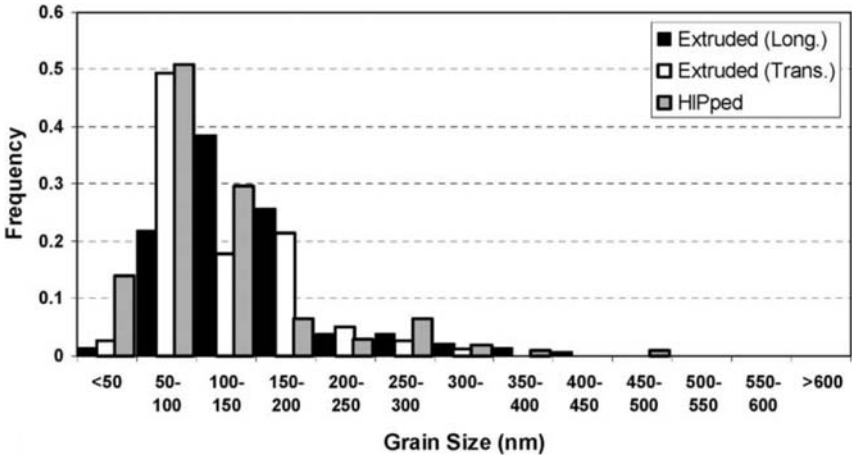

Fig. 12.3 Grain-size distributions of both as-HIPped and as-extruded cryomilled Al 5083 [36].

A technique, such as quasi-isostatic forging, commonly known as the Ceracon process [51–53], which can enable both consolidation and impart shear stresses to improve ductility, thus removing the need for HIP or extrusion, is very attractive for larger-scale consolidation. Ceracon forging was a conventional forging press [52], combined with a heated granular pressure-transmitting medium to achieve full density. As a cost competitive alternative to HIP, the Ceracon forging of canned powders can be used as an effective preparation step for secondary operations such as rolling and superplastic forming.

To enable increased retention of ball-milled structures, and nanoscale powders in general, a number of innovative methods of consolidation have been investigated, with a purpose to minimize the period of time spent at high temperature. These methods include spark-plasma sintering (SPS) (also known as plasma-activated sintering – PAS), the use of ultrahigh pressures (UHP) during pressing, and shock consolidation [35].

SPS, the combined application of pressure and a pulsed electrical current, can enable a rapid heating rate, obtaining high temperatures with a short densification time. Activated sintering may be achieved by increasing the driving force or enhancing kinetics via physical or chemical treatments. For instance, changes in interfacial properties may induce higher driving forces. Kinetically, activated sintering is a result of lowering the activation energies for densification [54]. Typical features of activated sintering are the reduction of sintering time and temperature, or increase of sintering degree. In SPS, the powders are consolidated in vacuum at high temperatures under high pressure. As a physical treatment, the imposition of an electric current is known to enhance sintering kinetics, and therefore, achieve high densities in shorter times or at lower temperatures as compared to a conventional sintering approach. To avoid undesired grain growth, the sintering process is usually applied for a few minutes or less. Microdischarge takes place among the powder particle, which generates a plasma. Hence, the atoms on the surface of each particle are activated, and grain growth during sintering can be minimized. In addition, the SPS technique does not result in significant compositional and/or structural changes of the sintered powders.

12.5 Mechanical Properties of Bulk Nanostructured Metallic Materials

The mechanical properties of BNMs consolidated from milled powders using approaches including SPS, ultrahigh pressures (UHP), and shock consolidation [35] have been studied. The possibility of porosity or incomplete bonding, which has a significant effect on the mechanical performance, might exist in these materials, since consolidation is usually accomplished rapidly in order to avoid significant grain growth. Porosity, like the lack of dislocation activity, is argued to be responsible for poor tensile performance [55, 56]. An example in support of this argument can be provided by comparing the tensile yield strength to the

compression yield strength for ball-milled Cu. The values of tensile yield strength are clearly lower than those in compression [55]. It is suggested that the asymmetry of yield strength between tension and compression is attributed to the existence of porosity in the consolidated nanostructured materials.

A high compressive strength of 692 MPa is observed in a Al-5at%Ti alloy with grain sizes of 50–100 nm, consolidated by SPS of reactive ball-mill powder [57]. However, the material was rather brittle and there was only about 5% compressive plastic strain. Similar behavior is also observed in MA vanadium with grain sizes of ~100 nm [58]. Although a compression strength of higher than 2000 MPa was observed, stress softening occurred, and the materials failed at a strain of only 5% [58].

A MA Al containing 5 at% Ti was warm pressed at 120 °C for only 250 s using a UHP of 4.8 GPa [59]. Despite the low temperature and short time, full density compacts were obtained with a grain size of 50 nm. The retention of a small grain size in this case was aided by the presence of Al_3Ti, Al_2O_3 and Al_4C_3 dispersoids. Even with this high thermal stability, at higher temperatures, e.g., at 360 °C, the grain-size increased to 160 nm, with some abnormal grain growth resulting in grains of 600 nm. At room temperature, the material pressed at 120 °C exhibited greater compressive strength (1.01 GPa) and ductility (20%) than powder consolidated by hot extrusion (grain size 50–100 nm and strength of 630 MPa) and SPS (grain size 50–70 nm and strength of 780 MPa). The material consolidated by hot extrusion and SPS displayed minimal ductility [60].

MA Fe-0.8wt.%C has been consolidated by SPS under a load of 70 MPa for 10 min [60]. Although an average grain size of 34 nm was achieved after a sintering temperature of 400 °C, the density of the compact was low (78%). It required a temperature of 600 °C to obtain nearly full density, but the ferrite and cementite grains formed had grown to ~150 nm, with some as large as 450 nm. Even so, the material still displayed excellent compressive strength, yielding at 1.9 GPa and failing at 3.5 GPa, and exhibiting a plastic strain of ~40%. This good compressive ductility is attributed to the ability of SPS to achieve good bonding between the particles due to efficient surface oxide removal [60].

Shock wave, or dynamic, compaction, in which a plate moving at 1.5 km/s was fired at the powder compact, has been used to consolidate Fe-28Al-Cr with an as-ball-milled grain size of 7 nm [61]. The as-consolidated disk, 32 mm in diameter and 10 mm thickness, retained an average grain size of 80 nm, exhibited no evidence of porosity and had a density of 99.9% of the cast alloy. However, 4 mm of the disc thickness failed in compression at very low stress, indicating the powder was not all fully bonded. In compression, the good material yielded at 2.1 GPa, an order of magnitude greater than the value for the cast alloy (0.27 GPa), and did not fail even after a true plastic strain of ~1.4. In tension, the material failed in the elastic region at a stress similar to the cast alloy (0.64 GPa), probably by interparticle decohesion, suggesting that the particle bonding could be improved further. Despite the successful consolidation of the

ball-milled powder, commercialization of shock-wave compaction is unlikely because to the complexity and expense involved [61].

The combination of HIP or CIP with extrusion has been proved to be an effective route to fabricate large amounts of cryomilled 5083 Al alloys [36]. The tensile behavior of three cryomilled 5083 Al alloys [44, 62] and a conventionally processed 5083 Al [49], is shown in Fig. 12.4 (a). The first material, cryomilled 5083 Al alloy consolidated via CIP and extrusion, has a grain size of approximately 200 nm. The second material, cryomilled 5083 Al alloy consolidated via HIP and extrusion, has an average grain size of 220 nm. The third material is reported to have an average grain size of 139 nm. However, the cryomilled 5083 Al alloys after HIP treatment have a bimodal microstructure. Both HIP alloys are observed to also contain large grains of $\sim 1\,\mu m$. The highest yield strength of 713 MPa is observed in the cryomilled 5083 Al alloy consolidated via CIP and extrusion. Such a high strength is mostly attributed to a grain-size effect (e.g., Hall–Petch strengthening). However, an extremely low ductility of 0.3% is observed in the cryomilled 5083 Al alloy consolidated via CIP and extrusion. The cryomilled 5083 Al alloy consolidated by HIP has a smaller grain size, but both strength and ductility are lower than those of the cryomilled 5083 Al alloy consolidated via HIP and extrusion. The poor mechanical performance of the cryomilled 5083 Al alloy consolidated by HIP may be attributed to the residual porosity or poor interfacial bonding.

Bimodal 5083 Al alloys with volume fractions of 15%, 30% and 50% coarse grains have been developed as a means to enhance ductility through the blend-

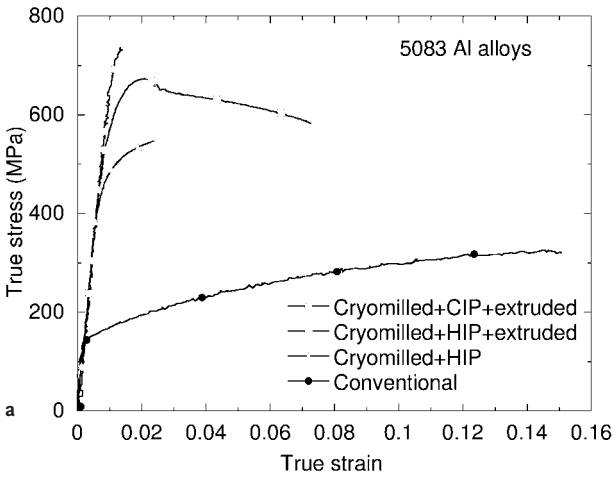

Fig. 12.4 (a) True tensile stress as a function of true strain for four 5083 Al alloys, i.e. a cryomilled nanostructured 5083 Al alloy consolidated via CIP and extrusion [44], and a cryomilled nanostructured 5083 Al alloy consolidated via HIP and extrusion [62], a cryomilled nanostructured 5083 Al alloy consolidated via HIP [62], and a conventional 5083 Al [49].

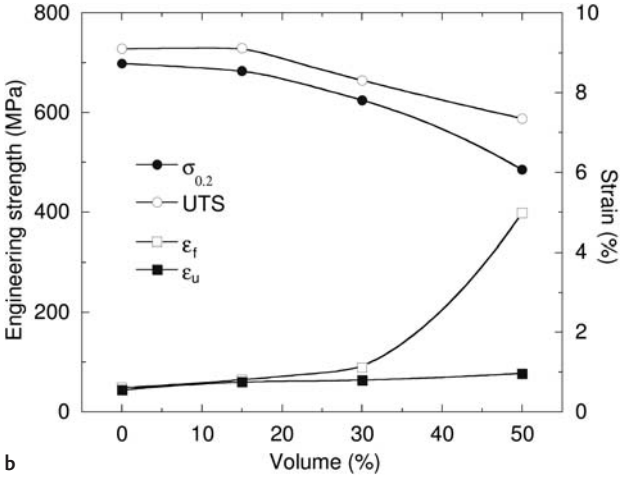

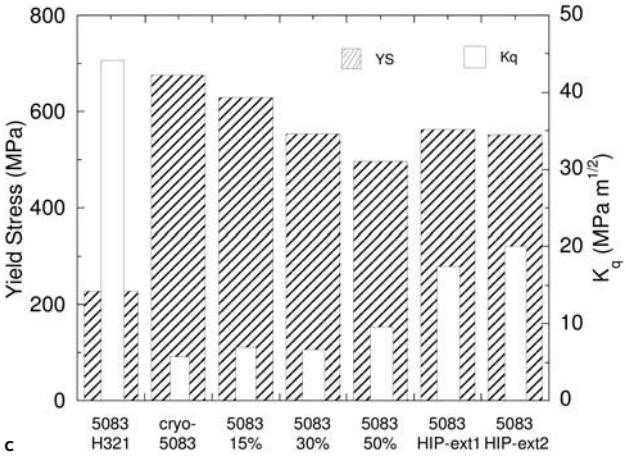

Fig. 12.4 b, c (b) Tensile stress as a function of strain of bimodal cryomilled Al 5083 alloys [44]. (c) Comparison of strength and fracture toughness of several cryomilled 5083 Al alloys [63] with those of a conventional 5083 Al alloy.

ing of cryomilled powder with unmilled powder [44]. After CIP and extrusion, the nanostructured regions have grain sizes of 100–300 nm. Larger-grained bands, originating from the unmilled powder, have a grain size of ~500 nm – 1 μm, elongated along the extrusion direction. There is a trend of decreasing strength and increasing elongation with increasing fraction of coarse-grain material, as shown in Fig. 12.4 (b). The bimodal microstructure in cryomilled Al alloys also leads to an enhancement of fracture toughness. Figure 12.4 (c) compares the strength and fracture toughness of several cryomilled 5083 Al alloys [63] with those of the conventionally processed 5083 Al alloy (a benchmark material). The cryomilled 5083 Al alloy is processed by CIP and followed by extru-

sion [44]. The cryomilled 5083 Al alloy (HIP and ext1) and the cryomilled 5083 Al alloy (HIP and ext2) are processed by HIP followed by extrusion at temperatures of 473 K and 498 K, respectively [45]. As shown in Fig. 12.4 (c), the 100% cryomilled 5083 Al alloy has a much higher strength, but with a low fracture toughness. With increasing volume fraction of coarse grains, the fracture toughness increases. Two cryomilled 5083 Al alloys processed by HIP and extrusion have both high strengths and reasonably high fracture toughness, because of the presence of an intrinsic bimodal microstructure that evolves during HIP, as discussed previously.

The microstructure produced by mixing cryomilled nanostructured powders with unmilled coarse-grained powders is analogous to that of short-fiber metal matrix composites, in that the larger-grain bands are distributed parallel to the extrusion direction. Microcracks are expected to nucleate in the nanostructured regions and then propagate along the grain boundaries during deformation. When a microcrack meets a large-grain band, the band will retard propagation by blunting the crack and delaminating the interfaces between the large-grain and fine-grain regions. When more dislocations are emitted into the large grain, a new slip surface may be formed, eventually leading to necking and cavitation within the large-grain bands. The bridging of ductile phase ligaments will restrict crack openings and undergo plastic stretching, thus promoting shielding of the crack tip. Both the delamination and the necking of ductile large-grain regions absorb significant energy, resulting in an enhanced tensile ductility and fracture toughness [44].

Inspection of the tensile stress–strain curves shown here, and published elsewhere, reveals a common characteristic: the presence of a short, rapid strain-hardening region, in which multiplication of dislocations may occur. Although it is expected that there are strong interactions between dislocations and dispersoids in nanostructured materials processed by consolidation of milled powders, the dislocations may be able to move after yielding, resulting in classic strain-hardening behavior [64].

The reported high strength in nanostructured metallic materials could be the result of the contributions of several types of strengthening mechanisms. It is expected that the following mechanisms may contribute to strengthening: grain-size effect, solid-solution hardening, dispersion strengthening, and precipitate strengthening, *etc.* On the basis of the Hall–Petch relationship ($\sigma_d = \sigma_0 + k_y \cdot d^{-1/2}$ where σ_0 is a frictional stress required to move dislocations and k_y is the locking parameter), there is an increase in strength with a decrease in grain size [65]. In addition to the increase in strength due to grain size, ball milling usually extends the solid solubility of solute elements [4], thus leading to the larger solid solution strengthening than that in conventional materials. A third contribution to strength involves strong interactions of dislocations with dispersoids or precipitates, i.e. Orowan strengthening. In addition to the above-mentioned strengthening mechanisms, composite strengthening due to the presence of a hard reinforcement exists in the nanostructured composites consolidated from milled nanocomposite powders [66].

Another frequently observed characteristic of ball-milled metallic materials, in common with many other BNMs, is the phenomenon of a stress drop. BNMs processed via consolidation of milled powders usually contain contamination elements and nanoscale dispersoids that are generated during milling [41, 50]. One possible explanation for the stress drop is the detachment of dislocations from ultrafine oxide or nitride dispersoids [49, 67]. Dislocations can accumulate around dispersoids during plastic deformation. When dislocations burst out from nanometric dispersoids under high applied stresses or annihilate each other in the vicinity of dispersoids, a stress drop can occur [49]. A similar stress drop observed in other UFG materials consolidated from milled powders [67–69], has been attributed to the collective movement of large numbers of mobile dislocations that were previously pinned by a complex network of fine dislocation cells. The subsequent flow stress plateau was attributed to the reduced resistance to glide of unpinned dislocations [68].

The stress-drop phenomenon that has been documented for several cryomilled nanostructured Al alloys has been associated with the initiation of Lüders bands [44]. After Lüders-band formation, plastic deformation is observed to accelerate on one side of the band. In addition, propagation of the Lüders band is limited by the presence of glide obstacles and does not extend. Therefore, it has been proposed that the deformation strain that follows the attainment of the peak stress is principally related to the formation and propagation of a Lüders strain [44]. Following the initiation of Lüders band or necking, the phenomenon of low strain hardening or work-softening behavior is often observed in nanostructured or UFG Al alloys [41, 50, 67–74]. Although the underlying mechanisms of the low strain-hardening or work-softening behavior are not fully understood, three possible explanations can be offered as follows.

First, in an investigation of MA Al alloys, the work-softening behavior was rationalized on the basis of a modified theory of low-energy dislocation structure (LEDS) [68, 75]. In this study it was proposed that the work softening was accomplished via a reduction of dislocation density or a reduction of the Hall–Petch strengthening effect. It is quite likely that during the course of MA, exceptionally high dislocation densities may have been introduced. In fact, high dislocation densities, on the order of 1.3×10^{17} m^{-2}, are indeed observed in cryomilled Al-Mg powders with a grain size of $\sim$25 nm [16, 18]. After consolidation, the dislocation densities in cryomilled Al alloys may remain high, since dislocations are likely to be stabilized via interactions with nanometric dispersoids documented for a variety of systems [50, 68, 76]. The dislocation densities in the dispersion-strengthened materials might be higher than those in dispersoid-free materials. Therefore, subsequent plastic deformation will cause the dislocation density to be reduced to that in the equilibrium status and thus the flow stress will not increase, since every new glide dislocation loop will give rise to the annihilation of more than its own length, resulting in work-softening behavior [68]. Work softening may also be related to a reduction in the friction stress of the Hall–Petch strengthening during the unlocking of dislocations from impurity or alloying atmospheres, and/or during the breaking of barriers in grain or dislocation structures [64].

A second explanation is the occurrence of dynamic recovery during plastic deformation [49, 64]. Mobile dislocations can be trapped by both impenetrable obstacles and forest dislocations, forming additional obstacles to glide that contribute to strain hardening. On the other hand, immobile dislocations may be annihilated due to cross-slip or rearrange to form subboundaries of relatively low energy, contributing to dynamic recovery [77, 78]. In a related study of the tensile and compressive behavior of an UFG AlFeVSi alloy, it has been proposed that dynamic recovery occurs in the low strain-hardening region [79]. Although solute additions usually retard dynamic recovery by increasing lattice frictional stress and thereby inhibiting dislocation slip, a high disorder region, as well as the associated high vacancy concentration in cryomilled Al alloys may facilitate recovery, causing low strain hardening and a relatively high ductility.

The third explanation is the notion that grain boundaries act as sources and sinks for dislocations that contribute to plastic deformation [80]. It is observed that there is a low value of the activation volume in cryomilled Al alloys with the grains on the order of 100–200 nm. The low value of activation volume during plastic deformation suggests that dislocations do not accumulate within the grains but glide to grain boundaries, resulting in the elastic-perfectly plastic behavior in cryomilled Al alloys as well as in other UFG materials [80]. Further investigation is necessary to fully explain the observed behavior.

12.6 Summary

During ball milling, the material experiences severe plastic deformation, which leads to the grain refinement and eventually the formation of nanostructured grains. Cryomilling, which is conducted in a liquid-nitrogen slurry, takes advantage of both the extremely low temperature of the liquid-nitrogen medium and the advantages that are provided with conventional mechanical milling. The extremely low milling temperature in cryomilling suppresses the recovery and recrystallization and leads to finer grain structures and more rapid grain refinement. The cryomilled powders exhibit grain sizes that are comparable to the minimum grain sizes achieved in mechanical milling. The milling time used for metal matrix composites was much shorter than that needed with normal mechanical milling. In addition, there is a uniform distribution of the reinforcement and good matrix/reinforcement interfaces in metal matrix composites processed by cryomilling.

Conventional powder metallurgy processes such as hot isostatic pressing or cold isostatic pressing have been used as primary consolidation approaches for bulk nanostructured metallic materials. The HIP process, which combines pressure and temperature, can be used to achieve a particular density at a lower temperature than would be required for sintering alone and at a lower pressure than required for CIP. After the primary processing such as HIP or CIP, a secondary processing such as extrusion or forging can be applied to remove residu-

al porosity and improve mechanical properties. Once consolidated, milled nanostructured materials typically possess considerable strength compared to both conventional and fine-grained materials processed by other methods. In order to avoid significant grain growth during consolidation, several rapid consolidation methods such as spark-plasma sintering have been developed. SPS, the combined application of pressure and a pulsed electrical current, can enable a rapid heating rate, with a short densification time. The consolidation conditions have a significant effect on the mechanical properties of bulk nanostructured metallic materials. Nanostructured materials usually have a significant increase in strength, however, at the expense of ductility and toughness, compared to their coarse-grained counterparts. The high strength is primarily attributed to the grain-size effect by the Hall–Petch relation, solid-solution hardening and Orowan dispersion strengthening. Low ductility and low toughness in nanostructured metallic materials can be overcome by adding submicrometer grains into the nanostructured region for the formation of bimodal microstructures. The low strain-hardening behavior in nanostructured metallic materials processed by milling can be attributed to dislocation annihilation or dynamic recovery during plastic deformation.

Acknowledgements

Support from the Office of Naval Research (under Grant No. N00014-04-1-0370 from Dr. Larry Kabakoff for fundamental investigations) and the Marine Corps (under Grant No. N00014-03-C-0163 from Mr. Rod Peterson for applications) is gratefully received.

References

1 H. Gleiter **1989**, *Prog. Mater. Sci.* 33, 223–315.
2 C.C. Koch **2002**, (ed.) *Nanostructured Materials: Processing, Properties and Potential Applications,* Noyes Publications (William Andrew Publishing), Norwich, NY.
3 C.C. Koch **1997**, *Nanostruct. Mater.* 9, 13–22.
4 C. Suryanarayana **2001**, *Prog. Mater. Sci.* 46, 1–184.
5 J.S. Benjamin **1970**, *Metall. Trans. A* 1, 2943–2951.
6 P.S. Gilman, J.S. Benjamin **1983**, *Annu. Rev. Mater. Sci.* 13, 279–300.
7 J.S. Benjamin, T.E. Volin **1974**, *Metall. Trans. A* 5, 1929–1934.
8 D.R. Mautice, T.H. Courtney **1990**, *Metall. Trans. A* 21, 289–303.
9 D.R. Mautice, T.H. Courtney **1995**, *Metall. Mater. Trans. A* 26, 2437–2444.
10 H.J. Fecht **1995**, *Nanostruct. Mater.* 6, 33–42.
11 H.J. Fecht **2002**, in: C.C. Koch (ed.), *Nanostructured Materials: Processing, Properties and Potential Applications,* Noyes Publications, Norwich, New York, pp. 73–113.
12 J. Eckert, J.C. Holzer, I.C.E. Krill, W.L. Johnson **1992**, *J. Mater. Res.* 7, 1751–1761.
13 F.A. Mohamed **2003**, *Acta Mater.* 51, 4107–4119.
14 M.J. Luton, C.S. Jayanth, M.M. Disko, S. Matras, J. Vallone **1989**, (eds), *MRS Proc.* 132, 79–86.

15 R. J. Perez, H. G. Jiang, C. P. Dogan, E. J. Lavernia **1998**, *Metall. Mater. Trans. A* 29, 2469–2475.

16 F. Zhou, X. Z. Liao, Y. T. Zhu, S. Dallek, E. J. Lavernia **2003**, *Acta Mater.* 51, 2777–2791.

17 F. Zhou, D. Witkin, S. Nutt, E. J. Lavernia **2004**, *Mater. Sci. Eng.* A375–377, 917–921.

18 X. Z. Liao, J. Y. Huang, Y. T. Zhu, F. Zhou, E. J. Lavernia **2003**, *Philos. Mag. A* 83, 3065–3075.

19 A. D. Jatkar, R. D. Schelleng, J. A. J. Varall **1986**, Process for producing composite materials, MPD Technology Corp., USA.

20 M. S. Zedalis, P. S. Gilman **1990**, Aluminum-based metal matrix composites from mechanically alloyed powder, Allied-Signal Inc., USA.

21 C. C. Koch **1993**, *Nanostruct. Mater.* 2, 109–29.

22 C. Goujon, P. Goeuriot, M. Chedru, J. Vicens, J. L. Chermant, F. Bernard, J. C. Niepce, P. Verdier, Y. Laurent **1999**, *Powder Technol.* 105, 328–336.

23 J. He, J. M. Schoenung **2003**, *Metall. Mater. Trans. A* 34, 673–683.

24 J. B. Fogagnolo, F. Velasco, M. H. Robert, J. M. Torralba **2003**, *Mater. Sci. Eng. A* 342, 131–143.

25 J. B. Fogagnolo, E. M. Ruiz-Navas, M. H. Robert, J. M. Torralba **2002**, *Scr. Mater.* 47, 243–248.

26 J. Ye, J. He, J. M. Schoenung **2006**, *Metall. Mater. Trans. A*, 37, 3099–3109.

27 K. H. Chung, J. He, D. H. Shin, J. M. Schoenung **2003**, *Mater. Sci. Eng. A* 356, 23–31.

28 M. S. El-Eskandarany **1998**, *J. Alloys Compd.* 279, 263–271.

29 V. V. Prasad, B. V. R. Bhat, Y. R. Mahajan, P. Ramakrishnan **2002**, *Mater. Sci. Eng. A* 337, 179–186.

30 H. Zhang, N. Maljkovic, B. S. Mitchell **2002**, *Mater. Sci. Eng. A* 326, 317–323.

31 S. L. U. Filho, R. Rodriguez, J. C. Earthman, E. J. Lavernia **2003**, *Mater. Sci. Forum* 416–418, 213–218.

32 F. Tang, M. Hagiwara, J. M. Schoenung **2005**, *Scr. Mater.* 53, 619–624.

33 J. R. Groza, R. J. Dowding **1996**, *Nanostruct. Mater.* 7, 749–768.

34 D. L. Bourell, J. R. Groza **2002**, *ASM Handbook – Powder Metal Technologies & Applications*, Vol. 7, ASM International, Materials Park, OH.

35 J. R. Groza **2002**, in: C. C. Koch (ed), *Nanostructured Materials: Processing, Properties and Potential Applications*, Noyes Publications, Norwich, New York, pp. 115–178.

36 D. B. Witkin, E. J. Lavernia **2006**, *Prog. Mater. Sci.* 51, 1–60.

37 F. Zhou, R. Rodriguez, E. J. Lavernia **2002**, *Mater. Sci. Forum* 386–388, 409–414.

38 M. F. Ashby, In: I. Jenkins, J. V. Wood **1991**, (eds.) *Powder Metallurgy: an Overview*, The Institute of Metals, London, pp. 144–166.

39 H. V. Atkinson, S. Davies **2000**, *Metall. Mater. Trans. A* 31, 2981–3000.

40 Z. Lee, R. Rodriguez, R. W. Hayes, E. J. Lavernia, S. R. Nutt **2003**, *Metall. Mater. Trans. A* 34, 1473–1481.

41 V. L. Tellkamp, A. Melmed, E. J. Lavernia **2001**, *Metall. Mater. Trans. A* 32, 2335–2343.

42 D. Witkin, E. J. Lavernia, **2003**, in L. L. Shaw, C. Suryanarayana, R. S. Mishra (eds.) *Processing and Properties of Structural Nanomaterials*, TMS, Warrendale, PA, p. 117–124.

43 Y. S. Park, K. H. Chung, N. J. Kim, E. J. Lavernia **2004**, *Mater. Sci. Eng. A* 374, 211–216.

44 B. Q. Han, Z. Lee, D. Witkin, S. R. Nutt, E. J. Lavernia **2005**, *Metall. Mater. Trans. A* 36, 957–965.

45 D. Witkin, B. Q. Han, E. J. Lavernia **2005**, *J. Mater. Res.* 20, 2117–2126.

46 J. D. Whittenberger, E. Arzt, M. J. Luton **1990**, *J. Mater. Res.* 5, 271–277.

47 J. D. Whittenberger, E. Arzt, M. J. Luton **1990**, *J. Mater. Res.* 5, 2819–2827.

48 J. E. Carsley, A. Fisher, W. W. Milligan, E. C. Aifantis **1998**, *Metall. Mater. Trans. A* 29, 2261–2271.

49 B. Q. Han, Z. Lee, S. R. Nutt, E. J. Lavernia, F. A. Mohamed **2003**, *Metall. Mater. Trans. A* 34, 603–613.

50 B. Q. Han, E. J. Lavernia, F. A. Mohamed **2005**, *Metall. Mater. Trans. A* 36, 345–355.

51 B. Lynn-Ferguson, O. D. Smith **1984**, *ASM Handbook – Powder Metallurgy*, Vol. 7, ASM International, Materials Park, pp. 537.

52 R. L. Anderson, J. Groza **1988**, *Metal Powder Report* 43, 678–681.

53 H.W. Chan **1988**, *Mater. Des.* 9, 355–358.
54 J.R. Groza, A. Zavaliangos **2000**, *Mater. Sci. Eng. A* 287, 171–177.
55 P.G. Sanders, J.A. Eastman, J.R. Weertman **1997**, *Acta Mater.* 45, 4019–4025.
56 C.J. Youngdahl, P.G. Sanders, J.A. Eastman, J.R. Weertman **1997**, *Scr. Mater.* 37, 1997.
57 J.R. Ryu, K.I. Moon, K.S. Lee **2000**, *J. Alloys Compd.* 296, 157–165.
58 Q. Wei, T. Jiao, K.T. Ramesh, E. Ma **2004**, *Scr. Mater.* 50, 359–364.
59 K.I. Moon, H.S. Park, K.S. Lee **2001**, *J. Alloys Compd.* 325, 236–244.
60 H.W. Zhang, R. Gopalan, T. Mukai, K. Hono **2005**, *Scr. Mater.* 53, 863–868.
61 M. Jain, T. Christman **1994**, *Acta Metall.* 42, 1901–1911.
62 D. Witkin, B.Q. Han, E.J. Lavernia **2006**, *Metall. Mater. Trans. A* 37, 185–194.
63 P.S. Pao **2005**, Fracture toughness of cryomilled Al alloys, ONR Report.
64 D. Kuhlmann-Wilsdorf, **1999**, *Philos. Mag. A* 79, 955–1008.
65 J.R. Weertman **1993**, *Mater. Sci. Eng. A* 166, 161–167.
66 J. Ye, B.Q. Han, Z. Lee, B. Ahn, S.R. Nutt, J.M. Schoenung **2005**, *Scr. Mater.* 53, 481–486.
67 Y.W. Kim, L.R. Bidwell **1982**, *Scr. Metall.* 16, 799–802.
68 H.G.F. Wilsdorf, D. Kuhlmann-Wilsdorf **1993**, *Mater. Sci. Eng. A* 164, 1–14.
69 H.R. Last, R.K. Garrett **1996**, *Metall. Mater. Trans. A* 27, 737–745.
70 T. Mukai, M. Kawazoe, K. Higashi **1998**, *Nanostruct. Mater.* 10, 755–765.
71 R.W. Hayes, R. Rodriguez, E.J. Lavernia **2001**, *Acta Mater.* 49, 4055–4068.
72 T. Hasegawa, T. Miura, T. Takahashi, T. Yakou **1992**, *ISIJ Int.* 32, 902–908.
73 X.K. Sun, H.T. Cong, M. Sun, M.C. Yang **2000**, *Metall. Mater. Trans. A* 31, 1017–1024.
74 Y. Champion, C. Langlois, S. Guerin-Mailly, P. Langlois, J.-L. Bonnentien, M.J. Hytch **2003**, *Science* 300, 310–311.
75 D. Kuhlmann-Wilsdorf, H.G.F. Wilsdorf **1992**, *phys. stat. sol. (a)* 172, 235–248.
76 B.S. Dehiya, J.R. Weertman, in J.C. Earthman, F.A. Mohamed **1997**, (eds.) *Creep and Fracture of Engineering Materials and Structures*, The Minerals, Metals & Materials Society, Warrendale, PA, p. 129–137.
77 R. Kral **1996**, *phys. stat. sol. (a)* 157, 255–263.
78 F.J. Humphreys, M. Hatherly **1995**, Recr*ystallization and Related Annealing Phenomena*, Pergamon, New York, pp. 127.
79 S. Hariprasad, S.M.L. Sastry, K.L. Jerina **1996**, *Acta Mater.* 44, 383–389.
80 R.W. Hayes, D. Witkin, F. Zhou, E.J. Lavernia **2004**, *Acta Mater.* 52, 4259–4271.

13
Bulk Nanostructured Materials from Amorphous Solids

Gerhard Wilde

13.1
Introduction

Nanostructured materials and composites present a promising class of engineering materials with structural length scales between about 5 nm and 100 nm. This microstructure characteristics result in properties and property combinations that are often enhanced or even unique compared to the polycrystalline counterparts [1, 2]. This attracts enormous interest in basic research as well as in the application-oriented engineering sciences or – more recently – even in the public media. In the historical perspective, and even disregarding the obvious coincidence of structure formation on a nanometer scale and basic synthetic chemistry, nanostructured materials have been around for a very long time. Natural examples can be found in abundance, such as the surface of butterfly wings, shark teeth or the Abalone shell (Fig. 13.1, upper half) – both latter examples utilize a nanocomposite approach to achieve high hardness or strength combined with a large toughness [3–6]. Early man-made examples (Fig. 13.1, lower half) include damascene sword making (or equivalently, the Japanese art of sword making), where layers of two different steel grades with largely different mechanical properties are welded and repeatedly forged in over a hundred layers, yielding a nanocomposite that combines high hardness and a large elastic limit. A different – and probably earlier – technique of damascene sword making was based on a banding phenomenon of Fe_3C precipitates in the legendary Indian wootz steel [7]. Even the size dependence of materials properties that represents the very foundation of today's interest in nanostructured materials has been exploited already several hundred years ago, although without addressing or understanding the underlying mechanisms. A prominent example is given by church windows from the middle ages; colloidal gold or silver nanocrystals are dispersed in window glass to obtain the special bright red or green colors [8]. In this case, the size-dependent shift of the surface plasmon wavelength of gold or silver is responsible for the color of these materials [9]. Thus, utilizing nanoparticles, the color could be tuned without hampering the transparency of the glass. However, further examples for utilizing an amorphous or

Bulk Nanostructured Materials. Edited by M. J. Zehetbauer and Y. T. Zhu

ISBN: 978-3-527-31524-6

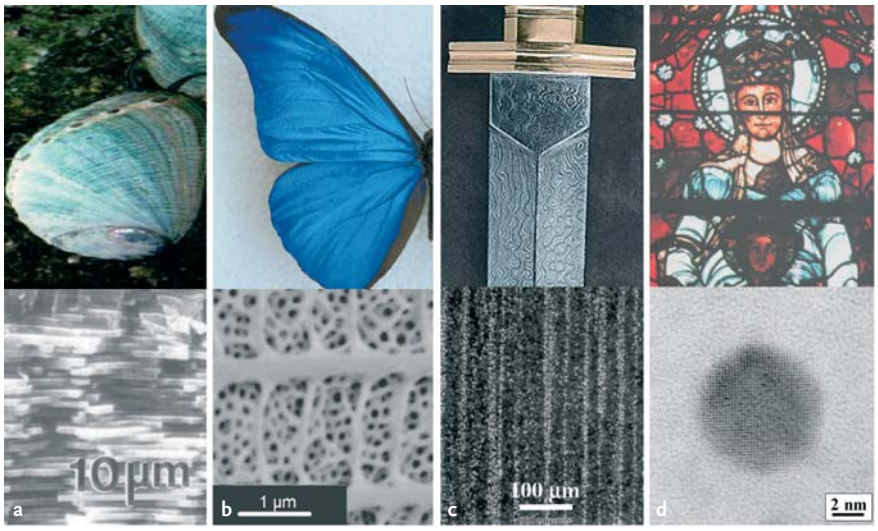

Fig. 13.1 Examples of natural and man-made nanostructures in normal view and at higher resolution revealing the nanoscale microstructure, respectively. (a) Abalone shell with the typical appearance of the outer shell. The microstructure reveals thin alternating layers of aragonite and layers of the protein matrix that form a composite with high strength and high toughness (reprinted with permission from the Materials Research Society, MRS, [4]). (b) Butterfly wing of the butterfly *Morpho rhetenor* (reprinted by permission from Macmillan Publishers Ltd, Nature [5], copyright 2003). The scanning electron microscopy image displays the photonic structure of the wing surface that causes the iridescence (reprinted figure with permission from [6], copyright (2003) by the American Physical Society). (c) Celtic sword that was forged in so-called "damascene" tradition, using so-called wootz steel. The surface pattern results from a carbide-banding phenomenon produced by the microsegregation of minor amounts of carbide-forming elements present in the wootz ingots (reprinted with permission from The Minerals, Metals and Materials Society, TMS, [7]). (d) Window of Notre Dame de la Belle Verrière. The red color in medieval church windows is often generated by gold nanoparticles, green is due to silver nanoparticles that are dispersed within the glass. The micrograph shows a silver nanoparticle in high resolution. (Reprinted with permission from the Materials Research Society, [8]).

a vitreous material to synthesize bulk nanostructured materials are rather sparse, and in some instances, such as in solid-state dielectrics for supercapacitors, nanostructure formation from the amorphous state often terminates the usability of the device due to the generation of conductive pathways that prevent or at least limit electrical charging [10].

Especially in the two decades after the pioneering work by H. Gleiter and coworkers in the early 1980s [11, 12], the major part of the published work on nanomaterials is related to nanocrystalline powders or to more massive structures that are obtained by cold or hot consolidation methods of powdery starting material. Yet, inherent to any powder processing approach are issues that are re-

lated to contamination due to the increased reactivity of surfaces and interfaces and to residual porosity, especially when the consolidation process needs to be performed at low homologous temperatures to avoid significant coarsening of the microstructure. With today's synthesis methods that utilize UHV-compatible instrumentation, the amount of surface contamination can be dramatically reduced – yet, with increased costs and without a clear perspective for upscaling. Thus, alternative methods for synthesizing bulk nanostructured materials that start from the bulk are attractive; both from the perspective of basic research and concerning applied materials science.

In the following, metallic materials will mostly be regarded, since the metallic bond results in rather isotropic materials that – in the amorphous state – are close to being real-world representatives of molecular liquids or glasses. In most cases, the discussion presented for the case of metals can – with slight modifications – also be applied for oxide glasses. In fact, the issue of phase separation that will be discussed shortly in Section 13.3 is, in practice, much more important for oxide glasses than for metals [13]. An additional and important class of materials that are often obtained in glassy form and that tend to nanocrystallize upon thermal attenuation and also – in particular cases – upon deformation, is presented by polymers and especially by polymer blends [14, 15]. These materials can also undergo a partial nanocrystallization upon plastic straining that is related to the entropic contribution of chain folds and the elastic anisotropy of the polymer chains. This combination of properties allows adjusting an ordered (crystalline) state by applying a mechanical load and a disordered (amorphous) state otherwise. The interested reader is referred to [16] for further information on polymers.

Within this book, several different synthesis methods and techniques are described that serve to produce bulk materials with ultrafine or even nanometer-scaled grain size from bulk polycrystalline material; that is, methods that reduce the size of millimeter- or micrometer-sized crystalline grains to the grain size range below 100 nm by introducing nonequilibrium amounts of defects into the material, mostly by means of continued plastic deformation [17, 18]. In this chapter, additional synthesis options are described that are based on starting from an amorphous rather than a crystalline bulk material. Aside from expanding the range of synthesis options, these methods can also yield bulk nanocrystalline materials with extremely small nanocrystal sizes [19] and narrow size distribution or bulk amorphous/nanocrystalline composites with unique property combinations that might not be obtainable by any other processing route [20, 21]. Two basically different underlying synthesis methods can be applied for synthesizing bulk nanostructured materials from an amorphous solid, rather classically by thermal attenuation or – alternatively – by plastic deformation, as recently described [22]. These two options are discussed in separate sections after a brief introduction into the basics of amorphization and devitrification in the following section.

13.2
Amorphization and Devitrification

A solid material that does not display a long-range translational periodicity of the atomic (or molecular) equilibrium positions in real space represents an amorphous solid. If the amorphous solid that reveals a nonequilibrium state can undergo a continuous transformation – the glass transition – to become a metastable undercooled liquid, then the amorphous solid belongs to the class of materials that are termed "glasses" [23]. In this chapter, amorphous structures will be termed "amorphous" whether or not they are glasses, since this distinction is of minor concern for the following. As a side note for the interested reader: the metallic systems that will be the basis for the major part of the present chapter are actually true glasses [24].

Often, the reactions that occur during the freezing of undercooled liquids are viewed as nonequilibrium processes. While such a claim is valid in one sense, since a finite rate of a transformation process does involve a departure from full equilibrium conditions, this identification is also somewhat misleading since the various stages of materials processing can involve different levels of departure from full equilibrium [25]. The transition from stable to metastable equilibrium is schematically illustrated in Figs. 13.2 (a)–(c) where the kinetic suppression of an equilibrium γ phase (Fig. 13.2 (a)) yields a metastable eutectic involving the α and β phases (Fig. 13.2 (b)). Under extreme conditions, significant loss

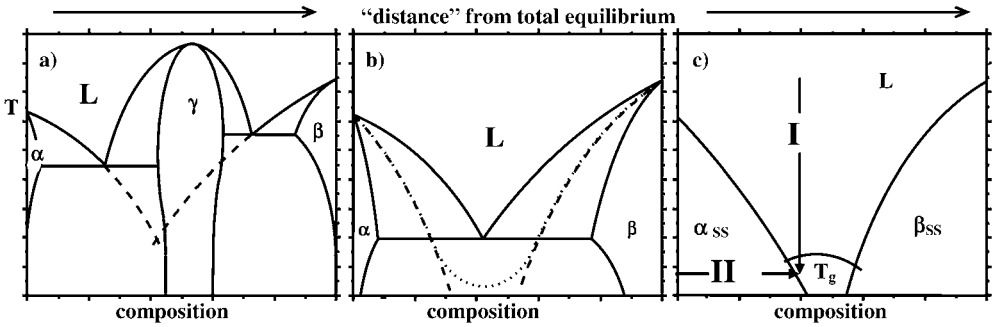

Fig. 13.2 Schematic of the evolution of metastable phase equilibria. The equilibrium phase diagram of a system with an intermediate phase is shown in (a) as an example. Included are the metastable extensions of the liquidus curves for the primary solution phases (dashed). Thus, solidification under metastable equilibrium conditions can result in bypassing of the intermediate phase yielding a metastable eutectic phase diagram as in (b). The T_0 curves for the primary solutions are included in (b), as dashed-dotted lines. The extensions of these curves to temperatures below the metastable eutectic are indicated as dashed and dotted curves, respectively. If the primary phases have different structures and low mutual solubility, then the T_0 curves might not intersect (c). Such a situation favors glass formation by either rapid quenching (pathway I) or by solid-state mixing (pathway II).

of interfacial equilibrium for either a stable or metastable phase can develop when even interfacial relaxation becomes too slow (Fig. 13.2 (c)). With the loss of interfacial equilibrium, thermodynamics can still be used to restrict the possible range of compositions that can exist at an interface at various temperatures since the selection must yield a net reduction in the free energy of the system. One way to represent the thermodynamic restrictions is based upon the application of T_0 curves, which represent the limiting condition for partitionless transformation [26]. For example, as interfacial equilibrium is lost, the liquidus and solidus boundaries in Fig. 13.2 (b) collapse to the T_0 curves. Because of the diffusional constraint due to partitioning, crystallization can be inhibited by rapid quenching to promote glass formation [27]. Solid-state glass formation as an alternative vitrification route is often viewed as a nonequilibrium process resulting from the destabilization of crystalline phases when the maximum metastable solubility is exceeded [28]. Within this framework, amorphization is depicted by a generalized phase diagram for partitionless transformations [29] as also indicated by Fig. 13.2 (c), i.e. the T_0 curve of a common solid-solution phase of the respective system and the composition-dependent glass temperature. According to this perspective, glass formation is enabled by rapidly quenching a homogeneous melt (Fig. 13.2 (c), pathway I) or, alternatively, by compositional variation at a constant low temperature (Fig. 13.2 (c), pathway II) leading to equivalent glassy states, except for relaxation.

Thus, techniques for amorphization include a synthesis pathway that prevents the material from attaining the stable equilibrium. Basic thermodynamics thus state that after finite time at finite temperature, the unstable solid or the metastable liquid will attain the stable state by a devitrification transformation, i.e. by crystallization. This process – in accordance with Ostwald's step rule – often involves metastable transient states of intermediate free energies [30]. In reality, the time for this transformation to occur might be very long if the material is kept at temperatures sufficiently below the glass transition [23]. However, if heated to temperatures in the vicinity of or above the glass transition, crystallization is prone to occur rather rapidly, especially for the amorphous metallic alloys known so far. Rare exceptions that are related to specific kinetic "barriers" are presented by some polymeric materials or e.g. by boron oxide (B_2O_3) that do not show a distinct tendency to crystallize at any temperature [31].

In accordance with classical nucleation theory [32], the overall transformation rate can be represented by $I = \Omega \exp(-\Delta G^*/k_{bB}T)$ with an effective activation energy, ΔG^*, that depends on the respective changes of the free enthalpy per volume and the interfacial free energy density and a prefactor, Ω, that depends on the density of nucleation sites on a volume or surface basis and an attempt frequency. T is the absolute temperature and k_B is Boltzmann's constant. While the specifics of the nucleation process in multicomponent materials, such as glass formers, require detailed analyses of the nucleating phases and the coupled fluxes of solute and solvent [33], experimental analyses of the nucleation kinetics in agreement with simplified theoretical analyses have indicated that a typical value for the nucleation site density for heterogeneous nucleation

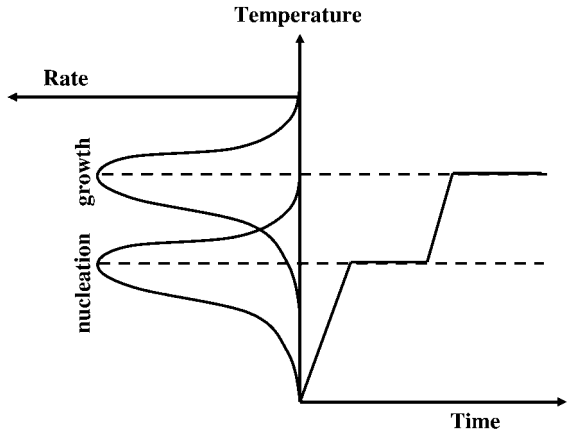

Fig. 13.3 Schematic representation of the dependence of nucleation rate and growth rate on temperature. On the right side of the diagram, a temperature–time profile is indicated that is commonly applied for synthesizing glass ceramics from silicate glasses. Holding near temperatures where the nucleation rate attains its maximum yields a high number density of small crystallites. Rapid heating to higher temperatures and annealing at a temperature where the growth rate is high serves to fully crystallize the material by rather uniform growth of all crystals. The final product microstructure is thus characterized by a narrow size distribution of rather small grains.

in the volume of an undercooled liquid is about 10^{13} sites/m^3 [32, 34]. Thus, the spacing between individual nucleation sites on average is on a scale of several micrometers to several tens of micrometers. If it were assumed that every nucleation site generates one stable crystallite and that all crystallites would grow isotropically at the same rate, then the resulting microstructure would consist of micrometer-scaled, equiaxed grains, as frequently observed by microstructure analyses of devitrified materials with a rather high stability of the amorphous state against crystallization. Here, the fact that the maximum of nucleation rate and growth rate are often displaced on the temperature scale (Fig. 13.3) such that the maximum nucleation rate occurs at temperatures that are lower than the temperature where the growth rate has its maximum [35] helps preventing rapid growth of only a few crystallites that nucleated first, as conventionally observed after solidification near the melting temperature [36].

Although some product structures that are based on partially or fully crystallizing bulk amorphous materials have interesting properties [37–39], it is obvious that the large potential given by nanocrystalline materials can not be accessed by amorphous materials that devitrify in accordance with classical nucleation theory, since the resulting microstructures are far too coarse. Thus, alternative mechanisms need to be operative to obtain bulk nanostructured materials from processing an amorphous precursor state. The following sections will present an overview on some new opportunities for bulk nanostructure formation that are based on "nonclassical" nucleation kinetics.

13.3
Thermally Induced Nanocrystallization

However different and/or beneficial the properties of nanostructured materials are with respect to the respective bulk material, stabilizing the material against detrimental coarsening presents in all cases a basic precondition for any technical use. Apart from restricting the range of candidate materials to the class of refractories such as ceramics or high melting point metals that are kinetically stabilized at or near ambient conditions, a composite approach involving either two nanosized crystalline or amorphous phases or an extended polycrystalline or amorphous matrix and one nanocrystalline phase are obvious solutions for the latter issue since the material transport required for coarsening is severely hampered by a composite structure with limited mutual solubility.

In recent years, the spectrum of synthesis options for producing nanocrystalline materials and nanocomposites has become considerably broader. Apart from inert-gas condensation [12], ball milling [40] or different deposition processes, rapid progress towards bulk quantity production has been made with severe plastic deformation processes [2]. Yet, synthesizing kinetically stabilized two-phase composite nanostructures by plastic-deformation processing does not seem to be straightforward, although nanocomposites of two immiscible components [41] or of two components that require large activation energies for mixing [42] have been obtained. An alternative nonequilibrium synthesis route utilizes so-called marginal glass formers – a class of alloys based on Al, Mg or Fe – that require extremely high quenching rates to prevent complete crystallization [43].

In these cases, primary crystallization reactions represent the key to achieving the microstructural designs associated with the most attractive structural properties, however, these same reactions also appear to contribute to the marginal glass-forming behavior. Based upon the comprehensive analysis developed by Inoue [44] it is clear that glass formation is favored for hypereutectic compositions. However, for the hypereutectic composition range, it is somewhat unexpected that the kinetic competition during crystallization would favor the terminal solution phase as the primary reaction product. For the most part, the kinetic competition is largely determined by the relative magnitudes for the activation barrier for nucleation, ΔG^*, which is proportional to $(\sigma_{ls})^3/(\Delta G_v)^2$ where σ_{ls} is the liquid-solid interfacial energy and ΔG_v is the driving free energy for nucleation. For primary crystallization that involves solute partitioning, the maximum value for ΔG_v is determined by the parallel tangent construction [45], where the individual undercooling levels of the precipitating phases are taken into account, as shown in Fig. 13.4 (a) for the example of an Al-rich Al-Sm alloy. The result of the parallel tangent analysis is presented in Fig. 13.4 (b) where it appears that over the entire hypereutectic composition range of glass formation between 8 to 12 at% Sm, the $Al_{11}Sm_3$ intermetallic phase is favored, yet the primary Al phase is observed [46, 47]. This indicates that there is a heterogeneous nucleation reaction to favor the Al phase [48].

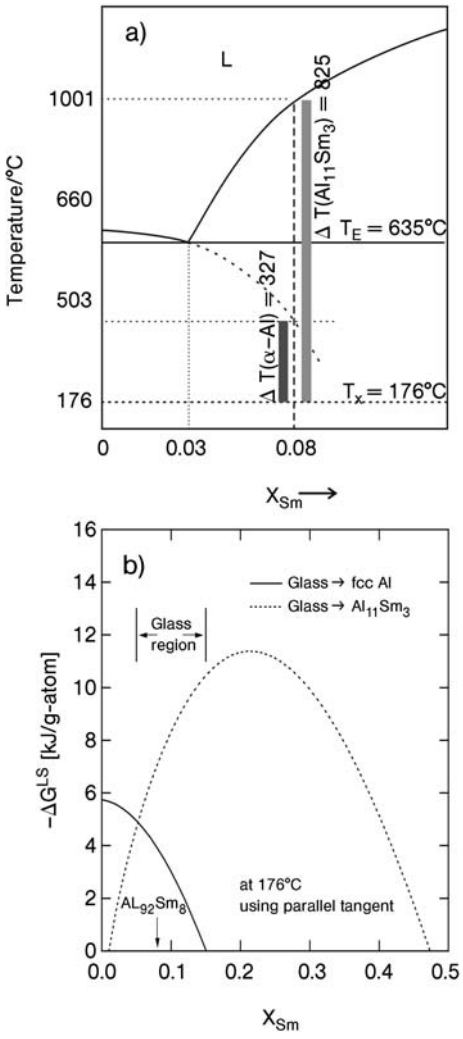

Fig. 13.4 (a) The Al-rich portion of the Al-Sm phase diagram showing the relative undercooling for crystallization of the terminal aluminum solid solution (Al) and of the intermetallic $Al_{11}Sm_3$ phase. (b) The composition dependence of the driving free energy for nucleation of Al and $Al_{11}Sm_3$ at 176 °C from the glass, according to the parallel tangent construction.

With respect to the underlying process, it is well accepted that impurity-mediated heterogeneous nucleation cannot account for the observed microstructures. The amount of impurities required to be in accordance with the high nanocrystal number densities far exceeds the amount of impurities in the starting material as well as the detection limit in chemical analyses. However, there are structural arrangements in the melt that may act to serve as a high density of viable catalysts at high undercooling. Some of the possibilities have been suggested by Turnbull [49] as either heterophase or homophase catalysts where minute levels of solute either serve as discrete cores for a catalyst or promote aggregations that act as catalysts. These catalyst effects can be active at low solute levels in the ppm range, but their impact may well dominate the nanocrys-

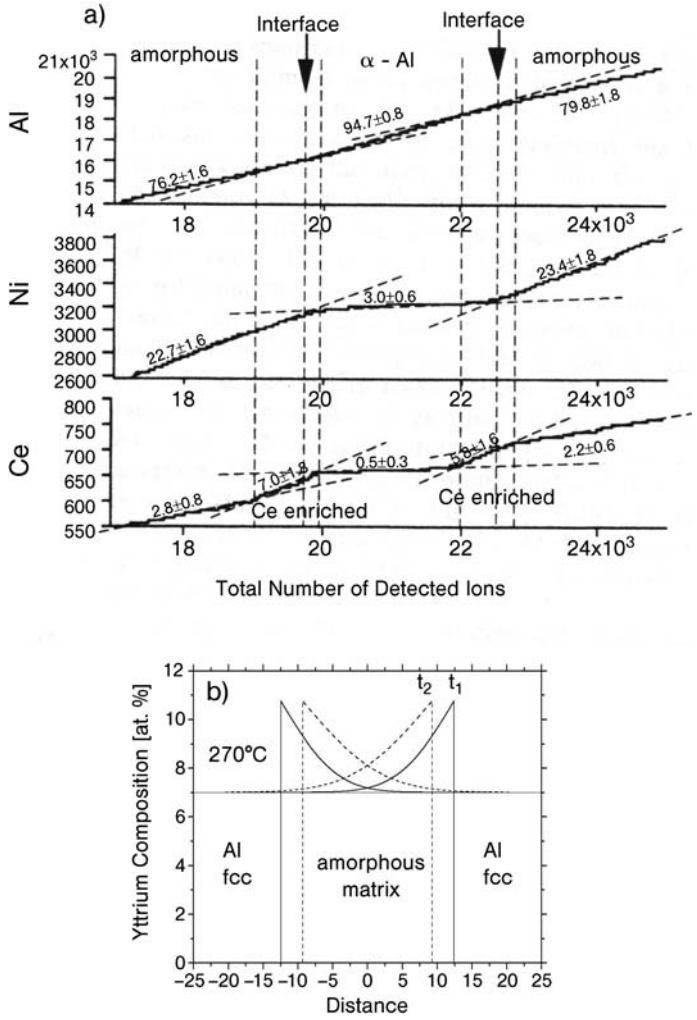

Fig. 13.5 (a) Intensity profiles obtained by atom-probe field-ion microscopy on a partially nanocrystallized ternary Al-Ni-Ce alloy. The (local) magnitude of the slope of the measured data corresponds to the local concentration of the respective atomic species. The data show that Al is slightly enriched in the nanocrystal region (denoted as α-Al) while Ni and Ce are depleted in that region. Clearly, the region surrounding the nanocrystal is enriched in Ce. (Reproduced with permission from *Materials Science and Engineering A*, [53], copyright 1997, Elsevier). (b) The enrichment of the amorphous matrix surrounding the nanocrystals leads to diffusion-field impingement, which slows down the growth of the nanocrystals. The concentration profiles that were calculated for an $Al_{88}Y_7Fe_5$ alloy in accordance with a growth kinetics model [54] are indicated for two different times with $t_2 > t_1$, indicating the progressive overlap of the diffusion fields.

tal formation process. In fact, detailed analyses of the nucleation and growth behavior by calorimetry and quantitative electron microscopy methods have revealed that the size distribution consists of two contributions, i.e. from growth of pre-existing nuclei that were produced during the initial quench and that form crystals that originated from additional nucleation [50]. These results indicate that one option for enhancing the nanocrystal number density is to modify the rapid cooling pathway, although that option might be limited in practice.

In addition, it is evident that one consequence of the solute partitioning during primary crystallization is an enrichment of the amorphous matrix composition. If all of the solute rejected by the growing Al nanocrystal were distributed uniformly within the amorphous matrix, then the application of the parallel tangent construction reveals that the driving free energy for continued nanocrystal nucleation would decrease continuously with further reaction. In effect, the reduction in ΔG_v would yield a reduction in nucleation rate even in the presence of a high heterogeneous nucleation site density [48]. However, it has been established by 3-dimensional atom-probe investigations that the large rare-earth atom solutes do not distribute uniformly within the amorphous matrix, but tend to pile up at the interface between the nanocrystal and the matrix [51, 52], as indicated in Fig. 13.5. The non-uniform distribution will inhibit further transformation of existing nanocrystals, restrict the volume that is available for further nucleation and will also lead to a reduction in nucleation rate. Therefore, and in addition to property enhancements that will be discussed in Section 13.5, the composite nanostructure is self-stabilizing due to overlapping diffusion fields surrounding the nanocrystals [54]. Thus, the key strategy in enhancing the nanocrystal number density, and to improve both property performance and microstructure stability, is to promote the nucleation density of nanocrystals while minimizing the change of the amorphous matrix phase. One successful approach towards this goal is represented by deformation processing of marginal glass formers, as highlighted in Section 13.4.

13.3.1
Phase Separation of Glasses

Recently, the idea of creating amorphous/amorphous or crystalline/amorphous nanocomposites by utilizing phase-separation processes in metallic glasses has generated significant attention [55, 56]. An additional and not yet explored option is presented by nanoglasses (Fig. 13.6), that is, nanostructured materials that consist of nanoscaled amorphous structural units, which offer an interesting future perspective with potentially unprecedented capabilities to tune the properties of the material. Although a phase separation would potentially have a detrimental effect on the thermal stability, the phase-separation reaction could also be used for the formation of materials with a fine uniform grain-size distribution. This microstructure requires a high internal site density, which can be achieved by the promotion of phase-separation reactions. The basic idea goes back to earlier work on silicate glasses, where the separation of the homoge-

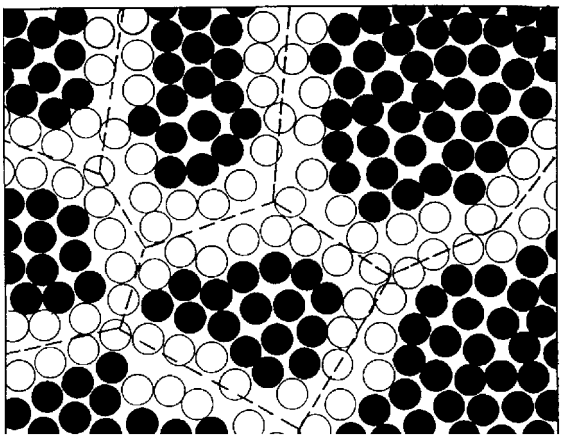

Fig. 13.6 Two-dimensional schematic representation of a nanoglass that consists of two components, as indicated by the black and white disks. Naturally, straight grain boundaries are not defined. Yet, the free volume within the boundary regions is enhanced. By modifying the size of the individual "grains" as well as by modifying the compaction and the relaxation of the boundary regions, the amount of free volume should become tunable over a much wider range than by the classical "aging" of glasses. Thus, materials properties can become adjustable.

neous quenching product into two amorphous phases with different chemical composition and – in certain cases – the selective crystallization of one component is well documented and technologically utilized in the production of advanced glass ceramics [13, 57]. Similarly to these systems and in contrast to most of the earlier reports on metallic systems that have now proven to be erroneous, phase separation in a bulk metallic glass has recently been verified unequivocally for a multicomponent alloy that has been assembled from two binary glass-forming systems with immiscible majority constituents [58]. From a thermodynamic point of view, it seems unexpected that phase separation via a binodal mechanism should occur in such alloys, since a high tendency for glass formation requires a strong negative heat of mixing [59], which favors the formation of dissimilar associates (as opposed to self-associates that form in demixing liquids), as, e.g. pointed out by the association model for the liquid specific heat by Sommer [60]. In fact, for most glass-forming alloys including the marginal glass formers, current evidence by transmission electron microscopy or by 3-dimensional atom-probe investigations [61] suggests that primary crystallization rather than phase separation causes the compositional modulation. Thus, except for specific alloy compositions, phase separation of amorphous precursors does not represent a viable route for the synthesis of bulk nanostructured materials.

13.4
BNM Formation by Plastic Deformation

One new opportunity for enhancing the number density of nanocrystals is presented by severe plastic deformation treatments of amorphous quenching products [19, 62]. In addition to nanostructure formation, the deformation treatment can also serve as a consolidation step, which is important for producing bulk shapes. The new advancement of deformation-based methods for nanostructure formation has been initiated by observations of nanocrystal formation during nanoindentation experiments on metallic glasses [22]. It is well known that amorphous materials do not show homogeneous plastic deformation upon applying external strain. Instead, the deformation is localized in narrow regions, so-called shear bands that carry the entire response of the material to external stresses [63], as also shown in Fig. 13.7 (a). While recent experiments indicate that to a certain extent, the amorphous material might also be affected in its volume by externally applied stresses [65], the major part of the deformation is certainly localized in the shear-band regions. These regions are distinctly different from shear bands in plastically deformed nanocrystalline materials: while the latter are the microstructural response to strain localization due to negligible strain hardening capacity and low strain rate sensitivity of the flow stress [66], shear bands in amorphous materials are to be treated as an effective second phase. These shear bands are characterized by a decreased mass density that, for example, changes the contrast in transmission electron microscopy analyses and that provides for faster atomic transport [67]. Both aspects are directly coupled to the increased amount of volume that can be freely distributed in a glass, so-called *free volume* [68, 69], and that allows for atomic rearrangements under applied stress. Thus, the formation of shear bands leads to an effective work softening, which gives rise to plastic instability in tension and to inadequate fatigue-test performance of bulk metallic glasses. In this context it is still actively debated whether the shear softening and related microstructural features such as the vein pattern on fracture surfaces of amorphous materials is related to a local temperature rise due to adiabatic heating. Estimates between several tenths of a Kelvin and several thousand Kelvin for the temperature rise of the material within a shear band have been published [70, 71]. While recent studies that utilized a clever and simple local melting probe indicate that the temperature rise during shear-band formation is significant and affects a rather large volume of several 100 nm in the direction perpendicular to the shear plane [72], it is not clear how the magnitude of the offset of the two sides of a shear band (i.e. the large difference on the surface of a material on both sides of the intersection line of a shear band with the surface) affects the heat balance. Independent studies on shear-band generation by bending (with significantly smaller shear displacement) find that the microstructural response of the material adjacent to a shear band is different for the compressive and the tensile sides [73]. Such a finding is at least unexpected if one would assume a massive heat release during shear-band formation. Thus, at present it appears that

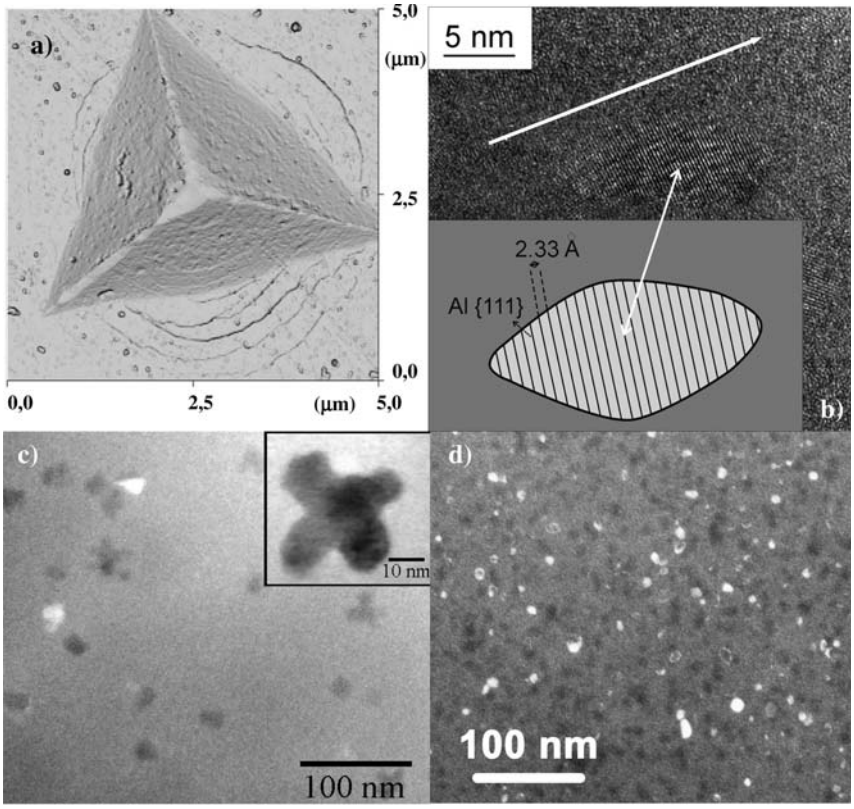

Fig. 13.7 Microstructures of metallic glasses that developed during plastic deformation. (a) Shear-band formation at an indentation site, imaged by atomic force microscopy. The circular patterns at the periphery of the indent impression constitute pileup due to overlapping layers of displaced material (reprinted with permission from [64], copyright (2002) AAAS). (b) High-resolution transmission electron microscopy image of an $Al_{88}Y_7Fe_5$ alloy that was deformed by cold rolling. The white arrow indicates the inplane direction of a shear band. The fringe contrast inside the shear-band region is due to a nanocrystal that is schematically depicted in the inset. (c) Bright-field TEM image after annealing an as-quenched $Al_{88}Y_7Fe_5$ alloy at 245 °C for 30 min. The nanocrystal number density is drastically lower compared to the material after severe plastic deformation by high-pressure torsion straining, as shown in (d). The dark-field transmission electron microscopy image shows a high number density of Al-nanocrystals with a size of about 12 nm that developed during the deformation within the amorphous matrix.

both underlying processes: an increase of the amount of free volume and a localized increase of the temperature contribute to the observed nanocrystal formation at ambient conditions within shear bands. Interestingly, recent investigations on the deformation of amorphous Al-based alloys indicate that the nanocrystals within shear bands induced by cold rolling have a cigar-shaped morphology with the long axis oriented parallel to the direction of the shear bands

(Fig. 13.7 (b)) [65]. The elongated morphology of the deformation-induced nanocrystals along with the common orientation of the (111) lattice planes relative to the longer axis of the nanocrystals indicates the importance of the details concerning the redistribution of free volume. In addition to generating nanocrystals by plastic deformation, for partially devitrified Al-rich material it was also shown that plastic deformation caused the disruption of the nanocrystals that exceeded a critical size of about 15 nm [74]. The resulting smaller nanocrystals were found to be dispersed in the matrix. Dislocations that were observed in the few remaining larger nanocrystals suggest a shear-induced fragmentation mechanism. These results indicate that plastic deformation can yield nanocrystals within the amorphous matrix and that it can also limit the size of these nanocrystals [74]. Thus, nanocrystalline/amorphous composites with a rather narrow grain-size distribution of small nanocrystals and with extremely high nanocrystal number densities might be obtainable if a deformation treatment is applied that affects the volume of the material. A recent investigation on an Al-rich amorphous alloy that was plastically deformed by high-pressure torsion verifies this expectation [19]. Figure 13.7 also displays representative examples of partially nanocrystallized $Al_{88}Y_7Fe_5$ samples after (c) thermally induced and (d) deformation-induced nanocrystallization. The comparison indicates clearly the enhanced nanocrystal number density that can be obtained by combining rapid quenching and severe plastic deformation pathways sequentially. Additionally, the increase of the nanocrystal number density with the applied strain demonstrates the possibility to produce homogeneous ultrafine nanostructures in bulk shape that yet wait to be explored.

13.5 Properties of BNM from Amorphous Precursors – Selected Examples

A broad range of nanostructured materials exist that are obtained by processing amorphous precursor structures and that provide enhanced properties with a high potential for applications. Concerning nonmetallic materials, glass-ceramics that have already been discussed briefly in Section 13.3.1 represent an important class of engineering materials due to their improved mechanical performance, e.g. the high strength at low mass density and due to the retained functional properties of the oxide materials, e.g. their transparency if the crystal diameter is kept below the wavelength of the light that should be transmitted [13]. In addition, the combination of different crystalline phases with different functional properties within the residual amorphous matrix allows for designing truly multifunctional materials, such as glass-ceramics that combine biocompatibility and ferromagnetism with reasonable mechanical strength for applications in bone-tumor treatment [75].

With metallic alloys, materials based on the famous Metglass^{TM}-type compositions that show nanocrystallization of Fe-rich crystals or variants that include e.g. neodymium are already commercialized as either extremely soft or hard

magnetic materials with high saturation polarization [76, 77]. While the size of the Fe-rich nanocrystals can effectively be used to optimize the coercivity, as detailed in the comprehensive treatment by Herzer [78], the coupling between the ferromagnetic nanocrystals can also be tuned by compositional variation or by annealing treatments. Aside from the possibility to adjust extremely small crystal sizes, starting from an amorphous state provides additional options due to the increased solubility limit of the amorphous phase compared with the respective crystalline state.

With Al-base marginal glass-formers, the mechanical properties such as the hardness and strength that show unprecedented performance compared to conventional lightweight alloys are in the focus of application-oriented research [21]. In the analysis of the exceptional strength, the high solute content of the nanostructured Al alloys compared to crystalline Al alloys appears to be one important factor, but the interaction between the Al nanocrystal dispersion and the shear bands that develop upon deformation of the amorphous matrix is also likely to be important. A useful perspective on the structural performance of Al-based systems based upon the relationship between tensile strength and the microstructural scale has been presented by Greer [20] and has been adapted in Fig. 13.8 to provide a comparison to some other common high strength alloys. It is evident from Fig. 13.8 that even in terms of a direct comparison of absolute strength values, the nanostructured Al alloys offer advantages even compared to advanced structural materials, such as ultrafine grained low-carbon steel. More-

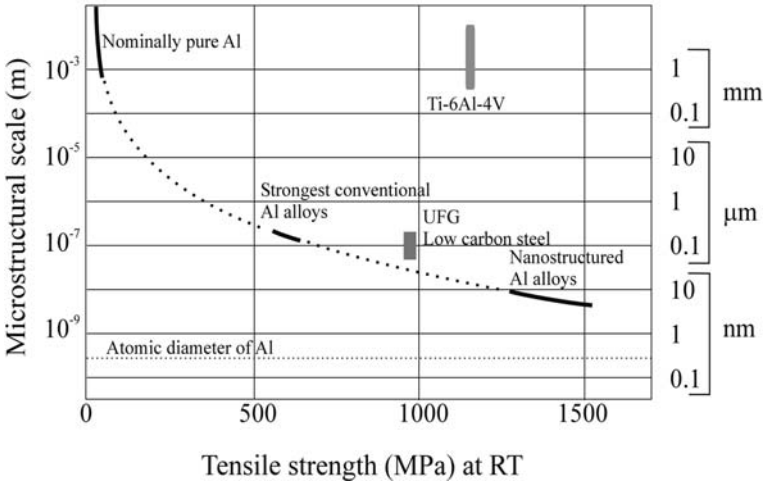

Fig. 13.8 Relationship between the characteristic scale of the microstructure and the tensile strength at room temperature for Al-based alloys. Strength values for a Ti alloy and for an ultrafine-grained (UFG) steel are shown for comparison. The results indicate the enormous benefits that can be entailed with nanostructuring. It also indicates the importance of retaining the size of the microstructure on the nanoscale.

over, these advantages are even further enhanced when the relative density is considered as a basis for a specific strength comparison [20, 78]. In that respect, the Al-base nanocomposites effectively enter the performance domain of technical ceramics while retaining a finite ductility.

13.6 Summary and Outlook

One basic requirement for an application of nanostructured materials is their stability under thermal or mechanical load as well as at least sufficient reliability characteristics. While a broad range of basic issues still need to be addressed concerning the coupling between stabilization strategies and materials properties, it seems clear that a composite approach that enables an effective diffusion control is suitable and most probably also necessary. As such, nanostructure formation starting from an amorphous precursor state offers interesting perspectives in preparing nanostructured materials with different interface types, i.e. crystalline/crystalline or crystalline/amorphous interfaces. New routes for nanostructure formation are provided by sequentially combining different nonequilibrium processing pathways that are based on rapid cooling or continuous strain-energy input. The available permutations offer a wide range of options for tailoring the microstructure and the shape and quantity of the product nanostructure and – at the same time – represent a wide field yet to be explored. In fact, these advanced synthesis pathways might also offer attractive options for the synthesis of nanostructured materials starting from bulk metallic glasses. Moreover, these strategies allow for a large leverage concerning the preparation of stable, metastable or even unstable product phases with properties that might be improved or even completely unique.

Acknowledgements

The continuous financial support by the Deutsche Forschungsgemeinschaft, the Helmholtz Association of National Research Centres and the Alexander von Humboldt-Foundation are gratefully acknowledged. The author would like to thank all co-workers and colleagues who have contributed to this topic, in particular Dr. N. Boucharat, Dr. G.P. Dinda, Prof. H. Gleiter, Dr. R. Hebert, Prof. J.H. Perepezko, Dr. H. Rösner, Dr. T. Scherer and Prof. R.Z. Valiev.

References

1 H. Gleiter, **2000**, *Acta Mater.* 48, 1–29.
2 R. Valiev, **2002**, *Nature* 419, 887–889.
3 H. Hahn, **2003**, *Adv. Eng. Mater.* 5, 277–284.
4 E. DiMasi, M. Sarikaya, **2004**, *J. Mater. Res.* 19, 1471–1476.
5 P. Vukusic, J.R. Sambles, **2003**, *Nature* 424, 852–855.
6 L.P. Biro, Z. Balint, K. Kertesz, Z. Vertesy, G.I. Mark, Z.E. Horvath, J. Balazs, D. Mehn, I. Kiricsi, V. Lousse, J.-P. Vigneron, **2003**, *Phys. Rev. E* 67, 0219071–7.
7 J.D. Verhoeven, A.H. Pendray, W. E. Dauksch, **1998**, *JOM* 50, 58–64.
8 H. Hofmeister, G.L. Tan, M. Dubiel, **2005**, *J. Mater. Res.* 20, 1551–1562.
9 S. Linden, J. Kuhl, H. Giessen, **2001**, *Phys. Rev. Lett.* 86, 4688–4691.
10 J. Xu, W. Menesklou, E. Ivers-Tiffee, **2004**, *J. Electroceram.* 13, 229–233.
11 H. Gleiter, **1981**, *Proceedings of the Second Risø International Symposium on Metallurgy and Materials Science*, eds. N. Hansen, T. Leffers, H. Lilholt, Risø National Laboratory (Risø), Roskilde, Denmark.
12 R. Birringer, H. Gleiter, H.-P. Klein, P. Marquardt, **1984**, *Phys. Lett. A* 102, 365–369.
13 P.W. McMillan, **1979**, *Glass-Ceramics*, Academic Press, London.
14 K.D. Jandt, L.M. Eng, J. Petermann, H. Fuchs, **1992**, *Polymer* 33, 5331–5333.
15 J. Petermann, Y. Xu, **1991**, *J. Mater. Sci.* 26, 1211–1215.
16 H.G. Elias, **1997**, *An Introduction to Polymer Science*, Wiley-VCH, Weinheim.
17 R.Z. Valiev, R.K. Islamgaliev, I.V. Alexandrov, **2000**, *Prog. Mater. Sci.* 45, 103–189.
18 M. Zehetbauer, R.Z. Valiev, **2004**, *Nanomaterials by Severe Plastic Deformation*, Wiley-VCH, Weinheim.
19 N. Boucharat, R.J. Hebert, H. Rösner, R.Z. Valiev, G. Wilde, **2005**, *Scr. Mater.* 53, 823–828.
20 A.L. Greer, **1995**, *Science* 267, 1947–1953.
21 H. Chen, Y. He, G.J. Shiflet, S.J. Poon, **1991**, *Scr. Metall. Mater.* 25, 1421–1424.
22 H. Chen, Y. He, G.J. Shiflet, S.J. Poon, **1994**, *Nature* 367, 541.
23 R. Zallen, **1983**, *The Physics of Amorphous Solids*, Interscience, New York.
24 G. Wilde, R. Wu, J.H. Perepezko, **2000**, *Adv. Solid State Phys.* 40, 391–405.
25 J.H. Perepezko, G. Wilde, **1998**, *Ber. Bunsenges. Phys. Chem.* 102, 1074.
26 J.W. Cahn, **1980**, *Bull. Alloy Phase Diag.* 1, 27–41.
27 W.J. Boettinger, **1982**, in *Rapidly Solidified Amorphous and Crystalline Alloys*, eds. B.H. Kear, B.C. Giessen, M. Cohen, North-Holland, Amsterdam. Elsevier Science Publishing, Dordrecht, The Netherlands.
28 H.J. Fecht, **1992**, *Nature* 356, 133–135.
29 W.L. Johnson, **1986**, *Prog. Mater. Sci.* 30, 81–134.
30 W. Ostwald, **1890**, *Outlines of General Chemistry*, Translated by J. Walker, MacMillan, London.
31 P.B. Macedo, A. Napolitano, **1968**, *J. Chem. Phys.* 49, 1887–1898.
32 D. Turnbull, **1950**, *J. Chem. Phys.* 18, 198–203.
33 K. Kelton, **2000**, *Acta Mater.* 48, 1967–1980.
34 B.A. Mueller, J.H. Perepezko, **1987**, *Met. Trans. A* 18, 1143–1152.
35 J. Schroers, A. Masuhr, W.L. Johnson, R. Busch, **1999**, *Phys. Rev. B* 60, 11855–11858.
36 M. Schwarz, A. Karma, K. Eckler, D.M. Herlach, **1994**, *Phys. Rev. Lett.* 73, 2940–2940.
37 G.J. Fan, W. Löser, S. Roth, J. Eckert, L. Schultz, **1999**, *Appl. Phys. Lett.* 75, 2984–2986.
38 H. Choi-Yim, R.D. Conner, W.L. Johnson, **2005**, *Scr. Mater.* 53, 1467–1470.
39 W. Zhang, P. Sharma, K. Shin, D.V. Louzguine, A. Inoue, **2006**, *Scr. Mater.* 54, 431–435.
40 C. Suryanarayana, **2001**, *Prog. Mater. Sci.* 46, 1–184.
41 H. Ehrhardt, J. Weissmüller, G. Wilde, **2001**, *Mater. Res. Soc. Symp. Proc.* 634, B8.6.1–B8.6.6.
42 G.P. Dinda, H. Rösner, G. Wilde, **2005**, *Solid State Phenom.* 101–102, 55–60.
43 J.H. Perepezko, G. Wilde, **2000**, *J. Non-Cryst. Solids* 274, 271–281.

44 A. Inoue, **1998**, *Prog. Mater. Sci.* 43, 365–520.

45 M. Hillert, **1998**, *Phase Equilibria, Phase Diagrams and Phase Transformations: Their Thermodynamic Basis*, Cambridge University Press, Cambridge, UK.

46 M. Baricco, P. Tiberto, L. Battezzati, **1995**, *Mater. Sci. Forum*, 195, 73–78.

47 L. Battezzati, M. Baricco, P. Schumacher, W. C. Shih, A. L. Greer, **1994**, *Mater. Sci. Eng. A* 179/180, 600–604.

48 J. H. Perepezko, R. J. Hebert, W. S. Tong, J. Hamann, H. Rösner, G. Wilde, **2003**, *Mater. Trans. JIM* 44, 1982–1992.

49 D. Turnbull, **1981**, *Prog. Mater. Sci.* Chalmers Ann. Vol., 269–275.

50 G. Wilde, N. Boucharat, R. J. Hebert, H. Rösner, S. Tong, J. H. Perepezko, **2003**, *Adv. Eng. Mater.* 5, 125–130.

51 T. Gloriant, D. H. Ping, K. Hono, A. L. Greer, M. D. Baró, **2001**, *Mater. Sci. Eng. A* 304, 315–320.

52 K. Hono, Y. Zhang, A. P. Tsai, A. Inoue, R. Sakurai, **1995**, *Scr. Mater.* 32, 191–196.

53 K. Hono, Y. Zhang, A. Inoue, T. Sakurai, **1997**, *Mater. Sci. Eng. A* 226–228, 498–502.

54 D. R. Allen, J. C. Foley, J.H. Perepezko, **1998**, *Acta Mater.* 46, 431–440.

55 J. F. Löffler, W. L. Johnson, W. Wagner, P. Thiyagarajan, **2000**, *Mater. Sci. Forum* 343, 179–184.

56 M. K. Miller, D. J. Larson, R. B. Schwarz, Y. He, **1998**, *Mater. Sci. Eng. A* 250, 141–145.

57 R. F. Cooper, W. Y. Yoon, J. H. Perepezko, **1991**, *J. Am. Ceram. Soc.* 74, 1312–1319.

58 J. C. Oh, T. Okubo, Y. C. Kim, E. Fleury, K. Hono, **2005**, *Scr. Mater.* 53, 165–169.

59 D. Turnbull, **1988**, *J. Non-Cryst. Solids* 102, 117–124.

60 R. N. Singh, F. Sommer, **1992**, *Z. Metallkde.* 83, 553–540.

61 A. A. Kündig, M. Ohnuma, T. Ohkubo, K. Hono, **2005**, *Acta Mater.* 53, 2091–2099.

62 N. Boucharat, H. Rösner, R. Valiev, G. Wilde, **2005**, *Arch. Mater. Sci.* 25, 357–363.

63 A. S. Argon, **1979**, *Acta Metall.* 27, 47–58.

64 J. J. Kim, Y. Choi, S. Suresh, A. S. Argon, **2002**, *Science* 295, 654–657.

65 R. J. Hebert, J. H. Perepezko, H. Rösner, G. Wilde, **2006**, *Scr. Mater.* 54, 25–29.

66 Q. Wei, D. Jia, K. T. Ramesh, E. Ma, **2002**, *Appl. Phys. Lett.* 81, 1240–1242.

67 Q. Y. Zhu, A. S. Argon, R. E. Cohen, **2001**, *Polymer* 42, 613–621.

68 M. H. Cohen, D. Turnbull, **1959**, *J. Chem. Phys.* 31, 1164–1169.

69 M. H. Cohen, G. S. Grest, **1979**, *Phys. Rev. B* 20, 1077–1098.

70 K. M. Flores, R. H. Dauskardt, **1999**, *J. Mater. Res.* 14, 638–643.

71 H. A. Bruck, A. J. Rosakis, W. L. Johnson, **1996**, *J. Mater. Res.* 11, 503–511.

72 J. J. Lewandowski, A. L. Greer, **2006**, *Nature Mater.* 5, 15–18.

73 W. H. Jiang, M. Atzmon, **2003**, *Acta Mater.* 51, 4095–4105.

74 G. Wilde, N. Boucharat, R. Hebert, H. Rösner, R. Valiev, **2007**, *Mater. Sci. Eng. A*, 449–451, 825–828.

75 D. Holland, **2001**, *Glass Ceramics*, in Encyclopedia of Materials: Science and Technology, eds. K. H. J. Buschow, R. W. Cahn, M. C. Flemings, B. Ilschner, E. J. Kramer, S. Mahajan, P. Veyssière, Elsevier, Oxford, UK.

76 Y. Yoshizawa, S. Oguma, K. Yamauchi, **1988**, *J. Appl. Phys.* 64, 6044–6046.

77 J. J. Croat, J. F. Herbst, R. W. Lee, F. E. Pinkerton, **1984**, *J. Appl. Phys.* 55, 2078–2082.

78 G. Herzer, **1990**, *IEEE Trans. Magn.* 26, 1397–1402.

14
Continuous SPD Techniques, and Post-SPD Processing

Igor V. Alexandrov

14.1
Introduction

As is known, severe plastic deformation (SPD) offers the possibility to form unique ultrafine-grained (UFG) and nanostructured states and, as a result, rather attractive mechanical and physical properties in bulk billets from different metallic materials for instance [1]. At the same time it should be noted that along with the obvious advantages the SPD technique possesses a number of disadvantages and restrictions. In particular, the process requires construction of expensive special-purpose die-sets. It can not be widely used in the conveyor mode, as the given process is not a continuous production process. A low ratio of material utilization is typical of it, etc. In connection with this it is necessary to find ways of further perfection of SPD processes.

The most promising trends of SPD are development of continuous equal-channel angular pressing (ECAP) or equal-channel angular extrusion (ECAE), and utilization of post-SPD processing. Elaboration and application of continuous SPD techniques serve to significantly enhance the output ratio of good material to raw material, and make the process close to the industrial conditions. We should note that the number of papers dealing with the processing of bulk nanostructured billets by SPD techniques is quite large, however, the number of papers dealing with post-SPD processing and continuous SPD techniques is rather limited and they have mainly been published just recently. Control of structure, crystallographic texture, properties, shape and geometrical sizes of bulk nanostructured billets processed by SPD is possible, as a result of application of conventional techniques of metal forming, like rolling, extrusion, forging, drawing, *etc.* Hence, the problem of putting billets into the shapes of rods or plates, convenient for further production of units from bulk nanostructured billets in the industrial conditions, can be solved.

The aim of the present chapter is to overview investigations conducted with the aim to develop continuous ECAP to make the SPD process an industrially valuable one and post-SPD processing for further refinement of the microstructure, enhancement of mechanical properties and also the industrialization of SPD processes.

Bulk Nanostructured Materials. Edited by M. J. Zehetbauer and Y. T. Zhu

ISBN: 978-3-527-31524-6

14.2 Continuous SPD Techniques

It is of significant importance to address the issues of enhancing the output factor of homogeneous bulk nanostructured material, reducing energy consumption and labor cost, increasing the economical effectiveness when using the conventional ECAP process. It is possible to solve these issues by increasing the sizes of the work piece in one or two dimensions up to several meters or tens of meters. In this case the SPD process should be applied to wires or sheet billets and to satisfy one of the most important requirements, which is its continuance. Without this, none of the technological processes will be introduced into production.

The aspect ratio (c/a = length/diameter or length/thickness) of a work piece up to a value higher than 8–10, used in the traditional ECAP scheme, is quite problematic. As shown in [2] for the case of a billet with the square cross section, the applied pressure on the punch is proportional to the ratio c/a. As a result, the pressure can exceed the material yield stress by several times. Therefore, the punch will lose stability and its buckling will take place.

The attempts to decrease heterogeneity of the head and tail ends of billets at the expense of using different inserts can promote the improvement of the situation to some degree, but do not solve the problem in general [2, 3].

14.2.1 ECAP-Conform Process

The concept of continuous ECAP was first developed by Segal in the Physical and Technical Institute of Minsk (Belorussia) in 1976 [4]. One of the schemes of continuous ECAP uses the principle of the so-called "Conform" extrusion, developed in 1974 by Etherington [5]. During the conform extrusion material 5 is extruded through the die with the channels formed by slot 1 of roll 2, segment 3 and support 4 (Fig. 14.1 [2]). The active friction force that appears between the

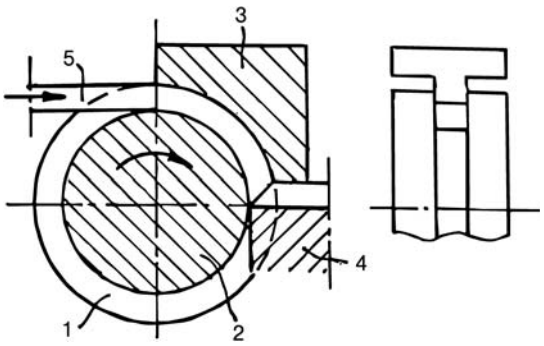

Fig. 14.1 Concept of the continuous equal-channel angular extrusion [2].

deformed material and rotating roll makes continuous extrusion possible without any decrease of the cross section and heating of the material.

The process of continuous ECAP was realized by V. M. Segal on the example of Cu wire with a cross-section of 8×8 mm. Meanwhile, the die-set mentioned above and a semi-industrial rolling mill were used.

In [6] the results of a combination of the Conform process and ECAP, called the "ECAP-Conform process", are presented. An Al rod with a diameter of 3.4 mm was pulled through a rectangular channel made on the surface of the rotating shaft. Then the billet was subjected to shear in a zone, similar to the scenario in traditional ECAP. When passing through the outlet, the billet's length was more than 1 m. The billet was rotated about its axis for 180° between the passes, which corresponded to ECAP route C. In total, 4 ECAP-Conform passes were performed.

TEM investigations showed that the ECAP-Conform process produced microstructure similar to that produced by traditional ECAP. After 4 ECAP-Conform passes UFG structure with a mean grain size of about 650 nm and a high volume of high-angle boundaries formed. Mechanical tensile testing indicates the increase of yield strength σ_y by approximately 3 times and the ultimate strength σ_u by about 2.5 times as compared to the initial state. The elongation to failure falls from 28% to 13% after the 1st pass and practically did not change further after more passes.

The authors of Ref. [6] highlighted a number of differences between the ECAP-Conform process and the conventional Conform process. The main difference is the more complicated scheme of loading during the conventional Conform process. The ECAP-Conform process actually occurs by means of simple shear as well as the conventional ECAP.

14.2.2
Equal-channel Angular Drawing (ECAD) Process

Equal-channel angular drawing (ECAD) is another promising process for continuous industrial production. When conducting ECAD, material in the form of a bar is drawn through two intersecting channels [7]. In Ref. [8] the process of microstructure refinement during ECAD of pure Al is investigated.

It is shown that the angle of channels' intersection of 135° has some advantages as compared to the angle 90°, which is most frequently used during ECAP or ECAE. Moreover, risk of a rod failure during drawing decreases, as the drawing load lessens. ECAD was performed on CP Al bars with a square cross section with an edge of 15 mm and length of 750 mm. The angle of the channels' intersection was 135°. The microstructure of the ECAD rods was characterized by low-angle (1–4°) misorientations.

The ultimate tensile strength increased by about 60% and the elongation to failure decreased as a result of the two first passes. During the following passes the changes of these values were insignificant.

14.2.3
Conshearing Process

ECAP of sheet materials means that continuous ECAP is performed, as the ratio "length:thickness" is very high in the given case. The method, used for the continuous ECAP of Al [9–11] and steel strips [11], is based on a novel continuous shear-deformation process, called the continuous shearing deformation (conshearing) process.

The idea of using the continuous ECAP arose when the authors [9–11] wanted to enhance the *r* value (Lankford value). This parameter reflects the tendency of material to deep drawing, but in the case of fcc metals (Cu, Al) strong cubic crystallographic texture $\{100\}\langle 001\rangle$ forms during annealing after cold rolling. The texture does not promote enhancement of the Langford value. On the other hand, {111}//ND shear texture is favorable for increase of the *r* value. Such texture is observed in a thin layer of the deformed material, bearing to the rolls. As the ECAP is implemented mostly by simple shear, the authors of Ref. [9] came to the idea of using ECAP to process sheet materials. Thus, they intended to solve the problem of enhancing the *r* value at the expense of increasing the volume of the material with favorable texture.

The scheme of the conshearing process is presented in Fig. 14.2 [9]. During this process, a strip of the sheet material is forced against the rotating central roll with the help of guide shoes and satellite rolls. The friction force makes the strip move through the channel between the cover and the abutment. Hence, the die between the channel axis and the tangent to the central roll is equal to θ. Thus, it is possible to solve the problem of introducing continuous shearing deformation into a strip of sheet material.

The given process was applied at room temperature to long Al (1100-H24) strips 1.0 mm thick and 20 mm wide. The shearing angle $\theta = 55^\circ$. It turned out that the increase of the number of passes up to 4 did not practically change the tensile strength and the elongation to failure. At the same time, as a result of

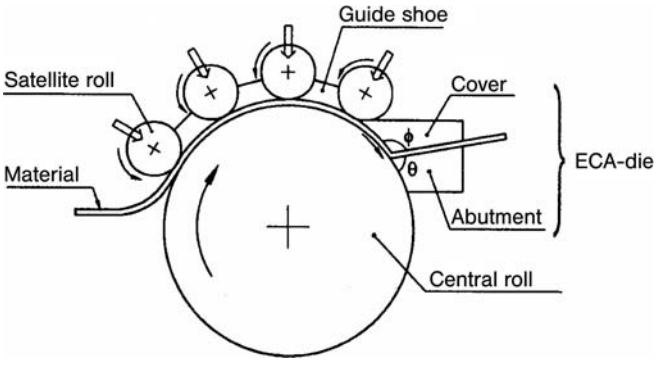

Fig. 14.2 Schematic illustration of the conshearing process [9].

using the conshearing process the ⟨111⟩//ND shear texture was formed and as a result of the subsequent annealing the corresponding r_0 value was significantly enhanced.

In [10, 11] it was stated that in the case of Al (AA1100) strips with a thickness of 2 mm the optimal shear angle = 65°. Hence, after 6 passes a banded microstructure with UFG grains was formed. The grain thickness was 0.42 μm, their length was 1.4 μm. The tensile strength increased by 70% after deformation, and the elongation to failure fell from 50% to 23%.

The application of the conshearing process in the case of steel (JIS SPCC 0.044%C) strips pointed to the formation of the microstructure of lamellar subgrains with small misorientations [11]. The tensile strength increased from 380 MPa in the initial state to 700 MPa after six passes.

14.2.4
Continuous Confined Strip Shearing (C2S2) Process

A new conceptual process, named the continuous confined strip shearing (C2S2) process was elaborated and used in [12, 13]. As in the previous case of the conshearing process, the aim of the C2S2 process was formation of shearing texture, favorable from the point of view of obtaining high formability of Al alloy sheets.

During the C2S2 process a thin strip of the deformed 1050 Al alloy with a thickness of 1.55 mm enters the space between the rolls with a diameter of 10 cm, is reduced to the thickness 1.45 mm and forced through the die for ECAP (Fig. 14.3 [12]). The feeding speed is rather high at 5 to 50 m min^{-1}. The oblique angle between the inlet and outlet channels can be from 100 to 140°. The thickness of the horizontal channel corresponds to the thickness of the strip before entering into the space between the rolls.

Actually, the dissimilar channel angular pressing (DCAP) lies in the basis of the C2S2 process. The results of application of the given process [12] indicated

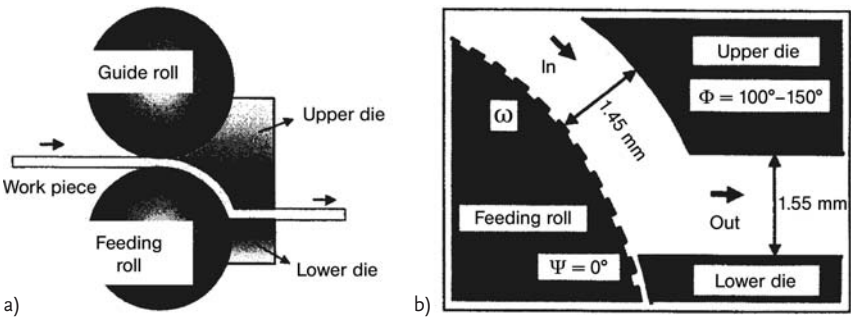

Fig. 14.3 (a) Scheme of the C2S2 process, and (b) of a detailed die configuration of the forming zone [12].

the formation of shear texture, favorable from the point of view of the sheet-forming application of the Al alloy.

In [13] the data on the multiple (up to 100 times) application of the C2S2 process are presented. The size of billets from the commercial 1050 Al alloy was 20 mm×1.55 mm×1000 mm. Analysis formulated evolution of microstructure and mechanical properties, depending on the processing parameters. In particular, it is shown that both the accumulative strain and the strain level imparted to the specimen per passage must exceed some critical levels for the formation of the UFG microstructures. Temperature rise as a result of the high speed of the processing, $\sim 5\ \mathrm{m\ min^{-1}}$, provides the formation of the UFG microstructures with high-angle grain boundaries.

Thus, on the basis of the conducted analysis one can conclude that at present two (conshearing and C2S2) schemes of continuous ECAP processing are developed and implemented. These schemes are mainly applied to rather easy-to-deform Al strips with limited sizes. The formation of shearing textures, favorable from the point of view of high formability of Al sheets, is demonstrated. The UFG microstructures are obtained at definite processing parameters. But it is revealed that after refinement during the 1st C2S2 pass, the grain size grows to some extent during the subsequent passes. The size of the elongated grains is relatively large. The strength increased, but quickly reached saturation.

The application of continuous SPD techniques implies realization of a new (different from the conventional ECAP case) mechanics of the flow of the deformed material. In particular, one of the walls of the vertical channel of the die for ECAP is in motion, which lessens the degree of friction and consequently the character of the accumulated strain distribution in the billet. Due to the increased length the change of the accumulated strain fields at the ends of the deformed billet has less impact.

14.3 Post-SPD Processing

Additional cold deformation and thermal treatment after SPD are considered now as a promising approach to further improve UFG and nanostructures and mechanical properties. This approach is based on traditional metal forming. The additional cold deformation, although its degree is rather small, allows the dislocation density in UFG materials to be increased considerably. As a result, their strength increases while retaining good plasticity. This approach can be also used when shaping ECAP billets. Several examples are discussed below.

14.3.1 ECAP plus Forging or Cold Rolling

Recent researches are dedicated to studying the influence of post-SPD processing on the structure and properties of commercially pure (CP) Ti. CP Ti is widely used

for manufacturing different articles. Besides, significant microstructure refinement and enhancement of mechanical properties can be achieved in it.

The basics of this approach is protected by the patent [14], granted in Russia in 2001. In the description of the invention, covered by the patent, the possibility of using the combination of SPD and further thermomechanical treatment at 250–500 °C for 0.5–2 h applied to CP Ti billets is highlighted. This makes it possible to form a thermally stable UFG structure with the grain size not more than 0.1 μm and enhance the tensile strength and fatigue strength.

Later in 2002, an American patent appeared [15] that suggested that ECAP CP Ti should be subjected to cold rolling and/or cold extrusion in order to significantly enhance mechanical properties and further use it in manufacturing medical implants. In this patent, CP Ti is subjected to ECAP at a temperature $T \geq 400$ °C. This is connected with its low ductility at lower temperatures. At the same time, high ECAP temperature leads to relatively low strength. Therefore, strengthening by additional post-SPD processing can be expected. Conventional techniques of metal forming do not require such high strain degrees to be achieved as in the case of ECAP and can be implemented at room temperature.

The results of investigations of the influence of ECAP and post-SPD processing on the structure and properties of CP Ti billets are presented in a number of papers [16–23]. Billets were processed by ECAP route B_C with temperature decreasing from 450 °C to 400 °C after 8 passes and 350 °C after 12 passes. The main post-SPD processing technique was cold rolling [17–23] and only in one case cold extrusion [16].

Cold extrusion was carried out in 3 or 5 stages up to reaching total reduction in cross-sectional area equaling to 47% and 75%, respectively [16]. The 47% extrusion did not practically change the grain size, typical of the microstructure after ECAP, although the dislocation density increased and the grain boundaries became less sharp. The grain boundaries are a mixture of low- and high-angle boundaries. Increasing the reduction in cross-sectional area to 75% resulted in the formation of grains with irregular shape in the cross section and elongated grains in the longitudinal section. Meanwhile, the grain size in the cross section decreased significantly. Most of the grain boundaries became high angle. Internal elastic stresses appeared in grains.

Investigation of mechanical properties showed that 47% extrusion increased the microhardness slightly. At the same time, tensile testing revealed considerable increase in yield strength and ultimate strength and some reduction of the elongation to failure. The above trends became more marked after 75% extrusion. The yield and ultimate strengths are 640 and 710 MPa, respectively, in the ECAP CP Ti, the 75% extrusion enhanced them up to 970 and 1050 MPa, respectively. The obtained mechanical properties are much higher than those of Ti-6Al-4V alloy. Grain-boundary strengthening, associated with a small grain size, and dislocation strengthening, associated with cold deformation, are considered as the causes of the strength enhancements.

Cold extruded ECAP CP Ti billets were subjected to annealing for 30 min at different temperatures. The conducted tensile testing allowed the thermostabil-

ity of the strength and the recovery of ductility with increasing annealing temperature to be estimated. It appeared that the processed billets preserve high yield stress and ultimate tensile strength after annealing at 300 °C. Annealing at 400 °C did not change the mechanical properties of billets, subjected to extrusion with larger reduction in cross-sectional area.

Thus, the positive influence of post-SPD processing on the structure and properties of ECAP CP Ti is demonstrated.

The analysis of microstructure and mechanical properties of CP Ti, subjected to 8 ECAP passes and further cold rolling showed the following [17, 18]. Cold rolling of billets with a diameter of about 20 mm to strain of 35% and 55% resulted in transformation of the equi-axed UFG structure, formed as a result of ECAP, into a structure that is strongly elongated in the rolling direction. Meanwhile, in the cross section the grains remained mostly equi-axed, but their average size decreased slightly. Strong fragmentation was observed inside grains. The mechanical properties of CP Ti VT1-0 increased considerably to the level of those of Ti alloys. The yield strength σ_y increased from 640 MPa up to 1020 MPa, the ultimate strength σ_u from 460 MPa to 1050 MPa, the elongation to failure δ decreased from 27% to 6%.

In Ref. [19] rolling of billets with a diameter 16 mm was conducted in shaped rolls up to the total reduction in cross-sectional area of 35–75%. The cross section of a billet changed its shape from round to oval and then to square. During the rolling self-heating of work piece up to 100 °C took place. Because of this, the billets were cooled down between passes.

In the case of 35% strain, the mean grain size decreased from 280 nm to 170 nm in the cross section. In the longitudinal section the grains elongated. The dislocation density in the grain interior increased significantly. The 55% strain distorted the equiaxed shape of grains in the cross section. The process of grain refinement in the cross section and grain elongation in the longitudinal section continued. Strong fragmentation of elongated grains was accompanied by formation of low-angle subgrain boundaries. It was revealed that further increase of the strain degree did not result in any considerable changes in the microstructure. The fragmentation of the filamentary structure continued. Some low-angle boundaries turned into high-angle ones.

The number of ECAP passes influenced significantly the evolution of microstructure during subsequent cold rolling [19]. The microstructures became similar for the cases of fewer ECAP passes and larger strain degree during the subsequent cold rolling and more ECAP passes and less strain during cold rolling. On the other hand, an increase in the number of passes, up to 4, resulted in the growth of the fraction of high-angle grain boundaries with practically unchanged grain size. The grain boundaries became sharper, which, according to the authors' assumption, can be connected with higher probability of trapping lattice dislocations by high-angle grain boundaries. The grains became less filamentary and more fragmentary.

Mechanical tensile testing showed that rolling can increase the strength ECAP CP Ti by 50% to an ultimate tensile strength of 1050 MPa [19]. At the

same time, the value of the ductility fell by more than a factor of two (to 6%). Annealing after rolling enhanced the ductility up to 12.5%, i.e. practically to the level typical of the ECAP billet, ~14%, without significantly decreasing the strength. The formed microstructure became thermostable up to 400 °C.

Thus, the conducted investigations [19] demonstrated that post-SPD processing, consisting of cold rolling and subsequent low-temperature annealing, can produce excellent mechanical properties in the case of CP Ti.

In Ref. [20] the results of investigation of the influence of cold rolling on the microstructure and mechanical properties of two kinds of CP Ti billets with the initial coarse-grained (a mean grain size 15 μm) microstructure and the microstructure obtained as a result of ECAP UFG (a mean grain size about 500 nm), are presented. Before ECAP, the billets had a diameter of 60 mm, and before cold rolling the diameter was 54 mm and the length was 120 mm. The large billet size, subjected to ECAP and post-SPD processing, is of great interest from the point of view of enhancing the prospects of their subsequent application. Besides, the increased initial diameter of ECAP billets makes it possible to reach high strain degrees during the following rolling.

The positive influences of ECAP on the microstructure and mechanical properties of CP Ti, subjected to the subsequent cold rolling up to 80% accumulative rolling strain, include finer grain size, more homogeneous strength and good elongation to failure.

Rigorous TEM investigations of the evolution of the microstructure of CP Ti, subjected to cold flat rolling with strain degrees of 18, 45 and 88% after ECAP (billet diameter 40 mm, 8 passes), were conducted in [21]. It was shown that cold rolling results in fragmentation of the UFG structure produced ECAP. The size of the grains that have an equi-axed shape as well as an elongated one becomes less than 100 nm.

Tensile tests showed that increasing cold rolling strain from 0% to 88% leads to an increase in strength (for example, the yield stress σ_y increases from 549 MPa up to 629 MPa, the ultimate stress σ_u increases from 633 MPa to 941 MPa, the elongation to failure falls from 27% to 17%). The cause of these changes of mechanical properties is the formation of subgrain structure with the high dislocation density and low-angle boundaries inside the grains.

Rigorous investigations of the microstructure of the CP Ti billets, subjected to 8 ECAP passes and further cold rolling with 73% strain, were conducted in [22]. TEM investigations revealed considerable scatter in the grain size and character of the subgrain structure. In particular, it was revealed that there may be large grains (> 320 nm) in the microstructure. The large grains may contain subgrains, which in turn may contain dislocation cells. Grains with intermediate size (130–600 nm) may contain dislocation cell structure without formation of subgrains. Dislocation cells can not be observed in the grains and subgrains with a size less than 150 nm. Dislocations were absent in the grains with the typical size of 75 nm, being absorbed by grain boundaries.

XRD investigations revealed an arithmetic mean crystallite size of 39±4 nm. The given size corresponded to a mean size of dislocation cells that was equal

to 45 nm, obtained by the TEM method. It is shown that most of the dislocations are dislocations of type $\langle a \rangle$. An important role of the dislocations of type $\langle c \rangle$ is also noted.

One of the important applications of CP Ti is its use for producing medical devices, including hearing aids. For this, high-strength foil should be obtained. In [23] the results of an investigation of the influence of cold rolling on the microstructure and mechanical properties of CP Ti (ECAP, 8 passes) are presented. The initial thickness of a billet was 2.65 mm, and the final thickness of the foil was 20 μm. Cold rolling was carried out with a thickness reduction of 15–5% per pass and by three intermediate annealing stages at 350 °C for 1 h between certain passes.

A mean grain size was ~350 nm in the initial state after ECAP and before cold rolling. After cold rolling by 75% strain the microstructure was homogeneous with a mean grain size ~150 nm, which did not change on further thinning of the foil. Similar treatment of coarse-grained CP Ti resulted in a microstructure with a mixture of nanostructured and coarse-grained areas.

The dependence of the mechanical properties of coarse-grained and UFG ECAP CP Ti, subjected to cold rolling with intermediate annealing, is nonmonotonous with an intermediate maximum for each of the considered cases [23]. At the same time, much higher strength properties and the elongation to failure are typical of the UFG ECAP CP Ti at each considered stage of processing. Maximal values of the yield stress σ_y exceeded 900 MPa, the ultimate strength σ_u reached almost 1000 MPa, and the elongation to failure was 8%. These characteristics became 10–20% higher than those that are typical of the coarse-grained CP Ti, subjected to the same treatment.

In a number of papers [24–28] the influence of cold rolling on the structure and properties of ECAP/ECAE Cu ingots was investigated. In particular, it was shown in [24] that cold rolling of ECAP (a die angle 90°, 16 passes, route B_C, room temperature) Cu (99.98%) billets with 83% reduction changes the XRD pattern, which corresponds to the ECAP state, significantly. These changes reflect the increase of the size of coherent scattering domain from 37±3 nm to 104 ± 5 nm, the drop in the level of elastic microdistortions from $(52 \pm 4) \times 10^{-4}$ to $(37 \pm 3) \times 10^{-4}$, the higher Debye-Waller parameter, and the change of the crystallographic texture. The obtained results testify to the flow of recovery in the microstructure and formation of preferred orientations, typical of Cu, cold rolled from the coarse-grained state.

It is shown in Refs. [25–27], that the microstructure of ECAP Cu, cold rolled with the 83% reduction, is rather homogeneous and characterized by elongated grains, which corresponds to the character of the deformation scheme. At the same time recrystallized grains of the cube $\{001\}\langle 100 \rangle$ orientation are revealed in the microstructure. The fraction of such grains grows considerably with the reduction rising from 83% to 95%.

Flow of recovery and even recrystallization during cold rolling of the ECAP Cu should enhance ductility and promote shaping of the deformed billets. At the same time the recrystallization can reduce their strength properties.

The results of investigations of ECAE (a die angle 120°, 3 passes, routes A and C, room temperature) of Cu (99.8%) billets, subjected to cold rolling up to ~50% reduction, are presented in Ref. [28]. In general, a positive, but insignificant influence of cold rolling on mechanical properties is demonstrated. We should note that the processing parameters (the die angle, the chosen routes, the number of ECAE passes, the reduction during cold rolling) cannot be considered as successfully chosen from the point of view of achieving optimal structure and properties.

Twist hydroextrusion (THE) is another SPD scheme. Cold rolling (total relative deformation under rolling $e = 1.36$) of plates, cut out parallel and normal to the axes of THE processing (degree of deformation $e = 2.7$) Cu billets, results in the formation of equiaxed grain structure, unusual for cold-rolled microstructures. Thus, not only high level but also isotropy of mechanical properties are typical of such microstructures [29]. The obtained results are attributed to the peculiarities of THE processing by the authors.

The authors of Refs. [30–32] demonstrated the possibilities of processing UFG structures in sheets of Al alloys as a result of the combined treatment that includes ECAE and subsequent rolling. In particular, application of the isothermal rolling at 250 °C (a total reduction of 85% in seven passes) to the 7055 Al alloy billets, with sizes of 115 mm×115 mm×15 mm and obtained as a result of ECAE (a die angle 90°, 10 passes, route A, temperature $T = 250$ °C) made it possible to form microstructure with a mean grain size ~1.4 μm and a high fraction (~67%) of high-angle boundaries. The obtained microstructure had attractive superplastic properties.

14.3.2
ECAP plus Additional Thermomechanical Treatment

Recently, the combined SPD technique underwent further development. Special attention was paid to the processing of ECAP Grade 2 CP Ti billets by additional thermomechanical treatment (TMT) processing [33], the details of which are not revealed in connection with the forthcoming patent defense.

ECAP is an initial stage of such a combined treatment. This stage is necessary for preliminary microstructure refinement. Lessening of the total number of passes is possible, as after 4 passes along the route B_C homogeneous UFG structure forms, and mechanical properties reach their saturation level. It is shown that at the preliminary stage the usage of two ECAP passes is possible but with the preliminary forging, which is supposed to enhance homogeneity of the microstructure. The conducted microstructure investigations showed that after 4 ECAP passes the microstructure is characterized by equi-axed UFG grains with a mean size of about 600 nm.

The subsequent TMT was carried out in several stages and the total accumulated strain was 80%. As a result of such treatment, the ECAP billets with a diameter of 40 mm turned into rods with a diameter of 6.5 mm and up to 1 m long (Fig. 14.4 [33]).

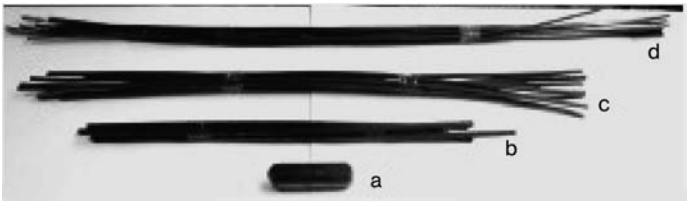

Fig. 14.4 Photographs of billets at various stages of SPD: (a) billets after ECAP; (b)–(d) billets at various stages of post-SPD TMT [33].

The elongated grains with predominantly high-angle grain boundaries were formed. A mean grain size was about 100 nm in the cross section. Inside the grains a developed substructure with a high dislocation density was observed. The mechanical properties of the billets, obtained with the help of the mentioned combined treatment, became rather attractive. Specifically, the yield stress σ_y reached 1100 MPa, the ultimate strength σ_u was 1150 MPa, and the elongation to failure was 11%.

It was stated that the microstructure and mechanical properties are quite homogeneous along the length of the rods and the scatter in strength and ductility of samples for the mechanical tensile testing did not exceed 7%.

Thus, as a result of the combined treatment that includes ECAP and subsequent TMT, the most significant microstructural refinement and the highest level of mechanical properties were achieved in CP Ti. The process produced very long rods [33].

Post-SPD processing was also recently applied to the electrotechnical alloy Cu-1%Cr-0.7%Al [34]. It is shown that the combined treatment (forging, drawing and annealing) produces a significantly enhanced microhardness (from 1781 MPa in the ECAP state to 2343 MPa after additional TMT), a higher strength $\sim$700 MPa and preserved high ductility $\sim$16%.

The observed changes in the structure and properties of bulk nanostructured billets during post-SPD processing are connected with the change of the stress–strain state. As known, the main deformation mechanism during SPD is simple shear. Tensile and compressing deformation modes become predominant during conventional methods of metal-forming treatment. As a result, post-SPD processing should lead to significant changes in a mean size and shape of grains, character of grain boundaries, dislocation structure, *etc.*

The results of the conducted investigations demonstrate high potential of application of post-SPD processing for additional enhancement of UFG and nanostructured states, mechanical properties and shaping of bulk ECAP billets.

14.4 Conclusions

Continuous ECAP, a combination of different SPD schemes and also consecutive application of SPD and conventional deformation are important promising trends that have potential for industrial processing bulk nanostructured billets with the necessary geometries and sizes, further refinement of UFG and nanostructures and enhancement of their mechanical properties. At the same time the work done in this area is still in its first stages. The aspects dealing with deformation mechanisms in UFG materials subjected to ECA pressing with subsequent cold deformation are topical. The schemes and approaches that are now being developed require further development and optimization.

References

1 R. Z. Valiev, R. K. Islamgaliev, I. V. Alexandrov **2000**, *Prog. Mater. Sci.* 45, 103–189.
2 V. M. Segal **2004**, *Mater. Sci. Eng.* A 386, 131–135.
3 G. Krallics, D. Malgin, G. I. Raab, I. V. Alaexandrov **2004**, *Ultrafine Grained Materials III* (eds.) Y. T. Zhu, T. G. Langdon, R. Z. Valiev, S. L. Semiatin, D. H. Shin, T. C. Lowe (TMS, The Minerals, Metals & Materials Society), Warrendale, Pennsylvania, USA, pp. 179–184.
4 V. M. Segal, V. I. Reznikov, V. I. Kopylov, D. A. Pavlik, V. F. Malyshev **1994**, *Processy Plasticheskogo Structyroobrazovania Metallov*, Sci. Eng., Minsk p. 231 (in Russian).
5 C. Etherington, **1974**, *J. Eng. Ind.* (August), 893.
6 G. J. Raab, R. Z. Valiev, T. C. Lowe, Y. T. Zhu **2004**, *Mater. Sci. Eng.* A 382, 30–34.
7 U. Chakkingal, A. B. Suriadi, and P. F. Thomson **1998**, *Scr. Mater.* 39, 677–684.
8 U. Chakkingal, A. B. Suriadi, and P. F. Thomson **1999**, *Mater. Sci. Eng.* A266, 241–249
9 Y. Saito, H. Utsunomiya, H. Suzuki, T. Sakai **2000**, *Scr. Mater.* 42, 1139–1144.
10 H. Utsunomiya, K. Hatsuda, T. Sakai, Y. Saito **2004**, *Mater. Sci. Eng.* A 372, 199–206.
11 H. Utsunomiya, K. Hatsuda, Y. Okamura, T. Sakai and Y. Saito **2004**, *Ultrafine Grained Materials III* (eds.) Y. T. Zhu, T. G. Langdon, R. Z. Valiev, S. L. Semiatin, D. H. Shin, T. C. Lowe (TMS, The Minerals, Metals & Materials Society), Warrendale, Pennsylvania, USA, pp. 149–154.
12 J.-C. Lee, H. K. Seok, J. H. Han, Y. H. Chung **2001**, *Mater. Res. Bull.* 36, 997–1004.
13 J.-C. Lee, H. K. Seok, J.-Y. Suh **2002**, *Acta Mater.* 50, 4005–4019.
14 Russian Patent No RU 2175685 C1 7 C 22 F 1/18, B 21 J 5/00 "Sposob polucheniya ultramelkozernistyh titanivuh zagotovok". Printed on 10.11. 2001.
15 USA Patent No 6, 399,215, IlC7 C22C 014/00; C22F 001/18 "Ultrafine-grained titanium for medical implants". Printed on 4.07. 2002.
16 V. V. Stolyarov, Y. T. Zhu, T. C. Lowe, R. Z. Valiev **2001**, *Mater. Sci. Eng.* A 303, 82–89.
17 V. V. Stolyarov, Y. T. Zhu, T. C. Lowe, R. Z. Valiev **2001**, *J. Nanosci. Nanotech.* 1, No. 2, 237–242.
18 R. Z. Valiev, V. V. Stolyarov, V. V. Latysh **2001**, *New Technologies for the 21st Century* 5, 15–17.
19 V. V. Stolyarov, Y. T. Zhu, I. V. Alexandrov, T. C. Lowe, R. Z. Valiev **2003**, *Mater. Sci. Eng.* A 343, 43–50.
20 V. V. Stolyarov, Y. T. Zhu, G. I. Raab, A. I. Zharikov, R. Z. Valiev **2001**, *Mater. Sci. Eng.* A 385, 309–313.

21 B. Mingler, V. V. Stolyarov, M. Zehetbauer, W. Lacom, H. P. Karnthaler **2006**, *Mater. Sci. Forum* 503–504, 805–810.

22 Y. T. Zhu., J. Y. Huang, J. Gubicza, T. Ungar, Y. M. Wang, E. Ma, R. Z. Valiev **2003**, *J. Mater. Res.* 18, 1908–1917.

23 Y. T. Zhu, Y. R. Kolobov, G. P. Grabovetskaya, V. V. Stolyarov, N. V. Girsova, R. Z. Valiev **2003**, *J. Mater. Res.* 18, 1011–1016.

24 I. V. Alexandrov, Y. D. Wang, K. Zhang, K. Lu, R. Z. Valiev **1996**, *Proc. ICOTOM 11,* (eds.) Z. Liang, L. Zuo, Y. Chu (International Academic Publications, Xi'an) pp. 929–940.

25 O. V. Mishin, G. Gottstein **1998**, *Philos. Mag. A* 78, No. 2, 373–388.

26 O. V. Mishin, V. Y. Gertsman, G. Gottstein **1996**, *Proc. ICOTOM 11,* (eds.) Z. Liang, L. Zuo, Y. Chu (International Academic Publications, Xi'an), pp. 1015–1020.

27 O. V. Mishin, V. Y. Gertsman, R. Z. Valiev, G. Gottstein **1996**, *Scr. Mater.* 35, 873–878.

28 A. Krishnaiah, Uday Chakkingal, P. Venugopal **2006**, *Mater. Sci. Forum* 503–504, 733–738.

29 V. N. Varykhin, E. G. Pashinskaya, V. M. Tkachenko, V. M. Bilousov **2006**, *Mater. Sci. Forum* 503–504, 591–596.

30 H. Akamatsu, T. Fujinami, Z. Horita, T. G. Langdon **2001**, *Scr. Mater.* 44, 759–764.

31 K. T. Park, H. J. Lee, C. S. Lee, W. J. Nam, D. H. Shin **2004**, *Scr. Mater.* 51, 479–483.

32 I. Nikitin, R. Kaibyshev, T. Sakai **2005**, *Mater. Sci. Eng.* A 407, 62–70.

33 V. V. Latysh, I. P. Semenova, G. H. Salimgareeva, I. V. Kandarov, Y. T. Zhu, T. C. Lowe, R. Z. Valiev **2006**, *Mater. Sci. Forum* 503–504, 763–768.

34 I. V. Alexandrov, V. V. Latysh, S. I. Hong, S. N. Faizova, V. M. Polovnikov **2006**, *Mater. Sci. Forum* 503–504, 515–520.

Part Four
Characterization

Bulk Nanostructured Materials. Edited by M. J. Zehetbauer and Y. T. Zhu

ISBN: 978-3-527-31524-6

15
Transmission Electron Microscopy of Bulk Nanostructured Metals

Xiaozhou Liao and Xiaoxu Huang

15.1
Investigation of Deformation Mechanisms of Nanostructured Metals

Nanostructured materials have been arguably the hottest research area for more than a decade [1, 2]. Nanostructured materials are defined as materials with structural features (e.g., grain sizes and/or domain structures separated by small-angle grain boundaries, *etc.*) smaller than 100 nm in at least one dimension. Because of the very small structural dimension, nanostructured materials have demonstrated unique mechanical, chemical and physical properties, which are not available to their coarse-grained counterparts. For example, material scientists have been working strenuously to make structural materials that have both high strength and high ductility so that structural components made from the materials are able to carry high loads and to prevent catastrophic failure. However, the combination of high strength and good ductility is rare in coarse-grained materials. In contrast, combined high strength and good ductility have been realized in some nanostructured materials, for example, nanostructured Cu-Zn alloy [3], Al alloy [4], Cu, and Ti processed by severe plastic deformation [1, 5, 6] and nanostructured Cu with a mean grain size of 26 nm obtained by *in-situ* consolidation [7]. Unfortunately, only a few nanostructured materials have demonstrated a combination of high strength and good ductility, while most have ductility that is too low for structural applications [8].

It is well known that the mechanical behaviors of materials are determined by their deformation mechanisms while, the deformation mechanisms are controlled by the structures of the materials. The unique mechanical properties of nanostructured materials are believed to be caused by the unique deformation mechanisms operating in the nanostructured materials. In conventional coarse-grained materials, plastic deformation occurs mainly through dislocation slip and twinning. When a dislocation passes through a grain, it will deform the grain with the amount of the deformation being equal to the Burgers vector of the dislocation. Dislocation sources required for sustained dislocation slip in coarse-grained materials include the Frank–Read source [9]. Twinning in coarse-grained materials occurs through the well-known pole mechanism [10, 11], in

Bulk Nanostructured Materials. Edited by M. J. Zehetbauer and Y. T. Zhu

ISBN: 978-3-527-31524-6

which one partial dislocation forms a whole twin via climbing a screw dislocation pole to adjacent slip planes. However, as grain sizes are reduced to the nanometer regime and the percentage of grain-boundary atoms increases correspondingly, the pole mechanism for twinning and the traditional sources for dislocation multiplication (e.g., the Frank–Read source) no longer work. As a result, the traditional view of dislocation-driven plasticity in coarse-grained materials needs to be reconsidered and new mechanisms are needed for the plastic deformation of nanostructured materials.

To understand how nanostructured materials deform, extensive investigations using molecular dynamics (MD) simulations and transmission electron microscopy (TEM) have been carried out. Using MD simulations, Schiøtz et al. suggested that the plastic deformation in nanostructured materials with grain sizes from 3.3 to 6.6 nm, in which 30–50% of atoms are located at grain boundaries, is mainly due to grain-boundary sliding [12]. Grain-boundary sliding can be triggered by uncorrelated shuffling and to some extent by stress-assisted diffusion [13], or governed by enhanced grain-boundary diffusion ("Coble creep") [14], depending on the experimental temperatures. Recent *in-situ* TEM experimental observations have presented evidence of grain-boundary sliding and rotation during the deformation of nanocrystalline Ni [15–17] and Au [18]. *Ex-situ* TEM investigation of different deformation stages of nanocrystalline Cu processed by high-pressure torsion (HPT) also confirms grain rotation at the smallest grain sizes [19]. At the stage immediately before the structure of HPT Cu evolved into the smallest grains, elongated nanodomains with widths of 10–20 nm were formed from originally submicrometer-sized (100–200 nm) grains. Nanodomains formed within a submicrometer-sized grain were of the same orientation. This orientation relationship was later broken and transformed to random orientation through grain-boundary sliding and rotation when the nanodomains evolved into the smallest grains with grain sizes in the range of 10–20 nm during the further HPT deformation. Figure 15.1 shows a typical bright-field TEM image of HPT Cu with the smallest grain sizes of 10–20 nm. Most of the grain

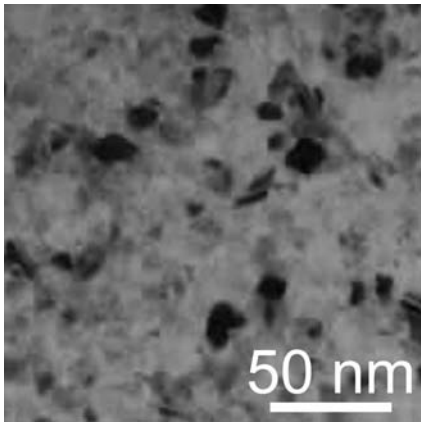

Fig. 15.1 A typical bright-field TEM image of HPT Cu with the smallest grain sizes of 10–20 nm.

boundaries are large-angle boundaries, as evidenced by the sharp diffraction contrast variation among neighboring grains. Grain-boundary sliding at the smallest grain sizes is believed to be a mechanism responsible for the reverse Hall–Petch effect, i.e. the material strength decreases with reducing grain sizes, observed in very small grain sizes [20, 21].

For grain sizes larger than a critical value (typically 20–30 nm) [22] deformation mode switches from grain-boundary sliding to dislocation processes and material behavior above this critical size follows the normal Hall–Petch relationship [23, 24], i.e. the materials strength increases with reducing grain sizes. This critical size therefore corresponds to the strongest grain size at which the material is hardest to deform [25]. Above this critical grain size (but less than 100 nm), MD simulations suggest that deformation occurs through partial dislocation emissions from grain boundaries [26]. As grain sizes increase, partial dislocations nucleate in different regions of the grain boundaries [27]. Depending on the sample structures used in MD simulations, full dislocations can also be observed in nanostructured materials with grain sizes of 30 nm [28].

Partial dislocation emissions from grain boundaries were later observed experimentally in nanostructured Cu [29] and Al [30, 31] resulting in some structural phenomena that are not seen in coarse-grained Cu and Al. Figure 15.2 shows a typical high-resolution TEM image of nanocrystalline Cu processed by HPT. Only one twin boundary is seen in the left part of Fig. 15.2 that divides twin domains I and II. However, high densities of nanotwins and stacking faults are observed in the right part of II. These nanotwins and stacking faults do not pass across the whole grain, but stop in the grain interior with Shockley partial dislocations (Burgers vectors $\frac{1}{6}\langle 112\rangle$) located at the front boundaries of the nanotwins and stacking faults. It is obvious that these twins were *heterogeneously* nucleated at a grain boundary and grew into the grain interior via partial dislocation emission from the grain boundary.

According to previous experimental results of coarse-grained Cu, deformation twinning usually occurs at high strain rates and/or low temperature and reduc-

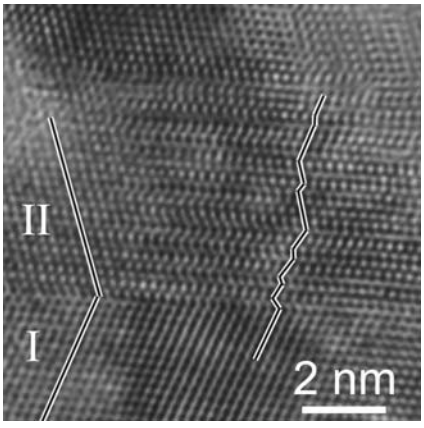

Fig. 15.2 A typical high-resolution TEM image of part of a HPT nanocrystalline Cu grain. The left part of the image shows only two twin domains, marked as I and II, while the right part of II has a lot of nanotwins and stacking faults with one end of the nanotwins/stacking faults ends within the grain.

ing grain size makes twinning more difficult because the critical twinning stress is larger than the critical slip stress when a copper grain is smaller than a certain size [32]. This result is consistent with the observation that no twin is seen in HPT Cu when the grain sizes are in the range of 100–200 nm [19]. However, the observation of twinning in nanocrystalline HPT Cu contradicts the conclusion that smaller grains are less likely to twin. The reason for the contradiction is that twining in coarse-grained copper occurs via the pole mechanism [10, 33], while twinning in HPT nanocrystalline copper occurs through heterogeneous partial dislocation emission from grain boundaries. Furthermore, because of the change in the twinning mechanism, high strain rates and/or low temperature, which are essential for deformation twinning in coarse-grained materials, are no longer necessary conditions for deformation twinning to occur in nanocrystals, as evidenced by the fact that the HPT nanostructured Cu was processed at room temperature and a low strain rate [29].

In addition to the above-mentioned *heterogeneous* twinning mechanism in nanocrystalline materials, MD simulations also predict two other twinning mechanisms: *homogeneous* twinning [26, 34] and twin lamellae formed via the dissociation and migration of grain boundaries [34]. Twins formed by these two mechanisms have also been found experimentally [30, 35]. Figures 15.3 (a) and (b) show high-resolution TEM images of a two-atomic-layer thick nanotwin and a nanotwin with a zigzag-shaped twin boundary, respectively, observed in cryogenically ball-milled Al nanocrystalline grains. The nanotwin in Fig. 15.3 (a) was

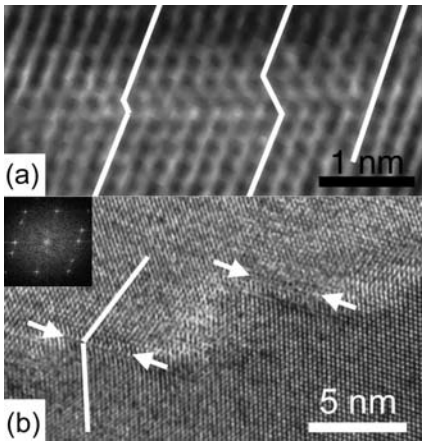

Fig. 15.3 High-resolution TEM images of a cryogenically ball-milled Al nanocrystalline grains: (a) an image showing a deformation twin formed by the overlapping of two extended dislocations on adjacent slip planes and (b) an image of part of a twin with a zigzag-shaped twin boundary. The boundary consists of short, straight, coherent {111} twinning planes (marked by arrows) connected by incoherent, noncrystallographic segments. The insert in (b) shows the Fourier transformation, indicating the twinning relationship.

formed through *homogeneous* dynamic overlapping of two stacking faults on adjacent slip planes. The two stacking faults in Fig. 15.3 (a) are only partially overlapped. The widths of the two stacking faults are unexpectedly wide considering that Al has very high stacking faults energy. An analytical model suggests that the wide stacking faults are formed due to the small grain sizes and possibly also to the interaction of stacking-fault ribbons with the high density of dislocations [36]. The zigzag-shaped twin boundary seen in Fig. 15.3 (b) is very different from conventional twin boundaries that usually appear as atomic sharp planes. Some segments of the boundary in Fig. 15.3 (b) are straight, coherent {111} twin boundaries as indicated by white arrows. These segments, which are connected by noncrystallographic segments, form a zigzag boundary between the two twinning areas. Examination of the local twinning morphology in Fig. 15.3 (b) reveals that the twin strikingly resembles a type of twin observed in MD simulations [34]. According to the MD simulations, this type of twin is formed by an entirely different mechanism, which involves the splitting and subsequent migration of a grain-boundary segment, leaving behind two coherent twin boundaries. More specifically, a grain-boundary segment was dissociated into a twin boundary and a new grain boundary [34]. A twin lamella was formed via the migration of the new grain boundary. The boundaries of twin lamellae formed at different time frames joined together to form the zigzag boundary. The noncrystallographic segments observed here were actually the new grain boundaries in this mechanism. Note that the observation of deformation stacking faults and nanotwins in nanocrystalline Al is very surprising because deformation stacking faults and twinning have never been reported in coarse-grained Al due to its very high stacking-fault energy.

Although MD simulations and TEM observations have predicted and observed deformation twins in nanocrystalline face-centered-cubic metals (e.g., Al, Cu, and Ni), respectively, they do not provide insight into the formation mechanism of the deformation twins. An analytical model based on the classical dislocation theory [37] has been proposed to successfully explain the nucleation and growth of deformation twins in face-centered-cubic metals [38, 39]. The model suggests that the stress for twin growth is much smaller than that for its nucleation. The model also suggests that there exists an optimum grain-size range in which deformation twins nucleate most readily. The critical twinning stress is found to be determined primarily by the stacking-fault energy, while the optimum grain size is largely determined by ratio of shear modulus to stacking-fault energy.

So far, we have demonstrated that several deformation mechanisms predicted by MD simulations were confirmed experimentally. On the other hand, MD simulations are usually based on structural models with equilibrium grain boundaries and deformation conditions with uniaxial stresses and extremely high strain rates (e.g., of the order of 10^6–10^8 s^{-1}) [26]. However, grain boundaries in nanostructured materials are usually in a nonequilibrium state [40] and the deformation strain rates in reality are usually several orders of magnitude lower than those used in MD simulations. Because both boundary structures [41] and strain rates [42, 43] will significantly affect the deformation behavior of materi-

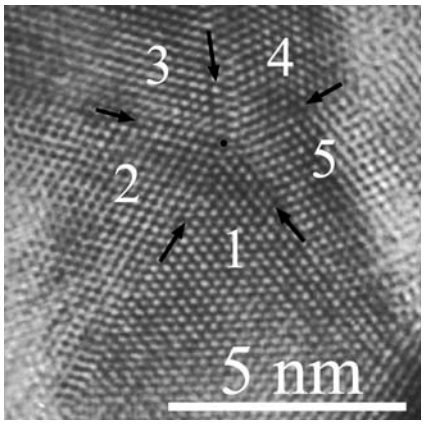

Fig. 15.4 A typical high-resolution TEM image of a fivefold twin in HPT Cu. The twin boundaries are indicated by black arrows, and each twin domain is marked with 1 to 5, respectively. A black dot is placed at the center of the fivefold twin.

als, some discrepancies between MD-simulation data and experimental observations have been reported. For example, unexpectedly wide stacking faults were observed in cryogenically ball-milled nanostructured Al, while the twin density in the same sample was much lower than that predicted by MD simulations [36, 44]. Such wide stacking faults will significantly affect the mechanical properties of the nanostructured Al because they make Shockley partial dislocations harder to constrict for cross-slip from one {111} plane to another [45].

MD simulations have never observed fivefold deformation twins, which contradicts the experimental results that fivefold deformation twins have been frequently seen in severely deformed nanocrystalline face-centered-cubic metals and alloys with grain sizes of ~ 20 nm or smaller [19, 29, 46, 47]. A typical image of a fivefold deformation twin observed in HPT Cu is shown in Fig. 15.4. The formation mechanism of fivefold twins in severely deformed metals and alloys has been discussed in detail using a sequential twinning mechanism [48]. Based on the sequential twinning mechanism, a fivefold twin is formed step-by-step: first twofold, then threefold, fourfold and finally fivefold through the emissions of Shockley partial dislocations from grain boundaries and twin boundaries. Indeed, twofold, threefold, fourfold and fivefold twins have all been observed in severely deformed face-centered-cubic metals [48]. For this sequential twinning mechanism to work, a critical requirement is that the applied stresses should vary in direction at different deformation stages so that to activate different dislocation slip systems for different twin domains. The requirement can be realized in ball milling, which provides a rapid change in stress orientation, and HPT in which compressive stress perpendicular to the specimen surface and pure shear stress along the tangential direction are applied. This critical requirement also explains why no fivefold twin is predicted in MD simulations that usually apply only uniaxial stresses to the specimens under investigation.

A discrepancy also occurs between MD simulations and experimental results on the effect of generalized planar fault energy (GPFE) curves [49] on the par-

tial-dislocation-mediated deformation processes in nanostructured materials. Based on GPFE curves, MD simulations predicted that nanocrystalline Ni, with very high unstable stacking-fault energy γ_{usf} and even higher unstable twin fault energy γ_{utf}, tends to deform through the emissions of leading partial dislocations from grain boundaries, leaving behind stacking faults, but is less likely to deform via twinning at some moderate external stresses unless the stresses are high enough to overcome γ_{utf} [49]. However, experimental observations of deformed nanocrystalline Ni suggest that twinning is a more preferred deformation mechanism than slipping of individual leading partial dislocations, which leave behind extended stacking faults [50, 51]. Wu and Zhu [51] discussed the discrepancy based on the fact that nanocrystalline metals (including Ni in their study) are usually of nonequilibrium grain boundaries, in which high densities of excessive or geometrically unnecessary dislocations are located [19, 40]. They argued that (i) stress concentrations caused by the high density of excessive dislocations at grain boundaries are so high that they could overcome any energy barriers for twin nucleation, (ii) some grain-boundary dislocations have been dissociated into leading and trailing partials, making the successive emissions of leading and trailing partial dislocations easy, which would eliminate the stacking fault behind each leading partial dislocation, and (iii) the GPFE curves used in the MD simulations might be significantly different from the real physical curves [52].

Most of the literature reports on the deformation mechanisms of nanostructured materials have been related to metals and alloys with face-centered-cubic structures [53–57], there are only a few reports on the deformation mechanisms of nanostructured materials with other crystalline structures. For example, Frederiksen et al. [58] used MD simulations to investigate the plastic deformation of nanocrystalline molybdenum, which is of a body-centered-cubic structure, with a grain size of 12 nm at high strain rates and concluded that the plastic deformation involves both grain-boundary processes and dislocation migration that in some cases lead to twin-boundary formation. Most strikingly, the simulations show that a large component of the strain is accommodated through the formation of cracks in the grain boundaries, which would greatly limit the potential mechanical applications of the material. Experimental investigation of body-centered-cubic nanocrystalline tantalum with grain sizes in the range of 10–30 nm suggested that the plastic deformation of the material during nanoindentation is controlled by deformation twinning [59].

In summary, extensive investigations on the deformation mechanisms of nanostructured materials mainly with face-centered-cubic structures have been carried out worldwide. Results suggested that (i) for the finest grain sizes deformation occurs through grain-boundary sliding and rotation, (ii) for grain sizes larger than 20–30 nm but smaller than 100 nm, partial dislocation emissions from grain boundaries play a significant role during plastic deformation, resulting in the formation of high densities of nanotwins and stacking faults, and (iii) other twinning mechanisms not seen in coarse-grained materials are also possible.

15.2
Nanostructured Metals Produced by Severe Plastic Deformation

Severe plastic deformation (SPD)-produced nanostructures are characterized by several structural parameters such as structural morphology, boundary spacing, boundary misorientation and interior dislocation density. A precise characterization of these structural parameters is essential for understanding the mechanical and thermal behaviour of these fine-scaled metals. Various techniques, such as conventional TEM, high-resolution TEM, backscatter electron diffraction (EBSD) in a scanning electron microscope (SEM) and X-ray diffraction (XRD), can be used in these structural studies. This section focuses on TEM characterization and in some cases EBSD results are also shown for comparison. Results obtained from pure Ni processed by high-pressure torsion (HPT) and pure Al processed by accumulative roll bonding (ARB) are taken as examples to demonstrate the characterization of structural parameters and the importance of selecting a proper sample plane and characterization technique is discussed.

15.2.1
Structural Morphology

SPD-produced nanostructures exhibit typically an elongated (lamellar) or an equiaxed appearance. The elongated structure is often observed in nanostructures produced by monotonic deformation, such as cold rolling [60], ARB [61] and HPT [62]. An equiaxed structure is typically the result of more complicated deformation modes or strain path changes such as equal-channel angular pressing (ECAP) routes involving sample rotation between passes [63], multiple directional forging [64] and surface mechanical attrition [65]. The structural morphology is also affected by the deformation conditions (e.g. strain, strain rate and temperature) and material parameters (e.g. stacking-fault energy, impurity level and the presence of second-phase particles).

In the case where an elongated structure is formed, a proper selection of the sample plane is critical to properly reveal the elongated morphology. In the case of HPT-processed metals, the microstructures have been characterized by many

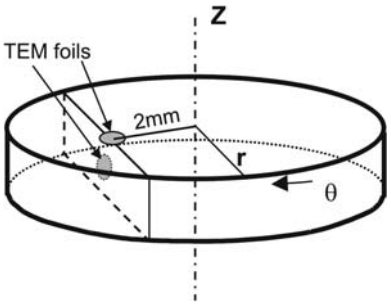

Fig. 15.5 Schematic drawing of the HPT sample and the sample panes for TEM observations. *Z*: torsion axis. *r*: radius, θ: shear direction. The TEM foils samples are prepared from a location 2 mm from the disc center and therefore the strain is well defined.

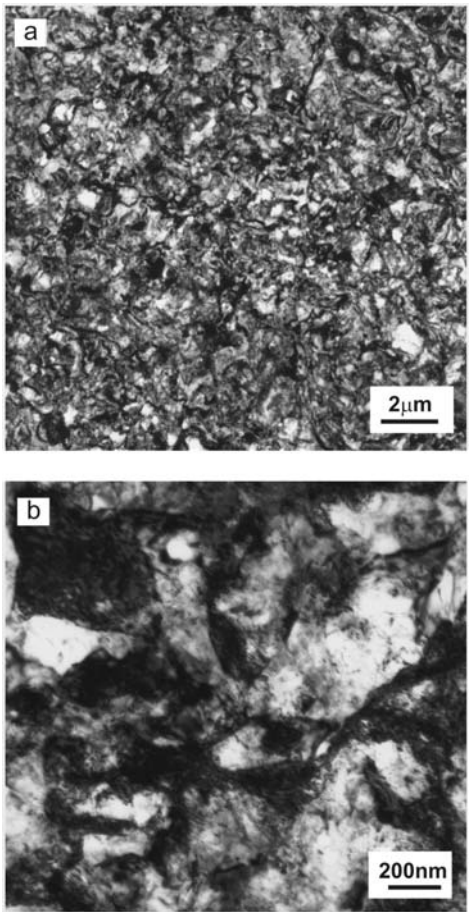

Fig. 15.6 Microstructural morphology of HPT-deformed Ni viewed in the torsion plane at a strain $\varepsilon_{vM} = 5.2$ at two different magnifications (a) and (b). HPT was carried out under a hydrostatic pressure of 4 GPa.

researchers only in the torsion plane [66–68], probably due to the difficulty in preparing TEM foil samples from the longitudinal plane (see Fig. 15.5) of the small disc samples (typically with a thickness of 1 mm and a diameter of 10 mm) processed by HPT. The morphology observed in the torsion plane is in general described as equiaxed, similar to the early rolling-plane observations in cold-rolled or ARB-processed metals [69]. An example of the torsion plane observations is shown in Fig. 15.6 for a Ni sample processed to a strain of 5.2. In Fig. 15.6 (a), which is a low magnification observation covering a relatively large area, only a dislocation structure of complicated morphology is seen. Even at higher magnification (Fig. 15.6 (b)), detailed structural features such as dislocation boundaries are not clearly revealed, although areas with light or dark contrast and irregular shapes can be identified. However, in the longitudinal plane, a well-defined lamellar structure was observed at the same strain of 5.2, and an example is shown in Fig. 15.7 (a). As schematically shown in Fig. 15.7 (b), the la-

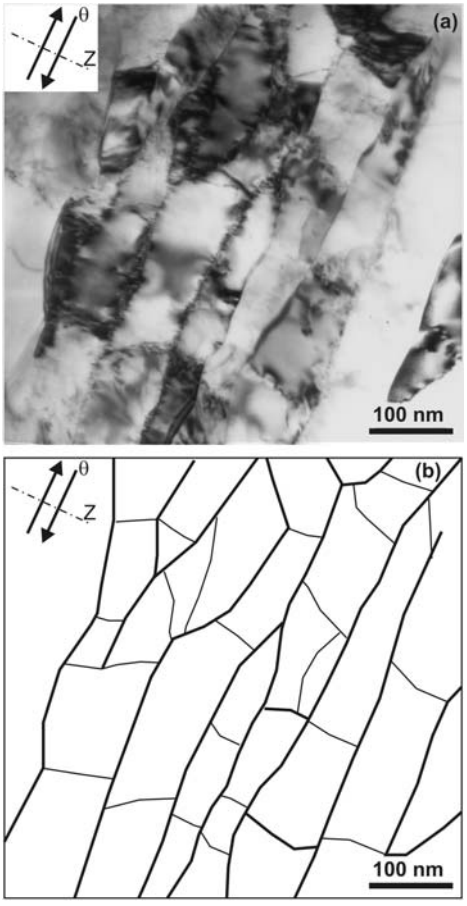

Fig. 15.7 (a) TEM image observed in the longitudinal plane of HPT Ni showing the development of a lamellar structure with the lamellar boundaries approximately parallel to the torsion plane (perpendicular to the torsion axis *Z*). Interconnecting boundaries are formed between the lamellar boundaries. (b) A sketch of the lamellar structure seen in (a). The boundary spacings for the lamellar boundaries *D* and interconnecting boundaries *d* are measured, respectively, in the torsion-axis direction and the shear direction.

mellar structure is delineated by the lamellar boundaries approximately parallel to the torsion plane. Within the lamellae, short boundaries interconnecting the lamellar boundaries are formed. This lamellar structure is similar to that observed after high strain rolling [60, 70] or ARB processing [71].

15.2.2 Boundary Spacing

During plastic deformation, the mean boundary spacing decreases with increasing strain due to grain subdivision. The boundary spacing in deformation-pro-

Table 15.1 Lamellar boundary spacing (D) and interconnecting boundary spacing (d) measured in HPT Ni deformed to two different van Mises strains.

van Mises strain, ε_{vM}	D [nm]	d [nm]	Aspect ratio
12	75	200	2.7
33	60	150	2.5

duced nanostructures is typically in the range from a few hundred nanometres to about 100 nm. At very large strains, the boundary spacing can be reduced to about 10 nm [72].

To measure the boundary spacing on transmission electron micrographs, it is necessary to clearly reveal the structural morphology. For the lamellar structure, as shown in Fig. 15.7 (b), there are two boundary spacings, namely the spacing between the lamellar boundaries (D) and the spacing between the interconnecting boundaries (d). The mean spacings measured at two different van Mises strains, $\varepsilon_{vM} = 12$ and $\varepsilon_{vM} = 33$ are given in Table 15.1. In the literature, the grain size measured from the torsion plane of HPT Ni deformed under various hydrostatic pressures (3–9 GPa) and van Mises strains ($\varepsilon_{vM} > 5$) varies in a range of 100–200 nm [67, 68]. These values are comparable with the spacing of interconnecting boundaries measured in the longitudinal plane but significantly larger than the lamellar boundary spacing.

The boundary spacing may also be measured from EBSD orientation image maps or boundary maps when the structural size is larger than the EBSD spatial resolution, which is typically above 50–100 nm. However, due to the problem of limited angular resolution, which will be discussed in the next section, low-angle boundaries (typically less than 2°) cannot be revealed in the EBSD maps. Therefore, the boundary spacing measured from the EBSD maps is larger than the value measured from the TEM images. When the grain size is smaller than 50–100 nm, the spacing can only be measured by TEM and high-resolution TEM methods or by the XRD method. However, it should be noted that the grain-size distribution may have a strong effect on the grain size measured by the XRD analysis [73].

15.2.3 Boundary Misorientation

During plastic deformation, the mean boundary misorientation increases with increasing strain due to a continuous increase in the fraction of high-angle boundaries that are formed by the transformation of low-angle dislocation boundaries into high-angle boundaries and by the generation of boundaries separating different texture components [74]. Electron-diffraction-based techniques, namely selected area electron diffraction (SAD) and convergent-beam Kikuchi electron diffraction in a TEM and EBSD in a SEM, have been exten-

sively used to measure the orientation and misorientation in deformation-induced nanostructures. These techniques have different angular resolutions and spatial resolutions, and caution is required when interpreting the measured results. Moreover, they have different efficiencies in their data acquisition, which is also an issue when selecting a technique.

SAD is a traditional and simple method to determine the crystallographic orientation. Since it has been used extensively for characterizing the SPD-produced nanostructured metals, it is worth discussing the issues that may cause misinterpretation of the SAD patterns obtained from the nanostructured metals. In the literature, the formation of a ring-like SAD pattern has often been taken as evidence of the generation of high-angle boundaries in the area from which the SAD pattern is obtained. However, an SAD pattern provides only qualitative information on the spread of orientations present in the selected area but no information on the spatial distribution of these orientations. In other words, although grains of many different orientations can produce a ring-like SAD pattern, the formation of such a pattern does not necessarily indicate the presence of high-angle boundaries in the structure. For example, a smooth and continuous lattice curvature over a large angular range can also produce a similar ring-like pattern. In a deformed structure, it is likely that a continuous lattice curvature or an accumulative misorientation is formed over a distance of several hundred nanometres (comparable with the smallest selected-area aperture size available in modern electron microscopes). Therefore, the formation of a ring-like SAD pattern does not provide conclusive information about the development of high-angle boundaries.

EBSD is a fully commercialized and automated method. It is a powerful technique to map orientation and misorientation over rather large areas (for example, up to the scale of mm^2) and to obtain the misorientation distribution. However, this technique suffers from problems in both the angular resolution and the spatial resolution (about 50 nm). The angular resolution depends on the diffraction-pattern quality that is affected by many factors such as the quality of the polished sample surface for the EBSD measurements and the dislocation content in the area analyzed. For samples deformed to large strains, the angular resolution is in general not better than 2°. Figure 15.8(a) shows an example of misorientation distributions obtained by EBSD for a high-purity (99.99%) Al processed by ARB to 6 cycles ($\varepsilon_{vM} = 4.8$) [75]. In this distribution, the misorientation angles below 2° are not included due to the uncertainty in the misorientation determination. The relatively large spatial resolution (typically >50 nm) limits the application of the EBSD technique to the characterization of the misorientation in nanostructured metals when the grain size is below the EBSD spatial resolution.

The TEM Kikuchi diffraction method has advantages in both angular and spatial resolution, and thus is an ideal tool to study misorientations in nanostructured metals. However, the analysis of Kikuchi patterns is still manually based in many laboratories and it is thus a time-consuming process. In some laboratories, a semiautomatic Kikuchi pattern analysis method has been developed

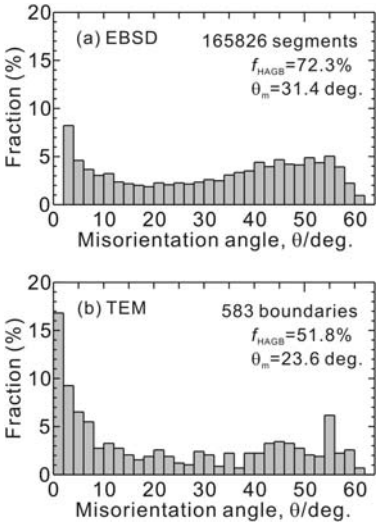

Fig. 15.8 Misorientation distribution obtained by (a) EBSD, and (b) TEM methods in high-purity aluminum processed by 6 cycles of ARB. Note the absence of misorientation angles $<2^\circ$ in the second distribution.

[76] and applied to measure boundary misorientations in several nanostructured metals [60, 75]. One example of the results obtained is shown [75] in Fig. 15.8 (b) from the same sample as was used for EBSD analysis (Fig. 15.8 (a)) for comparison. It is seen that both EBSD and TEM measurements demonstrate a bimodal distribution with one peak located in the lower end of the misorientation angles and the other located in the upper end. Similar distributions have also been obtained in other nanostructured metals [60, 70, 77], indicating that the bimodal misorientation distribution is a characteristic feature of nanostructured metals. However, as shown in Fig. 15.8 (b), about 17% of the boundaries have misorientation angles less than 2°, which are not detected by EBSD (Fig. 15.8 (a)). This result indicates that to achieve a complete characterization of the misorientation distribution the EBSD technique is not appropriate but that the use of the TEM Kikuchi diffraction technique is required. It should also be noted that the concentration of low-angle boundaries with misorientations of less than a few degrees is rather high even for the high-purity Al studied (Fig. 15.8 (b)). The quantification of these low-angle boundaries is crucial to establish the correlation between the structural parameters and the mechanical properties of the deformation-induced nanostructures as has been suggested that the low-angle boundaries contribute to dislocation strengthening [78]. However, it should be pointed out that most of the TEM analyses of misorientation distributions have been made for a structure coarser than 100–200 nm. More measurements in finer structures (<100 nm) are required to prove the presence and evolution of low-angle dislocation boundaries when the structure is refined down to a scale smaller than 100 nm.

In summary, due to the different angular and spatial resolutions associated with different electron-diffraction techniques, careful selection of the technique

is required depending on the purpose and care is required to interpret the results. The boundary misorientation angles in the deformation-produced nanostructures exhibit a characteristic bimodal distribution with one peak located in the lower end of misorientation angles and the other located in the upper end. This bimodal distribution clearly illustrates a difference between the boundaries characterizing the deformation-produced nanostructures and those present in a recrystallized structure.

15.2.4 Interior Dislocation Density

As a product of high-strain deformation, the SPD-produced nanostructures always contain a certain number of interior dislocations and the dislocation density varies depending on which metal and the procession conditions. The existence of interior dislocations may play a key role in determining the mechanical behaviour of nanostructured metals [79]. The dislocation density can be determined by XRD, high-resolution TEM and conventional TEM techniques. The XRD only gives a mean density, while the high-resolution TEM and conventional TEM methods allow both the density and the spatial distribution of dislocations to be determined. The determination of dislocation density by high-resolution TEMS relies on the identification of individual dislocations on high-resolution TEM images. Special care is required to avoid the misidentification of Moiré-effect-induced lattice-image shifting as dislocations [80]. In the TEM method, the crucial issues are the precise determination of the foil thickness and the complete manifestation of all the dislocations present in the structure. Convergent-beam diffraction can be used to precisely determine the foil thickness and multiple-beam diffraction is required to reveal the dislocations.

15.2.5 Summary

SPD-produced nanostructured metals often exhibit characteristic structural features such as elongated morphology, a bimodal misorientation distribution and the presence of interior dislocations. TEM characterization of these parameters has been demonstrated by results obtained in pure Ni processed by high-pressure torsion (HPT) and pure Al processed by accumulative roll bonding (ARB). The care needed in selecting the sample plane and the characterization technique has been discussed.

Acknowledgment

Xiaozhou Liao thanks the Australian Research Council for financial support (Grant # DP0772880). Xiaoxu Huang gratefully acknowledges the Danish National Research Foundation for supporting the Center for Fundamental Re-

search: Metal Structures in Four Dimensions, within which part of this work was performed.

References

1 R. Z. Valiev, **2004**, *Nature Mater.* 3, 511–516.
2 R. Z. Valiev, R. K. Islamgaliev, I. V. Alexandrov, **2000**, *Prog. Mater. Sci.* 45, 103–189.
3 Y. H. Zhao, Y. T. Zhu, X. Z. Liao, Z. Horita, T. G. Langdon, **2006**, *Appl. Phys. Lett.* 89, 121906.
4 Y. H. Zhao, X. Z. Liao, S. Cheng, E. Ma, Y. T. Zhu, **2006**, *Adv. Mater.* 18, 2280–2283.
5 R. Z. Valiev, I. V. Alexandrov, Y. T. Zhu, T. C. Lowe, **2002**, *J. Mater. Res.* 17, 5–8.
6 Y. M. Wang, M. W. Chen, F. H. Zhou, E. Ma, **2002**, *Nature* 419, 912–915.
7 K. M. Youssef, R. O. Scattergood, K. L. Murty, J. A. Horton, C. C. Koch, **2005**, *Appl. Phys. Lett.* 87, 091904.
8 Y. T. Zhu, X. Z. Liao, **2004**, *Nature Mater.* **3**, 351–352.
9 F. C. Frank, W. T. Read, **1950**, *Phys. Rev.* 79, 722–723.
10 J. A. Venables, **1961**, *Philos. Mag.* 6, 379–396.
11 J. A. Venables, **1964**, *J. Phys. Chem. Solids* 25, 693.
12 J. Schiøtz, F. D. Ditolla, K. W. Jacobsen, **1998**, *Nature* 391, 561–563.
13 H. Van Swygenhoven, P. M. Derlet, **2001**, *Phys. Rev. B* 64, 224105–224109.
14 V. Yamakov, D. Wolf, S. R. Phillpot, H. Gleiter, **2002**, *Acta Mater.* 50, 61–73.
15 Z. W. Shan, E. A. Stach, J. M. K. Wiezorek, J. A. Knapp, D. M. Follstaedt, S. X. Mao, **2004**, *Science* 305, 654–657.
16 M. W. Chen, X. Q. Yan, **2005**, S*cience* 308, 356c.
17 Z. W. Shan, E. A. Stach, J. M. K. Wiezorek, J. A. Knapp, D. M. Follstaedt, S. X. Mao, **2005**, *Science* 308, 356d.
18 M. Ke, S. A. Hackney, W. W. Milligan, E. C. Aifantis, **1995**, *Nanostruct. Mater.* 5, 689–697.
19 X. Z. Liao, Y. H. Zhao, Y. T. Zhu, R. Z. Valiev, D. V. Gunderov, **2004**, *J. Appl. Phys.* 96, 636–640.
20 K. Lu, **1996**, *Mater. Sci. Eng. R-Rep.* 16, 161–221.
21 J. Schiøtz, K. W. Jacobsen, **2003**, *Science* 301, 1357–1359.
22 G. E. Fougere, J. R. Weertman, R. W. Siegel, S. Kim, **1992**, *Scr. Metall. Mater.* 26, 1879–1883.
23 E. O. Hall, **1951**, *Proc. Phys. Soc. London B* 64, 747–753.
24 N. J. Petch, **1953**, *J. Iron Steel Inst.* 174, 25–28.
25 V. Yamakov, D. Wolf, S. R. Phillpot, A. K. Mukherjee, H. Gleiter, **2004**, *Nature Mater.* 3, 43–47.
26 V. Yamakov, D. Wolf, S. R. Phillpot, A. K. Mukherjee, H. Gleiter, **2002**, *Nature Mater.* 1, 45–49.
27 H. Van Swygenhoven, M. Spacer, A. Caro, **1999**, *Acta Mater.* 47, 3117–3126.
28 V. Yamakov, D. Wolf, M. Salazar, S. R. Phillpot, H. Gleiter, **2001**, *Acta Mater.* 49, 2713–2722.
29 X. Z. Liao, Y. H. Zhao, S. G. Srinivasan, Y. T. Zhu, R. Z. Valiev, D. V. Gunderov, **2004**, *Appl. Phys. Lett.* 84, 592–594.
30 X. Z. Liao, F. Zhou, E. J. Lavernia, S. G. Srinivasan, M. I. Baskes, D. W. He, Y. T. Zhu, **2003**, *Appl. Phys. Lett.* 83, 632–634.
31 M. W. Chen, E. Ma, K. J. Hemker, H. W. Sheng, Y. M. Wang, X. M. Cheng, **2003**, *Science* 300, 1275–1277.
32 M. A. Meyers, O. Vohringer, V. A. Lubarda, **2001**, *Acta Mater.* 49, 4025–4039.
33 J. W. Christian, S. Mahajan, **1995**, *Prog. Mater. Sci.* 39, 1–157.
34 V. Yamakov, D. Wolf, S. R. Phillpot, H. Gleiter, **2002**, *Acta Mater.* 50, 5005–5020.
35 X. Z. Liao, F. Zhou, E. J. Lavernia, D. W. He, Y. T. Zhu, **2003**, *Appl. Phys. Lett.* 83, 5062–5064.
36 X. Z. Liao, S. G. Srinivasan, Y. H. Zhao, M. I. Baskes, Y. T. Zhu, F. Zhou, E. J. Lavernia, H. F. Xu, **2004**, *Appl. Phys. Lett.* 84, 3564–3566.
37 J. P. Hirth, J. Lothe, **1982**, *Theory of Dislocations,* Wiley, New York.

38 Y. T. Zhu, X. Z. Liao, S. G. Srinivasan, Y. H. Zhao, M. I. Baskes, F. Zhou, E. J. Lavernia, **2004**, *Appl. Phys. Lett.* 85, 5049–5051.

39 Y. T. Zhu, X. Z. Liao, S. G. Srinivasan, E. J. Lavernia, **2005**, *J. Appl. Phys.* 98, 034319.

40 J. Y. Huang, Y. T. Zhu, H. G. Jiang, T. C. Lowe, **2001**, *Acta Mater.* 49, 1497–1505.

41 A.A. Nazarov, A. E. Romanov, R. Z. Valiev, **1993**, *Acta Metall. Mater.* 41, 1033–1040.

42 K. Zhang, J. R. Weertman, J. A. Eastman, **2004**, *Appl. Phys. Lett.* 85, 5197–5199.

43 E. M. Bringa, A. Caro, Y. M. Wang, M. Victoria, J. M. McNaney, B. A. Remington, R. F. Smith, B. R. Torralva, H. V. Swygenhoven, **2005**, *Science* 309, 1838–1841.

44 S. G. Srinivasan, X. Z. Liao, M. I. Baskes, R. J. McCabe, Y. H. Zhao, Y. T. Zhu, **2005**, *Phys. Rev. Lett.* 94, 125502.

45 A. Rohatgi, K. S. Vecchio, G. T. Gray III, **1999**, *Metall. Mater. Trans.* 32A, 135–145.

46 X. Z. Liao, J. Y. Huang, Y. T. Zhu, F. Zhou, E. J. Lavernia, **2003**, *Philos. Mag.* 83, 3065–3075.

47 J. Y. Huang, Y. K. Wu, H. Q. Ye, **1996**, *Acta Mater.* 44, 1211–1221.

48 **Y. T. Zhu, X. Z. Liao, R. Z. Valiev, 2005**, *Appl. Phys. Lett.* 86, 103112.

49 H. Van Swygenhoven, P. M. Derlet, A. G. Frøseth, **2004**, *Nature Mater.* 3, 399–403.

50 X. L. Wu, Y. T. Zhu, E. Ma, **2006**, *Appl. Phys. Lett.* 88, 121905.

51 X. L. Wu, Y. T. Zhu, **2006**, *Appl. Phys. Lett.* 89, 031922.

52 J. A. Zimmerman, H. J. Gao, F. F. Abraham, **2000**,*Modell. Simul. Mater. Sci. Eng.* 8, 103–115.

53 D. Wolf, V. Yamakov, S. R. Phillpot, A. Mukherjee, H. Gleiter, **2005**, *Acta Mater.* 53, 1–40.

54 X. L. Wu, E. Ma, **2006**, *Appl. Phys. Lett.* 88, 231911.

55 X. L. Wu, E. Ma, **2006**, *Appl. Phys. Lett.* 88, 061905.

56 C. X. Huang, K. Wang, S. D. Wu, Z. F. Zhang, G. Y. Li, S. Li, **2006**, *Acta Mater.* 54, 655–665.

57 J. Wang, H. C. Huang, **2004**, *Appl. Phys. Lett.* 85, 5983–5985.

58 S. L. Frederiksen, K. W. Jacobsen, J. Schiotz, **2004**, *Acta Mater.* 52, 5019–5029.

59 Y. M. Wang, A. M. Hodge, J. Biener, A. V. Hamza, D. E. Barnes, K. Liu, T. G. Nieh, **2005**, *Appl. Phys. Lett.* 86, 101915.

60 Q. Liu, X. Huang, D. J. Lloyd, N. Hansen, **2002**, *Acta Mater.* 53, 3789.

61 N. Tsuji, Y. Saito, S. H. Lee, Y. Minamino, **2003**, *Adv. Eng. Mater.* 5, 338.

62 X. Huang, A. Vorhauer, G. Winther, N. Hansen, R. Pippan, M. Zehetbauer, **2004**, in *Ultrafine Grained Materials III*, eds. Y. T. Zhu, T. G. Langdon, R. Z. Valiev, D. H. Shin, T. C. Lowe, TMS, 235.

63 M. Furukawa, Z. Horita, T. G. Langdon, **2002**, *Mater. Sci. Eng. A.* 332, 97.

64 O. Sitdikov, T. Sakai, A. Goloborodko, H. Miura, R. Kaibyshev, **2005**, *Philos. Mag.* 85, 1159.

65 H. W. Zhang, Z. K. Hei, G. Liu, J. Lu, K. Lu, **2003**, *Acta Mater.* 51, 1871.

66 R. Z. Valiev, Y. V. Ivanisenko, E. F. Rauch, B. Baudelet, **1996**, *Acta Mater.* 44, 4705.

67 A. P. Zhilyaev, G. V. Nurislamova, B.-K. Kim, M. D. Baró, J. A. Szpunar, T.G. Langdon, **2003**, *Acta Mater.* 51, 753.

68 F. Dalla Torre, P. Spätig, R. Schäublin, M. Victoria, **2005**, *Acta Mater.* 53, 2337.

69 Y. Saito, N. Tsuji, H. Utsunomiya, T. Sakau, R. G. Hong, **1998**, *Scr. Mater.* 39, 1221.

70 D. A. Hughes, N. Hansen, **2000**, *Acta Mater.* 48, 2985.

71 X. Huang, N. Tsuji, N. Hansen, Y. Minamino, **2003**, *Mater. Sci. Eng.* A340, 265.

72 D. A. Hughes, N. Hansen, **2001**, *Phys. Rev. Lett.* 87, 135503.

73 R. Mitra, T. Ungar, J. R. Weertman, **2005**, *Trans. Indian. Met.* 58, 1125.

74 D. A. Hughes, N. Hansen, **1997**, *Acta Mater.* 45, 3871.

75 N. Kamikawa, N. Tsuji, X. Huang, N. Hansen, **2006**, *Acta Mater.* 54, 3055.

76 Q. Liu, **1995**, *Ultramicroscopy* 60, 81.

77 X. Huang, N. Kamikawa, N. Hansen, **2008**, *Mater. Sci. Eng. A* 483, 102–104.

78 N. Hansen, **2004**, *Scr. Mater.* 51, 801.

79 X. Huang, N. Hansen, N. Tsuji, **2006**, *Science* 312, 249.

80 C. Rentenberger, T. Waitz, H. P. Karnthaler, **2004**, *Scr. Mater.* 51, 789.

16
Bulk Nanostructured Intermetallic Alloys Studied by Transmission Electron Microscopy

Thomas Waitz, Christian Rentenberger, and H. Peter Karnthaler

16.1 Introduction

During the past decade, bulk nanostructured materials have stimulated numerous research activities to elucidate the fundamental physical reasons for their novel and enhanced properties [1–8]. In the case of alloys and intermetallic compounds, methods of severe plastic deformation (SPD) can lead to grain sizes that are significantly smaller than those of pure metals after SPD [9]. In addition, unique phase structures of nanocrystalline alloys and intermetallic compounds can be obtained that differ significantly from those of their coarse-grained counterparts. Striking examples of new-phase structures include disordering [10] and even amorphization [11–14], the dissolution of second-phase particles and the enhanced solubility of otherwise immiscible elements [9]. It should be noted that most of the studies of nanostructured intermetallic compounds are based on materials processed by mechanical alloying and milling of powders [15], whereas, investigations of bulk nanostructured intermetallics are still rare.

Transmission electron microscopy (TEM) methods provide an excellent tool to study nanostructures. TEM investigations of various isolated nanostructures such as nanoparticles and nanotubes were excellently reviewed previously [16]. Since by SPD considerable local changes of the phase structures can occur down to the atomic scale, it is the objective of this chapter to give an overview on TEM studies including high-resolution transmission electron microscopy (HRTEM) of bulk nanostructured materials. The very high density of the grain boundaries requires special care when the results of the TEM experiments are analyzed in terms of crystalline lattices and lattice defects such as dislocations. Therefore, this chapter focuses initially on possible contrast artefacts arising by nanograins that overlap in the TEM projection. After solving these problems of methodology, TEM investigations of bulk nanostructured alloys are presented. The nanostructured alloys were obtained from ordered intermetallic alloys by SPD. Coarse-grained starting materials were subjected to high-pressure torsion (HPT). From the HPT discs, TEM specimens with marked orientations and well-defined deformation degrees were prepared by electropolishing.

Bulk Nanostructured Materials. Edited by M. J. Zehetbauer and Y. T. Zhu

ISBN: 978-3-527-31524-6

16.2
TEM Analysis of Lattice Defects in Nanostructured Materials: Possible Pitfalls

Severe plastic deformation of alloys and intermetallics can facilitate the formation of bulk nanocrystalline structures with grain sizes down to a few nanometers. Therefore, even the very thin TEM foils will frequently contain areas where several grains overlap in the TEM projection (foils of a thickness of about 100 nm and ~10 nm or less are suitable for TEM and HRTEM, respectively). As a consequence, TEM bright-field, dark-field and HRTEM images frequently show moiré effects [17]. Moiré pattern arise by the interference of diffracted beams $\boldsymbol{g}_1$ and $\boldsymbol{g}_2$ that correspond to different grains located on top of each other in the TEM projection; their interference leads to a moiré reflection $\Delta\boldsymbol{g}=\boldsymbol{g}_1-\boldsymbol{g}_2$. In the case of TEM diffraction contrast images, a moiré interference pattern will arise in bright- and dark-field images when the modulus Δg of the moiré reflection is sufficiently small to be included in the objective aperture (i.e. $\Delta g < g_1, g_2$). When an objective aperture is not used as in the case of HRTEM images, Δg having a value similar to that of g_1 and g_2 will contribute to the image and give rise to unique moiré contrast artefacts.

These moiré effects can be very complex; they often dominate the contrast of structural images and therefore lead to misinterpretations [18]. Figure 16.1 shows a HRTEM image of nanocrystalline Ni_3Al revealing {111} lattice planes of two adjacent grains; the angle between the two sets of {111} lattice planes is 52°. A moiré pattern containing a periodic array of bright dots similar to a structural image is formed where the grains overlap. It is important to realize that the periodic pattern does not correspond to projected atomic columns and that its symmetry does not agree with the crystalline symmetry of Ni_3Al. The HRTEM contrast pattern arising by overlapping grains was also calculated using an image simulation software [19], which clearly shows the occurrence of moiré

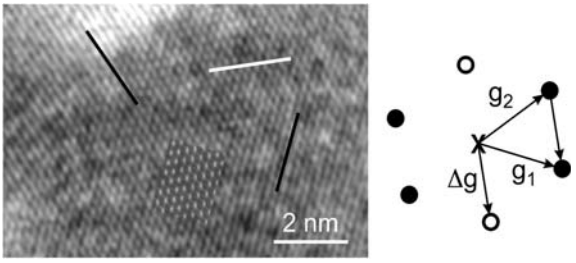

Fig. 16.1 Nanocrystalline Ni_3Al produced by HPT. The HRTEM image of two overlapping grains shows moiré fringes parallel to the white line. The superposition of the {111} lattice fringes (parallel to the dark lines) leads to an image characterized by a periodic pattern of white dots. (For comparison an image simulation is shown as an inset.) The structural image of overlapping grains does not reflect the real crystal structure. In the power spectrum the beating of the reflections $\boldsymbol{g}_1$ and $\boldsymbol{g}_2$ corresponding to the {111} lattice fringes causes the moiré reflection $\Delta\boldsymbol{g}$.

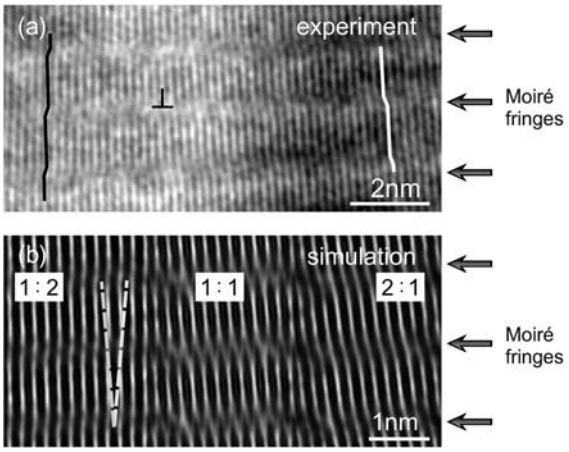

Fig. 16.2 Nanocrystalline Ni_3Al produced by HPT. (a) Experimental HRTEM image of an area of overlapping grains showing lattice fringes and moiré fringes. Bent and interrupted lattice fringes occur not reflecting the real structure. (b) Simulated HRTEM image based on overlapping grains of varying relative thickness. Depending on the ratio of their thickness (1:2, 1:1, 2:1) different shifts of the contrast lines occur. These observed lattice fringes should not be interpreted as bent or terminating lattice planes of the real crystal.

effects. In the present case of overlapping grains ({111} planes in Bragg orientation and rotated by 52°), a calculated image shown as an inset in Fig. 16.1 agrees with the experiment.

When the relative rotations between overlapping grains are in the range of a few degrees, moiré fringes of large spacings (as compared to the lattice spacing) arise. The moiré fringes can significantly impact lattice fringe images. In this case, bent or terminating lattice fringes are frequently observed (cf. Fig. 16.2). The fringes have almost the correct spacing of the lattice planes but their arrangement does not reflect the local orientation of the lattice planes. Therefore, it is not possible to interpret the bent lattice fringes as localized distortions of the lattice planes. Also, contrast fringes that are interrupted cannot be interpreted as terminating lattice planes and are therefore not an indication of a high density of dislocations. As shown by simulations (cf. Fig. 16.2 (b)) the pattern of lattice fringes depends on the relative thickness of the overlapping grains (1:2, 1:1, 2:1). The lattice fringes observed in the TEM image do not correspond to the real structure of the grains since in the simulation the grains (rotated by 10°) were considered to be free of defects. Therefore, special care is needed when images with inclined grain boundaries are interpreted in terms of lattice defects.

16.3
Evolution of Nanostructures by SPD

TEM methods are very suitable to study the evolution of nanograins from the coarse-grained structure by quantitative analysis of their structural morphology including grain subdivision, boundary spacing and boundary misorientation. This topic is covered by the contribution of Liao and Huang (see Chapter 15 of this book), presenting TEM results on the continuous evolution of the nanostructure by homogenous grain fragmentation in pure metals. However, in intermetallic alloys a different, very localized transformation to a nanocrystalline structure or even to an amorphous phase can occur. In the following, TEM results on the SPD-induced heterogeneous formation of nanocrystalline (NC) and amorphous structures are presented.

In the case of intermetallic alloys, a heterogeneous formation of the nanocrystalline structure arises by severe plastic deformation using HPT. Intermetallic alloys with crystal structures based on the fcc structure (e.g. $L1_2$ ordered Ni_3Al [10, 20]) or based on the bcc structure (e.g. B2 ordered FeAl [21]) were studied. Concomitant with the formation of the nanograins disordering is observed (cf. Section 16.4.1). In the initial stages of the plastic deformation, the NC structure frequently forms within narrow bands (width of a few hundred nanometers) and shows a sharp transition to the coarse-grained structure. Comparing TEM micrographs with optical images of deformation marks on etched crystal surfaces revealed that the bands are shear bands representing areas of high local shear. Similar bands denoted as brass-type shear bands were observed in cold-rolled Ni_3Al [22]. In the case of HPT, the orientation of the bands (projected onto the shear plane) lies preferentially perpendicular or parallel to the shear direction of the HPT disc; the latter is interpreted as a consequence of the accumulation of geometrically necessary dislocations accommodating the strain gradient of the HPT deformation [10]. Figure 16.3 shows a TEM image of a NC

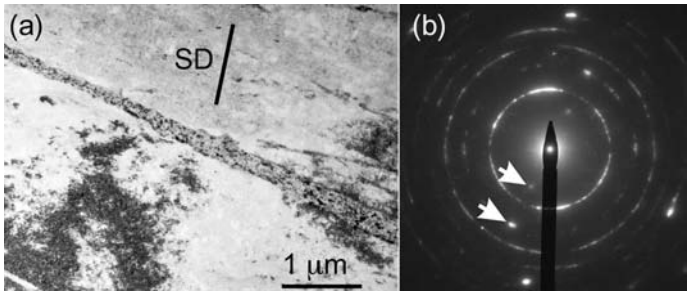

Fig. 16.3 FeAl deformed by HPT. Bright-field image and corresponding diffraction pattern of a narrow band consisting of nanograins. The band running from the upper left corner to the bottom right corner lies nearly perpendicular to the shear direction SD. The SA diffraction pattern of an area 0.3 µm in diameter of the band shows a ring pattern indicating a large variety of grains of different orientations. The spots indicated by the arrows originate from the coarse-grained area next to the band.

band in FeAl lying nearly perpendicular to the shear direction; the band is about 300 nm wide and consists of grains with a size below 100 nm. In the case of Ni_3Al, both a crystallographic and a strain-gradient-dependent orientation relationship of the band and the adjacent area is observed; the orientation correlates with both the trace of {111} glide planes and the shear direction [10].

With increasing strain, the volume fraction of the NC structure increases by autocatalytic growth of NC volume that already exists [10] and by the nucleation of new bands that, finally, merge. TEM studies of Ni_3Al and FeAl show large grains that are embedded in the NC structure [23, 24]. It is concluded that even at large strains a few coarse grains survive the HTP as a consequence of the heterogeneous formation of the nanograins. The highly symmetric orientations of these coarse grains indicate that their homogeneous deformation distributed onto several noncoplanar slip systems hampers the transformation into the NC structure [23].

In NiTi shape-memory alloys, severe plastic deformation by HPT [14, 25–29] and even by cold rolling [13, 30–33] can cause localized deformation that destroys the crystalline lattice, leading to a crystalline to amorphous phase transformation. It was proposed that the accumulation of a high density of lattice defects such as dislocations and grain boundaries is a major driving force for amorphization. The amorphization occurs on the nanoscale and TEM methods can be used to analyze the heterogeneous microstructure. Based on a detailed

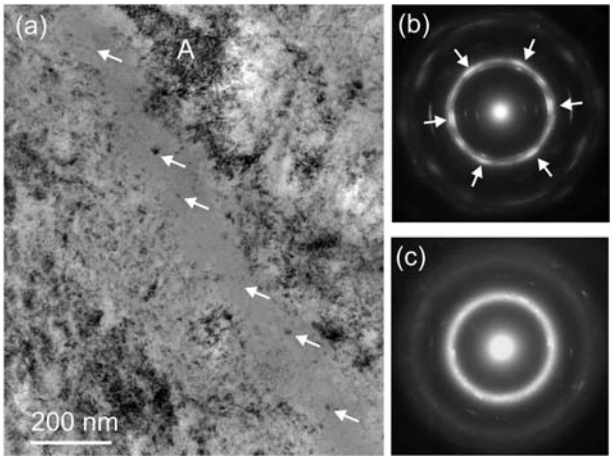

Fig. 16.4 NiTi deformed by HPT (strain <1000%). (a) TEM bright-field image of the severely strained crystalline matrix containing an amorphous shear band. In the crystalline phase, strong changes of the contrast occur even on the nanometer scale that are caused by moiré effects. Whereas, the contrast of the amorphous band is rather uniform and diffuse. Retained nanocrystals are marked by arrows. (b) SA diffraction pattern of nanocrystalline B2 and B19́ phases yield a ring pattern. Caused by a texture, six-fold intensity variations occur (indicated by arrows). (c) SA diffraction pattern taken from the amorphous shear band. Weak spots of the retained nanocrystals superimpose the diffuse ring pattern of the amorphous phase.

HRTEM analysis, as the initial step amorphization at the core of dislocations and at grain boundaries was observed [14]. A high density of dislocations might also trigger the SPD-induced formation of amorphous bands caused by a shear strain instability [30]. Figure 16.4 (a) shows a TEM bright-field image of a specimen taken near the centre of the HPT disc where the strain is relatively low (< 1000%). The amorphous band-shaped area is embedded in a severely deformed crystalline matrix. The crystalline phase shows a complex contrast; strong local variations of the contrast, e.g. near A arise by a moiré effect [18]. Selected area (SA) diffraction taken from the crystalline areas yields ring patterns that are caused by the strong grain refinement and by large lattice strains (cf. Fig. 16.4 (b)). The diffraction pattern comprises both reflections from the B2 austenite and the B19′ martensite; a six-fold intensity variation is caused by a crystallographic texture. In the TEM bright-field images, the amorphous bands that have a width of about 100 nm show up by a uniform and rather diffuse contrast. In the corresponding SA diffraction pattern broad and diffuse rings are observed (cf. Fig. 16.4 (c)). The ring pattern is superimposed by diffraction spots that arise from nanocrystals embedded in the amorphous bands. Most of the nanocrystals have a size of less than 30 nm (some of them are indicated in Fig. 16.4 (a)).

It should be noted that the interface between the crystalline and the amorphous phase is rather fuzzy [33, 34]. HRTEM methods used to analyze the structure of the interface reveal a transition zone that contains nanocrystals partially detached from the crystalline phase (cf. Fig. 16.5). It is interesting to note that the crystalline lattice is still ordered right up to the interface with the amorphous phase since spots corresponding to B2 superlattice reflections occur in

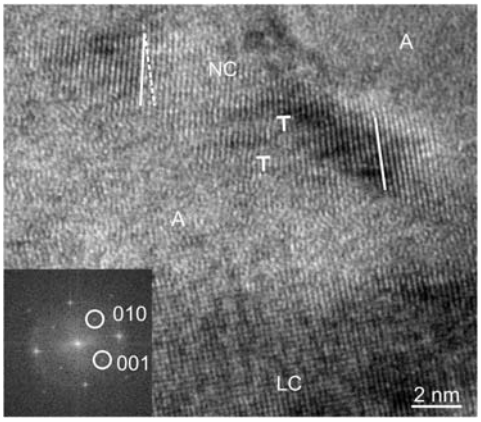

Fig. 16.5 NiTi deformed by HPT. HRTEM image of the transition zone between large crystals (LC) and the amorphous phase (A). A calculated power spectrum of LC shows spots that correspond to ⟨100⟩ superlattice reflections. Marked by NC, a nanocrystal is detached from LC. Lattice fringes of NC are bent, gradually rotated (cf. the full and dashed lines) and frequently terminating (some of them indicated by T).

calculated power spectra (cf. the inset of Fig. 16.5). Near the transition zone, HRTEM images of the crystalline lattice frequently show lattice planes that seem to be heavily bent, gradually rotated and terminating. This could indicate the occurrence of severe lattice strains caused by a high density of dislocations. However, the possibility of moiré effects should also be considered. Caused by two overlapping nanocrystals that are rotated with respect to each other, moiré effects might occur that would lead to bent lattice fringes even when lattice strains are not present (cf. Fig. 16.2).

16.4 Local Phase Analysis

In ordered intermetallic alloys processed by HPT, the structures of the crystalline lattices frequently differ from those of the corresponding coarse-grained materials. In the following, two examples are presented. Firstly, TEM is used to clarify the mechanisms of the local disordering in $L1_2$ and B2 long-range ordered intermetallic alloys that arises upon severe plastic deformation. Secondly, HRTEM methods are applied to analyze the lattice structure of the thermally induced martensitic phase in nanograins of NiTi shape-memory alloys.

16.4.1 SPD-induced Order–Disorder Transition

SPD of long-range ordered (LRO) intermetallic alloys leads to disordered metastable states that cannot be obtained by any annealing heat treatments. Even in intermetallic alloys showing no thermal order–disorder transition, the chemical order can be completely destroyed by the severe plastic deformation since the superlattice structure is entirely lost. Experimentally, the state of order can be deduced measuring the intensities of the superlattice reflections with respect to those of the fundamental reflections. Using X-ray diffraction, several investigations of mechanically disordered powders processed by ball milling were carried out (for a review see [35]); whereas, studies of disordered bulk materials are still rare. By X-ray diffraction methods only the integral value of the order and its dependence on strain and annealing temperature can be measured, yielding an average that does not reveal the strong local effects occurring in the SPD-processed bulk nanostructures (e.g. [36–38]).

Using TEM methods, the local state of order and the defects that lead to disorder can be studied in reciprocal space (selected area electron diffraction SAED, convergent-beam electron diffraction CBED) and in real space; in the latter case the comparison of dark-field images using fundamental and superlattice reflections is essential. Comparison of X-ray diffraction and electron-diffraction data of DO_{19} LRO Ti_3Al indicate that electron diffraction is more sensitive to detect some remaining atomic order; i.e. superlattice reflections disappear in TEM SAED patterns at a substantial higher degree of the plastic strain than in the

case of X-ray diffraction [38]. In the following, examples of TEM results on deformation-induced disordering corresponding to the phase transformation from $L1_2$ LRO to the fcc solid solution and from B2 LRO to bcc solid solution are presented.

In the case of $L1_2$ LRO alloys, disordering of Cu_3Au and Ni_3Al subjected to HPT was studied by TEM using electron diffraction and dark-field images. Dark-field images reveal a very localized destruction of the order on the nanometer scale within coarse grains [10, 39]. These disordered narrow zones correlate with highly activated glide planes and also occur at crystallographic boundaries fragmenting the coarse grains. Disordering requires the formation of antisite defects (i.e. unlike A-B type atomic neighbors are replaced by A-A and B-B type neighbors). Therefore, the deformation induced accumulation of antiphase boundary (APB) faults is an important process since the APB displace A-B neighbors to antisite A-A and B-B positions across the interface. APB faults can be created (i) by APB ribbons of superlattice dislocations [40], (ii) by APB tubes [41, 42] and (iii) by additional APBs generated by the fragmentation of the grown-in domain structure. Cu_3Au shows a domain structure bounded by grown-in APB already in the coarse-grained material. Therefore, in HPT-processed Cu_3Au, all three mechanisms of APB formation occur, as analyzed by TEM. Their simultaneous activation might explain why in Cu_3Au complete disordering takes place by deformation in coarse grains.

In $L1_2$ LRO Ni_3Al deformed by HPT, complete disordering is directly connected with the dynamic formation of the nanocrystalline structure as analyzed by SAED patterns [10, 43]. In this case, disordering is expected to occur by the formation of APBs during the localized formation of nanograins by dynamic recovery. Since the disordered nanocrystalline structure is formed heterogeneously, the coexistence of an ordered coarse-grained structure and a disordered nanocrystalline structure can be clearly revealed by TEM [10]. Figure 16.6 shows the TEM bright-field image of this duplex structure; the corresponding SAED pattern reveals the grain-size-dependent state of order. Similar, strong heterogeneous disordering is accompanied by the formation of nanocrystals in the case of B2 ordered FeAl deformed by HPT [21]. Thus, the monotonic decrease of the global order parameter measured by X-ray diffraction with increasing deformation [44] should be reconsidered; on the basis of the TEM results this monotonic decrease rather reflects the increase of the volume fraction of the disordered nanocrystalline structure at the expense of the ordered coarse grains. It is interesting to note that SPD of $L1_0$ ordered TiAl (ordered structure based on fcc) leads to a weak disordering of the nanocrystalline structure only [45]. This can be attributed to the different deformation mode since TiAl deforms mainly by twinning and not by the glide of superlattice dislocations.

Upon annealing recovery processes including reordering of SPD intermetallic alloys can be studied by *in-situ* TEM [46] and *post-mortem* TEM [37, 38, 47, 48]. In the case of reordering the nucleation and growth of ordered domains, the evolution of their morphology and the structure of the APB can be followed during the thermal treatment and correlated to DSC measurements. Even in in-

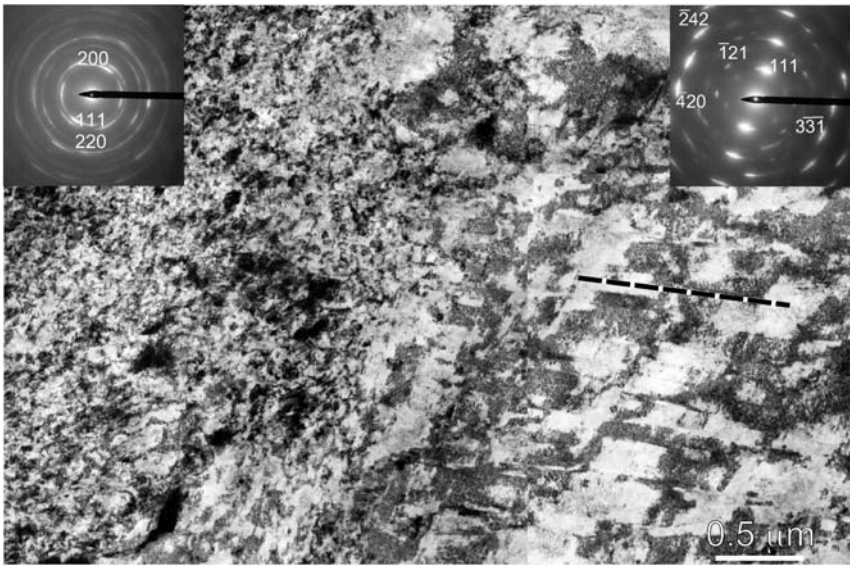

Fig. 16.6 Ni_3Al deformed by HPT. TEM bright-field image of a duplex structure consisting of a disordered nanocrystalline structure (left) and an ordered coarse-grained structure (right) fragmented parallel to glide planes (indicated by the dashed line). Superlattice reflections are absent and present in diffraction patterns that correspond to the nanocrystalline and the coarse-grained structure, respectively (cf. the insets) [10].

termetallic alloys showing no thermally induced order–disorder transition, due to the high ordering energy, domains of nanometer size are found within nanograins.

16.4.2
Thermally Induced Crystalline–Crystalline Phase Transformation in Nanograins

NiTi shape-memory alloys show a martensitic phase transformation from the cubic B2 high-temperature phase (the austenite) to the monoclinic B19′ martensite that causes large transformation strains. In the case of nanocrystalline NiTi, the high density of grain boundaries that act as obstacles significantly impact the phase transformation. In the nanograins, the transformation to martensite is hindered since both the transformation temperatures and the volume fraction of the martensite decrease with decreasing grain size [27]. As analyzed by TEM, the transformation to martensite is even completely suppressed in grains with a size less than a critical grain size of 50 nm. In addition to the phase stability, the nanograins strongly impact the morphology of the martensite [49, 50]. Figure 16.7 shows a HRTEM image of a martensitic nanograin that contains numerous twins that occur at an atomic scale. Frequently, twins are observed that have a thickness of 4 and 6 atomic layers only. On tilting the specimen, different beam directions were selected to analyze both the lattice structure and the

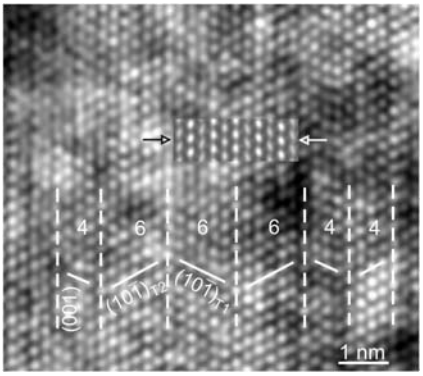

Fig. 16.7 HPT nanocrystalline NiTi. Atomic structure of the martensite. Experimental HRTEM image of (00$\bar{1}$) compound twins. (10$\bar{1}$) lattice planes of the twins and the twin boundaries are marked by full and dashed lines, respectively. The bright dots correspond to positions between the atomic columns. As an inset (between the arrows) a calculated HRTEM image is shown for comparison.

atomic structure of the twin boundaries. The lattice structure agrees with that expected in the case of the B19′ martensite as it is observed in coarse grains. Contrary to this, different twins are encountered in nanograins: the twins are of the (001) compound type (based on the HRTEM analysis, an atomic model of the twin boundaries was set up and used to carry out image simulations that are in good agreement with the experiment; cf. the calculated image shown as an inset in Fig. 16.7). It should be noted that (001) compound twinning of B19′ violates the theory of martensite formation since an invariant martensite/austenite interface does not exist [51]. However, in the nanograins fine twins are favored since they yield effective compensation of the transformation strains [52]. Since the formation of fine twins is opposed by the high total twin-boundary energy, the question arises why atomic scale (001) twinning is possible in the case of the NiTi nanograins. To answer this question, *ab-initio* total-energy calculations based on the atomic model obtained by the HRTEM analysis were carried out. As a result, the calculations yield a low specific energy of the twin interfaces that facilitates the formation of the atomic-scale (001) compound twins in the nanograins [52].

16.4.3
Amorphous–Crystalline Phase Transformation

Nanocrystallization of amorphous phases is a very promising route to obtain bulk nanostructured materials (see Chapter 13 of this book, by Wilde). Devitrification of amorphous solids can occur upon annealing, irradiation and mechanical straining [53]. Devitrification is most commonly induced thermally, and the mechanisms of the crystallization strongly depend on the conditions of the annealing and on the chemical composition and the structure of the amorphous

phase. The ability to control and to predict the evolution of a nanocrystalline structure that occurs by devitrification requires in-depth knowledge of the crystallization kinetics and the analysis of the crystalline lattice, chemistry and morphology of the nanocrystals. In this respect, investigations of the nanostructures by TEM methods provide valuable insight into the physical mechanisms of the nanocrystallization.

Two main experimental approaches of the TEM analysis can be distinguished. Firstly, we can investigate *post-mortem* specimens that were obtained by partial or complete devitrification of the bulk amorphous specimens. Partial devitrification facilitates the analysis of the morphology of the nanocrystals and of the local composition [54, 55] (this can be used to distinguish between the different modes of the crystallization: polymorphous, primary and eutectic; for an excellent introduction to crystallization, cf. e.g. [53]). Secondly, *in-situ* TEM experiments offer the challenging opportunity to directly study the formation of the nanocrystals in an amorphous matrix. The nanocrystallization can be induced thermally by heating the thin TEM foils [56], mechanically using *in-situ* straining devices [57] or by radiation using the electron beam [58]. Isothermal *in-situ* heating experiments carried out at different temperatures, yield the kinetics of the devitrification by direct measurements of the rates of the nucleation and growth as well as the corresponding activation energies [59]. Counting the number of new crystallites formed in a given volume of the thin TEM foil as a function of time directly yields the nucleation rate (the thickness of the thin TEM foil can be measured precisely using electron energy-loss spectroscopy [60]). Since the nanocrystallization might occur heterogeneously, *in-situ* TEM offers a unique tool to measure the local kinetics of the devitrification.

Figures 16.8 and 16.9 show TEM bright-field images obtained by *in-situ* heating that were used to analyze the structures and the kinetics of the devitrification of amorphous Ni-50at.%Ti shape-memory alloys processed by HPT. Figure 16.8 shows that the devitrification occurs heterogeneously. Pre-existing nanocrystals that have survived the severe plastic deformation start to grow and new crystallites nucleate predominantly near clusters of pre-existing nanocrystals (marked by C). Most of the nanocrystals show bright contrast with respect to the amorphous phase. They scatter less than the amorphous matrix since they have a random orientation with respect to the incident electron beam, whereas some crystals close to a Bragg or Laue orientation cause dark contrast. Figure 16.9 shows nanocrystals that were nucleated in the amorphous matrix and grow spherically until they impinge upon each other (TEM bright-field images were recorded using a TV-rate camera system; in this case nanocrystals of weak contrast show up when their size exceeds 5 to 10 nm). TEM SA diffraction methods applied during the *in-situ* heating yield the result that the devitrification occurs by the formation of nanocrystals that have the ordered B2 high-temperature phase of NiTi. The devitrification is polymorphous since no apparent change of the chemical composition upon crystallization was encountered using energy dispersive X-ray measurements. Based on the analysis of TEM micrographs similar to that of Fig. 16.9, the rate of the nucleation and growth were measured

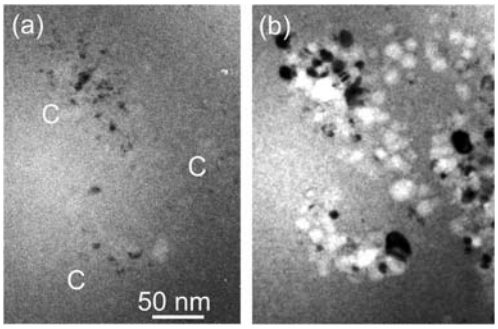

Fig. 16.8 HPT NiTi. TEM bright-field images of the same area (a) prior and (b) after *in-situ* heating. (a) Clusters of nanocrystals surviving the HPT deformation are marked by C. (b) Structure obtained by annealing at a temperature of ~370 °C for about 4 h. New crystals form almost entirely near pre-existing nanocrystalline clusters.

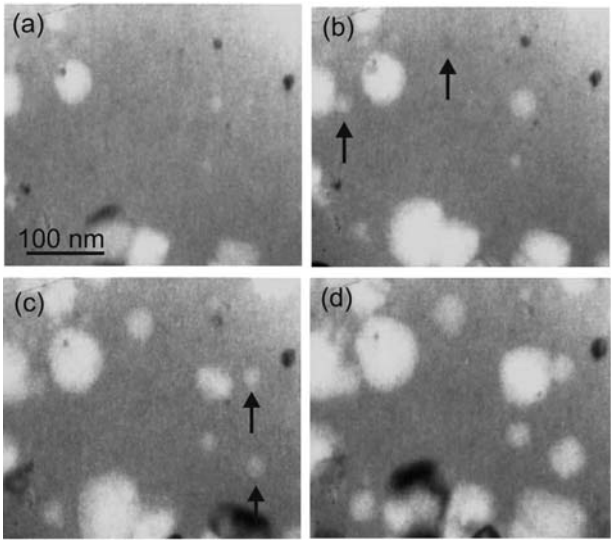

Fig. 16.9 HPT NiTi. Devitrification process recorded during *in-situ* heating. Crystals nucleated during the *in-situ* heating (marked by arrows) grow spherically at a constant rate till they impinge upon each other. The time intervals from (a) to (b), (a) to (c) and (a) to (d) is 19, 49 and 85 min, respectively (the temperature of the TEM heating holder is ~370 °C).

[61]. It is interesting to note that the kinetics of the devitrification of the present HPT-processed amorphous NiTi alloys differ considerably from those obtained in the case of thin films of amorphous NiTi made by sputter deposition or melt spinning. This is caused by different structures of the amorphous phases obtained by the different processing routes.

16.5
Local Texture Analysis by SAED, HRTEM and Dark-field Images

Crystallographic texture that is a basic parameter for the evolution and formation of the nanocrystalline structure is generally investigated by X-ray diffraction or electron back-scattered diffraction in a scanning electron microscope. In addition, TEM methods using SAED, CBED, HRTEM and dark-field images can be applied to obtain information on the local orientation distribution of nanograins. SAED allows qualitative texture measurements of an ensemble of grains, whereas CBED is applied on individual grains giving additional information on the misorientation between neighboring grains. For a reliable measurement of the texture using SAED patterns, it is important that the information of different tilting positions of the specimen is considered. Using HRTEM images and dark-field images, grains of selected orientations can be located; grain orientations can be correlated with grain morphology, grain size and macroscopic orientations. Dark-field images can be used also for small grains with high density of defects. However, depending on the size and position of the objective aperture used to obtain the dark-field images the angular resolution is small (typically $>5^{\circ}$).

The texture analysis of Ni_3Al and FeAl shows that a highly random orientation distribution of the nanograins occurs when the samples are deformed to large deformation strain under SPD condition [10, 21]. Upon further straining, the grain structure and the texture do not change significantly. In HPT-processed Ni_3Al, a texture component $\{112\}\langle 110\rangle$ was encountered using SAED that agrees with results obtained by X-ray measurements [36]. The results on textures can be used to determine the deformation process occurring under SPD conditions: weak textures are a strong indication for grain-boundary-mediated processes like grain-boundary sliding [62] or dynamic recrystallization [63]. Using SAED patterns and dark-field images of different sections of the

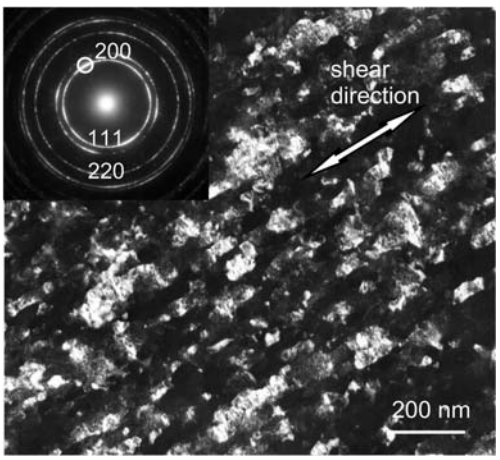

Fig. 16.10 Nanocrystalline Ni_3Al obtained by HPT (strain of about 80 000%). The TEM dark-field image using $\langle 111\rangle$ reflections indicates that some grains are elongated along the shear direction (beam direction is parallel to the normal of the shear plane). In the corresponding diffraction pattern shown in the inset the position of the aperture is indicated.

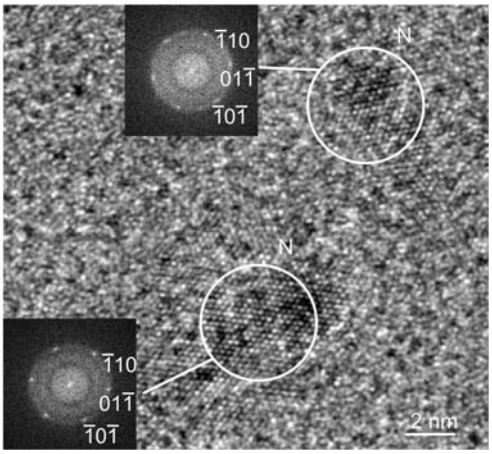

Fig. 16.11 NiTi after HPT. HRTEM image of nanocrystallites (marked N) embedded in an amorphous matrix. The nanocrystallites have similar orientations since ⟨111⟩ is almost parallel to **FN** (insets show calculated power spectra of the encircled areas).

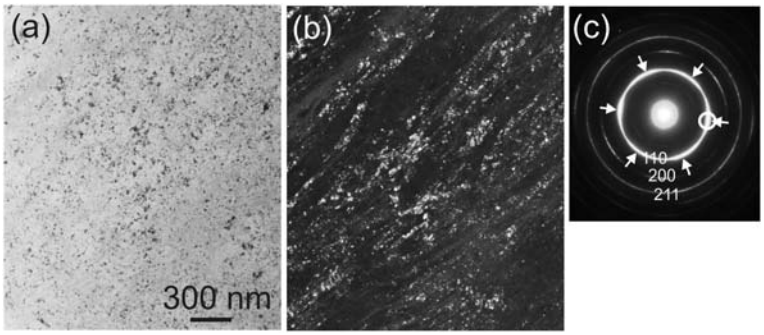

Fig. 16.12 HPT NiTi. Nanocrystalline structure obtained after complete devitrification of the amorphous phase. a) TEM bright-field image. A texture is hardly visible. b) TEM dark-field image. The texture shows up clearly: Nanograins of similar orientations are contained in band-shaped areas. c) SA diffraction pattern. A 6-fold pattern of intensity maxima indicated by arrows is caused by preferred orientations of the nanograins (⟨111⟩ zone axis parallel to **FN**). The circle marks the position of the objective aperture used to obtain the dark-field image.

HPT disc, a correlation of grain morphology and texture is found in nanocrystalline Ni_3Al (cf. Fig. 16.10). The TEM observations also show that the texture can differ on the micrometer scale.

When NiTi shape-memory alloys are subjected to plastic deformation, a strong crystallographic texture arises [64, 65]. Severe plastic deformation causes refinement of the textured grain structure and concomitant amorphization until, finally, only nanocrystallites survive the HPT. The nanocrystallites embedded in the amorphous matrix still show the crystallographic texture. HRTEM images directly reveal the texture of the nanocrystals that frequently have a ⟨111⟩ or ⟨100⟩ zone axis almost parallel to the foil normal (**FN** is perpendicular to the

plane of the HPT disc; cf. Fig. 16.11). After complete devitrification by annealing, a nanocrystalline structure is obtained in the amorphous specimens (cf. Fig. 16.12). It is interesting to note that this undeformed nanocrystalline structure also shows a texture. In TEM dark-field images, band-shaped structures made up of nanograins with similar orientations showed up (cf. Figs. 16.12 (b) and (c), respectively). The preferred orientation of the nanograins corresponds to that of the nanocrystalline debris that survived the HPT. The texture is preserved by the nanocrystallites that act as heterogeneous nucleation sites of the devitrification. The texture strongly depends on the density of the nanocrystallites acting as nuclei and decreases with increasing HPT strain. Finally, it should be noted that the present result of texture formation by heterogeneous nucleation of HPT bulk amorphous alloys disagrees with the observation of devitrification by laser annealing of thin amorphous films of NiTi obtained by sputtering [66]. In the latter case, a texture has not been observed after devitrification and it was concluded that nucleation occurs homogeneously in these thin films.

16.6 Summary

To summarize, it is shown that TEM studies of bulk nanostructured intermetallic alloys provide valuable insight into both their structures and the physical mechanisms of their formation. With careful consideration to avoid possible pitfalls arising by moiré effects of overlapping nanograins, the analysis by TEM and HRTEM can yield details on crystalline lattice structure, crystallographic orientation, and phase stability. In addition, TEM is an excellent tool for nanoscale studies of the SPD-induced amorphization and loss of chemical order.

A main result is that intermetallic alloys subjected to severe plastic deformation by high-pressure torsion show a heterogeneous development of the nanostructure caused by shear-band formation. In the case of Ni_3Al and FeAl, nanograins arise in narrow bands. In NiTi even a crystalline to amorphous phase transformation is caused by the large localized plastic strains. TEM selected-area diffraction and HRTEM were used to analyze the local chemical order of the nanostructures. HPT of Ni_3Al and FeAl causes the formation of a metastable state of complete disorder even at room temperature, whereas in the thermodynamic equilibrium both alloys are ordered up to the melting point. TEM analyses revealed that the disordering occurred by the accumulation of lattice defects such as APB ribbons and APB tubes existing in coarse grains (e.g. in Cu_3Au) or concomitant with the formation of the nanocrystalline structure (as in the case of Ni_3Al and FeAl). SAED, HRTEM and dark-field images were used to analyze the local texture that reflects the mechanism of the SPD-induced deformation. In the case of the formation of bulk nanocrystalline alloys by devitrification of an amorphous phase, the thermally induced nanocrystallization was analyzed in detail by TEM *in-situ* heating experiments. It is shown that the kinetics of the

devitrification of the SPD-induced amorphous phase of NiTi differ considerably from those of melt-spun or sputter-deposited amorphous NiTi alloys.

The TEM analysis of nanocrystalline structures revealed that thermally induced phase transformations can be considerably affected by small grain size. In the case of the martensitic phase transformation of nanocrystalline NiTi shape-memory alloys, the formation of the martensite is hindered by the high density of grain boundaries acting as obstacles. With decreasing grain size the transformed volume fraction decreases and finally, the transformation to martensite is completely suppressed in grains smaller than a critical size ($\sim$50 nm). Using HRTEM, a unique morphology of atomic-scale twinning is observed in the nanograins that violates the standard theory of martensite formation.

It is strongly emphasized that in the case of nanostructures even in the very thin TEM foils suitable for HRTEM experiments, frequently moiré effects are caused by overlapping grains and nanocrystals. Moiré effects might dominate the contrast of TEM images and are open to misinterpretations. In HRTEM images, moiré effects can lead to the artefact of a periodic spot pattern that occurs at an atomic scale similar to that caused by projected atomic columns. However, the symmetry of the spot pattern is determined by the relative orientation of the overlapping grains. Moiré effects can also lead to the artefact of bent lattice fringes or even to a high density of terminating lattices fringes that must not be interpreted by large lattice strains or by a high density of dislocations.

Note added in proof. Ideas put forward in this article have been proved in a recent publication: Evidence for the extensive disordering by APB faults during SPD (see 16.4.1) is shown in [67].

Acknowledgments

The authors would like to thank the group of Professor R. Pippan from the Erich Schmid Institute Leoben (Austria) for the kind help during HPT and Professor R. Z. Valiev from the Ufa State Aviation Technical University (Russia) for provision of some HPT deformed samples. The support by the research project "Bulk Nanostructured Materials" within the research focus "Materials Science" of the University of Vienna is acknowledged.

References

1 S. X. McFadden, R. S. Mishra, R. Z. Valiev, A. P. Zhilyaev, A. K. Mukherjee, **1999**, *Nature* 398, 684–686.
2 Y. M. Wang, M. Chen, F. Zhou, E. Ma, **2002**, *Nature* 419, 912–914.
3 C. C. Koch, **2003**, *Scr. Mater.* 49, 657–662.
4 K. S. Kumar, H. Van Swygenhoven, S. Suresh, **2003**, *Acta Mater.* 51, 5743–5774.
5 K. S. Kumar, S. Suresh, M. R. Chisholm, J. A. Horton, P. Wang, **2003**, *Acta Mater.* 51, 387–405.
6 Y. M. Wang, E. Ma, **2004**, *Acta Mater.* 52, 1699–1709.
7 D. Wolf, V. Yamakov, S. R. Phillpot, A. Mukherjee, H. Gleiter, **2005**, *Acta Mater.* 53, 1–40.

8 R. Z. Valiev, A. K. Mukherjee, **2001**, *Scr. Mater.* 44, 1747–1750.
9 X. Sauvage, R. Pippan, **2005**, *Mater. Sci. Eng.* A 410–411, 345–347.
10 C. Rentenberger, H. P. Karnthaler, **2005**, *Acta Mater.* 53, 3031–3040.
11 K. Yamada, C. C. Koch, **1993**, *J. Mater. Res.* 8, 1317–1326.
12 D. Kuhlmann-Wilsdorf, M. S. Bednar, **1993**, *Scr. Metall. Mater.* 28, 371–376.
13 J. Koike, D. M. Parkin, M. Nastasi, **1990**, *J. Mater. Res.* 5, 1414–1418.
14 J. Y. Huang, Y. T. Zhu, X. Z. Liao, R. Z. Valiev, **2004**, *Philos. Mag. Lett.* 84, 183–190.
15 C. Suryanarayana, **2001**, *Prog. Mater. Sci.* 46, 1–184.
16 Z. L. Wang, **2003**, *Adv. Mater. 15*, 1497–1514.
17 D. B. Williams, C. B. Carter, **1996**, *Transmission Electron Microscopy; A Textbook for Materials Science*. Plenum Press, New York, pp. 444.
18 C. Rentenberger, T. Waitz, H. P. Karnthaler, **2004**, *Scr. Mater.* 51, 789–794.
19 P. A. Stadelmann, **1987**, *Ultramicroscopy* 21, 131–145.
20 A. N. Tyumentsev, M. V. Tret'yak, Y. P. Pinzhin, A. D. Korotaev, R. Z. Valiev, R. K. Islamgaliev, A. V. Korznikov, **2000**, *Phys. Met. Metall.* 90, 461–470.
21 C. Mangler, C. Rentenberger, H. P. Karnthaler, **2006**, *Proc. 16th Int. Microsc. Congr., Japan* 1656.
22 J. Ball, G. Gottstein, **1993**, *Intermet.* 1, 171–185.
23 C. Rentenberger, H. P. Karnthaler, **2007**, *Int. J. Mater. Res.* 98, 255–258.
24 C. Rentenberger, T. Waitz, H. P. Karnthaler, **2007**, *Mater. Sci. Eng. A* 462, 283–288.
25 Y. V. Tatyanin, V. G. Kurdyumov, V. B. Fedorov, **1986**, *Phys. Met. Metall.* 62, 118–124.
26 A. V. Sergueeva, C. Song, R. Z. Valiev, A. K. Mukherjee, **2003**, *Mater. Sci. Eng. A* 339, 159–165.
27 T. Waitz, V. Kazykhanov, H. P. Karnthaler, **2004**, *Acta Mater.* 52, 137–147.
28 H. P. Karnthaler, T. Waitz, C. Rentenberger, B. Mingler, **2004**, *Mater. Sci. Eng. A* 387–389, 777–782.
29 S. D. Prokoshkin, I.Yu. Khmelevskay, S. V. Dobatkin, I. B. Trubitsyna, E. V. Tatyanin, V. V. Stolyarov, E. A. Prokofiev, **2005**, *Acta Mater.* 53, 2703–2714.
30 J. Koike, D. M. Parkin, M. Nastasi, **1990**, *Philos. Mag. Lett.* 84, 183–190.
31 J. C. Ewert, I. Böhm, R. Peter, F. Haider, **1997**, *Acta Mater.* 45, 2197–2206.
32 H. Nakayama, K. Tsuchiya, M. Umemoto, **2001**, *Scr. Mater.* 44, 1781–1785.
33 K. Tsuchiya, M. Inuzuka, D. Tomusa, A. Hosokawa, H. Nakayama, K. Morii, Y. Todaka, M. Umemoto, **2006**, *Mater. Sci. Eng. A* 438–440, 643–648.
34 T. Waitz, H. P. Karnthaler, R. Z. Valiev, **2004**, in: R. Z. Valiev, M. Zehetbauer, (eds.) *Proceedings of the Second International Conference on Nanomaterials by Severe Plastic Deformation*, VCH Weinheim, J. Wiley, pp. 339–344. |**AQ1**|
35 H. Bakker, G. F. Zhou, H. Yang, **1995**, *Prog. Mater. Sci.* 39, 159–241.
36 J. Languillaume, F. Chmelik, G. Kapelski, F. Bordeaux, A. A. Nazarov, G. Canova, C. Esling, R. Z. Valiev, B. Baudelet, **1993**, *Acta Metall. Mater.* 41, 2953–2962.
37 A. V. Korznikov, O. Dimitrov, G. F. Korznikova, J. P. Dallas, S. R. Idrisova, R. Z. Valiev, F. Faudot, **1999**, *Acta Mater.* 47, 3301–3311.
38 R. N. Eshchenko, O. A. Elkina, A. M. Patselov, V. P. Pilyugin, **2006**, *Phys. Met. Metall.* 102, 611–618.
39 C. Rentenberger, C. Mangler, H. P. Karnthaler, **2004**, *Mater. Sci. Eng. A* 387, 795–798.
40 D. P. Pope, S. S. Ezz, **1984**, *Int. Met. Rev.* 29, 136–167.
41 C. T. Chou, P. M. Hazzledine, P. B. Hirsch, G. R. Anstis, **1987**, *Philos. Mag. A* 56, 799–813.
42 C. Rentenberger, T. Waitz, H. P. Karnthaler, **2003**, *Phys. Rev. B* 67, 094109.
43 A. V. Korznikov, G. Tram, O. Dimitrov, G. F. Korznikova, S. R. Idirisova, Z. Pakiela, **2001**, *Acta Mater.* 49, 663–671.
44 S. Gialanella, M. D. Baro, L. Lutterotti, S. Surinach, **1995**, *Mater. Res. Soc. Symp. Proc.* 364, 213–218.
45 O. Dimitrov, A. V. Korznikov, G. F. Korznikova, G. Tram, **2000**, *J. Phys. IV* 10, 33–38.

46 W. Zielinski, Z. Pakiela, K. J. Kurzydlowski, **2003**, *Mater. Chem. Phys.* 81, 452–456.

47 H. P. Karnthaler, T. Waitz, C. Rentenberger, B. Mingler, **2004**, *Mater. Sci. Eng. A* 387, 777–782.

48 R. Z. Valiev, C. Song, S. X. McFadden, A. K. Mukherjee, R. S. Mishra, **2001**, *Philos. Mag. A* 81, 25–36.

49 T. Waitz, T. Antretter, F. D. Fischer, N. K. Simha, H. P. Karnthaler, **2007**, *J. Mech. Phys. Sol.* 55, 419–444.

50 T. Waitz, **2005**, *Acta Mater.* 53, 2273–2283.

51 K. Otsuka, X. Ren, **2005**, *Prog. Mater. Sci.* 50, 511–678.

52 T. Waitz, D. Spišák, J. Hafner, H. P. Karnthaler. **2005**, *Europhys. Lett.* 71, 98–103.

53 K. Lu, **1996**, *Mater. Sci. Eng. R* 16, 161–221.

54 R. I. Wu, G. Wilde, J. H. Perepezko, **2001**, *Mater. Sci. Eng. A* 301, 12–17.

55 A. Hirata, Y. Hirotsu, **2006**, *J. Mater. Sci.* 41, 2597–2600.

56 X. Sun, A. Cabral-Prieto, M. Jose Yacaman, J. Reyes-Gasga, R. Hernandez-Reyes, A. Morales, W. Sun, **2000**, *Physica B* 291, 173–179.

57 N. Boucharat, R. Hebert, H. Roesner, R. Z. Valiev, G. Wilde, **2007**, *J. Alloys Compd.* 434, 252–254.

58 M. Libera, **1996**, *Appl. Phys. Lett.* 68, 331–333.

59 H. J. Lee, H. Ni, D. T. Wu, A. Ramirez, **2005**, *Appl. Phys. Lett.* 123102.

60 R. V. Ramanujan, Y. R. Zhang, **2006**, *Phys. Rev. B* 74, 224408.

61 M. Peterlechner, T. Waitz, H. P. Karnthaler, **2008**, *Scr. Mater.* 59, 566–569.

62 J. Weissmüller, J. Markmann, **2005**, *Adv. Eng. Mater. 7*, 202–207.

63 T. Hebesberger, H. P. Stüwe, A. Vorhauer, F. Wetscher, R. Pippan, **2005**, *Acta Mater.* 53, 393–402.

64 Y. Liu, Z. L. Xie, J. Van Humbeeck, L. Delaey, **1999**, *Acta Mater.* 47, 645–660.

65 C. Frick, A. Ortega, J. Tyber, K. Gall, H. Maier, **2004**, *Metall. Mater. Trans. A* 35, 2013–2025.

66 X. Wang, Y. Bellouard, J. J. Vlassak, **2005**, *Acta Mater.* 53, 4955–4961.

67 C. Rentenberger, H. P. Karnthaler, **2008**, *Acta Mater.* 56, 2526–2530.

17
Microstructure of Bulk Nanomaterials Determined by X-Ray Line-profile Analysis

Tamás Ungár, Erhard Schafler, and Jenö Gubicza

17.1 Introduction

The physical properties of structural materials are determined by their microstructure. The microstructure can be investigated either by direct methods, especially transmission or scanning electron microscopy (TEM or SEM), or by the indirect methods, like X-ray line-profile analysis (XLPA), differential scanning calorimetry (DSC), residual electrical resistivity (RER) or the different methods of mechanical testing. All these methods, irrespective of whether direct or indirect, reflect different aspects of the different microstructure features. The more methods that are used, the more comprehensive will be the microstructural characterization. In the present work the method of XLPA is summarized and discussed in comparison with other methods listed here. It is attempted to reveal how XLPA can contribute to a more complete characterization of the microstructure of bulk nanomaterials, especially when combined with other methods.

17.2
General Concept and the Basic Ideas of X-ray Line-profile Analysis

Within the framework of the kinematical scattering theory, the ideal diffraction pattern of a polycrystalline specimen consists of narrow, symmetrical, delta-function-like peaks at the positions of the exact Bragg angles according to the well-defined unit cell of the crystal [1]. Several aberrations of the ideal powder pattern are related to the microstructure of materials and are the subject of XLPA. (i) Peak shift is related to internal stresses [2] or planar faults, especially stacking faults or twinning [1–4], or chemical heterogeneities [1]. (ii) Peak broadening indicates small crystallites [5–7], grains or subgrains [8], and/or the presence of microstresses [1, 9–14]. (iii) Stress gradients and/or chemical heterogeneities can also cause peak broadening [1, 15–17]. (iv) Peak asymmetries can be caused by long-range internal stresses [12, 13, 16–20], planar faults [3, 4, 21–23] or chemical heterogeneities [1]. (v) Anisotropic peak broadening can result

Bulk Nanostructured Materials. Edited by M. J. Zehetbauer and Y. T. Zhu

ISBN: 978-3-527-31524-6

from anisotropic crystallite shape [24, 25] or anisotropic strain [9, 10, 26–32]. (vi) When the lattice parameter is large and the specimen has either a local or general texture, unusual peak narrowing can be observed, especially in the first few Bragg reflections [33, 34]. Microstructural properties can be summarized at least into the following different categories: (1) internal stresses, (2) stacking faults, (3) twinning, (4) crystallite size or subgrains, (5) microstresses, (6) long-range internal stresses, (7) chemical heterogeneities, (8) anisotropic crystallite shape or (9) anisotropic strain. There is no one-to-one correlation between the different peak profile features and the different microstructure properties, as can be seen in Table 17.1, where the line-profile features and the microstructure elements are listed.

Both the different line-profile features and the different microstructure properties are complex, and the two sides, e.g. the experimental features and the microstructure properties, can be combined in many different ways. This fact makes it practically impossible (at least at this time) to have a general description of XLPA that would be able to treat all the microstructural properties by a unified general theory or model. It is the experimentator's task to select those microstructure properties that are most relevant to be considered in a particular experiment. At the same time, just because of the complexity of both the experiment and the microstructure properties, it is probably not possible to produce a *model-independent general* theory for XLPA. For the same reason, though there have been many attempts to develop model-independent descriptions of line

Table 17.1 Correlations between peak profile features, i.e. broadening, shifts, asymmetries or shape, and the different microstructure elements.

Peak profile features Microstructure properties	Peak shift	Peak broadening	Peak asymmetry	Anisotropic peak broadening	Peak shape
Dislocations		+	+	+	+
Stacking faults	+	+	+	+	+
Twinning		+	+	+	+
Microstresses		+			
Long-range internal stresses or stress gradients	+		+	+	
Grain boundaries	+	+			
Subboundaries	+	+			
Internal stresses	+				
Coherency strains	+	+	+	+	
Chemical heterogeneities or chemical gradients	+	+	+		
Point defects					+
Precipitates, inclusions	+		+		+
Crystallite or grain smallness or subgrains		+		+	+

broadening, these have not been too successful. In the present work a brief summary of XLPA is presented that is based on well-defined specific microstructure models, in particular on the model that the microstructure consists fundamentally of (a) subgrains with a simple and well-defined size distribution and that (b) the main source of microstrains are dislocations or dislocation-type lattice defects, e.g. triple junctions or sinter stresses.

17.3
Basic Principles of X-ray Line-profile Analysis

Assuming that size (S) and lattice distortion (D) are the two sources of X-ray line broadening, the profile of a Bragg reflection can be given by the convolution of the size and the distortion profiles [1]:

$$I^{\mathrm{F}} = I^{\mathrm{S}} \times I^{\mathrm{D}} \tag{17.1}$$

where the superscript F indicates that I^{F} is the physical profile that does not contain instrumental effects. The Fourier transform of this expression is the Warren–Averbach equation [35]:

$$\ln A(L) \cong \ln A_{\mathrm{L}}^{\mathrm{S}} - 2\pi^2 L^2 g^2 \langle \varepsilon_{\mathrm{g},L^2} \rangle \tag{17.2}$$

where $A(L)$ are the absolute values of the Fourier coefficients of I^{F}, $A_{\mathrm{L}}^{\mathrm{S}}$ are the size Fourier coefficients, g is the absolute value of the diffraction vector and $\langle \varepsilon_{\mathrm{g},L^2} \rangle$ is the mean square strain. L is the Fourier length defined as $L = na_3$, where $a_3 = \lambda/2(\sin\theta_2 - \sin\theta_1)$, n are integers starting from zero, λ is the wavelength of the X-rays and $(\theta_2 - \theta_1)$ is the angular range of the measured diffraction profile. When strain is caused by dislocations or dislocation-type defects, $\langle \varepsilon_{\mathrm{g},L^2} \rangle$ can be expressed as [10]:

$$\langle \varepsilon_{\mathrm{g},L^2} \rangle = (b/2\pi)^2 \pi \rho C f(\eta) \tag{17.3}$$

where $\eta = L/R_{\mathrm{e}}$, R_{e} is the effective outer cutoff radius and b is the Burgers vector of dislocations and C is the contrast or orientation factor of dislocations. Wilkens determined the $f(\eta)$ function for parallel straight screw dislocations in the entire L range from zero to infinity, see, e.g. Eqs. (A.6) to (A.8) in [10]. It can be shown that the Wilkens function, $f(\eta)$, has a more general validity, i.e. it is also valid for edge dislocations and for curved dislocations, and it can be extended in a simple way for infinitesimal dislocation dipoles when M goes to zero, cf. [36], where $M = R_{\mathrm{e}}\sqrt{\rho}$ is the dislocation arrangement parameter [10, 11]. M is smaller or larger than unity if the dislocations have strong or weak dipole character, or in other words, when the effect of screening of the deformation fields is strong or weak, respectively [10, 14].

17.3.1 Strain Anisotropy

Strain anisotropy means that neither the breadths nor the Fourier coefficients of the diffraction profiles are monotonous functions of the diffraction angle or g [27–32]. Strain anisotropy proved to be a powerful feature in XLPA, especially for determining Burgers-vector populations or active slip systems [37–49].

The orientation or hkl dependence of the contrast of dislocations is well known in TEM. It is expressed explicitly in Eq. (17.3) by the contrast factor C. If dislocations are the major source of strain in a crystal the values of C depend on the relative orientation of the Burgers, the line and the diffraction vectors, $\boldsymbol{b}$, $\boldsymbol{l}$ and $\boldsymbol{g}$, respectively. If either all possible slip systems in a crystal are more-or-less equally populated or, if a polycrystal is more-or-less texture free, the contrast factors corresponding to one particular hkl can be averaged over the permutations of these hkl indices. It can been shown that, in a dislocated crystal, the average contrast factors, $\bar{C}$, are linear functions of the fourth-order invariants of hkl [32]. For cubic crystals $\bar{C}$ is [32]:

$$\bar{C} = \bar{C}_{\mathrm{h00}}(1 - qH^2) \tag{17.4}$$

where $\bar{C}_{\mathrm{h00}}$ is the average dislocation contrast factor of the $h00$ type reflections and $H^2 = (h^2k^2 + h^2l^2 + k^2l^2)/(h^2 + k^2 + l^2)^2$. The values of $\bar{C}_{\mathrm{h00}}$ and the q parameter can be obtained numerically for different dislocation types as functions of the elastic properties of a crystal [37]. For hexagonal crystals $\bar{C}$ is [32, 43]:

$$\bar{C}_{hk.l} = a + \frac{[\beta(h^2 + k^2 + i^2) + \gamma l^2]l^2}{\left[h^2 + k^2 + i^2 + \frac{3}{2}\left(\frac{a}{c}\right)^2 l^2\right]^2} \tag{17.5}$$

where a, β and γ are constants depending on the elastic constants of the crystal and the type of dislocations (e.g. basal, prismatic, pyramidal and/or any subslip-system, or slip-system family) and on c/a, the ratio of the two lattice constants in the hexagonal crystal. The value of a is the average contrast factor corresponding to the $hk.0$ reflection: $\bar{C}_{hk.0} = a$. Equation (17.5) can be rationalized as [43, 50]:

$$\bar{C}_{hk.l} = \bar{C}_{hk.0}[1 + q_1 x + q_2 x^2] \tag{17.6}$$

where $x = (2/3)(l/ga)^2$, $q_1 = a_1$ and $q_2 = -a_1\lambda^{-2} + a_2$. Equation (17.6) means that the average contrast factors corresponding to a specific slip system family (these are the 11 most likely slip systems in a hexagonal crystal according to Jones and Hutchinson [51]) and materials constants (lattice parameters and elastic constants) have to follow a parabola as a function of x. The $\bar{C}_{hk.0} = a$ and the q_1 and q_2 parameters have been numerically evaluated and compiled for a large number of hexagonal crystals in [43].

17.3.2
Breadth Methods

The two simplest measures of peak broadening are the full width at half-maximum (FWHM) and the integral breadths, the two are denoted here as: ΔK_{FWHM} and ΔK_{β}, where $\Delta K = (\cos\theta/\lambda)\Delta(2\theta)$, θ is the Bragg angle and $\Delta(2\theta)$ is the FWHM or the integral breadth in radians, respectively. Since size is independent and strain is increasing with diffraction order, in order to separate size and strain effects, Williamson and Hall [52] suggested plotting the breadth of profiles *versus* $\sin\theta$. The extrapolated intercept of such a plot at $\sin\theta = 0$ should give the inverse of an "apparent" size and the slope should be proportional to strain. A typical Williamson–Hall plot of a copper specimen deformed by equal channel angular pressing (ECAP) in a single pass is shown in Fig. 17.1(a). The

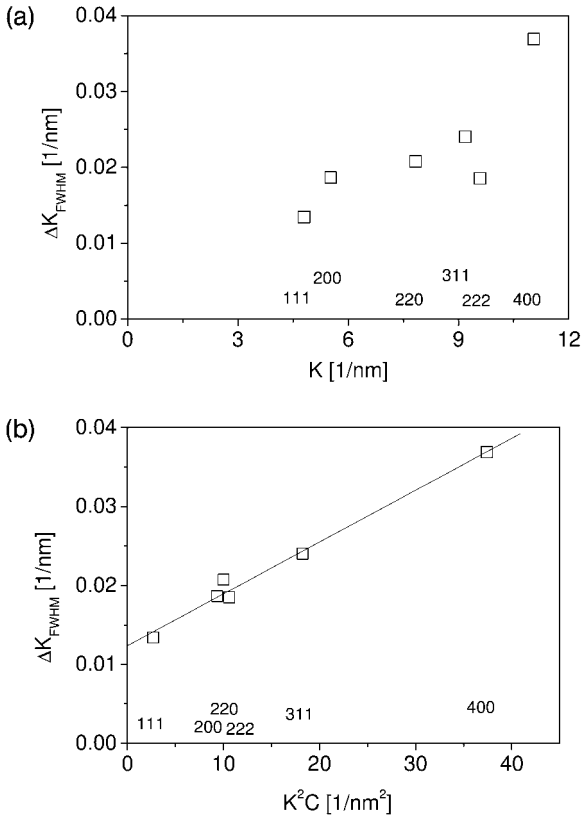

Fig. 17.1 The full width at half-maximum (FWHM) as a function of $K = 2\sin\theta/\lambda$ in the *classical* (a) $K\bar{C}^2$ in the *modified* Williamson–Hall plot (b) for Cu deformed by 1 ECAP pass, where 2θ and λ are the diffraction angle and the X-ray wavelength and C is the average dislocation contrast factor, respectively.

apparent scattering of the data is far beyond experimental error, the figure indicates a strong strain anisotropy. This effect makes a simple interpretation of the Williamson–Hall plot impossible. However, strain anisotropy in the classical Williamson–Hall plot can be rationalized by the contrast factors of dislocations in the *modified* Williamson–Hall plot [30, 37, 40, 41, 53]. Two versions of the *modified* Williamson–Hall plot are suggested in [30, 53, 54]:

$$\Delta K_{\mathrm{FWHM}} \text{ or } \Delta K_\beta = 0.9/D + (\pi A^2 b^2/2)^{1/2}\rho^{1/2}(K\bar{C}^{1/2} + O(K^2\,\bar{C}) \tag{17.7}$$

and

$$\Delta K_\beta = 1/d + aK^2\bar{C} + O(K^2\,\bar{C})^2 \tag{17.8}$$

In Eq. (17.7) D is an apparent crystallite size, $K = 2\sin\theta/\lambda$, A is a constant depending on the M parameter of dislocations, b and ρ are the Burgers vector and the average density of dislocations, respectively, and O stands for higher-order terms in $K\bar{C}^{1/2}$. In Eq. (17.8) d is an apparent crystallite size, a is a constant and O stands for higher-order terms in $K^2\bar{C}$, not interpreted here. In [53] it has been shown by dimensionality analysis that the order dependent strain part of either the ΔK_{FWHM} or the integral breadths, ΔK_β, can only have even-power terms of K. Therefore, Eq. (17.8) is physically more appropriate. However, the breadth methods should only be used for qualitative purposes, as pointed out in [55], thus, both Eqs. (17.7) and (17.8) can be used alternatively. For spherical crystallites the volume-weighted mean diameter $\langle x\rangle_{\mathrm{vol}}$ is directly related to d: $\langle x\rangle_{\mathrm{vol}} = (4/3)d$ [5]. The same data as in Fig. 17.1 (a), are plotted according to Eq. (17.8) in Fig. 17.1 (b), and show a smooth behavior *versus* $K^2\bar{C}$.

17.3.3
Whole-profile Fitting Methods

The idea of whole-profile fitting goes back to Rietveld, who suggested producing the measured diffraction pattern by taking into account all possible effects that contribute to the intensity distribution, including all instrumental effects [56, 57]. The purpose of this method was to refine the structure parameters from powder-diffraction patterns. Well-defined analytical profile functions are used in the Rietveld method, such as the Voigt or pseudo-Voigt functions. However, profile shapes corresponding to dislocated crystals cannot be described by simple analytical functions [9–14, 17, 18, 37, 53]. Therefore procedures have been worked out, in which the diffraction pattern is simulated by using *ab-initio* physically established functions for both the size and the strain profiles [37, 42, 50, 53, 58]. In [53] and [58] the size profile, I^{S}, is given by assuming either spherical or ellipsoidal crystallite shape and log-normal size distribution. In the case when spherical crystallite shape can be assumed, the function is defined by the two parameters of the size-distribution function: the median, m, and the variance, σ. The strain function, I^{D}, is given by using the Wilkens function $f(\eta)$, as

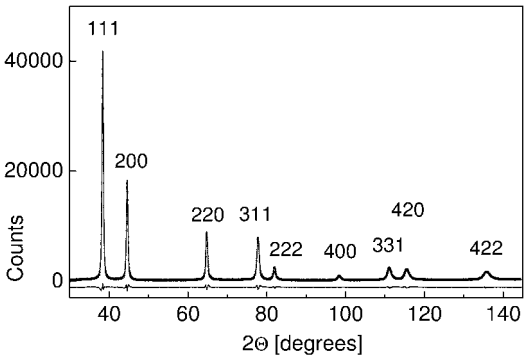

Fig. 17.2 The measured X-ray diffractogram (open circles) and the pattern obtained as a result of the CMWP fitting procedure (solid line) for Al-6wt.%Mg ball milled for 6 h [50].

defined in Eq. (17.3). The I^D function is defined by two parameters: the dislocation density, ρ and the dislocation-arrangement parameter, M. This means that in the simplest case, together with the q parameter in the contrast factors for cubic crystals, the numerical procedure is operating with five independent parameters: m, σ, ρ, M and q. Here, we note that, due to the nature of the microstructure, this is the minimum number of parameters that have to be used. The instrumental profile, I^i, has to be measured. The convolutional multiple whole-profile (CMWP) fitting procedure is a numerical method, producing the convolution of the three functions, I^S, I^D and I^i, i.e. $I^{SIM} = I^S \times I^D \times I^i$ [59]. The procedure is freely available through the web: http://www.renyi.hu/cmwp/. The background, I^{BG}, is determined before the simulated I^{SIM} function is fitted to the measured diffraction pattern [38]. The measured X-ray diffractogram (open circles) and the pattern obtained as a result of the CMWP fitting procedure (solid line) for Al-6wt.%Mg ball milled for 6 h is shown in Fig. 17.2. When individual profiles can be measured, the numerical procedure, called the multiple whole-profile (MWP) fitting procedure [50], is operating on the Fourier coefficients of the measured and the theoretical profiles. This method is also available at the same web address. The effect of stacking faults and twinning has been elaborated and incorporated into the CMWP procedure by evaluating the faulting effect on powder patterns of cubic crystals, for details see [23, 60].

17.4 Interpretation of Crystallite Size in Bulk Materials in Terms of Subgrains

Crystallite size determined by XLPA is often smaller than the grain or subgrain size obtained by TEM [45, 53, 60–64], especially when the material has been processed by plastic deformation. It can be shown that besides differences in orientation between grains or subgrains, cf. [65], subgrains separated by dipolar dislocation walls, but without differences in orientation, can also break down coherency of X-rays scattering [8]. Dipolar dislocation walls are one of the most

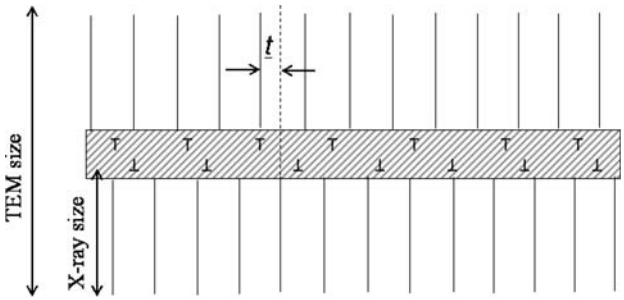

Fig. 17.3 A schematic dipolar dislocation wall. The symbol $\underline{t}$ represents the shift of the two lattice-halves on the two sides of the dipolar wall.

common dislocation configurations in plastically deformed crystalline materials [66]. They do not cause a tilt or twist between the two delineated regions [67] therefore, it is not trivial whether that breaks down coherent scattering. A schematic dipolar dislocation wall is shown in the striated region in Fig. 17.3. In [8] it was shown that the lattice planes on the two sides of the dipolar dislocation wall will be shifted relative to each other as shown schematically in the figure. The shift, t, is varying randomly from subgrain to subgrain between $t=0$ and $t=b/2$, where b is the Burgers vector of dislocations. The shifts of the lattice planes induce phase shifts in the scattered X-rays. Since there is no correlation between the shifts caused by the different subgrains, the phase shifts on the scattered rays will also be uncorrelated. As a result, the intensities and not the amplitudes of the scattered rays will add up, which means that there will be no coherency between the rays scattered by the different subgrains, and the line broadening will be determined by the average subgrain size. The subgrains separated by small-angle grain boundaries or dipolar dislocation walls are shown schematically in Figs. 17.4 (a) and (b), respectively. The two models, i.e. the small-angle grain-boundary model, cf. [65], and the dipolar dislocation-wall model [8] of subgrain boundaries, provide together a physically well-established basis for the assumption that size and size-distributions determined by XLPA correspond to subgrains or dislocation cells. In those cases, however, when the subgrains and the metallographic or TEM grains are identical, as might happen in many cases, the TEM and X-ray size data can be identical. It has to be noted that, neither dipolar dislocation walls nor small-angle grain boundaries are such perfect arrays of dislocations as shown in Fig. 17.4. The arrays will not be perfectly regular and the dislocations may be of different type and/or orientation and/or sign. There may be some dipoles within the small-angle grain boundaries or, the dipolar walls may contain surplus dislocations of one sign causing orientation differences between the neighboring subgrains. The main message of the calculation in [8] is that dislocation subboundaries or dislocation walls break down the coherent scattering of X-rays, thus the X-ray size is probably closest to the subgrain size in bulk materials.

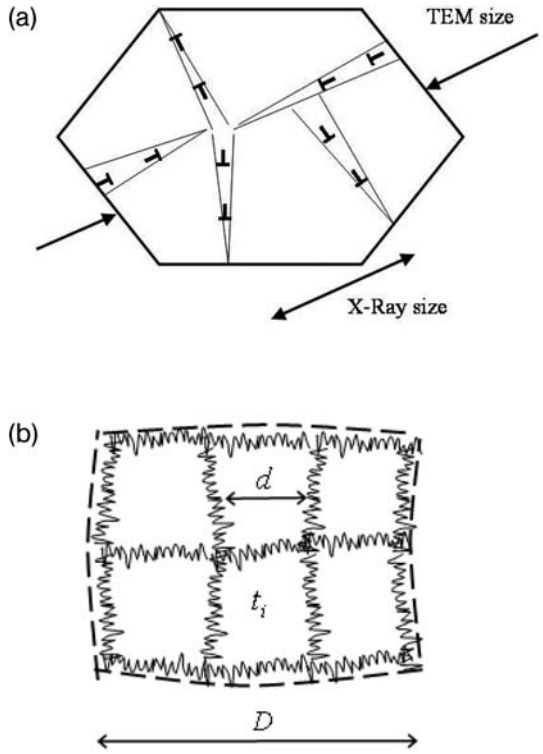

Fig. 17.4 (a) Schematic picture of subgrain or cell structure where dislocations constitute the boundaries of subgrains or cells with small misorientations. (b) A schematic representation of the structure of a grain interior containing dipolar dislocation walls. The randomly hatched regions are for the subgrain boundaries, in the present case they are assumed to be dipolar dislocation walls. The thick dashed lines represent the large-angle grain boundaries. D and d are the grain and subgrain size, respectively. The lattice shift relative to the adjacent subgrain lattice in the ith subgrain is t_i.

17.5
Dislocation Structure of Bulk Nanomaterials Determined by X-ray Line-profile Analysis

17.5.1
Characteristic Parameters of the Dislocation Structure from Line Profiles

The X-ray line-profile analysis gives the density and the arrangement parameter of dislocations, ρ and M, as well as the q parameter(s) in the contrast factors of dislocations [50, 53]. The magnitude of M describes the strength of the dipole character of dislocations: a higher M value corresponds to a weaker dipole character, i.e. a weaker screening of the displacement fields of dislocations [53]. For polycrystalline cubic crystals the anisotropic contrast effect of dislocations on

the peak broadening is characterized by one q parameter, while for hexagonal structures two parameters, q_1 and q_2 are obtained from the evaluation of line profiles [37, 43, 68].

The values of q (q_1, q_2) parameter(s) are determined by the elastic constants and the dislocation slip systems activated in the crystal. For cubic structures, the Burgers vector of the prevailing dislocations is the shortest lattice vector. For example, in *fcc* materials the Burgers vector is $1/2\langle 110\rangle$, while in *bcc* structure it is $1/2\langle 111\rangle$. For a particular slip system, the value of the q parameter depends on the angle between the dislocation line and Burgers vectors. The lower and upper limits of the q values correspond to edge and screw dislocations, respectively. Assuming that the Burgers vector is the shortest lattice vector, the theoretical q values for pure edge and screw dislocations in some frequently studied cubic materials are listed in Table 17.2 [37]. The comparison of the experimental q value obtained from line-profile analysis with the theoretical values for pure edge and screw dislocations enables the determination of edge/screw character of prevailing dislocations. If the experimental q value is close to the arithmetic average of the theoretical values for pure edge and screw dislocations, the dislocation structure has mixed character. When the experimental q value is higher or lower than the theoretical average, the character of dislocations can be regarded as rather screw or rather edge, respectively.

In hexagonal materials the momentum of the shortest lattice vector equals the a lattice parameter in the basal plane, therefore the directions of easy slip are the three $\boldsymbol{a}$-type directions. According to von Mises for plastic deformation of a polycrystalline material the activation of at least five independent slip systems is needed, therefore beside the three basal slip systems other dislocations should contribute to plastic flow. Moreover, the Burgers vectors of basal dislocations are perpendicular to the c-axis, therefore basal slips can not produce strain to the c direction. Consequently, another nonbasal slip systems with Burgers vectors having a component parallel to the c-axis should be activated to deform hexagonal polycrystals. The prismatic and pyramidal slip systems and twinning are most probably required for plastic deformation of hexagonal polycrystals. As a consequence, all the eleven slip systems in hexagonal materials should be taken into account in studying the dislocation structure.

Table 17.2 The theoretically calculated values of q parameter in the cases of pure edge, screw dislocations for some cubic materials [37].

	q (edge)	q (screw)
Al	0.36	1.33
Cu	1.68	2.37
Ni	1.42	2.24
Fe	1.28	2.67
Diamond	0.3	1.35

Each of the eleven slip systems has different theoretical values of the q_1 and q_2 parameters, therefore the evaluation of the experimental q_1 and q_2 values enables the determination of the prevailing dislocation slip systems in the specimen. The theoretical q_1 and q_2 values for the eleven possible slip systems in the most common hexagonal materials have been calculated according to the work of Kužel and Klimanek [29] and listed in the paper of Dragomir and Ungár [43]. The eleven dislocation slip systems can be classified into three groups based on their Burgers vectors: $b_1 = 1/3\langle\bar{2}110\rangle$ ($\langle \boldsymbol{a} \rangle$ type), $b_2 = \langle 0001 \rangle$ ($\langle \boldsymbol{c} \rangle$ type) and $b_3 = 1/3\langle\bar{2}113\rangle$ ($\langle \boldsymbol{c} + \boldsymbol{a} \rangle$ type). There are 4, 2 and 5 slip systems in the $\langle \boldsymbol{a} \rangle$, $\langle \boldsymbol{c} \rangle$ and $\langle \boldsymbol{c} + \boldsymbol{a} \rangle$ Burgers vector groups, respectively. A computer program was elaborated to determine the Burgers-vector population from the measured values of $q_1^{(m)}$ and $q_2^{(m)}$ [46]. First, the program selects some slip systems from one of the three groups. In the second step the calculated $\bar{C}_{hk0}q_1$ and $\bar{C}_{hk0}q_1$ values of the selected slip systems are averaged with equal weights, where $\bar{C}_{hk0}$ is the average contrast factor corresponding to the $hk0$ type of reflections. This procedure is carried out for each of the three Burgers-vector groups. The relative fractions of the three groups, $h_i (i = 1, 2, 3)$ are calculated by solving the following three equations:

$$q_1^{(m)} = \frac{1}{P}\sum_{i=1}^{3} h_i b_i^2 \left(\overline{\bar{C}_{hk0}q_1}\right)_i \tag{17.9}$$

$$q_2^{(m)} = \frac{1}{P}\sum_{i=1}^{3} h_i b_i^2 \left(\overline{\bar{C}_{hk0}q_2}\right)_i \tag{17.10}$$

and

$$\sum_{i=1}^{3} h_i = 1 \tag{17.11}$$

where $\left(\overline{\bar{C}_{hk0}q_1}\right)_i$ and $\left(\overline{\bar{C}_{hk0}q_2}\right)_i$ are obtained by averaging for the ith Burgers vector group and P is given as $P = \sum_{i=1}^{3} h_i b_i^2 \left(\overline{\bar{C}_{hk0}}\right)_i$. *If the three* h_i weights have positive values the program stores them as one of the possible solutions. After examining all the possible combinations of the slip systems (1395 combinations), ranges of the three weights are obtained as the final solution. The detailed description of the procedure is given in Ref. [46]. In the next two sections, results obtained on the dislocation structures in bulk cubic and hexagonal nanomaterials by X-ray line-profile analysis are summarized.

17.5.2
Dislocation Structure in Cubic Nanomaterials

Severe plastic-deformation (SPD) techniques are effective methods for producing bulk, porosity- and contamination-free ultrafine-grained (UFG) or nanostructured materials. As the grain refinement during SPD-processed materials occurs by the arrangement of dislocations into dislocation walls that separate misoriented domains, the investigation of the dislocation structure is essential for understanding the evolution of fine-grained microstructure. Dislocations have been intensively studied in cubic metals [69] (Al [70], Al-alloys [70–72], Cu [73–80], Ni [81–83]) processed at room temperature by SPD procedures, e.g. by equal-channel angular pressing (ECAP) or high-pressure torsion (HPT). These two techniques are described in detail elsewhere [84]. One pass of ECAP corresponds to an equivalent strain value of about 1. The imposed strain increases proportionally by the increase of the number of passes. It was found that the dislocation density increases with increasing strain for any studied cubic metals. As an example, the dislocation density *versus* the imposed strain for Al-3%Mg specimen is plotted in Fig. 17.5 [70].

As the deformation proceeds, the dislocation arrangement parameter, M, decreases, indicating that dislocations are arranged into dipoles minimizing the energy of their strain field [71, 72, 74]. This arrangement of dislocations is associated with the formation of dislocation walls resulting in the decrease of crystallite size, as mentioned above. After room-temperature SPD processes, the q parameter is usually close to or less than the arithmetic mean of the theoretical values for pure edge and screw dislocations, which indicates a rather edge type character of the dislocation structure. This can be explained by the annihilation of screw dislocations resulted by their relatively easy cross-slip. It was shown that the parameters of the dislocation structure saturate after about 4 ECAP passes at room temperature for Al [70], Al-Mg alloys [70], commercial Al-Mg-Si alloy (Al 6082) [72] and Cu [74] specimens. This saturation was also observed after 3 revolutions of HPT for Al-Mg-Sc-Zr alloys [71]. The saturation values correspond to the dynamic equilibrium state between formation and annihilation

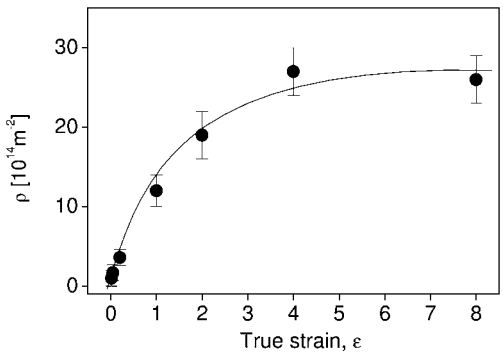

Fig. 17.5 The dislocation density (ρ) for Al-3%Mg processed by ECAP as a function of the imposed strain [70].

Table 17.3 The measured saturation values of the area-weighted mean crystallite size ($\langle x \rangle_{area}$), the dislocation density (ρ) for different fcc metals processed by SPD methods [69].

Sample	$\langle x \rangle_{area}$ [nm]	ρ [10^{14} m^{-2}]
Al, 8ECAP	272 ± 30	1.8 ± 0.3
Al-1%Mg, 8ECAP	88 ± 10	3.9 ± 0.4
Al-3%Mg, 8ECAP	65 ± 7	23 ± 2
Cu, 8ECAP	64 ± 7	26 ± 3
Ni, 8ECAP+6HPT	48 ± 6	25 ± 2

of dislocations. The maximum dislocation densities at room temperature for different cubic materials are listed in Table 17.3. The saturation value of the dislocation density is higher for a metal where the annihilation of dislocations is more difficult. For example, in Al-3%Mg alloy the Mg atoms hinder the dislocation motion, consequently the maximum dislocation density is approximately 13 times higher than for Al [70]. As grain refinement in SPD metals occurs by the arrangement of dislocations into cell boundaries, the higher dislocation density results in a decrease of crystallite size for higher Mg concentrations. The higher saturation dislocation density at room temperature for Cu compared to Al is explained by the lower self-diffusion rate as the dislocation annihilation is controlled by the diffusion of vacancies [76]. It should be noted, however, that several authors have found that after 12–16 ECAP passes at room temperature the dislocation density in Cu decreased as a result of dynamic recovery [75].

The combination of SPD procedures was applied to achieve further grain refinement in pure Ni [82, 83]. HPT and cold rolling were carried out on specimens processed by ECAP previously. It was found that the additional deformation after ECAP resulted in a further grain refinement (46 nm) and an increase of the dislocation density up to 25×10^{14} m^{-2}, which can be reached after 8 ECAP passes and additional 5 revolutions of HPT. However, the specimen produced by electrodeposition has even finer microstructure (24 nm) and much higher dislocation density (82×10^{14} m^{-2}) than the materials processed by any combination of SPD methods.

The thermal stability of the ultrafine-grained microstructure is an important issue from the point of view of the practical application of nanomaterials. The recovery of the dislocation structure and the recrystallization in SPD processed ultrafine-grained fcc metals has been extensively studied [76, 85]. The crystallite size and the dislocation density as a function of the annealing temperature were measured for Ni deformed by HPT [85] and ECAP-processed Cu [76]. The differential scanning calorimetry (DSC) measurements of Cu samples show a broad exothermic peak that corresponds to the recovery of the microstructure. The maximum of the exothermic peak in the DSC trace shifted to lower temperature values and the heat released during the annealing increases with the increase of strain and saturate at about $\varepsilon = 4$. The increase of the stored energy can be at-

tributed to the rise of the dislocation density with increasing strain. The higher strain energy raises the driving force for nucleation of new dislocation-free grains, i.e. the recovery starts at lower temperatures [76].

The dislocation density and the area-weighted mean crystallite size as a function of the temperature at the DSC curve for a Cu specimen processed by 8 ECAP passes are shown in Fig. 17.6 [76]. At the temperature corresponding to the beginning of the DSC peak, each X-ray profile appears to be the sum of a narrow and a broad peak. This special shape of the diffraction lines has been also observed by Kužel [78] for a copper sample deformed by HPT under 6 GPa pressure and annealed at 250 °C for 100 min. In Fig. 4 in [76] the intensity distribution of the 200 Bragg reflection is shown in linear (a) and double-logarithmic (b) scales, respectively. This figure shows that the intensity distribution goes through a well-defined inflection point at around $\Delta K \sim 0.006\ \mathrm{nm}^{-1}$, indicating that the diffraction profile consists of two peaks. It was found that the broad peak can be well approximated by the profile measured before the heat-treatment, which suggests that the broad subprofile corresponds to the nonrecovered regions of the material. The profile for the non annealed specimen (the solid lines in Fig. 4 in [76]) matches perfectly the tail part of the peak recorded after annealing (open circles in Fig. 4 in [76]) after dividing the intensity by an appropriate factor. The difference between the two profiles (the solid line and the open circles) gives a sharp peak that is related to the recovered volume of the material. The other peaks of the specimen quenched from 500 K can be also decomposed into narrow and broad subprofiles. At the temperature corresponding to the maximum of the DSC peak, the mean crystallite size is about 8 times higher, while the dislocation density is 50 times lower than before annealing. After the DSC peak the crystallite size and the dislocation density reach their

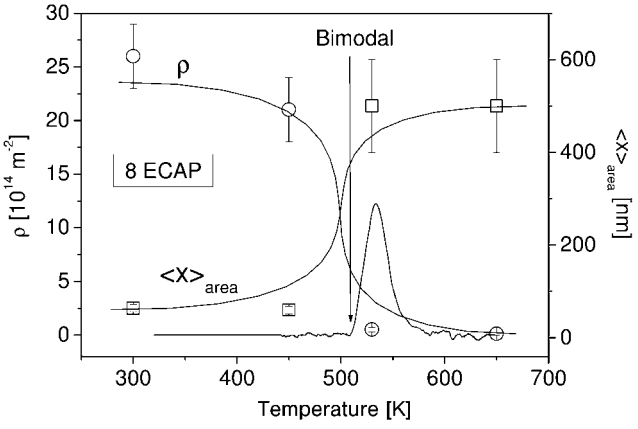

Fig. 17.6 The dislocation density and the area-weighted mean crystallite size as a function of temperature for Cu processed by 8 ECAP passes. The DSC curve obtained at 40 K/min is also shown in the figure [76].

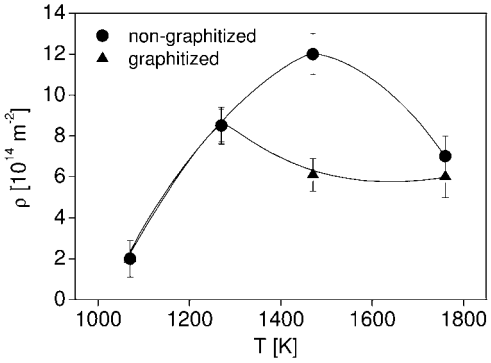

Fig. 17.7 Dislocation density in graphitized and nongraphitized samples of nanocrystalline diamond as a function of the sintering temperature [86].

highest and lowest limiting values, 500 nm and $10^{13}\,m^{-2}$, respectively, which are detectable by X-ray peak profile analysis.

Besides the UFG metals processed by SPD methods, X-ray line-profile analysis has been also applied for the characterization of the dislocations structure in nonmetallic bulk cubic nanomaterials. Nanostructured diamond specimens were prepared from micrometer-sized (30–40 μm) synthetic diamond powder by high-pressure–high-temperature (HPHT) compaction at a pressure of 2.0 GPa and at selected temperatures in the 1070–1760 K range [86]. The increase of the dislocation density during HPHT compression is associated with the decrease of the crystallite size down to about 50–100 nm. The grain refinement in HPHT-treated diamond results from the rearrangement of the dislocation structure into a lower-energy configuration. The density of dislocations was always greater in samples that were compressed and heated in water-free environments (did not graphitize) than in partially graphitized samples [86]. At the lowest temperatures used in the experiments the difference in the population of dislocations between the two sets of samples was very small, but quickly increased and reached a maximum at 1470 K and then decreased with further increase in temperature, as shown in Fig. 17.7, cf. [86–88].

17.5.3
Dislocations in Hexagonal Nanomaterials

For obtaining fine-grained microstructure with high dislocation density SPD procedures were applied also to hexagonal metals, e.g. on commercially pure Ti [45, 63, 64, 74, 89–91] and AZ91 Mg alloy [92]. Generally, the SPD processes on hexagonal materials are carried out at elevated temperatures because of the rigidity of the specimens at room temperature. In a commercially pure Ti specimen processed by 8 ECAP passes at 400–450 °C, the dislocation density obtained from X-ray line-profile analysis is $44 \times 10^{14}\,m^{-2}$. The relative fractions of the $\langle a \rangle$, $\langle c \rangle$ and $\langle c + a \rangle$ Burgers vectors are 62%, 0–4% and 32–36%, respectively. The abundance of $\langle a \rangle$-type dislocations besides the $\langle c \rangle$- and $\langle c + a \rangle$-type dislocations has been also found for other bulk hexagonal nanomaterials, e.g

sintered WC [93, 94] and SPD processed Mg alloys [93]. This observation is in agreement with TEM results carried out on other coarse-grained specimens [95]. The relatively high fraction of $\langle c + a \rangle$ dislocations in Ti processed by ECAP can be attributed to the high temperature of deformation. Theoretical calculations and TEM observations for hexagonal metallic materials suggest the activation of $\langle c + a \rangle$ dislocations by strong deformation at elevated temperatures [45]. At room temperature the critical resolved shear stress of pyramidal $\langle c + a \rangle$ dislocations is about five times larger than that for basal slip [96], but this value decreases with increasing temperature.

The thermal stability of the ultrafine-grained microstructure in Ti was investigated by DSC [74]. The volume-weighted mean crystallite size and the dislocation density as a function of temperature are shown in Fig. 17.8. It can be seen that the recovery of the dislocation structure starts before the appearance of the exothermic DSC peak. At 800 K, where the DSC peak starts, the dislocation density has already decreased from $44\times10^{14}\ m^{-2}$ to $9\times10^{14}\ m^{-2}$. However, the increase of the crystallite size accelerates only after 800 K. The dislocation density decreases further after 800 K and at 850 K it has a value of $8\times10^{13}\ m^{-2}$. As the temperature increases the relative fraction of the $\langle c + a \rangle$-type dislocations decreases to between 0 and 4%, indicating that these dislocations disappear faster than the $\langle a \rangle$ or $\langle c \rangle$-type ones (see Fig. 17.9). This can be explained by the fact that the $\langle c + a \rangle$-type dislocations have larger Burgers vectors and consequently higher formation energies than the other two types.

The ECAP process of AZ91 magnesium alloy was also carried out at high temperature (270 °C) [92]. The main alloying elements in the AZ91 alloy are 9 wt.% Al, 1 wt.% Zn and 0.2 wt.% Mn. The dislocation density increases from $0.4\times10^{14}\ m^{-2}$ to $2\times10^{14}\ m^{-2}$ and the mean crystallite size decreases from 563 nm to 97 nm as a result of 8 ECAP passes. It was found that before ECAP the

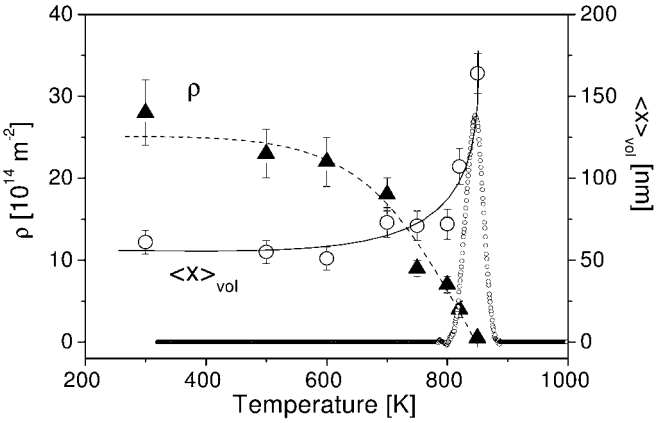

Fig. 17.8 The dislocation density, the volume-weighted mean crystallite size and the heat flow as a function of annealing temperature for Ti processed by ECAP [74].

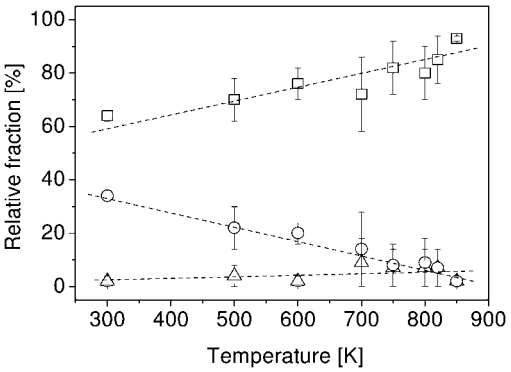

Fig. 17.9 Burgers-vector populations as a function of annealing temperature for Ti processed by ECAP [74]. Burgers vector types are denoted as: open squares – $\langle a \rangle$-type, oben circles – $\langle c+a \rangle$-type and open triangles – $\langle c \rangle$-type.

relative fractions of the $\langle a \rangle$, $\langle c \rangle$ and $\langle c + a \rangle$ Burgers vectors are 68–86%, 0–15% and 0–14%, respectively. The abundance of $\langle a \rangle$-type dislocations can be explained similarly as for Ti. After high-temperature ECAP the relative fractions of the $\langle a \rangle$, $\langle c \rangle$ and $\langle c + a \rangle$ Burgers vectors are changed to 54–58%, 0–2% and 38–42%, respectively. The increase of the relative fraction of $\langle c + a \rangle$ dislocations results from the strong deformation at high temperature. The specimen processed by 8 ECAP passes was further deformed by tension at different temperatures [92]. At relatively low temperature the dominance of $\langle a \rangle$-type dislocations can be established. At high temperature, i.e. at 300 °C, the relative fraction of the $\langle a \rangle$ Burgers vector types decreases and the relative fraction of $\langle c + a \rangle$ dislocations increases. This is in agreement with the general observation that $\langle c + a \rangle$ dislocations are activated during strong plastic deformation at elevated temperatures.

17.6 Vacancies and X-ray Line-profile Analysis

It is well known that during conventional deformation beside dislocations vacancies are also formed, which during severe plastic deformation may be enforced. The mechanisms of plastic deformation and strain hardening in large-strain deformation, i.e. in stages IV and V are relevant for severe plastic-deformation modes, with the additional feature of an enhanced hydrostatic-pressure component [97, 98]. The specific evolution of lattice defect types and their densities, their interaction mechanisms and arrangements control the hardening behavior, but also seem to be responsible for the enhanced ductility that has been repeatedly observed as a special feature of SPD metals [97–99]. In particular, the deformation-induced vacancies appear to play a major role here.

Since electrical resistivity [100] and calorimetric measurements [101] provide the total concentration of vacancies together with dislocations, whereas XLPA gives only the dislocation density [10, 17], the combination of these three different types of investigations enable determination of the vacancy and dislocation

densities separately. It is shown further that *in-situ* diffuse X-ray scattering measurements at a synchrotron radiation source can also provide information about the evolution of lattice defects, especially of vacancies, and about vacancy distribution in grain-interior and grain-boundary regions.

The diffuse scattering from crystals containing defects with displacements was first calculated by Eckstein [102] and Huang [103], and in more detail in [104–106]. For more details about diffuse scattering of point defects see [107–116].

Here, we show that a systematic analysis of the diffuse background scattering corresponding to deformed metals can be interpreted in terms of point defect production. *In-situ* XLPA measurements were carried out at the ELETTRA synchrotron in Trieste [20]. Single- and polycrystalline copper specimens of high purity have been deformed in compression by a compact test machine mounted on a 5-axis goniometer for the compensation of the shape and orientation changes during the deformation process. The (400) peak profiles of the specimen were measured in reflection by a linear position-sensitive detector (OED-50 Braun, Munich). A [001]-oriented Cu single crystal and a polycrystalline copper specimen of about 80 μm average grain size have been investigated *in situ* with a very low strain rate $\dot{\varepsilon} \sim 5 \times 10^{-5}\ s^{-1}$. The diffraction peaks were recorded in 30 to 60 s, in this time the true strain deformation ε was less than 10^{-3}. More details of such an *in-situ* synchrotron experiment can be found in [20]. From the diffraction peaks the dislocation densities were evaluated by the procedure described in Section 17.3 and in detail in [20] by fitting the Wilkens-type strain profile functions to the measured profiles according to the numerical procedure described in [50, 53]. Due to the low noise of the detector the increase of the background to peak ratio, R, is considered to be a physical effect due to the increase of the diffuse scattering caused by point defects, in particular by vacancies and/or vacancy clusters.

In the case of the undeformed specimens only a vanishing background intensity was observed, for the single as well as the polycrystal. With increasing deformation the diffuse background intensity increased considerably. For the quantification of the diffuse background scattering, the ratio of the integrated background, A_{BG}, and the integrated peak intensity, A_{Peak}, $R = A_{BG}/A_{Peak}$, was defined according to Fig. 2 in [117]. The evolution of R as a function of strain can be seen in Figs. 4 (a) and (b), in [117], on linear and logarithmic scales, respectively. It has been found that in the polycrystalline specimen the ratio, R_{PX}, increases much faster at the initial strain values than the ratio, R_{SX}, in the single-crystalline sample and that R_{PX} remains much larger than R_{SX} throughout the entire deformation range.

During plastic deformation vacancies and dislocations are produced concomitantly, cf. [118–123]. Experimental data suggest that the vacancy concentration, C_{vac} starts increasing with the dislocation density, ρ, only beyond a certain threshold and saturates at very large ρ values. The correlation between the average vacancy concentration, C_{vac}, and the dislocation density measured in $10^{14}\ m^{-2}$ units, ρ_{14}, is determined on the basis of data obtained on specimens deformed by cold rolling, C_{vac}^{CR}, and by ECAP, C_{vac}^{ECAP} [80, 124, 125]:

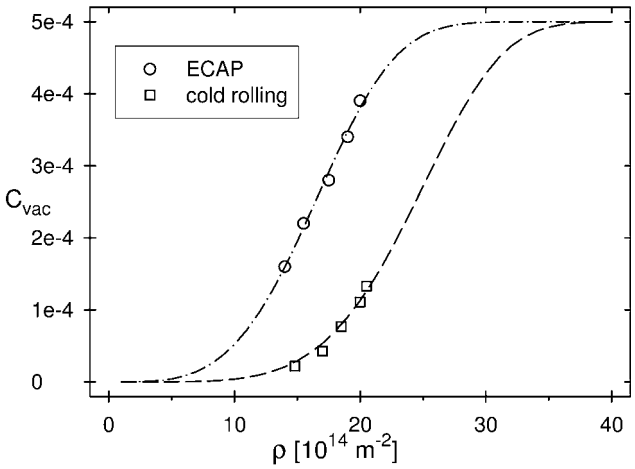

Fig. 17.10 The vacancy concentrations determined from the difference between the true and apparent dislocation densities determined by the X-ray and calorimetric or residual electrical resistivity methods. The open circles or squares correspond to copper specimens deformed by ECAP and interrupted cold rolling, respectively. The dashed and dash dotted lines correspond to Eqs. (17.12a) and (17.12b), respectively [125].

$$C_{vac}^{CR} \cong 5 \times 10^{-4}\{1 - \exp[-8 \times 10^{-8}(\rho_{14})^5]\} \tag{17.12a}$$

$$C_{vac}^{ECAP} \cong 5 \times 10^{-4}\{1 - \exp[-2.2 \times 10^{-5}(\rho_{14})^{3.7}]\} \tag{17.12b}$$

Equations (17.12a) and (17.12b) are shown in Fig. 17.10 with the measured data points for cold-rolled and ECAP-deformed Cu, respectively. The saturation value of $C_{vac}^{SAT} = 5 \times 10^{-4}$ has been determined as the lowest value that can satisfy Eqs. (17.12) for both sets of experimental data. In Fig. 7 in [117] it has been shown that the diffuse background scattering ratios for the single crystal, R_{SX}, and polycrystal, R_{PX} specimens are proportional to the dislocation densities, i.e. $(R_{PX}/\rho_{14}^{PX}) \cong 13(R_{SX}/\rho_{14}^{SX})$. This indicates a much faster vacancy accumulation in the polycrystalline specimen. The polycrystal is considered as a composite of grain boundary (GB) and grain interior or *matrix* (M) regions. It can be assumed that the vacancy production rates in the single crystal and in the *matrix* (of the polycrystal) are the same, thus the *average* vacancy concentration in the polycrystal can be given as the weighted sum of vacancy concentrations in the *matrix* and GB regions:

$$C_{vac}^{average} = f_{GB} C_{vac}^{GB} + (1 - f_{GB}) C_{vac}^{M} \tag{17.13}$$

where f_{GB} is the volume fraction of the grain boundary (GB) region, and C_{vac}^{GB} and C_{vac}^{M} are the local vacancy concentrations in the grain-boundary and the matrix regions. Assuming a volume fraction of the grain-boundary region of about 5%, the *average* vacancy concentration then can be given to the two regions *pro*

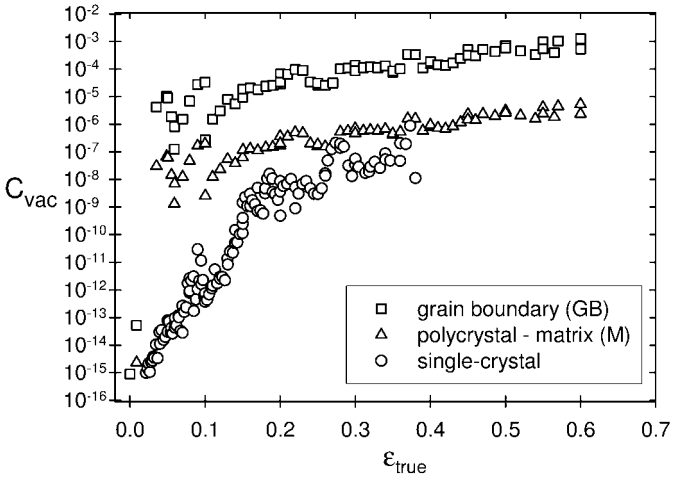

Fig. 17.11 The local vacancy concentrations, produced by plastic deformation, as a function of true strain ε, in the single-crystal (open circles), and in the grain-interior (open triangles) and grain-boundary (open squares) regions in the polycrystalline specimens, respectively [125].

rata. In Fig. 17.11 the vacancy concentrations in the single-crystal specimen and the local vacancy concentrations in the matrix and in the grain-boundary region are shown. In the single-crystalline state the vacancy concentration increases by about 8 orders of magnitude during deformation up to $\varepsilon \sim 40\%$. The evolution in the *matrix* (or grain interior) region is similar, while in the grain-boundary region the vacancy concentration grows much stronger to extremely high values between 10^{-4} and 10^{-3} corresponding to those at the melting point of copper. We note that these vacancy concentrations are the *excess* vacancy concentrations produced and stored during plastic deformation. The extremely large vacancy concentration values, especially in the GB region are probably present in the form of free volumes, rather than single vacancies, as results from molecular dynamics simulation suggest (D. L. McDowell, private communication).

From these more qualitative considerations it follows that the storage of vacancies or free volume produced during plastic deformation depends (i) on the structure and volume fraction of grain boundaries in the crystal (ii) on the deformation mode and conditions. The latter is indicated by the variation of factor and exponent in Eqs. (17.12 a) and (17.12 b) for two different cases.

17.7
Stacking Faults and Twinning in Nanostructured Materials Determined by X-ray Line-profile Analysis

The formation of planar defects, especially twinning has been shown to be an important mechanism, alternative to dislocation glide, even in materials of high stacking-fault energy, like aluminum and copper, when the grain size is reduced below a certain critical value [54, 60, 126–139]. In one of the models of deformation twinning the authors suggested that the critical stress to move a twinning partial increases slower with decreasing grain size than for lattice dislocations [127]. This model, however, turns out not to be supported by experimental data in the literature [128]. An alternative model was worked out, according to which an optimum grain-size range can be found in which the critical stress for the nucleation of deformation twins is lower than the stress necssary to move full dislocations [129–133]. Zhu and coworkers [134] have shown the existence of deformation twins in copper produced by high-pressure torsion (HPT). A model was developed in which leading and trailing partials form deformation twins where the trailing partials are less mobile than the leading one, thus creating large twins. Nongeometrically necessary dislocations at grain boundaries play an important role in the model that are substantiated by experiment and theory [135–137]. Both, experiment and the model suggest critical grain sizes, below which twinning occurs in Cu and Al at about 40 and 20 nm, respectively.

A systematic method to determine the density of intrinsic and extrinsic stacking faults, and twin boundaries together with the dislocation density and arrangement, and the average grain size and grain-size distribution, by X-ray line-profile analysis, has been developed recently [23, 138]. The effect of stacking faults, and twin boundaries on X-ray diffraction patterns was calculated numerically by using the DIFFaX software of Treacy et al. [4] for the first 15 Bragg reflections in *fcc* crystals up to 20% fault densities [23]. It was found that the Bragg reflections consist of 5 types of subreflections, where the subreflection types are determined by specific conditions of the *hkl* indices, in good agreement with the theory developed in the early 1950s by Warren [1]. It was shown that the profiles of the subreflections are of Lorentzian- (or Cauchy-) type functions. Analyzing about 15 000 subreflections the breadths (FWHM) and the shifts relative to the exact Bragg angles were determined. The values of FWHM and shifts of the subreflections were given by 5th-order polynomials as a function of the densities of intrinsic and extrinsic stacking faults, and twin boundaries, β_{intr}, β_{extr} and α, respectively. The coefficients of the 5th-order polynomials and the fractions of the different subreflection types were compiled in three separate data files that are accessible at the website: http://metal.elte.hu/~levente/stacking. The data files were incorporated into the CMWP software [50, 53, 59] for evaluating planar faults together with dislocations and crystallite and/or subgrain-size distributions. The extended software, eCMWP, was applied to inert-gas condensed nanocrystalline [54, 139–141], and submicrometer grain-size copper specimens deformed by the method of ECAP [142, 143]. The X-ray

line-profile analysis results substantiated the TEM results of the group of Zhu [127, 129–131, 133, 134], that in copper twinning becomes essential below a critical crystallite or subgrain size, of about 40 nm.

17.8 Conclusions

1. It has been shown that X-ray line-profile analysis can be used as a powerful tool to characterize the microstructure of bulk nanomaterials in terms of (i) grains or subgrains, (ii) dislocation densities, (iii) Burgers-vector population and slip activity, (iv) stacking faults and twin boundaries, and (v) excess vacancy concentrations.
2. Whenever this was possible, the data provided by the X-ray method, have been analyzed in comparison with TEM results. It has been shown that either there is a good correlation between the X-ray and TEM results, or, if there are differences, these can be used to learn more details about the microstructure, especially in terms of grains *versus* subgrains.
3. It is found that bulk nanomaterials produced by severe plastic deformation, usually contain extremely high dislocation densities up to the order of 10^{16} m^{-2}, and these values have been confirmed by high-resolution TEM investigations.
4. The discrepancy between dislocation densities determined by the X-ray method or TEM and other procedures like residual electrical resistivity (RER) or differential scanning calorimetry (DSC) has been shown to enable the determination of excess vacancy concentrations produced by plastic deformation. It has been shown that the methods of RER and DSC provide an apparent dislocation density, a part of which can, and has to, be expressed in terms of vacancy concentration.
5. It has been shown that the dislocation mechanism is replaced by faulting or twinning when the grain or subgrain size becomes smaller than certain critical values, of about 40 and 20 nm in the case of copper and aluminium, respectively, in good correlation with TEM observations.
6. It has been shown that the breadth methods provide a very useful qualitative guidance, before more sophisticated full-profile methods are applied.

Acknowledgements

The authors are grateful to the Hungarian National Science Foundation, OTKA T46990, F47057 and T43247, for supporting this work.

References

1 B. E. Warren **1996**, *X-ray Diffraction*, Dover Publications, New York.

2 I. C. Noyan, J. B. Cohen **1987**, *Residual Stress Determination by Diffraction*, Springer, Berlin.

3 A. J. C. Wilson **1962**, The Diffraction of X-Rays by Finite and Imperfect Crystals, in *X-Ray Optics*, London, Methuen.

4 M. M. J. Treacy, J. M. Newsam, M. W. Deem **1991**, *Proc. Roy. Soc. London A* 433, 499.

5 J. I. Langford, D. Louer **1991**, *J. Appl. Crystallogr.* 24, 149.

6 N. C. Popa, D. Balzar **2002**, *J. Appl. Crystallogr.* 35, 338.

7 J. I. Langford, D. Louër, P. Scardi **2000**, *J. Appl. Crystallogr.* 33, 964.

8 T Ungár, G Tichy, J Gubicza, R Hellmig **2005**, *Powder Diff.* 20, 366.

9 M. A. Krivoglaz **1996**, *Theory of X-ray, Thermal Neutron Scattering by Real Crystals*, Springer-Verlag, Berlin.

10 M. Wilkens **1970**, *Fundamental Aspects of Dislocation Theory*, J. A. Simmons, R. de Wit, R. Bullough (eds.), Vol. II. Nat. Bur. Stand. (US) Spec. Publ. No. 317, Washington, DC. USA, p. 1195.

11 M. Wilkens **1970**, *phys. stat. sol. (a)* 2, 359.

12 I. Gaál **1984**, in *Proceedings of the 5th Riso International Symposium on Metallurgy Materials Science*, (eds.) N. H. Andersen, M. Eldrup, N. Hansen, D. Juul Jense, T. Leffer, H. Lifholt, O. B. Pedersen, B. N. Singer, Riso Nat. Lab, Roskilde, Denmark, p. 245.

13 I. Groma, T. Ungár, M. Wilkens **1988**, *J. Appl. Crystallogr.* 21, 47.

14 I. Groma **1998**, *Phys. Rev.* B 57, 7535.

15 E. Macherauch, V. Hauk **1986**, (eds.) *Residual Stresses in Science and Technology*, DGM-Informationsstelle, Germany.

16 H. Mughrabi **1983**, *Acta Metall.* 31, 1367.

17 T. Ungár, H. Mughrabi, D. Rönnpagel, M. Wilkens **1984**, *Acta Metall.* 32, 333.

18 H. Mughrabi, T. Ungár, W. Kienle, M. Wilkens **1986**, *Philos. Mag. A* 53, 793.

19 H. Mughrabi, T. Ungár **2002**, in *Dislocations in Solids*, F. R. N. Nabarro, M. S. Duesbury (eds.), Vol. 11, NH-Elsevier, Amsterdam, p. 343.

20 E. Schafler, K. Simon, S. Bernstorff, P. Hanák, G. Tichy, T. Ungár, M. J. Zehetbauer **2005**, *Acta Mater.* 53, 315.

21 A. I. Ustinov, L. O. Olikhovska, N. M. Budarina, F. Bernard **2004**, in *Diffraction Analysis of the Microstructure of Materials*, E. J. Mittemeijer, P. Scardi (eds.) Springer, Berlin-Heidelberg, pp. 309.

22 E. Estevez-Rams, M.Leoni, P. Scardi, B. Aragon-Fernandez, H. Fuess **2003**, *Philos. Mag.* 83, 4045.

23 L. Balogh, G. Ribárik, T. Ungár **2006**, *J. Appl. Phys.* 100, 023512.

24 A.Guinier **1963**, *X-ray Diffraction*, Freeman, San Francisco, CA.

25 P. Scardi, M. Leoni **1999**, *J. Appl. Crystallogr.* 32, 671.

26 A. R. Stokes, A. J. C. Wilson **1944**, *Proc. Cambridge Philos. Soc.* 40, 197.

27 G. Caglioti, A. Paoletti, F. P. Ricci **1958**, *Nucl. Instrum.* 3, 223.

28 P. Klimanek, R. Kužel Jr. **1988**, *J. Appl. Crystallogr.* 21, 59.

29 R. Kužel Jr., P. Klimanek **1988**, *J. Appl. Crystallogr.* 21, 363.

30 T. Ungár,A. Borbély **1996**, *Appl. Phys. Lett.* 69, 3173.

31 P. W. Stephens **1999**, *J. Appl. Crystallogr.* 32, 281.

32 T. Ungár, G. Tichy **1999**, *phys. stat. sol. (a)* 171, 425.

33 D. Rafaja, V. Klemm, G. Schreiber, M. Knapp, R. Kužel **2004**, *J. Appl. Crystallogr.* 37, 613.

34 G. Ribárik, N. Audebrand, H. Palancher, T. Ungár, D. Lour **2005**, *J. Appl. Crystallogr.* 38, 912.

35 B. E. Warren, B. L. Averbach **1950**, *J. Appl. Phys.* 21, 595.

36 F. F. Csikor, I. Groma **2004**, *Phys. Rev. B* 70, 064106.

37 T. Ungár, I. Dragomir, Á. Révész, A. Borbély **1999**, *J. Appl. Crystallogr.* 32. 992.

38 P. Chatterjee, S. P. Sen Gupta **1999**, *J. Appl. Crystallogr.* 32, 1060.

39 R. Cerny, J. M. Joubert, M. Latroche, A. Percheron-Guegan, K. Yvon **2000**, *J. Appl. Crystallogr.* 33, 997.

40 R. W. Cheary, E. Dooryhee, P. Lynch, N. Armstrong, S. Dligatch **2000**, *J. Appl. Crystallogr.* 33, 1271.

41 P. Chatterjee, S. P. Sen Gupta **2001**, *Philos. Mag. A* 81, 49.

42 P. Scardi, M. Leoni **2002**, *Acta Crysallogr. A* 58, 190.

43 C. Dragomir, T. Ungár **2002**, *J. Appl. Crystallogr.* 35, 556.

44 E. Schafler, Ch. Sitkovitch, I. Dragomir, Á. Révész, M. Zehetbauer, T. Ungár **2000**, *Mater. Sci. Forum* 321–324, 92.

45 Y. T. Zhu, J. Y. Huang, J. Gubicza, T. Ungár, Y. M. Wang, E. Ma, R. Z. Valiev **2003**, *J. Mater. Res.* 18, 1908.

46 K. Máthis, K. Nyilas, A. Axt, I. D. Cernatescu, T. Ungár, P. Lukáè **2004**, *Acta Mater.* 52, 2889.

47 P. Cordier, T. Ungár, L. Zsoldos, G. Tichy **2004**, *Nature,* 428, 837.

48 I. C. Dragomir, D. S. Li, G. A. Castello-Branco, H. Garmestani, R. L. Snyder, G. Ribárik, T. Ungár **2005**, *Mater. Charac.* 55, 66.

49 E. Schafler, M. Zehetbauer **2005**, *Rev. Adv .Mater. Sci.* 10, 28.

50 G. Ribárik, T. Ungár, J. Gubicza **2001**, *Mater. Sci. Eng. A,* 34. 669.

51 I. P. Jones, W. B. Hutchinson **1981**, *Acta Metall.* 29, 951.

52 G. K. Williamson, W. H. Hall **1953**, *Acta Metall.* 1, 22.

53 T. Ungár, J. Gubicza, G. Ribárik, A. Borbély **2001**, *J. Appl. Crystallogr.* 34, 298.

54 T. Ungár, S. Ott, P. Sanders, A. Borbély, J. R. Weertman **1998**, *Acta Mater.* 46, 3693.

55 P. Scardi, M. Leoni, R. Delhez **2004**, *J. Appl. Crystallogr.* 37, 381.

56 H. M. Rietveld **1969**, *J. Appl. Crystallogr.* 2, 65.

57 P. Suortti **1993**, in *The Rietveld Method, IUCr Monographs on Crystallography,* R. A. Young (ed.) Vol. 5, Oxford University Press, Oxford, p. 167.

58 T. Ungár, P. Martinetto, G. Ribárik, E. Dooryhée, Ph. Walter, M. Anne **2002**, *J. Appl. Phys.* 91, 2455.

59 G. Ribárik, J. Gubicza, T. Ungár **2004**, *Mater. Sci. Eng. A* 387–389, 343.

60 T. Ungár, L. Balogh, Y. T. Zhu, C. Xu, G. Ribárik, Z. Horita, T. G. Langdon **2006**, in *Proc. Ultrafine Grained Materials IV,* Y. T. Zhu, T. G. Langdon, Z. Horita, M. J. Zehetbauer, S. L. Semiatin, T. C. Lowe (eds.), The Minerals, Metals & Materials Society, Warrendale, USA.

61 T. Ungár, M. Victoria, P. Marmy, P. Hanák, G. Szenes **1999**, *Nucl. Instrum. Methods A.* 11995. 1.

62 T. Ungár, M. Victoria, P. Marmy **2000**, *J. Nucl. Mater.* 276, 278.

63 J. Gubicza, I. C. Dragomir, G. Ribárik, S. C. Baik, Y. T. Zhu, R. Z. Valiev, T. Ungár **2003**, *Z. Met.kd.* 94, 1185.

64 J. Gubicza I. C. Dragomir, G. Ribárik, Y. T. Zhu, R. Z. Valiev, T. Ungár **2003**, *Mater. Sci. Forum,* 414-415, 229.

65 R. E. Bolmaro, H. G. Brokmeier, J. W. Signorelli, A. Fourtz, M. A. Bertinetti **2004**, in *Diffraction Analysis of the Microstructure of Materials,* E. J. Mittemeijer, P. Scardi, P. (eds.), Springer, Berlin-Heidelberg, p. 391.

66 D. Kuhlmann-Wilsdorf **2002**, in *Dislocations in Solids,* F. R. N.Nabarro, M. S. Duesbery (eds.), Elsevier, Amsterdam, p. 211.

67 M. Wilkens, T. Ungár, H. Mughrabi **1987**, *phys. stat. sol. (a)* 104, 157.

68 A. Borbely, I. Dragomir-Cernatescu, G. Ribarik, T. Ungar **2003**, *J. Appl. Crystallogr.* 36, 160.

69 J. Gubicza, N. Q. Chinh, Gy. Krállics, I. Schiller, T. Ungár **2006**, *Curr. Appl. Phys.* 6, 194.

70 J. Gubicza J., N. Q. Chinh, Z. Horita, T. G. Langdon **2004**, *Mater. Sci. Eng. A* 387-389, 55.

71 D. Fátay, E. Bastarash, K. Nyilas, S. Dobatkin, J. Gubicza, T. Ungár **2003**, *Z. Met.kd.* 94, 842.

72 J. Gubicza, Gy. Krállics, I. Schiller, D. Malgin **2004**, *Mater. Sci. Forum* 473–474, 453.

73 A. Dubravina, M. J. Zehetbauer, E. Schafler, I. V. Alexandrov **2004**, *Mater. Sci. Eng. A* 387, 817.

74 J. Gubicza, N. H. Nam, L. Balogh, R. J. Hellmig, V. V. Stolyarov, Y. Estrin, T. Ungár **2004**, *J. Alloys Compd.* 378, 248.

75 F. Dalla Torre, R. Lapovok, J. Sandlin, P. F. Thomson, C. H. J. Davies, E. V. Pereloma **2004**, *Acta Mater.* 52, 4819.

76 J. Gubicza, L. Balogh, R. J. Hellmig, Y. Estrin, T. Ungár **2005**, *Mater. Sci. Eng. A* 400–401, 334.

77 R. Kužel, Z. Matej, V. Cherkaska, J. Pesicka, J. Cízek, I. Procházka, R. K. Islamgaliev **2004**, *J. Alloys Compd.* 378, 242.

78 R. Kužel, M. Cernansky, V. Holy, J. Kubena, D. Simek, J. Kub **2004**, in: *Diffraction Analysis of the Microstructure of Materials*, E. J. Mittemeijer, P. Scardi (eds.), Springer, Berlin, p. 229.

79 E. Schafler, G. Steiner, E. Korznikova, M. Kerber, M. J. Zehetbauer **2005**, *Mater. Sci. Eng. A* 410–411, 169.

80 E. Schafler, A. Dubravina, B. Mingler, H. P. Karnthaler, M. Zehetbauer **2006**, *Mater. Sci. Forum*, 503-504, 51.

81 W. Skrotzki, R. Tamm, R. Klemm, E. Thiele, C. Holste, H. Baum **2002**, *Mater. Sci. Forum*, 408, 667.

82 A. P. Zhilyaev, J. Gubicza, G. Nurislamova, Á. Révész, S. Suriñach, M. D. Baró, T. Ungár **2003**, *phys. stat. sol. (a)* 198, 263.

83 A. P. Zhilyaev, J. Gubicza, S. Suriñach, M. D. Baró, T. G. Langdon **2003**, *Mater. Sci. Forum* 426, 4507.

84 R. Z. Valiev, R. K. Ishlamgaliev, I,V. Alexandrov **2000**, *Prog. Mater. Sci.* 45, 103.

85 E. Schafler, R. Pippan **2004**, *Mater. Sci. Eng A* 387-389, 799.

86 C. Pantea, J. Gubicza, T. Ungár, G. Voronin, T. W. Zerda **2002**, *Phys. Rev. B*, 66, 094106.

87 C. Pantea, J. Gubicza, T. Ungár, G. A. Voronin, N. H. Nam, T. W. Zerda **2004**, *Diamond Relat. Mater.* 13, 1753.

88 G. A. Voronin, T. W. Zerda, J. Gubicza, T. Ungár, S. N. Dub **2004**, *J. Mater. Res.* 19, 2703.

89 E. Schafler, L. Zeipper, M. J. Zehetbauer **2004**, in *Proc. 2nd International Conference on Nanomaterials by Severe Plastic Deformation: Fundamentals – Processing – Applications*, M. J. Zehetbauer, R. Z. Valiev (eds.) Wien, Austria, Wiley-VCH Weinheim, Germany, pp. 426–432.

90 L. F. Zeipper, M. J. Zehetbauer, Ch. Holzleithner **2005**, *Mater. Sci. Eng. A* 410-411, 217.

91 B. Mingler, V. V. Stolyarov, M. Zehetbauer, W. Lacom, H. P. Karnthaler **2006**, *Mater. Sci. Forum* 503-504, 805.

92 K. Máthis, J. Gubicza, N. H. Nam **2005**, *J. Alloys Compd.* 394, 194.

93 J. Gubicza, G. Ribárik, G. R. Goren-Muginstein, A. R. Rosen, T. Ungár **2001**, *Mater. Sci. Eng. A* 309-310, 60.

94 T. Ungár, J. Gubicza **2002**, *Z. Met.kd.* 93, 694.

95 D. R. Chichili, R. K. T. Ramesh, K. J. Hemker **1998**, *Acta Mater.* 46, 1025.

96 M. H. Yoo **1981**, *Metall. Trans. A* 12, 12.

97 M. Zehetbauer, H. P. Stuewe, A. Vorhauer, E. Schafler, J. Kohout **2003**, *Adv. Eng. Mater.* 5, 330.

98 M. Zehetbauer, J. Kohout, A. Dubravina, E. Schafler, A. Vorhauer **2004**, *J. Alloys Compd.* 378, 329.

99 M. J. Zehetbauer, L. Zeipper, E. Schafler **2005**, in *Proc. NATO-ARW Workshop Nanostructured Materials by High-Pressure Severe Plastic Deformation*, Y. Zhu, V. Varyukhin (eds), Donetsk, Ukraine, *Nato Science Series II: Mathematics, Physics and Chemistry, Vol.* 212, Springer Berlin.

100 M. Zehetbauer **1994**, *Key Eng. Mater.* 97–98, 287.

101 M. B. Beaver, D. L. Holt, A. L. Titchener **1973**, *Prog. Mater. Sci.* 17, 5.

102 H. Eckstein **1945**, *Phys. Rev.* 68, 120.

103 K. Huang **1947**, *Proc. R. Soc. A*, 190, 102.

104 R. Cochran, G. Kartha **1956**, *Acta Crystallogr.* 9, 941.

105 B. Borie **1959**, *Acta Crystallogr.* 12, 280.

106 M. A. Krivoglaz **1969**, *Theory of X-Ray and Thermal Neutron Scattering by Real Crystals*, Plenum Press, New York.

107 T. O. Baldwin, F. A. Sherrill, F. W. Young **1968**, *J. Appl. Phys.* 39, 1541.

108 R. Collella, A. Merlini **1966**, *phys. stat. sol.* 14, 81.

109 S. B. Austermann, K. T. Miller **1965**, *phys. stat. sol.* 11, 241.

110 R. G. Perret, D. T. Keating **1967**, in: *Small Angle X-Ray Scattering*, H. Brum-

berger (ed.), Gordon, Breach, New York, p. 373.
111 H. Trinkhaus, H. Spalt, H. Peisl **1970**, *phys. stat. sol. (a)* 2, K97.
112 W. Schmatz **1970**, in: *Vacancies and Interstitials in Metals*, A. Seeger et al. (eds.), North Holland, Amsterdam, p. 589.
113 P. Ehrhart, W. Schilling **1973**, *Phys. Rev. B*, 8, 2604.
114 H. Trinkhaus **1972**, *phys. stat. sol. (b)* 51, 307.
115 P. H. Dederichs **1970**, *Phys. Rev. B*, 1, 1306.
116 P. H. Dederichs **1973**, *J. Phys. F*, 3, 471.
117 T. Ungár, E. Schafler, P. Hanák, S. Bernstorff, M. Zehetbauer **2005**, *Z. Met.kd.* 96, 578.
118 A. Seeger **1955**, *Handbuch der Physik III*, Springer-Verlag, Berlin.
119 I. Kovács **1967**, *Acta Metall.* 15, 1731.
120 A. Van den Beukel **1970**, in *Vacancies and Interstitials in Metals*, A. Seeger et al. (eds.), North Holland, Amsterdam, p. 427.
121 H. G. Van Bueren **1955**, *Acta Metall.* 3, 519.
122 G. Saada **1963**, in: *Electron Microscopy and Strength of Crystals*, G. Thomas, J. Washburn (eds.), Interscience, New York.
123 U. Essmann, U. Goesele, H. Mughrabi **1981**, *Philos. Mag. A*, 44, 405.
124 M. Zehetbauer, E. Schafler, T. Ungár **2005**, *Z. Met.kd.* 96, 1044.
125 T. Ungár, E. Schafler, P. Hanák, S. Bernstorff, M. Zehetbauer **2007**, *Mater. Sci. Eng A*, 462, 398–401
126 M. Chen, E. Ma, K. J. Hemker, H. Sheng, Y. M. Wang, X. Cheng **2003**, *Science.* 300, 1275.
127 X. Z. Liao, J. Y. Huang, Y. T. Zhu, F. Zhou, E. J. Lavernia **2003**, *Philos. Mag.* 83, 3065.
128 M. A. Meyers, O. Vöhringer, V. A. Lubarda **2001**, *Acta Mater.* 49, 4025.
129 X. Z. Liao, F. Zhou, E. J. Lavernia, D. W. He, Y. T. Zhu **2003**, *Appl. Phys. Lett.* 83, 5062.
130 X. Z. Liao, Y. H. Zhao, Y. T. Zhu, R. Z. Valiev, D. V. Gunderov **2004**, *J. Appl. Phys.* 96, 636.
131 X. Z. Liao, Y. H. Zhao, S. G. Srinivasan, Y. T. Zhu, R. Z. Valiev, D. V. Gunderov **2004**, *Appl. Phys. Lett.* 84, 592.
132 R. J. Asaro, P. Krysl, B. Kad **2003**, *Philos. Mag. Lett.* 83, 733.
133 Y. T. Zhu, X. Z. Liao, S. G. Srinivasan, Y. H. Zhao, M. I. Baskes, F. Zhou, E. J. Lavernia **2004**, *Appl. Phys. Lett.* 85, 5049.
134 Y. T. Zhu, X. Z. Liao, S. G. Srinivasan, E. J. Lavernia **2005**, *J. Appl. Phys.* 98, 034319/1-8.
135 Z. Budrovic Van Swygenhoven, H. Derlet, P. M. Van Petegem, S. B. Schmitt **2003**, *Science*, 304, 273.
136 J. Schiøtz, K. W. Jacobsen **2003**, *Science.* 301, 1357.
137 H. Van Swygenhoven, P. M. Derlet, A. G. Frøseth **2004**, *Nature Mater.* 3, 399.
138 T. Ungár, L. Balogh, Y. T. Zhu, Z. Horita, C. Xu, T. G. Langdon **2007**, *Mater. Sci. Eng.* 444, 153–156.
139 J. R. Weertman, P. G. Sanders **1994**, *Solid State Phenom.* 35-36, 249.
140 P. G. Sanders **1996**, *Ph. D. Thesis*, Northwestern University, Evanston, IL, USA 60208.
141 P. G. Sanders, G. E. Fougere, L. J. Thompson, J. A. Eastman, J. R. Weertman **1997**, *Nanostruct. Mater.* 8, 243.
142 R. Z. Valiev, E. V. Kozlov, Yu. F. Ivanov, J. Lian, A. A. Nazarov, B. Baudelet **1994**, *Acta Metall. Mater.* 42, 2467.
143 T. Ungár, J. Gubicza, P. Hanák, I. Alexandrov **2001**, *Mater. Sci. Eng. A*, 319–321, 274.

18
Texture Evolution in Equal-channel Angular Extrusion

Irene J. Beyerlein and László S. Tóth

18.1
Introduction

In order to understand and predict the bulk properties of a polycrystalline material one needs to know and predict its texture. Texture is a microstructural property of the polycrystal (PX), which describes the distribution of crystallographic orientations of its grains. This distribution directly affects the applied flow stresses required to accommodate a given applied deformation. The "harder" grain orientations of the distribution that are unfavorably oriented for deformation require higher flow stresses than the "softer" orientations, which are favorably oriented. Texture also affects the microscale deformation mechanisms by influencing the choice and number of slip/twinning systems used by each grain. Grain orientations, which operate several slip systems, contribute to a higher flow stress than those operating fewer slip systems. Other critical properties, such as fracture stress and strain, fracture toughness, internal stress distributions, and electronic properties also depend on texture. For instance, the enhanced formability of ECAE Mg alloys is attributed to texture evolution [3, 4]. Texture has been most appreciated for its affects on anisotropy, that is, a dependence of material response on direction and sense of loading. Observed plastic anisotropy and differences between the tensile and compression responses of ECAE materials [5, 6], for instance, can be partly attributed to texture.

A review of texture evolution in ECAE is complicated by the number of factors that influence texture evolution. These factors can be broadly categorized as (i) those affecting the applied strain path, (ii) microscale deformation mechanisms (material parameters), or (iii) initial texture. The applied straining in ECAE can vary in intensity, uniformity, complexity, and strain path change. The controlling input variables are ECAE route, number of passes N, die angle Φ and corner angle Ψ (see Fig. 18.1), backpressure, pressing rate, temperature, and material response. The deformation mechanisms will vary widely with crystal properties, alloying, strain rate and temperature. Even for the same material under the same applied deformation, the initial grain orientations can affect subsequent re-orientation.

Bulk Nanostructured Materials. Edited by M. J. Zehetbauer and Y. T. Zhu

ISBN: 978-3-527-31524-6

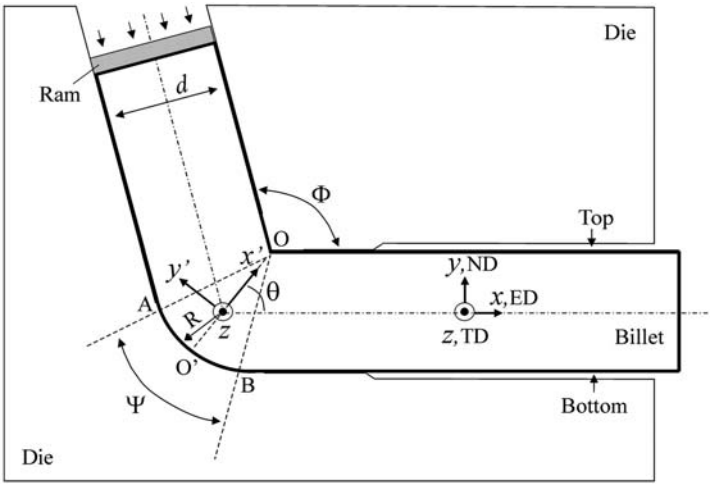

Fig. 18.1 Typical ECAE die geometry with die angle Φ and outer-corner angle Ψ defined. Also displayed is the fixed coordinate system used in this chapter. This illustration is taken from Li et al. [31].

Following this categorization, we review what has been observed or predicted to be relevant factors affecting texture evolution in ECAE. This discussion will aid in explaining why experimental observations of textures of materials can differ widely, even among the same material across different studies. Often times slight differences in processing conditions or in the state of the starting material can lead to differences in observed textures. Next, we discuss models of texture evolution and their performance against experimental measurement. We finally end with relationships between texture evolution and other properties, such as grain refinement and mechanical properties.

18.2 Background

18.2.1 Macroscopic Deformation in ECAE

18.2.1.1 Simple Shear Model

The first and simplest model of ECAE deformation is the simple shear model (SS), assuming simple shearing concentrated along the intersection plane of the two channels [1, 2]. This model represents the theoretically ideal situation of zero friction, perfectly plastic material and sharp inner and outer corners. Under these conditions, the deformation and velocity gradients, F and L, are functions of Φ only [7, 8]

$$F = \begin{bmatrix} 2+\cos\Phi & -\sin\Phi & 0 \\ (\cos\Phi+1)^2/\sin\Phi & -\cos\Phi & 0 \\ 0 & 0 & 1 \end{bmatrix}, \quad L = \dot{\gamma}\begin{bmatrix} \sin\Phi & \cos\Phi-1 & 0 \\ \cos\Phi+1 & -\sin\Phi & 0 \\ 0 & 0 & 0 \end{bmatrix} \tag{18.1}$$

where $\dot{\gamma}$ is the shear strain rate. F and L are expressed in the fixed laboratory coordinate system x-y-z, see Fig. 18.1. Note that in this fixed system, all inplane components become nonzero.

ECAE deformation is often visualized by the distortion of either an initial sphere or a cube element. The two will deform differently under the same deformation. Using F for SS deformation in (18.1), the angle of orientation of that side of the cube, which is initially perpendicular to the flow, will be inclined at an angle θ_r with respect to the axis of the exit channel:

$$\theta_r = \cot^{-1}\left(2\cot\left(\frac{\Phi}{2}\right)\right) \tag{18.2}$$

A sphere transforms into an ellipsoid with its long axis oriented θ_s with respect to the exit-channel:

$$\theta_s = \tan^{-1}\left(\operatorname{cosec}\left(\frac{\Phi}{2}\right) - \cot\frac{\Phi}{2}\right) = \frac{\Phi}{4} \tag{18.3}$$

Note that $\theta_r \neq \theta_s$. For $\Phi = 90^\circ$ (or 120°) die, the θ_r of a cube "grain" deformed after one pass is 26.6° (or 40.9°) but for a spherical "grain", θ_s is less being 22.5° (or 30°). Figure 18.2 shows the resulting distorted ellipsoid inscribed in the parallelogram for a 90° die. As shown, the long axis of the ellipsoid is not aligned with the inclination angle of the parallelogram. Neither θ_r nor θ_s results from a simple shear on the y plane in the x direction and neither one is aligned with the shear plane at $\Phi/2$. However, they can both be obtained by assuming a negative simple shear parallel to the intersection plane of the channel.

18.2.1.2 **Finite-element Modeling**

Finite-element (FE) simulations of the ECAE process are another method of calculating F and L in ECAE. These numerical calculations have been useful in revealing how ECAE deformation can change with material, die geometry and processing conditions and deviate from ideal SS. Figure 18.3 is an example of a steady-state strain rate field calculated from a 2D FE simulation [9] assuming either (a) a strain-hardening material or (b) an elastic-perfectly plastic one. Because of the rounded outer corner, plastic deformation takes place in a broad zone, called a plastic-deformation zone (PDZ), spread around the intersection plane. The upper portion resembles a fan emanating from the inner corner (Fig. 18.3 (c)). The bottom portion of the billet experiences little shear but large rotations. The strain-hardening case, Fig. 18.3 (a), shows formation of a corner

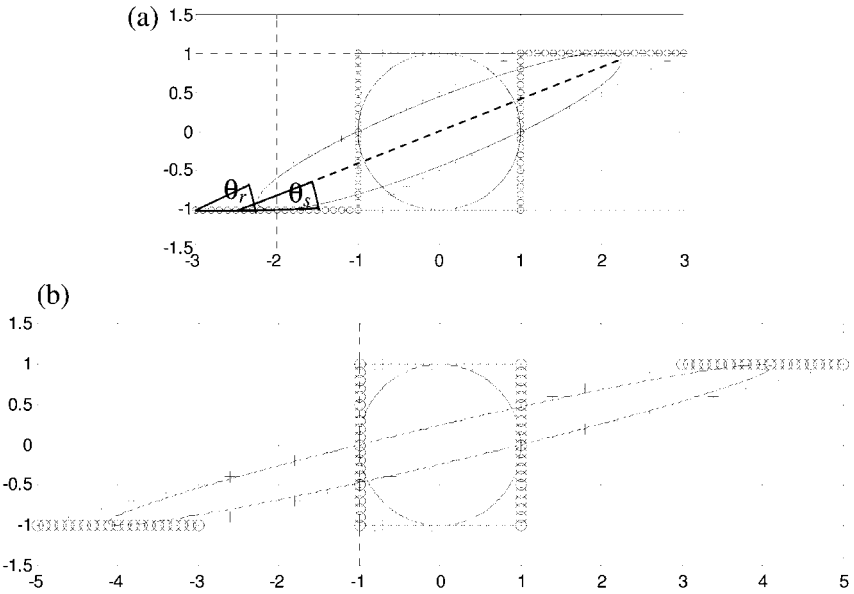

Fig. 18.2 Distortion of an initial sphere inscribed in a cube (a) after one pass of ECAE assuming $\Phi = 90^\circ$ and (b) after two passes of route A. The sphere distorts into an ellipsoid with its long axis inclined θ_s from the extrusion axis and the cube distorts into a parallelogram with its lateral sides inclined θ_r from the extrusion axis. Note that θ_s and θ_r are not equal. This figure is taken from Beyerlein and Tomé [7].

gap. The gap causes the strain-rate distribution within the PDZ to skew towards the exit channel [9–12]. Generally, 3D FE models predict smaller corner gaps and lower accumulated strains than 2D ones [13–15].

18.2.1.3 **Analytical Flow Models**

Many researchers would prefer to use the SS model for its simplicity, ease in use, and efficiency, despite undisputed evidence that FE is more accurate in some cases. A good alternative are analytical flow models.

The first one was derived for $\Psi = 0$ dies by Segal [2] using a slip-line field analysis, which assumes a rigid plastic isotropic material. Segal showed that die surface friction results in a fan-shaped PDZ, symmetric about the intersection plane. The internal angle of the fan $\beta(< \Phi)$ increases with the friction coefficient. Later, the same slip field analysis [16] was applied to rounded dies ($\Psi(> 0)$). In agreement with FE calculations, the analysis revealed that the rounded outer corner has two effects; it tends to broaden the PDZ and break it up into two parts, an upper shear fan and a lower part with little applied shearing (Fig. 18.3 (c)), and mostly rigid-body rotation [9]. Following this analysis, Beyerlein and Tomé [7] derived the analytical form for F and L in each part (for $\Phi = 90^\circ$). Because deformation by the shear fan is *homogeneous* [9], it is more convenient to use a normalized form ($\bar{L}$) for L. For $\bar{L}$ of the upper shear fan, they obtain

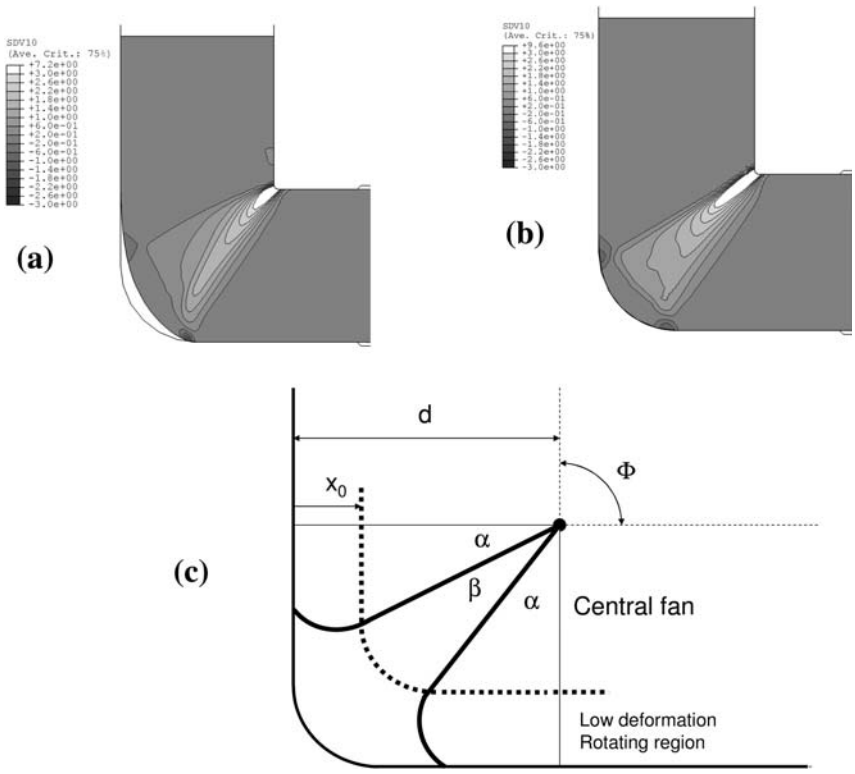

Fig. 18.3 The plastic-deformation zones (PDZ) revealed by strain-rate field plots calculated by finite element modelling (a) and (b) Beyerlein et al. [9] and (c) modeled analytically as two parts, found in [7]. In (a), the material behavior is strain hardening and in (b) it is perfectly plastic.

$$\bar{\mathrm{L}} = \frac{t_{\mathrm{n}} L}{\cos^2 \alpha} = \begin{bmatrix} \dfrac{\sin 2(\alpha+\bar{\beta})}{2} & -\cos^2(\alpha+\bar{\beta}) & 0 \\ \sin^2(\alpha+\bar{\beta}) & -\dfrac{\sin 2(\alpha+\bar{\beta})}{2} & 0 \\ 0 & 0 & 0 \end{bmatrix}, \quad \alpha = \frac{\pi/2-\beta}{2} \tag{18.4}$$

where $\bar{\beta}(T') = T' \cos^2 \alpha$ is the angular position of the material as it flows through the fan and T' is a normalized time in the fan since t_1 when the material point reaches the first fan boundary, i.e. $T' = (t\text{–}t_1)/t_{\mathrm{n}}$. The normalization constant $t_{\mathrm{n}} = (d\text{–}x_0)/V$ contains information concerning the width of the channel d (Fig. 18.3 (c)), initial point in the channel x_0, and the pressing speed, V. Therefore, the first relationship in Eq. (18.4) implies that L (or strain rates) increases with V and x_0 and decreases with d and β, as predicted by FE [17].

When β is nonzero and constant, deformation is homogeneous and dependent only on β [7]. In this case, plastic deformation takes place on a series of rotating planes rather than being concentrated on a single plane with additional shears entering and leaving the fan. Consequently, $\beta > 0$ causes texture components to deviate from their ideal positions. When $\beta = 0$, SS is recovered and texture components are predicted to be close to ideal. Beyerlein and Tomé [7] find that using Eq. (18.4) leads to the same texture predictions as FE across the sample [9] and better agreement with measurement than SS in single and multiple pass deformation [9, 18, 19].

Another model is the flow-line model of Tóth et al. [20, 21] for a 90° die and also for a 120° die [22] that expresses L along a preselected flow line ϕ. For $\Phi = 90°$, $\Psi = 0°$, ϕ is:

$$\phi = (d - x)'' + (d - y)'' = (d - x_0)'' \tag{18.5}$$

where x_0 is the incoming position of the line. L is readily obtained from Eq. (18.5), see [21]). The curvature of the flow line is governed by the parameter n, which equals 2 for a circular curvature and ∞ for the simple shear model. Reasonable n-values were deduced from FE simulations by fitting the flow lines. Values of $n < \infty$ also lead to deviations of the texture components from their expected symmetry positions in agreement with experiments [20, 21].

18.2.1.4 **Multiple Passes**

In multipass ECAE, at least one (usually two) rotation is performed after each pass. One rotation simulates the reinsertion of the "head" of the sample into the die entrance. Another rotation simulates the twist about the billet axis that depends on route and N. For Routes A, C and Bc, they are rotated clockwise (CW) 0°, 180° and 90° after every pass, respectively. For Route Ba, they are rotated CW 90° after each odd pass and CCW 90° after each even pass. The first rotation of any ECAE route already imposes a strain-path change. In Routes A, Ba and Bc, the shear planes intersect between sequential passes, resulting in a cross-shear path change. In contrast, the strain-path change of Route C is a shear reversal. In the second pass of Route C, the sample experiences a reverse shear along the intersection plane and in the third pass, a forward shear and so on. In Route Bc, there is a shear reversal, although it is not sequential; the third pass is the reverse shear of the first pass and the fourth pass is the reverse shear of the second pass. In Route A, the strain-rate tensor (the symmetric part of L) in the second pass is reversed from that of the first pass, but the spins (skew parts) are equal [23, 24]. Figure 18.2 (b) shows the distorted shapes of the sphere and cube elements after two passes of Route A. Note that the height of the deformed shapes is the same as that of the original side of the cube. This distortion after two passes of Route A is different than that after monotonic shear deformation of 2×2.0, which is the same accumulated strain [7].

There are two ways that multipass ECAE deformation has been modeled in the literature. One way is to rotate the *die* for each pass and extruding the billet through a network of connecting dies. In this method, L changes from pass to pass. The other way is to rotate the *sample* while keeping the die fixed. In the latter case, the location of the shear plane does not change during the ECAE process and L retains its orientation with respect to the laboratory. To simulate rigid rotation of the billet between passes, both the crystallographic and morphological (grain shape) texture are rotated relative to a fixed global coordinate system. This method has been used successfully to simulate all four routes in e.g. [19, 21, 25–27] for all types of L, from homogeneous SS to inhomogeneous FE-calculated deformations. For inhomogeneous deformations, one needs to account for the change of material positions in the billet with each pass. In Routes C, Bc, and Ba, material points in the top and bottom layers differ with N, while they are maintained in Route A.

18.2.2 Crystal Plasticity and Polycrystal Modeling

18.2.2.1 Crystal Structure

Over the past decade, materials processed by ECAE have one of three crystal structures, face-centered cubic (fcc): Cu, Ni, Al, Ag, Au, and alloys; body centered cubic (bcc): IF steel, Ta, low-carbon steel, Fe; or hexagonal close packed (hcp): Ti, Zr, Be, and Mg alloys. Texture evolves differently for each structure.

The crystal structure determines the planes $\{hkl\}$ and directions $\langle hkl \rangle$ of slip and twinning systems under which a crystal can deform. A family of slip or twinning systems with the same type of crystallographic planes and directions under symmetry operations are denoted, respectively, as a slip mode or twinning mode. Fcc crystals with high to medium stacking-fault energies (SFE), like pure Al, Ni, and Cu, typically deform by only one slip mode, $\{111\}\langle 110 \rangle$, containing 12 slip systems. Low-SFE fcc crystals, such as Ag and brass tend to deform also on the $\{111\}\ \langle 112 \rangle$ twin systems. In bcc materials, slip can take place on three planes {110}, {112}, and {123}, all sharing the same slip direction $\langle 111 \rangle$ (motivating the term "pencil glide").

Due to its low-symmetry crystal structure, a hcp grain needs to call up a combination of several possible slip or twinning modes to accommodate deformation. The choice depends heavily on their crystallographic orientation. Unlike cubic materials (fcc and bcc), not every hcp material uses the same set of slip and twinning modes. For the same orientation, one type of hcp crystal would use one or two slip modes, while another type would use a combination of twinning and slip.

18.2.2.2 Texture Measurement and Presentation

Compared to other microstructural features, such as grain size, boundary misorientation, and other material properties, such as yield or fracture stress, textures

are relatively easier to measure and predict. The methods of measurement are X-rays, neutron diffraction (NT), Orientation Imaging Microscopy/Electron Backscattering Diffraction (OIM/EBSD), and synchrotron. With X-rays or OIM/EBSD, only small sample volumes close to the surface are probed. Synchrotron measurements can also capture small dimensions but with larger grain numbers as the texture of the whole irradiated volume is detected. On the other hand, NT provides a nondestructive bulk texture measurement.

Pole figures (PFs) are perhaps the most popular method for describing and presenting textures in ECAE, ODFs being a close second. Both are suitable descriptions for ECAE textures. The advantage of an ODF representation is that it can isolate a component completely within the two-dimensional sections of the ODF. In PFs, the same component can appear in many areas and overlap with others. When only some of these sections are displayed, limited usually to those that contain the main texture components, the three-dimensional ODF texture presentation is not complete. A PF is more compact and shows more completely the fibers existing in the textures. Complete PFs can be obtained from the ODFs.

18.2.2.3 **Texture Characterization**

ECAE textures can be related to classic shear texture components defined by Canova et al. [28], and later examined in detail by Tóth et al. [29, 30]. They categorized the preferred orientations of fcc torsion textures as either lying on the A fiber ($\{111\}||SP$) or the B fiber ($\langle 110\rangle||SD$) where SP is the shear plane and SD is the shear direction. Along the A fiber, the most intense are the A, $\bar{A}$, A_1^* and A_2^* components, while the B fiber contains the A, $\bar{A}$, B, $\bar{B}$ and C ideal orientations. Figure 18.4(a) shows all these components in a (111) PF. For positive and negative shear the location of the components are the same; however, the thick solid lines in Fig. 18.4(a) indicate the partial fiber textures resulting from negative simple shear. For simple shear, two-fold symmetry is valid around the TD axis. When this symmetry applies, A and $\bar{A}$ must have the same intensity, so too must the B and $\bar{B}$. The C component ($\{001\}\langle 110\rangle$) is self-symmetric. However, a two-fold symmetry does not apply to A_1^* and A_2^*, so they can have different intensities even in simple shear. Analogous components and fibers for bcc materials have been identified as well [32].

In ECAE, SS occurs in the negative sense on a plane oriented $\Phi/2$ from the billet axis [31]. Let an ideal orientation $g=(\varphi_1, \phi, \varphi_2)$ be defined by set of Euler angles φ_1, ϕ, φ_2. The ideal orientations for negative shear are rotated accordingly to define the "ideal ECAE components":

$$g_\Phi = (\varphi_1 + \Phi/2, \phi, \varphi_2) \tag{18.6}$$

The ideal ECAE components for fcc and bcc materials assuming $\Phi=90^\circ$, for example, are listed in Table 18.1. The subscript Φ signifies a dependency on Φ. These components are also indicated on a key PF in Fig. 18.5 in three views, the TD (z-plane), ND (y-plane), and ED (x-plane) for both $\Phi=90^\circ$ and 120°. As an example, Fig. 18.6 shows two sections of the ODF for the fcc case. These sec-

Table 18.1 Ideal ECAE orientations and fibers for fcc materials using a $\Phi = 90^\circ$ die.

Notation	Euler angles (°) [a]			Miller indices			Fibers it belongs to
	φ_1	ϕ	φ_2	ND	ED	TD	
$A^*_{1\Phi}$	80.26/260.26	45	0	$[81\bar{1}]$	$[1\bar{4}4]$	[011]	$\{111\}_\Phi$
	170.26/350.26	90	45				
$A^*_{2\Phi}$	9.74/189.74	45	0	$[1\bar{4}4]$	$[81\bar{1}]$	[011]	$\{111\}_\Phi$
	99.74/279.74	90	45				
A_Φ	45	35.26	45	[914]	$[111\bar{5}]$	$[\bar{1}12]$	$\{111\}_\Phi$, $\langle 110\rangle_\Phi$
$\bar{A}_\Phi$	225	35.26	45	$[1\bar{1}\bar{1}5]$	$[9\bar{1}\bar{4}]$	$[\bar{1}12]$	$\{111\}_\Phi$, $\langle 110\rangle_\Phi$
B_Φ	45/165/285	54.74	45	[15411]	$[726\bar{1}9]$	$[\bar{1}11]$	$\langle 110\rangle_\Phi$
$\bar{B}_\Phi$	105/225/345	54.74	45	$[\bar{7}\bar{2}619]$	$[\bar{1}54\bar{1}\bar{1}]$	$[\bar{1}11]$	$\langle 110\rangle_\Phi$
C_Φ	135/315	45	0	[334]	$[22\bar{3}]$	$[\bar{1}10]$	$\langle 110\rangle_\Phi$
	45/225	90	45				

a) Given in the $\varphi = 0^\circ$ sections only.

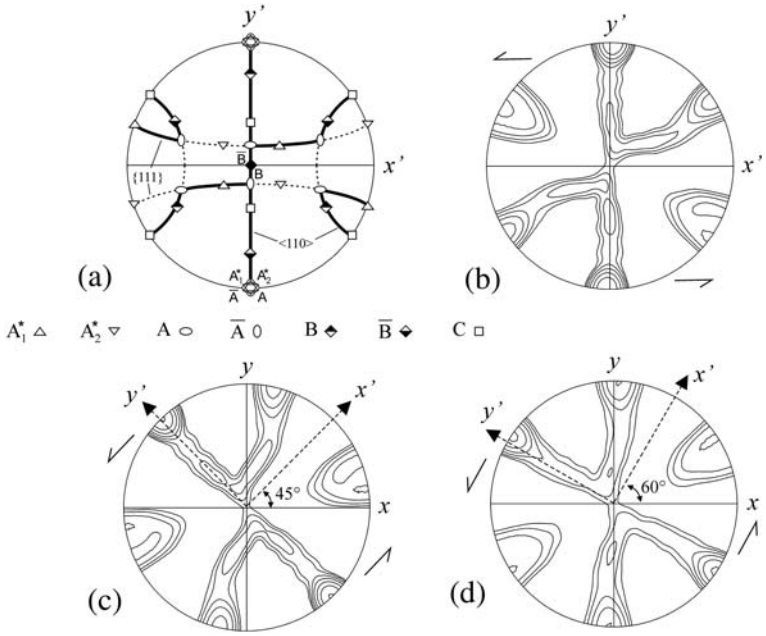

Fig. 18.4 (a): (111) pole figure showing the main ideal orientations and fibers associated with simple shear deformation of fcc materials, Li et al. [31]. The thick solid lines in (a) indicate the partial fiber textures resulting from *negative* simple shear (when the A^*_2 component is much weaker than A^*_1). Simulated textures in (111) pole figures obtained by the Taylor model for fcc materials after (b): negative simple shear ($\gamma \cong 2$) applied in x'–y', (c): one pass of ideal simple shear ECAE deformation with $\Phi = 90^\circ$ and (d): one pass of ideal simple shear ECAE deformation with $\Phi = 120^\circ$, respectively. The arrows indicate the sense of shear. Contour levels: 1/1.4/2/2.8/4/5.6/8/11.

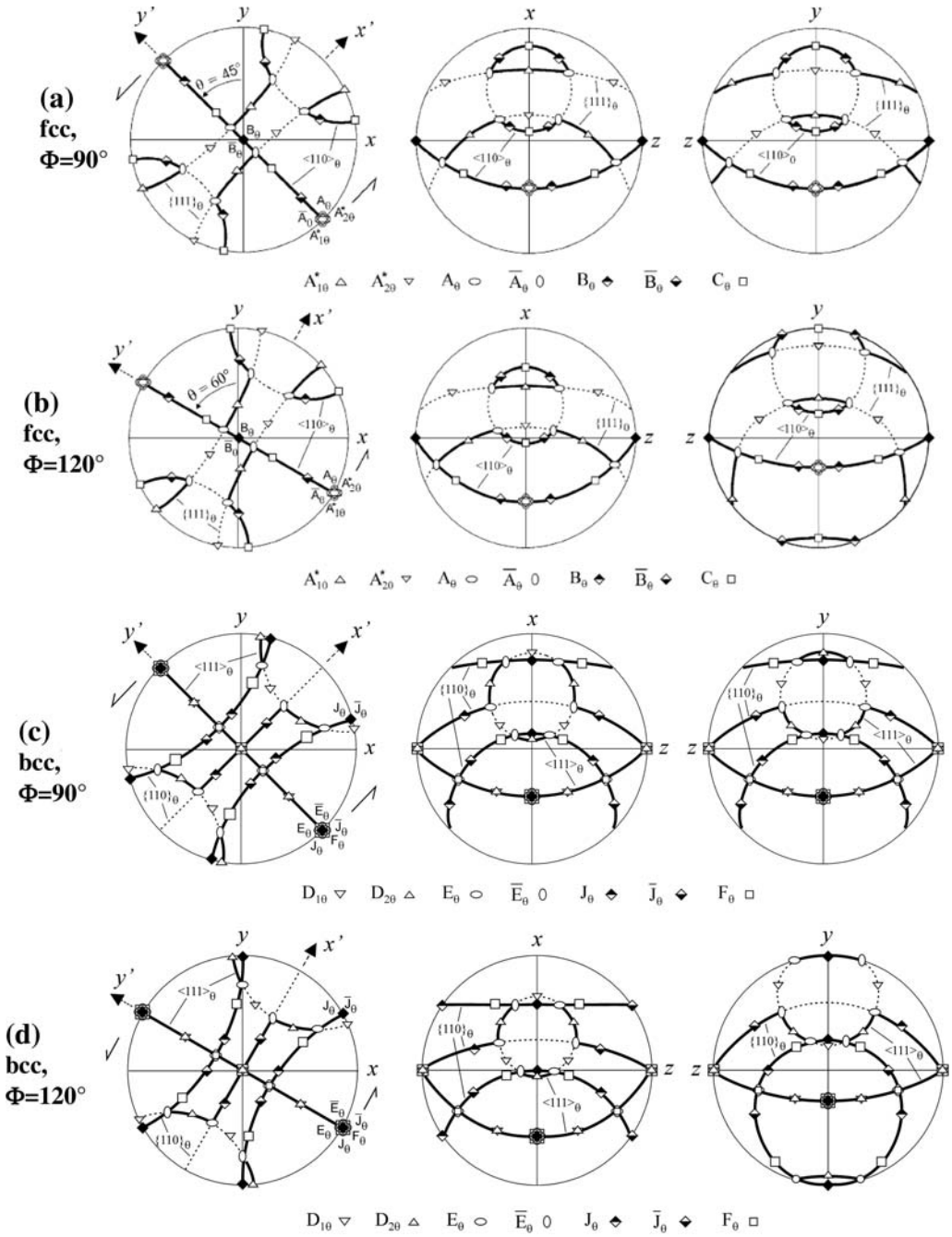

Fig. 18.5 (111) pole figures on the TD, ND and ED planes showing the ideal orientations of ECAE textures defined by the simple shear model in (a) fcc and 90° die; (b) fcc and 120° die; (c) bcc and 90° die; (d) bcc and 120° die, Li et al. [31]. The subscript θ is Φ in the present chapter.

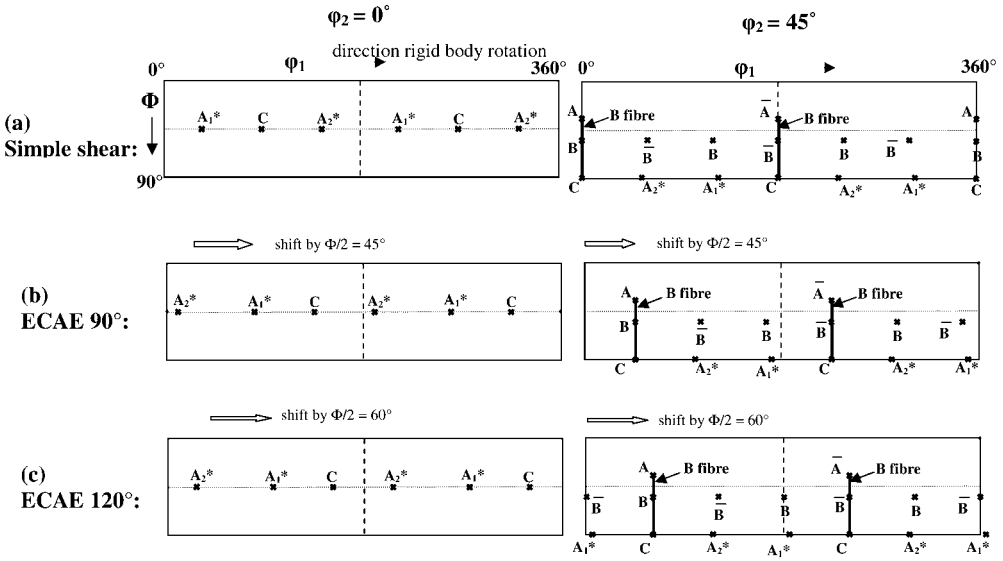

Fig. 18.6 Relationship between ideal positions of simple shear (a) and ECAE deformation (b) and (c) in orientation space using two different sections, $\phi_2 = 0^\circ$ and $\phi_2 = 45^\circ$, for (b) $\Phi = 90^\circ$ and (c) 120°. Rather than use the subscript Φ, as we do in the text, we note that for $\Phi = 90^\circ$ the ideal orientations are shifted $\Phi/2 = 45^\circ$ and for $\Phi = 120^\circ$, they are shifted $\Phi/2 = 60^\circ$.

tions contain all ideal components (except the A fiber) for ECAE dies of $\Phi = 90^\circ$and 120°.

One-pass textures can be completely described by these ideal ECAE components. Measured texture components can deviate from these ideal positions, however. Some of the known causes for these deviations will be explained later in Sections 18.3.1.1 and 18.4.1.

Texture characterization after multiple passes has not been a trivial task due to the number of possible strain path change sequences and strain levels. While not necessary for the first pass, it is important to use a fixed lab coordinate system, such as in Fig. 18.1, for defining components in multipass textures. With respect to the billet, the history of shearing does not necessarily occur on the same plane.

Some researchers elect to relate the texture of each route to a different deformation mode, such as rolling, drawing, or shearing on a plane parallel to the exit flow plane. Such analyses, however, are erroneous. It is not possible, for example, to develop textures in rolling (pure shear) the same as those in simple shear, regardless of the rotations required to make them coincide. Any coincidence is superficial. The reason is the difference in the sample symmetries. For rolling, an orthotropic symmetry prevails while for simple shear, only a two-fold symmetry. That can lead to a complete non-existence of a component in the other texture (the A_1^* and A_2^* components) or "tilts" of the components from their ideal positions in simple shear, non-existent in pure shear. The differences are striking in the rotation fields of the two deformation modes: while for roll-

ing, ideal components are within a convergent flow field in orientation space [33], in simple shear they lie at the boundaries of convergent/divergent regions [34]. From a pure mechanics point of view, while the symmetric parts of L are the same, the skew parts for pure shear and simple shear are different. Perhaps most importantly once a strain-path change is made, one cannot deduce the deformation purely from analysis of its texture components.

When the sample is reinserted into the die, the whole ODF is shifted in the lab system. For Route A, for example, the ODF simply shifts according to:

$$g_{\Phi}(\text{Route A}) = (\varphi_1 - \Phi, \phi, \varphi_2) \tag{18.7}$$

This shift means that all preferably oriented grains will be rotated to orientations that are *not* stable when the next pass begins. (One exception is the $\Phi = 120^\circ$ die where the B and $\bar{\text{B}}$ components are replaced with each other.)

For characterizing textures after multiple passes, it has been customary to either use the ideal ECAE texture components in Tables 18.1 and 18.2 (or defined by Eq. (18.6) for a general Φ) or to identify of sets of texture components (e.g. partial fibers) found repeatedly across different routes and from pass to pass. The former method has worked well; ECAE textures after multiple passes have been successfully characterized by the evolution (strengthening or loss) of these ideal ECAE components [21, 27]. The latter task has been attempted by [27, 35, 36]. For instance, Li et al. [27] found that Cu textures after subsequent passes of Routes Bc, C, and A consist of components distributed along three partial fibers f_1–f_3, established in the first pass (see Table 18.3). Within these fibers, ideal orientations come and go with N and route. A similar analysis identified analogous fibers for bcc materials, b_1–b_3, in IF steel processed by different Φ and Routes A, Bc, Ba, and C (Table 18.3) [25, 26, 36].

A characterization method for hcp ECAE materials has yet to be developed.

Table 18.2 Ideal ECAE orientations and fibers for bcc materials using a $\Phi = 90^\circ$ die.

Notation	Euler angles (°) [a]			Miller indices			Fibers it belongs to
	φ_1	ϕ	φ_2	ND	ED	TD	
$D_{1\Phi}$	99.74/279.74	45	0	[118]	[44$\bar{1}$]	[1$\bar{1}$0]	$\langle 111\rangle_{\Phi}$
	9.74/189.74	90	45				
$D_{2\Phi}$	170.26/350.26	45	0	[$\bar{4}$41]	[118]	[$\bar{1}$10]	$\langle 111\rangle_{\Phi}$
	80.26/260.26	90	45				
E_{Φ}	135	35.26	45	[914]	[$\bar{1}\bar{1}\bar{1}$5]	[$\bar{1}$12]	$\langle 111\rangle_{\Phi}$, $\{110\}_{\Phi}$
$\bar{E}_{\Phi}$	315	35.26	45	[$\bar{9}\bar{1}\bar{4}$]	[111$\bar{5}$]	[$\bar{1}$12]	$\langle 111\rangle_{\Phi}$, $\{110\}_{\Phi}$
J_{Φ}	15/135/255	54.74	45	[15411]	[$\bar{7}\bar{2}$6$\bar{1}$9]	[$\bar{1}$11]	$\{110\}_{\Phi}$
$\bar{J}_{\Phi}$	75/195/315	54.74	45	[$\bar{1}\bar{5}\bar{4}\bar{1}\bar{1}$]	[726$\bar{1}\bar{9}$]	[$\bar{1}$11]	$\{110\}_{\Phi}$
F_{Φ}	45/225	45	0	[334]	[$\bar{2}\bar{2}$3]	[$\bar{1}$10]	$\{110\}_{\Phi}$
	135/315	90	45				

Table 18.3 Definition of fibers in fcc (f_1, f_2, f_3) and bcc (b_1, b_2, b_3) ECAE textures.

Notation of fiber	Orientations in fiber
f_1	$A^*_{1\Phi} - A_\Phi/\bar{A}_\Phi - A^*_{2\Phi}$ $\{111\}_\Phi$ partial fiber
f_2	$C_\Phi - \bar{B}_\Phi/\bar{B}_\Phi - \bar{A}_\Phi/A_\Phi$ $\langle 110\rangle_\Phi$ partial fiber; $\bar{A}_\Phi/A_\Phi - A^*_{1\Phi}$ $\{111\}_\Phi$ partial fiber
f_3	$C_\Phi - B_\Phi/\bar{B}_\Phi - A_\Phi/\bar{A}_\Phi$ $\langle 110\rangle_\Phi$ partial fiber; $A_\Phi/\bar{A}_\Phi - A^*_{2\Phi}$ $\{111\}_\Phi$ partial fiber
b_1	$D_{2\Phi} - E_\Phi - D_{1\Phi}$ $\langle 111\rangle_\Phi$ partial fiber
b_2	$F_\Phi - J_\Phi - E_\Phi$ $\{110\}_\Phi$ partial fiber; $E_\Phi - D_{2\Phi}$ $\langle 111\rangle_\Phi$ partial fiber;
b_3	$D_{1\Phi} - \bar{E}_\Phi$ $\langle 111\rangle_\Phi$ partial fiber; $-\bar{E}_\Phi - \bar{J}_\Phi - F_\Phi$ $\{110\}_\Phi$ partial fiber;

18.2.2.4 **Polycrystal Modeling**

To predict texture evolution, one must treat the material as a polycrystal (PX), neither as a continuum nor as a single crystal. PX models relate the bulk plastic response of an aggregate to the deformation of the individual grains. The two main PX models used in ECAE are the full constraints Taylor (FC) and viscoplastic self-consistent (VPSC) [37, 38] models. These are more appropriate for modeling the general deformation modes found in ECAE than the relaxed constraints (RC) Taylor model. In both models, the PX is represented as a number of orientations each with a given volume fraction. In order for PX models to apply to the ECAE experiment, the model material must contain at least 20 to 100 grains in the cross section, such that nearest-neighbor correlation effects are not strong.

The FC model is perhaps the simplest to understand, implement and use. It assumes that the strain is uniform throughout the PX, that is, the strain in each grain equals the macroscopic strain, and provides an upper-bound solution. It best applies to cubic materials, in which there are at least five independent slip systems available, and at low strains, prior to any development in plastic heterogeneities (such as subgrain-induced anisotropy). Even for cubic materials, the FC model can quickly become inaccurate at large strains.

VPSC is a rate-dependent PX model, which neglects the elastic contribution to deformation. VPSC is well suited for modeling large strain deformation in ECAE, because it accounts for the plastic anisotropy of each grain and strain and stress variations between grains. A representative grain is modeled as an ellipsoid embedded in a homogeneous effective medium (HEM) with average properties of all the grains. At each increment, the viscoplastic compliance of the PX is determined self-consistently. Each grain does not deform independently, but rather according to its interaction with the HEM, as well as its morphological and crystallographic orientation. Consequently, it is not necessary for each grain to activate at least five slip systems. Indeed, in ECAE deformations, we find the number to be less, in the order of two to four. This feature will be particularly important when considering crystal symmetries other than cubic, such as Mg, Zr, Be, and Ti. Any given hcp slip mode is likely to have fewer than five independent systems, like basal slip which has only two.

18.2.2.5 Comparing Measurement and Prediction

Most comparisons are qualitative. For this reason, it is best to use the same format and same software when presenting textures so that the reader can make his/her own judgment.

Let $f(g)$ be the ODF representation of a texture. The strength of $f(g)$ is usually measured by the texture index T defined as,

$$T = \int [f(g)]^2 \mathrm{d}g \tag{18.8}$$

To quantitatively assess the quality of a predicted texture $f_{\mathrm{sim}}(g)$ with respect to a measured one $f_{\mathrm{exp}}(g)$, the normalized texture index $\hat{T}^{\mathrm{d}}$ of the difference ODF (DODF) can be used [27]

$$\hat{T}^{\mathrm{d}} = \frac{T^{\mathrm{d}}}{T} = \frac{\int [f_{\mathrm{sim}}(g) - f_{\mathrm{exp}}(g)]^2 \mathrm{d}g}{\int [f_{\mathrm{exp}}(g)]^2 \mathrm{d}g} \tag{18.9}$$

where T^{d} is the texture index of the DODF, i.e. $f_{\mathrm{sim}}(g) - f_{\mathrm{exp}}(g)$. T^{d} is a measure of the error in the predicted texture. The prediction with the smaller better reproduces the experimental one. Compared to T^{d}, $\hat{T}^{\mathrm{d}}$ allows direct comparisons between predicted textures with different reference textures, such as those generated from different materials or deformations.

18.3 Texture Results

18.3.1 Cubic Textures

18.3.1.1 Influence of Die Angle Φ

Measured textures show that Φ has two primary effects. First, due to its effect on the orientation of the shear plane, Φ causes a deviation in the shear components from the classic shear components of Canova et al. [28] according to Eq. (18.6). Using FC, Fig. 18.4 shows the shear textures as (111) pole figures in the TD plane in (a,b) the classical situation and (c, d) ECAE situations. In Fig. 18.4 (b) the classic shear texture is shown next to the marked components (18.4 a) of Canova et al. [28] under a negative shear ($\gamma = -2$) acting in the x'–γ' reference system. Figures 18.4 (c) and (d) show the textures generated using an ideal (SS) ECAE deformation under two different Φ, 90° and 120°, which appear to be rotated by 45° and 60°, respectively, from Fig. 18.4 (b). Secondly, the larger the Φ, the lower is the accumulated strain per pass. Therefore, larger Φ is expected to lead to weaker textures, with all else being the same. This tendency has been observed, particularly with higher N [26]. In addition to average intensities, the relative intensities of the components change with Φ. For example, in IF steel, after one pass, a stronger $D_{1\Phi}$ component is seen in the $\Phi = 90°$ case than for $\Phi = 120°$ [26]. In Cu, there is a weak or absent C_{Φ} in 120° while it is significant in 90° [22].

According to Eq. (18.6), textures developed with two different die angles Φ_1 and Φ_2 are expected to differ by a TD-rotation equal to half the difference between their die angles, i.e. $\Delta\Theta = (\Phi_1 - \Phi_2)/2$. For example $\Delta\Theta$, should be 15° between textures developed in $\Phi_1 = 90°$ and $\Phi_2 = 120°$ dies, which are predicted by the FC model (Figs. 18.4 (c) and (d)). Measured textures generated from these two Φ in Cu after one pass [39], an Al alloy after route A [40], and in IF steel [26] after A, Bc, and C, show approximately a $\Delta\theta \approx 15°$ difference. However, the difference between the textures in Figs. 18.4 (c) and (d) is 12°. This discrepancy occurs because the smaller strain for a lower Φ leads to *larger* rotations of the ideal components from their ideal positions (opposite to the shear) (as explained for simple shear in [29]).

18.3.1.2 **Influence of Route and Pass Number**

Next to Φ, ECAE route and N make a significant impact on texture evolution. Their influence has been most comprehensively studied in cubic materials. As representative examples, Figs. 18.7–18.9 display the PFs and ODFs of Cu (fcc) by NT ($\Psi = 37°$) [27] and IF steel (bcc) by X-ray diffraction ($\Psi = 0°$) [25], both with initially weak textures and processed by Routes A, Bc, Ba, and C using a $\Phi = 90°$ die. Note that due to the symmetry found in Routes A and C, one only needs to show ODF sections for $0° < \varphi_1 < 180°$. In Routes Bc and Ba, however, $0° < \varphi_2 < 360°$ is necessary due to the lack of symmetry.

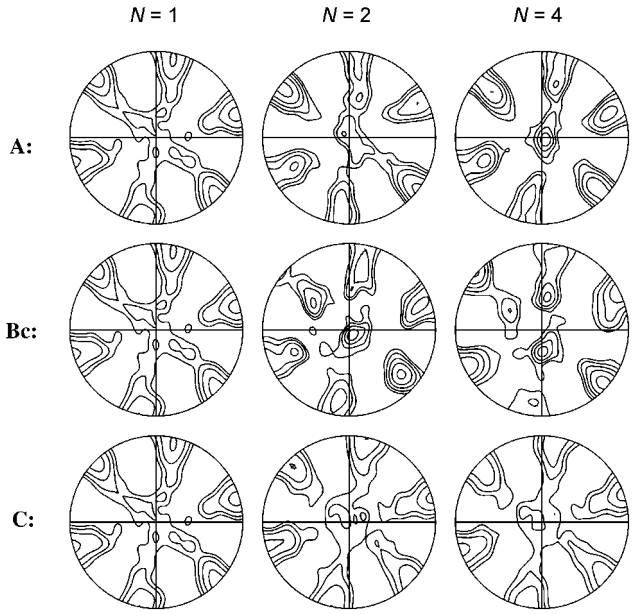

Fig. 18.7 (111) pole figures of textures in Cu in Routes A [47], Bc, and C [27] in a 90° die with a rounding of $\Psi = 37°$. Axis *x* is horizontal and *y* is vertical. Isolevels: 1/1.4/2/2.8/4.

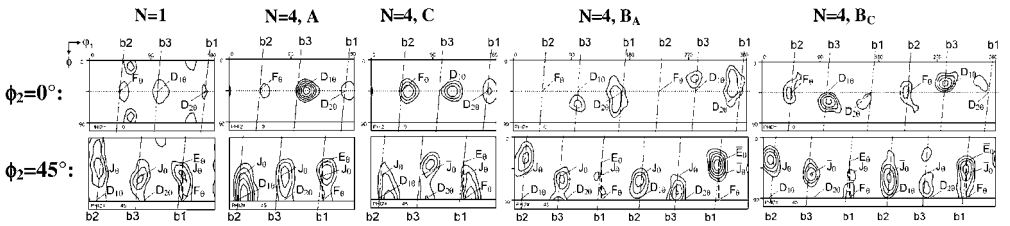

Fig. 18.8 φ_2 = constant ODF sections of textures in IF steel in a 90° a sharp corner die [25] for the first pass and all four routes. Contours: 1.4/2/2.8/4/5.6/8. Near vertical lines connect ideal positions in the full ODF.

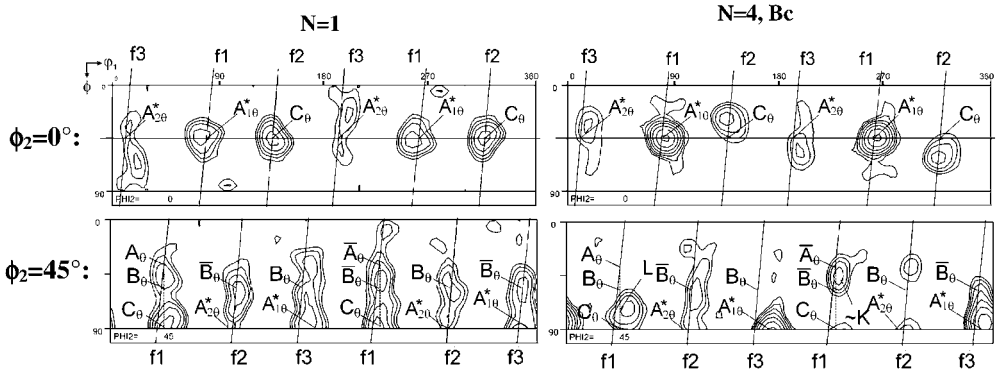

Fig. 18.9 φ_2 = constant ODF sections of texture measured in the billet after one and four passes in Route Bc [27]. Contours: 1.4/2/2.8/4/5.6/8. The f1–f3 lines connect ideal positions in the full ODF. The index θ is Φ in the present work.

First-pass cubic textures have been analyzed in several works (for sharp 90° dies: [20, 21, 41–44], for 120° sharp dies: [11, 22, 45, 22], for rounded 90° dies: [31, 46]). When the initial texture has monoclinic symmetry, it is always maintained in the first pass. For course-grained material, this symmetry is lost even in the first pass [41]. Generally, it is found that all the ideal shear components appear. In Cu (Figs. 18.7–18.9), C_{Φ} is the strongest component followed by $A_{1\Phi}$ and $B_{\Phi}/\bar{B}_{\Phi}$ and last $A_{2\Phi}$, which is the weakest. In IF steel (Fig. 18.8), $J_{\Phi}/\bar{J}_{\Phi}$ are strong, while $D_{1\Phi}$, $D_{2\Phi}$, and $E_{\Phi}/\bar{E}_{\Phi}$ are relatively weak.

Route A textures are similar to the first pass and maintain a monoclinic symmetry for up to many passes when the initial texture is monoclinic (Fig. 18.7 A) [11, 21, 25, 26, 40]. In the second through fourth passes in Cu (Fig. 18.9), $A_{1\Phi}$ becomes the main component and C weakens [21, 47]. Compared to the one-pass IF steel texture, the four-pass Route A texture (Fig. 18.8) depicts higher orientation densities around the $J_{\Phi}/\bar{J}_{\Phi}$ and $E_{\Phi}/\bar{E}_{\Phi}$ and lower orientation densities near $D_{1\Phi}$ and F_{Φ}.

In Route C, the grains do not necessarily recover their original crystallographic orientation. A large number of studies, examining a wide range of materials (e.g. Cu [10, 27, 48, 49], Al [50], Fe [35, 51], IF steel [23, 25, 26], Ti [52],

Zr [53]) have shown that the monoclinic sample symmetry as seen for the one-pass billet is preserved after multiple passes, even up to 16 passes in Cu [49]. Most works like to refer to these shear-like textures after reversal as a "retained" texture, as if some grain orientations are retained, unchanged during reverse deformation. However, this is not the case; these texture components are obtained by deformation.

In Cu, Route C does not show a cyclic evolution (Fig. 18.7). Textures in subsequent passes are all very similar to the first-pass texture, depicting main texture components near the C_{Φ}, $A^{*}_{1\Phi}$, A_{Φ}, $B_{\Phi}/\bar{B}_{\Phi}$ orientations, together with a much weaker $A^{*}_{2\Phi}$ component. The strengths of the main texture components along these fibers differ between these textures. Compared to those for the odd-numbered passes, the textures for the even-numbered passes show slightly weaker $A^{*}_{1\Phi}$, C_{Φ} and $B_{\Phi}/\bar{B}_{\Phi}$ but a stronger $A^{*}_{2\Phi}$ component. When texture evolution is slowed down, such as under high temperatures or low strain levels per pass (high Φ or Ψ), the more the initial texture components are recovered for large N. For example, in [54] coarse-grained pure Al was processed at 500 °C ($\Phi = 120^{\circ}$). The original texture was recovered up to three passes of Route C and persisted up to five passes in Route A. In IF steel, however, cyclic texture evolution is apparent from the similarities between textures after two and four passes and, to a lesser extent, between one and three passes. The primary texture components are located between the F_{Φ} and $J_{\Phi}/\bar{J}_{\Phi}$ orientations along the $\{110\}_{\Phi}$ fibers.

For Routes Bc and Ba, the monoclinic symmetry of the first pass is lost in subsequent passes (Figs. 18.7 and 18.8). In Cu, after two passes of Route Bc (and Ba), $\bar{A}_{\Phi}$ is the strongest, $A_{1\Phi}$ is weaker and A_{Φ} and C_{Φ} are absent [27]. In the fourth pass of Route Bc (Fig. 18.9) and thereafter, $A_{1\Phi}$ becomes the strongest and C_{Φ} reappears (Fig. 18.9). The texture repeats in both characteristics and strength after eight passes. Route Bc textures can also be described as showing orientation concentrations around the f_1–f_3 partial fibers within which main components vary in position and intensities with N up to 16 passes [27].

In IF steel for Routes Bc and Ba, the $\{110\}_{\Phi}$ fibers ($F_{\Phi} - J_{\Phi}/\bar{J}_{\Phi} - E_{\Phi}/\bar{E}_{\Phi}$) become less apparent than $\langle 111\rangle_{\Phi}$ fiber with N. After four passes (Fig. 18.8), the b_3 fiber passing through $D_{1\Phi} - \bar{E}_{\Phi} - F_{\Phi}$ depicts the most complete orientation distribution with its main-texture components located between $D_{1\Phi}$ and $E_{\Phi}/\bar{E}_{\Phi}$. After four passes of route Ba (Fig. 18.8), the most complete fiber is the b_1 (or $\langle 111\rangle_{\Phi}$) fiber passing through $D_{2\Phi} - \bar{E}_{\Phi} - D_{1\Phi}$, with the maximum orientation density near $\bar{E}_{\Phi}$. Li et al. [25] found that the three-pass texture is approximately the same as the two- or four-pass texture, but rotated by 180° about the TD, a relationship that they attribute to the alternating ±90° rotations of the Route B_A billet longitudinal axis during each two successive passes [36].

18.3.2 HCP Textures

Table 18.4 lists some of the recent ECAE hcp studies and their conclusions on deformation mechanisms. The current variation in Φ, Ψ, processing tempera-

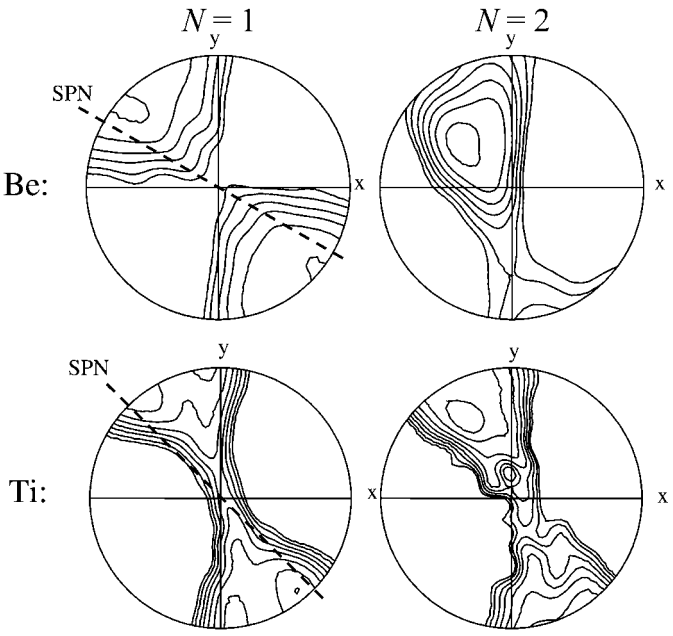

Fig. 18.10 Textures in (0001) pole figures measured in Route Bc for Be, 120° die [59], and for Ti, 90° die [64]. SPN denotes the direction perpendicular to the shear plane. Isolevels: 0.8/1/1.3/1.6/2/2.5/3.2/4.

tures, routes, N, alloying elements across the literature is quite large. While these works are informative, still many more texture studies are needed.

As an example of hcp ECAE textures, Fig. 18.10 shows the (0001) pole figures of the first- and second-pass (Route Bc) textures of pure Ti and Be in the TD view [59, 64]. The one-pass textures are symmetrical about a single plane, which is misaligned from the intersection plane. The maxima are tilted approximately 50° from the y-axis in the Be processed using $\Phi = 120°$ and 35° in the Ti processed using $\Phi = 90°$. Interestingly, the tilts differ by $\Delta\theta = 15°$, which can be explained by the difference in their Φ (see Section 18.3.1.1; Eq. (18.6)).

Similar features, such as the symmetry and approximate maxima location, are found in the one-pass textures of other hcp materials: Mg alloys [4, 66, 67], Ti [48 ,56–65], and Zr [53, 56], processed with $\Phi = 90°$, in spite of likely differences in alloying, deformation mechanisms, and initial textures. However, there are subtle differences, such as in the concentration of basal poles close to the TD (z-axis), spread of poles at the maxima, and single *vs* split maxima. The Ti in Fig. 18.10 has a higher concentration along the TD and split maxima compared to the Be that has no TD concentration and one maximum. In the Ti, the second maximum is located near the y-axis, approximately 7°. Reported studies on Ti, Zr, Mg and Be propose that basal, prismatic or some combination of the two are most dominant in the first pass [58, 60, 66, 67], and pyramidal $\langle c + a \rangle$ and

twinning are less so. One plausible reason for the common features in the one-pass hcp textures is the predominance of $\langle a \rangle$-slip.

As in cubic, texture development in hcp materials vary greatly with processing route and N. In Fig. 18.10, one can see how the textures have evolved after the second pass of Route Bc to be different in features from those in the first pass. Moreover, the hcp textures after even passes of Route C are unlike the starting textures. In Ti64 [61], despite being extremely strong (12×mr, multiply random), the initial texture was not recovered in the second pass. Likewise in [48], the Ti did not recover the initial rolling texture by the second pass.

18.3.3 Influence of Microstructure

18.3.3.1 Influence of Initial Texture

Most starting materials are likely to have some initial texture which is a signature of the manufacturing process that made and shaped the material billet. Regardless of the strength of the initial texture, most of it is *not* retained after a single pass of ECAE. Also, it is expected, that in Route C in every second pass the initial texture should be reconstructed, but this is not the case. However, loss of initial texture components in these cases does not imply that they had no effect on texture development. Because the initial texture can favor the increase of one component, while reducing another, the texture development in materials with different initial textures can be different.

It is difficult to analyze deformation textures without knowledge of the initial texture. Knowing it, texture analyses can separate initial texture effects from other effects such as those of material, like SFE or grain size, or recrystallization, or deviations in the macroscopic deformation from SS. Vogel et al. [58] studied the first-pass textures of pure Cu, Ni, and Al. Cu and Ni with a nearly random initial texture show strong A_{Φ} fibers, but weak B_{Φ} fibers, whereas Al with a swaged, asymmetric initial texture, shows both A_{Φ} and B_{Φ} fibers. A second study on the same material was conducted using VPSC, which accounted for the initial texture and not the material differences [19]. Differences in texture evolution between Al and Cu up to four passes (Route Bc) could be fully explained by initial texture effects. This result implies that differences in subgrain microstructures of the two materials [69] due to SFE, although important for grain refinement and mechanical properties, are not reflected in the texture evolution (at least up to four passes).

Textures generated from simple shearing, like torsion testing, are generally not considered to be strong ($1.0 < T < 6.0$). ECAE textures in materials with weak starting textures are therefore expected to have strengths within this range too. Likewise, when there is a relatively strong initial texture, a reduction in texture strength is observed in the first few passes. For instance, DeLo et al. [61] observed a reduction from 12.0 mr in the initial texture of Ti64 to ∼4.0 mr after the first pass, and Kim et al. [4] noted a decrease from an initial axisymmetric texture of 7.0 mr in AZ61 (an Mg alloy) to 5.6 mr after first pass and then to

2.8 mr after second pass. Ferrasse et al. [35] and Suwas et al. [41] studied initial texture effects in various cubic materials. The texture strengths (but not the texture features) suggest that initial texture effects disappear after three passes for all four routes [35] and for Route A [41].

For hcp materials, the initial orientations will strongly determine which slip and twinning modes grains will access in order to deform. Agnew et al. [67] showed that texture development in Mg alloy samples (AZ31) evolved differently depending on their initial texture. From the initial extruded texture, basal poles aligned 20° left from the y-axis whereas from the initial plate texture, they were more diffuse and closer to the y-axis. A theoretical study using VPSC showed that an initially random texture would promote nearly all basal slip in the otherwise same PX. Introducing an initial texture had the effect of increasing the non-basal activity.

18.3.3.2 **Stacking-fault Energy/Twinning in Cubic Materials**

SFE is a material property that varies in pure metals, and can be lowered by alloying. It has been found in many metals that as the SFE is lowered, some noticeable texture transitions take place. Possible mechanisms are slip of partial dislocations, stacking fault formations, shear banding and twinning. Both shear banding and twinning can result in large misorientations across their boundaries. For instance, in fcc materials, $\{111\}\langle 112\rangle$ twins result in a 60° misorientation across the twin/matrix interface. When twinning has reoriented a non-negligible portion of the grain (10% or higher) texture evolution will be altered. The boundaries of twins can present directional barriers to some slip systems leading to anisotropic hardening. The conditions that promote twinning are generally found to be low temperatures, low stacking-fault energies, high strain rates, large grain sizes, and low-symmetry crystallographic structures.

Recent studies [70, 71] on Ag, which slips and twins, have shown that twinning plays an important role in texture evolution. Compared to Cu, which does not twin, the relative intensities and evolution of the texture components from pass to pass were different. In the first pass in Ag (Fig. 18.11), the $B_{\Phi}/\bar{B}_{\Phi}$ components are the strongest, followed by the $A_{2\Phi}$, then C_{Φ}, and finally the weakest is $A_{1\Phi}$. In contrast, in Cu (in the same die), the C_{Φ}, $A_{1\Phi}$, and $B_{\Phi}/\bar{B}_{\Phi}$ components are equally strong, while the $A_{2\Phi}$ component is the weakest [21]. In the subsequent passes (Fig. 18.11), the $B_{\Phi}/\bar{B}_{\Phi}$ component strengthens even further, the $A_{2\Phi}$ component maintains approximately the same strength, while the $A_{1\Phi}$ and C_{Φ} components weaken, whereas in Cu the C_{Φ} and $A_{2\Phi}$ components weaken [21].

Both microscopy and VPSC calculations show that in Ag grains near the $A_{1\Phi}$ orientation twin readily under simple shear, explaining why this component is consistently weak in *all* passes (Fig. 18.11). At the same time, the $A_{2\Phi}$ and the $B_{\Phi}/\bar{B}_{\Phi}$ components are the least likely to twin, which explains why they are the strongest. The strain-path changes associated with Route A and a $\Phi = 90°$ die allow this twinning mechanism to repeat in each pass. In the first pass, the

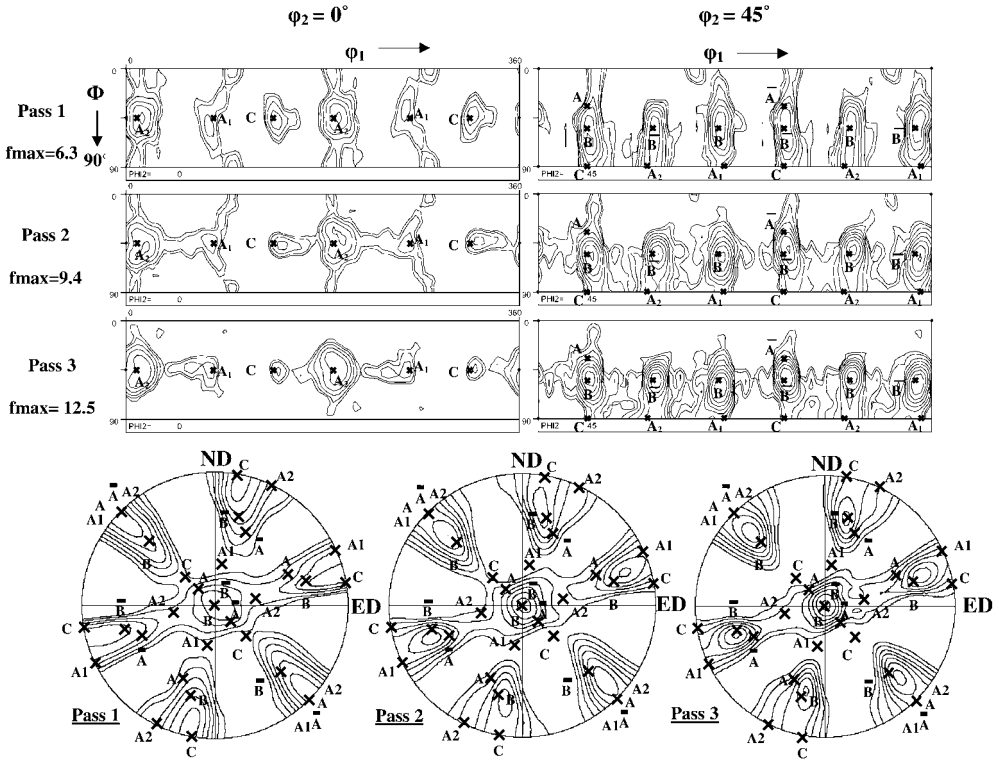

Fig. 18.11 Experimental ODFs and {111} pole figures corresponding to ECAE passes one, two and three for Ag [70]. Isovalues in ODF: 0.8, 1, 1.4, 2, 2.8, 4, 5.6, 8. Isovalues in pole figures: 0.8, 1, 1.3, 1.6, 2, 2.5, 3.2, 4, 5, 6.4.

$A_{1\Phi}$-oriented grains twin into the $A_{2\Phi}$ orientation. The rotation of the billet between passes causes grains and twinned domains in the $A_{2\Phi}$ orientation to be placed near the unstable $A_{1\Phi}$ position prior to second-pass shearing. During the second pass, these preferentially repositioned elements reorient again into the $A_{2\Phi}$ orientation. This process is repeated even in the third pass. This work demonstrates how route and Φ can influence twinning in each pass. It would be compelling to study how other combinations can promote or hinder twinning in subsequent ECAE passes.

18.3.3.3 **Influence of Deformation Mechanisms in hcp Materials**

Table 18.4 summarizes the microscale deformation mechanisms that have been inferred or identified in ECAE-processed hcp materials. As shown, the deformation modes are highly dependent on temperature and alloying. What is not apparent but is also important is the initial texture used. Some initial textures can, for instance, promote twinning in the first pass in a material that would otherwise prefer to deform by slip. Because of the strong initial texture of basal

Table 18.4 Recent ECAE hcp studies.

Materia l	Passes/Routes	Processing Temp Φ/Ψ	Reference	Conclusions [a]
Zr702	4/A, Ba,C	RT, 135°/45°	[55]	prismatic, TTW, CTW
Zr702	1st pass	350 °C, 90°/20°	[53]	mostly basal
Zr702	2–4/Bc,C	350 °C, 90°/20°	[53]	basal, prismatic, pyramidal
Zr702	1st pass	350 °C, 90°/20°	[56]	basal, prismatic, $\{10\bar{1}1\}$ CTW
Zr702	4/Bc	350 °C, 90°/20°	[57]	basal
Be		1st pass 425 °C, 120°	[58, 59]	basal
Be		1st pass 425 °C, 90° (10 1/s)	[60]	basal, prismatic
Ti64	1–2/A,C	preheat 900 °C, 90°	[61]	prismatic
α-Ti	2/C	400 °C, 90°	[52]	basal, twinning
CP-Ti	1st pass	250–550 °C, 90°/20°	[62]	prism..>basal, pyram.., $\{10\bar{1}1\}$ CTW
CP-Ti	1st pass	350 °C, 90°/20°	[63]	$\{10\bar{1}1\}$ CTW
CP-Ti	2/Bc	350 °C, 90°/20°	[63]	prismatic
Pure Ti	1–4/Bc	200 °C, 90°/37°	[64]	basal, prismatic
CP-Ti	1st pass	350 °C, 90°/20°	[65]	$\{10\bar{1}1\}$ CTW
CP-Ti	2/C,	350 °C, 90°/20°	[65]	prism, pyramidal
CP-Ti	2/A	350 °C, 90°/20°	[65]	basal, twinning
CP-Ti	2/Bc,	350 °C, 90°/20°	[65]	prismatic
Mg-AZ61	8/A,Bc	275 °C, 90°/30°	[4]	basal, prismatic
Mg-3.3% Li	4/A,Bc	250 °C, 90°	[3]	basal, prismatic, pyramidal $\langle c+a \rangle$
Mg-4Li	1–4/A	260 °C, 90°	[66, 67]	basal, prismatic
Mg-AZ31	1–4/A	200 & 300 °C, 90°	[66, 67]	basal, prismatic, pyramidal $\langle c+a \rangle$
Mg-ZK60	1–4/A	260–325°C, 90°	[66, 67]	basal, prismatic, pyramidal $\langle c+a \rangle$
Mg-WE43	1–4/A	260–325°C, 90°	[66, 67]	basal, prismatic, pyramidal $\langle c+a \rangle$
Mg-AZ31	1st pass	200 °C, 90°/37°	[68]	basal, prismatic, TTW
Mg-AZ31	1st pass	250 °C, 90°/37°	[68]	basal, pyramidal $\langle c+a \rangle$

a) The conclusions on deformation mechanisms will be dependent on the method used to determine them. Some studies used modeling, others used microscopy, and a few, both methods. These conclusions are what is reported in the corresponding reference and are not reflective of our independent interpretation of their results. These results listed are general and the reader is encouraged to consult the reference for more details on the dependence of deformation mechanism on route and pass number. TTW stands for tensile twinning and CTW stands for compression twinning.

poles aligned favorably for twinning, Yu et al. [62] observed $\{10\bar{1}1\}$ compressive twins (for 250–550 °C) in CP-Ti after the first pass, but none after the fourth pass of route Bc. In Agnew et al. [67] it was found that both initial texture effects and alloying had large effects on texture evolution of various Mg alloys. Two alloys (AZ80 and AZ31) with similar solid-solution Al content but different initial textures had the same texture evolution dominated by basal slip. The Mg-4Li alloy, however, had a different one-pass texture due to the nonbasal activity promoted by Li.

One can appreciate form Table 18.4 that deformation mechanisms will also be highly dependent on *N* and processing route. Each route has a different "entry" texture that may invoke different deformation modes in hcp crystals. Also, each mode hardens differently so that their relative activities in the first pass may not be repeated in subsequent passes. Generally, in subsequent passes twinning will not be favored over slip due to the combination of grain refinement and high processing temperatures. Dependencies of slip and twinning modes on route have been observed in CP-Zr [55] for Routes A, Bc and Ba and in CP-Ti [65] for Routes A, Bc and C (see Table 18.4).

18.3.3.4 **ECAE of Single Crystals**

The study of texture development in SX during ECAE is very recent with the first report from 2003 [72]. In that work, OFHC Cu SX was extruded in a 90° die in Route C up to five passes. The occurrence of dynamic recrystallization and misorientation distributions were documented [72, 73]. Since then, SX studies involved only single pass. Fukuda et al. [74] processed a SX of Al in a 90° rounded die, which was initially oriented with a (111) plane parallel to the ideal shear plane and a [110] direction coincident with the shear direction of ideal SS. At many locations before and after the PDZ, the SX showed a significant CCW rotation of 60°, close to the theoretical value of 57.3° for SS [7]. After extrusion, shear bands and stringers were observed, within which the initial orientation was retained. In principle, the initial orientation, which corresponds to the A_{Φ} orientation, should remain stable in simple shear. The actual initial orientation, however, was slightly off (see inserts 1 and 6 in Fig. 6 of [74]), making it unstable. Consequently, after ECAE, the SX reoriented to the ideal $\bar{B}_{\Phi}$ position. This rotation is a natural consequence as $\bar{B}_{\Phi}$ lies 60° away from the A_{Φ} orientation (see Fig. 18.6). They interpreted this B_{Φ} orientation as an ideal position of the rolling process; however, this interpretation does not hold true, as the number of operating slip systems is not enough for stability. The number should be at least four for rolling [75], while it is only two in simple shear for the $\bar{B}_{\Phi}$ component [34].

Starting with an initial cube orientation, Ni SX was also studied under ECAE [76]. Very inhomogeneous deformation with wildly varying microstructures was found across the cross section. The main feature of texture development was the rotation of the cube into the C_{Φ} component. In the work of Miyamoto et al. [77, 78] seven different initial orientations of SX Cu were processed using

$\Phi = 90^\circ$. The final orientations of A_2^*, C_Φ, and $B_\Phi/\bar{B}_\Phi$ as well as the propensity for deformation twinning and heterogeneous deformation, depended on initial orientation. It is clear from these SX studies that good crystal plasticity simulations of substructure development are still needed for relating slip patterns to texture and microstructural evolution.

18.3.4 Effect of Temperature

At temperatures higher than room temperature, texture develops more slowly as most of the deformation can be accommodated by diffusion and less by slip-induced grain reorientation. Higher temperatures also enable dislocation maneuvers involved in plastic relaxation, allowing stress-free, low-energy, high-angle boundary (HAB) dislocation structures to form, thus enabling subgrains to behave more like individual grains. Huang et al. [79] ECAE processed Cu in the range of $0.22\,T_m$ to $0.35T_m$. They see larger cell sizes and cleaner, larger fractions of HABs, as temperature increases. Both grains and subgrains alike rotate towards the preferred ideal ECAE shear orientations during extrusion but the subgrains with the larger boundary misorientations can result in a measurable spread about these components. Therefore, higher temperatures could lead to more diffuse textures than observed at lower temperatures, but with the same features. In [54] pure Al was processed at 500 °C ($\Phi = 120^\circ$) and no sharp deformation textures were generated and texture evolution became more diffuse with N. Dynamic recrystallization was suspected to occur in both Routes A and C.

There are two main factors determining the temperature of the billet during ECAE processing. One is the processing temperature controlled by the operator and the other one is that due to adiabatic heating of the material under deformation, which can be a significant contribution as the pressing rate increases. For instance, Field et al. [60] reported that under an ECAE processing strain rate of 10 1/s, the adiabatic heating resulted in a rise from a 425 °C applied temp to 475 °C in pure Be.

In hcp materials, increasing the temperature can alter the type of deformation mechanism, (such as from twinning to slip), also the relative activities of these mechanisms, or the fraction of recrystallized grains. In these situations, noticeable transitions in the texture evolution with temperature take place. For instance, in Mg alloys, basal slip is the easiest and most common slip mode at room temperature [80], having the lowest CRSS. Increases in temperature lower the differences between the CRSS of basal slip and those of the nonbasal slip modes, such as prismatic and $\langle c + a \rangle$ pyramidal. Therefore, during high-temperature ECAE processing, it is possible that prismatic and pyramidal modes are activated, in combination with basal slip, producing observable changes in texture evolution after the first pass [66–68].

Some hcp studies find, however, that temperature has little effect on texture. Li et al. [64] observe similar four-pass Route Bc textures in pure Ti between 200 °C (Fig. 18.10) and 400 °C. For CP-Ti, Yu et al. [62] found that as the tem-

perature increased, 250–550 °C, the texture intensities reduced, but the features were still the same. In these cases, the temperature changes did not invoke a transition in deformation mechanisms.

18.4 Model Performance

18.4.1 Macroscale

Most texture predictions are calculated from either a FC or VPSC scheme, likely with some variation in application across studies. Earlier theoretical work [81] using a standard VPSC model for a hypothetical fcc PX, assuming initially random texture, ideal SS, and no hardening, demonstrated that the texture predictions closely followed what would be expected by the strain-path changes associated with each route. The inplane, pseudo-continuous Route A strain-path change displays a shear texture that intensifies with N. The reversal Route C also displays a shear texture in the odd passes and recovers the initial texture every even pass. Routes Bc and Ba show different and mixed-type textures, as expected from the out-of-plane cross-shearing imposed by them. To first order, these predictions agree with measurements on materials under nearly SS conditions and initially weak textures, with the exception of Route C.

Agreement improves greatly when a deformation scheme more realistic than SS, such as FE or analytical flow models, is used [20, 21, 27]. For instance in [27] when the initial texture and an FE history are input into VPSC, the model predicts the texture evolution much better in Route C up to four passes and Route Bc up to 16 passes compared when an SS history is used. Polycrystal texture predictions using the fan or flow-line model also lead to improvements, comparable to FE [9, 19, 21]. In these models (see Section 18.2.1.3), deformation is described by a single parameter. Figure 18.12 shows one-pass fcc ECAE textures in the form of (111) pole figures in the TD view, for both models (fan and flow line) assuming different β and n. These models shift the texture components from the ideal positions, proportional to β or n. In this viewpoint, the shift translates to a CCW rotation (or "tilt") about the TD. Note that the strengths of the textures only depend slightly on β or n. This signature shift enables characterization of β or n through comparisons with texture measurement [9, 19].

The SS model ($\beta = 0$), shear fan ($\beta > 0$), and flow-line model are examples of deformations that are symmetric about the intersection plane. For Route C, they would produce perfect reversals and near recovery of the original texture [10, 18, 81]. As demonstrated by the FE simulations in Fig. 18.3 [9], strain hardening affects the strain-rate field within the PDZ, skewing this distribution towards the exit channel. Mahesh et al. [18] analytically captured the strain-hardening effect, by rotating (skewing) the shear fan slightly by an angle ϕ about the inner

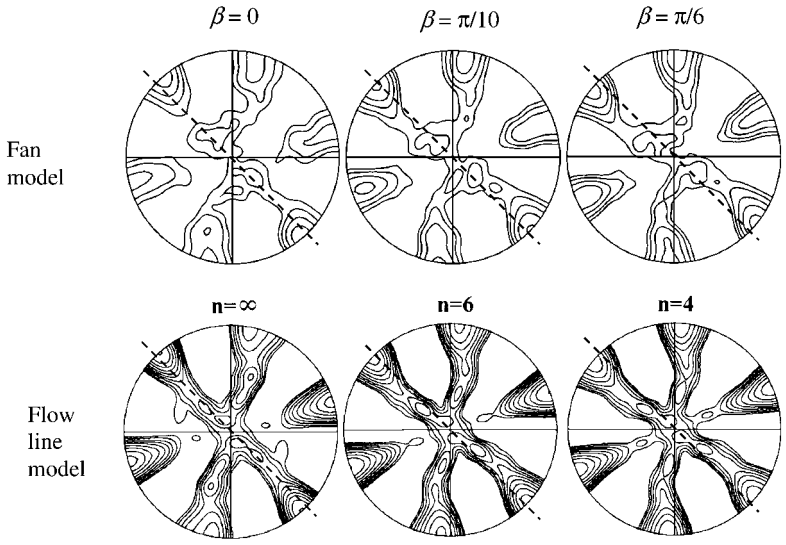

Fig. 18.12 Rotations from ideal positions predicted by the fan [7] and flow-line models [21] for ECAE of fcc in the first pass for a 90° die with no rounding. Axis *x* is on the right and axis *y* is vertical. The broken line indicates the direction perpendicular (or normal) to the shear plane. Isolines; fan: 1.0/1.4/2.0/2.8/4.0, flow line model: 0.8/1/1.3/1.6/2/2.5/3.2/4/5/6.4.

corner. The "skewed" fan improved predictions because it did not affect the already good agreement for the first pass and generated shear-like textures in the second pass of Route C.

18.4.2 Mesoscale

The most commonly used PX model is the FC model. FC performs the best for fcc materials, which deform by only one slip mode. However, early work by Canova et al. and others [28, 82, 83] shows that FC is not as good as the relaxed constraints Taylor (RC) or VPSC after 300% straining. The latter two do not require that five independent slip systems be available or activated, a requirement that is likely not to be the case when strains become large.

Comparing FC texture predictions to measurement suggest that this model is unsatisfactory for modeling texture development in cubic materials processed by ECAE [10, 21, 35, 40, 43, 66, 67]. Agnew et al. [24] performed the first of these studies, wherein they compared measured textures in Cu up to four passes of Route A with those predicted with VPSC and FC, and showed that VPSC textures achieved better agreement. The FC-predicted textures were sharper than either the texture measurement or VPSC-predicted textures and it did not capture some of the features observed in the third and fourth passes. Using $\hat{T}^{d}$ in Eq. (18.9) as a measure of performance, Li et al. [10] found that irrespective of

whether an FE or SS deformation model was introduced, VPSC outperformed FC up to 16 passes in Cu, processed by Route Bc. The VPSC-predicted textures reproduce the positions, as well as the relative intensities of all the main components in the experimental textures. Although the quality of VPSC predictions declines with N for the first four passes, it does not worsen with further increase of N. As far as location of texture components, FC seems to perform better with Route A than the other routes [25, 26, 84]. The FC model can also perform well if deformation closely follows SS [26].

18.4.3 Microscale

There have been many attempts to introduce microscale features into the PX model in order to improve its texture predictions. In standard form, PX models neglect grain interactions and assume each grain to be homogeneous, resulting in an overestimation of texture strength. Models for grain–grain interactions [11, 27, 85, 86] help to slow down texture evolution and lower intensities in better agreement with experiment. A few studies have found that VPSC with a corotation scheme for grain interaction performs well in Route A up to three passes [11] and in Route Bc up to 16 passes [27] and notably does not grossly overestimate texture intensities. There is also a class of subgrain evolution models [8, 18, 87–89] that predict the formation of deformation substructures and the misorientations across the subgrain boundaries. While these substructure elements do not deform independently, they do operate using slip systems different from their neighbor, which can lead to a further growth in misorientation during deformation. The orientations of the subgrain boundaries (bands, lamella or subgrains) are predicted to be noncrystallographic. These models predict more diffuse textures than the standard PX models after one pass and shear-like textures after two passes of Route C, in agreement with measured NT [27] or OIM textures [10]. Twins and twin boundaries can also affect texture evolution directly, by reorienting substantial volume fraction of the grains, or indirectly, by acting as directional barriers for slip systems not closely parallel to the twin interface. In [71], a twin reorientation model was introduced to VPSC, enabling texture predictions in Ag up to three passes of Route A.

Texture can also be affected by the CRSS hardening law, when it is assumed to be anisotropic. Otherwise, if single-crystal hardening is isotropic, meaning that the CRSS of all slip systems harden equally irrespective of slip activity, changes in CRSS evolution will not change the texture prediction. Good examples of how anisotropic hardening can influence texture evolution, which introduces variation in hardening among slip and twinning systems (or modes), are found in [66, 67] for hcp materials and [10, 71, 90] for cubic.

18.4.4
Factors Affecting Comparisons Between Experiment and Prediction

One needs to be mindful of several unphysical factors that can affect texture measurement or prediction and potentially the conclusions made when comparing them. First, consider the measurement technique; NT appears to give lower values than OIM. On the same first-pass sample, OIM made in the center gives $\sim$5 to 6 mr [9], whereas NT gives 2.3 [27]. Surface measurements like X-ray diffraction and OIM are sensitive to heterogeneities, so that the scan area, scan location, and grain number in the scan can influence texture intensities. Next, numerical studies are subject to possible dependencies on discretization, such as coarseness of mesh in FE or number of grains in the PX model. Li et al. [27] show that when more grains are used to represent the same initial texture, e.g. 8000 versus 1000 grains, more of the initial texture components are recovered. Model billet lengths that are too short (< 3–5 times the billet width, d), coarse meshes, or friction coefficients above an applicable value [91] can prevent attainment of steady-state deformation in an FE simulation. Another potential source, whose degree of impact is unknown, is the ECAE billet geometry. Billet lengths range from as short as 4 cm [23] to as long as 15 cm [51] and billet cross sections range from a flat plate [35], circular [46], and to the most common, square.

Subjective examinations by eye are the most common tool in comparative texture analysis in ECAE. It is therefore important to make the same choices in presenting both experiment and predicted textures. For instance in PFs, choosing the same poles, level lines, viewpoints (TD *vs* ED view), and in ODFs, choosing the same sections and level lines are recommended. Different texture presentations across studies make it difficult to compare them. An established standard for texture measurement and presentation in the ECAE community would aid utilizing results across studies and expediting our understanding in texture evolution.

Finally, the texture gradient existing between the top and the bottom of the billet is a factor that can influence significantly the measured texture. When the texture is measured on the whole lateral surface, an average texture will be influenced by the gradient [21, 27]. One can avoid this gradient effect by measuring the texture on the ED-TD (x–z) plane [21].

18.5
Additional Features

18.5.1
Heterogeneity

Inhomogeneous texture evolution results when the deformation is inhomogeneous (such as when $\Psi > 0$ or free surface corner gap forms, e.g., Fig. 18.3(b) [46]) or the texture of the starting material of each pass is inhomogeneous [10].

The former is likely to influence all passes and the latter, mainly subsequent passes. Skrotzki et al. [92–95] presented detailed experimental results for the texture heterogeneities in Cu and Ag for Route A using a synchrotron. Signorelli et al. [11] measured a gradient in texture of Al-Cu alloy across the ED-TD plane for route A up to five passes.

The first-order inhomogeneity is the formation of a lower region of little plastic deformation and large rigid-body rotations, which is distinct from the intense plastic shearing of the upper portion (see Sections 18.2.1.3 and 18.2.1.4). Deformation in this lower region has been modeled numerically using 2D or 3D FE [9, 14, 43, 46, 84] and analytically [7, 96]. The size of this undeformed zone is proportional to Ψ and to the corner gap size [14, 97]. Baik et al. [84] predicted more heterogeneity in the texture of Cu after one pass when the outer corner is rounded than when it is sharp, even though a corner gap was predicted for the sharp corner die. Observations and discussion on second-order heterogeneity within the fan region can be found in [9, 48].

After multiple passes, the parts of the billet affected by this low-deformation region depend on route. For example in Route A, the locations of material points in the billet are unchanged from pass to pass, so any heterogeneity or initial texture effects will remain, as observed in [11] and predicted in [46]. In Route C, however, the bottom and top material points are interchanged, and therefore the heterogeneity or the influence of initial texture is expected to diminish, albeit slower than the material in the center. Similarly, in Route Bc and Ba, the outer layers change their orientation in the die from pass to pass, possibly creating an outer perimeter of microstructure and texture different from the center. The tendency for increased homogeneity in Route C with N has been observed in [10, 48, 49] and predicted in [46]. In [48] the two-pass Route C copper displayed large variations with the top and bottom having more dispersed textures than in the center. The material was more homogeneous by the fourth pass. On the other hand, Ti exhibited more uniformity than Cu, which the authors attributed to higher processing temperatures and a finer grain size. These factors help to reduce the work hardening in Ti making the deformation more uniform in the die.

18.5.2
Texture Strength

Texture strength, Eq. (18.9), is often reported as a function of N and route. Strengths of ECAE textures do not vary significantly unless there is an unusually strong initial texture, from which it drops and then stabilizes with N (see Section 18.3.3.1).

There are some differences in the evolution of texture strengths with N in the literature. Take, for instance, observations made on cubic processed by Route Bc. Using NT, Li et al. [27] observed an increase in texture strength in Cu, although slight, up to 16 passes. The textures after eight and 16 passes depict a similar strength that is much stronger than that for $N=4$. Also using NT, Baik

et al. [97], see the opposite trend for Cu, a weakening in Route Bc up to four passes. In an Al alloy, Ferrasse et al. [35] found that texture strengths fluctuate in C, Ba, and Bc (more than in Route A) but then stabilize after three passes. Using EBSD, Cao et al. [98], observe a strengthening in Al with N. In contrast, using X-rays, Li et al. [25, 26] did not observe any weakening or strengthening with N for both $\Phi = 90^\circ$ and 120° in IF steel.

Textures in Route A will be particularly vulnerable to growing end effects with N. After one pass, the length of the nonuniformly deformed head region ranges from 1–2 times the width of the billet, and increases with Ψ [91]. Unlike in Routes C, Bc, and Ba, there is no exchange of the top, middle, bottom, and side layers with each pass of Route A. Consequently, folded material from both ends tend to build and propagate to the center at a faster rate in Route A than the other routes, possibly leading to weak and nonshear like textures in the central portion of the billet. This phenomenon may explain why some studies report a drop in texture strength after 6–8 passes of Route A [23, 40, 42].

18.5.3
Influence on Grain Refinement

At large strains, coupling between texture and subgrain microstructures becomes stronger. Together they determine the slip activity within the grains. It has been shown in cubic materials under monotonic straining that grain orientation can influence the morphology of the substructure formed (e.g. [99]). These substructures can in turn affect directional hardening and slip activity and hence grain reorientation. In ECAE, texture plays additional roles in grain refinement due to the continuously varying shearing of the PDZ and strain-path changes between passes. Using TEM, Xue et al. [100] studied subgrain microstructural evolution in Cu during one pass in a rounded corner die, in which deformation does not follow the SS model. They find that the best grain orientations for grain refinement are those that promote a transition from planar slip on one plane to a different one during the course of extrusion. The first slip activity builds dislocation boundaries that are intersected by new boundaries formed by the second slip activity, fragmenting the grain. With each new pass, the grains and subgrains will likely activate slip systems that lie on different slip planes or act in the opposite sense as those in the previous pass. New substructure can channel locally through the old substructure, build up on it, or further stabilize it, depending on the grain orientation. Another texture-related deformation mechanism that can aid grain refinement is deformation twinning [71].

18.5.4
Influence on Mechanical Properties

Texture influences the anisotropy of a material and its flow strength. Texture changes the portion of grains that have “hard” or “soft” orientations with respect to the loading direction. When substantial texture has developed, mechanical

testing of the processed material then needs to be performed in many directions or modes (e.g., compression, shearing, tension). Only a handful of studies to date have experimentally evaluated the anisotropy of ECAE materials in this way. They have shown that ECAE-processed Ti [101, 102], Mg alloy [103], Al [104], and Cu [5, 105] exhibit an anisotropic response. For instance, when reloaded in compression in three orthogonal directions, ECAE Cu exhibited considerable anisotropy (TD > ND > ED), after all N up to 16 passes of Route Bc and four passes of Route C [5, 105]. Likewise, the hardness of a Mg alloy in the TD was greater than in the ED [4]. Along the ED, ECAE material is observed to be weaker in compression, yet stronger in tension for Fe [106]. Even fewer studies have predicted mechanical properties accounting for texture development [90, 107, 108]. For instance, it was shown in [90] that a change in β resulted in noticeable changes in the mechanical anisotropy. In a hardening study based on a dislocation cell-hardening model, Tóth pointed out [107] that the strain-rate variations during the passage of the PDZ may even lead to some softening of the material when it leaves the PDZ.

For hcp or highly anisotropic crystals, texture can have an even bigger impact on strength and anisotropy than on cubic as crystal orientations determine the deformation modes. In two studies, two different Mg alloys (AZ61 [103] and Mg-Li alloy [3]) processed by Routes A and Bc were studied. Not surprisingly, after four passes they report different textures. Both had axisymmetric initial textures, but one had basal poles concentrated close to the billet axis (8.2 mr) [3] and the other a weaker one (7 mr) normal to the billet axis [103]. Both find that Route Bc has a lower yield stress (after four passes in [3] and eight passes in [103]), but a larger elongation to failure than Route A. Both speculate that Route A is stronger and less ductile because it has more nonbasal activity unlike Route Bc, which develops a texture that promotes mostly basal activity. Liu et al. [3] show a strengthening in the UTS after four passes of both routes, while Kim et al. [103] observe a decrease after four (and eight passes) of Route Bc. Kim et al. [103] explain the decrease due to the texture formation favorably oriented for easier basal slip in Mg alloy. This reduction occurs in spite of the refined grain size, emphasizing the importance of texture considerations.

References

1 V. M. Segal, V. I. Reznikov, A. E. Drobyshevski, V. I. Kopylov **1981**, *Russ. Metall.* 1, 99–105.

2 V. M. Segal **1999**, *Mater. Sci. Eng.* A 271, 322–333.

3 T. Liu, Y. D. Wang, S. D. Wu, R. Lin Peng, C. X. Huang, C. B. Jiang, S. X. Li **2004**, *Scr. Mater.* 51, 1057–1061.

4 W. J. Kim, S. I. Hong, Y. S. Kim, S. H. Min, H. T. Jeong, J. D. Lee **2003**, *Acta Mater.* 51, 3293–3307.

5 D. J. Alexander, I. J. Beyerlein **2005**, *Mater. Sci. Eng.* A410–411, 201–206.

6 H. J. Roven, H. Nesboe, J. C. Werenskiold, T. Seibert **2005**, *Mater. Sci. Eng. A* 410–411, 426–429.

7 I. J. Beyerlein, C. N. Tomé, **2004** *Mater. Sci. Eng.* A380, 171–190.

8 S. M. Sivakumar, M. Ortiz, **2004** *Comput. Methods Appl. Mech. Eng.* 193, 5177–5194.

9 I. J. Beyerlein, S. Li, C. T. Necker, D. J. Alexander, C. N. Tomé, **2005** *Philos. Mag.* 85, 1359–1394.

10 S. Li, I. J. Beyerlein, C. T. Necker **2006**, *Acta Mater.* 54, 1397–1408.

11 J. W. Signorelli, R. Loge, P. A. Turner, V. Sordi, E. A. Vieira, M. Ferrante, R. E. Bolmaro **2005**, *Mater. Sci. Forum* (ICOTOM-14) 495–497, 775–784.

12 H. S. Kim, M. H. Seo, S. I. Hong **2000**, *Mater. Sci. Eng. A* 291, 86–90.

13 I. N. Budilov, I. V. Alexandrov, Y. V. Lukaschuk, I. J. Beyerlein, *Ultrafine Grained Materials III*, (eds.) Y. T. Zhu, T. G. Langdon, R. Z. Valiev, S. L. Semiatin, D. H. Shin, T. C. Lowe, **2004**, TMS (The Minerals, Metals & Materials Society), Warrendale, USA, 193–198.

14 V. S. Zhernakov, I. N. Budilov, V. Alexandrov, I. J. Beyerlein **2007**, *J. Mater. Res.* 98, 178–183.

15 S. W. Chung, H. Somekawa, T. Kinoshita, W. J. Kim, K. Higashi **2004**, *Scr. Mater.* 50, 1079–1083.

16 V. M. Segal **2003**, *Mater. Sci. Eng.* A345, 36–46.

17 H. S. Kim **2002**, *J. Mater. Res.* 17, 172–179.

18 S. Mahesh, I. J. Beyerlein, C. N. Tomé **2005**, *Scr. Mater.* 53, 965–969.

19 S. Li, I. J. Beyerlein, D. J. Alexander **2005**, *Scr. Mater.* 52, 1099–1104.

20 L. S. Tóth **2003**, *Adv. Eng. Mater.* 5, 308–316.

21 L. S. Tóth, R. Arruffat-Massion, L. Germain, S. C. Baik, S. Suwas **2004**, *Acta Mater.* 52, 1885–1898.

22 R. Arruffat-Massion, L. S. Tóth, J-P. Mathieu **2006**, *Scr. Mater.* 54, 1667–1672.

23 J. De Messemaeker, B. Verlinden, J. Van Humbeeck **2005**, *Acta Mater.* 53, 4245–4257.

24 S. R. Agnew, U. F. Kocks, K. T. Hartwig, J. R. Weertman **1998**, *Proc. 19th Riso Int. Symp. Mater. Sci.* Riso Nat. Lab. Roskilde, Denmark, 201–206.

25 S. Li, A. A. Gazder, I. J. Beyerlein, E.V. Pereloma, C. H. J. Davies **2006**, *Acta Mater.* 55, 1087–1100.

26 S. Li, A. A. Gazder, I. J. Beyerlein, E.V. Pereloma, C. H. J. Davies **2007**, *Acta Mater.* 55, 1017–1032.

27 S. Li, I. J. Beyerlein, D. J. Alexander, S. C. Vogel **2005**, *Acta Mater.* 53, 2111–2125.

28 G. R. Canova, U. F. Kocks, J. J. Jonas **1984**, *Acta Metall.* 32, 211–226.

29 L. S. Tóth, P. Gilormini, J. J. Jonas **1988**, *Acta Metall.* 36, 3077–3091.

30 L. S. Tóth, K. W. Neale, J. J. Jonas **1989**, *Acta Metall.* 37, 2197–2210.

31 S. Li, I. J. Beyerlein, M. A. M. Bourke **2005**, *Mater. Sci. Eng.* A394, 66–77.

32 J. Baczynski, J. J. Jonas **1996**, *Acta Metall.* 44, 4273–4288.

33 L. S. Tóth, J. J. Jonas, D. Daniel, R. K. Ray **1990**, *Met. Trans. A* 21, 2985–3000.

34 L. S. Tóth, K. W. Neale, J. J. Jonas **1989**, *Acta Metall.* 37, 2197–2210.

35 S. Ferrasse, V. M. Segal, S. R. Kalidindi, F. Alford **2004**, *Mater. Sci. Eng.* A368, 28–40.

36 S. Li, I. J. Beyerlein **2005**, *Modell. Simul. Mater. Sci. Eng.* 13, 509–530.

37 A. Molinari, G. R. Canova, S. Ahzi **1987**, *Acta Metall.* 35, 2983–2994.

38 R. A. Lebensohn, C. N. Tomé **1993**, *Acta Metall.* Mater. 41, 2611–2624.

39 W. H. Huang, L. Chang, P. W. Kao, C. P. Chang **2001**, *Mater. Sci. Eng. A* 307, 113–118.

40 A. Gholinia, P. Bate, P. B. Prangnell **2002**, *Acta Mater.* 50, 2121–2136.

41 S. Suwas, R. Arruffat Massion, L. S. Tóth, J.-J. Fundenberger, A. Eberhardt, W. Skrotzki **2006**, *Metall. Mater. Trans. A* 37, 739–753.

42 X. Molodova, G. Gottstein **2005**, *Mater. Sci. Forum* (ICOTOM-14) 495–497, 791–796.

43 I. V. Alexandrov, M. V. Zhilina, A V. Scherbakov, J. T. Bonarski **2005**, *Mater. Sci. Eng.* A410–411, 332–336.

44 A. A. Gazdar, S. Li, F. H. Dalla Torre, I. J. Beyerlein, C. F. Gu, C. H. J. Davies, E.V. Pereloma **2006**, *Mat. Sci. Eng. A* 437, 259–267.

45 I. Kopacz, M. Zehetbauer, L. S. Tóth, I.V. Alexandrov **2001**, *Proc. 22nd Riso Int. Symp. on Mechanical Science: Science of Metastable and Nanocrystalline Alloys Structure, Properties and Modelling*, (eds.) A. R. Dinesen et al., Roskilde, Denmark, Sept. 2001, pp. 295–300.

46 S. Li, I. J. Beyerlein, C. T. Necker, D. J. Alexander, M. A. M. Bourke **2004**, *Acta Mater.* 52, 4859–4875.

47 S. Li, I. J. Beyerlein, D. J. Alexander **2006**, *Mat. Sci. Eng. A* 431, 339–345.

48 Y. Perlovich, M. Isaenkova, V. Fesenko, M. Grekhov, I. Alexandrov, I. J. Beyerlein **2006**, *Mater. Sci. Forum* (NanoSPD3 Conf., Fukuoka, Japan, 2005 Sept.) 503–504, 853–858.

49 A. Tidu, F. Wagner, W. H. Huang, P.W. Kao, C. P. Chang, T. Grosdidier **2000**, *J. Phys. IV France* 10, 211–217.

50 T. R. McNelley, D. L. Swisher, **2004**, *Ultrafine Grained Materials III*, (eds.) Y. T. Zhu, T. G. Langdon, R. Z. Valiev, S. L. Semiatin, D. H. Shin, T. C. Lowe. TMS (The Minerals, Metals & Materials Society), Warrendale, USA, pp. 89–94.

51 M. A. Gibbs, K. T. Hartwig, L. R. Cornwell, R. E. Goforth, E. A. Payzant **1998**, *Scr. Mater.* 39, 1699–1704.

52 M. Isaenkova, Y. Perlovich, V. Fesenko, M. Grekhov, I. Alexandrov, I. J. Beyerlein **2005**, *Mater. Sci. Forum* (ICOTOM-14) 495–497, 827–832.

53 Y. Perlovich, M. Isaenkova, V. Fesenko, M. Grekhov, S. H. Yu, S. K. Hwang, D. H. Shin **2005**, *Mater. Sci. Forum* 503–504, 859–864.

54 U. Chakkingal, P. F. Thompson **2001**, *J. Mater. Proc. Tech.* 117, 169–177.

55 W. S. Choi, H. S. Ryoo, S. K. Hwang, M. H. Kim, S. I. Kwun, S. W. Chae **2002**, *Metall. Mater. Trans.* 33A, 973–980.

56 S. H. Yu, D. H. Shin, N. J. Park, M. Y. Huh, S. K. Hwang **2002**, *Mater. Sci. Forum* (ICOTOM-13), 408–412, 661–666.

57 H.S Ryoo, S. H. Yu, K. H. Oh, S. K. Hwang **2002**, *Mater. Sci. Forum* 408–412, 655–660.

58 S. C. Vogel, D. J. Alexander, I. J. Beyerlein, M. A. M. Bourke, D. W. Brown, B. Clausen, C. N. Tomé, R. B. Von Dreele, C. Xu, T. G. Langdon **2003**, *Mater. Sci. Forum* 426–432, 2661–2666.

59 S. Li, I. J. Beyerlein, D. J. Alexander, D. W. Brown **2008**, Proceedings of ICOTOM-15, Cd-rom.

60 R. D. Field, K. T. Hartwig, C. T. Necker, J. F. Bingert, S. R. Agnew **2002**, *Metall. Mater. Trans.* A33, 965–972.

61 D. P. DeLo, T. R. Bieler, S. L. Semiatin **2000**, *Ultra Fine-Grain Symposium*, March 12–16, (eds.) Y. T. Zhu et al., TMS (The Minerals, Metals & Materials Society), Warrendale, USA, pp. 257–266.

62 S. H. Yu, D. H. Shin, S. K. Hwang **2004**, *Ultra Fine-Grain Symposium III*, (eds.) Y. T. Zhu et al., TMS (The Minerals, Metals & Materials Society), Warrendale, USA, pp. 227–234.

63 Y. S. Him, J. Kim, I. Kim, D. H. Shin **2002**, *Ultra Fine-Grain Symposium II*, (eds.) Y. T. Zhu et al., TMS (The Minerals, Metals & Materials Society), Warrendale, USA, pp. 99–104.

64 S. Li, I. J. Beyerlein, D. J. Alexander, unpublished data from 2004

65 D. H. Shin, I. Kim, J. Kim, Y. S. Kim, S. L. Semiatin **2003**, *Acta Mater.* 51, 983–996.

66 S. R. Agnew, P. Mehrotra, T. M. Lillo, G. M. Stoica, P. K. Liaw **2005**, *Mater. Sci. Eng.* A408, 72–78.

67 S. R. Agnew, P. Mehrotra, T. M. Lillo, G. M. Stoica, P. K. Liaw **2005**, *Acta Mater.* 53, 3135–3146.

68 Y. Yoshida, L. Cisar, S. Kamado, J-I. Koike, Y. Kojima **2003**, *Mater. Sci. Forum*, 419–422, 533–538.

69 S. Komura, Z. Horita, M. Nemoto, T. G. Langdon **1999**, *J. Mater. Res.* 14, 4044–4050.

70 S. Suwas, L. S. Tóth, J. J. Fundenberger, A. Eberhardt, W. Skrotzki **2003**, *Scr. Mater.* 49, 1203–1208.

71 I. J. Beyerlein, L. S. Tóth, C. N. Tomé, S. Suwas **2007**, *Phil. Mag.* 87, 885–906.

72 G. Wang, S. D. Wu, L. Zuo, C. Esling, Z. G. Wang and G. Y. Li **2003**, *Mater. Sci. Eng. A* 346, 83–90.

73 G. Wang, S. D. Wu, Q. W. Jiang, Y. D. Wang, Y. P. Zong, C. Esling, L. Zuo **2005**, *Mater. Sci. Forum* (ICOTOM-14) 495–497, 815–820.

74 Y. Fukuda, K. Oh-ishi, M. Furukawa, Z. Horita, T. G. Langdon **2004**, *Acta Mater.* 52, 1387–1395.

75 L. S. Tóth, J. J. Jonas, K. W. Neale **1990**, *Proc. Roy. Soc. Lond. A* 427, 201–219.

76 D. Goran, J.-J. Fundenberger, S. Suwas, E. Bouzy, L. S. Tóth, W. Skrotzki, T. Grosdidier **2005**, *Mater. Sci. Forum* (ICOTOM-14) 495–497, 833–838.

77 H. Miyamoto, U. Erb, T. Koyama, T. Mimaki, A. Vinogradov, S. Hashimoto **2004**, *Philos. Mag. Lett.* 84, 235–243.

78 H. Miyamoto, J. Fushimi, T. Mimaki, A. Vinogradov, S. Hashimoto **2005**, *Mater. Sci. Eng.* A405, 221–232.

79 W. H. Huang, C. Y. Yu, P. W. Kao, C. P. Chang, **2004** *Mater. Sci. Eng. A* 366, 221–228.

80 A. Ahmadieh, J. Mitchell, J. E. Dorn, **1965** *Trans. Met. Soc. AIME*, 233, 1130–1138.

81 I. J. Beyerlein, R. A. Lebensohn, C. N. Tomé **2003**, *Mater. Sci. Eng.* A345, 122–138.

82 U. F. Kocks, C. N. Tomé, H. R. Wenk **2000**, *Texture and Anisotropy*, 2nd edn, Cambridge University Press.

83 L. S. Tóth, A. Molinari **1994**, *Acta Met. Mater.* 42, 2459–2466.

84 S. C. Baik, Y. Estrin, H. S. Kim, R. J. Hellmig **2003**, *Mater. Sci. Eng.* A351, 86–97.

85 S. Li, S. R. Kalidindi, I. J. Beyerlein **2005**, *Mater. Sci. Eng. A*, 207–212, 410–411.

86 S. C. Vogel, I. J. Beyerlein, M. A. M. Bourke, C. N. Tomé, P. Rangaswamy, C. Xu, T. G. Langdon **2002**, *Mater. Sci. Forum*, 408–412, 673–678.

87 A. A. Nazarov, N. A. Enikeev, A. E. Romanov, T. S. Orlova, I. V. Alexandrov, I. J. Beyerlein, R. Z. Valiev **2006**, *Acta Mater.* 54, 985–993.

88 A. A. Nazarov, I. V. Alexandrov, I. J. Beyerlein, N. A. Enikeev, T. S. Orlova, A. E. Romanov and R. Z. Valiev **2006**, *Ultrafine Grained Materials IV.* (eds.) Y. T. Zhu, T. G. Langdon, Z. Horita, M. J. Zehetbauer, S. L. Semiatin, and T. C. Lowe, TMS, Warrendale, USA, pp. 215–221.

89 Y. Estrin, L. S. Tóth, Y. Brechet, H. S. Kim **2006**, *Mater. Sci. Forum* (NanoSPD3, Fukuoka, Japan, 2005 Sept.) 503–504, 675–680.

90 I. J. Beyerlein, S. Li, and D. J. Alexander **2005**, *Mater. Sci. Eng. A*, 201–206, 410–411.

91 S. Li, M. A. M. Bourke, I. J. Beyerlein, D. J. Alexander, B. Clausen **2004**, *Mater. Sci. Eng. A* 382, 217–236.

92 W. Skrotzki, N. Scheerbaum, C.-G. Oertel, H.-G. Brokmeier, S. Suwas, L. S. Tóth **2003**, *Solid State Phenom.* 105, 327–332.

93 W. Skrotzki, N. Scheerbaum, C.-G. Oertel, R. Arruffat-Massion, S. Suwas, L. S. Tóth **2007**, *Acta Mater.* 55, 2013–2024.

94 W. Skrotzki, B. Klöden, C.-G. Oertel, N. Scheerbaum, H.-G. Brokmeier, S. Suwas and L. S. Tóth **2006**, *Ultrafine Grained Materials IV.* (eds.) Y. T. Zhu, T. G. Langdon, Z. Horita, M. J. Zehetbauer, S. L. Semiatin, and T. C. Lowe, TMS, Warrendale, USA, pp. 283–288.

95 W. Skrotzki, N. Scheerbaum, C.-G. Oertel, H.-G. Brokmeier, S. Suwas, L. S. Tóth **2005**, *Mater. Sci. Forum* (ICOTOM-14), 495–497, 821–826.

96 G. M. Stoica, P. K. Liaw **2003**, TMS, 119–133 (Procceedings).

97 S. C. Baik, Y. Estrin, R. J. Hellmig, H-T. Jeong, H-G Brokmeier, H. S. Kim **2003**, *Z. Metallkd.* 94, 1189–1198.

98 W. Q. Cao, A. Godfrey, Q. Liu **2003**, *Mater. Sci. Eng. A* 361, 9–14.

99 X. Huang, A. Borrego, W. Pantleon **2001**, *Mater. Sci. Eng. A* 319–321, 237–241.

100 Q. Xue Q, I. J. Beyerlein, D. J. Alexander, G. T. Gray, III **2007**, *Acta Mater.* 55, 655–668.

101 V. V. Stolyarov, Y. T. Zhu, I. V. Alexandrov, T. C. Lowe, R. Z. Valiev **2001**, *Mater. Sci. Eng. A* 299, 59–67.

102 V. Z. Bengus, E. D. Tabachnikova, V. D. Natsik, I. Mishkuf, K. Chakh, V. V. Stolyarov, R. Z. Valiev **2002**, *Low Temp. Phys.* 28, 864–874.

103 W.-J. Kim, S. W. Chung, C. S. Chung and D. Kum **2001**, *Acta Mater.* 49, 3337–3345.

104 Z. Horita, T. Fujinami, T. G. Langdon **2001**, *Mater. Sci. Eng.* A318, 34–41.

105 D. J. Alexander, I. J. Beyerlein **2004**, *Ultrafine Grained Materials III*, (eds.) Y. T. Zhu, T. G. Langdon, R. Z. Valiev, S. L. Semiatin, D. H. Shin, and T. C. Lowe, TMS, Warrendale, USA, pp. 517–522.

106 B. Q. Han, E. J. Lavernia, F. A. Mohamed **2003**, *Metall. Mater. Trans. A* 34, 71–83.

107 L. S. Tóth **2005**, *Comput. Mater. Sci.* 32, 568–576.

108 I. J. Beyerlein, C. N. Tomé **2006**, *Ultrafine Grained Materials IV,* (eds.) Y. T. Zhu, T. G. Langdon, Z. Horita, M. J. Zehetbauer, S. L. Semiatin, T. C. Lowe. TMS, Warrendale, USA, pp. 63–71.

Part Five
Properties

Bulk Nanostructured Materials. Edited by M. J. Zehetbauer and Y. T. Zhu

ISBN: 978-3-527-31524-6

19
Mechanical Properties of Bulk Nanostructured Metals

Yinmin M. Wang and Evan Ma

19.1
Introduction

Because of their extremely small grain sizes, nanocrystalline (NC) materials [1] exhibit high strength and hardness [2], high wear and corrosion resistance [3], enhanced diffusivity [4], and other attractive properties [5]. However, truly NC materials (grain sizes well below 100 nm) also have drawbacks: they are often produced in small quantities, exhibit limited tensile elongation to failure [6–10], and may suffer from unstable microstructures. For better ductility and grain stability, as well as larger sample dimensions, the so-called ultrafine-grained (UFG) materials are appealing [11]. The grain sizes of this class of metals are in the range of 100–1000 nm. Porosity-free samples can be made in bulk forms (centimeters in size) and exhibit tensile elongation better than $\sim$10%. The UFG materials are often considered nanostructured as well, because they contain substantial microstructural features such as dislocation cells, mosaic/subgrain structures, and/or nanotwins that have scales/spacings below 100 nm. In this chapter, we use the term nanostructured (NS) metals to refer to both NC and UFG materials [12].

The mechanical properties of bulk NS metals are the most important for their structural applications. In the following, we will discuss several of these properties. The successful synthesis of NS materials with sufficiently large sample sizes for mechanical testing represents a major breakthrough in the pursuit of their intrinsic mechanical properties, as discussed in previous chapters. Serious discrepancies of mechanical properties were found in the earlier work, due to flaws (porosity) present in the consolidated samples [13]. These flaws led to low Young's modulus, low hardness and, most significantly, dismal ductility in tension. Several excellent reviews have addressed these issues in detail [1, 2, 14]. Here, we focus our attention on the mechanical properties of NS materials with very low or no flaw contents, produced in recent years via electrodeposition [15–19], equal-channel angular pressing [11], surface mechanical attrition [20], physical vapor deposition [21], *in-situ* consolidation [22, 23], and pulsed laser deposition [24].

Bulk Nanostructured Materials. Edited by M. J. Zehetbauer and Y. T. Zhu

ISBN: 978-3-527-31524-6

Similar to conventional coarse-grained counterparts, NS metals can also be subdivided into three groups according to their crystal structures, namely, fcc (Cu, Ni, Al, Au, Al alloys, Ni alloys), bcc (Fe, Ta, W, steels), and hcp (Co, Ti, Ti alloys) nanostructured materials. While alloys are preferable in engineering applications, in this chapter we will focus on pure NS metals to exclude effects other than those due to grain size. When relevant, the mechanical behavior of NS alloys will be mentioned briefly. We concentrate on plastic-deformation properties (mostly tensile and compressive strength and ductility) of NS metals at low homologous temperatures, i.e. room temperature and below. The strain rate and temperature dependence of the strength and ductility, as well as observations of deformation modes (such as shear banding) will also be covered. The topic of creep and fatigue behavior of NS materials is left for discussions in the subsequent chapters [25].

Our discussions below will focus on the phenomenology of the deformation behavior, rather than mechanistic details; the latter will be discussed in depth in other chapters. In other words, our purpose is to provide an outline of the general behavior of the NS metals in response to applied stresses. As we use mostly our own results and figures to illustrate the properties observed, the coverage here is not meant to be a thorough review of the field and contributions by various groups.

19.2 Elastic Properties

Earlier studies on elastic properties of NC materials focused on the samples synthesized by the inert-gas-condensation (IGC) technique. Because of imperfections and pores present in these samples, the Young's modulus was measured to be lower than that of the coarse-grained material [2, 26]. More recently, experimental results in NC samples with improved qualities have indicated that the Young's modulus is hardly affected by the grain size. Kristic et al. [27] measured the elastic modulus of 7-nm grain-sized Ni-P samples prepared by electrodeposition and observed virtually the same Young's modulus as that of the corresponding polycrystals. Nearly identical results have been attained by other researchers and also supported by computer simulations [28]. It is now generally recognized that the elastic property of NC materials is insensitive to the grain size until the grain size reaches a few nanometers, and therefore is no longer a subject of intense research. Alloying, of course, can substantially reduce the Young's modulus of nanostructured materials [29]. A low-modulus and high-strength NS alloy is desirable for biomedical implant applications.

19.3
Hardness and Strength

The yield strength, along with the hardness, of nanostructured materials follows the empirical Hall–Petch (H–P) relationship down to very small grain sizes, i.e. the yield stress increases proportional to the inverse square root of the grain size. But the strength plateaus or even drops sometimes as the grain size decreases into the range of 10–20 nm. The exact grain size at which such strength falloff occurs depends on the material and remains uncertain.

Because of the small sample sizes, hardness measurement is one of the most convenient ways to probe the mechanical strength of nanocrystalline materials. Chokshi et al. [30], in one of the earliest groundbreaking and yet controversial discoveries, measured the hardness of nanocrystalline Cu and Pd synthesized by IGC with grain sizes of ~7–16 nm and found a negative H–P slope (i.e. inverse H–P behavior). These results were rationalized by the authors in terms of room-temperature Coble creep, arising from the large volume fractions of disordered intercrystalline grain boundaries. Ever since then, tremendous experimental and theoretical effort has been devoted to clarifying such inverse Hall–Petch relationship in nanocrystalline materials. Table 19.1 is a partial list of the H–P breakdown experimentally observed in several material systems [19, 24, 31–36]. Of particular interest is the recent work by Knapp et al. [24] in a pulse-laser deposited nanocrystalline nickel. In addition to the grain-size effect, Knapp pointed out that the grown-in twin boundaries frequently observed in as-synthesized nanocrystalline materials should also be taken into account. They found that the H–P relationship can be maintained well up to an approximately

Table 19.1 A partial list of Hall–Petch breakdown experimentally observed in nanocrystalline materials. Note that not all experimental measurements indicate a breakdown of Hall–Petch relationship. (IGC = inert-gas condensation; ED = electrodeposition; PLD = pulsed laser deposition; PVD = physical vapor deposition).

Materials	Breakdown grain sizes (nm)	Synthesis techniques	Autors and references	Year
Ni	12 (hold)	ED	Hughes [31]	1986
Cu, Pd	7–16	IGC	Choksi [30]	1989
Cu, Pd	5–10 (Pd) 25–35 (Cu)	IGC	Nieman [32]	1989
Ni	11–25	ED	Erb [33]	1995
Ni	10 (hold)	ED	Ebrahimi [34]	1999
Ni	12	ED	Schuh [35]	2002
Ni	10 (hold)	PLD	Knapp [24]	2004
Ni-Co	15	ED	Wu [19]	2005
Cu	10 (hold)	PVD	Chen [36]	2006

10 nm grain size. Despite the scatter in data, there seems to be a consensus that the breakdown of the H–P relationship does not occur at a grain size of $\gtrsim 10$ nm.

Explanations offered for the reduced or even negative H–P slope include room-temperature Coble creep [2], onset of grain-boundary sliding [37], approach to the amorphous state (the amorphous phase is supposed to be weaker than the crystalline phase) [18], and development of cracks/voids in triple junctions [1]. In recent experiments Wang et al. [38, 39] measured the activation volumes of electrodeposited nanocrystalline Ni (~ 30 nm) and Co (~ 15 nm) in quasistatic tensile testing, and found a value of $\sim 10\,b^3$, where b is the Burgers vector. This value is one order of magnitude higher than that would be expected from the Coble creep mechanism ($\sim 1\,b^3$), suggesting a minor role of the Coble creep hypothesized by earlier authors. A large decrease in hardness at grain sizes well above 10 nm is likely due to porosity and/or contaminations [1].

The grain-boundary sliding mechanism was proposed in molecular dynamics simulations [37, 40] and later observed during *in-situ* transmission electron microscopy experiments in nanocrystalline Ni with an average grain size of 10 nm [41, 42]. The grain-boundary sliding hypothesis provides a possible explanation to the abnormal H–P slope observed so far from experiments. The question remains, however, as to at what grain size this transition occurs and how it depends upon different material systems. To experimentally pinpoint such transition grain size is difficult. There are several factors that complicate the issue. (1) The majority of samples contain porosity and/or contaminations; (2) the *average* grain size used in H–P relationship is usually obtained from X-ray measurements, which alone does not represent the internal structures of nanocrystalline materials with a grain-size distribution. Other factors, such as twin boundaries [24] and impurities, could also impact the measured hardness/strength.

The high strength of nanocrystalline materials can be readily confirmed from compression tests [43], where the flaws are less damaging. The measured compressive strength values are often close to those deduced from hardness measurements, i.e. H/3. High compressive strengths have been seen in nanocrystalline Cu and Ni samples processed by IGC techniques [43]. More recently, mini-compression experiments have been adopted to measure the compressive strength of thin-sheet electrodeposited nanocrystalline nickel and revealed a high yield strength [44].

As porosity and imperfections are especially devastating to the tensile properties of nanostructured materials, tensile strength is one of the most important parameters to evaluate the quality of the samples. Due to sample flaws, earlier work on *tensile* strength measurements usually observes a much lower strength than that obtained from compression tests or deduced from hardness measurements. This problem is being alleviated with the improvement of sample quality. As shown in Fig. 19.1, Youssef et al. [45] and Cheng et al. [23] used an *in-situ* milling technique to synthesize nanocrystalline Cu (~ 23 nm) and measured a very high yield strength of ~ 1.1 GPa, in line with the extrapolation of H–P rela-

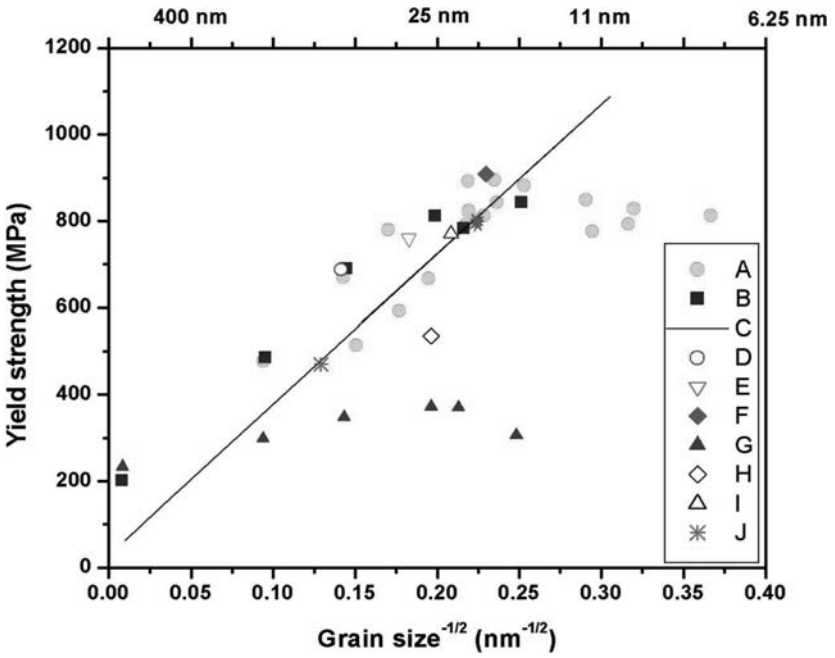

Fig. 19.1 Summary of the yield stress of nanocrystalline Cu from the literature. This figure is adapted from Ref. [23], added with recent data (red symbol) from Ref. [45]. The solid line is the Hall–Petch relationship for the yield strength of Cu given by Meyers and Chawia, $\sigma_y = 25.5 + 3478\, d^{-1/2}$.

tionship from the coarse-grained regime. Evidently, the improvement of the sample quality has drastically increased the tensile strength measured for nanocrystalline Cu.

Because of the pressure-dependent yield behavior observed in nanocrystalline materials, it is believed that there exists an asymmetry between the tension and compression strength. Computer simulations suggest that such strength difference can reach up to $\sim$30% as the grain sizes decreases down to 2–4 nm [46]. The experimental evidence regarding the tension/compression strength asymmetry, however, remains inconclusive. This is partially due to the facts that at such small grain sizes, materials are very difficult to synthesize, and that most nanocrystalline metals already tested contained processing flaws, which reduced the tensile strength.

19.4
Strain-hardening Behavior

The strain-hardening behavior of NS materials has been documented recently. In some cases (most of them in electrodeposits), nanocrystalline metals are found to exhibit strong strain hardening up to failure [22, 45, 47–51]; whereas in others, little strain hardening was observed [52]. Careful examinations of these studies are necessary as the strain-hardening behavior of nanostructured materials are affected by a number of microstructural parameters such as grain-size distribution, dislocation density, internal stress, twin boundaries [47, 48, 50], low/high-angle grain boundaries [16, 53], and so forth.

Because of the flaws and tensile instability, the strain-hardening behavior of NS metals is better revealed in compression tests, which provide a direct evaluation of the strain-hardening response as a function of strain. For most UFG materials prepared by severe plastic deformation, a flat compressive stress–strain curve is common, two examples of which are shown in Fig. 19.2. In such compressive curves, a short region of strain hardening is immediately followed by a long region of negligible work hardening or even work softening. The strain-hardening region is rather small and in the strain range of 1–3%. Such near-perfect elastoplastic behavior is different from normal single-crystal or polycrystalline materials, which typically show strong strain hardening to very large strains.

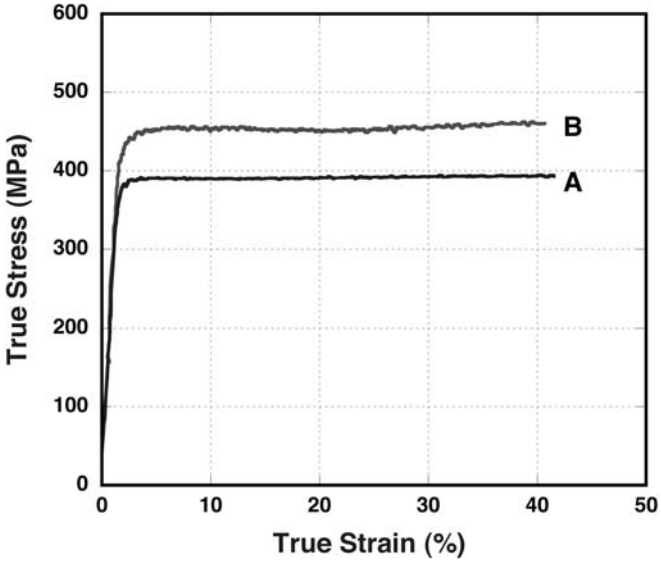

Fig. 19.2 Compressive true stress–strain curves of the ECAP-Cu (curve A) and cryorolling plus 180 °C annealed Cu (curve B) at a strain rate of 1×10^{-3} s^{-1}. This curve is adapted from Ref. [52].

That such NS metals prepared by severe plastic deformation show flat stress–strain curves is easy to understand. This is because the decomposition of originally large grains into nano/ultrafine-grain structures is achieved through accumulation and rearrangement of dense dislocations. These NS materials usually contain a high density of dislocations and other defect structures. Similar to the late work-hardening stages of heavily deformed conventional metals. The strain-hardening rate in these nanostructured metals is very low because the density of dislocations reaches a saturation level in the presence of dynamic recovery. Work hardening is observable only when very large additional strain is imposed. Over a range of plastic strains, the flow stress would appear to have reached a steady state. Several examples of nanostructured materials that exhibit flat stress–strain curves include ECAP Cu [54], ECAP Ti [55], and hot-consolidated Fe [56].

Unlike the stress–strain curves of the UFG materials, the tensile stress–strain curves of some electrodeposits such as nanocrystalline Co [47] and nanocrystalline Ni-Fe [49] show strong strain-hardening behavior up to failure. The mechanism responsible for strain hardening in these nanocrystalline materials is currently not well established. The stress increase could arise from the "exhaustion" phenomenon, possibly due to gradual exhaustion of grain-boundary dislocation sources, and/or the increase of the internal stress as a result of grain-boundary sliding [37, 40]. Both of these could cause some apparent strain hardening for a nanocrystalline metal. One supporting piece of evidence for such reasoning is the increase of strength in nanocrystalline materials after short time low temperature annealing [57–59]. Another possibility is the gradual involvement of grains of different sizes (hence different apparent strength) due to the presence of a grain-size distribution. Dislocation pile-ups may still be possible: some recent experiments in an *in-situ* consolidated nanocrystalline copper have suggested such pile up in grains as small as 10 nm [45]. Strong strain hardening has recently also been seen in an ultrafine-grained Cu containing a high density of growth twins [48, 50]. The origin of such a strain-hardening behavior will be discussed in Section 19.6.1.

19.5
Strain-rate Sensitivity

The strain-rate sensitivity, m, is commonly defined as

$$m = \left\{ \frac{\partial \log \sigma}{\partial \log \dot{\varepsilon}} \right\}_{\varepsilon,\mathrm{T}} \tag{19.1}$$

where σ is the follow stress, and $\dot{\varepsilon}$ is the corresponding strain rate. This engineering parameter is linked with the activation volume, V, through

$$m = \frac{\sqrt{3}kT}{\sigma V} \tag{19.2}$$

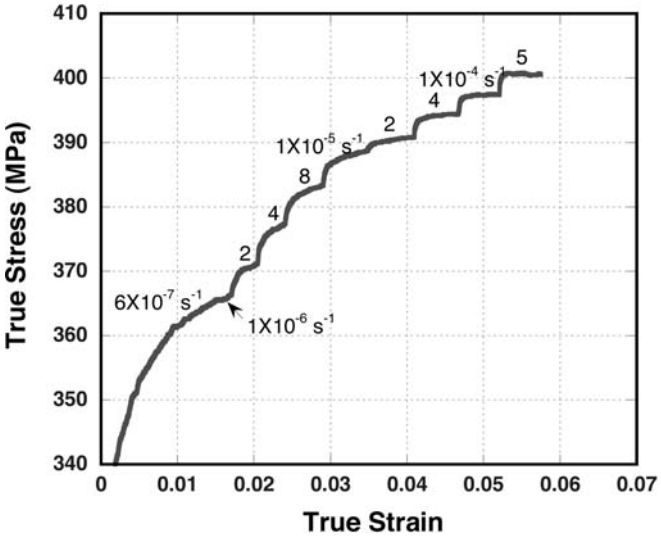

Fig. 19.3 An example [52] of a strain-rate jump test in an ECAP-Cu (average grain size ~300 nm), with the strain rate varied from 6×10^{-7} to 5×10^{-4} s^{-1}.

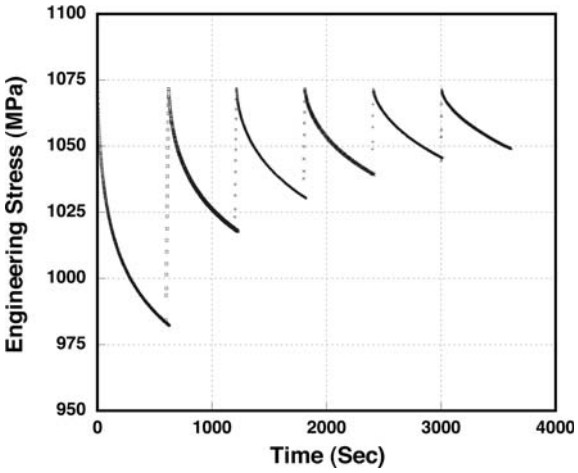

Fig. 19.4 An example of stress-relaxation tests in an electrodeposited nanocrystalline Ni with an average grain size of ~30 nm, showing several relaxation cycles.

Here, k is the Boltzmann constant, T is the absolute temperature, and V is the activation volume of the flow stress [39, 60].

The strain-rate sensitivity is an indicator of the strain-rate response of the flow stress and is useful for technological comparisons and applications. For nanostructured materials having large enough sample sizes and at least several

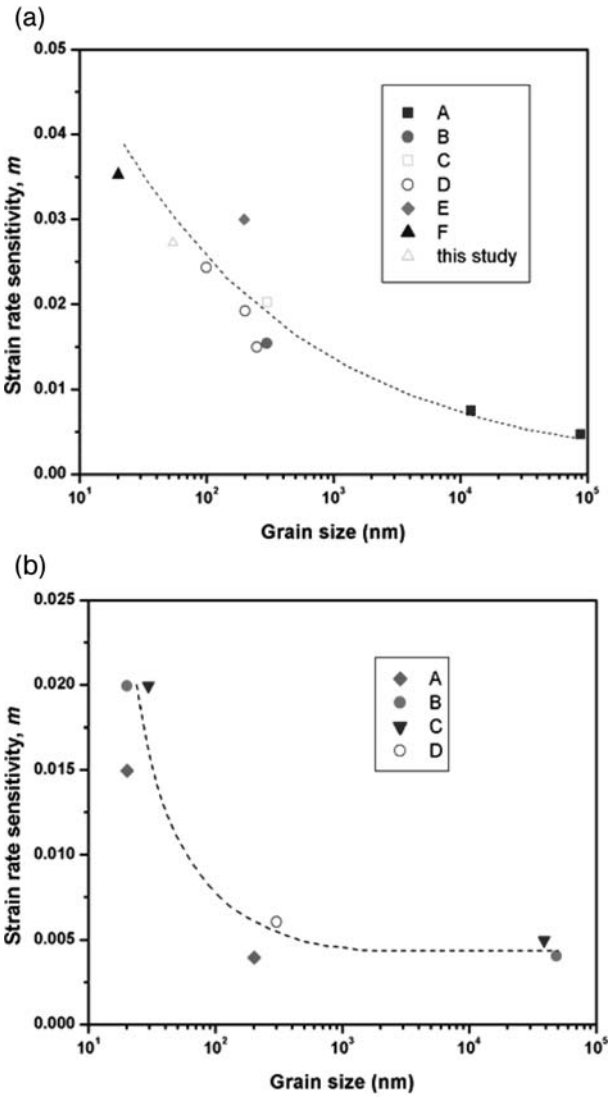

Fig. 19.5 Summary of strain-rate sensitivity *m vs* grain size for (a) Cu and Ni (b) from the open literature. In both cases, *m* shows an increasing trend as grain size decreases [23].

per cent tensile strain, the magnitude of the strain-rate sensitivity *m* can be routinely determined (using Eq. (19.1)) through jump tests (see Fig. 19.3) that can be carried out over a range of strain rates, at different temperatures. The strain-rate jump test is particularly useful for characterizing ultrafine-grained materials prepared through the ECAP technique, as these materials do have large sample sizes and decent tensile ductility. For truly nanocrystalline materials

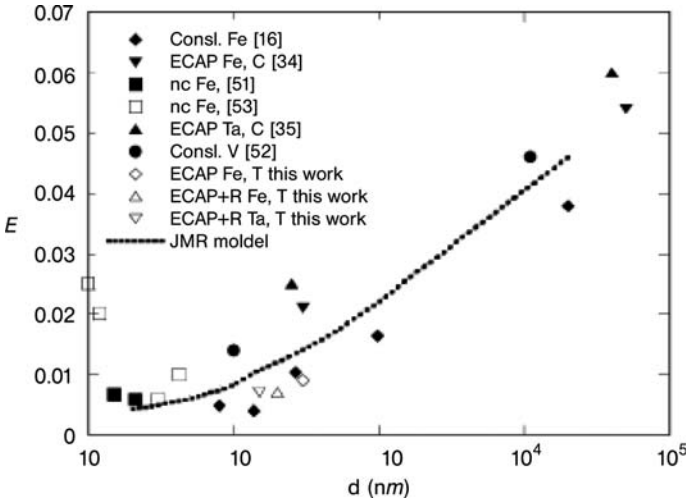

Fig. 19.6 Strain-rate sensitivity as a function of grain size for some bcc nanostructured metals, including Fe, Ta, and V. These data are from Ref. [60].

(such as those prepared by electrodeposition), the strain-rate jump test may not be applicable due to the small tensile strains these samples can sustain. Instead, a transient (stress-relaxation) test may be performed to extract the strain-rate sensitivity. The activation volume can be obtained as well (using Eq. (19.2)). One example of such a stress-relaxation test is shown in Fig. 19.4.

There have been many cases where the synthesized nanostructured samples were not sufficiently large for tensile testing. Multiple compression tests at different strain rates were usually performed to probe the strain-rate sensitivity. For very thin sheets or films, nanoindentation at different loading rates was also applied as an alternative but indirect way to measure the strain-rate sensitivity [61]. As strain-rate sensitivity is a function of both strain and strain rate (see Eq. (19.1)), caution needs to be exercised when comparing strain-rate sensitivity from different tests. Since the (dislocation and grain-boundary) microstructures of nanomaterials can change upon straining, one should be careful about deducing deformation mechanisms using the apparent m or V values obtained.

Recent experimental evidence suggests that the strain-rate sensitivity in nanostructured metals is a function of grain size. Cheng et al. [23] and Wei et al. [60] have recently documented their observations in fcc and bcc nanostructured materials processed through different routes. Their findings are shown in Fig. 19.5 and Fig. 19.6. According to these observations, an enhanced value of strain-rate sensitivity is manifested in fcc nanostructured Cu and Ni as the grain size decreases (Fig. 19.5) [39, 62, 63], in contrast to the decreasing trend seen in bcc nanostructured metals such as Fe, Ta, Va (Fig. 19.6). These findings are corroborated by other research groups. At room temperature, elevated values of strain-

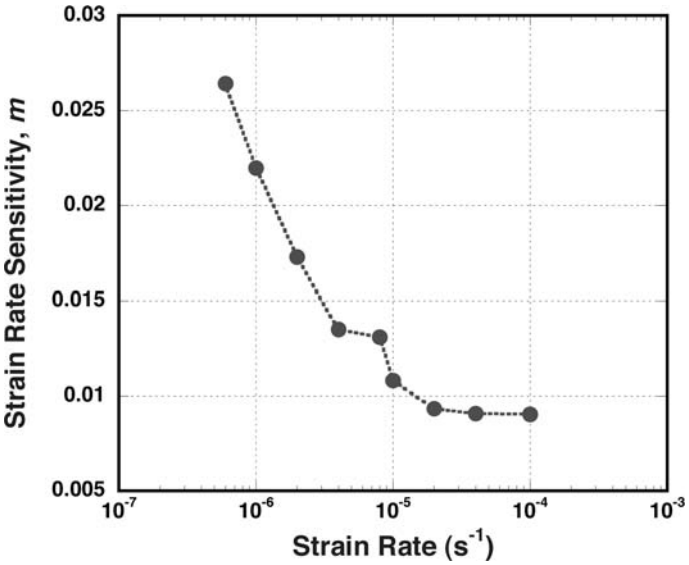

Fig. 19.7 The strain-rate sensitivity as a function of strain rate in an ECAP Cu. The strain rate range is 6×10^{-7} s^{-1} to 1×10^{-7} s^{-1}. With the increasing strain rate, the m value decreases from 0.026 to 0.010 [52].

rate sensitivity have been observed in Ni [63, 64], Au [66], electrodeposited Cu [66], Al [67], and so forth. It appears that all the fcc nanostructured materials show increasing strain-rate sensitivity with decreasing grain size. In contrast, bcc nanostructured metals exhibit decreasing strain-rate sensitivity as the grain size is reduced to the NS regime. This trend is believed to preserve at least in the grain-size regime where the H–P relationship apparently holds.

For the strain-rate sensitivity of hcp nanostructured metals, Zhang et al. [51] performed strain-rate jump tests on the ball-milled Zn samples and obtained an m value of 0.15 at room temperature. This value is substantially higher than those seen in nanostructured Cu and Ni. One plausible explanation is that Zn has a low melting temperature (693 K), and therefore room temperature represents a high homologous temperature for Zn (0.43 T_m). In contrast, studies on hcp ECAP Ti ($\sim$260 nm) revealed that the strain-rate sensitivity drops from 0.025 of the coarse-grained value to 0.009 when nanostructured [55]. A similar reduction of the strain-rate sensitivity was also reported for an electrodeposited hcp Co [47].

It is known that deformation conditions such as strain rate and temperature have a strong influence on the strain-rate sensitivity of nanostructured materials. As shown in Fig. 19.7, the strain-rate jump tests of an ECAP Cu (average grain size $\sim$300 nm) indicate that it has a strain-rate sensitivity value of 0.026 when the strain rate is 6×10^{7} s^{-1}, in contrast with the 0.010 value when the strain rate is 1×10^{-4} s^{-1} [52]. Much higher values of strain-rate sensitivity were

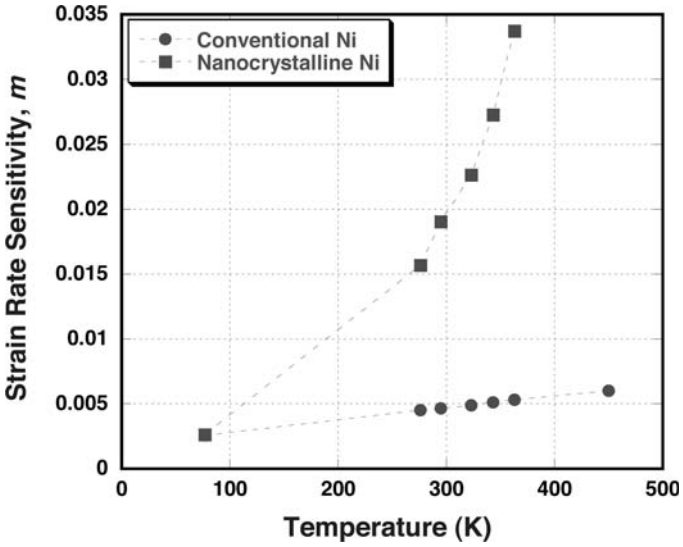

Fig. 19.8. The strain-rate sensitivity of an electrodeposited nanocrystalline Ni (~30 nm) as a function of temperature, in compared with that of conventional polycrystalline Ni. A strong increase of m with increasing temperature is evident in nanocrystalline Ni.

observed during creep (extremely low strain rates) tests of nanocrystalline Cu [66], Ni [4], and Au [65], where the grain-boundary deformation mechanism can be dominant. These high values have no direct relevance in normal quasistatic tensile tests where the strain rates are several orders of magnitude higher.

The effect of deformation temperature is stronger than the strain rate on the strain-rate sensitivity of nanostructured materials; this has recently been documented in an electrodeposited nanocrystalline Ni with an average grain size of ~30 nm [39]. These results are shown in Fig. 19.8. As the temperature increases from 77 K to 363 K, the strain-rate sensitivity of the electrodeposited nanocrystalline Ni rises an order of magnitude, from 0.003 to 0.035. This observation is in stark contrast to conventional coarse-grained Ni, the strain-rate sensitivity of which shows a weak temperature-dependent behavior (from 0.003 to 0.005). When other mechanisms come in at high temperatures, the m value increases drastically as expected. An m value of 0.5 was seen in nanocrystalline Ni when the temperature increased to 623 K [68].

19.6 Tensile Ductility

In conventional coarse-grained (1–100 μm) engineering materials, the tensile ductility sometimes increases with decreasing grain size, due to the inhabitation effects of small grain sizes on nucleation and propagation of cracks [7, 9]. In

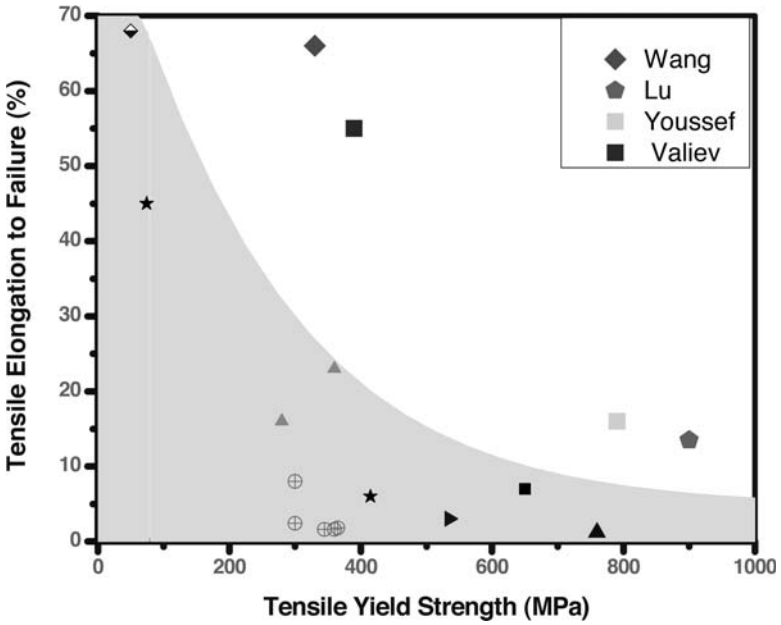

Fig. 19.9 Summary of tensile yield strength *vs* tensile elongation to failure in various nanostructured copper from the open literature. In general, the tensile ductility of nanostructured metals decreases with increasing strength. The few promising data points with good combination of strength and ductility are from Wang [74], Lu [48], Youssef [45], and Valiev [83].

contrast, as summarized in Fig. 19.9 using Cu as a model system, the tensile elongation to failure of NS materials decreases monotonically with increased strength (with the several exceptions to be discussed later in this section). Similar trends have also been observed in other nanostructured metals such as Ni, Fe, and Ti. However, despite such a decrease of the tensile elongation, nanocrystalline or ultrafine-grained materials are intrinsically ductile, judging from the often-seen ductile dimples from the fracture surface [57, 64, 69], Fig. 19.10. These dimples have sizes significantly larger than the grain sizes. It has been proposed that the dimples are formed through collectively shearing of a group of nanograins during deformation [70].

Koch et al. [9] pointed out three major sources for the low tensile ductility observed in nanostructured materials. They are (1) processing porosities and imperfections; (2) tensile instability; (3) crack nucleation or propagation instability, where the imposed stress at an existing flaw exceeds the critical toughness of the material. The first source is processing related and somewhat material-system dependent; therefore it is not an intrinsic property of nanostructured materials. With the improvement of processing routes, porosity- and contamination-free nanostructured samples have become available to avoid such problems.

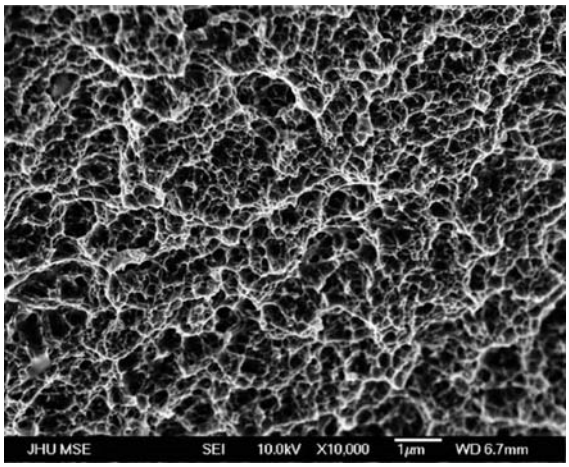

Fig. 19.10 Ductile dimple features typically seen from the fracture surface of electrodeposited nanocrystalline nickel, suggesting the ductile nature of nanocrystalline materials.

The tensile instability is closely tied to the strain-hardening rate and strain-rate sensitivity (strain-rate hardening), both of which are indicative of the intrinsic resistance of nanostructured materials to strain localization. According to Hart's criteria for a strain-rate sensitive material [71],

$$\frac{1}{\sigma}\left(\frac{\partial\sigma}{\partial\varepsilon}\right)_{\dot{\varepsilon}} + m - 1 \leq 0 \tag{19.3}$$

where the first term is the normalized strain-hardening rate, and the second term is the strain-rate sensitivity as defined by Eqs. (19.1) and (19.2). The tensile instability sets in when the condition in Eq. (19.3) is reached. According to this criteria, higher values of strain-hardening rate and/or strain-rate sensitivity help to stop early necking and prolong the tensile elongation to failure.

As discussed in Section 19.4, the majority of nanostructured materials exhibit a low strain-hardening rate, i.e. the strain-hardening rate approaches zero as soon as the yielding occurs. This is especially true for the nanostructured materials prepared through severe plastic deformation. These materials are saturated with dense dislocations and dynamic recovery occurs as deformation progresses. Such a low strain-hardening rate promotes tensile instability and is one of the major obstacles to overcome before the tensile ductility of nanostructured materials can be improved.

Of equal importance, the strain-rate sensitivity of nanostructured materials also has a direct impact on the tensile ductility. The enhanced strain-rate sensitivity slows down early necking and prevents catastrophic failure. Due to the increased strain-rate sensitivity (Section 19.5) seen in some fcc nanostructured metals, it is anticipated that they would exhibit higher tensile ductility than

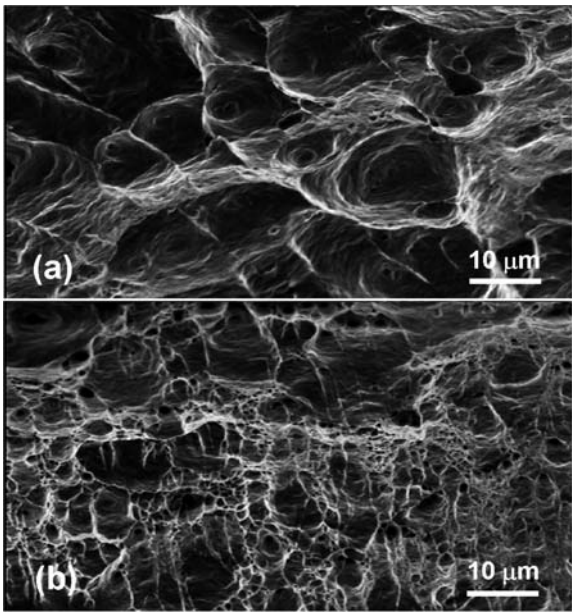

Fig. 19.11 Scanning electron micrographs of the fracture surfaces of (a) ECAP-Cu, and (b) ECAP-Cu plus cryorolling to the strain of 1340% and annealing at 100 °C for 2 h. The dimple sizes are smaller after cryorolling.

those of bcc and hcp nanostructured materials [23]. The moderately enhanced m value in fcc nanostructured metals at room temperature, however, is still too small to prevent shear localization [23].

The decrease of grain size to the nanometer regime, on the other hand, is potentially conducive to reduced flaw sizes (on the same order as grain sizes) and subsequently helps suppress the crack nucleation and propagation instability. It is known from conventional materials that both yield stress and fracture stress increase as grain sizes decrease, with the fracture strength increasing faster. Given the strong increase of the flow stress with decreasing grain size at the nanoscale, the competition between plastic flow and fracture becomes difficult to predict. By continuously refining the grain sizes and other microstructural features in the nanoscale regime, a concurrent enhancement of tensile strength and ductility was observed in cryorolled ECAP Cu [72]. The dimples from the fracture surface were also found to be finer with decreasing grain sizes, Fig. 19.11.

As the tensile ductility of nanostructured materials is of crucial importance to the structural applications, in the following we will discuss several approaches developed in recent years to improve this critical mechanical property.

19.6.1 Bimodal and/or Multimodal Microstructures

The distribution of grain size in NS metals has profound effects not only on their strength but also on the tensile ductility [73]. It is our experience from coarse-grained materials that large grains have relatively low yield strength, but offer ample room for dislocation strain hardening and thus large uniform elongation. A useful strategy is therefore to develop a bimodal or even multimodal grain structure with the micrometer-sized large grains embedded in nano- or ultrafine-grained matrix. As such, the nanograins impart high strength, whereas the micrometer-sized grains provide strain-hardening mechanisms and potentially high tensile ductility.

Wang et al. [74] achieved such bimodal distributed grain structures in copper through a combination of cryorolling (rolling of ECAE (equal channel angular extrusion) samples at cryogenic temperatures) and controlled annealing. Such a bimodal structure contains about 25% volume fraction of microsized grains ($\sim$1.7 μm) and 75% percent of UFG grains (average $\sim$190 nm). The coarse grains have been formed through an abnormal grain-growth mechanism. As expected, such a bimodal microstructure (see Fig. 19.12), though having a reduced yield strength of 330 MPa compared with the $\sim$400 MPa of the ECAP Cu, exhibits strong strain hardening and a large tensile elongation to failure almost comparable to coarse-grained Cu. The strong strain-hardening mechanism originates from deformation twinning as well as dislocation mechanisms. Recently, similar bimodal structures have been developed by other research groups [75–

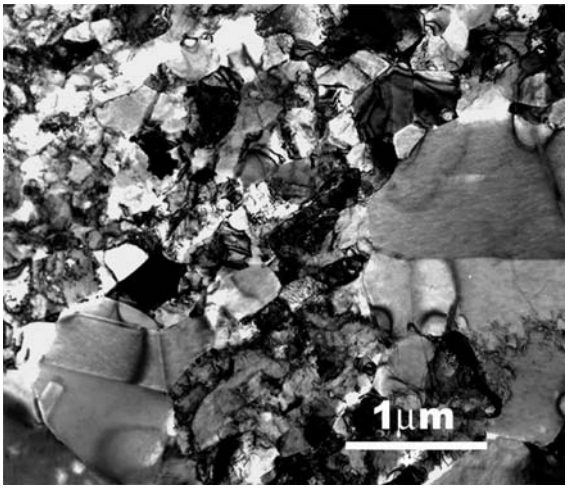

Fig. 19.12 The bimodal microstructure developed in a nanostructured Cu through cryorolling and low-temperature annealing. Such bimodal structure exhibits concomitant high strength and high ductility.

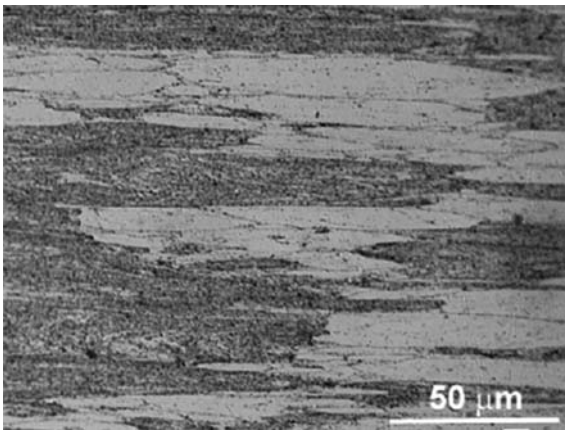

Fig. 19.13 The bimodal microstructure developed in Al-Mg alloys, through mixing the unmilled powder with cryomilled powder. The gray is the micrometer-sized grain area and the dark is the nanograined region. An optimized strength and ductility can be achieved when the gray area reaches 30% volume fraction. The image is from Ref. [76].

77] to improve tensile ductility in nanostructured Al-Mg alloys. The bimodal heterogeneous structure was achieved by mixing different volume fractions (15–30 wt.%) of unmilled submicrometer-grained powder with cryomilled (ball milling at 77 K) NC powder. After hot consolidation, the products were extruded to eliminate porosity and poor bonding. An optical micrograph of such a bimodal microstructure is shown in Fig. 19.13. The dark areas are cryomilled NS regions and the gray areas are unmilled ones. The grain size in the nanostructured region and micrometer-sized region is 100–300 nm and 1 μm, respectively. Figure 19.14 reveals an increased tensile ductility with increasing fraction of the micrometer-grained material, disobeying the simple rule of mixture. A good combination of tensile strength and ductility was achieved when the micrometer-grained regions reached 30% [75].

The use of bimodal or multimodal microstructures is likely to be a valuable approach to develop useful materials based on nanostructures. By adjusting the volume fraction, size, shape, and distributions of coarse grains, one has ample room and opportunities to tailor the mechanical properties of nanostructured materials, to optimize strength, ductility, or a combination of both. Note that a porosity-free highly uniform nanocrystalline grain structure is not only extremely difficult to process but also not necessary or beneficial for properties and structural applications. In fact, for most nanocrystalline metals that showed ductility, the microstructures usually contained a certain fraction of larger grains. Even though the number fraction of these large grains may be small, their volume fraction can be sufficiently high to influence the plastic deformation behavior. In a more generic case, the large grains can also be ductile second phase,

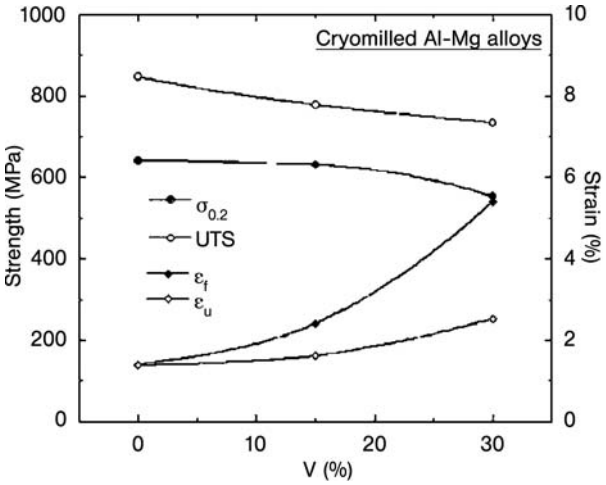

Fig. 19.14 The tensile strength and ductility as a function of submicrometer grain sizes for the bimodal structure shown in Fig. 19.13. The ductility does not follow the simple rule of mixture.

particles, or dendrite structure, which will act as roadblocks for shear localizations or crack propagation [78]. The success of such an approach has recently been documented in pure nanostructured metals [74], alloys [77, 78], and metallic glasses [79].

19.6.2 Growth Twins

A twin boundary is a special kind of grain boundary that can effectively impede the motion of dislocations and increase the strength of the material. A twin boundary also allows nonglissile partial dislocations to deposit on its twin plane and accommodates plastic strain. In addition, the twin lamellar structure may be viewed as inherently bimodal (see discussion in Section 19.6.1), because the length scale parallel to twin boundaries is significantly larger than the nanoscale twin lamellar width (harder direction or the direction perpendicular to twin boundaries). Dislocations can accumulate and form tangles, cutting the twin ribbons into cells.

High-density growth twins can be produced using electrodeposition by increasing the current density and lowering the temperature during the deposition. Figure 19.15 shows a transmission electron micrograph of nanotwinned copper in the as-synthesized condition. Growth twins are visible in all grains. Even though the grain sizes are $\sim$500 nm on average, the grains are further subdivided into twin/matrix lamellar structures with nanoscale (a few to a few hundred nm) twin-boundary spacing. The density of the twins is adjustable by modifying the electrodeposition parameters. Figure 19.16 shows that the nano-

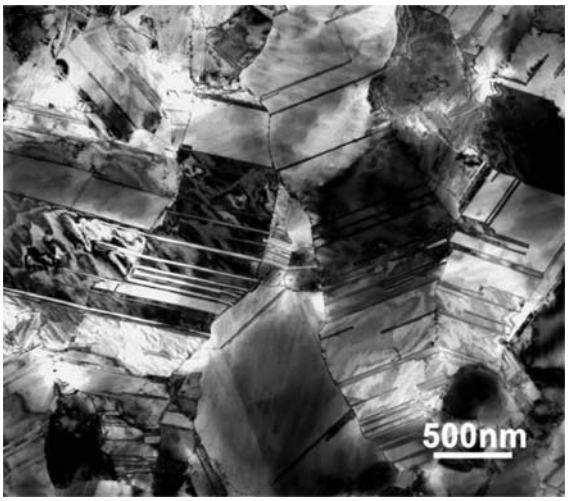

Fig. 19.15 Transmission electron micrograph of a nanotwinning Cu, showing a high density of growth twins inside submicrometer-sized grains. The material was prepared through electrodeposition. By adjusting the deposition parameters, different twin densities can be achieved.

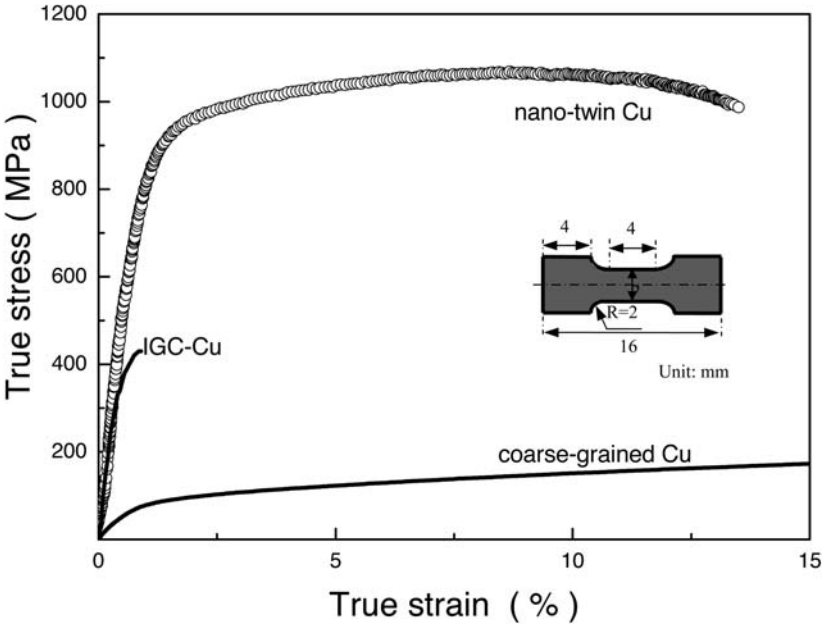

Fig. 19.16 Tensile properties of nanotwinned Cu shown in Fig. 19.15. The strong nanotwinned copper has a yield stress of 900 MPa, and a tensile elongation to failure of 13.5% [48].

twinned Cu has a tensile strength of 1070 MPa and an elongation to failure of 13.5% [48]. The strong strain hardening persists to rather large strains. It is further observed that both the tensile strength and tensile ductility increased with increasing twin density. A similar hardness increase was reported in sputter-deposited 330 stainless-steel thin films [80]. The twin spacing in these stainless steel films is as small as about 4 nm. However, there was no mention of tensile ductility in these films.

19.6.3 Deformation at Low Temperature and/or High Strain Rates

It is known for conventional fcc polycrystalline materials that their yield strength is not sensitive to temperature and strain rate, whereas their strain-hardening rate is. When nanostructured, however, an elevated strain-rate sensitivity and small activation volume are observed at room temperature in fcc metals [38, 39]. This is indicative of a change of thermally activated deformation processes in these nanostructured materials. By deforming nanostructured materials at low temperature and/or high strain rates [81], the dynamic recovery can be suppressed. The material gains the ability to work harden and, as a result, uniform and overall tensile elongation is improved, together with an elevated strength at cryogenic temperature. A high density of dislocations is accumulated when an ECAP Cu is deformed at cryogenic temperatures [81], as shown in Fig. 19.17. Some deformation twins are also observed.

The strategy of using low-temperature deformation to derive higher ductility may be applicable mostly to ultrafine-grained materials. For truly nanocrystal-

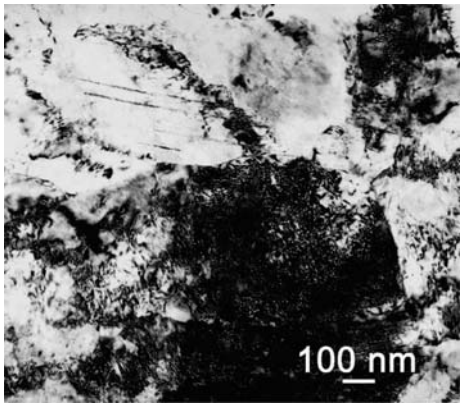

Fig. 19.17 High density of dislocations is observed to accumulate in an ECAP Cu (~300 nm) after being deformed at 77 K. The deformation twins are also visible. Low-temperature deformation helps to suppress dynamic recovery and thus improve the tensile ductility of nanostructured metals.

line materials, a very high strength is observed at cryogenic temperatures (such as 77 K). But the dislocation activities and its storage may not be sufficient to give rise to a high enough strain rate in such small grains.

19.6.4
Taking Advantage of Elevated Strain-rate Sensitivity

To date, there have been only a limited number of experiments, all of which are in nanostructured Cu, that take advantage of the elevated strain-rate sensitivity to stabilize the nearly uniform tensile deformation and thus enhance the tensile ductility. This strategy is based on Hart's criterion that if a metal has a larger value of m, necking can be delayed and thus near-uniform tensile elongation can be extended to larger strains. As discussed in Section 19.5, the strain-rate sensitivity of nanostructured materials is dependent on strain rate (Fig. 19.7). For example, an ECAP Cu was observed to have an m value of 0.025 when deformed at the strain rate of 6×10^{-7} s^{-1}, and 0.010 when the strain rate is 1×10^{-4} s^{-1} [52]. A near elastic-perfectly plastic behavior with a uniform tensile strain of $\sim$12% was observed when this nanostructured Cu was tested at the strain rate of 6×10^{-7} s^{-1} [52]. Champion et al. [82] observed similar nearly uniform plastic strains in the absence of work hardening, at a similarly low strain rate in another nanostructured Cu prepared through a powder metallurgy process, possibly due to the same reason.

In one special case, an m value as large as 0.14 was reported at room temperature in an ECAP Cu after 16 passes [83]. The average grain size of this material was 100 nm. Tensile results revealed a very large tensile elongation to failure of over 50%. It is postulated that the unusually high strain-rate sensitivity originated from the nonequilibrium grain-boundary structures that led to considerable grain-boundary deformation processes.

Based on our previous discussions, a moderately enhanced value of strain-rate sensitivity is commonly achieved in fcc nanostructured materials. This effect may become more pronounced when the grain size is reduced to well below 30 nm. Computer simulations have indeed predicted that at grain sizes below 10 nm, grain-boundary sliding and diffusional mechanisms could take control of the plastic deformation, leading to m values in the range of 0.5–1.0. Such high values of m will obviously be useful in terms of achieving high tensile ductility (or even superplasticity) in nanostructured materials. So far, this has not materialized for NS metals at or near room temperature.

19.6.5
Other Possible Approaches

Some nanostructured materials, ECAP ones in particular, bear similarity to heavily cold-worked samples; it is conceivable that annihilation and recovery of stored dislocations through proper heat treatment could help to regain strain hardening in these metals and thus achieve a higher value of tensile elongation.

Thermal annealing could also help to optimize the nonequilibrium grain-boundary structures and improve the mechanical properties. Note that high-temperature annealing is not an option in this situation, as excessive grain growth will occur. A concurrent increase of strength and ductility after low temperature annealing has been indeed seen in several ECAP metals [59].

The high strength and high ductility have also been achieved in certain nanostructured aluminum alloys, through long-time aging treatments. For example, the precipitation-hardened Al-Ag nanostructured alloys can achieve optimized strength and high tensile ductility by introducing intermediate metastable phases into ultrafine-grained microstructures [84].

Recently, several truly nanocrystalline metals also exhibited decent tensile ductility [23, 45, 47, 85]. Li and Ebrahimi [85] reported that without using plating additives, a nanocrystalline Ni-Fe ($\sim$9 nm) showed 8% tensile elongation to failure and 2.2 GPa strength. In another report by Erb et al. [47], nanocrystalline cobalt ($\sim$12 nm) was shown to exhibit $\sim$9% tensile strain and 2.2 GPa fracture strength. Perhaps more impressive are the results of Youssef et al. [45] in an *in-situ* consolidated nanocrystalline pure Cu (23 nm), showing tensile ductility of 14% and a fracture strength as high as 1.1 GPa. One common feature of all these nanocrystalline materials is the high quality of the samples. Currently, the strain-hardening mechanisms of these truly nanocrystalline materials are not well understood but clearly worth further investigations. Nonetheless, these examples suggest that there are practical paths to simultaneously achieve high strength and high ductility in truly nanocrystalline materials.

19.7 Temperature Dependence

The mechanical strength and ductility of nanostructured materials, as already discussed above, depend strongly on temperature. The rapid increase of the strain-rate sensitivity (discussed in Section 19.5) with increasing temperatures opens new opportunities for (superplastic) forming of nanostructured materials at relatively low temperatures or high strain rates. It is known that superplastic materials typically require an m value of 0.3 or larger and that grain-boundary sliding is an important deformation mechanism during superplasticity. The large volume fraction of grain boundaries in nanostructured materials is conducive to such superplastic formability. To date, a large number of nanostructured metals and alloys have been found to exhibit superplastic behavior at moderately elevated temperatures (low homologous temperatures) [86, 87].

In addition, the mechanical properties of ECAP Cu, Ti, and Fe at cryogenic temperature (77 K) were investigated [88]. These findings are summarized in Fig. 19.18. At 77 K, all three crystal structures show ultrahigh strength that is not expected from the simple extrapolation of the coarse-grained materials. In particular, the ratios of the yield strength for nanostructured Cu (and Ti) at 77 K and RT are much higher than those of the coarse-grained counterpart. This

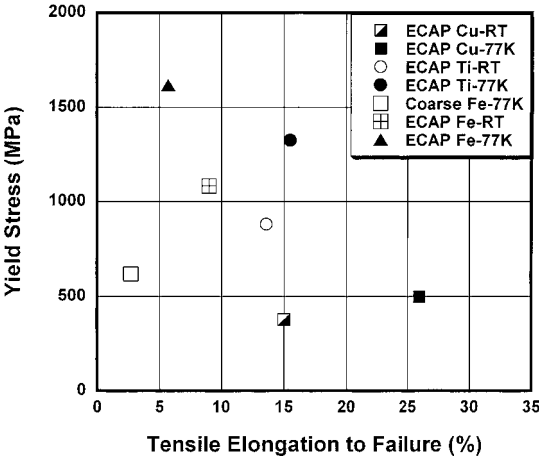

Fig. 19.18 Summary of tensile strength and ductility observed in ECAP Cu (full square, half square), Ti (circle), and Fe (open square, crossed square, triangle). The data of room temperature are the crossed square and open circle. The others are of 77 K. For reference, the tensile data of a coarse-grained Fe deformed 77 K is also included (triangle). The excellent combination of strength and ductility of nanostructured materials is evident at cryogenic temperatures.

temperature dependence of the yield strength is believed to be associated with the small activation volume measured in these materials. A similar elevation of strength was also observed in electrodeposited NC Ni [34, 38] and IGC Cu [89]. For bcc nanostructured Fe, a much larger tensile elongation to failure was observed at 77 K, in contrast to that bordering brittle behavior for the coarse-grained counterparts [88]. The ultrahigh strength and high ductility at cryogenic temperature suggest that some NS materials could be useful for low-temperature processing and load-bearing applications.

19.8 Deformation Modes

The unique mechanical behavior of nanostructured materials arises from their unusual deformation mechanisms that often differ from the coarse-grained counterparts. The research on deformation mechanisms of bulk NS metals has been primarily focused on the materials with the grain size below ~ 30 nm. This is motivated by the conviction that a mechanism change would occur in the regime of such small grain sizes. Because of the difficulties in producing quality samples with such small grain sizes, molecular dynamic simulations have far outpaced the experiments in the search for mechanism changes [90]. The subject of molecular dynamic simulations of NC metals has recently been reviewed by Wolf et al. [90]. A number of deformation mechanisms have been proposed from such simulations. Some are verified by experimental investiga-

tions, while others remain debatable. In the following, we will make a brief survey on experimental findings pertaining to deformation modes and mechanisms of NC metals.

Twinning is a viable deformation mode in conventional materials. Since the critical stress for twinning is higher than for slip at small grain sizes, twinning is not expected to be a major deformation mode in nanocrystalline materials. Therefore, the discovery of deformation twinning [91–93] in high stacking-fault energy ($\sim$160 mJ/m^2 [94]) nanocrystalline aluminum has triggered a considerable debate over the applicability of the traditional twinning model in the NS regime [88]. The deformation twinning has also been revealed in a variety of other nanocrystalline metals, including Cu [95], Ni [96], Pd [97], Ta [21], and Al-Mg alloys [98]. In addition to the grain-size effect, it is now more or less accepted that deformation conditions have a strong impact on the twinning mechanism [96]. As twinning requires high nucleation stress, a high strain rate and/or a low deformation temperature are the deformation conditions that favor the formation of mechanical twins. One point to be emphasized here, however, is that the activation of twinning by no means excludes the dislocation mechanisms, which may well be active down to the grain size of 10 nm [45].

Because of low strain-hardening capacity and reduced strain-rate sensitivity, shear banding has been documented as one of the important deformation modes, especially in some bcc nanostructured metals. Following the earlier work of Carsley et al. [99], Jia et al. [56] reported shear banding in consolidated nanostructured Fe with an average grain size of 80–300 nm. Careful transmission electron microscopy (TEM) examinations revealed that the grains in the shear localization zone are highly elongated and decorated with dislocations [100], Fig. 19.19. The shear localization has also been observed in an *in-situ* consolidated nanocrystalline Cu [23] and an ECAP W [101].

As the grain size approaches 10 nm, it is believed that the dislocation mechanism becomes increasingly difficult and the grain-boundary-based processes could take over for the plastic deformation in nanocrystalline metals [36, 40]. *In-situ* TEM experiments on thin foils of NC Ni with an average grain size of 10 nm showed that grain rotation and/or grain-boundary sliding became an important mode of deformation [41]. However, the question remains as to whether these *in-situ* TEM observations are representative of bulk behavior.

In some cases, the deformation of nanocrystalline metals is accompanied by stress-assisted concomitant grain growth. This could become a concern when nanocrystalline metals are deformed under highly localized stresses and/or high strains. The indentation-induced grain growth has been seen in nanocrystalline Cu and Al [102, 103]. In another observation, electrodeposited Ni subjected to high pressure torsion also showed grain-growth behavior [104]. The stress-assisted grain growth in nanocrystalline metals has only been documented very recently. It is not clear yet when and how this process is coupled with stresses and plastic deformation in nanocrystalline metals.

The wide spectrum of deformation behavior documented so far suggests that the deformation mechanism of nanocrystalline materials is not yet fully under-

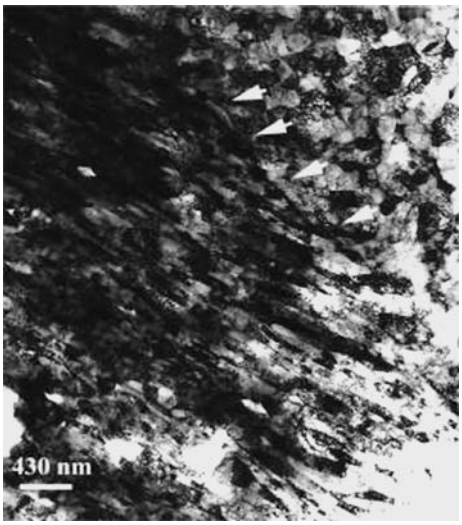

Fig. 19.19 Shear banding observed in nanostructured Fe from Ref. [100]. The grains are elongated and decorated with dislocations inside shear bands.

stood. This situation is in part due to the various preparation procedures applied to produce nanocrystalline materials, which lead to variations in internal structures such as grain-size distribution (albeit perhaps the same average grain size), impurities (batch dependent) [63], nanovoids (difficult to detect) [105], and so forth. Accurate determination of the average grain size and its distribution represents a significant experimental challenge in the analysis of the H–P relationship. Comparisons of grain-size distributions obtained from TEM and X-ray line-profiling measurements indicate that the difference can be substantial [106]. In addition, the grain-boundary structures can be vastly different in the nanostructured materials prepared by different methods [59]. Further experimental studies on well-characterized model systems are needed to paint a clearer and more complete picture than the one we have so far. Computer modeling capable of handling less-idealized microstructures (e.g., with flaws and impurities) will also bring us a step closer to a better understanding of the experimental observations.

19.9 Concluding Remarks

The macroscopic deformation behavior of bulk nanostructured materials (including nanocrystalline and ultrafine-grained materials) are briefly surveyed, with emphasis on their principal mechanical properties, including tensile/compressive strength, strain hardening, strain rate and temperature dependence,

and tensile ductility. Our focus is on the effect of the grain size on the intrinsic and general mechanical response of nanostructured metals, without paying detailed attention to subtle microstructural differences in these materials.

In line with expectations, the strength of nanostructured materials is observed to be very high. Their relatively low ductility is due in part to the lack of sufficient strain hardening and strain-rate hardening. There are cases, however, where the tensile ductility is surprisingly high. Contrasting behavior has been observed with regard to strain-rate sensitivity in fcc and bcc NS metals. Deformation temperature has been found to be an important parameter affecting strength and ductility. To improve tensile ductility, a number of strategies have been proposed in the literature. The applications of these approaches to different material systems have generated some fruitful results.

To obtain the benefit of the high strength of nanostructured materials, a thorough understanding of their deformation modes is imperative but also challenging. The divergence of experimental evidence on deformation behavior suggests that despite years of research, a consensus on the deformation mechanisms of nanostructured materials has not yet been reached. However, recent progress on several different fronts has begun to paint a unifying picture of the deformation physics of NS metals. Advances in characterization tools and computational simulations are needed to aid future progress in this field.

Acknowledgements

The authors are grateful for the help of Dr. B.Q. Han of UC Davis, Dr. L. Lu of Institute of Metal Research in China, and Prof. Q. Wei of University of North Carolina in providing some original figures used in this article.

References

1 J. R. Weertman **2002**, in: Koch C, (ed.) *Nanostructured Materials*, Noyes Publications, Norwich, NY, p. 393–417.
2 H. Gleiter **1989**, *Prog. Mater. Sci.* 33, 223–315.
3 S. H. Kim, K. T. Aust, U. Erb, F. Gonzalez, G. Palumbo **2003**, *Scr. Mater.* 48, 1379–1384.
4 N. Wang, Z. R. Wang, K. T. Aust, U. Erb **1997**, *Mater. Sci. Eng. A* 237, 150–158.
5 H. Gleiter **1995**, *Nanostruct. Mater.* 6, 3–14.
6 E. Ma **2003**, *Scr. Mater.* 49, 663–668.
7 C. C. Koch **2003**, *Scr. Mater.* 49, 657–662.
8 P. G. Sanders, J. A. Eastman, J. R. Weertman **1997**, *Acta Mater.* 45, 4019–4025.
9 C. C. Koch, D. G. Morris, K. Lu, A. Inoue **1999**, *MRS Bull.* 24, 54–58.
10 J. R. Weertman, D. Farkas, K. J. Hemker, H. Kung, M. Mayo, R. Mitra, H. van Swygenhoven **1999**, *MRS Bull.* 24, 44–50.
11 R. Z. Valiev, R. K. Islamgaliev, I. V. Alexandrov **2000**, *Prog. Mater. Sci.* 45, 103–189.
12 C. Suryanarayana **2005**, *Adv. Eng. Mater.* 7, 983–992.
13 P. G. Sanders, J. A. Eastman, J. R. Weertman **1998**, *Acta Mater.* 46, 4195–4202.
14 C. Suryanarayana, C. C. Koch **2000**, *Hyperfine Interact.* 130, 5–44.
15 G. D. Hibbard, J. L. McCrea, G. Palumbo, K. T. Aust, U. Erb **2002**, *Scr. Mater.* 47, 83–87.

16 L. Lu, M. L. Sui, K. Lu **2000**, *Science* 287, 1463–1466.
17 H. Q. Li, F. Ebrahimi **2003**, *Acta Mater.* 51, 3905–3913.
18 H. Iwasaki, K. Higashi, T. G. Nieh **2004**, *Scr. Mater.* 50, 395–399.
19 B. Y. C. Wu, P. J. Ferreira, C. A. Schuh **2005**, *Metall. Mater. Trans. A* 36, 1927–1936.
20 Y. M. Wang, K. Wang, D. Pan, K. Lu, K. J. Hemker, E. Ma **2003**, *Scr. Mater.* 48, 1581–1586.
21 Y. M. Wang, A. M. Hodge, J. Biener, A. V. Hamza, D. E. Barnes, K. Liu, T. G. Nieh **2005**, *Appl. Phys. Lett.* 86, 101915.
22 K. M. Youssef, R. O. Scattergood RO, K. L. Murty, C. C. Koch **2004**, *Appl. Phys. Lett.* 85, 929–931.
23 S. Cheng, E. Ma, Y. M. Wang, L. J. Kecskes, K. M. Youssef, C. C. Koch, U. P. Trociewitz, K. Han **2005**, *Acta Mater.* 53, 1521–1533.
24 J. A. Knapp, D. M. Follstaedt **2004**, *J. Mater. Res.* 19, 218–227.
25 F. A. Mohamed, Y. Li **2001**, *Mater. Sci. Eng. A* 298, 1–15.
26 G. W. Nieman, J. R. Weertman, R. W. Siegel **1991**, *J. Mater. Res.* 6, 1012–1027.
27 V. Kristic, U. Erb, G. Palumbo **1993**, *Scr. Metall. Mater.* 29, 1501–1504.
28 T. D. Shen, C. C. Koch, T. Y. Tsui, G. M. Pharr **1995**, *J. Mater. Res.* 10, 2892–2896.
29 G. He, J. Eckert, Q. L. Dai, M. L. Sui, W. Loser, M. Hagiwara, E. Ma **2003**, *Biomater.* 24, 5115–5120.
30 A. H. Chokshi, A. Rosen, J. Karch, H. Gleiter **1989**, *Scr. Metall.* 23, 1679–1984.
31 G. D. Hughes, S. D. Smith, C. S. Pande, H. R. Johnson, R. W. Armstrong **1986**, *Scr. Metall.* 20, 93–97.
32 G. W. Nieman, J. R. Weertman, R. W. Siegel **1989**, *Scr. Metall.* 23, 2013–2018.
33 U. Erb **1995**, *Nanostruct. Mater.* 6, 533–538.
34 F. Ebrahimi, G. R. Bourne, M. S. Kelly, T. E. Matthews **1999**, *Nanostruct. Mater.* 11, 343–350.
35 C. A. Schuh, T. G. Nieh, T. Yamasaki **2002**, *Scr. Mater.* 46, 735–740.
36 J. Chen, L. Lu, K. Lu **2006**, *Scr. Mater.* 54, 1913–1918.
37 J. Schiotz, F. D. Di Tolla, K. W. Jacobsen **1998**, *Nature* 391, 561–563.
38 Y. M. Wang, E. Ma **2004**, *Appl. Phys. Lett.* 85, 2750–2752.
39 Y. M. Wang, A. V. Hamza, E. Ma **2006**, *Acta Mater.* 54, 2715–2726.
40. J. Schiotz, K. W. Jacobsen **2003**, *Science* 301, 1357–1359.
41 Z. W. Shan, E. A. Stach, J. M. K. Wiezorek, J. A. Knapp, D. M. Follstaedt, S. X. Ma **2004**, *Science* 305, 654–657.
42 E. Ma **2004**, *Science* 305, 623–624.
43 P. G. Sanders, C. J. Youngdahl, J. R. Weertman **1997**, *Mater. Sci. Eng. A* 234, 77–82.
44 B. E. Schuster, Q. Wei, H. Zhang, K. T. Ramesh **2006**, *Appl. Phys. Lett.* 88, 103112.
45 K. M. Youssef, R. O. Scattergood, K. L. Murty, J. A. Horton, C. C. Koch **2005**, *Appl. Phys. Lett.* 87, 091904.
46 A. C. Lund, T. G. Nieh, C. A. Schuh **2004**, *Phys. Rev. B* 69, 012102.
47 A. A. Karimpoor, U. Erb, K. T. Aust, G. Palumbo **2003**, *Scr. Mater.* 49, 651–656.
48 L. Lu, Y. F. Shen, X. H. Chen, L. H. Qian, K. Lu **2004**, *Science* 304, 422–426.
49 F. Ebrahimi, Z. Ahmed, H. Li **2004**, *Appl. Phys. Lett.* 85, 3749–3751.
50 E. Ma, Y. M. Wang, Q. H. Lu, M. L. Sui, L. Lu, K. Lu **2004**, *Appl. Phys. Lett.* 85, 4932–4934.
51 X. Zhang, H. Wang, R. O. Scattergood, J. Narayan, C. C. Koch, A. V. Sergueeva, A. K. Mukherjee **2002**, *Appl. Phys. Lett.* 81, 823–825.
52 Y.M. Wang, E. Ma **2004**, *Acta Mater.* 52, 1699–1709.
53 M. J. Caturla, T. G. Nieh, J. S. Stolken **2004**, *Appl. Phys. Lett.* 84, 598–600.
54 Y. M. Wang, E. Ma **2004**, *Mater. Sci. Eng. A* 375–377, 46–52.
55 D. Jia, Y. M. Wang, K. T. Ramesh, E. Ma, Y. T. Zhu, R. Z. Valiev **2001**, *Appl. Phys. Lett.* 79, 611–613.
56 D. Jia, K. T. Ramesh, E. Ma **2003**, *Acta Mater.* 51, 3495–3509.
57 Y. M. Wang, S. Cheng, Q. M. Wei, E. Ma, T. G. Nieh, A. V. Hamza **2004**, *Scr. Mater.* 51, 1023–1028.
58 J. R. Weertman, P. G. Sanders **1994**, *Solid State Phenom.* 35–36, 249–262.
59 R. Z. Valiev, A. V. Sergueeva, A. K. Mukherjee **2003**, *Scr. Mater.* 49, 669–674.

60 Q. Wei, S. Cheng, K. T. Ramesh, E. Ma **2004**, *Mater. Sci. Eng. A* 381, 71–79.
61 L. Lu, R. Schwaiger, Z. W. Shan, M. Dao, K. Lu, S. Suresh **2005**, *Acta Mater.* 53, 2169–2179.
62 G. T. Gray, T. C. Lowe, C. M. Cady, R. Z. Valiev, I. V. Aleksandrov **1997**, *Nanostruct. Mater.* 9, 477–480.
63 F. Dalla Torre, H. Van Swygenhoven, M. Victoria **2002**, *Acta Mater.* 50, 3957–3970.
64 H. Tanimoto, S. Sakai, H. Mizubayashi **1999**, *Nanostruct. Mater.* 12, 751–756.
65 B. Cai, Q.P. Kong, P. Cui, L. Lu, K. Lu **2001**, *Scr. Mater.* 45, 1407–1413.
66 J. May J, H. W. Hoppel, M. Goken **2005**, *Scr. Mater.* 53, 189–194.
67 S. X. McFadden, A. P. Zhilyaev, R. S. Mishra, A. K. Mukherjee **2000**, *Mater. Lett.* 45, 345–349.
68 R. Schwaiger, B. Moser, M. Dao, N. Chollacoop, S. Suresh **2003**, *Acta Mater.* 51, 5159–5172.
69 K. S. Kumar, H. Van Swygenhoven, S. Suresh **2003**, *Acta Mater.* 51, 5743–5774.
70 A. Hasnaoui, H. Van Swygenhoven, P.M. Derlet **2003**, *Science* 300, 1550–1552.
71 E. W. Hart **1967**, *Acta Metall.* 15, 351–355.
72 Y. M. Wang, E. Ma, M. W. Chen **2002**, *Appl. Phys. Lett.* 80, 2395–2397.
73 R. J. Asaro, S. Suresh **2005**, *Acta Mater.* 53, 3369–3382.
74 Y. M. Wang, M. W. Chen, F. H. Zhou, E. Ma **2002**, *Nature* 419, 912–915.
75 D. B. Witkin, Z. Lee, S. R. Nutt, E. J. Lavernia **2003**, *Scr. Mater.* 49, 297–302.
76 B. Q. Han, E. J. Lavernia, F. A. Mohamed **2005**, *Rev. Adv. Mater. Sci.* 9, 1–16.
77 D. B. Witkin, E. J. Lavernia **2006**, *Prog. Mater. Sci.* 51, 1–60.
78 G. He, J. Eckert, W. Loser, L. Schultz **2003**, *Nature Mater.* 2, 33–37.
79 C. Fan, R. T. Ott, T. C. Hufnagel **2002**, *Appl. Phys. Lett.* 81, 1020–1022.
80 X. Zhang, A. Misra, H. Wang, M. Nastasi, J. D. Embury, T. E. Mitchell, R. G. Hoagland, J. P. Hirth **2004**, *Appl. Phys. Lett.* 84, 1096–1098.
81 Y. M. Wang, E. Ma **2003**, *Appl. Phys. Lett.* 83, 3165–3167.
82 Y. Champion, C. Langlois, S. Guerin-Mailly, P. Langlois, J. L. Bonnentien, M. J. Hytch **2003**, *Science* 300, 310–311.
83 R. Z. Valiev, I. V. Alexandrov, Y. T. Zhu, T. C. Lowe **2002**, *J. Mater. Res.* 17, 5–8.
84 Z. Horita, K. Ohashi, T. Fujita, K. Kaneko, T. G. Langdon **2005**, *Adv. Mater.* 17, 1599–1602.
85 H. Li, F. Ebrahimi **2004**, *Appl. Phys. Lett.* 84, 4307–4309.
86 S. X. Mcfadden, R. S. Mishra, R. Z. Valiev, A. P. Zhilyaev, A. K. Mukherjee **1999**, *Nature* 398, 684–686.
87 S. V. Dobatkin, E. N. Bastarache, G. Sakai, T. Fujita, Z. Horita, T. G. Langdon **2005**, *Mater. Sci. Eng. A* 408, 141–146.
88 Y. M. Wang, E. Ma, R. Z. Valiev, Y. T. Zhu **2004**, *Adv. Mater.* 16, 328–331.
89 Z. Huang, L. Y. Gu, J. R. Weertman **1997**, *Scr. Mater.* 37, 1071–1075.
90 D. Wolf, V. Yamakov, S. R. Phillpot, A. Mukherjee, H. Gleiter **2005**, *Acta Mater.* 53, 1–40.
91 M. W. Chen, E. Ma, K. J. Hemker, H. W. Sheng, Y. M. Wang, X. M. Cheng **2003**, *Science* 300, 1275–1277.
92 X. Z. Liao, F. Zhou, E. J. Lavernia, D. W. He, Y. T. Zhu **2003**, *Appl. Phys. Lett.* 83, 5062–5064.
93 X. Z. Liao, F. Zhou, E. J. Lavernia, S. G. Srinivasan, M. I. Baskes, D. W. He, Y. T. Zhu **2003**, *Appl. Phys. Lett.* 83, 632–634.
94 M. A. Meyers, A. Mishra, D. J. Benson **2006**, *Prog. Mater. Sci.* 51, 427–556.
95 X. Z. Liao, Y. H. Zhao, S. G. Srinivasan, Y. T. Zhu, R. Z. Valiev, D. V. Gunderov **2004**, *Appl. Phys. Lett.* 84, 592–594.
96 X. L. Wu, E. Ma **2006**, *Appl. Phys. Lett.* 88, 061905.
97 H. Rosner, J. Markmann, J. Weissmuller **2004**, *Philos. Mag. Lett.* 84, 321–334.
98 X. Z. Liao, J. Y. Huang, Y. T. Zhu, F. Zhou, E. J. Lavernia **2003**, *Philos. Mag.* 83, 3065–3075.
99 J. E. Carsley, W. W. Milligan, S. A. Hackney, E. C. Aifantis **1995**, *Metall. Trans. A* 26, 2479–2481.
100 Q. Wei, D. Jia, K. T. Ramesh, E. Ma **2002**, *Appl. Phys. Lett.* 81, 1240–1242.

101 Q. Wei, K. T. Ramesh, E. Ma, L. J. Kesckes, R. J. Dowding, V. U. Kazykhanov, R. Z. Valiev **2005**, *Appl. Phys. Lett.* 86, 101907.

102 K. Zhang K, J. R. Weertman, J. A. Eastman **2005**, *Appl. Phys. Lett.* 87, 061921.

103 M. Jin, A. M. Minor, E. A. Stach, J. W. Morris **2004**, *Acta Mater.* 52, 5381–5387.

104 X. Z. Liao, A. R. Kilmametov, R. Z. Valiev, H. S. Gao, X. D. Li, A. K. Mukherjee, J. F. Bingert, Y. T. Zhu **2006**, *Appl. Phys. Lett.* 88, 021909.

105 S. Van Petegem, F. Dalla Torre, D. Segers, H. Van Swygenhoven **2003**, *Scr. Mater.* 48, 17–22.

106 G. W. Nieman, J. R. Weertman **1991**, in: *The Morris E. Fine Symposium*, The Minerals, Metals and Materials Society, Warrendale, PA.

20
Superplasticity of Bulk Nanostructured Materials

Terence G. Langdon

20.1
Principles of Superplasticity

When metallic specimens are pulled in tension, they generally fracture after relatively small amounts of ductility. However, some materials are capable of exhibiting superplastic behavior in which the samples pull out uniformly without failure and ultimately break at very high tensile elongations. This phenomenon of superplasticity is the basis for the superplastic forming industry in which complex shapes are formed from sheet metals for use in applications ranging from aerospace and transportation to architectural decorations.

It is now recognized that two requirements must be fulfilled in order to achieve superplastic ductilities [1]. First, the grain size of the material must be very small and typically less than $\sim$10 μm. Second, since superplastic flow is a diffusion-controlled process, the temperature of deformation must be sufficiently high that diffusion rates are reasonably rapid. This means in practice that the temperatures associated with superplasticity are at and above $\sim 0.5\ T_m$ where T_m is the absolute melting temperature of the material.

It is standard practice in the superplastic forming industry to achieve a superplastic-forming capability in sheet metals by using appropriate thermomechanical treatments in which the materials are subjected to predetermined schedules of annealing, ageing and mechanical processing. However, this treatment leads to average grain sizes lying typically within the range of $\sim$1–10 μm and it is generally not feasible to achieve grain refinement to the submicrometer level. Accordingly, the processing of metals by severe plastic deformation (SPD) and the consequent refining of grain sizes to the submicrometer range provides a unique opportunity for attaining ultrafine grain sizes that are approximately one order of magnitude smaller than those achieved in conventional practice. It is important to first examine the implication of this reduction in grain size.

When materials deform under conditions of high-temperature creep, the steady-state strain rate, $\dot{\varepsilon}$, varies both with the applied stress, σ, through a power-law relationship in which the stress is raised to a stress exponent of n and inversely with the grain size raised to a power of p. For conventional creep

Bulk Nanostructured Materials. Edited by M. J. Zehetbauer and Y. T. Zhu

ISBN: 978-3-527-31524-6

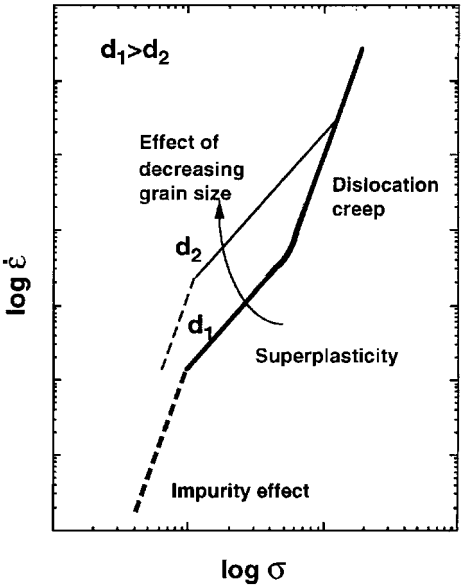

Fig. 20.1 Schematic illustration of strain rate versus stress on a double-logarithmic plot showing the effect of decreasing the grain size from d_1 to d_2.

by dislocation processes within the grains, termed dislocation creep, the value of n is typically ~ 5 and there is no dependence on grain size so that $p=0$ [2], whereas in the superplastic regime it is well established, both experimentally [3] and theoretically [4], that the strain rate varies with stress raised to a power of 2 and inversely with grain size raised to a power of 2 [4]. Figure 20.1 shows a schematic illustration of the variation of strain rate with stress in a double-logarithmic plot. Thus, at high stresses flow occurs by dislocation creep with $n \approx 5$ but at lower stresses the flow falls within the superplastic regime and $n=2$ and at even lower stresses there is usually an impurity effect where n again is close to ~5: this latter region (termed region I in superplasticity) is associated with grain-boundary impurities that inhibit the movement of dislocations in grain-boundary sliding and the region may be removed by using samples of exceptionally high purity [5, 6]. The lower line delineates the behavior of a material with a grain size of d_1 and the upper line shows the effect of decreasing the grain size to a smaller value of d_2. Thus, in the superplastic region where $p=2$, and also in region I where there is a similar dependence on grain size, the curve moves upwards to higher strain rates, whereas the region of dislocation creep remains unaffected because $p=0$. This means in practice that the superplastic regime is displaced to higher strain rates when the grain size is decreased.

The effect of this displacement on the elongation to failure is depicted schematically in the semilogarithmic plot in Fig. 20.2 where the elongation to failure is plotted against the strain rate for the two grain sizes of d_1 and d_2. Thus, decreasing the strain rate displaces the peak ductility to higher strain rates and, in addition, the anticipated elongations to failure are now higher because less time

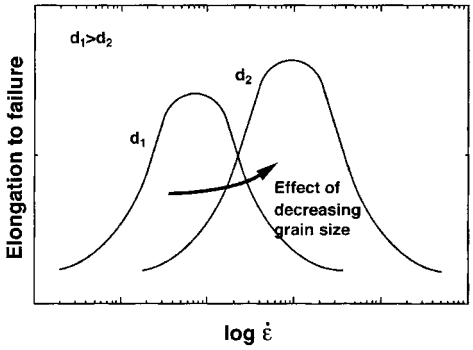

Fig. 20.2 Elongation to failure versus strain rate showing the peak elongations within the superplastic regime and the displacement to higher strain rates when the grain size is reduced.

is available for the diffusive growth of internal cavities and the consequent breaking of the material through cavitation failure.

The ability to achieve superplastic ductilities at higher strain rates has important implications for the superplastic forming industry. Currently, superplastic metals are formed industrially within the strain-rate range of $\sim 10^{-3}$ to 10^{-2} s^{-1} so that the forming time for each separate component is of the order of ~20–30 min; but if the grain size is reduced by one order of magnitude through SPD processing, it follows that, since the strain rate is proportional to $(1/d)^2$, the optimum strain-rate range will increase to $\sim 10^{-1}$–1 s^{-1} and the individual forming times will be reduced to <60 s. Formally, superplasticity occurring at strain rates at and above 10^{-2} s^{-1} is termed *high strain-rate superplasticity* [7] and it is apparent that SPD processing and the production of bulk nanostructured metals has the potential of achieving very rapid superplastic flow and thereby substantially reducing the forming times in industrial operations. This reduction in forming time implies also a potential for expanding the industrial use of the superplastic forming technology into high-volume applications as in the automotive and consumer-product industries. Accordingly, the purpose of this chapter is to examine recent progress in achieving these objectives.

20.2
Achieving Superplasticity after SPD Processing

The possibility of achieving high strain-rate superplasticity after SPD processing, and thus rapid industrial superplastic forming, was first proposed in 1996 in a report noting that equal-channel angular pressing (ECAP) and high-pressure torsion (HPT) should both have the capability of producing ultrafine-grained materials capable of exceptionally rapid superplastic flow [8]. This proposal was followed in 1997 by the first report documenting the occurrence of high strain-rate superplasticity in two commercial aluminum-based alloys where, after processing by ECAP, elongations of up to >1000% were achieved without failure within the regime of high strain-rate superplasticity [9]. Follow-

ing this early report, there have been several subsequent demonstrations of both the occurrence of superplastic flow at very rapid strain rates after SPD processing and the potential for achieving remarkably high elongations to failure in these ultrafine-grained materials. For example, there are numerous reports describing the use of ECAP to achieve tensile elongations of >2000% in several aluminum alloys [10–18], in the ZK60 magnesium alloy [19, 20] and in the Zn-22% Al eutectoid alloy [21]. These results confirm the potential for utilizing SPD processing in achieving exceptional superplastic ductilities with the as-processed ultrafine microstructures.

To examine this potential in more detail, it is worthwhile considering some of the experimental results reported when testing an Al-3% Mg-0.2% Sc alloy that was fabricated in the laboratory by casting and solution treated to give an initial grain size of ~200 μm [10–13]. Samples were processed by ECAP at room temperature using a die with an angle of $\Phi = 90^\circ$ between the two parts of the channel and a pressing speed of ~19 mm s^{-1}. Each sample was processed through a total of 8 passes to give an imposed strain of ~8 [22] and the samples were rotated by 90° in the same sense between each pass in the procedure known as processing route B_C [23]. This processing gave a grain size of ~0.2 μm.

Following SPD processing, tensile specimens were machined parallel to the pressing direction and Fig. 20.3 shows the variation of the maximum flow stress with the imposed strain rate at a testing temperature of 673 K [10]. These results show that the strain-rate sensitivity, m, is close to ~0.5 in the intermediate range of strain rates, where this is equivalent to a stress exponent of $n = 1/m \approx 2$, which suggests the occurrence of superplastic flow at strain rates in the vicinity of ~10^{-2}–10^{-1} s^{-1}. This is confirmed in Fig. 20.4, which shows the specimens after testing to failure over strain rates from 1.0×10^{-4} to 3.3 s^{-1} where the upper specimen is untested. The remarkably high elongation of 2280% at an imposed strain rate of 3.3×10^{-2} s^{-1} confirms the occurrence of high strain-rate superplasticity in this alloy.

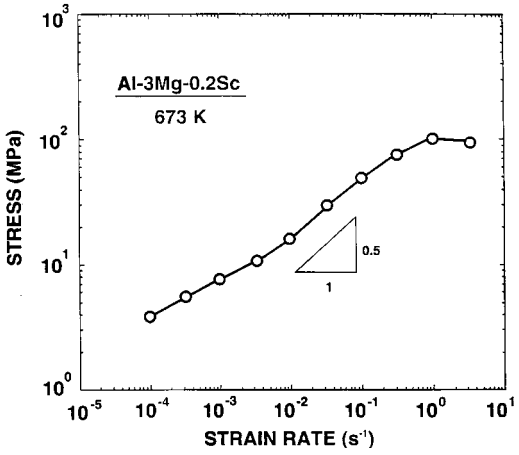

Fig. 20.3 Flow stress versus strain rate for the Al-3% Mg-0.2% Sc alloy at 673 K showing the occurrence of an intermediate region where the strain-rate sensitivity is ~ 0.5 [10].

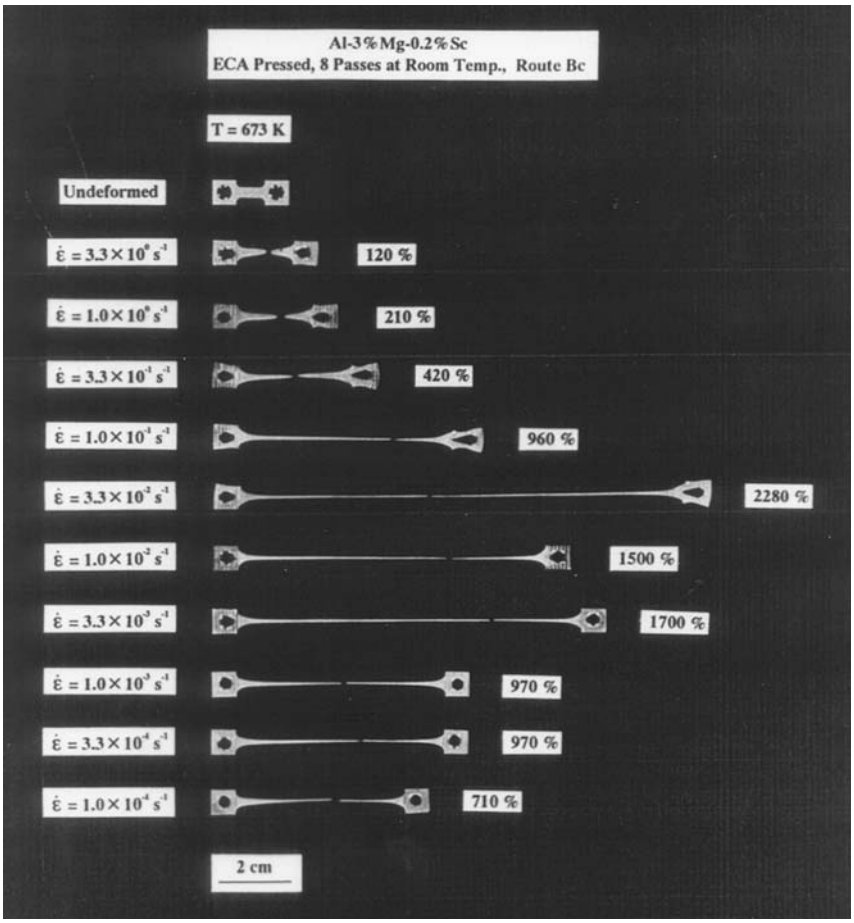

Fig. 20.4 Tensile specimens of the Al-3% Mg-0.2% Sc alloy after pulling to failure over a range of strain rates at 673 K: the upper specimen is untested [10].

In practice, the superplastic elongations achieved after processing by ECAP are dependent upon the precise nature of the pressing operation. This is illustrated in Fig. 20.5 where experimental results are shown for a commercial Al-1420 Al-5.5% Mg-2.2% Li-0.12% Zr alloy with an initial grain size of $\sim$400 μm. This alloy was processed by ECAP under two different conditions: (a) using route B_C for a total of 4 passes at 673 K to give a grain size of $\sim$1.3 μm and (b) using route B_C for a total of 8 passes at 673 K and, in order to minimize grain growth during pressing, an additional 4 passes at 473 K to give a grain size of $\sim$0.8 μm [24]. In Fig. 20.5, the upper open points show results obtained at temperatures from 573 to 723 K using the as-pressed samples for these two pressing conditions and the lower closed points show the results obtained for the unpressed alloy when testing at 603 K. Thus, this commercial alloy exhibits re-

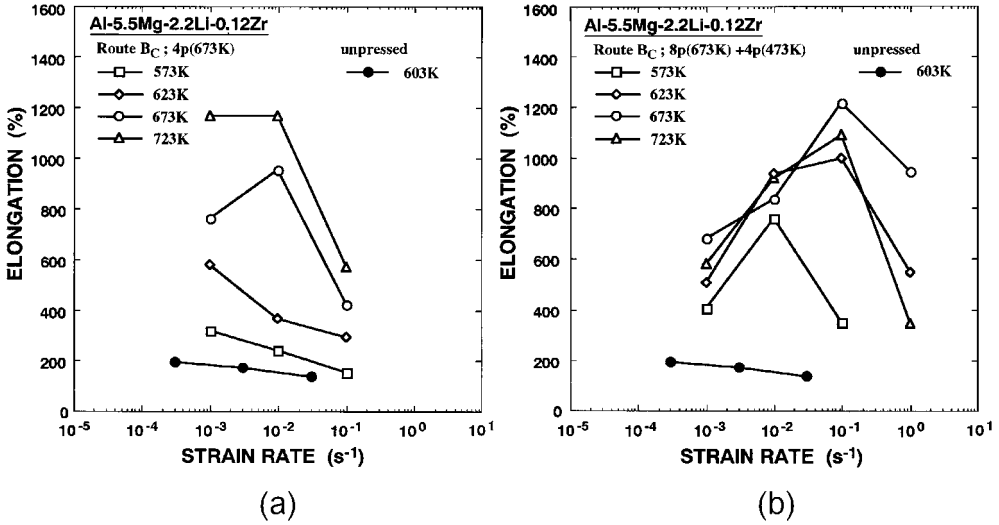

Fig. 20.5 Elongation to failure versus strain rate for an Al-5.5% Mg-2.2% Li-0.12% Zr alloy over temperatures from 573 to 723 K after (a) 4 passes of ECAP at 673 K and (b) 8 passes of ECAP at 673 K and an additional 4 passes at 473 K: the lower closed points are for the unpressed alloy at 603 K [24].

markable superplastic properties after processing by ECAP including elongations to failure of >1000% and, in Fig. 20.5 (b), exceptionally high elongations even at strain rates of 10^{-1} and 1 s^{-1}. The displacement of the curves to higher strain rates in Fig. 20.5 (b) is due in a minor way to the smaller grain size achieved after 12 passes of ECAP but primarily it arises because of the evolution of the microstructure with increasing numbers of passes through the die. It is well established in materials such as pure aluminum that the fraction of high-angle grain boundaries introduced by ECAP increases with increasing strain [25]. Since high-angle boundaries are a necessary prerequisite for grain-boundary sliding, and sliding and the relative displacements of adjacent grains represent the flow mechanism in superplasticity [26], it follows that the pressing of materials through a larger numbers of passes in ECAP leads to microstructures that are more conducive to the occurrence of grain-boundary sliding and thus to the advent of superplastic flow.

Although the pressing of face-centered cubic metals is generally relatively easy, the successful pressing, and especially the attainment of superplastic elongations, becomes more difficult in hexagonal close-packed systems where there are only a limited number of slip systems. In cast pure magnesium, for example, early experiments showed a reduction in the grain size only from ~400 μm to ~120 μm when pressing through 3 passes of ECAP at 673 K [27]. However, it is possible to obtain good grain refinement and superplastic properties in magnesium-based alloys by making use of a two-step process of extrusion followed by ECAP [28]. This two-step procedure, designated by the acronym

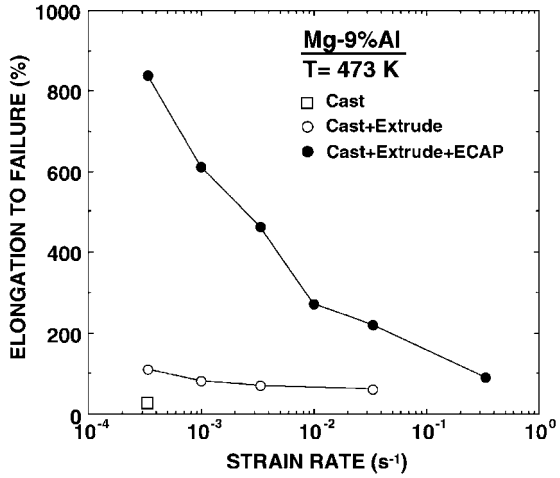

Fig. 20.6 Elongation to failure versus strain rate for a Mg-9% Al alloy in the cast condition, after casting and extrusion and after casting and EX-ECAP [29].

EX-ECAP, was used successfully with several Mg-based alloys and Fig. 20.6 shows an example of the superplastic behavior achieved in a Mg-9% Al alloy where results are shown for the cast alloy, the cast and extruded alloy and the alloy in the cast and EX-ECAP condition [29]. Thus, the latter procedure leads to superplastic flow that is otherwise absent, with a maximum elongation of up to >800% under optimum conditions. A similar result was achieved also using EX-ECAP with a Mg-7.5% Al-0.2% Zr alloy [30].

20.3
Achieving a Superplastic-forming Capability

The results described in the preceding section show that SPD processing can be used to achieve superplastic elongations in tensile testing in the laboratory but it does not provide a direct confirmation that it is possible also to achieve a superplastic-forming capability. Accordingly, the potential for using this approach for forming operations was addressed using two different but complementary procedures.

First, it was shown in Fig. 20.4 that the Al-3% Mg-0.2% Sc alloy exhibits excellent superplastic behavior at strain rates of the order of 10^{-1} s^{-1} when testing at a temperature of 673 K. This suggests, therefore, that the as-pressed material should be capable of easy and rapid forming when heated to this temperature. To check this hypothesis, small disks were cut from an as-pressed billet and they were inserted into a biaxial gas-pressure forming facility, heated to 673 K and then subjected to a constant pressure of argon gas for short but controlled

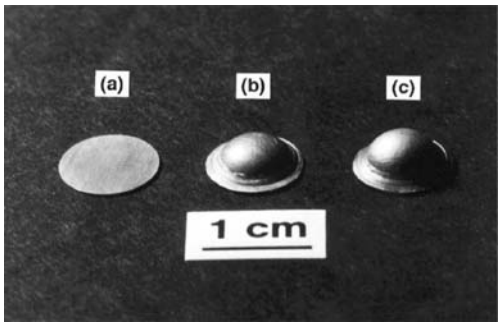

Fig. 20.7 Domes formed in an Al-3% Mg-0.2% Sc alloy by imposing an argon gas pressure after ECAP: the disk at (a) is untested and the other disks were subjected to a pressure for periods of (b) 30 s and (c) 60 s [10].

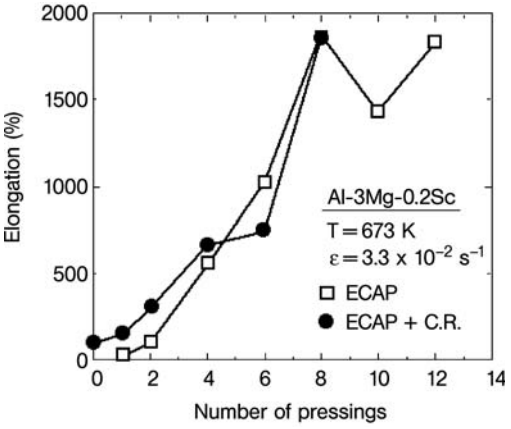

Fig. 20.8 Elongation to failure versus number of passes in ECAP for an Al-3% Mg-0.2% Sc alloy at 673 K after ECAP and after ECAP plus cold rolling (CR) [31].

periods of time. The result is shown in Fig. 20.7 where the disk marked (a) is untested and the disks marked (b) and (c) were subjected to a gas pressure of 10 atm, equivalent to 1 MPa, for periods of (b) 30 s and (c) 60 s [10]. Thus, it is apparent that the as-pressed material blows out readily under this relatively low pressure and thus the forming capability of the alloy is excellent.

Secondly, and noting that the industrial superplastic forming industry uses sheet metals for their forming operations, it is necessary to take as-pressed billets and cold roll these into sheets to determine whether the superplastic capabilities are retained after the rolling operation. The result from this type of procedure is shown in Fig. 20.8 where the elongations to failure are plotted against the number of passes through the die for samples of the Al-Mg-Sc alloy tested at a strain rate of 3.3×10^{-2} s^{-1} at 673 K after ECAP and after ECAP plus cold rolling (CR) [31]. These results confirm that there is no loss in the superplastic characteristics if the as-pressed samples are rolled into sheets after pressing, thereby suggesting that the grain boundaries retain their high angles of misorientation during the subsequent rolling operation. Very recent results suggest that a better procedure may be to press the samples to strains that are below the optimum superplastic condition and then to cold roll these into a sheet

[32, 33]. Using this approach, increased elongations to failure were achieved in a modified Al-5154 alloy containing 0.13% Sc when the rolling reductions were >70%. All of these results confirm, therefore, the potential for producing superplastic sheet metals using appropriate combinations of ECAP and cold rolling.

20.4
Cavitation in Superplasticity after SPD Processing

It was demonstrated in very early experiments on superplastic alloys that internal cavities develop when materials pull out to very high elongations [34] and this led to numerous investigations of the role of cavitation in superplastic flow [35]. However, there is only one detailed report to date describing quantitative measurements of the cavity shapes and sizes occurring in the tensile testing of samples after processing by ECAP [36]. In this work, a commercial Al-7034 alloy containing Al-11.5% Zn-2.5% Mg-0.9% Cu-0.20% Zr was fabricated by spray casting to produce an alloy with a grain size of $\sim$2.1 μm and the alloy was pressed in ECAP for different numbers of passes using route B_C at 473 K to give a grain size of $\sim$0.3 μm after 6 and 8 passes [37, 38]. This alloy is attractive for investigations of superplasticity because the ultrafine grains are reasonably stable at elevated temperatures due to the presence of MgZn2 and Al3Zr precipitates [39].

Figure 20.9 shows the variation of the elongation to failure with the imposed strain rate for specimens tested in tension at 673 K where the closed points denote the as-received alloy and the open points are for the samples pressed through 1, 2, 6 and 8 passes at 473 K [39]. It is apparent that elongations of >1000% are achieved after ECAP through 6 and 8 passes and, as shown earlier in Fig. 20.5 for the Al-Mg-Li-Zr alloy, the peak elongation is displaced to a high-

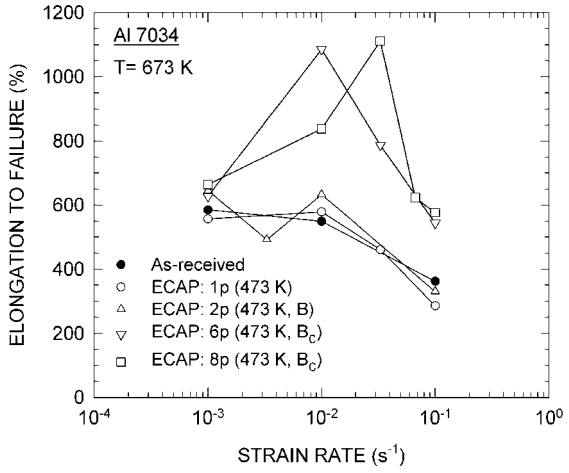

Fig. 20.9 Elongation to failure versus strain rate for an Al-7034 alloy at 673 K after pressing through 1, 2, 6 and 8 passes of ECAP: the closed points show data for the as-received unpressed alloy [39].

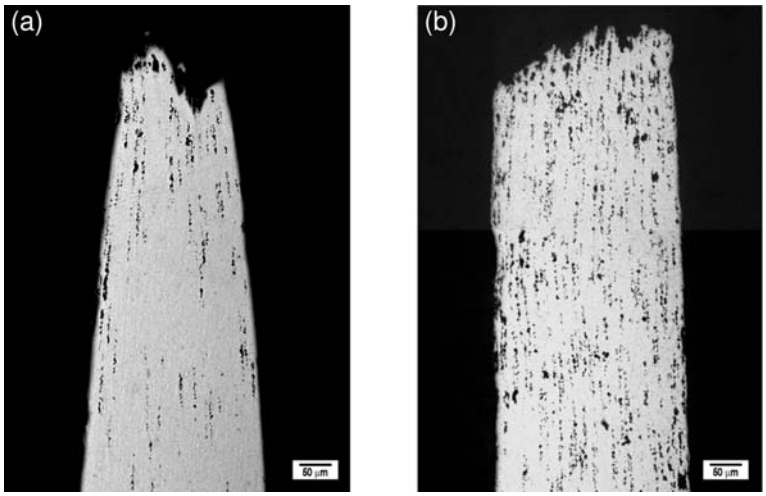

Fig. 20.10 The appearance of the fracture tips of specimens of the Al-7034 alloy after pulling to failure at 673 K at a strain rate of 1.0×10^{-2} s^{-1}: the specimen at (a) is in the as-received unpressed condition and the specimen at (b) was pressed in ECAP for 6 passes at 473 K [36].

er strain rate when the samples are pressed through larger numbers of passes. There is an important difference in the macroscopic failure behavior of the as-received and the as-pressed material and this difference is visible from inspection of the fracture tips in Fig. 20.10 where both specimens were tested at 673 K at an initial strain rate of 1.0×10^{-2} s^{-1} but the sample in (a) is for the as-received condition where the specimen failed at an elongation of ~550% and the sample in (b) is for the as-pressed condition after 6 passes of ECAP where the sample failed at an elongation of ~1085% [36]. Thus, both specimens reveal the development of internal cavitation during the tensile testing with the formation of stringers of cavities aligned approximately along the tensile axes but the as-received material fails prematurely by necking, whereas the sample processed by ECAP exhibits typical cavity interlinkage where failure occurs without any macroscopic necking: it is well known that the latter behavior is characteristic of many conventional superplastic alloys [40].

When cavities form in superplastic nanostructured materials, they may grow either by the diffusion of vacancies into the cavities in the superplastic diffusion growth process [41] or by deformation in the surrounding crystalline lattice through the plasticity-controlled growth process [42]. These two mechanisms lead to different cavity shapes because superplastic diffusion growth gives cavities that are essentially spherical, whereas in plasticity-controlled growth the cavities pull out and become elongated along the tensile axis. This difference can be measured quantitatively by recording the values of the roundness coefficient for each individual cavity, where a roundness coefficient equal to 1.0 corresponds to a circular cavity and the values become increasingly lower than 1 as

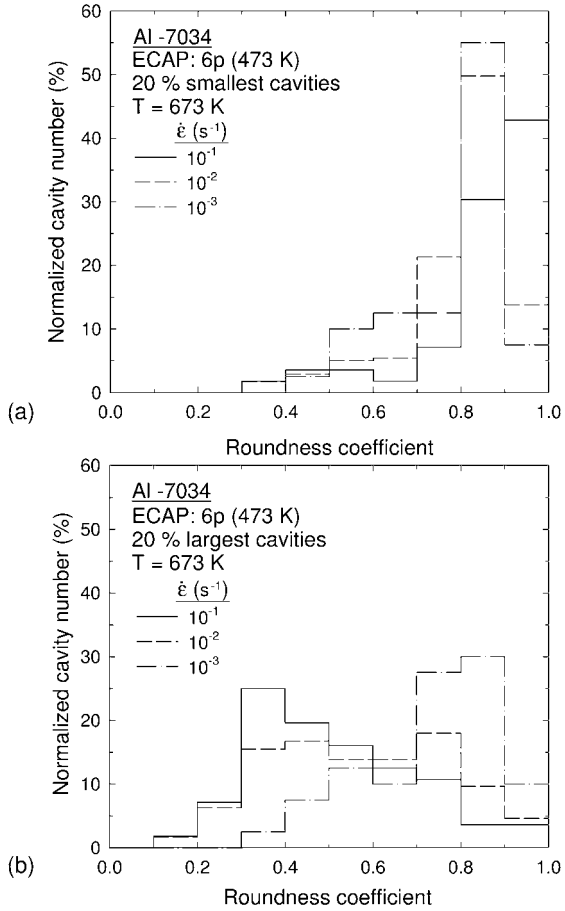

Fig. 20.11 Values of the roundness coefficient in samples of the Al-7034 alloy processed by ECAP for 6 passes at 473 K and then pulled to failure at 673 K at strain rates from 10^{-3} to 10^{-2} s^{-1}: (a) data for the 20% smallest cavities and (b) data for the 20% largest cavities [36].

the cavity further deviates from a circular shape. To obtain a reasonable analysis of quantitative measurements, it is convenient to divide the cavity population into two separate groups. Thus, Fig. 20.11 shows data for the 20% of smallest cavities in (a) and for the 20% of largest cavities in (b), where information is given for three specimens of the Al-7034 alloy processed by ECAP through 6 passes at 473 K and then tested to failure at 673 K at strain rates of 10^{-1}, 10^{-2} and 10^{-3} s^{-1}, respectively. It is readily apparent from inspection of Fig. 20.11 that in (a) the smallest cavities tend to have a rounded appearance with peak values of the roundness coefficient >0.8 whereas in (b) the largest cavities are elongated and this elongation is especially visible when testing at the fastest strain rate of 10^{-1} s^{-1}. These results provide a direct confirmation for a change

in the cavity growth process from superplastic diffusion growth at the smaller cavity radii to plasticity-controlled growth at the larger radii [36].

20.5
Future Prospects for Superplasticity in Nanostructured Materials

The early prediction that the ultrafine grains introduced by SPD processing would lead to excellent superplastic properties [8], including the occurrence of superplastic flow at very rapid strain rates, has been fulfilled by the very extensive experimental data now available documenting the occurrence of superplasticity in a number of different alloy systems. Furthermore, there are numerous clear demonstrations that the superplastic effect is achieved in these nanostructured materials at strain rates that are significantly faster than those in conventional micrometer-grained materials. Nevertheless, it is important to recognize that superplasticity can be achieved only in those materials where the ultrafine grain sizes introduced through processing remain small and reasonably stable at the temperatures needed to attain diffusion-controlled plastic flow. This means in practice that superplastic flow is not easily achieved in pure metals or solid solution alloys where the grains grow rapidly when heated to high temperatures. All of the examples of superplasticity given in this chapter refer either to alloys where precipitates are available to inhibit grain-boundary movement (as in the Al-3% Mg-0.2% Sc alloy) or two phases are present to prevent easy grain growth (as in the Zn-22% Al eutectoid alloy). With favorable materials, the extent of superplastic deformation is often remarkable: for example, elongations of up to >2300% without failure were achieved at a strain rate of $1\ s^{-1}$ in the Zn-22% Al alloy [21]. All of these results suggest, therefore, that SPD processing can play a very significant role in providing useful materials for superplastic forming operations.

More work is now needed to obtain a thorough understanding of the superplastic process in bulk nanostructured materials. For example, there are only two experimental reports to date describing measurements taken using surface marker lines in order to estimate the importance of grain-boundary sliding within the superplastic regime [43, 44] and both of these experiments confirm the importance of sliding as the dominant flow process. There is also only a single recent report where any attempt was made to correlate the experimental data directly with a theoretical model for superplasticity [45]. Undoubtedly, much more work will now develop along these lines to provide a reasonably complete understanding of the factors influencing the superplastic flow processes in these bulk nanostructured solids.

References

1 T.G. Langdon **1982**, *Metall. Trans. A* 13A, 689–702.
2 T.G. Langdon **2005**, *Z. Met.kd.* 96, 522–531.
3 A. Ball, M.M. Hutchison **1969**, *Met. Sci. J.* 3, 1–6.
4 T.G. Langdon **1994**, *Acta Metall. Mater.* 42, 2437–2443.
5 P.K. Chaudhury, F.A. Mohamed **1988**, *Acta Mater.* 36, 1099–1110.
6 S. Yan, J.C. Earthman, F.A. Mohamed **1994**, *Philos. Mag. A* 69, 1017–1038.
7 K. Higashi, M. Mabuchi, T.G. Langdon **1996**, *ISIJ Int.* 36, 1423–1438.
8 Y. Ma, M. Furukawa, Z. Horita, M. Nemoto, R.Z. Valiev, T.G. Langdon **1996**, *Mater. Trans. JIM* 37, 336–339.
9 R.Z. Valiev, D.A. Salimonenko, N.K. Tsenev, P.B. Berbon, T.G. Langdon **1997**, *Scr. Mater.* 37, 1945–1950.
10 Z. Horita, M. Furukawa, M. Nemoto, A.J. Barnes, T.G. Langdon **2000**, *Acta Mater.* 48, 3633–3640.
11 S. Komura, Z. Horita, M. Furukawa, M. Nemoto, T.G. Langdon **2000**, *J. Mater. Res.* 15, 2571–2576.
12 S. Komura, Z. Horita, M. Furukawa, M. Nemoto, T.G. Langdon **2001**, *Metall. Mater. Trans. A* 32A, 707–716.
13 S. Komura, M. Furukawa, Z. Horita, M. Nemoto, T.G. Langdon **2001**, *Mater. Sci. Eng.* A297, 111–118.
14 F. Musin, R. Kaibyshev, Y. Motohashi, G. Itoh **2004**, *Scr. Mater.* 50, 511–516.
15 F. Musin, R. Kaibyshev, Y. Motohashi, G. Itoh **2004**, *Metall. Mater. Trans. A* 35A, 2383–2392.
16 V.M. Perevezentsev, V.N. Chuvil'deev, A.N. Sysoev, V.I. Kopylov, T.G. Langdon **2003**, *Problems Mater. Sci.* N1(33), 400–408.
17 V.N. Perevezentsev, V.N. Chuvil'deev, A.N. Sysoev, V.I. Kopylov, T.G. Langdon **2002**, *Phys. Met. Metall.* 94, Suppl. 1, S 45–S53.
18 R. Kaibyshev, K. Shipilova, F. Musin, Y. Motohashi **2005**, *Mater. Sci. Tech.* 21, 408–418.
19 R. Lapovok, R. Cottam, P. Thomson, Y. Estrin **2005**, *J. Mater. Res.* 20, 1375–1378.
20 R. Lapovok, P.F. Thomson, R. Cottam, Y. Estrin **2005**, *Mater. Sci. Eng. A* 410–411, 390–393.
21 S.M. Lee, T.G. Langdon **2001**, *Mater. Sci. Forum* 357–359, 321–326.
22 Y. Iwahashi, J. Wang, Z. Horita, M. Nemoto, T.G. Langdon **1996**, *Scr. Mater.* 35, 143–146.
23 M. Furukawa, Y. Iwahashi, Z. Horita, M. Nemoto, T.G. Langdon **1998**, *Mater. Sci. Eng. A* 257, 328–332.
24 S. Lee, P.B. Berbon, M. Furukawa, Z. Horita, M. Nemoto, N.K. Tsenev, R.Z. Valiev, T.G. Langdon **1999**, *Mater. Sci. Eng. A* 272, 63–72.
25 S.D. Terhune D.L. Swisher, K. Oh-ishi, Z. Horita, T.G. Langdon, T.R. McNelley **2002**, *Metall. Mater. Trans. A* 33, 2173–2184.
26 T.G. Langdon **1994**, *Mater. Sci. Eng. A* 174, 225–230.
27 A. Yamashita, Z. Horita, T.G. Langdon **2001**, *Mater. Sci. Eng. A* 300, 142–147.
28 Z. Horita, K. Matsubara, K. Makii, T.G. Langdon **2002**, *Scr. Mater.* 47, 255–260.
29 K. Matsubara, Y. Miyahara, Z. Horita, T.G. Langdon **2003**, *Acta Mater.* 51, 3073–3084.
30 Y. Miyahara, K. Matsubara, Z. Horita, T.G. Langdon **2005**, *Metall. Mater. Trans. A* 36, 1705–1711.
31 H. Akamatsu, T. Fujinami, Z. Horita, T.G. Langdon **2001**, *Scr. Mater.* 44, 759–764.
32 K.T. Park, H.J. Lee, C.S. Lee, W.J. Nam, D.H. Shin **2004**, *Scr. Mater.* 51, 479–483.
33 K.T. Park, H.J. Lee, C.S. Lee, D.H. Shin **2005**, *Mater. Sci. Eng. A* 393, 118–124.
34 H. Ishikawa, D.G. Bhat, F.A. Mohamed, T. G. Langdon **1977**, *Metall Trans. A* 8, 523–525.
35 X.G. Jiang, J. Earthman, F.A. Mohamed **1994**, *J. Mater. Sci.* 29, 5499–5514.
36 M. Kawasaki, C. Xu, T.G. Langdon **2005**, *Acta Mater.* 53, 5353–5364.
37 C. Xu, M. Furukawa, Z. Horita, T.G. Langdon, **2003** *Acta Mater.* 51, 6139–6148.
38 C. Xu, W. Dixon, M. Furukawa, Z. Horita, T.G. Langdon **2003**, *Mater. Lett.* 57, 3588–3592.

39 C. Xu, M. Furukawa, Z. Horita, T. G. Langdon **2005**, *Acta Mater.* 53, 749–758.
40 T. G. Langdon **1982**, *Met. Sci.* 16, 175–183.
41 A. H. Chokshi, T. G. Langdon **1987**, *Acta Metall.* 35, 1089–1101.
42 J. W. Hancock **1976**, *Met. Sci.* 10, 319–325.
43 R. K. Islamgaliev, N. F. Yunusova, R. Z. Valiev, N. K. Tsenev, V. N. Perevezentsev, T. G. Langdon **2003**, *Scr. Mater.* 49, 467–472.
44 P. Kumar, C. Xu, T. G. Langdon **2005**, *Mater. Sci. Eng. A* 410–411, 447–450.
45 N. Balasubramanian, T. G. Langdon **2005**, *Mater. Sci. Eng. A* 410–411, 476–479.

21
Fracture and Crack Growth in Bulk Nanostructured Materials

Ruth Schwaiger, Benedikt Moser, and Timothy Hanlon

21.1
Introduction

Bulk forms of nanostructured metals and alloys exhibit extraordinarily high strength and their mechanical properties have been studied extensively for a few decades. Many attractive features of nanostructured metals, such as high strength, high hardness, and improved wear and corrosion resistance compared to conventional coarse-grained metals, will likely be rendered futile if the damage tolerance of these materials does not meet a certain level that is acceptable for a particular application. Most studies, though, focused on the high yield strength and the Hall–Petch behavior, whereas experimental investigations on the evolution of damage and the fracture behavior of nanostructured materials have been limited in scope and quantity. This is due to the fact that efforts to synthesize nanostructured materials into sizable bulk forms have had limited success so far. Due to the paucity of experimental data, the validity of trends extracted from larger-grained materials to bulk nanostructured materials is largely unknown.

The difficulties associated with characterizing the fracture properties of bulk nanostructured materials of relatively uniform purity and grain size mainly stem from current limitations in the processing of specimens of good quality with sufficient dimensions for "valid" testing. This pertains to fracture under monotonic loads as well as to crack growth under the application of cyclic loads. Processing methods such as electrodeposition or electron-beam deposition, which are used to produce fully dense nanostructured materials with uniform purity and of small grain size (< 100 nm), typically yield thin foils of only a few hundred micrometers in thickness. Experimental difficulties related to the mechanical testing of such small thickness specimens are not only problems in gripping the test specimen but also imposing controlled loads and stress states without experimental artifacts such as out-of-plane bending or buckling of the specimen. Also, due to the small thickness of the specimens, the applied loading may represent plane stress states since the plastic zone size at the tip of the crack is comparable to or larger than the specimen thickness. These problems

Bulk Nanostructured Materials. Edited by M. J. Zehetbauer and Y. T. Zhu

ISBN: 978-3-527-31524-6

can be overcome by severe plastic deformation (SPD) methods, such as equal-channel angular pressing (ECAP) techniques and high-pressure torsion (HPT). These methods provide materials of sufficient volume but a main drawback is that they produce microstructures with pronounced variations in grain size (ranging from 50 nm to 500 nm) and grain structure as well as high density of crystal lattice defects. This makes it difficult to use such materials for studying fundamental fracture mechanisms and the correlation between structure and damage tolerance.

In this chapter, we will focus on the fracture behavior of bulk nanostructured metals and alloys and review findings from investigations on fracture and crack growth behavior in recent years. We will critically discuss the available data and elaborate on the problems that are related with fracture experiments in BNMs. This includes free-standing nanocrystalline foils of several hundreds of micrometers thickness but not thin films, which are also often considered to behave like bulk material as long as their thickness is significantly larger than the grain size. In general, "nanoscale" is defined as being of dimensions of less than 100 nm. We will use the term "nanostructured" or "nanocrystalline" for metals and alloys with an average grain size and also a range of grain sizes smaller than 100 nm, since the properties of nanostructured metals are very sensitive not only to the average grain size but also to the distribution of grain sizes. In some places, we will also describe results obtained on larger-grained samples, that is ultrafine crystalline, with grain sizes in the range of 100–1000 nm. The results highlighted primarily deal with face-centered cubic (fcc) materials because the majority of available results on this topic pertain to this class of metals; however, references to other crystal structures are included, wherever available. This article is broadly divided into three major sections: (1) fracture toughness, (2) fracture mechanisms, (3) crack growth.

21.2
Fracture Toughness

Fracture-toughness measurements are critical to assess the potential of BNMs as structural materials but are difficult to perform due to the limited availability of high-quality nanostructured materials. Hence, the specimen geometry required by the testing standards often cannot be fulfilled. To the best of our knowledge, no plane strain fracture-toughness values from truly nanocrystalline and dense pure metals are available in the open literature. This is related to the fact that no truly nanocrystalline and dense material with sufficient size in all three dimensions is available to perform standardized tests, such as single edge notched beam tests, compact tension tests, or chevron notch tests and to compare the results with conventional metals.

Mirshams et al. [1] studied the fracture behavior of electrodeposited pure nanocrystalline Ni and electrodeposited carbon-doped nanocrystalline Ni. Thin sheets (220–350 μm) in the shape of small compact tension specimens were

tested with a special antibuckling fixture. The crack-opening displacement was measured using a clip-on extensometer. Crack-mouth opening displacement curves and crack-growth resistance curves have been given for the as-deposited material as well as annealed Ni sheets. However, the validity of the fracture-toughness values is difficult to judge as no information on total crack length is given in the paper. Further, given the small thickness of the specimens, it is evident that large-scale yielding was present in these experiments. This certainly precludes the use of linear elastic fracture mechanics (LEFM) for the extraction of fracture-toughness values, which may exhibit thickness-dependent behavior. As no plane strain conditions are found at the crack front, the crack-growth resistance values that are presented cannot be seen and compared with conventional fracture-toughness values, K_{Ic}. It can, however, be said from the available data presented by Mirshams et al. [1] that annealing reduces the toughness of the electrodeposits significantly.

Materials produced with methods other than electrodeposition often suffer from some deficiencies. Either the density is significantly smaller than 100% and the material contains pores, or the grain size is not uniform and the material contains a few larger grains (>100 nm) that dominate the deformation behavior, or the defect density (the dislocation density, for instance) is extremely high. Morris-Munoz et al. [2] produced nanocrystalline FeAl by ball milling and hot compacting a mixture of the elemental powders. Below 40 nm grain size, they found both the fracture toughness and the hardness to decrease significantly with decreasing grain size; the fracture toughness decreased from more than 12 MPa $m^{1/2}$ for 40 nm grain size to about 5 MPa $m^{1/2}$ for 20 nm grain size, while the hardness decreased from HV = 650 to HV = 490 in the same grain size range as determined from Vickers hardness testing with a 300 g load. It is not clear whether the reduction in fracture toughness is due to poor powder consolidation or related to strain localization and/or lack of work hardening. However, the samples tested exhibited flaws on the order of 300 μm in size, which makes it very likely that strength and toughness were controlled by the quality of the specimens.

Another binary alloy with grain sizes in the ultrafine crystalline and microcrystalline range has been investigated by Morris and Leboeuf [3]. They produced TiAl alloys by compaction of atomized and ball-milled powders. Grain sizes ranged from 80 μm to 200 nm. Fracture-toughness tests were done using a three-point bend test. The values for K_{Ic} decreased monotonically with (grain size)$^{-1/2}$, whereas hardness and yield stress were found to increase with (grain size)$^{-1/2}$. Tensile fracture was transgranular for conventionally hot isostatically pressed specimens with grain sizes between 40 and 80 μm, but was intergranular for grain sizes below 10 μm.

Han et al. [4] produced an Al-7.5%Mg alloy by cryomilling commercially pure Al powders and high-Mg Al alloy powders. The cryomilled powders were consolidated by hot isostatic pressing; the remaining porosity was removed by extrusion. The average grain size of this material was approximately 260 nm with some small dispersoid particles of 5 to 10 nm in size. Fracture toughness was

measured using notched 3-point bend specimens and K_{Ic} was around 8 MPa $m^{1/2}$ for the as-extruded material. Annealing the material for 2.5 h at 773 K increased the size of some grains to 550 nm, while large areas remained fine grained. In this case, the fracture-toughness values more than doubled to about 17 MPa $m^{1/2}$. Annealing for 23 h resulted in a fully recrystallized microstructure with a grain size of 550 nm, but K_{Ic} remained at 17 MPa $m^{1/2}$. The increase in fracture toughness was accompanied by a slight decrease in yield strength and an almost three-fold increase in elongation at failure (14%).

With respect to density and grain size, nanocrystalline metals produced by crystallization of amorphous metals are comparable to electrodeposited nanocrystalline metals. Gan and Zhou [5, 6] annealed amorphous $(Fe_{0.99}Mo_{0.01})_{78}Si_9B_{13}$ ribbons to produce a fully dense and fully crystallized metal with a grain size of the α-Fe phase between 11 and 35 nm. The dimensions of the ribbon were 8 mm × 30 mm × 25 μm. A hole was then laser drilled in the center of the specimen; several radial cracks were produced around the hole by this process. These cracks were then propagated by tensile testing. The plastic zone size has been estimated by the authors and they concluded that, despite the small specimen thickness, conditions were fulfilled for plane strain fracture-toughness testing. The measured K_{Ic} was generally low (< 4.6 MPa $m^{1/2}$) and decreased with decreasing grain size. The yield strength was also found to decrease in the same grain size range (< 50 nm). It seems that intergranular decohesion was the dominant failure process and that the material tested in general showed brittle behavior.

In contrast to some of the experimental results described above [2, 3, 5, 6], molecular dynamics (MD) simulations showed an opposite trend: the fracture toughness of nanostructured α-Fe (bcc) increased with decreasing grain size [7]. However, the grain size range investigated in the MD simulations by Latapie and Farkas was 6 to 12 nm, which is much smaller than the grains in the experimental studies.

At this point, we also want to describe the few studies on SPD materials. Although often the reported average grain size is below 100 nm, SPD materials cannot directly be compared with nanocrystalline materials produced by other methods such as electrodeposition. Bansal et al. [8] studied SPD Cu and Ni with an average grain size of 60 nm. However, typical microstructures contain high dislocation densities as well as steps and facets at the grain boundaries. Grain size was determined by X-ray diffraction peak broadening, but as peak broadening is influenced by the defect density, the grain size was very likely underestimated. However, the authors did not provide micrographs of the materials studied. Despite the possibly high defect density, the SPD Cu and Ni tested by Bansal et al. behaved in a rather ductile way with considerable necking and elongations at failure between 10% and 20% for Ni and Cu, respectively. Fracture toughness has been determined using a single-edge-notch beam test. J_c values of 12 kJ m^{-2} and 22 kJ m^{-2} for Ni and Cu, respectively, have been reported.

As shown above, it is very difficult to conclude on the overall trend of fracture toughness as a function of grain size on the basis of the currently available

data. Trends are partially contradictory and more systematic studies on model material systems are necessary. Recently, a method has been suggested for the microfabrication of fracture-toughness specimens [9]. The proposed method is based on the UV-LIGA process and could potentially be applied for any nanocrystalline material that can be produced by electrodeposition.

21.3 Fracture Mechanisms

An example of a fracture surface obtained from a tensile specimen of electrodeposited nanocrystalline Ni with a grain size of about 25–30 nm is shown in Fig. 21.1. Typically, dimple diameters as well as dimple depths were found to be significantly larger than the average grain size. These dimples, as shown in Fig. 21.1, are indicative of local plasticity during the failure event and point towards a microvoid coalescence mechanism, similar as in conventional ductile metals.

Similar findings have been reported for electrodeposited nanocrystalline Ni [10–13], Al-Fe [14], Ni-Fe [15], Ni-W [16], and Cu [17]. When the grain size is reduced to ~10 nm or less, as in the case of electrodeposited Ni-W [16] and Ni-Fe [15] alloys, the resulting fracture surfaces from tensile specimens still show dimpled rupture with the dimples being larger than the grain size, but shallower and smaller in diameter compared to the 30 nm grain size materials. Whether these observations are a consequence of the smaller grain size or whether they are related to the presence of W and Fe, respectively, is unclear. It

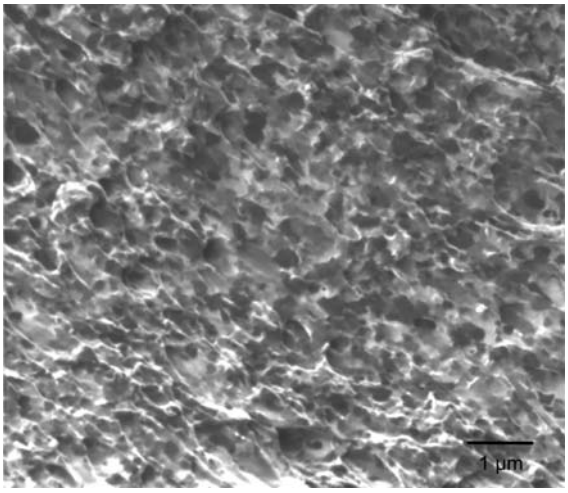

Fig. 21.1 Fracture surface of a ~30 nm grain size electrodeposited Ni tensile specimen: dimpled rupture with a range of dimple sizes that are larger in diameter (100–200 nm) than the grain size.

is interesting to note that, in general, the fracture surfaces of nanocrystalline Ni under monotonic tensile stresses showed indications for ductile fracture, such as dimples, whereas under cyclic loading of nanocrystalline Ni fracture surfaces consisting of rough areas and fast fracture zones have been reported [18, 19].

Besides dimpled rupture, specimens often show necking before the actual fracture, both of which being typical of a ductile material. However, there is also a lack of substantial macroscopic ductility in nanocrystalline fcc metals. Most nanocrystalline materials with an average grain size of about 30 nm show little ductility in tension, typically less than 5% elongation to failure (for example [10, 12, 13, 17, 20–22]). This might not be an intrinsic property of these materials, though, but rather is expected to be related to failure caused by existing flaws. However, most nanocrystalline materials made by electrodeposition, which are expected to be fully dense and to have almost no flaws, have also exhibited very poor ductility. It has been argued that this may be due to additives often needed in the electrodeposition bath in order to attain a nanoscale grain structure [10, 23]. The additives are typically organic materials, which can leave a residue of impurity atoms such as sulfur trapped at the grain boundaries presumably leading to embrittlement resulting in the low ductilities. This assumption is supported by Li and Ebrahimi [15] who investigated nanocrystalline fcc Ni-15% Fe and pure Ni both produced by electrodeposition without the use of additives; in both materials, they found a surprisingly high tensile elongation, that is 9% and 7% in pure Ni of 44 nm grain size and Ni-15%Fe alloy of 9 nm grain size, respectively. This is a significant improvement compared to other reports [10, 12, 13]. However, Stauss et al. [24] investigated commercially produced nanocrystalline Ni produced with additives and observed strains at failure of about 10% in the as-received material. After annealing, though, the samples showed brittle behavior presumably due to sulfur segregation to the grain boundaries. Also, a lack of strain hardening that has been observed in some fine-grained metals may limit the ductility and result in shear instability and premature failure [25].

In several tensile tests on pure Ni, extensive necking was observed [10, 12, 15, 21]. In Ni-Fe [15], however, no reduction in area was observed, which is characteristic of a brittle material. Surprisingly, the stress–strain curve indicated that shear instability preceded fracture. The fracture surface showed shallow voids inside which the fracture was intergranular. Furthermore, deformation bands within the region close to the fracture surface were found, with microcracks inside the bands. The elongation observed in this material was believed to be associated with the stable propagation of the microcracks. Porosity was also seen to influence the fracture behavior: nanocrystalline Ni with high porosity along grain boundaries behaved in a brittle manner. At the grain boundaries, voids formed secondary cracks that coalesced into a primary crack that finally led to failure [26].

Improved ductility with decreasing grain size was observed in SPD Cu [27]. Again, a direct comparison with true nanocrystalline materials is difficult since the grain size and the defect structures are very different. Wang et al. [27] stud-

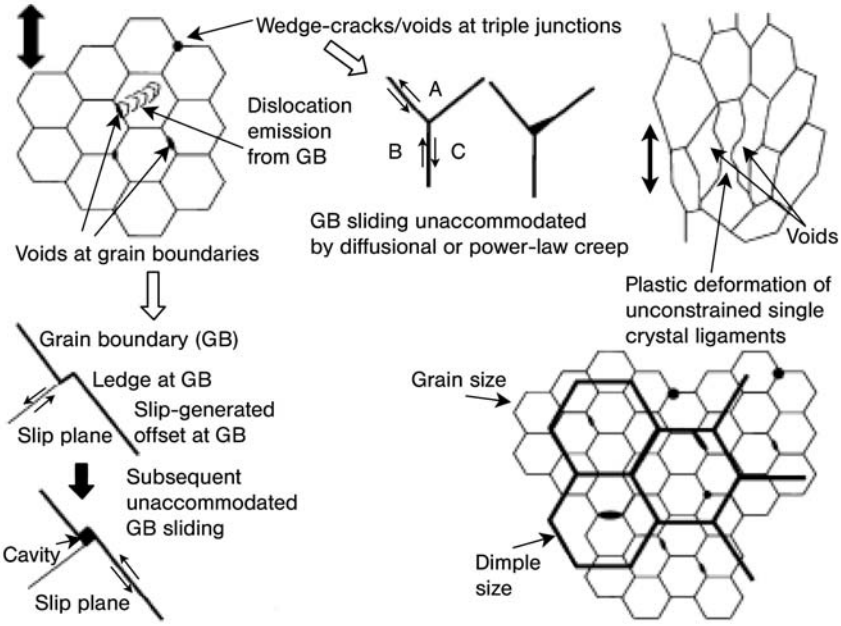

Fig. 21.2 A schematic illustrating how deformation evolves in the nanocrystalline Ni: Dislocation motion, void formation/growth at grain boundaries and triple junctions, formation of ligaments that deform plastically. The interaction of these features may produce the fracture morphology as described above [10].

ied SPD Cu with an average grain size of 300 nm, an inhomogeneous microstructure, and a large fraction of low-angle grain boundaries. Further refinement of the microstructure to grain sizes of 190 nm was achieved by cold rolling at liquid-nitrogen temperature and low-temperature annealing also resulting in a more uniform grain structure. This procedure was found to increase the strength as well as the tensile elongation significantly.

As becomes evident from the preceding discussion, the fracture process in bulk nanostructured metals and alloys is only at the beginning of being understood. Kumar et al. [10] describe the fracture process in nanocrystalline metals as a combination of dislocation motion, void formation and growth at grain boundaries and triple junctions, and the formation of partially unconstrained ligaments that deform plastically (see Fig. 21.2).

This description has been supported not only by their own *in-situ* and *ex-situ* electron microscopy studies on nanocrystalline Ni [10], but also by other groups: Dislocation activity ahead of a crack tip was observed in-situ in nanocrystalline Cu in grains with a size of 100 nm [28] and in grains in nanocrystalline Ni as small as 10 nm [26]. *In-situ* TEM studies on Au with grain sizes of 8 and 25 nm showed nanopores at grain boundaries and evidence for plastically deformed ligaments [29]. There is admittedly uncertainty about the validity of extending

TEM observations to bulk behavior, but analyses of fracture surfaces support the suggested mechanisms.

For materials with grains in the nanoregime, a large fraction of atoms can be considered as grain-boundary atoms; therefore intergranular deformation mechanisms are expected to become relevant, in contrast to intragranular mechanisms based on dislocation activity. This was shown in a number of computer simulations of plastic deformation in nanocrystalline fcc materials (for example [30–33]). Atomistic simulations also showed that a small grain size affects the crack propagation [34]; the crack propagates via an intergranular mechanism creating nanovoids ahead of the crack tip which gradually coalesce. These observations also support the fracture mechanisms proposed by Kumar et al. [10].

21.4
Fatigue Crack Growth

It is well established that the resistance to fatigue crack initiation and propagation in most metals and alloys is significantly influenced by grain size (for example [35]). On the basis of experimental results obtained in microcrystalline metals with grain sizes typically well above 1 μm, it is widely recognized that an increase in grain size generally results in a reduction in the fatigue endurance limit. Here, with all other structural factors approximately held fixed, the endurance limit of initially smooth-surfaced specimens generally scales with the strength of the material, which increases with decreasing grain size. On the other hand, a coarse grain structure can lead to an increase in the fatigue crack growth threshold stress intensity factor range and a decrease in the rate of crack growth owing to such mechanisms as periodic deflections in the path of the fatigue crack at grain boundaries during crystallographic crack propagation [36], especially in the near-threshold regime of fatigue crack growth (for example [37]). The relevance of such broad trends extracted from conventional microcrystalline alloys to ultrafine crystalline and nanocrystalline metals is largely unknown at this time.

Typically, two stages of microscopic fatigue crack growth can be identified [38]. Stage I growth takes place when the crack and its associated plastic zone are confined within a few grains. Here, crack growth occurs primarily by single slip along the primary slip system. Considering a crack must propagate (on average) in a direction perpendicular to the tensile axis during Mode I loading, Stage I crack growth leads to a relatively tortuous crack path. As the level of applied stress increases, the crack tip plastic zone size becomes large, relative to the characteristic grain dimension, and crack growth occurs via duplex slip (Stage II). In this case, the crack propagates in a planar fashion between slip bands, normal to the tensile axis. Grain refinement to the nanocrystalline regime can therefore have a significant effect on the level of crack-path tortuosity, independent of whether a crack grows in a transgranular or intergranular fashion. This is illustrated in Fig. 21.3, which shows that the crack paths emerging

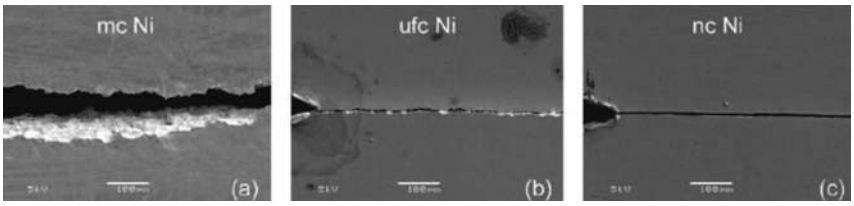

Fig. 21.3 Scanning electron micrographs of (a) microcrystalline, (b) ultrafine crystalline, and (c) nanocrystalline Ni subjected to sinusoidal fatigue loading at initial ΔK values of 10, 6.2, and 8.5 MPa $m^{1/2}$, respectively. A cyclic frequency of 10 Hz and load ratio, $R = 0.3$ were used in all cases. Crack-path tortuosity clearly decreases with grain refinement [35].

in microcrystalline and ultrafine crystalline Ni are crystallographic with the extent of crack-face roughness significantly diminishing from the larger to the smaller grain size. Nanocrystalline Ni shows a straighter fracture path than the ultrafine crystalline and microcrystalline materials.

To date, only few studies of fatigue crack growth behavior in nanocrystalline and ultrafine crystalline metals and alloys exists [39, 40]. Hanlon et al. [39] studied a variety of grain sizes and materials; in this study, the grain size of fully dense electrodeposited Ni was systematically varied from the nanocrystalline to the ultrafine crystalline regime. While the inplane dimensions of the electrodeposited Ni were relatively large (80 mm × 80 mm), the thickness was limited to ~150 μm. Single-edge notched crack growth specimens were extracted from the Ni foils via electrodischarge machining. Additional crack-growth experiments were conducted in a cryomilled ultrafine crystalline Al-Mg alloy and an ECAP Grade 2 ultrafine crystalline pure Ti, for which sizeable quantities of bulk specimens were available such that conventional fatigue testing could be employed. The fatigue crack growth behavior in each material system was assessed over a broad range of load ratios, from threshold to final failure. In order to enforce the assumptions inherent to LEFM, all data collection was truncated to incorporate only those data points corresponding to an uncracked ligament length of at least 20 times the plastic zone size at the tip of the crack during fatigue crack growth experiments.

In each material system investigated, grain refinement resulted in a marked reduction in the resistance to fatigue crack propagation. As described above, grain refinement to the nanocrystalline regime considerably reduces the extent of crack path tortuosity during Stage I propagation (compare Fig. 21.3). It is well known that crack-path deflection can lead to a reduction in *effective* ΔK, as a result of the mixed mode loading conditions that exist at the tip of a deflected crack [36]. In addition, increased levels of crack deflection typically exacerbate partial crack-closure effects. Such phenomena can be used to interpret the observed increased resistance to subcritical fatigue crack growth in coarse grain materials, relative to their finer-grain counterparts. Crack propagation rates at elevated ΔK were found to be independent of grain size, as a result of the tran-

sition from a tortuous Stage I-type mechanism in coarse-grain materials, to that of a more planar crack growth observed during Stage II propagation.

Similar findings have been reported by Pao et al. [40], who studied bulk Al-7.5%Mg with an average grain size of about 250 nm. The material was produced by ball milling followed by hot isostatic pressing, extrusion and annealing. The crack growth rate was significantly higher in the ultrafine crystalline Al-7.5Mg alloy than the rate in coarse grain Al 7050-T74 with grains in the range of 20 μm, which was tested for comparison. Furthermore, the threshold stress for crack growth decreased to half the value of that of the coarse-grained alloy. The increased fatigue crack growth rates and reduced thresholds were accompanied by a much smoother fracture surface morphology and, thus, lower roughness-induced crack closure.

21.5 Conclusion

In conclusion, it can be said that fracture of bulk nanocrystalline materials is not well understood and has not yet been extensively investigated. Contradictory observations, such as brittle behavior on a global scale and indicators for ductility on a local scale, that is reduced ductility and dimples on the fracture surface, respectively, make this a wide open field for additional studies. Also, the differences between experimental and simulated fracture-toughness values are important issues to be investigated. In the future, progress in the development of new experimental techniques including the processing of high quality materials in large quantities as well as theoretical advancements may help to better describe and understand fracture mechanisms with the goal to improve and tailor bulk nanostructured materials for application in structural components.

References

1 R. A. Mirshams, C. H. Xiao, S. H. Whang, W. M. Yin **2001**, *Mater. Sci. Eng.* A 315(1–2), 21–27.
2 M. A. Morris-Munoz, A. Dodge, D. G. Morris **1999**, *Nanostruct. Mater.* 11(7), 873–885.
3 M. A. Morris, M. Leboeuf **1997**, *Mater. Sci. Eng. A* 224(1–2), 1–11.
4 B. Q. Han, F. A. Mohamed, C. C. Bampton, E. J. Lavernia **2005**, *Metall. Mater. Trans. A* 36(8), 2081–2091.
5 Y. Gan, B. L. Zhou **2001**, *Scr. Mater. 45(6),* 625–630.
6 Y. Gan, B. L. Zhou **2001**, *Acta Metall. Sin.* 37(4), 391–394.
7 A. Latapie, D. Farkas **2004**, *Phys. Rev. B* 69, 134110.
8 S. Bansal, A. Saxena, T. Hartwig, R. R. Tummala **2005**, *J. Metastable Nanocryst. Mater.* 23, 183–186.
9 W. Dai, C. Oropeza, K. Lian, W. Wang **2006**, *Microsyst. Technolog.* 12(4), 306–314.
10 K. S. Kumar, S. Suresh, M. F. Chisholm, J. A. Horton, P. Wang **2003**, *Acta Mater.* 51(2), 387–405.
11 A. Hasnaoui, H. V. Swygenhoven, M. Derlet, **2003,** *Science* 300.
12 F. D. Dalla Torre, H. Van Swygenhoven, M. Victoria, **2002,** *Acta Mater.* 50, 3957–3970.

13 R. Schwaiger, B. Moser, M. Dao, N. Chollacoop, S. Suresh, **2003,** *Acta Mater.* 51(17), 5159–5172.

14 T. Mukai, S. Suresh, K. Kita, H. Sasaki, N. Kobayashi, K. Higashi, A. Inoue **2003**, *Acta Mater.* 51(14), 4197–4208.

15 H. Li, F. Ebrahimi **2004**, *Appl. Phys. Lett.* 84(21), 4307–4309.

16 K. S. Kumar, H. Van Swygenhoven, S. Suresh **2003**, *Acta Mater.* 51(19), 5743–5774.

17 F. Ebrahimi, Q. Zhai, D. Kong **1998**, *Scr. Mater.* 39(3), 315–321.

18 B. Moser, T. Hanlon, K. S. Kumar, S. Suresh **2006**, *Scr. Mater.* 54(6), 1151–1155.

19 J. Aktaa, J. T. Reszat, M. Walter, K. Bade, K. J. Hemker **2005**, *Scr. Mater.* 52(12), 1217–1221.

20 G. Sanders, J. A. Eastman, J. R. Weertman **1997**, *Acta Mater.* 45(10), 4019–4025.

21 F. Ebrahimi, G. R. Bourne, M. S. Kelly, T. E. Matthews **1999**, *Nanostruct. Mater.* 11(3), 343–350.

22 G. W. Niemann, J. R. Weertman, R. W. Siegel **1991**, *J. Mater. Res.* 6(5), 1012–1027.

23 C. C. Koch, K. M. Youssef, R. O. Scattergood, K. L. Murty **2005**, *Adv. Eng. Mater.* 7(9), 787–794.

24 S. Stauss, Schwaller, J.-L. Bucaille, R. Rabe, L. Rohr, J. Michler, E. Blank **2003**, *Microelectron. Eng.* 67–68, 818–825.

25 D. Jia, Y. M. Wang, K. T. Ramesh, E. Ma, Y. T. Zhu, R. Z. Valiev, **2001,** *Appl. Phys. Lett.* 79(5), 611.

26 R. C. Hugo, H. Kung, J. R. Weertman, R. Mitra, J. A. Knapp, D. M. Follstaedt **2003**, *Acta Mater.* 51(7), 1937–1943.

27 Y. M. Wang, E. Ma, M. W. Chen **2002**, *Appl. Phys. Lett.* 80(13), 2395.

28 C. J. Youngdahl, J. R. Weertman, R. C. Hugo, H. H. Kung **2001**, *Scr. Mater.* 44, 1475–1478.

29 W.W. Milligan, S.A. Hackney, M. Ke, E.C. Aifantis **1993**, *Nanostruct. Mater.* 2(3), 267–276.

30 J. Schiotz, T. Vegge, F.-D. Di-Tolla, K.-W. Jacobsen **1999**, Atomic-scale simulations of the mechanical deformation of nanocrystalline metals, *Phys. Rev. B* 60(17), 11971.

31 H. van Swygenhoven, M. Derlet **2001**, Grain-boundary sliding in nanocrystalline fcc metals, *Phys. Rev. B* 64, 224105.

32 H. van Swygenhoven, M. Derlet, A. Hasnaoui **2002**, Atomic mechanism for dislocation emission from nanosized grain boundaries. *Phys. Rev. B*. 66, 024101.

33 V. Yamakov, D. Wolf, S. R. Phillpot, A. K. Mukherjee, H. Gleiter **2004**, Deformation-mechanism map for nanocrystalline metals by molecular-dynamics simulation. *Nature Mater.* 3, 43.

34 D. Farkas, S. Van Petegem, M. Derlet, H. van Swygenhoven **2005**, Dislocation activity and nano-void formation near crack tips in nanocrystalline Ni, *Acta Mater.* 53(11), 3115.

35 S. Suresh **1998**, *Fatigue of Materials*. 2nd edn, Cambridge University Press, Cambridge.

36 S. Suresh **1985**, *Metall. Trans. A 16*, 249–260.

37 A. K. Vasudevan, K. Sadananda, K. Rajan **1997**, *Int. J. Fatigue* 19, 151–159.

38 J. E. Forsyth **1962**, in *Crack Propagation: Proceedings of Cranfield Symposium*, HMSO, London, 76–94.

39 T. Hanlon, E. D. Tabachnikova, S. Suresh **2005**, *Int. J. Fatigue* 27(10–12), 1147–1158.

40 S. Pao, H. N. Jones, S. J. Gill, C. R. Feng **2002,** *Mater. Res. Soc. Symp. Proc.* 740, I1.4.

22
Fatigue Properties of Bulk Nanostructured Materials

Heinz-Werner Höppel, Hael Mughrabi, and Alexey Vinogradov

22.1
Introduction and Motivation

For many potential technological applications of bulk nanostructured materials, the fatigue properties are key features for a successful use of this new class of materials. Strictly speaking, the expression "bulk nanostructured materials" refers to materials with grain sizes below 100 nm. However, since there are only very few publications on the fatigue behavior of "truly" nanocrystalline materials available, see [1–6], this chapter will deal mainly with ultrafine-grained (UFG) materials with grain sizes up to one micrometer. As UFG metals rather than "truly" nanocrystalline materials became available in technologically relevant dimensions and quantities, there is an increasing scientific as well as technological interest in these materials. This development is mainly due to the progress in the field of severe plastic-deformation (SPD) techniques, like, for example, Equal-Channel Angular Pressing (ECAP) or accumulative roll bonding (ARB), producing UFG microstructures with grain sizes in the range of some hundred nanometers up to the micrometer range. Current research on continuous SPD techniques, like ECAP-Conform [7] or Continuous Confined Strip Shearing (C2S2) [8], show also the great technological potential of these materials. Hence, fundamental investigations and, derived therefrom, a detailed understanding of the fatigue mechanisms of UFG materials are indispensable. In general, UFG metals exhibit very promising mechanical properties under monotonic loads: High specific strength is paired with a relatively high ductility, which is sometimes found to be higher than for cold worked conventional grain size (CG) materials. Some authors reported a strongly increased ductility (elongation to failure), depending on the strain rate, while others observed a reduced ductility compared to the CG counterparts. The enhanced ductility has been found so far for ECAP-processed Cu and Al [9, 10] as well as for ARB-processed UFG Al [11] and the aluminium alloy AA6016 [11] and just recently also for the ARB-processed aluminium alloy AA8011 [12]. In all these cases, the ductility increases as the strain rate decreases [10, 13].

The paradox of strength and ductility [9, 11] provides a great technological potential for the use of UFG materials for metal-forming processes, like deep

Bulk Nanostructured Materials. Edited by M. J. Zehetbauer and Y. T. Zhu

ISBN: 978-3-527-31524-6

drawing. In practical applications, not only the performance under monotonic loads is of technological relevance. In addition, the cyclic deformation behavior and fatigue life play a very significant role for many prospective engineering applications. CG materials will only be replaced by UFG materials for cyclically loaded parts if their fatigue properties also meet the requirements. Beside the technological view, the cyclic deformation behavior and fatigue lives of UFG materials are also of high scientific interest, as the grain size now becomes the dominating microstructural length scale. This change in the dominating microstructural feature will strongly affect the deformation mechanisms, as will be discussed later. Understanding fatigue phenomena is always strongly related to the question of the dominating cyclic deformation mechanisms. As these mechanisms change due to the UFG microstructure, (cyclic) deformation behavior or, more generally, the mechanical properties of UFG materials cannot simply be explained by the well-known Hall–Petch [14, 15] relationship. In particular, the following key features must be regarded carefully for UFG materials:

- Microstructural stability under cyclic and/or thermal loads;
- Strain rate dependence of the deformation behavior and the mechanical properties;
- Effect of the grain size on the cyclic deformation behavior and the fatigue life;
- Potential changes in the mechanisms of localization of plastic deformation compared to CG materials.

In this context, modeling approaches can help to understand more clearly the dominating mechanisms during cyclic loading. Only when the dominating deformation mechanisms are identified, and attempts for a further improvement of the cyclic deformation behavior and consequently of the fatigue lives can be made with foresight.

The first investigations on the cyclic deformation behavior of UFG materials were performed on copper, by Vinogradov et al. [16] and Agnew and Weertman [17] almost one decade ago. Until now, only a few systematic investigations on the fatigue behavior were performed by several groups on UFG copper [18–30] and UFG nickel [31–33] as the most prominent model materials, but also on UFG aluminum and UFG α-brass [26, 28, 34]. Although these investigations were mainly confined to single-phase (model) materials, the fatigue properties of multiphase materials also came into the focus of research. Due to the progress in the SPD processes, UFG multiphase materials, like Al alloys [35, 36], Mg alloys [37, 38], FeCr alloy [39] and titanium alloys [40–42], can nowadays be processed successfully by ECAP and their fatigue properties have been investigated.

Although there are some interesting investigations on the fatigue properties of multiphase materials, this chapter will focus mainly on the fatigue properties of single-phase materials, as the effects of the UFG microstructure on the dominating fatigue mechanisms can be understood more easily. Nevertheless, it will also provide a small outlook on multiphase materials. The main objective of this chapter will be, based on the current understanding of the fatigue phenomena

in UFG-materials, to provide a more generalized framework for understanding the fatigue behavior of UFG materials.

22.2
Fatigue Life of UFG Materials

Discussing fatigue life, the classical Wöhler (*S–N*)-plot is used most commonly, in which the fatigue life is plotted with regard to the stress amplitude. As UFG materials generally show a significantly higher monotonic strength, which is due to a much higher athermal stress component σ_G, the fatigue lives are also superior compared to that of the CG counterparts. This statement holds for the low cycle-fatigue (LCF) regime as well as for the high cycle-fatigue (HCF) regime and for all UFG materials investigated so far. Most recently, it was found for UFG copper that in the very high cycle-fatigue (VHCF) regime [27] the fatigue lives are also superior to that of the CG counterpart. Fig. 22.1 shows, as examples, the *S–N* diagrams for copper, aluminum and α-brass.

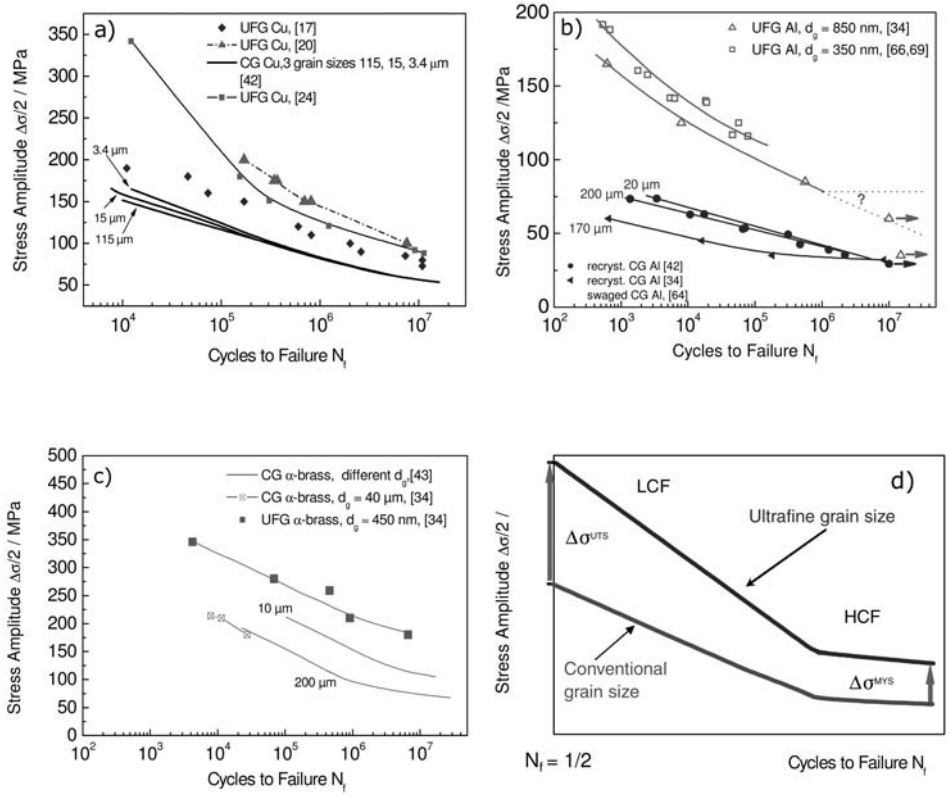

Fig. 22.1 Wöhler *S–N* diagrams for (a) copper, (b) commercial purity (CP) aluminum, (c) α-brass for different grain sizes and (d) schematic view. Data from [17, 20, 24, 34, 43, 63, 73].

Fig. 22.1 (d) shows schematically the changes in the *S–N* plot when changing the microstructure from conventional to ultrafine grain size. Due to the significantly enhanced ultimate tensile strength (UTS) of UFG materials compared to the CG counterparts, the sustainable stress level at a given fatigue life is markedly increased in the LCF regime. As the stress amplitude decreases, the plastic-strain amplitude decreases and work hardening as an additional hardening mechanism is reduced. Hence, in the HCF regime the sustainable stress levels of the UFG materials at a given fatigue life are still superior to those of the CG condition, but the differences are not as high as in the LCF regime. The difference between UFG and CG materials is due to their significantly different microyielding behavior, see [22, 26, 44], which is schematically indicated in Fig. 22.1 (d) by $\Delta\sigma^{MYS}$. In particular, these explanations are supported by the fatigue-life diagrams obtained for UFG Cu and Al, by the increased stresses for the onset of microyielding and also by the work-hardening behavior of UFG materials under monotonic loading, see for example [11, 13]. The cyclic stress–strain curves (CSS) for UFG Ni and UFG Cu also reflect the enhanced properties of UFG materials, see Fig. 22.2. As can be seen for copper, data from [45, 46], and also nickel, data from [31, 47], the UFG microstructures lead, in both materials, to a significantly improved cyclic saturation stress and, with increasing plastic-strain amplitude, to a more than proportional increase in the cyclic saturation stress, compared to the CG counterparts.

According to [48, 54] the dependence between the cyclic saturation stress and the plastic-strain amplitude can be described as follows:

$$\frac{\Delta\sigma}{2} = k\left(\frac{\Delta\varepsilon_{pl}}{2}\right)^{n'} \tag{22.1}$$

with:
k cyclic hardening coefficient
η' cyclic hardening exponent.

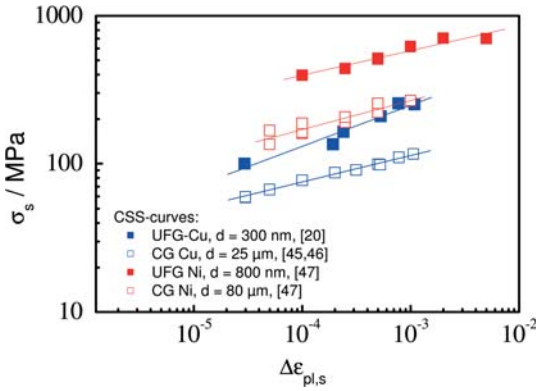

Fig. 22.2 Cyclic stress–strain curves (cyclic saturation stress σ_s *vs.* plastic-strain amplitude at cyclic saturation $\Delta\varepsilon_{pl,s}$) for copper and nickel in the CG and UFG condition. Data from [20, 45, 46, 47].

Table 22.1 Cyclic-hardening coefficients and exponents for CG and UFG copper and nickel.

Material	CG Cu	UFG Cu	CG Ni	UFG Ni
$\log k$	2.59	3.51	2.75	3.26
n'	0.175	0.364	0.145	0.166

As can be seen from Table 22.1, both the cyclic hardening exponents as well as the cyclic hardening coefficients are significantly higher for UFG than for CG material. This behavior can be interpreted as follows: In UFG materials, the onset of microplastic flow takes place at markedly higher stresses and the cyclic hardening coefficients are enlarged. Moreover, UFG microstructures show an enhanced sensitivity to the plastic strain amplitude, which is reflected by the cyclic hardening exponent.

In this context, the influence of the grain size on the *S–N* fatigue-life diagram must be discussed in more detail. Based on investigations on CG materials from Thompson and Backofen [43] and Lukáš and Kunz [49], the influence of the grain size, (in the range from some micrometers up to some millimeters) on the fatigue lives is strongly related to the glide character of the material. If the material exhibits a wavy glide character (which is supposed to be mainly influenced by the ease of cross-slip) as in the case of aluminum and copper, only a small influence of the grain size is detectable in the lower LCF regime (intermediate to short fatigue lives), while in the upper LCF and the HCF regime no grain-size effect is found. When the glide character is planar, as for example in α-brass, a pronounced grain-size effect on the fatigue lives is found throughout the complete fatigue life range. Regarding the UFG materials, this situation changes drastically. From the LCF regime to the HCF regime there is a strong grain-size dependence of the fatigue lives irrespective of the glide character. This behavior can only be explained by the change in the dominating microstructural length scale. In UFG materials, the grain size is in the range of the slip distances of the dislocations. Hence, the probability of an individual gliding dislocation interacting with the grain boundary or grain-boundary dislocations is much higher than in CG materials. In this context, it should be stated that the term grain size is used irrespective of the angle of misorientation between the adjacent (sub)grains. Although the characters of the boundaries are different, the hardening effects of subgrains or grains are supposed to be qualitatively similar. According to the Hall–Petch relationship the hardening effect is inversely proportional to the square root of the grain size while for subgrains the hardening effect is inversely proportional to the grain size. Under cyclic loading, the plastic-strain amplitudes are normally far beyond the macroscopic yielding point. Hence, in CG materials, the gliding distance of dislocations is much smaller than the grain size for intermediate to low plastic-strain amplitudes. Only pile-up effects of dislocations moving on a particular glide plane, like in planar glide materials, will lead to a grain-size effect on the fatigue properties.

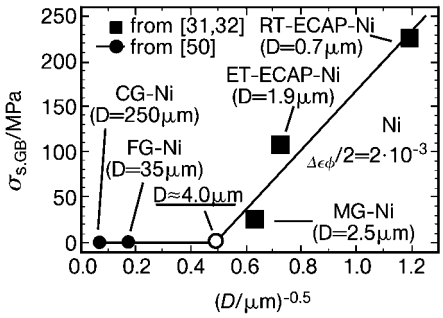

Fig. 23.3 Cyclic saturation stress $\sigma_{s,GB}$ (grain-boundary contribution) *vs.* the inverse square root of the grain size D (Hall–Petch plot) for nickel deformed cyclically at $\Delta\varepsilon_{pl}/2 = 2\times10^{-3}$. FG: fine-grained, MC: microcrystalline, RT-ECAP and ET-ECAP refer to ECAP at room and at elevated temperature. After [31, 32, 50], as modified in [26].

At high plastic strain amplitudes, the fatigue properties of wavy slip materials can also be affected by the grain size. This situation changes completely when UFG materials are considered. Due to the small grain size, the back stresses of the boundaries can either affect the source stress for emitting a gliding dislocation or the gliding stress itself. With this assumption a grain or even a subgrain boundary will affect the fatigue behavior due to either a direct interaction of a moving dislocation with the boundaries or an interaction between the stress field of the boundary and the dislocation source. Hence, the cyclic saturation state should be affected by the grain size, as discussed by Thiele et al. [4, 32, 33] and Klemm [31]. According to the authors, the cyclic saturation stress of nickel is affected by the grain size, if the grain size is smaller than about 4 μm. With decreasing grain size the grain-boundary contribution to the cyclic saturation stress increases further, following a Hall–Petch type relationship as shown in Fig. 22.3, for a plastic-strain amplitude of 2×10^{-3}.

When fatigue lives are considered in terms of strain amplitudes (rather than stress amplitudes), the situation is quite different. In the regime of low to intermediate total strain amplitudes, i.e. in the HCF regime, the fatigue lives of UFG materials are much higher than those of the CG counterparts, while in the LCF regime of intermediate to high total strain amplitudes, the fatigue lives are distinctively shorter. Based on earlier considerations of Mughrabi and Höppel [20], a cross-over of the fatigue-life graphs for the CG and UFG condition was predicted, see Fig. 22.4. In the meanwhile, it has been shown that all available experimental data with the exception of UFG titanium verify this prediction. Fig. 22.4 (b)–(e) show the data for UFG aluminum and UFG α-brass. This cross-over can easily be explained by using the well-known laws of Coffin [51] and Manson [52] and Basquin [53], as in the form first proposed by Morrow [54] and Landgraf [55]:

$$\Delta\varepsilon_t/2 = \Delta\varepsilon_{el}/2 + \Delta\varepsilon_{pl}/2 = \frac{\sigma'_f}{E}(2N_f)^b + \varepsilon'_f(2N_f)^c \qquad (22.2)$$

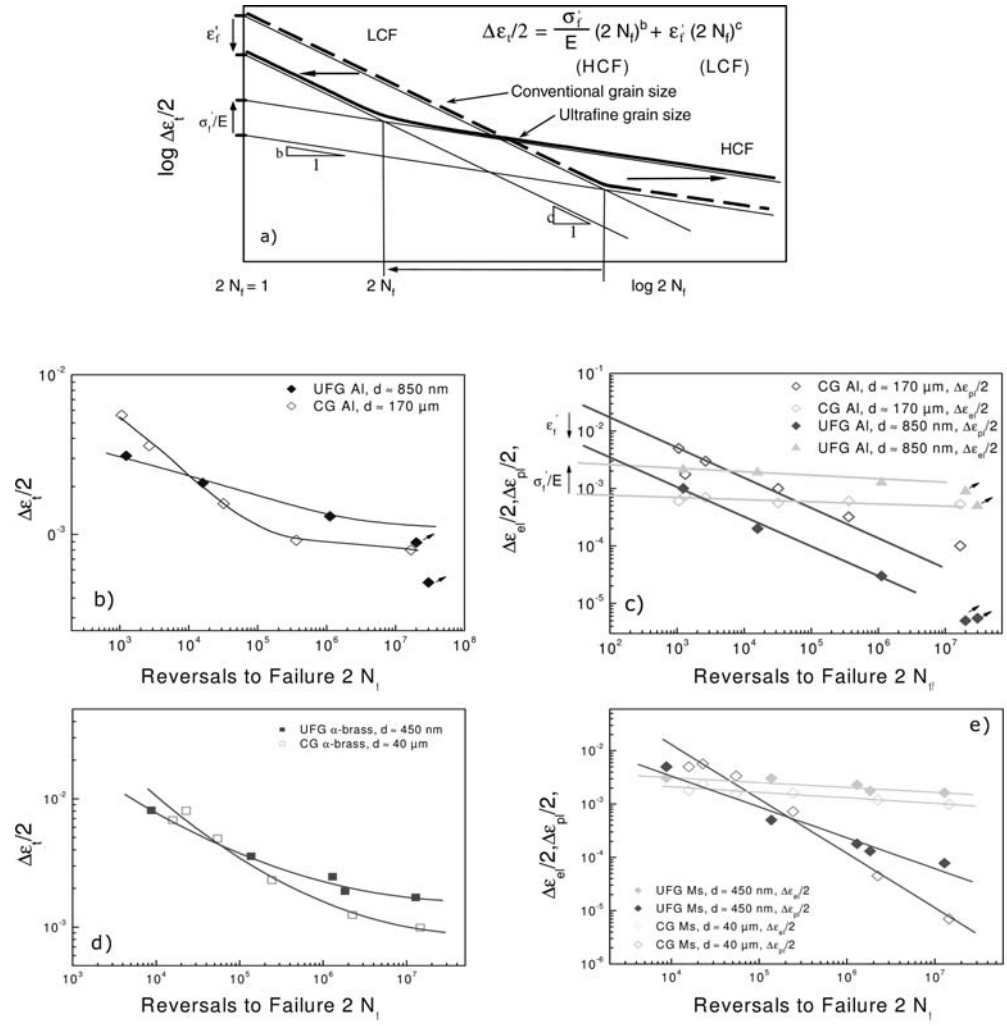

Fig. 22.4 (a) Schematic total strain fatigue-life diagram for UFG and CG materials, from [20]. (b) Total strain fatigue-life diagram for UFG Al and CG Al, (c) Corresponding fatigue-life diagram according to Coffin–Manson and Basquin laws for CG and UFG Al, (d) Total strain fatigue-life diagram for UFG α-brass and CG α-brass, (e) Corresponding fatigue-life diagram according to Coffin–Manson and Basquin laws for CG and UFG α-brass. Both materials were fatigued in symmetrical fully reversed total strain control with limitation of the plastic strain, or, respectively, under stress control. Data of (b), (c), (d) and (e) from [34], see also [59, 60].

According to Eq. (22.2), the fatigue life for a given total strain amplitude $\Delta\varepsilon_t/2$ can be calculated from the combination of the Coffin–Manson and Basquin laws. With the exception of UFG titanium, it was found for all other UFG materials that the fatigue ductility coefficient ε'_f of the Coffin–Manson law is drastically reduced compared to the CG condition while the fatigue strength coefficient σ'_f of the Basquin law is increased significantly. The exponents for both laws remain more or less unchanged, see [56–58]. Consequently, in the HCF regime, i.e. in the regime of small plastic strain amplitudes that is usually studied in stress-controlled tests, and that is primarily governed by the Basquin law, the increased fatigue strength coefficient σ'_f accounts for the enhancement in fatigue life. On the other hand, in the LCF regime, i.e. in the regime of intermediate to high plastic strain amplitudes, in which usually strain-controlled experiments are performed and that is primarily governed by the Coffin–Manson law, the decreased fatigue ductility coefficient ε'_f will lead to a deterioration of the fatigue life, see [59, 60].

Based on the above considerations concerning the interaction of dislocations with the grain boundaries, the observed cross-over in the total strain fatigue-life diagram can be easily understood. According to Orowan's equation, the slip length can be calculated by a simple estimate. At the point of crossover, the slip length is rather close to the measured grain size, see [28, 60]. Hence, it is supposed that the reduced fatigue lives in the regime of intermediate to high plastic-strain amplitudes are due to a limitation of the possible slip length of the dislocations by the UFG grain structure.

In this context, it should be noted that, in the case of α-brass, the fatigue ductility exponent c from the Coffin–Manson law differs significantly for the CG and UFG materials, while the exponents are nearly identical for aluminum and also copper. This change in the slope of the fatigue life plot probably indicates a change in the deformation mechanism.

22.3
Cyclic Deformation Behavior and Damage Mechanisms

When discussing the cyclic deformation behavior and, in particular, the phenomenon of cyclic softening in combination with the microstructural stability of UFG materials produced by SPD techniques such as ECAP, it is important to note the following differences with respect to the related cyclic softening behavior in CG materials that have been predeformed. In the latter case, as has been well documented in the classical work of Feltner and Laird [61], it is the dislocation cell/subgrain structure that readjusts itself and undergoes coarsening during cyclic softening. On the other hand, in UFG materials, it is the refined grain structure that contains a large fraction of high-angle grain boundaries and that is inherited from the ECAP process that coarsens during cyclic softening. In this case, a deformation-induced dislocation substructure that is strikingly absent in the grains of the original UFG microstructure can develop

in the coarsened grains, once they have become larger than the characteristic spacings of the dislocation substructure.

In this context, it can be stated that cyclic deformation behavior of UFG materials is significantly different from the behavior of the CG counterparts. Beside the different levels of the materials response (stress or strain amplitude), pronounced cyclic softening is often observed for rather pure single-phase UFG materials, see [17, 18, 21, 23] and Fig. 22.5 (a). In this context, systematic investigations on UFG Cu [23] reveal that the microstructural stability plays a key role in the cyclic deformation behavior. From such studies on pure and less pure UFG copper and of other materials of different purity it can be concluded that UFG materials of commercial purity frequently are cyclically stable, whereas high-purity UFG materials usually undergo severe cyclic softening. This behavior can be attributed to the stable grain-boundary structure in the former case, as compared to the much less stable grain structure in the latter case. Thus, it was found for high-purity UFG copper in the LCF regime, dynamic grain growth occurs at a low homologous temperature of 0.22, see Fig. 22.6 (a) and [20, 23]. More specifically, the grain growth was found to be time and temperature dependent and to also depend in a particular way on the plastic-strain amplitude. All these effects were related to the strong cyclic softening observed. Moreover, dynamic grain coarsening has been considered as a crucial microstructural event for the formation of macroscopic shear bands, see [23]. In the case of less-pure single-phase materials, like less-pure copper [27, 62] and commercial-purity UFG Al [22, 34, 73], the reduced purity leads to a drastically reduced dynamic grain-coarsening effect, which is also reflected in a significantly different cyclic deformation behavior, see Fig. 22.5 (b). For commercial-purity

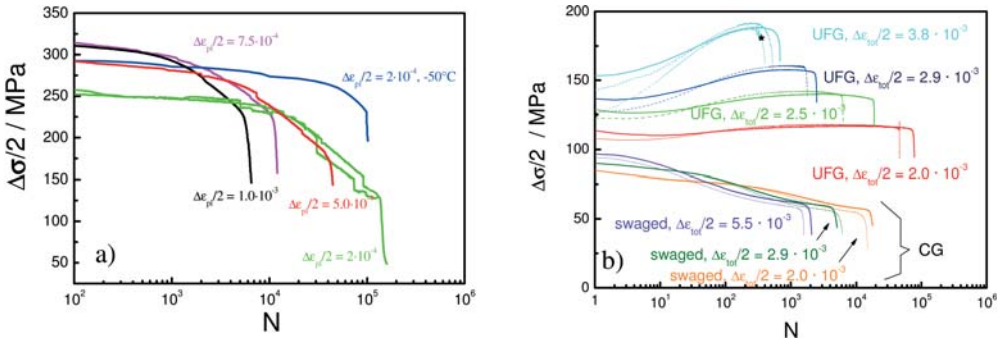

Fig. 22.5 Cyclic deformation curves for (a) UFG Cu fatigued at different constant plastic-strain amplitudes. If not indicated otherwise, the experiments were performed at room temperature at a strain rate of 1×10^{-3} s^{-1}. From [23]. (b) Cyclic deformation curves of UFG Al and swaged CG Al, respectively, fatigued at different constant total strain amplitudes and at two different strain rates: solid lines: 5×10^{-3} s^{-1} and dotted lines: 5×10^{-4} s^{-1}. For an amplitude of $\Delta\varepsilon_{tot}/2=3.8\times10^{-3}$ an additional test at a strain rate of 5×10^{-5} s^{-1} was also performed (indicated by an asterisk. Courtesy of D. Amberger [63]).

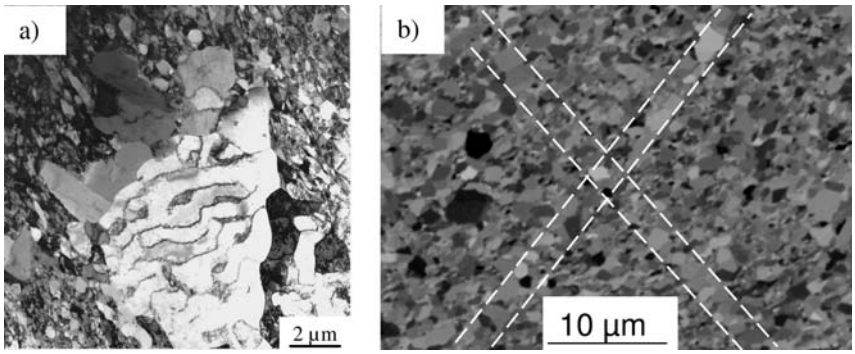

Fig. 22.6 (a) Markedly coarsened patch in UFG Cu fatigued at $\Delta\varepsilon_{pl}/2=1\times10^{-3}$. Please note the dislocation substructure formed in the coarsened patch. (b) Intersecting shear bands in UFG Cu fatigued at $\Delta\varepsilon_{pl}/2=1\times10^{-3}$. Stress axis horizontal. From [23].

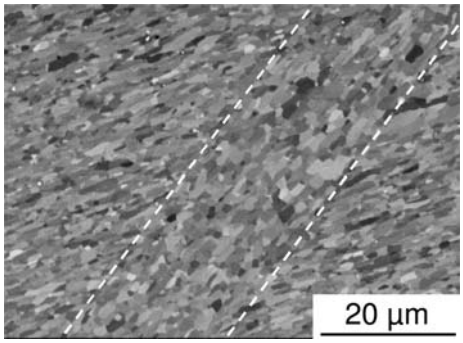

Fig. 22.7 Macroscopic shear band formed in UFG Al fatigued at $\Delta\varepsilon_{pl}/2=1\times10^{-3}$. Within the shear band a possibly noncrystallographic grain rotation and slight grain coarsening can be detected. Stress axis horizontal. From [44].

UFG Al with a grain size of 350 nm cyclic hardening was found for all amplitudes applied due to the absence of intense dynamic grain coarsening. In contrast, the swaged CG reference material shows pronounced cyclic softening. For UFG Al with the grain size of 350 nm no macroscopic shear bands were found. On the other hand, in the case of UFG Al with a grain size of 850 nm and with a slightly lower amount and different kind of impurities only few but severe and extended macroscopic shear bands do form during cyclic loading, see Fig. 22.7 (a) and [22, 26, 28, 34]. Only within these shear bands did the grain structure markedly coarsen. The strength within the shear band determined by nanoindentation tests is reduced by almost 30% compared to the hardness of the vicinity. Switching to single-phase materials with a high amount of solution-hardening elements, like α-brass, a very pronounced microstructural stability is found, which leads to a marked cyclic saturation level. Macroscopic shear bands are absent in these materials. Furthermore, in the case of α-brass, it can be concluded that the planar type of deformation typical for the CG condition becomes less dominating in the case of an ultrafine-grained microstructure. In the UFG α-brass, the slip lines are less planar and shorter than in the CG counterpart.

Many individual microcracks starting mainly at the remaining but comparably small slip bands appear. For the coarser microstructures introduced by a post-ECAP annealing heat treatment, the character of deformation switches to the planar type back again. Hence, the slip mode obviously varies with the grain size.

Evaluating the above-mentioned results in combination with other investigations on multiphase materials like the alloy AA6061, it can be concluded that the boundary mobility in UFG microstructures is one of the relevant features for the stability of the microstructure. Hence, an enhanced microstructural stability of the UFG grain structure, accompanied by an improved fatigue resistance, can be expected when the grain-boundary mobility is reduced. Moreover, it can be stated that as long as the grain size is small enough, typical substructures such as di-/multipolar dislocation veins/walls, which are commonly observed in fatigued wavy-slip CG material, cannot form and are hence absent [19, 32, 64]. Thus, variations in the dislocation density and arrangements in UFG materials during cycling must also be considered.

In UFG materials, gliding dislocations can interact much more easily either with the grain boundaries or with the so-called grain-boundary-affected zone (GBAZ) [65] than in the CG counterparts, as the grain size is in the range of the slip distance. This enhanced probability for the interaction with the grain boundaries or the GBAZ plays a significant role in understanding the deformation behavior of UFG materials. As mentioned above, UFG materials show enhanced strain-rate sensitivity under monotonic loading [11, 13, 66]. The reasons for the enhanced SRS are until now under discussion. Grain-boundary sliding and Coble creep are mainly used to explain this behavior. As suggested earlier [11, 13] and also proposed by Li et al. [67] thermally activated annihilation of dislocations at the grain boundaries or in the GBAZ in UFG materials are also brought into the discussion. The influence of the increased SRS on the fatigue lives and the deformation behavior fatigue tests on UFG Al at two different strain rates of $5\times10^{-3}\,s^{-1}$ and $5\times10^{-4}\,s^{-1}$ were investigated recently in total strain-controlled tests [60, 63, 68]. There is a clear influence of the strain rate on the fatigue lives as well as on the cyclic deformation behavior, Fig. 22.5 (b). At the lower strain rate, the UFG material is softer for the first approximately hundred cycles and the fatigue life is reduced by approximately a factor of two. After the first hundred cycles, pronounced hardening takes place and for all amplitudes applied the corresponding stress amplitudes for the tests performed at the lower strain rate slightly exceed the levels of the experiments at the higher strain rate. Such an influence was not found for the swaged CG condition. Hence, it can be concluded that dislocation-annihilation mechanisms rather than grain-boundary sliding or Coble creep play an important role.

According to Essmann and Mughrabi [69] the differential change of dislocation density $d\rho$ occurring in a particular glide system in an interval of shear strain $d\gamma$ can be written as:

$$\frac{d\rho}{d\gamma} = \frac{2}{bL} - \frac{2}{b}y\rho \tag{22.3}$$

with:
b: modulus of the Burgers vector,
L: dislocation glide path, usually a function of the shear strain γ,
y: annihilation distance within which two dislocations of opposite sign on neighboring glide planes can annihilate spontaneously.

Equation (22.3) combines a term for the rate of production of dislocations and a term for the rate of annihilation. The annihilation distance y depends, of course, on the dislocation character and on the temperature. The spontaneous annihilation distance y becomes larger with increasing temperature. If additionally, high-temperature processes, like dislocation climb, must be taken into account, the annihilation distance becomes also time dependent. Considering ECAP-processed UFG materials, usually high (local) dislocation densities of 10^{14}–10^{16} m^{-2} are obtained by X-ray peak broadening analysis. In addition, as known from TEM observations, the dislocations are mainly stored at the grain boundaries. Cyclic deformation of SPD-processed materials will, very likely, lead to a change in the activated slip planes due to the change in the deformation mode. Hence, only those dislocations introduced by SPD that belong to an active glide system can be annihilated. Based on these fundamental considerations, the cyclic deformation behavior of UFG materials can be understood more easily.

The following sequence of events is visualized: Dislocations are gliding into the grain boundaries or GBAZ and annihilate spontaneously with those dislocations of opposite sign that are spaced at the annihilation distance or closer. Subsequently, dislocations of opposite signs spaced further apart can only annihilate by thermally activated (time-dependent) climb. Hence, annihilation processes of gliding dislocations with grain-boundary dislocations or dislocations stored in the GBAZ will occur much more easily at the beginning of the cyclic deformation test. During further cycling, the appropriate annihilation partners are spaced further apart, and hence the annihilation rate decreases. This proposed scenario is also strongly supported by the found strain-rate-dependent deformation behavior, see Fig. 22.5 (b). The slight cyclic softening and the consecutive strain-rate-dependent cyclic hardening of the material at the beginning of the deformation can easily be explained by the influence of thermally activated processes on the annihilation distance, as described above. In this context, it should be mentioned, that also a significantly increased amount of vacancies found in the UFG materials may contribute to the time- and temperature-dependent deformation behavior, see [70]. It is worth mentioning that a similar strain-rate-dependent cyclic deformation behavior for truly nanocrystalline nickel was reported very recently by Moser et al. [2].

As mentioned above, localization of deformation in macroscopic shear bands occurs frequently in UFG materials, see Fig. 22.6 (b) and Fig. 22.7. As localiza-

tion of plastic deformation is always a prerequisite for fatigue crack nucleation and propagation, the formation mechanisms responsible for these shear bands deserve special attention. Up to now, there is an ongoing discussion whether the shear bands are inherently formed during the ECAP process, whether they form due to a strain-path change from ECAP shear deformation to symmetrical push-pull deformation, or whether they form as a consequence to the local onset of grain coarsening, see [20, 25, 71]. Shear bands that are inherently formed during ECAP will of course seriously affect the cyclic deformation behavior. According to Iwahashi et al. [72] and to a recent investigation [73], they are expected to occur if improper ECAP parameters are applied or if the material is strongly solid-solution hardened. In the mean time it is well known that the UFG microstructure obtained depends strongly on the individual ECAP routes, the number of ECAP passes and also the materials used. The formation of shear bands during fatigue is supposed to be related also to the fraction of boundaries that are high-angle grain boundaries. If there are, on the one hand, many elongated grains with manifold low-angle grain boundaries as a substructure in between, the formation of shear bands during cycling will be rather easy. On the other hand, the situation for UFG materials produced by more appropriate ECAP processes, like route C, route B_c or related routes, leading to a more equiaxed microstructure with about 60–70% high-angle grain boundaries is not so clear. For these kinds of materials, macroscopic shear banding can be more easily attributed to a strain-path change or to grain coarsening and grain rotation than to inherently formed shear bands, see [20, 28]. Alternatively, there is also the possibility that the shear deformation during ECAP leads to nonhomogeneous band-like shaped grains, which will then be easily detectable by a thorough microstructural investigation. As proposed earlier by two of the authors [20], the following two mechanisms are supposed to govern the shear-banding mechanism, Fig. 22.8:

(a) The shear band starts at a locally coarsened grain/subgrain or at a patch, which is much more easily deformed. Triggered by the localized plastic deformation, the coarsened/weakened patch spreads out and the macroscopic

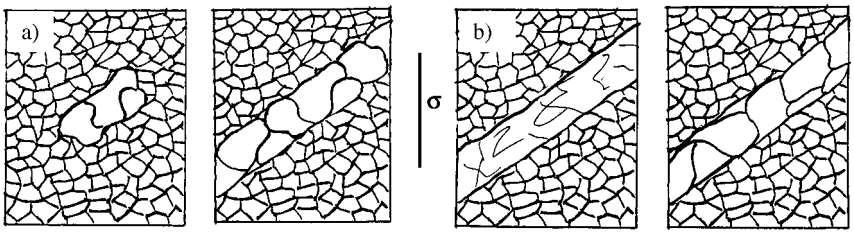

Fig. 22.8 Alternative scenarios of formation of large-scale fatigue shear bands with coarsened microstructure. Stress axis vertical. (a) Local grain/subgrain coarsening spreading out, forming a shear band. (b) Catastrophic extended shear band, caused by "strain-path change", with subsequent formation of coarsened microstructure in the shear band. From [20].

shear band forms. As pointed out earlier, grain coarsening was found to be also dependent on the plastic-strain amplitude. Hence, localized plastic deformation will be the starting point for these kinds of shear banding.

(b) The extended shear band is caused by a strain-path change (from simple shear by ECAP to push-pull deformation in the fatigue test). Catastrophic shear instability will be the consequence. Depending on the grain-boundary mobility, the microstructure in the so-formed shear band will coarsen. In this context, it should be pointed out that the grain coarsening for that mechanism can be more or less marked and can also be completely absent, if the grain-boundary mobility is small enough, as in impure or solid-solution-strengthened materials.

For both cases, the shear bands should be oriented more or less at 45° to the stress axis, which is also clearly visible in Fig. 22.6 (b) and Fig. 22.7. For shear bands formed inherently during the ECAP process, the shear bands should be, from a theoretical point of view, inclined under approximately 26° [74]. As reported in [27, 39], for less-pure Invar and copper it was found that the shear bands after fatigue exposure form along the last shear plane of the ECAP process. These observations are not contradictory to the scenarios proposed above, but are in fact compatible with the scenario of the strain-path change.

In this context, it should also be noted that a post-ECAP recovery heat treatment was shown to increase the microstructural stability and to have the potential to increase the fatigue life in the LCF regime of the total strain fatigue-life diagram, see [20–23, 26, 34, 75]. Triggered by recovery processes, where sometimes a bimodal grain-size distribution is obtained (see next section for details), under cyclic loading the microstructure is much more stable, dynamic grain coarsening will be diminished, shear banding will be significantly reduced and the fatigue life in the LCF regime of the total strain fatigue-life diagram is enhanced. However, the corresponding stress amplitude at a given strain amplitude is significantly reduced. Consequently, compared to the as-ECAP-processed counterparts, a deteriorated fatigue life in the Wöhler (*S*–*N*) plot is obtained. Nevertheless, compared to the CG counterparts, the fatigue life is still (slightly) increased.

22.4 Modeling

The attempts to model the fatigue behavior of UFG metals are still scarce. Despite the complexity and thermal and mechanical instability of UFG structures discussed above, their fatigue behavior in many ways can be visualized more simply than that of ordinary poly- and single crystals due to lacking of dislocation patterning. Patlan et al. [76] and Vinogradov et al. [77] have suggested that the shape of a stable hysteresis loop and the cyclic stress–strain curve can be described, at least semiquantitatively, by considering only the kinetics of the average dislocation den-

sity within the framework of a simplified one-parameter model based on the Eq. (22.3). Assuming the annihilation parameter y and the slip length L do not vary with straining after some elementary transformations one obtains the stress–strain relation approximating roughly the cyclic hysteresis loop

$$\tau = \tau_0 + \alpha\mu b\sqrt{\frac{1-\exp(-2y\gamma/b)}{Ly}} \tag{22.4}$$

As an example, a typical ascending part of the stable hysteresis loop of the 5056 Al alloy is plotted in Fig. 22.1 in the so-called relative coordinates σ_r–$\varepsilon_{pl\,r}$, where the tip of the compressive half-loop is set at the origin coordinates and both half-loops are considered identical. The nonlinear curve fit of experimental points by the function (22.4) with two fitting parameters – L and y – provides a reasonable agreement between the experimental and calculated loops with L and y of 1.4×10^{-7} m and 2.3×10^{-8} m, respectively, Fig. 22.1. It is worth noticing that the mean free pass of dislocations L appears to be of the order of the half-grain diameter d being typically 200–300 nm, which is a quite plausible assumption as discussed above. Similarly, one can calculate peak stresses, $\Delta\sigma/2$, at different plastic-strain amplitudes, giving an approximation of the cyclic stress–strain curve such as shown in Fig. 22.2, see Fig. 22.9 (b) [76, 77]. Furthermore, in the low-strain limit, the formulae (22.4) can be rewritten as

$$\tau = \tau_0 + \alpha\mu b\sqrt{\frac{2\gamma}{bL}} = \tau_0 + 2\alpha\mu(\gamma b)^{1/2}d^{-1/2} \tag{22.5}$$

which agrees with the Ashby expression of the Hall–Petch work-hardening stress $\tau=\tau_0+kd^{-1/2}$ (τ_0 and $k=k(\gamma)$ materials properties) if $L=d/2$. In other words, from Eq. (22.5) the $d^{-1/2}$ dependence of the flow stress agrees with the

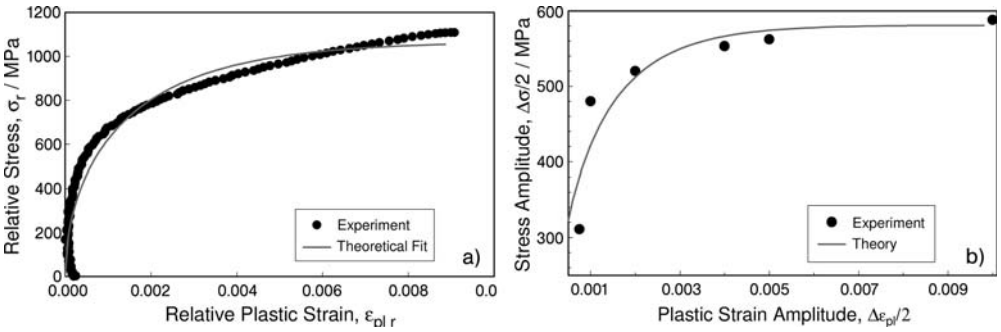

Fig. 22.9 (a) ascending part of the hysteresis loop in relative coordinates at the beginning of saturation during cycling of ECAP Ti at $\Delta\varepsilon_{pl}/2$ of 5×10^{-3} – the solid line corresponds to the linear fit of the experimental data by function (22.4); (b) fragment of the cyclic stress–strain curve for the same material the solid line corresponds to the linear fit of experimental data by function (22.5). From [77].

experimentally observed Hall–Petch behavior of the cyclic stress–strain curve and the fatigue limit. Due to the model simplicity, the qualitative agreement between experimental results and calculations is surprising. Although this modeling does not pretend to be a complete description, it emphasizes the significance of two factors in the fatigue behavior of UFG materials – dislocation accumulation and annihilation of a general kind, which are most essential and common processes in plasticity and fatigue of metals, both UFG and CG. Thus, despite oversimplification, this approach is capable to explain qualitatively such experimental results as

i) saturation of the cyclic stress amplitude,
ii) high saturation stress,
iii) rapid hardening/softening in the early stage of cycling (softening is naturally explained if one assume the initial dislocation density for differential equation (3) to be high enough),
iv) shape of the cyclic stress–strain curve and
v) Hall–Petch behavior of the fatigue limit.

Comprehensive modeling of fatigue in UFG materials should (a) be microstructurally based and (b) be able to account for the features of the cyclic behavior discussed above and (c) give reasonable estimates of cyclic life parameters, σ'_f, ε'_f, b and c, entering in Eq. (22.2) for fatigue-life prediction. When successful, such modeling could serve as a theoretical ground for optimizing the fatigue performance from the stand point of materials physics, in particular with respect to the relevant deformation mechanisms.

22.5
Criteria for Optimizing the Cyclic Deformation Behavior

Based on the fundamental aspects of the fatigue properties described above, attempts to enhance the fatigue properties of UFG materials must therefore aim at enhancing the microstructural stability of the UFG microstructures under cyclic loading and at the same time, improve the ductility. In detail, the following points are considered to play an important role, compare [20]:

- Microstructural stability: The microstructural stability is strongly affected by the ECAP process parameters, in particular by the route and number of passes and the amount and the kind of impurities of the materials used. Although these are very important factors, a fundamental knowledge of the influence of the individual microstructures on the fatigue behavior is still lacking.
- Post-ECAP recovery heat treatment: Suitable annealing treatments after ECAP have a positive effect on the fatigue lives in the LCF regime in the total strain fatigue-life diagram. The increase in fatigue ductility can be explained by a reduction of the dislocation density, which will on the one hand also affect the driving force for cyclically induced grain coarsening. On the other hand, due to the high density of dislocations introduced during the ECAP process, a

heat treatment will rearrange the dislocations lying at the grain boundaries or in the GBAZ. Rearranging the dislocations in the grain-boundary-affected zone may also affect the maximum possible slip distance positively.

- Positive effect of a bimodal microstructure: In some cases, bimodal grain-size distributions, consisting of large grains in the micrometer range embedded in an ultrafine-grained matrix, form during annealing and have a positive effect on the LCF fatigue behavior, see [20, 21]. For heat-treated UFG Cu with a bimodal microstructure, a significantly increased fatigue life reaching the value of the CG counterpart but at a higher stress level is obtained. In general however, the introduction of a bimodal microstructure by heat treatment is not always possible [22, 75]. Also, as emphasized elsewhere [22, 26, 59], a bimodal grain distribution does not always enhance the fatigue performance markedly. Hence, further attempts to introduce bimodal grain-size distributions in different UFG materials and to study and optimize their effect on the fatigue performance are desirable.
- Effect of grain size: From a more general point of view, the grain size itself should also be considered as an essential microstructural design feature influencing the fatigue life in the LCF regime, as is visible in Fig. 22.1 (b) and Fig. 22.3. As discussed above, in UFG materials the slip distance of the mobile dislocations is of the order of the grain size. Consequently, a moderate increase of the grain size is supposed to shift the intersection point in Fig. 22.4 (b) and Fig. 22.4 (d) towards higher plastic strain amplitudes. The strong influence of the grain size on the fatigue life for wavy slip UFG materials, like Cu and Al, is in contrast to the classical behavior of the CG counterparts, where a slight grain-size effect is reported only at rather high strain amplitudes, see Fig. 22.1. As described above, the grain-size dependence of the cyclic deformation behavior can be easily explained as long as the slip distance of gliding dislocations is of the order of the grain size. On the other hand, the increase of the fatigue life of UFG materials in the HCF regime cannot be explained easily by a pile-up effect of gliding dislocations at the grain boundaries as the slip distances of the gliding dislocations become significantly smaller than the grain size. For the HCF regime, it is supposed that the strongly increased stresses for the onset of microyielding in UFG materials, see [22, 44], will play a key role in enhanced fatigue lives. To conclude, a few words on the role of crack propagation are relevant. The total fatigue life results from the sum of the cycles consumed during the crack initiation period and cycles consumed in the crack propagation period. In this context, it should be noted that the reduction of the grain size from CG to UFG has a small but negative effect on the rate of fatigue-crack propagation. Thus, in the work of Kim et al. [78] on a low carbon steel, of Hanlon et al. [6] on electrodeposited Ni, of Vinogradov et al. [79] on a CuCrZr alloy or on an Al-Mg alloy [80], and of Hübner et al. [81] on Cu, Ti and Al-1.5MgScZr it has been shown that the fatigue threshold value is decreased and the fatigue crack growth rate is increased as the grain size diminishes. Further investigations should also clarify this point in more detail.

References

1 A. B. Witney, P. G. Sanders, J. R. Weertman, J. A. Eastman **1995**, *Scr. Met.* 35, 2025.
2 B. Moser, T. Hanlon, K.S. Kumar, S. Suresh **2006** *Scr. Mater.* 54, 1151.
3 D. Farkas, M. Willemann, B. Hyde **2005** *Phys. Rev. Lett.* 94, 321.
4 E. Thiele, R. Klemm, L. Hollang, C. Holste, N. Schell, H. Natter, R. Hempelmann **2005**, *Mater. Sci. Eng. A* 390, 42.
5 R. Schwaiger, B. Moser, M. Dao, N. Chollacoop, S. Suresh **2003**, *Acta Mater.* 51, 5159.
6 T. Hanlon, Y. N. Kwon, S. Suresh **200**3, *Scr. Mater.* 49, 675.
7 G. J. Raab, R. Z. Valiev, T. C. Lowe, Y. T. Zhu **2004** *Mater. Sci. Eng. A* 382, 30.
8 J. C. Lee, H.K. Seok, J. H. Han, Y. H. Chung **2001**, *Mater. Res. Bull.* 36(5–6), 997.
9 R. Z. Valiev, I. V. Alexandrov **2002**, *J. Mater. Res.* 17(1), 5.
10 H. W. Höppel, J. May, P. Eisenlohr, M. Göken **2005**, *Z. Met.kd.* 96, 566
11 H. W. Höppel, J. May, M. Göken **2004**, *Adv. Eng. Mater.* 6, 781; and unpublished work.
12 H. S. Kim, W. S. Ryu, M. Janacek, SC. Baik, Y. Estrin **2005**, *Adv. Eng. Mater.* 7, 43.
13 J. May, H. W. Höppel, M. Göken **2006**, *Mater. Sci. Forum* 503–504, 781.
14 E.O. Hall **1951**, *Proc. Phys. Soc. B* 64, 747
15 N. J. Petch **1953**, *Iron Steel Inst.* 174, 25.
16 A. Vinogradov, Y. Kaneko, K. Kitagawa, S. Hashimoto, R.Z. Valiev **1998**, *Mater. Sci. Forum* 269–272, 987.
17 S.R. Agnew, J.R. Weertman **1998**, *Mater. Sci. Eng. A* 244, 145.
18 S. R. Agnew, A. Vinogradov, S. Hashimoto, J. R. Weertman **1999** *J. Electron. Mater.* 28, 1038.
19 H. Mughrabi **2000**, in: Lowe T.C., Valiev R. Z. (eds.) *Investigations and Applications of Severe Plastic Deformation*, Kluwer Academic Publishers, Dordrecht, p. 241.
20 H. Mughrabi, H.W. Höppel, **2001**, in: D. Farkas, H. Kung, M. Mayo, H. v. Swygenhoven, J. Weertman (eds.) *Structure and Mechanical Properties of Nanophase Materials-Theory and Computer Simulation vs. Experiment, Mater. Res. Soc. Symp. Proc.* 634, B 2.1.1.
21 H. W. Höppel, M. Brunnbauer, H. Mughrabi, R. Z. Valiev, A.P. Zhilyaev **2001**, in: *Proc. of Werkstoffwoche 2000, http://www.materialsweek.org/proceedings.*
22 H. Mughrabi, H. W. Höppel, M. Kautz **2004**, *Scr. Mater.* 51, 807.
23 H. W. Höppel, Z. M. Zhou, H. Mughrabi, R. Z. Valiev **2002**, *Philos. Mag. A* 82, 1781.
24 A. Vinogradov, S. Hashimoto **2001**, *Mater. Trans.* 42, 74.
25 A. Vinogradov, S. Hashimoto **2004**, in: M. Zehetbauer, R. Z. Valiev (eds.) *Proc. of. 2nd Int. Conf on Nanomaterials by Severe Plastic Deformation Nanospd 2*, Wiley-VCH, Weinheim, p. 663.
26 H. Mughrabi, H. W. Höppel, M. Kautz **2006**, in: Y.T. Zhu and V. Varyukhin (eds.) *Nanostructured Materials by High-Pressure Severe Plastic Deformation* NATO ARW, Springer, Dordrecht, pp. 209–216.
27 P. Lukáš, L. Kunz, M. Svoboda **2006**, in: *Proc. of 9th Int. Fatigue Congress, Fatigue FT62.* CD – Elsevier Ltd.
28 H. W. Höppel, M. Kautz, C. Xu, M. Murashkin, T. G. Langdon, R.Z. Valiev, H. Mughrabi **2006**, *Int. J. Fatigue* 28, 1001.
29 H. J. Maier, P. Gabor, I. Karaman **2005**, *Mater. Sci. Eng. A* 410–411, 457.
30 L. Kunz, P. Lukáš, M. Svoboda **2006**, *Mater. Sci. Eng. A* 424, 97.
31 R. Klemm **2004**, Doctorate Thesis, Technische Universität Dresden.
32 E. Thiele, C. Holste, R. Klemm **2002**, *Z. Met.kd.* 93, 730.
33 E. Thiele, J. Bretschneider, L. Hollang, N. Schell, C. Holste **2000**, in: T. C. Lowe, R. Z. Valiev (eds.) *Investigations and Applications of Severe Plastic Deformation*, Kluwer Academic Publishers, Dordrecht, p. 173.
34 M. Kautz **2005**, Doctorate Thesis, Universität Erlangen-Nürnberg, and unpublished work.
35 H. W. Höppel, M. Kautz, H. Mughrabi **2006**, in: *Proc. of 9th Int. Fatigue Congress, Fatigue FT* 207. CD – Elsevier Ltd.
36 R. Lapovok, C. Loader, F. H. Dalla Torre, S. L. Semiatin **2006**, *Mater. Sci. Eng. A* 425, 36.

37 T.T. Lanmark, R.J. Helmig, Y. Estrin **2006**, *Mater. Sci. Forum* 503–504, 889.
38 Y. Estrin, R. Hellmig, M.J. Ek, T.T. Lanmark, Z. Zuberova, R. Lapovok, M.V. Popov **2006**, in: Y.T. Zhu, T.G. Langdon, Z. Horita, M. Zehetbauer, S.L. Semiatin, T.C. Lowe (eds.), *Ultrafine Grained Materials IV*, TMS, Warrendale, PA, USA, p. 381.
39 A. Vinogradov, S. Hashimoto, V. Kopylov **2003**, *Mater. Sci. Eng. A* 355, 277
40 V.V. Stolyarov, Y.T. Zhu , I.V. Alexandrov, T.C. Lowe, R.Z. Valiev **2003**, *Mater. Sci. Eng. A*. 343, 43.
41 A.V. Sergueeva, V.V. Stolyarov, R.Z. Valiev, A.K. Mukherjee **2002**, *Mater. Sci. Eng. A* 323, 318.
42 S. Zherebtsov, G. Salishchev, R. Galeyev, K. Maekawa **2005**, *Mater. Trans.* 46, 2020.
43 A.W. Thompson, W.A. Backofen **1971**, *Acta Metall.* 19, 597.
44 H.W. Höppel, C. Xu, M. Kautz, N. Barta-Schreiber, T.G. Langdon, H. Mughrabi **2004**, in: M. Zehetbauer, R.Z. Valiev (eds.) *Proc. of. 2nd Int. Conf on Nanomaterials by Severe Plastic Deformation Nanospd 2*, Wiley-VCH, Weinheim, p. 677.
45 H. Mughrabi, R. Wang **1988**, in: P. Lukáš, J. Polák (eds.) *Basic Mechanisms in Fatigue*, Academia, Prague and Elsevier Science Publ. Co., p. 1.
46 M. Falkner **1997**, Diplomarbeit, Universität Erlangen-Nürnberg.
47 E. Thiele **2000**, private communication.
48 P. Lukáš, M. Klesnil, J. Polak **1974**, *J. Mater. Sci.* 15, 239.
49 P. Lukáš, L. Kunz **1987**, *Mater. Sci. Eng.* 85, 67.
50 C. Buque, J. Bretschneider, A. Schwab, C. Holste **2001**, *Mater. Sci. Eng. A* 319–321, 631.
51 L.F. Coffin **1954**, *Trans. ASME* 76, 9310.
52 S.S. Manson **1953**, *NACA TN-2933.*
53 O.H. Basquin **1910**, *Proc. ASTM* 11, 625.
54 J.D. Morrow **1965**, in: *Internal Friction, Damping and Cyclic Plasticity, ASTM STP 378*, American Society for Testing Materials, Philadelphia, PA, p. 45.
55 R.W. Landgraf **1970**, in: *Achievement of High Fatigue Resistance in Metals and Alloys*, ASTM STP 467, American Soc. for Testing and Materials, Philadelphia, PA, p. 3.
56 V. Patlan, K. Higashi, K. Kitagawa, A. Vinogradov, M. Kawazoe **2001**, *Mater. Sci. Eng. A* 319–321, 587.
57 S. Hashimoto, Y. Kaneko, K. Kitagawa, A. Vinogradov, R.Z. Valiev **1999**, *Mater. Sci. Forum* 312–314, 593.
58 H.W. Höppel, R.Z. Valiev **2002**, *Z. Met.kd.* 93, 641.
59 H. Mughrabi, H.W. Höppel, M. Kautz **2006**, in: Y.T. Zhu, T.G. Langdon, Z. Horita, M. Zehetbauer, S.L. Semiatin, T.C. Lowe (eds.), *Ultrafine Grained Materials IV*, TMS, Warrendale, PA, USA, p. 47.
60 H.W. Höppel **2006**, *Mater. Sci. Forum* 503–504, 259.
61 C.E. Feltner, C. Laird **1967**, *Acta. Metall.* 15, part I: 1621, part II: 1633.
62 P. Lukáš, L. Kunz, M. Svoboda **2005**, *Mater. Sci. Eng. A* 391, 337.
63 D. Amberger **2005**, Diplomarbeit, Universtät Erlangen-Nürnberg.
64 C. Holste **2004**, *Philos. Mag. A* 84, 299.
65 R. Schwaiger, B. Moser, M. Dao, N. Chollacoop, S. Suresh **2003**, *Acta Mater.* 51, 5159.
66 L. Hollang, E. Hieckmann, D. Brunner, C. Holste and W. Skrotzki **2006**, *Mater. Sci. Eng. A* 424, 138.
67 Y.J. Li, X.H. Zeng and W. Blum **2004**, *Acta Mater.* 52, 5009.
68 D. Amberger, M. Kautz, J. May, H.W. Höppel, H. Mughrabi, M. Göken, to be submitted to *Acta. Mater.*
69 U. Essmann, H. Mughrabi **1979**, *Philos. Mag. A 40*, 731.
70 M.J. Zehetbauer, G. Steiner, E. Schafler, A. Korznikov, E. Korznikova **2006**, *Mater. Sci. Forum* 503–504, 57.
71 S.D. Wu, Z.G. Wang, C.B. Jiang, G.Y. Li, I.V. Alexandrov, R.Z. Valiev **2004**, *Mater. Sci. Eng. A* 387–389, 560.
72 Y. Iwahashi, Z. Horita, M. Nemoto, T.G. Langdon **1988**, *Acta Mater.* 46, 3317.
73 J. May **2007**, private communication.
74 A. Shang, I.G. Moon, H.S. Ko, J.W. Park **1999**, *Scr. Mat*er. 41, 353
75 H. Mughrabi, H.W. Höppel, M. Kautz, R.Z. Valiev **2003** *Z. Met.kd.* 94, 1079.

76 V. Patlan, A.Vinogradov, K. Higashi, K. Kitagawa **2001**, *Mater. Sci. Eng. A* 300, 171.
77 A. Vinogradov, V.V. Stolyarov, S. Hashimoto, R. Z. Valiev **2001**, *Mater. Sci. Eng. A* 318, 163.
78 H. K. Kim, M. I. Choi, C.S. Chung, D. H. Shin **2003**, *Mater. Sci. Eng. A* 340, 243.
79 A. Vinogradov, K. Kitagawa, V. I. Kopylov **2006**, *Mater. Science Forum* 503–504, 811.
80 A. Vinogradov, V. Patlan, K. Kitagawa, M. Kawazoe **1999**, *Nanostruct. Mater.* 11, 925.
81 P. Hübner, R. Kießling, H. Biermann, A. Vinogradov **2006**, *Int. J. Mater. Res.* 97, 1566.

23
Diffusion in Nanocrystalline Metallic Materials

Wolfgang Sprengel and Roland Würschum

23.1
Introduction

Since the pioneering research work on nanocrystalline materials by Gleiter and coworkers in 1984 [1], diffusion processes in these novel types of materials have attracted considerable interest, largely because material transport belongs to the group of physical properties differing most in nanocrystalline materials in comparison to their coarse-grained or single-crystalline counterparts. In nanocrystalline specimens, rapid mass transport can occur because of the high number density of crystallite interfaces and the fact that diffusion along interfaces is usually much faster than in crystals.

Diffusion is a determining feature of a number of application-oriented properties of nanocrystalline materials, such as enhanced ductility, diffusion-induced magnetic anisotropy, enhanced ionic mass transport, and improved catalytic activity [2, 3]. Moreover, diffusion in nanocrystalline materials is also relevant for the understanding of the basic physics of interfaces. Since interface diffusion is highly structure sensitive, diffusion studies can provide valuable insight into the question of the extent to which interfaces in nanocrystalline materials differ from conventional grain boundaries (GBs).

This chapter is an updated version of our review on diffusion in nanocrystalline metals and alloys [4]. Following a brief description of GB diffusion models (Section 23.2) and an introductory overview of experimental results (Section 23.3.1), focus is laid on the effects of structural relaxation and grain growth (Section 23.3.2), different types of interfaces (Section 23.3.3), intergranular amorphous phases (Section 23.3.4) and intergranular melting (Section 23.3.5). Specific aspects of atomistic simulations of GB structures related to diffusion are briefly summarized in Section 23.4. An assessment of the diffusion-mediated processes of deformation and induced magnetic anisotropy is given in Section 23.5 on the basis of the available diffusion data.

For a summary of diffusion data on hydrogen diffusion in nanocrystalline metals as well as diffusion in nanocrystalline ceramics, the reader is referred to

Bulk Nanostructured Materials. Edited by M. J. Zehetbauer and Y. T. Zhu

ISBN: 978-3-527-31524-6

Ref. [5]. Furthermore, reviews of GB diffusion in coarse-grained materials and bicrystals have been published by Mishin and Herzig [6, 7].

23.2 Modelling

Diffusion coefficients in solids are most precisely determined from concentration-penetration profiles obtained from long-range diffusion experiments with radioactive tracer atoms. In the general case of interface diffusion in polycrystalline materials, two simultaneous diffusion processes have to be taken into account: rapid diffusion in the crystallite interfaces (GB diffusion coefficient D_{GB}), and diffusion from the interfaces and the specimen surface into the volume of the crystallites (diffusion coefficient D_V). According to Harrison's classification scheme, three different diffusion regimes denoted by A, B, and C can be observed in polycrystalline materials. In regime A, the diffusion length in the grains is significantly longer than the average grain size d, i.e. diffusion inside the grains is dominating. The regime denoted as diffusion regime C describes the situation where diffusion occurs in grain boundaries exclusively or, in other words, where diffusion inside the grains can be neglected. The diffusion regime B falls between these two extreme cases. Here, diffusion from the grain boundary into the grains occurs but the penetration length inside the grains is smaller than the grain size. The diffusion regimes are thus characterized by appropriate ratios between the diffusion length L_V in the crystallites ($\propto (D_V t)^{0.5}$, with diffusion time t) and the crystallite diameter d or the interface thickness δ. In each of these regimes, the evaluation of the diffusion penetration profile is relatively straightforward (see, e.g., Ref. [8]).

In the case of type A ($L_V > d$) and type C ($L_V < \delta$) diffusion regimes the diffusion profiles can be described by a Gaussian distribution from which D_{GB} (type C) or an average value of D_{GB} and D_V (type A) are directly determined. In the type-B regime ($d > L_V > \delta$), in addition to the Gaussian contribution characterizing the volume diffusion, a second, deep penetrating part is observed, from which D_{GB} can only indirectly be determined, if the value of D_V is known, because only the product $s\delta D_{GB} D_V^{-0.5}$ (s denotes a segregation factor) is analytically accessible. Transitions between the regimes A and B or B and C can be treated numerically [9–11]. Moreover, an immobilization of diffusing atoms from fast interfacial diffusion paths in the crystallites that arise from the migration of GBs in the wake of grain growth can be taken into account quantitatively [12].

For fine-grained materials, Mishin and Herzig proposed an extension of the aforementioned scheme, based on different ratios of the diffusion length along the interfaces and the crystallite diameter (see Ref. [8]). For a number of recent measurements of diffusion in nanocrystalline materials, it turned out to be useful to extend the GB diffusion model to include two types of interfaces manifesting low and high diffusivity (see Section 23.3.3). Between fast and slow interface diffusion, relationships can be derived that are analogous to those valid

for the case of type-B kinetics of GB diffusion [11, 13, 14]. In another extension, Peteline and coworkers [15] considered the possibility of diffusion along the triple-line intersections of interfaces in addition to diffusion within the interfaces and crystallites.

23.3 Diffusion Measurements

23.3.1 Overview

An overview of diffusion measurements that have been performed on nanocrystalline metals and alloys is given in Table 23.1. The first diffusion study in this field was published by Horváth et al. in 1987 [16], in which self-diffusivities in nanocrystalline Cu were measured to be about three orders of magnitude higher than in grain boundaries. Subsequently, further findings of extraordinarily high diffusivities were reported in nanocrystalline metals (Table 23.1), such as the diffusivity of Ag in nanocrystalline Cu [17]. In the period following this initial era, however, it was realized that factors like structural relaxation, grain growth and residual porosity must be taken into account in order to obtain an unambiguous assessment of the diffusion in nanocrystalline metals. As a consequence of experimental advances in preparing porosity-free nanocrystalline metals of high purity, grain growth became even more prevalent during the diffusion annealing performed in subsequent studies, because of the absence of pinning centers for interfaces [18–21]. However, thermally stable nanostructures could be achieved for alloys, which permitted the study of diffusion without grain-boundary migration in a number of cases [11, 14, 22–26]. As outlined in the following, most of the studies taking these factors into consideration (Sections 23.3.2 and 23.3.3) have concluded that the diffusivities in relaxed interfaces of nanocrystalline materials are similar to or only slightly higher than diffusivities in conventional grain boundaries. However, a particular situation appears to apply to nanocrystalline alloys prepared by crystallization, in which lower interfacial diffusivities are observed, presumably as a result of the presence of residual intergranular phases (Section 23.3.4).

A wide spectrum of well-established experimental techniques has been applied to the measurement of diffusion in nanocrystalline materials, including the radiotracer method with sputter or mechanical sectioning, electron-beam microanalysis, Auger electron or secondary ion mass spectroscopy with depth profiling, Rutherford backscattering and nuclear magnetic resonance. These techniques are described in textbooks on diffusion (see, e.g., Ref. [8]) or in the respective references quoted in Table 23.1.

Table 23.1 Overview of diffusion studies on nanocrystalline materials. Pure metals: Diffusivities D at 1/4 of the melting temperature T_M obtained by linear interpolation of the experimental data. D values obtained by linear extrapolation are given in parentheses. Grain-boundary (GB) diffusivities in coarse-grained metals and bicrystals are given for comparison. Alloys: Activation energy Q and pre-exponential factors δD_0 or D_0 of diffusion. Model used for analysis: GB diffusion kinetics of type A, B, or C; models with two different types of interfaces (2 IF); brick-layer model (BL); Boltzmann–Matano technique (BM). T_a: preannealing temperature; T_d: temperature range of diffusion; d: crystallite size prior to diffusion. Synthesis route: crystallite condensation and compaction (CC), severe plastic deformation (SPD), electrodeposition (ED), melt spinning and crystallization (MS/CRY), melt spinning and hot compaction (MS/HC), mechanical alloying and hot compaction (MA/HC). Experimental method: radiotracer (RT), electron-probe microanalysis (EPMA), Auger electron spectroscopy (AES); secondary ion mass spectroscopy (SIMS), Rutherford backscattering (RBS). (Adopted from Ref. [4]).

Pure metals	Synthesis	Diffusor	T_a [K]	T_d [K]	D (0.25 T_M) [m^2 s^{-1}]	Model	d [nm]	Exp. Method	Ref.
Pd	CC	Fe	373 [a]	423–523	2.8×10^{-20}	C	50 [b]	RT	[18]
	SPD	Fe	293–673	371–623	3×10^{-20}	C	80 [b]	RT	[19]
Fe	CC	Fe	403 [a]	452–499	1×10^{-21} [c]	C	31 [b]	RT	[4]
	SPD	Fe	527	527	3×10^{-19} [c] (0.29 T_M)	C	NS	RT	[4]
Cu	CC	Cu	293	293–393	9.2×10^{-19}	C	8 [d]	RT	[16]
	CC	Ag	293	303–373	1.6×10^{-18}	C	8	EPMA	[17]
	CC	Au	293	373	4.8×10^{-22} (0.27 T_M)	C	10	AES	[65]
	CC	Bi	293	293–413	3×10^{-20} [c]	C	10	RBS	[65]
	CC	Sb	293	323–373	2.4×10^{-21} 1.3×10^{-22}	2 IF [e]	50	RBS	[66]
Ni	CC	Ni	773 [b]	293–473	5.9×10^{-18} 1.6×10^{-19} (0.27 T_M)	2 IF [e]	70	RT	[67]
	SPD	Cu	398	398–448	9.6×10^{-15} [c] (0.245 T_M)	C	300 d)	SIMS	[68]
	ED	Cu	–	423	3.8×10^{-17} (0.245 T_M)	C	30	SIMS	[68]
Fe	CC	B	–	293–383	(4.5×10^{-18})	C	7	SIMS	[69]
Grain boundary (GB) diffusion in coarse-grained metals and bicrystals									
fcc, general					(1.7×10^{-21}) [f]				[70]
bcc, general					(7.1×10^{-23}) [f]				[70]
Ag					1.2×10^{-16} (0.29 T_M)				[71]
Σ5-tilt-GB Ag/Au					(2.7×10^{-19}) [f]				[48]

Table 23.1 (Fortsetzung)

Alloys	Synthesis	Diffusor	T_a [K]	T_d [K]	δD_0 or D_0	Q [eV]	Model	d [nm]	Method	Ref.
$Fe_{73.5}Si_{13.5}B_9Nb_3Cu_1$	MS/CRY	Fe	810–818	628–773	–	1.9	BL	13 [d]	RT	[22]
		Ge	817	735–783	1.1×10^{-8} m^3 s^{-1}	2.91	B	13 [d]	RT	[40]
$Fe_{90}Zr_7B_3$	MS/CRY	Fe	873	593–773	2.8×10^{-7} m^2 s^{-1}	1.70	2 IF [e]	18 [d]	RT	[37]
				623–741	6.8×10^{-14} m^3 s^{-1}	1.64				
$Nd_{14.2}Fe_{80.8}B_5$	MS/HC	Fe	1048	689–951	1.5×10^{-11} m^3 s^{-1}	1.74	B	100 [d]	RT	[23, 24]
		Nd	1048	623–950	1.7×10^{4} m^2 s^{-1}	2.65	C	100–500 [d]	RT	[26]
γ-$Fe_{61.2}Ni_{38.8}$	MA/HC	Fe	1123	636–1013	4.2×10^{-3} m^2 s^{-1}	1.93	A, AB	80–100 [d]	RT	[11]
					3.4×10^{-3} m^2 s^{-1}	1.53	B, 2 IF [e]			
$Al_{91.9}Ti_{7.8}Fe_{0.3}$	MA/HC	Cu	673	371–571	2.4×10^{-12} m^2 s^{-1}	0.364	C	22	SIMS	[72]
$Al_{96.8}Mg_3Sc_{0.2}$/ $Al_{99.8}Sc_{0.2}$	SPD		293	523–723	–	1.02 [g]	BM	200 [b]	EPMA	[73]

a) Temperature of crystallite compaction.
b) Crystallite growth during diffusion annealing observed.
c) Variation with temperature of preanneal or with diffusion time observed.
d) Crystallite size constant upon diffusion annealing.
e) 2-IF diffusion model (the two values in the 1st and 2nd lines refer to diffusion along two types of interfaces).
f) Related to grain-boundary thickness $\delta = 1$ nm.
g) Interdiffusion.

23.3.2 Structural Relaxation and Grain Growth

Since the conditions prevalent during the synthesis of nanocrystalline materials are far from thermodynamic equilibrium, the initial structure of interfaces in such samples may depend sensitively on the time–temperature history. For nanocrystalline metals prepared by crystallite condensation in an inert-gas atmosphere with subsequent crystallite compaction, extensive experimental evidence exists that structural relaxation occurs at slightly elevated temperatures. That this structural relaxation exerts an influence on the diffusion behavior can be concluded from the decrease in the self-diffusion coefficient with increasing time of diffusion annealing, as measured, for instance, in nanocrystalline Fe prepared by the cluster condensation and compaction route and by severe plastic deformation [20]. Similar observations were made by Kolobov et al. [27] on nanostructured Ni prepared by severe plastic deformation. In that case, the diffusivity of Cu at 423 K was found to decrease by more than three orders of magnitude upon preannealing of the sample at 523 K prior to the onset of grain growth [27]. Both in nanocrystalline Fe [20] and in nanocrystalline Ni [27], the interfacial diffusion coefficients in the relaxed state appear to be similar to or only slightly higher than the values expected for conventional GBs in coarse-grained materials from an extrapolation of high-temperature data.

The enhanced diffusivity observed in nanocrystalline metals prior to relaxation may indicate a nonequilibrium structure of the interfaces. Nonequilibrium GBs are known in the case of cold-worked metals, where they exhibit a gradual relaxation behavior or a metastable character [28]. The enhanced diffusivities found in such samples are ascribed to the absorption of lattice dislocations at GBs [28, 29]. In the case of nanocrystalline metals, in which dislocation activity ceases due to the small crystallite size [30], enhanced diffusivities may arise from local excess free volume, which, in the case of inert-gas-condensed samples, may remain following the high-pressure compaction step. Evidence for the existence of vacancy-type interfacial free volumes and their variation upon annealing at slightly elevated temperatures could be derived from positron annihilation studies [31]. This situation resembles the well-known structural relaxation in amorphous alloys, where the annealing out of excess volume gives rise to a decrease in diffusivity (see, e.g., Ref. [32]). Unlike the case of amorphous alloys, the microstructure of which remains stable over a relatively wide temperature range below the onset of crystallization, the relaxed structure of nanocrystalline metals is highly prone to interface migration and grain growth. This is particularly true for pore-free nanocrystalline metals of high purity, in which pinning centers for interfaces have largely been eliminated [18]. In that case, the assessment of the diffusion behavior is affected by the concomitant GB migration.

The occurrence of crystallite growth during diffusion gives rise to a decrease in the fraction of interfaces and, as a consequence of growth-induced interface migration, to a slowing down of tracer diffusion, since the tracer atoms are immobilized by incorporation at lattice sites of the crystallites. Although this leads

to deviations from Gaussian diffusion profiles, the diffusivities derived from fits of Gaussians to the diffusion tails according to type-C kinetics (see Section 23.2) may still lie fairly close to the actual values of D_{GB}. This follows from the fact that the tails of the diffusion profiles are least affected by grain growth, because the tails are governed by those GBs that migrate at the lowest rate [21]. Here, it is useful to note that regions with low or negligible GB migration are commonly observed during inhomogeneous grain growth, which frequently prevails in nanocrystalline samples [5, 21].

The complications introduced by grain growth in nanocrystalline metals are even more serious when attempting to ascribe a physical interpretation to experimental values for the activation energies of diffusion, because grain growth seriously limits the temperature range of such studies. For this reason, only characteristic diffusion coefficients are quoted for nanocrystalline metals in Table 23.1, rather than activation energies.

An enhanced stability of nanocrystalline metals with respect to grain growth may be obtained in the case of thin films, as studied by Erdélyi et al. [33]. In nanocrystalline Cu films, the diffusion of Ag in the low-temperature regime of type-C kinetics was found to be consistent with the GB diffusion and segregation data obtained for conventional GBs in the type-B regime (see Section 23.2) [33].

23.3.3
Different Types of Interfaces

In a number of nanocrystalline alloys, it has been possible to carry out diffusion studies over a wide temperature range without complications arising from grain growth (Section 23.3.2). Despite the stable microstructure, the diffusion characteristics of such nanocrystalline alloys may be quite complex, owing to the presence of various types of interfaces (this section), intergranular amorphous phases (Section 23.3.4), or the occurrence of intergranular phase melting (Section 23.3.5).

Different types of interfaces even in the same material may be a characteristic feature of nanocrystalline materials, particularly in those cases in which bulk materials are prepared from powders consisting of agglomerates of nanocrystallites. The interfaces between these μm-sized agglomerates (i.e. interagglomerate boundaries) as well as residual porosity between the agglomerates provide pathways of higher diffusivity, whereas a lower diffusivity occurs along the interfaces between the nanocrystallites located within the agglomerates (so-called intra-agglomerate boundaries). A first diffusion study taking these two types of interfaces into account was performed by Bokstein et al. [13] on cluster-assembled nanocrystalline Ni with a density of 92–93% of the bulk density. This approach was generalized in a model for diffusion in two-scale interface materials by Divinski et al. [11] by employing relationships analogous to those of type-B GB diffusion kinetics (see Section 23.2). A fast diffusion process is ascribed to diffusion in the interagglomerate boundaries compared to a second process of slower diffusion fluxes from the interagglomerate into the intra-agglomerate bound-

aries. The much lower diffusion fluxes from the intra-agglomerate boundaries into the volume are negligible in this case. The analysis method was applied to Fe [11] and Ni [34] self-diffusion and Ag [35] impurity diffusion studies in 98%-dense nanocrystalline γ-Fe–40wt%Ni prepared by mechanical alloying and hot compaction. In all cases of diffusion in nanocrystalline Ni [13] and γ-$Fe_{61.2}Ni_{38.8}$ [11, 34–36], the diffusion in the interagglomerate boundaries occurs at rates that are several orders of magnitudes higher than diffusion in the intra-agglomerate boundaries. On the other hand, the diffusion in the intra-agglomerate boundaries, that is in the boundaries between the nanocrystals, was found to be of the same order and with similar Arrhenius-type temperature characteristics as for conventional GBs.

Evidence for the presence of various types of interfaces has also been obtained in nanocrystalline Fe-based alloys prepared by crystallization [14, 37]. In these highly dense alloys, residual intergranular amorphous phases rather than interagglomerate boundaries give rise to additional interfacial diffusion paths, as outlined in the following section.

23.3.4
Intergranular Amorphous Phases

Nanocrystalline Fe-based alloys prepared by crystallization are of high technical relevance due to their superior soft-magnetic properties [38]. The two basic types of alloys are $Fe_{73.5}Fe_{13.5}B_9Nb_3Cu_1$ (VITROPERM^{TM}) and $Fe_{90}Zr_7B_3$ (NANOPERM^{TM}), consisting of $D0_3$-Fe_3Si or α-Fe nanocrystallites, respectively, with sizes of 10 to 15 nm embedded in a residual amorphous matrix. Larger crystallite sizes of ca. 30 nm with a two-phase structure of α-Fe and Fe-Zr nanocrystallites are formed upon crystallization of $Fe_{90}Zr_{10}$ [14].

As these materials are highly dense, pore free, and thermally stable, interface diffusion can be studied without any influence of porosity, relaxation, or grain growth. Each of the three Fe-based alloys manifests Fe-tracer diffusivities that are substantially lower than those of GBs in α-Fe (Fig. 23.1, [14, 22, 23]). This particular feature strongly differs from the diffusion behavior observed in other nanocrystalline metals and alloys (see above). The reduced interfacial diffusivities, which are similar to ($Fe_{73.5}Si_{13.5}B_9Nb_3Cu_1$) or even lower ($Fe_{90}Zr_7B_3$, $Fe_{90}Zr_{10}$) than those of the initial amorphous phases, are considered to arise from the residual intergranular amorphous phases (interface type I).

In addition to the slow interface diffusivity, indications for a second fast diffusion process have been deduced from the tails of the diffusion profiles measured in nanocrystalline $Fe_{90}Zr_7B_3$ [23] and $Fe_{90}Zr_{10}$ [14, 39]. Adopting the simple picture of the existence of two types of interfaces with high and low interface diffusivities – which can be described with diffusion kinetics analogous to those of type B – we find the fast process to be characteristic of diffusion along conventional GBs (interface type II; Figs. 23.1 and 23.2, [23, 39]). Although the description in the framework of a two-interface type model is conceptually the same as in the case of powder-compacted nanocrystalline materials (see Section

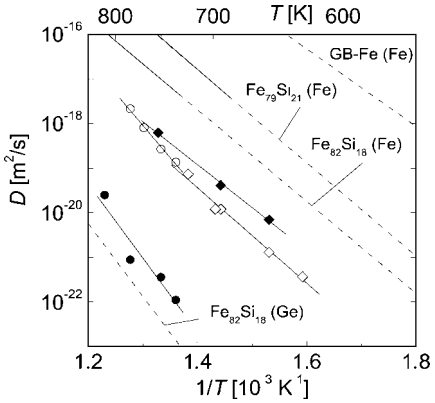

Fig. 23.1 Temperature dependence of Ge and Fe diffusivities in $Fe_{73.5}Si_{13.5}B_9Nb_3Cu_1$: ^{71}Ge diffusion in nanocrystallites (●, D_V) and in interfaces (○, D_B) [40]; ^{59}Fe diffusion in the nanocrystalline state (◆) and in the initial amorphous state (◇) [22]. The data are compared to diffusion in coarse-grained polycrystalline $D0_3$-$Fe_{82}Si_{18}$ and $D0_3$-$Fe_{79}Si_{21}$ [41] and in grain boundaries (GBs) of α-Fe [42], the diffusing element is given in parentheses, dashed lines indicate extrapolation of the literature data. (Adopted from Ref. [40], http://www.tandf.co.uk/journals).

23.3.3), the character of the various types of interfaces is quite different. In the alloy obtained from crystallization, the major diffusion path with the lower diffusivity (interface type I) is given by the interfaces with the intergranular amorphous phase, whereas in the metals obtained from the compaction of agglomerates the intra-agglomerate boundaries represent the major diffusion path with the lower diffusivity [35].

In the case of $Fe_{73.5}Si_{13.5}B_9Nb_3Cu_1$, a rather detailed picture of diffusion characteristics is obtained from data on the Fe- [22] and Ge-tracer diffusivities [40] as well as on the thermal formation of lattice vacancies as deduced from positron annihilation [22]. Ge diffusion is considered to characterize Si self-diffusion. Like the Fe interface diffusion, the interface diffusion of Ge is rather similar to the Fe diffusion in the amorphous state, i.e. both the Ge and the Fe interface diffusivities are therefore determined by the amorphous intergranular phase. In contrast to the interfacial diffusivities, the diffusivities of Ge and Fe in the nanocrystallites differ substantially, reflecting the peculiar diffusion behavior of Fe and Ge in crystalline $D0_3$-type Fe_3Si. The Fe diffusion in $D0_3$-type Fe_3Si is extraordinarily fast [41] owing to a high concentration of thermal vacancies [43]. The Ge diffusion in $D0_3$-type Fe_3Si, on the other hand, is orders of magnitude lower [41] presumably because of a much lower thermal vacancy concentration and a longer vacancy jump distance on the Si sublattice [43]. A similar situation is considered to prevail in the Fe_3Si nanocrystallites of $Fe_{73.5}Si_{13.5}B_9Nb_3Cu_1$, as deduced from the Fe- and Ge-tracer diffusion data in combination with the high-temperature positron lifetime data [40]. Owing to the strongly differing diffusivities of Fe and Ge in the nanocrystallites but the similar diffusivities in the amorphous intergranular layers, the particular situation

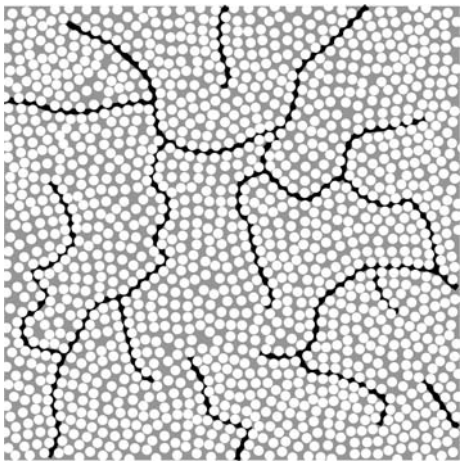

Fig. 23.2 Model for the microstructure of a nanocrystalline alloy obtained from crystallization of an amorphous precursor with two different types of interfaces. Nanocrystallites (white circles) embedded in an amorphous intergranular phase (interface type I). Black lines indicate interfaces without an amorphous phase (interface type II) with properties similar to grain boundaries in crystals. (Adopted from Ref. [37]).

arises that the Fe diffusion in the nanocrystallites is faster than in the interfaces, whereas the opposite is true for the Ge diffusion [40].

23.3.5 Intergranular Melting

Diffusion studies of nanocrystalline alloys and compounds have also been performed on $Nd_2Fe_{14}B$-based materials, which manifest an intergranular melting transition of Nd-enriched grain boundaries [45]. These studies are motivated by the important role played by intergranular melting in the technological application of this permanent magnetic material. The powder-metallurgical processing of $Nd_2Fe_{14}B$ takes advantage of intergranular melting in order to induce crystallographic and thus magnetic texture [45].

The diffusion studies performed on nanocrystalline $Nd_2Fe_{14}B$ shed light on a novel type of diffusion behavior in nanocrystalline materials. Radiotracer measurements carried out with the isotopes ^{59}Fe and ^{147}Nd show a substantial increase of the interface diffusion coefficient D_B for temperatures above the intergranular melting transition [23–26]. The increase of D_B reaching high values characteristic of diffusivities in bulk melts occurs over a distinct temperature range, rather than abruptly. Such a gradual change could result either from confinement effects or from an initially local melting. Both effects give rise to reduced long-range diffusivities compared to bulk melts, as long as the dimensions of the molten region are small or an interconnected network of liquid regions has not yet been formed during the initial stage of melting. Below the inter-

granular melting transition, the grain-boundary diffusivities in nanocrystalline $Nd_2Fe_{14}B$ are found to be similar to those of α-Fe, within a framework of grain-boundary diffusion kinetics of type B with an assumed volume self-diffusivity as in α-Fe (see Fig. 23.3). This assumption is supported by a quantitative consideration of the different regimes of interface diffusion [25]. In the case of Nd-diffusion experiments the diffusivities were directly determined from experiments in the kinetic regime of type C and are similar to the ones reported for Fe diffusion [26]. It turned out that neither the Nd nor the Fe diffusion is rate controlling for the thermodynamically induced generation of the texture observed for magnetic $Nd_2Fe_{14}B$ compounds. For a more detailed analysis of the diffusion characteristics of ultrafine-grained $Nd_2Fe_{14}B$ measurements of bulk diffusion coefficients in single-crystalline or coarse-grained $Nd_2Fe_{14}B$ would be desirable.

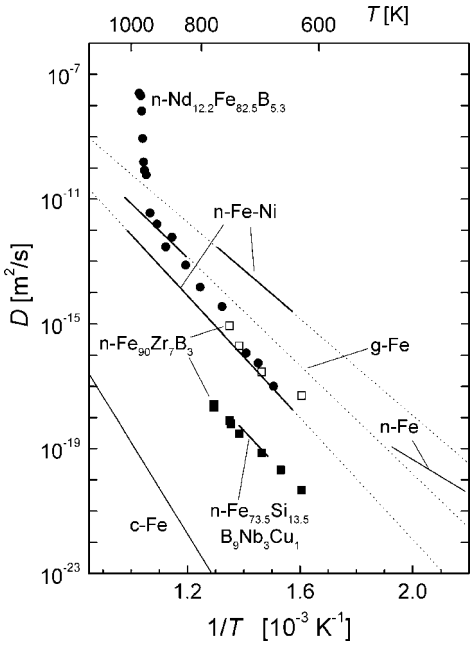

Fig. 23.3 Arrhenius plots of ^{59}Fe-tracer diffusivities in nanocrystalline Fe [20] and the Fe-rich nanocrystalline alloys $Fe_{73.5}Si_{13.5}B_9Nb_3Cu_1$ [40], $Fe_{90}Zr_7B_3$ [37] and $Nd_{12.2}Fe_{81.8}B_6$ [23] (interface thickness $\delta = 1$ nm). For $Fe_{90}Zr_7B_3$ the diffusivities in the two types of interfaces (■ and □) are shown. The data of n-Fe refer to relaxed GBs. Data of Fe diffusion in the ferromagnetic phase of crystalline α-Fe (c-Fe, [46]) and in grain boundaries of Fe (g-Fe, [42]) are shown for comparison (extrapolations are dotted). (Adopted from Ref. [4]).

23.4
Atomistic Simulations

Atomistic simulations have become a valuable tool for gaining additional insights into interfacial diffusion processes in bicrystals (for reviews see, e.g., Refs. [6, 47]) and nanocrystalline materials [30].

In coincidence site GBs of metals, which represent special GBs, diffusion is found to be mediated by point defects with reduced activation energies of formation and migration compared to the lattice. In contrast to lattice diffusion in metals, where vacancy-mediated diffusion prevails, computer simulations show that GB diffusion can be dominated either by vacancy- or by interstitial-related mechanisms, depending on the GB structure [48, 49]. The picture of single point defects in ordered GBs appears to be restricted to low and moderate temperatures, where the thermal motion of atoms induces only limited distortions of the GB structure. At high temperatures according to molecular dynamics simulations performed by Keblinski et al. [50] – high-energy GBs may undergo a transition from a solid to a confined liquid state, accompanied by a decrease in the activation energy for diffusion.

Nanocrystalline structures were also studied by Wolf and coworkers [30, 51, 52] in a number of computer simulations. They find that low-angle and special boundaries are absent in nanocrystalline materials; according to these studies, nanocrystalline materials contain only high-energy GBs, with atomic structures like those of high-energy GBs in bicrystals. Therefore, nanocrystalline materials are characterized by a narrow distribution of interfacial widths and energy densities. As far as diffusion is concerned, simulations of GB diffusion creep in a nanocrystalline Pd model structure at high temperatures of 900 K and above reveal a Coble-creep-type behavior, with a fast liquid-like self-diffusivity as found in high-energy GBs at high temperatures [30]. So far, an unambiguous comparison with experimental diffusion data is hampered by the drastically different temperature regimes accessible in computer simulations ($T > 900$ K) and experimental studies ($T < 600$ K, see Table 23.1).

23.5
Comparison with Diffusion-mediated Processes of Deformation and Induced Magnetic Anisotropy

Diffusion is particularly relevant for the deformation behavior of nanocrystalline metals and alloys, as, with small crystallite sizes, conventional dislocation mechanisms may be suppressed and grain-boundary-mediated deformation processes may dominate [30]. From a comparison of the diffusion and deformation characteristics of nanocrystalline metals and alloys a basic understanding of the deformation mechanisms may be obtained.

In molecular-dynamics simulations of high-temperature deformation of nanocrystalline Pd, Yamakov et al. [30] observed the steady-state strain rate to obey

Coble-creep behavior, as characteristic of a GB-diffusion-mediated deformation. Grain-boundary sliding was found to be an accommodation mechanism for the Coble creep, with the entire deformation process being controlled by GB diffusion [30].

The occurrence of a GB-diffusion-mediated deformation process is also the conclusion reached by room-temperature creep experiments performed by Wang et al. [53] on electrodeposited nanocrystalline Ni. At small grain sizes of 6 nm, the strain rate $d\varepsilon/dt \sim \sigma^n$ is found to be related to the stress σ by a stress exponent n of 1.2 – a value lying between that of Coble creep ($n=1$) and GB-diffusion-controlled GB sliding ($n=2$) [53]. At grain sizes between 20 nm and 40 nm, higher values of n up to 5.3 indicate a transition to dislocation creep with increasing crystallite size [53]. Creep studies carried out on electrodeposited n-Cu by Cai et al. [54] also revealed a linear relation between strain rate and stress (i.e. $n=1$), as characteristic of GB-diffusion-controlled Coble creep. This is further supported by the observed increase of the strain rate of n-Cu with temperature, from which an activation energy for diffusion creep of 0.72 eV [54] – rather similar to the activation energy for GB self-diffusion in coarse-grained Cu [55] – is derived. For nanostructured Ni prepared by severe plastic deformation Kolobov et al. [56] deduced an apparent creep activation energy of 1.2 eV. Although this value again nearly equals the activation energy for GB self-diffusion in coarse-grained Ni [8], in this case other creep mechanisms in addition to GB diffusion may be operative, owing to the larger grain size of 300 nm. In combined diffusion and plasticity studies of submicrocrystalline Ni, Ti, Cu, and Al-base alloys [57] and Ti and Ti-base alloys [58] Kolobov et al. found an increased GB diffusivity of up to 5 orders of magnitude higher for ultrafine-grained materials prepared by severe plastic deformation if compared to coarse-grained materials. The activation energy for Co diffusion in the grain boundaries of ultrafine-grained Ti is much lower than for the coarse grained counterpart [58].

An important application-relevant issue concerning the high-temperature deformation of nanocrystalline materials is the processing and magnetic anisotropy of soft-magnetic and hard-magnetic nanocrystalline alloys. A high-temperature treatment of magnetic alloys placed under mechanical load or in an external magnetic field may give rise to diffusion-mediated magnetic anisotropy or texture, which may be desirable for tailoring the hysteresis loop [44, 45, 59]. Recently obtained diffusion data and their comparison with deformation characteristics may offer insight into the microscopic processes underlying the magnetic anisotropy induced during the processing of magnetic nanocrystalline alloys.

Based on a model developed by Néel, the induced anisotropy in the soft-magnetic nanocrystalline alloy $Fe_{73.5}Si_{13.5}B_9Nb_3Cu_1$ can be considered to arise from atomic pair ordering [44]. According to Emura et al. [60], the activation energy of 2.9 eV measured for the formation of magnetic anisotropy in the nanocrystalline state of $Fe_{73.5}Si_{13.5}B_9Nb_3Cu_1$ is higher than the corresponding value – 1.92 eV – of the amorphous state [60]. In addition, the magnetic anisotropy was found to be induced more efficiently during crystallization (so-called one-step

annealing) than by a two-step annealing procedure of crystallization followed by anisotropy formation [61]. A comparison of both results with the diffusion data of nanocrystalline $Fe_{73.5}Si_{13.5}B_9Nb_3Cu_1$ (Table 23.1) shows that, for the following reasons, the diffusivity of Fe can be excluded as the controlling factor for anisotropy formation [22]: (i) The Fe diffusivity increases upon crystallization, in contrast to the efficiency of anisotropy formation. (ii) The activation energy of 1.9 eV for Fe diffusion in the nanocrystalline state is substantially lower than the activation energy of 2.9 eV for anisotropy formation. (iii) On the time scale of anisotropy formation, the Fe diffusion length substantially exceeds the crystallite diameter, which is considered to be an upper bound for the characteristic diffusion length required for anisotropy formation by atomic pair ordering. Instead of Fe diffusion, the anisotropy formation appears to be controlled by diffusion of Si. Indeed, the diffusion of Ge in $Fe_{73.5}Si_{13.5}B_9Nb_3Cu_1$, which is considered to resemble Si diffusion, is found to be much slower than Fe diffusion, with an activation energy similar to that of anisotropy formation [40]. From a detailed analysis of Ge diffusion profiles, it can be concluded that the limiting factor for anisotropy formation in n-$Fe_{73.5}Si_{13.5}B_9Nb_3Cu_1$ is Si diffusion in the nanocrystallites, rather than through the intergranular amorphous matrix, indicating that the development of magnetic anisotropy requires diffusion-mediated Fe-Si pair ordering to occur within the nanocrystallites. This view is also supported by the observation that the induced magnetic anisotropy sensitively depends on the Si content of the $D0_3$-type Fe_3Si compound [62]. The smaller the deviation from the stoichiometric composition, the smaller is the anisotropy constant, which indicates that with decreasing deviation from stochiometry it becomes more difficult to disturb the cubic symmetry, which is necessary for magnetic anisotropy. Unlike field-induced anisotropy, the anisotropy induced by mechanical stress is considered to arise mainly due to distortions in the intergranular amorphous and the crystalline phase by internal stress [63]. Similarly, diffusion creep appears also to be governed by GB diffusion rather than by diffusion in the nanocrystallites. In fact, in nanocrystalline Fe-Si-B – prepared by crystallization with a composition similar to that of $Fe_{73.5}Si_{13.5}B_9Nb_3Cu_1$ – a low activation energy of 1.5 eV is found for diffusion creep [64], which is characteristic of Fe diffusion in Fe-rich amorphous alloys.

During the processing of nanocrystalline $Nd_2Fe_{14}B$ permanent magnets, hot deformation is applied in order to induce a magnetic texture. Although the deformation of these materials is promoted by the presence of a liquid grain-boundary phase, which forms as a consequence of an excess content of Nd, the stress exponent n of the strain rate and the activation energy of deformation does not depend on the structure of the grain-boundary phase, that is whether it is liquid or solid [45]. This contrasts with the aforementioned Fe self-diffusion studies of nanocrystalline $Nd_2Fe_{14}B$ (Section 23.3.5, Table 23.1), which show a pronounced increase of D_{GB} upon intergranular melting. Moreover, the activation energy of 2.9 eV for deformation [45] is higher than the value of 1.74 eV for grain-boundary diffusivity (Table 23.1). These discrepancies between the characteristics of deformation and Fe diffusion confirm prior conclusions that,

in this case, the deformation process is controlled by a solution-precipitation process occurring at GBs, rather than by GB diffusion [45] – a notion further supported by Nd self-diffusion studies [26].

References

1 R. Birringer, H. Gleiter, H.-P. Klein, P. Marquardt **1984**, *Phys. Lett. A* 102, 365–369.

2 A. S. Edelstein, R. C. Camarata (eds.) **1996**, *Nanomaterials: Synthesis, Properties, and Applications* Institute of Physics, Bristol.

3 C. C. Koch (ed.) **2002**, *Nanostructured Materials: Processing, Properties and Applications*, Noyes Publications, William Andrew Publishing, Norwich, NY.

4 R. Würschum, S. Herth, U. Brossmann **2003**, *Adv. Eng. Mater.* 5, 365–372.

5 R. Würschum, U. Brossmann, H.-E. Schaefer, in Ref. [3], 267–299.

6 Y. Mishin, Chr. Herzig **1999**, *Mater. Sci. Eng. A* 260, 55–71.

7 Y. Mishin, **2001**, *Defect Diffus. Forum* 194–199, 1113–1126.

8 I. Kaur, Y. Mishin, W. Gust **1995**, *Fundamentals of Grain and Interphase Boundary Diffusion*, John Wiley, Chichester.

9 I. A. Szabó, D. L. Beke, F. J. Kedves **1990**, *Philos. Mag. A* 62, 227–239.

10 I. V. Belova, G. E. Murch **2001**, *Philos. Mag. A* 81, 2447–2455.

11 S. V. Divinski, F. Hisker, Y.-S. Kang, J.-S. Lee, C. Herzig **2002**, *Z. Metallkd.* 93, 256–264; 265–272.

12 A. M. Glaeser, J. W. Evans, **1986**, Acta Metall. 34, 1545; F. Güthoff, Y. Mishin, C. Herzig **1993**, *Z. Metallkd.* 84, 584–591.

13 B. S. Bokstein, H. D. Bröse, L. I. Trusov, T. P. Khvostantseva **1995**, *Nanostruct. Mater.* 6, 873–876.

14 R. Würschum, T. Michel, P. Scharwaechter, W. Frank, H.-E. Schaefer **1999**, *Nanostruct. Mater.* 12, 555–558.

15 L. M. Klinger, L. A. Levin, A. L. Peteline **1997**, *Defect Diffus. Forum* 143–147, 1523–1526; A. L. Peteline, S. Peteline, O. Oreshina **1996**, *Defect Diffus. Forum* 194–199, 1265–1270.

16 J. Horváth, R. Birringer, H. Gleiter **1987**, *Solid State Commun.* 62, 319–322.

17 S. Schumacher, R. Birringer, R. Strauß, H. Gleiter **1989**, *Acta Metall.* 37, 2485–2488.

18 R. Würschum, K. Reimann, S. Gruß, A. Kübler, P. Scharwaechter, W. Frank, O. Kruse, H. D. Carstanjen, H.-E. Schaefer **1997**, *Philos. Mag. B* 76, 407–417.

19 R. Würschum, A. Kübler, S. Gruß, P. Scharwaechter, W. Frank, R. Z. Valiev, R. R. Mulyukov, H.-E. Schaefer **1996**, *Annal. Chim. – Sci. Matér.* 21, 471–482.

20 H. Tanimoto, P. Farber, R. Würschum, R. Z. Valiev, H.-E. Schaefer **1999**, *Nanostruct. Mater.* 12, 681–684.

21 R. Würschum, K. Reimann, P. Farber **1997**, *Defect Diffus. Forum* 143–147, 1463–1468.

22 R. Würschum, P. Farber, R. Dittmar, P. Scharwaechter, W. Frank, H.-E. Schaefer **1997**, *Phys. Rev. Lett.* 79, 4918–4921.

23 S. Herth, M. Eggersmann, P. D. Eversheim, R. Würschum **2004**, *J. Appl. Phys.* 95, 5075–5080.

24 S. Herth, F. Ye, M. Eggersmann, O. Gutfleisch, R. Würschum **2004**, *Phys. Rev. Lett.* 92, 095901/1–4.

25 S. Herth, F. Ye, M. Eggersmann, H. Rösner, O. Gutfleisch, R. Würschum **2004**, *Z. Metallkde* 95, 895–903.

26 W. Sprengel, S. Herth, V, Barbe, H.-E. Schaefer, T. Wejrzanowski, O. Gutfleisch, R. Würschum **2005**, *J. Appl. Phys.* 98, 074314/1–5.

27 Y. R. Kolobov, G. P. Grabovetskaya, M. B. Ivanov, A. P. Zhilyaev, R. Z. Valiev **2001**, *Scr. Mater.* 44, 873–878.

28 L. G. Kornelyuk, A. Yu Lozovoi, I. M. Razumovskii **1997**, *Defect Diffus. Forum* 143–147, 1481–1486.

29 R. Z. Valiev, I. M. Razumovskii, V. I. Sergeev **1993**, *phys. stat. sol. (a)* 139, 321–335.

30 V. Yamakov, D. Wolf, S. R. Phillpot, H. Gleiter **2002**, *Acta Mater.* 50, 61–73.

31 R. Würschum, H.-E. Schaefer, in Ref. [2], pp. 277–301.

32 W. Frank **1997**, *Defect Diffus. Forum* 143–147, 695–710.

33 Z. Erdélyi, Ch. Girardeaux, G. A. Langer, D. L. Beke, A. Rolland, J. Bernardini **2001**, *J. Appl. Phys.* 89, 3971–3975.

34 S. V. Divinski, F. Hisker, Y.-S. Kang, J.-S Lee, Chr. Herzig **2003**, *Interface Sci.* 11, 67–80.

35 S. V. Divinski, F. Hisker, Y.-S. Kang, J.-S Lee, Chr. Herzig **2003**, *Acta Mater.* 52, 631–645.

36 Y.-S. Kang, J.-S. Lee, S.V. Divinski, Chr. Herzig **2004**, *Z. Metallkd* 95, 76–79.

37 S. Herth, M. Eggersmann, P.-D. M. Eversheim, P.-D. Eversheim, R. Würschum **2004**, *J. Appl. Phys.* 95, 5075–5080.

38 Y. Yoshizawa, S. Oguma, K. Yamauchi **1988**, *J. Appl. Phys.* 64, 6044–6046; G. Herzer, **1989**, *IEEE Trans. Magn.* 25, 3327–3329.

39 S. Herth, T. Michel, H. Tanimoto, M. Eggersmann, R. Dittmar, H.-E. Schaefer, W. Frank, R. Würschum **2001**, *Defect Diffus. Forum* 194–199, 1199–1204.

40 S. Herth, M. Eggersmann, G. Herzer, R. Würschum **2004**, *Philos. Mag. Lett.* 84, 531–537.

41 A. Gude, H. Mehrer **1997**, *Philos. Mag. A* 76, 1–30.

42 J. Bernardini, P. Gas, E. D. Hondros, M. P. Seah **1982**, *Proc. Roy. Soc. Lond. A* 379, 159–178.

43 E. A. Kümmerle, K. Badura, B. Sepiol, H. Mehrer, H.-E. Schaefer **1995**, *Phys. Rev. B* 52, R6947–R6950.

44 B. Hofmann, H. Kronmüller **1996**, *J. Magn. Magn. Mater.* 152, 91–98.

45 W. Grünberger, D. Hinz, A. Kirchner, K.-H. Müller, L. Schultz **1997**, *J. Alloys Compd.* 257, 293–301.

46 M. Lübbehusen, H. Mehrer **1990**, *Acta Metall. Mater.* 38, 283–292.

47 Y. Mishin, C. Herzig, J. Bernadini, W. Gust **1997**, *Int. Mater. Rev.* 42, 155–178.

48 Qing Ma, C. L. Liu, J. B. Adams, R. W. Balluffi **1993**, *Acta Metall. Mater.* 41, 143–151.

49 M. R. Sørensen, Y. Mishin, A. F. Voter **2000**, *Phys. Rev. B* 62, 3658–3673.

50 P. Keblinski, D. Wolf, s. R. Phillpot, H. Gleiter **1999**, *Philos. Mag. A* 79, 2735–2761.

51 P. Keblinski, D. Wolf, S. R. Phillpot, H. Gleiter **1999**, *Scr. Mater.* 41, 631–636.

52 P. Keblinski, D. Wolf, H. Gleiter **1998**, *Interface Sci.* 6, 205–212.

53 N. Wang, Z. Wang, K. T. Aust, U. Erb **1997**, *Mater. Sci. Eng. A* 237, 150–158.

54 B. Cai, Q. P. Kong, L. Lu, K. Lu **1999**, *Scr. Mater.* 41, 755–759.

55 T. Surholt, C. Herzig **1997**, *Defect Diffus. Forum* 143–147, 1391–1396.

56 Y. R. Kolobov, G. P. Grabovetskaya, K. V. Ivanov, M. B. Ivanov **2002**, *Interface Sci.* 10, 31–36.

57 Y. Kolobov, G. Grabovetskaya, K. Ivanov, M. Ivanov, E. Naidenkin **2003**, *Solid State Phenom.* 94, 35–40.

58 Y. R. Kolobov, G. P. Grabovetskaya, K. V. Ivanov, R. Z. Valiev, Y. T. Zhu **2004**, *Ultrafine Grained Materials III,* Y. T. Zhu, T. G. Langdon, R. Z. Valiev, S. L. Semiatin, D. H. Shin, T. C. Lowe, (eds.) TMS, Warrendale, pp. 621–628.

59 G. Herzer **1995**, *Scr. Metall. Mater.* 33, 1741–1756.

60 M. Emura, A. M. Severino, A. D. Santos, F. P. Missell **1994**, *IEEE Trans. Magn.* 30, 4785–4787.

61 A. Lovas, L. F. Kiss, B. Varga, P. Kamasa, I. Balogh, I. Bakonyi **1998**, *J. Phys. IV* 8, 291–298.

62 G. Herzer **1994**, *IEEE Trans. Magn.* MAG-30, 4800–4802.

63 G. Herzer **1997**, in *Handbook of Magnetic Materials*, Vol. 3, (ed.) K. H. J. Buschow, Elsevier Science, Amsterdam, pp. 415–462.

64. M. L Xiao, Q. P. Kong **1997**, Scr. Mater. *36*, 299–303; Q. P. Kong, B. Cai, M. L. Xiao **1997**, *Mater. Sci. Eng. A* 234–236, 91–93.

65 H. J. Höfler, R. S. Averback, H. Hahn, H. Gleiter **1993**, *J. Appl. Phys.* 74, 3832–3939.

66 I. L. Balandin, B. S. Bokstein, V. K. Egorov, P. V. Kurkin **1997**, *Defect Diffus. Forum* 143–147, 1475–1480.

67 B. S. Bokstein, H. D. Bröse, L. I. Trusov, T. P. Khvostantseva **1995**, *Nanostruct. Mater.* 6, 873–876.

68 Y. R. Kolobov, G. P. Grabovetskaya, M. B. Ivanov, A. P. Zhilyaev, R. Z. Valiev **2001**, *Scr. Mater.* 44, 873–878.

69 H. J. Höfler, R. S. Averback, H. Gleiter **1993**, *Philos. Mag. Lett.* 68, 99–105.
70 W. Gust, S. Mayer, A. Bögel, B. Predel **1985**, *J. Phys. Colloq.,* C4, 46, 537–544
71 J. Sommer, C. Herzig **1992**, *J. Appl. Phys.* 72, 2758–2766
72 Y. Minamino, S. Saji, K. Hirao, K. Ogawa, H. Araki, Y. Miyamoto, T. Yamane **1996**, *Mater. Trans. JIM* 37, 130–137.
73 T. Fujita, H. Hasegawa, Z. Horita, T. G. Langdon **2001**, *Defect Diffus. Forum* 194–199, 1205–1210.

24
Creep Behavior of Bulk Nanostructured Materials – Time-dependent Deformation and Deformation Kinetics

Wolfgang Blum, Philip Eisenlohr, and Vaclav Sklenička

24.1
Introduction

At low homologous temperatures T_{hom} a decrease in grain size d generally leads to an increase in flow stress σ in proportion to $d^{-0,5}$; this is the well-known Hall–Petch strengthening resulting from interaction of dislocations with grain boundaries. At high T_{hom} and low strain rates $\dot{\varepsilon}$ thermally activated grain-boundary processes come into play. The rate $\dot{\varepsilon}$ of creep due to grain-boundary sliding and diffusive flow via grain boundaries (Coble creep) varies with grain size as $1/d^p$ with $1 \leq p \leq 3$ at a given stress σ and temperature T [1]. Therefore ultrafine-grained (ufg, 100 nm < d < 1 μm) and nanocrystalline (d < 100 nm) materials may creep faster than materials with conventional grain size (cg) [2–6].

Whether or not grain boundary effects become significant in crystalline materials, can be seen from the microstructure by comparing the grain and dislocation structures [7]. In cg materials the dislocations form subgrains of size $w \ll d$, which approaches a stress-dependent steady-state value

$$w_\infty = k_w bG/\sigma \tag{24.1}$$

within limited strain intervals; b is the length of the Burgers vector, G the shear modulus and k_w a material-dependent numerical factor of the order of 20 [8, 9]. The significance of w_∞ lies in the fact that it represents a rough measure of the mean-free path of dislocations; according to the data in [10, 11] the mean-free path is about four times w_∞. When w_∞ approaches d, dislocations are no longer stored predominantly in the subgrain interior, but at the grain boundaries. This is an important change that allows the special properties of grain boundaries to become dominant. The ratio

$$f_{\mathrm{hb}} = \frac{c_d}{c_w}\frac{w}{d} \leq 1 \tag{24.2}$$

is the areal fraction of high-angle grain boundaries within a given subgrain structure. This follows directly from the fact that c_x/x is the boundary area per

Bulk Nanostructured Materials. Edited by M. J. Zehetbauer and Y. T. Zhu

ISBN: 978-3-527-31524-6

volume for a granular structure with spacing (linear intercept) x of boundaries; the factor c_x depends weakly on grain geometry and equals 2 for equiaxed (sub-) grains [12]; in the following we will neglect the deviation c_d/c_w from 1. According to the above, grain boundary effects will dominate when f_{hb} approaches 1 and $f_{lb} = 1 - f_{hb}$ goes to zero. In the following we will therefore not restrict our attention to nanostructured materials only, but look at cases where the condition $f_{lb} \approx 0$ is fulfilled.

Bulk ufg materials are often produced by severe plastic deformation (SPD) up to large prestrains $\varepsilon_{pre} \approx 10$ [13]. Figure 24.1(a) shows the flow stress σ of cg Cu under conditions equal or similar to those of predeformation as a function of cumulative prestrain ε_{pre} imposed at room temperature by multiple compression and equal-channel angular pressing (ECAP). The lower intervals and rates of predeformation may be the causes of the slightly lower σ values found after compression compared to ECAP. The increase in flow stress with $\varepsilon_{pre} < 1$ is consistent with the work-hardening behavior in torsion (Fig. 24.1(a)). For $\varepsilon_{pre} > 2$ there is little change in flow stress with ε_{pre} in Fig. 24.1(a), even though d decreases significantly (see e.g. [14, 15]). Yet the changes of the grain structure do affect the flow stress as is seen from the significant increase in sensitivity of flow stress to strain rate with ε_{pre}; it occurs at elevated temperature (Fig. 24.1(b)) as well as room temperature [16] and means that ufg material softens faster with decreasing strain rate $\dot{\varepsilon}$ than cg material.

In the following, we will demonstrate that the decrease in f_{lb} towards zero has a profound influence on the creep behavior of Al and Cu. Then, tests with

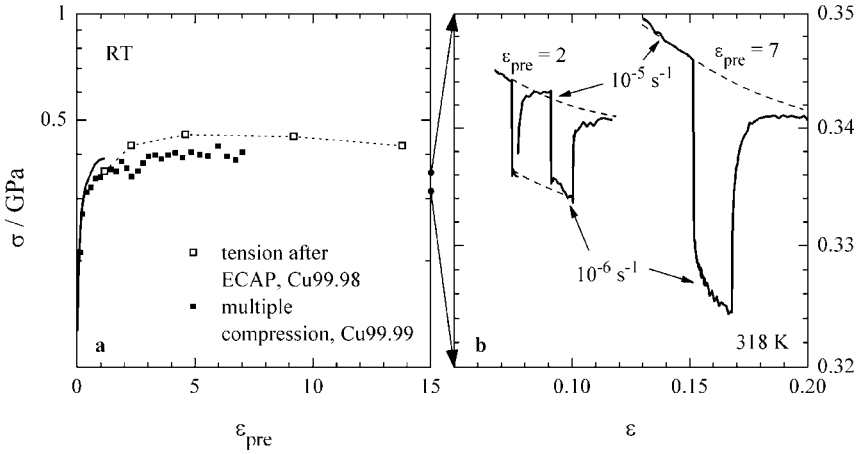

Fig. 24.1 (a) Flow stresses during prestraining at 298 K measured at ends of steps of multiple compression in three alternating orthogonal directions at 10^{-3} s^{-1} [49] and as ultimate tensile stresses at $1.6\times10^{-3}s^{-1}$ after ECAP on route B_C (rotation by 90° between passes, $\varepsilon_{pre} \approx 1.15$ per pass) [14]; σ–ε curve from torsion at room temperature [50] shown for comparison. (b) Strain-rate jumps demonstrating strong increase in strain-rate sensitivity of compressive flow stress at 318 K with ε_{pre} of multiply compressed Cu (after [49, 40]).

changes of stress σ or temperature T will be presented to display the special properties of materials with low f_{lb} in contrast to conventional materials with low f_{hb}. It will be shown that the strengthening by grain boundaries observed at low T_{hom} continuously diminishes as T increases and $\dot{\varepsilon}$ decreases and may even switch to softening. This trend of diminishing grain-boundary strengthening corresponds directly to the increase in strain-rate sensitivity of flow stress. The microstructural mechanisms causing this trend will be briefly discussed. The creep data will be used to estimate the creep life of ufg Cu at elevated temperature.

24.2
Deformation Resistance in Creep

24.2.1
Nanocrystalline Ni

In the search for grain-boundary-controlled creep in nanocrystalline materials, the traditional approach is to determine the (absolute) minimum of creep rate, $\dot{\varepsilon}_{min}$, from the progress of strain ε with time t at constant σ and T, mostly in tension. Wang et al. [17] reported the $\dot{\varepsilon}_{min}$ data for electrodeposited Ni with

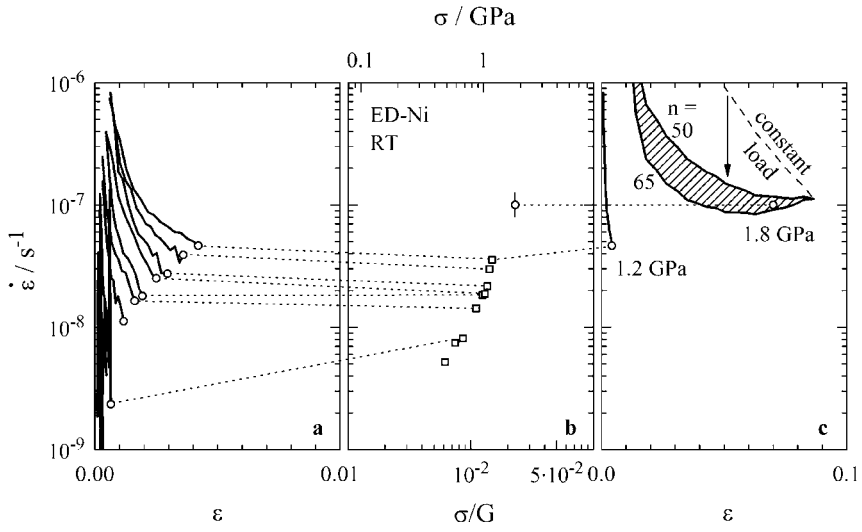

Fig. 24.2 Creep behavior of electrodeposited nanocrystalline Ni at room temperature: (a) tensile $\dot{\varepsilon} - \varepsilon$ curves derived from smoothed ε–t data of Wang et al. [17] for reported $d = 20$ nm; (b) $\dot{\varepsilon}_{min}$ reported in [17] and from (c) as a function of normalized stress (G from [33]); (c) compressive $\dot{\varepsilon} - \varepsilon$ curve for 1.8 GPa; the dashed field was derived with two estimates of n [23] from the dashed curve measured at constant load by Kottada and Chokshi [20] for the reported $d \approx 40$ nm; curve for 1.2 GPa from (a) for comparison. Dotted lines connect data from same test.

20 nm grain size shown in Fig. 24.2 (b). It is seen that the stress exponent of $\dot{\varepsilon}_{min}$ (slope of the $\log \dot{\varepsilon}_{min}$–$\log \sigma$ curve) declines to values of about 3 as expected for grain-boundary sliding (see [18]).

However, this analysis is valid only, if $\dot{\varepsilon}_{min}$ represents the *steady-state* creep rate. In order to check this important condition, the measured $\varepsilon - t$ curves from [17] were converted to $\dot{\varepsilon} - \varepsilon$ curves by smoothing and differentiating. Figure 24.2 (a) clearly shows that all the $\dot{\varepsilon} - \varepsilon$ curves end within the primary stage of creep where $\dot{\varepsilon}$ is still decreasing with ε. The $\dot{\varepsilon}_{min}$ data derived from Fig. 24.2 (a) agree well to the ones reported in [17] for high stresses; for low stresses there is some disagreement, probably due to uncertainties in differentiation. The distance of the measured $\dot{\varepsilon}_{min}$ to the steady-state creep rate appears to increase with decreasing stress. This causes a systematic error resulting in reduction of the stress exponent of the creep rate as demonstrated, for example, in [19, 20]. A similar error was found in literature data claiming the existence of Coble creep by stress directed diffusion via grain boundaries in ufg Cu [21] and nanocrystalline Ni [22].

Our analysis of the data of [17] is consistent with recent measurements of Kottada and Chokshi [20]. This follows from comparison of the two curves displayed in Fig. 24.2 (c). The uncertainty of the curve for 1.8 MPa results from the uncertainty of the value of the stress exponent n [23] in the power law $\dot{\varepsilon} \propto \sigma^n$ used for converting the reported $\dot{\varepsilon} - \varepsilon$ curve in compression at constant load to a curve at constant stress. It is seen that the primary stage of creep extends over a strain interval of about 0.07. This is in the order of the range of work hardening at constant deformation rate [23]. This range is small due to the high rate of work hardening in fine-grained structures.

It should be noted that our description is in conflict with the statement of Kottada and Chokshi who reported that there is no steady-state creep, but only primary creep, in their tests on nanocrystalline Ni, extending beyond a strain of 0.27 [20]. However, this statement was based on the assumption $n < 22$ that appears to be invalid, if the strong dependence of on stress and grain size is taken into account [23].

We conclude that (i) the measured $\dot{\varepsilon}_{min}$ do not correspond to the steady-state creep rates, (ii) the low n-values discussed by Wang et al. [17] do not give information on the steady-state creep mechanism and (iii) there is no indication of creep being solely due to grain-boundary activity like Coble creep in nanocrystalline Ni at $T_{hom} \leq 0.2$. The high stress exponents $\gg 4$ [20, 23] rather suggest that nanocrystalline Ni with $d \approx 40$ nm creeps via dislocation mechanisms.

24.2.2 Fine-grained Al

Pure Al was predeformed by ECAP on route A at room temperature to different values of ε_{pre} [24, 25]. Due to deformation-induced heating the temperature T_{pre} during local shearing in ECAP lies somewhat above room temperature. After ≥ 2 passes of ECAP ($\varepsilon_{pre} \geq 2.1$) the subgrain size $w_0(T_{pre})$ was 1.0 μm [26]. Ac-

cording to Eq. (24.1) this value corresponds to a flow stress of 145 MPa building up in ECAP; it is consistent with the steady-state flow stress of Al near room temperature [11, 27]. During heating a specimen with $\varepsilon_{pre} = 4$ to the temperature $T = 473$ K ($T_{hom} = 0.51$) of creep testing and subsequent annealing for 2 h, the subgrains coarsened to $w_0(T) = 7$ μm. TEM observations indicate that $f_{hb} > 0.5$ in this state, so that the grain size can be estimated from Eq. (24.2) as $d_0 = w_0(T)/f_{hb} < 14$ μm. At the given conditions of creep (Fig. 24.3) the steady-state subgrain size in cg Al is found from Eq. (24.1) to be $w_\infty = 14$ μm. The fact that $w_\infty > d_0$ for $\varepsilon_{pre} \geq 4$ means that new low-angle boundaries will not be generated during creep of Al with $\varepsilon_{pre} \geq 4$; rather, still existing low-angle boundaries will leave the crystal by migration and recombination with other boundaries, bringing f_{lb} down to zero. The significant changes of f_{lb} and subgrain size w associated with deformation before and during creep suggest strong changes of creep resistance. These are in fact seen in Fig. 24.3.

The cg Al ($\varepsilon_{pre} = 0$) in Fig. 24.3 displays normal transient creep at a rate declining towards the steady-state rate of about 1.5×10^{-6} s^{-1} within a strain interval of about 0.4 due to formation and refinement of the steady-state subgrain structure with low-angle boundaries ($d\dot{\varepsilon}/dw > 0$).

Predeformation by $\varepsilon_{pre} \approx 1$ introduces an initial subgrain structure at the beginning of creep with a subgrain size w_0 lying between $w_0(T_{pre})$ and $w_0(T)$. The steady-state subgrain size w_∞ exceeds $w_0(T)$ by a significant factor >2. Due to the initially present subgrain hardening $\dot{\varepsilon}$ drops to a (relative) minimum $\dot{\varepsilon}_{min}$ within a strain interval of about 0.05, where the existing dislocation structure inherited from pretreatment by ECAP plus heating to the test temperature adjusts to the conditions of compressive creep. Beyond $\varepsilon = 0.05$ the creep rate increases with creep strain ε, as the coarsening of subgrains towards w_∞ by migration of the low-angle boundaries now is the dominating process. This tertiary stage of creep constitutes normal transient-creep behavior with $d\dot{\varepsilon}/dw > 0$ as in the previous case $\varepsilon_{pre} = 0$.

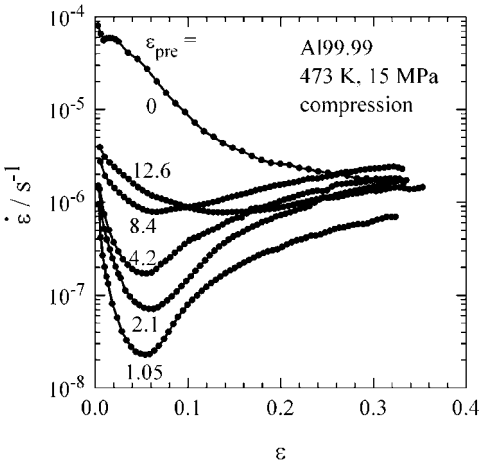

Fig. 24.3 Compressive creep-rate–strain curves of pure Al with initial grain size $d_0 = 5$ mm at $T_{hom} = 0.51$ after predeformation by $0 \leq \varepsilon_{pre} \leq 12.6$ at room temperature by ECAP-A (prestrain/pass ≈1.05). Initial aspect ratio of specimens is 2.

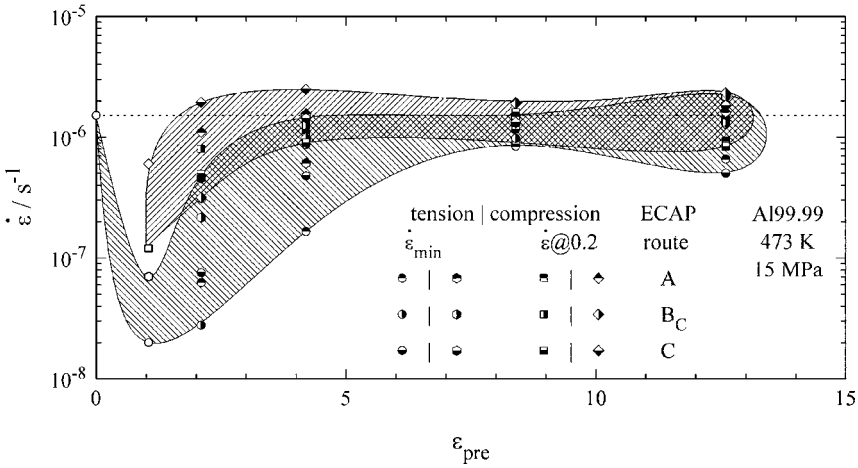

Fig. 24.4 Creep rates at minimum (lower hatched area) and at $\varepsilon = 0.2$ (upper hatched area) for Al99.99 with initial grain size $d_0 = 5$ mm after predeformation by ε_{pre} at room temperature on different routes of ECAP.

With increasing $\varepsilon_{pre} > 1$ the $\dot{\varepsilon} - \varepsilon$ curves shift continuously upward. There is indication of a crossover of the curves for $\varepsilon_{pre} = 0$ and ≥ 2 at $\varepsilon \approx 0.3$, meaning that the material with $\varepsilon_{pre} \geq 2$ may have a lower steady-state creep resistance than Al with $\varepsilon_{pre} \leq 1$.

These creep results from compression tests on fine-grained Al produced by ECAP-A are confirmed by the results of tests in compression as well as tension performed on Al subjected to various routes of ECAP. Figure 24.4 displays the fields of $\dot{\varepsilon}_{min}$ and $\dot{\varepsilon}$ at $\varepsilon = 0.2$; this strain was chosen to minimize the distance from steady state on the one hand and possible influences of non-axial deformation in compression and tensile instability on the other hand. One sees that $\dot{\varepsilon}_{min}$ quickly increases with $\varepsilon_{pre} > 1$ by a factor of about 50. The increase of $\dot{\varepsilon}$ with ε beyond the minimum, in the ε interval from 0.05 to 0.2, becomes relatively small for $\varepsilon_{pre} \geq 8$. The spread between the different ECAP routes is largest for $\varepsilon_{pre} = 4$ where the sequence in direction of increasing softening is A, C, B_C.

Our interpretation of results can be summarized as follows: The softening that is apparent from the upward shift of $\dot{\varepsilon}_{min}$ with $\dot{\varepsilon}_{pre}$ in Fig. 24.3 is related to the decrease of the spacing of high-angle boundaries d at approximately constant subgrain size (due to flow stress saturation in ECAP) with predeformation ε_{pre}, leading f_{lb} to decrease from about 1 to < 0.5. The increase of $\dot{\varepsilon}$ with ε during creep is related to the increase of subgrain size w at approximately constant grain size $d_0(\varepsilon_{pre})$, resulting in a further decrease of f_{lb} in each test to values that may come close to 0 for $\varepsilon_{pre} > 4$.

24.2.3
Ultrafine-grained Cu

Predeformation influences the mechanical behavior of pure Cu in a similar manner as reported above for pure Al. Results obtained at $T_{hom} = 0.275$ for predeformation by multiple compression at room temperature have been reported in [28]. Figure 24.5 shows additional results for Cu predeformed by ECAP-B_C. For cg Cu ($\varepsilon_{pre} = 0$) it needs a strain interval of 0.30 of work hardening to increase the flow stress to 250 MPa at $\dot{\varepsilon} = 10^{-4}\,s^{-1}$. Work hardening goes on during creep and is far from finished when the test ends at $\varepsilon = 0.5$. Predeformation by $\varepsilon_{pre} \approx 1$ significantly reduces the range of work hardening (the difference to the curve for $\varepsilon_{pre} \approx 1$ reported in [28] is attributed to the extraordinarily large initial grain size d_0 of the present material, see caption of Fig. 24.5); while the steady-state creep rate $\dot{\varepsilon}_{min}$ at $\varepsilon \approx 0.45$ is not accessible to direct observation at 250 MPa due to its low value outside the experimental window, it can be estimated from the stress-corrected data (open symbols) with acceptable accuracy to lie near $10^{-10}\,s^{-1}$. The strain hardening related with $\varepsilon_{pre} \approx 2$ is sufficient to raise the yield stress to a value above the creep stress so that rapid work hardening at the beginning of creep results in analogy to the case of Al with $\varepsilon_{pre} \approx 1$ (Fig. 24.3), driving $\dot{\varepsilon}$ again out of the experimental window. For $\varepsilon_{pre} \approx 4$ and 8, on the other hand, relative minima $\dot{\varepsilon}_{min}$ of creep rate are found that increase with ε_{pre} and exceed by far the steady-state creep rate $\dot{\varepsilon}_\infty$ determined in the test with $\varepsilon_{pre} \approx 1$. The steady-state values of $\dot{\varepsilon}$ for $\varepsilon_{pre} > 4$ lie about 5±1 orders of magnitude above this value of $\dot{\varepsilon}_\infty$. This is a much stronger effect of ε_{pre} on steady

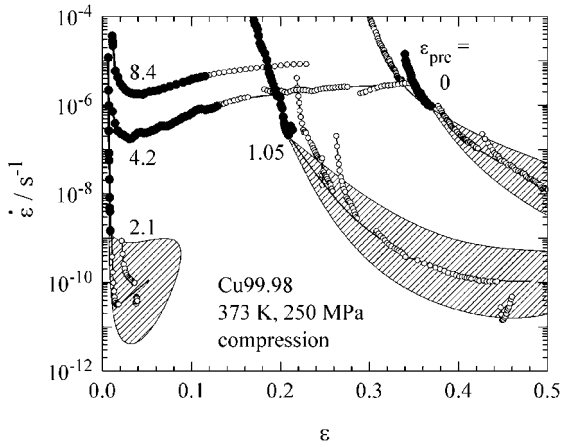

Fig. 24.5 Creep-rate–strain curves for pure Cu99.98 with initial grain size $d_0 \approx 4$ mm for $\varepsilon_{pre} > 0$ and Cu99.99 with $d_0 \approx 60$ µm for $\varepsilon_{pre} = 0$ at $T_{hom} = 0.27$ and 250 MPa after predeformation by $0 \le \varepsilon_{pre} \le 12.6$ at room temperature by ECAP-B_C (prestrain/pass ≈ 1.05) from measurements at $\sigma = f \cdot 250$ MPa with $0.94 \le f \le 1.28$. Filled symbols: $f = 1$, open symbols: corrected by multiplication with $(1/f)^n$ with $n = 120$, 90, 40, 23, 15 in sequence of increasing ε_{pre}. Shaded areas mark estimated uncertainty of correction. Based on unpublished results of Y. J. Li.

state as observed in the case of Al (see Section 24.2.2). The difference can be attributed to the distinctly lower value of T_{hom} used for Cu, causing higher levels of stress and higher stress exponents of creep rate and a higher difference between lattice and grain boundary diffusivity.

The fraction f_{lb} of low-angle grain boundaries after predeformation by $\varepsilon_{pre} \approx 8$ and 12 is known to be ≤ 0.5 [14, 15]. This is confirmed by the following consideration: The initial subgrain size w_0 after ECAP is (280±40) nm [29]. According to Eq. (24.1) with $k_w = 14$ for Cu [10] this value corresponds to a flow stress of (500±75) MPa for ECAP, consistent with the data from Fig. 24.1. A thermomechanical treatment of the ECAPed material with stepwise deformation at increasing temperature, ending at 245 MPa, 403 K, 10^{-5} s^{-1} after a total compressive strain of 0.08, raises the subgrain size to $w_1 = (500 \pm 70)$ nm [30]. This value is slightly below the steady-state subgrain size of 591 nm calculated from Eq. (24.1) for the conditions at the end of the thermomechanical treatment. It is plausible to assume that the low-angle boundaries have left the ECAPed material during thermomechanical treatment by migration and recombination with other boundaries in the move towards steady state. Then, w_1 corresponds to the grain size d_0. This leads to a fraction of high-angle grain boundaries in the structure after $\varepsilon_{pre} \approx 8$ by ECAP-B_C of $f_{hb} = w_0/w_1 = 0.56$, in agreement with the literature data cited above.

On the basis of the low values of f_{lb} established by ECAP the results obtained for Cu can be explained in a similar manner as the Al results: The refinement of the dislocation structure during predeformation increases the creep resistance and leads to a minimum of creep rate, once the subgrain size established during predeformation becomes smaller than the steady-state subgrain size of cg material in creep at 250 MPa that is calculated from Eq. (24.1) as $w = 586$ nm. The minimum creep rate as well as the steady-state creep rate increase as the spacing d of high-angle boundaries decreases with $\varepsilon_{pre} > 2$ at approximately constant subgrain size w (due to approximately constant flow stress, see Fig. 24.1 (a)) and f_{lb} decreases correspondingly down to < 0.5 for $\varepsilon_{pre} \approx 8$, where a significant influence of grain boundaries on deformation resistance may well be expected. When ε_{pre} is large enough to make the subgrain size smaller than the steady-state value w_∞ under subsequent creep conditions, the resulting increase of w with strain at approximately constant d_0 during creep causes the softening manifested in the increase in creep rate beyond the minimum for $\varepsilon_{pre} > 2$.

24.3 Creep Response to Changes in Deformation Conditions

Abrupt stress changes in conditions of creep are a valuable tool to investigate the dynamics of and the structural changes during deformation. In the following, we describe the information gained from changes in stress and temperature.

24.3.1
Stress Changes

Figure 24.6 compares the transient responses to stress reductions during creep of ufg Cu produced by severe predeformation and cg Cu. In order to achieve similar starting values of $\dot{\varepsilon}$ and σ at the points of stress reduction and similar magnitudes of $\dot{\varepsilon}$ change, the test temperatures and magnitudes of stress reductions were chosen accordingly. The cg Cu ($\varepsilon_{pre} = 0$) is still work hardening as seen from the continuous decrease of $\dot{\varepsilon}$ at constant σ. The ufg Cu, on the other hand, is work softening in the manner known qualitatively from Fig. 24.5. The response to the stress reduction is normal for cg Cu with an increase in $\dot{\varepsilon}$ due to subgrain coarsening superimposed to the general hardening trend. Such normal type of transient creep is absent in the ufg Cu. This is a clear indication that low-angle subgrain boundaries are virtually absent in this material.

Interestingly, a transient response to stress reduction is not completely absent in ufg Cu. Rather, there is a small initial transient extending over a strain interval of about 0.01 that is similar in character to that found in cg materials, with softening upon small and hardening upon larger reductions in σ [31]; an indication of the latter is seen in Fig. 24.6 (see [29] for more pronounced examples). These reactions point to changes in the defect structure of the ufg material that, due to their similarity to those of cg material, are probably related to dislocations. In analogy to the interpretation of the behavior of the cg material, it has been proposed in [29] that there is a certain defect content including dislocations in the deformed ufg material, e.g. at grain boundaries, which produces a thermal stress component opposing the glide of dislocations. This explains the normal transient behavior observed after stress increases and small stress reductions. The decrease in creep rate found after larger stress reductions is at least

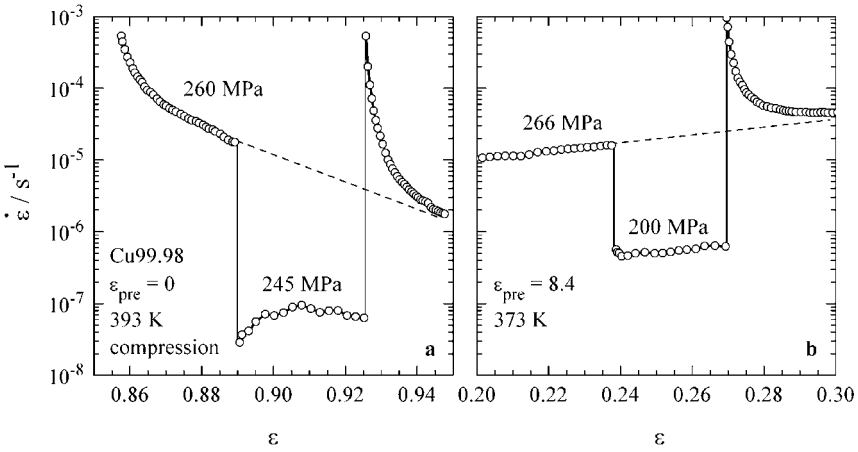

Fig. 24.6 Transient creep after stress reduction; (a) coarse-grained Cu ($\varepsilon_{pre} = 0$) at $T_{hom} = 0.290$, (b) ufg Cu ($\varepsilon_{pre} = 8.4$ by ECAP-B_C) at $T_{hom} = 0.275$. After [29].

partly due to the strain contribution associated with the recovery of the dislocation structure; an additional contribution will be due to the decrease in density of mechanical vacancies [32] following the decrease of $\dot{\varepsilon}$ and leading to reduction in the rate of annihilation/absorption of edge dislocations.

The transients after stress increases are distinctly more pronounced in ufg Cu than those due to stress reductions, but still distinctly weaker than those of cg Cu, given the strong difference in relative change in stress in Figs. 24.6 (a) and (b). The apparent asymmetry of the transients in ufg Cu has been discussed in [29] in terms of the high rate of recovery of defects with time, making it more difficult to increase the defect level than to let it fall; this asymmetry argument does not apply to the transients in cg material as the changes in subgrain size are coupled to strain, not to time.

24.3.2 Temperature Changes

Temperature-change tests allow one to determine the operational activation energy $Q = -R\Delta \ln \dot{\varepsilon}/\Delta(T^{-1})$ of creep at constant stress (R: general gas constant). Figures 24.7 and 24.8 display two tests on cg and ufg Cu showing that introduction of the ufg structure leads to lower Q at similar T. In comparing the data it must be noted that the activation energies are not constant, but depend on stress, as displayed in Fig. 24.9. However, even at equal stress a significant difference between the activation energies for cg and ufg Cu remains. As Q is commonly not significantly dependent on ε in pure metals, one may argue that the high fraction of high-angle grain boundaries in ufg material reduces the operational activation energy of deformation to values in the direction of those of thermally activated grain boundary processes like grain boundary diffusion (104 kJ mol^{-1} [33] and 78 kJ mol^{-1} [34]).

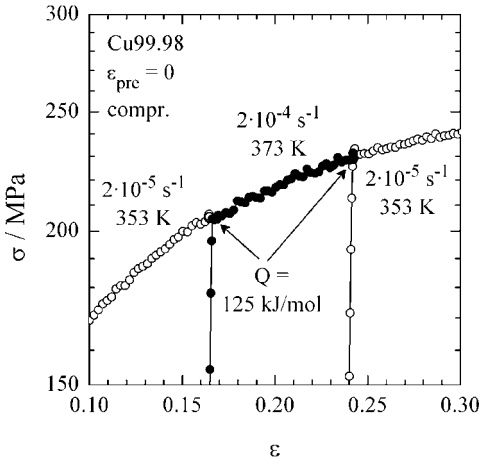

Fig. 24.7 Test on coarse-grained Cu99.98 ($\varepsilon_{pre} = 0$) with simultaneous changes of $\dot{\varepsilon}$ and T chosen such as to keep flow stress constant. Unpublished result of Y. J. Li.

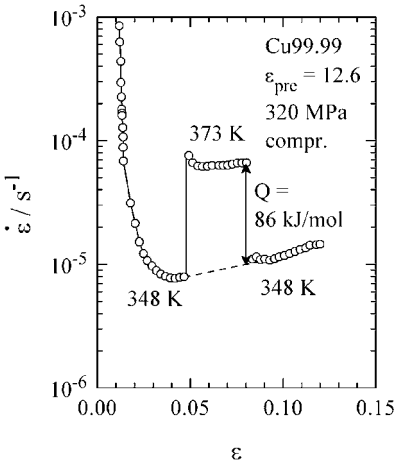

Fig. 24.8 Temperature changes during creep of ufg Cu99.99 ($w_0 = (250 \pm 50)$ nm) produced by 12 passes of ECAP-C with T changes. From [7].

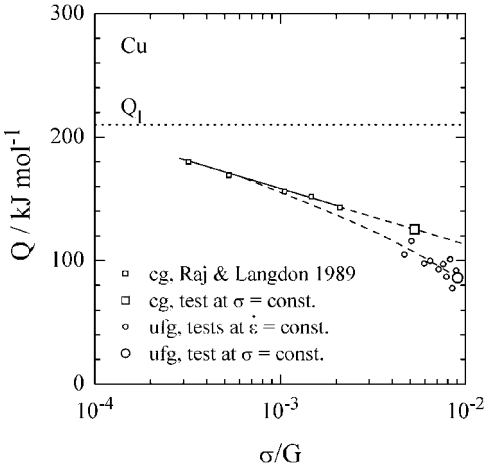

Fig. 24.9 Activation energy of creep of Cu as function of stress σ. With data for cg Cu from [51] and ufg Cu from [7]; Q_l: activation energy for lattice diffusion in Cu.

The test on ufg Al99.5 (Fig. 24.10) comprises a number of T changes near $T_{hom} = 0.41$ in an extended strain interval. In contrast to pure ufg Cu (Fig. 24.8) there is distinct strain hardening as is evident from the decrease of $\dot{\varepsilon}$ with ε that is accompanied by a significant increase in the activation energies determined from the T-changes by about 20%. A tentative, consistent explanation of these effects can be given in terms of diffusion. If diffusion is (i) controlling the rate of creep and (ii) shifting with strain from grain boundary towards lattice diffusion, the effective diffusion coefficient D_{eff} will develop from a high value for diffusion in nonequilibrium grain boundaries with low activation energy towards a low value for lattice diffusion with a high activation energy. Proportionality between $\dot{\varepsilon}$ and D_{eff} qualitatively explains the observed behavior of Al99.5.

The postulated shift in D_{eff} with strain may be explained in two ways. One is by invoking a decrease in rate of dislocation annihilation at grain boundaries due to a

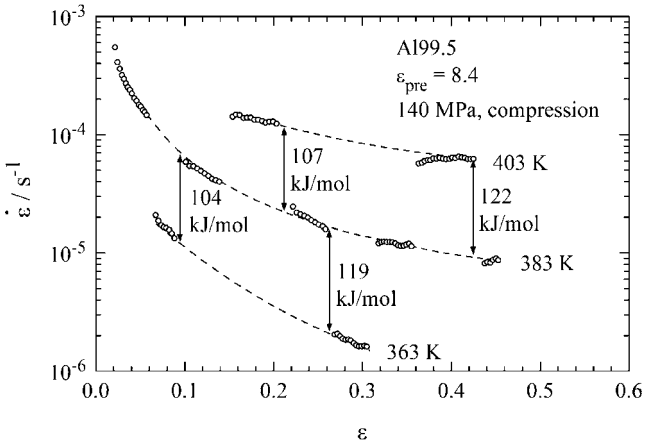

Fig. 24.10 Temperature changes during creep of ufg Al99.5 produced by 8 passes of ECAP-B_C at room temperature ($w_0 = (350 \pm 50)$ nm).

change in grain-boundary structure from nonequilibrium grain boundaries [35] to more relaxed grain boundaries with lower defect concentration [35]. Another, more probable way is to invoke dynamic strain aging, which has been reported to occur also in ufg metals [36–38]. The accumulation of solute atoms around dislocations in ufg Al99.5 may slow down dislocation glide in the grain interior. The necessity of dragging a cloud of solute atoms with the gliding dislocations may shift the overall activation energy of deformation towards lattice diffusion.

24.4 Creep Resistance at Saturation

Figure 24.11 shows the minimum creep rates $\dot{\varepsilon}_{\min}$ (large open circles) of ufg Cu produced by ECAP and multiple compression at room temperature as a function of σ. The data from different T have been normalized according to the proposal of Kocks and Mecking [39] for the saturation stress of stage III work hardening. The $\dot{\varepsilon}_{\min} - \sigma$ data fall into the data band of maximum flow stress at constant $\dot{\varepsilon}$ (small open circles). There is no significant difference between the different paths of predeformation. The fact that the band of normalized data is independent of T and $\dot{\varepsilon}$ means that the operational activation energy Q (defined for constant σ/G) of the maximum deformation resistance of ufg Cu varies with T and $\dot{\varepsilon}$ as $Q = RT(\ln \dot{\varepsilon}_0 - \ln \dot{\varepsilon})(1 - \mathrm{d} \ln G / \mathrm{d} \ln T)$, that is, from 64 kJ mol^{-1} at 300 K and 10^{-3}s^{-1} to 141 kJ mol^{-1} at 473 K and 10^{-6} s^{-1}. Note that the value of $\dot{\varepsilon}_0 = 10^7$ s^{-1} chosen for Fig. 24.11 is in good agreement with the value following from the temperature change test of Fig. 24.8.

There are several possible explanations for the increase in activation energy of the maximum deformation resistance of ufg Cu with increasing T, for instance:

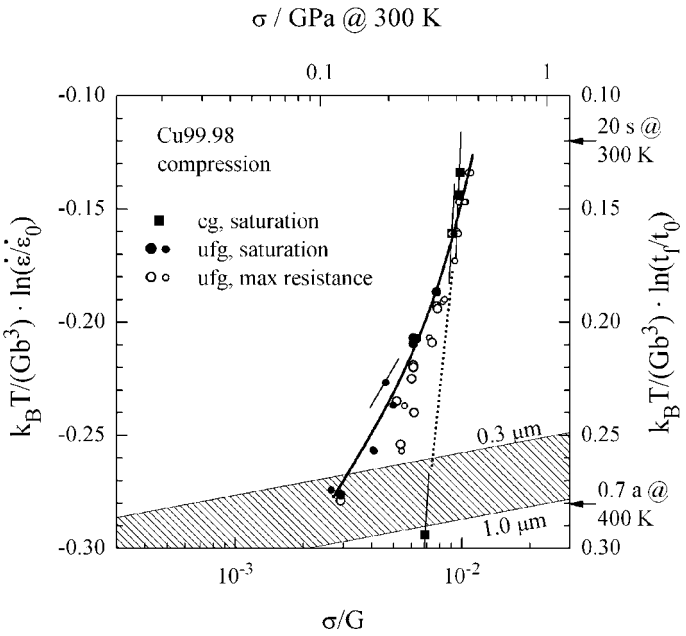

Fig. 24.11 Normalized $\dot{\varepsilon} - \sigma$ relation for ufg ($\varepsilon_{pre} \geq 8$) and cg ($\varepsilon_{pre} = 0$) Cu in uniaxial compression in the interval $298 \leq T/K \leq 473$ corresponding to $0.22 \leq T_{hom} \leq 0.35$ for saturation and maximum deformation resistance. Large symbols from creep tests ($\dot{\varepsilon}_\infty$, $\dot{\varepsilon}_{min}$), small symbols from tests at constant rate, lines through data points indicate slopes from change tests. With data from [7, 40]. Hatched area: Coble creep at 400 K for two grain sizes. Right ordinate axis: normalized creep rupture time t_f; $\dot{\varepsilon}_0 = 10^7\ s^{-1}$, $t_0 = 2.5 \times 10^{-8}$ s, $b = 0.256$ nm.

(i) the T dependence may reflect the σ-dependence of the activation energy shown in Fig. 24.9, (ii) Q_{gb} may increase from the level for nonequilibrium boundaries to that of relaxed boundaries, (iii) the contribution of lattice diffusion to the effective diffusion coefficient combining lattice and grain boundary diffusion may increase.

Due to the observed strain softening (Fig. 24.5) the deformation resistance of ufg Cu at mechanical saturation differs slightly from the maximum deformation resistance. The two lines for mechanical saturation for (initially) cg and ufg Cu in Fig. 24.11 clearly demonstrate that ufg Cu is softer than cg Cu in mechanical saturation at sufficiently high T_{hom} and low $\dot{\varepsilon}$. As texture has been reported [7, 40] to have limited influence only, the difference is most probably due to the grain size. The softening in saturation under creep conditions contrasts the well-established strengthening by grain refinement at low homologous temperatures that holds not only for the yield stress, but extends into the saturation stage (see e.g. [41]).

Figure 24.11 contains a band (hatched) for diffusive flow by Coble creep. Interestingly, the measured data approach this band [42]. This may indicate that

diffusive flow and related processes like grain-boundary sliding become more prominent as temperature increases. The observation that the fraction of strain due to grain-boundary sliding equals as much as 33% in the case of severely plastically predeformed Al [26], underlines the importance of direct contributions of high-angle grain boundaries to strain, in addition to the indirect ones caused by dislocation–grain boundary interactions.

In principle, ufg and nc materials have the potential of superplasticity at sufficiently high temperatures due to grain-boundary sliding supported by grain-accommodation processes. The extremely small grain sizes will shift the range of superplasticity to lower temperatures. However, instability of the grain structure limits the T range where ufg and nc materials may be applied, so that the range of superplastic behavior with n near 2 may not be achieved in pure materials. However, grain refinement in more-stable two-phase superplastic materials like Zn-22%Al leads to shift of optimum superplasticity to higher $\dot{\varepsilon}$ and lower T [43, 44].

24.5 Creep Life

The creep rupture time can be estimated as $t_f = c_{MG}/\dot{\varepsilon}_{min}$ from the minimum creep rate $\dot{\varepsilon}_{min}$, if c_{MG} is a constant (Monkman–Grant relation [45]). Figure 24.12 shows that this is the case for the fine-grained Al treated in Section 24.2.2, with $c_{MG} = 0.25$.

Using the same value for Cu, the T-normalized $\dot{\varepsilon}$ scale can be transformed into a T-normalized t_f scale given on the right ordinate axis of Fig. 24.11, from

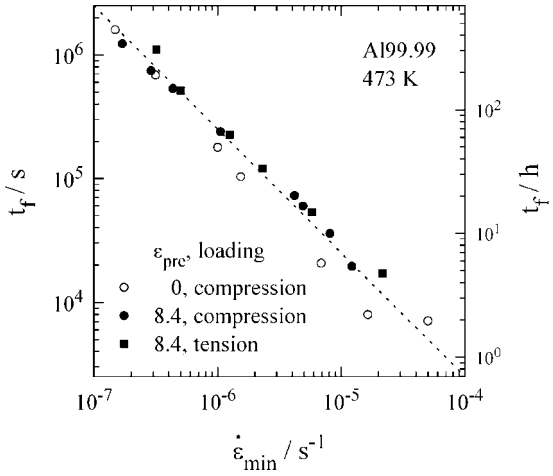

Fig. 24.12 Relation between minimum creep rate and creep lifetime (to fracture in tension and $\varepsilon = 0.35$ in compression) for Al99.99 without and with predeformation by ECAP.

which t_f can be determined. It is seen that the creep resistance of ufg Cu is very high within the T limits of grain stability of ufg Cu. In spite of the softening action of grain boundaries in the steady state of ufg Cu at elevated temperatures, cg Cu has distinctly lower creep resistance than ufg and nanocrystalline Cu due to its much lower yield stress and extended range of work hardening.

24.6 Microstructural Interpretation of Grain-size Effects

The common explanation of the Hall–Petch relation is based on the assumption that slip must be transferred via the grain boundaries into fine grains. This implies that easy dislocation sources are not generally available in those grains.

The considerations in the last section have indicated that the direct contribution of high-angle grain boundaries to deformation is significant only at relatively high T_{hom} and does not cover 100% of strain. Therefore, an indirect influence of the boundaries needs to be invoked to explain the reduction of the creep resistance of ufg compared to cg material.

The reported increase of $\dot{\varepsilon}_{min}$ with ε_{pre} and f_{hb} (Fig. 24.4) is inconsistent with a shortage of dislocation sources in fine grains. It can be explained in terms of strengthening by low-angle subgrain boundaries (see, e.g., [46]). Replacement of low-angle boundaries by high-angle ones increases the spacing of low-angle boundaries. This will diminish the subgrain strengthening caused by low-angle boundaries. It appears that the high-angle grain boundaries do not compensate this diminution. Probably, the high-angle grain boundaries not only contribute to deformation in a direct manner, but also act as easy sinks for lattice dislocations under these conditions as frequently proposed (for instance in [7, 47]).

In order to quantitatively assess the softening for the case $f_{hb} \approx 1$ a model was developed [48] that extends the picture proposed in the appendix of [7]. In this model the dislocation structure is simplified to a scalar dislocation density within grains and at grain boundaries, which in general are impenetrable. Production terms for both densities are formulated, which account for the reduction of storage rate of interior dislocations with decreasing grain size and the increase in the rate of dislocation storage at boundaries. The main difference in the annihilation terms of both dislocation populations is the accelerated dislocation dipole dissolution at grain boundaries due to locally enhanced diffusivity (see [48] for details). When such structure evolution is linked to an expression for the flow stress, set (approximately) proportional to the square root of the total (volumetric) dislocation density, a significant softening with increasing temperature results in the ufg case, qualitatively similar to that shown in Fig. 24.11. The minimum stress exponent $n \approx 8$ resulting from the model agrees well with the experimental data for low stresses; it is twice as large as that previously predicted (see Chuvil'deev [35]). The model also predicts that $\dot{\varepsilon}$ will vary with grain size as d^4 at elevated temperature in contrast to [35], where $\dot{\varepsilon}$ is formulated to be independent of d. At low T_{hom}, where annihilation is athermal (spontaneous

annihilation), the Hall–Petch hardening of grain boundaries due to an enhanced rate of dislocation generation prevails. In spite of its simplicity the model may catch the essential features of the influence of grain boundaries on the deformation behavior.

24.7 Conclusions

Plastic predeformation generates a material in which the fraction f_{hb} of high-angle grain boundaries increases with increasing prestrain ε_{pre} within the strain-induced subgrain structure. During creep at elevated temperatures predeformed pure metals exhibit a primary stage with decreasing creep rate $\dot{\varepsilon}$, a secondary stage with a relative minimum $\dot{\varepsilon}_{min}$ of creep rate and a tertiary stage with increasing $\dot{\varepsilon}$ due to subgrain coarsening by migration of low-angle boundaries. In ufg and nanocrystalline materials that have not undergone severe plastic deformation this type of tertiary creep is missing. $\dot{\varepsilon}_{min}$ increases distinctly with increasing ε_{pre}, i.e. with increasing initial fraction of high-angle boundaries in the initial subgrain structure of predeformed material, when f_{hb} rises to about 0.5. This indicates that high-angle grain boundaries have lower strengthening effect under creep conditions than low-angle ones. In pure Cu at a homologous temperature $T_{hom} \approx 0.3$ there is evidence that even the steady-state creep rate increases with decreasing grain size $d > 350$ nm due to an increase of f_{hb}. This softening by high-angle grain boundaries is explained in terms of the indirect effect that grain boundaries exert on the creep resistance by influencing the evolution of the dislocation structure in modifying the rates of generation and annihilation of dislocations. This modification results in a lowering of stress exponents of creep rate and enhancement of strain-rate sensitivities of the flow stress.

At sufficiently high T_{hom} the direct contributions of grain boundaries to strain gain in importance and add to the softening.

Acknowledgements

Thanks are due to Dr.-Ing. Y. J. Li, Dr.-Ing. X. H. Zeng, Dr. J. Dvořák, Dr. M. Svoboda and P. Kumar for help in preparing figures and interpreting the results, to cand. Ing. G. Hullin for the tests on Al99.5, to Dipl.-Phys. J. Mueller, Dr.-Ing. H.W. Höppel and Prof. M. Göken for stimulating discussions and to the Deutsche Forschungsgemeinschaft for funding the project BL135/30.

References

1 Y.T. Zhu, T.G. Langdon **2005**, Influence of grain size on deformation mechanisms, An extension to nanocrystalline materials, *Mater. Sci. Eng. A* 409, 234–242.

2 F.A. Mohamed, Y. Li **2001**, Creep and superplasticity in nanocrystalline materials, current understanding and future prospects, *Mater. Sci. Eng. A* 298, 1–15.

3 Y.R. Kolobov, G.P. Grabovetskaya, K.V. Ivanov, M.B. Ivanov **2002**, Diffusion and properties of bulk nanostructured metals and alloys processed by severe plastic deformation, *Defect Diffus. Forum* 216, 253–261.

4 G.P. Grabovetskaja, K.V. Ivanov, Y.R. Kolobov **2002**, Creep features of nanostructured materials produced by severe plastic deformation, *Ann. Chim. – Sci. Mat*er. 27, 89–98.

5 C. Xu, T.G. Langdon **2005**, Creep and superplasticity in a spray-cast aluminum alloy processed by ECA pressing, *Mater. Sci. Eng. A* 410-411, 398–401.

6 V. Skleniïcka, J. Dvoïrák, M. Svoboda, P. Král, M. Kvapilová, Z. Horita **2006**, Compressive creep in an Al-3%Mg-0.2%Sc alloy processed by equal-channel angular pressing, in Y. Zhu, T.G. Langdon, Z. Horita, M.J. Zehetbauer, S.L. Semiatin, T.C. Lowe, (eds.) *Ultrafine Grained Materials IV*, TMS, Warrendale, PA, pp. 459–464.

7 Y.J. Li, X.H. Zeng, W. Blum **2004**, Transition from strengthening to softening by grain boundaries in ultrafine-grained Cu, *Acta Mater.* 52(17), 5009–5018.

8 S.V. Raj, G. Pharr **1986**, A compilation and analysis of data for the stress dependence of the subgrain size, *Mater. Sci. Eng.* 81, 217–237.

9 A. Orlová, J. ïCadek **1986**, Dislocation structures and structural steady state in steady-state creep, *Mater. Sci. Eng.* 81, 371–377.

10 W. Blum **1993**, High-Temperature Deformation and Creep of Crystalline Solids, in H. Mughrabi, (ed.) *Plastic Deformation and Fracture of Materials*, Vol. 6 of Materials Science and Technology, (eds.) Cahn, R. W. Haasen, P. Kramer, E. J., VCH Verlagsgesellschaft, Weinheim, pp. 359–405.

11 E. Nes **1998**, Modelling work hardening and stress saturation in FCC metals, *Prog. Mater. Sci.* 41(3), 129–193.

12 E. E. Underwood **1970**, *Quantitative Stereology*, Addison-Wesley Publishing Company, Reading, MA.

13 R.Z. Valiev, R.K. Islamgaliev, I.V. Alexandrov **2000**, Bulk nanostructured materials from severe plastic deformation, *Prog. Mater Sci.* 45, 103–189.

14 F. Dalla Torre, R. Lapovok, J. Sandlin, P.F. Thomson, C.H.J. Davies, E.V. Pereloma. **2004**, Microstructures and properties of copper processed by equal-channel angular extrusion for 1–16 passes, *Acta Mater.* 52, 4819–4832.

15 X. Molodova, S. Bhaumik, M. Winning, G. Gottstein **2005**, ECAP processed copper during deformation and subsequent annealing, in Z. Horita, (ed.) *Proc. of 3rd Int. Conf. on Nanomaterials by Severe Plastic Deformation NANOSPD3*, Fukuoka, Japan, Materials Science Forum 503–504, pages 469– 474, Trans Tech Publications, Uetikon, Switzerland.

16 F.H. Dalla Torre, E.V. Pereloma, C.H.J. Davies **2004**, Strain-rate sensitivity and apparent activation volume measurements on equal-channel angular extruded Cu processed by one to twelve passes, *Scr. Mater.* 51, 367–371.

17 N. Wang, Z.R. Wang, K.T. Aust, U. Erb **1997**, Room temperature creep behavior of nanocrystalline nickel produced by an electrodeposition technique, *Mater. Sci. Eng.* A, 237, 150–158.

18 T. G. Langdon **2005**, Identifying creep mechanisms in plastic flow, *Z. Met.kd.* 96, 522–531.

19 D.A. Woodford **1969**, Measurement and interpretation of the stress dependence of creep at low stresses, *Mater. Sci. Eng.* 4, 146–154.

20 R.S. Kottada, A.H. Chokshi **2005**, Low temperature compressive creep in electrodeposited nanocrystalline nickel, *Scr. Mater.* 53, 887–892.

21 Y.J. Li, W. Blum, F. Breutinger **2004**, Does nanocrystalline Cu deform by Co-

ble creep? *Mater. Sci. Eng. A* 387–389, 585–589.
22 W. M. Yin, S. H. Wang, R. Mirshams, C. H. Xiao **2001**, Creep behavior of nanocrystalline nickel at 290 and 373 K, *Mater. Sci. Eng. A* 301, 18–22.
23 W. Blum, Y. J. Li **2007**, Flow stress and creep rate of nanocrystalline nickel, *Scr. Mater.* 57(5), 429–431.
24 V. Skleniicka, J. Dvoïrák, M. Svoboda, P. Král, B. Vlach **2005**, Effect of processing route on microstructure and mechanical behaviour of ultrafine grained metals processed by severe plastic deformation, *Mater. Sci. Forum*, 482, 83– 88.
25 V. Skleniicka, J. Dvoïrák, M. Svoboda **2004**, Creep in ultrafine grained aluminium, *Mater. Sci. Eng. A* 387-389, 696–701.
26 V. Skleniicka, J. Dvoïrák, P. Král, Z. Stonawska, M. Svoboda **2005**, Creep processes in pure aluminium processed by equal-channel angular pressing, *Mater. Sci. Eng. A* 410-411, 408–412.
27 P. Eisenlohr, W. Blum **2005**, Bridging steady-state deformation behavior at low and high temperature by considering dislocation dipole annihilation, *Mater. Sci. Eng. A* 400–401, 175–181.
28 W. Blum, Y. J. Li **2005**, Creep of ultrafine-grained Al and Cu, in R. S. Mishra, J. C. Earthman, S. V. Raj, R. Viswanathan, (eds.) *Creep Deformation and Fracture, Design, and Life Extension*, Symposium at MST'05 Fall Meeting, *Mat. Sci. Tech.* 1, 65–74.
29 R. Kapoor, Y. J. Li, J. T. Wang, W. Blum **2006**, Creep transients during stress changes in ultrafine-grained copper, *Scr. Mater.* 54, 1803–1807.
30 Y. J. Li, R. Kapoor, J. T. Wang, W. Blum **2006**, Deformation resistance of ultrafine-grained copper at elevated temperature, Poster at TMS annual meeting, San Antonio, USA.
31 W. Blum, A. Rosen, A. Cegielska, J. L. Martin **1989**, Two mechanisms of dislocation motion during creep, *Acta Metall.* 37, 2439–2453.
32 T. Ungár, E. Schafler, P. Hanák, S. Bernstorff, M. Zehetbauer **2005**, Vacancy concentrations determined from the diffuse background scattering of X-rays in plastically deformed copper, *Z. Met.kd.* 96, 578–583.
33 H. J. Frost, M. F. Ashby **1982**, *Deformation-Mechanism Maps*, Pergamon Press, Oxford.
34 R. Z. Valiev, E. V. Kozlov, Yu. F. Ivanov, J. Lian, A. A. Nazarov, B. Baudelet **1994**, Deformation behaviour of ultra-fine-grained copper, *Acta Metall. Mater.* 42(7), 2467–2475.
35 V. N. Chuvil'deev **2004**, *Nonequilibrium Grain Boundaries in Metals, Theory and Applications*, Physico-Mathematical Literature, Moscow.
36 Y. J. Li, R. Valiev, W. Blum **2005**, Deformation kinetics of ultrafine-grained Cu and Ti, *Mater. Sci. Eng. A* 410–411, 451–456.
37 W. Blum, Y. J. Li, F. Breutinger **2006**, Deformation kinetics of coarse-grained and ultrafine-grained commercially pure Ti, *Mater. Sci. Eng. A*, 462(1/2), 275–278.
38 J. May, H. W. Höppel, M. Göken **2005**, Strain-rate sensitivity of ultrafine grained aluminium processed by severe plastic deformation, *Scr. Mater.* 53(2), 189–194.
39 U. F. Kocks, H. Mecking **2003**, Physics and phenomenology of strain hardening, the FCC case, *Prog. Mater. Sci.* 48(3), 171–273.
40 Y. J. Li **2006**, Deformation behavior of ultrafine-grained copper, Dr.-Ing. thesis, University of Erlangen-Nürnberg.
41 J. Chen, L. Lu, K. Lu **2006**, Hardness and strain-rate sensitivity of nanocrystalline Cu, *Scr. Mater.* 54, 1913–1918.
42 X. H. Zeng, Y. J. Li, W. Blum **2004**, On Coble creep in ultrafine-grained Cu, *phys. stat. sol. (a)*, 201, R114–R117.
43 P. Kumar, C. Xu, T. G. Langdon **2006**, Mechanical characteristics of a Zn22% Al alloy processed to very high strains by ECAP, *Scr. Mater.* 429(12), 324–328.
44 T. G. Langdon **2008**, Superplasticity of bulk nanostructured materials, Ch. 20, this book.
45 F. C. Monkman, N. J. Grant **1956**, *Proc. ASTM* 56, 593–605.
46 W. Blum **2004**, Creep Simulation, in D. Raabe, F. Roters, F. Barlat, L.-Q. Chen, (eds.) *Continuum Scale Simulation of Engineering Materials Fundamentals, Microstructures, Process Applications*. Wiley-VCH, Weinheim.

47 A. A. Nazarov, A. E. Romanov, R. Z. Valiev **1990**, Incorporation model for the spreading of extrinsic grain boundary dislocations, *Scr. Metall. Mater.* 24, 1929–1934.

48 X. H. Zeng, P. Eisenlohr, W. Blum **2006**, Modelling the transition from strengthening to softening by grain boundaries, in *Proc. ICSMA 14*, Xi'an, China, *Mat. Sci. Eng. A.* (1/2 C), 95–98, 483–484.

49 Y. J. Li, W. Blum **2005**, Strain-rate sensitivity of Cu after severe plastic deformation by multiple compression, *phys. stat. sol. (a)* 202(11), R119– R121.

50 M. Zehetbauer, V. Seumer **1993**, Cold Work Hardening in Stages IV and V of f.c.c. Metals – I. Experiments and Interpretation, *Acta Metall. Mater.* 41, 577–588.

51 S. V. Raj, T. G. Langdon **1989**, Creep behavior of copper at intermediate temperatures—I. mechanical characteristics, *Acta Metall.* 37(3), 843–852.

25
Structural Properties of Bulk Nanostructured Ceramics

Alla V. Sergueeva, Dongtao T. Jiang, Katherine E. Thomson, Dustin M. Hulbert, and Amiya K. Mukherjee

25.1
Introduction

Advanced ceramic materials are attractive because of their low density, chemical inertness, high strength, high hardness and high-temperature capability. Nanocrystalline ceramics are commonly defined as having a grain size of 100 nm or less. While this definition is rather arbitrary, nanocrystalline ceramics are known to possess unique mechanical properties, including enhanced superplasticity and superior strength. Pilot-scale facilities for nanopowder synthesis and the commercialization of sizable quantities of certain types of nanosize powders have been achieved. The fabrication of nanopowders into fully dense components that retain a nanocrystalline grain size has lagged behind powder synthesis and characterization. In part, the gap between powder synthesis and bulk fabrication is related to an incomplete theoretical understanding of the mechanisms associated with densification and sintering when grain-interfacial regions comprise a large volume fraction of the material. Equally relevant is the incomplete understanding of the particular experimental conditions that yield high-density compacts without microstructural coarsening. The available experimental work in this area clearly demonstrates that the conditions for densification and sinterability of nanocrystalline ceramics is system specific and is not readily deduced from theory alone at the present time.

25.2
Highly Creep Resistant Ceramics

Covalent ceramics such as silicon nitride and silicon carbide require liquid-phase sintering to reach high density [1–3]. This is usually realized by addition (either singularly or in combination) of sintering aids such as Al_2O_3, MgO, AlN, SiO_2, Y_2O_3, and rare earth oxides, to the starting powder [4–7]. At the tem-

Bulk Nanostructured Materials. Edited by M. J. Zehetbauer and Y. T. Zhu

ISBN: 978-3-527-31524-6

perature of sintering, the sintering additives react with the silicon oxide layer, which is always present at the surface of silicon nitride particles, and form a silicate liquid phase to promote sintering. The liquid phase then forms a glassy phase with a thickness of about 0.5–2 nm at the grain boundaries upon cooling [3, 6, 8]. It is now well established that the superplasticity and creep deformation of silicon-nitride ceramics is dictated by the behavior of this glassy grain-boundary phase [9–14].

Marked improvement in creep resistance of nanocomposite ceramics has been achieved by dispersing hard secondary-phase nanoparticles such as SiC into the intergranular glassy phase in the matrix [15–17], in so-called micro-nanocomposites (nanosized SiC included in submicrometer Si_3N_4). For the silicon-nitride-based ceramics, it is not possible to establish a deformation mechanism under general conditions because it is a very complex system that generally contains more than one phase and their intrinsic properties are greatly influenced by external factors [14]. Also, the deformation mechanisms for tensile and compressive creep are different. Thus, it has been necessary to explain the creep of silicon-nitride ceramics by a series of mechanisms occurring simultaneously [14]. Generally, it has been realized that compressive creep takes place through grain-boundary sliding, mainly accommodated by a solution-precipitation process [14, 18–23]. The intergranular glassy phase plays a role in high diffusivity paths for atomic diffusion. The structural change in the intergranular film leads to a greater resistance to creep under compressive force [24]. Tensile creep is largely affected by the nucleation and growth of cavities when the tension-stress field favors the formation of cavitation [14].

In most cases, the solution-precipitation process associated with the deformation mechanism for steady-state compressive creep of silicon nitride involves three distinct processes. The first step is the dissolution of the crystalline grains into the glassy phase followed by diffusion of the dissolved atoms through the glassy phase, and, finally, the reprecipitation of these atoms onto some other crystalline grains [25, 26]. This multistep process can be controlled by the interface reaction or the diffusion through glassy phases. Therefore, the focus of efforts in enhancing the creep property has been on controlling the chemistry and amount of the glassy phase, which is determined by the amount/species of additive as well as the oxygen content at particle surface of the starting powders. A number of approaches have been attempted for this purpose [27–30]. However, owing to the thermodynamically stable nature of the glassy phases, and the fact that it is impractical to prevent surface oxidation of the powders, these efforts have led to only limited success. Even in the case where no oxide additive was used in sintering, glassy phases were still found at grain boundaries [31].

25.2.1
Nano-nano Ceramic Composites

A formation of a nano-nano structure (nanosized SiC and Si_3N_4 in dual-phase mixture) by a novel synthesis method [32] resulted in an exceptional creep resistance of the material [33]. Starting from an amorphous Si-C-N powder derived from the pyrolysis of a liquid-polymer precursor, nanocrystalline silicon nitride/silicon carbide ceramic composites with a grain size of 30–50 nm were synthesized without using sintering additive (Fig. 25.1). The grain-size distribution in such nanocomposites was fairly narrow. EELS analysis was conducted to examine the elemental distribution of the nano-nano composites. For the composite sintered without additive (Fig. 25.1), the EELS mapping of Si, C, N and O is shown in Fig. 25.2. It is quite clear that the two phases in this material, Si_3N_4 and SiC were randomly mixed with roughly equal grain size. The most important information from these maps is that, oxygen, which is the main element responsible for forming glassy grain-boundary phases in the absence of metal-oxide sintering additives, was found to exist at almost all the intergranular regions, including triple junction pockets and dual-grain boundaries. This is an explicit indication that the oxygen that originally exists mainly at the particle surface of the starting amorphous powder (in the form of either silica or silicon oxynitride) has diffused into the interior of the particles during sintering, and is distributed along the grain boundaries.

High-resolution transmission electron microscopy (HRTEM) of the grain-boundary regions of the synthesized material revealed that a significant population of grain boundaries do not have an apparent amorphous layer (as the example in Fig. 25.3 (a) demonstrates), although EELS reveals that oxygen exists at almost all grain-boundary regions (Fig. 25.2). Shinoda's research [34] on SiC polycrystalline ceramics also reported that no glassy film was formed even though some oxygen had segregated into the grain boundary. This is because the amount of segregated oxygen is not sufficient to form an intergranular glassy phase [34]. However, some of the dual-grain junctions (grain boundaries)

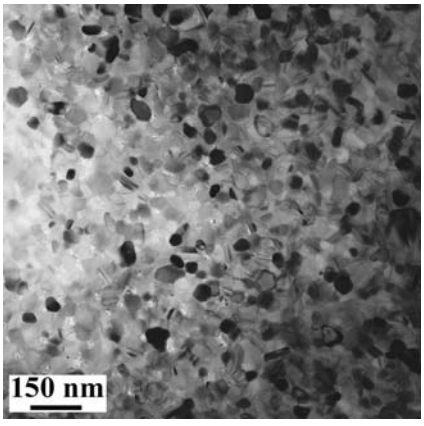

Fig. 25.1 Transmission electron microscopy (TEM) observations of nanocomposites of Si_3N_4-SiC sintered without additive at 1600 °C for 30 min, nano-nanostructure. (From Ref. [33]).

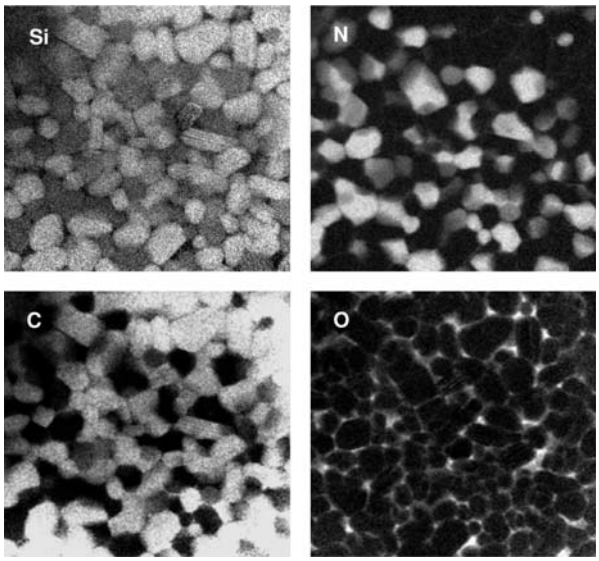

Fig. 25.2 Electron energy-loss spectroscopy (EELS) analysis of the component elements in the Si_3N_4-SiC nanocomposite sintered at 1600 °C for 30 min without additive. (From Ref. [33]).

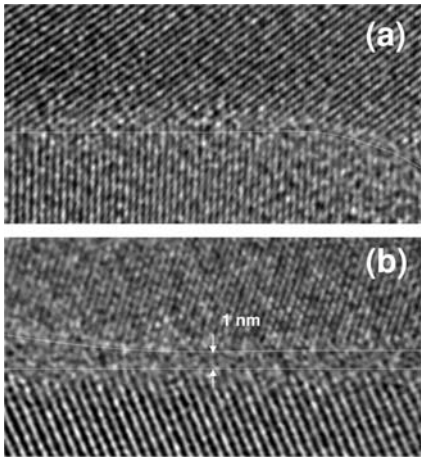

Fig. 25.3 High-resolution transmission electron microscopy (HRTEM) analysis of the grain boundary of the nano-nanocomposite (no additive, 1600 °C/30 min sintered). (a) Glass-free grain boundary, (b) Grain boundary containing glassy layer. (From Ref. [33]).

do contain an amorphous layer (Fig. 25.3 (b)). In this particular example, the thickness of the amorphous layer is about 1 nm, in accordance with the glassy-layer thickness in silicon nitride that contains silica as the only oxide species. It seems that the oxygen elements are not homogeneously distributed in grain-boundary regions, some grain boundaries having more oxygen and some others having less. As in microcrystalline silicon nitride or silicon carbide, most of the glassy grain-boundary phase exists at multigrain junctions.

25.2.2
Creep Resistance

The comparison between the creep property of nano-nano composites and that of microcrystalline silicon-nitride ceramics from literature data is given in Fig. 25.4. The data can be divided into four groups. The first group is composed of conventional silicon-nitride ceramics (including silicon nitride/silicon carbide microcrystalline composites) with a high level of additive amount (various additives are used by different researchers, as indicated in the legend of this plot [19–23, 33, 35–41]), most were sintered by hot pressing. This group has the lowest creep resistance of the silicon-nitride ceramics. For example, the steady-state creep rate at the reference test condition 1400 °C/100 MPa ranges from about 3×10^{-8} to 3×10^{-6} s^{-1}. Using high-purity silicon nitride powder, incorporation of less additive (e.g., less than 4 wt% Y_2O_3), and applying hot-isostatic pressing or gas-pressure sintering generates silicon-nitride ceramics of higher creep property, which are included in the group of new generation ceramics with reduced additive. These ceramics show a secondary creep rate of about 1×10^{-9} to 3×10^{-8} s^{-1}, roughly two or three orders of magnitude lower than ceramics in the first group. The micro-na-

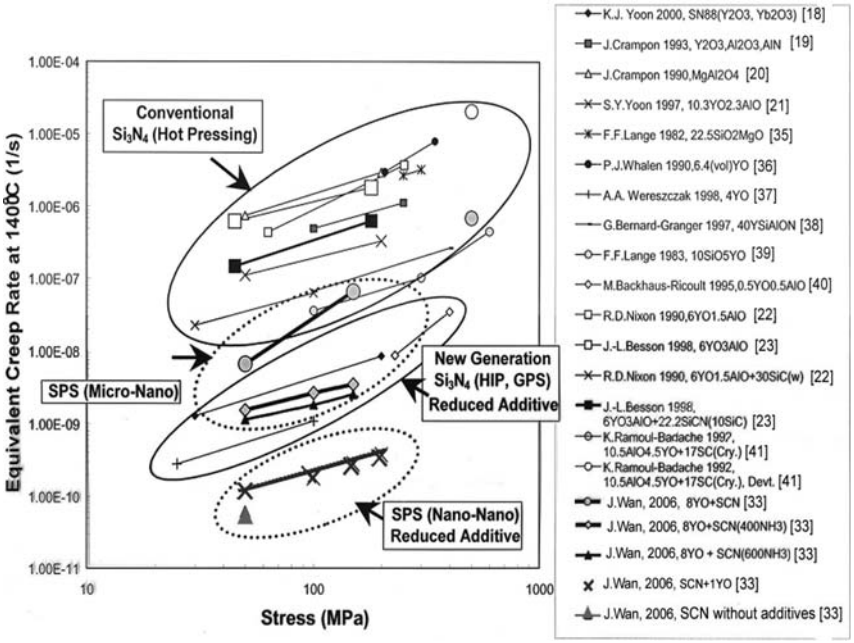

Fig. 25.4 Comparison of the compression-creep property of nanocomposites with those of existing silicon-nitride ceramics (additive in weight percentage unless specified, molecular formula simplified for clarity. For instance, "6YO" in figure legend stands for "6wt% Y_2O_3").

nocomposites have approximately similar levels of additives as conventional ceramics but exhibit higher creep resistance. However, their creep rate is faster than that of ceramics with reduced additive. The nano-nano composites demonstrate the highest creep resistance of all, as shown in Fig. 25.4. At the reference testing condition of 1400 °C/100 MPa, the steady-state creep rate of the nanocomposite sintered with 1 wt% Y_2O_3 is about 1.67×10^{-10} s^{-1}, while the nanocomposite sintered without additive shows a creep rate as low as 6.3×10^{-11} s^{-1} at 50 MPa stress. At this creep rate, most creep-testing equipment is at the limit of transducer resolution.

The steady-state creep deformation of crystalline materials can usually be described phenomenologically by the following equation:

$$\dot{\varepsilon} = A\frac{\sigma^n}{d^p}\exp\left(-\frac{Q}{RT}\right) \tag{25.1}$$

in which $\dot{\varepsilon}$ is the strain rate, A is a constant, σ the applied stress, n the stress exponent, d the grain size, p the grain-size dependence coefficient, Q the activation energy, R the gas constant and T the absolute temperature. Experimentally acquired creep data are usually compared with the established theoretical models for their n, p and Q value, in order to determine the creep deformation mechanism. Owing to the widely varied chemistry, microstructure, for compression-creep tests alone (where cavitation does not complicate issues), the experimentally determined stress exponent n for various silicon-nitride system ceramics can be as low as <1 to as high as >3; and the activation energy Q can be as low as 300 kJ/mol to as high as 1200 kJ/mol [42–44]. This discrepancy in n and Q values becomes even larger for tensile data where the strain rate and stress data are affected by intergranular cavitation. In spite of these discrepancies, it is generally agreed that the steady-state creep for silicon nitride (and silicon carbide) with a grain-boundary glassy phase proceeds by a solution-precipitation mechanism through the amorphous (liquid) grain-boundary phase, which has been modeled by Raj [25] and by Wakai [26]. Grain-size dependence p takes a value of about 1–3 [45–47]. This means a strong dependence of creep rate on grain size: the creep rate is supposed to increase at least for 1–3 orders of magnitude with the grain-size decrease from micrometer size (500–1000 nm or larger), as in most of the microcrystalline silicon nitride studies, to nanometer size [33]. The extraordinary high creep resistance found in the nanocomposites strongly suggests a fundamental change in creep mechanism. Another indication that the creep mechanism may be different in nano-nano composites is the low activation energy found in these materials. For example, the apparent activation energy for the 1 wt% Y_2O_3 nanocomposite was determined to be about 205 kJ/mol, significantly lower than that of microcrystalline silicon nitride.

Owing to the strong covalent bonds and high Peierls forces, which rule out the possibility of dislocation-based creep mechanisms in silicon nitride and silicon carbide at the test temperatures of this work, the only alternative to the liquid-phase-based mechanisms is solid-state-diffusion-based mechanisms, includ-

Table 25.1 Activation energy for diffusion processes in the Si_3N_4/SiC system.

Medium	Diffusing particle	Temperature range (°C)	Activation energy (kJ/mol)	Note	Reference
α-Si_3N_4	Si	1400–1600	199	Self-diffusion	Kunz [48]
	N	1200–1410	233	Lattice diffusion	Kijima and Shirasaki [49]
	Si	NA	NA	Grain-boundary diffusion	NA
	N	NA	NA	Grain-boundary diffusion	NA
β-Si_3N_4	Si	1490–1750	390	Lattice diffusion (β with some α)	Batha and Whitney [50]
	N	1200–1410	777	Lattice diffusion	Kijima and Shirasaki [49]
	Si	NA	NA	Grain-boundary diffusion	NA
	N	NA	NA	Grain-boundary diffusion	NA
β-SiC	Si	1960–2260	911	Lattice diffusion	Ziegler et al. [2]
	Si	2010–2270	612	Grain-boundary diffusion	Hon et al. [51]
	C	1860–2230	841	Lattice diffusion	Ziegler et al. [2]
	C	1855–2100	564	Grain-boundary diffusion	Hon and Davis [52]
In GB of HPSN (10 wt%Y_2O_3)	Si/N	1450–1550	448	Grain-boundary diffusion	Ziegler et al. [2]
	Si/N	1550–1760	695	Grain-boundary diffusion	Ziegler et al. [2]

ing lattice (Nabarro–Herring) diffusion or grain boundary (Coble) diffusion. The known activation values for various diffusion processes that may be involved are shown in Table 25.1 [2, 48–52].

It can be seen that the measured apparent activation energy in the nanocomposites is much lower than any value other than the lattice diffusion of N or Si in α-Si_3N_4. However, X-ray diffraction revealed that the silicon nitride in the sintered nanocomposites is β-Si_3N_4. Comparison of the measured activation energy in the nano-nano composites suggests that, the creep is controlled neither by diffusion processes in silicon carbide, nor by the lattice diffusion in β-Si_3N_4. The only option left is the grain-boundary diffusion in β-Si_3N_4, for which unfortunately there is no established diffusion data. Considering that N is the slower-diffusing species in Si_3N_4, and that the activation energy for grain-boundary diffusion is lower than that for lattice diffusion, N diffusion through (oxygen-enriched) grain boundaries might be the controlling mechanism in the creep of the nano-nano composites. It should be noted that the final grain size in the

nano-nano composites is much smaller than the particle size of the starting powder. Normally, silicon-nitride ceramics start with a fine powder (several tens or hundreds of nanometers), the grain size of the sintered materials is larger than, or at least close to, the particle size (or crystallite size in the case of agglomerated powder) of the starting powder. The oxygen content at grain boundaries, therefore, would very likely be greater than, or at least close to, the oxygen content at the particle surfaces. In contrast, the grain size of the nano-nano microstructure is determined by the concurrent crystallization process during sintering from an amorphous powder, and there the sintered materials can have a grain size much smaller than the original particle size. If, as in silicon nitride powders, oxygen also mainly exists at particle surfaces of the amorphous Si-C-N powder (it should be pointed out that there might be a small amount of network oxygen in the amorphous powder), and that the oxygen diffuse from the original particle surfaces into the interior regions (the grain boundaries), as the EELS mapping confirmed, the oxygen content at each individual grain boundary can be much lower than that at the particle surface. This "diluting" effect is possibly reducing the oxygen content to the extent that in some of the grain boundaries no effective glassy grain-boundary layer can be formed. Thus, diffusion-based mechanisms other than solution-precipitation become the dominant mechanisms. This transition in creep mechanism has such a strong effect that it produces a lower creep rate in the nanostructure with no effective glassy phase in the intergranular region other than that observed with the microcrystalline matrix with a significant amount of glassy phase having a much larger grain size. It is apparent that in order to further establish this concept, quantitative (and statistically valid) examination of the grain-boundary chemistry and structure is called for. Nonetheless, the low creep rate observed in the nano-nano composites brings us one step closer to the extremely high creep resistance that is promised by the strong covalent bonds and low diffusivity in silicon nitride and silicon carbide.

25.3 Superplasticity in Ceramics

Superplasticity was first widely studied in metals and alloys. The constitutive relation for superplastic deformation (SPD) usually takes the form of Mukherjee–Bird–Dorn equation [45]:

$$\dot{\varepsilon} = A\frac{DGb}{kT}\left(\frac{b}{d}\right)^{p}\left(\frac{\sigma}{G}\right)^{n} e^{-\frac{Q}{RT}} \tag{25.2}$$

in which G is the elastic shear modulus, b is the Burger's vector, k is the Boltzmann constant, T is absolute temperature, d is grain size, p is a grain-size-dependent coefficient, n is the stress exponent, Q is activation energy, D is the diffusion coefficient and R is the gas constant. The inverse of n is the strain-rate sensitivity, m. Grain-boundary sliding is generally the predominant mode of de-

formation during the superplastic flow. Plastic deformation by grain-boundary sliding is generally characterized by $n = 2$ ($m = 0.5$) and an activation energy that is either equal to the activation for lattice diffusion or to the activation energy for grain-boundary diffusion.

From Eq. (25.2) it is clear that for elevated temperature deformation at a constant temperature, a high strain rate is more easily realized in specimens with smaller grains. Generally, superplasticity of ceramics requires a microstructure with a fine grain size (< 1 μm) that is stable against coarsening during sintering and deformation [13]. A low sintering temperature is not enough to obtain the required fine-grain structure. In most cases, sintering aids and grain-growth inhibitors are used to achieve such structure [13]. Second-phase particles are especially effective in inducing superplasticity in ceramics [10–14, 34, 46]. With the development of ceramic processing, the particle sizes are now made smaller and smaller into the nanometer range and, therefore, so are the grain sizes in dense compacts. Superplasticity in ceramics has been studied since the first observation of the phenomena in yttria-stabilized tetragonal zirconia (YTZP) by Wakai in 1986 [47]. A number of fine-grained polycrystalline ceramics have demonstrated superplasticity, such as YTZP [53], magnesia-doped alumina [54], and alumina-reinforced YTZP [11]. Unfortunately, the superplastic temperatures were typically above 1450 °C and the strain rates were relatively low (10^{-4} s^{-1} or lower). Recently, Kim, et al. [46] realized a high strain rate of 0.1 s^{-1} in a zirconia-alumina-spinel triphase composite (volume ratio 4 : 3 : 3), but at a rather high temperature of 1650 °C.

25.3.1
Low-temperature Superplasticity

More recently, superplasticity of the zirconia-alumina-spinel triphase ceramic composite at temperatures as low as 1350 °C was demonstrated in samples processed by spark-plasma sintering (SPS) [55]. The system of nano Al_2O_3-based composites is one of the most difficult to produce, since Al_2O_3 possesses one of the highest homologous temperatures for full-density sintering. These high sintering temperatures lead to aggressive grain growth as the compacts reach full density. The realization of nano-Al_2O_3-based nanocomposites, e.g., successful suppression of Al_2O_3 grain growth, depends on the application of lower sintering temperature and/or shorter sintering time. Conventional processing routes such as hot pressing or pressureless sintering will not serve this purpose. Utilization of spark-plasma sintering (SPS) significantly reduced sintering temperatures and sintering times, and has achieved remarkable success in producing nanocomposites [56]. SPS is the third and newest generation of a sintering process based on the theory of high-temperature plasma momentarily generated in the gaps between powder materials by electrical discharge during DC pulsing [57]. Unlike the first-generation spark sintering and the second-generation plasma-activated sintering (PAS), SPS has gained a reputation as a new industrial process for the processing of a broad variety of materials including metals,

intermetallics, ceramics, composites and polymers. It has been suggested [57] that the ON-OFF DC pulse energizing method could generate: (1) spark plasma, (2) spark impact pressure, (3) Joule heating, and (4) an electrical-field-diffusion effect. SPS can rapidly consolidate powders to near theoretical density through the combined actions of a rapid heating rate, pressure application, and proposed powder-surface cleaning. In nanocrystalline materials, which are difficult to sinter by conventional methods, the advantages of SPS are more directly evident. With low sintering temperatures and short sintering times, SPS can result in better control of the microstructure and final properties of materials.

Because of the rather low sintering temperatures (1100–1200 °C) and the very short sintering time (a few minutes), the grain sizes in the synthesized zirconia-alumina-spinel triphase ceramic composite were about 50 nm to 100 nm (Fig. 25.5) [55, 56]. This material was fully dense after SPS and revealed superplasticity at relatively low temperature of 1350 °C (*vs.* Japanese researchers 1650 °C) and at a strain rate of 10^{-2} s^{-1}. A typical stress–strain curve for these testing conditions is shown in Fig. 25.6 (a). Figure 25.6 (b) represents an example of the sample view before and after testing. The stress–strain rate relationship and strain-rate–temperature relationship revealed a strain-rate sensitivity of 0.5 and activation energy of around 622 kJ/mol, pointing to dislocation-accommodated grain-boundary sliding as the deformation mechanism. However, the complicated grain boundaries and phase interfaces in the triphase composite make it difficult to study the rate-controlling mechanisms during the high-tem-

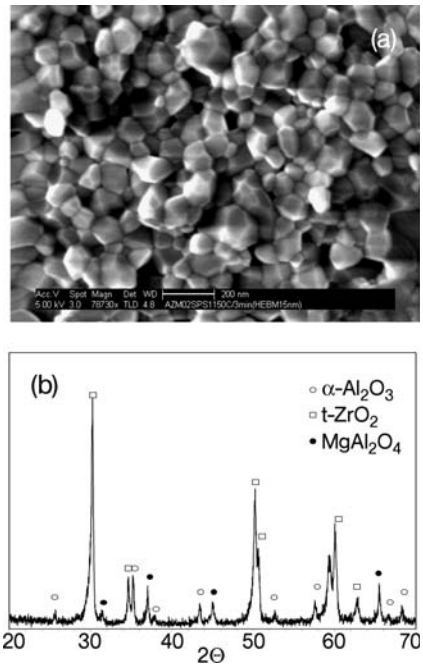

Fig. 25.5 Triphasic nanocomposite: (a) SEM image of the synthesized material; (b) phase composition determined by X-ray analysis.

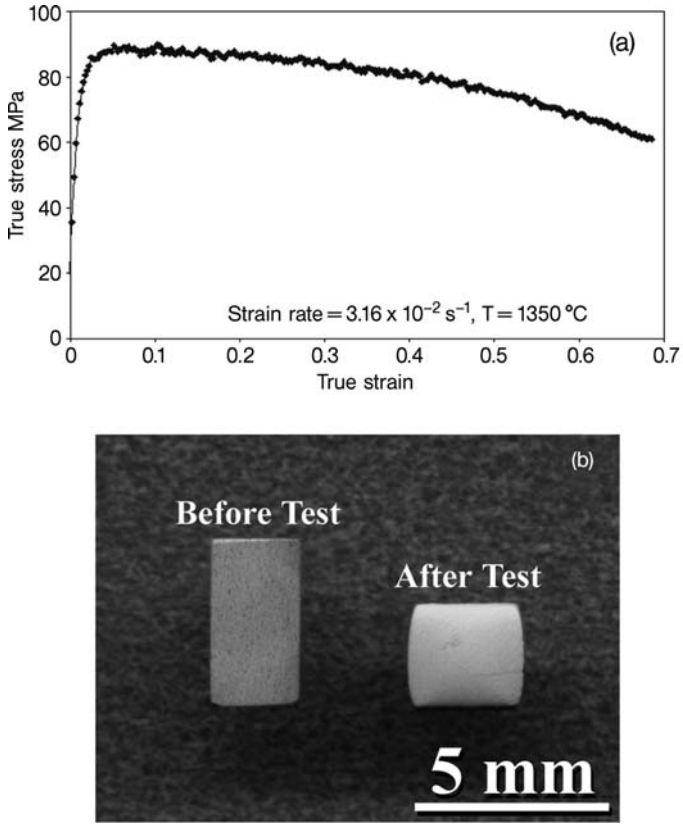

Fig. 25.6 (a) True-stress–true-strain curve of superplastic flow of zirconia-alumina-spinel triphase ceramic composite; (b) a sample view before and after the test.

perature deformation. In the triphase ceramic composite, there are three grain boundaries (zirconia-zirconia, alumina-alumina, and spinel-spinel), and three interphases (zirconia-alumina, zirconia-spinel and spinel-alumina) in the triphase ceramic. In order to deconvolute the rate-controlling mechanisms in the triphase ceramic composite, three biphase composites (zirconia-alumina, alumina-spinel and zirconia-spinel) of the zirconia-alumina-spinel ceramic were processed separately from nanosized alumina, zirconia and magnesia powders by Zhou et al. [58]. The samples became nearly fully dense after spark-plasma sintering at 1050–1100 °C, with the grain sizes between 50 nm and a few hundred nanometers. It was concluded that in the triphase ceramic composite, zirconia-alumina and zirconia-spinel contributed more to the grain-boundary sliding during superplastic flow (with the activation energies of 597 and 522 kJ/mol, respectively) [58]. Although alumina-spinel was not superplastic, spinel played a role in hindering the grain growth of the other two phases. It is interesting to notice that the activation energy of zirconia-spinel is lower than that of zirconia-

alumina, although the spinel grain size is larger than that of the alumina grains, while the zirconia grains are of similar sizes in both cases. The interface microstructures might play an important role.

25.3.2 Effect of the Processing Route

The above ceramic composites were processed by mechanically mixing nanoparticles and subsequent sintering. A new parallel process to make monolithic nanoceramic composites is plasma spraying [59] of spray-dried aggregates of a mixture of different ceramic particles, followed by sintering of the plasma-sprayed powders. The advantage of this method is that the nanophases in plasma-sprayed powders are more uniformly distributed. This is due to high nucleation rates and limited grain growth of each phase from the liquid state in the unique plasma melting and fast quenching process [60]. Another advantage is that starting materials are not necessarily nanoparticles. Typical spray-dried particles are composed in an aggregate of micrometer-sized primary particles consisting of all components of the composite. In most cases, the plasma-sprayed particles have large strain energies and usually contain metastable and even amorphous phases [60], which have a considerable driving force to form an equilibrium state and thus can help in consolidation. Duan et al. [61] studied the phase transformations in the consolidation by SPS of plasma-sprayed metastable Al_2TiO_5 powder and of mixtures of nano-Al_2O_3, TiO_2 powder with and without MgO additive. SPS of plasma-sprayed particles with and without preliminary high-energy ball milling (HEBM) led to a theoretical density over 99% in all sintered compacts [62]. The absence of HEBM in the processing route resulted in larger hard agglomerates with strong bonding between the nanograins inside these agglomerates. The difference in the superplastic behavior, especially in activation energy, implies different energetics of grain-boundary sliding. The grains in the specimen processed from nanopowder mixtures are more random in orientation and the grain boundaries are more prone to have high angles and high energies. As a result, grain-boundary sliding should be easier [63]. For plasma-sprayed powders, the strong low-angle grain boundaries between primary grains inside the particle formed by nucleation and growth from the metastable phase at elevated temperatures did not change during deformation. This suggests that the whole hard agglomerate acts as one entity during SPS and high-temperature deformation. Therefore, the sliding unit is not individual grains, but the whole particle or hard agglomerate. This could explain the lack of superplasticity in specimens from plasma-sprayed particles synthesized by SPS, i.e. the microstructure behaved as a course-grained sample. The application of HEBM of plasma-sprayed particles made the synthesized specimens superplastic because of smaller effective grain sizes. However, the apparent activation energy of superplastic flow in these materials was much higher than that of the specimens synthesized by SPS from nanopowder mixtures [62]. Low impurity (e.g. W, Co from HEBM) segregation may be responsible for the significant increase in the apparent activation energy for the grain-boundary diffusion.

25.3.3
SPS Accelerated Superplasticity

SPS has been demonstrated not only to be an effective sintering process to fabricate fully dense nanocrystalline ceramics and composites but also to be a new forming method to enhance ceramic ductility [64, 65]. The first attempt to apply the SPS approach to speed up superplastic forming was by Shen et al. [65] who started with fully dense ceramics that sinter via either transient or permanent liquid-phase modes. The observed enhanced ductility is thought to be associated with the enhanced grain sliding at the boundary of the glassy/liquid phase resulting from the electric-field-induced motion of charged species. Despite remarkable success (rapid superplastic deformation with high strain rates in the range 10^{-2} to 10^{-3} s^{-1}), the deformation temperatures were still extremely high (1500 °C is typical). A completely different strategy of using a porous preform instead of fully dense blanks and *simultaneously* consolidated and superplastically formed the specimens in the SPS equipment had been shown to be an effective way of utilization of low-temperature superplasticity of ceramics. The use of concurrent deformation and consolidation provides nanoceramic superplasticity with many advantages [66]. First, porous preforms are easy to produce (75–90% TD) by different methods such as pressureless sintering, plasma spray, SPS, *etc*. Secondly, by the presence of an open porosity network in the materials at densities below 90% TD was found to seriously inhibit static grain growth during the sintering. However, at densities over 90% TD density, as the porosity network closes, the pores become less effective at pinning grain boundaries, thus, beyond this point the grain size begins to increase dramatically. It has been found that the open porosity can also limit dynamic grain growth during the deformation. Finally, a microstructure with a nanocrystalline grain size can lead to much lower deformation temperatures and higher strain rates. As a result, the near net shape forming of a nearly dense (98%) nanoceramic was demonstrated at a temperature as low as 1150 °C (Fig. 25.7). This temperature is remarkably lower than those found for conventional superplastic ceramics. These record low temperatures are comparable to that of Ni-based superalloys (typically, 950 °C), suggesting that an existing metallic superplastic shape tooling might be applied to nanoceramic composites. The strain rate of the deformation process was about 10^{-2} s^{-1} and the final density was 100%. The same composites did not exhibit superplasticity by conventional deformation methods since both static grain growth during the slow heating and dynamic grain growth during high-temperature deformation occur. It can be noted that nearly nanosized microstructure has been obtained in the SPS-deformed composites whereas extensive grain growth was observed in the nondeformed samples even at the same SPS temperature.

It is generally accepted that application of mechanical pressure is helpful in removing pores from compacts. The increasing applied pressure during deformation is expected to promote rapid densification and grain-boundary sliding. Therefore, applying a high pressure at low temperature that allows the grain-

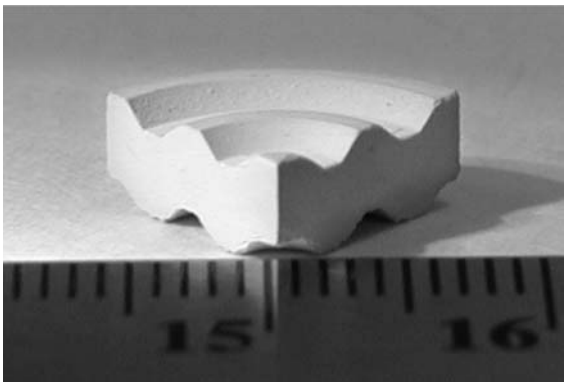

Fig. 25.7 A sectioned quadrant of the zirconia-alumina-spinel triphase ceramic sample superplastically deformed by SPS at 1150 °C.

boundary sliding to become kinetically favorable can enhance deformation rates. This is consistent with our findings where the strain rate increases with increasing loading rate. When a constant load instead of a constant stress is applied, the strain rates are significantly decreased. The latter is similar to the observations of Shen et al.'s [65] work where they applied a constant load during the deformation, indicating a decreasing applied stress. It can also be noted that the strain rates are significantly increased when a slightly higher deformation temperature is applied [66] even though the loading rates are slightly lower, suggesting the temperature has a profound effect on deformation.

In conclusion, this new SPS-forming approach provides a new route for low temperature and high strain-rate superplasticity for nanostructured materials and should impact and interest a broad range of scientists in materials research and superplastic forming technology.

25.4
Nanocomposites with Enhanced Fracture Toughness

Nanocrystalline ceramics do not appear to possess higher fracture toughness than conventional microcrystalline ceramics. Therefore, it is very likely that, in spite of the significant advantage in other properties, toughness is likely to be the bottleneck that controls the application of nanocrystalline ceramics in both structural and functional applications. In the last two decades significant advancements have been made in the understanding of toughening mechanisms in microcrystalline ceramics. Unfortunately, many of the microcrystalline material systems with improved fracture toughness have shown significant degradation of strength and hardness. This has led to interest in nanocrystalline ceramic composites where the possibility exists to offset this property degradation through the increases in strength and hardness typically seen in nanocrystalline

materials. Production of nanoceramic composites provides a promising route to enhance toughness. Most "nanocomposites" currently investigated are actually composites with microcrystalline matrixes and nanoscale second phases, very few composites with truly nanocrystalline matrix have been produced. Toughening mechanisms in ceramic composites, which have been reasonably well investigated in microcrystalline ceramics, need to be reinvestigated in their applicability to nanoceramics. Advanced consolidation techniques, such as SPS, can be used to produce nanocrystalline ceramic composites from nanopowders (see Section 25.2). These composites can then be analyzed for a comparison of toughening data and microstructural details versus material-system variables to develop analytical models for toughening mechanisms in ceramic composites with nanocrystalline matrices.

In the effort to produce ceramic nanocomposites, the introduction of a second phase is helpful in two ways; one is that the second phase will prevent grain growth of the matrix to some extent; the other is that toughening of the material can be made possible if the second phase is chosen with appropriate properties. Depending on the matrix grain size and second-phase particle size, Niihara et al. [67] have classified the nanocomposites in four groups. The first three types of nanocomposite fall into the micro-nano category, i.e. with nanosized second phase dispersed in a microcrystalline matrix. With only very few exceptions, the large majority of so-called "nanocomposites" developed to-date are micro-nanocomposites, rather than nano-nano composites (where both the matrix and inclusion grain size are in the nanometer range). Advances in the synthesis of nanocrystalline ceramics call for a reclassification that has been proposed by Kuntz et al. [68]. In this new classification the matrix phase is continuously nanocrystalline while the second phase varies, leading to four nanocomposite types: the nano-nano type, the nano-micro type, the nano-fiber type, and the nano-nanolayer type.

The enthusiasm in developing "nanocomposites" was triggered by Niihara's pioneering work in the late 1980s, who reported a significant increase in flexure strength from 350 MPa to 1–1.5 GPa accompanied by increase in fracture toughness from 3.5 $MPa \cdot m^{1/2}$ to 4.8 $MPa \cdot m^{1/2}$, by introducing 5% SiC nanoparticles into microcrystalline Al_2O_3 [69, 70]. Since then the research activity in this topic has been very intense, the new concept of adding nanometric particles has been introduced into various material systems. An extensive review has been made by Sternitzke [71] and by Awaji [72]. Some of the more recent results [75–85] are listed in Table 25.2. The selected examples are on alumina-based "nanocomposites."

Most of the work on ceramic/ceramic "nanocomposites" is concentrated on SiC-nanoparticle-strengthened materials. The large majority of the work has found obvious enhancement in strength or toughness or both. The increase in strength is usually more remarkable than that in toughness. A number of mechanisms were proposed to account for the toughening in Al_2O_3/SiC micro-nano composites, e.g., switch from intergranular to transgranular fracture because of the intergranular SiC particles, crack deflection by the internal stress

Table 25.2 Strength and fracture toughness of alumina-based "nanocomposites".

Material system	Microstructural description (grain size)	Strength (MPa)	Fracture toughness ($MPam^{1/2}$)	Reference
Micro-nanocomposites				
Al_2O_3	3.5 μm monolith	475	3.6	Ji and
Al_2O_3/5%Cr	Al_2O_3-0.68 μm, Cr-124 nm	736	4.0	Yeomans, 2002 [75]
Al_2O_3	1.2 μm monolith	683	3.5	Sekino et al.
Al_2O_3/15%Ni	Al_2O_3-1 μm, Ni-180 nm	1090	4.2	1997 [76]
Al_2O_3	0.89 μm monolith	536	3.57	Oh et al. 1997
Al_2O_3/5%Cu	Al_2O_3-0.63 μm, Cu-200 nm	707	4.28	[77]
Al_2O_3	N/A	528	3.2	Sekino and
Al_2O_3/5%W	W < 100 nm intragranular 1 μm intergranular	645–1105	3.6–3.8	Niihara, 1995 [78]
Al_2O_3	N/A	–	3.5	Siegel et al.,
Al_2O_3/10%MWCN [a] Al_2O_3	Al_2O_3-0.5 μm	–	4.2	2001 [79]
Al_2O_3/8.5%SWCN [b]-4.3%Fe	~1 μm monolith	335	4.4	Flahaut et al.,
	Al_2O_3-0.5 μm	400	5.0	2000 [80]
Al_2O_3/10%SWCN [b]-4.3%Fe	Al_2O_3-0.5 μm	296	3.1	
Al_2O_3	4.1 μm monolith	371	2.6	Maensiri and
Al_2O_3/1%SiC	Al_2O_3-6.85 μm, SiC-200 nm	369	2.3	Roberts, 2002
Al_2O_3/2.5%SiC	Al_2O_3-6.66 μm, SiC-200 nm	409	2.2	[81]
Al_2O_3/5%SiC	Al_2O_3-2.82 μm, SiC-200 nm	417	2.6	
Al_2O_3	3.5 μm monolith	430	3.2	
Al_2O_3/5%SiC	Al_2O_3-4.0 μm, SiC-200 nm	646	4.6	Anya, 1999
Al_2O_3/10%SiC	Al_2O_3-2.9 μm, SiC-200 nm	560	5.2	[82]
Al_2O_3/15%SiC	Al_2O_3-2.6 μm, SiC-200 nm	549	5.5	
Al_2O_3	2~3 μm monolith	460	3.1	Davidge et al.
Al_2O_3/5-10%SiC	Al_2O_3-2~3 μm, SiC-200 nm	760–800	3.3–3.6	1997 [83]
Al_2O_3	~1 μm monolith	380	3.91	
Al_2O_3/15%Si_3N_4	Al_2O_3~ μm Si3N_4-200~300 nm intergranular 80 nm intragranular	820	6.00	Zhu et al. 1997 [84]
Nano-nanocomposites				
Al_2O_3-10%ZrO_2	Al_2O_3-35–44 nm ZrO_2-20–30 nm	–-	8.38	Bhaduri and Bhaduri, 1997 [85]

a) MWCN: multiwalled carbon nanotubes
b) SWCN; single-wall carbon nanotubes

around the intragranular particles (also resulting in intergranular to transgranular fracture), crack bridging by SiC particles, or clinched rough crack surfaces, *etc*. [73, 74]. Reduction in critical flaw size in the "nanocomposites" is commonly accepted as an important reason for the strength increase.

Adding a small amount of metallic phases to alumina can also effectively increase both the strength and toughness of the material, as shown by the examples in Table 25.2. The metallic phases in these "nanocomposites" are all in the form of particles, either intergranular or intragranular, with the alumina forming the continuous phase. The enhancement is attributable to metal plasticity, or to crack-deflection due to residue stress, or to crack bridging.

In the sole example of a nano-nano composite shown in Table 25.2, remarkable toughness was achieved. The authors [85] did not attribute the high toughness to phase transformation, they declared that only 5% of the total zirconia undergoes t–m transformation under stress. The toughening might be due to ferroelastic-domain switching or crushing of well-distributed pores under the indenter.

Certain toughening mechanisms in microcrystalline ceramic systems have been reasonably well developed and investigated. It has yet to be determined whether these same mechanisms will be germane to the corresponding nanocrystalline systems.

25.4.1
Fiber Toughening

The most common toughening mechanism that is associated with the incorporation of fibers into a ceramic matrix is fiber bridging. This toughening mechanism involves the bridging of the crack wake by the second-phase fibers (Fig. 25.8). The toughening effect is achieved when the fibers either shed load from the crack tip while remaining intact (Fig. 25.8(c)), the interface debonds between the fiber and the matrix followed by pull out (Fig. 25.8(b)), and/or the individual fibers fracture followed by energy adsorption through pull out of the

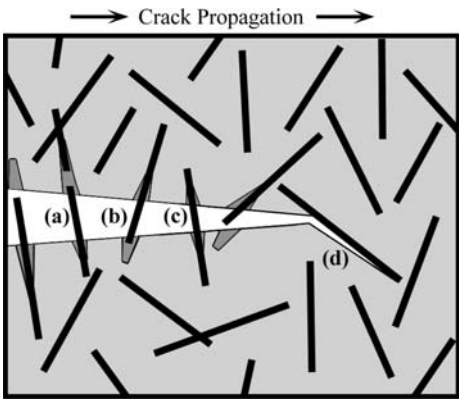

Fig. 25.8 Schematic of the fiber-toughening mechanism in a ceramic matrix composite: (a) fiber rupture followed by pull-out, (b) debonding and fiber pull-out, (c) fiber bridging in the crack wake, and (d) crack deflection along fiber–matrix boundary (From Ref. [86]).

broken fiber (Fig. 25.8 (a)). These effects lead to increased extrinsic toughness. Another possible toughening mechanism as seen in fiber-reinforced ceramic composites, is crack deflection. When the fiber is of a particular orientation (Fig. 25.8 (d)), the crack-propagation direction can be deflected away from the axis of highest stress to a less-efficient orientation directed by the longitudinal orientation of the fiber. This leads to increased fracture energy through increased fracture surface area and lower driving forces due to the reduced resolved normal stresses at the crack tip. This phenomenon will enhance the intrinsic toughness. Both crack deflection and fiber bridging should be pertinent to nanoceramic composites, since neither method is inherently dependent on the matrix grain size.

For example, addition of SiC whiskers to an alumina nanocrystalline matrix has been able to produce toughness values as high as 6.17 $MPa \cdot m^{1/2}$, while improving the hardness to 26 GPa [87]. A more detailed investigation on fiber toughening of nanocomposites was conducted by introducing single-walled carbon nanotubes (SWCN) into nanocrystalline alumina [88].

Carbon nanotubes (CNT), originally discovered as a byproduct of fullerene research, are attracting increasing interest as constituents of novel nanostructured materials for a wide range of applications [89–91]. There are two main types of carbon nanotubes, single-wall carbon nanotubes (SWCN) and multiwall carbon nanotubes (MWCN). Both of these types can have high structural perfection, however, SWCN have a particularly desirable combination of mechanical properties. Specifically, they have an elastic stiffness comparable to that of diamond $\sim$1.5 TPa, and they are several times as strong (yield strength 52 GPa) [89]. The size, shape, and properties of SWCN make them prime candidates for use in the development of potentially revolutionary composite materials. Attempts have been made to develop advanced engineering materials with improved mechanical properties through the incorporation of CNT in various matrices (polymers, metals, and ceramics) by taking advantage of the exceptional strength of the nanotubes [79, 89, 92–95]. Most of the investigations on carbon-nanotube-containing composites have so far focused on polymer-based composites with improved electrical and mechanical properties. For example, their addition to a polymer matrix leads to a very low electrical percolation threshold and improved electrical conductivity. Work on carbon nanotubes in metals and ceramics has been much less focused.

SWCN tend to self-organize into "ropes" that consist in many (typically, 10–100) tubes running together along their length in van der Waals bonding with one another. Due to their high surface area and high aspect ratio, the ability to homogeneously disperse the nanotubes into the matrix is a processing challenge. In the open literature [79, 92], all the other carbon-nanotubes-reinforced ceramic composites have been consolidated by hot-pressing methods that require higher temperatures and longer duration. These sintering parameters damage the carbon nanotubes in the composites, leading to decreases in, or total loss in, reinforcing effects. For example, in carbon nanotubes-metal-ceramic composite systems some of the hot-pressing temperatures were as high as

1600 °C. This damaged most of carbon nanotubes and decreased the quantity and quality of carbon nanotubes in the sintered composites. No reinforcing effect was noted in the *in-situ* carbon-nanotubes-Fe-Al_2O_3 nanocomposites in the investigation of Peigney et al. [92, 93]. The best reported result by Siegel et al. [79] was a 24% increase in toughness in 10 vol.% MWCN/Al_2O_3 nanocomposites produced by the hot-pressing method at 1300 °C/1 h. Full density of alumina-based nanocomposites with incorporated multiwall carbon nanotubes was achieved but the matrix grain size was in the submicrometer range.

The SPS technique, as it was shown earlier (Section 25.2) allows much lower sintering temperatures and shorter times for obtaining dense nanocrystalline ceramics as compared to conventional sintering techniques. As a result, in the alumina/SWCN system the best results to date have a toughness value of 9.7 $MPa \cdot m^{1/2}$ (nearly three times pure alumina) with only 10 vol.% SWCN added [88]. This remarkable toughening stands out as the only ceramic composite to realize the promise of significant toughening through the addition of carbon nanotubes into a nanocrystalline matrix (Fig. 25.9, solid squares). Structural investigation of the nanocomposites have shown that carbon nanotubes are fairly homogeneously distributed along grain boundaries to develop an intertwining network microstructure (Fig. 25.10 (a)) and are entangled with alumina grains when some of them encapsulated alumina nanoscale grains with good bonding (Fig. 25.10 (b)). This microstructure simultaneously provides stiffness, toughness, and strength to the ceramic. A strong toughening effect in these nanocomposites may likely be related to the number of factors. First, it is due to the extraordinary mechanical properties and the more perfect structure of SWCN. MWCN are similar to SWCN, but contain more defects, which limit their properties. Furthermore, there are differences in the ability to transfer load from the matrix to the nanotubes between SWCNT and MWCN. Secondly, the crack deflection along the continuous interface between carbon nanotubes and

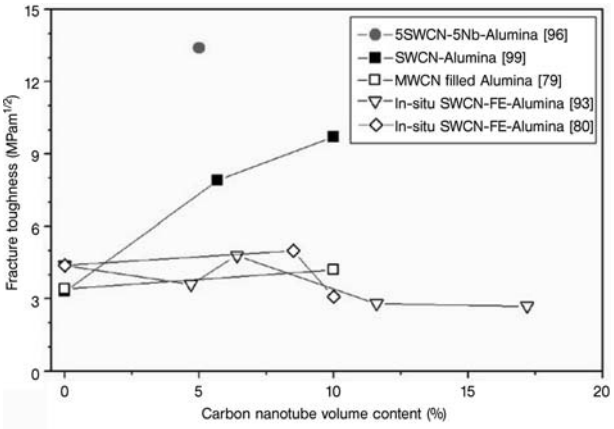

Fig. 25.9 Fracture toughness versus carbon-nanotube volume content in alumina-based composites [86].

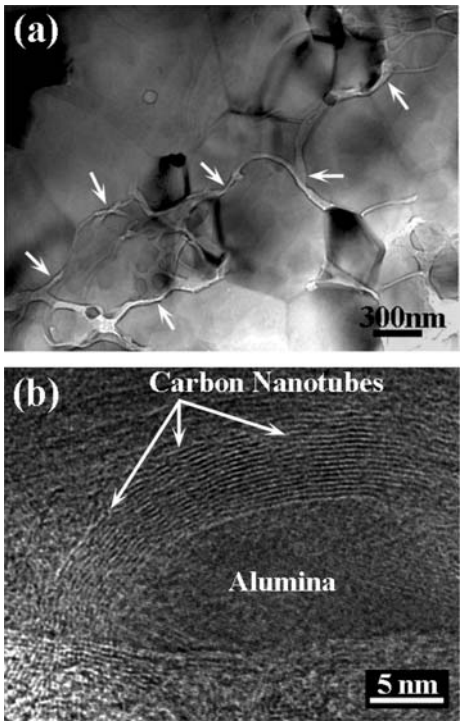

Fig. 25.10 (a) Bright-field TEM image and (b) high-resolution TEM image of the 5.7 vol.% SWCNT/Al_2O_3 composite. The arrows indicate the SWCNT. (From Ref. [88].)

nanocrystalline matrix grains might significantly contribute to the toughening effect (Fig. 25.6 (d), Fig. 25.11 (a)). Such toughening mechanisms as fiber bridging (Fig. 25.6 (c)) and fiber pull-outs (Figs. 25.6 (a) and (b)) were also experimentally observed in alumina/SWCN nanocomposites (Figs. 25.11 (b) and (c), respectively). Thirdly, it is related to a fast-sintering technique that allows lower sintering temperatures and shorter durations. Therefore, the high-quality ropes of single-wall carbon nanotubes can be retained in the sintered compacts. Raman spectroscopy of the sintered Al_2O_3/SWCN composites have shown that both composite and raw SWCN spectra have a sharp peak at $\sim$1595 cm^{-1} and a shoulder in the 1550–1575 cm^{-1} region (Fig. 25.12). No graphite peak in Al_2O_3/SWCN composite spectra was revealed.

This is also consistent with the results by Flahaut et al. [80] where the increase in the quality and quantity of SWCN may result in an easier transfer of the stress and, thus, can account for the increase in the toughness in the *in-situ* SWCN/Fe/Al_2O_3 nanocomposites. In order to be effective as reinforcing elements, high-quality carbon nanotubes, without damage during consolidation, must be effectively bonded to the matrix so that they can actually carry the loads. The dependence of toughness on density directly supports this statement.

These studies give a promising future for application of carbon nanotubes in reinforcing structural ceramic composites and other materials systems as well.

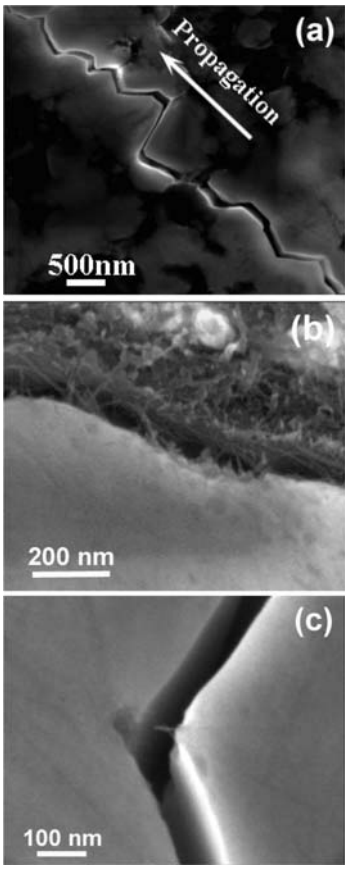

Fig. 25.11 (a) Indentation-induced intergranular crack; (b) SWCNT bridging and (c) SWCNT pull-out in the 5.7 vol.% SWCNT/Al_2O_3 nanocomposite.

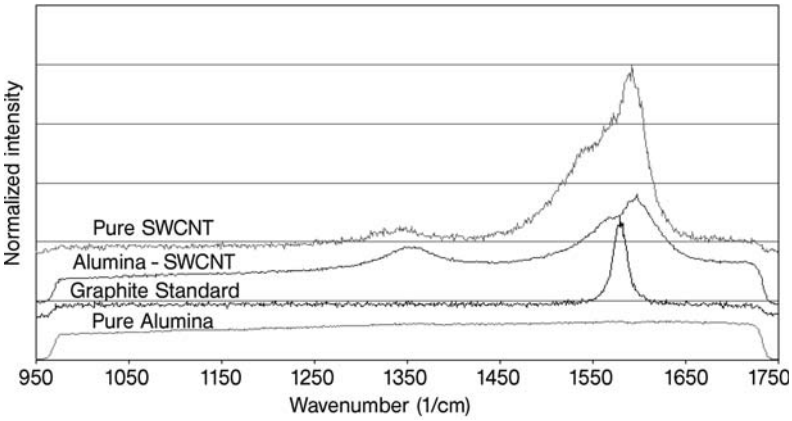

Fig. 25.12 Raman spectroscopy at 522–488 nm, 60-s scan.

25.4.2
Ductile-phase Toughening

The addition of certain ductile phases (metals) to ceramic matrixes has proven to be an effective toughening mechanism. The ductile phase can lead to the toughening of the composite through two distinct mechanisms. The first is through ductile yielding in the process zone of a propagating crack to increase intrinsic toughness. The stress field around the crack tip can be relieved through adsorption of energy through the deformation of the ductile phase or blunting of the crack tip at a ductile particle. The second manner a ductile phase can lead to toughening of a ceramic composite is by ductile bridging ligaments in the crack wake, increasing extrinsic toughness. This occurs when the crack tip propagates past a ductile phase grain that then bridges the crack wake and must be pulled to failure or debond from the surrounding matrix. These toughening effects should be applicable in nanocrystalline ceramic matrix composites as long as the ductile-phase grain size is large enough to support plastic deformation.

The addition of a ductile phase to examine the effect of ductile-phase toughening in a nanocomposite has been investigated through the addition of niobium to an alumina matrix. Nb was added through high-energy ball milling (HEBM) with the nano-Al_2O_3 powder and sintered by SPS at only 1100 °C for 3 min [86]. The product was a nano-nano type composite combined with nano-nano layer type. The 10-vol.% Nb nanocomposite has a fracture toughness value of 7 $MPa \cdot m^{1/2}$ without a decrease in hardness [96]. This is twice as tough as a pressureless sintered composite of the same composition reported in work by Garcia et al. [97]. This increase in toughness may be attributed to the novel microstructure in the nanocomposite where the Nb phase distributed as particles of $\sim$20 nm along with a continuous 3–4 nm layer at boundaries between Al_2O_3 grains (Fig. 25.13). This microstructure should lead to toughening by increasing ductility at the crack tip instead of the traditional ligament bridging in the crack wake that is typical of micrometer-scaled metallic-phase toughened ceramics. An addition of Nb to the alumina/SWCN system resulted in an exceptional value of the fracture toughness of 13.5 $MPa \cdot m^{1/2}$ (Fig. 25.9, solid circle).

25.4.3
Transformation Toughening

Transformation toughening has been investigated in ceramics containing zirconia as a second phase. This relies on the transformation of zirconia from the tetragonal to the monoclinic phase under applied stress. This transformation occurs in the stress field around the crack tip and the resultant strain involved in the transformation locally relieves the stress field and adsorbs fracture energy. The resultant zone of transformed particles left in the crack wake. This will increase intrinsic toughness. The transformation toughening mechanism is directly affected by the stability of the tetragonal phase of the zirconia. The phase sta-

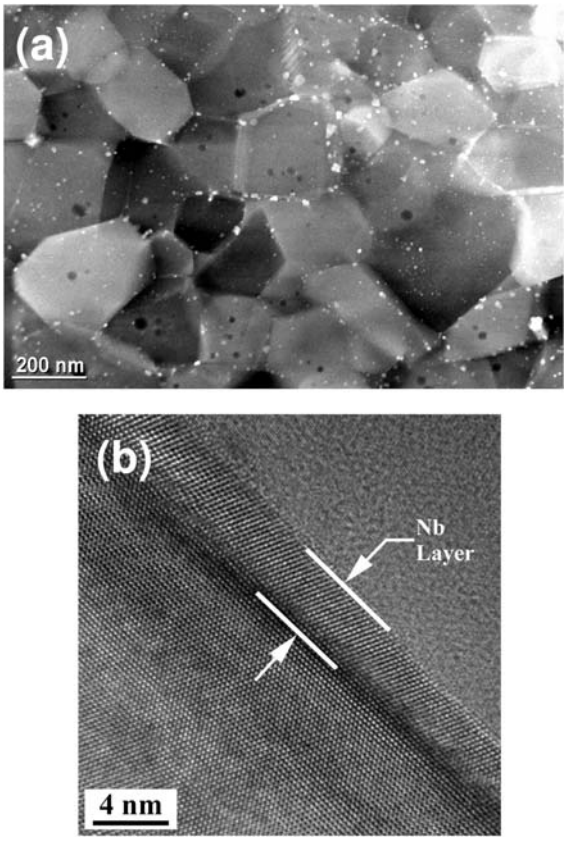

Fig. 25.13 Dark-field STEM and HRTEM images of 10 vol.% Nb-alumina composite.

bility is dependent on dopant concentration, the grain size of the zirconia phase and the testing temperature. Due to the fine balance of dopants and grain size, it is not clear whether transformation toughening will be a feasible toughening mechanism in nanoceramic composites.

The transformation that is being taken advantage of in ZrO_2 is the tetragonal to monoclinic phase transformation that has been investigated extensively in microcrystalline alumina-ZrO_2 composites [98]. In the alumina-based composites with $BaTiO_3$ as a second phase, a domain-switching effect that occurs during applied stress is believed to be a possible toughening mechanism [99]. The material systems we used for the investigation of transformation toughening in nanoceramic composites are alumina-ZrO_2 and alumina-$BaTiO_3$. Both of these systems were nano-nano type composites. The initial results from both of these composites have been very promising. The alumina-$BaTiO_3$ composite has already produced a fracture toughness of 5.26 $MPa \cdot m^{1/2}$ and the alumina-ZrO_2

composite has been measured at an impressive 8.9 $MPa \cdot m^{1/2}$ with a nanocrystalline matrix grain size of 96 nm. It is also interesting to note that in spite of the improved toughness in this composite the dilatational tetragonal to monoclinic phase transformation has not occurred during fracture. Virkar and Matsumoto [100] have proposed ferroelastic domain switching as a toughening mechanism in tetragonal zirconia ceramics that do not undergo a phase transformation.

25.4.4 Microcrack Toughening

Analogous to the tetragonal to monoclinic transformation behavior of zirconia, stress-induced microcrack formation represents an irreversible deformation phenomenon that is associated with energy dissipation and stress shielding. Microcracking is induced by the combined action of the thermal residual stress and the applied stress field at the crack tips. This can be observed in single-phase material (with anisotropic thermal expansion coefficient) as well as multiphase material (with different thermal expansion coefficients between the phases) [101, 102]. The presence of microcracks deflects or branches out the main crack as well as shield stress at the crack tip, increasing the intrinsic toughness. When it is effective, microcrack toughening can increase the fracture energy of ceramics by 20–40%. Pure alumina, alumina reinforced with monoclinic zirconia [103] and SiC reinforced with TiB_2 [104] have shown toughening due to this mechanism. The ability to apply the mechanism of microcrack toughening to composites with nanocrystalline ceramic matrices is still uncertain because of the dependence of the toughening on microcrack length, which is undoubtedly grain-size dependent since microcracks are typically generated at grain boundaries.

25.4.5 Future Perspectives

Carbon nanotubes are usually synthesized by carbon arc discharge, laser ablation of carbon, chemical vapor deposition (CVD), or high-pressure carbon monoxide carrier gas (HiPco) process [105–107]. Because of the morphological integrity of carbon nanotubes, which spatially confine the reaction, carbon nanotubes have been used as templates to synthesize other one-dimensional nanomaterials with diameters, lengths, and orientations close, or similar, to those of the carbon nanotube [108]. By filling the inside of the hollow space of CNT with other elements or through decorating the outside surfaces, different kinds of one-dimensional nanomaterials with heterostructures have been fabricated. For example, silicon-carbide nanotubes, nanorods or nanowires [108–112], gallium-nitride nanowires [113], Si-B-C-N nanocables [114], titanium carbide and niobium-nitride nanotubes or nanorods [115], heterostructural carbon nanotubes and carbide nanorods [116], and SiC-SiO_x biaxial nanowires [117] have recently been synthesized using carbon na-

notubes as templates. Another important method to synthesize one-dimensional nanomaterials is laser-assisted catalytic growth (LCG) where a laser was used to ablate the target materials to produce the nanocluster catalyst particles within a reactor, and then one-dimensional nanomaterials were grown as the reactant, such as single-crystalline silicon and germanium nanowires [118, 119] single-crystalline indium phosphide (InP) nanowires [120–122] single crystalline gallium nitride (GaN) nanowires [123, 124] and single-crystalline gallium phosphide (GaP) [125], *etc*. Recently, a novel and simple method of heat treatment of the polymer functionalized SWCNs has been successfully used in this investigation to synthesize the multielemental $Si_3C_xO_y\square_zN_{4-(x+y+z)}$ nanoscrews and nanowires [126]. These one-dimensional nanomaterials possess a diameter from a few nanometers to around 100 nm and a length up to a few tens of micrometers, with a structure like β-Si_3N_4 crystal. These novel $Si_3C_xO_y\square_zN_{4-(x+y+z)}$ nanoscrews and nanowires may exhibit unique properties with potential for utilization in nanotechnology, for example, for fiber toughening of nanoceramics.

Moreover, a number of studies have shown that sintering at high pressures can yield full densification of nanocrystalline powders with minimal grain growth. One such example is given by Hahn [127] who sintered n-TiO_2 to its theoretical density with no grain growth at 450–550 °C ($\sim$0.35 T_m) and 1 GPa. Mayo et al. [128] found that for the same final density (91%), sinter-forging n-TiO_2 retained a grain size of 87 nm, while pressureless sintering resulted in a grain size of 400 nm. Pechenik et al. [129, 130] and Gallas et al. [131] have been successful in suppressing grain coarsening in the fabrication of transparent nanocrystalline silicon nitride and alumina by applying pressures up to 5 GPa and modest temperatures.

25.5 Concluding Remarks

Advances in synthesis and processing of ceramic nanocomposites have opened up new vistas for practical utilization of such materials. A ceramic nanocomposite based on silicon nitride and silicon carbide has been produced by pyrolysis of a liquid-polymer precursor. It has demonstrated one of the lowest creep rates (greatest creep strength) as compared to all other results on silicon-nitride-based materials at a common reference temperature. This was achieved by either eliminating or minimizing the amount of oxynitride glassy phase in the intergrain and interphase boundaries of the microstructure.

Superplasticity has been demonstrated at a low temperature in an alumina/zirconia/magnesia spinel nanocomposite when the grain size was significantly lowered by using spark-plasma sintering (SPS) process. Furthermore, by using the SPS chamber as a forming environment, superplasticity was obtained at an astonishingly low temperature (1150 °C) with an extremely fast forming time (3 to 4 min).

Single-wall carbon-nanotube- (SWCN) reinforced alumina-based nanocomposites consolidated by an SPS process yielded a very significant increase in frac-

ture toughness that has not been attained before. Incorporating a nanocrystalline layer of niobium between the alumina grains in such alumina/SWCN nanocomposites yielded a fracture toughness value equal to that for metallic materials.

These studies do point to an attractive processing methodology where using SPS as a processing tool, one can engineer microstructures that have either much improved creep resistance or significantly enhanced superplastic formability or much improved fracture toughness.

Acknowledgements

This investigation was supported in part by a grant (G-DAAD19-00-1-0185) from U.S. Army Research Office with Dr. William Mullins as the Program Manager, a grant (N00014-03-1-0148) from Office of Naval Research with Dr. Lawrence Kabacoff as Program Manager, the HTML Proposal #2003-025 by Oak Ridge National Laboratory, and the EMSL Proposal No. 3385 (2003) by Pacific Northwest National Laboratory. The authors would like to acknowledge Dr. G.-D. Zhan, Dr. X. Zhou, Dr. M. Gasch, Dr. J. Wan, Dr. R.-G. Duan, and Dr. J. Kuntz for their input to the current investigations.

References

1 F. L. Riley **2000**, *J. Am. Ceram. Soc.* 83, 245–265.
2 G. Ziegler, J. Heinrich, G. Wötting **1987**, *J. Mater. Sci.* 22, 3041–3086.
3 R. G. Duan, G. Roebben, J. Vleugels, O. Van der Biest **2002**, *J. Eur. Ceram. Soc.* 22, 1897–1904.
4 R. W. Trice, J. W. Halloran **1999**, *J. Am. Ceram. Soc.* 82, 2633–2640.
5 H.-J. Choi, J.-G. Lee, Y.-W. Kim **1999**, *J. Eur. Ceram. Soc.* 19, 2757–2762.
6 G. Roebben, R. G. Duan, D. Sciti, O. Van der Biest **2002**, *J. Eur. Ceram. Soc.* 22, 2501–2509.
7 K. Okada, K. Fukuyama, Y. Kameshima **1995**, *J. Am. Ceram. Soc.* 78, 2021–2026.
8 H.-J. Kleebe, M. K. Cinibulk, R. M. Cannon, M. Rüler **1993**, *J. Am. Ceram. Soc.* 76, 1969–1977.
9 R. F. Pabst **1985**, Progress in Creep, Fracture, in: *Creep Behavior of Crystalline Solids,* Vol. 3, B. Wilshire, R. W. Evans (eds.), Pineridge Press, Swansea, UK, p. 254.
10 F. Wakai, Y. Kodama, S. Sakaguchi, N. Murayama, K. Izaki, K. Niihara **1990**, *Nature* 344, 421–423.
11 F. Wakai, H. Kato **1988**, *Adv. Ceram. Mater.* 3, 71–76.
12 T. Rouxel, F. Wakai, K. Izaki **1992**, *J. Am. Ceram. Soc.* 75, 2363–2372.
13 I.-W. Chen, L. A. Xue **1990**, *J. Am. Ceram. Soc.* 73, 2585–2609.
14 J. J. Meléndez-Martínez, A. Domínguez-Rodríguez **2004**, *Prog. Mater. Sci.* 49, 19–107.
15 T. Ohji, A. Nakahira, T. Hirano, K. Niihara **1994**, *J. Am. Ceram. Soc.* 77, 3259–3262.
16 T. Hirano, K. Niihara, T. Ohji, F. Wakai **1996**, *J. Mater. Sci. Lett.* 15, 505–507.
17 A. M. Thompson, H. M. Chan, M. P. Harmer **1997**, *J. Am. Ceram. Soc.* 80, 2221–2228.
18 K. J. Yoon, S. M. Wiederhorn, W. E. Luecke **2000**, *J. Am. Ceram. Soc.* 83, 2017–2023.
19 J. Crampon, R. Duclos, N. Rakotoharisoa **1993**, *J. Mater. Sci.* 28, 909–916.

20 J. Crampon, R. Duclos, N. Rakotoharisoa **1990**, *J. Mater. Sci.* 25, 1203–1208.
21 S. Y. Yoon, T. Akatsu, E. Yasuda **1997**, *J. Mater. Sci.* 32, 3813–3819.
22 R. D. Nixon, D. A. Koester, S. Chevacharoenkul, R. F. Davis **1990**, *Compos. Sci. Technol.* 37, 313–328.
23 J.-L. Besson, M. Mayne, D. Bahloul-Hourlier, P. Goursat **1998**, *J. Eur. Ceram. Soc.* 18, 1893–1904.
24 C. J. Gasdaska **1994**, *J. Am. Ceram. Soc.* 77, 2408–2418.
25 R. Raj **1982**, *J. Geophys. Res.* 87, 4731–4739.
26 F. Wakai **1994**, *Acta Metall. Mater.* 42, 1163–1172.
27 H. Mandal, D. P. Thompson, **2000**, *J. Mater. Sci.* 35, 6285–6292.
28 M. K. Cinibulk, G. Thomas **1992**, *J. Am. Ceram. Soc.* 75, 2037–2043.
29 M. Mitomo **1976**, *J. Mater. Sci.* 11, 1103–1107.
30 A. Tsuge, K. Nishida, M. Komatsu **1975**, *J. Am. Ceram. Soc.* 58, 323–326.
31 I. Tanaka, G. Pezzotti, T. Okamoto, Y. Miyamoto, M. Koizumi **1989**, *J. Am. Ceram. Soc.* 72, 1656–1660.
32 J. Wan, M. J. Gasch, A. K. Mukherjee **2000**, *J. Mater. Res.* 15, 1657–1660.
33 J. Wan, R.-G. Duan, M. J. Gasch, A. K. Mukherjee **2006**, *J. Am. Ceram. Soc.* 89, 274–280.
34 Y. Shinoda, T. Nagano, H. Gu, F. Wakai **1999**, *J. Am. Ceram. Soc.* 82, 2916–2918.
35 F. F. Lange, B. I. Davis **1982**, *J. Mater. Sci.* 17, 3637–3640.
36 P. J. Whalen, C. Gasdaska, R. D. Silvers **1990**, *Ceram. Eng. Sci. Proc.* 11, 633–649.
37 A. A. Wereszczak, M. K. Ferber, T. P. Kirkland, A. S. Barnes, E. L. Frome, M. N. Menon **1999**, *J. Eur. Ceram. Soc.* 19, 227–237.
38 G. Bernard-Granger, J. Crampon, R. Duclos, B. Cales **1997**, *J. Eur. Ceram. Soc.* 17, 1647–1654.
39 F. F. Lange, B. I. Davis, H. C. Graham **1983**, *J. Am. Ceram. Soc.* 66, C98–C99.
40 M. Backhaus-Ricoult, P. Eveno, J. Castaing, H. J. Kleebe **1995**, in: *Plastic Deformation of Ceramics*, p. 555, R. C. Bradt, C. A. Brookes, J. L. Routbort (eds.), Plenum Publishing Corporation, Plenum Publishing, New York.
41 K. Ramoul-Badache, M. Lancin **1992**, *J. Eur. Ceram. Soc.* 10, 369–379.
42 S. Y. Yoon, T. Akatsu, E. Yasuda **1996**, *J. Mater. Sci.* 32, 120–126.
43 F. F. Lange, B. I. Davis, D. R. Clarke **1980**, *J. Mater. Sci.* 15, 601–610.
44 M. S. Seltzer **1977**, *Am. Ceram. Soc. Bull.* 56, 418–423.
45 A. K. Mukherjee, J. E. Bird, J. E. Dorn **1969**, *ASM Trans.* 62, 155–179.
46 B.-N. Kim, K. Hiraga, K. Morita, Y. Sakka **2001**, *Nature* 413, 288–291.
47 F. Wakai, S. Sakaguchi, Y. Matsuno **1986**, *Adv. Ceram. Mater.* 1, 259–263.
48 K. P. Kunz, V. K. Sarin, R. F. Davis, S. R. Bryan **1988**, *Mater. Sci. Eng. A* 105/106, 47–54.
49 K. Kijima, S. Shirasaki **1976**, *J. Chem. Phys.* 65, 2668–2671.
50 H. D. Batha, E. D. Whitney **1973**, *J. Am. Ceram. Soc.* 56, 365–369.
51 H. Hon, R. F. Davis, D. E. Newbury **1980**, *J. Mater. Sci.* 15, 2073–2080.
52 M. H. Hon, R. F. Davis **1979**, *J. Mater. Sci.* 14, 2411–2421.
53 T. G. Nieh, J. Wadsworth **1990**, *Acta Metall. Mater.* 38, 1121–1133.
54 Y. Yoshizawa, T. Sakuma **1992**, *Acta Metall. Mater.* 40, 2943–2950.
55 J. D. Kuntz, J. Wan, A. K. Mukherjee, unpublished results.
56 G. D. Zhan, J. Kuntz, J. Wan, J. Garay, A. K. Mukherjee **2002**, *J. Am. Ceram. Soc.* 86, 200–202.
57 M. Omori **2000**, *Mater. Sci. Eng.* A 287, 183–188.
58 X. Zhou, D. M. Hulbert, J. D. Kuntz, J. E. Garay, A. K. Mukherjee **2004**, *Adv. Ceram. Matrix Compos.* 155–164.
59 B. H. Kear, Z. Kalman, R. K. Sadangi, G. Skandan, J. Colaizzi, W. E. Mayo **2000**, *J. Therm. Spray Technol.* 9, 483–487.
60 X. Zhou, V. Shukla, W. R. Cannon, B. H. Kear **2003**, *J. Am. Ceram. Soc.* 86, 1415–1420.
61 R. G. Duan, G. D. Zhan, J. D. Kuntz, B. H. Kear, A. K. Mukherjee **2004**, *Mater. Sci. Eng. A* 373, 180–186.

62 X. Zhou, D.M. Hulbert, J.D. Kuntz, R.K. Sadangi, V. Shukla, B.H. Kear, A.K. Mukherjee **2005**, *Mater. Sci. Eng. A* 394, 353–359.

63 H. Kokawa, T. Watanabe, S. Karashima **1981**, *Philos. Mag. A* 44, 1239–1254.

64 R. A. Hawsey, A. W. Murphy, W. S. Koncinski **2002**, ORNL Superconducting Technology Program for Electrical Power Systems, Annual Report, FY 2001, (published Feb.), p. 45.

65 Z. Shen, H. Peng, M. Nygren **2003**, *Adv. Mater.* 15, 1006–1009.

66 Guo-Dong Zhan, J.E. Garay, A.K. Mukherjee **2005**, *Nano Lett.* 5, 2593–2597.

67 K. Niihara, A. Nakahira, T. Sekino **1993**, New Nanocomposite Structural Ceramics, in: *Nanophase and Nanocomposite Materials Symposium*, p. 405, S. Komarneni, J.C. Parker, G.J. Thomas (eds.) Materials Research Society, Pittsburgh, PA.

68 J.D. Kuntz, G.-D. Zhan, A. K. Mukherjee **2004**, *MRS Bull.* January, 22–27.

69 K. Niihara, A. Nakahira, G. Sakai, M. Hirabayashi **1989**, *MRS International Meeting on Advanced Materials*, Vol. 4, p. 129.

70 K. Niihara, A. Nakahira **1991**, Analysis of Toughening Mechanisms of ZrO_2/Nano-SiC Ceramic Composites, in: *Advanced Structural Inorganic Composites*, P. Vincenzini (ed.) Elsevier, Amsterdam, The Netherlands, p. 637.

71 M. Sternitzke **1997**, *J. Eur. Ceram. Soc.* 17, 1061–1082.

72 H. Awaji, S.-M. Choi, E. Yagi **2002**, *Mech. Mater.* 34, 411–422.

73 I. Levin, W. D. Kaplan, D. G. Brandon, A. A. Layyous **1995**, *J. Am. Ceram. Soc.* 78, 254–257.

74 T. Ohji, J. Young-Keun, C. Yong-Ho, K. Niihara **1998**, *J. Am. Ceram. Soc.* 81, 1453–1461.

75 Y. Ji, J. A. Yeomans **2002**, *J. Eur. Ceram. Soc.* 22, 1927–1936.

76 T. Sekino, T. Nakajima, S. Ueda, K. Niihara **1997**, *J. Am. Ceram. Soc.* 80, 1139–1149.

77 S. T. Oh, T. Sekino, K. Niihara **1998**, *J. Euro. Ceram. Soc.* 18, 31–37.

78 T. Sekino, K. Niihara **1995**, *Nanostruct. Mater.* 6, 663–666.

79 R. W. Siegel, S. K. Chang, B. J. Ash, J. Stone, P. M. Ajayan, R. W. Doremus, L. S. Schadler **2001**, *Scr. Mater.* 44, 2061–2064.

80 E. Flahaut, A. Peigney, C. Laurent, C. Marliere, F. Chastel, A. Rousset **2000**, *Acta Mater.* 48, 3803–3812.

81 S. Maensiri, S. G. Roberts **2002**, *J. Eur. Ceram. Soc.* 22, 2945–2956.

82 C. C. Anya **1999**, *J. Mater. Sci.* 34, 5557–5567.

83 R. W. Davidge, R. J. Brook, F. Cambier, M. Poorteman, A. Leriche, D. O'Sullivan, S. Hampshire, T. Kennedy **1997**, *Br. Ceram. Trans.* 96, 121–127.

84 W. Z. Zhu, J. H. Gag, Z. S. Ding **1997**, *J. Mater. Sci.* 32, 537–542.

85 S. Bhaduri, S. B. Bhaduri **1997**, *Nanostruct. Mater.* 8, 755–763.

86 J.D. Kuntz, G.-D. Zhan, A. K. Mukherjee **2004**, *Mater. Res. Soc. Symp. Proc.* 821, 7.5.1–7.5.6.

87 G. D. Zhan, J. D. Kuntz, R. G. Duan, A. K. Mukherjee **2004**, *J. Am. Ceram. Soc.* 87, 2297–2300.

88 G. D. Zhan, J. D. Kuntz, J. L. Wan, A. K. Mukherjee **2003**, *Nature Mater.* 1, 38–42.

89 Yu, M.-F., B.S. Files, S. Arepalli, R.S. Ruoff **2000**, *Phys. Rev. Lett.* 84, 5552–5555.

90 A. Thess, R. Lee, P. Nikolaev, H. Dai, D. Petit, J. Robert, C. Xu, Y.H. Lee, S.G. Kim, A.G. Rinzler, D.T. Colbert, G.E. Sursevia, D. Tománek, J.E. Fischer, R.E. Smaley **1996**, *Science* 273, 483–487.

91 Baughman, R.H., A.A. Zakhidov, W.A. de Heer **2002**, *Science* 297, 787–792.

92 A. Peigney, Ch. Laurent, O. Dumortier, A. Rousset **1998**, *J. Eur. Ceram. Soc.* 18, 1995–2004.

93 A. Peigney, Ch. Laurent, E. Flahaut, A. Rousset **2000**, *Ceram. Int.* 26, 677–683.

94 G.-D. Zhan, J. D. Kuntz, H. Wang, C.-M. Wang, A. K. Mukherjee **2004**, *Philos. Mag. Lett.* 84, 419–423.

95 G.-D. Zhan, J. D. Kuntz, J. Garay, A. K. Mukherjee **2003**, *Appl. Phys. Lett.* 83, 1228–1230.

96 J. D. Kuntz, W. Julin, Z. Guo-Dong, A. K. Mukherjee **2002**, in *Ultrafine Grained Materials II*, Y. T. Zhu, T. G.

Langdon, R. S. Mishra, S. L. Semiatin, M. J. Sharan, T. C. Lowe (eds.) p. 225.
97 D. E. Garcia, S. Schicker, J. Bruhn, R. Janssen, N. Claussen **1998**, *J. Am. Ceram. Soc.* 81, 429–433.
98 G. D. Zhan, J. D. Kuntz, J. Wan, J. E. Garay, A. K. Mukherjee **2003**, *J. Am. Ceram. Soc.* 86, 200–203.
99 G. D. Zhan, J. D. Kuntz, J. Wan, J. E. Garay, A. K. Mukherjee **2003**, *Mater. Sci. Eng. A* 356, 443–446.
100 A. N. Virkar, R. L. K. Matsumoto **1986**, *J. Am. Ceram. Soc.* 69, 224–226.
101 A. G. Evans **1990**, *J. Am. Ceram. Soc.* 73, 187–207.
102 I. E. Reimanis, **1997**, *Mater. Sci. Eng. A* 237, 159–167.
103 M. Ruhle, A. G. Evans, R. M. McMeeking, P. G. Charalambides, J. W. Hutchinson **1987**, *Acta Metall.* 35, 2701–2710.
104 W.-H. Gu, K. T. Faber, R. W. Steinbrech **1992**, *Acta Metall. Mater.* 40, 3121–3128.
105 R. H. Baughman, A. A. Zakhidov, W. A. de Heer **2002**, *Science* 297, 787–792.
106 S. Lijima, T. Ichihashi **1993**, *Nature* 363, 603–605.
107 J. C. Charlier, A. De Vita, X. Blasé, R. Car **1997**, *Science* 275, 647–649.
108 C. L. Cheung, A. Kurtz, H. Park, C. M. Lieber **2002**, *J. Phys. Chem. B* 106, 2429–2433.
109 E. Munoz, A. B. Dalton, S. Collins, A. A. Zakhidov, R. H. Baughman, W. L. Zhou, J. He, C. J. O'Connor, B. McCarthy, B. J. Blau **2002**, *Chem. Phys. Lett.* 359, 397–402.
110 H. J. Dai, E. W. Wong, Y. Z. Lu, S. S. Fan, C. M. Lieber **1995**, *Nature* 375, 769–772.
111 Z. Pan, H. L. Lai, F. C. K. Au, X. F. Duan, W. Y. Zhou, W. S. Shi, N. Wong, C. S. Lee, N. B. Wong, S. T. Lee **2000**, *Adv. Mater.* 12, 1186–1190.
112 W. Q. Han, S. S. Fan, Q. Q. Li, W. J. Liang, B. L. Gu, D. P. Yu **1997**, *Chem. Phys. Lett.* 265, 374–378.
113 W. Q. Han, S. S. Fan, Q. Q. Li, Y. D. Hu **1997**, *Science* 277, 1287–1289.
114 Y. Zhang, K. Suenaga, C. Colliex, S. Lijima **1998**, *Science* 281, 973–975.
115 E. W. Wong, B. W. Maynor, L. D. Burns, C. M. Lieber **1996**, *Chem. Mater.* 8, 2041–2046.
116 Y. Zhang, T. Ichihashi, E. Landree, F. Nihey, S. Lijima **1999**, *Science* 285, 1719–1722.
117 Z. L. Wang, Z. R. Dai, R. P. Gao, Z. G. Bai, J. L. Gole **2000**, *Appl. Phys. Lett.* 77, 3349–3351.
118 A. M. Morales, C. M. Lieber **1998**, *Science* 279, 208–211.
119 Y. Cui, X. Duan, J. Hu, C. M. Lieber **2000**, *J. Phys. Chem. B* 104, 5213–5216.
120 M. S. Gudiksen, J. Wang, C. M. Lieber **2001**, *J. Phys. Chem. B* 105, 4062–4064.
121 M. S. Gudiksen, J. Wang, C. M. Lieber **2002**, *J. Phys. Chem. B* 106, 4036–4039.
122 X. Duan, Y. Huang, Y. Cui, J. Wang, C. M. Lieber **2001**, *Nature* 409, 66–69.
123 Y. Huang, X. Duan, Y. Cui, C. M. Lieber **2002**, *Nano Lett.* 2, 101–104.
124 X. Duan, C. M. Lieber **2000**, *J. Am. Chem. Soc.* 122, 188–189.
125 M. S. Gudiksen, C. M. Lieber **2000**, *J. Am. Chem. Soc.* 122, 8801–8802.
126 R.-G. Duan, A. K. Mukherjee **2005**, *Scr. Mater.* 53, 1071–1075.
127 H. Hahn **1993**, *Nanostruct. Mater.* 2, 251–265.
128 M. J. Mayo, D. C. Hague, D. J. Chen **1993**, *Mater. Sci. Eng. A* 166, 145.
129 A. Pechenik, G. J. Piermarini, S. C. Danforth **1992**, *J. Am. Ceram. Soc.* 75, 3283–3288.
130 A. Pechenik, G. J. Piermarini, S. C. Danforth **1993**, *Nanostruct. Mater.* 2, 479–486.
131 M. R. Gallas, B. Hockey, A. Pechenik, G. J. Piermarini **1994**, *J. Am. Ceram. Soc.* 77, 2107–2112.

Part Six
Applications

Bulk Nanostructured Materials. Edited by M. J. Zehetbauer and Y. T. Zhu

ISBN: 978-3-527-31524-6

26
Bulk Nanostructured Multiphase Ferrous and Nonferrous Alloys

Sergey Dobatkin and Xavier Sauvage

26.1
Introduction

The mechanisms of microstructural evolution during severe plastic deformation (SPD) and the specific features of these structures are already well described both for pure metals and for alloys [1–6]. Alloys processed by SPD are of special interest because of the variety of structural changes and phase transformations that may occur during deformation or post-processing annealing. Both the initial state (composition, microstructure) and the processing parameters affect the final microstructure and properties of SPD-processed alloys. For example, further grain refinement might be obtained thanks to phase transformations, or a higher thermal stability could be achieved thanks to second-phase particles. In this chapter, SPD processing of multiphase alloys is reviewed with a special emphasis on mechanical and functional properties. The first part deals exclusively with bulk nanostructured materials from ferrous alloys, e.g. mostly steels, while the second part deals with nonferrous multiphase materials, e.g. light alloys, intermetallics, copper alloys and composite materials.

26.2
Bulk Nanostructured Multiphase Ferrous Alloys

26.2.1
Introduction

Among all alloys, steels occupy a special position due to their diversity in chemical compositions, structures, and phase states. It was shown that, upon SPD, steels undergo carbide precipitation and dissolution, decomposition of supersaturated solid solutions, pearlite spheroidization, martensitic transformation, *etc.* Severe plastic deformation (SPD) in combination with possible pre- and post-SPD heat treatments allows for the desired control of the final steel structure.

In this chapter, the steels are classified based on their chemical composition and initial microstructure: low-carbon ferritic–pearlitic steels, low-carbon mar-

Bulk Nanostructured Materials. Edited by M. J. Zehetbauer and Y. T. Zhu

ISBN: 978-3-527-31524-6

tensitic steels, low-carbon ferritic–martensitic steels, high-carbon pearlitic steels, austenitic steels, and austenitic–ferritic steels.

It should be noted that such classification is rather arbitrary, especially because dramatic modifications of microstructures might occur during SPD. For example, the ferritic–pearlitic, pearlitic, and martensitic steels remain in such states only at the initial SPD stages. After significant degrees of deformation and upon subsequent heat treatment they exhibit ferrite–carbide structure with a uniform distribution of fine particles. The initially austenitic steels become austenitic–martensitic upon deformation and austenitic–ferritic upon subsequent heat treatment. In other words, the classification here corresponds to the initial phase state. The ferrite–martensite structure corresponds to the final state of the steel after heating and quenching of the ferritic–pearlitic steel.

26.2.2 Low-carbon Ferritic–Pearlitic Steels

26.2.2.1 Cold SPD Processing of Low-carbon Steels

In this section, cold SPD is referred to deformation at temperatures below 350 °C where the carbon diffusion rate and recovery mechanisms might be significant but recrystallization usually does not occur.

Low-carbon ferritic–pearlitic steels are generally used for building constructions, gas- and oil-pipeline, and machinery parts. A submicrocrystalline structure in bulk low-carbon steels can be produced by equal-channel angular pressing (ECAP) [7, 8]. Upon ECAP at room temperature, low-carbon steels can usually be subjected to three-four ECAP passes at the most efficient angle of channel intersection (90°) without failure. This deformation imparts only an accumulated strain of ~ 4 [7, 9], and for effective grain refinement, an accumulated strain over ~ 4–7 is generally needed [10]. The lower the deformation temperature, the higher the strain is required for the formation of high-angle boundaries, i.e. new grains [11]. Simultaneous deformation of ferrite and pearlite (usually < 20 vol.%) in low-carbon steels by ECAP leads to elongation of both phases. At large strain the new submicrometer grains of ferrite are formed [12–14].

Structure Formation in Ferrites

Structure formation inside initial ferritic grains depends on ECAP route. In [15–17] structural evolution in BCC commercial low carbon (0.15%C–0.52%Mn) ferritic–pearlitic (15 vol.%) steel during ECAP at room temperature was investigated for routes C and B_C. It is found that an equiaxed grain structure with the grain size of ferrite at ~ 0.2 μm and high-angle grain boundaries dominate the microstructure after 4 ECAP passes via route B_C at an channel intersection angle 90° [16] (Fig. 26.1), while nearly parallel bands of elongated substructures dominate after up to 11 ECAP passes via route C [15, 16]. An essentially equiaxed microstructure with high-angle grain boundaries and an average grain

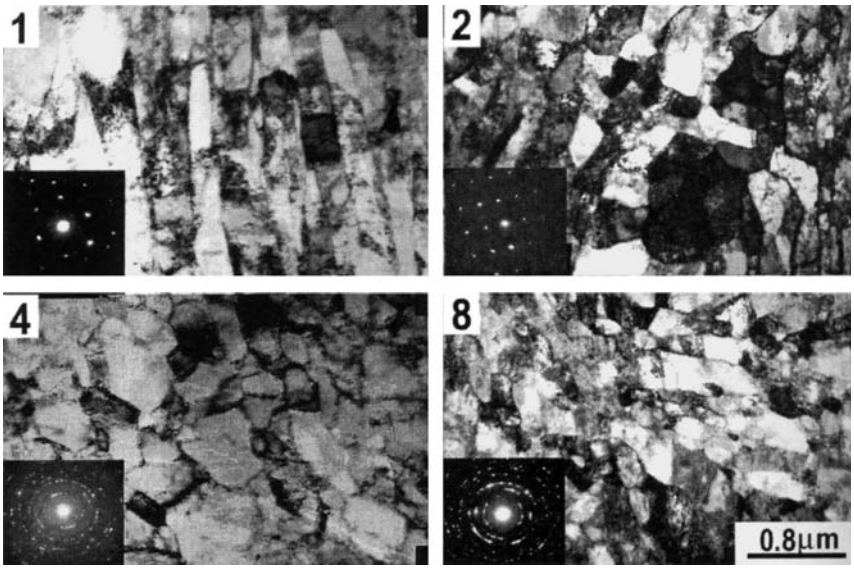

Fig. 26.1 Typical TEM microstructures of the low-carbon Fe–0.15%C–0.52%Mn steel after different ECAP passes via route B_C (number on each photo indicating ECAP passes). (Courtesy of J.T. Wang et al. [16]).

size of ~0.2 μm was achieved after 3 passes of ECAP of a 0.08%C–0.18%Si–0.42%Mn steel at room temperature using route B_C [18]. These results confirm that route B_C, in which the sample rotates 90° around its axis after each pass, is more efficient for the formation of an equiaxed-grained structure in bcc low-carbon steels at room temperature than route C, in which the sample rotates 180°.

Carbide Transformations

During ECAP, the morphology of cementite lamellae is significantly changed: they become wavy and fragmented [12, 19, 20]. The spheroidization of cementite in ECAPed low-carbon steel accelerated with annealing temperature and time [20, 21]. For example, after ECAP of 0.15%C–0.25%Si–1.1%Mn steel the spheroidization occurred during annealing at 480 °C for 72 h and at 510 °C for 1 h (Fig. 26.2) [20]. The spheroidized cementite (0.06 μm in diameter) is significantly smaller than that obtained through conventional spheroidization treatment (0.1–1 μm). Increasing accumulated ECAP strain leads to a decrease in spheroidization temperature and time. It is interesting to note that spheroidization is observed during the ECAP processing of 0.15%C–0.25%Si–1.1%Mn steel at 450 °C up to 12 passes [20]. Shin and coworkers [20, 22] observed that cementite spheroidization occurred in former pearlite colonies but also inside ferrite grains at the boundaries of submicrometer grains when the annealing temperature was increased to ≤700 °C. Surprisingly, the ferrite grain size remains close

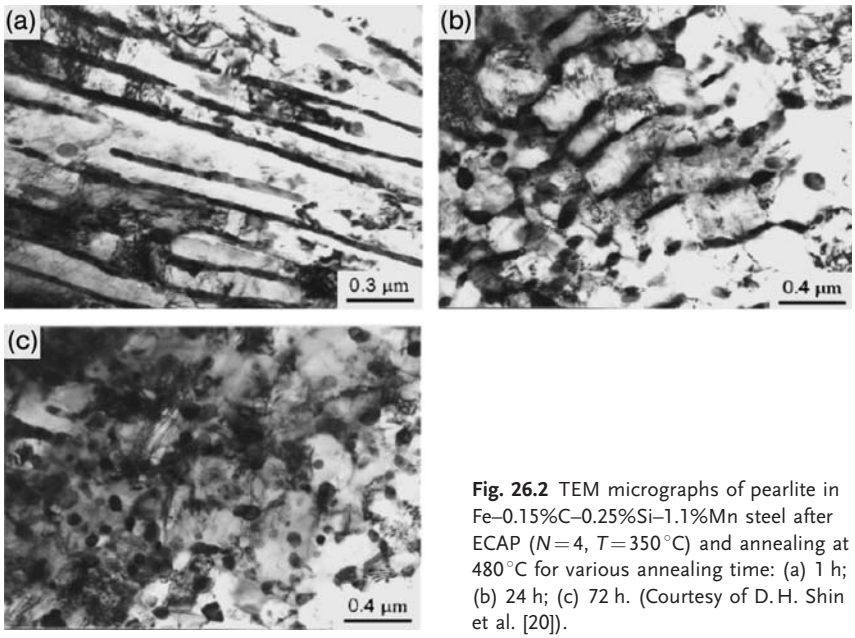

Fig. 26.2 TEM micrographs of pearlite in Fe–0.15%C–0.25%Si–1.1%Mn steel after ECAP ($N=4$, $T=350\,^{\circ}C$) and annealing at 480 °C for various annealing time: (a) 1 h; (b) 24 h; (c) 72 h. (Courtesy of D. H. Shin et al. [20]).

to only 0.3 μm, which is attributed to a pinning effect of grain boundary by cementite particles.

For practical applications, it is essential to ensure thermal stability of UFG structures. Shin and coworkers [23] successfully improved the thermal stability of low-carbon steels processed by ECAP thanks to the increase of ECAP strain (a) and microalloying (b). The first concept (a) is related to carbon atoms resulting from cementite decomposition that would slow down recovery, recrystallization and grain growth. The dissolution of carbides during large-strain deformation is indeed widely reported in the literature [24–31]. Shin and coworkers [23] also observed that the larger the strain, the higher the decomposition rate. The second concept (b) relies on dilute addition of carbide- and/or nitride-forming elements to increase the recrystallization temperature and to impede grain growth.

The mechanical properties of low-carbon steels depend on strain during ECAP at room temperature. Increase in the number of ECAP passes has a very substantial effect in increasing the strength and the increase of the yield stress can really be significant, up to 1200 MPa [13, 15, 18, 19]. Figure 26.3 (a) shows the evolution of yield stress with the number of ECAP passes, together with the evolution of the elongation to failure [15]. After an initial decrease in elongation, there is a subsequent increase when ECAP is continued to more than 4 passes. Ultrafine-grained materials fabricated by ECAP exhibit a very low strain hardening. Strain hardening is very important for structural applications. Shin and coworkers [32] suggested using second-phase particles to improve this property.

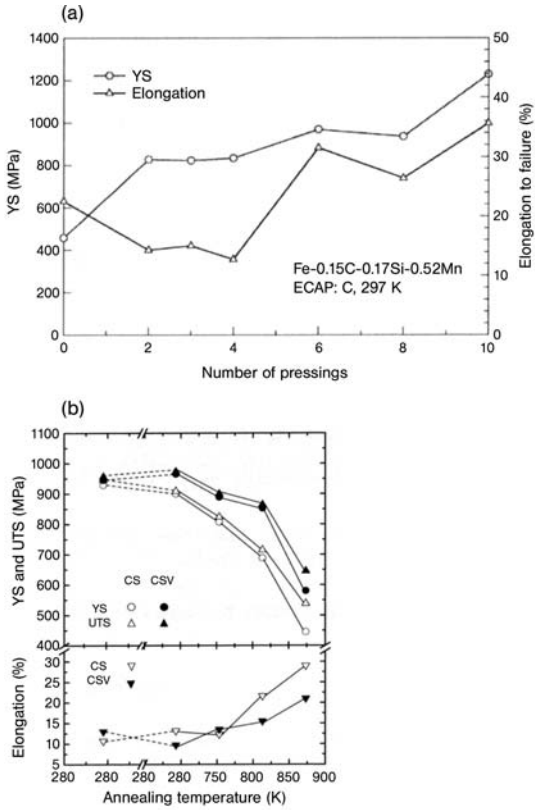

Fig. 26.3 Dependence of mechanical properties of low-carbon steels on number of ECAP passes [15] and annealing temperature after ECAP (b) [33]: (a) Fe–0.15%C–0.17%Si–0.52%Mn steel; ECAP at 25 °C; (b) (CS) – Fe–0.15%C–0.25%Si–1.1%Mn steel (CSV) – Fe–0.15%C–0.25%Si–1.1%Mn–0.06%V–0.008%N steel, ECAP at 350 °C, $N = 4$. (Courtesy of J. Wang et al. [15] and D.H. Shin and coworkers [33]).

Fukuda and coworkers [18] demonstrated that ECAP processing route B_C gives a large region of strain hardening, whereas there is essentially no strain hardening in the samples processed by routes A [33] and C [19]. The reason for this difference is probably the greater degree of homogeneity, and the more equiaxed nature of the microstructure.

The variation of the room-temperature tensile properties of low-carbon 0.15%C–0.25%Si–1.1%Mn (in wt.%) (hereafter, CS steel) and low carbon with V addition 0.15%C–0.25%Si–1.1%Mn–0.06%V–0.008%N (in wt.%) (hereafter, CSV steel) steels after 4 passes at 350 °C with annealing temperature is plotted in Fig. 26.3 (b) [23]. The extension of the mechanical stability in the CSV steel to higher temperatures in comparison with CS steel resulted mainly from the preservation of a UFG ferrite grains associated with homogeneously distributed nanosized cementite particles.

26.2.2.2 Warm SPD of Low-carbon Steels

In the previous section, only cold deformation (20–350 °C) was considered, but some low-carbon steels (for example low-alloyed steels), can be processed by ECAP only at higher temperatures. That is why in this section, warm SPD is considered, e.g. deformation in the temperature range of 400 to 600 °C. One should note also that warm SPD has some significant advantages comparing to cold SPD: the deformation load is much lower and post-SPD annealing treatments could be suppressed.

Shin and coworkers [34] investigated two grades of low-carbon steels, one containing vanadium (0.15%C–0.25%Si–1.1%Mn–0.06%V–0.008%N) and the other without vanadium (0.15%C–0.25%Si–1.1%Mn), after ECAP processing in the temperature range of 350–600 °C. At higher pressing temperatures, coarser grains with low-angle boundaries were formed, which indicates significant recovery occurs during SPD. Addition of vanadium preserved the high dislocation density up to a pressing temperature of 600 °C. In the steel pressed at 600 °C, pearlite colonies completely dissolved and a reprecipitation of nanosized cementite particles distributed uniformly was observed, while the grain size in the ferritic matrix was less than 1 μm. The yield stress of the steel without V pressed at 350 °C was up to 937 MPa, significantly higher than that of the as-received material (310 MPa). When the pressing temperature was increased, the yield stress significantly decreased, down to 600 MPa at 480 °C and down to 480 MPa at 600 °C. Concerning the steel with vanadium, the yield stress of the sample pressed at 350°C was similar to that of the plain low-carbon steel. However, the drastic drop in the yield stress was not observed with increasing the pressing temperature – 800 MPa at 480 °C with an elongation to failure of 16% and 640 MPa at 600 °C.

Three low-carbon 0.17%C–0.21%C–0.89%Mn–0.78%Si–0.16%V and 0.23%C–1.24%Mn–0.75%Si steels were studied after warm ECA pressing at 500–550 °C [35–38]. A TEM study revealed both ferrite subgrains, which were formed within ferrite grains and are separated by low-angle boundaries, and a submicrocrystalline structure characterized by high-angle grain boundaries [35, 37, 38]. Subgrain and grain structures featured structural elements 0.3–0.5 μm in size. The steels differ in the fractions of low- and high-angle grain misorientations. The partially submicrocrystalline structure led to substantial hardening of the steels: YS = 840, 1000 and 1110 MPa for 0.17%C–0.23%C–1.24%Mn–0.75%Si and 0.21%C–0.89%Mn–0.78%Si–0.16%V steels, respectively [35–38]. In all cases, the elongation to failure was about ~10%. Unfortunately, the steels with the partially submicrocrystalline structure had low impact toughness. It was shown that impact toughness could be improved by subsequent heating or using the hot ECAP at 750 °C [37, 38].

Up to now we have considered the structure and properties of low-carbon steels after ECAP – one of the advanced schemes of SPD. Note that there are also reports of formation of submicrocrystalline (grain size less than 1 μm) structure by conventional large-strain deformation processes.

26.2.2.3 Formation of Submicrocrystalline Structure by Conventional Processes

Ultrafine-grained steel bars were produced through a multipass warm caliber rolling to large cumulated strains of 2 or 3 for a SM490 (wt% 0.15%C–0.30%Si–1.50%Mn–0.01%P–0.002%S) steel [39]. Average ferrite grain sizes of 0.43 μm, 0.70 μm and 1.2 μm were obtained in the isothermal warm caliber rolling processes at 500 °C, 550 °C and 600 °C, respectively. Mechanical testing revealed a dramatic improvement in yield strength and a reduction in the ductile–brittle transition temperature by refinement of ferrite structure. In [40], ultrafine ferrite (sub)grains (0.60–0.85 μm) and uniformly distributed cementite particles (20–350 nm) were produced in two steels with 0.2% carbon and different Mn contents (0.7% and 1.5%) by using heavy warm deformation by multistep plain-strain compression at 550 °C ($\varepsilon = 1.6$). This processing can be readily applied in the industry. The ultimate tensile strength increased from 590 MPa to 680 MPa with increasing Mn content, while the total elongation of 18% was the same for both materials [40]. Low-carbon microalloyed steels (C < 0.1%, 0.5% < Mn < 1.5%, Si < 0.4%, 0.024–0.067%V) were intensively warm rolled in the ferritic region (400–700 °C) after austenitic hot rolling on a laboratory rolling mill ($\varepsilon = 1.9$) [41]. This study shows that warm deformation in the ferritic region is indeed able to induce fragmentation of grains. The EBSD analyses suggest that warm rolling induces continuous dynamic recrystallization, albeit heterogeneous. In [42], low-carbon low-alloy (0.07%C–0.22%Si–1.48%Mn–0.2%Ni–0.23%Cu–0.04%Nb–0.02%Ti) submicrocrystalline steel sheet was developed successfully by severe warm rolling at 500 °C through a single pass (reduction: 80%). Such steel revealed grain sizes of 300–600 nm and a large amount of nanoprecipitates (10–30 nm) that leads to enhanced thermal stability. Submicrocrystalline structure gives rise to a yield stress of 915 MPa and an elongation to failure of 18%.

26.2.3 Low-carbon Martensitic and Ferritic–Martensitic Steels

26.2.3.1 Low-carbon Martensitic Steels

Low-carbon 0.1%C–1.12%Mn–0.08%V–0.07%Ti steel was deformed by high-pressure torsion (HPT) at $T = 20$–500 °C to the strain $\varepsilon = 6.3$. The steel used had two initial states: martensitic (as-quenched) and ferritic–pearlitic (as hot forged) [43]. TEM examination of martensitic steel after HPT at 20 °C revealed a cellular-like oriented fragmented structure with isolated equiaxed grains of $\sim$65 nm in size. With increasing deformation temperature up to 500 °C, the fraction of nanograins and the average grain size increased to up to 85 nm. After HPT, the 0.1%C–1.12%Mn–0.08%V–0.07%Ti steel with initial ferritic–pearlitic microstructure had average grain sizes of 95 and 120 nm at $T = 20$ and 500 °C, respectively, which are larger than those observed in the quenched and deformed state. TEM study of a 0.1%C–1.12%Mn–0.08%V–0.07%Ti steel subjected to torsion and heated to 500 °C showed that the quenched initial state led to smaller grain

sizes than the hot-forged state. The average grain size of the 0.1%C–1.12%Mn–0.08%V–0.07%Ti steel with initial martensitic state after HPT and heating to 500 °C is 450 nm, which is smaller by a factor of two than that with the initial ferritic–pearlitic state – 860 nm. This observation can be explained by smaller grain size after HPT in the steel with initial quenched state, a higher total dislocation density resulting in a larger area of interfaces, probably, by a higher carbon content in the solid solution, and the presence of fine carbides suppressing the grain growth upon heating.

As reported in [44], the carbide phase in the 0.2%C–Mn–B low-carbon steel is completely dissolved upon SPD only in the initially quenched steel, while in the steel deformed after quenching and high-temperature tempering the carbide phase is not dissolved. ECAP was used to process low-carbon 0.1%C–1.6%Mn–0.1%V–0.08% Ti steel samples with two initial states: the ferritic–pearlitic and the martensitic (bainitic) state [45]. The cold ECAP at 20–400 °C resulted predominantly in a cellular and subgrain structure with separated grains of 150–350 nm. The sample with initial martensitic structure exhibited finer microstructure after ECAP than the sample with initial ferritic–pearlitic structure, possibly due to the initially higher dislocation density in the former. In addition, the former was also found to have much higher thermal stability after ECAP. This is attributed to (1) the higher homogeneity of the initial martensite (bainite) structure, (2) the higher initial dislocation density, and (3) the precipitation of fine uniformly distributed carbides upon heating. The ECAP-processed 0.1%C–1.6%Mn–0.1%V–0.08%Ti steel had high strength (ultimate tensile stress >1000 MPa) and ductility (elongation >20%). Specifically, the yield stress increased by about 100% from 510 to 1000 MPa for the initial ferritic–pearlitic steel and from 600 to 1110 MPa for the initial martensitic steel [45]. Note also that the strength of the steel with initial martensitic structure is higher upon heating to 700 °C, and its yield stress remains above 1015 MPa even after heating at 600 °C, along with a significant ductility of 28%.

26.2.3.2 Low-carbon Ferritic–Martensitic Steels

Ultrafine-grained (UFG) ferritic–martensitic dual-phase 0.15%C–0.25%Si–1.06%Mn (hereafter, DP0), 0.15%C–0.25%Si–1.11%Mn–0.06%V (hereafter, DP1) and 0.15%C–0.24%Si–1.12%Mn–0.12%V (hereafter, DP2) steels were fabricated by equal-channel angular pressing (ECAP) with an effective strain of ~4 at 500 °C and subsequent annealing of 730 °C for 10 min in the a–γ region [46, 47]. Under these processing conditions, the microstructure of dual-phase steels consisted of UFG ferrite with uniformly distributed blocky martensite islands of ~1 μm. Their room-temperature tensile properties were examined and compared to those of a coarse-grained (CG) counterpart (Table 26.1) [46, 47]. The strength of UFG dual-phase steels was much higher than that of their coarse-grained counterparts, but uniform and total elongations were not degraded. The present UFG dual-phase steels exhibited extensive rapid strain hardening unlike

Table 26.1 The microstructural and tensile characteristics of the dual-phase steels [48]. V_m, martensite volume fraction; d_m, martensite island size; d_f, ferrite grain size; σ_{YS}, yield strength; σ_{TS}, ultimate tensile strength; ε_u, true uniform strain; ε_f, engineering total elongation.

Designation	V_m (%)	d_m (μm)	d_f (μm)	σ_{YS} (MPa)	σ_{TS} (MPa)	ε_u (%)	ε_f (%)
CG-DP0	22	9.8	19.4	510	843	9.8	13.5
UFG-DP0	28	0.8	0.8	581	978	9.3	17.6
UFG-DP1	35	1.1	0.9	540	1044	11.5	18.1
UFG-DP2	32	1.1	1.2	565	1015	10.4	16.6

most UFG materials. The addition of vanadium slightly increased the strength and elongation (Table 26.1) [46, 47].

26.2.4 High-carbon Pearlitic Steels

In this section, the structural evolution during SPD by ECAP and HPT in high-carbon steels containing 0.6–0.8%C is reviewed. Steels were used in the normalized state with fully lamellar structure before SPD. These steels are generally used as tool steels, rails, cables or springs.

A high-carbon steel (0.65%C–0.90%Mn) with a fully pearlitic structure was successfully processed by ECAP at 650 °C via route C for up to 5 passes [48]. The lamellar structure transformed into a homogeneous ultrafine-grained ferrite matrix (average grain size of ~0.3 μm) with dispersed spheroidized cementite particles (average diameter of ~0.2 μm) (Fig. 26.4(f)). The pearlitic structure reacted through mild to sharp shear regular banding, irregular bending and distortion, and even planar shear breaking of cementite plates, to accommodate the strong shear strain of ECAP in the first pass (Figs. 26.4(a)–(e)). Wetscher and coworkers [49] also observed a decrease in lamellae spacing, a heavy fragmentation of the lamellae and increasing misorientation both in the cementite lamellae and the ferrite in the pearlitic rail steel UIC 900A during HPT at room temperature. The nanocrystalline structure of a eutectoid steel UIC 860 (0.6–0.8%C, 0.8–1.3%Mn, 0.1–0.5%Si, 0.04%P(max), 0.04%S(max)) after SPD by HPT was studied using TEM, HRTEM, energy-filtered TEM (EFTEM) and 3D atom probe (3DAP) analyses [29, 50–53]. According to [54, 55], the formation of nanostructure during SPD consists of three stages. The first stage corresponds to the formation of cell structure. Further increase of strain leads to an increase in dislocations in cell walls and rearrangements and annihilation of dislocations in cell boundaries, which results in high-angle grain boundary formation in the third stage. Ivanisenko and coworkers [29] showed that structure formation and decomposition of cementite in high-carbon steel UIC 860V during HPT also proceeds in three stages. In the shear-strain range of $\gamma < 100$ ($n = 1$–1.5 turns) dissolution of ~50% of cementite phase occurred. This was accompanied by

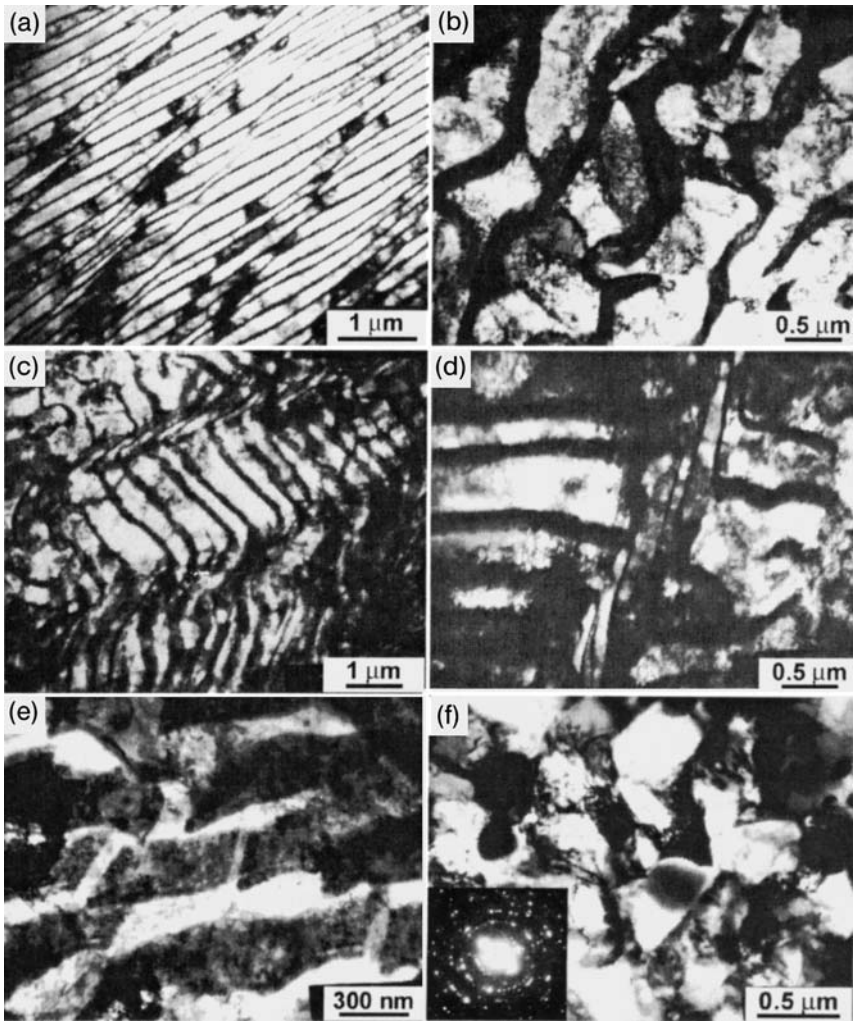

Fig. 26.4 Typical deformation accommodations in Fe–0.65%C–0.9%Mn commercial steel during ECAP at 650 °C (a) evenly interspaced regular necking, (b) irregular bending and twisting, (c) regular bending forming shear bands, (d) concentrated sharp shear band, (e) planar shear breaking of the cementite in pearlite lamellae of during ECAP, (f) typical microstructure after 5 passes of ECAP. (Courtesy of J.T. Wang et al. [48]).

the formation of a cellular structure in the ferrite phase, alignment of cementite colonies in the shear direction and thinning and elongation of cementite platelets. Even at first stage of deformation (1 turn by HPT), cementite lamellae were uniformly nanocrystalline with crystals in the size range of 5–20 nm [53].

During the second stage, corresponding to $100 < \gamma < 200$ ($n = 1.5$–3 turns), the rate of cementite dissolution decreases [29]. In this strain range a nanostructure

forms in cementite colonies oriented parallel to the shear plane with a fibrous appearance that can be observed by scanning electron microscopy (SEM). The rate of cementite dissolution increases again in the third stage, in the strain range $200 < \gamma < 300$ ($n = 3$–5), where the material has a nanocrystalline structure with a grain size of ~ 10 nm. The question of the distribution of the carbon in the structure of severely deformed steel has been widely discussed in the literature. It was proposed that carbon atoms concentrate in microcracks, or form graphite clusters [24], or that they segregate at grain boundaries and dislocation cores [25, 56], the concept of nanomartensite formation was even suggested [57]. It was shown [29, 58] that the flow of carbon in the ferrite phase (i.e. mechanism of dissolution) can be considered as a mechanically driven mass-transport process. It was suggested also [31] that the dissolution of cementite by heavy deformation at high strain rates might be attributed to a thermal effect. For the first time, a stress-induced a–γ transformation in nanocrystalline ferrite as a consequence of HPT at room temperature of an initially pearlitic eutectoid steel UIC 860 has been experimentally demonstrated [53, 59]. Nanocrystalline grains of austenite 10–20 nm in diameter are formed, having a Kurdjumov–Sachs orientation relationship with the neighboring ferrite. This was concluded to have occurred due to a stress-induced reverse martensitic transformation, and this additionally confirms earlier predictions of such transformations by molecular dynamics simulations. The stress-induced phase transformation represents a new deformation mode that can be activated when alternative deformation mechanisms, such as slip of lattice dislocations, are blocked by the nanostructure.

Ultrahigh-carbon steel wire can achieve very high strength after SPD, because of the fine substructure produced [26–28, 57, 60, 61]. Typically, these steels are eutectoid and hypereutectoid steels and drawing strains up to 4 are used during processing. SPD during wire drawing leads to an alignment of cementite plates and the development of a substructure that resists dynamic recovery [61]. In this way, nanoscaled substructures (e.g. interlamellar spacing < 10 nm) are commonly achieved thanks to industrial processes. Very high strengths are possible in hypereutectoid steel wire. At 1.8%C, hypereutectoid steel wires are projected to have a strength approaching 6000 MPa.

26.2.5
Austenitic and Austenitic–Ferritic Stainless Steels

Austenitic and austenitic–ferritic steels are widely used in chemical industry and power engineering as corrosion-resistant materials and in medicine for tools and implants.

26.2.5.1 Austenitic Stainless Steels

Room-temperature deformation of 0.08%C–18.3%Cr–9.8%Ni–0.6%Ti austenitic steel by HPT ($P = 6$ GPa) with $e = 5.8$ (5 revolutions) leads to the formation of a nanocrystalline structure with a grain size of 50 nm [62, 63] (Fig. 26.5).

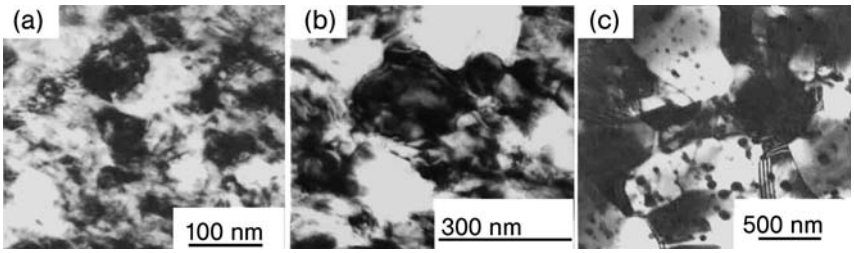

Fig. 26.5 Structure of austenitic Cr–Ni–Ti steel after severe plastic deformation (SPD) by HPT [64]: (a) $\varepsilon = 6.3$ (5 turns), (b) $\varepsilon = 6.3$; heating 500 °C (1 h), (c) $\varepsilon = 6.3$ heating 700 °C (1 h).

SPD induces a martensitic transformation in austenitic steels [62–65]. For example, the martensite content in the 0.08%C–18.3%Cr–9.8%Ni–0.6%Ti steel is 50% after one revolution and up to about 60% after five revolutions [62]. Not only $\gamma \rightarrow \alpha$, but also $\gamma \rightarrow \varepsilon \rightarrow \alpha$ transformation was reported [62, 64]. Efros and coworkers [66] also showed that HPT can result in a considerable destabilization of stable austenitic steels ($Fe_{85.8}Mn_{13}C_{1.2}$, $Fe_{79.55}Mn_{17}Al_3C_{0.45}$ and $Fe_{61.2}Cr_{18}Mn_{20}N_{0.7}C_{0.1}$). In [67], the complete $\gamma \rightarrow \alpha$ transformation during cold rolling (true strain 2.3) and partial $\alpha \rightarrow \varepsilon$ transformation during subsequent HPT at room temperature are reported. In any case, HPT led to the formation of a two-phase austenitic–martensitic structure, which should increase the thermal stability of the material. Upon heating of the nanocrystalline 0.08%C–18.3%Cr–9.8%Ni–0.6%Ti steel after HPT, the initial grain size of 50 nm remained virtually unchanged up to 400 °C. The grain size slightly increased at 500 °C (250 nm) and started to grow intensively at temperatures above 600 °C (Figs. 26.5 (b) and (c)) [63]. One should note that in [68], the grain growth in austenitic 0.05%C–15%Cr–25.3%Ni–0.3%V steel (size of structural elements 80 nm) after HPT started only at 700 °C. The martensite (ferrite) fraction begins to decrease upon heating above 400 °C. After heating to 550 °C, the phase composition corresponds to a ratio 50%:50%. This still suppressed an intense grain growth, which begun at 600 °C, when the austenite content is ~80%.

Even the imperfect and oriented submicrocrystalline structure of 0.07%C–17.3%Cr–9.2%Ni–0.7%Ti steel after ECAP provides a good combination of mechanical properties: yield stress = 1315 MPa and elongation to failure = 11% [63]. The high level of deformation and the high pressure used in [64] give rise to a more homogenous structure with a grain size of ~100 nm and, therefore a higher ductility (elongation of 27.5%) along with a somewhat higher yield stress (1340 MPa). Strain-induced fine-grain evolution taking place in a 304-type austenitic stainless steel (0.058%C–0.7%Si–0.95%Mn–0.029%P–0.008%S–8.35%Ni–18.09%Cr–0.15%Cu–0.13%Mo) under severe warm deformation was studied in multipass compression at 600 °C [69]. The microstructural changes are characterized by evolution of subgrains. These subgrains became more equiaxed and the misorientations between them gradually increased with increasing cumula-

tive strain, finally leading to the fine grains with an average size of about 0.3 μm.

The deformation behavior of a 304-type stainless steel with a grain size of 0.3 μm was studied in uniaxial compression at temperatures of 600–800 °C and under strain rates of 10^{-4} to 10^{-2} s^{-1} [70]. At high temperatures, the resulting fine-grained steel has a low dislocation density and steady-state flow stresses lower than those of an annealed coarse-grained steel. Moreover, the strain-rate sensitivity of the fine-grained material reaches high values, up to 0.3, which clearly differs from that of 0.1–0.2 for the coarse-grained steel. At room temperature, the initially fine-grained steel has higher hardness after warm deformation than the conventional steel.

The initial grain-size effect on submicrocrystalline structure evolution was studied in multiple compressions of a 304 stainless steel at 600 °C (0.5 T_m) [71]. The final microstructure with a grain size of about 0.25 μm that developed at large strains does not depend on the initial one. A decrease in the initial grain size can accelerate the kinetics of grain refinement significantly under a large-strain deformation. For instance, the fraction of the strain-induced high-angle boundaries in samples with initial grain sizes of $D_0 = 3.5$ μm increases rapidly to above 60% with multiple working to a cumulative strain of 1.5. On the other hand, the same fraction of high-angle boundaries of 60% in the samples with $D_0 = 15$ μm needs much more straining of about ~ 6.

The effect of a large amount of dispersed particles on the grain-size evolution in an austenitic stainless steel (0.07%C–18%Cr–10%Ni–0.56%Nb) processed by multidirectional forging (MDF) was investigated in [72, 73]. Austenitic stainless steels with about one volume per cent of second-phase particles (diameter in the range of 8 to 140 nm), were MDFed at 400 °C and 600 °C to strains up to $\varepsilon = 6$. During the MDF process, the particles become incoherent. However, comparing to the plain Fe–Ni austenitic steel, the grain-size reduction seems to saturate due to the presence of the particles.

ECAP processing (one pass) of AISI 316L (0.019%C–16.9%Cr–10.3%Ni–2.14%Mo–0.08%N) austenitic stainless steel was successfully carried out in the temperature range of 450–800 °C [74]. ECAP leads to deformation twinning as an effective deformation mechanism in AISI 316L at relatively high temperatures (0.4–0.65 T_m). Higher tensile and compressive strengths are obtained after ECAP compared to as-received values in relation to the microstructural refinement and deformation twinning. The highest yield stress of 1010 MPa with an elongation of 30% is observed after ECAP at 700 °C. It is shown [75] that twinning plays a critical role in the initiation of nanostructures within adiabatic shear bands formed in SS 316L (0.019%C–16.82%Cr–1.72%Mn–2.07%Mo–10.04%Ni–0.028%P–0.01%S–0.4%Si) stainless-steel samples deformed by high-strain-rate forced shear. Secondary twins directly led to the formation of elongated subgrains. Microtwins inside shear bands promoted division and breakdown of the subgrains, which further refined the microstructures.

26.2.5.2 **Austenitic–Ferritic Stainless Steels**

Deformation structures were studied in a two-phase austenitic (40%)–ferritic (60%) 27%Cr–9%Ni stainless steel. Severe plastic working was carried out by rolling followed by swaging at room temperature, providing a total strain of 6.9 [76, 77]. The severe deformation resulted in highly elongated (sub)grains with the final transverse (sub)grain size of about 0.1 μm. However, the kinetics of microstructure evolution in the two phases was different. The transverse (sub)-grain size decreased gradually during processing in the ferrite phase and rapidly in the austenite phase. Such a structural response in the austenite was associated with deformation twinning and microshearing. The number fraction of high-angle boundaries increased to a saturation of about 50–70%. After a rapid increase in the hardness at an early deformation, the rate of the strain hardening gradually decreased to almost zero at large strains above 4. In other words, the hardness approached a saturation level, leading to an apparent steady-state deformation behavior during cold working [77].

26.2.6
Summary

Severe plastic deformation (SPD) of steels results in grain refinement down to the nanoscale. Structure is characterized by a low density of internal dislocation and the nonequilibrium state of grain boundaries. Bulk nano- and submicrocrystalline steels in the equilibrium state could be obtained by SPD and subsequent low-temperature heating or by warm large-strain deformation. Such structure leads to high strength and sufficient ductility. In spite of the high mechanical properties of bulk nanostructured materials, the whole set of mechanical and service properties of these materials is poorly understood, which makes their possible application difficult [78]. Moreover, it is difficult to widely apply severe plastic deformation in industry. Nevertheless, it is important to study the structural states of commercial steels and a combination of their mechanical and service properties.

26.3
Bulk Nanostructured Multiphase Nonferrous Alloys

26.3.1
Introduction

Many different kinds of multiphase nonferrous alloys have been processed by SPD to achieve BNM. Through grain-size reduction, it is possible to get an excellent combination of high strength and a good level of ductility, or to obtain some superplastic ductility in Al- and Mg-based alloys or to improve the room-temperature ductility like in magnesium alloys. Due to the tremendous number

of multiphase nonferrous alloys that have been processed by SPD a standard classification based on their composition (e.g. Al alloys, Mg alloys, Cu alloys,...) cannot give a clear overview of SPD-induced features. Therefore, in this section, the following classification was chosen: cast and wrought alloys, age-hardenable alloys, eutectic and eutectoid alloys, intermetallics and composite materials.

26.3.2 Cast and Wrought Alloys

There are several motivations for processing cast and wrought alloys by SPD. The first one is to reduce the grain size to improve the mechanical strength and eventually to obtain some superplastic ductility. But the main motivation is to homogenize the structure. Thanks to SPD, it is possible to get smaller second-phase particles with a homogeneous distribution or to modify significantly the crystallographic texture.

26.3.2.1 Cast and Wrought Magnesium Alloys

Mg alloys are very attractive because of their low density and they have recently becoming more popular for structural applications in the automotive or aerospace industry. However, these alloys usually exhibit a low cold workability that is a strong limitation for further applications. This low-level ductility is inherent to the HCP structure of the α-Mg phase [79] but is also due to the strong crystallographic texture of wrought magnesium alloys [80]. Addition of Li as an alloying element [81], reduction of the grain size [73, 82] or modification of the crystallographic texture [80] of magnesium alloys could significantly improve their ductility. And it has been shown in various wrought magnesium alloys that SPD processing and particularly ECAP can be successfully applied [80, 83–91]. However, magnesium alloys cannot be processed by ECAP at low temperatures because of cracking. Therefore, they are usually processed in the temperature range of 127 °C to 327 °C but smaller grain sizes are achieved at lower temperatures [80, 83].

Cast magnesium alloys from the Mg–Al system are the most widely used and therefore investigated. For aluminum contents in the range of 2 to 10 wt.%, these alloys contain two phases: α-Mg (HCP) and β-$Mg_{17}Al_{12}$ [79]. The discontinuous precipitation of this latter phase without the formation of intermediate metastable phases gives rise to a low age-hardening response of these alloys and moderate tensile properties. In this system, several commercial alloys processed by ECAP have been investigated: AZ31 [80, 84–87], AZ61 [87, 88], AZ70 [89] and AZ91 [91–94] (a small amount of zinc is usually added to improve the tensile properties [79]). For all these alloys, it has been demonstrated that the grain size could be significantly reduced through ECAP processing (Fig. 26.6). This usually leads to a strong improvement of ductility [80, 89, 91]. However, even if magnesium alloys follow the Hall–Petch rule, Yoshida and coauthors have shown that the crystallographic texture is the main factor controlling the

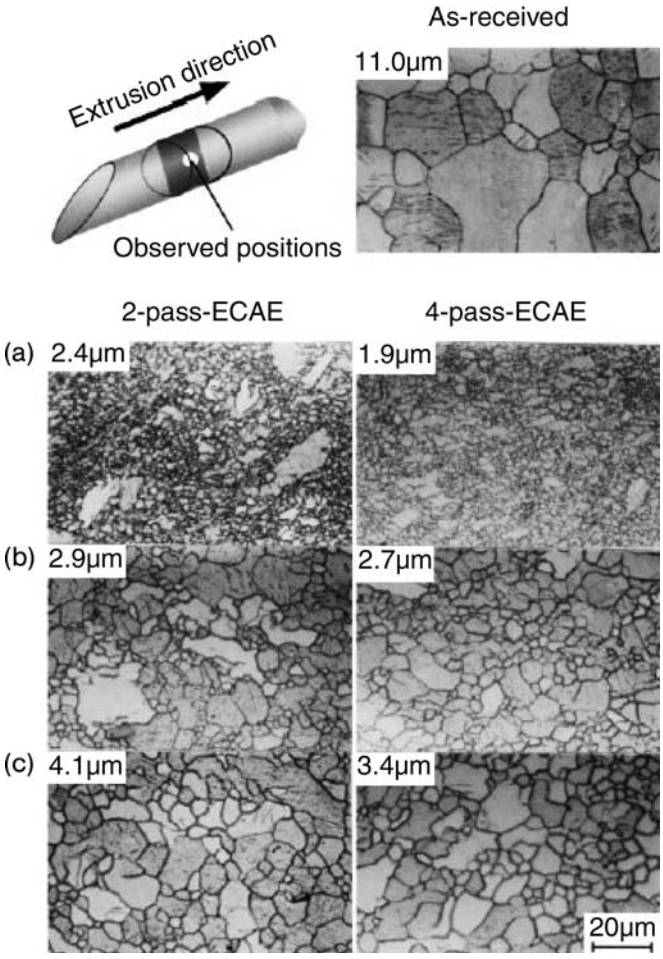

Fig. 26.6 Microstructure of AZ31 Mg alloy as-received and after ECAE processing at 200 °C (a), 250 °C (b) and 300 °C (c). (Courtesy of Y. Yoshida et al. [80]).

tensile properties [80]. The ECAP process dramatically changed the extrusion texture, and as shown by Mukai and coauthors, post-annealing treatment could give rise to an excellent combination of strain hardening and ductility at room temperature [84].

The combination of extrusion and ECAP (designated EX-ECAP) was first introduced by Matsubara and coauthors with a model Mg–9%Al alloy [83]. These authors have shown that at a low ECAP temperature (200 °C), β-$Mg_{17}Al_{12}$ second-phase particles are strongly fragmented, preventing grain growth and leading to a final β-Mg grain size of only 0.7 μm. The role of the β-$Mg_{17}Al_{12}$ phase has also been discussed by Mussi and coauthors for an AZ91 commercial alloy

[94]. Such material exhibits very attractive low-temperature superplasticity (800% elongation at 150 °C at 10^{-4} s^{-1}) and high-strain-rate superplasticity (360% elongation at 225 °C at 10^{-2} s^{-1}).

In a commercial alloy containing a similar amount of aluminum (AZ91) and processed by a combination of extrusion and ECAP, Mabuchi and coauthors obtained a similar grain size (0.5 μm) but much lower superplastic elongations (approx. 150% at 150 °C at 10^{-4} s^{-1}) [92]. This feature may indicate that a small amount of Zn (less than 1%) could dramatically affect the superplastic properties of magnesium alloys processed by ECAP. However, Mussi and coauthor seem to overcome this problem with an original method consisting of progressively decreasing the ECAP temperature, starting at 265 °C down to 150 °C for the 8th pass [94]. In this way, the final grain size is only 0.3 μm, which gives rise to an increase of the yield stress and improved superplastic properties.

Addition of Li to magnesium alloys is known to improve the ductility but to lower the yield stress [81]. Liu and coauthors have applied ECAP processing to an extruded LA81 commercial alloy (Mg–8%Li–1%Al) [95]. This alloy has a two-phase structure with α-Mg (HCP) and β (BCC) phase grains. They have demonstrated that ECAP processing (4 passes) leads to a strong refinement of the grain size of both phases: 0.5 μm for the α phase and 0.2 μm for the β phase, but the phase dispersion is not affected by the severe plastic deformation. This grain-size reduction leads to an important increase of the yield stress along with a good level of ductility if the material is subjected to at least three ECAP passes at 130 °C.

Watanabe and coauthors have investigated the properties of a commercial magnesium alloy from the Mg–Zn system (ZK60) [96]. Superplastic properties were also achieved, but the main difference with alloys from the Mg–Al system is the fairly constant strain-rate sensitivity during superplastic flow. This feature was attributed to the formation of equilibrium grain boundaries during ECAP processing.

Lamark and coauthors have applied the EX-ECAP process to a high-pressure die cast AS21X magnesium alloy [97]. Experimental data show that EX-ECAP improves the yield stress and elastic properties of the original material.

26.3.2.2 **Cast and Wrought Aluminum Alloys**

In cast aluminum alloys, the grain size and second-phase particles are usually large. SPD processing seems to be a promising technique to refine the structure and to obtain a fine distribution of second-phase particles. In this way, both ECAP [98] and ARB [99] have been successfully applied to a commercial AA8079 alloy containing 1.3%Fe and 0.09%Si. It has been indeed demonstrated that Fe-rich second-phase particles significantly improve the grain refinement compared to commercial-purity aluminum. This is attributed to a fastest generation of HAGBs in deformation zones surrounding second-phase particles that stabilize GBs as well. An extremely fine grain size in a range of 0.1 to 0.3 μm was also obtained by Homola and coauthors in a commercial twin-roll cast

AA8006 alloy with a similar Fe content [100]. In the Al–Fe system, Stolyarov and coauthors have investigated the microstructure of a model alloy containing 5 wt.% Fe processed ECAP [101]. Coarse $Al_{13}Fe_4$ particles of the as-cast structure are fragmented during ECAP and the grain size is only 0.3 μm, which gives rise to a strong increase of the hardness up to about 70 HV. Moreover, some particles are dissolved during SPD, forming a supersaturated solid solution with up to 0.6 wt.% Fe in solid solution. This feature allows post-ECAP age-hardening treatment in this conventionally nonhardenable alloy and an additional increase of the hardness up to about 80 HV. It is, however, interesting to note that in a recycled cast alloy containing Al_8Fe_2Si coarse particles, Korchef and coauthors did not observed a significant fragmentation of these second-phase particles [102]. The ECAP processing was, however, slightly different: route A without backpressure instead of route B_C with a backpressure used by Stolyarov and coauthors [101]. Thus, these parameters seem to play an important role in the particle-fragmentation mechanisms.

Xu and coauthors have investigated the precipitate distribution in a spray-cast aluminum 7034 alloy [103–106]. Before ECAP, this alloy from the Al–Zn system, contains an array of rod-like η-phase ($MgZn_2$) precipitates, but also nanoscaled metastable η'-phase and Al_3Zr particles. The yield stress of this alloy is quite high due to all these second-phase particles, and ECAP processing was therefore performed at 200 °C. After 8 passes, the material exhibits a grain size of only 0.3 μm (Fig. 26.7) leading to superplastic properties (elongation >1000% at 400 °C and 10^{-2} s^{-1}). η-phase ($MgZn_2$) precipitates are fragmented and most of them are no longer needle-shaped but almost spherical. Due to the signifi-

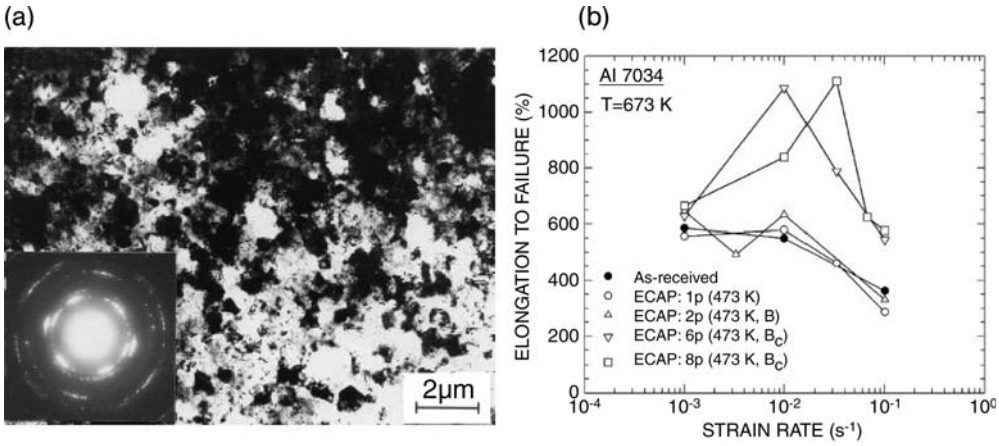

Fig. 26.7 (a) Microstructure after 8 passes of ECAP at 200 °C of a spray-cast aluminum alloy. (b) Elongation to failure versus strain rate at 400 °C for the as-received spray-cast aluminum alloy and after ECAP processing through 1, 2, 6 and 8 passes at 200 °C. (Courtesy of C. Xu et al. [103]).

cant processing temperature (200 °C), metastable η'-phase particles have been transformed into stable η-phase with subsequent coarsening. This feature gives rise to a significant decrease of the tensile strength. It is, however, interesting to note that nanoscaled Al_3Zr stable particles remain mostly unchanged.

Actually, the microstructures induced by ECAP processing of aluminum alloys containing Sc and/or Zr have been widely investigated [107–120]. Depending on the nominal composition, these alloys exhibit a fine dispersion of nanoscaled Al_3Sc, Al_3Zr or $Al_3(Zr_xSc_{x-1})$ ordered precipitates. They are usually processed by ECAP at room temperature via the route B_c up to 8 passes. After such processing the grain size is in the range of 0.2 to 0.3 μm and superplastic ductility is observed (typically >2000% at 400 °C and 3.3×10^{-2} s^{-1} [107]). Such properties result from the excellent thermal stability of the microstructure due to Al_3Sc, Al_3Zr or $Al_3(Zr_xSc_{x-1})$ precipitates that inhibit recrystallization and grain growth. Lee and coauthors have extensively investigated the influence of the alloy composition on the thermal stability of the microstructure [108]. In a AlMgZr alloy, the grain-growth onset was observed at only 300 °C, and superplasticity was not achieved. However, in a AlMgSc alloy the grain growth starts at 500 °C and superplastic ductility was recorded in the vicinity of 10^{-2} s^{-1} at 300 °C and 400 °C. This behavior is attributed to Al_3Sc precipitates that are more stable than Al_3Zr. Finally, the AlMgScZr alloy is shown to exhibit the better thermal stability (up to 550 °C) because of the higher stability of $Al_3(Zr_xSc_{x-1})$ precipitates. This allows superplastic ductility at high strain rate (10^{-1} s^{-1}) up to 730% at 500 °C, which seems very promising for industrial applications.

26.3.2.3 **Cast and Wrought Copper Alloys**

Only few data are reported about cast copper alloys processed by SPD. Such alloys are designed to produce a good combination of electrical conductivity and high strength. Joo and coauthors have investigated a Cu–9Fe–1.2Cr cast alloy processed by ECAP [121]. They have shown that routes C and B_C lead to the fragmentation of Fe–Cr dendrites, while they are elongated via route A. After 8 passes, the average grain size is about 0.2 μm, which gives rise to a significant increase of the hardness. However, the authors argue that drawing or extrusion is more efficient to increase the strength of such alloys thanks to the formation of an elongated nanoscaled structure.

26.3.3
Age-hardenable Alloys

26.3.3.1 **Age-hardenable Magnesium Alloys**

Magnesium alloys containing rare-earth elements (RE), like Y, Nd, Th, Sm or Gd usually exhibit high strength at elevated temperatures and good creep resistance [79]. These alloys are age hardenable, and their improved properties compared to other Mg alloys result from the precipitation of metastable phases like Guinier-Preston (GP) zones [122]. SPD processes have been successfully applied

on various Mg–RE alloys, leading to significant increase of strength and ductility thanks to grain refinement [123–125]. However, Cizek and coauthors revealed that in a Mg–10Nd alloy processed by HPT at room temperature, metastable β'' and β' phases do not precipitate and the stable FCC β phase directly precipitates at only 260 °C instead of 400 °C in the coarse-grain alloy [126]. On the other hand, Rohklin and coauthors observed that SPD intensifies the decomposition of Mg supersaturated solid solution upon ageing in MgSm alloys processed by HPT [127]. Thus, SPD could significantly affect the age-hardening properties of Mg–RE alloys. It is also important to mention that Yoshimoto and coauthors have shown that a Mg–Zn_1–Y_2 alloy with long-period stacking ordered structure (LPSO phase – $Mg_{12}ZnY$) exhibits higher strength and elongation after ECAP than non-LPSO-type Mg–Zn_1–La_2 and Mg–Zn_1–Yb_2 alloys processed under the same conditions [125].

26.3.3.2 **Age-hardenable Aluminum Alloys**

Aluminum alloys from the Al–Mg–Si (6xxx), AlCuZn (2xxx), AlZnMg (7xxx) and AlMgLi systems are widely used as structural materials in the automotive or aerospace industry. All these alloys are age hardenable, e.g. the yield stress is significantly improved by a high density of nanoscaled precipitates resulting from appropriate ageing treatments. The main motivation for the application of SPD to these alloys is to reduce the grain size to obtain a further increase of the yield stress.

6xxx alloys processed by SPD have been widely investigated [128–137]. The resulting microstructures and related properties strongly depend on the thermal treatment applied before SPD (annealed and quenched [129, 133, 135–137], aged [136, 137], as-extruded [130, 136, 137], fully annealed [131, 132]). ECAP processing of the annealed and quenched state gave the most promising results and, for example, a significant improvement of the mechanical strength comparing to the T6 state was obtained by Kim and coauthors [129] in an ECAPed 6061 alloy (Fig. 26.8). It is interesting to note that post-ECAP ageing treatments lead to further increase of strength. This could be attributed to SPD-induced precipitation and to a modification of the precipitation sequence and of the ageing kinetics [133]. Similar phenomena have been observed in 2xxx [106, 115, 117], 7xxx [106, 138] and Al–Ag [139, 140] alloys. On the other hand, as observed by Muruyama and coauthors, SPD processing could also lead to the dissolution of second-phase particles in an Al–Cu model alloy [141]. Improved hot forgeability of a 6061 alloy [53] and superplastic properties [115, 142–145] have also been obtained thanks to ECAP in several age-hardenable aluminum alloys.

26.3.3.3 **Age-hardenable Copper Alloys**

Age-hardenable copper alloys exhibit a unique combination of high strength, low electrical resistivity and high thermal conductivity that gives rise to numerous industrial applications. The best combination of properties is obtained in

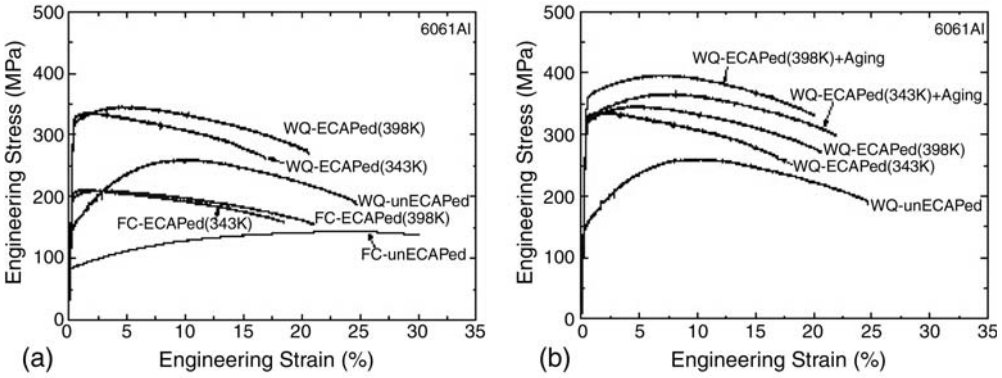

Fig. 26.8 Engineering stress–strain curves of a (a) furnace-cooled (FC) and water-quenched (WQ) ECAPed 6061 alloy without ageing treatment, and (b) with post-ECAP ageing treatments. (Courtesy of J. K. Kim et al. [129]).

the Cu–Cr system thanks to the extremely low solubility of Cr in copper at room temperature. The processing of these alloys by SPD was motivated by grain-size refinement that could bring further strength increase. It has been shown that a better combination of properties could be obtained if the material is aged after ECAP processing of the homogenized state (homogenization treatment followed by water quenching) [146–150]. Since the distribution and the size of precipitates directly influence the yield stress, a different precipitation kinetics induced by SPD could explain this feature. Actually, Vinogradov and coauthors have shown by DSC that in a Cu–0.44%Cr–0.21%Zr alloy, the precipitation sequence is reversed in the ECAPed material: Cu3Zr precipitates start to nucleate at 370 °C instead of 520 °C in the nondeformed samples and Cr precipitates appear secondly at a slightly lower temperature (425 °C instead of 440 °C in the nondeformed state) [149]. Such a decrease of the precipitation temperatures may indicate that SPD-induced defects (dislocations, dislocation cells, vacancies) could enhance atomic mobility and act as nucleation site. Otherwise, it is interesting to note that substantial improvement of fatigue life was also reported for various ECAPed alloys from the Cu–Cr system [147–150].

Dilute alloys from the Cu–Co system are also age hardenable. During ageing, small ferromagnetic Co-rich precipitates are formed in the nonmagnetic copper matrix. Fukita and coauthors have shown that one pass of ECAP could significantly increase the coercivity of these precipitates [176]. This effect is attributed to the anisotropic shape of precipitates resulting from the deformation during ECAP. At higher level of deformation (4 passes), theses authors report, however, that precipitates are partly dissolved in the Cu matrix.

26.3.4
Eutectic and Eutectoid Alloys

Eutectic and eutectoid alloys exhibit a lamellar structure in the as-transformed state. The behavior of such particular microstructures during SPD has been especially investigated by Wang and coauthors for the eutectic Al–33%Cu alloy [147–152]. Due to the low ductility of this alloy at room temperature, ECAP processing was performed at 400 °C, leading to a progressive spheroidization of the lamellar structure during processing along with a strong grain-size refinement. After 8 passes of ECAP, a homogeneous equiaxed duplex structure with an average grain size of about 1 μm was obtained. These authors have also investigated the deformation mechanisms of the lamellar structure: periodical bending, periodical shear banding, parallel shear and periodical shear cutting was reported (Fig. 26.9). However, shear banding is the dominant lamellae accommodation mode under ECAP.

Furukawa and coauthors have investigated the microstructure and the properties of a eutectoid Al–22%Zn alloy processed by ECAP [153]. However, the starting

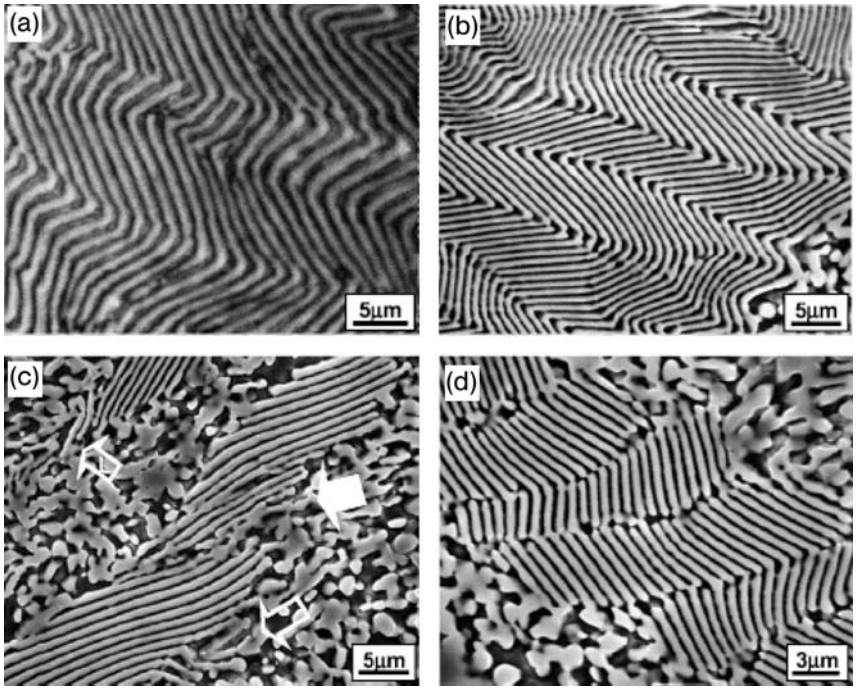

Fig. 26.9 Typical deformation mode accommodation modes: (a) periodical bending, (b) periodical shearing, (c) parallel shear and (d) periodical cutting in lamellae Al–33%Cu eutectics during equal channel angular processing.(Courtesy of J. Wang et al. [152]).

microstructure was not a lamellar structure but a homogeneous equiaxed grain structure obtained in superplastic conditions. After ECAP processing, a large grain-size distribution in a range of 0.1 to 0.5 μm was reported for this alloy. This gives rise to a superplastic elongation of 1540% at 200 °C at 3.3×10^{-1} s^{-1}. It is worth noting that after HPT processing, evidence of Al–Zn mixing and formation of supersaturated solid solutions was also reported [138].

26.3.5 Intermetallics

26.3.5.1 Ni–Ti Alloys

Shape-memory alloys (SMA) from the Ni–Ti system exhibit a unique combination of properties such as strength, biocompatibility, corrosion resistance and shape recovery. These functional materials are, therefore, very attractive for various applications like actuators, heat-sensitive elements or in medical field as implants or instruments. The physical properties of Ni–Ti based SMA are related to the inverse martensitic transformation that is controlled by microstructural features and composition. As shown by several authors, SPD could induce significant modifications of the microstructure, and thus improve the properties of NiTi alloys, especially through grain-size reduction [154–163].

HPT is the more efficient process to reduce the grain size of Ni–Ti-based SMA. A fully amorphous structure is indeed usually obtained, and post-deformation annealing treatments lead to the nucleation of new grains that could give rise to a homogeneous nanocrystalline structure with a grain size smaller than 50 nm (Fig. 26.10) [155–161]. Prokoshikin and coauthors have investigated the effect of the alloy composition and of processing parameters (temperature and pressure) on the amorphization induced by HPT [155]. Higher transformation rates were observed for alloys with a higher martensite start temperature (M_s). This easier amorphization of martensite or premartensitic structures in comparison with the austenite is attributed to crystal defects like distortions and boundaries. Thus, a full amorphization could be obtained only if the processing temperature was lower than the M_s temperature. The influence of the pressure during HPT is also important: the higher the pressure, the lower the transformation rate. This feature could be attributed to a pronounced decrease of the M_s temperature under compression strains and to the lower density of the amorphous phase compared to the crystal [155].

After post-deformation annealing, an excellent combination of strength and ductility is usually obtained (UTS >2 GPa, and elongation to failure >40% [156, 160]). Full shape recovery and superplastic properties were also reported (1200% elongation at 500 °C at 10^{-3} s^{-1}). However, the size of HPT samples is quite small and usually not suitable for application, there is therefore a strong motivation for the production of nanocrystalline Ni–Ti-based SMA by ECAP. Due to the high strength of Ni–Ti alloys, ECAP has to be performed in the temperature range of 400–500 °C [154, 157, 161, 163] and in such conditions

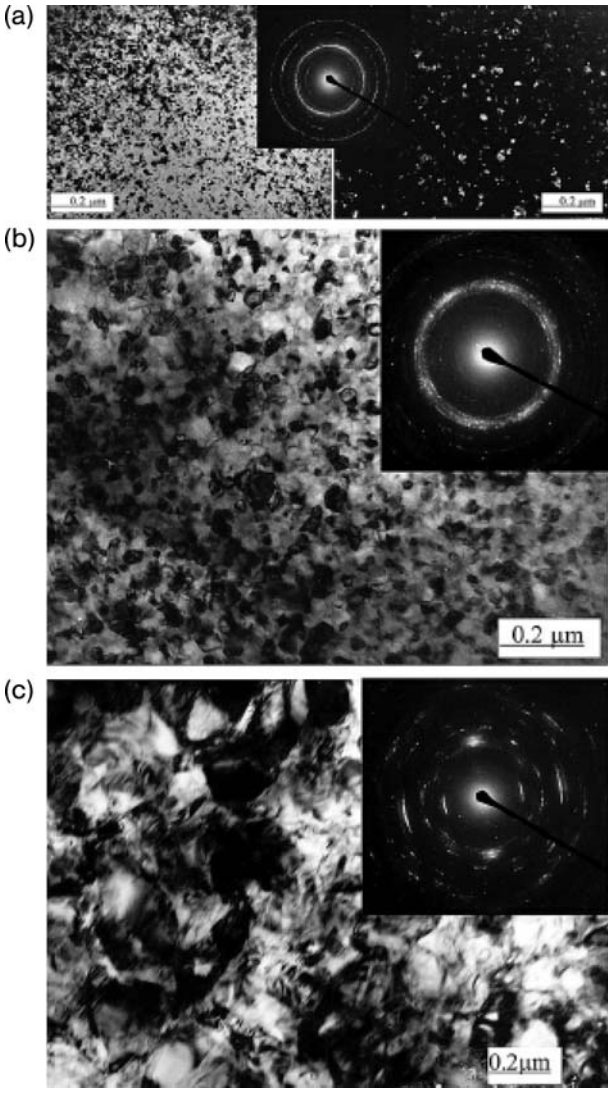

Fig. 26.10 Structures and electron diffraction patterns of Ti-50.0at.%Ni alloy after HPT at room temperature followed by annealing at 300 °C (a), 350 °C (b), 400 °C (c). (Courtesy of S.D. Prokoshkin et al. [155]).

amorphization does not occur. After ECAP, the grain size is typically in a range of 200–300 nm, which gives rise to a significant increase of the strength, while the ductility is kept. Functional properties are also improved [154]. Moreover, Pushin and coauthors have shown that a combination of ECAP and cold rolling leads to a further increase of the ultimate tensile stress up to 2 GPa [161].

26.3.5.2 Ni–Al, Ti–Al and Cu–Au Ordered Alloys

The microstructure evolution of ordered intermetallic alloys subjected to HPT as been investigated for $L1_2$ phases: Ni_3Al [164–166], Cu_3Au [165] and $L1_0$ phases: NiAl [167], TiAl [168]. Although these alloys exhibit a very limited ductility at room temperature, they were successfully processed by SPD and a crystallite size as small as 25 nm was even obtained for Ni_3Al [164, 166] and TiAl [168]. The propagation of deformation twins is reported as the main mechanism of plastic deformation of $L1_2$ and $L1_0$ phases. SPD-induced disordering was also observed. This phenomena is more pronounced in Ni_3Al than in TiAl, but is not reported for Cu_3Au. In TiAl, the disordering gives rise to the transformation of the $L1_0$ phase into the hcp (A3) phase. It is interesting to note that a small amount of boron in the Ni_3Al alloy does not promote the grain-size reduction and does not affect the disordering process, however, it seems to improve the thermal stability of the nanostructure [166].

26.3.6 Composite Materials

Metal matrix composites (MMCs) are usually made of a ductile metallic matrix reinforced with oxide or ceramic particles. These materials are very attractive for industrial applications because of their high specific mechanical properties. However, their mechanical properties are strongly linked to the distribution of particles, and a homogeneous distribution of particles is required for optimal properties. Since it is very difficult to achieve a homogeneous particle distribution in Al–MMCs, attempts have been made to improve this distribution through SPD [169–171]. Chang and coauthors have shown that coarse SiC particles (> 30 m) are fragmented during ECAP and their distribution in the Al matrix is improved [169]. However, they demonstrate that the smaller the initial grain size, the more uniform was the distribution of the reinforcement. Low ECAP temperatures and more ECAP passes improve the distribution as well. Similar features are reported for a 6061 aluminum alloy reinforced with Al_2O_3 or SiC particles and processed by HPT [171].

A large volume fraction (10%) of coarse Al_2O_3 particles (10 μm) in an aluminum alloy does not significantly affect the grain-size reduction during ECAP [170]. However, as reported by Islamgaliev and coauthors [172], a low volume fraction (0.5 wt.%) of small Al_2O_3 particles in copper leads to a stronger grain refinement of the matrix by HPT (down to 80 nm, instead of 150 nm in pure copper). Moreover, the fine distribution of nanoscaled Al_2O_3 particles leads to a better thermal stability and better creep properties. Similar improvement of grain refinement in multiphase composite materials processed by HPT was also reported for W–Cu [171, 173, 174] and Cu–Fe [175] composites. In this latter case, it is interesting to note that SPD leads to room-temperature interdiffusion of Cu and Fe and to the formation of supersaturated solid solutions, like in ball-milled powders.

26.3.7
Final Remarks

In the wide variety of bulk nanostructured nonferrous multiphase alloys, it seems clear that the most promising materials are among light alloys. As reported in the present review, SPD processes could give rise to some significant improvement of the ductility (critical issue for Mg alloys), superplastic properties (promising for metal forming applications) and the thermal stability (key point for nanostructured materials). Although they are used for some specific applications, bulk nanostructured shape-memory alloys (for instance, intermetallic NiTi alloys) also exhibit some unique functional properties. Finally, it is interesting to note that SPD processes could be applied to optimize the structure and the related mechanical properties of metal matrix composites.

26.4
Summary

The microstructure of multiphase metals processed by SPD exhibit some specific features related to deformation mechanisms of phases differing in hardness and morphology and also because of phase transformations occurring under nonequilibrium conditions (high level of stresses, high dislocation density and high vacancy concentration). SPD-induced phase transformations may indeed promote the grain-size refinement and also provide enhanced thermal stability of bulk nanostructured materials. These specific features give rise to unique properties, however, application of bulk nanostructured multiphase materials is still limited for the following reasons: i) the whole set of mechanical and service properties (including fracture toughness, impact toughness, fatigue strength, corrosion resistance, *etc.*) of most bulk nanostructured multiphase materials is poorly known, ii) the size of prepared billets is usually small, iii) the production cost is high, iv) industrial continuous technologies to make massive products with a homogeneous structure does not exist today. Anyway, there are some specific applications where bulk nanostructured multiphase alloys are used. For example, in medicine, some tools and implants are made with bulk nanostructured titanium alloys, shape-memory Ni–Ti base alloys or austenitic stainless steels. In machine building, fasteners such as bolts or pins are made of bulk nanostructured titanium alloys and steels, and thermomechanical clutches are made of bulk nanostructured shape-memory Ni–Ti alloys. The fast development and design of new SPD schemes will undoubtedly widen the field of bulk nanostructured applications in our everyday life if the challenge of large-scale bulk nanostructured production could be successfully overcome. It should be noted that a significant jump in BNM applications is soon expected thanks to the manufacture of bulk nanostructured sheets for applications based on the low-temperature and high-rate superplasticity established for light alloys.

References

1 *In vestigations and Applications of Severe Plastic Deformation* (eds.) T. C. Lowe, R. Z. Valiev, **2000**, Kluwer Academic Publishing, Dordrecht, The Netherlands, 395 pp.

2 *Ultrafine-grained Materials II* (eds.) Y. T. Zhu, T. G. Langdon, R. S. Mishra, S. L. Semiatin, M. J. Saran, T. C. Low, **2002**, TMS (The Minerals, Metals and Materials Society), Warrendale, USA, 685 p.

3 *Nanomaterials by Severe Plastic Deformation* (eds.) M. J. Zehetbauer, R. Z. Valiev, **2003**, Wiley-VCH, Vienna, Austria, 850 pp.

4 *Ultra Grained Materials III* (eds.) Y. T. Zhu, T. G. Langdon, R. Z. Valiev, S. L. Semiatin, D. H. Shin, T. C. Low, **2004**, TMS (The Minerals, Metals and Materials Society), Warrendale, USA, 686 pp.

5 *Nanomaterials by Severe Plastic Deformation* (ed.) Z. Horita, **2005**, TransTech Publications Ltd, Fukuoka, Japan, 1030 pp.

6 *Ultrafine-grained Materials IV* (eds.) Y. T. Zhu, T. G. Langdon, Z. Horita, M. J. Zehetbauer, S. L. Semiatin, T. C. Low, **2006**, TMS (The Minerals, Metals and Materials Society), Warrendale, USA, 497 pp.

7 V. M. Segal, V. I. Reznikov, V. I. Kopylov et al., **1994**, *Processes of Plastic Structure Formation in Metals*, Nauka i Tekhnika, Minsk, 232 pp. (in Russian).

8 V. Segal, **2002**, *Mater. Sci. Eng.* 338A, 331–344.

9 Y. Iwahashi, J. T. Wang, Z. Horita, M. Nemoto, T. G. Langdon, **1996**, *Scr. Mater.* 35, 143–146.

10 R. Z. Valiev, R. K. Islamgaliev, I. V. Alexandrov, **2000**, *Prog. Mater. Sci.* 45, 103–189.

11 S. V. Dobatkin, *Investigations and Applications of Severe Plastic Deformation* (eds.) T. C. Low, R. Z. Valiev, **2000**, NATO Science Series, Kluwer Academic Publishers, Dordrecht, Netherlands, 3/80, 13–22.

12 D. H. Shin, B. C. Kim, Y.-S. Kim M, K.-T. Park, **2000**, *Acta Mater.* 48, 2247–2255.

13 D. H. Shin, C. W. Seo, J. Kim, K.-T. Park, W. Y. Choo, **2000**, *Scr. Mater.* 42, 695–699.

14 D. H. Shin, I. Kim, J. Kim, K.-T. Park, **2001**, *Acta Mater.* 49, 1285–1292.

15 J. Wang, C. Xu, Y. Wang, Z. Du, Z. Zhang, L. Wang, X. Zhao, T. G. Langdon, **2002**, *Nanomaterials by Severe Plastic Deformation* (eds.) M. J. Zehetbauer, R. Z. Valiev, Wiley-VCH, Vienna, Austria, 829–834.

16 J.-T. Wang, X. Cao, Z. Du, Z. Zhang, X. Zhao, **2004**, *Ultra Grained Materials III* (eds.) Y. T. Zhu, T. G. Langdon, R. Z. Valiev, S. L. Semiatin, D. H. Shin, T. C. Low, TMS (The Minerals, Metals and Materials Society), Warrendale, USA, 345–350.

17 J. T. Wang, C. Xub, Z. Z. Duc, G. Z. Qua, T. G. Langdon, **2005**, *Mater. Sci. Eng.* A410–411, 312–315.

18 Y. Fukuda, K. Oh-ishi, Z. Horita, T. G. Langdon, **2002**, *Acta Mater.* 50, 1359–1368.

19 K.-T. Park, Y.-S. Kim, J. G. Lee, D. H. Shin, **2000**, *Mater. Sci. Eng.* A293, 165–172.

20 D. H. Shin, S. Y. Han, K.-T. Park, Y.-S. Kim Y.-N. Paik, **2003**, *Mater. Trans.* 44, 1630–1635.

21 D. H. Shin, B. C. Kim, K.-T. Park, W. Y. Choo, **2000**, *Acta Mater.* 48, 3245–3252.

22 D. H. Shin, Y.-S. Kim, E. J. Lavernia, **2001**, *Acta Mater.* 49, 2387–2393.

23 D. H. Shin, K.-T. Park, **2002**, *Nanomaterials by Severe Plastic Deformation* (eds.) M. J. Zehetbauer, R. Z. Valiev, Wiley-VCH, Vienna, Austria, 616–622.

24 V. N. Gridnev, V. G. Gavrilyuk, **1982**, *Metallofizika* 4 (3), 74–87 (in Russian).

25 A. V. Korznikov, Yu. V. Ivanisenko, D. V. Laptionok, I. M. Safarov, V. P. Pilyugin, R. Z. Valiev, **1994**, *Nanotsruct. Mater.* 4, 159.

26 J. Languillaume, G. Kapelski, B. Baudelet, **1997**, *Acta Mater.* 45, 1201.

27 M. H. Hong, W. T. Reynolds, Jr., T. Tarui, K. Hono, **1999**, *Met. Mater. Trans.* 30A, 717.

28 X. Sauvage, N. Guelton, D. Blavette, **2002**, *Scr. Mater.* 46, 459.

29 Yu. Ivanisenko, W. Lojkowski, R. Z. Valiev, H.-J. Fecht, **2003**, *Acta Mater.* 51, 5555–5570.

30 V. G. Gavriluk, **2003**, *Mater. Sci. Eng.* A345, 81.

31 M. Umemoto, Y. Todaka, A. Ohno, M. Suzuki, K. Tsuchiya, **2006**, *Mater. Sci. Forum*, 503–504, 461–466.

32 D. H. Shin, B. D. Ahn, H. S. Cho, K.-T. Park, **2004**, *Ultrafine-grained Materials III* (eds.) Y. T. Zhu, T. G. Langdon, R. Z. Valiev, S. L. Semiatin, D. H. Shin, T. C. Low, TMS (The Minerals, Metals and Materials Society), Warrendale, USA, 421–426.

33 K. Aoki, Y. Kimura, A. Azushima, **2001**, *Ultrafine-grained steels* (eds.) S. Takaki, T. Maki, The Iron and Steel Institute of Japan, Tokyo (Japan), 266.

34 D. H. Shin, J.-J. Pak, Y. K. Kim, K.-T. Park, Y.-S. Kim, **2002**, *Mater. Sci. Eng.* A325, 31–37.

35 S. V. Dobatkin, R. Z. Valiev, N. A. Krasilnikov, V. N. Konenkova, **1999**, *Recrystallization and Related Phenomena* (eds.) T. Sakai, H. G. Suzuki, JIM, Japan, 13, 913–918.

36 S. V. Dobatkin, P. D. Odessky, N. A. Krasilnikov, G. I. Raab, V. N. Konenkova, **2001**, *Recrystallization and Grain Growth* (eds.) G. Gottstein, D. A. Molodov, Spinger-Verlag, Germany, 543–548.

37 S. V. Dobatkin, P. D. Odessky, R. Pippan, G. I. Raab, N. A. Krasilnikov, A. M. Arsenkin, **2002**, *Nanomaterials by Severe Plastic Deformation* (eds.) M. J. Zehetbauer, R. Z. Valiev, Wiley-VCH, Vienna, Austria, 804–809.

38 S. V. Dobatkin, P. D. Odessky, R. Pippan et al., **2004**, *Russian Metallurgy (Metally)*, **2004**, No.1, 94–102 (Translated from *Metally*, **2004**, 1, 110–119).

39 S. Torizuka, S. V. S. N. Murty, A. Ohmori, K. Nagai, **2006**, *Ultrafine-grained Materials IV* (eds.) Y. T. Zhu, T. G. Langdon, Z. Horita, M. J. Zahetbauer, S. L. Semiatin, T. C. Low, TMS (The Minerals, Metals and Materials Society), Warrendale, USA, 165–170.

40 R. Song, R. Kaspar, D. Ponge, D. Raabe, **2004**, *Ultrafine-grained Materials III* (eds.) Y. T. Zhu, T. G. Langdon, R. Z. Valiev, S. L. Semiatin, D. H. Shin, T. C. Low, TMS (The Minerals, Metals and Materials Society), Warrendale, USA, 445–450.

41 G. Herman, B. Lechevalier, F. Montheillet, T. Oliveira, **2004**, *Ultrafine-grained Materials III* (eds.) Y. T. Zhu, T. G. Langdon, R. Z. Valiev, S. L. Semiatin, D. H. Shin, T. C. Low, TMS (The Minerals, Metals and Materials Society), Warrendale, USA, 357–362.

42 B. Shi, H.-W. Song, J.-B. Zhang, H.-Q. Cao, X.-F. Wang, **2006**, *Mater. Sci. Forum*, 503–504, 511–514.

43 S. V. Dobatkin, N. A. Krasilnikov, K. I. Yanushkevitch, **2004**, *Ultrafine-grained Materials III* (eds.) Y. T. Zhu, T. G. Langdon, R. Z. Valiev, S. L. Semiatin, D. H. Shin, T. C. Low, TMS (The Minerals, Metals and Materials Society), Warrendale, USA, 333–338.

44 M. V. Degtyarev, T. I. Chashchukhina, L. M. Voronova et al., **1994**, *Fiz. Met. Metalloved.* 77 (2), 141–146 (in Russian).

45 S. M. L. Sastry, S. V. Dobatkin, S. V. Sidorova, **2004**, *Russian Metallurgy (Metally)*, **2004**, No.2, 129–134 (Translated from *Metally*, **2004**, 2, 28–35).

46 D. H. Shin, W. G. Kim, J. Y. Ahn, K.-T. Park, Y. S. Kim, **2006**, *Mater. Sci. Forum*, 503–504, 447–454.

47 Y. I. Son, Y. K. Lee, K.-T. Park, C. S. Lee, D. H. Shin, **2005**, *Acta Mater.* 53, 3125–3134.

48 J. Wang, J. Huang, Z. De, Z. Zhang, X. Zhao, **2004**, *Ultrafine-grained Materials III* (eds.) Y. T. Zhu, T. G. Langdon, R. Z. Valiev, S. L. Semiatin, D. H. Shin, T. C. Low, TMS (The Minerals, Metals and Materials Society), Warrendale, USA, 673–678

49 F. Wetscher, R. Stock, B. Tian, R. Pippan, **2004**, *Ultrafine-grained Materials III* (eds.) Y. T. Zhu, T. G. Langdon, R. Z. Valiev, S. L. Semiatin, D. H. Shin, T. C. Low, TMS (The Minerals, Metals and Materials Society), Warrendale, USA, 315–320.

50 Y. Ivanisenko, R. Z. Valiev, W. Lojkowski, A. Grob, H.-J. Fecht, **2002**, *Ultrafine-grained Materials II* (eds.) Y. T. Zhu, T. G. Langdon, R. S. Mishra, S. L. Semiatin, M. J. Saran, T. C. Low, TMS (The Minerals, Metals and Materials Society), Warrendale, USA, 47–54.

51 Y. Ivanisenko, I. MacLaren, H. Rosner, H.-J. Fecht, **2004**, *Ultrafine-grained Materials III* (eds.) Y. T. Zhu, T. G. Langdon, R. Z. Valiev, S. L. Semiatin, D. H. Shin, T. C. Low, TMS (The Minerals,

Metals and Materials Society), Warrendale, USA, 387–392.
52 Y. Ivanisenko, I. MacLaren, R. Z. Valiev, H.-J. Fecht, **2006**, *Mater. Sci. Forum*, 503–504, 439–446.
53 I. MacLaren, Y. Ivanisenko, H.-J. Fecht, X. Sauvage, R. Z. Valiev, **2006**, *Ultrafine-grained Materials IV* (eds.) Y. T. Zhu, T. G. Langdon, Z. Horita, M. J. Zehetbauer, S. L. Semiatin, T. C. Low, TMS (The Minerals, Metals and Materials Society), Warrendale, USA, 251–256.
54 H.-J. Fecht, **1996**, *Nanomaterials: Synthesis, Properties, and Application* (eds.) A. S. Edestein, R. C. Cammarata, Bristol, Institute of Physics, J. W. Arrowsmith Ltd.
55 R. Z. Valiev, Yu. V. Ivanisenko, E. E. Rauch, B. Baudelet, **1996**, *Acta Mater.* 12, 4705.
56 W. Lojkowski, M. Djahanbakhsh, G. Burkle, S. Gierlotka, W. Zielinski, H.-J. Fecht, **2001**, *Mater. Sci. Eng.* A303, 197.
57 K. Hono, M. Omuma, M. Murayama et al., **2001**, *Scr. Mater.* 44, 977.
58 X. Sauvage, G. Dacosta, R. Z. Valiev, **2004**, *Ultrafine-grained Materials III* (eds.) Y. T. Zhu, T. G. Langdon, R. Z. Valiev, S. L. Semiatin, D. H. Shin, T. C. Low, TMS (The Minerals, Metals and Materials Society), Warrendale, USA, 31–36.
59 Yu. Ivanisenko, I. MacLaren, X. Sauvage, R. Z. Valiev, H.-J. Fecht, **2006**, *Acta Mater.* 54, 1659–1669.
60 E. Aernoudt, **2000**, *Investigations and Applications of Severe Plastic Deformation* (eds.) T. C. Low, R. Z. Valiev, NATO Science Series, Kluwer Academic Publishers, Dordrecht, Netherlands, 3/80, 373–381.
61 D. R. Lesuer, C. K. Syn, O. D. Sherby, **2000**, *Investigations and Applications of Severe Plastic Deformation* (eds.) T. C. Low, R. Z. Valiev, NATO Science Series, Kluwer Academic Publishers, Dordrecht, Netherlands, 3/80, 357–366.
62 S. V. Dobatkin, R. Z. Valiev, L. M. Kaputkina et al., **1999**, *Recrystallization and Related Phenomena* (eds.) T. Sakai, H. G. Suzuki, JIM, Japan, 13, 907–912.
63 O. V. Rybal'chenko, S. V. Dobatkin, L. M. Kaputkina et al., **2004**, *Mater. Sci. Eng.* A387–389, 244–248.
64 A. M. Patselov, V. P. Pilyugin, E. G. Chernyshov et al., **1999**, *Structure and Properties of Nanocrystalline Materials* (eds.) N. Noskova, G. Taluts, Ekaterinburg, Russia, 37–44 (in Russian).
65 I. I. Kositsyna, V. V. Sagaradze, V. I. Kopylov, **1999**, *Fizika Metalliv i Metallovedenie*, 88, 5, 84–94 (in Russian).
66 B. Efros, Y. Beygelzimer, A. Deryagin, N. Efros, V. Pilyugin, D. Orlov, **2004**, *Ultrafine-grained Materials III* (eds.) Y. T. Zhu, T. G. Langdon, R. Z. Valiev, S. L. Semiatin, D. H. Shin, T. C. Low, TMS (The Minerals, Metals and Materials Society), Warrendale, USA, 401–404.
67 S. S. M. Tavares, D. Gunderov, V. Stolyrov, J. M. Neto, **2003**, *Mater. Sci. Eng.* A358, 32–36.
68 A. Vorhauer, S. Kleber, R. Pippan, **2004**, *Ultrafine-grained Materials III* (eds.) Y. T. Zhu, T. G. Langdon, R. Z. Valiev, S. L. Semiatin, D. H. Shin, T. C. Low, TMS (The Minerals, Metals and Materials Society), Warrendale, USA, 629–634.
69 A. Belyakov, T. Sakai, H. Miura, R. Kaibyshev, **2000**, *Scr. Mater.* 42, 319–325.
70 A. Belyakov, T. Sakai, H. Miura, **2001**, *Mater. Sci. Eng.* A319–321, 867–871.
71 A. Belyakov, K. Tsuzaki, H. Miura, T. Sakai, **2003**, *Acta Mater.* 51, 847–861.
72 H. Miura, H. Hamaji, T. Sakai, **2002**, *Nanomaterials by Severe Plastic Deformation* (eds.) M. J. Zehetbauer, R. Z. Valiev, Wiley-VCH, Vienna, Austria, 375–380.
73 H. Miura, H. Hamaji, T. Sakai, N. Fujita, N. Yoshinaga, **2006**, *Mater. Sci. Forum*, 503–504, 293–298.
74 G. G. Yapici, I. Karaman, Z. P. Luo, Y. I. Chumlyakov, **2004**, *Ultrafine-grained Materials III* (eds.) Y. T. Zhu, T. G. Langdon, R. Z. Valiev, S. L. Semiatin, D. H. Shin, T. C. Low, TMS (The Minerals, Metals and Materials Society), Warrendale, USA, 291–296.
75 Q. Xue, X. Z. Liao, Y. T. Zhu, G. T. Gray III, **2005**, *Mater. Sci. Eng.* A410–411, 252–256.
76 K. Tsuzaki, A. Belyakov, Y. Kimura, **2006**, *Mater. Sci. Forum*, 503–504, 305–310.
77 A. Belyakov, Y. Kimura, K. Tsuzaki, **2006**, *Acta Mater.* 54, 2521–2532.

78 N. P. Lyakishev, M. I. Alymov, S. V. Dobatkin, **2003**, *Russian Metallurgy (Metally)*, **2003**, No. 3, 191–202 (Translated from Metally, **2003**, 3, 3–16).

79 I. J. Polmear, **2000**, *Light Alloys – Metallurgy of the Light Metals*, 3rd edn, Butterworth-Heinemann, Oxford, UK.

80 Y. Yoshida, L. Cisar, S. Kamado, Y. Kojima, **2003**, *Mater. Trans.* 44, 468–475.

81 T. Mukai, K. Ishikawa, Y. Okanda, M. Mabuchi, K. Kubota, K. Higashi, **1995**, *Light Weight Alloys for Aerospace Application III* (eds.) E. W. Lee, N. J. Kim, K. V. Jata, W. E. Frazier, TMS, Warrendale, USA pp. 483–488.

82 J. A. Chapman, D. V. Wilson, **1962**, *J. Inst. Met.* 91, 39–49.

83 K. Matsubara, Y. Miyahara, Z. Horita, T. G. Langdon, **2003**, *Acta Mater.* 51 3073–3084.

84 T. Mukai, M. Yamanoi, H. Watanabe, K. Higashi, **2001**, *Scr. Mater.* 45, 89–94.

85 H. Somekawa, T. Mukai, **2006**, *Mater. Sci. Forum* 503–504, 155–160.

86 X. Yang, J. Xing, H. Miura, T. Sakai, **2006**, *Mater. Sci. Forum* 503–504, 521–526.

87 Y. Chen, Q. Wang, J. Peng, C. Zhai, **2006**, *Mater. Sci. Forum* 503–504, 865–870.

88 Y. Miyahara, N. Emi, K. Neishi, K. Nakamura, K. Kaneko, M. Nakagaki, Z. Horita, **2006**, *Mater. Sci. Forum* 503–504, 949–954.

89 W. J. Kim, C. W. An, Y. S. Kim, S. I. Hong, **2002**, *Scr. Mater.* 47, 39–44.

90 Z. Horita, K. Matsubara, Y. Miyahara, T. G. Langdon, **2004**, *Nanomaterials by Severe Plastic Deformation* (eds.) M. J. Zehetbauer, R. Z. Valiev, Wiley-VCH, Weinheim, Germany, 711–716.

91 K. Mathis, A. Mussi, Z. Trojanova, P. Ludvac, E. Rauch J. Lendvai, **2004**, *Nanomaterials by Severe Plastic Deformation* (eds.) M. J. Zehetbauer, R. Z. Valiev, Wiley-VCH, Weinheim, Germany, 190–193.

92 M. Mabuchi, K. Ameyam, H. Iwasaki, K. Higashi, **1999**, *Acta Mater.* 47, 2047–2057.

93 M. Mabuchi, M. Nakamura, K. Ameyama, H. Iwasaki, K. Higashi, **1999**, *Mater. Sci. Forum* 304–306, 67–72.

94 A. Mussi, J. J. Blandin, E. F. Rauch, **2004**, *Nanomaterials by Severe Plastic Deformation* (eds.) M. J. Zehetbauer, R. Z. Valiev, Wiley-VCH, Weinheim, Germany, 740–745.

95 T. Liu, W. Zhang, S. D. Wu, C. B. Jiang, S. X. Li, Y. B. Xu, **2003**, *Mater. Sci. Eng.* A360, 345–349.

96 H. Watanabe, T. Mukai, K. Ishikawa, K. Higashi, **2002**, *Scr. Mater.* 46, 851–856.

97 T. T. Lamark, R. J Hellming, Y. Estrin, **2006**, *Mater. Sci. Forum* 503–504, 889–894.

98 P. J. Apps, J. R. Bowen, P. B. Prangnell, **2004**, *Nanomaterials by Severe Plastic Deformation* (eds.) M. J. Zehetbauer, R. Z. Valiev, Wiley-VCH, Weinheim, Germany, 138–144.

99 C. P. Heason, P. B. Prangnell, **2004**, *Nanomaterials by Severe Plastic Deformation* (eds.) M. J. Zehetbauer, R. Z. Valiev, Wiley-VCH, Weinheim, Germany, 498–504.

100 P. Homola, M. Slamova, M. Karlik, J. Cizek, I. Prochazka, **2006**, *Mater. Sci. Forum* 503–504, 281–286.

101 V. V. Stolyarov, R. Lapovok, I. G. Brodova, P. F. Thomson, **2003**, *Mater. Sci. Eng.* A357, 159–167.

102 A. Korchef, N. Njah, Y. Champion, S. Guerin, C. Leroux, J. Masmoudi, A. Kolsi, **2004**, *Adv. Eng. Mater.* 6 No. 4, 222–228.

103 C. Xu, M. Furukawa, Z. Horita, T. G. Langdon, **2005**, *Acta Mater.* 53, 749–758.

104 C. Xu, T. G. Langdon, **2006**, *Mater. Sci. Forum* 503–504, 77–82.

105 M. Kawasaki, C. Xu, T. G. Langdon, **2006**, *Mater. Sci. Forum* 503–504, 83–88.

106 N. Gao, M. J. Starink, M. Furukawa, Z. Horita, C. Xu, T. G. Langdon, **2006**, *Mater. Sci. Forum* 503–504, 275–280.

107 M. Furukawa, Z. Horita, M. Nemoto, T. G. Langdon, **2002**, *Mater. Sci. Eng.* A324, 82–89.

108 S. Lee, A. Utsunomiya, H. Akamatsu, K. Neishi, M. Furukawa, Z. Horita, T. G. Langdon, **2002**, *Acta Mater.* 50, 553–564.

109 V. N. Perevezentsev, V. N. Chuvil'deev, V. I. Kopylov, A. N. Sysoev, T. G. Lang-

don, **2002**, *Ann. Chim. Sci. Mater.* 27, 99–109.
110 M. Nemoto, Z. Horita, M. Furukawa, T. G. Langdon, **1999**, *Mater. Sci. Forum* 304–306, 59–66.
111 Z. Horita, T. Fujinami, M. Nemoto, T. G. Langdon, **2001**, *J. Mater. Proc. Tech.* 117, 288–292.
112 H. Hasegawa, S. Komura, A. Utsunomiya, Z. Horita, M. Furukawa, M. Nemoto, T. G. Langdon, **1999**, *Mater. Sci. Eng.* A265, 188–196.
113 H. Akamastu, T. Fujinami, Z. Horita, T. G. Langdon, **2001**, *Scr. Mater.* 44, 759–764.
114 S. V. Dobatkin, V. V. Zakharov, A. Y. Vinogradov, T. D. Rostova, N. A. Krasilnikov, E. N. Bastarash, I. B. Trubitsyna, **2004**, *Nanomaterials by Severe Plastic Deformation* (eds.) M. J. Zehetbauer, R. Z. Valiev, Wiley-VCH, Weinheim, Germany, 158–164.
115 C. Xu, M. Furukawa, Z. Horita, T. G. Langdon, **2004**, *Nanomaterials by Severe Plastic Deformation* (eds.) M. J. Zehetbauer, R. Z. Valiev, Wiley-VCH, Weinheim, Germany, 701–710.
116 K. T. Park, C. S. Lee, Y. S. Kim, D. H. Shin, **2006**, *Mater. Sci. Forum* 503–504, 119–124.
117 S. V. Dobatkin, V. V. Zakharov, L. L. Rokhlin, **2006**, *Mater. Sci. Forum* 503–504, 399–406.
118 G. Angella, P. Bassani, A. Tuissi, D. Ripamonti, M. Vedani, **2006**, *Mater. Sci. Forum* 503–504, 493–498.
119 O. Sitdikov, R. Kaibyshev, E. Avtokratova, K. Tsuzaki, **2006**, *Mater. Sci. Forum* 503–504, 721–726.
120 M. Cabibbo, E. Evangelista, C. Scalabroni, E. Bonetti, **2006**, *Mater. Sci. Forum* 503–504, 841–846.
121 K. H. Joo, K. I. Chang, H. S. Kim, S. I. Hong, **2006**, *Mater. Sci. Forum* 503–504, 71–76.
122 D. H. Ping, K. Hono, J. F. Nie, **2003**, *Scr. Mater.* 48, 1017–1022.
123 M. Y. Zheng, S. W. Xu, X. G. Qiao, W. M. Gan, K. Wu, S. Kamado, Y. Kojima, H. G. Brokmeier, **2006**, *Mater. Sci. Forum* 503–504, 527–532.
124 H. Watanabe, T. Mukai, S. Kamado, Y. Kojima, K. Higashi, **2003**, *Mater. Trans.* 44, 463–467.
125 S. Yoshimoto, Y. Miyahara, Z. Horita, Y. Kawamura, **2006**, *Mater. Sci. Forum* 503–504, 769–774.
126 J. Cizek, I. Prochazka, B. Smola, I. Stulikova, R. Kuzel, Z. Matej, V. Cherkaska, R. K. Islamgaliev, O. Kulyasova, **2006**, *Mater. Sci. Forum* 503–504, 149–154.
127 L. L. Rokhlin, S. V. Dobatkin, T. V. Dobatkina, N. I. Nikitina, M. V. Popov, **2006**, *Mater. Sci. Forum* 503–504, 961–966.
128 S. H. Lee, Y. Saito, T. Sakai, H. Utsunomiya, **2002**, *Mater. Sci. Eng.* A325, 228–235.
129 J. K. Kim, H. K. Kim, J. W. Park, W. J. Kim, **2005**, *Scr. Mater.* 53, 1207–1211.
130 E. Cerri, P. Leo, **2005**, *Mater. Sci. Eng.* $A410^{-4}11$, 226–229.
131 P. K. Chaudhury, B. Cherukuri, R. Srinivasan, **2005**, *Mater. Sci. Eng.* A410–411, 316–318.
132 J. C. Werenskiold, H. J. Roven, **2005**, *Mater. Sci. Eng.* A410–411, 174–177.
133 P. Bassani, L. Tasca, M. Vedani, **2004**, *Nanomaterials by Severe Plastic Deformation* (eds.) M. J. Zehetbauer, R. Z. Valiev, Wiley-VCH, Weinheim, Germany, 145–150.
134 G. Krallics, Z. Szeles, I. P. Semenova, T. V. Dotsenko, I. V. Alexandrov, **2004**, *Nanomaterials by Severe Plastic Deformation* (eds.) M. J. Zehetbauer, R. Z. Valiev, Wiley-VCH, Weinheim, Germany, 183–189.
135 P. W. J. McKenzie, R. Y. Lapakov, P. F. Thomson, **2006**, *Mater. Sci. Forum* 503–504, 657–662.
136 S. Amadori, L. Pasquini, E. Bonetti, M. Cabibbo, C. Scalabroni, E. Evangelista, **2006**, *Mater. Sci. Forum* 503–504, 835–840.
137 M. Cabibbo, E. Evangelista, C. Scalabroni, E. Bonetti, **2006**, *Mater. Sci. Forum* 503–504, 841–846.
138 B. B. Straumal, B. Baretzky, A. A. Mazilkin, F. Philipp, O. A. Kogtenkova, M. N. Volkov, R. Z. Valiev, **2004**, *Acta Mater.* 52, 4469–4478.
139 Z. Horita, K. Ohashi, T. Fujita, K. Kaneka, T. G. Langdon, **2005**, *Adv. Mater.* 17, 1599.
140 K. Inoke, K. Kaneko, Z. Horita, **2006**, *Mater. Sci. Forum* 503–504, 603–608.

141 M. Muruyama, K. Hono, Z. Horita, **1999**, *Mater. Trans. – JIM* 40, 938–941.

142 G. A. Lopez, B. B. Straumal, W. Gust, E. J. Mittemeijer, **2004**, *Nanomaterials by Severe Plastic Deformation* (eds.) M. J. Zehetbauer, R. Z. Valiev, Wiley-VCH, Weinheim, Germany, 642–647.

143 M. M. Myshlyaev, A. A. Mazilkin, M. M. Kamalov, **2004**, *Nanomaterials by Severe Plastic Deformation* (eds.) M. J. Zehetbauer, R. Z. Valiev, Wiley-VCH, Weinheim, Germany, 734–739.

144 M. M. Myshlyaev, M. M. Kamalov, M. M. Myshlyaeva, **2004**, *Nanomaterials by Severe Plastic Deformation* (eds.) M. J. Zehetbauer, R. Z. Valiev, Wiley-VCH, Weinheim, Germany, 717–721.

145 N. Llorca-Isern, P. A. Gonzalez, C. J. Luis, I. Laborde, **2006**, *Mater. Sci. Forum* 503–504, 871–876.

146 I. V. Alexandrov, V. V. Latysh, S. I. Hong, S. N. Faizova, V. M. Polovnikov, **2006**, *Mater. Sci. Forum* 503–504, 515–520.

147 A. Vinogradov, K. Kitagawa, V. I. Kopylov, **2006**, *Mater. Sci. Forum* 503–504, 811–816.

148 A. Vinogradov, V. Patlan, Y. Suzuki, K. Kitagawa, V. I. Kopylov, **2002**, *Acta Mater.* 50, 1639–1651.

149 A. Vinogradov, Y. Suzuki, T. Ishida, K. Kitawaga, V. I. Kopylov, **2004**, *Mater. Trans.* 45, 2187–2191.

150 A. Vinogradov, T. Ishida, K. Kitagawa, V. I. Kopylov, **2005**, *Acta Mater.* 53, 2181–2192.

151 J. Wang, S. B. Kang, H. W. Kim, Z. Horita, **2002**, *J. Mater. Sci.* 37, 5223–5227.

152 J. Wang, S. B. Kang, H. W. Kim, **2004**, *Mater. Sci. Eng.* A383, 356–361.

153 M. Furukawa, Y. Ma, Z. Horita, M. Nemoto, R. Z. Valiev, T. G. Langdon, **1998**, *Mater. Sci. Eng.* A241, 122–128.

154 V. V. Stolyarov, E. A. Prokofiev, S. D. Prokoshkin, S. B. Dobatkin, I. B. Trubitsyna, I. Y. Khmelevskaya, V. G. Pushin, R. Z. Valiev, **2005**, *Phys. Met. Metall.* 100, 608–618.

155 S. D. Prokoshkin, I. Y. Khmelevskaya, S. B. Dobatkin, I. B. Trubitsyna, E. V. Tatyanin, V. V. Stolyarov, E. A. Prokofiev, **2005**, *Acta Mater.* 53, 2703–2714.

156 A. V. Sergueeva, C. Song, R. Z. Valiev, A. K. Mukherjee, **2003**, *Mater. Sci. Eng.* A339, 159–165.

157 I. Y. Khmelevskaya, I. B. Trubitsyna, S. D. Prokoshkin, S. V. Dobatkin, V. V. Stolyarov, **2004**, *Nanomaterials by Severe Plastic Deformation* (eds.) M. J. Zehetbauer, R. Z. Valiev, Wiley-VCH, Weinheim, Germany, 170–176.

158 T. Waitz, H. P. Karnthaler, R. Z. Valiev, **2004**, *Nanomaterials by Severe Plastic Deformation* (eds.) M. J. Zehetbauer, R. Z. Valiev, Wiley-VCH, Weinheim, Germany, 339–344.

159 T. Waitz, V. Kazykhanov, H. P. Karnthaler, **2004**, *Nanomaterials by Severe Plastic Deformation* (eds.) M. J. Zehetbauer, R. Z. Valiev, Wiley-VCH, Weinheim, Germany, 351–356.

160 V. G. Pushin, **2004**, *Nanomaterials by Severe Plastic Deformation* (eds.) M. J. Zehetbauer, R. Z. Valiev, Wiley-VCH, Weinheim, Germany, 822–828.

161 V. G. Pushin, R. Z. Valiev, Y. T. Zhu, S. D. Prokoshkin, D. V. Gunderov, L. I. Yurchenko, **2006**, *Mater. Sci. Forum* 503–504, 539–544

162 K. E. Inaekyan, S. D. Prokoshkin, V. Brailovski, I. Y. Khmelevskaya, V. Demers, S. V. Dobatkin, E. V. Tatyanin, **2006**, E. Bastarache, *Mater. Sci. Forum* 503–504, 603–608.

163 C. Y. Xie, Z. G. Fan, Z. H. Li, G. Q. Xiang, X. H. Cheng, **2006**, *Mater. Sci. Forum* 503–504, 1013–1018.

164 A. V. Korznikov, G. Tram, O. Dimitrov, G. F. Korznikova, S. R. Idrisova, Z. Pakiela, **2001**, *Acta Mater.* 49, 663–671.

165 C. Rentenberger, H. P. Karnthaler, R. Z. Valiev, **2004**, *Nanomaterials by Severe Plastic Deformation* (eds.) M. J. Zehetbauer, R. Z. Valiev, Wiley-VCH, Weinheim, Germany, 80–86.

166 A. V. Korznikov, O. Dimitrov, G. F. Korznikova, J. P. Dallas, S. R. Idrisova, R. Z. Valiev, F. Faudot, **1999**, *Acta Mater.* 47, 3301–3311.

167 W. Skrotzki, B. Klöden, R. Tamm, C.-G. Oertel, L. Wcislak, E. Rybacki, **2004**, *Nanomaterials by Severe Plastic Deformation* (eds.) M. J. Zehetbauer, R. Z. Valiev, Wiley-VCH, Weinheim, Germany, 303–308.

168 A. V. Korznikov, O. Dimitrov, G. F. Korznikova, J. P. Dallas, A. Quivy, R. Z. Valiev, A. Mukherjee, **1999**, *Nanostruct. Mater.* 11, 17–23.

169 S.-Y. Chang, K. S. Lee, S. K. Ryu, K.-T. Park, D. H. Shin, **2002**, *Mater. Trans.* 43, 757–761.

170 B. Q. Han, T. G. Langdon, **2005**, *Mater. Sci. Eng.* A410–411, 430–434.

171 R. Pippan, A. Vorhauer, F. Wetscher, M. Faleschini, M. Hafok, I. Sabirov, **2006**, *Mater. Sci. Forum* 503–504, 407–412.

172 R. K. Islamgaliev, W. Buchgraber, Y. R. Kolobov, N. M. Amirkhanov, A. V. Sergueeva, K. V. Ivanov, G. P. Grabovetskaya, **2001**, *Mater. Sci. Eng.* A319–321, 872–876.

173 I. Sabirov, R. Pippan, **2005**, *Scr. Mater.* 52, 1293–1298.

174 I. Sabirov, T. Schoeberl, R. Pippan, **2006**, *Mater. Sci. Forum* 503–504, 561–566.

175 X. Sauvage, F. Wetscher, P. Pareige, **2005**, *Acta Mater.* 53, 2127–2135.

176 T. Fujita, S. Nishimura, T. Fujinami, K. Kaneko, Z. Horita, David J. Smith, **2006**, *Mater. Sci. Eng.* A417, 149–157.

27
Bulk Nanocrystalline and Amorphous Magnetic Materials

Roland Grössinger and Reiko Sato Turtelli

27.1
Introduction

There exist nowadays different families of magnetic materials that are suited for technical applications, e.g.: soft magnetic materials, hard magnetic materials, magnetostrictive materials and magnetoelectric materials, as a new multifunctional type. In many cases the "amorphous" or "nanocrystalline" state brought an enhancement of the magnetic properties mainly based on a changed type of coupling. It is the aim of this work to explain the physical background and to summarize the most interesting materials in this area. Additionally, this work is focused on bulk materials, but primarily on cast samples, ribbons, powders, and covers single-phase nanocrystalline and two-phase nanocomposite magnetic materials.

All these materials are characterized by their magnetic properties that can be subdivided into intrinsic and extrinsic properties. Intrinsic properties are mainly defined by the chemical composition as well as by the crystal structure. These are: Curie temperature, saturation magnetization, magnetocrystalline anisotropy, magnetostriction, etc. Extrinsic properties are mainly defined by the microstructure (such as: grain size, grain boundaries, crystallographical phases). These are: hysteresis loop, domain structure, losses, etc. These properties are important for all kinds of technical applications. The appearance of an amorphous or nanocrystalline state influences both types of properties.

For differentiating the magnetic behavior with respect to soft or hard magnetic properties the magnetization as function of the applied field, i.e. the hysteresis loop is best suited, see Fig. 27.1.

In both cases the saturation magnetization should be as high as possible but for soft magnetic materials the coercivity is small (typically between 1 and 1000 A/m), whereas for permanent magnets, coercivity values of 1 MA/m or more are achieved. The area of the loop describes for soft magnetic materials the losses and, for hard magnetic materials it is proportional to the stored energy $(B \cdot H)_{\max} < B_r^2/4$. ($B_r$ is the remanence). The shape and the area of the loop depend on the microstructure, which depends on the amorphous or nanocrystalline state of soft and hard magnetic materials.

Bulk Nanostructured Materials. Edited by M. J. Zehetbauer and Y. T. Zhu

ISBN: 978-3-527-31524-6

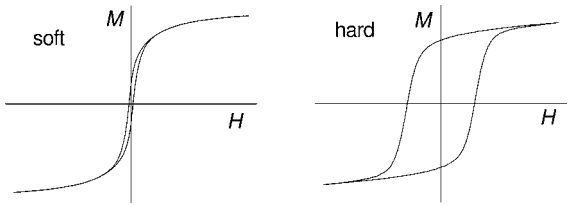

Fig. 27.1 Typical schematic hysteresis loop of a soft in comparison with a hard magnetic material.

27.2
Soft Magnetic Materials

New soft magnetic materials can be subdivided into: crystalline rapidly solidified materials, amorphous rapidly solidified materials and nanocrystalline materials. In the crystalline state the grain growth can be influenced by the quenching rate – if the quenching rate is very high nanocrystals (grains size between few nm and approximately 100 nm) or even an amorphous state can be achieved. The boundaries are not sharp because if a material is "truly" amorphous or nanocrystalline depends on the sensitivity of the method used for the characterization. Most of these materials are produced by a rapidly solidifying method.

Rapid solidification starts from the melt leading to a new state that can be amorphous, crystalline, nanocrystalline, metastable crystalline depending on the quenching rate and on the crystallization process. Applying a high quenching rate to a molten magnetic alloy can result into a material that presents generally new and interesting physical properties. Such materials are called "rapidly solidified". There exist different methods for producing metallic rapidly solidified materials. To form an amorphous state, the material must be cooled from the melting temperature T_m, to the glass-transition temperature T_g, without any crystallization. The cooling process must proceed fast enough from T_m down below T_g. Thus, the cooling time and the temperature range between T_m and T_g are the two most important factors for obtaining amorphous or nanocrystalline materials [1].

27.2.1
Rapidly Solidified Crystalline Materials

The main interesting crystalline rapidly solidified materials are Fe-Si with 6.5 wt% Si and Fe-Al-Si with Al (5–7 wt%) and Si (9–10 wt%), which is known as Sendust alloy. These compositions are chosen because the anisotropy and the magnetostriction of these materials are close to zero, which leads to very soft magnetic behavior. Therefore, the coercivity shows a minimum at this composition. These materials also have a high electrical resistivity. The disadvantageous is that the material becomes very brittle. This problem is partly overcome by rapidly quenching from the melt, where a small quantity of amorphous phase

Table 27.1 Physical properties of rapidly quenched Fe-6.5 wt%Si.

Property	Value
Density	7480 kg/m^3
Thermal conductivity (31 °C)	4.5 cal/m °C s
Specific heat (31 °C)	128 cal/°C kg
Thermal expansion coefficient (150 °C)	11.6×10^{-6}/°C
Electrical resistivity	82×10^{-8} Ωm
Tensile strength (ribbon 60 μm thick)	630 MPa
Saturation induction	1.8 T
Curie temperature	700 °C
Saturation magnetostriction	0.6×10^{-6}

can form among grains [2]. After a high-temperature annealing (above 1000 °C) one obtains large grains with a texture. In Table 27.1 the physical properties of Fe-Si with 6.5 wt% Si are summarized [3].

On the other hand, although Sendust alloy exhibits a low magnetostriction and the first-order anisotropy constant K_1 becomes nearly zero, a very high permeability, μ_{max} up to 130 000 and a rather low saturation polarization is obtained ($B_s = 0.89$ T) [4].

27.2.2
Amorphous Materials or Rapidly Quenched Glasses

Much progress in developing new soft magnetic materials was achieved in the last 20 years [see, e.g., 5]. Besides the well-known Fe-Si and the Fe-Ni alloys a new family of soft magnetic materials was discovered. These materials are based on amorphous alloys. Amorphous alloys are good candidates for soft magnetic materials because of the lack of crystal anisotropy and grain boundaries. The only sources of undesired anisotropies are shape anisotropy due to surface roughness and stress-induced anisotropy produced during the rapid quenching process. This is why amorphous materials became an established class of soft magnetic materials [6].

The general formula of amorphous alloys is $(\text{3d-metal})_{80}(\text{metalloid})_{20}$, where $\text{3d-metal} = \text{Fe, Co, Ni}$ and $\text{metalloid} = \text{B, Si, C}$, etc. The metalloid is necessary for lowering the melting point of the alloy, thus stabilizing the amorphous state. The absence of grains and grain boundaries lead to excellent soft magnetic properties [see, e.g., 7]. The easy substitution over a broad concentration range make these materials interesting from a basic point of view, but the excellent magnetic properties are also interesting for many applications [8]. The most promising systems here are Fe-Co-based amorphous alloys. Therefore many studies were already performed on these materials, describing the basic magnetic properties such as the concentration and temperature dependence of the magnetization, magnetic relaxation, the Curie temperatures, etc. [9–14], the crystallization behavior [15], the magnetostriction in these systems [13–16], the

induced anisotropy [13, 17] etc. These amorphous materials, which are also known as "rapidly quenched glasses" are generally obtained as thin ribbons (thickness 20–50 μm) by a melt-spinning technique [18, 19] or as wires (thickness 80–120 μm) by the in-water-quenching technique [20].

27.2.3 Bulk Amorphous Alloys

Bulk amorphous alloys or bulk metallic glasses are a subclass of metallic glasses, which can be prepared at relatively slow cooling rates, less than 10^3 K s^{-1}. Amorphous materials with a wide supercooled-liquid region, which is defined by the difference between the glass-transition temperature T_g and the crystallization temperature T_x, allowing the production of rods and plates with minimum dimensions of at least a few mm in an amorphous state [21]. In these materials cast to larger dimensions, the influence of the surface is reduced [22], and the existence of a wide supercooled-liquid region allows annealing at or above the glass-transition temperature in the supercooled liquid state, and nearly complete stress relief can be achieved [23].

There is great interest in the preparation of the bulk metallic glasses by consolidating amorphous powder precursors by virtue of their ability to be formed by injection molding. The main advantage of this technique is that it poses no limit on the size and shape of the amorphous product. The findings of several bulk amorphous alloys have enabled the derivation of three empirical rules for the achievement of large glass-forming ability [24–27]: i) multicomponent alloy systems consisting of more than three elements; ii) significantly different atomic size ratios above 12% among the constituent elements, and iii) large negative heats of mixing among the elements.

Prior to 1993 there were no bulk amorphous alloys developed that exhibit ferromagnetism at room temperature. In 1995 Inoue and coworkers reported the first results on ferromagnetic bulk metallic glasses: alloys containing a large number of elements such as: Fe–(Al, Ga)–(P, C, B, Si) [24] and Co–Cr–(Al, Ga)–(P, B, Si) [25].

Fe-based amorphous alloys in the system Fe-(Al, Ga)-(P, C, B) were found to exhibit a large glass-forming ability enabling the production of bulk materials up to a diameter of 2 mm by copper-mold casting [28], as well as of thick amorphous ribbons of more than 50 μm thickness by melt spinning [28]. Mizushima et al. [29] have reported that the replacement of *P* by 1–2 at% Si in $Fe_{72}Al_5Ga_2P_{11-x}C_6B_4Si_x$ causes an enlargement of the supercooled-liquid region, thereby increasing the thermal stability and leading to improved soft magnetic properties. They found that the soft magnetic properties at a ribbon thickness larger than 70 μm are improved as well by replacement of 1–2 at% Si, although the optimum magnetic properties occur for ribbons of a thickness of only around 40–50 μm. Heat treatment of amorphous ribbons of the Fe-(Al, Ga)-(P, C, B, Si) system leads to an obvious decrease of the coercive field, but this type of ribbons is characterized by some brittleness even in the as-cast state. Therefore, Sato Turtelli

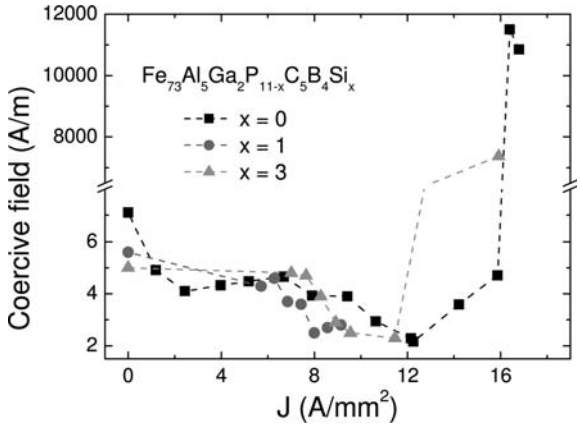

Fig. 27.2 Coercive field of $Fe_{73}Al_5Ga_2P_{11-x}C_5B_4Si_x$ ($x=1, 3$) as a function of current density (Joule-heating process) measured at room temperature [30].

et al. [30, 31] investigated the effect of annealing on magnetic and structural properties in amorphous $Fe_{73}Al_5Ga_2P_{11-x}C_5B_4Si_x$ ($x=1, 3$) ribbons, with a thickness about 40 μm, using a Joule-heating technique. Annealing generally reduces local stresses causing a reduction of the coercivity in soft magnetic amorphous materials. Figure 27.2 shows the current-density dependence of the coercivity measured at room temperature in these amorphous alloys.

$Fe_{65.5}Cr_4Mo_4Ga_4P_{12}C_5B_{5.5}$ shows, together with excellent soft magnetic behavior, a very high mechanical strength and a high resistance against corrosion that may be important for application as magnetic parts in valves, clutches, or relays [e.g., 32].

It is possible to cast such bulk amorphous alloys directly to use them as components of magnetic cores or to make dense powder compacts at a moderate pressing temperature between the glass-transition temperature and the crystallization temperature [33, 34]. Additionally, the low processing temperature allows the preparation of composites with temperature-sensitive additives such as $SmFe_2$ [35].

27.2.4
Nanocrystalline Soft Magnetic Materials

Nanocrystalline soft magnetic materials have attracted considerable interest in the last 20 years because of their excellent magnetic properties [36, 37]. These properties are different from those in amorphous and bulk soft magnetic materials because of grain sizes and surface/interface effects in the nanocrystalline state.

Soft magnetic nanocrystalline materials are produced by annealing amorphous ribbons at an optimum temperature for an optimum annealing time

thus forming nanoparticles embedded in an amorphous matrix. These nanocrystalline materials exhibit excellent soft magnetic properties due to the exchange coupling between nanoparticles by means of the magnetic amorphous phase. The softening occurs because the grain size is smaller than the magnetic exchange length, leading to an averaging of the magnetic anisotropy of the nanocrystals, consequently to a low value of the effective anisotropy [36, 37]. Macroscopically this exchange coupling causes a strong reduction of the coercivity and an increase of the permeability as described in the following formulas:

$$H_c = p_c \frac{K_1^4 \cdot D^6}{J_S A^3} \tag{27.1}$$

$$\mu_i = p_\mu \frac{J_S^2 A^3}{\mu_0 K_1^4 D^6} \tag{27.2}$$

J_S is the average saturation polarisation, K_1 the anisotropy constant; D the grain size, A the exchange stiffness constant, p_c and p_μ are dimensionless prefactors close to unity. The grain-size dependence of the coercivity of soft magnetic materials is shown in Figure 27.3.

The first soft magnetic nanocrystalline alloy that appears in literature is $Fe_{73.5}Cu_1Nb_3Si_{13.5}B_9$, which was developed by the Hitachi Metals Company [38]. The composition is mainly $Fe_{73.5}(Si, B)_{22.5}$ where the addition of Cu and Nb nucleates and hinders the grain growth, respectively, thus leading to crystals with grain sizes of about 10–20 nm [39]. This alloy and similar compositions were studied intensively by several groups (e.g. see [40–45]).The material consists of small α-Fe-Si grains that are embedded in an amorphous matrix, as shown in Fig. 27.4.

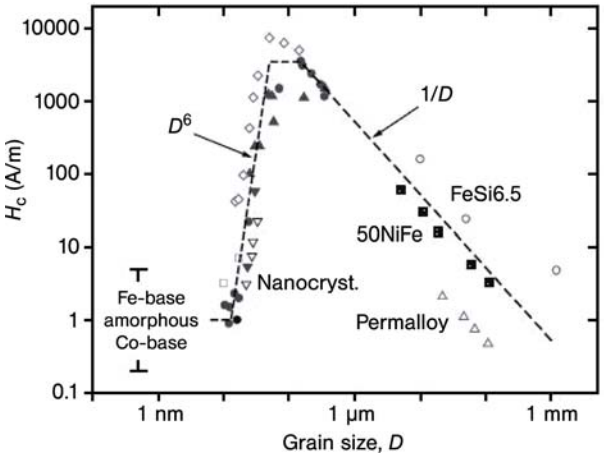

Fig. 27.3 Coercivity H_c versus grain size d for various soft magnetic alloys [36, 37].

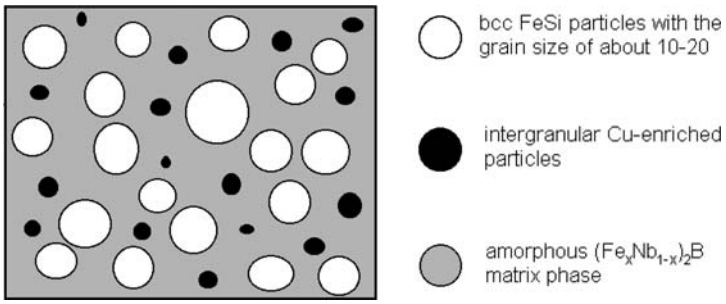

Fig. 27.4 Sketch of nanocrystalline FINEMET microstructure [40].

At elevated temperatures (above the magnetic-ordering temperature of the amorphous phase), where the amorphous phase becomes magnetically disordered, the decoupling between the grains finishes, leading to a magnetic hardening [44, 46]. Here especially interesting is a variation of the Si or Nb concentration. By varying these concentrations one can influence the Curie temperature, magnetization and the magnetostriction of the nanocrystalline alloy [47–50].

This kind of nanocrystalline material is already industrially available, such as in Japan under the name FINEMET and in Germany under the Trade name VITROPERM, which is used for tape wound cores or for magnetic amplifiers.

The second nanocrystalline system that was investigated is based on Fe-rich Fe-Zr-Cu-B alloys [51–53]. The magnetic-ordering temperature of the amorphous phase is between 50 and 100 °C and nanocrystals are formed of α-Fe. As in FINEMET, the exchange coupling between the nanocrystals leads to excellent soft magnetic properties. The Fe-Zr-Cu-B system is more difficult to produce (e.g. oxidation) which is technically disadvantageous. During the production a protective gas is necessary because of the highly reactive Zr. However, it exhibits a higher saturation magnetization in the nanocrystalline state than that of FINEMET and, from the experimental point of view, it is a simpler system due to the nanocrystals being only α-Fe. The existence and amount of nanocrystalline pure α-Fe is much easier to determine, e.g. with the Mössbauer effect, than the Fe-Si in FINEMET [54]. Due to the low ordering temperature (close to room temperature) of the amorphous phase, interesting investigations on a system of (partly) decoupled nanocrystals above this temperature are possible.

A recent review on soft magnetic nanocrystalline alloys gives the following as a general chemical composition for these materials [55]:

$$\begin{pmatrix} \text{Fe} \\ \text{Co} \\ \text{Ni} \end{pmatrix}_a \begin{pmatrix} \text{Ti, V, Cr} \\ \text{Zr, Nb, Mo} \\ \text{Hf, Ta, W} \end{pmatrix}_b \begin{pmatrix} \text{B, C} \\ \text{Al, Si, P} \\ \text{Ga, Ge} \end{pmatrix}_c \begin{pmatrix} \text{Cu} \\ \text{Ag} \\ \text{Au} \end{pmatrix}_d$$

with $a = 60$–90; $b = 2$–8; $c = 8$–31 and $d = 0$–1. This expression allows us to explore possibilities for new nanocrystalline alloys.

27.3 Hard Magnetic Materials

In the last 30 years dramatic improvements of the quality of permanent magnets were achieved. The reason is that intermetallic compounds between 3d–4f elements (Fe, Co-Sm, Nd) allows us to combine a high saturation magnetization at room temperature and a high Curie temperature with the unique high magnetocrystalline anisotropy of the 4f-metals. Modern permanent magnets are based on compounds such as: $SmCo_5$, Sm_2Co_{17} and $Nd_2Fe_{14}B$. These materials were long time only produced using a standard sintering technique (combined with a sophisticated heat treatment). However, later, applying the melt-spinning technique, high remanence values together with reasonable large H_c values on melt-spun Pr–Fe–B(Si) and Nd–Fe–B alloys with nanoscale grain sizes after melt spinning, or after crystallization were obtained [e.g., 56–59]. Thus, this discovery opened new horizons for permanent magnetic materials research and production. It is well known that the coercivity H_c, of permanent magnets increases with decreasing particle size, reaching a maximum at the single domain size, and then decreases again for ultrafine particles due to the thermal effect becoming zero at the superparamagnetic state.

Generally, the single-domain particle size is a fraction of a micrometer for hard magnetic materials with high anisotropy fields and reasonably high magnetization. For uncoupled single-domain particles the coercivity will reach its maximum value. However, for grain sizes in the nanometer range a rather low coercivity has to be expected. It was found that the remanence of isotropic hard magnetic materials with nanosized grains, becomes larger than that of uniaxial, uncoupled grains for which 50% of the saturation magnetization is expected. Later, nanocrystalline hard magnets have been prepared by a rapidly solidified method using other techniques, such as, e.g., by a mechanical alloying method with subsequent annealing. In late 1996, new bulk amorphous magnets or bulk metallic glasses were announced. In particular, a bulk metallic glass rod with a diameter between 1 and 12 mm of the composition Nd-(Fe,Co)-Al with appreciable coercivity at room temperature was found [e.g., 60–63].

27.3.1 Nanocrystalline Hard Magnetic Materials

Similar to amorphous materials various production techniques were established to produce nanocrystalline hard magnets, such as rapid solidification with different techniques: melt spinning, vapor deposition [e.g., 64–67], atomization [68], and mechanical alloying with subsequent annealing [69–73] and also direct powder production such as spark erosion. By melt spinning or rapid quenching, the nanocrystalline state can be obtained directly or after a heat treatment of an over-quenched material [74]. Additionally, sputtering techniques have also been used to prepare nanosized Sm-Co alloys [75, 76] and Co-Pt and Fe-Pt alloys for high-density recording media [77, 78].

The usual processing techniques to synthesize bulk nanocomposite magnets are melt spinning and mechanical alloying. Recently, some bulk nanocrystalline materials were also produced by severe mechanical deformation [79–81].

In contrast to soft magnetic materials, in hard magnetic nanocrystalline materials the magnetic exchange length is smaller than the grain size but still comparable. This leads to a remanence enhancement, which makes these materials interesting for applications. The remanence enhancement results in an increase of the maximum energy product $(BH)_{max}$ without a magnetic alignment of the grains. In relatively low fields and in any direction these materials can be magnetized, because they are crystallographically isotropic.

For nanocrystalline material the way in which the small grains couple is of great importance for the understanding of the exchange enhancement. For magnetic nanosized grains, three different exchange lengths have to be considered:
i) exchange length due to an external field:

$$l_H = \sqrt{\frac{2A}{H \cdot \mu_0 \cdot M_S}} \tag{27.3}$$

ii) exchange length due to the crystal energy:

$$l_C = \sqrt{\frac{A}{K}} \tag{27.4}$$

iii) exchange length due to stray fields:

$$l_s = \sqrt{\frac{2\mu_0 A}{(\mu_0 \cdot M_S)^2}} \tag{27.5}$$

M_S is the average saturation magnetisation, K the anisotropy constant; A the exchange stiffness constant, μ_0 the vacuum permeability. It depends on the considered material as to which exchange length is more important, however, for hard magnetic material the second type is the most important one, whereas for soft magnetic materials the stray-field contribution is more relevant. It turns out that the ratio between the mean grain diameter $\langle D \rangle_{grain}$ and the range of the exchange interaction given by the exchange length l_C mainly controls the magnetization distribution.

Most investigations were performed on R-Fe-B (R = Nd, Pr) based samples. This isotropic nanocrystalline material can be classified into three different ranges of compositions:

i) low R content: in this case nanocrystalline $R_2Fe_{14}B$ grains are mixed with nanocrystalline soft magnetic α-Fe grains or Fe_3B, if the amount of B is high enough. Here, an even higher remanence enhancement than for stochiometric R-Fe-B occurs due to polarization of the soft magnetic phase

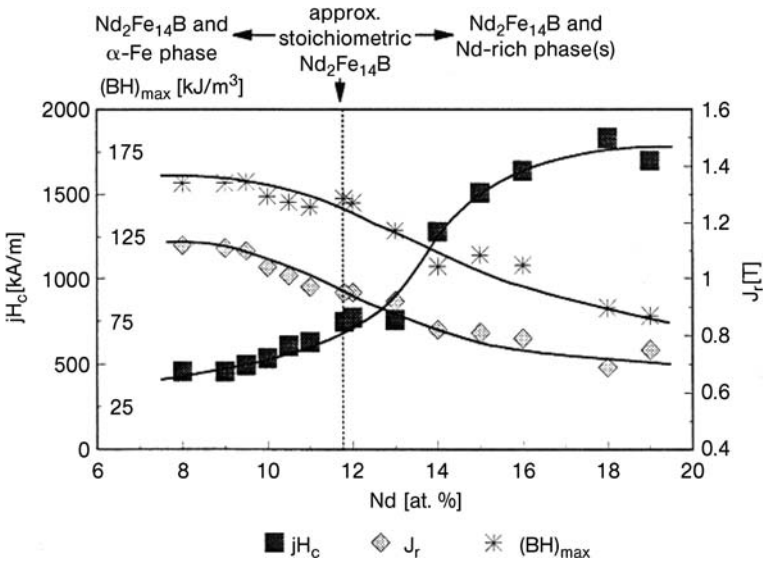

Fig. 27.5 Dependence of the coercivity ${}_jH_c$, the remanence J_r and the energy product $(BH)_{max}$ on the Nd content in a Nd-Fe-B alloy, after Davies et al. [82].

with a higher magnetic moment. These nanocrystalline materials are called nanocomposite magnets.

ii) stochiometric R-Fe-B: in this case, the pure exchange coupling between the nanocrystalline $R_2Fe_{14}B$ grains can be studied.

iii) high R content: the nanocrystalline $R_2Fe_{14}B$ grains are isolated by a R-rich, at room temperature non-magnetic, phase. This material exhibits a higher coercivity.

Davies et al. [82] carefully investigated the effect of varying the Nd content on the magnetic properties of nanocrystalline Nd-Fe-B magnets, as shown in Fig. 27.5.

27.3.1.1 **Nanocomposite Magnets**

The nanocomposite materials have a lower amount of the expensive rare-earth part than the single-phase hard magnetic materials. The reduction of the rare-earth-containing phase can be down to 40%. Therefore, from a commercial point of view the nanocomposites are an interesting competitor to the conventional rare-earth magnets.

In nanocomposites the magnetization of the soft magnetic phase should be higher than that of the hard magnetic phase in order to be attractive for technical applications. In this case, the magnetic moment of the soft magnetic grains will be polarized in the average direction of the surrounding magnetic moment of the hard magnetic grains, leading to a further enhancement of the rema-

nence. Therefore, a higher $(BH)_{max}$ would be expected in exchange-coupled magnets as compared to the conventional isotropic uncoupled magnets.

It should be noted that for α-Fe with cubic structure, the ratio of remanence to saturation polarization is, for isotropic noninteracting grains [83]:

$$\frac{6}{\pi\sqrt{2}}\operatorname{arctg}\frac{1}{\sqrt{2}} \approx 0.839 \tag{27.6}$$

Taking into account the stray field between α-Fe grains, the remanence to saturation ratio becomes smaller and can approach 0.5. Therefore, to examine if an enhanced remanence is due to interaction between the hard magnetic grains with uniaxial symmetry (hexagonal or tetragonal) and soft magnetic α-Fe grains with cubic structure, the ratio remanence to saturation has to exceed as an upper limit the theoretical one based on a simple addition of the two contributions of noninteracting grains as shown in the following equation:

$$\frac{J_r^{tot}}{J_s^{tot}} = \frac{1}{J_s^{tot}}\left(v_H\frac{1}{2}J_s^H + (1-v_H)\frac{6}{\pi\sqrt{2}}\operatorname{arctg}\left(\frac{1}{\sqrt{2}}\right)J_s^S\right) \tag{27.7}$$

where J_r^{tot} is the total value of remanence, J_s^{tot} the total value of saturation polarisation and, v_H is the volume fraction of the hard magnetic grains, J_s^H is the saturation polarization of the hard magnetic grains and J_s^S is saturation polarization of the soft magnetic grains.

To examine from the micromagnetic point of view how the polarization of the soft magnetic grains occurs, the different energy contributions have to be studied. If the soft magnetic grains are of several hundred nanometers in size, then the magnetic state would be determined by a competition between the stray field energy and the exchange energy ($K4\mu_0/J_s^2$ is much smaller than 1). But when the grains become smaller (less than 50 nm) the stray-field energy seems to be negligible. In this case even exchange coupling between the nanocrystalline soft magnetic grains has to be assumed. One example of this behavior are nanocrystalline soft magnetic materials. Their excellent soft magnetic properties are understood from an averaging of their anisotropy constant due to an exchange coupling of several grains. Here, the stray-field energy has more influence and exchange coupling is given by l_s. l_c is in this case much smaller than l_s. This can also be understood by the fact that stray field energy is a long-range interaction with a classical dipolar character, whereas exchange coupling is a short-range interaction.

The exchange hardening of the soft magnetic phase by the hard magnetic phase can be understood if the exchange coupling between the soft and hard magnetic grains acts as an exchange stiffness of the soft magnetic spins. Kneller and Hawig [84] developed a 1D model to describe how the exchange hardening occurs. The soft phase is effectively hardened by the magnetocrystalline anisotropy of the hard phase, because the large magnetocrystalline anisotropy results in a large domain-wall energy density for the hard phase.

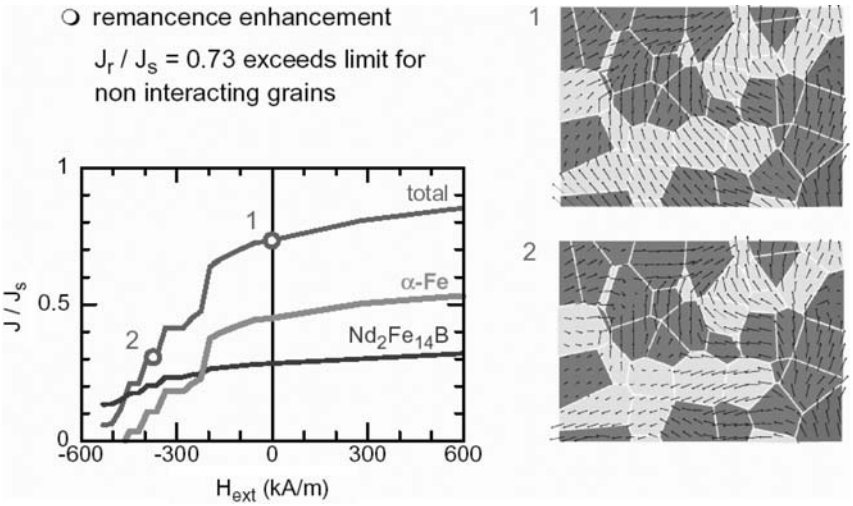

Fig. 27.6 FEM-simulation for a nanocomposite consisting of 10-nm-sized $Nd_2Fe_{14}B$ grains (50%) together with soft magnetic α-Fe (50%) [85].

Essentially the same process is described in a numerical model [85] for soft magnetic grains embedded in a hard magnetic matrix. Figure 27.6 shows here as an example the results of such a FEM-simulation of the microstructure (FEM = finite element method; numerical method to solve electromagnetic problems) performed for a nanocomposite consisting of $Nd_2Fe_{14}B$ grains together with soft magnetic α-Fe, which delivers as a result the demagnetizing curve, indicating remanence enhancement.

Several nanocomposite magnet systems such as: $R_2Fe_{14}B/Fe$, $R_2Fe_{14}C/Fe$ (R = Nd, Pr), $Sm_2Fe_{17}C_X/Fe$ have been extensively studied by Hadjipanayis and coworkers [86]; $Nd_2Fe_{14}B/Fe_3B$ by Coehoorn et al. [87]; $Pr_2Fe_{14}B/Fe$ and $Nd_2Fe_{14}B/Fe$ by our group [88–90], where a significant enhancement of the absolute remanence was found.

An interesting behavior of exchange-coupled magnets is the enhancement of Curie temperature of the hard phase due to the exchange-coupling effect. Lewis et al. [91] and Dahlgren et al. [88] have observed an enhancement in the Curie temperature of the $R_2Fe_{14}B$ phase in $R_2Fe_{14}B/Fe$ nanocomposite magnets. The enhancement in Curie temperature can result from the penetration of the exchange field of the higher Curie temperature (soft magnetic) phase into the adjacent lower Curie temperature (hard magnetic) phase.

The exchange coupling is strongly temperature dependent, and because of this, in some systems the two phases become coupled or decoupled at low temperatures depending on the composition and the magnetic properties of the nanocomposite magnets [e.g., 90].

27.3.1.1.1 Temperature Dependence of Anisotropy Field of Pr-Fe-B Nanocomposite Magnets

The anisotropy field H_A is an intrinsic property of a magnetic material and defined as the field necessary to rotate the magnetization vector from a hard crystallographic direction to an easy direction. A high uniaxial anisotropy is necessary for a material with a high coercivity. It is not an easy task to determine the anisotropy field in these intrinsic isotropic samples. In addition, the strong magnetic exchange interaction among nanocrystallites makes the measurements even more difficult. In this respect, the singular point detection (SPD) technique [90] provides a unique method in determining directly the anisotropy field of isotropic samples. The magnetic easy axes of the grains of a polycrystalline material are distributed over all possible directions. Now that grains where the easy axis is perpendicular to the external field causes a (nearly) linear increasing $M(H)$ curve up to the field where the anisotropy field H_A is achieved. There a kink becomes visible which can be measured as a singularity in d^2M/dH^2 exactly at $H = H_A$. This method allows to determine the anisotropy field. In Fig. 27.7 the temperature dependencies of the anisotropy field measured for $Pr_9Fe_{85}B_6$, $Pr_{11.76}Fe_{82.36}B_{5.88}$ and $Pr_{18}Fe_{76}B_6$ are shown [90].

It is worthwhile to note that the anisotropy field measured by using the SPD technique corresponds only to that of the hard magnetic phase. In the case of $Pr_9Fe_{85}B_6$, in which $Pr_2Fe_{14}B$ and α-Fe phases are formed, only the $Pr_2Fe_{14}B$ phase is responsible for the measured anisotropy field values H_A.

The reduction of the anisotropy field in the nanocrystalline $Pr_{12}Fe_{14}B$ grains is a strong indication of the presence of magnetic exchange interactions. From Fig. 27.7, the systematic decrease of $H_A(T)$ with increasing coupling between the grains, going from a too high Pr content (18% Pr) to stoichiometric sample (12% Pr), then to a low Pr content material (9% Pr), becomes clearly visible for higher temperatures. For lower temperatures a decoupling of the grains occurs due to the increase of anisotropy with decreasing temperature, causing equal

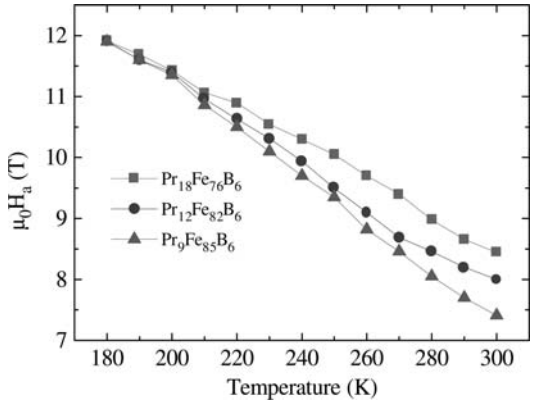

Fig. 27.7 Temperature dependence of the anisotropy field for hot-pressed mechanically alloyed Pr-Fe-B [90].

values of H_A for all three samples. This is also a proof that the differences in H_A as measured at room temperature are not a result of a disturbed surface but really due to exchange coupling.

27.3.1.1.2 Temperature Dependence of Magnetization and Remanence of Nanocomposites R-Fe-B (R = Pr, Nd)

From the measurements of the hysteresis loops, the coercivity and the remanence J_r are obtained. The saturation polarization J_S is determined by applying the law of approach to saturation. Figure 27.8 shows the temperature dependence of the saturation polarization, the remanence and the ratio J_r/J_s of the samples $Pr_9Fe_{85}B_6$, $Pr_{11.76}Fe_{82.36}B_{5.88}$ and $Pr_{18}Fe_{76}B_6$. Except for the sample with the highest Pr concentration, a decrease of J_r/J_S with decreasing temperature was found. This decrease indicates a decoupling due to the increase of the anisotropy at low temperatures (see Fig. 27.8). It is worth noting that for the $Pr_{18}Fe_{76}B_6$ sample, a J_r/J_s of about 0.5 was found for the whole temperature range, indicating that the grains should be decoupled due to the existence of a nonmagnetic Pr-rich phase.

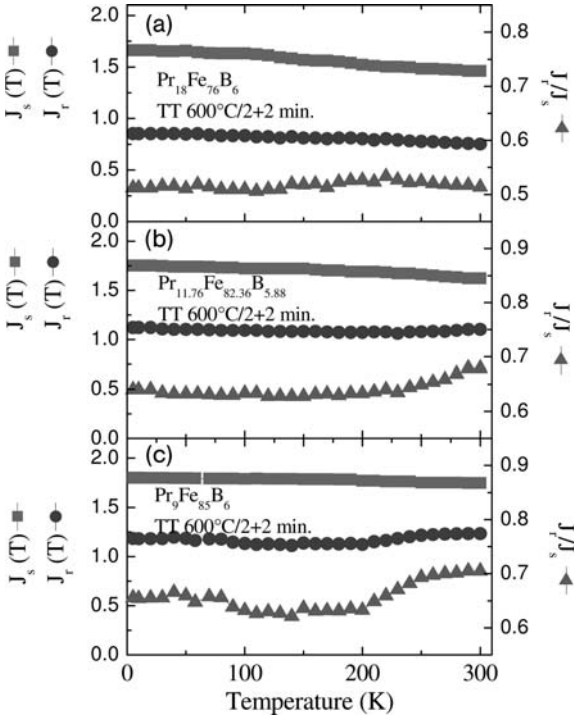

Fig. 27.8 Temperature dependence of the saturation polarization J_s, the remanence J_r and the ratio J_r/J_s for nanocrystalline mechanically alloyed: (a) $Pr_{18}Fe_{76}B_6$, (b) $Pr_{11.76}Fe_{82.36}B_{5.88}$ and (c) $Pr_9Fe_{85}B_6$ [90].

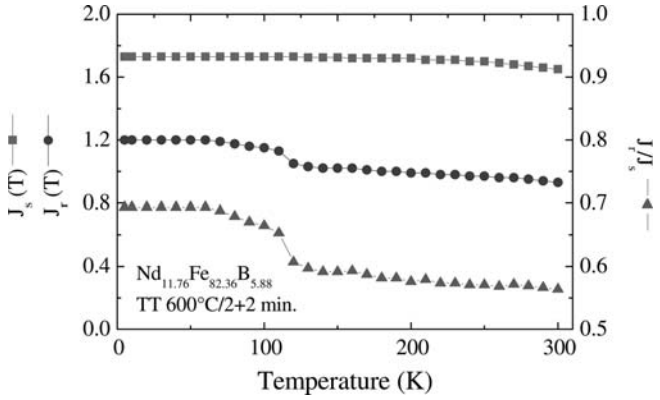

Fig. 27.9 Temperature dependence of the saturation polarization J_s, the remanence J_r and the ratio J_r/J_s for rapidly quenched nanocrystalline $Nd_{11.76}Fe_{82.36}B_6$ [90].

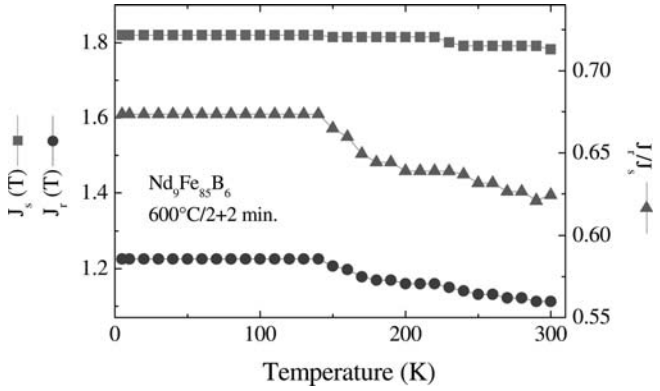

Fig. 27.10 Temperature dependence of the saturation polarization J_s the remanence J_r and the ratio $J_r/J_s$for rapidly quenched nanocrystalline $Nd_9Fe_{85}B_6$ [90].

In order to show a comparison, in Figs. 27.9 and 27.10 the same dependencies for rapidly solidified $Nd_{11.76}Fe_{82.36}B_6$ and $Nd_9Fe_{85}B_6$, in a nanocrystalline state, are shown. In understochiometric material, as in $Pr_9Fe_{85}B_6$, the measured ratio remanence to saturation polarization at room temperature clearly exceeds 0.5, showing also exchange-coupled grains. However, large ratio values were found for temperatures lower than 135 K. These large values are related to the spin reorientation (*c*-axis to easy cone) that occurs in $Nd_2Fe_{14}B$. For temperatures lower than 135 K, an easy cone is formed due to a reduction and change of sign of the first-order anisotropy constant.

27.3.1.1.3 Temperature Dependence of the Coercivity

Generally, the character of the temperature dependence of the coercivity in exchange coupled material is not significant (see Fig. 27.11). However, plotting the temperature dependence of the ratio between the coercivity and the anisotropy field, as shown in Fig. 27.12, the uncoupled sample (18% Pr) shows an usual high ratio for microcrystalline magnets of about 0.3. Due to the real microstructure only a part of the anisotropy field of a uniaxial material can be used for the coercivity. On the other hand, the exchange-coupled samples exhibit a significantly lower ratio, suggesting that the reduction of coercivity is due to the interaction between nanograins.

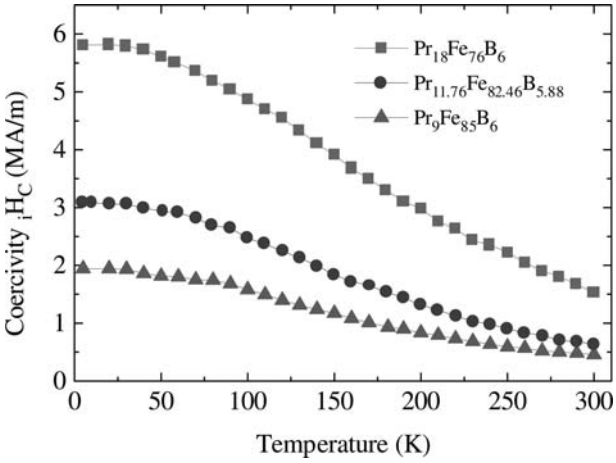

Fig. 27.11 Temperature dependence of the coercivity measured on mechanically alloyed Pr-Fe-B samples [90].

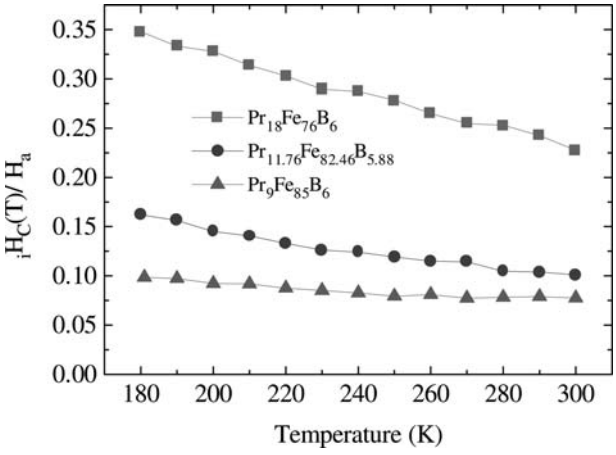

Fig. 27.12 Temperature dependence of the ratio coercivity to anisotropy field for mechanically alloyed nanocrystalline Pr-Fe-B [90].

27.3.1.2 Single-phase Nanocrystalline Magnets

In the 1980s, rapidly quenched single-phase rare-earth intermetallic compounds were used (initially $Nd_2Fe_{14}B$ compound) to obtain new anisotropic phases for permanent magnets by simply crystallizing the amorphous precursor. In fact, the coercivity of $Nd_2Fe_{14}B$ single-phase magnets produced by rapid quenching, which allows one to vary the grain size, can exhibit a higher coercivity than that of corresponding bulk magnets, especially sintered magnets. For example, melt-spun $Nd_2Fe_{14}B$ samples can easily attain coercivities beyond 15 kOe, while the coercivity of corresponding sintered Nd-Fe-B magnets is below 10 kOe [86]. Generally, the higher anisotropic material corresponds to a larger coercivity. In $Tb_2Fe_{14}B$ and $DyFe_{14}B$ with $H_A = 220$ and 150 kOe, respectively, coercivities in excess of 60 kOe have been reported [92]. Later, high-performance nanograined Sm_2Co_{17}, $PrCo_5$-based, YCo_5-based powders have been obtained by mechanical milling [93–96].

It is worth mentioning that although bulk YCo_5 exhibits a strong *c*-axis uniaxial anisotropy ($H_A \sim 130$ kOe), only rather low coercivity values could be obtained by traditional production methods [97]. The reported maximum value is only 2 kOe [98]. However, in powders with nanograins, produced by mechanical milling and subsequent convenient annealing, an improvement of the coercive field of a factor 8 could be achieved [95, 96]. Generally, in nanocrystalline single-phase magnets exchange coupling between grains enhancing the remanence can be expected.

27.3.2
Nd-(Fe,Co)-Al – a Hard Magnetic Amorphous System?

In 1996 Inoue and coworkers [60] announced the development of rods of bulk metallic glasses (1–12 mm diameter) of a $Nd_{30}Fe_{60}Al_{10}$ alloy with an appreciable coercive field at room temperature. This and related alloys modified by Co, have subsequently generated considerable interest of both applied and fundamental nature for other researchers including ourselves [63, 99–106], because the magnitude of this reported coercivity, up to 0.4 T at room temperature is an apparent contradiction of the conventional understanding of the relationship between structure and coercivity in amorphous materials. Both a very large anisotropy field and a very strong domain wall-pinning mechanism are required to account for the observed high coercivity. While the random anisotropy model [107] may account for the anisotropy field, the nature of the pinning sites in an amorphous material was unclear. Inoue et al. [108] have speculated that these bulk metallic glasses possess short-range order that confers coercivity. Other researchers [e.g., 61] have postulated the idea that ferromagnetic single-domain clusters are formed and they are responsible for the large coercivity [e.g., 62]. According to our point of view, the strong pinning model (a general coercivity model that describes the interaction of domain walls with pinning centers quantitatively) can be used to explain the coercivity mechanism of rapidly quenched ribbons and bulk Nd-(Fe,Co)-Al glasses. In these systems this model can de-

scribe the temperature dependence of the observed coercivity very well [63]. Electron microscopy investigations on rapidly quenched $Nd_{60}Fe_{30}Al_{10}$ ribbons showed precipitation of small crystalline nanoparticles of Nd-rich phases [103], which can act as pinning centers.

27.3.2.1 Magnetic Properties of Melt-spun $Nd_{60}Fe_{30}Al_{10}$ and $Nd_{60}Fe_{20}Co_{10}Al_{10}$ Alloys at 300 K

Due to the existence of precipitation of Nd-rich nanoparticles embedded in amorphous Nd-(Fe,Co)-Al, we can consider melt-spun Nd-Fe,Co-Al as a "quasi-amorphous" system. In the as-cast state, the microstructure, the coercive field (H_c) and the Curie temperature (T_C) are strongly dependent on the quenching rate (QR) and/or the production method. Typical hysteresis loops measured on as-cast ribbons and bulk materials (prepared by copper-mold casting) are shown in Fig. 27.13. The coercive field of ribbons and bulk alloys are 0.038 and 0.29 T, respectively. However, the magnetization at 2 T is very small. Generally at room temperature, the coercive field of melt-spun ribbons increases with the thickness, becoming comparable to that of bulk material. Additionally, the magnetization, M, and H_c show a strong time dependence [100], which is a consequence of domain-wall pinning. Figure 27.14 shows the hysteresis loops of melt-spun $Nd_{60}Fe_{30}Al_{10}$ measured at different field sweep rates of the applied field dH/dt.

The existence of the Nd-rich fine grains also becomes visible in the temperature dependence of various magnetic properties such as: coercive field [63], ac–susceptibility [104, 105], magnetostriction [106], where close to the magnetic-ordering temperature of the Nd-rich phase an anomaly was found. Additionally, the shape of the hysteresis loop below this temperature is typical of the existence of two magnetic phases [e.g., 63].

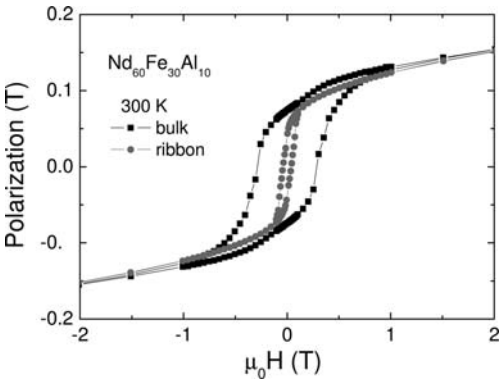

Fig. 27.13 Hysteresis loops of melt-spun ribbon and copper-mold bulk of $Nd_{60}Fe_{30}Al_{10}$ measured at 300 K.

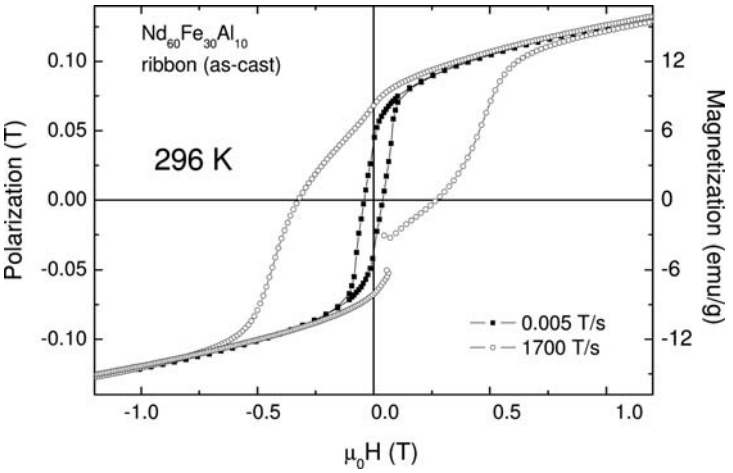

Fig. 27.14 Hysteresis loops of melt-spun $Nd_{60}Fe_{30}Al_{10}$ measured at $dH/dt = 0.005$ and 1700 T/s [100].

27.3.2.2 Temperature Dependence of Magnetic Properties of Melt-spun $Nd_{60}Fe_{30}Al_{10}$ and $Nd_{60}Fe_{20}Co_{10}Al_{10}$ Alloys

The temperature dependence of the coercive field, $H_c(T)$, for all samples investigated increases with decreasing temperature. Close to 70 K a maximum appears, where the coercive fields reach values between 2.5 and 5 T, depending on the preparation method and annealing procedure. Below this temperature, a Nd-rich crystalline phase becomes magnetically ordered. Then this phase behaves magnetically soft, which causes this maximum in $H_c(T)$ and then a decrease of the coercive field at low temperatures (see Fig. 27.15).

Assuming a region where the intrinsic magnetic properties can be considered constant, the strong-pinning model describes the coercive field H_c as given by [63]:

$$\sqrt{H_c} = \sqrt{H_0} - \sqrt{H_0}\left(\frac{\ln\frac{\tau}{\tau_0}k_B}{4bf}\right)^{2/3} T^{2/3} \tag{27.8}$$

where H_0 is the critical field in the absence of thermal activation, k_B is the Boltzmann constant, T the absolute temperature, τ is the time duration of measurement τ_0 is a time constant of order 10^{-7}–10^{-13} s and f is the maximum restoring pinning force from a single pin and $4b$ is the wall width. Plotting $(\mu_0 H_c)^{1/2}$ as a function of $(T)^{2/3}$ obtained for bulk $Nd_{60}Fe_{20}Co_{10}Al_{10}$ samples (Fig. 27.16), shows a very good agreement between the above equation and experimental data.

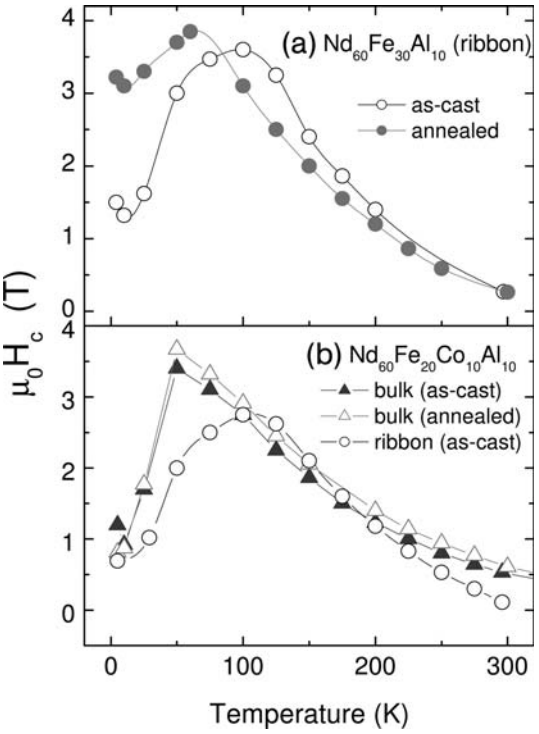

Fig. 27.15 Temperature dependence of the coercive field measured on ribbons and bulk materials [63].

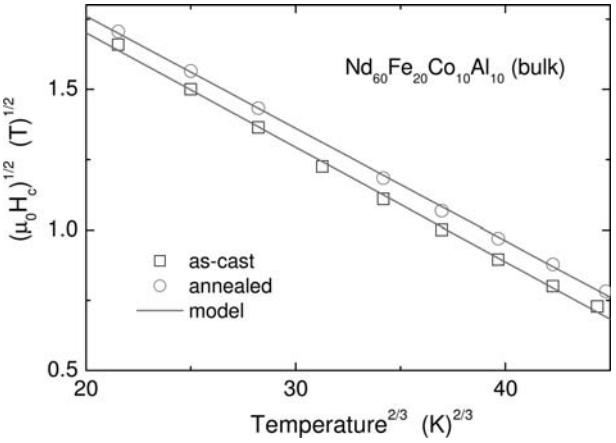

Fig. 27.16 $(\mu_0 H_c)^{1/2}$ as a function of $(T)^{2/3}$ obtained for bulk $Nd_{60}Fe_{20}Co_{10}Al_{10}$ samples. The symbols are the experimental data and the lines are the fitting of theoretical curve to the experimental data [63].

27.3.2.3 Temperature Dependence of the Magnetic After-effect

The magnetic after-effect becomes visible in a strong time dependence of the magnetization [100], susceptibility [104] and coercivity that was observed for temperatures between 4.2 and 300 K. Here, the coercivity as function of temperature is shown for bulk $Nd_{60}Fe_{20}Co_{10}Al_{10}$ in the as-cast state and after annealing at 773 K for 1 h, measured with different dH/dt (see Fig. 27.17). The coercivity increases with increasing field sweep rate, which manifests again a strong magnetic after-effect.

27.3.3 Industrial Nanocrystalline Hard Magnetic Material

Whereas soft magnetic nanocrystalline material is widely produced and used by industry, the situation for hard magnetic nanocrystalline materials is different. Only MAGNEQUENCH really offers commercial powder of nanosized Nd-Fe-B alloys, known as MQP^{TM} powders. MQP^{TM} powders are based upon MAGNEQUENCH's patented RE-Fe-B alloy compositions, the powders of which are obtained by rapidly solidification from the molten state at extremely high cooling rates ($\sim$1 000 000 degrees per second) resulting in a material constituted of extremely fine powders, with grain sizes typically of 30–50 nm. Because this grain size is smaller than that of the critical size for single magnetic domains, these materials are magnetically isotropic. Further, in contrast to the fine, anisotropic powders, which are used to manufacture sintered RE-Fe-B magnets, MQP^{TM} powder is relatively stable against oxidation and induced demagnetization. These characteristics make MQP^{TM} powders ideally suited for the production of bonded permanent magnets (see: *http://www.magnequench.com/*).

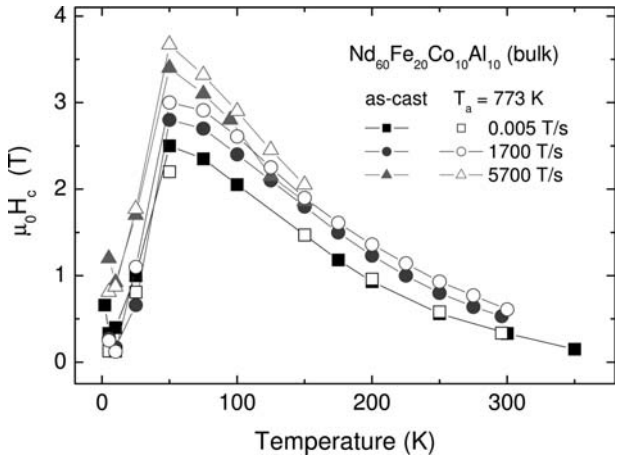

Fig. 27.17 Temperature dependence of the coercivity measured on bulk $Nd_{60}Fe_{20}Co_{10}Al_{10}$ in the as-cast, and annealed at 773 K measured with different dH/dt.

27.4 Magnetostrictive Materials

Applying a magnetic field to a magnetic material a change of length is exhibited, which lies between a few ppm and 2000 ppm. This property is generally called magnetostriction. For sensors, actuators and other applications, materials with a high magnetostriction are needed. At room temperature, the amorphous Fe-based alloys exhibit magnetostriction values of up to 46 ppm [14] together with excellent soft magnetic properties, which makes them very interesting for various stress–strain sensors. Rare-earth substitution does not enhance the magnetostriction in amorphous systems, even at low temperatures [109]. This might be due to the fact that the RKKY interaction is heavily disturbed in the amorphous state.

On the other hand, crystalline materials like $TbFe_2$ [110] or $SmFe_2$ [111] exhibit the highest magnetostriction values at room temperature. $TbFe_2$ exhibits the largest positive (+2600 ppm at room temperature) whereas $SmFe_2$ exhibits the largest negative magnetostriction (–2000 ppm). However, due to the rare earths involved these materials show a very high magnetocrystalline anisotropy. The high intrinsic rare-earth-based anisotropy can be overcome in the nanocrystalline state by the effect of exchange coupling, which reduces the "effective" anisotropy. Exchange coupling decreases the external field for saturation but it should not reduce the magnetostriction value. The effect of nanocrystallization was studied already by investigating the magnetostriction as a function of the applied field on rapidly quenched Tb-Dy-Fe-B alloys [112], however combined with high intrinsic magnetocrystalline anisotropy. In order to overcome the "anisotropy problem" materials, such as "Terfenol-D" ($Tb_{0.3}Dy_{0.7}Fe_2$) were invented [113] – the anisotropies of Tb and Dy have reciprocal sign, which cancel in Terfenol. It is worth noting that, very recently, the effect of magnetic softening in a high-magnetostriction material was nicely demonstrated for a multilayer system consisting of TbFeCo (high magnetostrictive) +Y-Fe-Co (soft magnetic) nanocrystalline layers. The coupling between the soft magnetic and the magnetostrictive layers combined with a nanocrystalline state (which also reduces the effective anisotropy and supports the coupling) leads to a soft magnetic material with a high magnetostriction. The total magnetostriction found in this system was about 400 ppm [114].

However, the search for new and economic bulk materials with high magnetostriction is ongoing, e.g., rapidly quenched Fe-Ga [115–118], Fe-Ga-X (X = Co, Ni, Al) [119], Fe-Al [120, 121] crystalline alloys. Among these alloys, the largest magnetostriction in the (100) direction of about 350 ppm was found for a single crystal with a composition of $Fe_{81}Ga_{19}$ [115]. Investigation of the magnetostriction in these alloys containing nanosized grains is in progress. The materials are being prepared by different techniques: melt spinning, splat cooling and severe plastic deformation (SPD).

27.5 Magnetoelectric Materials

Materials that are piezoelectric and magnetostrictive at the same time are generally called "magnetoelectric" or "multiferroic" materials. Magnetoelectric (ME) materials become magnetized when placed in an electric field and electrically polarized when placed in a magnetic field. These multifunctional materials exhibit a large potential for industrial applications. The nanocrystalline state with a high surface to volume ratio supports the coupling between the two phases, thus enhancing the magnetoelectric coefficient.

The first experimental observation of the ME effect was in 1960, when Astrov found the electric-field-induced magnetoelectric effect in Cr_2O_3 [122, 123]. One year later, the reverse effect in the same system was observed by Rado and coworkers [124, 125]. ME materials can be divided into two classes: single-phase compounds and composites.

27.5.1 Single-phase Materials

All single-phase multiferroic materials found up to now show this effect at low temperatures [126, 127]. Examples of single-phase multiferroic materials are: Cr_2O_3, which exhibits magnetoelectric behavior applying a rather high external magnetic field ($H > 10$ T) [128]. Materials such as $RMnO_3$ (R = Eu, Gd, Tb) [129], $BiMnO_3$ [127], $BiFeO_3$ [130]; and also other structure types such as $GdFe_3(BO_3)_4$ [131], all these materials exhibit magnetoelectric behavior, however, at low temperatures and sometimes even at high external field. A semitheoretical investigation tries to explain why only very few materials exist that are at the same time ferroelectric and magnetically ordered [132].

27.5.2 Magnetoelectric Composites

Only composites between a magnetostrictive and a piezoelectric material have shown up to now a magnetoelectric effect at room temperature [133, 134]. Materials with good magnetic properties (high magnetostriction, high saturation magnetization) can be combined with materials with piezoelectric properties leading to magnetoelectric composites even at room temperature. To achieve a high magnetoelectric coefficient, the magnetic phase should exhibit a high magnetostrictive coefficient and high electric resistance to avoid a discharging process, the piezoelectric coefficient (ratio between applied pressure and resulting electric charge) should be large too. The coupling between the phases should be optimized, which depends on the microstructure. It was recently shown that a nanocrystalline core-shell structure give the highest achieved magnetoelectric coefficient at room temperature. There exist hints that the magnetoelectric cou-

pling has also a direct component that acts between the magnetization and the electric polarization vector [135, 136].

The ME effect in composites started in 1972 when Van Suchetelene introduced the concept of "product properties" and used it to grow successfully the first magnetoelectric composite by unidirectional solidification of a $BaTiO_3$–$CoFe_2O_4$ eutectic liquid [133]. The product properties refer to ME composites, that is, the combination of magnetostrictive and piezoelectric materials causing the ME effect, but this effect does not exist in either magnetostrictive or in the piezoelectric phase alone. The ME effect is originated by applying a magnetic field; the magnetostrictive constituent will change its length (volume) causing a local stress, which will be passed into the piezoelectric phase, thus producing electric polarization (charge). Roughly, the ME effect in composites can be written as [137–139]:

$$\text{ME (effect)} = \frac{\text{magnetostriction}}{\text{mecheanical stress}} \times \frac{\text{mechanical stress}}{\text{electrical charge}}$$

Possible components of composites are based on magnetostrictive materials such as ferrites or manganates, which should be insulators, combined with piezoelectric materials such as $BaTiO_3$, PZT, Rochellesalt, $LiNbO_3$, $PbTiO_3$.

A wet chemically produced 50%$CoFe_2O_4$–50%$BaTiO_3$ (in mass) nanocomposite in a core-shell structure has been investigated magnetically. Magnetostriction measurements revealed the strong mechanical coupling between the two constituents. The ME coefficient was approximately 18 times higher than that of the mixed structure with the same composition [140]. The microstructure plays a very important role here. Nanosized particles gave the highest values of the ME coefficient. The main driving mechanism is the magnetomechanical coupling through magnetostriction of the magnetostrictive phase. The ME coefficient is found to be proportional to a coupling coefficient k, defined as $k = \lambda \cdot \partial\lambda/\partial \mathrm{H}$ where λ is the linear magnetostriction [136].

27.6 Summary

The microstructure determines, in all kinds of magnetic materials, technically useful properties such as: energy product, losses, permeability, etc. This means that an amorphous or a nanocrystalline state is an additionally very important possibility for influencing material parameters. In nanocrystalline materials the grain size becomes comparable to or even smaller than the exchange length. This causes, in soft magnetic materials, a significant decrease of the coercivity that is accompanied by an increase of the permeability.

On the other hand, in hard magnetic nanocrystalline materials a remanence enhancement ($M_r > 1/2 \cdot M_S$) occurs even for isotropic materials. The coercivity is reduced because of a reduction of the effective anisotropy. This effect can be

used for nanocrystalline magnetostrictive materials where due to a reduction of the effective anisotropy the for applications important $d\lambda/dH$ increases, which means that high magnetostriction values even at low external fields can be achieved. Also in composites (e.g. magnetoelectric composites) the nanocrystalline state enhances the coupling between the gains that causes a higher ME effect. There exist nowadays many different production routes leading to a nanocrystalline state. Here, the rather new method of severe plastic deformation should be mentioned for achieving nanocrystalline bulk materials.

References

1 K. Moorjani, J. M. D. Coey, **1984**, in *Metallic Glasses*, S. P. Wolsky, A. W. Czanderna (eds.), Elsevier, Amsterdam, pp. 6.
2 R. Sato Turtelli, E. de Morais, Vo. Hong Duong, G. Wiesinger, M. Dahlgren, E. Ferrara, **1998**, *J. Magn. Magn. Mater.* 177, 1389.
3 G. Bertotti, F. Fiorillo, **1994**, in *Landolt-Börnstein* Vol. 19, Springer-Verlag, ISBN: 978-3-540-55590-2, pp. 129.
4 T. Yamamoto, **1944**, *Trans. IEE Jpn.* 5, 175.
5 F. E. Luborsky, **1983**, in *Amorphous Metallic Alloys*, F. E. Luborsky (ed.) Butterworths, London.
6 F. Pfeifer, C. Radeloff, **1980**, *J. Magn. Magn. Mater.* 19, 190.
7 T. Egami, P. J. Flanders, C. D. Graham, **1974**, *AIP Conf. Proc.* 24, 697.
8 R. Boll, G. Hinz, **1985**, *Techn. Messen* 52(5), 189.
9 R. C. O'Handley, R. Hasegawa, R. Ray, C. P. Chew, **1976**, *Appl. Phys. Lett.* 29, 330.
10 R. C. O'Handley, D. S. Boudreaux, **1978**, *phys. stat. sol. A* 45, 607.
11 R. Sato Turtelli, R. Grössinger, C. Kussbach, J. P. Sinnecker, **1998**, *J. Appl. Phys.* 83(3), 1581.
12 R. Sato Turtelli, J. P. Sinnecker, R. Grössinger, M. Vázquéz, **1995**, *J. Appl. Phys.* 74(4), 2590.
13 Report of *PECO-COPERNICUS Program*, Contract CIPA-CT93-0239, **1995**, pp. 49.
14 R. Sato Turtelli, J. P. Sinnecker, R. Grössinger, G. Badurek, C. Kussbach, P. Allia, **2001**, *Phys. Rev.* 63, 094427-1.
15 U. Köster, **1984**, *Z. Metallkunde* 75(9), 691.
16 R. C. O'Handley, **1977**, *Solid State Commun.* 21, 1119.
17 M. Vasquez, E. Ascasibar, A. Hernando, O. V. Nielson, **1977**, *J. Magn. Magn. Mater.* 66, 37.
18 H. A. Davies, **1983**, in *Amorphous Metallic Alloys*, F. E. Luborsky (ed.) Butterworths, London, pp. 8.
19 R. Hasegawa, **1982**, in *Glassy Metals: Magnetic, Chemical and Structural Properties*, CRC Press, Boca Raton, Fl.
20 T. Matsumoto, I. Ohnaka, A. Inoue, M. Hagigawa, **1981**, *Scr. Metal.* 15, 293.
21 H. A. Davies, **1994**, in *Nanostructured and Non-Crystalline Materials*, M. Vázquez, A. Hernando (eds.) World Scientific, Singapore.
22 M. Stoica, S. Roth, J. Eckert, L. Schultz, **2004**, in: *16. Soft Magnetic Materials Conference Proc.*, D. Raabe (ed.), Stahl-Eisen, Düsseldorf, pp. 681.
23 S. Roth, M. Stoica, J. Degmova, U. Gaitzsch, J. Eckert, L. Schultz, **2006**, *J. Magn. Magn. Mater.* 304, 192.
24 A. Inoue, T. Zhang, T. Masumoto, **1993**, *J. Non-Cryst. Solids* 156, 473.
25 A. Inoue, **1995**, *Mater. Trans.* 36, 866.
26 A. Inoue, **1995**, *Mater. Sci. Forum* 179, 691.
27 A. Inoue, **1995**, in *Nanostructured and Non-Crystalline Materials*, M. Vazquez, A. Hernando (eds.), World Scientific, Singapore, pp. 15.
28 U. Gaitzsch, M. Stoica, A. Gebert, S. Roth, J. Eckert, L. Schultz, **2004**, *Proceedings of Soft Magnetic Material Conference*, D. Raabe (ed.), Stahl-Eisen, Düsseldorf, 2, 579.
29 T. Mizushima, A. Makino, A. Inoue, **1997**, *IEEE Trans. Magn.* 33, 3784.
30 R. Sato Turtelli, D. Triyono, G. Badurek, M. Schönhart, R. Grössinger, C. D. De-

whurst, H. Sassik, C. Bormio-Nunes, **2004**, *J. Magn. Magn. Mater.* 281, 364.
31 R. Sato Turtelli, D. Triyono, G. Badurek, R. Grössinger, C. D. Dewhurst, M. Scönhart, H. Sassik, **2004**, *Proceedings of Soft Magnetic Materials 16*, Düsseldorf, 2, 669.
32 M. Stoica, J. Eckert, S. Roth, Z. F. Zhang, L. Schultz, W. H. Wang, **2005**, *Intermetallics*, 13, 764.
33 M. Stoica, S. Roth, J. Eckert, L. Schultz, **2004**, *Proceedings of Soft Magnetic Materials 16*, D. Raabe (ed.), Stahl-Eisen, Düsseldorf, 2, 681.
34 J. Degmova, S. Roth, J. Eckert, H. Grahl, L. Schultz, **2004**, *Proceedings of Soft Magnetic Materials 16*, D. Raabe (ed.), Stahl-Eisen, Düsseldorf, 2, 269.
35 J. Degmova, J. Finnberg, S. Roth, **2006**, *J. Magn. Magn. Mater.* 301, 190.
36 G. Herzer, **1991**, *Mater. Sci. Eng. A* 133, 1.
37 G. Herzer, **1990**, *IEEE Trans. Magn.* 26, 1397.
38 Y. Yoshizawa, K. Yamauchi, S. Oguma, **1988**, European Patent, no. 0271657.
39 Y. Yoshizawa, S. Oguma, K. Yamauchi, **1988**, *J. Appl. Phys.* 64(10), 6044.
40 K. Hono, A. Inoue, T. Sakurai, **1991**, *Appl. Phys. Lett.* 58(9), 2180.
41 G. Herzer, **1992**, *J. Magn. Magn. Mater.* 112, 258.
42 A. Hernanodo, T. Kulik, **1994**, *Phys. Rev. B* 49(10), 7064.
43 R. Grössinger und R. Sato Turtelli, **1994**, *IEEE Trans. Magn.* 30, 445.
44 R. Grössinger, D. Holzer, C. Kussbach, J. P. Sinnecker, R. Sato Turtelli, H. Sassik, E. Wittig, **1995**, *IEEE Trans. Magn.* 31, 3883.
45 R. Grössinger, R. Sato Turtelli, Vo Hong Duong, C. Kuß, **1995**, *Proc. of III Latin American Workshop of Magnetism, Magnetic Materials and Their Applications*, F. Leccabue, V. Segredo (eds.), Mérida, Venezuela, 202.
46 T. Kulik, A. Hernanodo, **1994**, *J. Magn. Magn. Mater.* 138, 270.
47 Vo Hong Duong, R. Grössinger, R. Sato Turtelli, Ch. Polak, **1995**, *Proceedings of the Second International Workshop on Material Science*, Hanoi, Vietnam, pp. 460.
48 Vo Hong Duong, R. Sato Turtelli, R. Grössinger, K. Hiebl, P. Rogl, **1996**, *IEEE Trans. Magn.* 32, 4821.
49 Vo Hong Duong, R. Grössinger, R. Sato Turtelli, Ch. Polak, **1996**, *J. Magn. Magn. Mater.* 157/158, 193.
50 R. Grössinger, R. Sato Turtelli, Vo Hong Duong, Ch. Kuß, Ch. Polak, G. Herzer, **1999**, *Mater. Sci. Forum*, 307, 135, *J. Metastable Nanocryst. Mater.* **1999**, 1, 135.
51 R. Sato Turtelli, E. de Morais, R. Grössinger, M. Knobel, **1997**, *Suppl. Mater. Sci. Forum*, 235, 265.
52 M. Schwetz, R. Sato Turtelli, R. Grössinger, H. Sassik, **1998**, in *Non-crystalline and Nanoscale Materials*, J. Rivas, M. A. Lopez-Quintela (eds.), World Scientific, Singapore, pp. 329.
53 R. Matejko, R. Varga, P. Vojtaník, D. Holzer, R. Sato Turtelli, H. Sassik, R. Grössinger, **1998**, *Acta Phys. Slov.* 48, 667.
54 K. Suzuki, A. Makino, A. Inoue, T. Masumoto, **1991**, *J. Appl. Phys.* 70(10), 6232.
55 H. Hasegawa, **2004**, *J. Optoelectron. Adv. Mater.* 2, 503.
56 R. Grössinger, R. Sato Turtelli, **2004**, *Proc. of Workshop of the Metallurgy and Magnetism*, Freiberg.
57 R. Coehoorn, D. B. de Mooij, J. P. W. B Duchateau, K. H. J. Buschow, **1988**, *J. de Phys. C* 8, 669.
58 A. Jha, H. A. Davies, R. A. Buckley, **1989**, *J. Magn. Magn. Mater.* 80, 109.
59 H. A. Davies, J. F. Liu, G. Mendoza, **1996**, *Proceedings of the 9th International Symposium on Coercivity and Anisotropy*, F. P. Missell, V. Villos-Beas, H. R. Rechenberg, T. J. G. Landgraf (eds.), World Scientific, Singapore, 2, 251.
60 A. Inoue, T. Zhang, W. Zhang, A. Takeuchi, **1996**, *Mater. Trans. JIM* 37 (2), 99.
61 B. C. Wei, Y. Zhang, Y. X. Zhuang, D. Q. Zhao, M. X. Pan, W. H. Wang, W. R. Hu, **2001**, *J. Appl. Phys.* 89 (6), 3529.
62 H. Chiriac, N. Lupu, K. V. Rao, R. E. Vandenberghe, **2001**, *IEEE Trans. Magn.* 37 (4), 2509.
63 R. Sato Turtelli, D. Triyono, R. Grössinger, H. Michor, J. H. Espina, J. P. Sinnecker, H. Sassik, J. Eckert, G. Kumar, Z. G. Sun, G. J. Fan, **2002**, *Phys. Rev. B* 66, 054441-1.
64 F. J. Cadieu, **1995**, *Int. Mater. Rev.* 40, 137.

65 D. J. Sellmyer, **1992**, *J. Alloys Compd.* 181, 397.
66 E. Fullerton, J. S. Jang, M. Grimsditch, C. H. Sowers, S. D. Bader, **1998**, *Phys. Rev. B* 58, 12193.
67 O.Gutfleisch, **2000**, *J. Appl. Phys. D: Appl. Phys.* 33, R157.
68 K. Narasimhan, C. Willman, E. J. Dulis, **1986**, US Patent No. 4,588,439.
69 P. G. McCormick, W. F. Miao, P. A. I. Smith, J. Ding, R. Street, **1998**, *J. Appl. Phys.* 83, 6256.
70 L. Schultz, **1990**, in: *Science and Technology of Nanostructured Materials*, G. Prinz, G. C. Hadjipanayis (eds.), NATO ASI Series, 259, 583.
71 P. G. McCormick, **1997**, *Handbook on the Physics and Chemistry of Rare Earths*, K. A. Gscheidner, L. Eyring (eds.), Elsevier, Amsterdam, Chap. 16, Vol. 24.
72 J. Z. D. Zhang, W. Liu, J. P. Liu, D. J. Sellmyer, **2000**, *J. Phys. D: J. Appl. Phys.* 33, R217.
73 J. L. Sanchez, J. Elizalde-Galindo, J. A. Matutes-Aquino, **2003**, *Solid State Commun.* 127, 257.
74 G. C. Hadjipanayis, J. M. D. Coey, **1996**, *Rare Earth Fe Permanent Magnets*, Clarendon Press, Oxford, pp. 286.
75 D. Lambeth, **1996**, in: *Magnetic Hysteresis in Novel Magnetic Materials*, NATO ASI Series, G. C. Hadjipanayis (ed.), 338, 767.
76 D. J. Sellmyer, **1996**, in: *Magnetic Hysteresis of Novel Magnetic Materials*, NATO ASI Series, G. C. Hadjipanayis (ed.), 338, 419.
77 J. P. Liu, Y. Liu, C. P. Luo, Z. S. Shan, D. J. Sellmyer, **1998**, *Appl. Phys. Lett.* 72, 483.
78 S. Starroyiannis, I. Panagiotopoulos, D. Niarchos, J. Christodoulides, Y. Zhang, G. C. Hadjipanayis, **1998**, *Appl. Phys. Lett.* 73, 3453.
79 A. Giguère, N. H. Hai, N. M. Dempsey, D. Givord, **2002**, *J. Magn. Magn. Mater.* 242, 581.
80 A. Giguère, N. M. Dempsey, M. Verdier, L. Ortega, D. Givord, **2002**, *IEEE Trans. Magn.* 38, 2761.
81 V. V. Stolyarov, D. V. Gunderov, A. G. Popov, T. Z. Puzanova, G. I. Raab, A. R. Yavari, R. Z. Valiev, **2002**, *J. Magn. Magn. Mater.* 242, 1399.
82 H. A. Davies, A. Manaf, M. Leonowicz, P. Z. Zhang, S. J. Dobson, R. A. Buckley, **1993**, *Proc. of 1st Internat. Conf. on Nanostructured Materials*, Cancun (1992), *Nanostruct. Mater.* 2, 197.
83 R. Fischer, H. Kronmüller, **1996**, Phys. Rev. B 54, 7284.
84 E. F. Kneller, R. Hawig, **1991**, *IEEE Trans. Magn.* 27, 3588.
85 T. Schrefl, R. Fischer, J. Fidler, H. Kronmüller, **1994**, *J. Appl. Phys.* 76, 7053.
86 G. C. Hadjipanayis, **1999**, *J. Magn. Magn. Mater.* 200, 373.
87 R. Coehoorn, D. B. Mooji, C. DeWaard, **1989**, *J. Magn. Magn. Mater.* 89, 101.
88 M. Dahlgren, R. Grössinger, E. de Morais, S. Gama, G. Mendoza, J. F. Liu, H. A. Davies, **1997**, *IEEE Trans. Magn.* 33, 3895.
89 M. Dahlgren, R. Grössinger, **1998**, *Proc. of Rare Earth Magnets and their Applications*, Dresden, L. Schultz, K. H. Müller (eds.), pp. 253.
90 R. Grössinger, R. Sato Turtelli, **2003**, in: *Magnetic Amorphous Alloys: Structural Magnetic and Transport Properties*, P. Tiberto, F. Vinai (eds.), pp. 183.
91 L. H. Lewis, D. O. Welch, V. Panchanathan, **1997**, *J. Magn. Magn. Mater. 175*, 275.
92 F. E. Pinkerton, **1986**, *J. Magn. Magn. Mater.* 54, 579.
93 Z. Chen, X. Meng-Burany, H. Okumura, G. C. Hadjinapayis, **2000**, *J. Appl. Phys.* 87, 3409.
94 Z. Chen, X. Meng-Burany, H. Okumura, G. C. Hadjinapayis, **1999**, *J. Appl. Phys. Lett.* 75, 3165.
95 N. Tang, Z. Chen, Y. Zhang, G. C. Hadjipanayis, F. Yang, **2000**, *J. Magn. Magn. Mater.* 219, 173.
96 J. T. Elizalde Galindo, R. Sato Turtelli, R. Grössinger, J. A. Matutes Aquino, submitted to *J. of Materials Characterization* (Elsevier).
97 J. C. Téllez-Blanco, R. Grössinger, R. Sato Turtelli, E. Estévez-Rams, **2000**, *IEEE Trans. Magn.* 36, 3333.
98 K. Strnat, G. Hoffer, J. Olson, W. Ostertag, J. J. Becker, **1967**, *J. Appl. Phys.* 38, 1001.
99 D. Triyono, R. Sato Turtelli, R. Grössinger, H. Michor, K. R. Pirota, M. Kno-

bel, H. Sassik, T. Mathias, S. Höfinger, J. Fidler, **2002**, *J. Magn. Magn. Mater.* 242, 1321.

100 R. Sato Turtelli, D. Triyono, R. Grössinger, K. R. Pirota, M. Knobel, P. Kerschel, J. Eckert, S. Kato, **2002**, *Proceedings of the Seventeenth International Workshop on Rare Earth Magnets and Their Applications*, Newark, Delaware, pp. 161.

101 R. Sato Turtelli, J. P. Sinnecker, W. Steiner, G. Wiesinger, R. Grössinger, D. Triyono, **2003**, *Physica B* 327, 198.

102 R. Sato Turtelli, D. Triyono, G. Wiesinger, R. Grössinger, H. Michor, **2003**, *IEEE Trans. Magn.* 39, 2878.

103 R. Sato Turtelli, D. Triyono, R. Grössinger, H. Sassik, J. Fidler, T. Matthias, G. Badurek, C. Dewhurst, W. Steiner, G. Wiesinger, **2004**, *Mater. Sci. Eng. A* 375, 1129.

104 R. Sato Turtelli, J. P. Sinnecker, D. Triyono, R. Grössinger, **2004**, *J. Optoelectron. Adv. Mater.* 6, 609.

105 R. Sato Turtelli, D. Triyono, G. Wiesinger, M. Reissner, W. Steiner, J. P. Sinnecker, G. Badurek, R. Grössinger, **2004**, *J. Alloys Compd.* 369, 162.

106 R. Sato Turtelli, R. Grössinger, C. Bormio-Nunes, J. Eckert, **2004**, *Proceedings of the 18t*H *International Workshop on High Performance Magnets and their Applications*, N. M. Dempsey, P. de Rango (eds.), Annecy, France, l–2, 514.

107 E. Callen, Y. J. Liu, J. R. Cullen, **1977**, *Phys. Rev. B* 16 (1), 263.

108 A. Inoue, A. Takeuchi, T. Zhang, **1998**, *Metal. Mater. Trans. A* 29A, 1779.

109 R. Grössinger, H. Sassik, R. Wezulek, T. Tarnoczi, **1988**, *J. Physique* 49, C8-1337.

110 A. E. Clark, H. S. Belson, **1972**, *Phys. Rev. B* 5, 3642.

111 Hiroaki Samata, Nobuto Fujiwara, Yujiro Nagata, Takayuki Uchida, Ming Der Lan, **1999**, *J. Magn. Magn. Mater.* 195, 376.

112 S. I. Lim, S. Y. Kang, S. R. Kim, **1977**, *IEEE Trans. Magn.* 33 (5), 3943.

113 H. T. Savage, A. E. Clark, J. M. Powers, **1975**, *IEEE Trans. Magn.* 11, 1355.

114 N. H. Duc, D. T. Huong Giang, P. T. Thuong, **2004**, *Proc. 18th International Workshop on High Performance Magnets and their Applications*, pp. 881.

115 J. B. Restorf, M. Wun-Fogle, A. E. Clark, T. A. Lograsso, A. R. Ross, D. L. Schlagel, **2002**, *J. Appl. Phys.* 91, 8225.

116 A. E. Clark, J. B. Restorff, M. Wun-Fogle, T. A. Lograsso, D. L. Schlagel, **2000**, *IEEE Trans. Magn.* 36, (5), 3238.

117 C. Bormio-Nunes, M. A. Tirelli, R. Sato Turtelli, R. Grössinger, H. Müller, G. Wiesinger, H. Sassik, M. Reissner, **2005**, *J. Appl. Phys.* 97, 033901.

118 R. Sato Turtelli, C. Bormio-Nunes, J. P. Sinnecker, R. Grössinger, **2006**, *Physica B* 384, 265.

119 C. Bormio-Nunes, R. Sato Turtelli, H. Mueller, R. Grössinger, H. Sassik, M. A. Tirelli, **2005**, *J. Magn. Magn. Mater.* 290, 820.

120 A. E. Clark, J. B. Restorff, M. Wun-Fogle, D. Wu, T. A. Lagrasso, **2008**, *J. Appl. Phys. 103, 07B310.*

121 N. Mehmood, R. Sato Turtelli, R. Grössinger, M. Kriegisch, presented at JEMS '08 and submitted to *J. Magn. Magn. Mater.*

122 D. N. Astrov, **1960**, *Sov. Phys.-JETP* 11, 708.

123 D. N. Astrov, **1961**, *Sov. Phys.-JETP* 13, 729.

124 G. T. Rado, V. J. Folen, **1961**, *Phys. Rev. Lett.* 7, 310.

125 V. J. Folen, G. T. Rado, E. W. Stalder, **1961**, *Phys. Rev. Lett.* 6, 607.

126 S. S. Krotov, A. M. Kadomtseva, Yu. F. Popov, A. K. Zvezdin, G. P. Vorob'ev, D. V. Belov, **2001**, *J. Magn. Magn. Mater.* 226, 963.

127 K. Noda, M. Akaki, F. Nakamura, D. Akahoshi, H. Kuwahara, **2007**, *J. Magn. Magn. Mater.* 310, 1162.

128 S. S. Krotov, A. M. Kadomtseva, Yu. F. Popov, A. K. Zvezdin, G. P. Vorob'ev, D. V. Belov, **2001**, *J. Magn. Magn. Mater.* 226, 963.

129 Z. H. Chi, H. Yang, S. M. Feng, F. Y. Li, R. C. Yu, C. Q. Jin, **2007**, *J. Magn. Magn. Mater.* 310, 358.

130 M. M. Kumar, S. Srinath, G. S. Kumar, S. V. Suryanarayana, **1998**, *J. Magn. Magn. Mater.* 188, 203.

131 A. K. Zvezdin, A. M. Kadomtseva, S. S. Krotov, A. P. Pyatakov, Yu. F. Popov,

G. P. Vorob'ev, **2006**, *J. Magn. Magn. Mater.* 300, 224.
132 A. Hill, **2000**, *J. Phys. Chem. B* 104, 6694.
133 J. Van Suchetelene, **1972**, *Philips Res. Rep.* 27, 28.
134 Giap V. Duong, R. Groessinger, R. Sato Turtelli, **2006**, *IEEE Trans. Magn.* 42, 3611.
135 Giap V. Duong, R.Grössinger, R. Sato Turtelli, **2007**, *J. Magn. Magn. Mater.* 310, e361.
136 Giap V. Duong, R. Groessinger, R. Sato Turtelli, **2007**, *J. Magn. Magn. Mater.* 310, 1157.
137 C. W. Nan, **1994**, *Phys. Rev. B* 50, 6082.
138 M. Fiebig, **2005**, *J. Phys. D: Appl. Phys.* 38, R123.
139 Jungho-Ryu, Shashankprya Kenjiuchinoi, Hyoun-ee Kim, **2002**, *J. Electroceram. 8*, 107.
140 Giap V. Duong, R. Grössinger, **2007**, *J. Magn. Magn. Mater.* 316, 624.

28
Niche Applications of Bulk Nanostructured Materials Processed by Severe Plastic Deformation

Yuri Estrin and Michael J. Zehetbauer

28.1
Introduction

The main focus of research in the area of severe plastic deformation (SPD), which has experienced a period of rapid growth in the last decade, has been on improving mechanical properties of structural materials by extreme grain refinement (see [1, 2] and Chapter 20 of this book). Significant enhancement of mechanical performance achieved with bulk ultrafine-grained (UFG) materials has resulted in a strong drive for upscaling of the SPD processing techniques for their implementation in industry to become technologically and commercially viable. Other uses of UFG materials for *niche* applications, either based on downscaled processes or capitalizing, focusing on unusual properties of UFG materials other than the mechanical ones, have often been overlooked. In this chapter we address such niche applications and give an outlook for possible future directions of research in the area of nanomaterials produced by SPD.

28.2
Downscaling of Severe Plastic Deformation

For applications in miniaturized devices, such as micro-electro-mechanical systems (MEMS), structural materials with a grain size much smaller than the smallest dimension of a structural component (cross-sectional size of a wire or thickness of a thin foil-connect between electronic chips, the tooth size of cog wheels in MEMS, etc.) are required. This requirement is dictated by the need to ensure reproducibility of properties and reliability of performance. Besides, a small grain size provides the component with increased strength and fatigue life [1, 2]. The SPD technique of equal-channel angular pressing (ECAP) is capable of imparting the desired level of grain refinement to satisfy all these conditions. In a recent paper [3], it was proposed to use ECAP-processed magnesium alloy AZ31 for producing cog-wheel profiled parts by extruding the material through a millimeter-scale extrusion die. A drawback of this process that may

Bulk Nanostructured Materials. Edited by M. J. Zehetbauer and Y. T. Zhu

ISBN: 978-3-527-31524-6

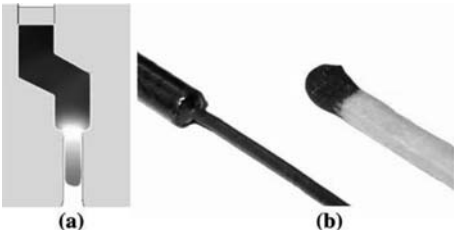

Fig. 28.1 Combined ECAP/extrusion process: (a) schematic die design and (b) Al alloy specimen that underwent integrated two-step ECAP + extrusion processing (a match is shown to indicate the size scale; from [4]).

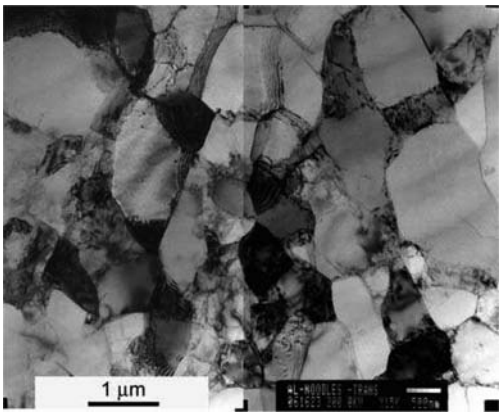

Fig. 28.2 Representative grain structure after a single pass through the miniaturized ECAP die (from [4]).

hinder its industrial use is its multistep character. Estrin et al. [4] suggested combining ECAP with an extrusion step in an integrated process illustrated by Fig. 28.1.

Through introducing a two-step ECAP die, the process proposed by Estrin et al. [4] also takes into account that a single ECAP step may not be sufficient to produce a well-established ultrafine grain structure [1, 2], at least as far as pure metals and dilute solid solutions are concerned. However, as long as grain refinement down to about 1 μm is required, single-pass 90° dies seem to be sufficient, as preliminary results obtained with a 3-mm thick die have demonstrated convincingly even for 99.99% purity aluminum. A characteristic micrometer-scale microstructure is obtained as shown in Fig. 28.2. These promising results, along with finite-element simulations supporting the viability of the miniaturized ECAP and/or ECAP+extrusion processing [4] give further motivation for studies into downscaling of SPD techniques.

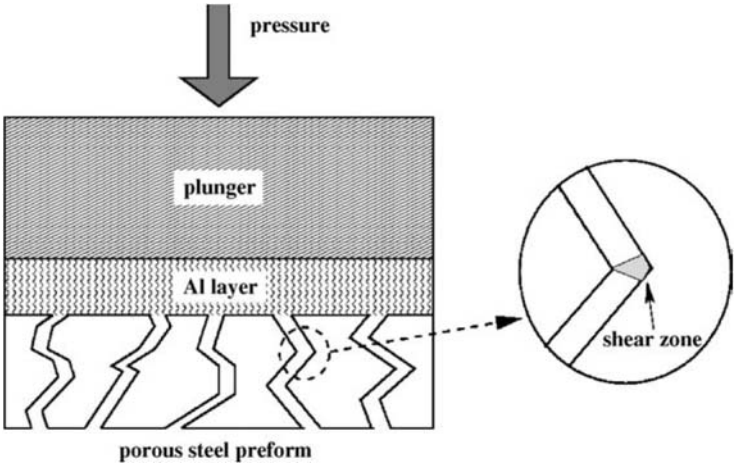

Fig. 28.3 ECAP-like principle of forcefill as applied to solid-state infiltration. The magnification on the right shows the shear zones formed in the kinks (from [5]).

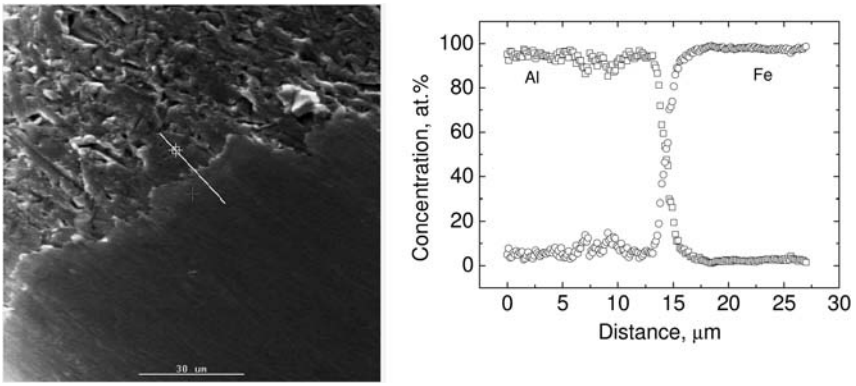

Fig. 28.4 Al and Fe concentration profiles across the interface measured by EDS along the line shown in blue in the left picture (after [7]).

A somewhat nonconventional application of the general idea of ECAP processing was considered in [5]. The process – called solid-state infiltration – utilizes penetration of solid aluminum in a porous iron preform under a high imposed pressure in a way similar to the forcefill process used for via filling in microelectronics [6]. During the plastic flow of Al through tortuous "channels" within the porous preform, the material repeatedly encounters configurations where significant shear deformation occurs in much the same way as under ECAP (Fig. 28.3, [5]). Technical viability of solid-state infiltration was demonstrated in a proof-of-concept study [5]. Several micrometer-deep penetration of Al in the porous steel preform measured in the cited article is illustrated in Fig. 28.4 [7].

28.3
Enhanced Reaction Kinetics

Extreme grain refinement produced by severe plastic deformation, as well as the concomitant increase in the dislocation density [8, 9] and/or in the deformation-induced vacancy concentration [10] can generally be expected to accelerate various kinetic processes involving "short-circuit" diffusion along grain boundaries and/or dislocation lines. Several metallurgical processes strongly affected by SPD will be discussed below.

28.3.1
Plasma Nitriding of Steels

The effect of severe plastic deformation by high-pressure torsion (HPT) [1, 2] on nitriding was investigated for pure iron and two steels (St2K50 and X5CrNi1810) [11]. Radio frequency (RF) plasma nitriding was conducted on virgin specimens and the HPT-processed ones. The results demonstrated that the thickness of the nitrided layer produced and its cohesion were improved by HPT preprocessing quite significantly. Figure 28.5, which shows scanning electron micrographs for specimens with different treatment histories, illustrates the favorable effect of SPD for the case of the steel X5CrNi1810. The upper pair of micrographs shows a through-thickness cut of the specimens in the as-received condition (left) and after HPT (right). The middle and lower pairs of pictures show the results of RF nitriding at 350 °C and 400 °C, respectively. The black horizontal lines seen in the pictures are not a signature of delamination, but rather come from the embedding medium. Increased thickness of the nitrided layers owing to HPT is clearly seen in the pictures in the middle and lower rows (e.g., 3–4 μm in the HPT-processed materials vs. 1–2 μm for that not pretreated by HPT in the case of 400 °C nitriding). A close nitride layer with good cohesion was produced in the HPT-treated material. Furthermore, element depth profile analysis showed that the nitrogen uptake in the HPT-processed material was enhanced.

Fig. 28.6 shows that the enhanced diffusion and thus nitriding in HPT-treated CrNi steel leads to an increase of the hardness at least by a factor of 1.4 with the same annealing time, or to the same hardness in half the annealing time [11]. The results of this investigation strongly suggest utilization by industry since pretreatment of CrNi steel by an SPD method before nitriding may markedly reduce time and cost of nitriding.

28.3.2
Accelerated Hydrogenation Kinetics of Magnesium Alloys

Despite the outstanding hydrogen-storage capacity (up to 7.6 wt.%) of magnesium alloys, their slow hydriding and dehydriding kinetics and low desorption pressures at the temperatures of interest (373–473 K) is a huge handicap to their application in automotive hydrogen-storage systems. One of the avenues

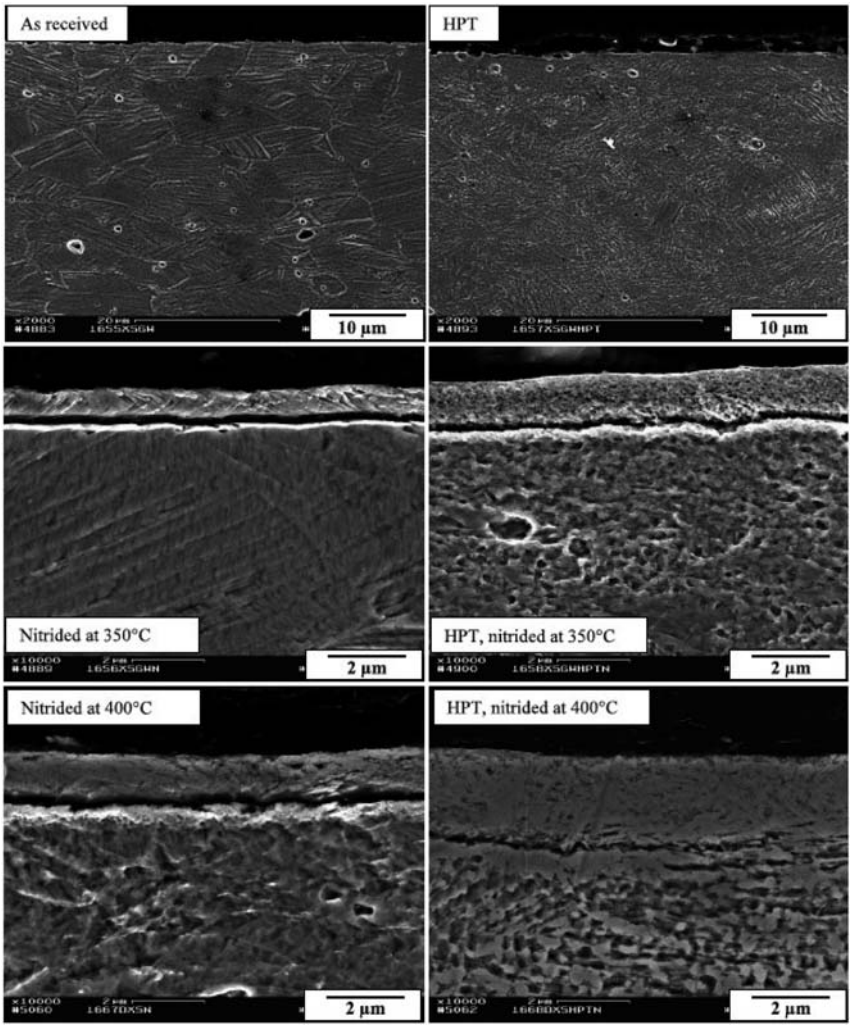

Fig. 28.5 SEM micrographs of sections through near-surface layers of steel X5CrNi1810 with different processing histories (see text for details, after [11]).

for accelerating the hydrogenation kinetics is a refinement of microstructure [12, 13]. A commonly used technique leading to grain refinement is high-energy ball milling (HEBM) [14]. Recent studies [15–17] have demonstrated that grain refinement by severe plastic deformation may provide a more economical way of enhancing the hydrogen absorption/desorption kinetics of Mg alloys, not only in terms of the throughput of the material, but also due to the possibility of its production in bulk form, avoiding contamination by impurities or health and environment hazards [18].

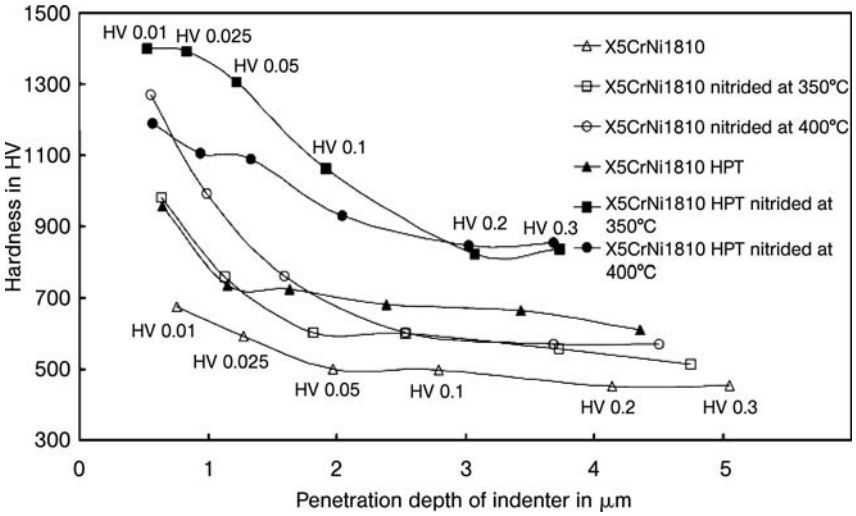

Fig. 28.6 Enhancement in hardness profiles due to accelerated diffusion of N_2 in CrNi steels due to HPT pretreatment (from [11]).

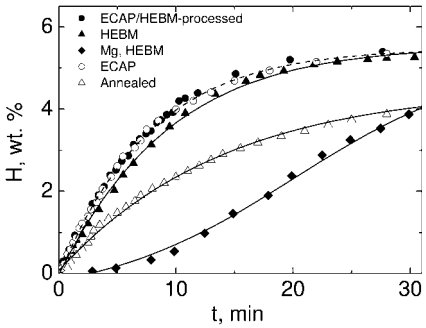

Fig. 28.7 Hydrogenation kinetics of Mg-alloy ZK60 after high-energy ball milling (HEBM), equal channel angular pressing (ECAP), and a combination of both methods (from [15, 16]).

The first hydrogenation experiments on SPD-processed materials were done on Mg alloy ZK60 [15, 16]. It was shown that preprocessing by ECAP provides absorption/desorption kinetics that are in no way inferior (and in some respects are superior) to those obtained by HEBM. A combination of ECAP and HEBM was also shown to eliminate undesirable pressure hysteresis in the absorption/desorption cycle. The hydrogenation curves for HEBM, ECAP and combined HEBM/ECAP-processed materials illustrating the excellent performance of the ECAP processed variants are presented in Fig. 28.7.

A striking effect of ECAP on the microstructure has been demonstrated recently for a eutectic Mg-Ni alloy ($Mg_{89}Ni_{11}$) [17]. As seen in Fig. 28.8, after 10

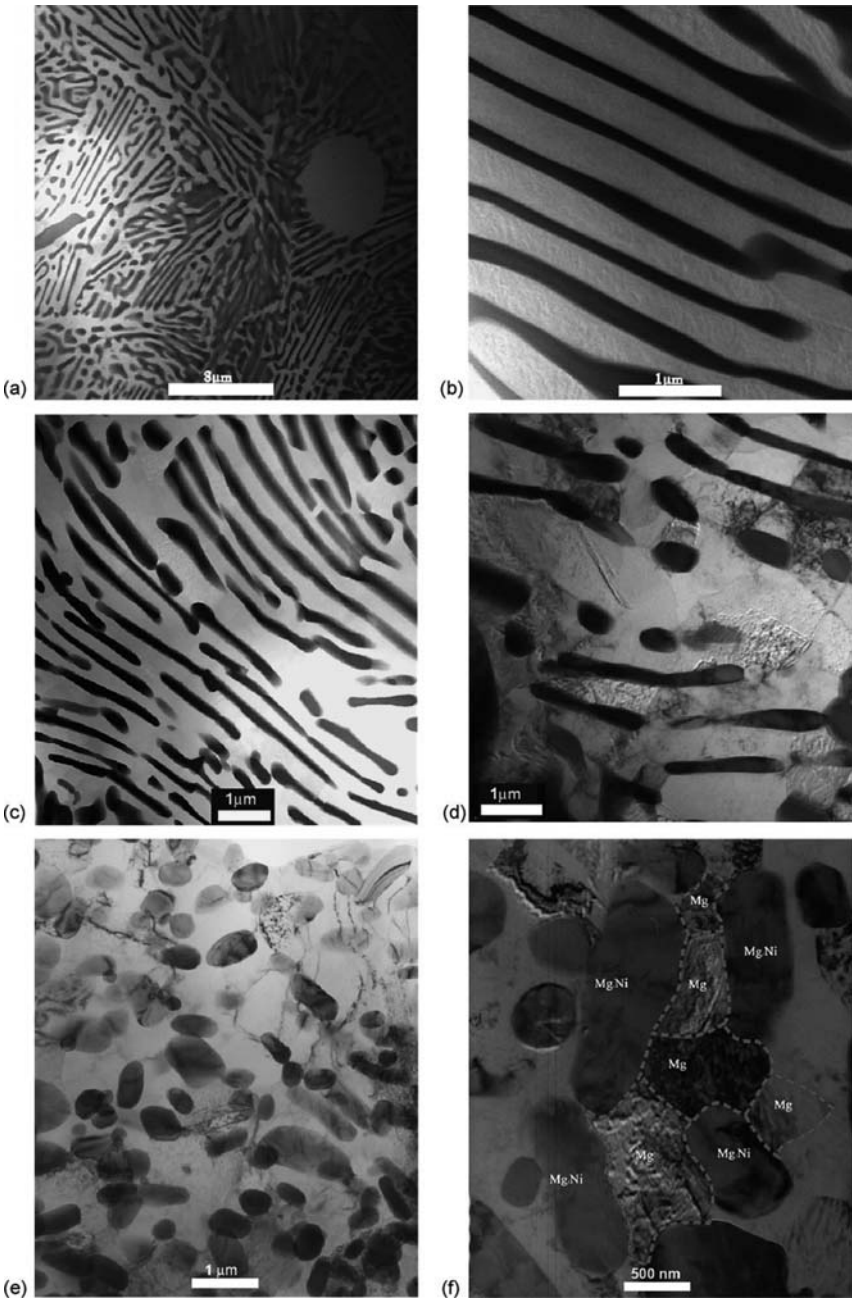

Fig. 28.8 Bright-field TEM micrographs of an as-cast $Mg_{89}Ni_{11}$ sample (a, b), a sample processed by a single ECAP pass (c, d) and one processed by ten ECAP passes (e, f). The dashed lines in (f) serve as a guide to the eye for recognizing the individual Mg grains and Mg_2Ni particles (after [17]).

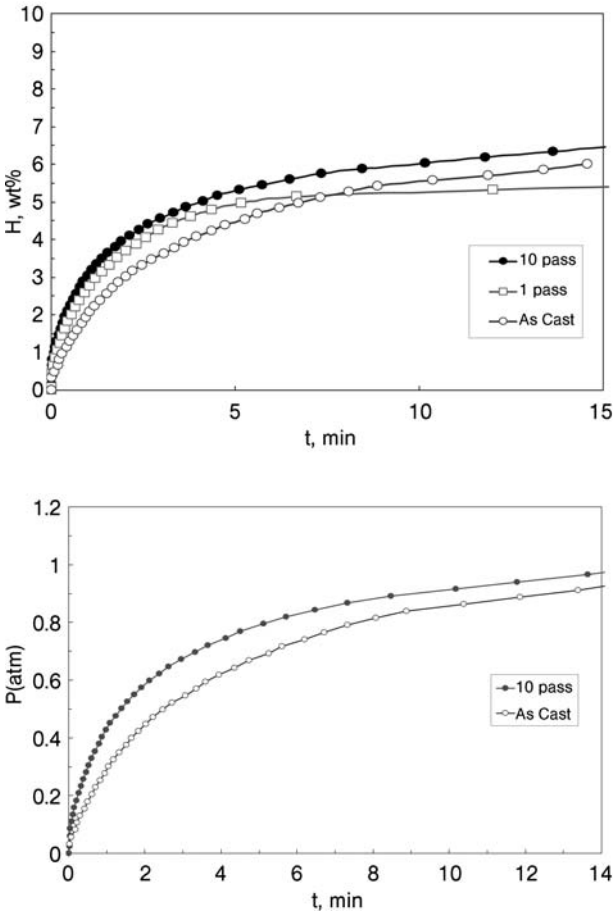

Fig. 28.9 The desorption kinetics in the as-cast and ECAP processed alloy $Mg_{89}Ni_{11}$ (upper diagram) and the concomitant variation of hydrogen pressure (lower diagram) in initially evacuated volume (after [17]).

ECAP passes (Route B_c with 90° rotations around the workpiece axis between the passes [1, 2], starting at 300 °C during the first pass and going down in temperature to 230 °C at the final 10^{th} pass), the initial microstructure gets refined down to the nanometer scale.

As in the case of ZK60 Mg alloy, the structural refinement allows for accelerated hydrogen-absorption/desorption kinetics [17]. The desorption curves for different structural states are shown in Fig. 28.9 (upper diagram). It is seen that for the sample processed by 10 ECAP passes it takes only about 6 min to desorb 5.5 wt.% of hydrogen compared to 10 min for the as-cast sample.

The pressures of hydrogen achieved during desorption in an initially evacuated volume are higher for the ECAP processed sample than for the as-cast one

for all desorption times (Fig. 28.9, lower diagram). Acceleration of hydrogenation kinetics in the Mg-Ni eutectic by ECAP was also found by the investigation of Fursikov et al. [19].

For both Mg alloys tested with regard to the effect of ECAP on the hydrogen-storage kinetics so far, the ECAP route and the number of billet passes through the die have been shown to have a strong effect on the parameters of the microstructure obtained and the resulting process rate. Hence, further progress with SPD processing as a means of boosting the hydrogen-absorption/desorption kinetics can be anticipated.

28.4 Biomedical Applications of Ultrafine-grained Materials

In an excellent review on the commercialization potential of bulk UFG materials [20], Lowe has identified the medical implant and prostheses market as a potential niche for commercialization of SPD-processed titanium. In 2001, Zhu et al. were granted a U.S. patent [21] utilizing the enhanced mechanical properties of ECAP-processed commercially pure titanium (see also the papers by Stolyarov et al. [22, 23], which suggests it for substitution of mostly applied Ti-6Al-4V for implant surgery, thus eliminating any concerns regarding toxicity of this alloy [24, 25]. Besides this advantage, it has been demonstrated [26] that nanocrystallization also has the potential for controlling initial cell responses. Recent studies have shown that attachment and proliferation of fibroblast [27] and preosteoblast [28] cells on ultrafine-grained titanium substrates processed by SPD are enhanced appreciably. Figure 28.10 provides a demonstration of this effect. In sum, it is believed that significant progress in the application of SPD-processed Ti and Ti alloys in medical implants can be expected in the near future.

While Ti-based alloys, along with stainless steel or NiTi (NITINOL), are preferably used for permanent implants and prostheses, there is often a need for temporary ones. Indeed, permanent implants may cause physical irritation and chronical inflammatory reaction. Sometimes, a repeat operation is needed for the implant to be removed. As the human body is able to regenerate damaged tissue, it would be ideal to have temporary, bioresorbable implants that would provide support during tissue recovery and get resorbed by the body once their function has been fulfilled. This alternative paradigm of implant surgery would be of particular interest for applications in vascular stents. The possibility of using Mg alloys for vascular stents has already been considered [29], and first clinical tests [30] have demonstrated the viability of this approach. However, the knowledge of the effect of the processing history and the resulting microstructure of the Mg alloys used on their performance is very scarce. This is why Wang et al. [31] undertook a study of the effect of mechanical processing, that is of achieving UFG microstructures, on both properties, which are of paramount importance for implant applications, viz. the fatigue life and the biocor-

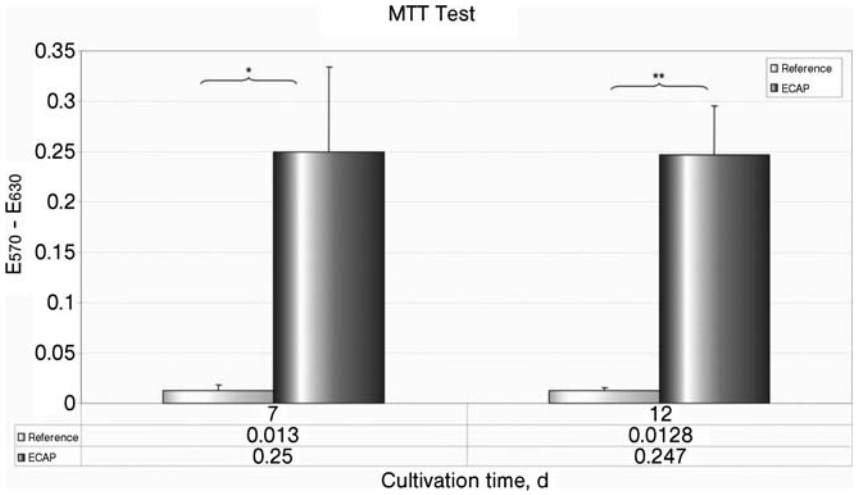

Fig. 28.10 Proliferation of preosteoblastic MC3T3-E1 cells extracted from mice embryos as expressed by light absorbance in MTT assays. The data on $E_{570} - E_{630}$ represented by the columns correspond to the mean values, which are also shown in the table below the diagrams. The light columns represent the as-received commercial purity Ti as a reference and the dark ones the ECAP-processed material. Error bars are also indicated (after Estrin et al. [28], (2008)).

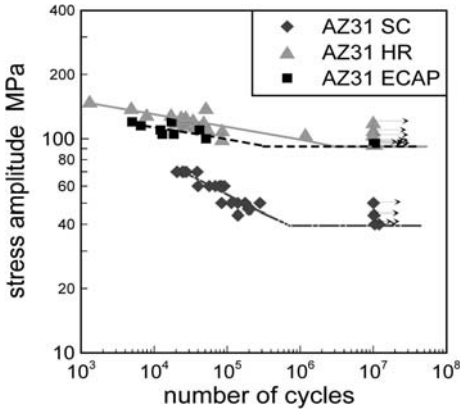

Fig. 28.11 Stress-amplitude dependence of the fatigue life for AZ31 with three different processing histories (from [31]). Arrows indicate run-outs.

rosion rate, for the case of a common structural Mg alloy AZ31 that was proposed for implant applications [29].

Three material states were investigated in [31]: squeeze-cast material (designated SC), SC subsequently hot rolled at 370 °C to a thickness reduction of 75% (designated HR) and, finally, a UFG one produced by additional ECAP processing of the HR material. 4 passes of ECAP (route B_c) through a 90° die at a die temperature of 200 °C. The grain structure in the three states was strongly dif-

ferent, the average grain size of the SC, HR and ECAP materials being, respectively, 450 μm, 20 μm, and 2.5 μm. The fatigue properties of the three materials are shown in Fig. 28.11. As is obvious from the curves, hot rolling produces a significant improvement of the fatigue response. However, further grain refinement of the HR alloy by ECAP did not lead to any further improvement – a result that is somewhat unexpected in the light of the literature on the effect of ECAP on fatigue resistance of alloys [1, 2].

28.5
Corrosion/Biocorrosion in SPD-processed Materials

As concerns the corrosion and biocorrosion resistance of UFG and nanocrystalline materials, these seem to be enhanced in comparison to their coarse-grained counterparts, although the extent of the improvement clearly depends on the material and the processing method considered, and in some cases is even not quantitatively reproduced by different research groups. For example, in the case of UFG Cu, Vinogradov et al. [32] found that the ultrafine-grained surface arising from ECAP rather contributes to the homogeneity of corrosion than to the corrosion resistance, while Hadzima et al. [33] found an improved corrosion resistance, too. The same beneficial effect has been observed by Hadzima et al. in UFG IF steel [34], and by Schneider et al. in nanocrystalline FeCr [35]. According to the investigations by the group of Rofagha [36, 37], nanocrystalline Ni from electrodeposition does not exhibit any increase in corrosion resistance but electrodeposited nano-Ni-P does. Consolidated ball-milled Ni, however, shows a marked increase of corrosion resistance [38]. As concerns hexagonal metals pro-

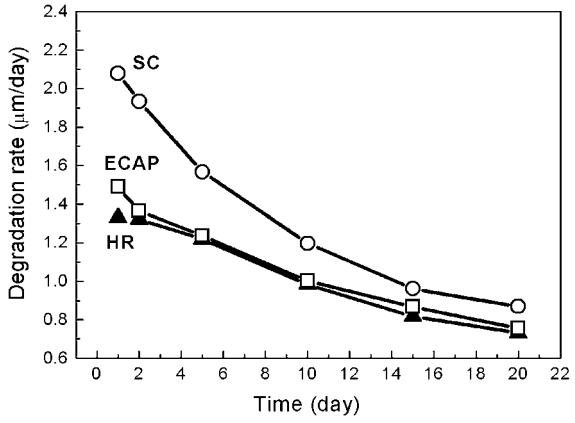

Fig. 28.12 The effect of the processing history on biodegradation rate of AZ31 in Hank's solution (after [31]). The acronyms SC, HR and ECAP stand for the squeeze cast, squeezed cast + hot rolled, and squeeze cast + hot rolled + ECAP-processed conditions.

cessed by SPD, Balyanov et al. [39] found that UFG Ti shows a much better corrosion resistance than coarse-grained (CG) Ti in both HCl and H_2SO_4 solutions as long as the concentration of the solutions were not too high. The improved corrosion resistance seems to arise from rapid formation of passive films due to an increase in the surface crystalline defects in the UFG material such as grain boundaries and dislocations, but not impurities segregated to grain boundaries. Also in Mg alloys grain refinement by hot rolling (HR) was shown to have a favorable effect, reducing the rate of biocorrosion. This is clearly seen from Fig. 28.12 [31] where specimens were immersed in Hank's solution, which simulates bodily fluids. However, as with the fatigue properties, ECAP did not give rise to a further biocorrosion retardation effect. While it is surprising that ECAP processing did not lead to the desired outcomes, there are further indications that grain refinement leads to enhanced corrosion resistance in Mg and Mg alloys [40, 41]. In their recent paper, Ben Hamu et al. [41] argue that deformation by ECAP not only reduces the grain size but also leaves a high dislocation density in the grain interior and in the wake of grain boundaries, whereas in hot-rolled Mg and Mg alloys no such dislocations have been observed. These defects are thus believed to be responsible for a marked enhancement of the corrosion and/or biodegradation rate, which suggests some thermal treatment of the as-deformed ECAP material should be carried out. It appears that more systematic studies are needed to tailor the ECAP-processing conditions for obtaining microstructures favorably affecting fatigue and biocorrosion resistance, and we definitely see some scope for SPD processing in producing novel biodegradable implants.

28.6 Summary

By several examples, it was shown that niche applications for alloys with extremely fine grain structure produced by severe plastic deformation exist in such high-tech areas as MEMS and force filling in electronics, hydrogen-storage systems, medical implants and prostheses, and corrosion-resistant tools. While the enhancement of mechanical properties by SPD is an important aspect of such technologies, it is often other improved properties achieved by SPD, such as hydrogen-storage kinetics or the rate of biodegradation, that make the materials attractive candidates for novel, marketable applications.

References

1 R. Z. Valiev, Y. Estrin, Z. Horita, T. G. Langdon, M. J. Zehetbauer, Y. T. Zhu, JOM 58 (4) 33 (2006).
2 R. Z. Valiev, M. J. Zehetbauer, Y. Estrin, H. W. Hoeppel, Y. Ivanisenko, H. Hahn, G. Wilde, H. J. Roven, X. Sauvage, T. G. Langdon, Adv. Eng. Mater. 9, 527 (2007)
3 W. K. Kim, Y. W. Sa, Scripta Mater. 54, 1391 (2006).
4 Y. Estrin, M. Janecek, G. I. Raab, R. Z. Valiev, A. Zi, Met. Mater. Trans. 38A (2007) 1906.
5 Y. Estrin, E. Rabkin, R. J. Hellmig, M. Kazakevich, A. Zi, Mater. Sci. Eng. A410–411 (2005) 165.
6 Y. Estrin, H. S. Kim, M. Kovler, G. Berler, R. Shaviv, E. Rabkin, J. Appl. Phys. 93 (2003) 5812.
7 Y. Estrin, E. Rabkin, R. J. Hellmig, M. Kazakevich, A. Zi, Int. J. Mater. Res. 96 (2005) 10.
8 M. J. Zehetbauer, H. P. Stuewe, A. Vorhauer, E. Schafler, J. Kohout, Adv. Eng. Mater. 5 (2003) 330.
9 S. C. Baik, R. J. Hellmig, Y. Estrin, H. S. Kim, Z. Metallk. 94 (2003) 754.
10 M. Zehetbauer, E. Schafler, G. Steiner, E. Korznikova, A. Korznikov, Mater. Sci. Forum 503–504 (2006) 57.
11 H. Ferkel, M. Glatzer, Y. Estrin, R. Z. Valiev, C. Blawert, B. L. Mordike, Mater. Sci. Eng. A 348 (2003) 100.
12 L. Zaluski, A. Zaluska, J. O. Ström-Olsen, J. Alloys Compd. 289 (1999) 197.
13 T. Spassov, U. Köster, J. Alloys Compd. 287 (1999) 243.
14 M. Dornheim, N. Eigen, G. Barkhordarian, T. Klassen, R. Bormann, Adv. Eng. Mater. 8 (2006) 377.
15 V. Skripnyuk, E. Rabkin, Y. Estrin, R. Lapovok, Acta Mater. 52 (2004) 405.
16 V. Skripnyuk, E. Rabkin, Y. Estrin, R. Lapovok, Proc. Ultrafine Grained Materials III, Y. T. Zhu et al., Eds., TMS 2004 (Charlotte, USA), p. 53.
17 V. Skripnyuk, E. Buchman, E. Rabkin, Y. Estrin, M. Popov, S. Jorgensen, J. Alloys Compd. 436 (2007) 99.
18 A. K.Wieczorek, M. Krystian, M. J. Zehetbauer, Solid State Phenom. 114 (2006) 177.
19 P. V. Fursikov, D. N. Borisov, M. V. Lototsky, Y. Estrin, V. A. Yartus, B. P. Tarasov, Int. Sci. J. Altern. Energy & Ecology ISJAEE 7 (2006) 23.
20 T. C. Lowe, JOM 58 (4) (2006) 28.
21 Y. T. Zhu, T. C. Lowe, R. Z. Valiev, V. V. Stolyarov, V. V. Latysh, G. I. Raab, SPD processing of Ultrafine-Grained Ti and Ti Alloy for medical implants, US patent No. 6,399.215 (2001).
22 V. V. Stolyarov, Y. T. Zhu, I. V. Alexandrov, T. C. Lowe, R. Z. Valiev, Mater. Sci. Eng. A343 (2003) 43.
23 V. V. Stolyarov, R. Z. Valiev, L. Zeipper, G. Korb, Proc. 10th Int. Conf. Titanium, Hamburg, Germany, July 13–18 (2003), ed. G. Lütjering (2004) p. 1437.
24 H. J. Rack, J. I. Qazi, Mater. Sci. Eng. C 26 (2006) 1269.
25 C. N.Elias, J. H.C. Lima, R. Valiev, M. A. Meyers, JOM 60 (3) 46 (2008).
26 H. Liu, T. G. Webster, Biomaterials 28 (2007) 354.
27 R. Z. Valiev, I. P. Semenova, V. V. Latysh, H. Rack, Terry C. Lowe, J. Petruzelka, L. Dluhos, D. Hrusak, J. Sochova, Adv. Eng. Mater. 10 (2008) B15.
28 Y. Estrin, C. Kasper, S. Diederichs, R. Lapovok, J. Biomed. Mater. Res. A, doi: 10.1002/jbm.a.32174 (2008).
29 F. Witte, V. Kaese, H. Haferkamp, E. Switzer, A. Meyer-Lindenberg, C. J. Wirth, H. Windhagen, Biomaterials 26 (2005) 3557.
30 R. Erbel, C. Di Mario, J. Bartunek, J. Bonnier, B. de Bruyne, F. R. Eberli, P. M. Haude, B. Heublein, M. Horrigan, C. Ilsley D. Boese, J. Koolen, T. F. Lüscher, N. Weissman, R. Waksman, The Lancet 369 (2007) 1869.
31 H. Wang, Y. Estrin, H. M. Fu, G. L. Song, Z. Zuberova, Adv. Eng. Mater. 9 (2007) 967.
32 A. Vinogradov, T. Mimaki, S. Hashimoto, R. Valiev, Scripta Mater. 41 (1999) 319.
33 B. Hadzima, M. Janecek, R. J. Hellmig, Y. Kutnyakova, Y. Estrin, Mater. Sci. Forum 503–504 (2006) 883.
34 B. Hadzima, M. Janecek, Y. Estrin, H. S. Kim, Mater. Sci. Eng. A 462 (2007) 243.

35 M. Schneider, W. Zeiger, D. Scharnweber, H. Woch, Mater. Sci. Forum 225–227 (1996) 819.
36 R. Rofagha, R. Langer, A. M. El-Sherik, U. Erb, G. Palumbo, K. T. Aust, Scripta Metall. 25 (1991) 2867.
37 R. Rofagha, U. Erb, D. Ostander, G. Palumbo, K. T. Aust, Nanostruct. Mater. 2 (1993) 12.
38 M. Schneider, W. Zeiger, U. Birth, K. Pischang, E. Gaffet, O. El kedim, Mater. Sci. Forum 235–238 (1997) 961.
39 A. Balyanov, J. Kutnyakova, N. A. Amirkhanova, V. V. Stolyarov, R. Z. Valiev, X. Z. Liao, Y. H. Zhao, Y. B. Jiang, H. F. Xu, T.C Lowe, Y. T. Zhu, Scripta Mater. 51 (2004) 225.
40 C.op't Hoog , N. Birbilis , Y. Estrin, Adv. Eng. Mater. 10 (2008) 579.
41 G. Ben Hamu, D. Eliezer, L. Wagner, J. Alloys Compd. (2008), doi:10.1016/j.jallcom.2008.01.084.

29
Bulk Materials with a Nanostructured Surface and Coarse-grained Interior

Ke Lu and Leon Shaw

29.1
Introduction

Refining grains of polycrystalline materials into the nanometer regime provides a unique approach to significantly enhance mechanical properties of conventional materials without changing their chemical compositions. Previous studies indicated that bulk nanostructured materials (with grain sizes below 100 nm) possess some novel properties and performances that differ fundamentally from those of their coarse-grained counterparts, such as high hardness and strength [1–3], enhanced chemical reactivity [4], improved tribological properties [5], and superplasticity at low temperatures [6, 7]. Nevertheless, technological applications of bulk nanostructured materials are restricted by the serious technical difficulties in their synthesis processes.

As most material failures occur on surfaces such as fatigue fracture, fretting fatigue, wear, corrosion, *etc*., a gradient structure of a nanostructured surface layer with a bulk coarse-grained interior is expected to be effective in improving the global properties and performance of the materials. Conventionally, a nanostructured surface layer can be made on a bulk material by means of various coating and deposition technologies such as PVD, CVD, sputtering, electrodeposition, *etc*. The predominant factors in this process are bonding of the coated layer with the matrix and bonding between particles inside the surface layer while maintaining nanostructures.

An alternative approach is to transform coarse grains in the surface layer of a conventional bulk material into nanosized grains while keeping the overall composition and/or phases unchanged [8]. Such an approach (referred to as surface self-nanocrystallization of bulk materials) can be realized by means of substantial grain refinement induced by plastic deformation in the surface layer. Its principle is similar to that in severe plastic deformation of bulk metals and alloys in which submicro-sized or nanosized grains are obtained [9]. Recently, pioneered by Lu and Lu [8, 10], a number of surface plastic-deformation processes have been developed aiming to create bulk materials with a nanostructured surface layer and a coarse-grained interior. These processes, which are generally re-

Bulk Nanostructured Materials. Edited by M. J. Zehetbauer and Y. T. Zhu

ISBN: 978-3-527-31524-6

ferred to as *surface mechanical attrition treatment (SMAT)*, rely on surface plastic deformation induced by impacts of high-velocity balls, hammer peening, surface rolling, laser shock treatment, or machining. The techniques have been successfully applied in various kinds of materials including pure metals, steels, and alloys [10–21], on which nanostructured surface layers up to about 50 μm thick have been obtained.

A common feature of these SMAT processes is surface severe plastic deformation (S^2PD). High-velocity ball-impact processes have received most of the attention because of their versatility in processing complex-shaped parts [10–25]. The high velocity of balls is generated through collision between balls and a vibrating chamber driven by an ultrasonic generator (previously termed ultrasonic shot peening (USSP) [10, 13, 15]) or by an electric motor (previously termed high-energy shot peening (HESP) [22] or SMAT [14, 15] or surface nanocrystallization and hardening (SNH) [17, 25]). The high velocity of balls can also be generated through a high-pressure light-gas gun that accelerates particles to a desired impact speed, named as the particle impact processing (PIP) [20, 21]. For these processes, different devices invented for generating high-speed balls offer a wide range of kinetic energies to produce various degrees of surface plastic deformation.

Table 29.1 lists typical values for the sizes and speeds of balls and their corresponding kinetic energies reported in the literature. For comparison, conventional shot peening (SP) is also included. It can be seen that PIP has the highest kinetic energy, followed by SNH and SMAT, and then HESP. SP has the lowest kinetic energy, which may overlap with the kinetic energy of USSP, depending on the diameter and velocity of balls and shots used. The kinetic energies of balls and shots are an important parameter in determining the degree of surface severe plastic deformation. As described in the following sections, many studies, both experiments and modeling, show unambiguously that the depth of plastic deformation zone is directly proportional to the kinetic energy of impacting balls and shots [26–29].

Table 29.1 Typical parameters of balls and shots used in SP and various SMAT processes.

Process	Diameter of balls or shots (mm)	Impact velocity (m/s)	Kinetic energy of balls or shots [a] (J)
SP [26]	0.25–1.0	20–150	9.2×10^{-6}–0.01
USSP [10, 13]	0.4–3.0	<20	0.0001–0.02
SMAT [14, 15]	2.0–10.0	2–5	<0.2
HESP [22]	4.0–8.0	2–3	<0.018
SNH [17, 25]	4.0–8.0	5–15	0.0063–0.43
PIP [20, 21]	4	120	1.88

a) Kinetic energy is also dependent of the density of the ball and shot used, which is not listed here.

29.2
Processing and Structure Characterization

29.2.1
Deformation Field

Quantification of the deformation field within the workpiece upon impact of high-energy balls is essential for understanding the structural evolution, residual stresses, and property improvements induced by S^2PD. The deformation field can be estimated using the analytical approach based on the Hertz theory of elastic contact [30]. The analysis of the elastic contact can be extended to describe the plastic deformation zone for an elastic, perfectly plastic solid [26, 31]. One of the most important parameters of the deformation zone in the workpiece is the depth of plastic zone, h, which determines the thickness of the work-hardened layer as well as the thickness of the surface layer within which residual compressive stresses are present. For an elastic, perfectly plastic solid the depth of plastic zone can be related to the processing parameters of S^2PD through the following equation [26]

$$\frac{h}{R} = 3\left(\frac{2}{3}\right)^{1/4}\left(\frac{\rho v_b}{\bar{P}}\right)^{1/4} \tag{29.1}$$

where R, ρ and v_b are the radius, density and velocity of the impacting ball, respectively, and $\bar{P}$ is the mean normal pressure in the circle of contact between the impacting ball and the workpiece. The depth of plastic zone estimated from Eq. (29.1) does not include work hardening, strain-rate sensitivity, and thermal effects. Nevertheless, Eq. (29.1) has provided the correct trend for the relationship between the depth of plastic zone and the parameters of shot peening [26, 31]. Since the mean normal pressure is proportional to the hardness of the workpiece, Eq. (29.1) reveals that the depth of plastic zone increases with the ball size, density and velocity, and decreases with an increase in the hardness of the workpiece. Based on these relationships, it can be concluded that the depth of the plastic zone increases with the kinetic energy of balls.

Numerical approaches such as finite-element analysis provide better evaluation of the deformation zone than the approximation of elastic contact or elastic-and-perfectly plastic contact. Based on a three-dimensional (3D) dynamic finite-element model (FEM) established in a recent study [32], the depth and the evolution of the plastic zone under a single and multiple impact conditions have been evaluated. Shown in Fig. 29.1 is the FEM that contains a high-velocity, rigid ball impacting the center of a plate made of an elastoplastic material with piecewise linear isotropic hardening behavior. By varying the input data the differences between shot-peening (SP) and S^2PD processes can be evaluated. Table 29.2 lists the depth of plastic zone and the maximum effective plastic strain within a nickel-based alloy induced by dynamic impact of a WC ball or shot with different processing parameters. SNH is assumed to have a WC ball

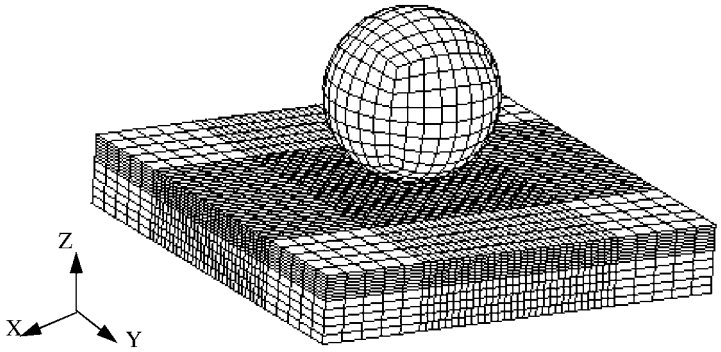

Fig. 29.1 Finite-element model describing single and multiple impacts at the same location on an elastoplastic plate by a high-velocity ball.

Table 29.2 Results of finite-element simulation of SNH and SP processes.

Process	Input data			Output data		
	Ball diameter (mm)	Ball density (g/cm^3)	Impact velocity (m/s)	Kinetic energy (J)	Depth of plastic zone (mm)	Maximum effective plastic strain
SNH	7.86	15	5	0.0476	1.6	0.18
SP	0.3	15	50	0.000265	0.15	0.0017
Hypo[a)]	0.3	15	670	0.0476	1.2	0.315

a) A hypothetical case that has the same kinetic energy as SNH, but with an extremely high impact velocity and a shot size equal to that in SP.

7.86 mm in diameter and traveling at a speed of 5 m/s, whereas SP is assumed to have a WC shot 0.3 mm in diameter with an impact velocity of 50 m/s. These assumptions are consistent with the typical processing parameters of SP, SMAT, HESP, and SNH [17, 22, 25, 26]. A hypothetic case, which has a shot size equal to that in SP but with a very large impact velocity so that the shot has the same kinetic energy as the ball in S^2PD, has also been included in Table 29.2 to evaluate the effect of S^2PD processing parameters.

Table 29.2 clearly reveals that the depth of the plastic zone increases with the kinetic energy of balls or shots. Furthermore, the depth of the plastic zone increases with shot size for a given kinetic energy. Since the kinetic energy of S^2PD is typically 50 to 500 times greater than that in SP, S^2PD processes produce a thicker plastically deformed layer than conventional shot peening. For the particular cases considered in Table 29.2, the kinetic energy of SNH is 180 times that of SP, which results in a plastic zone about 10 times deeper than that achieved from SP. Therefore, the SNH-processed workpiece will have a

thicker work-hardened layer than the shot-peened ones. Furthermore, since the thickness of the surface layer with residual compressive stresses coincides with the depth of the plastic zone [27], the SNH-processed workpiece also has a thicker surface layer with residual compressive stresses than the shot-peened workpiece. An additional important message from Table 29.2 is that each impact in SNH generates a larger maximum effective plastic strain than each impact in SP. As such, SNH is much more efficient in inducing the surface nanocrystallization than SP because a certain amount of plastic deformation is required for the formation of nanograins [23]. Finally, it is interesting to note that when the kinetic energy is kept constant, a larger ball produces a deeper plastic zone, whereas a smaller ball is more efficient in inducing the surface nanocrystallization.

These theoretical analyses explain why S^2PD processes induce the surface nanocrystallization, whereas SP usually does not. These analyses also predict better performance of the S^2PD-processed workpiece than the shot-peened workpiece because of the presence of a nanocrystalline surface layer, a thicker work-hardened layer, and a thicker surface region with residual compressive stresses in the S^2PD-processed workpiece.

29.2.2 Residual Stresses

Plastic deformation on the impacted surface not only causes the local property and microstructural changes, but also results in the formation of residual compressive stresses. Plastic deformation causes stretching of the top layer of the workpiece. Upon unloading, the elastically stressed subsurface layers tend to recover their original dimensions, but the continuity of the material in both zones, the elastic and the plastic, does not allow this to occur. As a result, a residual compressive stress field followed by a tensile field is formed in the impacted workpiece. Figure 29.2 shows the typical residual stress profile generated

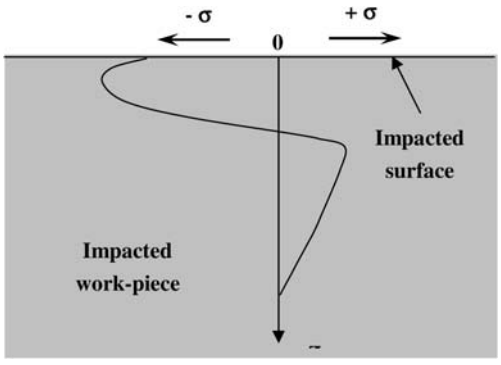

Fig. 29.2 The typical inplane residual stress profile produced by shot peening.

via shot peening. The inplane residual compressive stress normally increases as the position moves away from the shot-peened surface, reaches a maximum, then decreases continuously, and finally becomes tensile. Such a profile has been widely confirmed by both experiments and finite-element modeling [27, 28, 33]. However, when the workpiece to be processed is very soft, the maximum compressive stress can appear at the impacted surface rather than beneath it [33]. Thus, the details of the value and profile of the residual compressive stress depend on the mechanical properties of the workpiece and processing conditions (e.g., the shot size and velocity) of the shot-peening process [27, 28, 33, 34].

Figure 29.3 shows the residual stress profile just beneath the impact center within a nickel-based alloy after a single impact by a WC ball 7.86 mm in diameter and a speed of 5 m/s (i.e. a typical SNH condition as shown in Table 29.2), calculated using the FEM shown in Fig. 29.1. It is noted that the profile of the inplane residual compressive stresses (i.e. X-stress) is slightly more complicated than what is shown in Fig. 29.2. However, the overall conclusion remains the same; that is, there is a surface region that contains inplane residual compressive stresses for the S^2PD-processed workpiece. Thus, both shot-peening and S^2PD processes generate a surface region with residual compressive stresses, but the thickness of this compressive region is much thicker for the S^2PD-processed workpiece than for the SP workpiece.

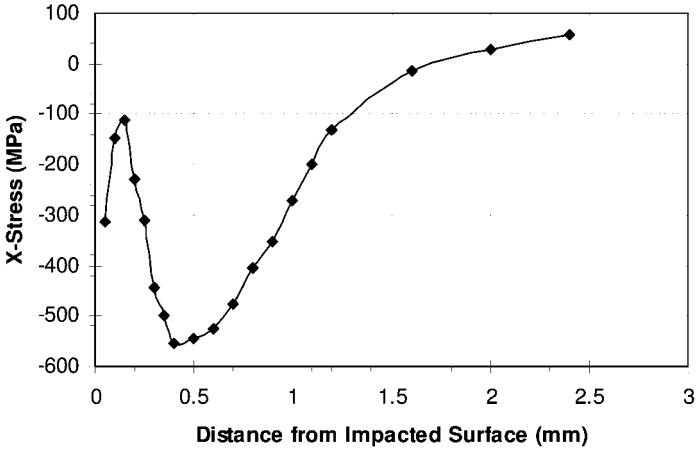

Fig. 29.3 The inplane residual X-stress profile beneath the impact center within a nickel-based alloy after a single impact by a WC ball, calculated from the FEM shown in Fig. 29.1.

29.2.3
Surface Roughness

Surface roughness typically increases after S^2PD [17, 35, 36]. Detailed studies [17, 35] indicated that surface roughening in S^2PD processes can be explained by the indentation process of impacting balls, and the surface-roughness evolution can be divided into three stages: the roughness-increase stage, the roughness-decrease stage, and finally the steady-state stage. These three stages are related to different stages of the surface coverage by indents generated by impacting balls. The steady-state stage corresponds to the impact coverage of the entire surface multiple times, and the surface roughness at the steady state increases with the ball size [35].

The dependence of the surface roughness on the S^2PD processing parameters has been investigated through experiments and numerical simulation [35, 36]. Analytical models have also been proposed and confirmed by experiments and numerical simulation [17]. The following equation shows how the peak-to-valley (PV) value of the workpiece surface, Z_{pv}, varies with the S^2PD processing parameters [17].

$$Z_{pv} \propto R, \quad Z_{pv} \propto v_b^{\frac{4}{n+4}}, \quad Z_{pv} \propto \rho^{\frac{-2}{n+4}}, \quad Z_{pv} \propto k^{\frac{-2}{n+4}} \tag{29.2}$$

where n and k are the strain-hardening exponent and the strength coefficient of the workpiece, respectively. R, v_b and ρ have been defined previously. Eq. (29.2) shows that the surface roughness increases linearly with the radius of the ball, whereas the effects of the ball velocity and density on surface roughness are described by power laws. Furthermore, the surface roughness is inversely proportional to the strength coefficient of the workpiece, i.e. increasing the strength coefficient of the workpiece reduces the surface roughness. The effect of the strain-hardening exponent cannot be expressed explicitly, but can be evaluated through curves with n as a variable. The analysis indicates that the surface roughness decreases as the resistance of the workpiece to plastic deformation increases [17]. Such a result is consistent with intuition.

It should be noted that in many cases the surface roughness is preferably characterized using the root-mean-square average (RMS) or arithmetic-mean value (AMV) rather than the PV value. In spite of this general practice, Eq. (29.2) still offers the guideline on how to minimize the surface roughness because a previous study [35] has established that RMS and AMV exhibit the same dependence on processing conditions as the PV value.

29.2.4
Grain Size and Grain-refinement Mechanism

As discussed in the previous sections, grain sizes and thickness of the nanostructured layer in the SMAT samples are strongly dependent upon the processing conditions (such as ball size, velocity of balls, *etc.*), and on the materials

Table 29.3 A list of minimum grain sizes (D_{min}) in the top surface layer and thickness of nanostructured layer (grain size $D<100$ nm) for some typical materials processed by means of SMAT.

Material	Process	D_{min} (nm)	Thickness (μm)	Reference
Fe	SMA T (60 min)	7 nm	15	[10]
Cu	SMAT (30 min)	10 nm	25	[37]
7075 Al alloy	USSP (15 min)	20 nm	22	[13]
AISI 304 stainless steel	SMAT (15 min)	8 nm	30	[38]

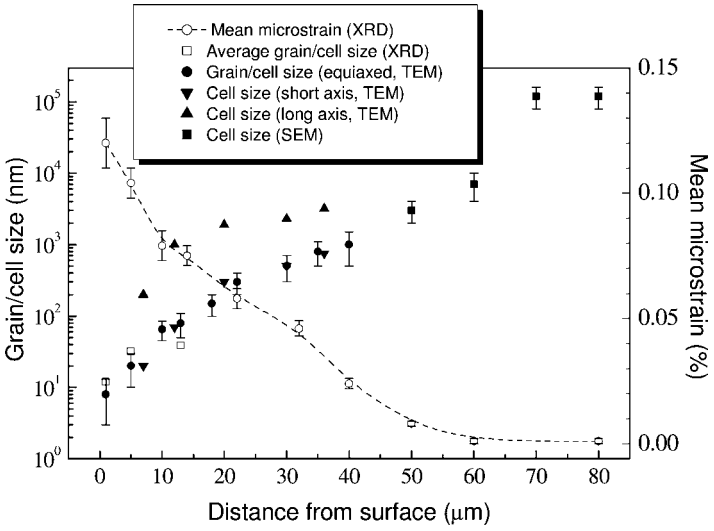

Fig. 29.4 Variations of the grain/cell size and the mean microstrain with the depth from the treated surface of a SMAT Fe sample determined by using XRD analysis, TEM and SEM observations. In TEM observations, the sizes of the equiaxed cells and the lamellar cells (along the short axis and long axis) are measured.

processed as well. Table 29.3 lists the minimum grain size in the top surface layer and thickness of nanostructured layer for some typical materials processed. Differences in the grain size and the thickness originate mainly from the different grain-refinement mechanisms involved, as will be discussed later in this section.

Figure 29.4 shows a measurement result of the variation of grain/cell size with the depth from the treated top surface in pure Fe processed by means of SMAT for 60 min [10]. From Fig. 29.4, one may see the surface layer after SMAT processing can be subdivided into four sections along the depth in terms of grain size: (i) nanostructured regime (0–15 μm), (ii) submicro-sized regime (15–40 μm), (iii) micro-sized regime (40–60 μm), and (iv) plastically deformed matrix (60–110 μm). Such a gradient variation of grain size along the depth re-

sults from the gradient variation of strain and strain rate from the treated top surface (both are very large) to the deep matrix (essentially zero) during SMAT. The underlying mechanism for deformation-induced grain refinement in the micrometer and nanometer regimes can be identified by examining the microstructure characteristics at different levels of strain and strain rate (at different depths from the top surface), which is crucial for development of the SMAT techniques [39].

Analogous to the grain-refinement mechanism during plastic deformation of bulk metals, formation of nanostructures from the coarse-grained polycrystals in the surface layer upon SMAT involves various dislocation activities and development of grain boundaries. Plastic deformation behaviors and dislocation activities in metals depend strongly on the lattice structure and the stacking-fault energy (SFE) of the materials treated, and the processing conditions (such as temperature, strain rate, and the kinetic energy of balls) as well. For example, in those materials with high SFEs, dislocation walls and cells will be formed to accumulate strains and subboundaries are developed to subdivide coarse grains. While for those with low SFEs, the plastic-deformation mode may change from dislocation slip to mechanical twinning (especially under a high strain rate and/or low temperatures). Here, three typical examples with different lattice structures and SFEs are taken to demonstrate the SMAT-induced grain-refinement processes.

Pure Fe: Fe is a typical bcc metal with a high SFE of about 200 mJ/m^2. Grain refinement was observed in the surface layer of a bulk Fe sample after SMAT and the top layer consists of crystallites of as small as about 10 nm in size, as indicated in Fig. 29.4. The grain/cell size increases gradually from 10 nm to several micrometers at about 60 μm deep. Detailed cross-sectional TEM observations of the as-treated Fe sample revealed the grain-refinement process, which involves the following elemental processes [10]:

(1) *Development of dense dislocation walls (DDWs) and dislocation tangles (DTs).* In order to accommodate plastic strains, dislocation activities are motivated in the original coarse grains, forming DDWs along (110) slip planes and random DTs in some grains (depending on the grain orientations). Development of these dislocation configurations results in subdivision of original grains by forming individual dislocation cells primarily separated by DDWs and DTs. The repeated multidirectional impacts on the sample surface may lead to a change of slip systems with the strain path even inside the same grain. The dislocations not only interact with other dislocations in the current active slip systems, but also interact with inactive dislocations generated in previous deformation. Therefore, the grains can be subdivided efficiently by the DDWs and DTs in the treatment.
(2) *Transformation of DDWs and DTs into subboundaries with small misorientations.* Formation of subgrain boundaries subdividing the original grains results from development of DDWs and DTs by accumulation of more and more dislocations with increasing strains. At a certain strain level, for mini-

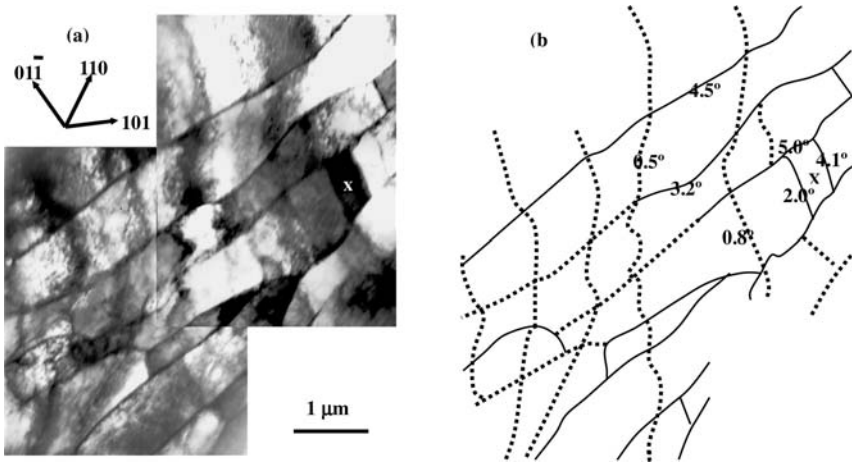

Fig. 29.5 Cross-sectional TEM images at 37 μm deep from the top surface of the SMAT Fe sample. Submicro-sized lamellar cells separated by DDWs (dotted lines) and subboundaries (solid lines) are seen. Numbers in (b) indicate misorientations across adjacent cells.

mizing the total system energy, dislocation annihilation and rearrangement occur in DDWs and DTs, which will transform into subboundaries (with larger misorientations across relative to the DDWs) separating individual cells. The subgrain boundaries are actually formed by recombination of a high density of dislocations and usually have small misorientations of a few degrees, i.e. small-angle grain boundaries, as can be clearly seen in Fig. 29.5.

(3) *Evolution of subboundaries to highly misoriented grain boundaries.* With further increasing strains, more dislocations are generated and annihilated at subboundaries, raising the energy of the subboundary and progressively increasing its misorientations. The orientations of grains with respect to their neighboring grains become completely random, forming highly misoriented grain boundaries. The increment of misorientations between neighboring grains can be realized by accumulating more dislocations with different Burgers vectors in grain boundaries, or alternatively, by rotation of grains (or grain-boundary sliding) with respect to each other when strains are large enough. The grain rotation process would be facilitated when the size of grains is reduced due to the obvious size dependence [18].

With further straining, DDWs and DTs could form inside the inner of the refined subgrains or grains, and these refined grains could be further subdivided following the similar mechanism. With increasing strain in the top surface layer, the subdivision takes place on a finer and finer scale. When dislocation multiplication rate is balanced by the annihilation rate, the increase of strains could not reduce the subgrain size any longer, and a stabilized grain size results.

In an Al alloy with a high SFE subjected to the SMAT, a similar grain-refinement mechanism was observed [13].

Pure Cu: Cu is an fcc metal with a medium SFE (about 78 mJ/m^2). After SMAT to a bulk Cu specimen, a nanostructured surface layer of about 25 μm thick was formed. Microstructure examination by means of cross-sectional TEM observations revealed a different grain-refinement mechanism [37]:

(1) *Development of equiaxed dislocation cells (DCs).* For the fcc structure, more dislocation slip planes exist compared with that in bcc Fe. The strain-induced dislocation activities lead to formation of equiaxed DCs (instead of DDWs or DTs as in Fe) where a high density of dislocations locate at the cell boundary with few dislocations inside the cell. The cell size observed ranges from a few micrometers to several tens of nanometer, depending upon the strain and strain rate. With increasing strains, the DC size decreases and forming a DC network that subdivides the original coarse grains.
(2) *Formation of twins and subboundaries with small misorientations.* At a certain strain and strain-rate level, mechanical twinning is activated in some grains with favorable orientations. Twins appear at depth from 10 to 100 μm from the top surface, implying the strains and strain rate within this depth regime is appropriate for formation of twins in Cu with the medium SFE. At the same time, in other grains, DCs transform into subboundaries with small misorientations with further straining, which is analogous to the transformation from DDWs as in Fe. These twin boundaries and subboundaries divide the original coarse grains into ultrafine (sub)grains.
(3) *Evolution of subboundaries to highly misoriented grain boundaries.* Increasing strains will drive the transformation from subgrain boundaries into conventional grain boundaries with large misorientations, similar to the process as in Fe.

AISI 304 stainless steel: AISI 304 stainless steel is a widely used engineering material with an fcc austenite structure and a very low SFE (about 17 mJ/m^2). Due to the low SFE, dislocation activities in plastic deformation are very different from the above two cases. The grain-refinement mechanism was found as follows [38]:

(1) *Formation of planar dislocation arrays and twins.* The strain-induced dislocations in the austenite phase slip mainly on their respective {111} planes, forming regular dislocation grids, instead of irregular DCs (as in fcc Al-alloy, Cu) or DDWs (as in bcc Fe). Such a difference originates from the low SFE that makes it difficult for partial dislocations to cross-slip for forming DCs, rather it favors formation of dislocation arrays and twins in {111} planes.
(2) *Grain subdivision by twins and martensite transformation.* With increasing strains, twins in different {111} planes intersect with each other and subdivide the original austenite grains into refined blocks. A strain-induced mar-

tensite transformation is the prevailing phenomenon in the plastic-deformed AISI 304 stainless steel. In the SMA-treated sample, we observed formation of martensite phase at intersections of the twins, of which the size ranges from several nm to submicrometers. Such a phase transformation is a unique process that facilitates grain-refinement procedures.

(3) *Formation of nanocrystallites.* In the top surface layer, nm-sized martensite crystallites are formed by means of further twin–twin intersection and martensite phase transformation under high strains and strain rates. Analogous to other systems, randomly oriented nanocrystallites are formed via grain rotation or other grain-boundary activities (motion or sliding) to accommodate the high strains.

29.3 Properties and Performance

29.3.1 Hardness and Strength

Plastic deformation during SMAT processes will alter the surface property of the workpiece dramatically. Shown in Fig. 29.6 are Vickers microhardness profiles of a nickel-based C-2000® Hastelloy plate (a single-phase, face-centered-cubic alloy with a nominal chemical composition of 23Cr, 16Mo, 1.6Cu, 0.01C,

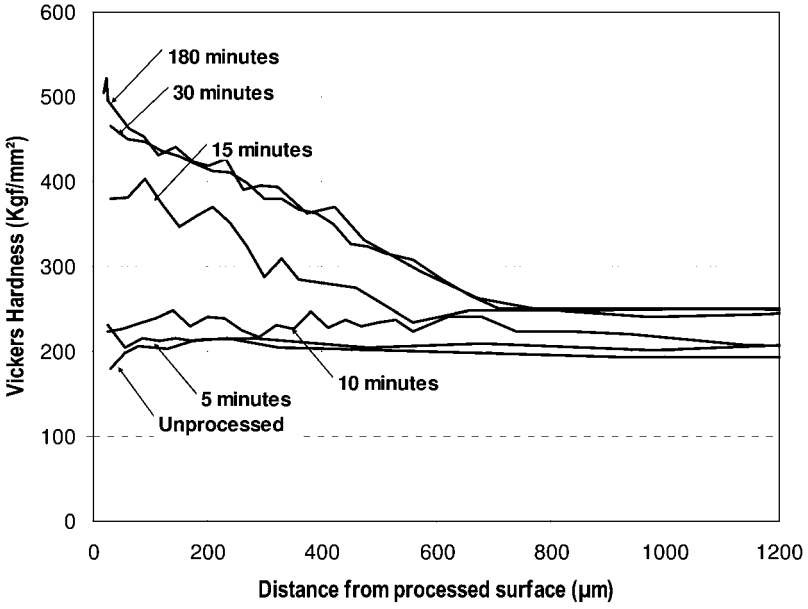

Fig. 29.6 Vickers hardness profiles of nickel C-2000® specimens treated with the SNH process for various periods of time.

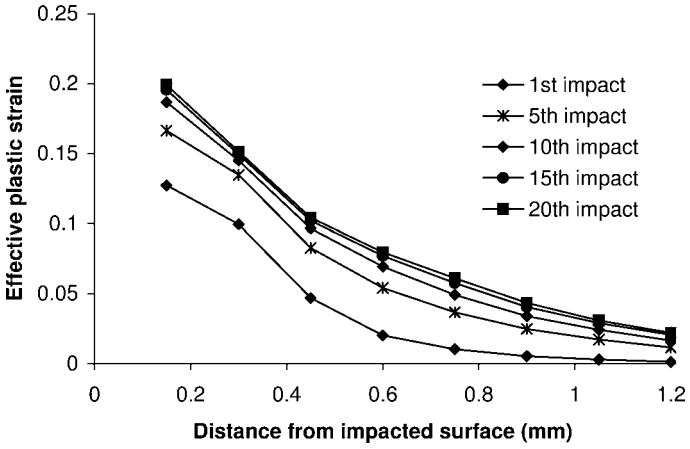

Fig. 29.7 Evolution of the effective plastic strain profile measured from the impacted surface as a function of the number of impacts. The data are generated via numerical simulation using the FEM shown in Fig. 29.1.

0.08Si, and the balance Ni in weight per cent) treated with the SNH process. Corresponding to the largest plastic deformation and thus the highest work hardening, the region near the impacted surface exhibits the highest hardness. This high hardness ($\sim$150% increase over the interior of the plate) derives mainly from work hardening because the nc surface layer is too thin ($\sim$50 μm for the sample processed for 180 min) to be measured with a Vickers indenter [40]. The hardness decreases gradually as the location moves away from the impacted surface due to the reduced plastic deformation. Commercially pure Ti produced using SP and HESP also exhibits similar phenomena [22, 24]. An interesting phenomenon to be noted in Fig. 29.6 is the surface-hardening saturation, i.e. no additional hardening is obtained beyond 30 min of processing. Such a phenomenon has also been observed with an Al-5052 alloy (not shown here). The surface-hardening saturation has important implications in process optimization because prolonged processing could result in surface contamination of the workpiece by impacting balls [36].

The surface hardening and the surface-hardening saturation have been predicted by finite-element modeling based on work hardening alone [32]. Shown in Fig. 29.7 are effective plastic-strain profiles directly beneath the center of impact as a function of the number of impacts, obtained through numerical simulation using the FEM shown in Fig. 29.1. It is noted that the curves of the effective plastic strain are very similar to the hardness profile observed in Fig. 29.6. Since work hardening is proportional to the effective plastic strain, Fig. 29.7 indicates that the surface hardening observed in Fig. 29.6 is mainly due to work hardening. Furthermore, the simulation reveals that a substantial amount of hardening is achieved in the early stage of impacting, whereas prolonged im-

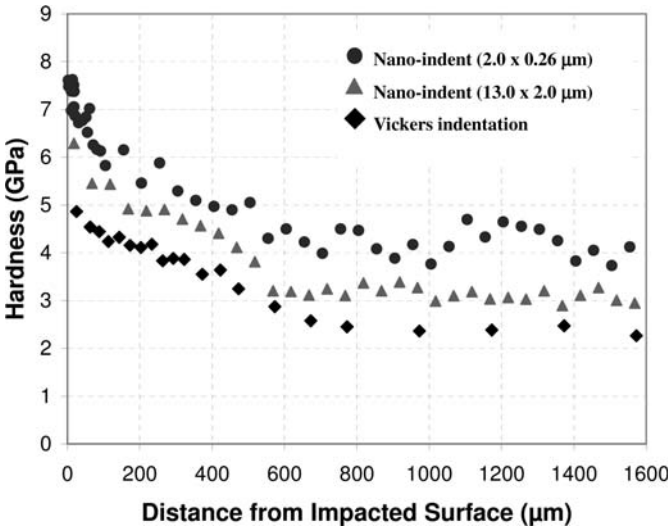

Fig. 29.8 Nanoindentation hardness profiles of nickel C-2000® specimens as a function of the distance from the impacted surface. The specimen has been processed with SNH for 180 min. The microhardness measured using a Vickers indenter is also included for comparison.

pacting provides little strengthening. Thus, the strengthening saturation predicted from the numerical simulation is consistent with the experimental observation.

In order to find out the hardness of the nc surface layer formed from SMAT processes, nanoindentation has been utilized by several groups [20, 25, 41]. Shown in Fig. 29.8 are hardness values of the nickel-based C-2000® Hastelloy after the SNH process, measured using a Berkovich indenter conducted in a displacement-controlled mode employing a computer-controlled Nano Indenter® XP system. Two displacement-controlled conditions have been used in nanoindentation measurements; one gives the indent size of 13 μm along one of the Berkovich triangle edge and 2 μm depth, whereas the corresponding values for the second loading condition are 2.0 and 0.26 μm, respectively. Note that the nanoindentation with smaller indent sizes gives higher hardness values than that with larger indent sizes. This phenomenon is consistent with the size effect established by many investigators [42, 43]. It is also noted that the hardness curve moves up and down more or less parallel regardless of the hardness value. Thus, both the Vickers indentation and nanoindentation reveal the same trend of increasing hardness as the location moves closer to the impacted surface. However, the advantage of nanoindentation is that the nanoindentation with the indent size of 2.0×0.26 μm has provided the valid hardness for locations that are only 10 μm away from the impacted surface.

One most interesting phenomenon revealed in Fig. 29.8 is the gradual increase in hardness from the work-hardened layer to the nc surface layer. Through detailed microstructural analysis using TEM, it has been established that the nickel-based alloy sample shown in Fig. 29.8 has a nc surface layer with grain sizes ranging from 10 to 50 nm and a thickness of 50 μm [40]. Thus, the nanoindentation measurement indicates that there is no sudden jump in the hardness value from the work-hardened layer to the nc surface layer for the nickel-based C-2000® Hastelloy. This is different from that in steels treated by means of a ball-drop technique in which a sudden jump in the hardness value was noticed [41].

The SMAT processes not only alter surface properties, but also change the tensile strength of bulk materials significantly. For a plate sample (or a rod geometry), a 35% improvement in the tensile yield strength of mild steels with minimum degradation in ductility and toughness has been demonstrated [12]. A recent study [44] indicates that about 100% improvements in the tensile yield strength of the nickel C-2000® Hastelloy can be achieved by SNH. Furthermore, it is noted that the ultimate tensile strength of the nickel C-2000® Hastelloy is also increased by SNH, suggesting that the improvement in tensile strength is not due to work hardening alone, but also due to the contribution from the nc surface layer.

To identify the effect of the nc layer on the tensile properties of SMAT samples, uniaxial tensile tests were performed on a thin-film specimen removed from the surface of a 316L austenitic stainless steel sheet processed by means of SMAT [45]. The nc 316L film sample (with a thickness of 15 μm and an average grain size of about 40 nm) exhibits a yield strength as high as 1450 MPa, which is about 6 times higher than that of the coarse-grained (CG) sample. This ultrahigh strength of the nc sample still follows the Hall–Petch relation extrapolated from CG structures. The result clearly indicated that formation of nanostructures in the top surface layer contributes significantly to the enhancement in surface hardness and strength.

29.3.2
Fatigue Resistance

Shot peening improves fatigue resistance [46–50], so do SMAT processes [25]. Figure 29.9 shows the applied stress versus fatigue-cycle–life (*S–N*) curves for the nickel C-2000® Hastelloy with and without 30 min of SNH processing. The SNH process has improved the fatigue endurance limit by as much as 50%. The improvement in the case of shot peening is generally attributed to the presence of residual compressive stresses at the surface region. Furthermore, many studies [46, 48, 50] seem to support the notion that improvements in fatigue resistance are mainly due to the ability of residual compressive stresses in stopping the microcrack propagation and not in preventing fatigue crack initiation. This notion is consistent with the fact that a thicker surface layer with residual compressive stresses is more effective in improving the fatigue strength

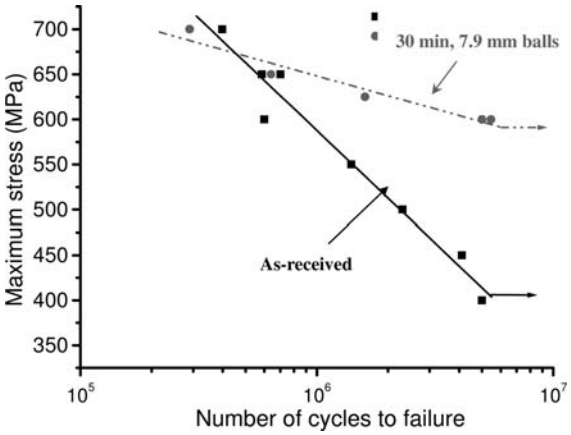

Fig. 29.9 Four-point-bend fatigue tests of the C-2000® alloy, showing improvements in the fatigue endurance limit by 50% after the SNH process.

[49], and larger shots, keeping other parameters constant, leads to better fatigue life [51]. Based on these results, it can be predicted that SMAT processes are likely to improve fatigue resistance more than shot peening because larger balls are used and a thicker surface layer with residual compressive stresses is created (Table 29.2).

The roles of the nc surface layer and work-hardened region in improving fatigue resistance have not been well quantified yet. Nevertheless, a recent study [25] using finite-element modeling to analyze the fatigue-resistance improvement via the SNH process has shown that the work-hardened layer makes more contribution to the fatigue-resistance improvement than residual compressive stresses. However, this may not be the case for shot peeing because SMAT processes create a thicker work-hardened layer than shot peening. Clearly, more detailed studies are needed to define the individual contributions of residual compressive stresses, work-hardened layer, and nanograins at the surface.

An additional factor to consider for the fatigue resistance of the SMAT-processed workpiece is the increased surface roughness and the possible surface contamination due to the material transfer between the workpiece and balls. The latter has been found when balls and the workpiece are not chemically inert and prolonged processing time has been employed [36]. Both increased surface roughness and surface contamination could be harmful to fatigue resistance. As such, fatigue-resistance improvements may not be observed if SMAT processes are not performed properly. "Overprocessing" has been observed on the nickel C-2000® Hastelloy treated with the SNH process [44].

In short, SMAT processes induce many changes to the workpiece. Many of these changes are expected to alter the fatigue properties of the workpiece. Such changes include (a) the formation of a nanocrystalline surface layer, (b) surface

work hardening, (c) the presence of residual inplane compressive stresses at the surface layer, (d) the increased surface roughness, and (e) the material transfer between balls and the workpiece if the balls and the workpiece are not chemically inert. Changes (a) to (c) are beneficial for fatigue properties, whereas changes (d) and (e) are detrimental. Process optimization is needed to enhance changes (a) to (c) and minimize (d) and (e).

29.3.3 Wear and Friction

Wear and friction properties of metallic materials with a nanostructured surface layer are obviously improved compared with their coarse-grained bulk counterparts [52–54]. The tribological behaviors of a SMAT pure Cu sample, in which the top layer of about 15 μm thick is nanostructured, were investigated under dry conditions. Experimental results showed that the load-bearing ability is markedly enhanced relative to the coarse-grained form. The friction coefficient and the wear-volume loss of the nanocrystalline layer are much smaller than those of the coarse-grained copper with a low applied load, as shown in Fig. 29.10. The wear-volume loss of SMAT Cu is less than half of that for the untreated sample for an applied load below 40 N. When the applied load exceeds a critical value, there occurs a transition of the wear regime from abrasion wear to adhesion wear, leading to an abrupt increase of the wear volume, which corresponds to the wear of the nanocrystalline layer in the SMAT Cu sample [54].

A similar observation was reported for a SMAT-processed low-carbon steel sheet of which the friction coefficient and the wear-volume loss are evidently smaller than those for the coarse-grained steel sheet [53]. The improved wear and friction properties can be attributed to the hard surface layer with nano-

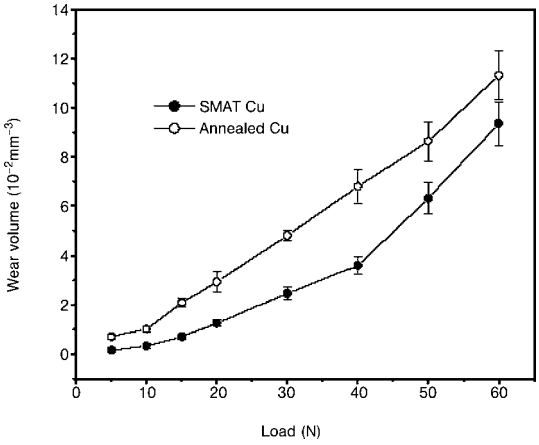

Fig. 29.10 Variation of wear volume with the applied load for the SMAT Cu and the annealed Cu samples.

grains and a gradient variation in the microstructure and properties along the depth from the top surface.

29.3.4 Diffusion and Surface Chemical Reaction

Atomic diffusivity in the nanocrystalline surface layer is expected to be considerably enhanced relative to the conventional coarse-grained polycrystals, as grain boundaries may act as fast-diffusion channels. Wang et al. [55] measured Cr diffusion kinetics in a nanocrystalline layer on a SMAT Fe sample within a temperature range of 573–653 K. They found that diffusivity of Cr in the nanocrystalline Fe is 7–9 orders of magnitude higher than that in Fe lattice and 4–5 orders of magnitude higher than that in the conventional grain boundaries (GBs) of α-Fe. The activation energy for Cr diffusion in the Fe nanophase is comparable to that of the GB diffusion, but the pre-exponential factor is much higher. The enhanced diffusivity of Cr may originate from a large volume fraction of nonequilibrium GBs and a considerable amount of triple junctions in the nanocrystalline Fe sample induced by plastic deformation.

The enhanced diffusivity in the nanostructures is very useful for advancing the traditional surface-modification techniques that are based on various chemical reactions, such as surface nitriding of steel. Surface nitriding of steels is extensively applied in industry to elevate the global performance of the materials especially the wear and/or corrosion resistance, owing to formation of a unique composite structure with a hard surface (a layer of Fe-nitride compounds) and a tough interior. However, widespread uses of the technique are frequently hindered by the reaction kinetics involved. Nitriding processes are performed at high temperatures ($>500\,^{\circ}C$) for a long duration ($\sim$20 to 80 h) [56] and may induce serious deterioration of the substrate in many families of materials.

With the nanocrystalline surface layer induced by SMAT, the nitriding kinetics can be significantly enhanced. Tong et al. [4] reported an investigation on nitriding behaviors of a SMAT pure Fe sample in comparison with the untreated coarse-grained Fe. Both samples were nitrided in flowing, high-purity ammonia gas (NH_3) at $300\,^{\circ}C$ for 9 h. After nitriding, a continuous dark gray surface layer about 10 μm thick was observed on the SMAT Fe sample (Fig. 29.11 (b)). This layer was not seen on the original (Fig. 29.11 (a)). Measurements of nitrogen-concentration profiles (Fig. 29.11 (c)) and phase identification by using TEM and XRD indicated that the dark gray layer consists of ultrafine polycrystalline ε-$Fe_{2\sim3}N$ and γ'-Fe_4N compounds, as well as a small amount of α-Fe phase. Underneath the compound layer was a mixture of nitrides and α-Fe solid solution. The constitution was identical to that of the compound layer formed during the conventional nitriding of coarse-grained Fe at high temperatures. The results clearly demonstrated that the surface chemical reaction occurred in the SMAT Fe with a nanostructured surface layer at $300\,^{\circ}C$, whereas no reaction was detected in the original coarse-grained sample under the same conditions. The obviously increased formation kinetics of nitrides in a nanocrys-

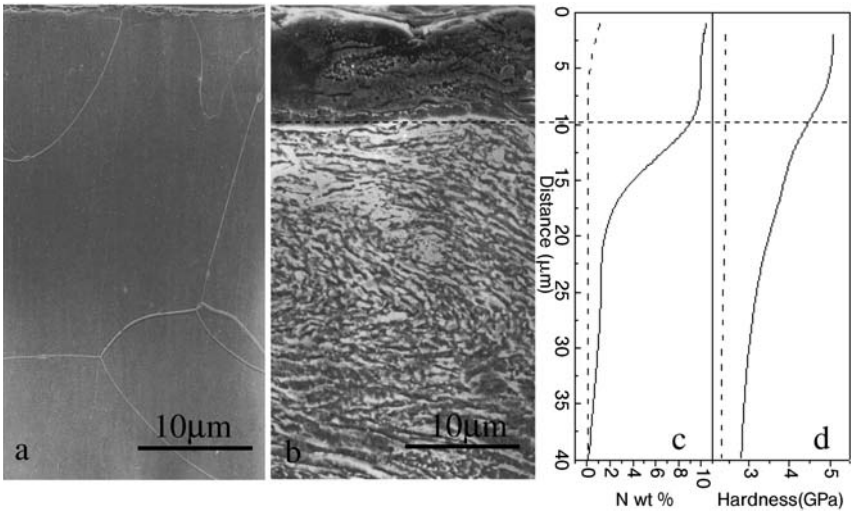

Fig. 29.11 Cross-sectional observations of the (a) original coarse-grained and the (b) SMAT Fe samples after nitriding at 300 °C for 9 h. (c) and (d) are measured nitrogen concentration (by using electron probe) and microhardness (using nanoindentation) along the depth from the top surface layer for the original Fe sample (dashed lines) and the treated one (solid lines), respectively.

talline α-Fe relative to that in the coarse-grained form can be attributed to the much-enhanced heterogeneous nucleation rate at numerous grain boundaries in the nanocrystalline α-Fe [57].

For an AISI 304 stainless steel, a nanostructured surface layer was produced after SMAT. Low-temperature plasma nitriding of the SMAT sample at 400 °C for 5 h resulted in formation of a much thicker nitrided layer compared to that in the coarse-grained counterpart nitrided under the same condition. The nitrided layer on the SMAT sample is composed of nanostructured austenite expansion and martensite expansion, both having much higher supersaturations of nitrogen relative to that in the nitrided coarse-grained sample [58].

The substantial reduction of the nitriding temperature by means of surface nanocrystallization is a marked advancement for materials processing. The reduced nitriding temperature may allow for the nitriding of materials families (such as alloys and steels) and workpieces that cannot be treated by conventional nitriding. In addition, this provides new alternative approaches to form functional surface structure by means of the nanostructure-selective reaction or diffusion.

Similarly, other surface chemical treatments controlled by diffusion of foreign atoms (such as chromium or aluminum) can be modified by means of surface nanocrystallization induced by SMAT. Chromizing behaviors of a SMAT low-carbon steel plate with a 20-μm thick nanostructured surface layer were investigated [59]. Experimental results showed that a much thicker Cr-diffusion layer

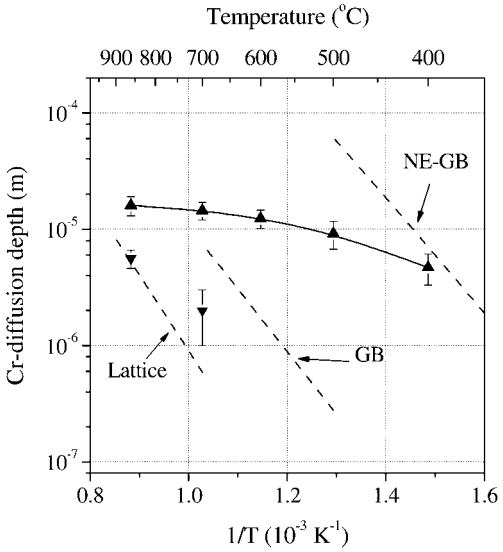

Fig. 29.12 Measured Cr-diffusion depth in the SMAT low-C steel sample (▲) and the coarse-grained low-C steel sample (▼) after chromizing at various temperatures, in comparison with the calculation results in terms of the lattice diffusion [24], and grain-boundary diffusions in the equilibrium state (GB) [25] and in the nonequilibrium state (NE-GB) [9], respectively.

was obtained in the SMAT sample than that in the coarse-grained one after the same chromizing treatment, especially at low temperatures, as shown in Fig. 29.12. The Cr-diffusion depth into the SMAT sample at 400 °C is about 5 μm, comparable to that into the coarse-grained sample at 860 °C. In the SMAT sample, the formation temperature of chromium compounds was found to be much lower and the amount of chromium carbides was higher than those in the coarse-grained counterpart. The enhanced chromizing kinetics originates from numerous grain boundaries with a high excess stored energy in the nanostructured surface layer due to severe plastic deformation during the SMAT.

29.4 Perspectives

The processing of nanostructured surface layer with a coarse-grained interior by means of SMAT techniques in metallic materials provides several unique opportunities for advancing both the basic understanding of nanostructured materials and their technological applications. It greatly facilitates the investigations on the strain-induced grain-refinement process in a rather wide grain-size scale from micrometer to nanometer. The studies on the structure–property relationship of solid, especially the grain-size dependence of various properties in me-

tals and alloys in the micro-nanometer regime will be enhanced as well. By means of the much-enhanced atomic diffusivity and chemical reactivity of the nanostructured surface layer, several conventional surface-modification techniques such as nitriding and chromizing of steels will be improved and their applications will be expanded. In addition, novel alternative approaches to functional surface structures by means of nanostructure-selective reaction will be feasible.

Enhancements in mechanical properties such as wear resistance, tensile strength and fatigue properties via SMAT are equally exciting, as demonstrated in multiple metals and alloys. In the engineering applications where wear, erosion and fatigue resistances are required simultaneously, SMAT is expected to provide its best values. This is the case because many current technologies, such as hard coatings, improve wear and erosion resistances at the expense of the fatigue resistance. In contrast, SMAT is expected to offer a unique solution to such problems because of the simultaneous improvement in wear, erosion and fatigue resistances.

Flexibility and low-cost SMAT procedures will greatly facilitate the widespread application of this technique to various industry areas. The process is also feasible to obtain a localized nanostructured surface layer in bulk materials and to realize surface nanocrystallization of components with complex shapes.

Other advantages of this technique include the fact that many existing processes can be used to obtain the nanostructured surface layer with a high productivity. Surface nanocrystallization of metallic materials will certainly provide a complementary process to the nanocrystallization process for bulk materials. With increasing investigations on the processing and properties of the nanostructured surface layer, industrial applications of this new technique to upgrade the traditional engineering materials and technologies in the near future can be anticipated.

Acknowledgments

The financial supports from the NSF of China, the Ministry of Science and Technology of China (Grant No. 2005CB623604) for K. Lu and from the U.S. National Science Foundation (Grant No. DMR-0207729) for L. Shaw are acknowledged. K. Lu would also like to thank J. Lu, G. Liu, N.R. Tao, H.W. Zhang, K. Wang, and W.P. Tong for their valuable contributions to the present work, while L. Shaw is indebted to his colleagues and students, P.K. Liaw, D.L. Klarstrom, K. Dai, Z. Stone, J. Tian, J.C. Villegas, and W. Yuan for their significant contributions to this work.

References

1 H. Gleiter **1989**, *Prog. Mater. Sci.* 33, 223–315.
2 C. Suryanarayana **1995**, *Int. Mater. Rev.* 40, 41–64.
3 K. Lu **1996**, *Mater. Sci. Eng. R* 16, 161–221.
4 W. P. Tong, N. R. Tao, Z. B. Wang, J. Lu, K. Lu **2003**, *Science* 299, 686–688.
5 Z. N. Farhat, Y. Ding, D. O. Northwood, A. T. Alpas **1996**, *Mater. Sci. Eng. A* 206, 302–313.
6 S. X. McFadden, R. S. Mishra, R. Z. Valiev, A. P. Zhilyaev, A. K. Mukherjee **1999**, *Nature* 398, 684–686.
7 L. Lu, M. L. Sui, K. Lu **2000**, *Science* 287, 1463–1466.
8 K. Lu, J. Lu **1999**, *J. Mater. Sci. Technol.* 15, 193–197.
9 R. Z. Valiev, R. K. Islamgaliev, I. V. Alexandrov **2000**, *Prog. Mater. Sci.* 45, 103–189.
10 N. R. Tao, M. L. Sui, J. Lu, K. Lu **1999**, *Nanostruct. Mater.* 11, 433–440.
11 G. Liu, J. Lu, K. Lu **2000**, *Mater. Sci. Eng. A* 286, 91–95.
12 G. Liu, S. C. Wang, X. F. Lou, J. Lu, K. Lu **2001**, *Scr. Mater.* 44, 1791–1795.
13 X. Wu, N. Tao, B. Xu, J. Lu, K. Lu **2002**, *Acta Mater.* 50, 2075–2084.
14 N. R. Tao, Z. B. Wang, W. P. Tong, M. L. Sui, J. Lu, K. Lu **2002**, *Acta Mater.* 50, 4603–4616.
15 K. Y. Zhu, A. Vassel, F. Brisset, K. Lu, J. Lu **2004**, *Acta Mater.* 52, 4101–4110.
16 X. Wu, N. Tao, Y. Hong, G. Liu, B. Xu, J. Lu, K. Lu **2005**, *Acta Mater.* 53, 681–691.
17 K. Dai, J. Villegas, L. Shaw **2005**, *Scr. Mater.* 52, 259–263.
18 N. Tao, X. Wu, M. Sui, J. Lu, K. Lu **2004**, *J. Mater. Res.* 19, 1623–1629.
19 X. P. Yong, G. Liu, K. Lu **2003**, *J. Mater. Sci. Technol.* 19, 1–4.
20 M. Umemoto, K. Todaka, K. Tsuchiya **2004**, *Mater. Sci. Eng. A* 375–377, 899–904.
21 Y. Todaka, M. Umemoto, Y. Watanabe, K. Tsuchiya **2004**. In *Designing, Processing and Properties of Advanced Engineering Materials:* Proceedings on the 3rd International Symposium on Designing, Processing and Properties of Advanced Engineering Materials. Jeju, Island, *Mater. Sci. Forum* 449–452, 1149–1152.
22 C.-H. Chen, R.-M. Ren, X.-J. Zhao, Y.-J. Zhang **2004**, *Trans. Nonferrous Met. Soc. China* 14, 215–218.
23 Y. Todaka, M. Umemoto, K. Tsuchiya **2004**, *Mater. Trans.* 45, 376–379.
24 G. Ma, Y. Luo, C.-H. Chen, R.-M. Ren, W. Wu, Z.-Q. Li, Y.-S. Zeng **2004**, *Trans. Nonferrous Met. Soc. China* 14, 204–209.
25 J. Villegas, L. Shaw, K. Dai, W. Yuan, J. Tian, P. Liaw, D. Klarstrom **2005**, *Philos. Mag. Lett.* 85, 427–438.
26 Y. Al-Obaid **1995**, *Mech. Mater.* 19, 251–260.
27 S. Meguid, G. Shagal, J. Stranart, J. Daly **1999**, *Finite Elem. Anal. Des.* 31, 179–191.
28 M. Guagliano **2001**, *J. Mater. Proc. Technol.* 110, 277–286.
29 R. M. Davies **1949**, *Proc. Royal Soc. London* 197A, 416–432.
30 H. Hertz **1896**, Misc. Papers, MacMillan, chap. Various, p. 146162.
31 M. C. Shaw, G. J. DeSalvo **1970**, *Trans. ASME, J. Eng. Ind,* 92, 480.
32 J. Villegas, K. Dai, L. Shaw, P. Liaw **2003**, in *Processing and Properties of Structural Nanomaterials,* L. Shaw, C. Suryanarayana, R. Mishra (eds.).
33 S. Wang, Y. Li, M. Yao, R. Wang **1998**, *J. Mater. Proc. Technol.* 73, 64–73.
34 M. Meo, R. Vignjevic **2003**, *Adv. Eng. Software* 34, 569–575.
35 K. Dai, J. Villegas, Z. Stone, L. Shaw **2004**, *Acta Mater.* 52, 5771–5782.
36 J. Villegas, K. Dai, L. Shaw **2003**, in *Processing and Fabrication of Advanced Materials XII,* Pittsburgh, PA, pp. 358–372.
37 K. Wang, unpublished work.
38 H. Zhang, Z. Hei, G. Liu, J. Lu, K. Lu **2003**, *Acta Mater.* 51, 1871–1881.
39 K. Lu, J. Lu **2004**, *Mater. Sci. Eng. A* 375–377, 38–45.
40 J. Villegas **2005**, *Investigation of the effects of the surface nanocrystallization and hardening (SNH) process on bulk metallic components,* PhD thesis, University of Connecticut.

41 M. Umemoto, Y. Todaka, K. Tsuchiya **2003**, in *Processing and Properties of Structural Nanomaterials*: Proceedings of Symposia held at Materials Science and Technology 2003 Meeting. L. Shaw, C. Suryanarayana, R. Mishra (eds.), Chicago, Il, pp. 125–132.

42 Q. Ma, D. R. Clarke **1995**, *J. Mater. Res.* 10, 853–863.

43 W. Nix, H. Gao **1998**, *J. Mech. Phys. Solids* 46, 411–425.

44 L. Shaw, P. Liaw **2005**, unpublished research.

45 X. Chen, J. Lu, L. Lu, K. Lu **2005**, *Scr. Mater.* 52, 1039–1044.

46 A. C. Batista, A. Dias, J. Lebrun, J. Le - Flour, G. Inglebert **2000**, *Fatigue Fract. Eng. Mater. Struct.* 23, 217–228.

47 D. Liu, J. He **2001**, *Acta Metall. Sin.* 37, 156.

48 L. Wagner **1999**, *Mater. Sci. Eng. A* 263, 210–216.

49 A. Drechsler, T. Dorr, L. Wagner **1998**, *Mater. Sci. Eng. A* 243, 217–220.

50 P. Song, C. Wen **1999**, *Eng. Fract. Mech.* 63, 295–304.

51 M. Guagliano, L. Vergani **2004**, *Eng. Fract. Mech.* 71, 501–512.

52 N. Tao, W. Tong, Z. Wang, W. Wang, M. Sui, J. Lu, K. Lu **2003**, *J. Mater. Sci. Tech.* 19, 563–566.

53 Z. Wang, N. Tao, S. Li, W. Wang, G. Liu, J. Lu, K. Lu **2003**, *Mater. Sci. Eng. A* 352, 144–149.

54 Y. S. Han, Z. Han, K. Wang, K. Lu **2006**, *Wear* 260, 942–948.

55 Z. Wang, N. Tao, W. Tong, J. Lu, K. Lu **2003**, *Acta Mater.* 51, 4319–4329.

56 J. Mongis, J. Peyre, C. Tournier **1984**, *Heat Treat. Met.* 3, 71–75.

57 W. Tong, N. Tao, Z. Wang, H. Zhang, J. Lu, K. Lu **2004**, *Scr. Mater.* 50, 647–650.

58 H. Zhang, L. Wang, Z. Hei, G. Liu, J. Lu, K. Lu **2003**, *Z. Metallkd.* 94, 1143–1147.

59 Z. Wang, J. Lu, K. Lu **2005**, *Acta Mater.* 53, 2081–2089.

30
Commercializing Bulk Nanostructured Metals and Alloys

Terry C. Lowe

30.1
The Innovation Process

The emergence of new technologies involves the interrelated processes of technological innovation and technology commercialization. These are distinct processes, the interleaving of which is important to the ultimate objective of introducing new products based upon new technologies. Though there is no single path that all innovation follows or that commercialization follows, one linear view of the innovation process and its connection to commercialization can be seen in Fig. 30.1.

The first step of innovation is sometimes discovery of new knowledge or of new capabilities. For the case of bulk nanostructured metals, there is not a clear single point of discovery. The virtues of ultrafine structure and grain refinement had been well known long before the notion of "nanostructure" developed [1–4]. Rather, the confluence of the availability of new instruments for characterizing nanoscale structure and the parallel emergence of multiple synthesis and processing technologies led to an awareness that ultrafine-grained materials with distinct desirable characteristics could be obtained solely by imposing large deformations. In essence, the second innovation step in Fig. 30.1, scientific exploration of the synthesis techniques and the resulting material properties is what has led to the emergence of bulk nanostructured materials as a distinct

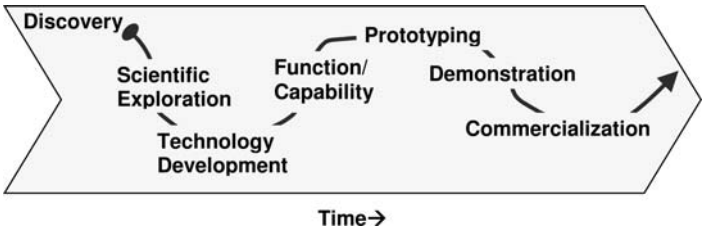

Fig. 30.1 Illustration of the steps in the process of innovation that precede commercialization.

Bulk Nanostructured Materials. Edited by M. J. Zehetbauer and Y. T. Zhu

ISBN: 978-3-527-31524-6

material class. Applied research on synthesis and processing methods increased the availability of homogeneous, high-quality material for scientific investigation. With this exploration came the third and fourth innovation steps, the awareness of special functionalities of these materials associated with their novel mechanical, physical, electronic, magnetic, and other properties. For example, the recognition that many ultrafine-grained alloys deform superplastically spawned special emphasis on alloy development to stabilize ultrafine grains against growth at elevated temperatures so that they retain their ability to sustain extraordinarily large strains. The unfolding of these earlier stages of innovation has been summarized in periodic overviews of the published body of knowledge of severe plastic-deformation processing by Lowe [5–7].

Once a technology is developed to the point of consistently exploiting one or more of its unique characteristics, then the prospect of creating prototype products emerges. This is the fifth step in Fig. 30.1. Whereas applications employing nanostructured materials have been envisioned for over 15 years, only most recently have these reached the prototype stage. Bulk nanostructured-metals prototypes that exploit the high intrinsic strength have appeared most prominently for specialty applications such as medical devices [8, 9]. Prototyping sometimes unveils the need for additional development of the underlying technology, and in some cases, even the need for additional scientific exploration. Successful prototyping is the basis for the sixth innovation step, product demonstrations. This stage is achieved only after the technological uncertainties and risks have been understood and mitigated to an extent to justify pilot-scale or even full-scale manufacturing evaluations. It is only at this point that the last step, commercialization, begins.

The steps in Fig. 30.1 portray innovation as a linear sequential process. This is rarely the case. Some steps may occur in parallel, in reverse order, or may be skipped entirely. Thus, innovation can follow a chaotic or seemingly random set of emergent pathways that defy the model portrayed in Fig. 30.1. The introduction of new materials is particularly prone to chaotic innovation, largely because of the complexity of the materials themselves. Only in the case of the simplest materials, such as pure metals, is the progression from scientific exploration to product demonstration relatively linear. For more complex materials like most bulk nanostructured materials the iterative interplay between scientific inquiry and subsequent phases of innovation may persist for many years. For example, in the earliest stages of investigating bulk nanostructured metals, hardness measurements were commonly used to contrast the mechanical properties with those of conventional metals. Microhardness was among the most widely measured properties, largely because the limited availability samples with sufficient geometric volume for other mechanical tests. Working with the limited insights into mechanical behavior provided by microhardness, researchers were able to evolve bulk nanostructured materials synthesis techniques to be able to produce materials with improved properties and with larger dimensions. This enabled a wider range of mechanical testing techniques to be employed, leading to further evolution of synthesis techniques and optimization of microstructures.

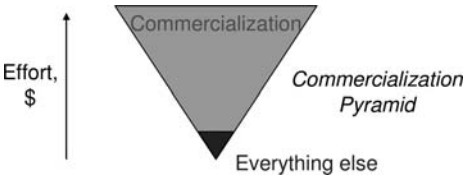

Fig. 30.2 Illustration of the relative magnitude of effort required in the early stages of innovation as compared to the later stages of commercialization.

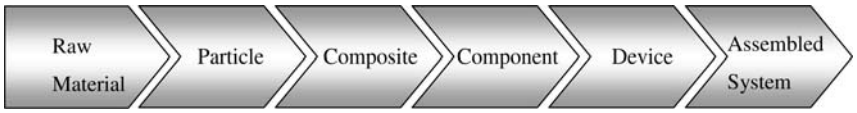

Fig. 30.3 The nanomaterials value chain.

The endpoint of the innovation process illustrated in Fig. 30.1 is the beginning of true commercialization. Figure 30.2 shows schematically the significant contrast between the level of effort involved in discovery and development of technology as compared to commercialization. In general, the costs of moving from discovery to commercialization increase at each stage of innovation. Figure 30.2 portrays the notion that the commercialization stage is typically an order of magnitude more costly than the sum of efforts involved in all preceding stages.

The activities contained under the heading commercialization include the elements that are prevalent in any technological business initiative: analyzing technical feasibility and market opportunities, establishing intellectual property protection, developing differentiated products, optimizing manufacturing processes, building distribution channels, and building an experienced sales team. One particularly important facet of commercializing bulk nanostructured materials is to consider where they fit in the product-value chain. Figure 30.3 illustrates the product-value chain for nanomaterials. At the beginning of the chain are the raw materials from which nanomaterials are made. The first addition of value in the chain is by creating particles, in particular nanoparticles. The term particle is a generic reference to the creation of desired nanoscale characteristics in raw materials. Thus, both nanosize powders, nanoscale films, ultrafine grains in metals are all examples of generic particles. Composites of nanoscale entities appear next in the value chain. Again, the use of the word composite is a reference to increasing value by combining nanoscale features into useful materials. Nanoscale composites engage the notion of engineered materials and materials design at the nanoscale. Next in the value chain are components. At this level one integrates nanomaterials, composite or otherwise, into larger scale subsystems that have specific functions. These subsystems then may be assembled function within devices. Devices may in turn function within assembled systems that incorporate multiple devices.

The multiple levels of hierarchy of systems within systems may seem excessively redundant. However, the distinctions between different levels of integration of nanomaterials becomes important when one attempts to understand the economic value and impact of bulk nanostructured metals. Consider the need to differentiate the economic value of nanomaterial foils used in microelectromechanical devices that are in turn used in electric motors. These motors may in turn be used in a variety of applications including household appliances, industrial machinery, and motor vehicles. The motor vehicle may also incorporate nanostructured metals separately in the suspension system and the structural frame. Each use occurs at a different level of integration. While one might associate the benefits of bulk nanomaterials used in an automobile with the large volume of material used in the frame, the greater value of nanomaterials may be found in their use in critical subsystems such as motors or actuators. The smaller the scale of integration of nanomaterials, the greater their potential to impact a diverse number of applications and markets.

The promise of superior value of bulk nanostructured metals raises the question about how this technology will enter the markets for metals and advanced materials. In the remainder of this chapter we will examine the prospects for commercializing bulk nanostructured metals technology, including some discussion of the impacts it may have on metals markets.

30.2
The Technology: Nanostructured Metals

The benefits of nanostructured metals have been the subject of multiple overviews and are illustrated throughout this book [6, 10–15]. Among the methods for nanostructuring metals, the only focus of this chapter is on those produced via severe plastic deformation (SPD) processing. SPD processing in particular has been applied to many commercially available metals and alloys [7]. From the perspective of commercialization it is most helpful to appreciate that the properties achieved by SPD processing result largely from the refinement of grain size during deformation. Whereas the mechanisms of grain refinement vary for different metals, virtually all metals undergo significant grain refinement and associated improvement in mechanical properties as the average grain size is reduced [16–21]. However, the degree of enhancement of properties varies for different metals.

It is also helpful to understand that SPD processing encompasses a family of processing methods that can impose extraordinarily large strains ($\varepsilon > 4$), for example high pressure torsion (HPT) [22–24], equal channel angular pressing (ECAP) [5], twist extrusion (TE) [25], accumulative roll bonding (ARB) [26–28]. Among SPD methods, ECAP remains the most extensively studied [5]. This is due largely to the fact that it was the earliest method to be systematically developed for the purpose of producing bulk nanostructured materials. Other methods such as HPT were derived from predecessor techniques such as diamond-

anvil apparatus that are appropriate for research-scale materials synthesis but not well suited for scale up to commercial production. Aluminum and its alloys are the most extensively studied family of metals.

Among the advantages of nanostructured metals, the enhancement of mechanical properties is the principal driver for their commercialization. Nanostructuring metals via SPD increases their tensile strength on the order of 25–150% over their conventional coarse-grain equivalents. Other properties such as hardness [29], fatigue strength [30, 31] also increase as grain size decreases. Corrosion resistance [32], electrical conductivity [33], and most physical properties are only mildly changed by nanostructuring. Overall, the suite of enhancements that bulk nanostructured-metals provide make them attractive for commercialization. However, enhanced properties alone are not sufficient to justify widespread commercialization without strong market drivers that capitalize on these properties.

30.3 Market drivers

Nanostructured metals possess characteristics that make them attractive in a diverse range of markets. Many product applications for which metallic materials are essential can benefit from the increment in mechanical and other properties that nanostructured-metals produced by SPD can provide. Some key markets are listed in Table 30.1. Distinct markets for nanomaterials are now being extensively researched, documented and frequently updated. Organizations such as the Freedonia Group (*www.Fredoniagroup.com*), SmallTimes (*www.smalltimes.com*), Business Communications Company (*www.bccresearch.com*), Mindbranch Inc. (*www.mindbranch.com*), Dedalus Consulting Inc. (*www.dedalusconsulting.com*),

Table 30.1 Markets for bulk nanostructured metals.

Aerospace structure
Archery products
Automobile components
Bicycle frames and component
Electrical contacts
Fishing equipment
Foils
Food and beverage packaging
Golf clubs
Heavy machinery and equipment
Medical devices
Petroleum exploration and recovery
Scuba-diving tanks and accessories
Sputtering targets
Wire

Lux Research Inc. (*www.luxresearchinc.com*), and others diligently analyzing markets for nanomaterials and providing frequently updated summaries. The market horizons are evolving rapidly as an increasing number of companies are recognizing the prospective benefits of nanomaterials in their products.

However, there are also distinct markets for which bulk nanostructured metals are not appropriate. The principal limitation of SPD-produced metals is that their strengthening is not necessarily stable at elevated temperatures. Thus applications and associated markets for high-temperature materials are not readily addressed. Similarly, applications where fusion welding or other very high temperature processing steps are involved in product manufacture are generally not viable. Furthermore, since large-volume production of nanostructured metals has yet to be implemented anywhere in the world, small-volume niche markets are the initial targets for commercialization efforts.

There are only a few markets that are being addressed at the time this volume is being published. One of these is the supply of ultrafine-grained copper and aluminum sputtering targets. These targets are used to produce thin films, particularly for electronic device applications. The driver for introducing bulk nanostructured metal targets is that SPD processing imparts finer grain sizes to the target material. The finer grain size allows sputtering of more uniform coatings. The market impact of this benefit is a result of using bulk nanostructured metals in material processing rather than being a direct result of their superior mechanical properties.

Specialty metals markets are attractive because drivers already exist that support the higher prices of specialty metals. These markets differ substantially from markets for more common metals such as steel and aluminum. Specialty metals possess particular combinations of engineering properties that justify the high cost of low-volume production. For example, titanium offers a combination of high strength, low density and corrosion resistance that makes it superior for many applications. Titanium is also highly biocompatible, making its use inside the human body for medical implants attractive. An emerging niche market sector is materials for medical devices. This market sector uses specialty metals such as titanium and its alloys, mainly in the form of mill products that are then machined or forged into final form. The market drivers for nanostructured titanium in medical devices vary depending upon the specific device type and market subsegment. However, in general, the global medical device market is highly competitive and highly innovative. Consequently, current and prospective manufacturers of medical implants compete for market share and create new markets based upon their ability to innovate. A significant enhancement of metal or alloy properties can be sufficient to provide a competitive edge in this market sector. Another driver in the medical device market is reduction of invasiveness of implants. Because nanostructured metals are stronger, it is possible to reduce their size in comparison to implants made from conventional metals.

The ultrafine grain sizes of bulk nanostructured metals offer additional benefits, for example in providing a more homogeneous and isotropic material. This

can be important in small-scale applications, for example, in microelectromechanical devices (MEMS) or miniscule structures such as the fine lattice structures of cardiovascular stents.

Once market drivers are established, it is important to consider an array of factors that can impede or augment commercialization. We will consider four of these, continuing to use the medical-implant markets as an example. The four factors we will consider are competition from other materials, appropriability, maturity of design paradigm, and distribution of complementary assets.

30.4 Competition from Other Materials

Commercialization of bulk nanostructured metals depends as much on the development and market position of competing materials as it does on characteristics of nanostructured materials themselves. It is important to recognize that other material technologies are evolving that can possibly eclipse the advantages of bulk nanostructured metals. For example, in the specialty-metals market novel alloys produced by new processing methods such as laser sintering of microalloyed powders, functionally graded alloys, and other advanced processing techniques appear promising. In the medical-metals market beta-phase titanium alloys, though heavier than workhorse alloys like Ti-6Al-4V, have strength that may in principle exceed the levels of nanostructured titanium. High-performance composite materials (e.g., reinforcing fibers in either a polymeric, metallic, or ceramic matrix) could be potential substitutes if fabrication costs can be reduced. Irrespective of progress that is being made developing bulk nanostructured metal technology, the parallel development of alternative materials is a constant threat.

30.4.1 Appropriability: Ability of Innovators to Capture Profit

For innovations in materials technology to be successful it is helpful if the innovators are able to profit from their inventions. This characteristic is formally described as appropriability, the regime of environmental factors, excluding company and market structure, that govern an innovator's ability to capture the profits generated by an innovation. The most important dimensions of such a regime are the nature of the technology and the virtues of the legal mechanisms to protect it [34].

Patenting is one means by which inventors increase appropriability. Research institutions and companies worldwide that have developed bulk nanostructured metals technology are protecting their intellectual property assets through patenting. A recent analysis of intellectual property related to bulk nanostructured-metals produced by severe plastic deformation found a total of 82 patents or other actions to protect intellectual property pertaining to SPD processing [5].

Another analysis of SPD intellectual property differentiated three categories of patents, those pertaining to: 1) processing methods, 2) processing apparatus, or 3) specific products [6]. This analysis showed that most SPD-related patents protect processing methods. Yet processing method patents are among the most difficult to enforce and are most readily "invented around." This liability is a result of the fact that it is nearly impossible to ascertain the methods by which materials were processed. Furthermore, SPD-technology development activities are truly global, including research and development in countries where the protection afforded by patents is weak. Most methods of nanostructuring bulk metals for which the early development has been globalized have the same challenge.

Trade secrets are a viable alternative to protecting innovations. However, prior publication in the open literature of bulk nanostructured metal innovations limits the value of this mechanism of protection. Since bulk nanostructured metals are the topic of extensive research, the open archival literature is replete with knowledge about methods of synthesis and the associated properties. There is an additional liability in that much research and development of bulk nanostructured metals involves collaborations that span multiple institutions, including industry–university partnerships. This makes trade secrets difficult to keep in-house. Furthermore, some large companies that would use nanostructured metals in their products engage multiple industrial manufacturing partners with facilities throughout the world. This exacerbates the challenge of maintaining trade secrets. A single tour of a manufacturing facility given to a visitor may be enough to compromise a secret of the trade.

From the perspective of legal protection, bulk nanostructured metals technology clearly falls into a weak appropriability regime. The preponderance of process patents and extensive international collaborations make the technology relatively difficult to protect. The process patents that already exist may readily make the technology of synthesis/fabrication apparent to those skilled in the art. Imitators could potentially invent around and add extensions at modest cost. Furthermore, small companies that tend to be stronger innovators do not often have the resources to participate in a patent dispute. Enforcement of a patent might require a court injunction to inspect the imitator's manufacturing facility. This would be especially difficult in view of the globally distributed development of bulk nanostructured-metals technology.

SPD methods for producing bulk nanostructured metals exist in a particularly weak appropriability regime. First, most of the existing patented SPD technology is associated with modifications to conventional metal-forming methods. For example, equal channel angular pressing is a variant of forging, twist extrusion is a variant of extrusion. Accumulative roll bonding is a variant of rolling. These variations require little in terms of specialized manufacturing assets. Conventional presses, extrusion apparatus, and rolling mills that are found in a standard mill-type environment do not require significant capitalization cost or unusual equipment modifications. Therefore, potential imitators do not have to invest heavily to have the hardware capacity to compete.

Next, the design of SPD technology may not be complex enough to prevent an engineer from understanding the overall process. With over 2500 publications on SPD in the open literature since 1990 there are a substantial number of researchers and engineers who have experience with the technology [5]. Furthermore, should even a single engineer or technician leave a company seeking to implement the technology, there could be a diffusion of the tacit knowledge associated with processing details into competing enterprises. Noncompete employment contracts only offer some marginal intellectual property protection of processing technology. They are particularly difficult to enforce across international borders.

Given the weak appropriability regime for SPD processing and the dominance of this method for nanostructuring bulk materials, there is a clear need to look to other factors to support the early commercialization of the technology.

30.5
Maturity of the Bulk Nanostructuring Metals Process Design Paradigm

Technology evolution is widely recognized to occur in at least two stages, a preparadigmatic and a paradigmatic phase [34]. In the preparadigmatic stage the body of knowledge is immature. There is not general agreement on the concepts and the body of theory upon which the technology is based. Standards of scientific understanding and engineering practice are not yet developed. In the paradigmatic phase a general understanding is established and standards emerge. From the viewpoint of commercialization, competition between companies during the preparadigmatic stage amount to contests amongst designs. For bulk nanostructured metals, these contests are between alternative processing methods. A dominant bulk nanostructured-metals process design that has differentiated itself as being advantageous or setting an industry standard doesn't yet exist. Whereas SPD is among the most widely studied processing methods, powder compaction, multilayer deposition, electrochemical forming, and microalloying are emerging as rival methods to economically manufacture bulk nanostructured metals. The foundations for all bulk nanometals synthesis are still evolving, as evidenced by the range of topics and debate at international conferences. It will remain unclear as to when a dominant nanostructured metal synthesis process may emerge until the economics of production are more fully understood.

Most recently there have been explicit efforts to contrast alternative SPD-processing methods, for example by Cherikuri et al. [28] or by Dutkiewicz et al. [35]. The work by Dutkiewicz et al. compares microstructures, microhardness, and basic tensile properties of titanium processed by ECAP, HPT, and hydrostatic extrusion. Consistent with the observations of others, they found that HPT creates the greatest grain-size refinement. However, because the levels of deformation imposed for each method were not the same, meaningful comparisons of mechanical properties could not be made. Additional work of this type,

but with attention to factors that influence manufacturability, uniformity of product, and the economics of production is needed before a dominant SPD process can become clear. In addition, though prototype facilities exist in research institutions, issues of scale and operation in an industrial environment remain to be addressed.

30.6 The Need for Complementary Assets

Once a dominant bulk nanostructured-metals processing technology emerges, is refined, and proven for widespread use, capitalizing on these innovations demands establishing a host of complementary assets to successfully commercialize the advancements. For SPD technology the principal complementary assets that are necessary to ensure the success of the innovations are manufacturing capability, robust distribution channels, sales and customer-service presence, and to a lesser extent a marketing organization.

Given the weak appropriability of the bulk nanostructured-metals technology, manufacturing capability will be among the most important for successful commercialization. Once a single bulk nanostructured-metals fabrication technology receives some publicity, it is almost certain that the current players in the metals markets will put tremendous effort towards duplicating the innovations of initial intellectual property generators and other early entrants into the field. They will also accelerate the development of alternative technologies that can be more quickly deployed on the largest possible scale. In essence, the success of just one early company in developing nanostructured metals will serve as a proof of capability to the metals industry. Once this occurs, there will be a race for the first firm to produce nanostructured materials in significant quantity to meet market demand. Unless significant effort is expended to develop the capabilities to meet this market demand, early innovators will find themselves in the precarious position of having superior technical capability but lacking the capability to address the market. Furthermore, early corporate innovators will find that their firm's technical advantage will be slowly whittled away as other firms increase their investment researching the production of nanostructured metals. It may be the access or control of complementary assets that is the most significant factor in determining who profits from bulk nanostructured metals innovations.

In view of the importance of complementary assets, there are three likely paths for commercialization of bulk nanostructured metals: 1) a large existing metal supplier develops and markets the technology into its existing markets and distribution channels, 2) a small new entrant acquires complementary assets, or 3) an end-product manufacturer introduces bulk nanostructured metals into a niche market.

The first path engages large metals industry producers. To date it appears that this path is not unfolding. There is little evidence of metals industry contribu-

tion to the technical literature or patent literature. This is to be expected since a dominant production paradigm has yet to unfold. Furthermore, since bulk nanostructured metal products would compete with existing products, the incentive is not yet large enough for the metals industry to invest in bulk nanostructured metals technology. In fact, there is greater incentive for existing metals suppliers to evolve the properties of existing products through enhanced process controls and optimization of existing alloy chemistries.

The second path involves one or more new entrants to the metals business, but only by acquiring complementary assets, potentially through strategic alliances. Several options exist to obtain complementary assets. Chief among these options is to build assets and capabilities internally. However, this requires significant financial resources and is likely the slowest option. Other options for new entrants include developing a contractual relationship with established firms to strengthen their market position. However, given the weak appropriabiltity of any entrant's technical capabilities, contractual relationships such as this are unlikely to provide a long-term path to success. The development of contractual relationships could also result in the uncontrolled diffusion of the firm's processes to the firm's partners and likely competitors.

A third option to building the portfolio of complementary assets to meet the firm's needs is to purchase an ownership position in firms that have already developed the necessary complementary assets. The success of this option relies heavily on the entrant's ability to gather enough capital to make such a strategic investment. The differential advantage of bulk nanostructured metals over competing technologies needs to be large and sustainable for a significant period of time to attract investment funds. For the venture capital markets that thrive largely in the US, and to a lesser extent in Europe, double to ten-fold product superiority for more than two years would be needed to justify multimillion-dollar capital investment.

The final option for building the necessary complementary assets would be for the entrant to be acquired by a firm that has demonstrated successful utilization of the aforementioned assets. Such an acquisition with the right firm would place the entrant in the position to gain significant market share by combining its intellectual property with access to the complementary assets of a parent company. More importantly, however, such an arrangement would better position the firm to defend itself against other competitors once the diffusion of knowledge occurs in the industry.

30.7
Impact on the Metals Industry

The significant players in the metals industry will respond to the developments that are emerging in bulk nanostructured metals technology when the processing methods become economically viable and that sufficient market demand is apparent. Since the first products are likely to appear in high-cost applications

within small-volume specialty-metal markets, the economics of production will become known in these areas first. Cost models for capitalization, capacity development, and product diversification will evolve based on these early experiences. Suppliers of more common metals, such as steel and aluminum are more likely to adopt the technology as the cost-benefit tradeoffs for large-scale production are better known.

There will be collateral benefits for the metals industry overall as nanoscale materials characterization tools that are essential for nanomaterials development emerge. These same tools serve to improve the characterization of conventional metals and alloys, further enabling their development and optimization. For example, the current strong research interest in ultrafine-grain metals certainly benefits the long-standing market for superplastically deformable alloys. Superplasticity depends on producing and maintaining fine grain sizes during their shaping and forming. Thus, the tools for examining the behavior of bulk nanostructured metals directly benefit the study and optimization of superplastic alloys. Furthermore, since superplastic forming offers the prospect of reducing manufacturing cost for some applications, interest in superplastically formable aluminum, magnesium, and titanium could lead to entry of bulk nanostructured metals into large-scale production.

Assuming that the economics for large-scale bulk nanostructured-metals processing become favorable, one can anticipate that the overall range of applications for which metals are selected over nonmetals could expand. Bulk nanostructured metals technology could expand the frontiers in which the metals industry competes successfully with nonmetals. Needless to say, this will trigger a competitive response from developers and suppliers of competing materials.

Even if the impact of bulk nanostructured metals is not broad, it is still probable that metal suppliers will eventually adopt bulk nanostructured metal products as a complementary higher-cost, higher-margin addition to their product lines.

30.8 Conclusions

The commercialization of bulk nanostructured metals technology is at an early stage. One can expect ongoing enhancement of bulk nanostructured-metals processing to achieve higher levels of strength, greater cost-effectiveness, and larger production volumes. Competition between alternative processing technologies and companies is inevitable and will eventually drive dramatic improvements in processed material performance as firms seek to establish a dominant design. Once key choices are made and a dominant design starts to appear progress will likely accelerate rapidly. As the technology matures and gains in performance become less, industry competitors may start to consolidate. Later, as the physical limits of the technology are approached, additional progress becomes much more expensive.

Early entrants into bulk nanostructured-metals processing may face these phases of competition and consolidation as they further develop bulk nanostructured-metals technology. The timeframe for this to occur is not yet clear.

As the metals industry becomes more aware of what bulk nanostructured-metals processing offers, assuming that the technology is developed to a level where reliable production is possible, it may view this as a technological discontinuity and, more specifically, a major product improvement. Such an improvement falls in a category of product competition known as competency enhancing. "Competency-enhancing discontinuities are order-of-magnitude improvements in price/performance that build on existing know-how within a product class. Such innovations substitute for older technologies, yet do not render obsolete skills required to master the older technologies" [36]. Generally, competency-enhancing discontinuities are initiated and exploited by existing firms and not by new, start-up firms. Thus, commercialization by larger firms with existing complementary assets may be a more probable avenue for bulk nanostructured metals technology to enter the markets for advanced materials if the improvements over competing technologies are great enough.

References

1 W. Reif **1998**, *Metall.* 52, 120.
2 N. Tsuji **2002**, *Tetsu-To-Hagane/J. Iron Steel Institute Jpn.* 88, 359.
3 R. Z. Valiev, R. K. Islamgaliev, N. F. Yunusova **2001**, *Mater. Sci. Forum* 357/359, 449.
4 P. D. Hodgson, H. Beladi, M. R. Barnett **2005**, *Mater. Sci. Forum* 500/501, 39.
5 T. C. Lowe **2006**, *Mater. Sci. Forum*, 503-504, 355.
6 T. C. Lowe, Y. T. Zhu **2003**, *Adv. Eng. Mater.* 5, 373.
7 T. C. Lowe, Y. T. Zhu, S. L. Semiatin, et al. **2000**, *Nato Science Series, Partnership Sub-Series 3:HighHTechnology* 80, 347.
8 V. V. Stolyarov, V. V. Latysh, R. Z. Valiev, et al. **2000**, *Nato Science Series, Partnership Sub-Series 3:HighHTechnology* 80, 367.
9 V. M. Segal **2004**, *Mater. Sci. Eng. A* 386, 269.
10 T. L. Brown, S. Swaminathan, S. Chandrasekar, et al. **2002**, *J. Mater. Res.* 17, 2484.
11 R. Valiev **2004**, *Nature Mater.* 3, 511.
12 K. Lu **2005**, *Mater. Sci. Forum* 475-479, 21.
13 Y. T. Zhu, J. Huang **2002**, in *Ultrafine-grained materials II. Proceedings of a Symposium*. 2002 TMS Annual Meeting, 17–21 Feb. 2002, Seattle, WA, USA, (eds.) Y. T. Zhu, T. G. Langdon, R. S. Mishra, S. L. Semiatin, M. J. Sharan, T. C. Lowe, TMS-Minerals Metals & Materials Society, Warrendale, PA, USA, p. 331.
14 E. Ma **2004**, *Met. Mater. Int.* 10, 527.
15 T. Lowe **2002**, *Adv. Mater. Process.* 160, 63.
16 O. A. Kaibyshev **2001**, *J. Mater. Process. Technol.* 117, 300.
17 Y. T. T. Zhu, T. C. Lowe **2000**, *Mater. Sci. Eng. A* 291, 46.
18 R. Kaibyshev, I. Mazurina **2004**, *Mater. Sci. Forum* 467/470, 1251.
19 A. L. M. Costa, A. C. C. Reis, L. Kestens, et al. **2005**, *Mater. Sci. Eng. A* 406, 279.
20 E. F. Rauch, L. Dupuy, J. J. Blandin **2002**, *Key Eng. Mater.* 230/232, 239.
21 T. C. Lowe, R. Z. Valiev **2004**, *Jom* 56, 64.
22 X. Z. Liao, Y. H. Zhao, Y. T. Zhu, et al. **2004**, *J. Appl. Phys.* 96, 636.
23 H. S. Kim **2001**, *J. Mater. Process. Technol.* 113, 617.

24 A. P. Zhilyaev, G. V. Nurislamova, B. K. Kim, et al. **2003**, *Acta Mater.* 51, 753.

25 D. V. Orlov, V. V. Stolyarov, H. S. Salimgareyev, et al. **2004**, *Ultrafine-grained materials III*, T. Z. Yuntian, T. G. Langdon, R. Z. Valiev, S. L. Semiatin, D. H. Shin, T. C. Lowe (eds.) The Mineralis, Metals & Materials Society, Warrendale, PA, 457.

26 G. Krallics, J. G. Lenard **2004**, *J. Mater. Process. Technol.* 152, 154.

27 S. H. Lee, T. Sakai, D. H. Shin **2003**, *Mater. Trans.* 44, 1382.

28 B. Cherukuri, T. S. Nedkova, R. Srinivasan **2005**, *Mater. Sci. Eng. A* 410-411, 394.

29 M. Furukawa, Z. Horita, M. Nemoto, et al. **1996**, *Acta Mater.* 44, 4619.

30 A. Vinogradov, S. Hashimoto **2003**, *Adv. Eng. Mater.* 5, 351.

31 H. Mughrabi, H. W. Hoppel, M. Kautz **2004**, *Scr. Mater.* 51, 807.

32 A. Vinogradov, H. Miyamoto, T. Mimaki, et al. **2002**, *Annal. Chimie Sci. Mater.* 27, 65.

33 A. Vinogradov, Y. Suzuki, T. Ishida, et al. **2004**, *Mater. Trans.* 45, 2187.

34 D. J. Teece **1986**, *Res. Policy* 186.

35 J. Dutkiewicz, J. Kusnierz, W. Maziarz, et al. **2005**, *phys. stat. sol.* (a) 202, 2309.

36 M. L. Tushman, P. Anderson **1986**, *Admin. Sci. Quart.* 439.

Subject Index

Bulk Nanostructured Materials. Edited by M. J. Zehetbauer and Y. T. Zhu

ISBN: 978-3-527-31524-6

f